Hydroelasticity 2026

HYDROELASTICITY IN MARINE TECHNOLOGY

Proceedings of the 10th International Conference on

HYDROELASTICITY IN MARINE TECHNOLOGY

Trondheim, Norway, June 16-18, 2026



Edited by

Trygve Kristiansen
Marilena Greco
David Kristiansen

Department of Marine Technology, NTNU



ISBN: 978-82-691120-6-1 (Hardcover)
June 2026

Editors:
Trygve Kristiansen, Marilena Greco and David Kristiansen

Publisher:
Department of Marine Technology,
Norwegian University of Science and Technology, NTNU

PREFACE

This volume contains the papers presented at the Hydroelasticity in Marine Technology conference held in Trondheim, June 16 – 18, 2026 – the tenth in a series convened approximately every three years since 1994. The contributions confirm that hydroelasticity remains a key topic across a broad and expanding range of applications, both traditional and emerging. These include ship whipping and springing, hydrofoils, offshore wind, floating solar, wave energy devices, bio-inspired propulsion, and seaweed systems. Over the roughly five decades since hydroelasticity emerged as a field in the 1970s, the number of relevant applications has steadily increased. The papers highlight its growing dual role: not only as a source of critical loads and responses that must be managed, but also as an enabling mechanism for innovative and energy-efficient designs. Despite substantial progress, many fundamental challenges remain unresolved. These include fluid-structure interaction under extreme loading (e.g., slamming and sloshing), ice-body-water interactions, membrane-wave interactions, hydro-plasticity, and higher-order wave loads. While new tools such as data-driven methods are advancing the field and CFD is more widely used, physical experiments and potential flow theory continue to play a vital role. This emphasizes the continued relevance and need of this conference also in the years to come.

INTERNATIONAL SCIENTIFIC COMMITTEE

Name	Affiliation	Nation
R. Cengiz Ertekin	University of Hawaii at Manoa	USA
Masashi Kashiwagi	Osaka University	Japan
Yonghwan Kim	Seoul National University	Korea
Alexander Korobkin	University of East Anglia	UK
Pandeli Temarel	University of Southampton	UK
Sime Malenica	Bureau Veritas	France
Daniele Dessi	CNR-INM	Italy
Kevin Maki	University of Michigan	USA
Jun Ding	CSSRC	China
Trygve Kristiansen	NTNU	Norway

LOCAL ORGANIZING COMMITTEE

Trygve Kristiansen	NTNU	Norway
Marilena Greco	NTNU	Norway
David Kristiansen	NTNU	Norway

PREVIOUS CONFERENCES

1	Trondheim, Norway	1994
2	Fukuoka, Japan	1998
3	Oxford, UK	2003
4	Wuxi, China	2006
5	Southampton, UK	2009
6	Tokyo, Japan	2012
7	Split, Croatia	2015
8	Seoul, Korea	2018
9	Rome, Italy	2022
10	Trondheim, Norway	2026

TABLE OF CONTENTS

Keynote lecture - Hydroelasticity of Marine Structures, Odd M. Faltinsen 3

1. Aquaculture Structures

A Study on the Hydroelastic Responses and Induced Loads of Aquaculture Lice-Skirts Exposed to Current. 17
Kristiansen, D., Fredriksen, A.G. and Kristiansen, T.

Computational Performance of Finite Elements Used in Hydroelastic Analysis of Aquaculture Nets. 27
Palaversa, M., Yu, Z. and Sævik, S.

Hydroelastic Behaviour of a Floating Hexagonal Net Cage under Regular Waves. 39
Mohapatra, S.C., Ji, J. and Guedes Soares, C.

2. Bio-inspired Concepts

Analytical Solutions of Two-Way Coupled Wave-Flexible Seagrass Interaction. 53
Wei, Z., Boyer, R. and Shao, Y.

Bending Modes and Fluid–Structure Interaction in Fish-Inspired Swimmers: Implications for Flexible Underwater Robot Design. 63
Norvik, C., Greco, M. and Lugni, C.

Experimental Characterization of Hydroelastic Dynamics in Biomimetic Caudal Fins. 73
Constantino Muniz, G., Paifelman, E., Aloisio, G., Sellini, M. and Ciappi, E.

3. Floating Bridges

Floating bridge global responses with wave-current-structure interaction. 85
Xiang, X. and Faltinsen, O.M.

Fully Coupled Hydroelastic Analysis of Curved Floating Bridges via DMB Method. 97
Song, J. and Kim, S.

4. Floating Structures and VLFS

Hydroelastic response of an articulated VLFS: Experimental, potential flow and CFD insights. 109
Arredondo-Galeana, A., Brown, S., Ogden, D., Greaves, D. and Brennan, F.

Numerical Analysis of a Barge's Torsional Hydroelastic Response. 119
Pascoaleto, V., Lopes, F.S. and Fernandes, A.C.

The Design, Production, and Verification of a Scaled Flexible Model of a Floating Truss Structure for Hydroelastic Experiments. 131
de Koning, J., Ruesen, J., Hoogendoorn, D. and Grammatikopoulos, A.

5. Floating Wind

Experimental Study of a Scaled Flexible Riser for Hydrogen Transport from a Floating Wind Turbine Platform to the Seabed. 145
Guichard, J., Hann, M., Tosdevin, T. and Greaves, D.

On Wave Load Mapping for Substructure Strength Assessment of FOWTs. 157
Zhiyuan, P., Wenzhe, Z., Alexandre, A., Won-Ho, L. and Caiwei, S.

Simulation of a SPAR-type deformable floater for offshore wind turbines: comparison with experimental and numerical data. 167
Halbout, C., Robaux, F., Ouvrard, T. and Peyrard, C.

Sum-frequency second-order wave loads and elastic response of the INO OptiFLEX 22 MW floating wind turbine. 177
Rajasree, V.R.N., Rogne, Ø.Y., Abdelmoteleb, S.E., Bachynski-Polić, E.E. and Sauder, T.

Wavelength and Wave-Steepness Effects on the Hydroelastic Response of Flexible Slender Offshore Components. 189
Zhang, Q., el Moctar, O., Qaimi, S., Galal, G., Brehm, A., Neugebauer, J. and Jiang, C.

6. Hydrofoils

A BEM-FEM model for the hydro-elastic analysis of passively controlled flexible foil-thrusters for ships and underwater vehicles. 201
Anevlavi, D. and Belibassakis, K.

Hydroelastic Consequences of Passive Vortex-Generator Control in Cavitating Flexible Hydrofoils. 211
Lin, Y., el Moctar, O. and Jiang, C.

7. Hydroelastic Problems and Methods

Data-driven prediction of design global bending loads in ships from model tests. 221
Drummen, I., Kaydihan, L., Düz, B. and Kurnia, R.

Generalized modal approach for marine and offshore engineering: key aspects and applications. 233
Jagite, G. and Malenica, S.

Hydroelastic Problems in Marine Seismic Acquisition. 245
Tønnessen, R. and Oscarsson-Nagel, M.D.

Inverse Wave Force Estimation Using Frequency- and Time-Domain Hydroelastic Models. 257
Van Zijl, C., Jovanova, J. and Grammatikopoulos, A.

New hydro-structure interface model based on Super Green functions accounting for forward-speed effects. 267
Chen, X., De Lauzon, J., Nguyen, M., Cao, K., Jagite, G. and Malenica, S.

Recent Developments in Modelling Flow-Induced Motions of Floating Offshore Wind Turbines During Wet-Tow. 279
Yin, D., Fonseca, N., and Jiang, F., Firoozkoohi, R., Indergård, R., Braaten, H. and Lie, H.

8. Ice-Body-Water Interactions

Analysis of Vertical Mode Expansions for Hydroelastic Waves in Viscoelastic Floating Ice Plates. 293
Shishmarev, K., Ni, B.-Y., Khabakhpasheva, T. and Korobkin, A.

Ice Sheet Response to a High-Speed Vessel Moving in Open Water along the Ice Edge. 305
Korobkin, A. and Khabakhpasheva, T.

Nonlinear Interaction Between an Ice Cover of Variable Thickness and a Bottom Obstruction in Channel Flow. 315
Liang, C., Ni, B.Y., Khabakhpasheva, T.I. and Semenov, Y.A.

Wave Scattering by a Submerged Porous Circular disc with Radially Varying Porosity below an Ice-Covered Surface. 325
Gayen, R. and Hoque, A.

9. Marine Membrane Structures

Assessing large hydroelastic parameter spaces through a table-top Faraday experiment. 339
Pot, H., Christiaens, B., Wellens, P., and Schreier S. and Westerweel J.

Effect of damping of floating flexible membrane exposed to water waves. 349
Maugsten, O. P. and Grue, J.

Non-linear hydro-elastic analysis of a vertical pre-tensioned membrane in waves. 359
Moreau, M. and Kristiansen, T.

Surge Motion and Hydroelastic Response of a Membrane-Based Floating Solar Island: An Uncertainty Study. 371
Skare, A. and Kristiansen, T.

10. Ship Loads and Responses

Comparative experimental investigation on springing responses of a 14,000 TEU containership. 383
Ye, Y., Fu, S., Jiang, J., Chen, X. and Huang, W.

Experimental Study on Influence of Bow Flare Shape above Waterline on Whipping Response of 14,000 TEU Container Ship. 393
Suzuki, K., Takeda, K., Sugimoto, K., Harada, M., Oka, M. and Matsui, S.

Variable-Stiffness Ship Elastic Models for Hydroelastic Digital Twinning. 403
Dessi, D., Passacantilli, F., Venturi, A., Delgado, D., van Dijke, R., Terroba Ramirez, F., Sbaruffati, C., Bardiani, J., Sandström, J. and Haridas, A.

11. Slamming Problems

Decomposition of Structural Response to Slamming Loads Based on Rigid Body Motions. 415
Ying-xu, M., Sun, Z., Korobkin, A. and Khabakhpasheva, T.

From hydroelasticity to hydro-elastoplasticity and hydroplasticity of structural responses subjected to extreme water impacts. 425
Yu, Z. and Fimreite, S.B.

Hydroelastic impacts with aerated water. 435
Wellens, P.R. and Bockstael, M.M.

Hydroelastic simulation for water entry slamming of a flat plate based on two-way CFD-FEM method. 445
Wang, Z., Wang, J., Xiao, J. and Wan, D.

Hydroelastoplasticity Effects on Water Impact Loads. 457
Tödter, S., Linde, J., Neugebauer, J. and el Moctar, O.

Investigation of the Dynamic Response of Elastic Circular Cylinders Subjected to Water Impact. 467
Taussé Kamdoum, F.L., Hascoët, R., El Malki Alaoui, A. and Jacques, N.

Mitigation of Hydroelastic Perturbations on Force Measurements During Water Impact Experiments with Pseudo-Rigid Impactors: Solutions and Challenges. 477
Tassin, A. and Jacques, N.

Physical and Numerical Experiment with Extreme Hydroelastic Wave Impacts at Scale. 487
Bockstael, M.M. and Wellens, P.R.

12. Sloshing

Effect of Liquid Materials on Sloshing Flows and Hydrodynamic Impact on a Rectangular Tank. 499
Park, G., Hwang, J., Park, T. and Kim, Y.

Experimental and Numerical Studies on Sloshing Flows in a Rectangular Tank with a Hyper-elastic Baffle. 509
Park, T., Park, C., Kim, Y. and Lee, J.

Numerical Study of Hydroelastic Response due to Slosh-Induced Impact. 519
Yang, K.-K., Kim, D.-H. and Kang, D.-Y.

13. Wave-Energy Concepts

Enhancing Floating Breakwater and Wave Energy Converter Performance Using Local Resonators. 529
Agarwal, S., Liang, C., Faragau, A. and Colomés, O.

Hydroelastic Response and Power Extraction in Wave-Energy-Integrated Aquaculture Systems. 541
Mi, S., Cheng, H., Avital, E.J., Chatjigeorgiou, I.K., Konispoliatis, D.N., Papadakis, G. and Samad, A.

Preliminary investigation into fully coupled solvers for flexible wave energy converters. 553
Capasso, S., Moretti, G., Rizzello, G., Flaßkamp, K., Martínez-Estévez, I., Altomare, C, Crespo, A. and Suzuki, T.

Wave energy conversion by a 3-raft piezoelectric system. 563
Dessi, D.

14. Wave-Plate Interaction

Comparative study of energy dissipation under capillary-gravity wave scattering by submerged porous, poroelastic, and porous piezoelectric plates. 575
Singh, M.

Flexural Gravity Wave Blocking in a Floating-Submerged Plate System Involving Compressive Force. 585
Boral, S., Sahoo, T. and Basu, B.

Keynote Lecture

10th International Conference on HYDROELASTICITY IN MARINE TECHNOLOGY
Trondheim, Norway, June 16th-18th, 2026

Hydroelasticity of Marine Structures

Faltinsen, O.M.

Norwegian University of Science and Technology,
Trondheim, Norway
(odd.faltinsen@ntnu.no)

Abstract. Applications are for ships, wind energy, solar islands, aquaculture and ultralong floating bridges. Both net cages and closed cages as well as operational conditions for well boats at net cages are discussed. Snap loads and sloshing are factors for net cages and closed cages, respectively. The influence of fish is examined. Slamming on ships and other marine structures causes local and global hydroelastic effects. Detailed hydrodynamics can be complicated involving, e.g., nonlinear free-surface effects, gas cushions, cavitation, acoustics and thermodynamics. What matters for hydroelastic response is the time duration of the loading relative to important structural natural periods. Considering this fact enables one to simplify the hydrodynamic problem. Slamming associated with sloshing in prismatic LNG tanks is challenging involving plunging breaking waves and flip-through in shallow-liquid conditions. Higher-order wave effects and hydroelasticity can matter in consideration of "springing" and "ringing". A case with a vertical free-surface piercing cylinder standing on the sea floor is experimentally and theoretically discussed. The current can by changing the wavelength significantly influence the wave loads on stationary marine structures and thereby the global hydroelastic behavior. The current can also block the waves in opposite wave heading and current directions. The current influences also the depth decay of the second-order sum-frequency pressure, which is a factor, e.g., for vertical resonant vibrations of a tension leg platform. It is pointed out that a realistic wind-induced current has a logarithmic profile relative to the free surface which causes challenges in model tests and by applying potential flow theory.

1. Introduction

Hydroelastic applications in mind are, e.g. for ships, wind energy, solar islands, aquaculture and ultralong floating bridges. Global challenges in the future are related to the climate, pollution and the need for food and energy.

The current can by changing the wavelength significantly influence the wave loads on stationary marine structures and thereby the global hydroelastic behavior. The current can also block the waves in opposite wave heading and current directions. The current influences the depth decay of the second-order sum-frequency pressure, which is a factor, e.g., for vertical resonant vibrations of a tension leg platform. Higher-order wave effects with current interaction and hydroelasticity can matter in consideration of "springing" and "ringing" of stationary marine structures. A realistic wind-induced current has a logarithmic profile relative to the free surface which causes challenges in model tests and by applying potential flow theory. Internal waves act as a current and can have a significant effect for structures in the South China Sea.

Hydroelasticity matters in aquaculture both for net cages and closed cages as well as operational conditions for well boats at net cages. Snap loads can occur in the netting and in flexible closed cages. Sloshing is a factor for closed cages, that can lead to strong free-surface nonlinearities that can be coupled with hydroelastic behavior. The influence of fish is an unknown factor for the behavior of aquaculture structures.

Slamming on ships and other marine structures causes local and global hydroelastic effects. Detailed hydrodynamics can be complicated involving, e.g., nonlinear free-surface effects, gas cushions,

cavitation, acoustics and thermodynamics. What matters for hydroelastic response is the time duration of the loading relative to important structural natural periods. Considering this fact enables one to simplify the hydrodynamic problem. Slamming associated with sloshing in prismatic LNG tanks is challenging involving plunging breaking waves and flip-through in shallow-liquid conditions.
We start by discussing wave-current-body interaction. Then continue with aquaculture and finally we discuss slamming.

2. Wave-current interaction and stationary structures

Vortex-Induced Vibrations (VIV) of risers and pipelines in current are of concern. VIV is a nonlinear resonant response due to vortex shedding. If we consider an ambient steady velocity U_c and a circular cylinder of diameter D with resonance period T_n, large and limited transverse response occurs for reduced velocity $U_c T_n/D$ between approximately 5 and 10. In-line VIV with lower amplitudes happens for lower reduced velocities. VIV was of concern in designing submerged floating tunnel crossing deep and broad fjords of Norway. Since transverse VIV can result in oscillation amplitudes of the order of the tunnel diameter, it must be avoided. It was possible to avoid transverse VIV but in-line VIV having much lower amplitude than transverse VIV could not be avoided. The hydrodynamic interaction between two nearby parallel tunnels was of concern. Hydrodynamic interaction is also a factor for riser bundles.
The wind, tidal flow, stratification, major ocean circulations and the topography such as islands, straits, fjords and the sea bottom influence the current. The wind speed, the wind-induced waves and the wind-induced current profile are connected. This fact is neither accounted for in a model basin with a wave maker nor in common state-of-the art potential-flow wave load calculations. The fact that the wind-induced current in the wind-direction has a turbulent logarithmic profile relative to the instantaneous wave surface was experimentally confirmed by Wu (1975) in 2D flow conditions and analytically derived by Madsen (1977) by considering the Coriolis force associated with rotation of the Earth and assuming a linearly varying eddy coefficient from the free surface. The penetration depth $h_0 = 0.25(g/2\pi)T_0^2(1 + 4\pi U/(T_0 g))$ of the wind-induced current depends on advection of vorticity with the Stokes wave drift velocity and is a function of the peak period T_0 of the wind-wave spectrum and the total current velocity U (Faltinsen et al, 2025). The wind-induced current velocity at the free surface is $0.02U_{10}$ where U_{10} is the sustained wind speed 10m above sea level that can be related to significant wave height and T_0. The logarithmic current profile has large variations in a very thin layer near the free surface. Since the current profile is described relative to the free surface of the wind waves, non-linear wave effects appear. Faltinsen et al. (2026a) demonstrated by using the Euler equations and assuming the current speed is small relative to the wave phase velocity that the wind-induced current shear matters in describing the ambient linear waves and suggested that the errors from neglecting wind-induced current shear may be comparable to those from ignoring viscous flow separation in linear wave excitation loads on a large-volume structure.
Ocean internal waves due to stratification typically have wavelengths ranging from hundreds of meters to tens of kilometers and periods from several minutes to several hours (Massel, 2015). The internal waves are associated with the thermocline, a transition layer in the sea between heated and lighter water above and colder and heavier water below. A thermocline in the ocean may exist at depths from about 50m to about 1000m. If we neglect continuous stratification and consider a two-layer model with different water densities, potential flow applies in each layer with a zero-thickness free shear layer and a jump in the horizontal velocity at the interface. Grue et al (1999) analyzed solitary waves by a strongly nonlinear numerical method that was compared with a weakly nonlinear Korteweg-de Vries (KdV) model and validated by model tests. Both the upper and lower layers were hydrodynamically shallow with a thin interface. If the depth of the lower layer is larger than the depth of the upper layer, a depression of the interface occurs. Internal waves act as current on wind waves and matter, for example, for marine structures in the South China Sea. Duan et al. (2023) analyzed the effect of internal solitary waves on the dynamic response of a vertical flexible riser by using the beam equation together with Morison's equation and empirical information about VIV for various ratios between the solitary wave amplitude and the upper layer depth. The depths of the upper and lower layers were 300m and 700m.

The internal wave period T_{iw} decreases with increasing solitary wave amplitude a. Using formulas in Grue et al. (1999) gives $T_{iw} = 1842s$ when $a = 30m$ and $T_{iw} = 742s$ when $a = 150\text{m}$. The natural periods of the considered riser with external diameter $D = 0.25m$ and pretension $1000kN$ can by neglecting bending stresses be estimated as $T_n = 40.7/n(s),\ n = 1,2,...$ (Faltinsen, 1990). It implies that the riser response is quasi-steady when the details of VIV are not considered. The transverse VIV can significantly affect the longitudinal drag coefficient according to empirical formulas (Faltinsen, 1990). When the internal wave amplitude is 150m, the predicted maximum stresses by Duan et al. on the riser part above and below the thermocline are 357 MPa and 269 MPa. If VIV is disregarded, the corresponding values are 227 MPa and 137 MPa. An error source is that Duan et al. (2023) did not consider the Reynolds number dependency of the drag coefficients and how it influences maximum stresses. Duan et al. (2023) presented values of U_c for their considered cases that make it possible to calculate the Reynolds numbers $Rn = U_c D/\nu$. Here ν is the kinematic viscosity coefficient. The maximum velocity increases with the solitary wave amplitude and is nearly constant within each layer. The flow velocity is in the wave propagation direction in the upper layer and opposite in the lower layer. If the highest examined wave amplitude is considered, the largest velocity for the upper layer is about $2.7ms^{-1}$ while the lowest value for the lower layer is $-2.3ms^{-1}$. It implies that the Reynolds number are in the critical and supercritical flow regimes with significant Reynolds and surface roughness number dependency of the drag coefficient (Faltinsen, 1990). VIV is influenced by the Strouhal number and thereby on the Reynolds number and roughness number.

How wind waves are affected by the internal waves depend on the depth h_1 of the thermocline and the wave number k of the wind waves. If $\exp(-2kh_1)$ is negligible, the effect of the internal waves is a current component in the free-surface conditions (Faltinsen et al, 2026b). If $\exp(-2kh_1)$ is not negligible, the effect of a jump in the horizontal wind wave velocity at the thermocline must be considered.

Faltinsen et al. (2025) studied experimentally and theoretically wave-current interaction with large-volume structures in deep water. The theory assumed incompressible water and irrotational flow, focusing on linear wave effects while omitting current shear. The experiments and presented theory showed that current significantly influences the linear wave excitation loads for a given wave frequency. This is associated with that the wavelength λ of the incident waves for a given wave frequency ω is affected by wave-current interaction in agreement with the pioneering work by Peregrine (1976). This leads to a relationship between the wave period and the wavelength, which may either have two solutions or no solution for the wavelength. When two solutions exist, one of the solutions may correspond to a very small wavelength that has no practical consequences for the behavior of the structure. The latter happens if the wave propagation and current directions are the same. No solution means that the current blocks the waves and corresponds to zero group velocity of the waves. The wavelengths of the two wave number solutions in blocking conditions for deep water regular waves with uniform current are one quarter of the wavelength without current interaction implying steepening of the waves which can increase the wave loads in the free-surface zone and motions of floating structures considerably. If one considers irregular waves described by a long-crested design wave spectrum, Faltinsen et al (2025) found by computations that the standard deviations of the wave pitch moment, longitudinal wave force, and vertical wave force on the considered pontoon in the design conditions are respectively 1.45, 1.11, and 1.56 times the standard deviations at zero current. The influence of current in regular waves could even be larger. However, the oscillations of the current dependent transfer functions of the longitudinal wave force as a function of wave frequency cause an important cancelling effect when the variance of the longitudinal force is obtained by frequency-integrating the product of the square of the transfer function times the wave spectrum.

Care must be shown when applying state-of-the-art potential flow codes, which accounts for the current effect by using a frequency of encounter approach assuming that the effect of current is equivalent to towing the body at the current speed in waves. The linear hydrodynamic variables oscillate then with the frequency of encounter, leaving the wavelength of the incident regular waves unchanged (relative to conditions without current). The studies by Faltinsen et al. (2025) resulted in a clarification of the wave-current problem in DNV's recommended practice DNV-RP-C205.

The findings also have consequences in analysis of higher-order wave-body-current interactions such as predictions of slow-drift hydroelastic oscillations of a planned floating bridge in Bjørnafjorden by the fact that the influence of current on the wave drift forces and wave drift damping on the pontoons must be reconsidered. This is a consequence of that wave drift forces according to second-order potential flow theory are related to the scattered and radiated waves by the structure which are not the same as when the structure is towed with the current velocity. There are 37 pontoons along the 5.4 km long bridge and hydrodynamic interaction between the pontoons, and the correlation of wave loads along the bridge must also be considered. The natural period corresponding to the highest natural mode of the bridge is 111.1s. Wind gusts matter also in this context.

Another example with current and free-surface nonlinearities is sum-frequency vertical wave excitation of resonant vibrations of a tension-leg platform. The elastic part is the tethers. The importance of the sum-frequency wave excitation is related to the small depth decay of the sum-frequency pressure. The depth decay of the second order sum-frequency pressure for a truncated vertical circular cylinder in waves with and without current was analytically studied by matched asymptotic expansions by Faltinsen et al. (2026b). It shows that the dominant depth decay both with and without current is proportional to D^{-1}. Here D is the depth below the mean free surface. The dependence of the wave frequency and the current on the depth decay requires a numerical solution. The depth decay of the sum frequency pressure for two monochromatic deep-water waves with opposite wave propagation directions can be more explicitly derived. When there are no current, deep water and the wave frequencies are the same, there is no depth decay (Longuet-Higgins, 1953). If current is present, the sum-frequency pressure decays with depth as $\exp\left(\left|k_{\omega_1} - k_{\omega_2}\right| z\right)$ where the vertical z-axis is upwards, $z = 0$ is at the mean free surface and k_{ω_i} are the wave numbers of the opposing wave components (Faltinsen et al., 2026b).

Higher-order horizontal wave-excited global vibrations of a vertical column is relevant for the Draugen platform standing on the sea floor at 251m depth in the North Sea as well as for supporting structures for a wind turbine. Sloshing of the internal water matters for the Draugen platform by e.g. influencing the structural natural period (Faltinsen and Timokha, 2009). Kristiansen and Faltinsen (2017) studied theoretically higher order horizontal wave load on a vertical free-surface piercing restrained circular cylinder standing on the sea floor in finite depth. There was no current and the FNV theory based on potential flow was modified to finite constant water depth. The FNV theory (Faltinsen et al., 1995) describes third order horizontal wave loads by assuming that the wavelength is large relative to the cylinder diameter and that the incident wave amplitude is of the same order as the cylinder diameter. Kristiansen and Faltinsen (2017) showed good agreement with experiments of higher-order wave effects for moderate wave steepness. Higher-order Stokes wave theory mattered in the generalized FNV theory for finite water depth. The experiments showed that a mound of water with locally large free-surface steepness was created at the rear end of the cylinder at the larger wave steepnesses. When the free surface subsequently propagated forward, local overturning waves happened at the cylinder surface. The fact that the free surface at the cylinder surface was not completely symmetric about the longitudinal x-axis implies that viscous flow separation may have played a role. In unpublished experiments with a restrained truncated surface-piercing circular cylinder, the mound of water was initially created at the front end of the cylinder. Very steep local waves were subsequently propagating at the two sides of the cylinder ending with that the two steep waves collided with a big splash at the downstream end of the cylinder. The observations suggest that a strongly nonlinear free-surface analysis is needed for the larger incident wave steepnesses.

Faltinsen et al. (2026b) modified the FNV theory to include a spatially uniform current. The studies of the third harmonic horizontal force for infinite water depth showed that current matters. When considering the FNV theory in finite water depth, higher-order Stokes theory matters. The mathematical expressions are the same as without current but the wave number in the expressions must account for wave-current interaction.

Floating solar islands have been proposed. An example is a circular horizontal membrane connected to an elastic floating collar that tends to follow the waves which minimize green water on the top and slamming underneath. Interaction between the floater and the membrane part matters. Experimental and theoretical studies in waves are presented by Skare and Kristiansen (2024).

Knowledge of the normal force on a cylinder in near-axial flow is needed in analyzing the motion of towed sonar and hydrophone arrays as well as current loading on pipelines and marine risers. Ersdal and Faltinsen (2006) consider experimentally the viscous hydrodynamic normal force and moment on a long cylinder of constant cross-section in infinite fluid when the angle of attack is small. The angle of attack is the angle between the ambient flow and the cylinder axis, and by small is meant that the angle is smaller than what is normally accepted as a valid region for the crossflow principle. The angles discussed range from 0° to 20° in the case of a stationary cylinder, while the amplitude of the angle varied from 4° and up to 50° in the oscillating case.

3. Aquaculture

Environmental footprints of fish farming are of concern. Our focus is on salmon farming. Salmon lice represent a problem that has led to closed cages. Rapid detection of fish escape is needed. One aspect is the economic losses. Another aspect is genetic contamination of wild stock. Our focus is on hydroelasticity.

Net cages and closed cages are separately discussed. The later presented theoretical studies are based on a spatially uniform current but did not correctly model wave-current interaction. The influence of wind induced current shear needs to be further studied. Icing can occur in exposed areas. It adds weight and increases the possibility that fish escape. Water quality inside the net cages depends on exchange of water to and from the net cages. Current flow removes waste and supplies oxygen and causes a turbulent wake that lowers the downstream velocity behind a cage. Løland's (1991) wake formula for small solidity ratios neglects exterior flow deviation due to the netting but illustrates in a simple way that number of downstream net cages must be restricted. He starts with considering 2D turbulent wake behind each twine by applying Schlichting's (1979) eddy viscosity model and relates it to the drag force on the twine. By linearly superposing contribution from each twine, it gives a spatially constant wake inside the net. The bottom weight influences net deformation and the net solidity ratio, marine growth, net deformation and current speed influence the wake.

A common type of net cage includes a floating collar of HDPE/plastic and either individual bottom weights or a bottom weight ring. The floater of a net cage tends to follow the waves well while that is not true for a nearby feed barge. However, in and out of water effects of existing floating collars may occur which implies that one should use floating collars with sufficient draft and freeboard. The netting may have ten million meshes which complicates the practical use of CFD and complete structural modelling in simulating the effect of a sea state during its duration. Kristiansen and Faltinsen (2012, 2014) use instead an equivalent truss model for the netting based on Bessonneau and Marichal (1998) combined with a screen model for the hydrodynamic loading. The screen model expresses the viscous loads by empirical pressure loss and tangential load coefficients that depend on the solidity ratio and the Reynolds number dependent drag coefficient of a twine. Non-zero tangential loads account for hydrodynamic shadow effects of twines. Since the Keulegan-Carpenter number based on twine diameter is large, the formulas apply to both wave and current loads. Current wake inside the net is considered on the downstream net part. A pragmatic way to account for biofouling is to increase the solidity ratio. The effect of knots and non-circular cross-sections of the twines are neglected and is an error source. The floater is modelled as a hydroelastic curved beam with tension and 3D potential flow in waves without current based on Li et al. (2016, 2018). 2D strip theory cannot describe the vertical wave loads on the floater in the range of non-dimensional wave frequencies needed. Morison's equation is applied for bottom weights and bottom weight rings. Løland's (1991) spatially constant current-wake model is used inside the net. The time domain solution starts at rest and a linear equation system for unknown tensions is solved for each time step. Shen et al. (2018) applied the method to a net cage with a realistic mooring system in irregular waves and current by hydrodynamically modelling the mooring lines by Morison's equation. Anchor and bridle loads agreed satisfactorily with model tests. An advantage of numerical simulations with the considered model is that the many needed realizations of a sea-state are not time consuming while that can represent a practical limitation if CFD and complete structural modelling are used as well as in model tests. Snap loads associated with the relative vertical motions between the floater and bottom weight may occur in the netting in severe sea states (Bardestani and Faltinsen, 2013). It causes possible netting damage and fish escape.

The previous studies neglect the effect of fish, which was experimentally studied by He et al. (2017). There are typically 100000-200000 salmon occupying 2.5% of the volume of a near-shore net cage. Model tests with 800 live fish occupying 2.5% of the volume were performed. The towing tests showed that the fish changes the net configurations and thereby increased the mooring loads with 10-27% in the considered cases by either touching the net or going to the bottom. Numerical simulations of the mooring loads agreed with the experiments by locally changing the solidity ratio in such a way that experimental and numerical net deformations are close. Towing tests with rigid fish models showed small effect on mooring loads. An important error source is scaling of the fish behavior to a realistic full-scale scenario. The fish have time to adapt to the environment in full scale. Numerically modelling the many fish is a challenging hydroelastic problem by itself.

Operational limits of a well boat at a moored net cage in waves and current was numerically studied by Shen et al. (2019). Well boats are used for transportation of fish from a fish farm to a factory for slaughtering and further processing. They are also used for delousing by pumping the fish into the well. Horizontal resonant slow drift oscillations of the interacting ship and net cage were important in the studies by Shen et al. (2019). It is equivalent to a coupled mass-spring system with damping. The mass is dominated by mass and sway-added mass of the ship while the spring is dominated by the fish cage with mooring. The viscous damping due to the ship and the netting matter. Second-order slowly varying potential-flow wave excitation of the well boat was considered. Wave drift damping of the ship was included. The contact between the ship and the floater can have a large influence on the floater. Large stresses at the contact points between the mooring and the floater of the cage were detected near the ship and will be a reason for operational limitations in terms of maximum operating sea-state. Another concern is that the propellers may damage netting and mooring lines. Other cases to be studied are the ship approach and departure phases as well as ship operations.

Closed cages can be divided into flexible structures (e.g. tarpaulin), semi-flexible structures (e.g. glass fiber) and rigid structures (steel and concrete). Sloshing of internal water becomes an issue. When the frequency of external wave excitation is in the vicinity of where the natural sloshing frequency is close to a natural frequency of the coupled system, strongly nonlinear internal free-surface flow can matter (Faltinsen and Timokha, 2021). Snap loads can occur in flexible cages as demonstrated in 2D linear hydroelastic studies by Strand (2018). The steady finite curvature of the membrane causes coupling between normal and tangential elastic modes. Strand and Faltinsen (2019) presented calculated maximum standard deviation of dynamic tension σ_τ along a fabric membrane cage in irregular waves versus peak wave period T_p for different significant wave heights $H_{1/3}$. The criterion used for snap loads was that the most probable largest tension $4\sigma_\tau$ should be larger than the static tension T_0. A cage radius of 12.5m was considered. As an example, snap loads were predicted for $H_{1/3} = 1m$ when $T_p > 5s$ and for $H_{1/3} = 2m$ when $T_p >\approx 4s$. Closed membrane cages were theoretically and numerically studied by Mukhlas et al. (2026), by generalizing the 2D linear model by Strand (2018) to 3D. The most dangerous situation is the resonant coupled floater heave with axisymmetric elastic bag modes, which represent the highest natural period of the system where the dynamic tension exceeds the static pre-tension in very calm sea-states. Moreau and Kristiansen (2025) studied nonlinear effects of a vertical elastic membrane attached to a floater in waves. Double-frequency in-plane tensions may dominate even when the dynamic tension is a small fraction of the pre-tension. The same applies to a mean set-down of the floater. Analysis of existing model tests of the bag and floater motions of a fabric membrane cage was presented by Mukhlas et al. (2021). They observed a strong mean set-down in low sea-states.

Shen et al. (2021) analyzed by linear hydroelastic theory a vertical cylinder-shaped semi-flexible fish cage in waves. Comparisons were made with model tests. The structural stiffness matrix and the dry structural modes were calculated by LS-DYNA while generalized hydrodynamic coefficients and wave excitation loads were obtained by WAMIT based on dry natural structural modes. Ovalizing structural deformations of the upper cylindrical cage part with nonlinear sloshing were experimentally evident in the vicinity of the highest wet natural period of the ovalizing mode which was close to a natural sloshing period T_{21}. The measured radial deformations at the freeboard level of the ovalizing modes close to T_{21} in regular waves varied as $\cos 2\theta$ and $\sin 2\theta$. The angle θ refers to the angle in a polar coordinate system with the vertical axis coinciding with the tank axis and $\theta = 0$ corresponding to the

incident wave propagation direction. The $\cos 2\theta$-mode increased initially more rapidly than the $\sin 2\theta$-mode. The behavior indicates nonlinear transfer of energy between the modes through sloshing. The $\cos 2\theta$ and $\sin 2\theta$ modes did not reach steady state during the examined duration of 170 times the wave period. The same was true for the internal measured wave elevation in regular waves. The reason may be that sloshing is associated with small damping and that it takes long time to develop steady-state oscillatory sloshing conditions (Faltinsen and Timokha, 2021). The internal wave elevation in irregular waves was also measured. If linear theory applies, the ratio between the "most probably largest value" and the standard deviation in the considered full-scale three hours storm should be 3.6 according to a Rayleigh distribution. Measured ratios up to six suggest nonlinearities. Since there was no closeness between natural surge-pitch natural periods and appropriate natural sloshing periods, linear theory agreed well with experiments in predicting the transfer functions of heave and pitch. Heave cannot excite linear sloshing in a rigid tank, but nonlinear Faraday waves may occur (Faltinsen and Timokha, 2021).

Multiple body interactions must be considered when analyzing closed fish cages in waves and current implying that spatial correlation of the waves can matter. The water is exchanged in a closed cage causing interior flow velocities of 0.2-0.4m/s. Full-scale tests indicate that the fish affect the pumping power. Interaction between the interior steady flow, sloshing and the fish needs to be studied.

Most of the fish farms are in protected coastal areas. However, there is a movement of fish farms towards the ocean by using knowledge from offshore engineering in structural designs. Fish comfort is an issue in large sea states and fish acceleration level is proposed as a measure. Service vessels as well as fish cages become larger. Severe damage or total collapse/sinking of the fish farm with resulting fish escape may occur because of a collision. Yu et al. (2019) simulated well boat collision with the salmon farm Ocean Farm 1 which has a cage diameter of 110m, height of 68m and a cage volume of 245000m^3. It is situated off the coast of Frøya, Norway and is a semi-submersible with a rigid net structure and a secondary net barrier. The design significant wave height is 5m. The ship in mind had length 81.3m, beam 22m, draft 7.8m with collision speed of 6m/s corresponding to kinetic energy 53.5 MJ.

A submersible cage with a submerged air cushion has been proposed. There are reduced wave loads on the netting and reduced exposure to sea lice in submerged conditions. The submerged air cushion solves the need for the salmon to fill the swim bladder with air.

There is a future potential for growing seaweed. Seaweeds are highly flexible with varying forms and properties. Neufeldt et al. (2025) have published a review article on physical and numerical modeling of seaweed in oceanic waters.

4. Slamming

Slamming causes local and global response of a structure. Our focus is on when hydroelasticity matters. A different problem with local and global consequences is underwater explosions and hydroelastic response of a ship. The initial acoustic phase and the later gas-bubble phase have local and global consequences, respectively (Greco et al, 2014).

The hydrodynamics associated with slamming can be complicated involving e.g. nonlinear free surface effects, turbulence, gas cushions, cavitation, acoustics and thermodynamics. The impact pressures can be very large, highly localized in space, very sensitive to inflow conditions and have very short duration. Kvålsvold et al. (1995) reported drop tests of elastic horizontal plates on calm water as well on regular waves of different steepnesses with different initial impact positions. The reported Froude-scaled maximum pressure with the same drop velocity V varied strongly in different tests with different impact scenarios and could be close to the acoustic pressure $\rho c V = 90 bar$ for the highest tested Froude-scaled $V = 6ms^{-1}$. Here ρ is the water density and c is the speed of sound in water. There is lack of correlation between the reported large impact pressures and maximum structural stresses (Kvålsvold et al, 1995). Hydroelasticity must then be considered with hydroplasticity in extreme cases (Abrahamsen et al., 2020). One can be lost in unnecessary details when focus is only on hydrodynamics. What matters is what is important for large structural stresses. Magnitude and time scales of hydrodynamic effects versus important structural natural periods matter. This is different for local and global slamming effects.

Faltinsen (1997) compared the experimental drop tests of horizontal elastic plates by Kvålsvold et al. (1995) with an approximate theoretical method that divides the analysis into an initial wetting phase and a free vibration phase. The important natural structural periods are assumed to be much larger than the wetting duration. If drop on an initially calm free surface is considered, an aircushion with very small height is formed during a very small initial period. The air cushion breaks subsequently down into bubbles. The consequence is that the space-averaged vertical deformation velocity goes towards the drop velocity at the end of the wetting phase, i.e. the plate stops. This provides initial conditions together with zero deformations for the subsequent free vibration phase. It implies that later resulting stresses in the plate in the free-vibration phase are proportional to the drop velocity. If an initial air cushion is formed, the scenario applies also for dropping on waves. This depends on the ratio L/R between the horizontal plate length and radius of curvature of the waves. Koehler and Kettleborough (1977) investigated the initial formation of an air cushion numerically in 2D by considering drop on calm water of a body where the lower part is a wedge and the upper part has vertical surfaces. If the deadrise angle of the wedge is 0.5 degrees and larger, an air cushion is not formed.

The plate is assumed to be fully wet in the free-vibration phase, and a beam model with proper end conditions is used. The hydrodynamic pressure is only due to beam vibrations. If only one structural mode is dominant, the maximum strain occurs at a quarter of its wet structural natural period. The hydrodynamic pressure is positive at maximum stress, but later hydrodynamic pressure can be negative depending on the beam vibrations. The magnitude of the negative pressure depends on the drop velocity and can be so large that the sum of the atmospheric and hydrodynamic pressure approaches zero, i.e. cavitation. Since the penetration of the plate is small, air ventilation occurs, i.e. the plate oscillates like it is in air with a smaller oscillation period (Faltinsen, 2005). However, since the maximum strain is smaller, we do not need to consider cavitation and ventilation to predict maximum strain. Kvålsvold et al (1995) presented experimental non-dimensional strain amplitude in the centers of dropped horizontal steel and aluminum plates as a function of nondimensional water entry velocity for different ratios L/R between the plate length and the radius of curvature of the waves at the impact position. The experiments by Kvålsvold et al (1995) are generally consistent with the theory by Faltinsen (1997) but show some difference for smaller non-dimensional impact velocities as well as for the largest tested $L/R = 0.198$, where the non-dimensional results were lower indicating that the model does not stop at the end of the wetting phase and that slam damping matters as explained by Abrahamsen et al (2023) and further discussed later.

Faltinsen (1999) studied theoretically hydroelastic water entry of a wedge by orthotropic plate theory without considering the wetting and free-vibration phases. The results show that hydroelastic slamming has analogy to transient response of a mass-spring system with time-dependent forcing. The Dynamic Amplification Factor (DAF), i.e. the ratio between the maximum response and the static response depends on the ratio T_d/T_n between the time duration of the loading and the natural period. When T_d/T_n is small, the DAF is less than one and decreases with decreasing T_d/T_n. DAF is influenced by the time history of the loading, including the rise time of the loading as it is illustrated in textbooks on dynamics of simple mass-spring systems.

If one considers steep wave impact on a vertical cylinder, the gravity does not matter in describing the local response. The problem is therefore analog to water entry of a 2D circular cylinder at a cross-section of the vertical cylinder. The rise time of the loading by potential flow theory of incompressible water is then zero. Since no initial air cushion is formed, one cannot divide the local hydroelastic response into an initial wetting and a free-vibration phase. The problem was theoretically considered by Abrahamsen et al. (2023) and experimentally validated by drop tests. Bending and membrane stiffness as well as the Poisson ratio matter which cause challenges in scaling model-test results to full scale. However, a validated theoretical method can facilitate scaling. 2D potential flow of incompressible water with high-frequency free-surface condition and “uprise” of the water was accounted for. Because slam loads depend on the relative normal velocity between impact and response, slam damping arises which reduces the response during slam loading. A small number of structural modes matter for maximum stress both in theory and experiments. The fact that acoustic pressure may occur initially as demonstrated experimentally by Hagiwara and Yuhara (1976) for impact of a circular section on calm water was not discussed. However, it lasts very short relative to the time scale of important structural response and has therefore a secondary effect.

Global wetdeck slamming response of a catamaran at forward speed in head sea was considered theoretically and experimentally by Ge et al. (2005). The global response causes that the important structural natural periods are significantly longer than for a local response. The latter fact simplifies the slamming model. Since the natural periods in heave and pitch are high relative to the wetdeck wetting duration, the water exit problem. i.e. diminishing wetdeck wetting had to be considered. The vertical force on the wetdeck is generally upwards during water entry while downwards during water exit resulting in a time-integrated wetdeck force during both water entry and exit clearly smaller than when only integrating the wetdeck force over the water entry phase. Since a Wagner-type of slamming model can only describe the water entry phase, a von-Karman type of method was used. It implies that water rise-up at the free surface during water entry was neglected. The theoretical predictions of the wetdeck force were validated by the experiments.

Many fluids dynamic parameter parameters, thermodynamics and hydroelasticity may matter in describing slamming-induced stresses in prismatic LNG tanks and represent challenges for numerical predictions and model test scaling (Faltinsen and Timokha, 2009). Sloshing depends on the filling depth and there are different violent impact scenarios such as plunging waves with gas cavity or flip-through in shallow depth. Slamming induced stresses associated with plunging breaker and an entrapped gas cavity depend on the cavitation and Euler numbers and requires depressurized model test conditions. The latter is complicated if a ship with LNG tanks in waves is investigated in model tests but is more feasible if forced oscillations with prescribed tank motions is studied. The structural details of a prismatic LNG tank can be complicated. A complete structural analysis with a simplified slamming model was made by Graczyk (2008). Bending stress spectra in the lowest and middle fiber of the plywood next to the resin ropes indicate that many structural natural periods matter in describing the effect of slamming. Since LNG is "boiling" and the sound speed can be significantly lowered in a mixture of gas and liquid, an unanswered question is if acoustic liquid effects matter for the smallest natural periods. Structural scaling of model tests is also an issue in this context. Tank roof impact with possible hydroelastic effects must be considered for large filling ratios. The roof may be rigid in this context but the slamming causes also loading at the vertical tank walls which can respond hydro-elastically (Rognebakke and Faltinsen, 2006).

Whipping of ships is transient hydroelastic response due to bow slamming is of concern for container vessels (Malenica and Tuitman J., 2008, Tuitman et al.,2013). The slamming loads are typically simplified by a 2D method to have time-efficient computation tools. A generalized Wagner-type method is e.g. used. It implies that the body-boundary conditions are correctly satisfied. A high-frequency free-surface condition is used, and the water up-rise is considered. It applies only during water-entry and does not consider possible non-viscous flow separation occurring from e.g. the bulb. CFD calculations of whipping are time consuming. Vladimir et al. (2025) combined CFD and potential flow to provide a time-efficient computation tool.

Springing refers to global continuously wave-excited steady-state hydroelastic vibrations of a ship that may occur in combination with whipping. Damping is an important issue for springing that was studied for a container vessel by Søding (2009). He investigated vibration damping by an immersed transom, wave radiation, bilge keels, propeller and hatch cover friction and concluded that the. damping is mostly due to the transom. The latter effect is also named hull-lift damping (Faltinsen, 2005) implying that the damping increases with the forward speed.

5. Conclusions

Wave-current-body interactions with possible hydroelasticity matters and is not the same as towing the structure with the current speed. The current can block the waves in opposing current and wave propagation directions. Current shear matters in describing internal waves and wind-induced current. Since the logarithmic wind-induced current profile is described relative to the wave surface, it causes higher-order harmonics. The fact that the boundary layer of the wind-induced current causes large variations of the horizontal velocity in a very thin layer near the free surface represents a challenge.

Numerical predictions of wave and current interaction with net cages require a hydroelastic analysis. The netting may have ten million meshes which complicates the practical use of CFD and complete structural modelling. Kristiansen and Faltinsen (2012, 2014) use instead an equivalent truss model for

the netting combined with a screen model for the hydrodynamic loading. Sloshing is a factor for closed fish cages. When the frequency of external wave excitation is in the vicinity of where the natural sloshing frequency is close to a natural frequency of the coupled system, strongly nonlinear internal free-surface flow can matter. Hydroelasticity matters for flexible and semi-flexible closed net cages. Snap loads should be recognized for nettings and flexible net cages. The fish is "hydroelastic" and can affect the flow and loads.
The hydrodynamics can be complicated in describing the details of liquid entry (slamming) and exit. There is a saying that one "can't see the forest for all the trees". It is the structural response and not the pressures that have practical interest in slamming. It requires a hydroelastic analysis recognizing the ratio between the slamming duration and important natural structural periods. The latter ratio determines what hydrodynamic details matter. Sloshing-induced slamming in prismatic LNG tanks involves hydroelasticity, many fluid mechanics and thermodynamic parameters with complicated inflows that remain a challenge in making simplifications, numerical simulations and model tests.
There must be a balance between hydrodynamics and structural mechanics in hydroelastic analysis. There is a saying "a chain is only as strong as its weakest point". Emphasis on error analysis is encouraged.
Future challenges relate to the need for food, energy and the climate. Problem areas have a return period. Will high-speed vessels return as an important topic in marine transportation?

References

Abrahamsen, B. C., Alsos, H. S., Aune, V., Fagerholt, E., Faltinsen, O. M., Hellan, Ø., 2020, *Hydroplastic response of a square plate due to impact on calm water*, Physics of Fluids.

Abrahamsen, B., Grytten, F., Hellan. Ø, Søreide, T., Faltinsen, O. M., 2023, *Hydroelastic response of concrete shells during impact on calm water*, Journal of Fluids and Structures.

Bardestani, M., Faltinsen, O. M., 2013, *A two-dimensional approximation of a floating fish farm in waves and current with the effect of snap loads*, Proc. 32nd International Conference on Ocean, Offshore and Arctic Engineering, Nantes, France.

Bessonneau, J.S., Marichal, D., 1998. *Study of the dynamics of submerged supply nets (applications to trawls)*. Ocean Engineering 25 (7), 563–583.

DNV-RP-C205, 2025. *Environmental conditions and environmental loads*. Det Norske Veritas.

Duan, J., Wang, X., Zhao, J., You, Y., 2023, *Effect of internal solitary wave on the dynamic response of a flexible riser*, Physics of Fluids.

Ersdal, S, Faltinsen, O.M., 2006, *Normal forces on cylinders in near-axial flow*, J. Fluids and Structures, 22.

Faltinsen, O.M., 1990, *Sea Loads on Ships and Offshore Structures*, Cambridge, England: Cambridge University Press.

Faltinsen, O.M., 1997, *The effect of hydroelasticity on ship slamming*, Phil. Trans. R. Soc. A., 355, 1-17

Faltinsen, O.M., 1999, *Water entry of a wedge by orthotropic plate theory*, Journal of Ship Res., Vol. 43, Sept., 180-193.

Faltinsen, O. M., 2005, *Hydrodynamics of High-Speed Marine Vehicles*, Cambridge University Press.

Faltinsen, O. M., Timokha, A. N., 2009, *Sloshing*, Cambridge University Press.

Faltinsen, O. M., Timokha, A. N., 2021, *Coupling between resonant sloshing and lateral motions of a two-dimensional rectangular tank*, J. Fluid Mech.

Faltinsen, O.M., Newman, J.N., Vinje, T., 1995, *Nonlinear wave loads on a slender vertical cylinder*, J. Fluid Mech. 289, 179-198.

Faltinsen, O. M., Shen, Y., 2018, *Wave and current effects on floating fish farms*, Journal of Marine Science and Application.

Faltinsen, O.M., Wang, J., Xiang, X., 2025, *Current-wave interaction with large-volume structures*, Physics of Fluids.

Faltinsen, O.M., Wang, J., Xiang, X., 2026a, *Water wave-current interaction with logarithmic wind-induced current*, Physics of Fluids,38,1.

Faltinsen, O.M., Wang, J., Xiang, X.,2026b. *Non-viscous and weakly nonlinear wave-current-body interaction*. Not published yet.

Ge, C., Faltinsen, O. M., Moan, T., 2005, *Global hydroelastic response of catamaran due to wetdeck slamming*, J. Ship Res, 49, 1, 24-42.

Graczyk, M, 2008, *Experimental investigation of sloshing loading and load effects in membrane LNG tanks subjected to random excitation*. Ph. D. thesis, Department of Marine Technology, NTNU, Trondheim.

Greco M., Colicchio G., Faltinsen O.M., 2014, *A domain-decomposition strategy for a compressible multi-phase flow interacting with a structure*, Int. J. for Numerical Methods in Engineering, 98.

Grue, J., Jensen, A., Rusås, P.-O., Sveen, J. K., 1999, *Properties of large amplitude internal waves*. J. Fluid Mech. 380: 257–278.

Hagiwara, K., Yuhara, T., 1976, *Fundamental study of wave impact loads on ship bow*. J. Soc. Nav. Arch., Japan, 14, 73-85.

He, Z., Faltinsen, O. M., Fredheim, A., Kristiansen, T., 2017, *The influence of fish on the mooring loads of a floating net cage*. J. Fluids Struct, 76: 384–395.

Koehler, B. R., Kettleborough, C.F., 1977, *Hydrodynamic of a falling body upon a viscous incompressible fluid*, J. Ship Research, 21,165-181

Kristiansen, T., Faltinsen, O. M., 2012, *Modeling of current loads on aquaculture net cages*. J Fluids Struct 34, 218–235.

Kristiansen, T., Faltinsen, O. M., 2014, *Experimental and numerical study of an aquaculture net cage with floater in waves and current*. J. Fluids Struct, 54:1–26.

Kristiansen, T., Faltinsen, O. M., 2017. *Higher harmonic wave loads on a vertical cylinder in finite water depth*. J. Fluid Mech.

Kvålsvold, J., Faltinsen, O.M., Aarsnes, J.V., 1995, *Effect of structural elasticity on slamming against wetdeck of multihull vessels*, PRADS'95, Seoul, Korea. Also published in Journal of Ship and Ocean Technology

Li, P., Faltinsen, O. M., Greco, M., 2018, *Wave-induced accelerations of a fish-farm elastic floater: experimental and numerical studie*s. J Offshore Mech Arct Eng, 140(1):011201.

Li P., Faltinsen, O. M., Lugni, C., 2016, *Nonlinear vertical accelerations of a floating torus in regular waves*. J. Fluids Struct 66:589–608.

Longuet-Higgins, M. S., 1953, *Can Sea waves cause microseisms?* Proc. Symp. On Microseism, 306, 74-93. New York: U. S. Nat. Sc.-Nat. Res. Council.

Løland, G. ,1991, *Current Forces on and Flow through Fish Farms*. Dr. Ing. Thesis. Division of Marine Hydrodynamics. The Norwegian Institute of Technology

Madsen, O. S. 1977. *A realistic model of wind-induced Ekman boundary layer*. Journal of Physical Oceanography, 7, 248-255.

Malenica, S., Tuitman, J., 2008, *3DFEM – 3DBEM model for springing and whipping analyses of ships*., RINA Conf. on Design and Operation of Container Vessels, London UK.

Massel, S.R., 2015, *Internal Gravity Waves in the Shallow Seas*, Springer International Publishing Switzerland.

Moreau, M., Kristiansen, T., 2025, *Numerical investigations of non-linear responses of a vertical membrane in waves*,16th Int. Conf. on Practical Design of Ships and Other Floating Structures, PRADS, Ann Arbor, Michigan, USA

Mukhlas, M., Lader, P., Kristiansen, D., Kristiansen, T., Motoyasu, K., 2021, *Bag and floater motions of a fabric membrane cage*, J. Fluids Struct, 106.

Mukhlas, M., Kristiansen, T., Moreau, M. K. I., Sævik, S., Lader, P., Kristiansen, D., 2026, *Development of a linear numerical model for closed membrane-type fish cage in waves*, submitted to JFS special invited issue on hydroelasticity.

Neufeldt, H., Windt, C., Buck, B. H., Heasman, K., Hildebrandt, A., Goseberg, N., 2025, *Physical and numerical modeling of seaweed in oceanic waters*, Aquacultural Engineering 110.

Peregrine, D., 1976. *Interaction of Water Waves and Currents*. Advances in Applied Mechanics, 16, Academic Press, New York, 9-117.

Rognebakke, O. F., Faltinsen, O.M., 2006, *Hydroelastic sloshing induced impact with entrapped air*, 4th Int. Conference on Hydroelasticity in Marine Technology, Wuxi, China.

Schlichting, H., 1979, *Boundary-Layer Theory*, McGraw-Hill series in Mechanical Engineering.

Shen Y., Greco M., Faltinsen O., Nygaard I., 2018, *Numerical and experimental investigations on mooring loads of a marine fish farm in waves and current*, J. Fluids Struct, 79.

Shen, Y.; Greco, M., Faltinsen, O. M., 2019. *Numerical study of a well boat operating at a fish farm in long-crested irregular waves and current*. J. Fluids Struct, 84, 97-121.

Shen, Y., Firoozkoohi, R., Greco, M., Faltinsen, O. M., 2021, *Experimental investigation of a closed vertical cylinder-shaped cage in waves*. Ocean Eng.

Shen, Y., Firoozkoohi, R., Greco, M., Faltinsen, O. M., 2022, *Comparative investigation: Closed versus semi-closed vertical cylinder-shaped fish cage in waves*. Ocean Eng.

Skare, A., Kristiansen, T., 2024, *Improved modelling of a floating membrane solar island in waves*, 15th International Conference on Hydrodynamics (ICHD 2024), Rome, Italy.

Strand, I. M., Faltinsen, O. M., 2017, *Linear sloshing in a 2D rectangular tank with a flexible sidewall*. J Fluids Struct, 73:70–81

Strand, I. M, 2018, *Sea Loads on closed flexible Fish Cages*. PhD thesis., Department of Mar Technol Norwegian University of Sci Technol, Trondheim

Aquaculture Structures

10th International Conference on HYDROELASTICITY IN MARINE TECHNOLOGY
Trondheim, Norway, June16th-18th, 2026

A Study on the Hydroelastic Responses and Induced Loads of Aquaculture Lice-Skirts Exposed to Current

Kristiansen, D.[1,*] Fredriksen, A.G.[2], and Kristiansen, T.[1]

[1] Norwegian University of Science and Technology, Trondheim, Norway
[2] Entail AS, Tromsø, Norway

Abstract. This paper addresses current-induced hydrodynamic effects of lice shielding skirts, which are flexible membrane structures for shielding of open net-cages used for salmon farming. The study is based on scaled model tests supplemented with numerical modeling and simulations. The focus is on the flexible deformations of the structure, the induced drag force, and the flow deviations caused by the skirt. Our results show that current exposure can cause large deformations interacting with flow deviations. This has an impact on the performance of the skirt as a flow barrier and influences the mooring loads.

Key words: *Aquaculture; Lice-skirt; Membrane; Current Drag; Flow deviations*

1. Introduction

This paper addresses the hydrodynamic effects of lice-skirts used in salmon aquaculture when exposed to current, by means of scaled model tests and numerical simulations. The work presented has relevance for the design and operation of such equipment for conventional fish cages. Lice-skirts are flexible membranes applied to floating aquaculture net cages as shielding against parasites (sea-lice) spread by natural convection of contaminated ambient surface water. Sea-lice infections represent one of the major challenges for sea-based salmon aquaculture in open net-cages, with negative consequences for fish health and for production. The application of lice-skirts as a barrier to displace the incident surface flow around the net-cages affects the hydrodynamic behavior of the net-cage structure, with expected implications for mooring loads and structural responses. The nature of flow deviations induced by the lice-skirt is also important from a protection performance point of view. The available literature on the hydrodynamic aspects of lice-skirts is scarce and more knowledge is needed to promote the design and operation of lice-skirts in aquaculture [1].

Flexible membrane structures are typically light-weight, complying with sea-loads, inexpensive and easy to install, making them attractive solutions in aquaculture. However, the compliant nature of such structures makes them complicated from a hydrodynamic point of view, as the hydrodynamic loads and structural deformations are mutually dependent. In addition, the in-plane tensions of the membrane are necessary for an unambiguously defined geometrical shape, where out-of-plane pressure forces are balanced by the in-plane stresses and curvature of the membrane. Consequently, loss of in-plane tensions or unfavorable membrane curvature relative to pressure loading can cause large deformations.

The present work focuses on the behavior of flexible lice-skirts exposed to steady current in terms of structural deformations, drag-induced mooring loads, and flow deviations. The paper is organized in the following sections: Introduction (1), Model experiments (2), Numerical model (3), Results and discussion (4) and Conclusions (5).

*Correspondence to: david.kristiansen@ntnu.no

2. Model experiments

Two dedicated experimental campaigns were conducted to investigate the current-induced effects of flexible lice-skirts applied to an elastic circular floater. The model tests were based on Froude-scaling due to the influence of weighted ballast, with a model scale factor 1/33.3. Different laboratories were used for the two test campaigns. The first test campaign, focusing on lice-skirts applied to floater without net, were conducted in the MC-lab at NTNU which is a medium sized towing tank measuring 40 m in length and 6.45 m width. The water depth was 1.5 m. The second test campaign was conducted with a complete net-cage equipped with lice-skirt in the Large Towing Tank at SINTEF Ocean measuring 10 m width and 10 m water depth. Steady uniform current was simulated by towing the model for a set of tow speeds corresponding to full-scale current speeds in the range from 0.2 m/s to 1.0 m/s, a procedure assumed adequate in the absence of waves. Froude number based on cage diameter was less than 0.05.

2.1. The models

The two lice-skirt model configurations N0S2 and N0S3 were tested in the first test campaign, with skirt depths $d_1 = 0.21$m and $d_2 = 0.30$m corresponding to 7 m (d_1) and 10 m (d_2) full scale, respectively (see Fig. 1). The chosen skirt depths are typical for present industrial use. Each skirt model was constructed from watertight parachute nylon fabric (0-P), a lightweight and highly flexible fabric material. A fold was prepared in the lower part to insert ballast weight (lead line) with wet weight 0.208 $\mathrm{N/m}$ in model scale. The upper rim of the skirt was connected to the inner perimeter of the floating collar using evenly spaced metal hooks. The inner circumference of the floater, corresponding to the circumference of the lice-skirt, was 4.80 m. The floating collar was constructed as a double torus using

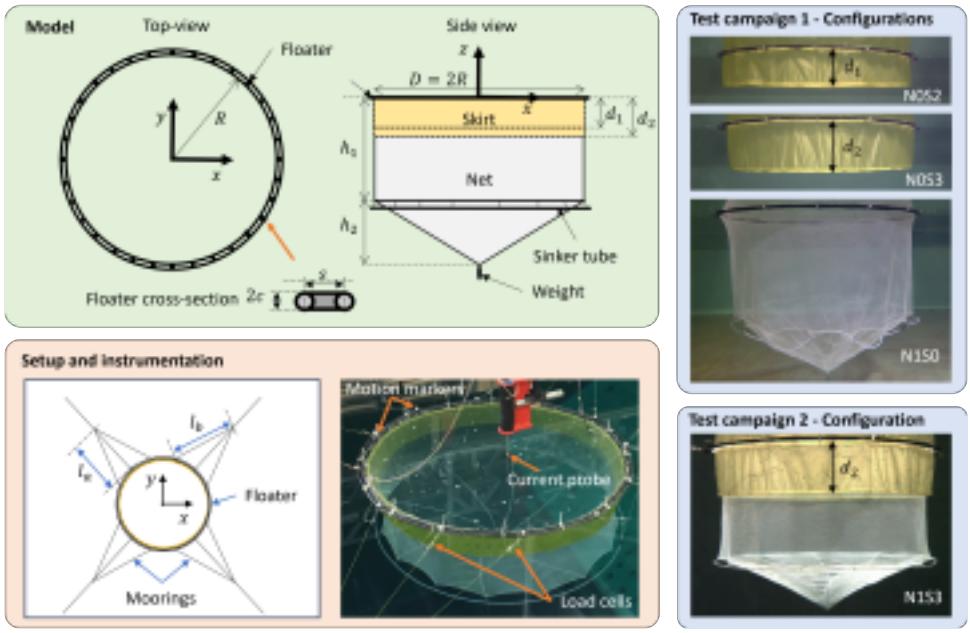


Figure 1: Overview of model geometry, configurations, setup and instrumentation. Upper left: Model geometry, top view and side view. Right: Different model configurations tested in the two test campaigns. Lower: Model setup and instrumentation.

flexible PVC tubes with an outer diameter of 15 mm. The two tori were connected by 16 3D-printed brackets and 32 cubes of 10 mm made from extruded polystyrene (XPS) evenly distributed around the collar, fixing the pipe axis-to-axis separation at 25 mm while increasing the floater's water-plane area by 3.3%.

In the second test campaign, the full cage configuration N1S3 was tested, where a circular cylindrical model net with a conical bottom was attached to the model with the deep draft skirt. The solidity ratio of the net, defined as $\mathrm{Sn} = 2d/l - (d/l)^2$, was $\mathrm{Sn} \approx 0.19$, with a twine diameter $d = 0.5$mm and a half-mesh width $l = 5.3$mm. The circumference of the cylindrical part of the net was 4.80 m, meaning 1.50 m diameter. Depth of the cylindrical part of the net model was 0.80 m. The slant height of the cone was 1.01 m, yielding an ideal full net-cage depth of 1.48 m. The cone was made up of eight triangular net pieces. A sinker-tube was applied to provide a cylindrical shaped net-cage at equilibrium. The outer diameter of the sinker-tube was 9,5 mm and the toroidal circumference was 4.80 m. The sinker tube consisted of a latex hose containing a lead line and a steel wire spring, providing weight and bending stiffness representative for a fish cage. The total wet weight of the whole sinker tube with included lead line and steel wire was 218.7 grams, corresponding to 8 tons full scale. A single 25 gram lead weight was attached to the cone apex of the net cage. The spring steel core had a circular cross-section diameter of 1.95 mm. The bending stiffness of the sinker tube governed by the spring steel thread was $0.147\,\mathrm{Nm}^2$.

2.2. Setup, instrumentation and measurements

The model was moored to the towing carriage using four pre-tensioned mooring lines, each connected to a coil spring with stiffness 24 N/m proven to be linear within the load range. Three bridles yield 12 attachment points evenly distributed around the circumference of the floating collar. The length of the center bridle was $l_a = 1.50$ m, while the length of the side-bridles was $l_b = 1.64$ m (see Fig. 1). The attachment points on the carriage were elevated 41 cm above the calm water level to keep the springs out of water during the tests. Pre-tension was applied to avoid the coil springs to go slack during testing.

Flexible motions of the collar were measured by the optical motion tracking system Qualisys Oqus, where twelve light weight reflective markers were fixed onto the floater. The markers were located next to attachment points of the mooring lines. In addition, markers were applied at the joints of the bridle lines, providing instantaneous mooring-line directions such that the directional mooring force is obtained when combined with the measured tension. Horizontal flow velocity components ($x-$ and $y-$ directions) were measured using Valeport electromagnetic current probes. The flow inside the cage was mapped by systematically changing the lateral position and depth of the probe. All measured signals were sampled at 200 Hz, except motion tracking that was sampled at 25 Hz. A low pass Butterworth filter of third order with cut frequency 2.0 Hz was applied on all channels. Video recordings of the model were made with cameras mounted to the towing carriage both above and below water.

3. Numerical lice-skirt model

We consider the lice skirt exposed to steady, horizontal, uniform ambient flow with magnitude U, as illustrated in the left and middle parts of Figure 2. The structural problem of the skirt is handled by a fully nonlinear, three-dimensional truss model, as illustrated by selected snapshots of the skirt as obtained by the presently implemented numerical code in Figure 3. The trusses form a rectangular mesh with additional diagonal trusses to represent membrane shear. This is not a rigorous representation of the membrane, but considered reasonable within other error sources of our method. The floater is considered rigid, but a generalization to flexible floater is straightforward.

The lice skirt is deformed due to the current. The deformation depends on the pressure distribution, and the steady drag load of the skirt depends on its steady shape. One main ingredient is therefore to represent the distribution of the pressure drop across the membrane in a rational manner. The hydrodynamic drag load model is based on empirical data and assumptions described in the following.

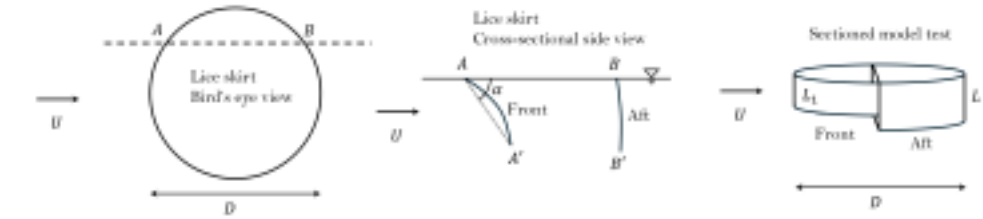


Figure 2: Sketches related to the lice skirt drag load model. The middle figure represent the vertical plane given by AB in the left figure. The right figure shows a sketch of the experiments by [2].

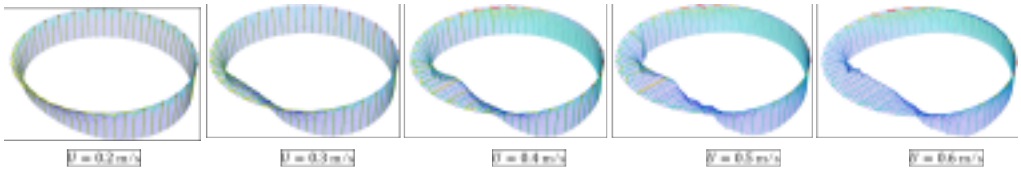


Figure 3: Snapshots of the skirt as obtained by our numerical predictions of the deep draft lice skirt in a relevant range of values of the steady current velocities U. The membrane is represented by a truss arrangement. The colors indicate tension level in each truss.

We assume strip theory in *vertical* planes, exemplified by the dashed curve AB in the left part of Figure 2. Strip theory means we neglect hydrodynamic interaction between the vertical planes and consider two-dimensional flow. Strip theory is commonly applied in cross-sectional planes of long cylindrical bodies. Our body is not long. The rational for assuming 2D flow in vertical planes instead, is based on the visual observations and theoretical considerations in [2]. We simplify the physical membrane shape by straight plates from a hydrodynamic point of view; see the dashed curve AA' for the front and similar for the aft. The front plate has an angle α as indicated in the figure. We apply a pressure drop distribution along the plate according to [3]. They reported numerical and experimental pressure drop distributions for two-dimensional wedges with internal angles in the range 30 to 90 degrees, referring to our angle α. Assuming the free surface to act as a rigid lid, we argue based on mirroring argument that we may use the bottom half of the wedge. The drag on each strip is weighed uniformly to sum up to a global drag coefficient of obtained in the experiments by [2]. They performed experiments on truncated, hollow, rigid cylinders of relevant aspect ratios in steady ambient flow. The model was cut in a front and a rear half, as illustrated in the right part of Figure 2. The drag load was measured on each half independently. In total, the drag coefficient for the whole cylinder was around 0.7. An important point is that the drag on the rear half was much lower than on the front half, even slightly negative for $L_1/L > 0.75$, while positive, although small for lower ratios of L_1/L. Consequently, there is in practice a very low contribution to the total drag from the rear half, unless the deformation of the front half is large. The value L_1/L for each strip (plane) is taken as the average over all strips and the weighing is made separately for the front and aft halves. Assuming strip theory is not well-justified for the lateral parts of the skirt. However, the majority of the drag is induced by the front and aft quarter sectors.

We acknowledge that there are many assumptions and simplifications in our load model. However, we justify the model by the reasonable comparisons with our experiments both in terms of skirt deformations and drag force. In future studies one can for instance perform CFD simulations for representative skirt shapes, and interpolate between these, to obtain pressure distributions more closely to first principle.

4. Results and discussion

We separate our results and discussions in three parts: current-induced deformations, drag forces and flow displacements.

4.1. Current-induced deformations

Steady-state deformations of the model skirt for selected current speeds are presented in Fig. 4. The

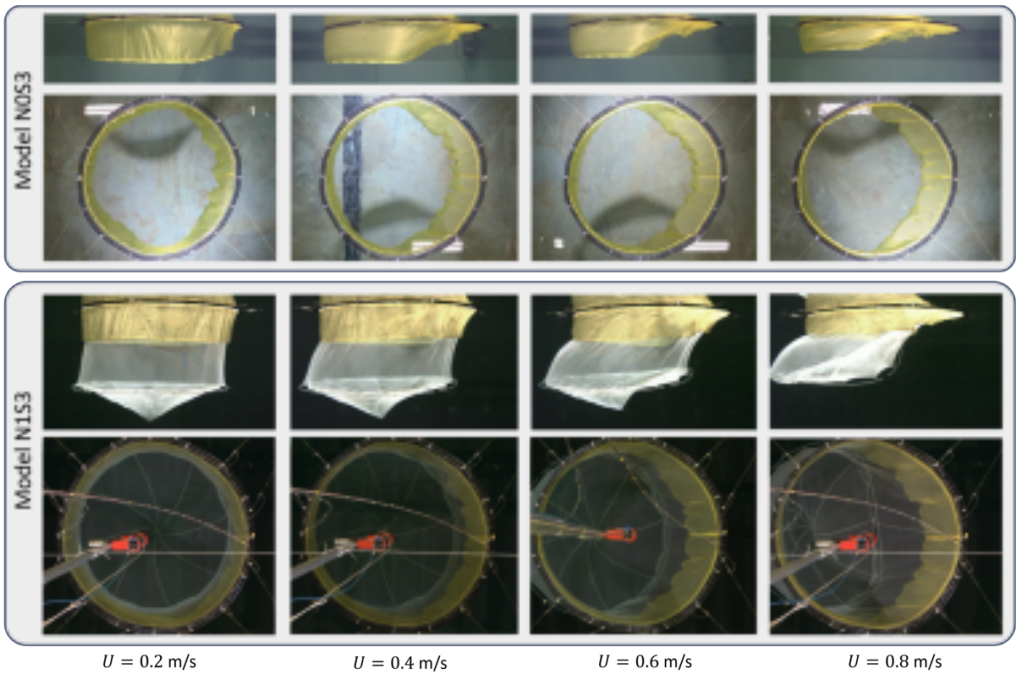


Figure 4: Selected snapshots of lice-skirt deformations in current simulated by towing, corresponding to the full-scale current speeds $U = \{0.2, 0.4, 0.6, 0.8\}$ m/s. Apparent inflow is from right towards left. Upper two rows: Tests with deep skirt attached to floater (N0S3). Lower two rows: Tests with skirt attached to full net-cage model (N1S3).

deformations were characterized by a deflection of the skirt front. The deflection lead to a reduced local draft of the front, implying increased current exposure to the aft side of the skirt. In the case without net (upper part of Fig. 4), the deflections were so large that a part of the skirt aligned with the free surface, leaving one side of the membrane dry. The figure shows the deep skirt (N0S3), but the medium draft skirt (N0S2) showed similar behavior. Some variability of the detailed deformation pattern was observed between repetition tests, in particular the folding pattern which was governed by the (discrete) connections to the floater.

The numerically obtained deformations for the deep skirt without net are presented in Fig. 3. The numerically predicted skirt deformations exposed to low and moderate current speeds are characterized by the same main deformations as observed in the experiments (Fig. 4), namely, that the front is deflected downstream and lifted so that more of the aft side is exposed. In addition, at moderate speeds, the front is partially aligned with the free surface. The lift-up causes increased current exposure of the aft, increasing the drag force on the skirt (discussed in the next section). In these simulations, the (numerical) skirt was

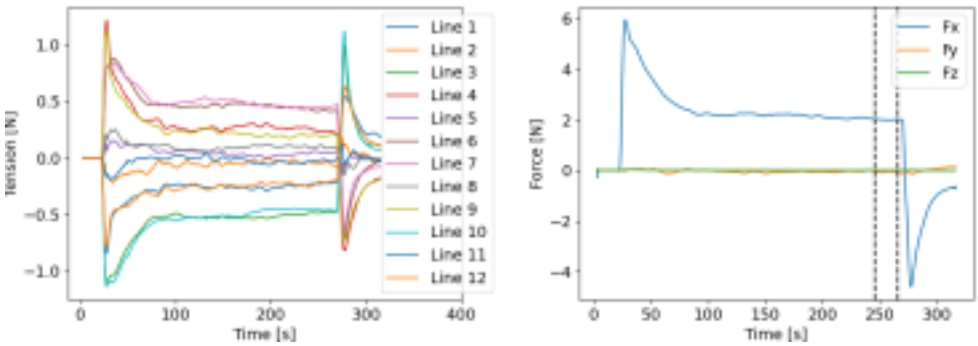
attached to the (rigid) floater at all trusses, so there was no folding pattern. In simulations where not all trusses were connected (not shown), similar folding patterns were obtained as in the experiments. The folding patterns were very sensitive to meshing, indicating sensitive physics, consistent with our experimental observations.

Skirt deformations observed in tests with the net applied (N1S3), presented in the lower part of Fig. 4, showed similar features as in the tests without net, although with some main differences. The deformations on the skirt front with the net present were smaller than for the tests without net as the presence of the net opposes deflections of the skirt through contact forces and geometric structural stiffness of the net-cage. Such contact is also pronounced on the aft side, where the skirt opposes the deflection of the net. The contact results in a discontinuous vertical slope of the net-cage, implying a positive vertical force component on the skirt from the net reducing the skirt draft on the aft side. Such contact with the net should be avoided as it can cause abrasion and wear of the net over time, in particular when combined with dynamic cage motions in waves, representing a possible failure mode.

The deformations of the elastic floater were deduced from measured motions of the position markers distributed on the floater. A modal representation of the floater in the horizontal plane was developed, where the modal amplitudes were obtained from fitting to measurements using least squares approximation. The observed deformations were small, less than 2% of the floater radius, and characterized by a negative radial displacement at the upstream side.

4.2. Drag forces

In Fig. 5 we present the bridle line tensions of all 12 bridles in the left part and the total mooring forces in the right part for a selected test with net and deep skirt (N1S3). By combining the measured



(a) Mooring line tension

(b) Resulting mooring force

Figure 5: Model scale mooring forces from towing of the large draft skirt applied to floater with net at tow speed $U_m = 0.07$ m/s ($U = 0.4$ m/s full scale). Left: Time-series of measured tension in each of the bridle lines. Right: Resulting directional mooring forces deduced from measured tension and mooring-line orientations.

mooring line tensions with the measured cage motions, the directional mooring forces were obtained, from which the resulting drag force on the model was calculated. The mooring force time-series can be described as follows: The first stage has a pronounced peak associated with added mass and inertia forces when accelerating the model to the given test speed. Thereafter, in the second stage, we observe a slow decay of the mooring force lasting for several units of non-dimensional time $\hat{t} = tU/D$, particularly for the lower tow speeds (0.2 m/s and 0.4 m/s full scale). The third stage starts when the decay trend expires and the measured force approaches a steady mean value. The steady state drag force was then obtained

as the average value over at least one diameter tow-length. During the second stage, we observed that the deflection of the front decreased with time, indicating a reduction in the pressure difference across the membrane. As this occurred during steady towing at constant speed, we attribute this to the evolution of an opposing flow inside the skirt on the front side. We also observed that the aft appeared not to be tensioned at the lowest tow speed, when the front deformations were small and the shape was close to circular cylindrical. This is in agreement with the experimental study of the steady drag force on truncated rigid circular cylinders [2], where a segmented model allowed one to isolate the drag contributions from the front and aft of the model. These tests showed that the drag on the aft side of the truncated cylinder approached zero for given conditions, whereas the total drag force yielded a drag coefficient $C_D \approx 0.7$.

The near steady drag forces are presented in Fig. 6 as function of towing speed. The black circular

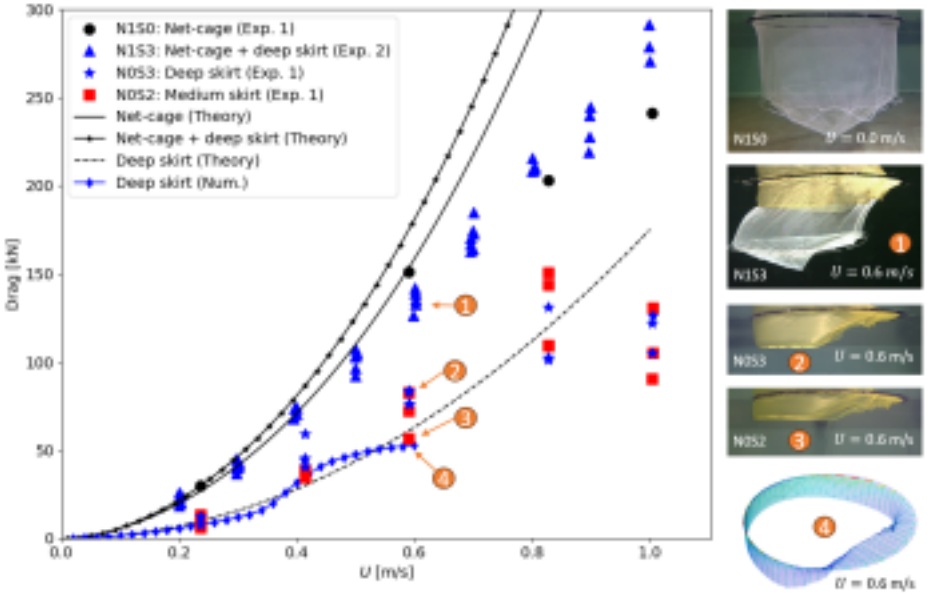


Figure 6: Full-scale steady drag force from towing in calm water. Theoretical estimates are based on quadratic drag model applied on the rigid initial geometry. Numerical results for deep skirt show effect of skirt deformation on drag, deviating from quadratic drag rule.

markers represent tests with net cage only (N1S0), the blue triangle markers both net and the deep skirt, the blue hexagon markers deep skirt only, while the red square markers medium skirt only. The solid black curve represents a theoretical prediction of the net cage only, as predicted by the screen load model by [4] given that it is undeformed. The solid black curve with markers represents similarly the undeformed net with the deep skirt attached. For the skirt, $C_D = 0.7$ is applied, based on the experiments by [2], and the part covered by the skirt is excluded in the drag calculation of the net. The dashed curve represents the drag load on the skirt if it was undeformed, using the projected area and $C_D = 0.7$. Last, the blue curve with markers represents the numerical predictions from our truss + rational drag load model. We consider the cases with net, with or without deep skirt first. The experimental values are in general lower than the theoretical curve, due to deformations. For the lowest towing velocity, the deformations are small, and the theoretical prediction is good. These observations are as expected. Perhaps less expected is that the total drag is very similar with and without skirt. This applies both to the theoretical estimate and the experiments. One would perhaps expect the total drag (and hence

mooring loads) to increase by adding a skirt. This is, however, not the case. We emphasize that this applies to steady current conditions only. In waves, inertia loads associated with the skirt will likely be considerable, with consequences not only for mooring but also for the loads transferred to the floater. We next consider the tests with skirt only. A first observation is that there is considerable spread in the experimental results. The measured line forces did not always reach a clear steady value, as exemplified in Fig. 5. We interpret this to be due to a slow convergence of the internal flow (discussed in the next section), some randomness in deformation pattern, as well as dynamic motions of the skirt (see Fig. 7). The spread is relatively less for the tests with net due to that there is less dynamic deformation in that case. A second observation is that the drag is lower for 1.0m/s than 0.8m/s. For these high velocities, the skirt gradually collapses with a reduced exposed area as consequence. See the upper right part of Fig. 4, where the case with 0.8 m/s is presented. The effect is even more pronounced for 1.0 m/s (not shown). On the contrary, for 0.4 m/s the deformation of the front part of the skirt gives the opposite effect: the measured drag is in fact significantly higher than that for a rigid (undeformed) cylinder. We interpret this to be caused by exposure of the rear part, with a larger drag due to parachute type effect where an adverse membrane curvature reduces compliance while increasing the momentum transfer to the fluid. The drag is very similar for the medium and deep skirts. The reason is at present not clearly understood. One candidate can be larger relative deformations of the deep skirt, but this is still under investigation.

Our numerical simulations with the truss + simplified drag model provide reasonable drag predictions, at least for velocities below 0.5 m/s. It appears that we are able to predict the "parachute" effect, with an increased drag in the range $0.4 - 0.5$ m/s, relative to undeformed cage (dashed curve). For 0.6 m/s the numerical model under predicts the drag. A feasible reason may be that our rational drag load model is not very good when the skirt deformations are as shown, characterized by a part that is horizontal, and one part that is nearly vertical. However, this type of skirt deformation does not occur when the net cage is there. Since the situation for design is with net cage, and not skirt alone, we conclude that our rational truss + simplified drag model may be of practical use in the case of current only. Future developments must include waves as well, i.e. wave-current-structure interaction.

A last comment goes to a flutter type motion. For the lowest test speed with the deep skirt and floater, we observed slow flutter type motions of the skirt. This occurred after the initial transient phase, where a steady-state drag force was expected. The flutter motions appeared to originate from the front and propagate towards the aft side. As shown in Figure 7, the drag force also shows an oscillating behavior at this stage. The oscillation period is around one non-dimensional unit of time ($\hat{t}$), corresponding to 43 s in model scale, or 4.1 minutes full scale. When this occurred, the membrane tension on the aft side seemed to be significantly reduced. The flutter-like behavior was observed in repetition tests, although with some differences in the phasing and amplitude of the oscillations.

4.3. Flow displacements

Example visualizations of flow displacements are presented in Fig. 8, where the images to the right show flow traces from a colorant (potassium permanganate) released upstream of the models' center-plane during tests with the skirt model N0S3. We observed that the skirt causes the incident flow to be deflected below the skirt. Some of the colorant was captured by the aft side of the skirt and circulated inside the cage. The compilation of images to the left in Fig. 8 is from a test with the deep skirt and net model N1S3, where stream traces obtained with particle tracking velocimetry (PTV) are drawn on top of the images. We divide the temporal evolution of the free surface flow into the following stages: 1) The inertial phase ($tU/D < 1$), startup where contained water is suddenly accelerated forward. 2) Transition phase ($1 < tU/D < 9$) where a viscous wake flow is gradually developing interior of the skirt. 3) steady vortex phase ($9 < tU/D$) where a vortex pair is formed, causing the surface flow along the center plane to be directed opposite to the outer incident current direction. Two internal stagnant regions appear on the free surface near the center plane of the cage both at the front and the aft side. Flow velocities inside the cage from the same test are shown in Fig. 9. The flow velocities are relative to a reference frame fixed to the model. The time-series on the left of Fig. 9 shows inline (u) and transverse

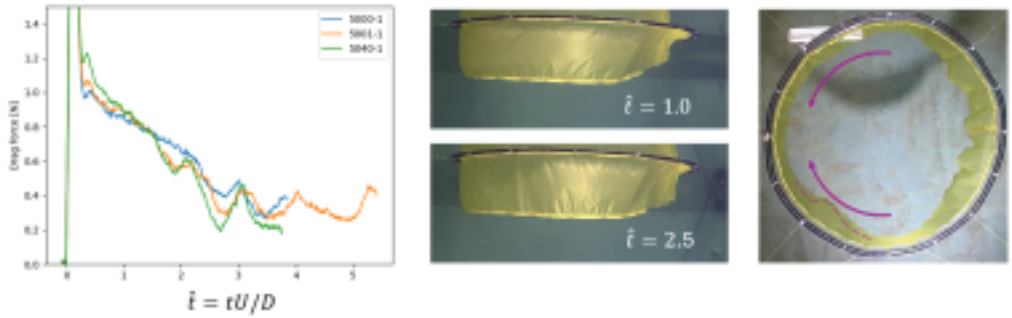


Figure 7: Dynamic skirt response at low speed steady towing. Left: Drag force time-series from repetition tests with model N0S3 corresponding to $U = 0.2$ m/s plotted against non-dimensional time. Low frequency drag oscillations occur for $\hat{t} > 2$. Center: Snapshots from before (upper image) and after (lower image) onset of flutter-like response. Right: Propagation direction of skirt deflections.

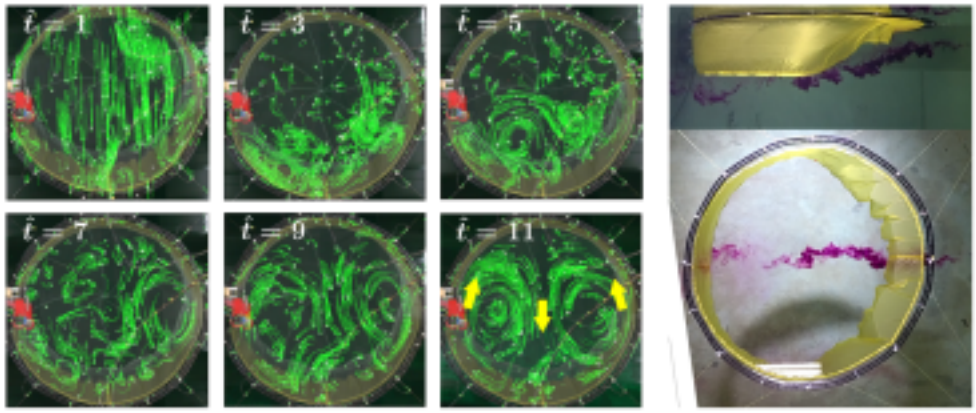


Figure 8: Free surface flow patterns obtained from tracing of floating marker particles (PTV) from evenly spaced intervals of non-dimensional time $\hat{t} = tU/D$ after start of towing with model N1S3. Full-scale current speed is $U = 0.4$ m/s. Incident flow direction is from bottom to top of the pictures. Right: Colorant released upstream shows vertical deflection of current from test with model N0S3.

(v) velocity components normalized by the tow speed, measured with a current probe at the center of the cage. Time-series for the two different depths are obtained from two repetition tests. The spikes of the inline component at the beginning and the end of the time-series are from acceleration and retardation of the model. For non-dimensional time $\hat{t} > 8$ we observe a significant positive inline velocity component, consistent with the steady vortex shown in Fig. 8, extending below the free surface. This inline velocity is almost absent at depths equal to half of the skirt draft (not shown). The free surface velocity field obtained with PTV is presented to the right in Fig. 9, corresponding to the stream traces in Fig. 8 for the non-dimensional time $\hat{t} = 11$. The obtained velocity field of the steady vortex phase appears to be consistent with current probe measurements at different locations below the free surface. The vortex pair in the free surface must be connected in the vertical plane, as the flow below the cage is directed in the negative $x-$direction. The slow time convergence of the interior flow explains the slow convergence of measured drag force.

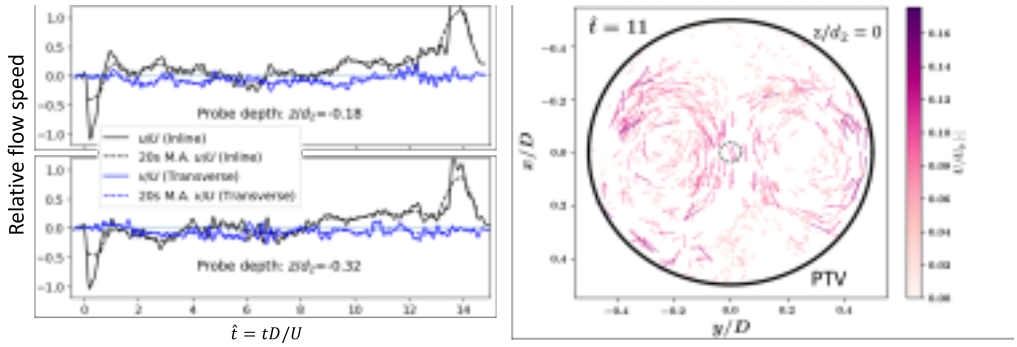


Figure 9: Normalized flow speed inside skirt in body-fixed reference for model N1S3. Moving averages for 20s time intervals are shown as dashed lines. Full scale current speed is $U = 0.4$ m/s. Left: Measured time-series of flow velocity (inline and transverse) at cage center for two different depths. Right: Vector field of surface flow obtained from PTV. Incident flow is in the negative $x-$direction.

5. Conclusion

A study on the current-induced hydrodynamics effects of aquaculture lice-skirts was presented. The study was based on model testing of skirt models fixed to a circular floater with and without net, supplemented by numerical simulations. In the model test of lice-skirt without net we observed large deflections of the lice-skirt reducing the skirt draft on the upstream side. This caused an increased current exposure on the downstream side, increasing the drag force at moderate current speeds. For tests with net included, the skirt deflections were less pronounced, due to contact forces from the net. Then, the increased drag from the skirt was mostly compensated for by a reduced drag on the net due to shielding. Investigation of flow deviations caused by the skirt reveals that incident current is mainly deflected downwards by the skirt and not around its sides as perhaps intended from a practical viewpoint. Further, we observe slow evolution of a viscous recirculation zone inside the cage, influencing the skirt deformations and the induced drag. We also observed that some of the incoming flow was captured and circulated within the skirt.

Acknowledgments

The work was funded by the Norwegian Research Council through the FlexAqua project (grant no. 284361) under the MARTERA program and by SFI Blues (grant no. 309281).

References

[1] Kristbjörg Edda Jónsdóttir, Andreas Ugelvik Misund, Leif Magne Sunde, Merete Bjørgan Schrøder, and Zsolt Volent. Lice shielding skirts through the decade: Efficiency, environmental interactions, and rearing challenges. *Aquaculture*, 562:738817, 2023.

[2] Trygve Kristiansen, David Kristiansen, and Arnt Fredriksen. Experimental study of drag loads on open and closed low-aspect-ratio circular cylinders in steady current. *Journal of Fluids and Structures*, 118:103851, April 2023.

[3] S. Mukherjea and G. Bandyopadhyay. Separated flow about a wedge. *The Aeronautical Journal*, 94(936):196–202, 1990.

[4] Trygve Kristiansen and Odd M. Faltinsen. Modelling of current loads on aquaculture net cages. *Journal of Fluids and Structures*, 34:218–235, October 2012.

10th International Conference on HYDROELASTICITY IN MARINE TECHNOLOGY
Trondheim, Norway, June16$^{\text{th}}$-18$^{\text{th}}$, 2026

Computational Performance of Finite Elements Used in Hydroelastic Analysis of Aquaculture Nets

Palaversa, M.[1,*] Yu, Z.[1], and Sævik, S.[1]

[1] Department of Marine Technology, Norwegian University of Science and Technology, Trondheim, Norway

Abstract. As aquaculture facilities move to more exposed, offshore locations, they are acted upon by much stronger waves, currents and winds causing greater operational loads and increasing probability of encountering extreme loads. Hydroelastic analyses of aquaculture nets exposed to the sea loads based on the finite element method (FEM) offer an accurate and a detailed picture of strains and stresses in the twines. However, this comes at a significant computational cost, which is often prohibitive to use of these approaches in engineering practice. In this paper, we study computational performance of a recently proposed membrane quadrilateral FE and two alternative approaches – one based on a triangular membrane FE and, a traditional one, based on the truss FE – when an explicit dynamic analysis is employed to calculate the structural response. A superior performance of the quadrilateral membrane element over the other two is demonstrated by means of a comparison with two experiments and available literature results including nets of increasing complexity in a steady uniform current.

Key words: *net-like structure; aquaculture; aquaculture net; membrane element; finite element analysis*

1. Introduction

As aquaculture facilities move to open sea, loads on them increase leading to potentially big deformations, which can result in their loss and escape of fish from the cages. This could have serious environmental and financial consequences [1]. Thus, it is important to know structural behaviour of the aquaculture structures, accurately assess their safety and reliability and manage risks arising in normal and extreme operational conditions [2].

Critical elements of the aquaculture structures are their nets. They prevent fish from escaping and transmit most of the environmental loads on rest of the structure. Since loads on the nets depend on their instantaneous shape, these analyses are a prime example of strongly coupled hydroelastic analyses [3].

Most research devoted to the hydroelastic behaviour of aquaculture and fishing nets was concerned with accurate assessment of hydrodynamic loads on the nets [4] establishing two dominant force models – one based on the Morison's equation [5], where each twine is considered in isolation when the loads are calculated, and another one which considers a portion of the net containing multiple twines. The latter one is referred to as the screen model [6].

Regarding assessment of the structural behaviour of the aquaculture and fishing nets, a 1D (truss) element is predominately used in scientific community. The main advantages of using this element are that it can be very easily implemented in a new code and that it is available in all commercial FE programs, which can then be used for this purpose [7].

The first FE derived specifically for the nets was a quadrilateral membrane FE for nets with diagonal meshes [8]. The second membrane FE was a triangular FE [9] that could be used for nets with diagonal

[*]Correspondence to: marin.palaversa@ntnu.no

and square meshes. This then allowed for application of the element in the analysis of aquaculture nets since these predominantly have square meshes. The element was later also extended such that it could be used for structural analysis of nets with hexagonal meshes [10]. There is also a quadrilateral membrane element that can be used for nets with square and hexagonal meshes implemented in a commercial program dedicated to the structural analysis of aquaculture nets called Aquasim [11]. Recently, a quadrilateral membrane element for nets with square meshes was proposed [12]. The element assumed linear distribution of load along its sides and was, thus, equivalent to FE discretisations including multiple triangular membrane or truss finite elements.

Regardless of the FE used, there are two groups of FE approaches in dynamic structural analysis: the explicit and the implicit ones [13]. The latter, being unconditionally stable, allow for use of a bigger time step in the analysis and are, thus, more computationally efficient in many engineering problems. The time step, however, must be reduced if relatively fast phenomena occur. One such phenomenon is the occurrence of snap loads in the nets due to their inability to withstand compressive load. It was recently shown [14] that the time step had to be reduced to as little as 1/3000 of the wave period (i.e. to about $5 \cdot 10^{-4}$ for the wave conditions in the study) in order to obtain tension forces occurring in the twines in those conditions. Additionally, the implicit dynamic approaches require assembly and decomposition of the global stiffness matrix – tasks which are difficult to parallelise. On the other hand, the explicit dynamic analysis does not require the global stiffness matrix if the lumped mass matrix is used making calculation of displacements and accelerations independent, i.e. these calculations can be performed on the element level. This then opens a question about potential gains in terms of computational efficiency and reduction of analysis times, which is often considered to be the main barrier to a widespread use of the finite element method in engineering practice [15], if the explicit dynamic analysis with the new quadrilateral FE is used.

In this paper, three finite elements, the truss FE (referred to as the consistent net element according to [16]), the triangular membrane element proposed in [9] and the quadrilateral membrane element proposed in [12], are compared in terms of their computational performance in hydroelastic analysis of aquaculture nets when the explicit structural dynamic analysis is used. Two examples, presented in Section 3, are used to this end: a simple square net and a more complex cylindrical net – both acted upon by a steady uniform current.

2. Explicit dynamic structural analysis of aquaculture nets

The discussion in this subsection is based on Bathe [13]. Check that reference for a more detailed exposition.

Equations of equilibrium governing the structural response of a non-linear dynamic system can be written as:

$$\mathbf{M}\ddot{\mathbf{U}} + \mathbf{C}\dot{\mathbf{U}} + \mathbf{K}\mathbf{U} = \mathbf{F} \tag{1}$$

where $\ddot{\mathbf{U}}$ is a vector of nodal accelerations, $\dot{\mathbf{U}}$ is a vector of nodal velocities and $\mathbf{U}$ is a vector of nodal displacements. $\mathbf{M}$, $\mathbf{C}$ and $\mathbf{K}$ are the mass, damping and stiffness matrix, respectively. $\mathbf{F}$ is a load vector. In this study, $\mathbf{C} = \mathbf{0}$ because the damping is provided by the hydrodynamic forces. Eq. (1) then reduces to:

$$\mathbf{M}\ddot{\mathbf{U}}(t) + \mathbf{K}(t)\mathbf{U}(t) = \mathbf{F}(t) \tag{2}$$

To solve for the displacements and the accelerations, Eq. (2) needs to be integrated in time. For that purpose, the central differences are used. The acceleration vector is approximated as follows:

$$\ddot{\mathbf{U}}(t) = \frac{1}{\Delta t_{an}^2}\left[\mathbf{U}\left(t - \Delta t_{an}\right) + 2\mathbf{U}(t) + \mathbf{U}\left(t + \Delta t_{an}\right)\right] \tag{3}$$

where Δt_{an} is a time step used in the analysis. If Eq. (3) is introduced to Eq. (2), an expression for the

displacement vector at $t + \Delta t_{an}$ is obtained:

$$\mathbf{U}\left(t + \Delta t_{an}\right) = \frac{\left[\mathbf{F}_{\text{ext}}(t) - \mathbf{F}_{\text{int}}(t)\right] \Delta t_{an}^2(t)}{\mathbf{M}} + \mathbf{U}(t) + \Delta\mathbf{U}(t - \Delta t_{an}) \tag{4}$$

If the mass matrix is diagonal, elements of the displacement and acceleration vector can be evaluated independently of each other:

$$U_i\left(t + \Delta t_{an}\right) = \frac{\left[F_i(t) - F_{\text{int},i}(t)\right] \Delta t_{an}^2(t)}{M_{ii}} + U_i(t) + \Delta U_i(t - \Delta t_{an}) \tag{5}$$

$$\ddot{U}_i(t) = \frac{1}{\Delta t_{an}^2}\left[U_i\left(t - \Delta t_{an}\right) + 2U_i(t) + U_i\left(t + \Delta t_{an}\right)\right] \tag{6}$$

Since all terms on the right-hand side of Eq. (5) are known at the current time t, $U_i\left(t + \Delta t_{an}\right)$ can be computed. This result is then introduced to Eq. (6) to find the acceleration vector. The fact that the solution can be obtained by solving for each element of $\mathbf{U}$ and $\ddot{\mathbf{U}}$ independently of the other elements means that the process can be parallelised, enhancing computational performance of the analysis.

For an explicit dynamic analysis to be stable, the analysis time step must be less than the critical time step:

$$\Delta t_{cr,\text{el}} = \frac{T_{min,\text{el}}}{\pi} \tag{7}$$

where $T_{min,\text{el}}$ is the shortest period of free vibrations (natural period) associated with a FE in the FE discretisation. It can be determined by finding the smallest value among all natural periods of the discretisation:

$$T_{ij,\text{el}} = \frac{2\pi}{\omega_{ij,\text{el}}} \tag{8}$$

where $\omega_{ij,\text{el}}$ is a frequency of the free vibrations (natural frequency) and el denotes the FE discretistion (based on CNEs, the triangular or quadrilateral membrane elements). The natural frequency can be obtained by the following expression:

$$\omega_{ij,\text{el}} = \sqrt{\frac{k_{ij,\text{el}}}{m_{ij,\text{el}}}} \tag{9}$$

where $k_{ij,\text{el}}$ and $m_{ij,\text{el}}$ are corresponding elements of element stiffness and mass matrix.

In this study, structural mass of the elements is lumped in the nodes resulting in a diagonal mass matrix (the lumped mass matrix):

$$\mathbf{m}_{\text{el}} = \begin{bmatrix} m_{11,\text{el}} & 0 & \cdots \\ 0 & m_{22,\text{el}} & \cdots \\ \vdots & \vdots & \ddots \end{bmatrix} \tag{10}$$

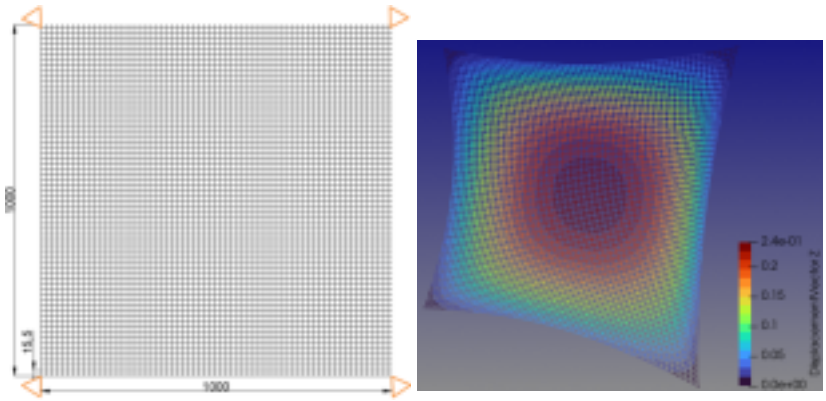
Since $\mathbf{m}_{\text{el}}$ is diagonal, it turns out that only diagonal elements in both the mass and the stiffness matrix need to be considered leading to the following expression for ω:

$$\omega_{ii,\text{el}} = \sqrt{\frac{k_{ii,\text{el}}}{m_{ii,\text{el}}}} \tag{11}$$

By introducing Eq. (11) to Eq. (8), the folowing natural periods are obtained:

$$T_{ii,\text{el}} = 2\pi\sqrt{\frac{m_{ii,\text{el}}}{k_{ii,\text{el}}}} \tag{12}$$

$T_{min,\text{el}}$ is then the shortest of the periods $T_{ii,\text{el}}$. Since the stiffness is a property of a given structure, it does not depend on the choice of a finite element used in the analysis. However, the mass depends on the element's ability to encompass as many twines as possible and, thus, increase the critical time step as will be demonstrated in examples provided in the remainder of this section.



(a) The square net in undeformed configuration. The dimensions are given in millimetres (mm).

(b) The square net in deformed configuration. The dimensions are given in metres (m).

Figure 1: The square net pinned at four vertices

3. Validation and verification examples

The three FEs, the consistent net element (CNE), the triangular and quadrilateral membrane element, together with the Morison's hydrodynamic model are implemented in OOFEM (Object-Oriented Finite Element Method), an open-source program for solving problems in continuum mechanics by the finite element method [17]. The code is available on GitHub (https://github.com/mpalaversa/oofem).

3.1. A square net in a steady current

A square net of a side $a = 1$ m consists of square meshes with a half-mesh $l_0 = 15.5$ mm and twines of a diameter $d_t = 1.6$ mm. The twines' material has density of $\rho_t = 1150$ kg/m^3 and a modulus of elasticity $E_t = 2 \cdot 10^9$ Pa. The net is pinned at its four vertices. It is under an action of a steady, uniform current normal to the plane of the undeformed net with a velocity of 1 m/s. Hydrodynamic loads are calculated by using the Morison's model as given in [5]. The net is shown in Figure 1a. More details can be found in [16].

There is in total 13 FE models built – 4 for each element with a varying FE mesh density shown in Figure 2 and an additional FE model where each twine is descritised by 1 truss element with non-linear material behaviour (no compressive stiffness). The coarsest FE mesh is obtained by subdividing the net into 16 basic units of discretisation (UDs). Each UD is then descritised by the minimum number of FEs possible, i.e. 4 CNEs, 2 triangular membrane elements and 1 quadrilateral membrane element. The next coarsest mesh is obtained by subdividing the net into 64 UDs and so on.

The dynamic hydroelastic analyses are run to simulate 5 s of the real process. The deformed net is shown in Figure 1b. Verification of the analyses' results is carried out by comparing the results with those available in the literature and the truss model. The comparison is provided in Table 1 for the drag force, vertical displacement and maximum stresses in twines.

The following conclusions can be drawn from the table:

- The drag force obtained by the 13 models is similar to the literature results, especially to the study in [16], which is also based on the Morison's hydrodynamic model and the finite element method,
- As the FE mesh gets refined, all the models converge to the results obtained by the truss FE model, i.e. the model where each twine is modelled by 1 truss FE,

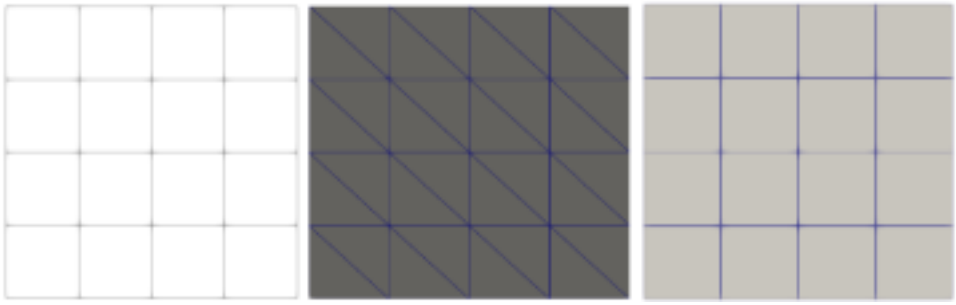


Figure 2: FE models of the square net in the steady uniform current for the FE mesh refinement of 4x4 UDs (units of discretisation). From left to right, the figures show the model consisting of CNEs, the model consisting of the triangular membrane elements and the model consisting of the quadrilateral membrane elements.

Table 1: The drag force, vertical displacement and maximum stress in the twines obtained by the 13 models in this study, by FEM/Morison model in [16] and by an empirical formula from of Aarsens et al. as presented in [16]. (CNE, Tri and Quad denote the consistent net element, the triangular membrane element and the quadrilateral membrane element, respectively. Numbers in parentheses denote the FE model.)

Model	Drag force (N)	Drag force diff. w.r.t truss (%)	Vertical displacement (mm)	Vertical displ. diff. w.r.t truss (%)	Max stress in twines (MPa)	Max stress diff. w.r.t truss (%)
Aarsnes et al.	135.61	29.61	N/A	N/A	N/A	N/A
Tsukrov et al.	106.50	1.79	N/A	N/A	N/A	N/A
CNE (4x4)	110.38	5.50	185.04	-22.53	9.45	-72.62
CNE (8x8)	107.52	2.76	202.14	-15.37	14.56	-57.81
CNE (16x16)	104.88	0.24	224.21	-6.13	22.02	-36.18
CNE (32x32)	102.40	-2.14	245.01	2.59	33.48	-2.98
Tri (4x4)	110.90	5.99	185.91	-22.16	9.57	-72.26
Tri (8x8)	108.16	3.37	202.95	-15.03	14.70	-57.41
Tri (16x16)	105.50	0.83	225.22	-5.70	22.24	-35.56
Tri (32x32)	102.83	-1.72	246.12	3.05	33.88	-1.83
Quad (4x4)	110.86	5.96	186.10	-22.08	9.60	-72.19
Quad (8x8)	108.15	3.36	202.99	-15.01	14.71	-57.39
Quad (16x16)	105.49	0.82	225.26	-5.69	22.24	-35.55
Quad (32x32)	102.82	-1.73	246.13	3.05	33.88	-1.82
Truss	104.63	N/A	238.84	N/A	34.51	N/A

- The results obtained by corresponding models based on the three FEs are very similar demonstrating that similar accuracy is achieved by the three elements when the equivalent FE discretisation is used (note that the similarity of the results here depends not only on the expected identical accuracy in terms of the elastic response, but also on similarity in applying the hydrodynamic loads,

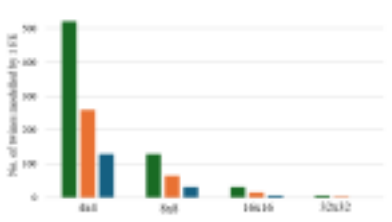
which might have led to the small difference in the results)

Table 2 provides measures of the computational performance. It is observed that the element's ability to encompass as many twines as possible leads to increase in the critical mass term, which results in bigger critical time steps. This also follows from the theoretical analysis of the previous section (see Eq. (12) and (7)). The consequence is shorter analysis times. This is demonstrated by the diagrams in Figure 3 as well.

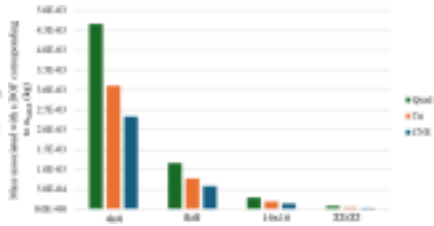
Table 2: Computational performance measures for the three FEs in each of the 12 FE models. The total time of the simulated (real) process is 5 s.

Model	No. of twines modelled by 1 FE	Critical time step Δt_{crit} (s)	Relevant stiff. mat. el., k_{ii}	Relevant mass mat. el., m_{ii}	Analysis time step Δt_{an} (s)	Analysis duration 1 core (min)	Analysis duration 4 cores (min)	Ratio 4 vs. 1 core
CNE (4x4)	130.07	2.68E-04	1.30E+05	2.33E-03	2.50E-05	1.92	0.40	0.21
CNE (8x8)	32.52	1.34E-04	1.30E+05	5.83E-04	1.25E-05	16.32	4.73	0.29
CNE (16x16)	8.13	6.70E-05	1.30E+05	1.46E-04	5.00E-06	54.68	21.35	0.39
CNE (32x32)	2.03	3.35E-05	1.30E+05	3.64E-05	2.50E-06	388.25	170.98	0.34
Tri (4x4)	260.15	3.08E-04	1.30E+05	3.11E-03	2.50E-05	1.03	0.33	0.32
Tri (8x8)	65.04	1.54E-04	1.30E+05	7.77E-04	1.25E-05	6.83	2.00	0.29
Tri (16x16)	16.26	7.73E-05	1.30E+05	1.94E-04	5.00E-06	70.60	27.53	0.39
Tri (32x32)	4.06	3.87E-05	1.30E+05	4.86E-05	2.50E-06	663.00	112.60	0.17
Quad (4x4)	520.29	3.79E-04	1.30E+05	4.66E-03	4.00E-05	0.58	0.25	0.43
Quad (8x8)	130.07	1.90E-04	1.30E+05	1.17E-03	2.00E-05	3.65	1.27	0.35
Quad (16x16)	32.52	9.48E-05	1.30E+05	2.91E-04	1.00E-05	73.88	8.15	0.11
Quad (32x32)	8.13	4.74E-05	1.30E+05	7.28E-05	5.00E-06	243.25	95.38	0.39

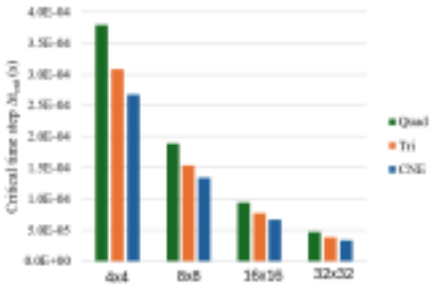
As can be seen, the difference in the critical time steps does not exactly correspond to the difference in the analysis durations. This is because the time step used in the analysis is smaller than the critical time step. This is usually the case in the explicit dynamic analysis [13]. In the analyses conducted in this study, the critical time step is determined for each of the 12 models. After that, the time step used



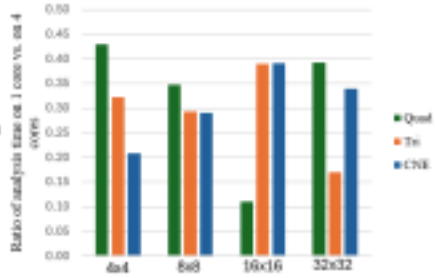
(a) Number of twines modelled by 1 FE in each of the 12 FE models



(b) Minimum element of the mass matrix for each of the 12 FE models



(c) Critical time steps for the 12 FE models



(d) Ratio of the analysis time on 4 cores vs. 1 core for the 12 FE models

Figure 3: Computational performance measures for the CNE, the triangular membrane and the quadrilateral membrane element in the square net example

in the analysis is determined by dividing the critical time step by 10 and rounding up the result to the closest divisor of 5. This is because the simulated process lasts for 5 s.

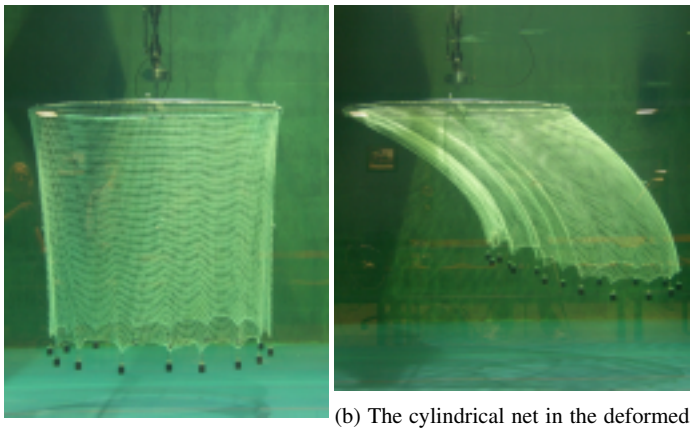
3.2. A cylindrical net in steady current

A cylindrical net, as given in [7] was considered (Figure 4). The net had a diameter of 1.75 m and a height of 1.5 m. It consisted of square meshes with a half-mesh of 8.3 mm and a twine diameter of 1.41 mm giving a solidity ratio of 0.35. The twines were made of Polyamide 6 (nylon) with a modulus of elasticity of 40 $\mathrm{N/mm^2}$ and a density of 1140 $\mathrm{kg/m^3}$.

The net was attached to a rigid steel ring along its upper edge and positioned in a flume tank with fresh water. The net was stretched by a system of 16 steel weights of a submerged weight of 4.48 N each.

The net was exposed to a steady uniform current of velocity of 0.5 $\mathrm{m/s}$ and a drag and lift force were measured. Deformation of the net was not measured directly, but photographs were taken during the experiment. Consequently, the deformation can be compared only qualitatively. More details about the experiment can be found in [7].

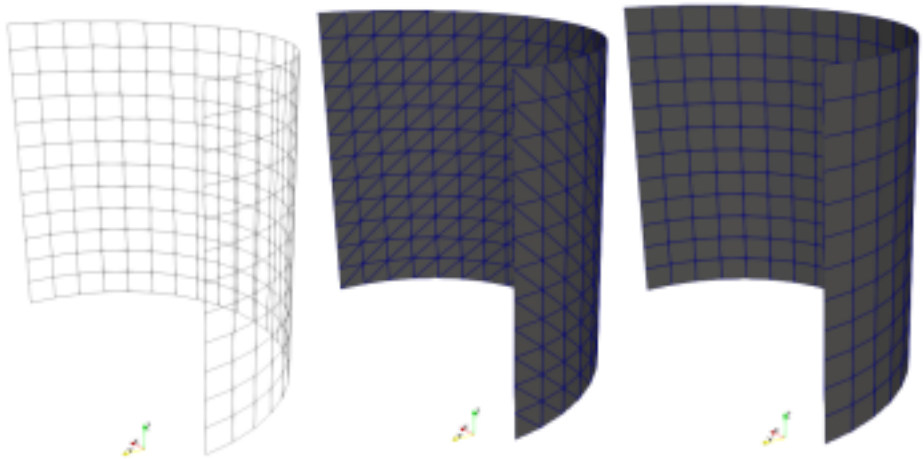
Based on the experimental set-up, a series of FE models consisting of the CNEs, the triangular membrane and the quadrilateral membrane elements was built (Figure 5) and compared with an FE model consisting of truss FEs built in [7]. The FE models built in this study differed in type of the FE used and density of the FE mesh. Figure 5 shows three FE models with the coarsest mesh consisting of 20 FEs in circumferential direction and 12 FEs depth-wise. Besides the three models shown in the figure, there are 6 more models built (consisting of 40×23 and 80×46 FEs) by refining the shown FE model. Both the FE models here and the truss FE model of [7] exploited the fact that the structure and loads were symmetric about the x-z plane (see Figure 5 for the coordinate system) and only a half of the structure was modelled.



(a) The cylindrical net in the undeformed configuration

(b) The cylindrical net in the deformed configuration at current velocity of 0.5 m/s

Figure 4: The cylindrical net during the experiment



(a) FE model of 20×12 CNEs

(b) FE model of 20×12 triangular membrane elements

(c) FE model of 20×12 quadrilateral membrane elements

Figure 5: FE models of the cylindrical net. The models as defined in the following way: $a \times b$. Here a represents a number of FEs in circumferential direction and b represents a number of FEs depth-wise

Hydrodynamic loads were calculated using the Morison's model both here (according to [5]) and in [7]. A constant drag coefficient of 1.15 was used in the calculation. The current had a constant uniform velocity in x-direction. More details about the hydrodynamic load model can be found in [12].

Table 3 gives hydrodynamic forces obtained by the 9 models of Figure 5, the truss model consisting of 40 elements in circumferential direction and 23 elements depth-wise (40×23) of Moe-Fore at al. [7] and the experiment. It can be seen that all the numerical models have approximately the same error compared to the experiment. These results are elaborated in more details in [12]. An additional verification of deformation of the net as obtained by the numerical model is also provided there (compare Figure 4b and Figure 6).

Table 4 shows the critical time step, the analysis time step and the total analysis time for the 9 FE models. The analysis time step is obtained by dividing the critical time step by 5 and rounding up the

Table 3: Hydrodynamic forces for the 9 FE models in the cylindrical net example, the study given in [7] and the experiment

Model	Drag force (N)	Lift force (N)	Drag force error (%)	Lift force error (%)
CNE (20x12)	122.48	34.80	-15.53	-26.33
CNE (40x23)	120.78	34.69	-16.70	-26.56
CNE (80x46)	118.27	32.42	-18.43	-31.36
Tri (20x12)	118.89	35.15	-18.01	-25.60
Tri (40x23)	118.36	34.56	-18.37	-26.84
Tri (80x46)	118.32	34.70	-18.40	-26.55
Quad (20x12)	118.61	35.42	-18.20	-25.02
Quad (40x23)	118.11	34.67	-18.54	-26.61
Quad (80x46)	118.32	34.70	-18.40	-26.55
Moe-Fore et al.	118.00	37.00	-18.62	-21.68
Experiment	145.00	47.24	N/A	N/A

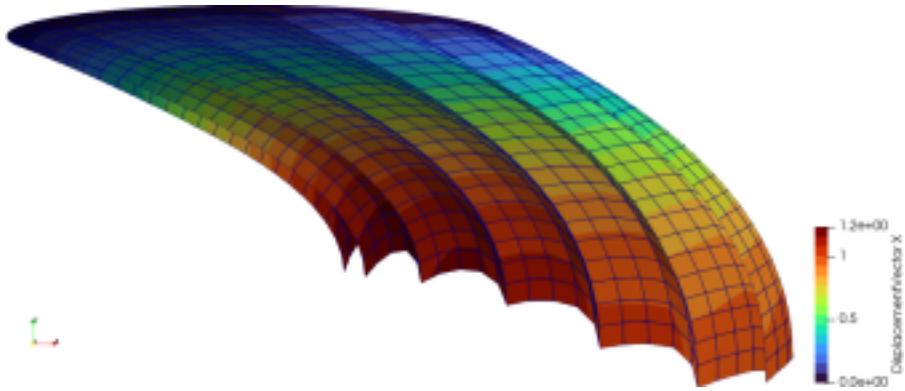


Figure 6: Deformed net at current velocity of 0.5 m/s – the FE model 40×23 with quadrilateral elements. Displacements in direction of the current (in m) are depicted.

result to the closest divisor of 30. This procedure is used because the analyses simulate 30 s of the real process.

As the FE meshes get refined from the models with 20×12 FEs to the models with 80×46 elements, the critical time steps decrease and, consequently, the corresponding analysis time steps. This leads to longer duration of the analyses as can be seen from the table. This increase in the analysis time is greatest for the models based on the CNEs, followed by the models based on the triangular element although the decrease in the critical time steps and the analysis steps is similar for models based on all three elements (the decrease in the analyses time steps is about 50% going from the 20×12 towards the 80×46 models). This observation implies that the time step size is not the only parameter governing the analyses' duration. The increase in the number of FEs in the models leads to an increased duration of each time step leading to the longer analyses. It can be then concluded that the critical time step is not the only parameter governing the computational performance. It is important to reduce the duration of individual time steps as well. The membrane elements have an advantage in this regard compared to

Table 4: Computational performance measures for the 9 FE models in the cylindrical net example. The analysis time refers to simulating 30 s of the real process.

Model	Critical time step (s)	Analysis time step (s)	Analysis time (min)
CNE (20x12)	$9.44 \cdot 10^{-4}$	$2 \cdot 10^{-4}$	10.5
CNE (40x23)	$4.91 \cdot 10^{-4}$	$1 \cdot 10^{-4}$	72.2
CNE (80x46)	$2.46 \cdot 10^{-4}$	$5 \cdot 10^{-5}$	1780.0
Tri (20x12)	$1.09 \cdot 10^{-3}$	$2.4 \cdot 10^{-4}$	8.6
Tri (40x23)	$5.64 \cdot 10^{-4}$	$1.2 \cdot 10^{-4}$	78.2
Tri (80x46)	$2.83 \cdot 10^{-4}$	$6 \cdot 10^{-5}$	460.2
Quad (20x12)	$1.33 \cdot 10^{-3}$	$2.5 \cdot 10^{-4}$	7.7
Quad (40x23)	$6.94 \cdot 10^{-4}$	$1.5 \cdot 10^{-4}$	49.3
Quad (80x46)	$3.48 \cdot 10^{-4}$	$6 \cdot 10^{-4}$	438.0

the CNEs and the quadrilateral membrane element in particular since they provide equal accuracy with smaller FE models.

4. Conclusion

This study showed that a hydroelastic analysis of aquaculture nets is computationally most efficient when quadrilateral membrane elements are used followed by triangular membrane elements. The least computationally efficient analysis can be expected when the consistent net element (truss) is used. Within the scope of explicit structural dynamic analysis, which is stable only if the analysis time step is smaller than a critical time step, it was shown that the critical time step is about 40% greater when the quadrilateral element is used than when the CNE is used and about 16% greater than when the triangular element is used. This translates to the analysis duration.

It was also shown that the reason for this relative behaviour of the FEs lies in the fact that the quadrilateral element can encompass most twines for the same accuracy of the analysis compared to the other two elements. This results in the greatest mass matrix term relevant for determination of the critical time steps, which increases with the increase of the element's mass. Thus, if one is concerned with designing new FEs for the net structures, one should seek to design an element that encompasses as many twines as possible. It then naturally follows that membrane (2D) elements have an advantage in terms of computational performance compared to 1D elements and that quadrilateral elements have the advantage over the triangular ones.

Apart from the critical time step size, it was demonstrated that duration of each time step also governs the computational performance and that the membrane elements, in general, and the quadrilateral membrane element, in particular, are preferred over the CNEs. This is because an increase in the number of FEs needed to achieve the same accuracy is much greater when the CNEs are used than when the membrane elements are used. It can then be concluded that the quadrilateral membrane elements increase the computational performance in two ways – first, by allowing the greatest analysis time step and second, by decreasing the size of the FE model used in the analysis and, consequently, the duration of each time step.

Finally, parallelisation of the code implementing the explicit dynamic structural analysis was investigated. It was shown that running the program on 4 cores reduces the analysis time by approximately 60% to 70%.

In our future work, we plan on investigating the parallelisation capabilities of the explicit dynamic analysis and compare it with implicit dynamic analysis of the same structures. It also remains to investigate a few outliers which show a much greater reduction of the computational time (of about 80% to 90%.

Acknowledgments

We are grateful to Pål Furset Lader from our department for providing us with photographs of the cylindrical net experiment.

References

[1] Holmer, M. Environmental issues of fish farming in offshore waters: Perspectives, concerns and research needs. *Aquacult. Environ. Interact.*, 1(1):57–70, August 2010.

[2] Føre, M., (first), Sørensen, A., Asbjørnslett, B. E., Greco, M., Hartmann, K., Halse, M., Hammernes, A., Hukkelås, T., Mjønes, J., Bjelland, H., and Størkersen, K. Offshore aquaculture (in Norwegian). Technical report, Workgroup for offshore aquaculture, Trondheim, 2022.

[3] Lader, P. F. and Fredheim, A. Dynamic properties of a flexible net sheet in waves and current—A numerical approach. *Aquacultural Engineering*, 35(3):228–238, October 2006.

[4] Cheng, H., Li, L., Aarsæther, K. G., and Ong, M. C. Typical hydrodynamic models for aquaculture nets: A comparative study under pure current conditions. *Aquacultural Engineering*, 90:102070, August 2020.

[5] Haritos, N. and He, D. Modelling the response of cable elements in an ocean environment. *Finite Elements in Analysis and Design*, 11(1):19–32, May 1992.

[6] Kristiansen, T. and Faltinsen, O. M. Modelling of current loads on aquaculture net cages. *Journal of Fluids and Structures*, 34:218–235, October 2012.

[7] Moe-Føre, H., Lader, P., Lien, E., and Hopperstad, O. Structural response of high solidity net cage models in uniform flow. *Journal of Fluids and Structures*, 65:180–195, August 2016.

[8] Tronstad, H. and Larsen, CM. NFEM Approaches for Calculating Fishing gear as a System of Flexible Lines. In *Proceedings of the 16th International Conference on Offshore Mechanics and Arctic Engineering*, volume 1-A, pages 101–108, Yokohama, Japan, 1997. American Society of Mechanical Engineers.

[9] Priour, D. Calculation of net shapes by the finite element method with triangular elements. *Commun. Numer. Meth. Engng.*, 15(10):755–763, October 1999.

[10] Priour, D. *A Finite Element Method for Netting: Application to Fish Cages and Fishing Gear*. SpringerBriefs in Environmental Science. Springer Netherlands, Dordrecht, 2013.

[11] Berstad, A. J. The Aquasim package theory user manual. Technical report, Aquastructures, Trondheim, Norway, 2023.

[12] Palaversa, M., Yu, Z., and Sævik, S. Structural modelling of aquaculture nets with square meshes by quadrilateral membrane finite elements. *Aquacultural Engineering*, 113:102706, March 2026.

[13] Bathe, KJ. *Finite Element Procedures*. Prentice Hall, Upper Saddle River, New Jersey, 2nd edition, 2014.

[14] Zhang, K., Liu, B., Yao, H.-D., Chen, H., and Chen, J. Numerical modeling of dynamic responses of aquaculture net cages in waves: Snap load prediction and the effect of nonlinear added mass. *Aquacultural Engineering*, 113:102701, March 2026.

[15] Slagstad, M., Yu, Z., and Amdahl, J. A simplified approach for fatigue life prediction of aquaculture nets under waves and currents. *Ocean Engineering*, 272:113859, March 2023.

[16] Tsukrov, I., Eroshkin, O., Fredriksson, D., Swift, M., and Celikkol, B. Finite element modeling of net panels using a consistent net element. *Ocean Engineering*, 30(2):251–270, February 2003.

[17] Patzak, B. and Bittnar, Z. Design of object oriented finite element code. *Adv. Eng. Softw.*, 32(10-11):759–767, 2001.

10th International Conference on HYDROELASTICITY IN MARINE TECHNOLOGY
Trondheim, Norway, June 16th-18th, 2026

Hydroelastic Behaviour of a Floating Hexagonal Net Cage under Regular Waves

Mohapatra, S.C.* Ji, J. and Guedes Soares, C.

Centre for Marine Technology and Ocean Engineering (CENTEC),
Instituto Superior Técnico, Universidade de Lisboa,
Av. Rovisco Pais, 1049-001 Lisboa, Portugal

Abstract. In this paper, a mathematical model of wave interaction with a hexagonal-shaped floating net cage model in finite water depth is developed. The hexagonal-shaped cage is modelled based on the cosine-type radial perturbation function, whilst the flexible net is designed using a porous membrane based on Darcy's Law. The velocity potentials are obtained via a Fourier-Bessel expansion, along with dual Bessel series relations associated with the radial function. The analytical solution of the model is derived by using the least-squares approximation method and the matching technique. The numerical results are produced by developing MATLAB code based on the analytical solutions. The analytical result of horizontal displacements of a hexagonal flexible net cage for two different values of mooring stiffnesses are compared with independent numerical AQWA model simulations. Further, the hydroelastic response of the hexagonal net cage under different model parameters is investigated.

Key words: *Hydroelastic response*; *Hexagonal net-cage*; *Mathematical formulation*; AQWA; *Displacements; Mooring lines*

1. Introduction

Offshore aquaculture represents a critical solution to the escalating problem of marine resource depletion and the dietary needs of a continuously growing world population. Its development is essential for addressing the current scarcity of fish and scaling up production to fulfil the world's demand. Therefore, the development of a moored hexagonal-shaped cage is an alternate and new solution that finds applications in offshore aquaculture for fish farming.

Designing reliable, budget-friendly fish farms using moored hexagonal net cages is a complex engineering task. Mastering this hydroelastic challenge is essential for allowing developing nations to unlock the economic potential of their marine environments through sustainable offshore aquaculture.

Studies were focused on the floating net cage to analyse the hydrodynamic characteristics of the net cage under mooring loads, and current, for regular and irregular waves based on numerical and physical model tests in [1]. Semi-closed (bottom part) floating net cage models based on numerical models of WAMIT and LS-DYNA and compared with the closed fish cage in [2]. The resistance capacity of the mooring system for offshore aquaculture farm using the reliability method was performed in [3].

An interesting and challenging aspect of the floating flexible net cage is the mathematical formulation and analytical/semi-analytical solution under marine environmental conditions. There have been a few potential and well-documented works reviewed here and discussed below: In [4], a mathematical model was formulated for a freely floating closed, 2D cage exposed to wave action and the wave-driven rigid-body responses, specifically sway, heave, and roll, were considered for the dynamic analysis. The floating net cage was used to analyze the hydrodynamic characteristics of the net cage under mooring loads, and current, for regular and irregular waves based on numerical and physical model tests [5]. Using ANSYS AQWA software, reference [6] established the design parameters for square semisubmersible open-net cages. The study assessed the hydrodynamic behavior of these cages across various configurations (single, double, and four-cage clusters) under the influence of regular sinusoidal waves. Researchers have employed a combination of mathematical techniques, including the eigenfunction expansion method, and the least-squares approximation, as outlined in [7], to investigate

* Correspondence to: sarat.mohapatra@centec.tecnico.ulisboa.pt

the interaction between surface waves and a vertically oriented, flexible net submerged in water of limited depth. A semi-analytical framework was introduced in [8] to calculate the vertical accelerations of a configuration of partially submerged, flexible circular floating structures exposed to regular wave conditions. This methodology integrated slender body theory with matched asymptotic expansions, all rooted in the foundations of linear wave theory.

A review of theoretical models of the hydroelastic behavior of net cages and elastic floaters was provided in [9]. An analytical model of an array of floating flexible net cages was developed and the flow field among the cages under current velocity was analysed in [10]. Recently, the effect of wave loading on the bottom fixed octagonal net cage platform based on experimental and numerical Star-CCM software [11]. The effect of wave-current on the floating circular elastic floater based on the theoretical approach was studied in [12].

From the literature, it is confirmed that there is no mathematical model associated with a floating hexagonal net cage developed and analysed its hydroelastic behaviour. Therefore, here, a mathematical model of wave interaction with a hexagonal-shaped floating net cage model in finite water depth is developed. The cage frame is modelled based on the elastic beam theory, whilst the flexible net is designed using a porous membrane based on Darcy's Law. The velocity potentials are obtained via a Fourier-Bessel expansion, along with dual Bessel series relations associated with the radial function. The analytical solution of the model is derived by using the least-squares approximation method and the matching technique. The analytically computed horizontal displacements of a flexible hexagonal cage, for two distinct mooring stiffness, are validated against independent numerical simulations performed using the AQWA-based BEM method. The numerical results are produced by developing MATLAB code based on the analytical solutions. The hydroelastic response of the net cage under physical and structural parameters is investigated.

2. Mathematical formulation

The mathematical model of the hexagonal floating net enclosure is expressed in a three-dimensional cylindrical coordinate system (r, θ, z) , which are assumed with its origin at the centre of the regular hexagonal-shaped cage. It is assumed that the undisturbed free surface of the water is situated at $z = 0$ and is considered to pierce the water surface within a water column of finite depth h (see Figure 1). The net is modelled as a flexible porous membrane that bears a uniform tension over a radius function. On the other hand, it is assumed that the hexagonal-shaped cage can be generated by adopting a radius function ($r = R(\theta)$) defined by the cosine-type radial perturbation as [13]

$$R(\theta) = A\{1 + \varepsilon cosn_r(\theta - \theta_0)\}, \tag{1}$$

where the values of $A, \varepsilon,\ n_r$, and θ_0 are chosen in the numerical computation.

The whole fluid domain is subdivided as follows:

$$\text{Fluid domain} = \begin{cases} 0 < r|_{r=R(\theta)} < \infty, -d < z < 0, \text{except cage by } D_1 \\ -d \le z \le 0, r \ge R(\theta) \text{ by } D_1 \\ -h \le z \le 0, r \le R(\theta) \text{ by } D_2 \\ -d \le z \le -h, r \le R(\theta) \text{ by } D_3 \end{cases}$$

Further, the notations R_{sp} and R_{gp} represent the submerged and the gap portions of the hexagonal net cage, respectively (see Fig. 1). Under the assumption of linear wave theory and fluid characteristics, there exist velocity potentials $\Phi_j(r, \theta, z, t) = Re\{\varphi_j(r, \theta, z)e^{i\omega t}$, where Re is the real part of the complex velocity potentials, with angular frequency ω , and $\varphi_j, j = 1$ (refered to D_1), 2(refered to D_2), 3(refered to D_3) are the spatial velocity potentials in the respective domains. The velocity potentials $\Phi_j(r, \theta, z, t)$ satisfy:

$$\frac{\partial^2 \Phi_j}{\partial r^2} + \frac{1}{r}\frac{\partial \Phi_j}{\partial r} + \frac{1}{r^2}\frac{\partial^2 \Phi_j}{\partial \theta^2} + \frac{\partial^2 \Phi_j}{\partial z^2} = 0, \tag{2}$$

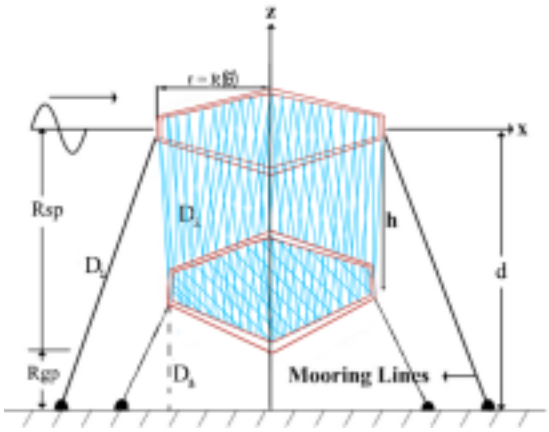


Figure 1: Prospective schematic diagram of a hexagonal net cage.

where r is the radial distance from the z-axis calculated as $r = R(\theta)$ and θ is the angle about the x-axis.

The linearized free surface condition (by combining the kinematic and dynamic boundary conditions) on $z = 0$, the impermeable seabed yield

$$\frac{\partial^2 \Phi_j}{\partial t^2} + g\frac{\partial \Phi_j}{\partial z} = 0 \quad \text{for } j = 1,2 \tag{3}$$

$$\frac{\partial \Phi_j}{\partial z} = 0 \text{ for } j = 1,3 \text{ on } z = -d. \tag{4}$$

where g is the acceleration due to gravity. The far-field condition can be assumed to be of the form

$$\lim_{r\to\infty} \sqrt{r}\frac{\partial \Phi_1}{\partial r} + ik_0\Phi_1 = 0, \tag{5}$$

where k_0 is the wave number of the gravity wave dispersion relation. The linearised kinematic and dynamic conditions on the vertical boundary of the hexagonal net cage at $r = R(\theta), z \in R_{sp}$ can be derived as:

$$\frac{\partial \Phi_j}{\partial r}\Big|_{r=R(\theta)} - ik_0\sigma(\Phi_2 - \Phi_1) - \xi_t cos\,\theta = 0 \text{ for } j = 1,2, \tag{6}$$

$$\left(m_m\frac{d^2}{dt^2} - T_f\frac{d^2}{dz^2}\right)\xi = 2R(\theta)\rho\int_0^{\pi}(\Phi_{2t} - \Phi_{1t})\,cos(\pi - \theta)d\theta, \tag{7}$$

where $\xi(z,t) = Re\{\zeta(z)e^{i\omega t}\}$ refers to the displacement of the vertical hexagonal net cage, T_f is the uniform tensile force acting on the vertical membrane of the cage, and m_m refers to the mass of the net. It is assumed that the bottom bed of the hexagonal cage is covered by a net-type structure, which is modelled as a flexible porous membrane that satisfies Darcy's law for flow past a porous medium ($\sigma = \text{porous} - \text{effect parameter}$). Therefore, the linearized kinematic boundary condition can be given by

$$\frac{\partial \Phi_2}{\partial z} = \frac{\partial \Phi_3}{\partial z} = \frac{\partial \eta}{\partial t} + ik_0\sigma(\Phi_3 - \Phi_2) \text{ at } z = -h, \quad r = R(\theta). \tag{8}$$

In this formulation, k_0 denotes the wave number associated with the plane gravity wave, while σ functions as the porous-effect parameter for the flexible membrane. The physical behavior of the cage bed is described by the two-dimensional string equation, and the fluid transmission through the porous structure is governed by a generalized Darcy's law that accounts for both inertial and frictional forces. Under this law, the normal fluid velocity across the membrane is directly proportional to the pressure differential; the resulting complex proportionality constant reflects these dynamics. Specifically, the imaginary component characterizes the inertial effect, whereas the real component, the porous-effect parameter, quantifies viscous resistance and is empirically determined [14].

Now, the dynamic condition on the submerged flexible porous membrane satisfies deflection η with the hydrodynamic pressure differences between the gap and submerged portion of the cage as:

$$\left(-T_g\nabla_{r\theta}^2 + m_m\frac{\partial}{\partial t^2}\right)\eta = -(P_3(r,\theta,z,t) - P_2(r,\theta,z,t)), \text{ for } \quad r = R(\theta), \tag{9}$$

where $\eta(r,\theta,t) = Re\{\varsigma(r,\theta)e^{i\omega t}\}$ is the deflection of the flexible porous membrane bed which is under the action of uniform tensile force, T_g, m_m is the mass of the membrane, and the hydrodynamic pressure read as:

$$P_j(x,y,z,t) = \rho g z - \rho\frac{\partial \Phi_j}{\partial t} \text{ for } j = 2,3, \text{ in } \quad D_2 \text{ and } D_3. \tag{10}$$

The continuity of pressure and normal velocity, at the interface $r = R(\theta)$, results

$$\Phi_{1r}|_{r=R(\theta)} = \Phi_{3r}|_{r=R(\theta)} \quad z \in R_{gp} \tag{11}$$

$$\Phi_1|_{r=R(\theta)} = \Phi_3|_{r=R(\theta)} \quad z \in R_{gp}. \tag{12}$$

where the subscript r in Eq. (11) denotes the partial derivative with respect to r.

To prevent the structure from failing under the onslaught of storm-generated waves and currents during typhoons, the upper and lower parts of the hexagonal net cage are anchored with mooring lines with stiffness q_{ju} and $q_{jl}, j = 1,2$ distributed along the perimeter of a regular hexagon at $r = R(\theta)$, which results in

$$T_f\xi_z = 2q_u\xi\, sin^2\alpha \quad \text{at } r = R(\theta), z = 0, \tag{13a}$$

$$T_f\xi_z = 2q_l\xi\, sin^2\beta \quad \text{at } r = R(\theta), z = -h, \tag{13b}$$

where α and β are the angles extended by the upper and lower mooring lines with respect to the negative z-axis. For the sake of simplicity, $q_{1u} = q_{2u} = q_u$ and $q_{1l} = q_{2l} = q_l$. The subscript "z" refers to the partial derivative with respect to z.

3. Method of solution

Using Fourier-Bessel series expansion and cosine-type radial perturbation, the velocity potentials satisfying Eqs. (1-5) and Eqs. (8-9) associated with each domain can be derived as:

$$\varphi_1(r|_{r=R(\theta)},\theta,z) = \frac{g}{2i\omega}U_0(z)\sum_{m=0}^{\infty} e^{im\pi/2}\varepsilon_m\{J_m(k_0r) + A_{m0}H_m^{(1)}(k_0r)\}\cos m\,\theta + \sum_{m=0}^{\infty}\sum_{n=1}^{\infty}\alpha_m A_{mn}\,K_m(k_nr)U_n(z)\cos m\,\theta \quad \text{for } D_1 \tag{14}$$

$$\varphi_2(r|_{r=R(\theta)},\theta,z) = \frac{g}{2i\omega}\sum_{m=0}^{\infty}\sum_{n=0}^{\infty}B_{mn}e^{im\pi/2}\varepsilon_m\, I_m(\lambda_nr)V_n(z)\cos m\,\theta \quad \text{for } D_2 \tag{15}$$

$$\varphi_3(r|_{r=R(\theta)},\theta,z) = \frac{g}{2i\omega}\sum_{m=0}^{\infty}\sum_{n=0}^{\infty}C_{mn}e^{im\pi/2}\varepsilon_m\, I_m(\lambda_nr)W_n(z)\cos m\,\theta \quad \text{for } D_3, \tag{16}$$

where $U(z)$, $V(z)$, and $W(z)$ are the vertical eigenfunctions in the respective domains. The parameter $\varepsilon_m = 1$ and $\varepsilon_m = 2$ for $m = 0$ and $m \geq 1$, respectively. $H_m(k_0 r)$ are the Bessel function and Hankel function of first kind of order m, respectively, $K_m(k_0 r)$ is the modified Bessel functions of first kind of order m. The wavenumbers k_n and λ_n satisfy the following dispersion relations

$$K = k_n \tanh(k_n d), \; K = \omega^2/g, \tag{17}$$

$$\{(T_f \lambda_n^2 - m_s) i k_0 \sigma - K\}(\lambda_n \sinh \lambda_n d - K \cosh \lambda_n d) = \lambda_n (T_f \lambda_n^2 - m_s) \sinh \lambda_n (d - h) \times (\lambda_n \sinh \lambda_n h - K \cosh \lambda_n h). \tag{18}$$

The four series relations associated with the can be obtained in the gap portion and the submerged portion of the hexagonal net cage as:

$$\left.\begin{aligned} \sum_{n=0}^{\infty} A_{1n} \Gamma_{an}(z) + \sum_{q=0}^{\infty} C_{1q} \Gamma_{cq}(z) + \Gamma_0(z) = 0 \\ \sum_{n=0}^{\infty} A_{1n} \Theta_{an}(z) + \sum_{q=0}^{\infty} C_{1q} \Theta_{cq}(z) + \Theta_0(z) = 0 \end{aligned}\right\} \text{ for } z \in R_{gp} \tag{19}$$

$$\left.\begin{aligned} \sum_{n=0}^{\infty} A_{1n} \Lambda_{an}(z) + \sum_{q=0}^{\infty} B_{1q} \Lambda_{bq}(z) + \Lambda_0(z) = 0 \\ \sum_{n=0}^{\infty} A_{1n} \Omega_{an}(z) + \sum_{q=0}^{\infty} B_{1q} \Omega_{bq}(z) + \Omega_0(z) = 0 \end{aligned}\right\} \text{ for } z \in R_{sp} \tag{20}$$

where the expressions $\Gamma_0, \Theta_0, \Lambda_0, \Omega_0, \Gamma_{an}, \Theta_{an}$, $\Lambda_{an}, \Omega_{an}, \Gamma_{cq}, \Theta_{cq}, \Lambda_{bq}$, and Ω_{bq} are associated with Hankel, Bessel, and modified Bessel functions.

Proceeding similarly to [10] and using the least squares approximation method by setting $r = R(\theta)$, the series relation from R_{sp} and R_{gp}, one can derive the following series relation as:

$$\mathcal{P}(R(\theta), z) = \sum_{n=0}^{N} A_{1n} S_n(R(\theta), z) + \sum_{q=0}^{M} B_{1q} G_q(R(\theta), z) + \sum_{q=0}^{M} C_{1q} T_q(R(\theta), z) + X_0(R(\theta), z) = 0, \tag{21}$$

where, $S_n(R(\theta), z)$, $G_q(R(\theta), z)$, $T_q(R(\theta), z)$, and $X_0(R(\theta), z)$ are the mathematical expressions associated with $H_1^{(1)'}$, $K_1'(k_n R(\theta))$, $I_1^{(1)'}(p_n R(\theta))$, $J_1'(k_0 R(\theta))$ over R_{sp} and R_{gp} along with vertical eigenfunctions $U_n(z)$, $V_n(z)$, and $W_n(z)$.
Applying the least-squares approximation again, Eq. (21) produces the result as:

$$\int_{-d}^{0} |\mathcal{P}(R(\theta), z)|^2 dz = \text{minimum}. \tag{22}$$

The unknowns in Eq. (21) are selected so that they minimize the integral shown in Eq. (22), which yields

$$\int_{-d}^{0} \mathcal{P}^*(R(\theta), z) \frac{\mathcal{P}(R(\theta), z)}{\partial A_{1n}} dz = 0, \tag{23}$$

where '*' denotes the complex conjugate. To satisfy the mooring conditions (13a) and (13b), we compute the displacement ζ of the hexagonal net cage by inserting the functions φ_1 and φ_2 into Eq. (7) and then solving the resulting partial differential equation with the appropriate analytical method.

$$\zeta = A\frac{cos(pz)}{cos(ph)} + B\frac{sin(pz)}{sin(ph)} + c_0U_0(z) + \sum_{n=0}^{N} A_{1n}\Upsilon_n U_n(z) + \sum_{q=0}^{M} B_{1q}\Upsilon_q\lambda_q V_n(z), \tag{24}$$

Using Eq. (24) in the mooring conditions (13a) and (13b), the following system of equations yields

$$\begin{aligned}\sum_{n=0}^{N} A_{1n}\Upsilon_n\{-2q_u(sin^2\,\alpha) + k_n\,tanh(\,k_n d)\} + \sum_{q=0}^{M}\frac{B_{1q}\Upsilon_q\lambda_q\{-2q_u(sin^2\,\alpha) + T_fK\}}{cosh\,\lambda_q\,h(K - \lambda_q\,tanh\,\lambda_q\,h)}\\ = 2q_uA\frac{(sin^2\,\alpha)}{cos\,p\,h} - \frac{T_fBp}{sin\,p\,h}\\ + \{2q_u(sin^2\,\alpha) - T_fk_0\,tanh(\,k_0 d)\}c_0,\end{aligned} \tag{25}$$

$$\begin{aligned}\sum_{n=0}^{N} A_{1n}\Upsilon_n\left\{-2q_l(sin^2\,\beta)\frac{cosh\,k_n\,(d-h)}{cosh\,k_n\,d} + T_fk_n\frac{sinh\,k_n\,(d-h)}{cosh\,k_n\,d}\right\}\\ + \sum_{q=0}^{M} B_{1q}\Upsilon_q\lambda_q\left[\frac{\{-2q_l(sin^2\,\beta)\}(K\,tanh\,\lambda_n\,h - \lambda_n)}{(K - \lambda_n\,tanh\,\lambda_n\,h)} + \lambda_n\right]\\ = A\big(2q_l\,sin^2\,\beta - T_fp\,tan\,p\,h\big) - B\big(2q_l\,sin^2\,\beta + T_fp\,cot\,p\,h\big)\\ + \left\{2q_l(sin^2\,\beta)\frac{cosh\,k_0\,(d-h)}{cosh\,k_0\,d} - T_fk_0\frac{sinh\,k_0\,(d-h)}{cosh\,k_0\,d}\right\}c_0.\end{aligned} \tag{26}$$

where

$$c_0 = 2\rho g\pi R(\theta)\frac{J_1(k_0R(\theta))}{\lambda_q^2+p^2},\ p = \omega(m_m)^{1/2},\ \Upsilon_n = \begin{cases}2\rho g\pi R(\theta)\frac{H_1^{(1)}(k_0R(\theta))}{k_0^2+p^2}, n = 0,\\ 2\rho i\omega\pi a_k\frac{K_1(k_nR(\theta))}{k_0^2+p^2},\ n \geq 1,\end{cases}$$

$$\Upsilon_q = -2\rho g\pi R(\theta)\frac{I_1\left(\lambda_qR(\theta)\right)}{\lambda_q^2 + p^2}, \text{ for } q \geq 0.$$

Another four systems of equations can be obtained: two of them are obtained by combining Equations (19)–(20). The other two are obtained from the moored edge condition as in Equations (25-26). Now, this system of equations will be solved numerically using the MATLAB code along with the Bessel, Hankel, and modified Bessel functions of the second kind, order to solve the systems using built-in MATLAB subroutine to present the numerical results. After determining the unknown constants that appear in the velocity potentials (14–16), the horizontal displacement ζ of the flexible hexagonal net cage follows directly from Eq. (24).

4. A concise overview of the numerical AQWA model

In this section, a numerical model of the floating hexagonal net cage is established using AQWA, a BEM method to simulate the cage displacements. The hydrodynamic forces acting on the fishing net are calculated using the Morison equation, where each twine is treated as an independent cylindrical element. The netting structure consists of a large number of slender net twines, and the lumped mass method is adopted to analyse the dynamic response of the mooring system. In the grouping process, several adjacent original meshes are merged into one equivalent grouped mesh for numerical modelling. In addition, the mooring line is divided into many segments using the lumped mass method (see Fig. 2).

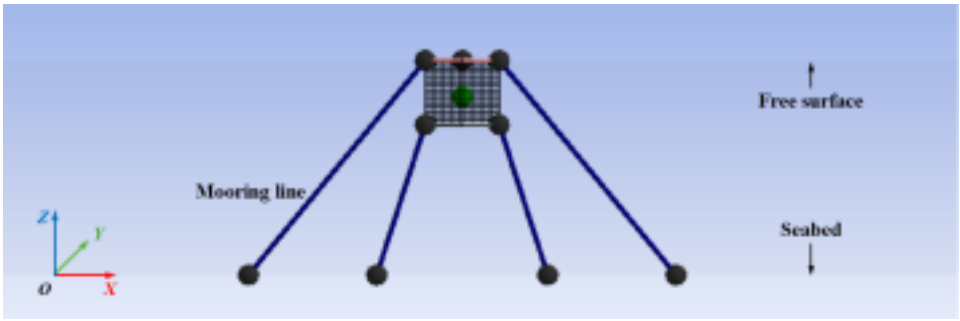


Figure 2: The numerical model of a moored hexagonal net cage.

The next section will present the numerical outcomes and their analysis by i) comparing the analytical and numerical AQWA simulations to assess the accuracy of the theoretical results and ii) studying the effect of cage height, tensile force, and theta on the cage displacements based on the analytical solution.

5. Numerical outcomes and their explanation

The computational results based on the analytical solution were performed in MATLAB R2022b (64-bit) running on a Windows 64-bit machine. The computer was equipped with an Intel Core i7-4790 CPU clocked at 3.6 GHz, 8 GB of DDR-3 RAM (running at 3601 MHz), and a solid-state drive. Each run took roughly 8–10 minutes to complete. On the other hand, in the case of AQWA simulations, the system used for this study featured a laptop powered by an Intel® Core i5-13500H processor running at 2.6 GHz, equipped with 32 GB of RAM, and a CPU architecture comprising 12 physical cores and 16 logical processors. On average, each AQWA model simulation required about 10 hours to complete. Therefore, the MATLAB code based on the analytical solution is computationally efficient and can be simulated in a daily-based normal-configured computer compared to numerical AQWA.

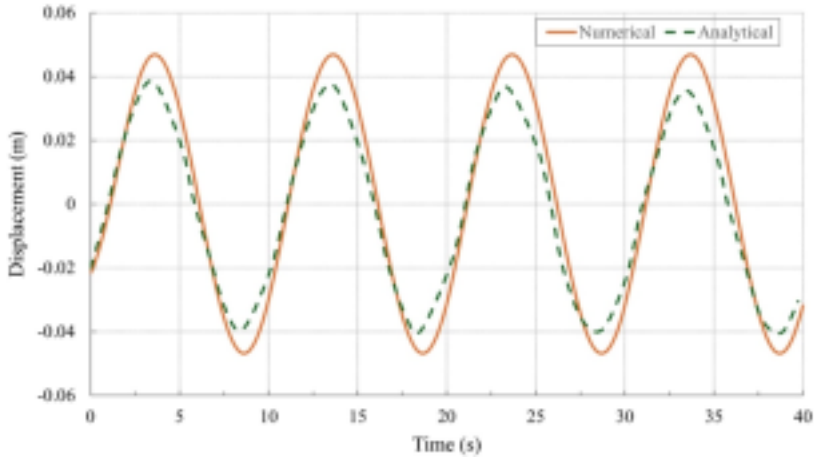
It may be noted that the convergence of the cage displacement (ζ) series is achieved when the vertical truncation order, 25; therefore, the number of Fourier–Bessel modes is 25 utilized for all calculations to maintain consistency and accuracy. Further, the parametric values used in the convergence study are the same as in Table 1. In the numerical results, the effect of model parameters on the cage displacements will be analysed in detail and the model parameters are provided in Table 1.

Table 1: Cage model properties.

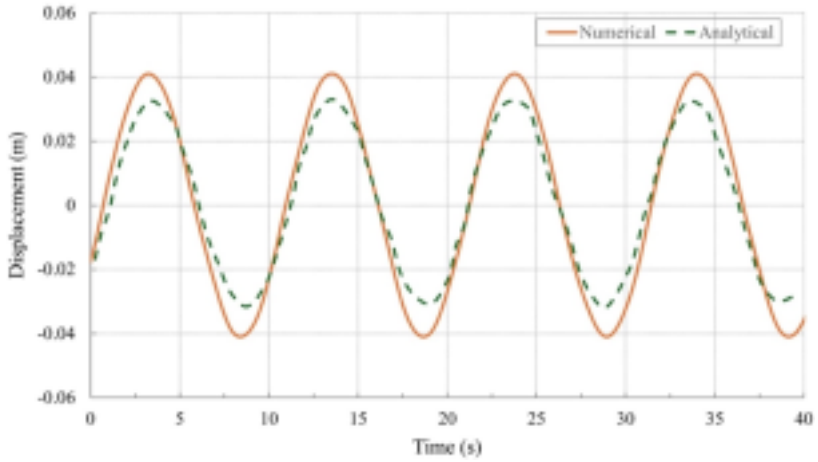
Model parameters	Values	Units
Water depth (d)	50	[m]
ε	0.03	[-]
θ_0	$\pi/6$	[-]
Water density (ρ)	1025	[kg/m^3]
Gravitational constant (g)	9.8	[ms^{-2}]
n_r	6	[-]
Tensile forcer (T_f)	10^2	[N/m]
Radius (A)	10	[m]
Lower mooring stiffness (q_l)	10^{11}	[N/m]
Upper mooring stiffness (q_u)	10^7	[N/m]
Net weight	8	[kg/m]

5. 1. Comparison between the analytical and numerical AQWA simulations

In Fig. 3, the influence of two different values of mooring stiffness (a) $q_u = q_l = 10^7 \mathrm{N/m}$ and (b) $q_u = q_l = 10^9 \mathrm{N/m}$ on horizontal displacement of the hexagonal cage between analytical and numerical AQWA simulations are compared versus time t (s) with the other parametric values being the same as provided in Table 1. Fig. 3 (a-b) reveals that increasing mooring stiffness leads to a reduction in the horizontal displacement of the hexagonal cage across both models. This inverse relationship suggests that enhanced mooring stiffness reinforces the stability of the floating structure, thereby limiting its movement. While the analytical findings align with the trends observed in the AQWA simulations, some variance in peak values is apparent. These discrepancies are likely attributable to variations in cage quality, differences in the center of gravity, and the inherent limitations of symmetrical computational modelling.



(a) Mooring stiffness = $q_u = q_l = 10^7 \mathrm{N/m}$.



(b)Mooring stiffness = $q_u = q_l = 10^9 \mathrm{N/m}$.

Figure 3: Comparison of horizontal displacement of hexagonal flexible net cage for (a) $q_u = q_l = 10^7 \mathrm{N/m}$ and (b) $q_u = q_l = 10^9$ between analytical and numerical AQWA simulations.

In Fig. 3a, the displacement from the analytical model is 0.0379 m, while the AQWA model is 0.0465 m, which is 22.7% larger. On the other hand, in Fig. 3b, the displacement from the analytical model is 0.0324 m, while the AQWA model is 0.0409 m, which is 26.2% larger. In case of analytical results, the

displacements from $q_u = q_l = 10^7 \mathrm{N/m}$ is 0.0379 m and from $q_u = q_l = 10^9 \mathrm{N/m}$ is 0.0324 which is 17% lower. Furthermore, a comparison of the analytical outcomes for two distinct mooring stiffness values reveals a displacement decrease of approximately 17%.

5.2. Effect of structural parameters on the cage displacements

Fig. 4 illustrates how the horizontal movement of the hexagonal net cage varies with time (*t, s*) for several non-dimensional cage-height configurations, using the parameter set listed in Table 1. The curves reveal a clear trend: as the cage height grows, the magnitude of horizontal displacement also rises. This pattern indicates that, given particular mooring-stiffness values applied to both the upper and lower sections of the cage, taller structures experience greater horizontal shifts.

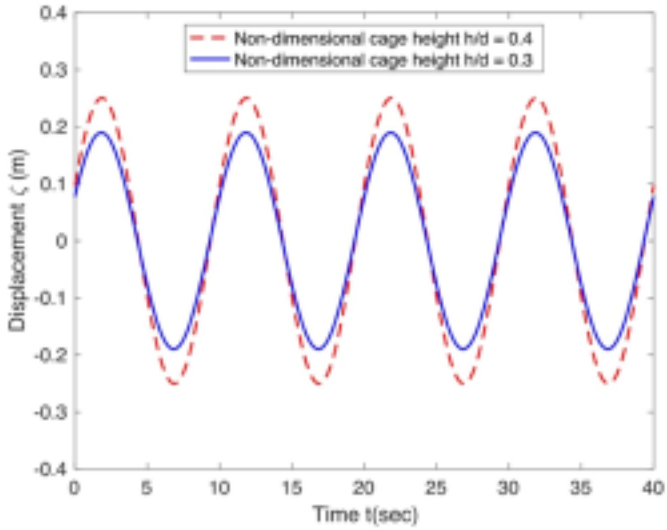


Figure 4: Effect of non-dimensional cage height on the horizontal hexagonal cage displacements with $h/d = 0.3$ (*solid blue line*) and $h/d = 0.4$ (*dashed red line*).

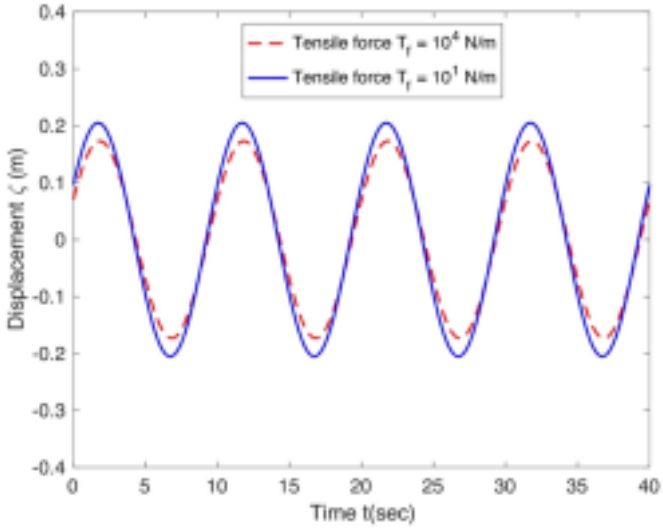


Figure 5: Variation of tensile force on the horizontal hexagonal cage displacements with $T_f = 10^1$ N/m (*solid blue line*) and $T_f = 10^4$ N/m (*dashed line*).

Further, in Fig. 4, it can be explained that when the structure's height is increased, the hexagonal cage exhibits more pronounced horizontal movement, which in turn leads to higher tension in the mooring lines. It indicates that a clear rise in mooring-line forces accompanied the increase in cage height.

Fig. 5 presents a series of simulations showing how the cage's horizontal movement varies over time (t, s) for several tensile-force levels (T_f), while all other parameters remain those specified in Table 1. The results clearly indicate that raising the net's tensile force leads to a reduction in the cage's horizontal displacement.

Fig. 6 illustrates how the parameter θ linked to the radial function affects the cage's horizontal movement over time (t in seconds) while keeping the other parameters identical to those listed in Table 1. The plot clearly shows that raising the value of θ leads to a larger horizontal shift of the cage. This trend arises because a greater θ enlarges the net's effective surface area, which in turn boosts the hydrodynamic forces acting on it. The increased wave-induced loading on the larger area translates into higher forces on the cage, producing correspondingly larger displacement.

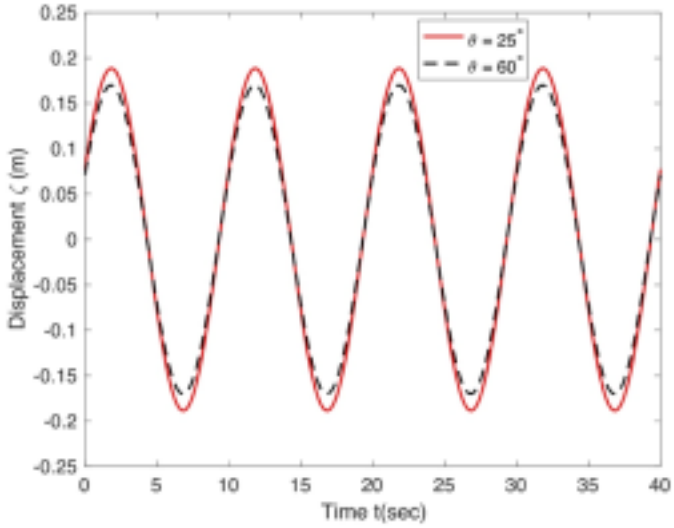


Figure 6: Impact of $R(\theta)$ on the horizontal hexagonal cage displacements with $\theta = 25^o$ (*solid red line*) and $\theta = 60^o$ (*dashed black line*).

6. Conclusion

In this paper, a mathematical formulation of a hexagonal net cage is proposed under linearized water wave theory, and the theoretical solution is obtained using Bessel's series function and the least square approximation method. The analytically computed horizontal displacements of a flexible hexagonal cage, for two distinct mooring stiffness, are validated against independent numerical simulations performed using the AQWA-based BEM method. The hydroelastic response of the cage is analysed by studying the numerical results for the horizontal displacements with different model parameters.

The analysis showed that boosting either the mooring stiffness or the membrane tension leads to a reduction in the cage's horizontal displacement. In contrast, raising the cage's height causes its horizontal displacement to grow, a pattern that mirrors the effect observed when θ is altered behaviour that is entirely consistent with physical intuition.

In the future, the present mathematical formulation will be extended to include current velocity and to provide a comprehensive understanding of its effects and wave-blocking phenomena. Further, a comparative analysis of the AQWA model simulations in the presence of current velocity will be performed.

Acknowledgements

This work is supported by the China Scholarship Council under Grant: 202306950024. This work contributes to the Strategic Research Plan of the Centre for Marine Technology and Ocean Engineering (CENTEC), funded by the Portuguese Foundation for Science and Technology (Fundação para a Ciência e Tecnologia—FCT) under contract UID/00134/2025 (https://doi.org/10.54499/UID/00134/2025)

References

[1] T. Kristiansen, and O.M. Faltinsen, *Modelling of current loads on aquaculture net cages*, Journal of Fluids and Structures, 34: 218-235, 2012. https://doi.org/10.1016/j.jfluidstructs.2012.04.001

[2] Y. Shen, R. Firoozkoohi, M. Greco, and O. M. Faltinsen, *Comparative investigation: Closed versus semi-closed vertical cylinder-shaped fish cage in waves*, Ocean Engineering, 245: 110397, 2022. https://doi.org/10.1016/j.oceaneng.2021.110397

[3] H.M. Hou, Y. Liu, G.H. Dong, and T.J. Xu, *Reliability assessment of mooring system for fish cage considering one damaged mooring line*, Ocean Engineering, 257: 111626, 2022. https://doi.org/10.1016/j.oceaneng.2022.111626

[4] I.M. Strand, and O.M. Faltinsen, *Linear wave response of a 2D closed flexible fish cage*, Journal of Fluids and Structures, 87: 58–83, 2019. https://doi.org/10.1016/j.jfluidstructs.2019.03.005

[5] O.M. Faltinsen, and Y. Shen, *Wave and Current Effects on Floating Fish Farms*, Journal of Marine Science and Application, 17(3): 284-296, 2018. https://doi.org/10.1007/s11804-018-0033-5

[6] A.S. Shaik, N. Thuvanismail, M. Vijayakumar, and P. Kumar, *Numerical Investigation on Different Configurations of Offshore Fish Cages in Submerged Conditions Subjected to Regular Waves*, Journal of Marine Science and Application, 22: 445–455, 2023. https://doi.org/10.1007/s11804-023-00361-7

[7] W, Su, J.M. Zhan, and H. Huang. *Analysis of a porous and flexible cylinder in waves*, China Ocean Engineering, 29: 357-68, 2015. https://doi.org/10.1007/s13344-015-0025-z

[8] A. Gharechae, and M.J. Ketabdari, *Semi-analytical study on regular sea wave interaction with circular elastic floaters of aquaculture fish cages*, Aquacultural Engineering, 91: 102125, 2020. https://doi.org/10.1016/j.aquaeng.2020.102125

[9] S.C. Mohapatra, and C. Guedes Soares, *A Review of the Hydroelastic Theoretical Models of Floating Porous Nets and Floaters for Offshore Aquaculture*, Journal of Marine Science and Engineering, 12: 1699, 2024. https://doi.org/10.3390/jmse12101699

[10] S.C. Mohapatra, and C. Guedes Soares, *A semi-analytical model of an array of moored floating flexible offshore net cages under current loads*, Ocean Engineering, 291: 116309, 2024. https://doi.org/10.1016/j.oceaneng.2023.116309

[11] J. Ji, B. Liu, L, Zhou, and C. Guedes Soares, *Experimental and numerical studies of a bottom-fixed aquaculture platform with different net configurations under wave loading*, Ocean Engineering, 348: 124081, 2026. https://doi.org/10.1016/j.oceaneng.2025.124081

[12] S.C. Mohapatra, Z. C. Liu, and C. Guedes Soares, *Motion response of a flexible floater with current loads for offshore aquaculture system*, Ocean Engineering, 125902, 2026. https://doi.org/10.1016/j.oceaneng.2026.125902

[13] A.M. Mansour, A.N. Williams, and K. Wang, *The diffraction of linear waves by a uniform vertical cylinder with cosine-type radial perturbations*, Ocean Engineering, 29: 239–259, 2002. https://doi.org/10.1016/S0029-8018(01)00003-8

[14]I.H. Cho, and M.H. Kim, *Transmission of oblique incident waves by a submerged horizontal porous plate*, Ocean Engineering, 61: 56-65, 2013. https://doi.org/10.1016/j.oceaneng.2012.12.044

Bio-inspired Concepts

10th International Conference on HYDROELASTICITY IN MARINE TECHNOLOGY
Trondheim, Norway, June16$^{\text{th}}$-18$^{\text{th}}$, 2026

Analytical Solutions of Two-Way Coupled Wave-Flexible Seagrass Interaction

Wei, Z.[1], Boyer, R.[2], and Shao, Y.[1,*]

[1] Technical University of Denmark, Department of Civil and Mechanical Engineering, 2800 Kgs. Lyngby, Denmark
[2] ENSTA Bretagne, 29200 Brest, France

Abstract. We present an analytical model for two-way coupled interactions between waves and a benthic, flexible seagrass canopy. The physical problem is formulated as a two-layer (water/canopy) system with linearized governing equations and boundary conditions, while quadratic Morison-type drag is retained as the dominant dissipation mechanism and the canopy motion is represented by prismatic Euler–Bernoulli cantilevers. An inviscid outer solution is obtained first, after which a laminar viscous closure is introduced via oscillatory boundary layers at the seabed and canopy–water interface to close tangential stresses and remove velocity discontinuities. The coupled solution yields a complex wave number and exponential wave-height decay. Attenuation over finite canopies is computed with an incremental marching scheme and extended to irregular waves using stochastic linearization to propagate the spectrum. Comparisons with laboratory measurements show reasonable first-order predictions of attenuation for both regular and irregular waves. Further validation of stem deflections and in-canopy velocity profiles, as well as turbulence (eddy-viscosity) closures, is left for future work.

Key words: *Wave attenuation; Seagrass; Euler–Bernoulli beam; Viscous closure; Stochastic linearization*

1. Introduction

Wave attenuation by coastal vegetation has long been recognized as an effective mechanism for reducing wave energy and associated hydrodynamic loads, with implications for coastal protection, habitat resilience, and nature-based solutions. Seagrass is one of the most widespread naturally occurring vegetation types, characterized by benthic growth and flexible stems.

The scientific community has devoted substantial effort to quantifying wave attenuation across submerged canopies; among the early analytical contributions, foundational models were developed in [1] and [2]. Although canopy flexibility was not considered, these studies set out the essential hydrodynamic framework. The energy-balance approach of [1] is based on time-averaged wave-energy conservation and does not resolve in-canopy velocity profiles. As a result, it is not readily suited for fully two-way coupling with flexible vegetation. In contrast, the problem was formulated in [2] from continuity and linearized momentum equations, providing a convenient basis for incorporating vegetation-induced hydrodynamic forces. For flexible canopies, this framework can be extended by adding stem motion equations. This formulation is particularly attractive because it provides phase shifts and in-canopy velocity profiles in addition to wave attenuation.

Based on this idea, vegetation motion was represented in [3] as a seabed-mounted pendulum with a single degree of freedom, with buoyancy and stiffness supplying the restoring moments. Similarly, suspended seaweed were modeled in [4] as a rigid bar pinned at the top, with buoyancy as the only restoring

*Correspondence to: yshao@dtu.dk

force owing to its high compliance. These two-way coupled formulations therefore remain confined to single-degree-of-freedom representations. For comparatively stiff seagrass, an Euler–Bernoulli beam model is more appropriate. While Euler–Bernoulli beams have been combined with energy-conservation approaches to predict wave attenuation [5], they have not yet been incorporated within a fully two-way coupled framework. Unlike a single-degree-of-freedom oscillator, a beam is a continuous system, introducing additional differential equations into the coupled problem rather than a single algebraic relation. There remains a clear need for a tractable analytical model that couples wave dynamics with Euler–Bernoulli stem motion to resolve both wave attenuation and seagrass canopy deformation in a fully two-way manner.

The framework of [2] neglects viscosity, leading to a discontinuity in the horizontal velocity across the water-canopy interface [6, 4], which is not physical. To address this issue, a viscous closure was introduced in [7] for the wave–vegetation interaction problem where the vegetation is assumed as fixed and rigid bars. As a lowest-order approximation, the boundary layer was assumed laminar, and only the interface boundary layer was considered. In principle, however, an additional boundary layer should also develop near the seabed. A viscous closure for wave–flexible-vegetation interaction that includes boundary layers at all relevant boundaries and interfaces is still lacking.

Considering the above scientific gaps in the literature, the present work will present an analytical model for wave interaction with flexible vegetation canopies that couples the dynamic fluid motion and vegetation deformation. Laminar boundary-layer theory with viscous closure is applied at the seafloor and the canopy–water interface to examine its implications for the resulting flow kinematics.

The rest of the paper is organized as follows. Section 2 presents the mathematical framework and derives the analytical solutions, including the inviscid wave solution and the combined solution with viscous closure. Section 3 validates the model against measured wave attenuation. Section 4 examines the implications of the viscous closure. Finally, conclusions are given in Section 5.

2. Theory

In this section, we first present the viscous governing equations and associated boundary conditions for infinitesimal wave amplitude. Recognizing that viscosity is confined to thin boundary layers near the seabed and the canopy–water interface, we neglect viscous terms in the bulk equations and boundary conditions to obtain the outer (wave) solution in the fluid core. We then incorporate viscosity through closure relations at the seabed and the canopy–water interface, assuming laminar boundary layers.

The general problem (without viscosity) is illustrated in Fig. 1. A benthic canopy of seagrass or other aquatic vegetation is rooted on the seabed. The water depth above the canopy is d_1, while the canopy height is d_2. The total water depth is $h = d_1 + d_2$. The canopy height at rest (with no deformation) is $l = d_2$. We define a Cartesian coordinate system Oxz fixed in space. The waves propagate along the positive x-direction. The calm-water surface is located at $z = 0$ and the surface elevation is denoted as $\eta(x, t)$. t denotes time. In Layer $j = 1, 2$, p_j is the dynamic pressure and $\boldsymbol{u}_j = [u_j, w_j]$ is the filter velocity [8], defined as the volume averaged ensemble averaged velocity over a total control volume including the canopy blades.

2.1. Problem formulation

The flow above the canopy ($j = 1$) and within the canopy ($j = 2$) is governed by the following continuity equation and momentum equation [9]:

$$\nabla \cdot \boldsymbol{u}_j = 0 \quad \text{and} \quad \frac{\partial}{\partial t}\frac{\boldsymbol{u}_j}{n} + \frac{1}{n^2}\boldsymbol{u}_j \cdot \nabla \boldsymbol{u}_j = -\frac{1}{\rho}\nabla p_j + \nu_e \nabla^2 \boldsymbol{u}_j - \delta_{2j}\frac{\boldsymbol{F}_{\text{hd}}}{\rho}, \tag{1}$$

where $\boldsymbol{u}_j = (u_j, w_j)$ is the filter velocity, $p_j = \mathcal{P}_j + \rho g z$ is the dynamic pressure, with $\mathcal{P}_j$ the total pressure, ρ the water density, and g the gravitational acceleration. Here $n = 1$ for $j = 1$ and $n = 1 -$

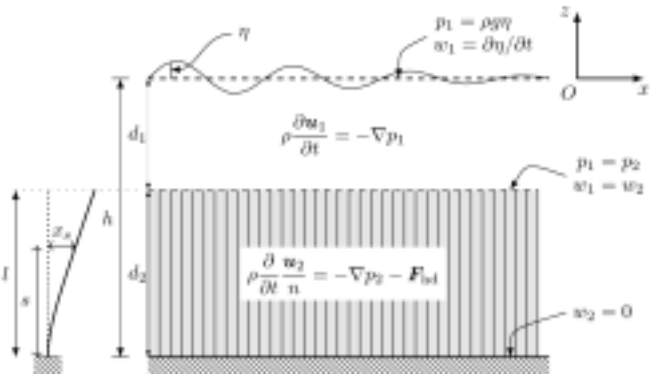


Figure 1: Governing equations for the outer solution (i.e., wave solution without viscosity) in each layer, boundary conditions at the interfaces, and the sketch of a stem rooted on the seabed.

NA_s for $j = 2$ is the volume fraction of water, i.e., porosity of the canopy, with N the number of stems per unit area and A_s the cross-sectional area of the stems. The effective viscosity is defined as $\nu_e = \nu/n$, where ν is the kinematic molecular viscosity. Further, $\boldsymbol{F}_{\text{hd}}$ is the volume-averaged hydrodynamic force exerted on the canopy, and $\delta_{2j} = 1$ for $j = 2$ and 0 otherwise.

On a water surface $F = z - \eta(x, t) = 0$, the kinematic condition is

$$\frac{\partial \eta}{\partial t} + u_1 \frac{\partial \eta}{\partial x} = w_1, \quad z = \eta. \tag{2}$$

The dynamic boundary condition is the continuity of normal and tangential stresses. The water surface is assumed to be free of atmospheric pressure and free of surface contamination. Dynamically, we require the vanishing of the normal stress and the tangential stresses

$$-p_1 + \rho g \eta + 2\mu \frac{\partial w_1}{\partial z} = 0 \quad \text{and} \quad \mu \left(\frac{\partial u_1}{\partial z} + \frac{\partial w_1}{\partial x} \right) = 0, \quad z = \eta, \tag{3}$$

where $\mu = \rho\nu$ is the dynamic viscosity.

To facilitate analysis, we assume infinitesimal amplitude and linearize Eq. (1),

$$\frac{\partial}{\partial t} \frac{\boldsymbol{u}_j}{n} = -\frac{1}{\rho} \nabla p_j + \nu_e \nabla^2 \boldsymbol{u}_j - \delta_{2j} \frac{\boldsymbol{F}_{\text{hd}}}{\rho}. \tag{4}$$

In addition, the kinematic free-surface boundary condition Eq. (2) can also be linearized into $\partial\eta/\partial t = w_1$ at $z = 0$. For the free-surface dynamic conditions, strictly speaking, the stress-free conditions cannot be applied on $z = 0$ unless the wave amplitude is much smaller than the boundary-layer thickness $\delta = O(\sqrt{\nu/\omega})$ [10]. The error induced from misplacing the free surface on $z = 0$ is only of higher order. The boundary layers at the water-canopy interface and near the seabed are of more interest and concern. The linearized dynamic free-surface boundary conditions are

$$-p_1 + \rho g \eta + 2\mu \frac{\partial w_1}{\partial z} = 0 \quad \text{and} \quad \mu \left(\frac{\partial u_1}{\partial z} + \frac{\partial w_1}{\partial x} \right) = 0, \quad z = 0. \tag{5}$$

Moreover, we also assume small-amplitude lateral deflection of the seagrass stems, i.e., $x_s \ll l$, where x_s and l are the lateral deflection and the stem length, respectively. Accordingly, the interface between the water and the canopy is linearized to $z = -d_1$, on which the interfacial conditions are enforced, i.e., continuity of velocities, normal and tangential stresses, i.e., $u_1 = u_2$ and $w_1 = w_2$ at $z = -d_1$ and

$$-p_1 + 2\mu \frac{\partial w_1}{\partial z} = -p_2 + 2\mu_e \frac{\partial w_2}{\partial z} \quad \text{and} \quad \mu \left(\frac{\partial u_1}{\partial z} + \frac{\partial w_1}{\partial x} \right) = \mu_e \left(\frac{\partial u_2}{\partial z} + \frac{\partial w_2}{\partial x} \right), \quad z = -d_1, \tag{6}$$

where $\mu_e = \rho\nu_e$ is the effective dynamic viscosity within the canopy. On the seabed, we impose impermeable and no-slip boundary conditions, $u_2 = w_2 = 0$ at $z = -h$.

We linearize the hydrodynamic equations and boundary conditions but retain the quadratic Morison drag to represent leading-order dissipation within the canopy. The hydrodynamic force $\boldsymbol{F}_{\text{hd}} = (F_{\text{hd},x}, F_{\text{hd},z})$ for small lateral deflection motion of the canopy stems is approximated by Morison's equation, i.e.,

$$F_{\text{hd},x} \simeq \rho C_A \frac{\pi}{4} b^2 N \left(\frac{\partial}{\partial t} \frac{u_2}{n} - \frac{\partial^2 x_s}{\partial t^2} \right) + \rho A_s N \left(\frac{\partial}{\partial t} \frac{u_2}{n} \right) + \frac{1}{2} \rho C_D b N \left| \frac{u_2}{n} - \frac{\partial x_s}{\partial t} \right| \left(\frac{u_2}{n} - \frac{\partial x_s}{\partial t} \right), \tag{7}$$

and $F_{\text{hd},z} \simeq 0$. Here, b is the projection width of the canopy stem, and C_D and C_A are the drag and added mass coefficients, respectively.

We model each seagrass stem as a prismatic Euler–Bernoulli cantilever. Let $s = z + h$ be the arclength from the fixed root ($s = 0$) to the free tip ($s = l = d_2$). The governing equation of motion of the vegetation stem reads

$$m_s \frac{\partial^2 x_s}{\partial t^2} + EI \frac{\partial^4 x_s}{\partial s^4} = \frac{F_{\text{hd},x}}{N} = \rho C_A \frac{\pi}{4} b^2 \left(\frac{\partial}{\partial t} \frac{u_2}{n} - \frac{\partial^2 x_s}{\partial t^2} \right) + \rho A_s \frac{\partial}{\partial t} \frac{u_2}{n} + \frac{1}{2} \rho C_D b \left| \frac{u_2}{n} - \frac{\partial x_s}{\partial t} \right| \left(\frac{u_2}{n} - \frac{\partial x_s}{\partial t} \right), \tag{8}$$

where E is Young's modulus, I the second moment of area, and $m_s = \rho_s A_s$ the blade mass per unit length, where ρ_s is the canopy stem density. Replacing $s = z + h$ and rearranging gives

$$\left(m_s + \rho C_A \frac{\pi}{4} b^2 \right) \frac{\partial^2 x_s}{\partial t^2} + EI \frac{\partial^4 x_s}{\partial z^4} = \rho \left(C_A \frac{\pi}{4} b^2 + A_s \right) \frac{\partial}{\partial t} \frac{u_2}{n} + \frac{1}{2} \rho C_D b \left| \frac{u_2}{n} - \frac{\partial x_s}{\partial t} \right| \left(\frac{u_2}{n} - \frac{\partial x_s}{\partial t} \right). \tag{9}$$

The boundary conditions are $x_s = \partial x_s/\partial z = 0$ at $z = -h$ and $\partial^2 x_s/\partial z^2 = \partial^3 x_s/\partial z^3 = 0$ at $z = -d_1$.

2.2. Wave solution

Taking the divergence removes the bulk viscous term because $\nabla \cdot \boldsymbol{u} = 0$. Consequently, viscosity does not enter the pressure equation in the outer region (i.e., inviscid region away from boundaries). The leading-order outer pressure satisfies the inviscid pressure equation; viscous effects enter through boundary layers and hence through effective boundary/interface conditions. We therefore solve an inviscid (outer) problem for the wave field and later account for dissipation separately. Similar approaches have been used for energy dissipation in porous seabeds [11] or wave attenuation by rigid canopies [7]. The solution without viscosity is called the wave solution or outer solution.

When viscosity is not included, the governing equations are

$$\nabla \cdot \boldsymbol{u}_j = 0 \quad \text{and} \quad \frac{\partial}{\partial t} \frac{\boldsymbol{u}_j}{n} = -\frac{1}{\rho} \nabla p_j - \delta_{2j} \frac{\boldsymbol{F}_{\text{hd}}}{\rho}. \tag{10}$$

The free-surface boundary conditions now are $\partial\eta/\partial t = w_1$ and $p_1 = \rho g \eta$ at $z = 0$. In the full viscous problem, tangential stress and velocity are continuous at $z = -d_1$. In the inviscid outer solution we enforce only pressure and normal-velocity continuity, with tangential matching provided by the boundary-layer closure. The interfacial conditions at $z = -d_1$ are $w_1 = w_2$ and $p_1 = p_2$ at $z = -d_1$. On the seabed, only the impermeable condition is applied, $w_2 = 0$ at $z = -h$. The governing equation of the stem motion and the corresponding boundary conditions remain the same.

All equations listed are linearized except for the quadratic drag in Eq. (7). To derive an analytical

solution, we first combine Eqs. (10) and (7),

$$\begin{aligned}\frac{1}{n}\left(1+C_A\frac{\pi}{4}b^2N+A_sN\right)\frac{\partial u_2}{\partial t} &= -\frac{1}{\rho}\frac{\partial p_2}{\partial x}+C_A\frac{\pi}{4}b^2N\frac{\partial^2 x_s}{\partial t^2}-\frac{1}{2}C_DbNn^{-2}\left|u_2-n\frac{\partial x_s}{\partial t}\right|\left(u_2-n\frac{\partial x_s}{\partial t}\right)\\ &\approx -\frac{1}{\rho}\frac{\partial p_2}{\partial x}+C_A\frac{\pi}{4}b^2N\frac{\partial^2 x_s}{\partial t^2}-D\left(u_2-n\frac{\partial x_s}{\partial t}\right),\end{aligned} \tag{11}$$

where the second line of the equation approximates the first line with an equivalent linearization defined below. For simplicity, we rewrite Eq. (11) as

$$\frac{1}{n}(1+A_1+A_2)\frac{\partial u_2}{\partial t}=-\frac{1}{\rho}\frac{\partial p_2}{\partial x}+A_1\frac{\partial^2 x_s}{\partial t^2}-D\left(u_2-n\frac{\partial x_s}{\partial t}\right), \tag{12}$$

where

$$D=\frac{1}{2}C_DbNn^{-2}\frac{\int_{-h}^{-d_1}\overline{|u_2-n\partial x_s/\partial t|^3}\,\mathrm{d}z}{\int_{-h}^{-d_1}\overline{(u_2-n\partial x_s/\partial t)^2}\,\mathrm{d}z},\quad A_1=C_A\frac{\pi}{4}b^2N,\quad\text{and}\quad A_2=A_sN. \tag{13}$$

Here, D in Eq. (13) is defined such that the work done by the linearized load on the vegetation over one wave period is identical to that done by the quadratic drag, which can be obtained through an iterative method. The overline $\overline{(\cdot)}$ denotes time average over one period. Eq. (13) has been widely used as the standard approach for the analytical solution to wave attenuation by vegetation [2, 6].

We consider steady-state solutions, and thus all solutions are harmonic functions oscillating with the same wave frequency. The free-surface elevation η can be expressed in the form (periodic in time, progressive and attenuating in space), $\eta=\Re\left\{H_0/2\mathrm{e}^{\mathrm{i}(\omega t-kx)}\right\}$, where $k=k_r+\mathrm{i}k_i$ is the complex wave number, ω is the (real) angular wave frequency, and H_0 is the incident wave height at $x=0$. The corresponding local wave height $H(x)$ decays exponentially and is expressed as $H(x)=H_0\mathrm{e}^{k_ix}$, where $k_i<0$ for attenuation in the positive x-direction.

As in linear wave theory, u_j, w_j, and p_j are proportional to $\mathrm{e}^{\mathrm{i}(\omega t-kx)}$ and take the separable forms

$$\{u_j,w_j,p_j\}(x,z,t)=\Re\left\{\{U_j(z),W_j(z),P_j(z)\}\,\mathrm{e}^{\mathrm{i}(\omega t-kx)}\right\}, \tag{14}$$

and the blade deflection is represented as $x_s=\Re\left\{X_s(d_j,\omega,H,\ldots;z)\,\mathrm{e}^{\mathrm{i}(\omega t-kx)}\right\}$.

Combining Eqs. (10) and (14) gives the velocity amplitudes in terms of pressure in Layer 1 and the ordinary differential equation (ODE) for P_1 due to the continuity equation:

$$U_1=\frac{k}{\rho\omega}P_1,\quad W_1=\frac{\mathrm{i}}{\rho\omega}\frac{\mathrm{d}P_1}{\mathrm{d}z},\quad\text{and}\quad\frac{\mathrm{d}^2P_1}{\mathrm{d}z^2}-k^2P_1=0. \tag{15}$$

Similarly, in Layer 2 for the canopy, we have

$$U_2=\frac{\mathrm{i}n}{\Gamma}\frac{k}{\rho\omega}P_2+\frac{n(-A_1+\mathrm{i}nD/\omega)}{\Gamma}\omega X_s,\quad W_2=\frac{\mathrm{i}n}{\rho\omega}\frac{\mathrm{d}P_2}{\mathrm{d}z},\quad\text{and}\quad\frac{\mathrm{d}^2P_2}{\mathrm{d}z^2}-\kappa^2P_2+\varsigma X_s=0, \tag{16}$$

where

$$\left(\frac{\kappa}{k}\right)^2=\frac{\mathrm{i}}{\Gamma},\quad\varsigma=\rho k\omega^2\frac{A_1-\mathrm{i}nD/\omega}{\Gamma},\quad\text{and}\quad\Gamma=\mathrm{i}(1+A_1+A_2)+nD/\omega. \tag{17}$$

Combining the free-surface boundary conditions yields $P_1=(g/\omega^2)\mathrm{d}P_1/\mathrm{d}z$ at $z=0$. The boundary conditions at the interfaces between the water layer and the canopy layer are expressed as $P_1=P_2$ and $\mathrm{d}P_1/\mathrm{d}z=n\mathrm{d}P_2/\mathrm{d}z$ at $z=-d_1$. The kinematic boundary condition at the horizontal impermeable bottom is given by $\mathrm{d}P_2/\mathrm{d}z=0$ at $z=-h$. Meanwhile, the ODE for X_s is deduced from Eq. (8) as

$$-\omega^2\left(m_s+\rho\frac{A_1}{N}\right)X_s+EI\frac{\mathrm{d}^4X_s}{\mathrm{d}z^4}=\mathrm{i}\omega\frac{\rho}{N}\left(A_1+A_2\right)\frac{U_2}{n}+\frac{\rho D}{N}\left(U_2-\mathrm{i}\omega nX_s\right). \tag{18}$$

After inserting Eq. (16) into the equation above and rearranging it, we obtain

$$\frac{\mathrm{d}^4 X_s}{\mathrm{d}z^4} + \lambda^4 X_s + \xi P_2 = 0, \tag{19}$$

where

$$\lambda^4 = -\frac{\omega^2}{EI}\left(m_s + \frac{\rho}{N}\frac{\mathrm{i}A_1 + nD/\omega}{\Gamma}\right), \quad \xi = \frac{1}{EI}\frac{k}{N}\frac{(A_1 + A_2) - \mathrm{i}nD/\omega}{\Gamma}. \tag{20}$$

The boundary conditions are $X_s = \partial X_s/\partial z = 0$ at $z = -h$ and $\partial^2 X_s/\partial z^2 = \partial^3 X_s/\partial z^3 = 0$ at $z = -d_1$. In conclusion, we have a system of three ODEs:

$$\frac{\mathrm{d}^4}{\mathrm{d}z^4}\begin{bmatrix}0\\0\\X_s\end{bmatrix} + \frac{\mathrm{d}^2}{\mathrm{d}z^2}\begin{bmatrix}P_1\\P_2\\0\end{bmatrix} + \begin{bmatrix}-k^2 & 0 & 0\\ 0 & -\kappa^2 & \varsigma\\ 0 & \xi & \lambda^4\end{bmatrix}\begin{bmatrix}P_1\\P_2\\X_s\end{bmatrix} = \begin{bmatrix}0\\0\\0\end{bmatrix} \tag{21}$$

The ODE for P_1 is uncoupled from the other two, though coupled through the boundary conditions. We can assume a solution in the form of $P_1 = C_1^{P_1}\cosh(k(z+d_1)) + C_2^{P_1}\sinh(k(z+d_1))$. On the contrary, P_2 and X_s are coupled. We assume exponential solutions of the form $P_2 = C^{P_2}\mathrm{e}^{r(z+h)}$ and $X_s = C^{X_s}\mathrm{e}^{r(z+h)}$. We substitute these assumed solutions into both equations to obtain a system of algebraic equations in terms of C^{P_2}, C^{X_s}, and r:

$$\begin{bmatrix}r^2 - \kappa^2 & \varsigma\\ \xi & r^4 + \lambda^4\end{bmatrix}\begin{bmatrix}C^{P_2}\\C^{X_s}\end{bmatrix} = \begin{bmatrix}0\\0\end{bmatrix}. \tag{22}$$

Let the determinant of the coefficient matrix be zero and we get the characteristic equation, $r^6 - \kappa^2 r^4 + \lambda^4 r^2 - (\kappa^2\lambda^4 + \xi\varsigma) = 0$, which is a sixth-degree polynomial in r. Substituting $y = r^2$ into the characteristic equation provides a cubic equation, $y^3 - \kappa^2 y^2 + \lambda^4 y - (\kappa^2\lambda^4 + \xi\varsigma) = 0$. We can solve this cubic equation using Cardano's formula. Let the three complex roots be y_1, y_2, and y_3, which are used to find r:

$$r_{1,4} = \pm\sqrt{y_1},\ r_{2,5} = \pm\sqrt{y_2}, r_{3,6} = \pm\sqrt{y_3}. \tag{23}$$

Since r_i and r_{i+3} are opposite numbers, the general solutions for P_2 and X_s are in the form of

$$P_2 = \sum_{i=1}^{3} C_{2i-1}^{P_2}\mathrm{e}^{r_i(z+h)} + C_{2i}^{P_2}\mathrm{e}^{-r_i(z+h)}, \quad X_s = \sum_{i=1}^{3} C_{2i-1}^{X_s}\mathrm{e}^{r_i(z+h)} + C_{2i}^{X_s}\mathrm{e}^{-r_i(z+h)}, \tag{24}$$

where $C_i^{X_s} = (\kappa^2 - r_i^2)/\varsigma C_i^{P_2}$ from the first row of Eq. (22).

In conclusion, there are eight unknowns, $C_1^{P_1}$, $C_2^{P_1}$, and $C_i^{P_2}, i = 1, \cdots, 6$, and one dispersion relation. The eight boundary conditions determine the integration constants up to an arbitrary amplitude. Enforcing a nontrivial solution yields the dispersion relation for k; the amplitude is then fixed by prescribing the local wave height H.

2.3. Viscous closure and laminar boundary layers

In the wave (outer) solution, we impose no constraints on the horizontal velocity or tangential stresses at the free surface, the water-canopy interface, or the seabed. As a consequence, the outer solution generally exhibits a finite jump in the horizontal velocity amplitude (and hence in the shear stress) across the water-canopy interface [6, 4]. To assess the role of viscosity and to close the tangential stress conditions, we introduce laminar oscillatory boundary layers at the water-canopy interface $z = -d_1$ and near the seabed $z = -h$. The weak boundary layer at the free surface is neglected.

The momentum equation (4) in the boundary layers can be approximated by [10]:

$$\frac{\partial}{\partial t}\frac{u_j}{n} = -\frac{1}{\rho}\frac{\partial p_j}{\partial x} + \nu_e\frac{\partial^2 u_j}{\partial z^2} - \delta_{2j}\frac{F_{\mathrm{hd},x}}{\rho}. \tag{25}$$

Here the dynamic pressure p_j is taken as prescribed by the wave solution presented in the previous section. After linearizing the term $F_{\text{hd},x}$ as before, Eq. (25) becomes a solvable linear partial differential equation. Substituting Eq. (14) into Eq. (25) yields, in the water layer and the canopy layer,

$$\frac{\mathrm{d}^2U_1}{\mathrm{d}z^2} - \beta^2 U_1 = \frac{\mathrm{i}k}{\rho\nu} P_1, \quad \text{and} \quad \frac{\mathrm{d}^2U_2}{\mathrm{d}z^2} - \alpha^2 U_2 = \frac{\mathrm{i}k}{\rho\nu_e} P_2 + \frac{1}{\nu_e}(-A_1\omega^2 + \mathrm{i}\omega n D) X_s, \tag{26}$$

where $\beta = \sqrt{\mathrm{i}\omega/\nu}$ and $\alpha = \sqrt{(\Gamma/n)\omega/\nu_e}$.

The wave (outer) solution provides a particular solution to (26). Accordingly, we write the total velocity amplitudes as $U_j(z) = U_j^I(z) + \widetilde{U}_j(z)$, where U_j^I denotes the inviscid outer solution and the boundary-layer correction $\widetilde{U}_j$ satisfies the homogeneous equations

$$\frac{\partial^2 \widetilde{U}_1}{\partial z^2} - \beta^2 \widetilde{U}_1 = 0, \qquad \frac{\partial^2 \widetilde{U}_2}{\partial z^2} - \alpha^2 \widetilde{U}_2 = 0. \tag{27}$$

We choose the branches of β and α such that $\Re(\beta) > 0$ and $\Re(\alpha) > 0$, ensuring exponential decay away from the interface. By imposing the continuity of tangential stress across $z = -d_1$, we obtain

$$U_1(z) = U_1^I(z) + \big(U_{d_1} - U_1^I(-d_1)\big)\, \mathrm{e}^{-\beta\,(z+d_1)}, \tag{28}$$

$$U_2(z) = U_2^I(z) + \big(U_{d_1} - U_2^I(-d_1)\big)\, \mathrm{e}^{\alpha(z+d_1)} - U_2^I(-h)\mathrm{e}^{-\alpha(z+h)}, \tag{29}$$

where

$$U_{d_1} = \frac{\nu\beta\, U_1^I(-d_1) + \nu_e\alpha\, U_2^I(-d_1) + \left(\nu\, \dfrac{\mathrm{d}U_1^I}{\mathrm{d}z} - \nu_e\, \dfrac{\mathrm{d}U_2^I}{\mathrm{d}z}\right)_{z=-d_1}}{\nu\beta + \nu_e\alpha}. \tag{30}$$

2.4. Wave attenuation

The theory presented in previous sections is based on local properties only. Accordingly, an exponential decay function is found, i.e., a complex k with negative imaginary part $k_i < 0$. An incremental method [12, 7, 4] is used to find wave attenuation across an entire canopy. The wave heights at x can be obtained numerically following $H(x + \Delta x) = H(x)\mathrm{e}^{k_i \Delta x}$, with $|k_i \Delta x| \ll 1$.

For irregular waves, the stochastic linearization is adopted to find the damping coefficient D:

$$D = \frac{1}{2} C_D b N n^{-2} \frac{\int_{-h}^{-d_1} \sigma_{u_{2,r}}^3 \mathrm{d}z}{\int_{-h}^{-d_1} \sigma_{u_{2,r}}^2 \mathrm{d}z}, \tag{31}$$

where $\sigma_{u_{2,r}}(z)$ is the standard deviation of the relative velocity $u_2 - n\partial x_s/\partial t$ at z in the canopy layer. The parameter D in Eqs. (17) and (19) should also be replaced with this new D. As in regular waves, the wave spectrum at $x + \Delta x$ is given by $S(\omega, x + \Delta x) = S(\omega, x)\mathrm{e}^{2k_i(\omega,x)\Delta x}$, where $S(\omega, x)$ is the wave spectrum at x.

3. Model validation

Experimental data on wave attenuation across a canopy of flexible mimics were reported in [13], which covered both regular waves and irregular waves. Each blade mimic measured $10\,\mathrm{cm}$ in length, $3\,\mathrm{mm}$ in width, and $0.1\,\mathrm{mm}$ in thickness, with a material density of $900 \pm 20\,\mathrm{kg/m^3}$ and an estimated Young's modulus of $1.6\,\mathrm{GPa}$. In our analytical model, we use $\rho_s = 910\,\mathrm{kg/m^3}$. The canopy was $9\,\mathrm{m}$ long with a distribution density $N = 40\,000\,\mathrm{stems/m^2}$. The water depths at the canopy were $0.30\,\mathrm{m}$, $0.50\,\mathrm{m}$, and $0.80\,\mathrm{m}$. Wave heights along the canopy were reported in their Figure 3 for $h = 0.30\,\mathrm{m}$ and $h = 0.50\,\mathrm{m}$ at four locations. In our model, we use the measured wave heights at the start of the canopy

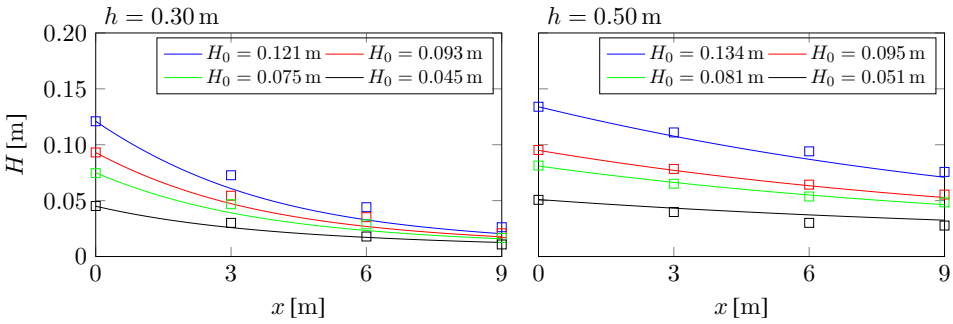


Figure 2: Comparison between measured and predicted regular wave attenuation. Lines represent the analytical solution, while square markers indicate experimental data.

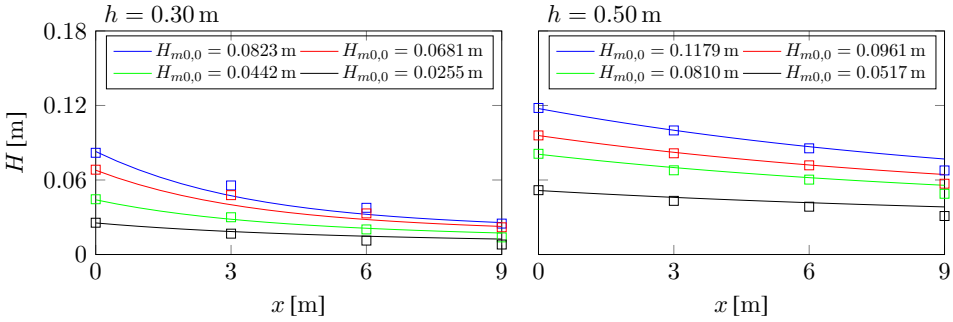


Figure 3: Comparison between measured and predicted irregular wave attenuation. Lines represent the analytical solution, while square markers indicate experimental data.

instead of the target wave heights (see their Table 1) as the incident wave height H_0 for regular waves and $H_{m0,0}$ for irregular waves. As suggested in [14], we use $C_D = 2.0$ and $C_A = 0.5$ for all cases.

For regular waves, we reproduce four wave heights at a fixed wave period $T = 1.25\,\text{s}$ for each water depth, $h = 0.30\,\text{m}$ and $h = 0.50\,\text{m}$. Since the along-canopy wave heights for $h = 0.80\,\text{m}$ were not reported in [13], this case is not included in the comparison. As shown in Fig. 2, the analytical predictions agree reasonably well with the measurements. The agreement is better for $h = 0.50\,\text{m}$ than for $h = 0.30\,\text{m}$, especially for the larger wave heights in shallower water. Since all cases fall within the Stokes second- to third-order regimes, while the stem deflections remain asymptotically small (less than 5% of the stem length), the discrepancies are more likely attributable to stronger wave nonlinearity in shallow water. The velocity profiles can no longer be adequately represented by linear wave theory. Overall, the model still provides reasonable first-order attenuation predictions for moderately nonlinear waves.

Irregular-wave attenuation across the same canopy was also examined at the two water depths, using a fixed peak period $T_p = 1.25\,\text{s}$. The incident waves followed a JONSWAP spectrum with peak enhancement factor $\gamma = 3.3$. Overall, the analytical predictions agree well with the measurements, see Fig. 3. The local zero-moment wave height H_{m0} is estimated from the wave spectrum using $H_{m0}(x) = 4\sqrt{\int_0^\infty S(x;\omega)\mathrm{d}\omega}$. Consistent with the regular-wave results in Fig. 2, the largest discrepancies occur for the highest $H_{m0,0}$ in the shallow-water case. Overall, the analytical model yields a reasonable first-order prediction of irregular-wave attenuation.

The blade lateral deflections were not reported in [13]. The canopy used in their experiments was

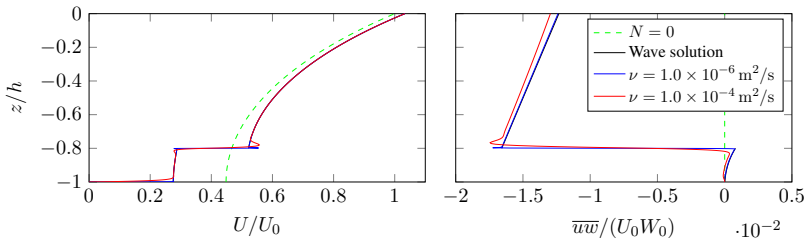


Figure 4: The wave-only solution and the combined solution including viscous boundary-layer effects, shown for two values of the kinematic viscosity. Left: horizontal velocity amplitude profiles. Right: period-averaged momentum flux $\overline{uw}$.

relatively rigid. Stem flexibility can be characterized by the parameter proposed by [15]:

$$CaL = \frac{\rho b U_w^2 l^3}{EI} \frac{2\pi l}{U_w T}, \tag{32}$$

where U_w is a representative wave orbital velocity. For a preliminary estimate in regular waves, we take U_w as the linear-theory velocity amplitude at the stem tip in the absence of the canopy. For irregular waves, we use the root-mean-square orbital velocity for U_w together with the mean wave period T_{m0} [14]. Smaller CaL indicates stiffer stems. In the experiments, $CaL \in [0.74,\ 2.97]$, and the model predicts a normalized tip deflection in the range $[0.004,\ 0.033]$, indicating only minor deflections.

The present formulation is intended as a first-order approximation and is expected to be most reliable when the wave remains approximately linear and the stem deflection remains small compared with the stem length. A precise validity envelope in terms of the governing non-dimensional parameters of the coupled wave–seagrass problem remains to be established and is left for future work. Beyond the present range, the model may still provide qualitative or first-order estimates, but its accuracy should be assessed with caution.

4. Discussion on the viscous closure

The viscous closure likely contributes less to wave attenuation than canopy-induced drag given its thin thickness compared to the canopy height, but it removes the discontinuity in the horizontal velocity profile and provides a first-order correction. It also enables a physically consistent estimate of shear stress. To illustrate its effect, we consider the regular-wave case with $H_0 = 0.134\,\mathrm{m}$, $T = 1.25\,\mathrm{s}$, and $h = 0.50\,\mathrm{m}$ at $x = 4.5\,\mathrm{m}$, where the local wave height is $H = 0.096\,\mathrm{m}$.

Using the molecular kinematic viscosity of water as a first-order approximation, Fig. 4 compares the horizontal velocity amplitude and the period-averaged momentum flux $\overline{uw}$ from linear wave theory without canopy, the outer wave solution, and the combined solutions with viscous boundary-layer effects for $\nu = 1.0 \times 10^{-6}\,\mathrm{m}^2/\mathrm{s}$ and $\nu = 1.0 \times 10^{-4}\,\mathrm{m}^2/\mathrm{s}$. Away from the seabed and canopy–water interface, the combined solution is nearly identical to the wave solution. The boundary-layer thickness increases from about $\delta \sim 4.0 \times 10^{-4}\,\mathrm{m}$ to $\delta \sim 4.0 \times 10^{-3}\,\mathrm{m}$ as ν increases, and is generally larger on the water side than within the canopy. The viscous closure causes only small changes in velocity amplitude, while enforcing a smooth transition near the seabed.

The momentum flux $\overline{uw}$ is more sensitive to ν than the velocity amplitude. In linear wave theory, $\overline{uw} = 0$, whereas with the canopy present the phase difference between u and w departs from $\pi/2$, giving $\overline{uw} > 0$ in the canopy and $\overline{uw} < 0$ in the water layer. Although amplitude changes are small, slight phase shifts produce noticeable differences in $\overline{uw}$. Further work is needed to clarify the role of the viscous closure.

5. Conclusions

We developed an analytical model for two-way coupled interactions between water waves and a submerged, flexible seagrass canopy. The hydrodynamics are formulated as a two-layer (water/canopy) system with linearized governing equations and boundary conditions, while quadratic Morison-type drag is retained as the primary dissipation mechanism. The canopy motion is represented by prismatic Euler–Bernoulli cantilevers forced by the wave-induced hydrodynamic loads. The model yields a complex wave number and exponential wave-height decay, and is extended to irregular waves through stochastic linearization. Comparisons with laboratory measurements show reasonable first-order predictions of attenuation for both regular and irregular waves, despite moderate wave nonlinearity. The viscous closure enforces no-slip at the seabed and smooths the horizontal-velocity transition across the canopy–water interface, but its appropriate parameterization remains uncertain. Further validation of stem deflections, in-canopy velocity profiles, and turbulence-based closures is needed.

References

[1] Robert A. Dalrymple, James T. Kirby, and Paul A. Hwang. Wave Diffraction Due to Areas of Energy Dissipation. *Journal of Waterway, Port, Coastal, and Ocean Engineering*, 110(1):67–79, February 1984.

[2] Nobuhisa Kobayashi, Andrew W. Raichle, and Toshiyuki Asano. Wave Attenuation by Vegetation. *Journal of Waterway, Port, Coastal, and Ocean Engineering*, 119(1):30–48, January 1993.

[3] Toshiyuki Asano, Hiroshi Deguchi, and Nobuhisa Kobayashi. INTERACTION BETWEEN WATER WAVES AND VEGETATION. *Coastal Engineering Proceedings*, 1(23), January 1992.

[4] Zhilong Wei, Morgane Weiss, Trygve Kristiansen, David Kristiansen, and Yanlin Shao. Wave attenuation by cultivated seaweeds: A linearized analytical model. *Coastal Engineering*, 195:104642, January 2025.

[5] Longhuan Zhu, Kimberly Huguenard, David W. Fredriksson, and Jiarui Lei. Wave attenuation by flexible vegetation (and suspended kelp) with blade motion: Analytical solutions. *Advances in Water Resources*, 162:104148, April 2022.

[6] Niels G. Jacobsen. Wave-averaged properties in a submerged canopy: Energy density energy flux radiation stresses and Stokes drift. *Coastal Engineering*, 117:57–69, November 2016.

[7] Niels G. Jacobsen and Brian C. McFall. Wave-averaged properties for non-breaking waves in a canopy: Viscous boundary layer and vertical shear stress distribution. *Coastal Engineering*, 174:104117, June 2022.

[8] Bjarne Jensen, Niels Gjøl Jacobsen, and Erik Damgaard Christensen. Investigations on the porous media equations and resistance coefficients for coastal structures. *Coastal Engineering*, 84:56–72, February 2014.

[9] Otto E. Neshamar, Niels G. Jacobsen, Dominic A. van der A, and Tom O'Donoghue. Linear and nonlinear frequency-domain modelling of oscillatory flow over submerged canopies. *Journal of Hydraulic Research*, 61(5):668–685, September 2023.

[10] Chiang C Mei, Michael Stiassnie, and Dick K-P Yue. *Theory and Applications of Ocean Surface Waves*. World Scientific, July 2005.

[11] Philip L.-F. Liu and Robert A. Dalrymple. The damping of gravity water-waves due to percolation. *Coastal Engineering*, 8(1):33–49, February 1984.

[12] Longhuan Zhu. *Wave Attenuation Capacity of Suspended Aquaculture Structures with Sugar Kelp and Mussels*. PhD thesis, The University of Maine, August 2020.

[13] José Francisco Sánchez-González, Virginia Sánchez-Rojas, and Constantine Demetrius Memos. Wave attenuation due to Posidonia oceanica meadows. *Journal of Hydraulic Research*, 49(4):503–514, July 2011.

[14] Niels Gjøl Jacobsen. A theoretical approach for irregular wave attenuation through vegetation and application to spectral wave models. *Applied Ocean Research*, 166:104915, January 2026.

[15] Jiarui Lei and Heidi Nepf. Wave damping by flexible vegetation: Connecting individual blade dynamics to the meadow scale. *Coastal Engineering*, 147:138–148, May 2019.

10th International Conference on HYDROELASTICITY IN MARINE TECHNOLOGY
Trondheim, Norway, June16th-18th, 2026

Bending Modes and Fluid–Structure Interaction in Fish-Inspired Swimmers: Implications for Flexible Underwater Robot Design

Norvik, C.[1,*] Greco, M.[1,2] and Lugni, C.[3,1,2]

[1] Department of Marine Technology, Norwegian University of Science and Technology, Trondheim, Norway
[2] Institute of Marine Engineering, CNR-INM, Rome, Italy
[3] University of Naples Federico II, Naples, Italy

Abstract. Body flexibility plays a crucial role in the interaction between swimming fish and its surrounding fluid. This study investigates the hydroelastic response of passive fish-like bodies with steady forward motion. Hydrodynamic loads are modeled using slender-body theory while internal forces and structural dynamics are represented by Euler-Bernoulli beam theory. A finite-element formulation was developed to determine the wet bending modes as a function of body geometry, stiffness and forward speed. The analysis found that primary modes correspond closely to the kinematic patterns observed in fish locomotion and were consistent with Strouhal numbers for efficient propulsion. It revealed how biological systems by increasing their effective body stiffness via muscle contraction can maintain similar deformation pattern and Strouhal number while raising tail-beat frequency and forward speed. A parametric scaling analysis further indicate that the relationship between swimming frequency and velocity observed across aquatic animals can be explained by the scaling of structural modes of the body. The results support the hypothesis that mechanical resonance plays an important role in swimming performance and highlight the interplay between body size, flexibility, and operating regime on the hydroelastic response. These findings provide physical insight that may guide the design of flexible fish-inspired underwater robots.

Key words: *fish-inspired swimming; hydroelastic modes; mechanical resonance; scaling relations*

1. Introduction

Nature has long inspired innovations in engineering. In marine technology, a major historical motivation has been to improve propulsive efficiency. Many fishes demonstrate exceptional performance, and still to this day outperform conventional AUVs (autonomous underwater vehicles) in swimming capabilities [1]. Despite extensive cross-disciplinary research, several aspects of fish-fluid interaction and the associated hydroelastic mechanisms remain unsolved, particularly how body flexibility and morphology influence propulsive performance [2]. Fish exhibit a wide diversity of body forms and swimming strategies, yet their locomotor patterns can be organized into overarching modes [3, 4]. Body-caudal-fin (BCF) propulsion enables efficient, high-speed locomotion and BCF swimming modes are commonly classified as anguilliform, subcarangiform, carangiform, thunniform and ostraciiform [5]. With the exception of ostraciiform, BCF swimmers generate a backward-traveling wave along the body, with a wavelength in the order of 0.5-2 times the body length [4, 5]. The wave phase speed exceeds the forward swimming speed during efficient locomotion, and the wave amplitude increases toward the tail, becoming progressively concentrated in the posterior body going from anguilliform to tunniform mode of swimming [4, 5].

A governing process underlying efficient propulsion in BCF swimmers is the generation of a coherent vortex wake that enhances thrust while limiting wasted energy. This performance is commonly

[*]Correspondence to: carina.norvik@ntnu.no

measured by the Strouhal number, St, which for fish swimming expresses the ratio between the product of the tail flapping frequency and amplitude and the forward swimming speed as

$$St = \frac{fA}{U} \tag{1}$$

where f is the tail-beat frequency, A the peak-to-peak trailing-edge amplitude and U the forward swimming velocity. The dominant vortex-shedding frequency in the wake is generally comparable to the tail-beat frequency, and the wake width scales with the lateral tail excursion [6]. At sufficiently high Reynolds numbers, for efficient locomotion across swimming and flying animals, the Strouhal number typically lies in the range of $0.2 \leq St \leq 0.4$ with a mean value of $St \approx 0.3$ [4, 7]. Recent kinematic analyses of BCF swimmers further show that their locomotion can broadly be categorized as standing-wave, mixed-wave, or traveling-wave mode, depending on the relative strengths of standing-wave and traveling-wave components [8]. These modal forms influence how energy is transferred to the fluid and how thrust is generated.

Previous modeling studies have identified mechanical resonance as one of the key mechanisms through which fluid-structure interaction influences swimming performance [9]. When the added-mass and structural-mass distributions along the body are similar, the resulting wet bending modes remain close in shape to the corresponding dry modes [10]. However, this similarity has been shown to break down in fish with truncated or forked caudal fins, where the added-mass distribution differs substantially from the structural-mass distribution [11]. Studies on flexible pitching panels have shown that optimal performance can be achieved when the structural natural frequency is tuned to wake hydrodynamic resonant frequency associated with maximum spatial growth of wake instabilities [12]. It was suggested that animals may tune their body resonance to the hydrodynamic resonance of their wake to improve efficiency. Analytical models further indicate that both internal material damping and external fluid-dynamic damping are crucial in shaping fish-like kinematics and determining propulsion efficiency [9]. Fish possess both passive stiffness and the capability to actively modulate their stiffness through muscle activation. Furthermore, experiments have shown that muscle activation can be the primary factor governing the midbody-caudal flexural rigidity [9].

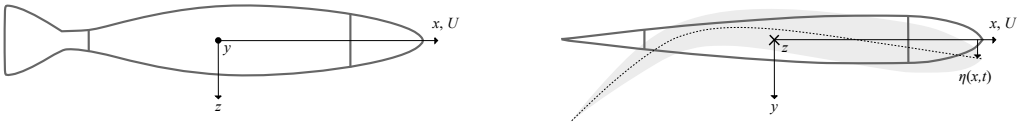
Our research reveals how forward velocity, stiffness distribution and body geometry can affect the hydroelastic response of a simplified fish-like system, through the estimation of bending modes and corresponding natural frequencies with finite-element method (FEM). Only passive stiffness is explicitly modeled. However, variations in trunk stiffness provide direct insight into the consequences of muscle activation and the associated changes in body mechanics. The paper is organized as follows. Section 2. outlines the proposed methodology; Section 3. presents the results on how the mechanical response changes with forward velocity and trunk stiffness, and introduces similarity scaling for the mechanical response; Section 4. discusses potential connections between bending modes and fish swimming modes and between muscle activation and Strouhal number, and compares our findings with proposed scaling laws for fish swimming; and finally Section 5. contains the main conclusions.

2. Mathematical and Numerical Modeling

The hydrodynamic loads were modeled with linear slender-body potential-flow theory, assuming high Reynolds number, geometric slenderness and small lateral slopes [13, 14]. Body flexibility was represented using Euler-Bernoulli beam theory, appropriate for slender structures undergoing bending-dominated deformation with negligible shear deformation [15]. Under the assumption of small body deformations, the added-mass distribution was taken as time invariant. The body was assumed to be neutrally buoyant with density equal to that of the surrounding water, aligned with typical swimming conditions for fish-like bodies.

Figure 1 shows the body-fixed coordinate system translating with the forward speed U and with the origin at the midpoint of the undeformed body. The simplified fish geometry with truncated caudal fin

adopted for the present investigations is also illustrated. The body was divided into three main regions – tail, trunk and head – with corresponding region-dependent stiffness denoted as $[E^{\text{tail}}, E^{\text{trunk}}, E^{\text{head}}]$. The tail is characterized by its thin shape and very low structural mass compared with its hydrodynamic added mass. The head region has structural mass and added mass of similar magnitude and exhibits high flexural rigidity due to skull bones stiffness and geometric thickness. The trunk, consisting of a series of vertebrae, is comparatively flexible and can exhibit different effective stiffnesses depending on muscle activity. In this study, the reference body has length of 1.0 m, a maximum depth of 0.17 m, and a maximum width of 70% of the maximum depth. The length was set to 1.0 m so that the body-length speed U_b (L/s) is identical to forward speed U (m/s). The reference tail-trunk-head stiffness distribution was $[E^{\text{tail}}_{\text{ref}}, E^{\text{trunk}}_{\text{ref}}, E^{\text{head}}_{\text{ref}}] = [15,\ 0.5,\ 1.5{\cdot}10^3]$ MPa, based on measurements and biological data reported by Aleyev [16] and Jimenez et al. [9].



(a) Side view (b) Top view

Figure 1: Coordinate system translating at the forward speed U with origin at the midpoint of the undeformed body. The body is divided into tail, trunk and head, and the local body deformation η is indicated from the top view.

The wet bending modes of the fish-like body with free-free boundary conditions and forward speed U can be estimated as steady-state oscillatory solutions of a system with hydrodynamic forces generated by the body lateral deformation. The transverse motion at a generic cross-section with coordinate x is governed by

$$m(x)\,\frac{\partial^2\eta(x,t)}{\partial t^2}\ +\ \frac{\partial^2}{\partial x^2}\left(EI(x)\,\frac{\partial^2\eta(x,t)}{\partial x^2}\right) = f_2^{\text{hyd}}(x,t)\,, \tag{2}$$

where $\eta(x,t)$ is the lateral midline displacement, and $m(x)$, $EI(x)$, and $f_2^{\text{hyd}}(x,t)$ denote, respectively, the structural mass, the flexural rigidity, and the motion-induced hydrodynamic sway force per unit length. In a coordinate system translating at constant forward speed U, the local two-dimensional hydrodynamic forces, generated by the deformations of a slender body in potential flow, can be written as

$$f_2^{\text{hyd}}(x,t) = -\left(\frac{\partial}{\partial t} - U\,\frac{\partial}{\partial x}\right)\left[\left(\frac{\partial\eta(x,t)}{\partial t} - U\,\frac{\partial\eta(x,t)}{\partial x}\right)a_{22}(x)\right], \tag{3}$$

where $a_{22}(x)$ is the added mass per unit length of the body at position x. This expression shows that the fluid forces modify the beam dynamics through added mass ($\propto \ddot{\eta}$), hydrodynamic damping ($\propto U\dot{\eta}$), and hydrodynamic stiffness ($\propto U^2\eta$). The hydrodynamic damping term arises due to reactive forces rather than viscous dissipation. Because we are interested in steady-state oscillatory (modal) solutions, the displacement is separated into spatial and temporal components,

$$\eta(x,t) := \Psi(x)q(t)\,, \tag{4}$$

where $\Psi(x)$ is the mode shape and $q(t)$ is the associated time-dependent generalized coordinate oscillating at the corresponding natural frequency. To estimate bending modes, the beam was discretized using a finite-element formulation, with Hermite-cubic interpolation functions and the elemental matrices were derived from kinetic energy, potential energy and virtual work [17]. The assembly of the

elemental contributions to the global system matrices lead to the governing equation of motion in matrix form as

$$\mathbf{M}^{\text{eff}}\,\underline{\ddot{q}}(t) + \mathbf{C}^{\text{eff}}\,\underline{\dot{q}}(t) + \mathbf{K}^{\text{eff}}\,\underline{q}(t) = \underline{0}\,. \tag{5}$$

Here the subscript eff denotes the effective system matrices accounting for fluid-structure interaction effects, defined as

$$\mathbf{M}^{\text{eff}} := \mathbf{M} + \mathbf{M}^{\text{hyd}}, \quad \mathbf{C}^{\text{eff}} := \mathbf{C}^{\text{hyd}}, \quad \mathbf{K}^{\text{eff}} := \mathbf{K} + \mathbf{K}^{\text{hyd}}, \tag{6}$$

where $\mathbf{M}$ and $\mathbf{K}$ denote the structural mass and stiffness matrices, while $\mathbf{M}^{\text{hyd}}$, $\mathbf{C}^{\text{hyd}}$, and $\mathbf{K}^{\text{hyd}}$ represent the hydrodynamic added-mass, damping, and stiffness contributions, respectively. Eq. (5) was solved to obtain the system eigenvalues and eigenvectors, to find the natural frequencies and bending modes of the body. The modes of the system at zero forward speed were ordered by their frequency, while subsequent modes were tracked using the modal assurance criterion (MAC) [18], as frequency alone did not uniquely identify the modes with increasing velocity. To examine the influence of the structural and hydrodynamic stiffness with increasing forward velocity, the mode shapes $\underline{\Psi}_i$ (real part of the right eigenvectors) were mass normalized with $\underline{\Psi}_i = \alpha_i \underline{\tilde{\Psi}}_i$ so that

$$\underline{\tilde{\Psi}}_i^T \mathbf{M}^{\text{eff}} \underline{\tilde{\Psi}}_i = 1, \qquad \underline{\tilde{\Psi}}_i^T \mathbf{K}^{\text{eff}} \underline{\tilde{\Psi}}_i = K_{ii}^{\text{eff}}\,. \tag{7}$$

Here K_{ii}^{eff} denotes the modal (projected) effective stiffness associated with mode i, which is equal to the corresponding natural angular frequency squared for real eigenvectors.

To examine how the body size and stiffness affect the wet mode shapes, we introduced the following geometric scaling parameters

$$s = \frac{(x, y, z)}{(x_{\text{ref}}, y_{\text{ref}}, z_{\text{ref}})}, \qquad s_x = \frac{x}{x_{\text{ref}}}, \qquad s_\varepsilon = \frac{\varepsilon}{\varepsilon_{\text{ref}}} \tag{8}$$

with ε as a slenderness parameter defined by the maximum depth-and-width-to-length ratio, and the stiffness-scaling parameters

$$\kappa = \frac{E}{E_{\text{ref}}}, \qquad \kappa_{\text{trunk}} \approx \frac{E^{\text{trunk}}}{E_{\text{ref}}^{\text{trunk}}} \tag{9}$$

where s and κ scale the body globally, while s_x, s_ε, and κ_{trunk} selectively scale the length, slenderness and trunk stiffness, respectively. Varying only the trunk stiffness allows us to assess how muscle activation could influence the natural modes and natural frequencies of the fish.

A preliminary verification of the implemented FEM formulation for the beam model was carried out with ABAQUS-based FEM models serving as reference solutions at zero forward speed [11]. To verify the formulation at non-zero forward speed, we adapted the closed-form solutions for free-free, non-uniform Euler-Bernoulli beams derived by Sarkar and Ganguli [19] to identify geometries with varying stiffness and forward speed. For identified cases, the closed-form solutions provide accurate benchmark mode shapes and frequencies for non-uniform beams in the absence of damping.

3. Results

In the preliminary verification with ABAQUS-based FEM models, the first mode shape and corresponding natural frequency for similar fish-like geometries were compared, and showed close agreement with frequency differences within 1-5$\%$. For the identified geometries by closed-form solutions, predicted mode shaped compared well and the natural frequencies agreed with our FEM results within approximately 1% for the cases found. However, the closed-form solutions could only be applied in configurations where forward-speed effects remained weak, and therefore provided verification over a limited subset of the parameter space.

3.1. Undamped bending modes

The undamped eigenvectors remained real unless modes coalesced. Figure 2 shows the first three bending modes as a functions of forward speed when only hydrodynamic stiffness was included, for both the reference body ($\kappa = 1$) and a body with trunk stiffness increased by a factor of four ($\kappa_{\text{trunk}} = 4$). At zero forward speed, the wet modes are qualitatively consistent with what is expected for a free-ends non-uniform beam, exhibiting one, two and three internal peaks for the first, second and third modes, respectively. Forward speed had a more pronounced effect on the first two modes, which coalesce at approximately 3.5 $\text{m}\,\text{s}^{-1}$ for $\kappa = 1$ and 6.3 $\text{m}\,\text{s}^{-1}$ for $\kappa_{\text{trunk}} = 4$. The third mode exhibits distinctive behavior, with decreasing frequency for $\kappa = 1$ with forward speed, but increasing frequency for $\kappa_{\text{trunk}} = 4$ due to a stronger interaction with the fourth mode (not shown). Increasing trunk stiffness modified the spatial mode distribution, with all examined modes showing a relative larger amplitude near the tail compared to the upstream body regions, reflecting greater resistance to deformation in the stiffened trunk.

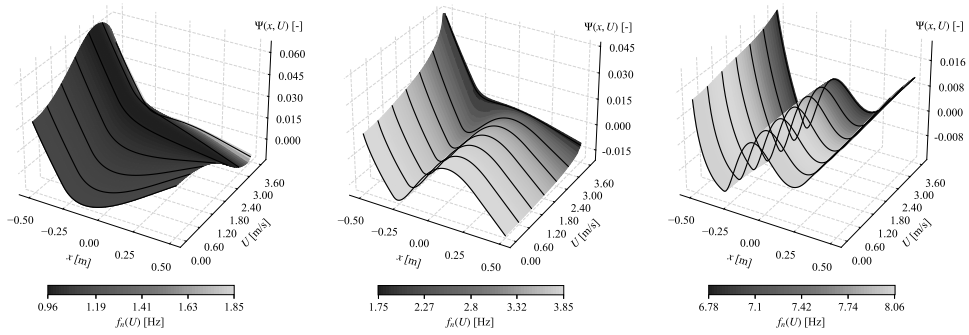
Figure 3 shows the contributions from the structural and hydrodynamic stiffness to the effective modal stiffness K_{ii}^{eff} for the two stiffness configurations. As expected, hydrodynamic stiffness is zero at zero forward speed, while at forward speed the hydrodynamic stiffness may be either positive or negative depending on the mode shape, which itself depends on forward speed. The coalescing of the first two modes is also reflected in the projected stiffness. Increasing the trunk stiffness shifts the modal deformation towards the tail, and the resulting increase in tail deflection leads to a larger added-stiffness contribution to the effective stiffness. Given the large added mass in the tail region and the reduced symmetry of the mode shape when the trunk is stiffened, these trends are physically consistent.

3.2. Damped bending modes

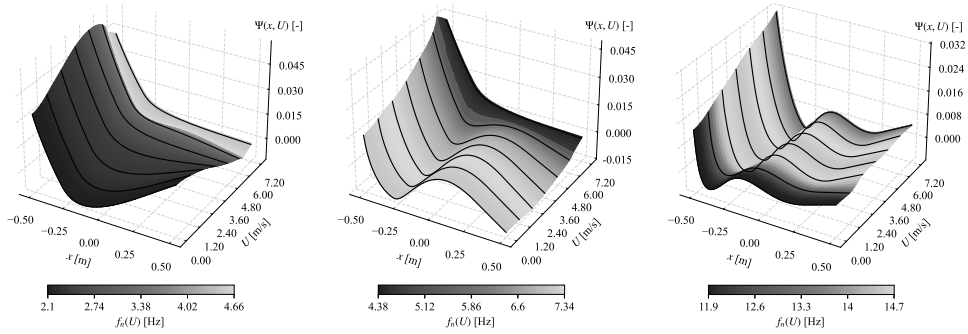
The damped eigenvectors were real at zero forward speed, but complex components arose with forward speed suggesting propagating wave behavior in the physical system. Figures 4 and 5 show the first three damped bending modes and their corresponding projected stiffness for the reference body and for the case with increased trunk stiffness. In contrast to when undamped, no coalescence was observed for the first two modes. As the forward speed increases, the natural frequency of the first mode decreases and eventually approaches zero, while the second and third modes progressively shift toward the first- and second-mode shapes, respectively, and their frequencies vary within similar ranges as the undamped case. The first-mode frequency reaches zero at approximately 1.7 $\text{m}\,\text{s}^{-1}$ for the reference body and 3.5 $\text{m}\,\text{s}^{-1}$ for the case with increased trunk stiffness. Overall, the natural frequencies decrease with sufficiently large speed. Introducing hydrodynamic damping modifies the mode shapes and reduces the projected stiffness relative to the undamped case. This reduction arises from both the structural- and hydrodynamic-stiffness components for the first and second modes. For the third mode, the structural contribution remains higher than in the undamped case when the trunk stiffness increases, likely due to increased interaction with the fourth mode (not shown).

3.3. Geometric and stiffness scaling relations for mode-shape similarity

To further assess the influence of geometry and stiffness, scaling transformations of the body were derived that preserve the spatial mode shapes, see Table 1. Using proportional arguments, we identified how global body size, length, slenderness and overall stiffness can be scaled together with forward speed to produce the same mode shapes with different natural frequencies. These scaling relations were subsequently verified numerically. By contrast, the trunk-stiffness scaling relations were acquired empirically from analysis of the numerical results presented in Figures 2-5 and additional runs with different trunk stiffnesses. Qualitatively, similar mode shapes are obtained when: (i) increasing overall size, length or bluntness (i.e. decreasing slenderness) is accompanied by a lower forward speed and leads to lower natural frequencies or (ii) increasing stiffness is accompanied by a higher forward speed

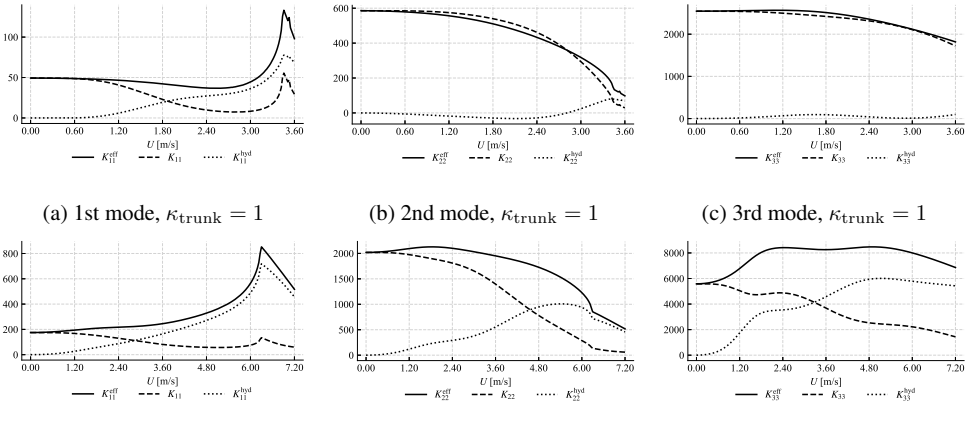


(a) 1st mode, $\kappa_{\text{trunk}} = 1$ (b) 2nd mode, $\kappa_{\text{trunk}} = 1$ (c) 3rd mode, $\kappa_{\text{trunk}} = 1$



(d) 1st mode, $\kappa_{\text{trunk}} = 4$ (e) 2nd mode, $\kappa_{\text{trunk}} = 4$ (f) 3rd mode, $\kappa_{\text{trunk}} = 4$

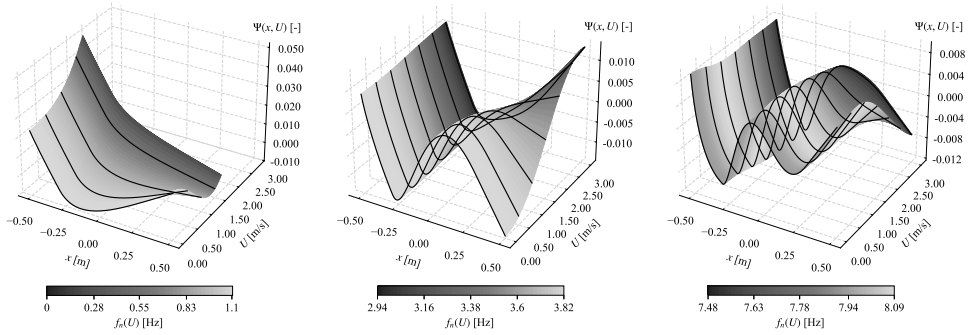
Figure 2: First three undamped bending modes and natural frequencies versus forward speed for two trunk stiffnesses of the reference body.



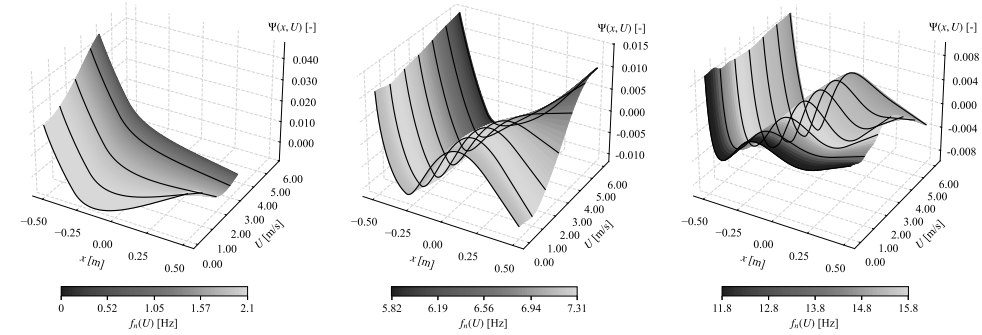
(a) 1st mode, $\kappa_{\text{trunk}} = 1$ (b) 2nd mode, $\kappa_{\text{trunk}} = 1$ (c) 3rd mode, $\kappa_{\text{trunk}} = 1$

(d) 1st mode, $\kappa_{\text{trunk}} = 4$ (e) 2nd mode, $\kappa_{\text{trunk}} = 4$ (f) 3rd mode, $\kappa_{\text{trunk}} = 4$

Figure 3: Projected stiffness for the first three undamped bending modes versus forward speed for two trunk stiffnesses of the reference body.

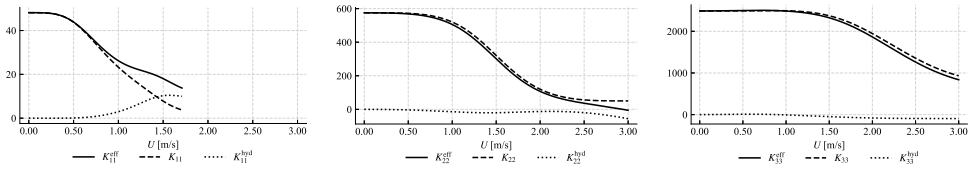


(a) 1st mode, $\kappa_{\text{trunk}} = 1$ (b) 2nd mode, $\kappa_{\text{trunk}} = 1$ (c) 3rd mode, $\kappa_{\text{trunk}} = 1$

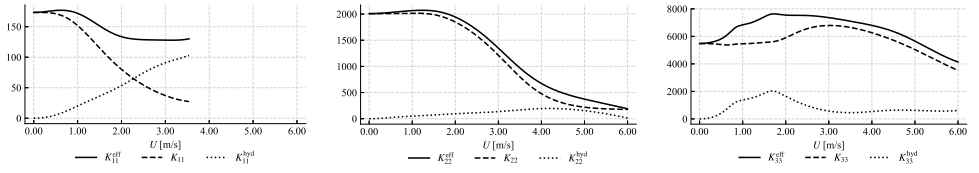


(d) 1st mode, $\kappa_{\text{trunk}} = 4$ (e) 2nd mode, $\kappa_{\text{trunk}} = 4$ (f) 3rd mode, $\kappa_{\text{trunk}} = 4$

Figure 4: The first three damped bending modes and natural frequencies versus forward speed for two trunk stiffnesses of the reference body.



(a) 1st mode, $\kappa_{\text{trunk}} = 1$ (b) 2nd mode, $\kappa_{\text{trunk}} = 1$ (c) 3rd mode, $\kappa_{\text{trunk}} = 1$



(d) 1st mode, $\kappa_{\text{trunk}} = 4$ (e) 2nd mode, $\kappa_{\text{trunk}} = 4$ (f) 3rd mode, $\kappa_{\text{trunk}} = 4$

Figure 5: Projected stiffness for the first three damped bending modes versus forward speed for two trunk stiffnesses of the reference body.

and leads to higher natural frequencies. Even though κ_{trunk} was found to scale similarly as the global stiffness parameter κ, qualitative differences become increasingly pronounced as trunk stiffness grows, as discussed in Section 3. These differences include an increased difference in amplitude envelope between the tail and head regions, and a stronger interaction between the third and fourth modes.

Table 1: Scaling parameters and scaling relations of forward speed and frequency for preserved mode shapes.

Scaling	Scaling parameter	$\frac{U}{U_{\text{ref}}}$	$\frac{U_b}{U_{b,\text{ref}}}$	$\frac{f_n}{f_{n,\text{ref}}}$
Size	$s = \frac{(x,y,z)}{(x_{\text{ref}},y_{\text{ref}},z_{\text{ref}})}$	1	s^{-1}	s^{-1}
Length	$s_x = \frac{x}{x_{\text{ref}}}$	s_x^{-1}	s_x^{-2}	s_x^{-2}
Slenderness	$s_\varepsilon = \frac{\varepsilon}{\varepsilon_{\text{ref}}}$	s_ε	s_ε	s_ε
Body stiffness	$\kappa = \frac{E}{E_{\text{ref}}}$	$\kappa^{1/2}$	$\kappa^{1/2}$	$\kappa^{1/2}$
Trunk stiffness	$\kappa_{\text{trunk}} \approx \frac{E^{\text{trunk}}}{E^{\text{trunk}}_{\text{ref}}}$	$\kappa_{\text{trunk}}^{1/2}$	$\kappa_{\text{trunk}}^{1/2}$	$\kappa_{\text{trunk}}^{1/2}$

4. Discussion

4.1. Swimming modes and mode shapes

Fish swimming modes can be classified according to the body wave pattern and portion of the body involved in the undulatory motion, in addition to body shape and other morphological features [5]. Carangiform swimmers display up to roughly half a wavelength on the body, subcarangiform swimmers typically between half to a full wavelength, and anguilliform swimmers more than a half-wave and often a full wavelength or more, distributed and propagating along their body. From Figure 4, at zero forward speed the first three bending modes of the fish-like model correspond to slightly more than a half-wave, one full wave, and three half-waves, respectively. When hydrodynamic damping is included, the visible wavelength shortens with forward speed for all three modes. Based on this, the first three modes can be associated, respectively, with a carangiform-, a subcarangiform- and an anguilliform-like pattern, for the range of velocities examined. The reference body has morphological characteristics typical of carangiform or subcarangiform swimmers, and the first and second natural frequencies fall within the expected swimming-frequency range for a fish of comparable body size and swimming speeds [20]. Furthermore, geometric scaling indicates that a slenderer (more anguilliform) body would exhibit its expected swimming frequencies in higher bending modes compared to the reference body, reinforcing the idea that structural resonance plays an important role in propulsion efficiency. Since our study is limited to a single simplified fish-like geometry, scaling results must be interpreted with caution. If fishes exploit structural resonance to enhance propulsion efficiency, morphological and stiffness-distribution differences across species should place different swimmers within the observed swimming-frequency ranges and associated mode shapes. In addition, investigations into the propagating wave behavior from complex eigenvectors may provide insight into the interplay between modal structure, body mechanics and propulsive performance. Further research on the structural response of more complex and diverse body shapes, including the effect of internal damping, is needed to enhance the understanding of role of mechanical resonance in fish swimming.

4.2. Strouhal number and muscle activation

Variation in trunk stiffness allowed us to examine how mode-shape similarity relates to the Strouhal number. While some fishes exhibit increasing tail-beat amplitude at higher velocities, others maintain a

nearly constant amplitude envelope [8]. For the present investigation we assume $A \approx (0.188 \pm 0.01)L$, consistent with large cross-species compiled dataset [20]. Because the relevant velocity and frequency parameters scale with $\kappa_{\text{trunk}}^{1/2}$ (see Table 1), the Strouhal number St remains approximately constant whenever the mode shape is preserved while forward speed and natural frequency increase. According to this physical model, a swimmer can therefore retain a given Strouhal number and mode shape while increasing its propulsion by raising the tail-beat frequency through muscle activation, which increases the effective trunk stiffness. This provides a mechanism for tuning the body's natural frequency to the tail-beat frequency, while maintaining a particular swimming mode, e.g., carangiform. These results support that structural resonance can contribute significantly to propulsive efficiency. Figures 2 and 4 show that increasing trunk stiffness reduces the deformation of the head and trunk relative to the tail, thereby increasing the contrast in the amplitude envelope. Conversely, the shape of the amplitude envelope is preserved for global stiffness and geometric scaling. This behavior is qualitatively consistent with observations of fish locomotion, where body undulations are typically concentrated toward the posterior part of the body while the head and anterior trunk exhibit relatively small lateral displacements, particularly at higher swimming speeds, and consequently larger muscle activation (see, e.g., [21]). The present results therefore suggest that variations in stiffness distribution may contribute to shaping the spatial amplitude distribution of the body wave during swimming.

4.3. Scaling of body size and stiffness

From Table 1, it can be seen that our size-scaling results reproduce the same scaling laws reported for swimmers above a certain body length, namely $f_n \propto s^{-1}$ with U remaining nearly size-independent [20]. It has been proposed that biological constraints at smaller sizes lead to deviations from this scaling law. From a resonance perspective, such deviations may also be explained by differences in body stiffness. According to our study, if smaller swimmers possess lower effective stiffness, either due to lower material stiffness or reduced muscle activation, their wet natural frequencies scale as $f_n \propto \kappa^{1/2} s^{-1}$ and the corresponding forward speed scales as $U \propto \kappa^{1/2}$, where κ represents either whole body stiffness or stiffness associated with muscle activation. This addition of a stiffness scaling parameter for smaller fishes fits with the observed data and proposed scaling laws [20]. It should be noted that our mathematical model assumes sufficiently large Reynolds numbers so that viscous effects are negligible. This assumption may break down at small body sizes, where viscous forces become increasingly important. Additionally, material damping is likely important [9], but was not considered in this research.

5. Conclusions

The study considers a simplified fish-like body modeled as an Euler-Bernoulli beam coupled to a linear slender-body hydrodynamic model. A finite-element formulation is used to compute wet bending modes and natural frequencies under varying forward speed, geometry, and stiffness distributions, enabling a parametric analysis of the hydroelastic response. The work demonstrates that fluid-structure interactions associated with forward speed significantly modify the structural response of a fish-like body. A simplified fish geometry and bio-inspired stiffness distribution produced wet-mode frequencies in reasonable agreement with observed swimming data and established scaling laws. Varying only the trunk stiffness, via muscle activation, was found to scale in a manner similar to variations in overall body stiffness with respect to mode shape, natural frequency and forward speed associated with a given mode. Thus, muscle activation can strongly influence the hydroelastic response. Within the present model, increases in stiffness through muscle activation allow a swimmer to retain the same Strouhal number and swimming mode while increasing tail-beat frequency and forward speed, thereby indicating that fish can tune their tail-beat frequency to their wet natural frequency to maintain efficiency. These findings support the view that mechanical resonance is an important mechanism influencing swimming performance. Modulating trunk stiffness is therefore a plausible strategy for shifting maneuvering-propulsion

balance in bio-inspired soft robots, highlighting the relevance of fluid-structure interaction effects in future biomimetic design.

Acknowledgments

This work was supported by the Research Council of Norway through the Centre of Excellence funding scheme (Grant No. 223254-AMOS).

References

[1] F. E. Fish. Advantages of aquatic animals as models for bio-inspired drones over present AUV technology. *Bioinspiration & Biomimetics*, 15(2), 2020.

[2] G. V. Lauder. Fish locomotion: recent advances and new directions. *Annual Review of Marine Science*, 7:521–545, 2015.

[3] C. M. Breder. The locomotion of fishes. *Zoologica : scientific contributions of the New York Zoological Society.*, 4(5):159–297, 1926.

[4] M. Sfakiotakis, D. M. Lane, and J. B. C. Davies. Review of fish swimming modes for aquatic locomotion. *IEEE Journal of Oceanic Engineering*, 24(2):237–252, 1999.

[5] C. C. Lindsey. Form, Function, and Locomotory Habits in Fish. In *Fish Physiology*, volume 7 of *Locomotion*, pages 1–100. Academic Press, 1978.

[6] G. V. Lauder and E. D. Tytell. Hydrodynamics of undulatory propulsion. In *Fish Physiology*, volume 23, pages 425–468. Academic Press, 2005.

[7] M. S. Triantafyllou and G. S. Triantafyllou. An efficient swimming machine. *Scientific American*, 272(3):64–70, 1995.

[8] Z. Cui, Z. Yang, L. Shen, and H. Z. Jiang. Complex modal analysis of the movements of swimming fish propelled by body and/or caudal fin. *Wave Motion*, 78:83–97, 2018.

[9] Y. E. Jimenez, K. N. Lucas, J. H. Long, Jr, and E. D. Tytell. Flexibility is a hidden axis of biomechanical diversity in fishes. *Journal of Experimental Biology*, 226(Suppl_1):jeb245308, 2023.

[10] O. M. Faltinsen. *Hydrodynamics of high-speed marine vehicles*. Cambridge University Press, 2005.

[11] C. Norvik, M. Greco, and C. Lugni. Effect of morphology and flexibility on directional stability of fish and bio-inspired robots. *Journal of Hydrodynamics*, 37:1133–1144, 2026.

[12] K. W. Moored, P. A. Dewey, B. M. Boschitsch, A. J. Smits, and H. Haj-Hariri. Linear instability mechanisms leading to optimally efficient locomotion with flexible propulsors. *Physics of Fluids*, 26(4):041905, 2014.

[13] M. J. Lighthill. Note on the swimming of slender fish. *Journal of Fluid Mechanics*, 9(2):305–317, 1960.

[14] J. N. Newman. *Marine Hydrodynamics*. MIT Press, Cambridge, MA, 1977.

[15] W. Weaver, S. P. Timoshenko, and D. H. Young. *Vibration Problems in Engineering*. John Wiley & Sons, New York, 5 edition, 1990.

[16] Y. G. Aleyev. *Nekton*. Springer, 1977.

[17] L. Meirovitch. *Elements of vibration analysis*. McGraw-Hill, New York, 2nd ed. edition, 1986.

[18] R. J. Allemang. The modal assurance criterion: Twenty years of use and abuse. *Sound and Vibration*, 37(8):14–23, 2003.

[19] K. Sarkar and R. Ganguli. Closed-form solutions for non-uniform euler–bernoulli free–free beams. *Journal of Sound and Vibration*, 332(23):6078–6092, 2013.

[20] J. Sánchez-Rodríguez, C. Raufaste, and M. Argentina. Scaling the tail beat frequency and swimming speed in underwater undulatory swimming. *Nature Communications*, 14(1):5569, 2023.

[21] J. J. Videler and F. Hess. Fast continuous swimming of two pelagic predators, saithe and mackerel. *Journal of Experimental Biology*, 109:209–228, 1984.

Experimental Characterization of Hydroelastic Dynamics in Biomimetic Caudal Fins

Costantino Muniz, G.[1], Paifelman, E.[2] Aloisio, G.[3], Sellini, M.[4] and Ciappi, E. [5*]

[1] Department of Mechanical and Aerospace Engineering, Sapienza University of Rome, Rome, Italy (gabriele.costantinomuniz@uniroma1.it)
[2] CNR-INM Institute of Marine Engineering, Rome, Italy (elena.paifelman@cnr.it)
[3] CNR-INM Institute of Marine Engineering, Rome, Italy (giovanni.aloisio@cnr.it)
[4] CNR-INM Institute of Marine Engineering, Rome, Italy (massimiliano.sellini@cnr.it)
[3] CNR-INM Institute of Marine Engineering, Rome, Italy (elena.ciappi@cnr.it)

Abstract. This study presents the results of an experimental campaign designed to investigate fluid–structure interaction mechanisms in flexible rectangular plates that emulate the caudal fins of subcarangiform fish. The aim is to understand the operational parameters, in terms of Strouhal number, conditioning thrust production and propulsion efficiency, and how to apply this knowledge. Tests were conducted in the recirculating hydraulic channel at CNR-INM using rectangular prototype panels that varied in stiffness and aspect ratio AR. Different operative conditions were obtained by varying the oscillation frequency, the pitch angle amplitude and the flow velocity. For panels with $AR > 1$, the non-dimensional thrust scaling law available in the literature is confirmed. However, for panels with $AR < 1$, which were the focus of the study, the same scaling does not provide a collapse of the curves. Nevertheless, a clear trade-off emerges between thrust and efficiency: stiffer plates favour thrust generation, while more compliant ones favour efficiency. This offers practical guidelines for designing and optimising biomimetic underwater propulsors.

Key words *biomimetic propeller; flexible fin; experimental test; efficiency*

1. Introduction

Most of the studies conducted on biomimetic underwater propulsors are based on numerical methods, using both high-fidelity [1,2] and low-fidelity models [3–5]. However, experimental data that can be used to validate models is limited, especially when flexible fins are considered. The experimental configurations studied are primarily rectangular plates or NACA0012 airfoil profiles. PIV measurements are performed to study the evolution of the wake structure generated by oscillating plates, to better understand its role in thrust production and control [6,7]. Force and fin displacement measurements provide quantitative information on propulsion efficiency, as well as further physical insights, especially in terms of hydroelastic coupling, that can be used to design biomimetic propellers. In this context, several experimental campaigns based on direct force and displacement measurements have explored different geometries and stiffness ranges. For instance, Floryan et al. [8] investigated teardrop-shaped rigid foils combining pitch and heave motions, while Fernandez-Prats et al. [9] analysed the effect of chordwise flexibility using stainless steel plates with increasing bending stiffness. Barannyk et al. [10] examined partially rigid Polydimethylsiloxane (PDMS) fins and highlighted the influence of immersion depth on thrust performance. Within this experimental framework, the contribution of Dewey et al. [11] stands out for its systematic investigation of flexible panels over a broad range of bending stiffness values. By combining direct measurements of thrust and efficiency with a non-dimensional scaling analysis, their study provided a consistent interpretation of hydroelastic

* Correspondence to: elena.ciappi@cnr.it

effects, including the identification of a thrust peak at frequencies higher than the first wet natural frequency. For this reason, their work represents a key experimental reference for the validation and interpretation of new results on flexible biomimetic propulsors. In this paper it is presented an experimental campaign carried out in a recirculating water channel, aimed at evaluating the propulsive performance of pitching flexible rectangular plates under different working conditions. To this end, experiments were conducted by prescribing different pitch amplitudes α and oscillation frequencies f, while the performance of each plate was evaluated by measuring the mean thrust $\bar{T}$ and the Strouhal number associated with each test case. To extend the experimental data and knowledge, attention is directed towards the behaviour of flexible plates with aspect ratio $AR < 1$ which, although less studied than those with $AR > 1$, are significant for a class of underwater robotic platforms [12, 13] that mimic the propulsion of fish characterised by moderately to high swimming speeds and moderate flexibility. By studying low-AR plates, our goal is to verify to what extent the knowledge obtained for high-AR plates still holds, to identify the leading parameters that must be considered when changing the aspect ratio, and to understand how the overall coupling behaviour changes.

2. Dimensional analysis and design of propulsive plates

Dimensional analysis has been performed to identify the dimensionless parameters needed to correctly design the propulsive flexible plates and the test matrix. Neglecting fluid viscosity, the relevant variables of the problem are: the flow velocity U_∞ the fluid density ρ_f, the material density ρ_s, the Young modulus E, the fin dimensions — length L, span d, and thickness h_b — the oscillation frequency f, and the pitch angle α. The relevant output quantities are the peak-to-peak amplitude χ and the thrust T.

Using dimensional analysis, the following dimensionless parameters are found:

$$\alpha, \quad K = \frac{fL}{U_\infty}, \quad R = \left(\frac{\rho_s}{\rho_f}\right)\left(\frac{h_b}{L}\right), \quad S = \frac{Eh_b^3}{\rho_f U_\infty^2 L^3}, \quad AR = \frac{d}{L}, \tag{1}$$
$$\lambda = \frac{h_b}{L}, \quad \mathrm{A}^* = \frac{\chi}{L}, \quad C_T = \frac{T}{\rho_f U_\infty^2 dL}, \quad St = \frac{f}{U_\infty}\frac{\chi}{2}$$

where K is the reduced frequency, R is the inertia ratio, S is the non-dimensional stiffness parameter, AR is the aspect ratio, λ is the slenderness parameter related to the structural model (*i.e.* thin plate theory), A^* is a measure of the problem linearity, and C_T is the thrust coefficient. In some cases, χ/U_∞ is used as the time scale, and the Strouhal number St is introduced. The experimental fins were designed to provide a variation of all dimensionless parameters within a realistic range for biomimetic applications. In this regard, biological studies [14-16] reveal that meaningful values for the flexural stiffness EI of fish fins varies between 10^{-6} and $10^{-2} Nm^2$, where $I = dh_b^3/12$ is the moment of inertia of the cross section. Considering representative sizes and velocities for fish species of interest (*i.e.* salmon, trout, tuna), S in nature ranges between 10^{-2} and 10^2. Most experiments cited above consider fin models with S ranging between 1 and 100. Although direct measurements of fin-lobe density are not available in the literature, the inertia ratio R can be estimated from biological considerations. In teleost fish, whole-body density is maintained very close to neutral buoyancy through swim bladder regulation, typically within a few percent of the surrounding water density. Experimental measurements on zebrafish report deviations smaller than approximately 2% throughout development [17]. It is therefore reasonable to assume $\rho_s/\rho_f = \mathcal{O}(1)$. The dominant contribution to R is thus the geometric slenderness ratio λ. Morphometric studies of fin rays indicate characteristic radii on the order of $\sim 100\,\mu m$ near distal regions [18], with thicker proximal sections but strong tapering toward the trailing edge. Even adopting a conservative equivalent thickness h_b

between 0.1 and 1 mm and characteristic fin lengths L between 1 and 5 cm for typical teleost caudal lobes, one obtains

$$\frac{h_b}{L} \sim 10^{-3} - 10^{-2}, \Rightarrow R_{bio} \sim 10^{-3} - 10^{-2}.$$

This estimate is consistent with hydroelastic studies showing that biological and bio-inspired fins operate in a fluid-dominated inertial regime where structural inertia remains small compared to fluid inertia [19–21]. Finally, considering facility constraints, six panels in the following indicated as P1-P6 have been designed. Their geometric characteristics and mechanical properties, as well as the values of the corresponding dimensionless parameters, are shown in Table 1 along with the same information on the panels (D1-D4) tested in [11] and used as a reference. Going from P1 to P4 the non-dimensional stiffness S is progressively reduced by varying either the plate thickness or material, while keeping AR = 0.33 fixed. Panels P5 and P6 share the higher AR = 2.4 geometry and are designed to match the S values of panels D1 and D4, enabling direct validation of the scaling laws.

Table 1: Characteristics of tested and reference panels.

Panel	L	d	AR	h_b	E	ρ_s	U	α	S	R
	m	m	-	m	GPa	Kg/m^3	m/s	∘	-	-
P1	0.5	0.15	0.33	$3 \cdot 10^{-3}$	3.27	1191.6	0.1	12.5	70.6	0.0071
P2	0.5	0.15	0.33	$1 \cdot 10^{-3}$	65.89	2633.6	0.1	12.5	52.7	0.0053
P3	0.5	0.15	0.33	$3 \cdot 10^{-3}$	1.96	933.42	0.1	12.5	42.3	0.0056
P4	0.5	0.15	0.33	$2 \cdot 10^{-3}$	3.27	1191.6	0.1	12.5	20.9	0.0048
P5	0.14	0.32	2.4	$5 \cdot 10^{-4}$	3.27	1191.6	0.1	12.5	14.9	0.0043
P6	0.14	0.34	2.4	$1 \cdot 10^{-3}$	1.96	933.42	0.1	12.5	71.4	0.0067
D1	0.12	0.28	2.4	$2.52 \cdot 10^{-4}$	5.37	1300	0.06	14.32	13.8	0.0027
D2	0.12	0.28	2.4	$3.84 \cdot 10^{-4}$	2.17	1300	0.06	14.32	19.7	0.0042
D3	0.12	0.28	2.4	$5 \cdot 10^{-4}$	1.96	1300	0.06	14.32	39.5	0.0054
D4	0.12	0.28	2.4	$6.4 \cdot 10^{-4}$	1.86	1300	0.06	14.32	76.9	0.0069

3. Experimental setup

The experimental campaign was conducted in the recirculating open channel flume of the Institute of Marine Engineering (see Figure 1) which has a test section 27 m long, 0.6 m wide and 0.7 m deep. The water is moved by three 16 kW pumps and, before entering the test section, flows through a settling chamber, a series of conditioning elements (honeycombs and grids), and a 3.5:1 contraction. The water velocity can be varied up to 1 m/s by adjusting the pump rotation speed. The vertical sides of the channel are made of tempered glass, and the bottom is made of stainless steel, except for two 1 m long transparent acrylic panels that allow optical access.

The experimental setup designed to evaluate the propulsive performance of the flexible fins is shown in Figure 2,3,4. The propulsive plates were mounted at mid-span to a vertical stainless-steel shaft 0.76 m high. The shaft was connected to a single-degree-of-freedom rotary actuator positioned above the free surface, enabling controlled pitching motion about the shaft axis. This configuration ensures that the top and bottom edges are subject to the same boundary conditions. This has been achieved by ensuring that the centreline of the plate is equidistant from the bottom edge and the free surface. The pitching kinematics were prescribed through a motor–gearbox–coupling assembly, imposing a

harmonic rotation of amplitude α and an oscillation frequency f. A flexible coupling element was included to compensate for minor alignment imperfections while limiting torsional compliance transmission to the measurement system.

The actuation unit consisted of a brushless Smart Automation motor (continuous torque 1.45 Nm, peak torque 3.39 Nm, encoder resolution 8000 $count/revs$) interfaced through a planetary gearbox. Below the gearbox, a 6-axis ME K6D40 load cell (full scale 50 N in force, 5 Nm in moment) was mounted in line between the actuation system and the supporting structure, enabling direct measurement of hydrodynamic loads. Per manufacturer specifications, mean thrust measurement uncertainty is within $\pm(1\text{-}2)\%$ of full scale, with repeatability errors below $\pm 1\%$ under steady-state conditions. However, before starting the hydrodynamic campaign, the load cell was recalibrated using a dedicated calibration rig designed to reproduce the mechanical boundary conditions of the experimental configuration. The flexible plate was replaced by a rigid extension beam of equivalent reference length (up to 0.5 m), allowing the controlled application of known forces at the geometric centroid of the plate. The calibration confirmed data reported by the manufacturer. The supporting frame was rigidly anchored to the lateral walls of the flume interposing rubber elements to mitigate the transmission of vibrations generated by the pumps.



Figure 1 Hydrodynamic channel.

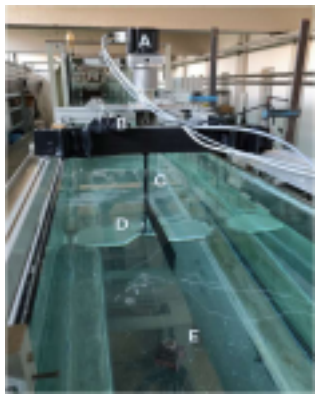
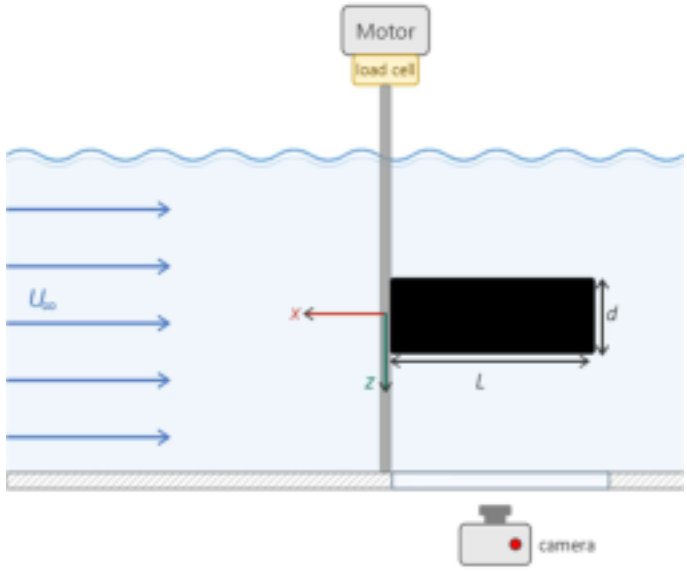


Figure 2 Experimental setup. A motor, B 6 load- axis cell, C support rod, D fin, E fast camera.

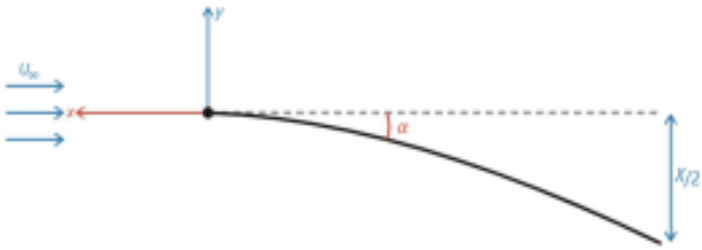
A Photron high-speed camera with $500\ fps$ was used to record the plate deformation enabling post- processing reconstruction of the kinematic response. The deformation is reconstructed by tracking the bottom edge of the plates, painted with a highly reflective paint: all other structural components were painted black to ensure robust image processing. Optical access was provided by the transparent acrylic window located beneath the plate, see Figure 2, 3(a)-(b).

The experimental campaign was conducted over a controlled range of inflow velocities U_∞ = 0.1, 0.2 and 0.4 m/s whose values have been checked through a Dantec Dynamics laser Doppler velocimetry system, and prescribed pitching amplitudes $\alpha = 5°$ and $12.5°$. The actuation frequency varied between $0.1 - 2\ Hz$, enabling exploration of both quasi-static and dynamically amplified response regimes.
Force signals were acquired using a Dewesoft data acquisition system, the acquisition time was 1 minute, and the sampling frequency was $2\ KHz$. Analog filtering and cycle-average digital post-processing were applied to mitigate high-frequency noise. Several repetitions of each test condition have been performed to check measurement repeatability and ensure statistical consistency of the mean thrust values. All measurement systems were temporally synchronized. Once the oscillatory motion reached periodic steady state, a hardware trigger activated the high-speed camera, recordings therefore correspond to fully developed fluid–structure interaction conditions. The camera acquisition time was set to capture at least 10 complete oscillation periods for each condition. Experimental dry modal

analysis was performed to evaluate the first natural frequencies f_n of all panels in the test configuration. Wet natural frequencies were determined numerically, owing to the inherent difficulties of conducting wet experimental modal analysis.



(a) Lateral view



(b) Top view

Figure 3 Schematic view of the kinematic parameters.

4. Results and discussion

The first set of experiments was conducted to verify some literature findings and the accuracy of the data acquired. For this purpose, we compared the present results with the experiment by Dewey et al. [11]. Specifically, we considered configurations with aspect ratio $AR > 1$ (panel D1-D4 of

Table 1) and compared them with panels $P5$ and $P6$. This configuration is practically identical to that in [11]: the aspect ratio is the same, the length L and span d are very similar, while the velocity and thickness differ. However, these latter parameters were selected to ensure that the non-dimensional stiffness S matches that of panels D1 and D4 (see Table 1). Figure 4 reports the scaling law for the thrust proposed in [11], namely $\widetilde{C_T} = C_T/S = TL^2/(Eh_b^3 d)$ as a function of $f^* = f/f_b$, where f_b is experimentally identified as the frequency at which maximum fin deformation occurs. An excellent collapse of all curves is observed up to $f^* \approx 1$. In particular, curves with similar S values (D1, P5 and D4, P6) show very close agreement. For frequencies beyond this threshold, all curves — both ours and those from the literature — progressively diverge from one another, regardless of the value of S.

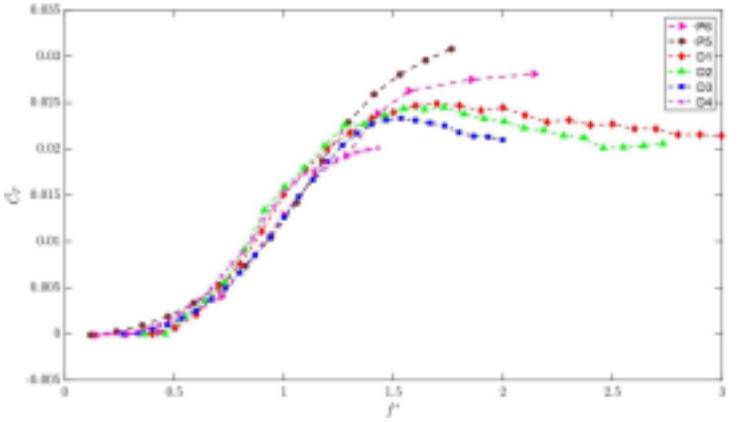


Figure 4 Scaling law for panels with $AR > 1$.

Following Dewey et al. [11], maximum efficiency is achieved at Strouhal numbers in the range 0.2–0.4 and when the oscillation frequency is close to resonance. The thrust coefficient C_T does not show a direct correlation with either the maximum deformation amplitude or the efficiency. Instead, it exhibits a plateau at a frequency approximately 50% higher than the fin's wet natural frequency, which corresponds to the peak of the deformation amplitude χ.

The next step was to verify whether the same scaling law holds for $AR < 1$. Our low-AR panels were tested following the same approach adopted in [11]: constant $L, d, U_\infty,$ and pitch angle amplitude α, varying only thickness or material to modify the non-dimensional stiffness S. Figures 5(a)–(c) show the peak-to-peak deformation amplitude χ, the mean thrust $\bar{T}$, and the propulsive efficiency η as functions of oscillation frequency f. The efficiency is defined as $\eta = \bar{T}U\infty/P$, where $P = Mz\omega$ is the input power computed from the shaft torque Mz and angular velocity ω averaged over an oscillation period.

By varying only S while keeping all other parameters constant, the resonance peak shifts clearly within the interval between $0.2\ Hz$ (for P3 and P4) and $0.3\ Hz$ (for P1 and P2). The onset of the thrust plateau occurs at a frequency approximately 2.5 times higher than the wet natural frequency identified from the peak of χ, likely because the lower AR value alters the two-dimensionality of the problem compared to [11]. Thrust magnitude decreases as S increases, while no consistent monotonic trend is observed for efficiency. The efficiency peak broadly follows that of thrust. However, no direct correspondence

between maximum efficiency and maximum thrust is observed. Panel P4, which is the most flexible panel (lowest S), achieves the highest efficiency but not the highest thrust.

(a) χ peak-to-peak vs f. (b) $\overline{T}$ Thrust force vs f. (c) 5 efficiency vs f.

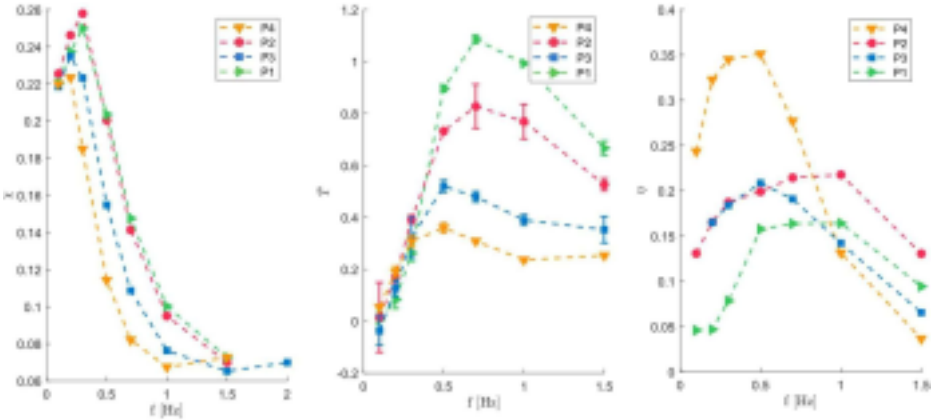


Figure 5 Experimental results for panels with $AR < 1$ for $U_\infty = 0.1m/s$ and $\alpha = 12.5°$.

These results seem to follow the trends identified by Dewey et al. [11] despite the different aspect ratio. We therefore attempted in Figure 6 to represent our data using the scaling law of Figure 4 which, in this case, for $AR < 1$ does not provide a collapse of the curves.

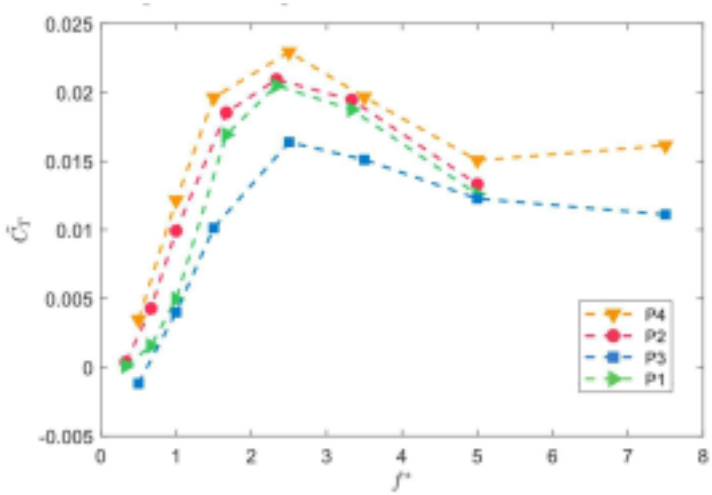


Figure 6 C_T vs f^*. Scaling law Dewey et al. [11] for our panels with $AR < 1$.

For this reason, we analyse the $AR < 1$ data to highlight the role of the Strouhal number and to demonstrate how it can be used to interpret the effects of flexibility on thrust production. Figure 7 shows that plotting the thrust coefficient C_T, as a function of the Strouhal number St generates an envelope defined by the peaks of the curves (see black dotted line) expressed by a fourth-degree polynomial of St:

$$C_T^{max} = 236.45 \cdot St^4 - 216.35 \cdot St^3 + 64.73 \cdot St^2 - 2.98 \cdot St + 0.023.$$

These peaks are ordered by increasing S: the lowest peak (leftmost) corresponds to the most flexible plate (P4), while the highest peak corresponds to the stiffest plate (P1). This indicates that plate stiffness governs the maximum achievable thrust.

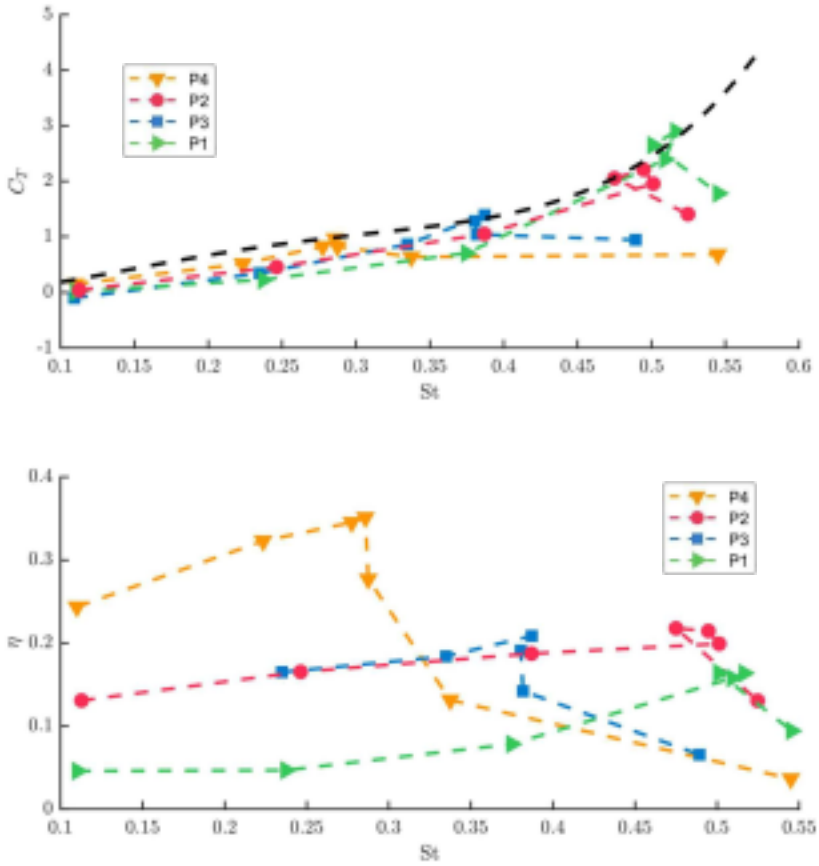


Figure 7 C_T (top) and η (bottom) as functions of St.

However, each plate exhibits a different optimal Strouhal number at which its maximum thrust occurs. Moreover, within a given Strouhal range, each plate can outperform the others. This suggests that, to obtain the highest thrust under specific operating conditions, the plate non-dimensional stiffness S must be tuned to the operational Strouhal number to ensure adequate thrust generation. From Figure 7 it is also evident that the frequency corresponding to the peak in C_T coincides with a peak in η. Nevertheless, the overall efficiency trend with respect to St is opposite to that observed for C_T. The most flexible plate achieves the highest efficiency (P4), which progressively decreases as the non- dimensional stiffness increases. Additionally, plates with resonance frequencies lying within the optimal Strouhal range $0.2 - 0.4$ exhibit higher

efficiencies, in agreement with Dewey et al. [11] findings. These observations indicate that stiffness tuning is equally important for efficiency: similarly to the thrust coefficient, each plate shows a specific Strouhal interval within which it performs better than the others. Combining these results reveals a clear trade-off between thrust and efficiency. Achieving high thrust peaks requires stiffer plates and more demanding operating conditions, such as higher actuation frequencies or larger pitching amplitudes, to match the desired swimming speed and thrust. However, these conditions inevitably lead to reduced efficiency, which instead is maximized under more compliant configurations and milder operating regimes.

Final remarks

This paper has presented part of the results of an experimental campaign carried out to characterize the hydroelastic dynamics of flexible pitching plates emulating fish-like caudal fins, with particular focus on low-AR configurations ($AR < 1$). The results were first compared with published data for panels with $AR > 1$, demonstrating close agreement and confirming the validity of the scaling law at least below the wet natural frequency. For plates with $AR < 1$, the non-dimensional stiffness emerges as the dominant parameter governing thrust production, resonance behaviour, and efficiency. Optimal performance is achieved by tuning structural properties to the operational Strouhal number. Overall, the study provides new experimental evidence on hydroelastic scaling for high AR and clarifies the trade-off between thrust maximization and propulsive efficiency, offering practical guidelines for the design and optimization of biomimetic underwater propulsors.

Acknowledgements

The authors would like to sincerely thank Roberto Zagaglia and Roberto Basti, together with their respective technical groups, for their essential contribution to the mechanical design and sensor integration of the experimental setup. Their expertise in the development, implementation, and calibration of the measurement systems was fundamental to the reliability and accuracy of the experimental campaign.

References

[1] C. Bai, P. Liu, Y. Lyu, S. Wang, (2026). Effect of variable stiffness characteristics on the propulsion performance of biomimetic caudal fin flexible plates, Ocean Engineering 352, 124486.
[2] E.I. Basri, A.A. Basri, K.A. Ahmad, (2023). Computational fluid dynamics analysis in biomimetics applications: a review from aerospace engineering perspective, Biomimetics 8(3), 319.
[3] A. Rehman, D. Floryan, (2025). Propulsion of a flexible foil in a wavy flow: resonance, antiresonance and destructive self-interference, Journal of Fluid Mechanics 1023, A11.
[4] R. Das, S.D. Peterson, M. Porfiri, (2023). Experimental study of the hydrodynamic interaction between a fish and an actively pitching airfoil, in: Bioinspiration, Biomimetics, and Bioreplication XIII, Vol. 12481, SPIE, pp. 85–91.
[5] E. Paifelman, G. Riccardi, E. Ciappi, (2024). Fluid-structure coupled analytical model for oscillatory fish-like propulsion, Ocean Engineering 299, 117292.
[6] J.H.J. Buchholz, A.J. Smits, (2006). On the evolution of the wake structure produced by a low-aspect-ratio pitching panel, Journal of Fluid Mechanics 546, 433–443.
[7] J. Moubogha Moubogha, U. Ehrenstein, J.A. Astolfi, (2017). Forces on a pitching plate: An experimental and numerical study, Applied Ocean Research 69, 27–37.
[8] D. Floryan, T. Van Buren, C.W. Rowley, A.J. Smits, (2017). Scaling the propulsive performance of heaving and pitching foils, Journal of Fluid Mechanics 822, 386–397.

[9] R. Fernandez-Prats, (2017). Effect of chordwise flexibility on pitching foil propulsion in a uniform current, Ocean Engineering 145, 24–33.
[10] O. Barannyk, B.J. Buckham, P. Oshkai, (2012). On performance of an oscillating plate underwater propulsion system with variable chordwise flexibility at different depths of submergence, Journal of Fluids and Structures 28, 152–166.
[11] P.A. Dewey, B.M. Boschitsch, K.W. Moored, H.A. Stone, A.J. Smits, (2013). Scaling laws for the thrust production of flexible pitching panels, Journal of Fluid Mechanics 732, 29–46.
[12] P. Piskur, P. Szymak, M. Przybylski, K. Naus, K. Jaskólski, M. Żokowski, (2021). Innovative energy-saving propulsion system for low-speed biomimetic underwater vehicles, Energies 14(24).
[13] E. Paifelman, A. Odetti, M. Bibuli, E. Ciappi, (2026). Estimating thrust in biomimetic underwater vehicles using design maps, Ocean Engineering 353, 124673.
[14] M.J. McHenry, C.A. Pell, J.H. Long Jr., (1995). Mechanical control of swimming speed: stiffness and axial wave form in undulating fish models, Journal of Experimental Biology 198(11), 2293–2305.
[15] J.H. Long Jr., M. Koob-Emunds, B. Sinwell, T.J. Koob, (2002). The notochord of hagfish Myxine glutinosa: visco-elastic properties and mechanical functions during steady swimming, Journal of Experimental Biology 205(24), 3819–3831.
[16] J.H. Long Jr., M.E. Hale, M.J. McHenry, M.W. Westneat, (1996). Functions of fish skin: flexural stiffness and steady swimming of longnose gar Lepisosteus osseus, Journal of Experimental Biology 199(10), 2139–2151.
[17] B. Pelster, (2003). Buoyancy at early life stages of fish, Comparative Biochemistry and Physiology Part A 135(1), 1–11.
[18] S. Alben, P.G.A. Madden, G.V. Lauder, (2007). The mechanics of active fin-shape control in ray-finned fishes, Journal of the Royal Society Interface 4(13), 243–256.
[19] Q. Zhu, M.J. Wolfgang, D.K.P. Yue, M.S. Triantafyllou, (2002). Three-dimensional flow structures and vorticity control in fish-like swimming, Journal of Fluid Mechanics 468, 1–28.
[20] K.N. Lucas et al., (2015). Bending rules for animal propulsion, Nature Communications 6, 7386.
[21] C.J. Esposito, J.L. Tangorra, B.E. Flammang, G.V. Lauder, (2012). A robotic fish caudal fin: effects of stiffness and motor program on locomotor performance, Journal of Experimental Biology 215, 56–67.

Floating Bridges

10th International Conference on HYDROELASTICITY IN MARINE TECHNOLOGY
Trondheim, Norway, June 16th-18th, 2026

Floating bridge global responses with wave-current-structure interaction

Xu Xiang [1*], O.M. Faltinsen [2]

[1)] Norwegian Public Roads Administration (NPRA), Oslo, Norway (xu.xiang@vegvesen.no)
[2)] Norwegian University of Science and Technology, Trondheim, Norway (odd.faltinsen@ntnu.no)

Abstract. This study investigates the hydro-elastic responses of the Bjørnafjorden floating bridge under wave-current-structure interaction. A simplified method is employed to account for that the incoming wave frequencies are maintained while the wavelength is modified due to wave-current interaction by using the zero-current-speed hydrodynamic coefficients of the pontoons. Hydrodynamic interaction between the pontoons is considered. This simplification was applied to a floating bridge with model tests under irregular waves combined with or without current. The floating bridge consists of 10 pontoons connected by elastic girders and columns and contains a cable-stay bridge. The comparison of numerical results with model tests demonstrates that wave-current-structure interaction has a significant impact on the loads and response of the floating bridge. Furthermore, the validation with model tests demonstrated that the simplified method yields meaningful loads and responses for practical engineering.

Key words: *Floating bridge; wave-current-structure interaction; hydrodynamic interaction*

1. Introduction

The planned Bjørnafjord floating bridge at the west coast of Norway has a length of around 5.5 km. The bridge is supported by floating pontoons of length 53m, width 14.9m and draft 5.0m. The distance between two pontoons is 125 meters for one of the concepts. There are both local wind waves and low-amplitude swell penetrated from the North Sea. An example of a 100-year wind wave condition is significant wave height Hs = 2.1m and peak period Tp = 5.5s. Further, current is relatively strong in the fjord and can be up to 1.7 m/s, depending on return period. During engineering design, both hydrodynamic interaction between pontoons, and the wave-current-structure interaction were identified as issues of interest, and a comprehensive model test campaign were designed and carried out in the ocean basin of SINTEF Ocean, Xiang [6]. The tests confirmed that both issues are important and should be considered in floating bridge response analysis. Especially, the tests revealed that wave-current-structure interaction had a significant impact on the floating bridge loads and responses, which were not understood by applying the traditional method of computing hydrodynamics via the forward speed/towing method.

Faltinsen et al. [1] studied the wave-current-structure interaction of the tested pontoon numerically and experimentally. The study pointed out that the traditional method of towing the body fails to account for the wavelength change under wave-current interaction. The consequence is that incorrect wave loads and global responses are computed. Faltinsen et al. [2] further studied the impact of wind-induced shear current on the wave loads of the same pontoon, concluding that neglecting current shear introduces an error like that of neglecting viscous effects for wave loads on large-volume structures.

The two studies mentioned above paved the theoretical foundation for further improvements of the floating bridge global response computation. This article considers constant current profile over the whole depth and the floating bridge global responses under wave-current interaction. The first order wave loads are approximated by a simplification method that maps the wave loads under wave-

* Correspondence to: xu.xiang@vegvesen.no

current interaction to the zero-current-wave-loads from the wave periods which have equal wavelengths. This method is consistent with the study of Faltinsen et al. [1] and Fredriksen et al. [3] showing that the wavelength plays a critical role in improving the computation of floating bridge loads and responses in wave-current conditions. The second order wave loads are approximated by Newman's approximation without accounting for the wave-current interaction.

2. Wave-current interaction

The first objective is to develop and validate a numerical framework to quantify the change in wavelength resulting from wave-current interaction. The investigation covers the full 360-degree range of relative angles between wave propagation and current direction, providing a comprehensive database of interaction effects on wavelength. This database serves as a foundational tool for more advanced hydrodynamic analyses, such as the global response of floating structures where accurate wavelength is critical. Thus, the correction of wave loads RAOs computed with zero-current solver can be implemented for the usage of wave-current-structure interaction computations.

2.1 Linear theoretical wave-current interaction

The theoretical framework for wave-current interaction is established for regular, linear gravity waves in a constant water depth. A Cartesian coordinate system, $OXYZ$, is defined with its origin at the mean free surface and the Z-axis pointing vertically upwards, as illustrated in Figure 3. The horizontal seabed is located at a constant depth $Z = -h$. We consider a linear, harmonic wave train propagating in the positive x-direction, characterized by its amplitude ζ_a, circular frequency $\omega = 2\pi/T$, and wavenumber $k = 2\pi/\lambda$, where T and λ are the wave period and wavelength, respectively.

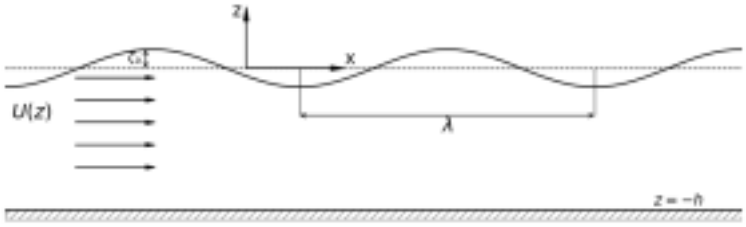


Figure 1: Coordinate system for definition of wave-current interaction

To account for the general case where the current is at a relative angle θ to the wave direction (with $\theta = 0°$ being a purely following current), the current velocity U is replaced by its component in the direction of wave propagation, $U\cos(\theta)$. A general dispersion relation that includes current shear, U'(z), as presented by Faltinsen et al. (2025) is:

$$(U(0)k - \omega)^2 = \Big(gk + U'(0)(U(0)k - \omega)\Big)\tanh(kh) \tag{1}$$

Here, $U(0)$ is the current velocity at the free surface. As current shear is not considered in the present study, the term U'(0) is zero, which reduces the dispersion relation to the form used herein throughout this work.

$$(kU\cos(\theta) - \omega)^2 = gk\tanh(kh) \tag{2}$$

To verify the implementation of the dispersion relationship, the wavelengths of wave under different wave periods combined with different same-direction current speeds are computed and compared with the experimental and CFD results from Faltinsen et al. [1]. The comparison is shown in **Error! Reference source not found.**. The L represent pontoon length of 53 meters. Full scale water depth was 77.5m for the tests where the wavelengths were extracted. One can see that the numerical implementation is validated.

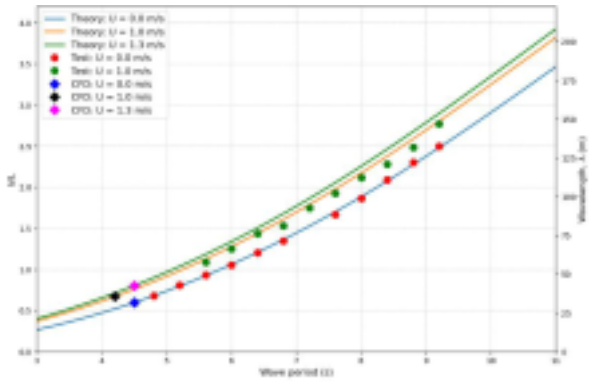


Figure 2: Wavelengths computed under different current speeds. Comparison with experimental and CFD results from Faltinsen et al. [1].

Now we consider the case with arbitrary relative angle between the long-crested waves and the current. Consider deep-water waves with a fixed direction of propagation, while a current of constant speed U flows at a relative angle θ. Thus, the wavelength change can be solved through Equation (2).

A special consideration that matters for numerical implementation is wave-blocking. Following Faltinsen et al.([1],[2]), the condition for wave blocking in deep water is given by the non-dimensional relationship $\omega U_{opp}/g = 0.25$, where U_{opp} is the component of the current that directly opposes the wave. For a general angle θ, this component is $U_{opp} = -U\cos(\theta)$, and the condition only has physical meaning in the opposing hemisphere (90° < θ < 270°). Substituting $\omega = 2\pi/T$ and $U_{opp} = -U\cos(\theta)$ into the blocking condition gives the analytical expression for the limiting (blocking) period T:

$$T = -(8\pi U / g)\cos(\theta) \tag{3}$$

This is the polar equation for a circle. The maximum blocking period occurs for a directly opposing current ($\theta = 180°$), where the equation simplifies to $T_{max} = 8\pi U/g$.

This is shown in **Error! Reference source not found.**. For a current speed of U = 1.5 m/s, the maximum blocking period is $T_{max} \approx 3.84$ seconds. The figure illustrates the non-dimensional wavelength L/L_0, where L_0 is the wavelength in zero current. The gray "Blocked Zone" visualizes the region of periods and angles for which no regular waves can propagate, enclosed by the red analytical blocking limit line.

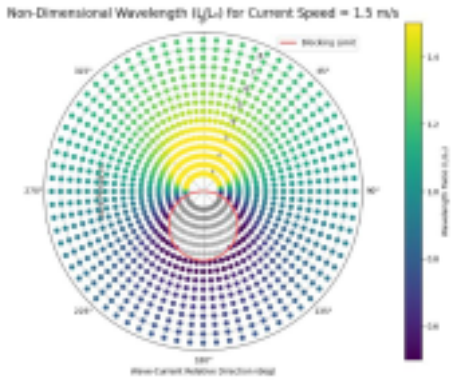


Figure 3: Nondimensional wavelength L/L_0 for a current speed of 1.5 m/s in deep water. The relative angle θ is 0° for following conditions and 180° for opposing conditions. The red line indicates the analytical blocking limit, and the gray area represents the zone where waves are blocked.

2.2 Wave loads under wave-current interaction

Now the wavelength changes are computed for arbitrary relative wave-current directions. Wave loads computed from frequency domain solver are needed as input to the global analysis model of a floating bridge with many pontoons. This means that ideally a Boundary Element Method (BEM) solution that accounts for wave-current-structure-interaction will provide the wave loads RAOs. However, there exists no commercial software that can provide such a full wave-direction-and-period-dependent RAOs sets directly. Thus, a simplification is to apply coefficients from zero current speed. As explained above, the simplification will maintain the wave frequency as incoming wave frequencies while mapping the load RAOs at a given incoming wave frequency to the load RAOs of a zero-current frequency that corresponds to the modified equivalent wavelength. An example of the wave force RAO in the longitudinal pontoon direction is provided by Figure 4. The relative direction between the waves and current is 113 degrees, meaning that the waves are shortened due to the wave-current condition. From the example it is also obvious that the shorter waves and loads are more affected than the longer waves.

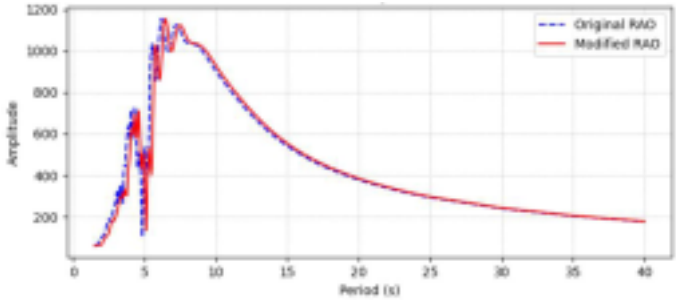


Figure 4: An example of wave force RAO (kN/m) in the longitudinal pontoon direction.

3. Floating bridge global responses with wave-current-structure interaction

To evaluate the global responses of the tested floating bridge under wave-current interaction, the OrcaFlex software is applied. For this study, the hydro-elastic floating bridge model tests carried out at SINTEF Ocean is applied for investigation of our implementation. The details of the model tests can be found in Viuff et al. [5]. The floating bridge model is explained in Figure 5. The model is composed of 10 pontoons, bridge girder (composed of connected segments between pontoons), pontoon columns and a cable-stay bridge at one end. The motions of pontoons and bridge girder, the section loads in the bridge girder and columns, and the cable tensions on the cable-stay bridge part were measured under regular and irregular waves with and without current combined. In total, more than 300 hydro-elastic model tests were performed, forming a valuable database of floating bridge global responses under waves and current.

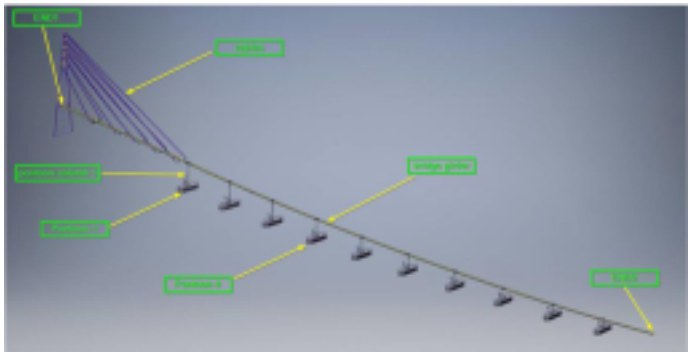


Figure 5 Floating bridge model tests: illustration of model components, Xiang [6].

3.1 Floating bridge components and modelling

An OrcaFlex model was setup based on the details of the bridge model tested. The pontoons are modelled as diffraction/radiation large volume structures, and the bridge girder is modelled as line elements with required section properties. Theory about OrcaFlex modelling is found in Orcina [4]. Xiang [6] also provided description on modelling the tested bridge in OrcaFlex. For clarification, the coordinate systems and definitions applied in a floating bridge model is briefly introduced here.

Waves and current are defined in the global coordinate system $OXYZ$, which has its origin at the mean free surface and the Z-axis pointing vertically upwards, as illustrated in Figure 6. The local coordinate $o_i x_i y_i z_i$ system of Pontoon-i has its origin $(X_i, Y_i, 0)$ at the free surface and z_i pointing upwards. Assume that the global directions of waves and current are γ_w and γ_c, respectively. The heading angle α_i of the Pontoon-i is defined as the angle from the global X-axis to the local x_i-axis. The wave direction in the local system $o_i x_i y_i z_i$ is defined as β_i, which is the angle from x_i-axis to the direction γ_w. Then $\gamma_w = \alpha_i + \beta_i$. Further, the angle from the wave direction γ_w to the direction of current U is defined as θ and $\gamma_c = \gamma_w + \theta$. As discussed earlier, only the current component projected onto the wave direction contributes to the change of wavelength.

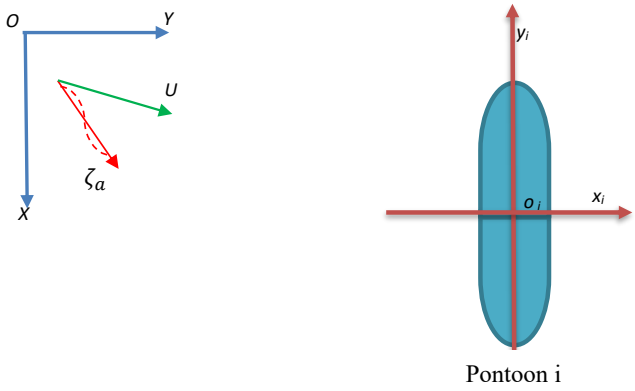


Figure 6: Definition of global coordinate system $OXYZ$, current, and ambient waves, and the pontoon local coordinate system.

In this article, computation and measurements are compared for loads along the bridge girder, and motions of the pontoons. Figure 7 shows coordinate systems used by pontoons and bridge girder sections. Table 1 lists information about the measurements carried and how they are named in comparison figures shown later. The pontoons are counted from 1 to 10 in the order illustrated in

Figure 5. In later comparison, all the measurement results related to full bridge girder is presented with the girder arc length, which is cumulative length of the girder starting from the cable stayed bridge END1 until END2, shown in Figure 5.

Table 1: Measurements for comparison in the floating bridge test and their reference coordinate systems.

Measurements /Computation	**Coordinate systems and names in the comparison figures**
Pontoon motions	6 DoF motions - translational x, y, z motions in local x_i, y_i, z_i directions, rotational Rx, Ry, Rz motions around axis x_i, y_i, z_i; measured for all pontoons; Refer to coordinate system shown in Figure 6.
Girder force and moments	Girder (vertical) x shear force x(v)_force, girder (transverse) y shear force y(t)_force, Mx, My, Mz moments around $x_{bg,k}$, $y_{bg,k}$,*and* $z_{bg,k}$ axis; measured along the bridge girder at 10 locations; Refer to coordinate system shown in Figure 7.

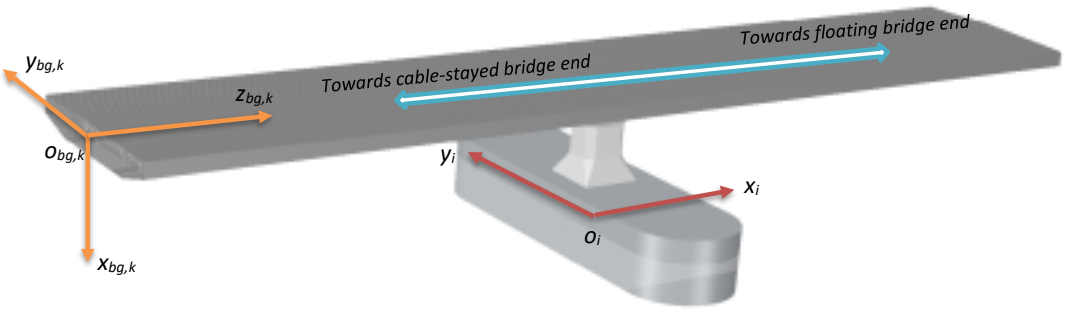


Figure 7: Bridge girder coordinate system $o_{bg,k}x_{bg,k}y_{bg,k}z_{bg,k}$ in a bridge section with pontoon and column; shown in the figure also an example of the ith pontoon coordinate system $o_ix_iy_iz_i$; At where pontoon column is connected to the bridge girder, the $y_{bg,k}$ is pointing in the same direction as the y_i direction of the pontoon coordinate system; The figure also shows the directions of girder towards cable-stayed bridge and floating bridge ends.

3.2 Modal analysis of the tested floating bridge

The undamped natural modes of the tested bridge model are evaluated through modal analysis in OrcaFlex. While the theory is based on the simple harmonic motion of a single mass-spring system ($mx''(t) = -kx(t)$), a floating bridge is a multi-degree-of-freedom (MDOF) system. By discretizing the structure into n degrees of freedom and assuming harmonic oscillation, the governing equations take the form of the generalized eigenvalue problem:

$$\omega^2 \boldsymbol{M}\boldsymbol{x} = \boldsymbol{K}\boldsymbol{x} \tag{4}$$

Here, **M** and **K** denote the $n \times n$ mass and stiffness matrices, and **x** is the n-element displacement vector. The mass matrix **M** includes frequency-dependent added mass. Further theoretical details regarding the modal analysis solver can be found in Orcina [4].

Hydrodynamic interaction matters for the pontoon added mass, as shown by Xiang [7]. In the modal analysis this interaction is included in the pontoon added mass matrix. Note that the cross-body interaction terms are not included, in consistency with the proposed simplification implementation.

The modal analysis was carried out iteratively. This means that for added mass of a given period, the modal period is considered as identified only when the computed modal period is numerically equal to the added mass period.

All the modal periods that are larger than 2.0s are given in Figure 8. It shows that there are 30 modes between 2s and 8s. This indicates that the response of the tested floating bridge is wind-wave dominated. And the first order loads and responses will be most significant. Considering that the hydrodynamic interaction and wave-current interaction are also more important under wind-wave-region, we expect that both effects will have an impact on the computation of the floating bridge responses under wind waves. This will be checked by comparison between computation, and the model test results in the following section.

The tested floating bridge represents about 1/3 of the full floating bridge length; thus, the full bridge will have much longer first modal periods. The longest modal period of the full bridge is 111.1s when no mooring lines are applied. With mooring lines, the first mode is reduced to around 1 minute. Xiang [8] provided an analysis of the floating bridge global responses under slowly varying wave loads. No mooring lines were included in the studied bridge. The study showed that the second order wave loads mainly have an impact on the horizontal motion of the bridge.

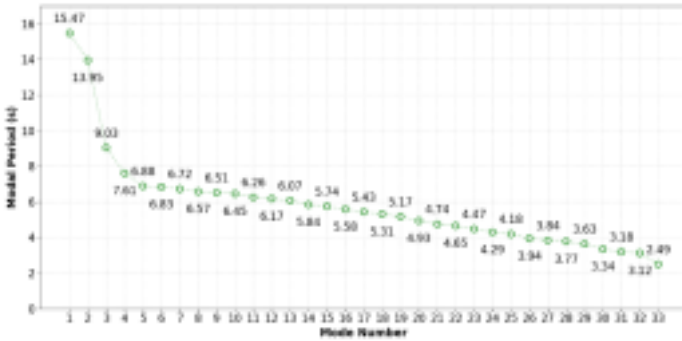


Figure 8: Modal periods of the tested floating bridge based on added masses accounting for hydrodynamic interaction between pontoons.

3.3 Floating bridge global responses under wave-current interaction in irregular waves

Two irregular waves test cases are selected to investigate wave-current-structure-interaction and hydrodynamic interaction on global responses of the tested floating bridge. The difference between two tests is that one without current and one with 1.0m/s current. The wave and current conditions are listed in Table 2**Error! Reference source not found.**. The values provided in the table are specified values meaning that the measured values will be slightly different. Both the current and the wave directions are 220 degrees, which corresponds to one of the main wind wave directions for the design.

It is important to emphasize the model test uncertainties. Due to the large area of ocean basin occupied by the model, the waves are not strictly homogeneous along the bridge, with around 5-15% variation of wave heights at different pontoons. This is a source of uncertainty, in addition to the current generation combined with wave generation which was pointed out in Faltinsen et al. [1].

The comparison of the results is provided in Figure 9 for floating bridge pontoon motions and Figure 10 for the bridge girder vertical/transverse shear forces and 3-DoF moments. The presented results are the standard deviation (STDV) of different bridge components responses. The model test results are denoted as Test_U0.0 (no current) and Test_U1.0 (with a 1.0 m/s current). Three numerical models are setup to investigate the importance of hydrodynamic interaction and wave-current-structure interaction. Table 3 provides a description of the different numerical models and model test cases. The same IDs are used in all the plots of comparison. In all the numerical models, a longitudinal Morison-type drag force coefficient Cd = 0.75 is applied in the y- direction of each pontoon.

Table 2: Comparison case from the floating bridge model tests; Hs: significant wave height; Tp: Peak period; Uc: current speed. Standard Jonswap Spectrum applied. Waves and current in same direction.

Case ID	Dir. (deg.)	Hs (m)	Tp (s)	Uc (m/s)	Gamma
Test_U0.0	220	2.1	5.5	0	2
Test_U1.0	220	2.1	5.5	1.0	2

Table 3: List of different numerical models and model test cases.

ID in plots	Comment
Test_U0.0	The model test results with no current**Error! Reference source not found.**.
Test_U1.0	The model test results with a 1.0 m/s current**Error! Reference source not found.**.
SB	The single-body model which applies hydrodynamic coefficients without hydrodynamic interaction or wave-current interaction modifications.
MB	The multi-body model which includes hydrodynamic interaction but no wave-current interaction modifications.
MB_U1.0	The multi-body model which accounts for both hydrodynamic and the 1.0 m/s wave-current interaction modifications.

For Test_U0.0, the SB model serves as baseline model, and the MB model serves as improved model for hydrodynamic interactions. For the Test_U1.0, the MB model serves as baseline model and the MB_U1.0 model serves as improved model for wave-current-structure interaction. Thus, the importance of included hydrodynamics effects can be studied based on comparisons.

The comparison between model test results demonstrates that the wave-current interaction has a non-trivial impact on most of the responses examined. For some of the responses (e.g. pontoon x-, z-, and Ry- motions, vertical girder motion and shear x(v) force, and weak-axis girder moment M_y), the impact is significant. This indicates also the importance of this effect in numerical implementation.

The comparison between model test results Test_U0.0 and numerical results shows that the responses (pontoon x-, z-, and Ry- motions, vertical girder motion and shear x(v) force, and weak-axis girder moment M_y) are underestimated by single body SB computation, and this underestimation can be largely corrected by including hydrodynamic interaction in the MB model. The different importance of hydrodynamic interaction to different responses can be explained by that the diffracted and radiated waves will mostly be reflected between the longitudinal sides of pontoons in vicinity.

The comparison between model test results Test_U1.0 and numerical results shows that the responses (pontoon x-, z-, and Ry- motions, vertical girder motion and shear x(v) force, and weak-axis girder moment M_y) are underestimated by multibody MB computation, and this underestimation can be much corrected by including wave-current-structure interaction in the MB_U1.0 model.

The comparison shows that the transverse girder shear force and strong-axis girder moment M_x are relatively insensitive to both hydrodynamic and wave-current interaction. These loads are related to the wave force in the pontoon y- direction. The regular wave loads comparison of Faltinsen et al. [1] showed that this force is significantly influenced by wave-current interaction. Thus, the insensitivity in irregular waves is related to the cancellation effects of wave excitation force in this direction.

The pontoon y- motion and girder torsional moment M_z are less sensitive to hydrodynamic interaction but more sensitive to wave-current-structure interaction. The deviation of all computations of pontoon Rx- motion of pontoons 7-10 can be observed in both model test cases. Since we have no good explanation for this, further study is necessary.

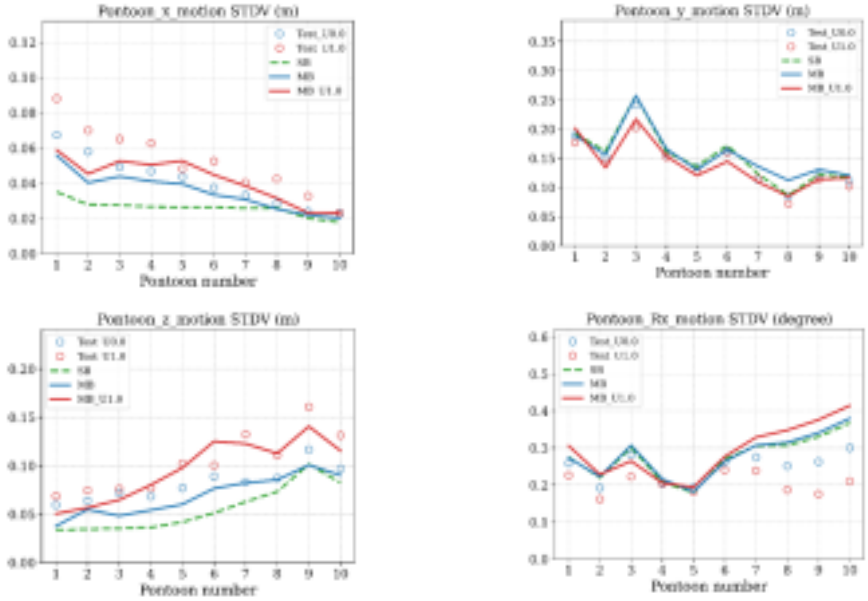
As observed in the comparison between model test results and different computations, the implementation of wave-current and hydrodynamic interaction provides a notable overall

improvement over the baseline numerical model, yielding results that agree much better with the model test measurements.

The computation shows that the strong-axis girder moment M_x and transverse shear y(t) force are much larger than weak axis bending moment M_y, torsional moment M_z and vertical shear x(v) force. But their contribution to cross section stress must be evaluated together with the section property.

The compared responses have practical implication to the bridge's service requirement and ultimate strength check. Excessive bridge girder and pontoon motions will cause that the bridge does not meet the requirement of driving safety and must be temporarily shut down. The driver comfort is mainly governed by the horizontal and vertical accelerations which may be set to 0.30 m/s^2 for the 1-hour extreme accelerations. The girder shear force, bending moments and torsional moment are directly related to the bridge girder cross-section stress level, and thus the bridge girder dimensions and the cost. One most dangerous situation is that if a numerical model underestimates the responses significantly, the subsequently structure strength will be greatly under-designed. In practice, the environmental loads will be multiplied with a factor of 1.6 before they are applied to strength computation, but even this may not be safe enough if one looks at the difference between the weak axis bending moment (M_y) predicted by the single body model (SB) and the model test results from both cases. The fact is that the SB model was the one applied traditionally before the importance of hydrodynamic interaction and wave-current interaction was introduced.

The model tests comparison with the computations are mainly considered as a process of software validation and identification of neglected physical effects in numerical models. The final design of the full bridge will eventually be carried out in the software considering also other loads from the wind, traffic, temperature and so on.



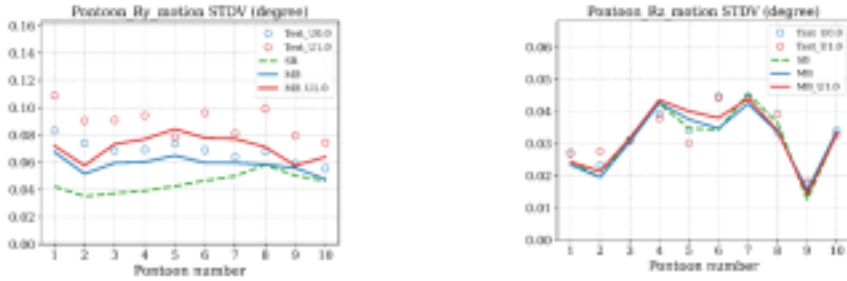


Figure 9: Standard deviation (STDV) of 6-DoF motions of 10 pontoons to the floating bridge test model. **'o'**: model test results, and 'U0.0' and 'U1.0' indicate the current speed (m/s) in the tests; **'-- SB'**: Numerical results with no wave-current and hydrodynamic interaction; **'- MB'**: Numerical results with hydrodynamic interaction but no wave-current accounted for; **'- MB_U1.0'**: Numerical results with hydrodynamic interaction and wave-current accounted for U = 1.0 m/s.

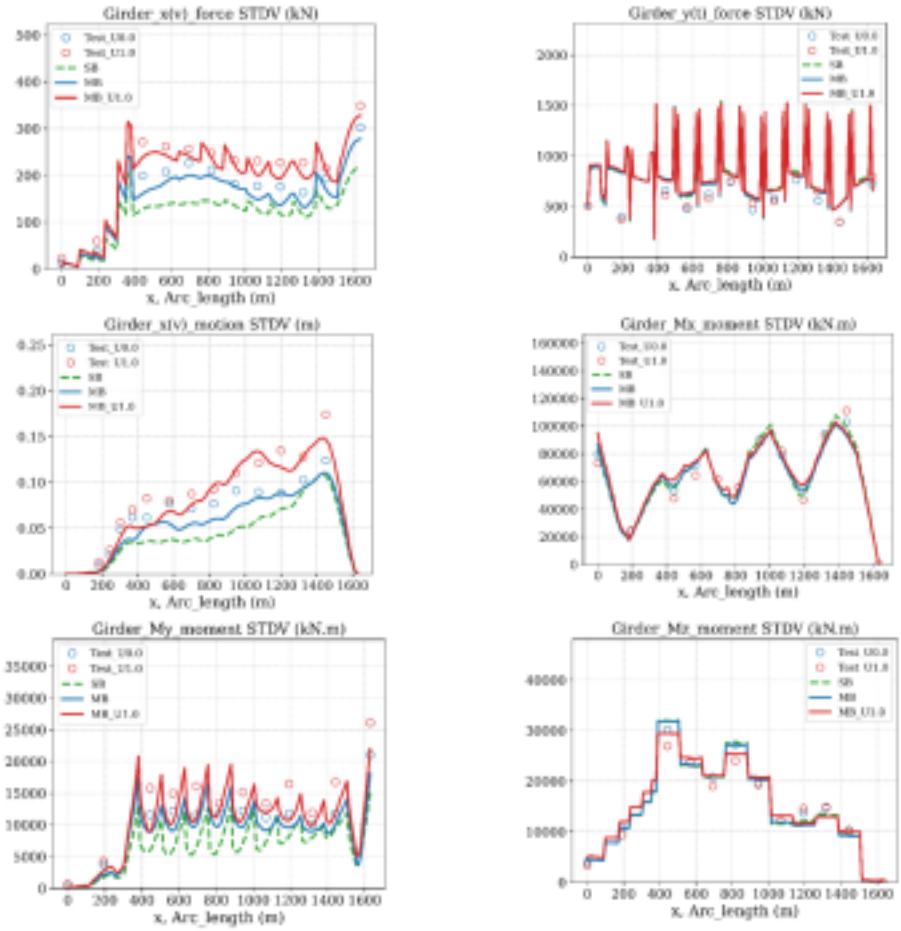


Figure 10: Standard deviation (STDV) of selected girder loads and stay-cable tension of the floating bridge test model. **'o'**: model test results, and 'U0.0' and 'U1.0' indicate the current speed (m/s) in the tests; **'-- SB'**: Numerical results with no wave-current and hydrodynamic interaction; **'- MB'**:

Numerical results with hydrodynamic interaction but no wave-current accounted for; **'- MB_U1.0'**: Numerical results with hydrodynamic interaction and wave-current accounted for U = 1.0 m/s.

4. Concluding remarks

This study investigated the hydro-elastic responses of a floating bridge under wave-current-structure interaction using a simplified, practical numerical approach. By mapping wave loads via equivalent wavelengths, the proposed method integrates complex wave-current effects into standard analyses that can be carried out in existing commercial software.

The comparison study of floating bridge responses under irregular waves with/without current proved the importance of including hydrodynamic interaction and wave-current-structure interaction in the numerical models. Neglecting these effects will underestimate critical structural responses, thus, can lead to non-conservative engineering designs.

Incorporating hydrodynamic interaction and wave-current-structure interaction corrected the substantial underestimations seen in the baseline models. It provided much improved agreement with the model tests for highly sensitive degrees of freedom, most notably x-, z-, and Ry- motions, as well as bridge girder's vertical shear forces, vertical motions and weak-axis bending moments. For degrees of freedom less sensitive to wave-current-structure and hydrodynamic interaction, the modified model maintains the same accuracy of the baseline results.

The validated framework presented in this article provides a tool for the practical engineering design of large-scale floating bridges in complex ocean environments.

References

[1] O.M. Faltinsen, J. Wang, and X. Xiang, *Current–wave interaction with large-volume structures*, Physics of Fluids, 37(6), 2025.
[2] O.M. Faltinsen, J. Wang, and X. Xiang, *Water wave-current interaction with logarithmic wind-induced current*, Physics of Fluids, 38:1, 2026.
[3] A.G. Fredriksen, K.A. Kvåle, and X. Xiang, *On the wave-current interaction effects on linear motion for floating bridges*, J Hydrodyn, 2026.
[4] Orcina, *OrcaFlex Help*, orcina.com, 2026.
[5] T. Viuff, S. Ravinthrakumar, O.D. Økland, O.A. Grytå, and X. Xiang, *Experimental study of floating bridge global response when subjected to waves and current*, Applied Ocean Research, 138:103588, 2023.
[6] X. Xiang, *Extensive hydro-elastic floating bridge tests: planning, design, implementation, and numerical comparison*, Applied Ocean Research, 140:103741, 2023.
[7] X. Xiang, *Floating bridge global responses with hydrodynamic interaction*. Ocean Engineering, 291: 116420 2024.
[8] X. Xiang, *Floating bridge global responses to slowly varying wave loads*. Ocean Engineering, 2024, 302: 117568.

10th International Conference on HYDROELASTICITY IN MARINE TECHNOLOGY
Trondheim, Norway, June 16th-18th, 2026

Fully Coupled Hydroelastic Analysis of Curved Floating Bridges via DMB Method

Song, J.[1] and Kim, S.[2*]

[1] School of Civil, Environmental, and Architectural Engineering, Korea University, Seoul, 02841, Korea (2016170334@korea.ac.)
[2] School of Civil, Environmental, and Architectural Engineering, Korea University, Seoul, 02841, Korea (rocksmell@korea.ac.kr)

Abstract. Floating girder bridges exhibit hydroelastic responses that arise indirectly from wave induced motions of their floating foundations. Preliminary designs commonly idealize the pontoons as rigid bodies, which can mask pontoon flexibility and the associated fluid structure interaction effects that influence global response predictions. This study proposes a fully coupled time domain framework based on the Discrete Module Beam method for the FLORA Pilot 1 curved pontoon bridge. Wave structure interaction is represented using linear potential flow hydrodynamics for discretized rigid modules, while equivalent beam connectors derived from pontoon sectional properties transfer internal forces and deformations within a coupled multibody system. The implementation is first examined against a rigid pontoon baseline in a stiffness dominant reference configuration. Pontoon sectional stiffness is then systematically reduced to quantify when and how bridge level motions and internal load envelopes depart from the rigid body assumption under representative wave headings. The results indicate that, for the end-fixed curved bridge considered, rigid-pontoon modeling is generally adequate for girder strength envelopes, while DMB-based hydroelastic refinement may be required for motion-sensitive serviceability assessments.

Key words: *Floating Bridge; Hydroelasticity; Discrete Module Beam; Fully Coupled Analysis*

1. Introduction

Floating bridges can be a viable solution for sites where pile foundations are impractical, such as locations with deep bedrock or significant water depth. For pontoon-supported bridges, particularly in a straight configuration, achieving sufficient lateral resistance solely through girder stiffness is inherently challenging. This limitation has motivated the adoption of planar curvature in conceptual designs, most notably for the Bjørnafjorden crossing in the Norwegian Public Roads Administration (NPRA) E39 ferry-free project, which has in turn accelerated research on curved floating bridges.

A floating bridge is a multi-component system in which the pontoons act as the primary bodies that directly interact with incident waves. Because the pontoons are connected to the bridge girder through columns, wave-induced motions and loads are transmitted to the superstructure, and the bridge consequently exhibits a coupled wave-induced response. From a hydroelastic perspective, the pontoon foundations can be sufficiently large and their structural flexibility can be sufficiently relevant that elastic deformation of the pontoon itself may influence the global bridge response, especially when the spatial scales of dominant structural deformation modes are comparable to incident wavelengths.

Extensive numerical studies have investigated the dynamic responses of curved floating bridges subjected to waves, wind, and current **[1-4]**. In addition, various numerical approaches have been proposed to evaluate accidental limit states **[5,6]**, and recent efforts have increasingly focused on hydrodynamic interaction and its influence on global responses **[7,8]**. More recently, experimental

* Correspondence to: abcdef@ntnu.no

campaigns have been conducted to validate numerical predictions and quantify inherent uncertainties **[9-11]**. Beyond response characterization, studies have examined structural behavior and vibration control strategies for curved floating bridges **[12]**, and practical design-oriented approaches and hydroelasticity considerations for continuous floating systems have been discussed **[13,14]**.

Despite these advances, in many floating-bridge analyses the pontoon foundations are still commonly modeled using rigid-body assumptions (e.g., lumped-mass representations or simplified supports with hydrodynamic effects), while the wave-induced structural response of the girder is evaluated through the coupled system dynamics. This approach is undoubtedly useful and can be regarded as a form of hydroelastic analysis at the system level; however, it differs from the classical offshore-engineering notion of hydroelasticity, where the elastic deformation of the wave-interacting floating body is explicitly accounted for in the fluid–structure interaction. Considering the scale of pontoons used in long-span floating bridges, pontoon flexibility may not always be negligible, and the validity range of the rigid-pontoon assumption—and its implications for global bridge response—remains insufficiently quantified in terms of pontoon sectional stiffness and practical design thresholds.

To address computational challenges associated with high-resolution hydroelastic modeling of large floating structures, the Discrete Module Beam (DMB) family of methods has emerged as an efficient mid-fidelity alternative. In DMB, a continuous floating body is discretized into multiple rigid hydrodynamic modules whose wave–structure interaction is evaluated (typically via potential-flow radiation/diffraction), while the internal structural behavior is represented through equivalent beam elements that connect the modules in a coupled multibody-dynamics formulation. DMB-based hydroelasticity has been developed and applied to very large floating structures and continuous floating systems, including time-domain formulations and extensions to practical structural representations.

Recent studies have progressively advanced DMB-type hydroelastic frameworks toward practical time-domain applications and more realistic structural representations. Zhang et al. extended the discrete-module-beam-bending formulation to a Cummins-equation–based time-domain scheme and further enhanced its applicability to complex geometries **[15,16]**. Ren et al. incorporated finite-element–based structural modeling within the DMB workflow for VLFS/FOPV-type platforms **[17]**, while Jin et al. demonstrated fully coupled DMB simulations for moored submerged floating tunnels under both regular and random waves **[18]**. A recent review by Loe et al. provides a consolidated overview of these developments and remaining challenges in DMB-based hydroelasticity **[19]**.

Against this background, the present study aims to assess the applicability of a DMB-based fully coupled time-domain framework for a curved floating bridge model designed in the FLORA Pilot-1 concept, and quantify how pontoon hydroelasticity, controlled through the pontoon sectional stiffness level, affects the wave-induced response of the bridge girder. To this end, the study formulates a practical hydroelastic modeling procedure in which a continuous pontoon is represented as an assembly of discretized hydrodynamic modules coupled through equivalent beam connectors derived from pontoon sectional properties, so that pontoon flexibility can be incorporated within a bridge-level multibody time-domain analysis. Specifically, the study first establishes a reference case where pontoon stiffness is sufficiently large such that rigid-like behavior is expected, thereby enabling a direct reference comparison between the assembled DMB model and a conventional rigid-pontoon representation in a stiffness-dominant regime. Finally, the study provides a practical criterion for when pontoon hydroelasticity should be included, based on the sensitivity of the global response to pontoon sectional stiffness. In this way, the study contributes both a modeling strategy for implementing pontoon hydroelasticity in curved floating bridges and a quantitative assessment of when such refinement becomes relevant for bridge-level response evaluation.

2. Methodology

2.1 Linear Wave–Structure Interaction Analysis

To perform a hydroelastic analysis of floating bridges, it is necessary to account for wave–structure interaction while also evaluating the behavior of the fully coupled system. In this study, a fully coupled global response analysis framework widely used in offshore engineering is adopted. The wave–structure interaction is characterized using linear potential-flow theory in the frequency domain, whereas the

overall system response is evaluated in the time domain through a Cummins-type formulation, which naturally accommodates nonlinearities arising from system-level effects

Based on potential-flow analysis, the hydrodynamic properties of the submerged part of a single rigid floating body are evaluated in the frequency domain for each wave heading. The added mass and radiation damping are obtained as frequency-dependent matrices, and the wave-excitation forces are obtained as frequency-dependent vectors. These quantities are then organized in tensor form as linear transfer functions with respect to unit incident waves and are referred to a chosen reference point (e.g., the body reference origin). The floating bodies are represented using a lumped-mass formulation, and the columns and girder are interconnected using line elements whose interactions are defined through connection stiffness to assemble the fully coupled system. By idealizing the girder ends as abutments and prescribing the corresponding boundary conditions, the floating bridge system of interest can be numerically implemented within the proposed framework.

The governing equation for pontoons of floating bridge in the time domain is given by Cummin's equation as

$$\left(\widetilde{M} + \widetilde{M}_a(\infty)\right)\ddot{\tilde{u}}_p(t) + \int_{-\infty}^{t} \tilde{R}(t-\tau)\dot{\tilde{u}}_p(\tau)d\tau + \left(\widetilde{K}_H + \widetilde{K}_s\right)\tilde{u}_p(t) = \tilde{F}_{ext}(t) \tag{1}$$

where $\widetilde{M}$ is the inertia matrix, $\widetilde{M}_a(\infty)$ represents the added mass at infinite frequency matrix, $\tilde{R}(t-\tau)$ is the retardation function to consider the energy dissipation corresponding to the motion of body, $\widetilde{K}_H$ is the hydrostatic stiffness matrix, $\widetilde{K}_s$ is the coupled stiffness matrix of the floating bridge, $\tilde{u}_p$ is the displacement vector, and $\tilde{F}_{ext}(t)$ is the external force vector including environmental loads.

Following this global response analysis procedure, the structural behavior of a floating bridge can be evaluated by applying wave-induced hydrodynamic terms that scale with the wave amplitude at each wave period. Although the bridge superstructure is not directly subjected to incident wave loads, it responds indirectly through the wave-driven motions of the floating foundations, enabling assessment of the resulting elastic response under the target environmental conditions. This approach constitutes a reference mid-fidelity methodology that has been extensively validated and widely adopted for global response predictions of floating offshore structures.

2.2 Discrete Module Beam Method

DMB is particularly effective for large-scale floating bridge systems in which the dominant structural deformation modes have spatial scales comparable to the incident wavelengths, and in which a fully resolved hydroelastic model would be computationally prohibitive. In essence, the DMB method preserves the potential-flow–based hydrodynamic analysis that is widely used in offshore engineering, but it represents a single, continuous floating body as an assembly of discretized modules. By doing so, wave–structure interaction can be captured at the module level within a multibody formulation.

The discretized modules are then coupled through equivalent beam elements that are constructed from the sectional details of the original floating body. This modeling choice introduces a clear separation of roles. The hydrodynamic modules are responsible for representing wave-induced loads and the hydrodynamic interaction among the modules, while the beam elements represent the internal structural stiffness and load transfer within the floating body. Together, the modules and the connecting beams are treated as one coupled hydroelastic system. From a computational perspective, this approach reformulates a complex hydroelastic problem into a multibody-dynamics framework, which substantially improves efficiency while retaining the key coupled-response characteristics of interest.

For the present curved pontoon bridge application, the discretized multibody model was implemented by attaching panel-based hydrodynamic modules to line elements defined using precomputed sectional properties. The multibody potential-flow problem for the discretized modules was solved using OrcaWave, while the assembled coupled system was modeled in OrcaFlex. Here, the hydrodynamic coefficients were evaluated in the frequency domain for the assembled mean configuration of the discretized modules, and the subsequent time-domain response was obtained using these precomputed coefficients within a Cummins-type formulation.

When each module is meshed as a fully closed body, duplicate end panels can be artificially generated at the common internal cut interfaces between adjacent modules. This does not imply physical overlap or interpenetration of floating bodies during the time-domain simulation; rather, it is a panelization artifact that arises when a continuous pontoon is subdivided into multiple hydrodynamic modules. In such cases, opposing outward normals at the same physical location can make the influence-coefficient matrix ill-conditioned (near-singular), leading to numerical instability. A commonly used remedy is to introduce a small artificial separation between modules to avoid exact overlap. However, if the imposed gap is narrow, this numerical treatment may introduce unintended high-frequency gap resonances that are unrelated to the hydroelastic response of interest.

To avoid both the overlap-induced ill-conditioning and the spurious resonance associated with narrow artificial gaps, the hydrodynamic modules were instead modeled using an open-surface panel strategy. In addition, because OrcaFlex line elements may otherwise introduce extra self-weight, buoyancy, and hydrostatic contributions through the specified diameter and mass properties, hydrodynamic loading on the line elements was suppressed by assigning near-zero values where appropriate. This ensures that the line elements function purely as structural connectors, while the intended sectional stiffness is enforced through the prescribed line properties and the chosen orientation of their principal axes.

3. Numerical Model of the Curved Pontoon Bridge

3.1 FLORA Pilot-1 Bridge

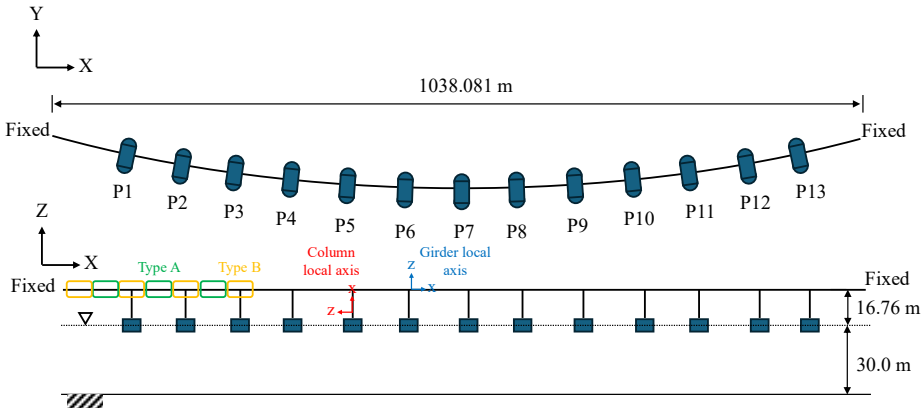
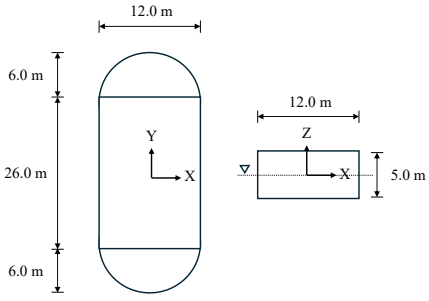
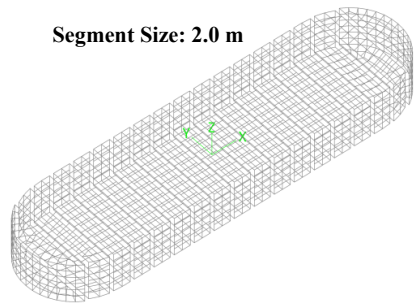


Figure 1: Geometry of the floating curved bridge



(a) Single pontoon



(b) Discretized pontoon

Figure 2: Pontoon geometry and Discretization

Fig. 1 presents schematic plan and side views of the curved floating bridge considered in this study. The bridge is supported by 13 pontoons connected to the superstructure through columns, which are uniformly spaced along the arc length. The total arc length is 1,060 m. The water depth is set to 30 m, representing the site conditions of the channel section connecting Nangdo and Dunbyeongdo in Yeosu, Republic of Korea. The clearance above mean sea level is 16.76 m, and the pontoon spacing exceeds 75.0 m to satisfy navigational clearance requirements.

Two girder cross-sections are adopted, with different configurations for the pier and mid-span regions. The curved bridge model is implemented in OrcaFlex. Because OrcaFlex does not provide a dedicated curved-beam element, the planar curvature is realized by constructing a sequence of straight line segments and assigning local constraint axes at prescribed locations so that the segment orientations follow the target curvature. The original design also incorporates vertical curvature, leading to different pier heights, to mitigate torsional response in the central span; however, the present study simplifies the geometry by considering planar curvature only. Both bridge ends are fully fixed. The girder is modeled using 112 straight line segments of equal length, and the end connections are configured to preserve the local orientation required by the planar curvature. The column height is set to 12.2 m; the column bottom is connected to the top-center of each pontoon, and the column top is positioned 2.06 m below the geometric centroid of the girder section.

Fig. 2 illustrates the pontoon geometry, which consists of a prismatic rectangular body with semicircular ends. The draft is set to 2.5 m. Additional geometric and modeling parameters are summarized in Tables 1 and 2. For application of the DMB method, the main pontoon body is discretized into 2 m segments, while the 3 m end regions with curvature are treated as single segments. Although a finer discretization improves spatial resolution, it also increases computational cost because the DMB formulation requires handling the full hydrodynamic coefficient tensors for each module, leading to a practical trade-off between accuracy and efficiency.

Table 1: Section properties

Section		A (m^2)	I_x (m^4)	I_y (m^4)	I_z (m^4)	E (Gpa)
Girder	Type-A	0.664	1.292	10.768	2.819	210
	Type-B	0.765	1.487	12.73	3.394	210
Pier		0.234	0.611	0.614	0.768	210
Pontoon		2.251	5.405	5.714	28.33	210

Table 2: Pontoon specifications

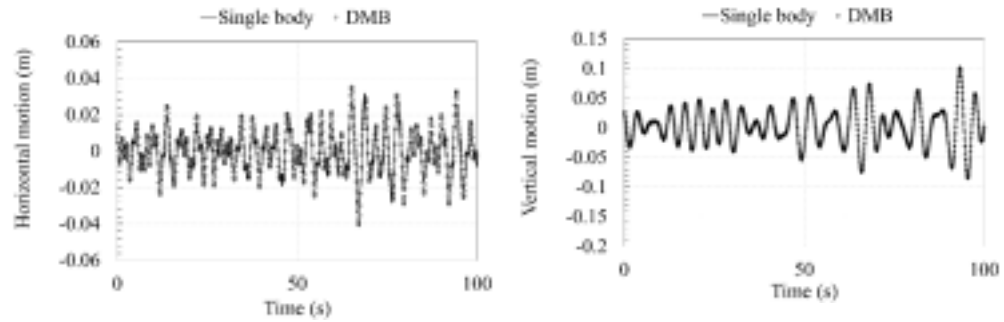
Category		Mass (t)	Mass moment Inertia ($t \cdot m^2$)
Local axis	x	439	551.8E+3
	y	439	96.6E+3
	z	439	606.9E+3

3.2 Reference Comparison for a Truncated Model

As summarized in Table 1, the sectional properties of the pontoons were simplified based on the detailed design of the FLORA Pilot model, including the compartment arrangement and internal stiffening system. As described in the methodology, a virtual line element—intended to represent only the structural role of the pontoon—is placed along the pontoon centerline, and the discretized pontoon modules are connected to this line to form an assembled configuration. Under the present design conditions, the computed pontoon sectional stiffness is sufficiently large that the pontoons exhibit little localized hydroelastic deformation and behave nearly as rigid bodies. Accordingly, whether the system is modeled as a single rigid floating body or through the DMB discretization, the responses are expected

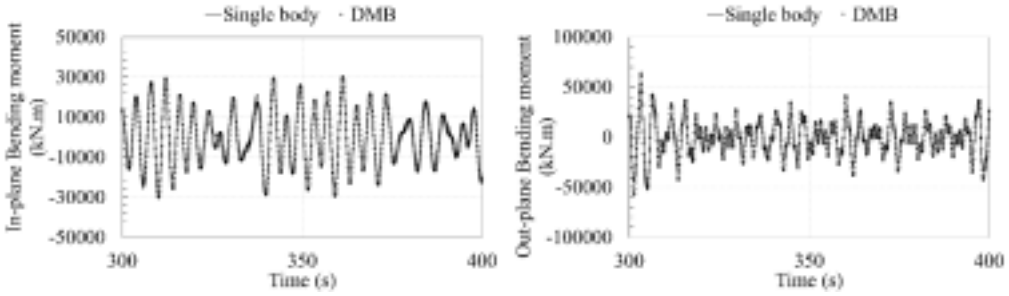
to be nearly identical for the current configuration. This expectation was preliminarily examined using a truncated model that includes the bridge up to the first pontoon bay.

Figure 3 compares the motions at the connection point between the pier and the girder in the truncated model, while Fig. 4 compares the reaction forces at the abutment. The results confirm that, when the discretized pontoon modules are assembled, the mass properties and the resultant hydrodynamic loads are consistently represented, and the resulting wave-induced motions are properly transmitted through the pier to the girder within the fully coupled system. In particular, the characteristic frequencies and the timing of peak responses (i.e., the motion phase) show very close agreement between the models. Although small differences are observed in the peak magnitudes, these discrepancies are unlikely to be caused by insufficient discretization, as the segment length is already sufficiently small. Rather, they can be attributed to the methodological difference that, in the multibody potential-flow solution, hydrodynamic interactions and the spatial distribution of wave-induced loads are explicitly represented, which can lead to slight deviations from the single-body baseline.



(a) Horizontal motion (b) Vertical motion

Figure 3: Time histories of the (a) horizontal and (b) vertical displacements at the connection point of the girder and the pier. The solid line denotes the reference model in which the pontoon is represented as a single rigid body, while the circular markers without connecting lines indicate the results obtained using the DMB-based discretized model.



(a) In-plane bending moment (b) Out-plane bending moment

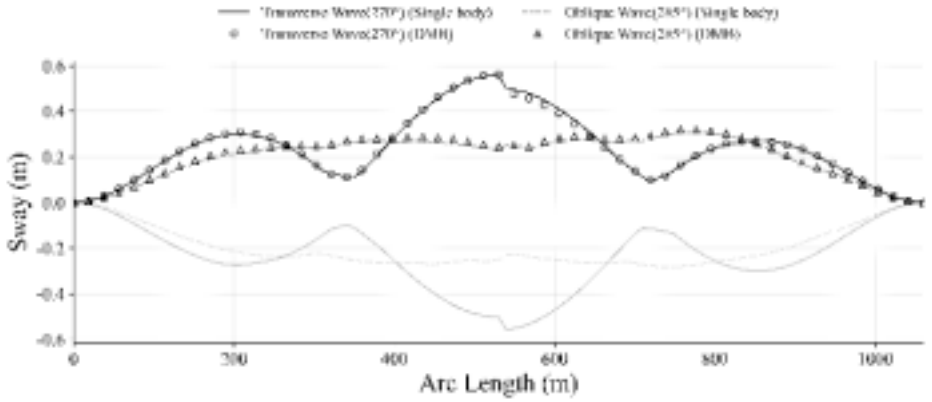
Figure 4: Time histories of the (a) In-plane and (b) Out-plane bending moments at the abutment. The solid line denotes the reference model in which the pontoon is represented as a single rigid body, while the circular markers without connecting lines indicate the results obtained using the DMB-based discretized model.

4. Results and Discussion

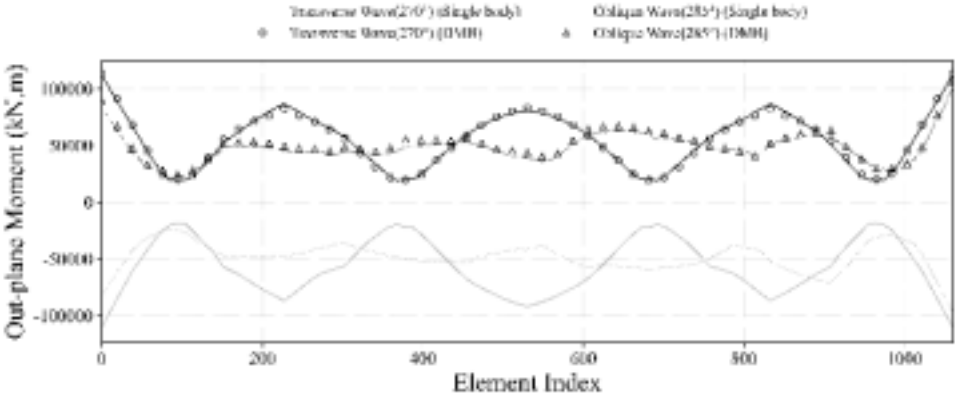
4.1 Examination of DMB Discretization: Rigid-Pontoon Baseline vs Hydroelastic Model

Building on the reference comparison using the truncated model, the DMB method was applied in the same manner to the full-bridge model. As the pontoon sectional stiffness is close to rigid, the DMB-based model is expected to yield responses similar to those of the single-body representation. This is confirmed in Fig. 5, where the maximum envelope distributions show nearly identical results between the two models.

The wave conditions correspond to a 100-year return-period irregular sea state. A JONSWAP spectrum was adopted with a peak period of 4.55 s and a significant wave height of 1.39 m. Because the pontoons are arranged with headings ranging from −18° to 18° with respect to the global coordinate system, the transverse-wave condition results in a system subjected to a range of effective wave headings along the bridge. Nevertheless, the DMB formulation preserves the global response characteristics of the single-body model, yielding nearly identical envelope shapes and peak values along the bridge. Comparable agreement is also observed for the oblique-wave condition, demonstrating the robustness of the DMB formulation under different wave headings. Due to space limitations, only the horizontal response components are presented; however, similar agreement was obtained for all six degrees of freedom.



(a) Horizontal displacement



(b) Internal forces in the girder

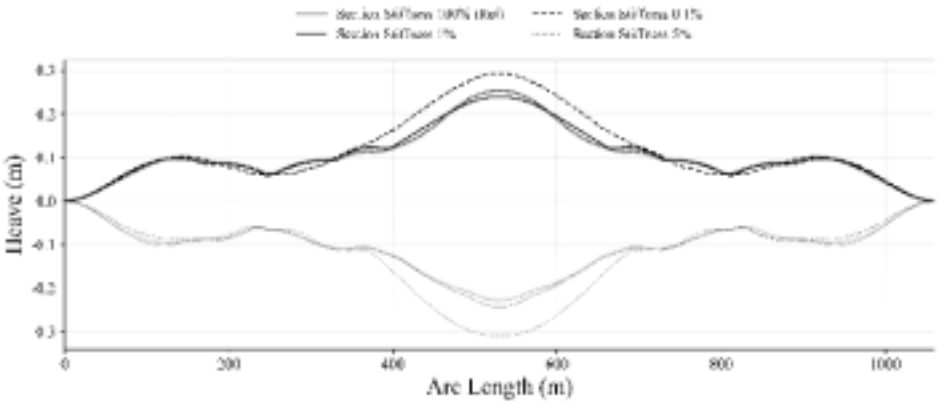
Figure 5: Envelope curves along the bridge girder for (a) sway displacement and (b) out-of-plane bending moment under transverse (270°) and oblique (285°) wave conditions. For each wave heading, the solid/dotted lines represent the reference model in which the pontoon is modeled as a single body,

while the corresponding circular and triangular markers without connecting lines denote the results obtained using the DMB-based discretized model.

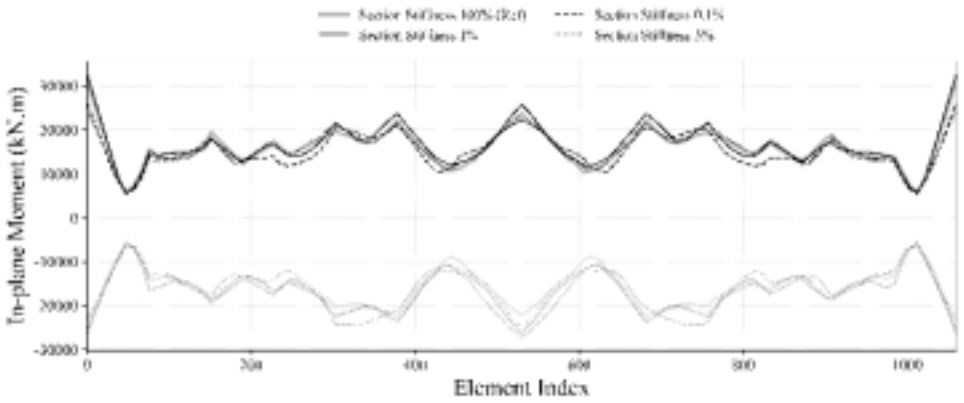
4.2 Influence of Pontoon Sectional Stiffness on Hydroelastic Bridge Response

Using the implemented DMB model, the present study investigated how changes in pontoon sectional stiffness affect the global response of the floating bridge system. Figure 6 presents the parametric results obtained by progressively reducing the sectional stiffness from the reference level of 100% (Ref) to 5%, 1%, and 0.1%. When the stiffness was reduced to 5%, the overall response distributions remained almost identical to those of the reference model. However, once the stiffness dropped below 1%, a noticeable increase in the maximum-envelope heave response emerged around the midspan region. This trend suggests that, as the pontoon becomes more flexible, local deformation of the pontoon is activated and a larger portion of the wave-induced deformation demand is redistributed to the floating foundation rather than being transmitted to the girder.

In contrast, as shown in Fig. 6(b), the maximum-envelope in-plane bending moment of the girder exhibited only limited changes even for substantial reductions in pontoon stiffness. Although an increase in deformation would generally be expected to increase internal forces for an unchanged girder stiffness, the envelope-based results imply that the peak values at different locations may occur at different instants, and that the spatial distribution of relative deformation demand does not deviate markedly from the baseline shape. Consequently, even when the pontoon sectional stiffness is reduced by up to three orders of magnitude relative to the reference design, local hydroelastic deformation of the floating foundation can increase the global displacement response, particularly the midspan heave, while the primary girder bending-demand envelopes remain relatively insensitive under the present modeling conditions.



(a) Vertical displacement



(b) Internal forces in the girder

Figure 6: Effect of pontoon sectional stiffness on the along-bridge envelope distributions of (a) heave displacement and (b) in-plane bending moment. The gray solid line denotes the reference case with 100% sectional stiffness, the black dotted line denotes 5% stiffness, the black solid line denotes 1% stiffness, and the black dashed line denotes 0.1% stiffness, where all stiffness levels are normalized by the reference design value.

5. Concluding Remarks

For the end-fixed curved pontoon bridge considered in this study, the global girder response is governed more strongly by the boundary constraints and the stiffness system shaped by the bridge geometry than by the hydroelastic deformation of the pontoons themselves. Within the investigated range, applying the DMB method led to noticeable changes in displacement responses, such as an increased midspan heave envelope at reduced pontoon stiffness, whereas the primary girder bending-demand envelopes showed no substantial deviation from the conventional rigid-pontoon idealization. In this sense, the present results provide an inverse, quantitative examination of the rigid-pontoon assumption for the examined configuration and wave conditions.

From a practical design perspective, the findings support the common workflow in which preliminary girder strength sizing can be performed independently of detailed pontoon structural design, enabling distinct optimization tracks without materially affecting the girder bending envelopes in the present case. Nevertheless, when motion-related performance metrics and serviceability requirements are critical, or when fatigue and local limit states of the substructure and connections are of interest, incorporating DMB-based hydroelastic analysis may still be warranted to increase modeling resolution and to capture stiffness-dependent response features.

The comparison presented herein should be interpreted as a consistency assessment between the discretized DMB model and the corresponding rigid-pontoon representation, rather than as a strict validation of absolute numerical accuracy. Since no experimental data or independently verified benchmark solution is provided in the present study, the results mainly serve to examine the relative response characteristics of the assembled model and the sensitivity of bridge-level responses to pontoon sectional stiffness. Further benchmark- or experiment-based validation would be needed to establish the absolute computational accuracy of the present framework.

Acknowledgements

This work was supported by a Korea Agency for Infrastructure Technology Advancement (KAIA) grant funded by the Ministry of Land, Infrastructure, and Transport (Grant RS-2023-00250727) through the Korea Floating Infrastructure Research Center at Seoul National University.

References

[1] Cheng, Z., Gao, Z., & Moan, T. (2018). Hydrodynamic load modeling and analysis of a floating bridge in homogeneous wave conditions. *Marine Structures*, *59*, 122-141.

[2] Xiang, X., & Løken, A. (2019, June). Hydroelastic analysis and validation of an end-anchored floating bridge under wave and current loads. In International Conference on Offshore Mechanics and Arctic Engineering (Vol. 58882, p. V009T12A018). American Society of Mechanical Engineers.

[3] Dai, J., Abrahamsen, B. C., Viuff, T., & Leira, B. J. (2022). Effect of wave-current interaction on a long fjord-crossing floating pontoon bridge. *Engineering Structures*, *266*, 114549.

[4] Wei, W., Fu, S., Moan, T., Song, C., Deng, S., & Lie, H. (2019). A time-domain method for hydroelasticity of a curved floating bridge in inhomogeneous waves. *Journal of Offshore Mechanics and Arctic Engineering*, *141*(1), 014501.

[5] Sha, Y., & Amdahl, J. (2019). Numerical investigations of a prestressed pontoon wall subjected to ship collision loads. *Ocean Engineering*, *172*, 234-244.

[6] Sha, Y., Amdahl, J., & Liu, K. (2019). Design of steel bridge girders against ship forecastle collisions. *Engineering structures*, *196*, 109277.

[7] Fenerci, A., Kvåle, K. A., Xiang, X., & Øiseth, O. (2022). Hydrodynamic interaction of floating bridge pontoons and its effect on the bridge dynamic responses. *Marine Structures*, *83*, 103174.

[8] Xiang, X. (2024). Floating bridge global responses with hydrodynamic interaction. *Ocean Engineering*, *291*, 116420.

[9] Rodrigues, J. M., Viuff, T., & Økland, O. D. (2022). Model tests of a hydroelastic truncated floating bridge. *Applied Ocean Research*, *125*, 103247.

[10] Viuff, T., Ravinthrakumar, S., Økland, O. D., Grytå, O. A., & Xiang, X. (2023). Experimental study of floating bridge global response when subjected to waves and current. *Applied Ocean Research*, *138*, 103588.

[11] Wang, C., Cui, M., Cheng, Z., & Moan, T. (2024). A review on design and analysis of floating bridges: Numerical simulations, model tests and field measurements. *Ocean Engineering*, *306*, 118065.

[12] Jin, C., Kim, S., Chung, W. C., Kang, B., & Kim, S. (2024). Feasibility investigation of tuned mass damper for vibration control of curved floating bridge in winds and waves. *Applied Ocean Research*, *148*, 104013.

[13] Song, J., Shin, H., Jin, C., & Kim, S. (2025). Simplified analysis method for pontoon-supported floating bridges under waves. *Ocean Engineering*, *324*, 120758.

[14] Jin, C., Lee, I., Bakti, F., Kim, D. K., Kim, S., & Kim, M. (2025). Multi-body-based 2D hydro-elasticity simulations in time domain for moored floating structure. *Engineering Structures*, *329*, 119789.

[15] Zhang, X., Lu, D., Gao, Y., & Chen, L. (2018). A time domain discrete-module-beam-bending-based hydroelasticity method for the transient response of very large floating structures under unsteady external loads. *Ocean Engineering*, *164*, 332-349.

[16] Zhang, X., & Lu, D. (2018). An extension of a discrete-module-beam-bending-based hydroelasticity method for a flexible structure with complex geometric features. *Ocean Engineering*, *163*, 22-28.

[17] Ren, X., Chen, Y., Zhang, Y., Zhang, X., Shen, K., Cui, L., & Lu, M. (2024). A discrete-module-beam hydroelasticity method with finite element theory in analyzing VLFS in different engineering scenarios. *Ocean Engineering*, *307*, 118121.

[18] Jin, C., Kim, G. J., Kim, S. J., Kim, M., & Kwak, H. G. (2023). Discrete-module-beam-based hydro-elasticity simulations for moored submerged floating tunnel under regular and random wave excitations. *Engineering Structures*, *275*, 115198.

[19] Loe, P. Y. A., Kim, M., Jin, C., Bakti, F. P., & Kim, D. K. (2025). Recent advances in Discrete-Module-Beam-based hydroelasticity method as an efficient tool approach for continuous very large floating structures. *Ocean Engineering*, *340*, 122229.

Floating Structures and VLFS

10th International Conference on Hydroelasticity in Marine Technology
Trondheim, Norway, June16th-18th, 2026

Hydroelastic response of an articulated VLFS: Experimental, potential flow and CFD insights.

Arredondo-Galeana, A.[1,*] Brown, S.[2,3], Ogden, D. [4], Greaves, D.[2] and Brennan, F.[1]

[1] Department of Naval Architecture, Ocean and Marine Engineering, University of Strathclyde, Glasgow, UK
[2] Department of Engineering Science, University of Oxford, Oxford, UK
[3] School of Engineering, Computing and Mathematics, University of Plymouth, UK
[4] Simocean, Manchester, UK

Abstract. A novel experimental campaign for an articulated VLFS is carried out to test the performance of the platform subject to irregular sea states. Rigid and hinged connectors are utilised to analyse performance. Different numerical methods are implemented to compare their accuracy. Two potential flow solvers, namely the discrete-module-beam (DMB) method and the open source potential flow solver SEA-Stack. And a CFD Openfoam framework specifically developed for articulated VLFS. We compare the performance of the numerical methods to predict the vertical and relative pitch angle motions of the platform. Limitations and strengths of the methods are analysed. In terms of performance, we find that the irregular sea state response of the VLFS is similar to that found previously in regular sea state studies, while the capability of load alleviation remains crucial with hinged connections as opposed to rigid connections. Extreme hinge angle responses show a potential range of 15-20° maximum response, both with experiments and CFD. This work paves the way to efficient low-order open source numerical methods in the field of articulated and hydroelastic VLFS.

Key words: *VLFS; Hydroelasticity; Hinge connected; Potential flow; CFD*

1. Introduction

As ocean levels rise and coastal areas become increasingly populated, the need to expand man-made infrastructure becomes more pressing. Very large floating structures (VLFS) offer a means to extend infrastructure offshore in the form of floating runways, cities, and marine tourism facilities [9, 16, 17]. Furthermore, VLFS can be deployed in deep water as foundations for offshore renewable energy systems. Such structures can be designed to host multiple wind or tidal turbines on a single platform, thereby reducing the number of mooring lines required per turbine [5]. Hence, these platforms present a promising solution for supporting ocean space utilisation.

One of the main engineering challenges for VLFS is the large hydrodynamic loads resulting from their extensive platform areas. This challenge can be mitigated through deformable structures. In particular, modular hinged VLFS can alleviate structural loads by allowing relative motion around the hinge connections [3]. Several numerical and experimental studies have investigated the performance of hinged VLFS under various wave conditions.

Although progress has been made in understanding the motion and structural response of VLFS under irregular waves, their extreme response requires further investigation to enable deployment in realistic deep-water environments [22]. Studies of modular VLFS under irregular waves have shown that loads at the connectors can increase significantly compared to regular-wave conditions [8]. Such high loads can pose substantial structural challenges to the survivability of these platforms.

*Correspondence to: abel.arredondo-galeana@strath.ac.uk

A common limitation of previous VLFS studies is that most have focused on two approaches: namely, low-order numerical modelling or experimental testing. This limits the ability to fully assess extreme responses, particularly the influence of non-linear dynamics such as vortex shedding or green-water events. In this work, we present an initial framework that combines experimental observations, high-fidelity CFD, and the evaluation of low-order methods.

To this end, an experimental campaign was carried out that included regular and irregular waves in the COAST laboratory at the University of Plymouth, while a high-fidelity CFD model was implemented in OpenFOAM. Although flow fields and green-water effects are not the focus of this paper, the manuscript introduces a framework for future comparisons of non-linear phenomena in articulated VLFS using three complementary approaches.

The main innovations of this work are summarised as follows: 1) An experimental campaign for articulated VLFS under regular and irregular waves. 2) A tailored OpenFOAM CFD framework for modelling articulated VLFS. 3) An open-source potential-flow framework in SEA-Stack for articulated VLFS. 4) A discrete-module-beam (DMB) approach with hydroelastic considerations is used as a baseline model to benchmark the alternative modelling approaches.

The structure of the paper is as follows. First, the articulated VLFS prototype is presented, followed by the experimental and numerical setups. Then, the selected sea states are introduced. Subsequently, comparative results from experiments, potential-flow models, and CFD are presented to assess the performance of the different approaches for modelling VLFS. Discussions of loading response and extreme pitch-angle response are also provided. Finally, conclusions are presented.

2. Method

2.1. Experimental setup

A hinged VLFS was built as part of a previous regular sea-state test campaign carried out in [3]. An image of the platform in calm water is shown in Figure 1. The VLFS consists of three pontoons connected by either hinges or rigid bars to test different structural configurations. Each pontoon measures 580 $\times$ 580 mm $\times$ 52 mm and is constructed as a sandwich structure, with a PVC foam bottom layer and a 2 mm carbon-fibre top layer. Eight strain gauges (four per connector) were mounted between the connectors and the pontoons to measure forces at the connection points.

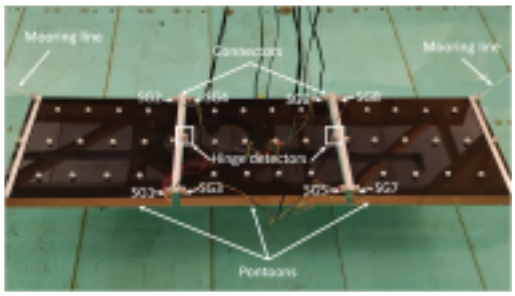


Figure 1: Experimental VLFS prototype built with three pontoons and two connectors. Strain gauges (SG1-SG8) are shown in the figure, with motion detection spheres on the platform.

The strain gauges are labelled SG1–SG4 and SG5–SG8, as shown in Figure 1, and were calibrated using weights in air to convert voltage measurements into force. Platform motion was tracked using a Qualisys system, with motion spheres mounted on both the pontoons and connectors, as illustrated in Figure 1.

The tests were conducted in the Ocean Basin at the COAST laboratory, University of Plymouth. The tank measures 35 m × 15.5 m, with an adjustable water depth of up to 3 m, which was used for this series of tests. The VLFS width results in a low blockage ratio, minimising wave reflection and improving data quality. Four soft mooring lines, attached to the corners of the platform, restrained its motion primarily to heave and pitch. For regular waves, a range of wave periods from $T = 6\,\mathrm{s}$ to $T = 20\,\mathrm{s}$ was tested at a wave amplitude of $A = 1\,\mathrm{mm}$. All results were normalised by wave height. For irregular waves, A JONSWAP wave energy spectrum was utilised in each run, following the ITTC recommended procedures [14]. Experimental motion amplitudes were measured directly and normalised by the significant wave height of the corresponding wave spectrum, defined as

$$H_s = 4\sigma, \tag{1}$$

where σ is the standard deviation of the wave-elevation time series.

2.2. CFD modelling

As part of the novelties of this work, a numerical CFD model was implemented in OpenFOAM for the articulated VLFS. A comparison between the experimental and numerical CFD prototypes is shown in Figure 2. The experimental prototype floating in water is shown in Figure 2a, while the numerical prototype is shown in Figure 2b. The dimensions of each pontoon of the platform are 58 m×58 m×5 m with a draft of 0.5 m.

The basis of the model is the open-source libraries provided by OpenFOAM v2212 (ESI-OpenCFD, 2022), and the interFoam solver [21], which solves the two-phase, incompressible, Reynolds-Averaged Navier-Stokes (RANS) equations

$$\frac{\partial(\rho\mathbf{u})}{\partial t} + \nabla\cdot(\rho\mathbf{u}\mathbf{u}) = -\nabla p + \nabla^2(\mu\mathbf{u}) + \rho\mathbf{g}, \tag{2}$$

$$\nabla\cdot\mathbf{u} = 0, \tag{3}$$

where p is the pressure, $\mathbf{u} = (u, v, w)$ is the fluid velocity, and $\mathbf{g}$ is acceleration due to gravity (Rusche, 2002). The fluid density, ρ, and dynamic viscosity, μ are determined using the volume of fluid (VOF) interface capturing scheme

$$\frac{\partial\alpha}{\partial t} + \nabla\cdot(\mathbf{u}\alpha) = 0, \tag{4}$$

$$\rho = \rho_w\alpha + \rho_a(1-\alpha), \tag{5}$$

$$\mu = \mu_w\alpha + \mu_a(1-\alpha), \tag{6}$$

where α is an indicator function representing the phase fraction of each mesh cell, and subscripts a and w represent air and water, respectively [21]. As discussed by Rusche (2002) [21], the interFoam solver uses an artificial compression term (C_α) when solving the transport equation for the volume fraction (equation 4), and this is set to $C_\alpha = 1$ in the present study. The Navier-Stokes equations (equations 2 and 3) are solved using a first order temporal scheme (Backwards Euler) and second order spatial schemes (Central Differencing and MUSCL). Pressure-velocity coupling is achieved via the Pressure Implicit with Splitting of Operators (PISO) algorithm [13] using 3 correctors. The k–ω SST turbulence closure model is used, which has been successfully demonstrated for other wave-driven flows [7].

The motion of the device is captured using OpenFOAM's 'rigidBodyDynamics' library, which uses a deforming mesh approach based on the spherical linear interpolation (SLERP) algorithm [23], and the Newmark method [18] to determine the instantaneous position of a rigid device. The rigidBodyDynamics library allows for a multibody structure to be modelled by applying an articulated body approach based on kinematics and forward-dynamics algorithms, to simulate a system of multiple interacting rigid bodies connected by joints [11]. In this work, a series of revolute and prismatic joints

are used to represent the hinged system, constraining the motion to rotation about the y-axis (pitch) and translation along the z-axis (vertical motion).

Wave generation and absorption is achieved via expression-based boundary conditions, which are supplied by the waves2Foam toolbox [15]. For the regular wave cases, stream function wave theory is used, with the coefficients determined by the method of Fenton [12]. For the irregular wave cases, linear superposition is utilised with 200 wave components, generated via a JONSWAP spectrum. For both cases, the generating-absorbing boundary condition (GABC) approach is utilised [6].

2.2.1. Regular Wave Setup

The simulations are set up such that the waves propagate in the positive x-direction. The y-axis is the transverse horizontal direction. The z-axis is the vertical direction, where upwards is positive, and the origin is set at the horizontal centre of the body at the still water level (SWL). To increase computational efficiency, a symmetry condition is utilised at the transverse centre of the device ($y = 0$).

The water depth is set as 100 m. A range of wave periods between 7.14 s and 12.5 s are considered, using a wave height of 4 m unless otherwise stated. The numerical domain is 460 m long ($-200 \leq x \leq 260$ m), 70 m wide ($0 \leq y \leq 70$ m) and 150 m high ($-100 \leq z \leq 50$ m). The discretisation in the free surface region ($-2 \leq z \leq 6$ m) is set to $\Delta z = 0.25$ m, which ensures that the wave is resolved within 1-2%, depending on wavelength [20]. Mesh grading is used in all dimensions to increase the computational efficiency, leading to a mesh size of approximately 18 million cells. A fixed timestep of 0.005 s is utilised.

The inlet and outlet boundaries specify GABC conditions for velocity and VOF. A symmetry plane is specified on the front of the domain. The bottom and back boundary are considered as solid walls and hence no-slip conditions have been applied along with zero gradient conditions for pressure and VOF. A zero-gradient condition is also applied on the top boundary for the VOF but the velocity boundary condition varies according to the near boundary flux; using a zero gradient condition for outflow and the internal cell value of the normal component to the patch face for the inflow. The top boundary is considered as an atmospheric condition, and hence for pressure a total pressure formulation is used:

$$p = p_0 + \frac{1}{2}|\mathbf{u}|^2, \tag{7}$$

where p_0 is the user defined reference value, and $\mathbf{u}$ is the velocity. For this case p_0 is set to zero since the solver uses the difference between total pressure and hydrostatic pressure. The structures are modelled as a rigid, moving wall with zero-gradient applied for the VOF and a consistent no-slip condition for the velocity and pressure. Wall functions are applied on the structures, back and bottom boundaries. Otherwise zero gradient is utilised for the turbulence model parameters, for outflow through boundaries, and a 1% turbulence intensity applied for inflow.

2.2.2. Irregular Wave Setup

The irregular wave cases are setup similar to the regular waves (Section 2.2.1.), with a few exceptions. The water depth is set to 70 m to more accurately represent the European Marine Energy Centre test site. The spectra is defined according to a peak wave period of 9 s and significant wave height 6.8 m, representing a 50-year return period wave obtained using the inverse first order method (IFORM) contour approach [24]. Given the longer simulation length, a 2D mesh is utilised to improve computational efficiency. The mesh is structured similar to that described for the regular waves, but the domain only contains one mesh cell in the y-direction. This leads to a mesh size of approximately 280,000 cells. A fixed time step of 0.001 s is utilised.

Potential flow modelling

Two potential flow solvers are analysed. The first one is the discrete-module-beam method developed in Zhang et al. [25], and applied for regular waves to rigid and hinged connected platforms in

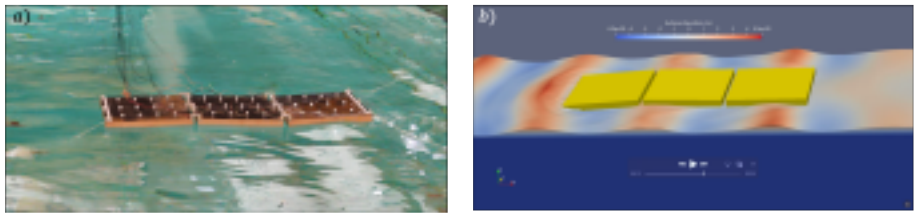


Figure 2: Side to side comparison of articulated VLFS in a) Experimental basin and b) Numerical setup in OpenFOAM.

Arredondo-Galeana et al. [3]. This method is based on frequency-domain linear hydrodynamics. The method accounts for hydro-elasticity by discretising the platform into a finite number of elements, which are then represented by lump masses connected to each other with elastic beams. Hinge kinematics are modelled assuming rigid connections between adjacent lump masses and hinges. A representative diagram of two pontoons connected with one hinge is depicted in Figure 3. For the case of Figure 3, two algebraic equations are solved as part of this method. Further details of the method are available in [5].

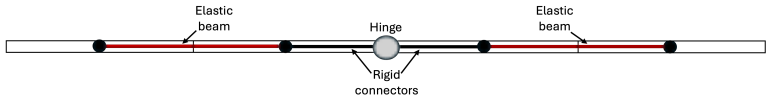


Figure 3: Schematic diagram of discrete-beam element to model elasticity and hinged connections.

The system of equations that is solved for a one-hinge two-pontoons system is

$$\begin{bmatrix} -\omega^2(\mathbf{M}+\mathbf{A}(\omega)) - i\omega\mathbf{B}(\omega) + \mathbf{C} + \mathbf{K}_S & \boldsymbol{\Xi}^T \\ \boldsymbol{\Xi} & \mathbf{0} \end{bmatrix} \begin{bmatrix} \boldsymbol{\zeta} \\ \mathbf{F}_J \end{bmatrix} = \begin{bmatrix} \mathbf{F}_E \\ \mathbf{0} \end{bmatrix}, \tag{8}$$

where $\mathbf{M}$ is the mass, $\mathbf{A}$ is the added, $\mathbf{B}$ is the radiation damping, $\mathbf{D_{pto}}$ is the PTO damping, $\mathbf{C}$ is the hydrostatic matrix, $\mathbf{K}$ is the stiffness matrix and $\mathbf{F_{wave}}$ is the wave excitation force. Note that for three pontoons, and two hinges, Equation (8) becomes a system of three algebraic equations.

The second potential flow solver used in this work is SEA-Stack, which is an open-source time-domain linear hydrodynamics solver, developed by the former National Renewable Energy Laboratory [19], to simulate wave energy converters. The motion of the platform is treated with a single algebraic equation. Solver Captayine 2.2 is used to compute the hydrodynamic coefficients. SEA-Stack uses a time-domain approach to compute the motion of the platform, but currently does not include structural stiffness effects. Further details of the method are available in [19].

2.3. Sea states

The sea states used in the irregular-wave experimental campaign were selected based on a site on the Atlantic Coast of France (47.84° N, 4.83° W). This location is relevant for offshore deployments due to its proximity to continental Europe and the availability of coastal infrastructure for assembling floating structures. Metocean data were obtained from the Homere database [1].

Wave scattered diagrams from the selected location are available in the literature [4], corresponding to 1-hour sea states over a 10-year period (2000–2010). The most probable sea state is selected as the design condition (sea state 1), while three additional less likely, but more severe sea states (sea states 2, 3 and 4) are selected as complementary cases. The corresponding wave periods, significant wave heights and probability of occurrences for the selected sea states are: sea state 1 (9 s, 1.2 m, 2%), sea state 2 (9

s, 4 m, 0.2%), sea state 3 (13.3 s, 6 m, 0.1%), and sea state 4 (15.6 s, 2 m, 0.1%). All sea states assume a wave incidence of 0°. Notably, the most severe conditions correspond to sea state 3, with a significant wave height of 6 m. Following the CFD irregular sea state considerations, a value of $H_s = 6.8$ m with a probability of occurrence of 0.1% is adopted as the worst-case scenario to assess hinge deflections in the final section.

The RAOs of the platform are used to obtain the response spectra in irregular sea states. Two types of motion are considered. Firstly, the vertical motion of different points along the platform, and secondly, the relative hinge rotation, computed from the difference in pitch angles between adjacent pontoons to the hinge. The regular wave RAOs are defined as the ratio between the response amplitude and the incident wave amplitude. The response spectrum $S_r(\omega)$, for either vertical motion or hinge rotation, is obtained by relating the regular wave RAOs of the system to the wave energy spectrum $S(\omega)$, such that

$$S_r(\omega) = |\mathrm{RAO}|^2 S(\omega), \tag{9}$$

where $S(\omega)$ is the JONSWAP spectrum. Note that for very large or flexible floating platforms, the vertical motion RAO varies with position along the structure (x/l), while the hinge rotation RAO is also hinge position dependent. The significant motion response is defined as

$$\Delta z_s = 4\sqrt{m_0}, \tag{10}$$

with m_0 the zero-th spectral moment of $S_r(\omega)$. All results are normalised by the significant wave height H_s to allow direct comparison between different sea states. The JONSWAP spectrum follows the definition in the DNV Environmental Conditions and Environmental Loads Practice Manual [10].

3. Results

3.1. Regular waves

The vertical motion (Δz) and relative pitch angle ($\Delta\theta$) RAOs of the upstream and downstream hinges under regular sea states are shown in Figure 4a and Figure 4b, respectively. Red and black curves denote the upstream and downstream hinges. The RAO curves computed with the discrete-module beam (DMB) potential flow model [3] are shown as solid lines. The hydrodynamic coefficients used to solve Eq. 8 are identical to those in [5]. Numerical results are interpolated using spline curves in both figures.

Experimental vertical motion measurements are shown in Figure 4a with cross markers and error bars. Unlike previous campaigns [3], vertical displacement was also measured at the hinge locations (see Figure 1). Relative pitch angles were derived from the vertical motion of adjacent pontoons, and are shown in Figure 4b with error bars.

CFD results for vertical motion and relative pitch angle are shown with filled markers in Figures 4a and 4b. The CFD model over predicts peak vertical response for both hinges but performs better for $T < 8\,\mathrm{s}$ and $T > 12\,\mathrm{s}$. For relative pitch, over prediction is approximately $0.8^\circ/\mathrm{m}$ (upstream) and $0.5^\circ/\mathrm{m}$ (downstream). These discrepancies may be due to rigid-body assumptions in the CFD model and damping effects in the physical prototype.

For clarity, results from SEA-Stack are shown only for the upstream hinge in both Figures 4a and 4b. A satisfactory agreement with the DMB model is observed for $T < 8\,\mathrm{s}$ and $T > 12\,\mathrm{s}$, while responses are over predicted in the intermediate range ($8\,\mathrm{s} \leq T \leq 12\,\mathrm{s}$), likely due to the absence of structural stiffness modelling.

Figure 4 confirms that upstream hinge response is higher than downstream response. CFD captures overall trends but deviates in magnitude, while the DMB model provides the closest agreement overall. SEA-Stack performs less well in the intermediate period range, likely due to missing elastic effects.

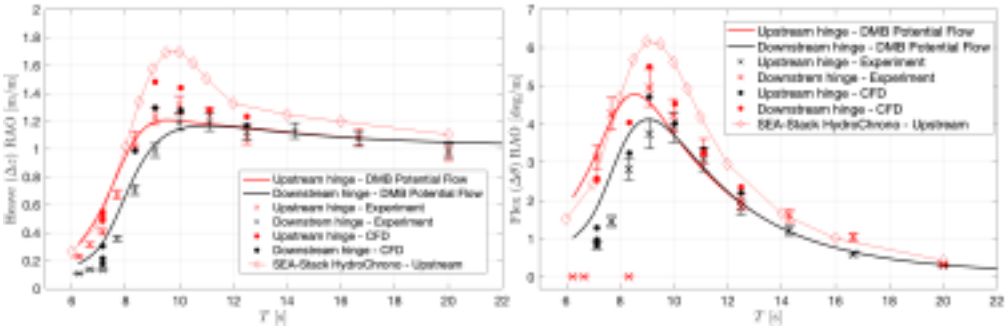


Figure 4: RAO of a) vertical motion and b) relative pitch angle for upstream ($x/l = 0.33$) and downstream ($x/l = 0.66$) hinge. Results from potential flow model, experiment and CFD are compared.

3.2. Irregular waves

In this section, we present results for sea state 1 ($T_p = 9\,\text{s}$) and sea state 3 ($T_p = 13.3\,\text{s}$), since sea state 2 ($T_p = 9\,\text{s}$) and sea state 4 ($T_p = 15.6\,\text{s}$) exhibit similar vertical motion patterns after normalisation by significant wave height. Figures 5a and 5b show the vertical motion response (Δz_s) for sea state 1, while Figures 5c and 5d show the corresponding results for sea state 3. The responses are evaluated at different positions along the platform (x/l) for both rigid (left column) and hinged (right column) configurations. Experimental measurements are shown in magenta, while numerical predictions are indicated by black markers. Only the potential flow DMB method is used in these comparisons.

In sea state 1 (top row, $T_p = 9s$), both Figures 5a and 5b show an asymmetric motion pattern, with the maximum displacement occurring at $x/l = 1$ (upstream) and the minimum at $x/l = 0$. The rigid configuration (Figure 5a) shows a maximum displacement that is approximately 20–40% lower than that of the hinged configuration (Figure 5b). The influence of the hinges is evident in Figure 5b, where two local peaks appear at $x/l = 0.33$ and $x/l = 0.66$, whereas no distinct midspan peaks are observed in the rigid case. Both figures also show that the experimental and numerical irregular wave responses follow trends consistent with those observed in regular wave analysis [2].

Figures 5c and 5d show the results for sea state 3 ($T_p \geq 12s$). The rigid configuration (Figure 5c) shows maximum displacement at the free ends of the platform ($x/l = 0$ and $x/l = 1$) and a minimum at midspan ($x/l = 0.5$). In contrast, the hinged configuration (Figure 5d) shows additional high response peaks at $x/l = 0.33$ and $x/l = 0.66$, corresponding to the hinge locations. Overall, the irregular wave

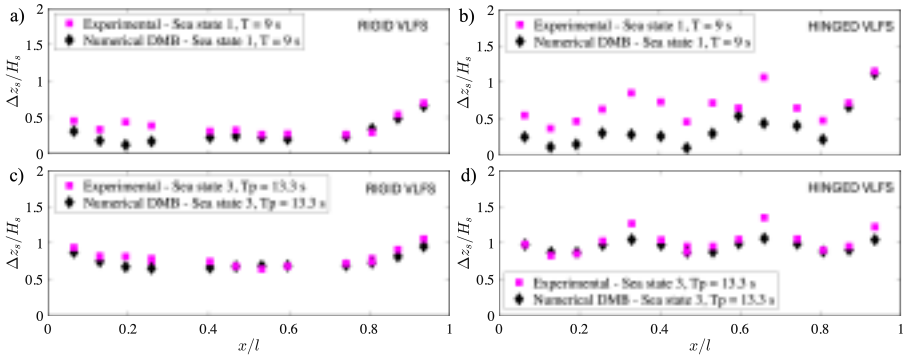


Figure 5: Experimental and numerical vertical point motion along the x-axis for irregular sea states for a rigid platform (a, c) and a hinged platform (b, d), at $T_p = 9, \text{s}$ (top row) and $T_p = 12\,\text{s}$ (bottom row).

results follow spatial trends consistent with those observed under regular wave conditions for both configurations.

3.3. Load alleviation

The load alleviation capabilities of the articulated VLFS are assessed in this section for the four tested sea states 1, 2, 3 and 4, ($H_s = 1\,\mathrm{m}, H_s = 4\,\mathrm{m}, H_s = 6\,\mathrm{m}, \mathrm{and}, H_s = 2\,\mathrm{m}$), at two wave directions, 0° and 90°. Results are presented in terms of the calibrated strain gauge response measured at gauge 1 (SG1 in Figure 1), which is taken as an indicator of the global structural response. The joint configuration is compared between rigid and hinged cases. Figure 6a shows the mean strain measured at SG1 for a wave incidence of 0°, for the rigid and hinged configurations of the VLFS, shown in black and grey respectively. Figure 6b presents the same results for a wave incidence of 90°.

Figure 6a shows that the rigid configuration (black bars) exhibits an overall increase in loading with significant wave height, with the highest response observed in sea state 3 ($H_s = 6\,\mathrm{m}$). In contrast, the hinged configuration (grey bars) reduces structural loading and results in comparatively uniform response levels across all sea states. For a wave heading of 90°, Figure 6b shows similar response levels for both configurations, as the hinges provide limited contribution to longitudinal bending in this orientation and the system behaves in a near rigid manner in the measured response direction.

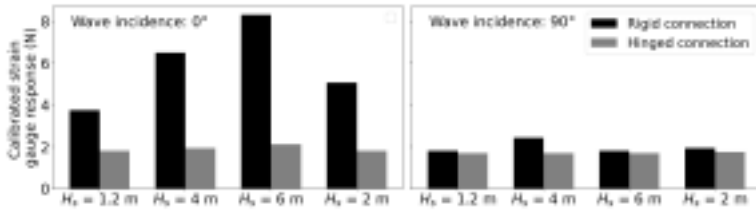


Figure 6: Calibrated strain gauge response (SG1) for rigid and hinged connected VLFS at significant wave heights $H_s = 1.2,\ 4,\ 6\,\mathrm{and}\,2\,\mathrm{m}$ at a) 0° and b) 90° wave incidences.

3.4. Hinge angle responses

The measured relative pitch-angle response of the VLFS is plotted in Figure 7a for all tested sea states ($H_s = 1.2\,\mathrm{m}$, $H_s = 2\,\mathrm{m}$, $H_s = 4\,\mathrm{m}$, and $H_s = 6\,\mathrm{m}$). The time series are shown in blue, green, red, and black for increasing H_s. Maximum hinge angles of approximately $12.5°$ are observed at $H_s = 6\,\mathrm{m}$, while the lowest response occurs at $H_s = 1.2\,\mathrm{m}$.

The worst case CFD scenario was $H_s = 6.8\,\mathrm{m}$, corresponding to the 50-year return period from the European Marine Energy Center (EMEC). Relative pitch angles at hinge 1 (upstream) and hinge

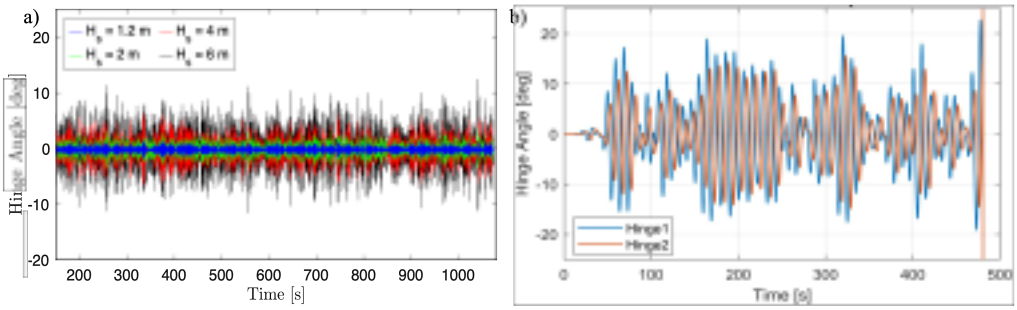


Figure 7: a) Upstream hinge relative pitch angle, experimental measurements for four sea states; b) numerical CFD simulations for the upstream (hinge 1) and downstream (hinge 2) hinges at $H_s = 6.8\,\mathrm{m}$.

2 (downstream) are shown in Figure 7b. The CFD model predicts maximum hinge angles of approximately 22° at hinge 1 and is likely to over predict the response due to the two dimensional simulation approach for irregular waves.

Both experimental and CFD results indicate that $H_s \geq 6, \mathrm{m}$ leads to significantly increased hinge rotations. Overtopping, aeration, and elevated turbulent kinetic energy are observed on the upstream side, where hinge 1 exhibits the largest motion. These effects are not fully captured by potential-flow models, highlighting the need for higher-order numerical approaches and experimental validation.

4. Conclusions

This study analyses the response of an articulated VLFS under irregular sea states using experimental testing, potential-flow solvers, and CFD. A dedicated experimental campaign at the COAST laboratory, University of Plymouth, was conducted to provide validation data under irregular wave conditions. Both rigid and hinged configurations were tested to assess differences in global structural response. The numerical methods considered include: (1) a discrete-module beam method (DMB) [2, 5], (2) the open-source potential-flow solver SEA-Stack [19], and (3) a CFD framework implemented in OpenFOAM.

The numerical models show differing levels of accuracy. The DMB method provides reliable predictions for hydroelastic interconnected VLFS, likely due to the inclusion of structural stiffness effects. SEA-Stack shows good agreement for shorter ($T < 8\,\mathrm{s}$) and longer ($T > 12\,\mathrm{s}$) wave periods, while over predicting peak platform response. These discrepancies are likely associated with the absence of structural stiffness effects. The CFD model over predicts maximum hinge angles by approximately $0.8°$ (upstream) and $0.5°$ (downstream), but captures non linear flow phenomena such as vorticity generation and green-water effects, which are not represented in potential-flow formulations.

Overall, the articulated platform exhibits response trends under irregular waves consistent with previous regular wave studies, with wave loading increasing with significant wave height and being mitigated by hinge flexibility. Experimentally, maximum hinge rotations of approximately $12.5°$ were observed at $H_s = 6\,\mathrm{m}$, while CFD predicted peak values of approximately 22° at $H_s = 6.8\,\mathrm{m}$.

This study provides a basis for further development of numerical tools for VLFS loading analysis, particularly for models that do not include structural stiffness effects.

Acknowledgments

This work was funded by the UK Engineering and Physical Sciences Research Council (EPSRC) under Supergen ORE Impact Hub 2023 Programme Grant EP/Y016297/1, and by the Early Career Research Grant "ECRRF2023 – (Call 6) – 11" awarded to Dr Abel Arredondo-Galeana and Dr Scott Brown. The first author thanks Dr Shaushai Dai, Director of the Kelvin Hydrodynamics Laboratory, for coordinating and supervising the experimental campaign, and PhD student Guangwei Zhao for executing the experiments. Gratitude is also extended to Yongqiang Chen (Shanghai Jiao Tong University) for providing hydrodynamic coefficients used in the discrete-module-beam method.

References

[1] M. Accensi and C. Maisondieu. Homere. ifremer - laboratoire comportement des structures en mer. 2015.

[2] A. Arredondo-Galeana, Y. Chen, S. Dai, X. Zhang, and F. Brennan. Experimental motion and load comparison of rigidly and hinged connected very large floating platforms. *Journal of Ocean Engineering and Science*, 11(1):222–237, 2026.

[3] A. Arredondo-Galeana, S. Dai, Y. Chen, X. Zhang, and F. Brennan. Understanding the force motion trade off of rigid and hinged floating platforms for marine renewables. *Proceedings of the European Wave and Tidal Energy Conference*, 15, Sep. 2023.

[4] A. Arredondo-Galeana, G. Olbert, W. Shi, and F. Brennan. Near wake hydrodynamics and structural design of a single foil cycloidal rotor in regular waves. *Renewable Energy*, 206:1020–1035, 2023.

[5] A. Arredondo-Galeana, G. T. Scarlett, M. Collu, and F. Brennan. A hybrid floating wind-wave energy platform for minimum power baseload. *Ocean Engineering*, 343:123090, 2026.

[6] M. Borsboom and N. G. Jacobsen. A generating-absorbing boundary condition for dispersive waves. *International Journal for Numerical Methods in Fluids*, 93(8):2443–2467, 2021.

[7] S. Brown, D. Greaves, V. Magar, and D. Conley. Evaluation of turbulence closure models under spilling and plunging breakers in the surf zone. *Coastal Engineering*, 114:177–193, 2016.

[8] J. Ding, Y. Geng, S. Xu, W. Yang, and Z. Xie. Experimental study on responses of an 8-module vlfs considering different encounter wave conditions. *Marine Structures*, 78:102959, 2021.

[9] J. Ding, Y. Wu, Z. Xie, W. Yang, S. Wang, J. Yu, and T. Yu. Overview: Research on hydroelastic responses of vlfs in complex environments. *Marine Structures*, 78:102978, 2021.

[10] DNV. *Recommended Practice DNV-RP-C205. Environmental conditions and environmental loads*. Det Norske Veritas, Høvik, Norway, 2007.

[11] R. Featherstone. Dynamics of rigid body systems. In *Rigid body dynamics algorithms*, pages 39–64. Springer, 2008.

[12] J. Fenton. The numerical solution of steady water wave problems. *Computer & Geosciences*, 14:357–368, 1988.

[13] R. I. Issa. Solution of the implicitly discretised fluid flow equations by operator-splitting. *J. Comput. Phys.*, 62:40–65, 1986.

[14] ITTC. Laboratory modelling of waves: Regular, irregular and extreme events. Technical Report 7.5-02-07-01.2, International Towing Tank Conference (ITTC), 2017.

[15] N. G. Jacobsen, D. R. Fuhrman, and J. Fredsøe. A wave generation toolbox for the open-source cfd library: Openfoam®. *International Journal for numerical methods in fluids*, 70(9):1073–1088, 2012.

[16] M. Lamas-Pardo, G. Iglesias, and L. Carral. A review of very large floating structures (vlfs) for coastal and offshore uses. *Ocean Engineering*, 109:677–690, 2015.

[17] B. Neumann, A. T. Vafeidis, J. Zimmermann, and R. J. Nicholls. Future coastal population growth and exposure to sea-level rise and coastal flooding - a global assessment. *PLOS ONE*, 10(3):1–34, 03 2015.

[18] N. M. Newmark. A method of computation for structural dynamics. *Journal of the engineering mechanics division*, 85(3):67–94, 1959.

[19] D. Ogden, Z. Quinton, T. de Lataillade, and M. Pallud. Hydrochrono: An open-source hydrodynamics package for project chrono. 2023. 15TH EUROPEAN WAVE AND TIDAL ENERGY CONFERENCE ; Conference date: 03-09-2023 Through 07-09-2023.

[20] E. Ransley. *Survivability of Wave Energy Converter and Mooring Coupled System using CFD*. PhD thesis, University of Plymouth, 2015.

[21] H. Rusche. *Computational fluid dynamics of dispersed two-phase flows at high phase fractions*. PhD thesis, Imperial College of Science, Technology and Medicine, 2002.

[22] H. Santo, P. Taylor, and P. Stansby. The performance of the three-float m4 wave energy converter off albany, on the south coast of western australia, compared to orkney (emec) in the u.k. *Renewable Energy*, 146:444–459, 2020.

[23] K. Shoemake. Animating rotation with quaternion curves. In *Proceedings of the 12th annual conference on Computer graphics and interactive techniques*, pages 245–254, 1985.

[24] S. R. Winterstein, T. C. Ude, C. A. Cornell, P. Bjerager, and S. Haver. Environmental parameters for extreme response: Inverse form with omission factors. *Proceedings of the ICOSSAR-93, Innsbruck, Austria*, pages 551–557, 1993.

[25] X. Zhang, D. Lu, Y. Gao, and L. Chen. A time domain discrete-module-beam-bending-based hydroelasticity method for the transient response of very large floating structures under unsteady external loads. *Ocean Engineering*, 164:332–349, 2018.

10th International Conference on HYDROELASTICITY IN MARINE TECHNOLOGY
Trondheim, Norway, June16th-18th, 2026

Numerical Analysis of a Barge's Torsional Hydroelastic Response

Pascoaleto, V.[1,*] Lopes, F.S[1], and Fernandes, A.C.[2]

[1] Poli/UFRJ, Rio de Janeiro, Brazil (pascoaleto.v.20222@poli.ufrj.br)
[2] COPPE/UFRJ, Rio de Janeiro, Brazil (filipe_salvador@oceanica.ufrj.br)
[3] COPPE/UFRJ, Rio de Janeiro, Brazil (acfernandes@oceanica.ufrj.br)

Abstract. With the great development of structural and hydrodynamic designs of offshore units, hydroelastic studies have shown great relevance to the modern engineering scenario. The elastic behavior of floating bodies due to environmental loads can be a concern to the operation, as damage due to fatigue can be accumulated throughout the years, resulting in the reduction of the structure's lifetime. Although typically associated with containerships due to the absence of the main deck, the torsional response can be relevant in large floating bodies, such as cargo ships and FPSOs. The focus of this works is on the development of numerical procedures capable of accurately reproducing the torsional response of floating bodies under wave excitation. To do so, a barge will be used in simulations. Data on the chosen barge is available in the literature, including experimental results, which allows it to be used as a benchmark to validate the numerical simulations conducted. The good agreement between the numerical results and the benchmark data indicates that the modelling of the problem was adequately performed. This study represents a first step towards the development of a consolidated methodology to replicate the torsional response of floating bodies, which in the future will include experiments with different approaches to build hydroelastic models in reduced scale.

Key words: *Hydroelasticity; Torsion; Numerical Simulation;Horizontal Bending*

1.. Introduction

The rigid body hypothesis is widely used in the early design stages of ships and offshore structures. However, it is well established that such structures exhibit elastic responses due to hydrostatic and hydrodynamic loads, which can be coupled with the rigid body degrees of freedom [1]. In the field of structural engineering, the next natural step is to treat the vessel as a deformable elastic body—an interaction known as hydroelasticity. This behavior is highly significant when determining the fatigue life and the extreme loads to which the structure can be subjected.

While many studies prioritize the vertical bending vibration response of a floating body due to its prevalence and substantial magnitude [2], open-deck structures, such as containerships, present unique challenges. For these vessels, torsional response is a primary design concern and must be carefully considered in both simulations and model tests [3]. This concern arises because the offset between the shear center and the center of gravity causes the structure to amplify the behavior, creating a strong coupling between horizontal bending and torsion.

To capture these complex effects, reduced-scale model tests are often performed to validate numerical simulations representing the hydroelastic behavior of the floating body. Typically, the model is built

*Correspondence to: pascoaleto.v.20222@poli.ufrj.br

in different segments connected by a backbone responsible for providing the required stiffness [4]. Alternatively, the model can be built using flexible materials, where the hull itself provides the required stiffness for different vibration modes [5]. Achieving the proper torsional response in these tests can be done in various ways, such as using elastic materials or alternatively shaped backbones [6].

The present study investigates the coupled horizontal bending and torsional response of a barge, reinforcing that these complex effects are predominantly excited by bow quartering waves. The barge considered in this research has been the focus of previous studies found in the literature, which include numerical simulations using different software [8] and model tests [9]. The goal of this work is to utilize an alternative set of well-known industry software tools to replicate this coupled response of the barge.

This serves as the first step in consolidating a robust, replicable methodology to assess the hydroelastic behavior of floating bodies, which will be complemented by model tests in the future. Furthermore, it invites the community to engage with the field of hydroelasticity by using this work as a starting point. To achieve this, the proposed method divides the problem into three separate stages: geometric modeling using Rhinoceros [16], a dry mode analysis utilizing Inventor Nastran [15] to obtain the dry natural frequencies and structural stiffness, and a hydrodynamic analysis conducted in WAMIT [7].

2.. Theoretical Background

Hydroelasticity may be studied in several degrees of accuracy and complexity, the most used model envolves separating the structural and hydrodynamic analysis apart for better visualization and understanding of the problem.

2.1. Dry modes

Natural dry modes are obtained by solving the undamped eigenvalue problem:

$$(\mathbf{K} - \omega^2 \mathbf{M})\mathbf{\Phi} = \mathbf{0} \tag{1}$$

where $\mathbf{K}$ is the global stiffness matrix, $\mathbf{M}$ is the global mass matrix, ω represents the natural circular dry frequencies, and $\mathbf{\Phi}$ denotes the corresponding mode shape vectors. For an Euler-Bernoulli beam approximation with constant properties, such as mass per unit length m', bending stiffness EI, and torsional stiffness GI_t, the analytical expressions for the modal mass and modal stiffness terms are given by the Rayleigh method [10]. For bending modes, the modal mass and stiffness terms are given by:

$$m_{bending} = \int_0^L m'[\phi]^2 dx \tag{2}$$

$$k_{bending} = \int_0^L EI \left[\frac{\partial^2 \phi}{\partial x^2}\right]^2 dx \tag{3}$$

where I is the second moment of area, L is the length of the beam, E is the Young's modulus, and ϕ is the transverse displacement part of the mode. On the other hand, the torsional modal mass and stiffness terms can be obtained through:

$$m_{torsion} = \int_0^L J'[\mathbf{\Psi}]^2 dx \tag{4}$$

$$k_{torsion} = \int_0^L GI_t \left[\frac{\partial \Psi}{\partial x}\right]^2 dx \tag{5}$$

where G is the shear modulus, J' is the polar mass moment of inertia per unit length, I_t is the torsional constant, and Ψ is the angular displacement part of the mode. While this analytical theory provides valuable insight into the physical dependencies of the mass and stiffness terms, numerical approaches are required for calculations that exceed the accuracy of this approximation. This is especially true because the beam's elastic axis often does not coincide with its center of mass. Therefore, the modal mass m and modal stiffness k must be calculated using the Finite Element Method (FEM):

$$m = [\delta]^{\mathbf{T}}\mathbf{M}[\delta] \tag{6}$$

$$k = [\delta]^{\mathbf{T}}\mathbf{K}[\delta] \tag{7}$$

where $[\delta]$ represents the discrete mode shape matrix. Since stress recovery will not be the primary focus of this study, it is possible to apply a nonlinear curve fitting to the discrete mode shapes $[\delta]$ in the form of:

$$\delta = \delta(\bar{x}) \tag{8}$$

where $\bar{x}$ is the normalized position along the beam, yielding approximate analytical equations for the mode shapes.

2.2. Wet surface

As the solution of the hydroelasticity problem follows the panel method together with potential wave theory, the creation of a faithful three-dimensional model is required in order to ensure sufficient accuracy in the simulation of the fluid–structure interaction. The transition from the FEM structural domain to the fluid domain relies on the structural properties to properly incorporate the displacement field, as described in Saint-Venant torsion theory [11].

$$\mathbf{h_{tor}} = \psi\mathbf{i} \times \mathbf{r} \tag{9}$$

where $\mathbf{h}$ is the wet surface displacement vector, ψ is the twist angle in the x axis and $\mathbf{r}$ is the position vector from the torsion center to the interested pannel centroid. As the initial barge building is made to strenghten the coupling between the horizontal bending and torsion the equation turns to:

$$\mathbf{h_{coupled}} = \mathbf{h_{hor}} + \psi\mathbf{i} \times \mathbf{r} \tag{10}$$

Where $\mathbf{h}_{\text{hor}}$ denotes the horizontal vibration mode displacement. Although the non-circular cross-section induces a warping effect, this phenomenon will not be considered in the present study and the displacement can therefore be expressed as:

$$\mathbf{h_{hor}} = v\mathbf{j} - \frac{dv}{dx}y\mathbf{i} \tag{11}$$

Where v is the $\mathbf{j}$ component of the displacement vector and $\frac{dv}{dx}$ is the slope of the horizontal displacement along the beam.

2.3. Hydrodynamics

To properly account for the wet-surface deformation induced by fluid excitation, the total displacement of the wetted boundary can be expressed as a modal superposition of the prescribed structural modes. This implies that the displacement of each panel is represented as a finite series of modal contributions, computed as:

$$\mathbf{H} = \sum_{i=1}^{N} \xi_i \mathbf{h_i} \tag{12}$$

Where ξ_i is the modal amplitude of the excitation and $\mathbf{H}$ is the total deflection of the wet surface.

The solution of the problem is formulated in terms of the velocity potential in the fluid domain, which neglects fluid viscosity and assumes the flow to be irrotational and incompressible [12].

$$\nabla\varphi = \mathbf{u} \tag{13}$$

$$\nabla \times \mathbf{u} = \nabla \cdot \mathbf{u} = 0 \tag{14}$$

Where $\mathbf{u}$ is the fluid velocity vector. The potential wave theory is used to model the hydrodynamics influences in the wet surface. Dividing apart the incident wave potential from diffraction and radiation wave potential parts to apply the modal superposition and determine hydrodynamics coefficients [13].

$$\varphi = \varphi_I + \varphi_D - i\omega_w \sum_k^N \xi_k \varphi_{R_k} \tag{15}$$

Where φ_D is the diffraction wave potential, ω ω_w is the wave frequency and φ_I is the incident wave potential and can be put as:

$$\varphi_I = i\frac{g\zeta}{\omega_w} e^{K(z+ix)} \tag{16}$$

Where ζ is the wave amplitude, g is the gravitational acceleration and K is the wave number. In the case of no forward speed, the boundary conditions for the problem may be putted as:

$$\Delta\varphi = 0 \tag{17}$$

$$-K\varphi + \frac{\partial\varphi}{\partial z} = 0 \tag{18}$$

$$\frac{\partial\varphi}{\partial n} = -i\omega_w(\mathbf{H}\cdot\mathbf{n}) \tag{19}$$

$$\frac{\partial\varphi_D}{\partial n} = -\frac{\partial\varphi_I}{\partial n} = \frac{\partial\varphi_{R_k}}{\partial n} = \mathbf{h_k}\cdot\mathbf{n} \tag{20}$$

Where $\mathbf{n}$ is the surface pannel normal vector.

Once the fluid potential has been determined, the linearized Bernoulli equation can be applied to accurately evaluate the dynamic pressure acting on the wetted surface.

$$p = i\omega_w\varphi + \rho g z \tag{21}$$

By integration over the surface the acting hydrodynamic forces $\mathbf{F_i^H}$ may be obtained:

Furthermore, the hydrodynamic force can be separated according to the potential fraction considered, which brings to:

$$\mathbf{F_i^H} = \mathbf{F_i^{DI}} + \mathbf{F_i^R} \tag{22}$$

$$\mathbf{F_i^{DI}} = i\omega\rho\int_S(\varphi_I + \varphi_D)\mathbf{h_i}\cdot\mathbf{dS} \tag{23}$$

$$\mathbf{F_i^R} = \omega^2\rho\sum_{K=1}^N \xi_K\int_S \varphi_R\mathbf{h_i}\cdot\mathbf{dS} \tag{24}$$

Where $\mathbf{F^{DI}}$ is the diffraction wave potential fraction and represents the modal excitation force [8] while $\mathbf{F^R}$ is the incident wave potential fraction. Noting that both forces are to be complex quantities, each

part (Re and Im) may represent a different contribution for both acceleration and velocity in the motion equation as:

$$F_i^a = \text{Re}(F_i^R) = \omega^2 \sum_k^N \xi_k A_{ik} \tag{25}$$

$$A_{ik} = \rho \text{Re} \int_S \varphi_{R_k} \mathbf{h_i} \cdot \mathbf{dS} \tag{26}$$

$$F_i^v = \text{Im}(F_i^R) = i\omega \sum_k^N \xi_k B_{ik} \tag{27}$$

$$B_{ik} = \rho\omega \text{Im} \int_S \varphi_{R_k} \mathbf{h_i} \cdot \mathbf{dS} \tag{28}$$

Where F_i^a is the acceleration force and F_i^v is the velocity force, A_{ik} and B_{ik} are the elements of added mass and damping matrixes coefficients.

2.4. Hydrostatics

It is assumed that the structural deformation is sufficiently small so as not to modify the body's wetted surface [14]. The restoring coefficient depends on the hydrostatic pressure distribution over the surface, together with the gravitational contribution c^m associated with the action of the gravitational field on the body. The hydrostatic component is further decomposed into a superposition of the pressure-variation term over the surface, c^p, and the contribution arising from the variation of the normal vector combined with the normal mode shape, c^{hn}

$$c_{ik}^p = \rho g \int_S h_z^k \mathbf{h_i} \cdot \mathbf{dS} \tag{29}$$

$$c_{ik}^{hn} = \rho g \int_S \nabla h^k \mathbf{h_i} \cdot \mathbf{dS} \tag{30}$$

$$c_{ik}^m = g \int_V \rho_S \nabla h_z^k \mathbf{h_i} \cdot \mathbf{dS} \tag{31}$$

Where V is the body's volume, ρ_S is its density and h_z is the vertical component of the displacement vector $\mathbf{h}$. Thus the total hydrostatic contribuition may be written as:

$$\mathbf{F_i^{HI}} = \sum_{K=1}^N c_{ik} \xi_k \tag{32}$$

2.5. Hydroelasticity

Hydroelasticity modeling is based on joining the structural parts obtained in subsections 2.1. and 2.2. and put it in a fluid environment, the equations presented in to obtain an elastic body analysis. In Figures 1 and 2 is possible to see how the structure behaves on each vibration mode.

The motion equation to be solved includes all previous discussions respective contributions as

$$\{[\mathbf{K}] - \omega^2[\mathbf{M}]\}\xi = \mathbf{F} \tag{33}$$

Where $\mathbf{F}$ is the total fluid force.

$$\mathbf{F} = \mathbf{F^a} + \mathbf{F^v} + \mathbf{F^{DI}} + \mathbf{F^{HI}} \tag{34}$$

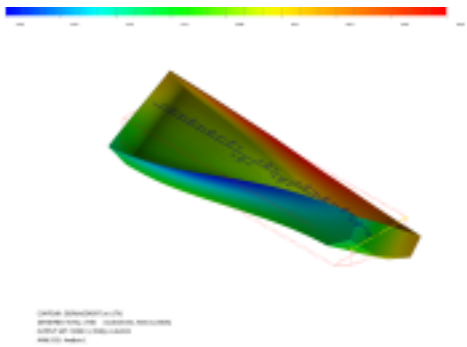


Figure 1: Torsional Vibration of the Barge

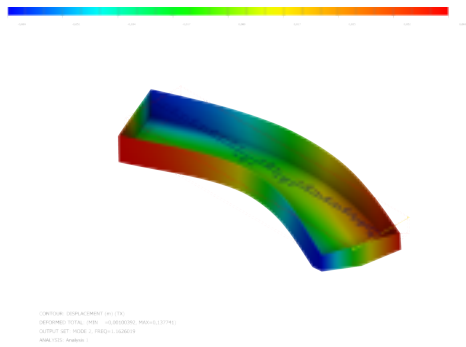


Figure 2: Horizontal Vibration of the Barge

Separating the terms into all $\{\xi\}$ dependancy, the governing matrix for floating structures motion is obtained as:

$$\{[\mathbf{K}] + [\mathbf{C}] - i\omega[\mathbf{B}] - \omega^2([\mathbf{M}] + [\mathbf{A}])\}\xi = \mathbf{F} \tag{35}$$

In this problem, the structural damping matrix is not included due to the reduced complexity of the structural model. However, additional damping mechanisms may be introduced artificially in order to account for viscosity-related effects.

The solution of Eq. 35 gives the modal amplitudes $\{\xi\}$ which can be used to solve the eigenvalue problem and obtain the wet natural modes in Eq. 36

$$\{[\mathbf{K}] + [\mathbf{C}] - \omega^{\mathbf{2}}([\mathbf{m}] + [\mathbf{A}])\}\{\xi\} = \mathbf{0} \tag{36}$$

As the added mass depends on the natural wet frequency, an iteractive procedure may be used to correctly obtain ω.

3.. Modeling

To correctly apply the methodology described in 2.3. the problem was split into three different environments, structural, geometric and hydrodynamic. Each part was modeled separately and then combined together to obtain the final solution.

3.1. FEM modeling

The finite element approach englobes an 1D construction of the structural properties. For this purpose, it was used a Nastran [15] environment to perform the calculations. The modeled beam receives properties shown in Table 1.:

To simulate the pontoons described in [8], the well-known CONM2 (Concentrated Mass) element was employed to define the center of gravity, total mass, and mass moments of inertia. As expected, this element does not contribute any structural stiffness to the model. In addition, the NSM (Non-Structural Mass) element was used to represent the remaining non-structural mass, such as sensing devices and calibration equipment. The parameters adopted for these external masses are presented in Table 2.

3.2. Hydrodynamic Modeling and Meshing

Hydrodynamic and hydrostatic aspects were considered to adequate mass and structural stiffness, Table 3 below summarizes the main parameters considered in the model.

Table 1: Beam properties.

Name	Unit	Value
Cross-section ($a \times a$)	mm	10×10
A	m^2	1.0×10^{-4}
$I_y = I_z$	m^4	8.333×10^{-10}
I_t	m^4	1.667×10^{-9}
E	Pa	2.1×10^{11}
G	Pa	0.808×10^{11}
L	m	2.445
ρ_s	kg/m^3	8027

Table 2: External mass parameters.

Name	Unit	Value
CONM2 A Mass	kg	11×13.7
CONM2 A r_{roll}	m	0.225
CONM2 A Vertical offset	mm	144
CONM2 B Mass	kg	10
CONM2 B r_{roll}	m	0.213
CONM2 B Vertical offset	mm	220
NSM	kg/m	6.17

Table 3: Rigid body properties.

Name	Unit	Value
L	m	2.445
B	mm	600
T	mm	120
KG	mm	163
M	kg	177.77
r_{roll}	mm	225
$r_{pitch} = r_{yaw}$	mm	611.25

More details can be found in [8] and [9]. To estimate the radii of inertia used in this study, the guidelines approved by the International Towing Tank Conference (ITTC) [17] are adopted as $0.375B$, where B is the beam width of the body.

The solution adopts a BEM formulation; therefore, the CAD software Rhinoceros 3D[16] is employed to construct the geometry and generate a sufficiently refined mesh, ensuring that numerical truncation errors are minimized.

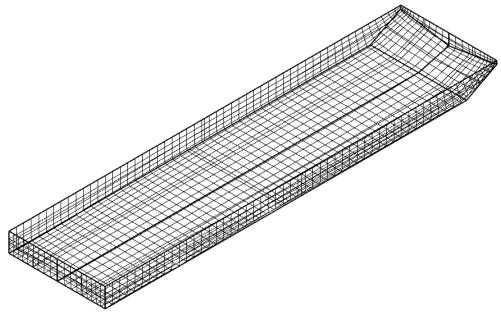


Figure 3: Meshing configuration

4.. Results

The results are presented in two distinct parts, obtaining the structural conditioning of the vibration modes and subsequently applying it to the hydroelastic analysis.

4.1. FEM analysis

The obtained dry natural frequencies, modal mass and stiffness are shown in Table 4; the modal shape $[\delta]$ is normalized to a maximum amplitude of 1.0.

Table 4: Natural dry frequencies, modal mass and stiffness.

Name	Horizontal bending	Torsional
Natural Frequency	5.744 rad/s	8.063 rad/s
Modal Mass	4.14E+01	4.28E+01
Modal Stiffness	$1.37E+03$	$2.78E+03$

4.2. Hydroelastic analysis

The elastic modal responses are displayed below. A heading angle of $\chi = 60^{\circ}$ and a damping coefficient equal to 5% of the critical damping value $\zeta = 2\sqrt{km}$ were used in these plots.



Figure 4: Torsional Vibration of the Barge Compared to [8]

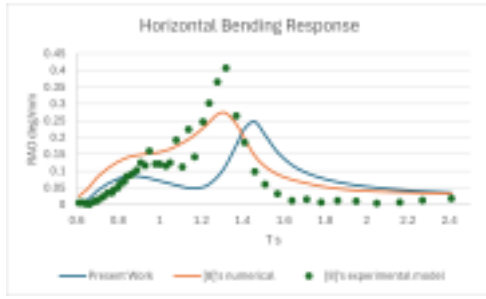


Figure 5: Horizontal Vibration of the Barge Compared to [8]

Coupling between the horizontal and torsional modes is observed as predicted. A higher torsional peak is also observed and can be adequately justified.

4.3. Discussion

Some features agree well with the findings of [8], especially regarding the structural analysis. Table 5 shows a comparison between the obtained dry frequencies.

Table 5: Comparison between coupled horizontal and torsional dry frequencies

Obtained	[8]	Difference
5.75	5.37	7%
8.04	7.92	2%

Discrepancies may arise because the NSM used in this study may not fully match the one adopted in the primary numerical model. In addition, the modal mass and stiffness could not be properly compared, which introduces fundamental error propagation into the hydroelastic analysis.

Regarding the hydroelastic response, several issues should be considered. The first is the omission of other vibration modes. As mentioned in [8], ten modes were considered to obtain the results; using only one mode may be inappropriate for more advanced analyses.

However, the obtained response shape agrees reasonably well; the resonant peaks occur in the same frequency domain for the torsional case, the horizontal bending peak is slightlty right shifted, this may be justified by the difference between the found dry frequencies for this case. The absence of adequate damping increases their amplitude and the absolute slope of the function, as described in [10]. Reference [8] considered higher damping for the horizontal bending mode; this choice is justified as a compensation for potential-flow assumptions that ignore fluid viscosity and vorticity together with the gaps of the segments of the physical model, and since the damping value was based on the decay rate of the segmented model (which differs from the numerical model presented). The discrepancy in the resonance peak's frequency of the horizontal vibration may therefore be due to differences from the original configuration of matrix elements.

5.. Conclusion

Comparing the modal shapes provides a means to validate the methodology adopted for predict-

ing the vibration behavior of the floating structure. Although the present formulation offers promising results, further refinement and experimental validation are necessary and are left for future work. Subsequent studies will focus on improving the procedure and assessing the influence of additional modes as they are incorporated into the analysis.

It is important to emphasize that the present work is conceived as an academic study aimed at broadening the hydroelasticity research community and increasing accessibility to the topic. By relying on transparent methodology and formulations that can be implemented with widely available tools, this study provides a foundation that can be adopted by academic institutions worldwide, including at early stages of engineering education such as the bachelor's level. This accessibility is intended to encourage new researchers to engage with hydroelasticity and to support the development of future contributions in the field.

6.. Acknowledgements

The authors would like to thank the Human Resources Program of the National Agency of Oil, Gas and Biofuels (PRH–ANP) for the financial support. This research was also supported by the "Coordenação de Aperfeiçoamento de Pessoal de Nível Superior – Brasil (CAPES)", the Department of Naval and Oceanic Engineering of the Federal University of Rio de Janeiro (DENO–UFRJ), the Waves and Currents Laboratory (LOC/COPPE/UFRJ), and the National Council for Scientific and Technological Development (CNPq), all of which are gratefully acknowledged.

References

[1] Grammatikopoulos, A. *A review of physical flexible ship models used for hydroelastic experiments*, Marine Structures 90th Edition, 2023.

[2] Kim, Y., Kim, J.H. *Benchmark study on motions and loads of a 6750-TEU containership*, Ocean Engineering, v. 119, p. 262-273, 2016.

[3] Hong SY, Kim BW, Nam BW. *Experimental study on torsion springing and whipping of a large container ship.*, In: Proceedings of the twenty-ffirst (2011) international ocean and polar engineering conference. 2011, p. 486–94.

[4] Drummen, I. *Experimental and numerical investigation of nonlinear wave-induced load effects in containerships*, Norwegian University of Science and Technology,2008

Ocean Engineering, v. 119, p. 262-273, 2016.

[5] Houtani, H., Komoriyama, Y., Matsui, S., Oka, M., Sawada, H., Tanaka, Y., Tanizawa, K.

Designing a Hydro-Structural Ship Model to Experimentally Measure its Vertical Bending and Torsional Vibrations. , Journal of Advanced Research in Ocean Engineering, v. 4, n. 4, p. 174-184, 2018.

[6] Kim BW, Kim K-H, Kim YS, Hong SY. *Torsion moment conversion methods in model test with U-shape backbone.* In: Proceedings of the twenty-fourth (2014) international ocean and polar engineering conference. 2014, p. 782–91.

[7] WAMIT, INC. *"WAMIT User Manual Version 7.5",* 2024.

[8] Senjanovic, I., Malenica, S., Tomasevic, S. *"Investigation of ship hydroelasticity"*, Ocean Engineering, v. 35, p. 523-535, 2008.

[9] Remy, F., Molin, B., Ledoux, A., 2006. *Experimental and numerical study of the wave response of a flexible barge*. Hydroelasticity in Marine Technology, Wuxi, China, pp. 255–264.

[10] Rao, S.S., 2016. *Mechanical Vibrations*. 6th ed. Pearson Education, Boston.

[11] Timoshenko, S.P., Goodier, J.N., 1970. *Theory of Elasticity*. 3rd ed. McGraw-Hill, New York.

[12] White, F.M., 2015. *Fluid Mechanics*. 8th ed. McGraw-Hill Education, New York.

[13] Faltinsen, O.M., 1990. *Sea Loads on Ships and Offshore Structures*. Cambridge University Press, Cambridge.

[14] Lopes, F.S., Fernandes, A.C., et al., 2025. *Hydroelastic Behavior of a Converted FPSO Platform in Head Excitation Waves*. Proceedings of the 44th International Conference on Ocean, Offshore and Arctic Engineering (OMAE 2025), Vancouver, Canada.

[15] Autodesk Inc., 2023. *Autodesk Inventor Nastran: User's Guide and Theory Manual*. Autodesk, San Rafael, CA.

[16] Robert McNeel & Associates, 2020. *Rhinoceros 3D*. Version 7.0, Seattle, WA.

[17] International Towing Tank Conference, 2017. *Seakeeping Tests*. ITTC Recommended Procedures and Guidelines

10th International Conference on HYDROELASTICITY IN MARINE TECHNOLOGY
Trondheim, Norway, June16$^{\text{th}}$-18$^{\text{th}}$, 2026

The Design, Production, and Verification of a Scaled Flexible Model of a Floating Truss Structure for Hydroelastic Experiments

de Koning, J.[1], Ruesen, J.[2], Hoogendoorn, D.[3], and Grammatikopoulos, A. [1,*]

[1] Department of Maritime & Transport Technology, Delft University of Technology, Delft, The Netherlands
[2] Mocean Offshore, Rotterdam, The Netherlands
[3] SolarDuck, Rotterdam, The Netherlands

Abstract. Flexible models have been used extensively in the literature to emulate hydroelastic behaviour at model scale. Such models mainly depict ships, with fewer examples representing other platforms, such as wind turbines. For both ships and wind turbines, the most common method to emulate the structure is to produce a model in rigid segments and introduce a stiffness source by linking them with a flexible backbone. This approximation can often be sufficient for both types of structures, as their behaviour in bending is beam-like. However, for floating platforms with a more 3-dimensional structure, the design of the model becomes significantly more complex. For instance, floating trusses are one of the suggested solutions for floating platforms of the future, but current studies are restricted to their bottom-fixed versions. In this study, the hydroelastic responses of a floating truss structure will be emulated. The platform has a triangular shape, with the truss system linking three cylindrical floaters at the points. A simplified model to emulate several of the mode shapes of the full-scale platform is designed, and produced using additive manufacturing. The instrumentation and calibration processes are described, and verification of the physical model against simulated responses is presented.

Key words: *Floating PV; Floating truss; Whipping; Multi-backbone system; Modal similarity*

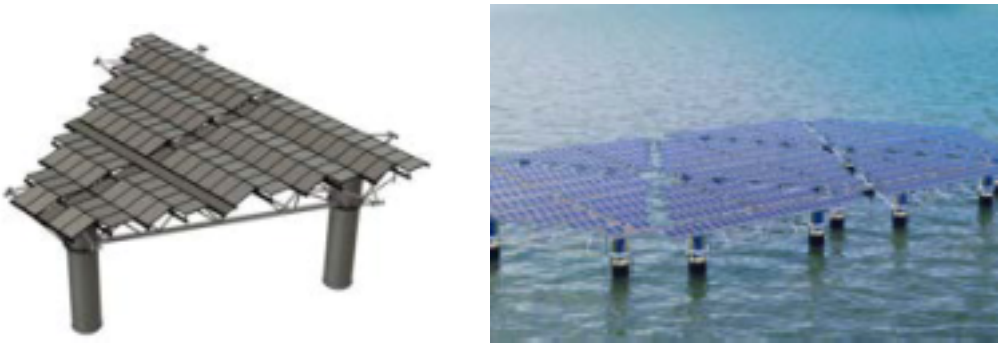
1. Introduction

The increasing demand for renewable energy, combined with the limited space on shore has generated a need for expansion of of photovoltaic farms offshore. Due to the low mass of PV panels, radically different designs are needed compared to what has been used historically, for instance in the oil and gas industry. One such example is the Merganser platform, as depicted in Figure 1, a modular triangular concept developed by SolarDuck, in which a truss structure elevates the PV system above the water surface by means of vertical cylindrical floaters located at each corner. The triangular geometry enables the interconnection of multiple units through flexible joints, forming a compliant and scalable array designed for operation in exposed offshore environments. This configuration leads to a flexible structure with relatively low natural frequencies and, potentially, significant slamming-induced whipping responses.

Use of models for hydroelastic experiments has a long history, but mainly pertaining to ships. The most popular approach is to use flexible backbone models, although flexible joint models and elastic models have also been popular for some applications [1]. Floating offshore wind turbines, like ships, can be often assumed to have a beam-like dynamic behaviour with only their tower considered flexible, resulting in backbone models being popular for such applications too (e.g. [2]).

Floating solar platforms fall into a separate category as they are inherently 2-dimensional, requiring more complex design of experimental models. Examples in the literature include tensioned membranes

*Correspondence to: A.Grammatikopoulos@tudelft.nl



(a) A single platform (b) Multiple platforms

Figure 1: A schematic of a single Merganser platform (a) of several interconnected platforms (b). The platforms are normally connected with flexible joints but this is not a part of the current investigation.

[3], un-tensioned membranes [4], and floating mattresses [5]. All of these are can be modelled by effectively extending the 1D beam approximation to a 2D deformable sheet. However, this is still not sufficient for the floating truss problem, in which the mechanical properties of the system as a whole cannot be replicated using an isotropic sheet. The only examples in the literature of experiments with deformable truss structures in the ocean involves a bottom-fixed arrangement [6]. Therefore, there is no established good practice to perform Froude scaling on the dynamic properties of such structures.

In this study, a methodology to produce scaled models of floating truss structures is developed. An equivalent geometry is generated, as scaling down the entire truss would result in sizes that cannot be manufactured. Inspiration is taken from the design of backbone models for ships [7] but is expanded for a 2-dimensional structure. Previous experience from ship models, suggesting backbone cut-outs to achieve concurrent scaling of bending and torsional properties is also utilised [8]. Due to mass limitations, polymers are selected as the backbone material, and specifically resin prints produced with SLA technology. Therefore, previous experience with additively manufactured structures and scaling of 2-dimensional mode shapes becomes relevant [9, 10]. The model's global modal properties in dry and wet conditions are compared to numerical predictions with good agreement. Special attention is given to mode similarity between predictions and measurements, something that is normally not a concern for beam-like structures but becomes essential for the application at hand.

2. Model design and production

2.1. Full-scale modal properties

Full-scale decay tests were performed on the Merganser plaform to identify its natural frequencies, mode shapes, and damping coefficients (Table 1 and Figure 2). Since the deflections were observed experimentally through discrete measurements, these full-scale results will be referred to as operational deflection shapes (ODS), rather than mode shapes.

The first three ODS corresponded to rigid body motion. As the platform does not feature a clear longitudinal axis, the two rotational motions observed were classified as "Pitch 1" and "Pitch 2" The naming convention adopted for the flexible ODS is summarised in Table 1. ODS 5 and 6 correspond to inward directed and tangential leg motions with respect to the platform centre, respectively, which induce dominant global bending and torsional deformation of the truss structure. These modes are therefore referred to as the global bending and torsion modes. ODS 4 exhibits a predominantly asymmetric deformation pattern and will be named as such.

These natural frequencies and ODS were used as the basis for the design of the scaled model. The

Table 1: Observed natural frequencies and damping ratios obtained from decay tests of the platform.

#	f [Hz]	ζ [%]	Shape description
1	0.18	2.19	Heave
2	0.19	0.40	Pitch 1
3	0.24	9.43	Pitch 2
4	2.37	0.90	Asymmetric
5	2.80	1.41	Bending
6	3.93	1.68	Torsion

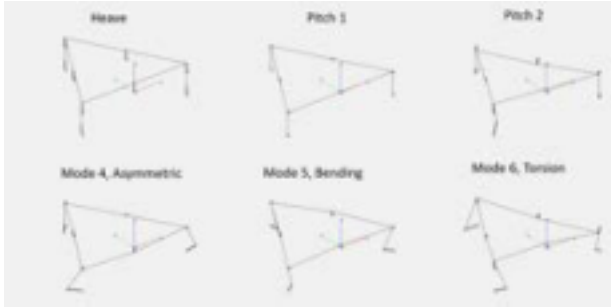


Figure 2: First six operational deflection shapes of the triangular platform, obtained through full-scale decay tests. The first three shapes are rigid body motion.

aim was to perform Froude scaling of the frequencies, while retaining the geometric characteristics of the global response.

2.2. Simplifying assumptions & modelling

Depending on the design of the three floaters, it is possible that impulsive loads can also excite flexible modes of this part of the structure. This could include beam-like behaviour of the floater, or even local deformation of its panels. However, in the present investigation the dynamic characterisation of the floating truss was prioritised, and floater flexibility was therefore omitted. As will be seen later in this document, the floaters were connected to the truss in a manner which allows them to potentially be replaced by flexible versions in future investigations, if desired. It was evident almost immediately that scaling of every single member of the truss structure was highly impractical or even impossible. However, evaluation of the observed ODS (Figure 2) indicated that they could be achieved with a less complex network of backbones. It was decided to design a triple-backbone model, where each side of the triangle coincided with a non-uniform backbone. Quantifying the effect of the connections of the three backbones to each other and to the floaters was challenging. Due to the limited measurement points for the full-scale ODS, the exact shape of the truss near these connection points and the corresponding boundary conditions were unclear. It was decided to assume that these backbone-floater interfaces behave in a manner which is very close to rigid.

The entire platform was modelled in ANSYS Mechanical APDL, using SHELL181 elements. The floaters and were modelled using the same elements, but with a significantly increased elastic modulus, rendering them effectively rigid. Different options to achieve the intended mode shapes and natural frequencies were tested, and it was demonstrated that backbones with uniform external dimensions and thickness but intermittent cut-outs were the easiest option. The rigid behaviour of the backbone-floater interface was emulated by allowing the outer backbone segments to intersect with the rigid shell of the top of the floaters. Additional masses, required primarily for the floaters, were modelled using MASS21 elements connected to the shell mesh with RBE3 links.

Python library Capytaine, a panel method code based on diffraction theory [11, 12], was used to identify the hydrodynamic characteristics of the mode shapes, and the calculation of the wet natural frequencies. The panel mesh of the three floaters is depicted in Figure 3b. Once the rigid body mesh is introduced in Capytaine, flexible modes can be defined through displacement of individual nodes of the mesh. The fully coupled model was used within an optimiser to iterate through different backbone geometries while attempting to minimise the error between the calculated & target natural frequencies and mode shapes.



(a) ANSYS structural mesh.

(b) Capytaine hydrodynamic mesh.

Figure 3: The meshes used for the structural (left) and hydrodynamic (right) calculations.

2.3. Material testing and final design

It has been demonstrated in previous work that the static and dynamic flexural moduli of 3D printed thermoplastics can differ from one another and that dynamic tests are, therefore, more appropriate to identify the mechanical properties relevant to vibration [13]. Specimens were produced using the same printer, material, and print settings as for the model. Modal tests were performed but, in the absence of a miniature instrumented hammer, the excitation was provided by a shaker. Unfortunately, it was found that, due to the small size of the specimens, the shaker attachment was interfering with the local stiffness drastically, and generating significant variation in the results. Despite the large spread of the results, the average flexural modulus was found to be 2.0 GPa, which was very close to the nominal value for the quasi-static flexural modulus of the material, and was therefore considered reliable. It was decided to use this value for the remainder of the design.

The final design consisted of three identical backbones, each produced in six identical segments. Each segment featured rectangular cut-outs on the sides, spanning the majority of its length (Figure 3a). The segments were designed so that a push-fit connection could be implemented, although glue would also be used to ensure a stable connection.

2.4. Materials and fabrication

The backbones were manufactured using the Form 4 printer and a patented engineering resin named Tough2000. The highest resolution settings available were used (layer height and in plane resolution of $50\ \mu m$), in order to minimise printing-induced geometric variability and to promote consistent material behaviour across all specimens and structural components. To further limit systematic variability, all SLA printed parts were printed with their longitudinal axis aligned with the build direction. All SLA printed parts were subsequently post-cured in accordance with the manufacturer's specifications to increase material stiffness. Curing time was monitored to reduce variability arising from differences in curing degree, both between individual parts and within more complex geometries.

2.5. Model assembly

Geometric measurements were performed using a caliper to assess printing accuracy. For components manufactured from Tough2000 (i.e. the backbones), reliable measurements proved challenging due to surface irregularities resulting from support removal and difficult accessibility of certain regions. The mean measured segment thicknesses difference from as designed thicknesses was $0.06\ \mathrm{mm}$. In contrast, the PLA–CF components (i.e. the backbone-floater interfaces and the floater end-pieces) were printed in orientations that required minimal support material, resulting in clean surfaces and consistent dimensions that closely matched the nominal CAD geometry, with only negligible deviations observed.

All printed components were weighed and compared against mass predictions obtained from CAD volumes and manufacturer specified material densities. Mean effective density for the Tough2000 components was within 2% of the nominal density, whereas larger deviations were found for the PLA–CF components (5-20%). Density of the PMMA tubes was also found to be 8.5% higher than what the manufacturer prescribes.

The Tough2000 backbone segments were snap-fit and glued together, as were the PLA–CF end-pieces to both ends of the PMMA tubes. All gluing was performed using Araldite 2011 epoxy adhesive. The PLA–CF parts connecting the former to the backbones were assembled mechanically using bolts, nuts, and washers (Figure 4). The steel mechanical fasteners further increased the total mass of the model.

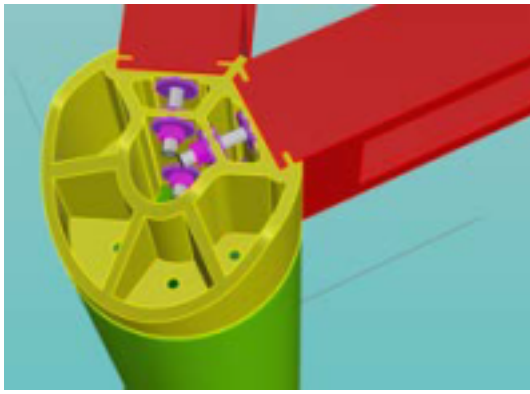


Figure 4: The backbone-floater interface (yellow) connecting the backbones (red) to one of the floaters (green). A slotting arrangement was used in conjunction with bolts.

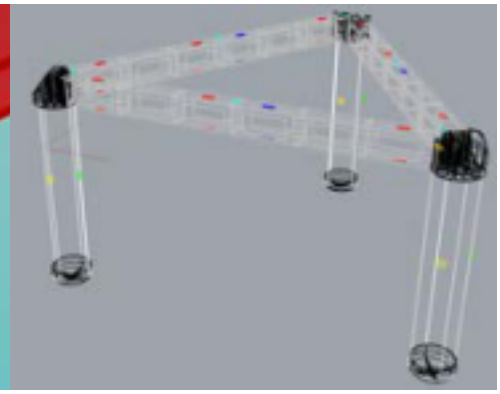


Figure 5: The instrumentation arrangement. The rectangles on the backbones correspond to strain gauges, and the circles on the floaters correspond to accelerometers.

2.6. Numerical model update

Based on measurements during assembly, the numerical modal predictions were refined through a series of targeted model updates. First, measured material densities were adopted in place of nominal values. The top-inserts were modelled by using CERIG constraints with the floater skin and bottom plate of the backbone-floater interface. In this manner, the floater insert and the backbone-floater interface were represented as an effectively rigid region, consisting of a $5\ \mathrm{mm}$ thick top insert combined with a $3\ \mathrm{mm}$ thick bottom plate. The PMMA tubes were modelled explicitly using their measured thickness, density, Young's modulus of 3.3 GPa, and Poisson ratio of 0.375. The updated total mass of the platform was then used to determine a revised static draft, which formed the basis for generating an updated floater surface mesh for the boundary element analysis. Based on the final mass of the model, and resulting draft, which was slightly higher than originally intended, the added mass calculations were repeated and the as-produced numerical model was finalised.

3. Experiments

3.1. Instrumentation

The model was instrumented with accelerometers and strain gauges. The strain gauges were installed before assembly. The overall instrumentation layout is shown in Figure 5. Strain gauge locations are

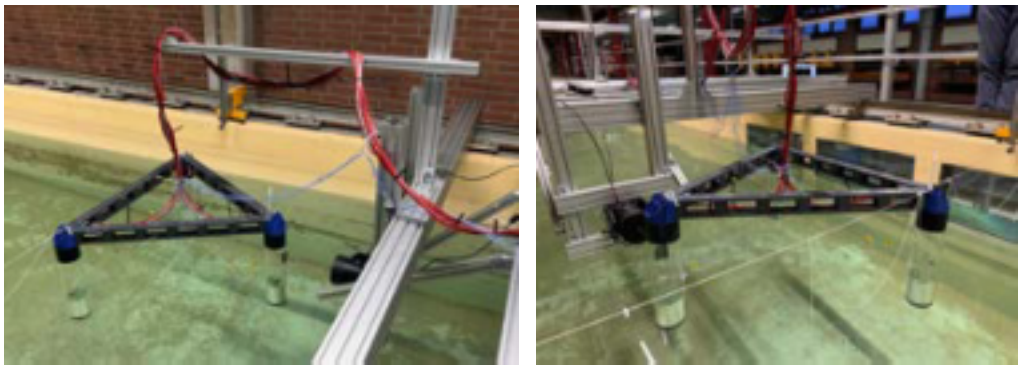
indicated by square markers, with red representing linear strain gauges and dark blue representing shear strain gauges. The linear strain gauges were HBM 1 LY16–3–350 gauges with a nominal resistance of $350\ \Omega$ and a nominal gauge factor of 2.09. These gauges were configured in half Wheatstone bridge arrangements. This configuration exploits the equal magnitude and opposite sign of bending strain at the top and bottom backbone surfaces, thereby increasing measurement sensitivity while suppressing uniform axial strain contributions. Shear strain was measured using HBM K 216.93 2217 strain gauge rosettes with a $(-45°, +45°)$ orientation. These rosettes were configured in full Wheatstone bridge arrangements to accurately measure the torsional shear strains present in the backbones.

A total of twelve single-axis accelerometers with a mean nominal sensitivity of $1.120\ \mathrm{mV/(m/s^2)}$ were installed on the model. Accelerometer locations are indicated by coloured circular markers, with green, yellow, and cyan denoting measurements in the global x, y, and z directions, respectively. As the global flexible modes are primarily characterised by the orientation of the horizontal rotation axes of the individual floaters, six accelerometers were mounted on the vertical outer walls of the floaters at a height of approximately $5\ \mathrm{cm}$ above the still waterline. These sensors were used to capture horizontal accelerations and thereby provide an indirect measure of the floater rotations relative to the backbone end assemblies. In addition to the floater motion, the vibration of the connecting backbones and their relative phase relationships constitute an important indicator of the global modal behaviour. For this reason, six additional accelerometers were positioned along the backbones, located at the backbone end assemblies and at mid span, and oriented in the global z direction to capture the vertical backbone response.

The data acquisition system was configured to sample all channels simultaneously at a fixed sampling frequency of $6000\ \mathrm{Hz}$. The strain gauge bridges were excited using a constant excitation voltage of $5\ \mathrm{V}$. Instrumentation cables were routed vertically above the geometric centre of the platform so that the cable weight is supported without introducing additional stiffness or mass. Applying small rigid body excitations confirmed that the platform was free to undergo heave and pitch motions while the cable bundle remained effectively stationary.

3.2. Modal testing in air & water

For testing in air, the model was suspended from linear springs at each corner, approximating free–free boundary condition. The springs had a nominal stiffness of $25\ \mathrm{N/m}$, which was verified through numerical simulations to be sufficiently low to have negligible influence on the global modal properties. To accommodate the relatively large spring lengths required, a triangular support tower constructed from aluminium extrusions was used to attach the springs above the model.



(a) Radial excitation (b) Tangential excitation

Figure 6: Modal tests in water with radial shaker excitation (left) and tangential shaker excitation (right).

A roving excitation strategy was adopted for both the dry and the wet tests in order to assess sensitivity to local boundary conditions associated with a single shaker location. Each floater was excited sequentially in two orthogonal horizontal directions: the radial direction along the line connecting the centre of the triangular platform to the excited floater which predominantly excites bending responses; and the tangential direction perpendicular to the former which predominantly excites torsional responses. This resulted in six distinct excitation configurations. The complete excitation sequence was repeated five times for a sufficient statistical sample. In the case of the dry tests, the shaker was placed close to the floor, therefore generating a force near the bottom of the floaters.

The tests were repeated with the platform floating instead of being suspended. Aluminium profiles were placed across the width of the towing tank to provide a rigid support for the modal shaker. This arrangement allowed the shaker to be positioned as close as possible to the waterline while being rigidly supported. The excitation location on the floater was selected to remain sufficiently distant from nodal regions of the targeted global modes, thereby promoting modal participation. The vertical position of the excitation connection point relative to the floater was fixed at $16.3\ \mathrm{cm}$ above the still waterline. The tank width was sufficiently large to allow the shaker to be rigidly fixed at approximately two thirds of the tank width, while the platform itself was repositioned to realise different excitation configurations. The same radial and tangential excitation locations as defined in the dry experimental procedure were employed.

To maintain the platform at a fixed mean position during the wet tests, two vertical flexible springs with a nominal stiffness of $25\ \mathrm{N/m}$ were applied using tensioned horizontal strings and pulley systems. These springs were oriented perpendicular to the stinger direction and were attached either to the two floaters furthest from the shaker for bending dominated tests, or to the single floater furthest from the shaker for torsion dominated tests. By carefully adjusting the string lengths, the springs were engaged with minimal pre-tension while still preventing drift of the platform during the measurements, thereby limiting their influence on the dynamic response. The shaker was repositioned once for each excitation configuration, and multiple measurements were performed without altering the boundary conditions.

For dry and wet tests, the excitation frequency range was limited to a maximum of $100\ \mathrm{Hz}$ and $70\ \mathrm{Hz}$, respectively. This range was selected based on numerical predictions indicating that higher order modes are increasingly local in nature.

4. Results and discussion

To avoid subjective manual filtering of the experimental data, and given the number of repeated test runs and excitation locations considered in this study, an automated post-processing procedure was required to consistently group modal identifications and quantify their scatter. To this end, a density-based spatial clustering (DBSCAN) algorithm was applied to the combined frequency and damping data. DBSCAN groups data points based on local density and does not require the number of clusters to be specified, which makes it suitable when the number of observable modes may vary between test conditions and when spurious identifications or noise points are present. The output of the clustering consists of a set of dense clusters representing repeatedly identified natural modes, as well as a set of noise points that do not belong to any cluster.

Table 2 summarises the behaviour of individual backbones in each of the numerically calculated mode shapes, which are depicted in Figure 7. Due to symmetry of the triangular platform, mode 1 and mode 4 repeat, as modes 1a and 1b, and 4a and 4b, respectively. It will also be seen later that these mode shapes have, as would be expected, almost the same natural frequency, with differences only present because of physical uncertainties. Comparison between the full-scale ODS and the numerical mode shapes was, unfortunately, impossible due to the limited data regarding the former (no strain measurements). However, extensive comparison was possible between numerical predictions and experimental measurements, for which the modal assurance criterion (MAC) was used.

MAC values comparing the numerically predicted mode shapes (columns) and clusters identified

Mode #	Backbone 1	Backbone 2	Backbone 3
1	T+	B+	B-
2	B-	B/T+	B/T+
3	B+	B+	B+
4	T+	T+	T+

Table 2: Type of response per backbone for the various mode shapes. Modes 1a and 1b and modes 4a and 4b are group together, respectively. T and B signify torsion-dominated and vertical-bending-dominated behaviour, respectively. + signifies same phase between backbones and - signifies opposite phase.

from the experimental measurements (rows) can be found in Tables 3 and 4 for dry and wet conditions, respectively. These clusters are named using the following convention: the first letter, D or W, signifies dry or wet conditions, respectively; The second letter, R or T, signifies radial or tangential excitation, and therefore bending-dominated or torsion-dominated response, respectively; the number signifies the number of the cluster, in ascending order of frequency, within that type of measurement.

It is evident that the similarity of numerically predicted mode shapes and experimentally measured ODS is very high, with a minimum value on the diagonal of 0.961. The only exception is the last entry from the wet experiments, which was not actually identified as a cluster using the DBSCAN algorithm and was identified manually. The increased noise in that part of the measurement resulted in an unsatisfactory MAC value. The off-diagonal terms are mostly equal to approximately zero, as expected, with the exception of modes 1a and 1b, and 4a and 4b, which are so similar to one another that they produce high MAC values. These similarities were also present when MAC was applied between only numerical or only experimental results.

Table 3: MAC values between numerical modes and experimental clusters in dry conditions.

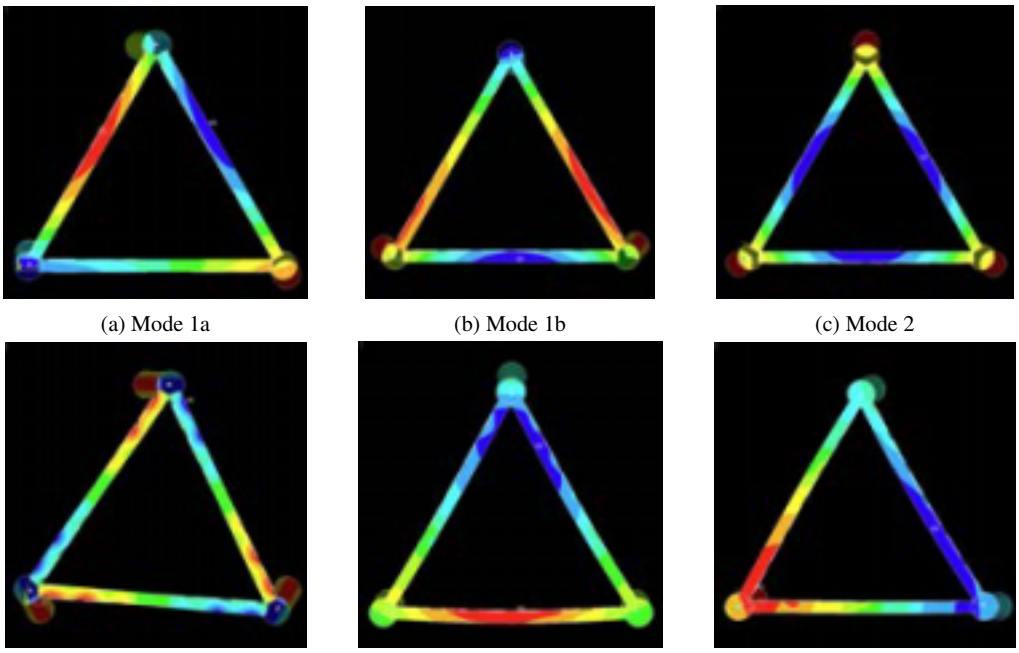
Mode	DR1	DT1	DR2	DT2	DT3	DR3
1a	.959	.903	.001	.000	.007	.073
1b	.816	.955	.000	.005	.004	0.009
2	.000	.000	.995	.031	.001	.017
3	.002	.000	.006	.986	.001	.000
4a	.008	.022	.000	.002	.974	0.757
4b	.179	.009	.001	.000	.813	.965

Table 4: MAC values between numerical modes and experimental clusters in wet conditions.

Mode	WR1	WT1	WR2	WT2	WT3	Man.
1a	.961	.685	.000	.000	.009	.084
1b	.657	.992	.000	.002	.004	.080
2	.018	.000	.976	.009	.000	.000
3	.004	.000	.002	.996	.000	.000
4a	.002	.004	.006	.000	.965	.462
4b	.002	.002	.000	.000	.939	.433

Table 5 summarises the comparison of modal properties between numerical predictions and experimental measurements. Columns 3 and 4 include the mean measured values for the natural frequency and damping coefficient of each ODS. Notably, the damping coefficients are quite large for this type of structure, with a value of approximately 3% for dry conditions and slightly higher for wet conditions. Based on observations during specimen testing, this is attributed mostly to the properties of the resin used for the backbones rather than the mechanical connections.

Columns 5 and 6 include the numerical predictions for the equivalent natural frequencies and the corresponding error %. These are based on the earlier assumption that the flexural modulus of the backbones is equal to 2.0 GPa. The errors are substantial and uniformly under-predicting the natural frequencies. This clear trend made evident a disparity between the assumed values in the numerical model and reality. Geometry and sizing was eliminated as a culprit, since they could be measured accu-



(a) Mode 1a (b) Mode 1b (c) Mode 2

(d) Mode 3 (e) Mode 4a (f) Mode 4b

Figure 7: Top view global mode shapes. Colours indicate vertical translation.

rately and reliably, as was mass/inertia for the same reasons. The behaviour of the interfaces is certainly, in reality, not perfectly rigid, but their finite stiffness could only result in lower natural frequencies. It was concluded that the flexural modulus, as provided by the manufacturers (and most likely obtained quasi-statically) differed from its effective dynamic counterpart, as previously observed with additively manufactured polymers [13]. Consequently, numerical iterations with different magnitudes of flexural modulus were performed, and it was found that a modulus of 2.5 GPa produces much more accurate results (most errors within 3%). This value is larger than both the tensile and flexural moduli provided by the material manufacturer, and indicates that strain-rate-dependent effects are present, necessitating the determination of a dynamic modulus. Further dedicated investigations at specimen-scale would be useful in the future.

5. Conclusions

Hydroelastic experiments usually involve models with a beam-like behaviour, such as ships or wind turbines, where a flexible backbone approach is often sufficient. When the interest is in floating solar platforms, experiments to date have primarily been performed on very flexible platforms, such as membranes or floating mattresses. The current investigation explores the possibility of creating a scaled model of a floating truss design. The triangular platform is supported by three cylindrical floaters, and the main consideration is scaling of the flexible response for experiments in slamming-induced vibrations.

Due to manufacturing limitations at scale, the model is designed with three flexible backbones forming the triangular shape, optimised to achieve the correct natural frequencies and mode shapes. SLA printing is used to produce the backbones; challenges with specimen tests did not allow good estimation of the flexural modulus, but dynamic tests of the entire model demonstrated significant differences from

Table 5: Consolidated modal identification results for dry and wet configurations.

Cluster	Mode	f_{mean} [Hz]	ζ_{mean} [%]	$f_{\text{num}}^{E=2.0}$ [Hz]	Err [%]	$f_{\text{num}}^{E=2.5}$ [Hz]	Err [%]
DT1	1a	21.97	2.95	19.28	-12.24	21.51	-2.09
DB1	1b	22.18	2.92	19.29	-13.03	21.52	-2.98
DB2	2	30.38	2.46	27.43	-9.44	30.54	0.83
DT2	3	30.63	3.34	25.57	-16.52	28.50	-6.95
DT3	4a	40.30	3.33	35.54	-11.81	39.55	-1.86
DB3	4b	39.55	3.07	35.63	-9.91	39.65	0.25
WB1	1a	11.82	3.62	10.60	-10.32	11.82	0.00
WT1	1b	11.72	4.05	10.60	-9.56	11.82	0.85
WB2	2	15.94	3.45	14.93	-6.34	16.60	4.14
WT2	3	20.37	3.19	17.41	-14.53	19.40	-4.76
WT3	4a	27.82	3.48	25.59	-8.02	28.43	2.19
Man.	4b	27.93	3.55	25.65	-8.16	28.49	2.01

the prescribed static flexural modulus, indicating strain rate effects, similar to previous reports in the literature. Despite some discrepancies between full-scale and model-scale properties, great agreement was achieved between numerical predictions and experimental measurements: the modal assurance criterion produced values of at least 0.961 when comparing strains from the FEA model and experimental measurements, and the natural frequencies with the adjusted flexural modulus come mostly within 3% between the two. Damping was found to be high, with coefficients of approximately 3% in air, which was found to be due to the material of the backbones.

Acknowledgements

This publication is part of the project MERGANSER with file number DEI122010 of the programme DEI+ from the Netherlands Enterprise Agency (RVO).

References

[1] Apostolos Grammatikopoulos. A review of physical flexible ship models used for hydroelastic experiments. *Marine Structures*, 90, 2023.

[2] Erin E. Bachynski, Maxime Thys, and Virgile Delhaye. Dynamic response of a monopile wind turbine in waves: Experimental uncertainty analysis for validation of numerical tools. *Applied Ocean Research*, 89:96–114, 8 2019.

[3] M. Mukhlas, T. Kristiansen, P.F. Lader, and D. Kristiansen. Experimental and numerical investigation of a vertical pre-tensioned membrane sheet in regular waves. In *9th International Conference on Hydroelasticity in Marine Technology*, pages 7823–7830, 2022.

[4] Esra Uksul, Angeliki Laskari, Sebastian Schreier, and Christian Poelma. Velocity field measurements under very large floating structures interacting with surface waves. *Ocean Engineering*, 315:119759, 2025.

[5] W.J. Otto, T.H.J. Bunnik, and L. Kaydihan. Hydro-elastic behaviour of an inflatable mattress in waves. In *9th International Conference on Hydroelasticity in Marine Technology*, pages 289–300, 2022.

[6] Ying Tu, Zhengshun Cheng, and Michael Muskulus. A global slamming force model for offshore wind jacket structures. *Marine Structures*, 60:201–217, 2018.

[7] Adolfo Marón and Geert K. Kapsenberg. Design of a ship model for hydro-elastic experiments in waves. *International Journal of Naval Architecture and Ocean Engineering*, 6:1130–1147, 1 2014.

[8] Suji Zhu, MingKang Wu, and Torgeir Moan. Experimental investigation of hull girder vibrations of a flexible backbone model in bending and torsion. *Applied Ocean Research*, 33:252–274, 2011.

[9] Apostolos Grammatikopoulos, Joseph Banks, and Pandeli Temarel. The design and commissioning of a fully elastic model of a uniform container ship. *Marine Structures*, 78, 2021.

[10] Anabel Keser, Michiel Verdult, Harleigh Seyffert, and Apostolos Grammatikopoulos. The design, production, verification, and calibration of an elastic model of a catamaran for hydroelastic experiments. In *13th Symposium on High Speed Marine Vehicles, HSMV 2023*, pages 139–148. IOS Press, 10 2023.

[11] Matthieu Ancellin and Frédéric Dias. Capytaine: a Python-based linear potential flow solver. *Journal of Open Source Software*, 4(36):1341, apr 2019.

[12] Aurélien Babarit and Gérard Delhommeau. Theoretical and numerical aspects of the open source BEM solver NEMOH. In *Proceedings of the 11th European Wave and Tidal Energy Conference (EWTEC2015)*, Nantes, France, 2015.

[13] Apostolos Grammatikopoulos, Joseph Banks, and Pandeli Temarel. Prediction of the vibratory properties of ship models with realistic structural configurations produced using additive manufacturing. *Marine Structures*, 73, 2020.

Floating Wind

10th International Conference on HYDROELASTICITY IN MARINE TECHNOLOGY
Trondheim, Norway, June 16th-18th, 2026

Experimental Study of a Scaled Flexible Riser for Hydrogen Transport from a Floating Wind Turbine Platform to the Seabed

Guichard, J.[1*], Hann, M.[2], Tosdevin, T.[3], and Greaves, D.[4]

[1] School of Engineering, Computing, and Mathematics, University of Plymouth, Plymouth, United Kingdom (jessica.guichard@plymouth.ac.uk)
[2] School of Engineering, Computing, and Mathematics, University of Plymouth, Plymouth, United Kingdom (martyn.hann@plymouth.ac.uk)
[3] Department of Engineering Science, University of Oxford, Oxford, United Kingdom (tom.tosdevin@eng.ox.ac.uk)
[4] Department of Engineering Science, University of Oxford, Oxford, United Kingdom (deborah.greaves@eng.ox.ac.uk)

Abstract. Dolphyn Hydrogen aims to support the UK Government's 2030 hydrogen targets by deploying a 10-15 MW Commercial Scale Demonstrator that produces hydrogen offshore using wind energy. To achieve this, hydrodynamic studies are required to optimise the flexible pipeline transporting hydrogen from a floating wind turbine to the seabed, as well as the buoyancy modules that create the riser's lazy-wave shape. A key parameter is ensuring the riser never bends below its minimum allowable radius. The hydrodynamic behaviour of a 6-inch NOV flexible pipe is tested at 1:62 scale in the University of Plymouth's COAST Laboratory Ocean Basin. The riser is connected to a semi-submersible platform with heave plates, and both operational and storm conditions representative of the Celtic Sea are examined. Design waves that maximise platform surge or mooring loads are also identified and tested. Underwater Qualisys cameras track ten markers along the riser, enabling reconstruction of its shape at each time step and calculation of the minimum bending radius. Comparing full sea-state results with those from Design waves helps assess whether Design waves can reliably predict minimum radii for flexible risers.

Key words: *Flexible riser; Semi-submersible platform; Design waves; Scaled tank testing; Offshore green hydrogen*

1. Introduction

To meet the UK's 2050 net zero targets, offshore wind capacity and green hydrogen production for hard to electrify sectors will expand. Producing hydrogen offshore can reduce costs by replacing expensive export cables with cheaper pipelines. Studies show offshore hydrogen production is more cost-effective than onshore, especially when kept as a gas [1, 2]. The cheapest option is decentralized hydrogen production on floating wind turbine platforms situated 50 km from shore [3]. Offshore hydrogen production also maximizes profit from an offshore wind farm 60 km from shore when hydrogen prices are 2.5 times higher than electricity prices [2]. Dolphyn aims to deploy a Commercial Scale Demonstrator (CSD) before 2030, the first commercial scale ultra low-carbon green hydrogen from floating offshore wind project [4]. The use of a flexible riser for transport of hydrogen produced on the platform to a rigid pipeline on the seabed requires investigation.
Orcaflex is frequently used to investigate configurations of dynamic power cables attached to floating wind turbines, such as in [5], where a suspended inter-array power cable is investigated, or a floating substation [6]. Experimental investigations for power cables have been carried out in [7], where a scaled

* Correspondence to: jessica.guichard@plymouth.ac.uk

model of a power cable in lazy wave configuration has been attached to a model at scale 1:70 of a semi-submersible floating wind turbine platform (VolturnUS) and the results compared to Orcaflex. In [8], a model of a dynamic power cable is investigated in a flume, exposed to waves and with forced surge motions. In [9], VIV are investigated on a lazy wave dynamic power cable in a steady current.
This study presents the experimental investigation of the riser to be used for the CSD developed by Dolphyn Hydrogen at scale 1:62, attached to a model of the CSD exposed to operational sea conditions and storm conditions. Platform geometry and mass properties were provided, and funding was available for building a model of the platform. This led to the simultaneous investigation of the platform motions alongside those of the riser, for determining lowest bending radius observed in storm conditions. In [7], a difference in acceleration of local positions on the riser was observed, with Orcaflex underpredicting acceleration by up to 15 %, and a difference of 10 % between maximum curvature predicted by Orcaflex when compared to experimental data was observed, suggesting that Orcaflex could underpredict curvature.
The study presented in [7] also investigated the case of wave loading on the riser only, with a stationary FOWT, and observed that, "modelling the waves only allowed for motion response to be well captured in the wave frequency region, but none of the low frequency response was captured". On the other hand, when considering platform motion only, without direct wave loading on the cable, low frequency motion at hog and sag bends was predicted well, and response in the wave frequency region was underpredicted. This emphasized the importance of accurately modelling wave loading on the cable.
Several other research objectives were pursued in this study: to find a material to represent a flexible riser at reduced scale and to determine optimum distances between underwater Qualisys markers for motion tracking. The concept of short design waves was applied to the platform, and it was investigated whether the concept of short design waves could also be applied to extreme values for the radius of the riser.
Scaled testing of a dynamic cable with a lazy wave shape for transmission of electricity from a floating wind turbine platform to the seabed is investigated in [7], which itself was building on investigations by [8]. The study presented in [7] inspired the use of fishing poppers combined with metal nuts for representing buoyancy modules, as well as the use of underwater Qualisys markers, weighted with metal nuts, to cancel buoyancy, for motion tracking of the riser. One difference to [7] was the use of a more flexible material, an FKM rubber cord, closer to the bending stiffness of a riser, instead of a helically wound steel wire with PVC coating used in [7] for representing a dynamic cable. As recommended in [7], a higher number of underwater Qualisys markers for motion tracking was used, spaced 20 cm, rather than 50 cm apart, which allowed determining the shape of the riser at each time step more reliably, and from it the curvature or radius.
Three hour long (at full scale) irregular wave time series for the 50-year sea state were run and a short design wave approach was applied to produce equivalent extreme surge, mooring load and platform pitch responses in a shorter time. The most likely extreme response (MLER) waves consist of short ~60 second focused waves conditioned on the linear RAOs of different responses. The approach was originally developed for ship design [10] but has recently been adapted to floating ORE (Offshore Renewable Energy) applications ([11, 12]), and expanded to include wind loading for floating wind turbines [13]. The wave only MLERs were applied in this work and a detailed account of the equations and their application can be found in [11] or [12].

2. Methodology

The properties of the full-scale riser and platform were aimed at being reproduced at a scale of 1:62. The riser investigated is a 6-inch riser (inner diameter = 152.4 mm) by NOV designed for transporting hydrogen. The outer diameter is 8.6" (=219.6 mm). The weight in air is 70.6 kg/m, giving a weight in the sea of 31.8 kg/m. The bending stiffness is 45 kNm^2. The length of the riser used is 250 m. The minimum bending radius is 1.87 m. The bending radius at each point on the riser should not go below this value to avoid damage to the riser.
Static simulations were carried out for several configurations of the riser, such as the distance between the attachment of the riser on the platform and on the seabed, keeping the length of the riser constant, using MoorDyn, a mooring system dynamics model based on a lumped-mass discretization of a

mooring line's dynamics [14] (Version 2, which includes bending stiffness, in WEC-Sim [15]). Buoyancy modules were represented by an equivalent buoyant section with total dry weight and volume identical to the buoyancy modules and the riser section. The equivalent diameter $Diam_{equ}$ of the buoyant section can be determined using Equation 1.

$$Diam_{equ} = \sqrt{\frac{4 \times (Vol_{bm} \times N + \frac{\pi}{4} Diam^2 \times L)}{\pi L}} = \sqrt{48 \frac{Vol_{bm}}{\pi L} + Diam^2} \quad (1)$$

Where Vol_{bm} is the volume of 1 buoyancy module, N is the number of modules (12 here), $Diam$ is the diameter of the riser, and L is the length of the buoyant section (see also Equation 2).

$$L = N \times l + (N - 1) \times d \quad (2)$$

With l the length of 1 buoyancy module (considered to be 1 m here), and d the distance between 2 buoyancy modules. The equivalent mass per length of the buoyant section M_{equ} can be calculated through Equation 3.

$$M_{equ} = N \times M_{bm} + M_{riser} \times L \quad (3)$$

Where M_{bm} is the mass of one buoyancy module and M_{riser} is the dry mass per length of the riser. The static simulations were run for a water depth of 65 m and several distances between the hang off point and the connection point to a rigid pipeline on the seabed. The buoyant section was assumed to start 55 m from the hang-off point. 12 modules were assumed to be used. The length of 1 module was assumed to be 1 m, the distance between two modules was selected to be 2 m, making the total length of the buoyant section 34 m. Properties of buoyancy modules, as well as distances between the hang-off point and the attachment point on the seabed that give the riser a lazy-wave shape, were determined (Figure 1, Table 1). The distances of 200 m and 210 m were selected to be investigated in the lab.

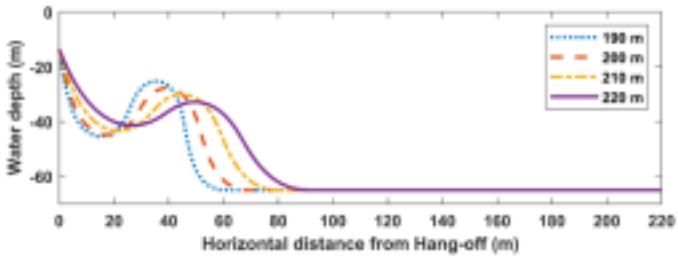


Figure 1 Shape of 6-inch riser, determined using MoorDyn, for a water depth of 65 m and various horizontal distances from the hang-off point.

Bending occurs at three locations with a radius of 11.8 m for the sag bend, 9.7 m for the hog bend, and 13.8 m for the bend near the seabed.

Table 1 Properties of buoyancy modules which would provide the correct buoyancy to the 6-inch riser.

Property	Value
Weight of 1 module (kg)	466
Volume (m^3)	0.656
Submerged weight (kg)	-206.20
Buoyancy of 1 module (N)	6,594
Density of buoyancy module (kg/m^3)	710.6

The sea conditions selected for the tank tests were for the Celtic Sea, where the Commercial Scale Demonstrator by Dolphyn Hydrogen is planned to be installed, and also location for the Floating

Offshore Wind Leasing Round 5 by the Crown Estate [16]. An operational sea state with a significant wave height Hs of 1.8 m and a peak period Tp of 9.1 s was selected, as well as a 1-in-50-year storm state, with a significant wave height Hs of 12 m and a Tp of 14.4 s. Wind was not used in the experiment, to focus on the underwater motions.
The effect of a white noise spectrum for frequencies between 0.038 and 0.25 Hz (0.3 to 2 Hz at reduced scale, corresponding to the extremes that can be produced in the lab), was recorded for the purpose of producing Short Design Wave spectra. Design waves were determined for maximum surge, maximum pitch, maximum loads in the front mooring lines and maximum loads in the aft mooring lines. Pitch and loads in aft mooring observed were not significant, which is why they are not shown here.
The floating wind turbine platform to which the riser is attached is a semi-submersible platform with heave plates in the shape of pentagons. The wind turbine tower is placed on top of a large column making up the summit of an isosceles triangle. The Commercial Scale Demonstrator will have hydrogen production facilities placed in between the three cylindrical columns, which provide the stability of the platform (Figure 2(a)). These facilities were not represented at reduced scale, only the weight distribution was aimed at being represented correctly for geometry situated out of the water. The main focus of the study were the movements of the riser which is why the platform is not described in detail, in addition to reasons of confidentiality. See Figure 2 (b) and (c) for photos of the experimental set up.

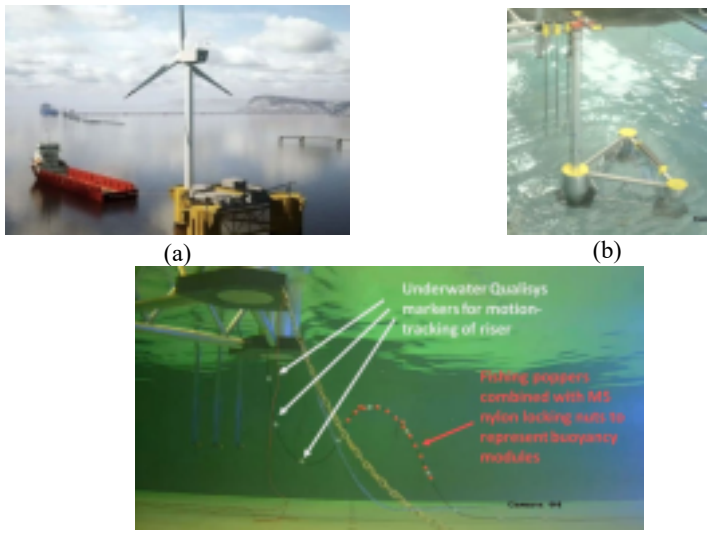


Figure 2 Virtual image of Commercial Scale Demonstrator (a) and experimental set up (b). Underwater image of experimental set-up for measurements of motions of the riser. In the foreground, one of three catenary mooring chains can be seen. The red line hanging down from the attachment point of the mooring on the platform is a cable for the load cell measuring mooring loads. In the background, a second mooring chain can be seen, as well as wave gauges (c).

The properties of the actual platform in the lab were different from the target properties, due to an accumulation of several errors, between the total buoyancy of the manufactured platform at the target draft being insufficient, the target weight of the platform including mooring being used, when the added ballast was determined, and the added ballast differing from the target weight (Table 2).
The small cross-sectional area of the platform caused a more significant error (8.8 %) in the draft, going from 13.5 m to 14.7 m, in spite of the rather small difference to the target weight. The second moment of area at the water surface for the new draft was almost the same as for the target draft, the cylindrical columns having a constant diameter, and the only difference was due to the different location of the relatively small waterplane area of the diagonal beams, so this is not expected to affect stability significantly. Concerning the difference in vertical distance between the attachment point of the riser on the platform and the seabed, the relative error (2.33 %, 50.3 m instead of 51.5 m) is not as important

as for the draft. This vertical distance affected the riser, as well as the mooring loads, as the mooring lines were a little slacker than if the platform was at the correct draft. In terms of weight of the platform, the weight used in the laboratory ended up being closer to the full size target than if the correct weight had been applied when taking into account the lack of buoyancy due to fresh water.

Table 2 Target and actual weights of the platform at full and reduced scale.

Property name	Total weight, excluding mooring
Target weight at full scale (mT)	11,680
Target property which should have been used at reduced scale for manufacture, when taking into account lack of buoyancy due to fresh water	47.7
Actual weight in Lab (kg), due to weight of ballast being different from target weight, and weight of mooring being included in calculations	49.19
Actual weight in lab converted to full size (mT)	11,723
Error (%)	0.37%

Table 3 shows the target moments of inertia determined using information on centers of gravity of individual components (Rotor Nacelle Assembly, Steel structure, Topside hydrogen equipment, Tower, Water ballast inside columns at full scale) as well as making additional assumptions. Actual properties for moments of inertia and positions of centers of gravity in the lab after manufacture were not verified. Given that the added ballast was above the target added ballast at reduced scale, it can be assumed that these properties differed slightly from the actual model platform used in the lab.

Table 3 Target properties of platform at full and model size.

Property	Target, full scale	Target, reduced scale
Longitudinal center of gravity (m)	4.2	0.068
Transverse centre of gravity (m)	0.0	0.0
Vertical centre of gravity or KG (m)	22.0	0.355
Ixx (kg.m^2)	2.0183×10^{10}	22.031
Iyy (kg.m^2)	2.2785×10^{10}	24.870
Izz (kg.m^2)	1.3921×10^{10}	15.195

The mooring which was set up in the lab did not correspond to the planned mooring at full scale, with the maximum length of the mooring lines being limited by the dimensions of the wave tank, and the use of three lines instead of 3 pairs of lines. Using Moorpy [17], the properties of a mooring line which would have similar added weight as the full-scale target (210 mT) were determined. A long-link stainless steel chain with links that have a 4 mm diameter was found to be closest to the target properties. Table 4 indicates the properties of the mooring chains used in the lab. There was a horizontal distance of 490 m at full scale between each attachment point of the riser on the platform and the attachment point on the seabed. The front mooring lines had an angle of 28.255º when compared to the y axis.

Figure 3 shows the experimental set-up seen from above. This is not necessarily the planned direction of the platform when compared to the waves. For simplicity reasons, the platform was set up symmetrically in the direction of the waves. The attachment point of the riser is also not necessarily the

one which will be used in the end. Rather, a position was selected which allowed both observing extreme motions in the default plane of the riser (movement is expected to be 2D) and motion tracking by underwater cameras. A propeller system which would allow reproducing effects of wind using a software-in-the-loop system was installed at the tower top (to represent the weight of the rotor nacelle assembly) but not used, as the development of a surrogate model for representing the aerodynamic loads of a 10 MW turbine was not ready.

Table 4 Properties of mooring chain used for experiments.

Property	At lab scale	At full scale
Length (m)	8.18	506.9
Dry mass per length (kg/m)	0.233	895.06
Equivalent diameter	0.0061	0.379
Submerged weight per length (kg/m)	0.204	782.38

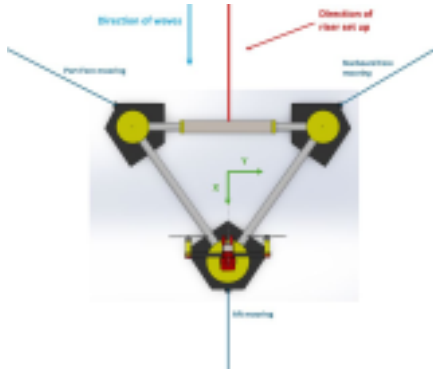


Figure 3 Schematic of experimental setup seen from above. Length and angle of mooring lines not to scale. Length of riser not to scale.

Several materials were considered for representing the riser at reduced scale, amongst which FKM (or Viton), EPDM, and NBR. According to [18], using an axial stiffness different from the actual axial stiffness does not affect the shape of the riser importantly, but staying close to the bending stiffness is important. The present study focuses on scaling the bending stiffness as closely as possible and neglect representing the axial stiffness correctly at reduced scale (Table 5).

Table 5 Properties aimed to be reproduced in the scaled experiment.

Property	Full scale	Target at reduced scale
Outer diameter (mm)	219.6	3.54
Weight in air (kg/m)	70.6	1.84×10^{-2}
Weight in sea (kg/m)	31.8	8.27×10^{-3}
Bending stiffness (Nm^2)	45,000	4.91×10^{-5}

The outer diameter was aimed at being reproduced, but priority was given to the weight in the sea, as well as the bending stiffness. The target Young's modulus of the model riser E_{model} can be expressed as a function of the density ρ of the material used for the model riser, the bending stiffness of the full-scale riser B_{fs}, the scale λ, the submerged weight of the full-scale riser Sw_{fs}, and the density of fresh water ρ_{fresh} using Equation 4.

$$E_{model} = \frac{4\pi B_{fs}\left(\rho - \rho_{fresh}\right)^2}{\lambda {Sw_{fs}}^2} \tag{4}$$

Figure 4 shows the target relation between the density and the Young's modulus of a material to be selected to represent the riser at reduced scale, for which several materials come close to the target with a slightly too high Young's modulus. Epichlorohydrin is in theory closer to the target line, but not available in the shape of rubber chords. The rubber chord also needed to be available at a diameter that would provide a submerged weight close to the target.

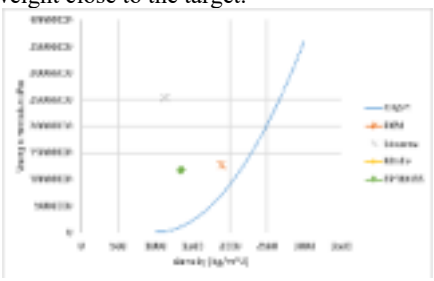


Figure 4 Target relation between density and Young's modulus of material to represent riser at reduced scale, as well as materials close to the target

Closest to the target properties was an FKM (or Viton) rubber cord, 3.44 mm (8.6 inches at full scale) thick, with a density of 1893 kg/m^3, a Young's modulus of 12.37 MPa, a submerged weight per length of 8.2×10^{-3} kg/m (1% difference to target), and a bending stiffness of 8.73×10^{-5}Nm^2 (79,941 Nm^2), 1.78 times higher than the target stiffness, which still gives a reasonably close shape to the shape of the riser if the correct bending stiffness was used, according to [18]. The outer diameter is close to the target diameter (3.54 mm).
To avoid confusion between Qualisys markers, as well as wasting an expensive ressource, the minimum number of Qualisys markers required to successfully determine the riser shape through interpolation was determined. Several curves (Figure 5) were traced, making different assumptions on the distances between 2 Qualisys markers, from 0.1 m to 0.5 m at reduced scale. The shape of the original curve can be determined well when using Qualisys markers spaced out by 0.20 m or less. The interpolation method used is Modified Akima ('makima" in Matlab).

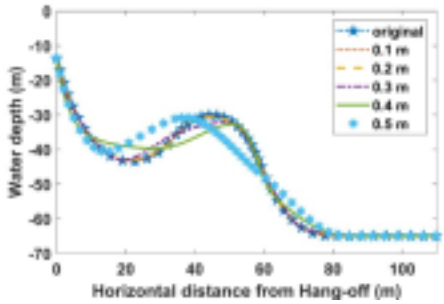


Figure 5 Interpolated shape of riser depending on the distance between two points where the position of the riser is indicated. The distance between the Qualisys markers is indicated at reduced scale, whereas the shape of the riser is shown at full scale. "original" designates the actual shape of the riser, whereas "0.x m" designates the curve that one would obtain if the Qualisys markers are spaced out by x dm at reduced scale in the wave tank.

Fishing poppers were combined with M5 nylon locking nuts to get close to the target properties of the buoyancy modules. Qualisys markers added to the riser for motion tracking were also combined with M5 nylon locking nuts, to get a submerged weight close to 0. Some errors were made on the exact weights and volumes of the fishing poppers and the Qualisys markers, in addition to the draft of the platform being larger than planned, which added up made the lazy wave shape sit lower in the water than planned. This was corrected by adding 3 additional fishing poppers onto the buoyant section. The properties of the components are indicated in Table 6. Figure 6 shows the actual shape of the riser

determined through the positions of the Qualisys markers in the laboratory compared to the shape predicted by MoorDyn using the properties for the actual riser in the laboratory, as well as the target shape at full scale.

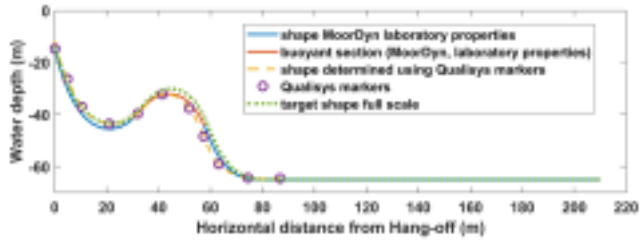


Figure 6 Comparison between static shape predicted by MoorDyn for riser used in the lab and shape of riser determined from underwater camera measurements, as well as target shape at full scale.

Table 6 Values for materials used (corrected values determined after experiments)

Property	Value at reduced scale	Value at full scale	Target
Volume of popper (m^3)	2.72×10^{-6}	0.649	0.656
Weight of popper (kg)	6.22×10^{-4}kg	148.15	466
Weight of M5 Nylon locking nut (kg)	1.35×10^{-3}		
Weight of M5 Nylon locking nut and popper (kg)	0.0020	470	466
Volume of M5 Nylon locking nut (m^3)	1.70×10^{-7}		
Volume of M5 Nylon locking nut and popper	2.90×10^{-6}	0.690	0.656
Submerged weight (kg)	-9.23×10^{-4}	-220	-206
Weight of one Qualisys marker (kg)	3.1×10^{-3}	738.82	
Volume of one Qualisys marker (m^3)	3.34×10^{-6}	0.795	
Weight of one Qualisys marker and one M5 Nylon locking nut (kg)	4.3×10^{-3}	1024	
Volume of one Qualisys marker and one M5 Nylon locking nut (m^3)	3.51×10^{-6}	0.837	
Submerged weight of one Qualisys marker (kg)	-2.36×10^{-4}	-56	
Submerged weight of one Qualisys marker and one M5 Nylon locking nut	7.89×10^{-4}	188	0

Three different set-ups were investigated, two different distances between the hang-off point and the attachment point on the seabed corresponding to 210 m and 200 m at full size, and for a distance of 200 m, one of the poppers which had been added to correct the water depth of the hog bend was taken off again, and further measurements were carried out.

3. Results

Highest values for surge, pitch and front mooring loads from the 6 sets of 3-hour long storm conditions were compared to the values determined for MLER and CMLER (constrained MLER) waves. Figure 7 shows those values for front mooring loads and surge. There was good agreement between the values for the front mooring loads, with an average of the maxima for storm conditions situated at about 37.7 N at reduced scale (~9000 kN), the maximum value for the MLER wave at 36 N, and the average of the CMLER waves at 38.6 N. For surge, the mean of maxima for the full storm conditions is 0.34 m at reduced scale (21 m at full scale), the maximum for the MLER wave is 0.33 m and the average of the maxima for the CMLER waves is at 0.37 m, which shows relatively good prediction by short design waves as well. For pitch, MLER and CMLER waves underpredicted the average highest pitch from the storms, with a maximum value below 1º for the MLER wave and an average of maxima of CMLER at around 1.8º, whereas the average of maxima for full storms is slightly above 2.5º. This could be due to the fact that wind was not included and that wind typically drives the extreme pitch response.

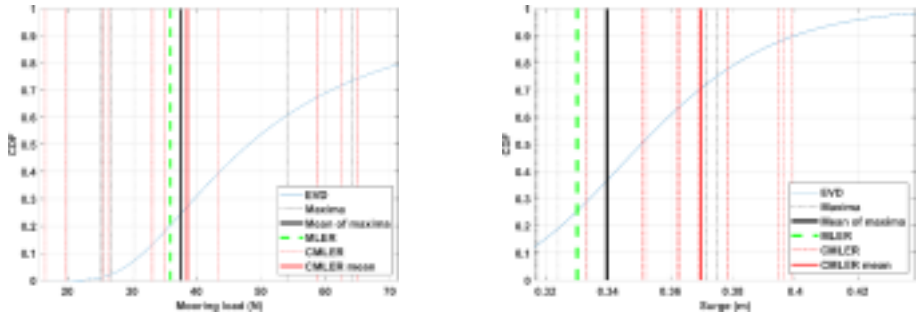


Figure 7 Comparison between maxima from full storm conditions, and values obtained from MLER or CMLER waves for front mooring loads and surge, at reduced scale. CDF: Cumulative Distribution Function. EVD: Extreme Value Distribution.

The 2 moments where the radius was lowest for each of 6 sets (5 sets only were analyzed for the distance of 210 m, due to issue in recorded data) of 3 hours of storm were determined for 3 different locations along the riser. Figure 8 shows superimposed curves for timelines of waves, front mooring loads, surge, and radius fluctuations 15 s before and 15 s after the moment when the radius is lowest, as well as the average of those curves at the hog bend. It can be observed that around the moment when this lowest radius occurs, the profile both of the incoming waves as well as the fluctuations of the riser are similar, which can be seen when tracing the average of all profiles. Similar observations can be made at the sag bend and at the bend near the seabed. From this, it can be intuited that there is a typical wave profile which would induce lowest radius for the sag bend, hog bend, or the bend near the seabed. The use of short design waves during tank experiments could replace running long duration runs corresponding to 6 sets of 3-hour storms.
The timelines for the front mooring loads and surge were also traced, to be able to observe the impact of important surge or the relation to front mooring loads. A typical average pattern can be observed for surge, but there are also some curves which do not fit this typical pattern. For the front mooring loads, a typical pattern can also be observed, again with some cases deviating from this pattern. Additional observations on cause and effect are expected to be observed when tracing heave and pitch, which is intended to be investigated at a later point.

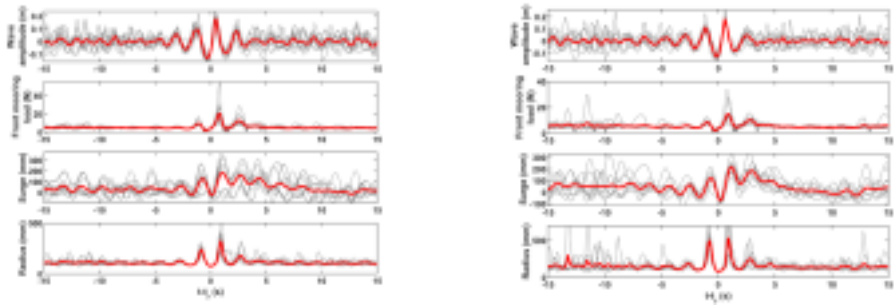


Figure 8 Timelines around moments when radius of hog bend is lowest during a storm. Left: 200 m. Right: 210 m. Thin grey lines are each one of a total of 12 timelines. Thick red line is the average of the individual timelines. t_r is the moment when the radius is determined to be lowest.

Table 7 shows the lowest radius determined at the hog bend for each sea state investigated. The hog bend experiences the lowest values for the bending radius. The lowest bending radius observed in storms is only slightly below the one observed for a short design wave for surge. When a short design wave for the front mooring load is applied, the lowest radius is still fairly low, but not as close to the one observed during storm as when using the short design wave for surge. It is expected that when determining a short design wave for the lowest radius, this would allow getting even closer to the one observed for storm conditions.

Table 7 Lowest radius in m at full scale determined for hog bend for each experimental set-up and type of waves

Experimental set-up	210 m between hang-off point and attachment on seabed	200 m between hang-off point and attachment on seabed	200 m between hang-off point and attachment on seabed, one less fishing popper
Operational sea state	7.0	6.0	
Storm (lowest)	4.8	4.4	4.7
Storm (average of 2 lowest of each storm)	5.0	4.6	4.8
MLER Surge	5.0	4.6	
MLER FTF	5.2	4.5	

It can be seen that for a distance of 210 m, bending is less extreme for the 3 locations investigated, than for the distance of 200 m. However, wind was not used and could create even higher surge. Tension was not measured, and is expected to be higher for 210 m. For a distance of 200 m, having the buoyant section hang lower (when taking away one of the fishing poppers) seems to lead to a higher lowest radius at the sag and the hog bend, to be confirmed by doing a full set of storm measurements (only one set was applied).
Another point to take into consideration when deciding on the best set up is the bending at the point of attachment. At full scale, a bend stiffener keeps the riser from experiencing extreme bending. This was not represented at reduced scale, so the riser was able to move more freely. In certain cases of extreme surge, the angle that the riser made when compared to the vertical axis of the platform became quite important, about 70º (This did not show up as an extremely low radius, as there were no Qualisys markers closer than 20 cm to the attachment point on the platform, and bending occurred very close to the attachment point). This angle was most extreme for the distance of 210 m. The value of this angle is something to be investigated further, and it should be considered that reducing the motion of the riser near the attachment point would affect the motions of the riser further along the length of the riser.

4. Conclusion

For the riser investigated in the laboratory, the radius consistently stayed above the minimum bending radius of 1.87 m at the hog bend, with the lowest value determined to be 4.4 m, obtained in an extreme storm, expected to occur every 50 years only in the Celtic Sea. The riser being aligned with the direction of the waves, it was exposed to maximum motion in a 2D plane. Waves could be arriving from various directions. The effect of the riser moving out of the plane has not been investigated here. Wind, expected to increase surge, should be included in future experiments. The installation of a load cell at the attachment point of the riser would allow determining extreme values for tension. Replicating the presence of a bend stiffener would be ideal to obtain motions closer to what the riser is expected to have at full scale. The experimental set-up indicates that it is possible to find materials to represent the riser and the buoyancy modules at reduced scale which give a static shape close to the target at full scale. For further improvement of confidence in the results, the riser could be retested with the correct submerged weight for the Qualisys markers (close to 0), as well as compared to dynamic simulations in MoorDyn or Orcaflex. The spacing of 20 cm between the Qualisys markers was a good distance. The markers allowed interpolation for subsequent tracing of the shape of the riser at each time step, and were not confused by the underwater motion tracking Qualisys cameras. Concerning the use of short design waves for faster prediction of extreme responses, this methodology worked well for surge and the front mooring loads of the platform, a little less well for pitch, expected to be different if wind loading is included. Being able to obtain a typical wave shape producing the same lowest radius as obtained during full storm measurements is a next step.

Acknowledgements

Funding came from the EPSRC-funded project EP/W003732/1, the R&D Solutions Fund by Enterprise Solutions from the University of Plymouth, the Supergen ORE ECR fund, the EPSRC IAA of the University of Plymouth, and GW Shift. The Ocean Basin of the COAST Laboratory of the University of Plymouth was used. We thank GMD Eurotool for the manufacture of the aluminum structure of the platform, Dr Kieran Monk for the assembly of the platform and the experimental setup, Dr Jeremy Clark for assistance in determining the mechanical properties of the flexible riser and Dr Anna Holcombe for advice on scaling the riser.

References

[1] Spyroudi, A., D. Wallace, K. Stefaniak, et al.: 'Offshore wind and hydrogen - Solving the integration challenge', ORE Catapult, 2020
[2] Guichard, J., R. Rawlinson-Smith, D. Coles, and D. Greaves: 'Decision-making tool for onshore vs. offshore hydrogen production from offshore wind', International Journal of Hydrogen Energy, 2026, 218, pp. 153966
[3] Caine, D., M. Iliffe, K. Kinsella, et al.: 'Dolphyn Hydrogen: Phase 1 - Final Report', Environmental Resources Management, Department for Business, Energy and Industrial Strategy, 2019
[4] Dolphyn Hydrogen: 'Producing Ultra Low Carbon Hydrogen Economically and at Scale', https://www.dolphynhydrogen.com/
[5] Ahmad, I.B., A. Schnepf, and M.C. Ong: 'An optimisation methodology for suspended inter-array power cable configurations between two floating offshore wind turbines', Ocean Engineering, 2023, 278, pp. 114406
[6] Hung, Y.-C. and R.-Y. Yang: 'Experimental and Numerical Study on Suitable Configuration of Dynamical Power Cable Connected to Floating Substation in Shallow Water', 2023
[7] Holcombe, A., S. Brown, S. Cheng, et al.: 'Experimental-numerical model comparison of a dynamic power cable for a floating offshore wind turbine', Ocean Engineering, 2024
[8] Somoano, M., D. Blanco, A. Rodríguez-Luis, and R. Guanche: 'Experimental Analysis of Mooring and Power Cable Dynamics When Using Elastic String Models', 2022,
[9] Moideen, R., V. Venugopal, J.R. Chaplin, and A.G.L. Borthwick: 'VIV-induced strain on a lazy wave dynamic marine power cable in a steady current', Ocean Engineering, 2025, 328, pp. 121081
[10] Adegeest L. J, M.: 'Use of Non-Linear Sea-Loads Simulations in Design of Ships', Proc. 7th PRADS, 1998, 1998
[11] Quon, E., A. Platt, Y.-H. Yu, and M. Lawson: 'Application of the Most Likely Extreme Response Method for Wave Energy Converters', 2016,
[12] Tosdevin, T., S. Jin, A. Caio, et al.: 'Extreme responses of a hinged raft type wave energy convertor', in *Proceedings of the European Wave and Tidal Energy Conference,* 2021,
[13] Tosdevin, T., S. Brown, F. Fàbregas Flavià, et al.: 'On the development and application of short design events for the prediction of extreme responses of floating offshore wind turbines', Ocean Engineering, 2025, 327, pp. 120929
[14] National Renewable Energy Laboratory: 'MoorDyn references', https://moordyn.readthedocs.io/en/latest/references.html#id2, 2024
[15] National Renewable Energy Laboratory and National Technology & Engineering Solutions of Sandia, L.N.: 'WEC-Sim', https://wec-sim.github.io/WEC-Sim/main/index.html, 2022
[16] The Crown Estate: 'Floating Offshore Wind Leasing Round 5 - Project Development Areas', https://www.thecrownestate.co.uk/our-business/marine/project-development-areas
[17] Hall, M.: 'Generalized Quasi-Static Mooring System Modeling with Analytic Jacobians', Energies, 2024, 17, (13), pp. 3155
[18] Holcombe, A., M. Hann, S. Brown, et al.: 'Sensitivity of small-scale global models of dynamic power cables to model material properties'. 2024

10th International Conference on HYDROELASTICITY IN MARINE TECHNOLOGY
Trondheim, Norway, June 16th-18th, 2026

On Wave Load Mapping for Substructure Strength Assessment of FOWTs

Zhiyuan, P. [*], Wenzhe Z , Alexandre A., Won-Ho, L. and Caiwei S.

DNV, Høvik, Norway ([*]peter.pan@dnv.com)

Abstract. In recent years, the development of floating offshore wind turbines (FOWTs) has brought challenges to the existing methodologies and software tools for the strength assessment of the floating substructures. First, the traditional frequency domain approach, which has been widely used in applied for the oil and gas offshore industry, is considered insufficient for FOWTs, as the nonlinear loads and responses are not well captured. Second, the elastic-response of the structure become of primary concern as the dimension of the FOWTs continue to grow and the need for less material, the vibration frequencies of the blades may be coupled with the responses of the substructure. Considering this, there has been a major effort to extend the capabilities of SESAM package, long established in offshore structural designs, to address these challenges and meet the advanced analysis requirements for the analyses and design of FOWTs.

A fully coupled analysis of the floating system, including the floater, tower, blades, and mooring system using a detailed structural finite element model is computationally demanding. Therefore, structural design analyses still need to be divided into two phases. In the first phase, the radiation and diffraction wave loads are mapped to the substructure represented by a simplified beam model, and a coupled analysis is carried out. In the second phase, the resulting dynamic responses are transferred into a FE analysis model with the same wave loads applied. Two key questions arising from this workflow. Firstly, if the structural elasticity is of concern, should radiation-induced added mass, damping matrices, and wave excitation forces be applied to the piece-wise sub-bodies for the substructure? Secondly, is the Distributed Potential Theory (DPT) approach applied to a single body sufficient for the radiation loads, or should hydrodynamic interactions due to the flexible motions of the substructure be included? The study with the intention to answer these questions is described in this paper, with a particular focus on the dynamic responses of motions and beam forces from the coupled analysis.

Key words: *Floating wind; Platform flexibility; Distributed hydrodynamic loads; Coupled analysis*

1. Introduction

As floating offshore wind turbine (FOWT) platforms scale towards 20+ MW and beyond, the structural flexibility of the floating substructure is becoming an increasingly important consideration in design. The primary driver is not hydroelasticity excitation - hydrodynamic loads on the flexibility modes of a semi-submersible remain small relative to first-order rigid-body wave loads — but rather the dynamic response of the floater to aerodynamic and turbine loads transmitted through the tower base. As platform dimensions grow, the natural frequencies of the lowest floater bending modes approach the rotor excitation frequencies, making the rigid substructure assumption progressively less tenable. Accounting for this flexibility in global coupled analysis requires that each structural segment of the floater carries

* Correspondence to: peter.pan@dnv.com

its own distributed hydrodynamic loading, rather than a single lumped load at the hull-tower interface. This raises a fundamental question: how should hydrodynamic loading be distributed across segments, and what level of accuracy is achievable with practical approaches?

Three broad approaches exist for computing distributed hydrodynamic loads on a segmented floater. The first - fully coupled hydroelastic analysis using generalized modes within a boundary element method (BEM) solver such WADAM [1] - is theoretically rigorous, fully resolving the radiation and diffraction interaction between deformation modes. However, this approach is currently not supported in the coupled aero-hydro-servo-elastic simulation tools used for FOWT design load case analysis, limiting its applicability in an industrial context. The second family uses modal or component mode synthesis (CMS) reduced-order structural representations, such as the Craig-Bampton substructuring method or the equivalent spring-mass formulation of Kim et al. [2] within coupled time-domain tools; these retain the single-body BEM and therefore make no explicit treatment of inter-segment hydrodynamic interaction. However, they present some limitations regarding the sectional loads sometimes required in the analysis, as well as need to have a FEM model of the platform at early stages of design. The third and most accessible approach is the segmented single-body BEM: the hydrodynamic pressure from a conventional single-body BEM analysis is decomposed by integrating panel pressures over subsets of the wetted surface, yielding a 6×6 coefficient matrix per segment. Luan et al. [3] [4] applied this method to a braceless semi-submersible to derive time-domain sectional loads; Alexandre et al. [5] adopted a similar methodology within Bladed, describing the simplification as expected to be valid for many platform types. Neither study, however, validated the approach against a multi-body BEM in which the hydrodynamic interaction between segments is fully resolved. The magnitude of the error introduced by neglecting this interaction — and the conditions under which it may be considered acceptable — remain unknown. IEA Wind Task 56 (OC7) Phase II, currently underway, has identified the validation of member-level hydrodynamic loads and floater flexibility effects as a priority for the international community [6].

This paper addresses this gap by presenting a direct comparison of the segmented single-body BEM and a full multi-body BEM - in which each structural segment is a separate hydrodynamic body with fully resolved inter-segment radiation and diffraction interaction - for a representative semi-submersible FOWT in time-domain coupled analysis. In addition to quantifying the error associated with the simpler approach, the paper provides practical guidance on how the segmented hydrodynamic analysis should be set up correctly, including the treatment of reference point consistency in the assembly of per-segment coefficient matrices. The results contribute directly to the broader question of how hydrodynamic models should be constructed when floater flexibility is included in FOWT design. The paper is organized as follows: Section 2 describes the structural model and coupled analysis framework; Section 3 presents the case study used here; Section 4 describes the hydrodynamic modelling and Section 5 presents and discusses the comparative results; and Section 6 draws conclusions.

2. Structural modelling and coupled analysis framework

Coupled analysis is employed to capture the interactions among the floating platform, mooring system, wind turbine, and environmental loads in the time domain. The coupled simulations are performed using multibody-based analysis tools, with the possibility of including flexible structural components, normally represented by beam elements. This modelling strategy is computationally efficient and well suited to engineering-level analyses. The overall system is divided into several subsystems to which aerodynamic and hydrodynamic loads are applied. Each subsystem has its own structural module for computing its structural response. For a wind turbine, these subsystems typically include the blades, drivetrain, tower, floating substructure, and mooring lines. The subsystems are then assembled within a multibody model, where appropriate boundary conditions are applied to solve the response of the complete system. Time-domain simulation tools are required for FOWTs because of the nonlinear control actions involved. Aerodynamic loading is typically computed using Blade Element Theory combined with engineering correction models, while hydrodynamic loads can be obtained from

boundary element methods and Morison-type loading on beam elements. Several commercial tools are available for this type of analysis, for example SIMA [9], Bladed [10], and OrcaFlex [11]. Further details on the theoretical formulations implemented in these tools can be found in their respective manuals.

In this work, SIMA is used as the coupled analysis software. Its structural finite element solver, RIFLEX, employs a nonlinear finite element formulation for slender structures in which beam elements are one of the available element types; both statically determinate and indeterminate configurations are supported. Further details are given in [9].

Most turbine system components—such as blades, towers, monopiles, and jackets—can be regarded as slender bodies and are therefore well represented using beam theory. Floating offshore wind turbine (FOWT) platforms, however, are relatively bulky structures whose structural design generally requires detailed finite element (FE) models developed separately from the coupled simulation model.

Because coupled analysis tools typically support only beam-element representations, an equivalent beam model of the platform is introduced. Although this approximation simplifies the structural description, it enables platform flexibility to be captured while maintaining compatibility with the multibody solver. Wave–structure interaction effects are then incorporated through hydrodynamic coefficients obtained from boundary element method (BEM) analyses.

Hydrodynamic loading

For rigid platform representations, hydrodynamic loads can be applied at a single reference point within the coupled analysis model. But when platform flexibility is considered, this simplification is no longer appropriate, as concentrated load application can lead to inaccurate local structural responses. Consequently, hydrodynamic loads are spatially distributed within the coupled analysis model.

The load distribution is achieved through a mapping procedure between the hydrodynamic model and the structural beam representation. Each hydrodynamic body is associated with a corresponding structural sub-body, which is modelled using two beam elements. Hydrodynamic forces and moments are transferred to the beam nodes of the sub-body, ensuring a consistent representation of distributed loading and structural deformation within the coupled analysis.

For a model where the platform is rigid the hydrodynamic loading can be defined in the following equation.

$$F_{hydro} = m_r(\infty)\,\ddot{x} + f_{hs}(t) + \int_{-\infty}^{t} k(t-\tau)\dot{x}\,(\tau)d\tau + f_e^{(1)} + f_{ext} \quad (1)$$

Where:

$m_r(\infty)$ is the added mass at infinite frequency
x is the displacement
$f_{hs}(t)$ is the hydrostatic force on the body
$k(t-\tau)$ is the retardation function
$f_e^{(1)}$ is the wave excitation force
f_{ext} is the external force acting on the platform (e.g. mooring lines)

When the platform is modelled with multiple hydrodynamic loading points, equation 1 needs to be adjusted such that the loading on each section is correctly computed. The modifications are on the radiation loads:

- When using the multibody variant: $m_{r_{i.j}}(\infty)$ and $k_{i,j}(t-\tau)$ where i,j are the degrees of freedom considered ($6\ N$) where N is the number of sub-bodies.

- When using the DPT: $m_{r_{i_n.j_n}}(\infty)$ and $k_{i_n,j_n}\ (t-\tau)$ where i_n, j_n are the degrees of freedom considered for each section.

Effectively the F_{hydro} will be computed and applied in the middle of the beams. This will lead to some local deformations, but the objective is to capture the global flexible behavior of the platform.

Coupled analysis model

The resultant structure for the example considered in this case study is illustrated in Figure 1. The hydrodynamic loading is applied to the seven bodies (shown in red), while the green beams represent the floating structure in the coupled analysis software used (SIMA). The hydrodynamic load is applied at the centre of each beam, and the internal loads at the beam interfaces are obtained as outputs of the computation. Other discretizations are also possible; in this case, the focus is primarily on the beam connections between the columns and the pontoons.

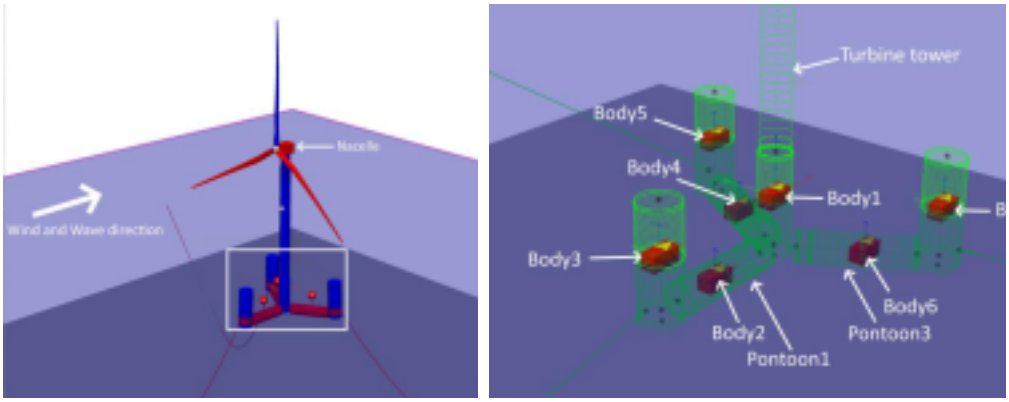


Figure 1: Platform modelling in Sima. Left – complete system modelled. Right – focus on platform.

3. FOWT definition and load cases

The VolturnUS-S semisubmersible structure that is made of four steel columns is used in this paper. Details of the substructure are reported by Allen et al [7]. The RNA specification is provided by Gaertner et al. [8]. A summary of key platform and mooring system properties is provided in Table 1.

Table 1: FOWT system main properties

Component	Value
Power rating	15 [MW]
Rotor diameter	241.9 [m]
Blade length	117.2 [m]
Hub height	149.8 [m]
RNA mass	945.8 [t]
Turbine mass	2412.4 [t]
Draft	20 [m]
Platform Column Height	35 [m]
Platform Column Diameter	12.5 [m]
Tower first bending moment	0.36 [Hz] – Original Stiffness 0.17 [Hz] – Reduced stiffness

This exercise used two platform stiffness values: the original, which resulted in a first tower bending frequency of about 0.36 Hz, and a less stiff model at approximately 0.17 Hz. The purpose was to study how increased platform deflections affect the response of the system, particularly the radiation forcing.

3.1 DLC conditions

Time domain analysis was conducted to assess how environmental conditions affect various parts of the turbine. The extreme idling scenario (DLC 6.1) was examined to determine whether wave loading could potentially trigger these platform modes. Table 2 presents the definition of this load case.

Table 2: Load case description (main parameters)

DLC	Operating conditions	Wind condition	Mean Wind Speed [m/s]	Wind dir. [°]	Hs [m]	Tp [s]	γ	Wave Dir. [°]
6.1	Idling	EWM 50yr	47.5	0	10.7	14.2	2.75	0

4. Hydrodynamic modelling

The substructure is divided into multiple bodies, connected by flexible beams in the coupled analysis in SIMA. The hydrodynamic coefficients for each body are obtained by using the frequency domain BEM tool WADAM. Two approaches to distribute hydrodynamic forces into each sub-body are examined. In the first one, the hydrodynamic coefficients are obtained from a conventional single body analysis. The hydrodynamic pressure is integrated over the wetted surface for each sub-body surrounded by a group of user defined cut planes, see Figure 2 where the wetted hull is divided by 6 cut planes into 7 sub-bodies, namely, 4 columns and 3 pontoons. The cut planes are perpendicular to the pontoons with distances of 11.48m and 45.5m from the geometry center of the floater.

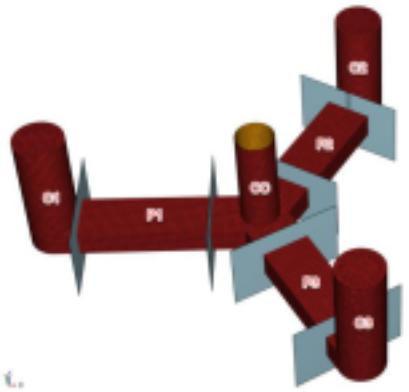


Figure 2: VolturnUS reference model, divided into 7 sub-bodies by 6 user defined cut planes.

In WADAM, the concept of cross-section, which is used to evaluate the sectional forces, is extended to define a sub-body. A cross-section involves a cut plane, defined by a refence point and the normal vector in parallel to one of the axes of the global coordinate system. The hydrodynamic forces are then integrated over the body up to such a cut plane from either side, with the resulting sectional forces referring to the same reference point on the cut plane. In comparison, a sub-body involves several surrounding cut planes, each of which with arbitrary orientation. The force reference point can be detached from these planes, up to the user's preference. With such an extension, the hydrodynamic

forces on any sub part of a floating can be obtained. The wave excitation forces, added mass and potential damping matrix on a sub-body can be converted to those in the format as if they are separated bodies. In this case, the force reference point could be preferred as the geometry center of the sub-body. The second approach involves multibody analysis with each sub-body of the wetted hull represented by a separate panel model. To match the first approach, the panel model shall be created with the origin located at the geometry center, namely the force reference point of the same sub-body in the first approach.

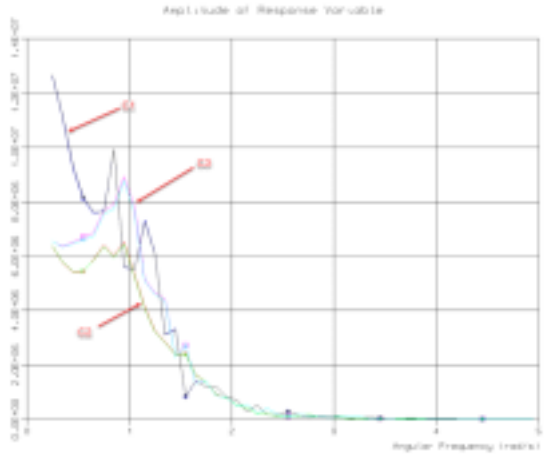


Figure 3: Pitch moment on each column C1, C2, C3, wave heading = 60 degree

As expected, the wave excitation forces acting on each sub-body for the two approaches are identical (Figure *3*). The figure shows 3 groups of curves representing the RAOs the pitch moments acting on each column. The two curves in each group are almost overlapping. This indicates the translation of forces for the sub-bodies in the single body analysis is in line with the handling of layout of bodies in the multibody analysis.

In comparison with the wave excitation forced from the diffraction problem, the added mass for each sub-body is quite different between the single body and multibody setups, as the boundary conditions are different. The total radiation force is larger when moving the entire body than the sum of forces moving each sub-part alone at a time, referring to Figure 4 for the added mass for each sub-body produced by running single and multibody analyses. In addition, it should be noted that the coupling between the sub-bodies can only be produced by running the multi-body analysis, the total size of added mass and potential damping matrix is $6N$ by $6N$, with N the number of bodies (or sub-bodies). The single body analysis only produced N times 6 by 6 matrices, which correspond to the diagonal band of those results from the multi-body runs.

The sub-body for pontoon P1 has zero surge pitch coupling from the multibody analysis, since all its panel elements are parallel to x axis and there is no pressure load due to its own vertical motions. However, non-zero added mass A51 can be found for the single body analysis, as the moment due to pressure loads are introduced by the motions of other parts of the body. Moreover, the added mass and potential damping matrices are generally not symmetrical as there are holes in all the sub-bodies where they are connected to their neighboring sub-bodies.

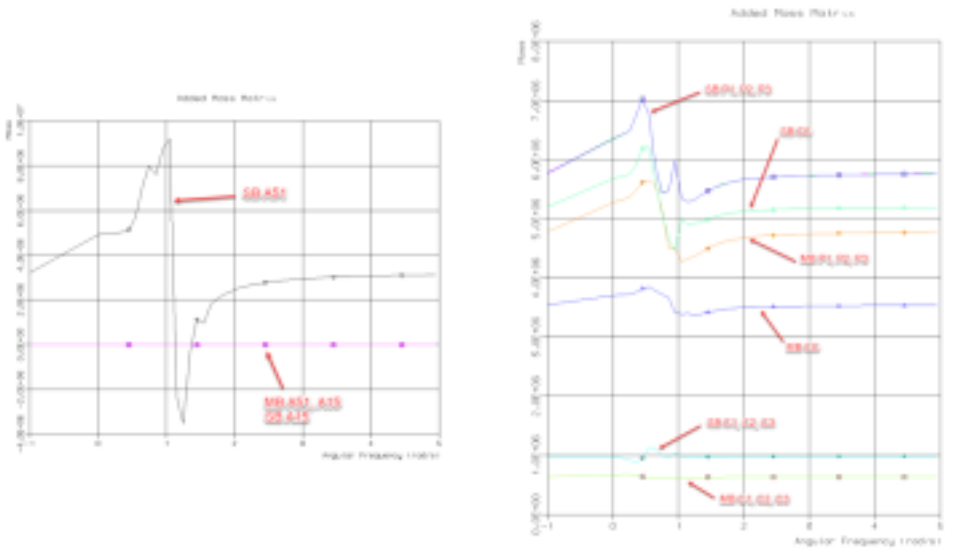


Figure 4: Left: Surge pitch coupling added mass A51, A15 for P1, SB: Single body analysis, MB: Multi-body analysis. Right: Heave added mass A33 for each sub-body. SB: Single body analysis, MB: Multi-body analysis

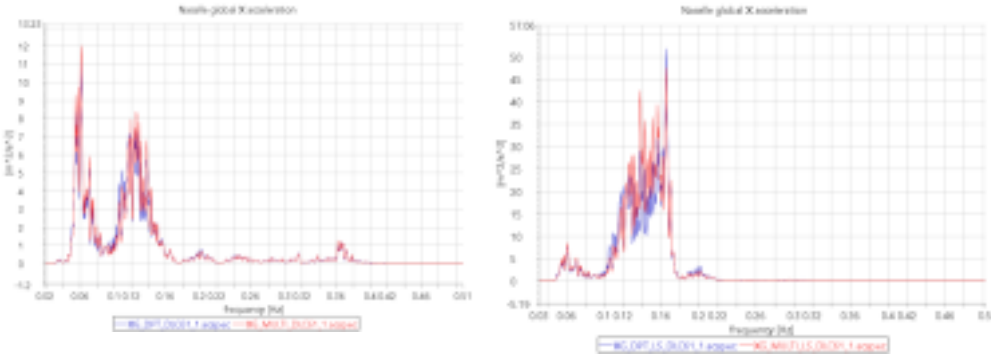
Nevertheless, in the coupled analysis, the sub-bodies are simulated by beams connected with nodes in the finite element code Riflex (part of SIMA). Therefore, the hydrodynamic coefficients from the single body analysis are only valid when the entire structure is moving as if they are a part of a single rigid body. When the floater is larger in size or the structural stiffness is smaller, the added mass and potential damping from the multi-body analysis could be preferred.

It should be noted that even though it is possible to include Morison elements in the coupled analysis models to include viscous effects, for this case study they were not considered.

5. Coupled simulations results

We conducted coupled analyses for the load case defined in Table 2 using two hydrodynamic loading approaches, and for both the original platform stiffness and a reduced-stiffness case. This allowed us to assess whether increased platform flexibility leads to differences in the predicted loading response.

First, the nacelle acceleration is compared for the different models in Figure 5. The first structural natural frequencies of the system can be identified at approximately 0.36 Hz and 0.17 Hz for the reference- and reduced-stiffness cases, respectively. However, the two modelling approaches produce similar nacelle acceleration responses, though the discrepancies is somewhat larger for the model with reduced structural stiffness.



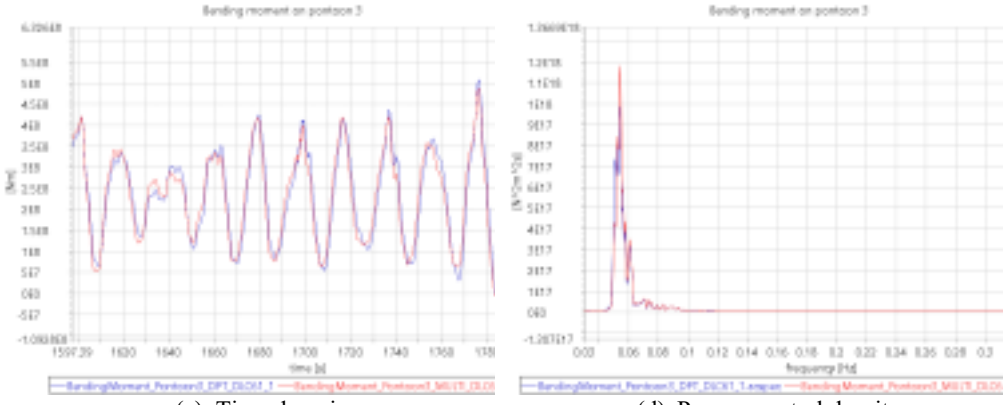
(a) Reference stiffness (b) Lower stiffness

Figure 5: Nacelle acceleration spectral power density for the two models. Results for multibody approach in Blue and DPT in Red.

We then focus on the bending moment and axial force acting on pontoon 1, as illustrated in Figure 6 and Figure 7. The total internal loads in the pontoons near the central tower are also very similar for the two modelling approaches. Only minor differences are observed near the peak frequencies, and the response around the first structural natural frequencies remains essentially unchanged.

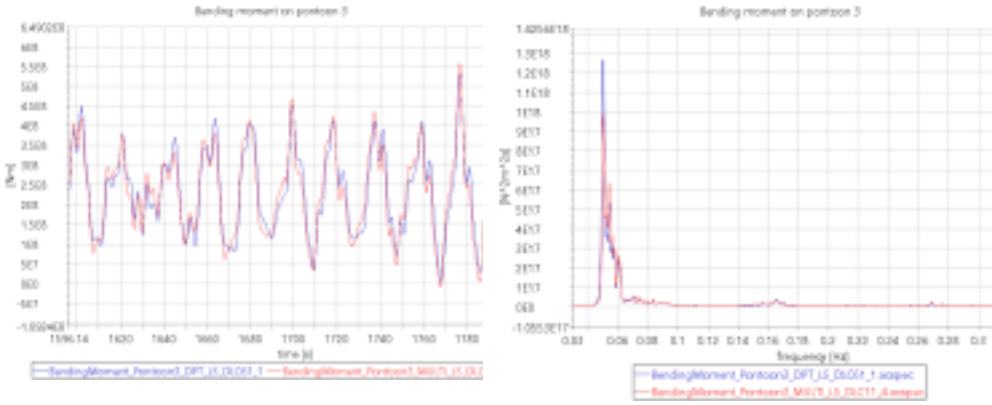
As discussed above, the different modelling approaches are expected to have a larger influence on radiation loading. A comparison of the total radiation load acting on pontoon 1 (Figure 8) shows a difference of approximately 16% between the DPT and multibody approaches. However, this difference has a relatively small effect on the overall system dynamics and internal loading, as illustrated in Figures 6 and 7.

To generalize these findings, further studies should examine other platform types and a wider range of operating conditions.



(c) Time domain (d) Power spectral density

Figure 6: Bending Moment of the pontoon 1, near the central column connection for reference stiffness case. Results for multibody approach in Blue and DPT in Red.



(e) Original model (f) Lower flexible model

Figure 7: Bending Moment of the pontoon 1, near the central column connection for the lower stiffness case. Results for multibody approach in Blue and DPT in Red.

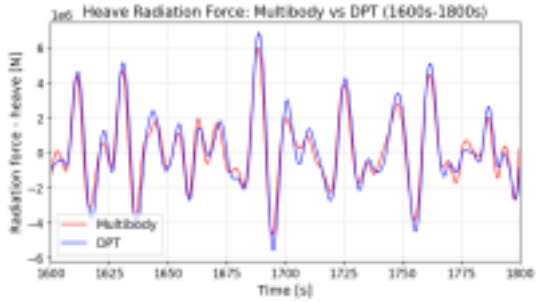


Figure 8: Heave radiation force. Results for multibody approach in Blue and DPT in Red.

6. Conclusions

This paper examined how to account for platform flexibility in coupled analyses. Two hydrodynamic modelling approaches were investigated for this purpose, namely a classical multibody approach and a segmented-model approach, in which the hydrodynamic properties of sub-bodies are derived from a single-body analysis. The latter approach was found to be more efficient for both boundary element method (BEM) analyses and coupled simulations – as the number of degrees of freedom to solve is smaller. However, differences remain in the way radiation loads are computed in the time domain for the two approaches. In the distributed property transfer (DPT) approach, radiation loads are calculated under the assumption that the entire structure moves as a rigid body. In contrast, in the pure multibody approach, only the panels associated with a given sub-body are displaced, while the remaining panels are held fixed. Despite these modelling differences, only small variations in platform internal loads were observed.

These differences become slightly more pronounced for cases involving more flexible structures; nevertheless, the overall impact on internal loading remains limited for the present case study.

Future work will extend the present study to other platform types and loading conditions. In addition, hybrid modelling strategies will be explored, for example by combining added mass obtained from multibody analyses with radiation damping derived from DPT bodies.

References

[1] Z. Pan, S. Zhang, and S. Fu, "Integrated hydrodynamic-structural analysis of flexible floating structures," *Ocean Engineering*, vol. 310, pt. 1, Art. no. 118644, 2024, doi:10.1016/j.oceaneng.2024.118644.

[2] Y. Kim, J. Lee, J. Kyoung, and J. Kim, "Equivalent spring-mass model for flexible floating offshore wind turbine platforms," *Journal of Marine Science and Application*, 2025, doi:10.1007/s11804-025-00758-6

[3] C. Luan, Z. Gao, and T. Moan, "Design and analysis of a braceless steel 5-MW semi-submersible wind turbine," *Proc. ASME 35th Int. Conf. on Ocean, Offshore and Arctic Engineering*, Busan, South Korea, 2016.

[4] C. Luan, Z. Gao, and T. Moan, "Development and verification of a time-domain approach for determining forces and moments in structural components of floaters with an application to floating wind turbines," *Marine Structures*, vol. 51, pp. 87–109, 2017.

[5] A. Alexandre, R. B. Urbano, J. Roadnight, and R. Harries, "Methodology for calculating floating offshore wind foundation internal loads using Bladed and a finite element analysis software," *Proc. ASME 37th Int. Conf. on Ocean, Offshore and Arctic Engineering (OMAE2018-78035)*, Madrid, Spain, 2018.

[6] L. Wang, A. Robertson, J. Jonkman, P. A. Berthelsen, and M. Thys, *OC7 Phase I definition document*, National Renewable Energy Laboratory Technical Report, 2025, doi:10.2172/2583478.

[7] C. Allen, A. Viscelli, H. Dagher, A. Goupee, E. Gaertner, N. Abbas, M. Hall, and G. Barter, Definition of the UMaine VolturnUS-S Reference Platform Developed for the IEA Wind 15-Megawatt Offshore Reference Wind Turbine, United States, 2020, doi:10.2172/1660012.

[8] E. Gaertner, J. Rinker, L. Sethuraman, F. Zahle, B. Anderson, G. E. Barter, N. J. Abbas, F. Meng, P. Bortolotti, W. Skrzypinski, G. N. Scott, R. Feil, H. Bredmose, K. Dykes, M. Shields, C. Allen, and A. Viselli, IEA Wind TCP Task 37: Definition of the IEA 15-Megawatt Offshore Reference Wind Turbine, National Renewable Energy Laboratory, United States, 2020, doi:10.2172/1603478.

[9] Sintef, Sima User Manual, https://sima.sintef.no/docs/5.0/riflex/index.html, accessed May 2026.

[10] DNV, Bladed user manual , https://mysoftware.dnv.com/download/public/renewables/bladed/documentation/index.html, accessed May 2026.

[11] Orcina, OrcaFlex user manual , https://www.orcina.com/webhelp/OrcaFlex/Default.htm, accessed May 2026.

10th International Conference on Hydroelasticity in Marine Technology
Trondheim, Norway, June16$^{\text{th}}$-18$^{\text{th}}$, 2026

Simulation of a SPAR-type deformable floater for offshore wind turbines: comparison with experimental and numerical data

*Claudine Halbout [1,2], Fabien Robaux [1], Titouan Ouvrard [1], Christophe Peyrard [1,2]

[1] EDF R&D, Chatou, France
[2] Saint-Venant Laboratory (LHSV), Chatou, France

Abstract. Structural integrity and design optimization are critical for Floating Offshore Wind Turbines (FOWT). Capturing structural deformation is essential for fatigue analysis and Ultimate Limit State (ULS) design, yet most academic work based on Hydro-Aero-Servo-Elastic (HASE) frameworks assume rigid floaters and focuses on other aspects of the multiphysic problem. Recent studies have begun addressing floater structural response. For instance, Hegseth et al. [1] validated distributed hydrodynamic load models in the modeling tool SIMA (Simulation of Marine operation) against hybrid tests of a semi-submersible and more recently, Jonkman et al. [2] extended OpenFAST with SubDyn-HydroDyn coupling for member-level load analysis. To advance this field, EDF R&D developed Turbine Emulator with Deformable DYnamics (TEDDY), integrated into the in-house HASE numerical model named DIEGO [3]. TEDDY couples the Chrono multibody dynamics library with hydrodynamic load models based on Morison's equation and weakly nonlinear potential-flow theory. This hydroelastic simulation approach yields valuable results for floater design, such as internal load distributions under hydrodynamic effects like radiation, diffraction, and added mass.

Few cases exist in the current literature to validate FOWT deformable models. Among these, we focus on the benchmark experiment conducted at Ecole Centrale de Nantes by Leroy et al. [4] along with its numerical modeling with SIMA (Ran et al. [5]). This benchmark investigated the hydroelastic behavior of a scaled spar-type FOWT under controlled wave conditions. We here present the numerical reproduction of this case with TEDDY, modeling the SPAR's elastic response during free-decay tests and regular wave scenarios, serving as further validation of TEDDY implementation.

The comparison focused on natural periods and Response Amplitude Operator (RAO) for surge, heave, pitch, strain, and tower base bending moments. Good agreement is found with experimental and numerical results, accurately predicting motions and internal loads. Additional tests under irregular wave conditions confirmed this consistency, validating the deformable-body approach for capturing hydroelastic effects.

Key words: *Hydroelasticity, internal loads, potential flow, validation, wave structure interaction*

1. Introduction

The European objective to increase offshore wind production by 45% by 2030 [6] has accelerated the deployment of numerous FOWT projects. As turbine ratings continue to rise, reaching up to 26 MW in recent developments, the structural design of floating platforms becomes increasingly critical. Reducing Levelized Cost of Energy (LCOE) while maintaining safety requires better prediction of fatigue damage, strains, and stresses within the floater. These aspects are often assessed outside fully integrated HASE models, introducing approximations when treating the floater as a rigid body.

To improve numerical capabilities, EDF R&D has developed TEDDY, a hydroelastic simulation tool integrated into the DIEGO framework which is a HASE model, able to simulate the coupled dynamics

*Correspondence to: claudine.halbout@edf.fr

of FOWT supporting hydrodynamic loading through Morison's equation, potential-flow from Boundary Element Method (BEM) solvers, or a combination of both to include drag and diffraction–radiation effects [3]. TEDDY couples DIEGO and the Chrono multibody solver [7, 8, 9], it allows to compute internal loads and to address relevant hydrodynamic issues for floater design.

This study evaluates TEDDY against one of the few hydroelastic benchmarks available: the flexible spar tested at Ecole Centrale de Nantes [4], whose numerical reproduction using SIMA was presented by Ran et al. [5]. This benchmark provides an extended evaluation of TEDDY in its ability to reproduce natural periods, decay responses, RAOs, strain measurements, and tower-base bending moments. The current work begins by validating the hydroelastic modeling strategy developed for the SPAR platform, focusing on its capability to capture internal forces, structural deformation, and natural modes. It then compares numerical predictions with experimental data under various environmental loading conditions, highlighting differences between potential-flow and Morison-based hydrodynamic approaches and presenting an illustrative example of the resulting RAO. Finally, preliminary results for the SPAR subjected to an irregular sea state are introduced and discussed.

2. Description of the numerical and experimental models

2.1. Presentation of TEDDY

As presented in the Section 1., TEDDY results from coupling the DIEGO library with the external Project:Chrono framework. This integration enables hydroelastic simulations of floating structures by incorporating the deformable-body dynamics provided by Chrono [8, 9]. This open-source multiphysics simulation library particularly is well suited for modeling systems undergoing large deformations and large-amplitude motions. It has been successfully used in combination with solvers such as REEF3D, a Computational Fluid Dynamics (CFD) tool [7], and QBlade [10].

TEDDY underwent a detailed verification process assessing its ability to reproduce natural modes and wave loading applied to submerged structural segments through code to code comparison. The focus of this paper is the comparison of the most recent version of the code with a complex experimental campaign. The objective is to replicate the results obtained by the authors of the original study conducted at Ecole Centrale de Nantes [4]. This campaign examines a scaled SPAR-type platform specifically designed to investigate internal forces and strain responses.

2.2. Experimental benchmark

The campaign presented by Leroy et al. [4] used a 1:40 Froude-scaled flexible SPAR composed of an aluminum backbone and six lightweight floaters. The campaign included free-decay tests, hammer tests, and regular and irregular wave conditions, with measurements of motions, strains, and tower-base bending moments. In parallel, Ran et al. [5] developed four numerical models in SIMA (potential-flow and Morison, each in rigid and flexible versions). Their results showed that the flexible potential-flow model provided the best agreement with experiments, highlighting the importance of structural flexibility and appropriate hydrodynamic modeling.

2.3. Numerical model in TEDDY

A full-scale numerical model of the SPAR described in [5] is built and presented in Figure 1. Froude similarity is preserved to retain gravity-driven effects. Viscous effects are expected to remain small compared to inertia and radiation loads.

In the experiment, five rigid bodies are used to represent the main floater and ballast components. Thus the numerical model copies that while the central backbone is represented as a deformable Euler–Bernoulli beam. These rigid solids are attached to selected Finite Element Analysis (FEA) nodes, where the hydrodynamic loads computed by the BEM solver Nemoh [11] are applied. Although Floater 3

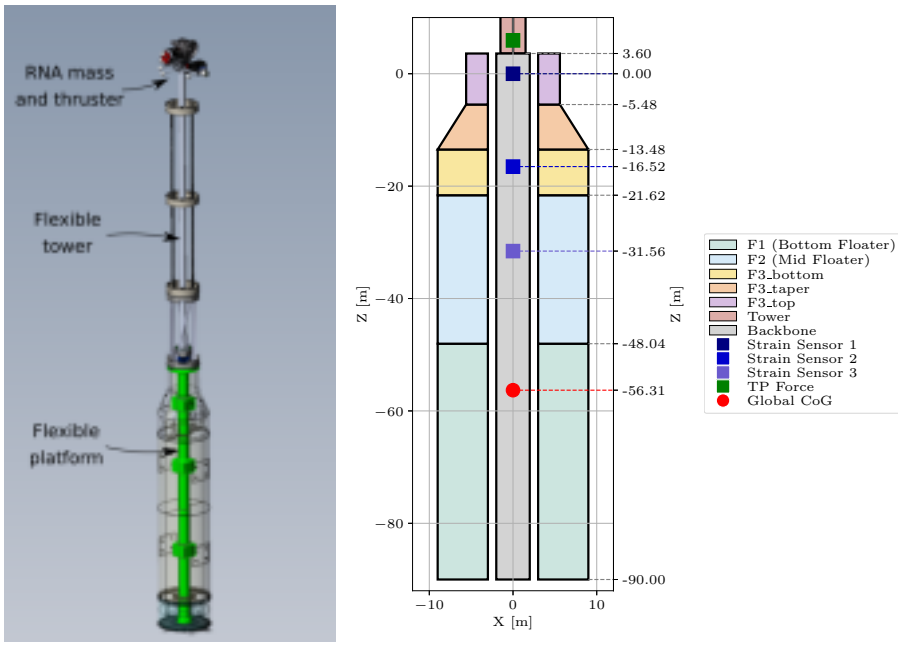


Figure 1 SPAR description from Leroy et al. [4] (left) and numerical representation (right).

is split into three elements in the Nemoh mesh, it is treated as a single rigid body in TEDDY to remain consistent with the physical setup. Mass properties are taken directly from the experimental publications and associated databases. The tower, approximately 90 m in length, is modeled as a uniform circular Euler beam of 2.4 m diameter, with the TP, nacelle, cables, and junction boxes represented as lumped masses. The combined RNA, tower, and TP mass is 2113 t, with a Center Of Gravity (CoG) located at $z = 53.02$ m. The backbone itself has a diameter of 4 m and a wall thickness of 0.2 m. Four additional rigid bodies are included to model the floaters and ballast, with their inertias computed analytically based on truncated cylindrical geometries.

To enable comparison with the work of Ran et al. [5], two hydrodynamic configurations are implemented. In the Morison-based model, each beam element is assigned a hydrodynamic diameter equal to the outer diameter of the SPAR. Radiation effects are not represented within the Morison formulation. Instead, a frequency dependent added mass is introduced based on the radiation matrix obtained with Nemoh at the pulsation $\omega = 0$ rd/s. In the potential-flow model, the full diffraction–radiation solution provided by Nemoh is used.

For both configurations, a Morison-type drag term is added to account for viscous damping, with a constant horizontal drag coefficient calibrated from the free-decay tests and applied to the backbone. The viscous effects are represented through a drag disk based on the bottom of the Floater 1, at the structure base. The final drag parameters adopted in this study are $C_{Dz} = 0.8$ and $C_{Dx} = 0.4$.

3. Results and comparison with experiments

3.1. Hammer test and tower frequency

The tower natural frequency is extracted from the Fourier transform of the nacelle horizontal acceleration, following the approach in the numerical campaign [5]. The unmodified model yields a period of 2.71 s, *i.e.* 4.6% higher than the experimental value. Ran et al. [5] also reported an underestimation

of the natural frequency and fixed it by increasing the young modulus by 5%.

In our case, slightly increasing the stiffness reduces the error to about 3%. Remaining differences may stem from coarse time discretization (0.1 s) and uncertainties in lumped-mass distribution (cables, boxes, load cells). To maintain coherence in the modeling approach, the original tower properties are retained. This choice must be kept in mind when interpreting the frequency-domain results.

3.2. Decay tests

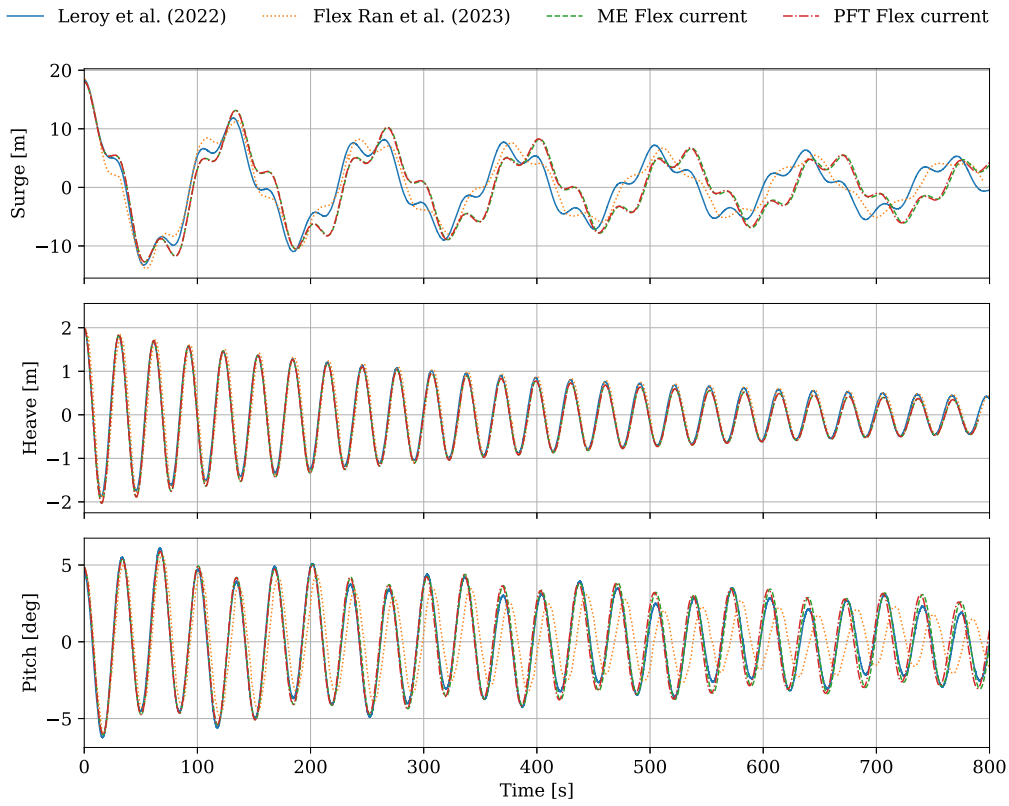


Figure 2 Simulated decay motions in surge, heave, and pitch.

Heave decay is generated by applying an external vertical force until a 2 m displacement is reached with nearly zero velocity. Surge and pitch decays follow the experimental procedure: horizontal forces are ramped at the fairlead and nacelle, respectively, then maintained constant for the floater to settle at the target position, and finally released to initiate free decay. In the following, the two numerical models are referred to as PFT for the potential-flow model and ME for the Morison-based model. Figure 2 shows a good agreement between simulations and experiments in heave and pitch, both in frequency and decay rate. Indeed, the obtained periods in Table 1 matches almost perfectly the natural period observed in the experiments for heave and pitch motions. The surge period, however, exhibits a slightly larger deviation, consistent with the observations made by Ran et al. [5]. The surge response is sensitive to both mooring properties and mass distribution due to strong surge–pitch coupling, which explains the

remaining discrepancy.

Table 1 Comparison of natural periods between numerical and experimental results

	Surge (s)		**Heave (s)**		**Pitch (s)**	
Case	Period	Dis. (%)	Period	Dis. (%)	Period	Dis. (%)
Exp. Leroy et al. 2022	128.0	–	30.70	–	33.70	–
ME Flex current	133.8	-4.53	30.71	-0.03	33.68	0.06
PFT Flex current	133.6	-4.37	30.70	0.0	33.59	0.3
PFT Flex Ran et al. 2023	128.73	0.6	30.67	-0.1	34.09	1.2

3.3. Regular wave tests

The model is subjected to the same regular wave conditions as in the experimental campaign. Time series of wave elevation, motions, strain, and tower-base moment were compared across all numerical configurations. The potential-flow model provides the most realistic reproduction and is therefore the one discussed here. Simulations show good agreement with experiments across all tested periods at a wave steepness of $H/\lambda = 2\%$. Figure 3 presents the resulting RAOs, which reproduce the experimental trends well, including for the strain measured at sensor 2 (see Figure 1). The tower-base moment amplitude is slightly overestimated (approximately 5%) over the full range of periods, likely due to uncertainties in the representation of the relatively heavy load cell and its exact mass location. The predicted strain response closely matches experimental measurements throughout the tested wave range, supporting the validity of the hydroelastic modeling approach.

3.4. First investigations on irregular wave tests

A first set of investigations examines the model under the irregular wave conditions listed in Table 2 and compares the numerical predictions to the experimental measurements, using the potential-flow model for the reasons discussed in Section 3.3.

Table 2 Irregular sea states used for the model tests.

Sea State	SS1	SS2	SS3	SS4	SS5	SS6	SS7	SS8
$\mathbf{T_p}$ **(s)**	5	6	6.5	8	10	13.4	13.8	13.83
$\mathbf{H_s}$ **(m)**	3	1.5	1.5	3.0	4.0	8.9	9.4	10.9

To replicate the experimental conditions, the numerical wave elevation was generated from a spectrum obtained via Fast Fourier Transform (FFT) of the experimental wave time series. Because the BEM solver Nemoh used for the selected model operates over a specific frequency range, the spectrum was truncated accordingly, removing only high-frequency components. The removed portion represented less than 1.5% of the total energy and the resulting change in significant wave height H_s remained below 1%. A natural extension of this work would be to recompute the hydrodynamic coefficients over a wider frequency range, eliminating the need for truncation.

After verifying that the reconstructed numerical wave field reproduced the experimental input with sufficient accuracy, numerical simulations were performed over the same experimental measurements.

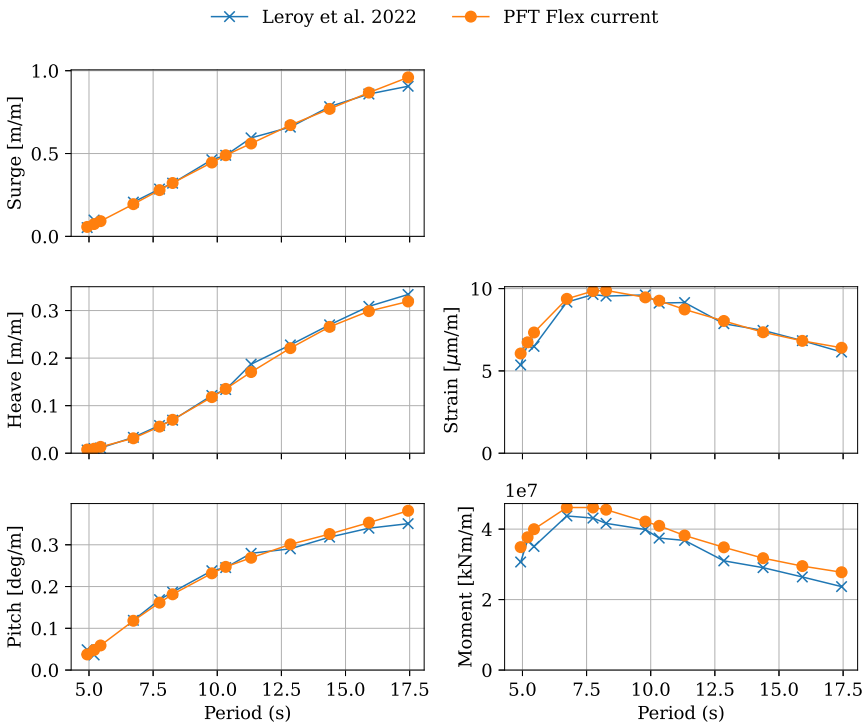


Figure 3 Response amplitude operators for $H/\lambda = 2\%$.

Across all tests, the reconstructed wave field was based on approximately 3,900 active Fourier components and covered a duration of 2100 s. This allowed a direct comparison of the surge, heave, pitch, strain, and tower-base bending-moment time series.

The potential-flow model provides reliable results in regular waves for RAO computations. For irregular seas, however, capturing low-frequency behavior is essential, and because Quadratic Transfer Functions (QTF) are not available in TEDDY, nonlinear effects were incorporated through modifications of the numerical model. Consequently, for Sea State SS1 to SS5, the hydrodynamic formulation remains based on the model described in Section 3.3., but with the following adjustments. To partially account for higher-order hydrodynamic effects, a Rainey correction is applied to the backbone and a McCamy–Fuchs correction is introduced for the effective pierce-water beam F3_top, showed in Figure 1. This replaces the excitation force from Nemoh on this section only. The McCamy-Fuchs approach takes into account the modification of the instantaneous wetted surface when the crest passes over the structure. Cases SS6 to SS8 are not presented here, as in these higher sea states the inclusion of QTF seems necessary to fit the experimental results. At the time of writing this paper, multi bodies QTFs were not available in DIEGO, and consequently in TEDDY.

A complementary analysis based on the Power Spectral Density (PSD) of each time series was carried out to evaluate the frequency distribution of the system's response and to compare this behavior with observations. Figure 4 and Figure 5 in Appendix 5. show a good agreement with the experimental spectra for sea states SS1 to SS5, particularly in TEDDY's ability to capture the low-frequency components. For clarity, PSD results obtained without the corrections described above are not shown, as the potential-flow model alone was insufficient to reproduce the low-frequency response observed experimentally. In the pitch PSD, the first low-frequency peak corresponds to the surge natural frequency, the second to the pitch

natural frequency, and the third to the incoming wave frequency. For the strain PSD, the first three peaks follow the same behavior, while the peak just bellow 0.4 Hz corresponds to the first bending mode of the tower for which the remaining difference in frequency between numerical and experimental is consistent with the modelling limitations discussed in Section 3.1. This peak is not generated directly by first-order wave loads. It may arise from higher-order wave excitation, but most likely it is driven by the floater motions, which induce deformation in the tower. This response reflects deformable-body dynamics and confirms that the model is able to reproduce such effects at least qualitatively For SS5, the low-frequency response is significantly amplified and a similar trend was reported by Ran et al. [5]. This should be further investigated by replacing the strip-theory-based loads with full QTF-based second-order forcing when such data become available.

4. Conclusions

This work presented a detailed numerical reproduction of the flexible spar benchmark from Ecole Centrale de Nantes using the hydroelastic simulation tool TEDDY. The numerical model was done at full scale to ensure a correct comparison with the scaled experimental results and it included a deformable Euler-beam backbone, rigidly connected floater components on which are applied hydrodynamic loads based either on Morison's equation or on weakly nonlinear potential-flow theory. The validation effort shows that TEDDY is able to accurately predict the main dynamic characteristics of the system. The hammer test reproduced the first tower bending frequency within a few percent of the experimental value. Free-decay tests in heave and pitch demonstrated excellent agreement with measurements, while the surge decay showed a slightly larger discrepancy, consistent with the sensitivity of this mode to mooring stiffness and mass distribution. Under regular waves, the model reproduced the motion RAOs, strain at sensor locations, and tower base bending moments with very good accuracy. The potential-flow-based hydrodynamic representation systematically provided better agreement than the Morison-only model, confirming observations from previous studies. The strain predictions, in particular, matched the experimental data across the full range of tested wave periods, reinforcing the validity of the flexible-body formulation and load transfer strategy. Eventually, the first investigations under irregular-wave conditions showed that for sea states up to SS5, the numerical results aligned well with experimental measurements across motions, strains, and bending moments when the model is extended with the Rainey and McCamy-Fuchs corrections. Beyond this range, however, the model exhibited instabilities probably due to the incomplete representation of second-order wave loads in the potential-flow formulation. The absence of QTF limits the model's ability to reproduce the higher-order effects that become important in harsher conditions and are particularly noticeable in the frequency domain, being the only contribution at high and low frequencies. Overall, the study confirms that TEDDY provides a reliable and accurate hydroelastic modeling framework for moderate sea states and regular-wave conditions, offering a high-fidelity representation of both global motions and local structural responses.

5. Further Work

The results of this study demonstrate that TEDDY can accurately reproduce the hydroelastic behavior of a real spar platform in free-decay and regular-wave conditions. The first tests in irregular seas also indicate that TEDDY is able to capture the correct low-frequency and wave-frequency responses associated with the main hydroelastic characteristics of the spar. Future developments will focus on several complementary directions. One priority is the computation of QTF for the full multibody system, as it would improve the prediction of slow-drift forces as well as springing and ringing responses. In parallel, additional work will address the correct application of hydrodynamic coefficients for deformable bodies when relying on external hydrodynamic databases. Improving the representation of damping is another important step, for instance by calibrating it directly from wave-test measurements rather than relying on decay tests. Finally, extending the validation to a wider set of irregular sea states, including

more severe conditions such as the 50 year return period, will help assess whether the model consistently captures nonlinear excitation and structural resonance effects across the full operational envelope.

References

[1] J. M. Hegseth, E. E. Bachynski, and M. Karimirad. Comparison and validation of hydrodynamic load models for a semi-submersible floating wind turbine. In *Proceedings of the ASME 37th International Conference on Ocean, Offshore and Arctic Engineering (OMAE)*, 2018.

[2] J. Jonkman, E. Branlard, M. Hall, G. Hayman, A. Platt, and A. Robertson. Implementation of substructure flexibility and member-level load capabilities for floating offshore wind turbines in openfast. Technical Report NREL/TP-5000-76822, National Renewable Energy Laboratory (NREL), 2020.

[3] D. Milano. *A Numerical Prototype for Floating Offshore Wind Turbines*. PhD thesis, University of Edinburgh, 2021.

[4] V. Leroy, S. Delacroix, A. Merrien, E. E. Bachynski-Polić, and J.-C. Gilloteaux. Experimental investigation of the hydro-elastic response of a spar-type floating offshore wind turbine. *Ocean Engineering*, 255:111430, 2022.

[5] X. Ran, V. Leroy, and E. E. Bachynski-Polić. Hydroelastic response of a flexible spar floating wind turbine: Numerical modelling and validation. *Ocean Engineering*, 286:115635, 2023.

[6] European Union. Directive (eu) 2023/2413 of the european parliament and of the council of 18 october 2023 on the promotion of the use of energy from renewable sources, 2023. Official Journal of the European Union.

[7] H. L. Aslaksen. Fluid–structure–interaction coupling between project chrono and reef3d. Master's thesis, Norwegian University of Science and Technology (NTNU), 2024.

[8] H. Mazhar, T. Heyn, A. Pazouki, D. Melanz, A. Seidl, A. Bartholomew, A. Tasora, and D. Negrut. Chrono: a parallel multi-physics library for rigid-body, flexible-body, and fluid dynamics. *Mechanical Sciences*, 4(1):49–64, 2013.

[9] A. Tasora, R. Serban, H. Mazhar, A. Pazouki, D. Melanz, J. Fleischmann, M. Taylor, H. Sugiyama, and D. Negrut. Chrono: An open source multi-physics dynamics engine. In *Proceedings of the International Conference on High Performance Computing in Science and Engineering*, pages 19–49. Springer, 2015.

[10] D. Marten, J. Saverin, R. Behrens de Luna, and S. Perez-Becker. *QBlade Documentation*, 2021.

[11] R. Kurnia and G. Ducrozet. *NEMOH v3.0: User Manual*, 2022.

Appendix

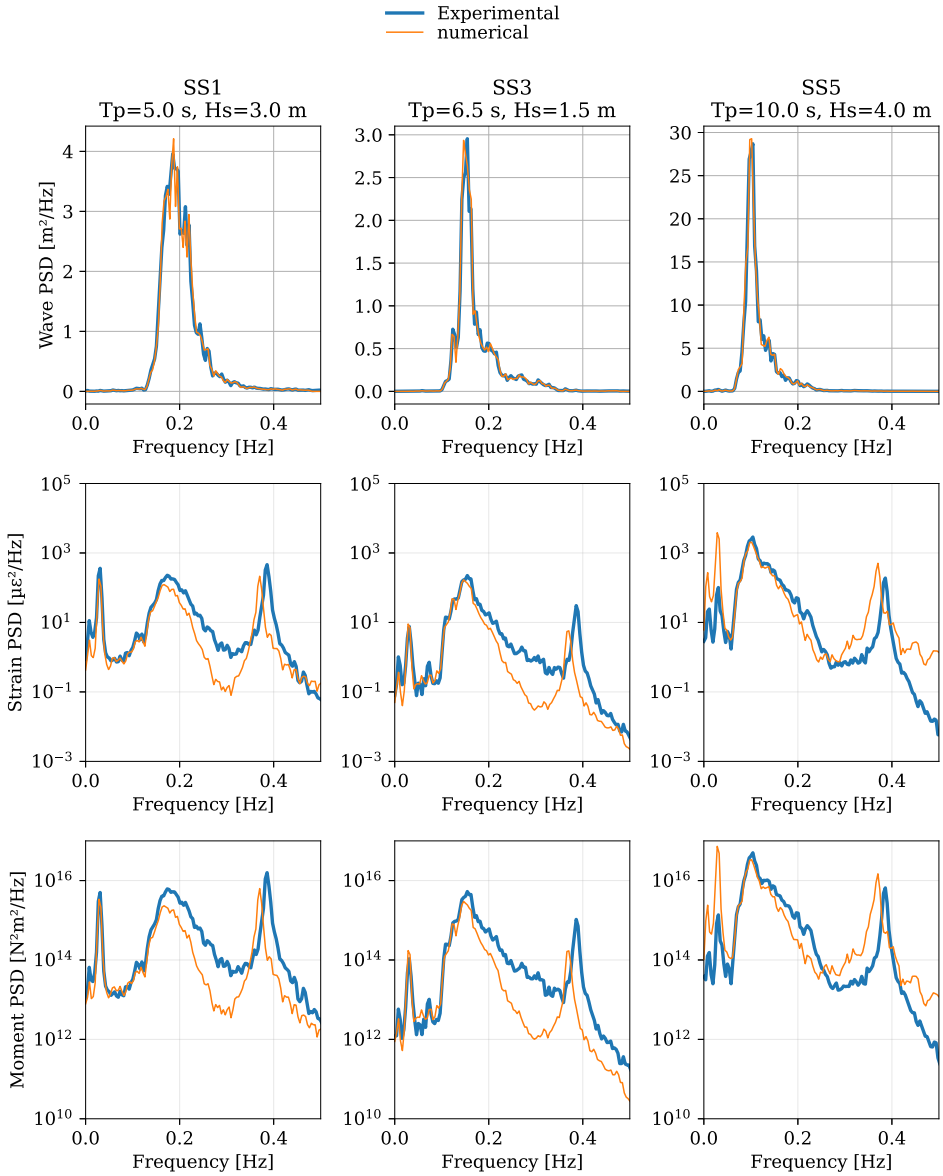


Figure 4 Power spectral density for strain at sensor 2 and tower base bending moment in irregular waves (SS1, SS3 and SS5): numerical and experimental comparison.

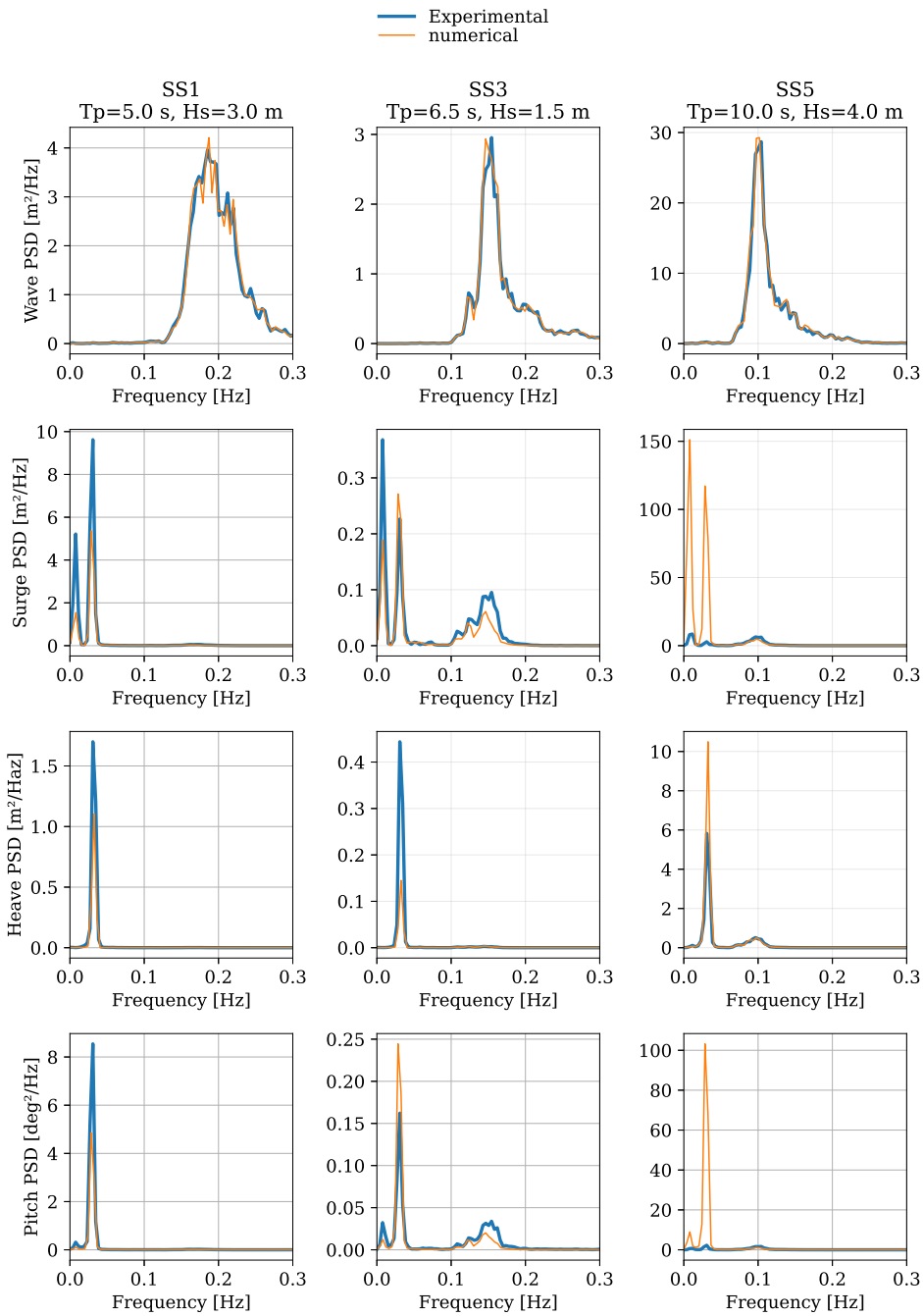


Figure 5 Power spectral density of wave, surge, heave, and pitch responses in irregular waves (SS1, SS3, and SS5): numerical and experimental comparison.

10th International Conference on HYDROELASTICITY IN MARINE TECHNOLOGY
Trondheim, Norway, June16$^{\text{th}}$-18$^{\text{th}}$, 2026

Sum-frequency second-order wave loads and elastic response of the INO OptiFLEX 22 MW floating wind turbine

Rajasree, V R N[1,*] Rogne, Ø Y [1], Abdelmoteleb, S E[1], Bachynski-Polić, E E[2], Sauder, T[1,2]

[1] SINTEF Ocean, P.O. Box 4762 Torgarden, Trondheim, 7465, Norway
[2] Department of Marine Technology, Norwegian University of Science and Technology, Trondheim, Norway

Abstract. Designing large floating wind turbines (FWTs) requires accurately quantifying relevant high-frequency (HF) excitation load and damping sources, and understanding their effect on extreme stresses, fatigue damage, and ultimately costs. Both aerodynamic and hydrodynamic loads contribute at these frequencies, and responses in the hull, mooring, tower, blades, and drivetrain are affected. The present work addresses second-order sum-frequency non-linear wave loads and the associated elastic response of the INO OptiFLEX 22 MW floating wind turbine. Second-order potential-flow calculations are performed using WADAM, and the results of the convergence study are presented. Subsequently, fatigue analysis is performed using time-domain simulations in relevant sea states, employing a new multi-body approach developed in SIMA. The sum-frequency second-order loads excite specific resonant modes of the flexible structure, especially in sea states with short, steep waves. However, the overall impact of the sum-frequency wave loads on the structure's fatigue life is minimal ($< 3\%$) at the considered site.

Key words: *Sum-frequency second-order loads; substructure flexibility; floating wind turbines; platform flexibility*

1. Introduction

The effects of hull elasticity for floating wind turbines (FWTs) are gaining increasing attention due to the trends toward increasing rotor size and reduced substructure mass. Experimental studies suggest that nonlinear high-frequency wave loads can excite resonant responses of these systems [1].

While several studies have documented the importance of hull elasticity on FWT natural frequencies and fatigue damage [2], and previous studies on models with rigid substructures document the importance of second-order wave loads on extreme responses [3], the importance of second-order distributed wave loads on FWTs with elastic hulls has not been addressed.

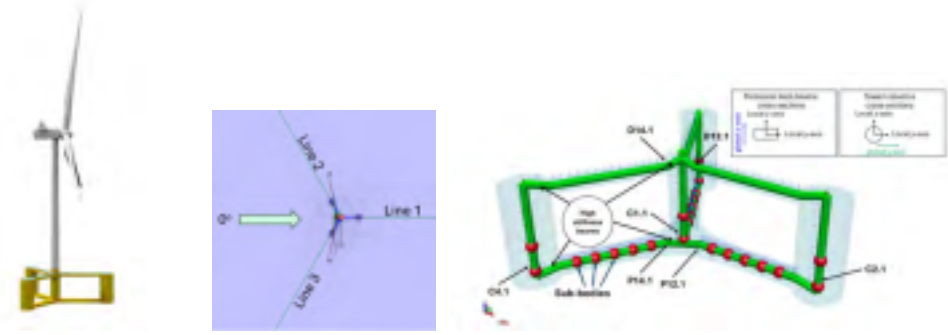
The paper is organized as follows. The flexible (elastic) model of the INO OptiFLEX 22 MW reference FWT [4] (Figure 1a) is briefly presented in Section 2.. Then, Section 3. presents the calculation of the sum-frequency quadratic transfer functions (QTFs). Finally, results from time-domain analyses, focusing on fatigue damage, are presented in Section 4. and conclusions given in Section 5..

2. Description of INO OptiFLEX 22MW

The INO OptiFLEX 22MW concept has been developed for the ongoing OptiFLEX research project, aiming at investigating coupled floater, tower and blade vibrations and associated high-frequency (HF) excitation and damping effects of large floating wind turbines.

INO OptiFLEX 22MW is a floating wind turbine consisting of a semi-submersible floater in steel (Figure 1a), with a central column supporting the IEA 22MW reference turbine, and connected to three

*Correspondence to: vishnu.rajasree@sintef.no



(a) Overview (b) Environment heading (c) Beam model for substructure in SIMA [6].

Figure 1: SIMA model setup for flexible INO OptiFLEX 22MW

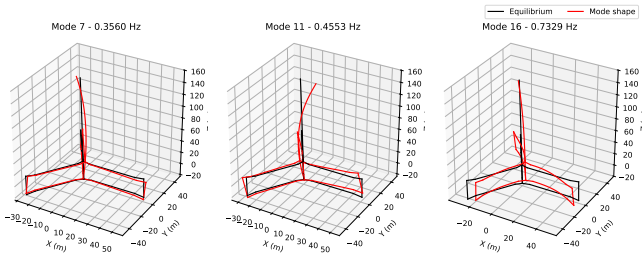


Figure 2: Visualization of selected eigenmodes of the flexible structure

side-columns via pontoons and deck beams. Sauder et al. [4] provide a complete description of the concept, including mass distribution and structural properties. Stationkeeping is ensured by a three-line semi-taut mooring system, where each line consists of a top chain segment, two polyester segments, and a bottom chain segment as shown in Figure 1b.

A numerical model of INO OptiFLEX 22MW has been established in SIMA [5] as a multi-body model, in which 23 sub-bodies are connected by beams, as shown in Figure 1c. The first-order wave, radiation, and hydrostatic loads are distributed among the sub-bodies as explained by Abdelmoteleb et al. [6]. The current work extends this model by including distributed sum-frequency second-order wave loads. Selected eigenmodes and eigenfrequencies of the flexible structure relevant to the present work are presented in Figure 2.

3. Calculation of the sum-frequency QTF

Section 3.1. describes the sum-frequency quadratic transfer functions (QTFs) calculated assuming a single body that encompasses the entire substructure. This setup is used to study the sensitivity of the resulting QTFs to the body and free-surface meshes. Subsequently, in Section 3.3., the calculation of the distributed sum-frequency QTFs is described, which provides the sum-frequency QTFs for each of the 23 sub-bodies indicated in Figure 1c. The sum-frequency QTFs are calculated using HydroD [7] using a development version of WADAM [8]. The sum frequencies are calculated for linear wave frequencies ranging from 0.1 Hz (10 s) to 0.55 Hz (1.82 s). The influence of first-order motions on the QTFs is assessed by calculating them using two approaches: fixed and floating. As detailed in Pinkster [9] - the second order forces can be split into 5 components based on their source : (1) first order variation of

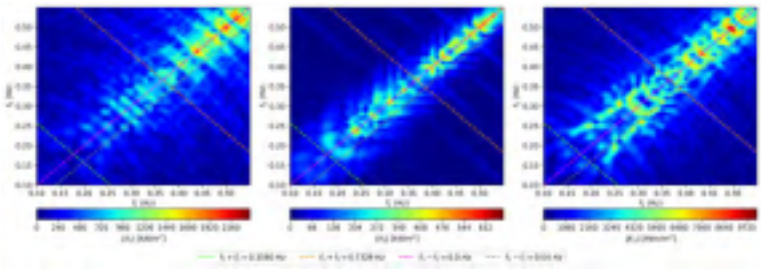


Figure 3: Contours of magnitude of sum-frequency QTFs for force/moment in the surge (X_1), heave (X_3), and pitch (X_5) degrees of freedom in the bi-frequency plane. The QTFs are calculated using mesh FS180-F_BM-C described in Table 1. Slices corresponding to constant difference frequency ($f_1 - f_2$) of 0 Hz and 0.04 Hz, and constant sum frequency ($f_1 + f_2$) of 0.3560 Hz and 0.7329 Hz are presented.

Table 1: Free surface and body mesh description for convergence study. r is the free surface mesh radius and dr is the typical mesh size in the radial direction, dl is the average panel diagonal length of the in the body mesh. $\lambda_{min} = 5.16\ m$ is the minimum wavelength considered.

ID	Free surface mesh				Body mesh		
	r [m]	dr (typical) [m]	λ_{min}/dr	No. of panels[b]	dl (average) [m]	λ_{min}/dl	No. of panels[b]
FS180-F_BM-C[a]	180	0.6	8.6	94700	1.3	4.0	2893
FS180-C_BM-C	180	**1.5**	3.4	15152	1.3	4.0	2893
FS240-F_BM-C	**240**	0.6	8.6	130700	1.3	4.0	2893
FS360-F_BM-C	**360**	0.6	8.6	200900	1.3	4.0	2893
FS180-F_BM-F	180	0.6	8.6	94700	**0.65**	7.9	10894

[a] Reference mesh
[b] Panel counts reported are for the symmetric half-body used in single-body simulations.

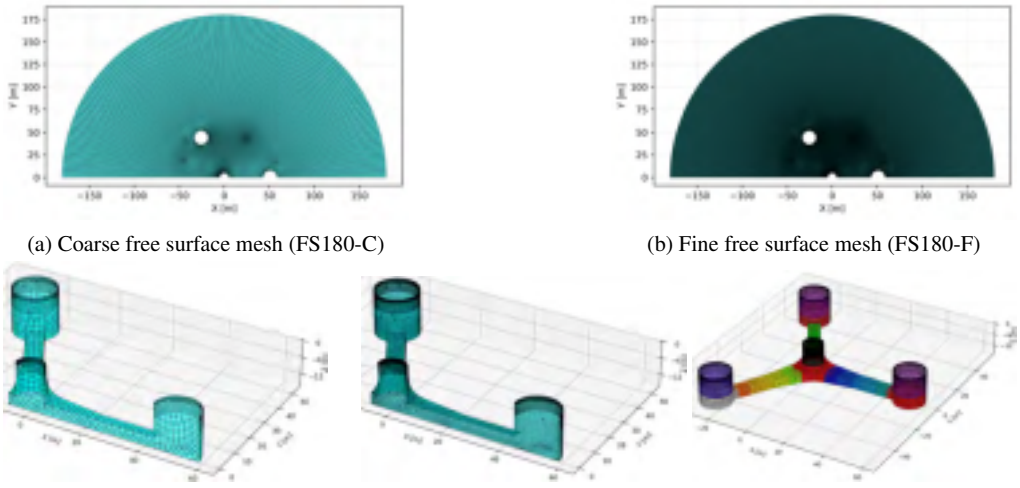
mean wetted surface, which depends on the relative wave elevation, (2) pressure due to velocity square term in Bernoulli's equation, (3) pressure from the integration of the second order potential (4) pressure due to first order motions of the body and (5) first order rotation of the normal vector to the panel surface. In the fixed case, only the contributions from (1), (2), and (3) are included, with (1) containing only the contribution from wave elevation, with the body considered to be fixed. Whereas, in the floating case, all the components are included.

3.1. Single body sum-frequency QTF - sensitivity to mesh

The body and free surface meshes used in the convergence study are described in Table 1. The contours of the absolute value of QTFs calculated using a reference mesh denoted FS180-F_BM-C are presented in Figure 3. The sensitivity of the QTFs to the free surface mesh density, free surface mesh radius, and body mesh density is assessed by comparing cross sections of the absolute value of the QTFs along constant difference frequencies ($f_1 - f_2$).

Free surface mesh density. Two different free-surface mesh densities were tested - Coarse (FS180-C_BM-C) and Fine (FS180-F_BM-C), with the panel size in radial direction as 1.5 m and 0.6 m. The meshes are presented in Figures 4a and 4b. Both simulations had the same free-surface mesh radius of 180 m and a coarse body mesh. The comparison of the absolute value of QTFs along the cross section with difference frequency of 0 Hz in Figure 5 suggests that the coarse free-surface mesh is unable to resolve the shortest wavelengths, leading to large over-prediction, especially in surge with a mean frequency larger than 0.35 Hz. The ratio between the wavelength and typical mesh size in the radial

direction dr for the coarse mesh at 0.35 Hz is 8.5. The free-surface mesh density is set to match the fine mesh in the subsequent analysis, which has this ratio to be 8.6 for the minimum wavelength considered.



(a) Coarse free surface mesh (FS180-C)

(b) Fine free surface mesh (FS180-F)

(c) Coarse body mesh (BM-C)

(d) Fine body mesh (BM-F)

(e) Multi-body coarse mesh (BM-C)

Figure 4: Body panel meshes and free surface meshes comparison (with radius 180 m) used in the sensitivity analysis

Free surface mesh radius. Three different free-surface mesh radii were tested - 180 m (FS180-F_BM-C), 240 m (FS240-F_BM-C), and 360 m (FS360-F_BM-C). All simulations used the same fine-mesh density for the free surface and the coarse density for the body mesh. The comparison of the absolute values of QTFs across different cross-sections indicated limited sensitivity to the free-surface mesh radius among the meshes tested. Hence, considering computational efficiency, the free-surface mesh radius is set as 180 m for subsequent analysis.

Body mesh. Two different body mesh densities were tested - coarse (FS180-F_BM-C) and fine (FS180-F_BM-F), with average panel diagonal sizes of 1.3 m and 0.65 m. In both cases, the body mesh near the waterline was refined, as shown in Figure 4c and Figure 4d. Both the simulations used a fine free-surface mesh with a radius of 180 m. The comparison of the absolute values of QTFs across different cross-sections indicated limited sensitivity to body mesh density among the meshes tested; however, the fine mesh showed a significant increase in computational time and memory requirements. Hence, the coarse body mesh is used in the subsequent analysis.

3.2. Influence of first-order motions on the second-order loads QTFs

Next, the impact of the first-order motions on the sum-frequency QTFs was investigated. In both fixed- and floating-analysis cases, mesh combination FS180-F_BM-C is used. The comparison of the absolute value of QTFs along a constant difference of 0 Hz shows good agreement; however, off-diagonal cross-sections show differences, for instance, the cross-section along a constant difference frequency of 0.04 Hz is plotted in Figure 6, which indicates differences in lower mean frequencies (< 0.3 Hz). Note, however, that the impact of these differences on the structure's response depends on the dynamic properties of the structure and input wave spectrum.

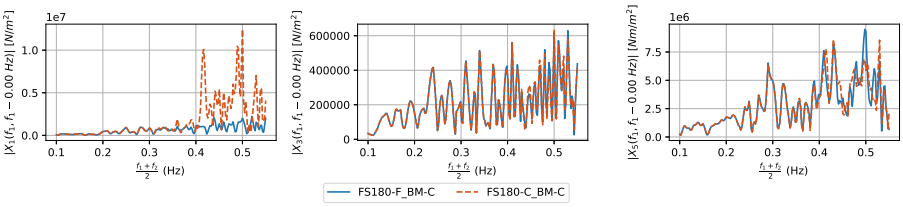


Figure 5: Magnitude of sum-frequency QTFs in the surge (X_1), heave (X_3), and pitch (X_5) degrees of freedom along constant difference frequency ($f_1 - f_2$) of 0.04 Hz for different free surface mesh densities. The mesh used in all the simulations is FS180-F_BM-C described in Table 1.

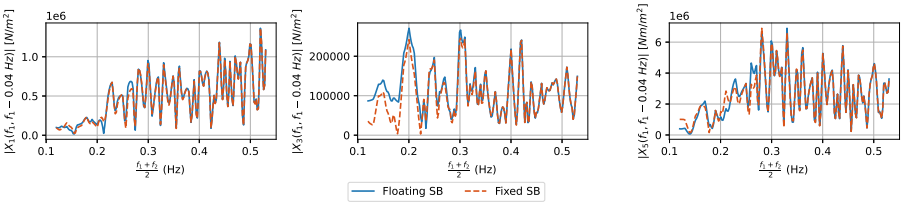


Figure 6: Magnitude of sum-frequency QTFs in the surge (X_1), heave (X_3), and pitch (X_5) degrees of freedom along constant difference frequency ($f_1 - f_2$) of 0.04 Hz for fixed and floating structure. The mesh used in all the simulations is FS180-F_BM-C described in Table 1.

3.3. Establishing multi-body sum-frequency QTFs

To apply second-order wave loads on a flexible structure in a time-domain analysis, it is necessary to provide the loading on each sub-body that composes the floater. The multibody panel mesh is generated by splitting the coarse body used in the single-body analysis into sub-bodies, as presented in Figure 4e, combined with the fine free-surface mesh. This resulted in 23 Nos. of 6-DOF bodies. Subsequently, a multibody analysis can be performed to obtain the QTF for each sub-body.

As in the single-body analysis, it is possible to compute fixed and floating QTFs in the multi-body analysis. To compute the "floating" multi-body QTF, the first-order motions of the sub-bodies must be physically consistent, representing the constraints between the motions of the sub-bodies. However, WADAM does not allow beam elements to connect sub-bodies. To get around this limitation, it was assumed that the impact of motions arising from *elastic* deformations of sub-bodies on the QTFs can be neglected in the calculations. This implies that the first-order motion response amplitude operators (RAOs) for each sub-body within the multi-body system can be calculated from the single-body RAO, assuming that all the sub-bodies move together as a rigid body. The calculated first-order RAOs are then prescribed to each sub-body and used in the sum-frequency QTF calculations in multi-body WADAM simulations. For the "fixed" multi-body QTFs, the sub-bodies were simply assumed to be fixed at their mean position during the analysis.

The distributed QTFs obtained across all sub-bodies are finally verified by summing up their contributions to obtain the total sum-frequency force/moment QTFs (called condensed QTFs), and comparing the results with those from the single-body QTF. The comparison of the sum-frequency QTFs along two sum-frequency diagonals corresponding to two eigenfrequencies of the structure (see Figure 2) of 0.3560 Hz (Mode 7) and 0.7329 Hz (Mode 16) is presented in Figure 7. The agreement between the condensed multi-body and single-body QTFs for both fixed and floating cases provides verification of the applied method for distributing QTFs. The effect of neglecting first-order motions when calculating the QTFs can be clearly observed in the lower sum-frequency diagonal (0.3560 Hz), but again, the actual consequence of such discrepancies will depend on the dynamic properties of the structure and on the

environmental conditions. At the higher frequency diagonal (0.7329 Hz), the floating and fixed QTFs are in agreement, as wave radiation effects are not significant at high frequencies.

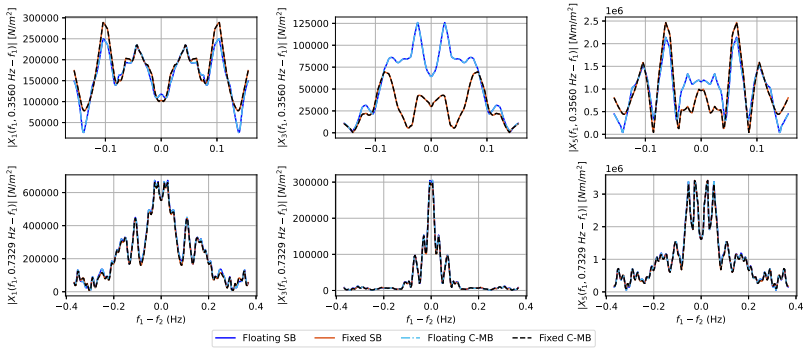


Figure 7: Magnitude of sum-frequency QTFs for force/moment in the surge (X_1), heave (X_3), and pitch (X_5) degrees of freedom along constant sum frequency ($f_1 + f_2$). SB indicates results from single-body simulations, and C-MB indicates single-body results condensed/summed up from multi-body simulations.

4. Time domain simulations

The present section examines (1) the impact of including second-order sum-frequency loads on the fatigue damage at various locations of the structure, (2) the impact of using sum-frequency QTFs computed from fixed bodies, i.e., neglecting first-order motions on the QTFs, and (3) the impact of linearizing the JONSWAP wave spectrum, in order to avoid double-counting of non-linearities in the high-frequency tail of the spectrum. This assessment is made in two sets of conditions: first, two irregular wave-only conditions, focusing on sea states dominated by short-steep waves, in which the sum-frequency QTFs are expected to be important; and then, 100 representative combined irregular wave and turbulent wind conditions. The wind and waves are assumed to be aligned with a heading of 0° as indicated in Figure 1b.

4.1. Impact of linearization and using fixed-body QTFs

4.1.1. Wave-only conditions

The two wave-only seastates described by the JONSWAP wave spectrum are selected as: for seastate SS1, the spectral peak frequency is selected to be half of the structural eigenfrequency of Mode 7 (see Figure 2), hence T_p is selected as 5.62 s. For seastate SS2, a higher T_P of 9 s is selected. The significant wave height (H_s) for both cases is selected to be the maximum significant wave height permitted as per the steepness criteria of DNV (Section 3.5.4 [10]). Hence, H_s for SS1 and SS2 are 3.29 m and 7.95 m, respectively. The seastate parameters and the wave spectrum for the two seastates are presented in Figure 8.

4.1.2. Wave spectrum linearisation

The calculated sum-frequency QTFs require linear wave elevation as input to compute the sum-frequency loads. However, the JONSWAP spectrum defines the total wave elevation, including higher-order wave components [11]. Hence, the wave spectrum has to be linearised [12]. Neglecting third- and higher-order contributions, the linearization involves removing second-order components to avoid

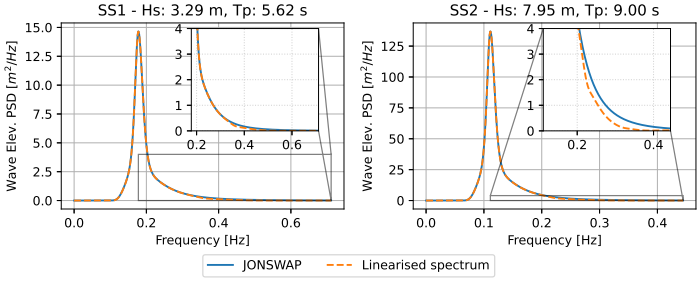


Figure 8: Linearised JONSWAP spectrum for the two sea states considered. A zoomed-in view of the high-frequency tail is presented for each case.

double-counting of second-order loads. The total spectrum, defined by JONSWAP ($S(\omega)$) can be approximated as : $S(\omega) \approx S_1(\omega) + S_{2+}(\omega; [S_1]) + S_{2-}(\omega; [S_1])$. Here S_1 is the desired linear spectrum and S_{2+} and S_{2-} are the sum- and difference-frequency wave elevation spectra, respectively. The sum- and difference-frequency wave elevation spectra can be calculated from the linear spectrum using the quadratic sum and difference frequency wave elevation transfer functions (Section 3.3.2.2 [10]), assuming deep water. The resulting linearised spectrum is compared against the JONSWAP spectrum for the two sea states in Figure 8. It is observed that as the peak spectral period increases, the contribution of the second-order components increases; consequently, the linearisation removes more energy from the high-frequency tail of the total spectrum.

4.1.3. Fatigue damage calculations

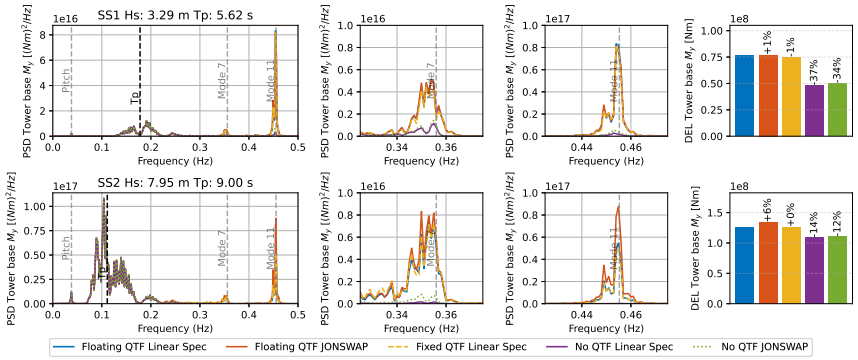
The impact of the sum-frequency QTFs is assessed by comparing the damage-equivalent load (DEL), which is calculated as : $DEL = \left(\frac{\sum_i n_i \cdot S_i^m}{N_{ref}}\right)^{\frac{1}{m}}$. Here, the number of cycles (n_i) at load range (S_i) is obtained by rainflow counting of the time series. The Wöhler exponent is taken as 4 as a compromise between the bi-linear SN curve with slope values of 3 and 5 recommended by DNV [13]. The simulations were conducted for 4600 s with the initial 1000 s discarded. N_{ref} is taken as 3600; hence, the DELs are computed at a reference frequency of 1 Hz. The spectral response and DEL calculated for tower base fore-aft bending moment (M_y) and vertical bending moment (M_z) of pontoon P14 at its mid-point are presented in Figure 9a and Figure 9b, respectively. We refer to Figure 1c for identification of the pontoon and the coordinate system for the moments.

4.1.4. Results

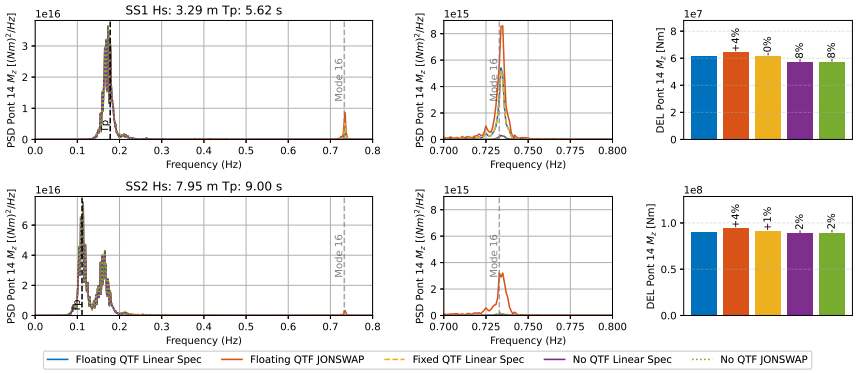
Five different simulations are presented in Figure 9 to assess the sensitivity of the DELs to different simulation approaches:

(1) Floating QTF Linear Spec: This is the base case combining the floating QTFs with linearised spectrum. The DELs using this approach are treated as the reference for each sea state.

(2) Floating QTF JONSWAP : The floating QTF is combined with the original JONSWAP spectrum without linearisation. Comparison with the base case is used to assess the impact of linearising the spectrum. For the tower base fore-aft bending moment M_y, it is observed that the DEL is increasingly over-predicted, from 1 % in SS1 to 6 % in SS2, due to the additional energy present in the spectrum compared to the base case. This trend is consistent with the increasing importance of sum-frequency wave elevation components as T_p increases, as observed in Figure 8. Further in SS2, a higher peak is observed in Modes 11 and 7 response compared to the base case, arising from the sum-frequency loads combined with the total spectrum. For P14 M_z, the over-prediction in DEL on account of the use of the total spectrum is 4% for the two sea states driven by the higher peaks observed for Mode 16 response.



(a) Tower base fore-aft bending moment (M_y)



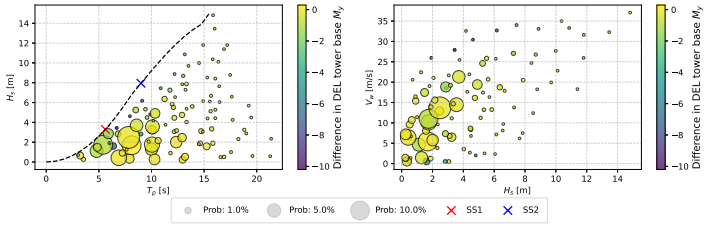
(b) Vertical bending moment (M_z) of pontoon P14 at its midpoint

Figure 9: PSD and DEL (right-end) for wave-only condition using different simulation approaches. Zoomed-in plots of relevant frequency ranges of the PSDs are also indicated. The value at the top of the bar in the bar plot is the percentage difference of the approach, with the floating QTF with linearised spectrum approach as the reference. The colors of the lines/bars are used to identify the approach.

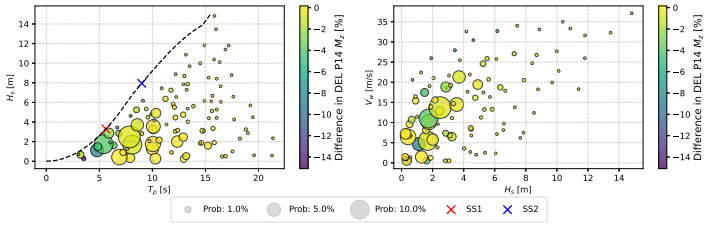
(3) Fixed QTF Linear Spec: The fixed body QTF is combined with a linearised spectrum in these simulations. The DELs for the tower base fore-aft bending moment and the vertical pontoon bending moments across all conditions show deviations of less than 1% from the base case, indicating that the effects of first-order motions on the QTFs-induced loading are not significant for these responses.

(4) No QTF Linear Spec: Sum frequency QTFs are not included in these simulations. Neglecting QTFs can lead to an under-prediction of the tower base fore-aft bending moment M_y DEL by up to 37% in SS1, with the deviation reducing with increasing T_p. The spectral plots indicate minimal responses in Modes 7 and 11 in this case compared to the base case, confirming that these resonant responses arise from sum-frequency QTFs. Similar observations also hold for pontoon vertical bending-moment DELs, which can be underpredicted by up to 8% in SS1. The spectral plots indicate that the resonant responses of Mode 16 nearly disappear if the sum-frequency QTF is removed from the simulations.

(5) No QTF JONSWAP: The sum-frequency QTFs are not included, and the total spectrum is utilised in these simulations. The comparison between this and "No QTF Linear Spec" provides a measure of the impact of linearisation on the DELS, mainly from the first-order loads. The tower base fore-aft bending moment DELs show a difference in the DELs by up to 3% between the two, whereas the impact is negligible in the pontoon DEL.



(a) Tower base fore-aft bending moment (M_y)



(b) Vertical bending moment (M_z) of pontoon P14 at its midpoint

Figure 10: Fatigue bins considered for Utsira Nord. Each dot indicates the combination of significant wave height (H_s), spectral peak period (T_p), and wind speed at hub height (V_w) for a bin. The size of the dots represents the probability of occurrence, and their color represents the percentage difference in the damage equivalent load (DEL) of the corresponding response between the simulation without the sum-frequency QTF and the one with the floating sum-frequency QTF. Both use the total spectrum without linearisation. The DNV steepness criteria, along with the selected two wave-only sea states, are also indicated.

4.2. Wind-wave conditions

4.2.1. Metocean conditions

To assess the impact of including second-order sum-frequency loads in representative combined wind-wave environmental conditions, the metocean data of Utsira Nord [14], off the coast of Norway, were used. They originate from the NORA3 database. The spatially averaged dataset [14] of significant wave height, spectral peak period, and mean wind speed at 150 m height over a period of 40 years (1982 to 2022) was binned into 100 bins by using the maximum dissimilarity algorithm [15]. The mean wind speed was adjusted to hub height (163 m) by using the power law with a shear exponent of 0.14. The resulting bins and their probability of occurrence are presented in Figure 10 as a pairwise plot of spectral peak period and wind speed at hub height against significant wave height. From the plot, it is observed that a very large proportion of the sea states have a significant wave height of less than 2.5 m, a peak period between 5-10 s, and wind speed at hub height ranging from 5-15 m/s.

4.2.2. Simulations and quantities of interest

Time-domain simulations were run for each bin using turbulent wind files generated for class C of the normal turbulence model (NTM). Two sets of simulations were performed - one including QTFs and the other without QTFs. Both used the total spectrum without linearization. Following the same approach as for wave-only conditions, the simulations were run for 4600 s, with the initial 1000 s discarded. The DEL for tower base fore-aft bending moment M_y and vertical bending moment M_z of P14 at the mid-point was computed for each bin. The difference between the DELs from the simulation without and with QTFs expressed as a percentage for each bin is presented in Figure 10a for the tower base fore-aft bending moment M_y and in Figure 10b for the vertical bending moment M_z of P14 at the mid-point.

In addition to DEL, the fatigue damage (D) due to stresses was also calculated using Miner's summation rule, which defines it as the summation over all the stress ranges ($\Delta\sigma_i$), the ratio of the number of cycles experienced (n_i) in the stress range to the total number of cycles to failure (N_i) for the stress range :$D = \sum_i \frac{n_i}{N_i}$. The number of cycles experienced was calculated using rainflow counting. The number of cycles to failure was calculated based on appropriate SN curves: for tower, Curve D for steel in air (Table 2-1 [13]), and for pontoon, Curve D for steel in seawater with cathodic protection (Table 2-2 [13]) was used. Thickness correction was not applied. For the beams, axial stress, computed by combining bending moments and axial force, was evaluated at 8 points around the circular sections and at the four corners of rectangular sections, and the location with maximum fatigue damage was considered in the analysis. No stress concentration factors were considered. The total accumulated damage was then computed by summing the 1-hour damage weighted by the probability of occurrence for each sea state, and accounting for the 20-year design operational lifetime.

4.2.3. Results

Comparison of DELs

For the tower base fore-aft bending moment M_y, Figure 10a shows that across 100 simulated bins, excluding QTFs can lead to an underprediction of DEL of tower base M_y by up to 10%. The majority of the sea states showing the highest increase in DELs with the inclusion of the QTFs lie along the steepness limit, with T_p ranging from 5-10 s. Further, the pairwise plot of H_s against V_w indicates that the bins sensitive to QTFs are predominantly either below the cut-in (3 m/s) or above the cut-off wind speeds (25 m/s), where wave loads are dominant and the tower base fore-aft bending moments are not driven by thrust loads, and aerodynamic damping from the rotor is negligible.

For the vertical bending moment M_z of P14 at the mid-point, Figure 10b indicates that exclusion of QTFs can lead to underprediction of DEL by up to 14%. The QTF-sensitive bins predominantly lie around a T_p of 5s; however, unlike the tower base fore-aft bending moment, they are also present in the operational region of the wind turbine.

Comparison of accumulated fatigue damage

From Figure 10, it is observed that the bins that are sensitive to QTFs have comparatively low probability of occurrence, especially in the case of the tower base fore-aft bending moment. The fatigue damage also follows a similar trend to the DELs. The total accumulated damage over the 20-year lifetime indicates that neglecting sum-frequency QTFs underpredicts fatigue by 1% for the tower base and by 3% at the pontoon P14 mid, suggesting a limited influence of sum-frequency QTFs on the overall fatigue response of the structure at the considered site.

5. Conclusion

A convergence study of the sum-frequency QTFs for the INO OptiFLEX 22 MW floating wind turbine was presented with respect to the free-surface and body meshes. The free-surface mesh, with a typical radial dimension of 0.6 m and a radius of 180 m, was found to be sufficient for the frequencies of interest, along with a body mesh with an average panel diagonal of 1.3 m. The distributed sum-frequency QTFs, including the effect of wave radiation, were computed by prescribing the RAOs for a multi-body configuration based on single-body simulations, neglecting elastic deformation. In the second part of the paper, the impact of several modeling approaches was investigated on the fatigue damage of the structure : (1) the impact of sum-frequency QTFs was investigated, considering both irregular wave-only conditions and a more representative turbulent wind - irregular wave conditions were used. It was concluded that sum-frequency loads can excite specific resonant modes of the structure and significantly increase fatigue damage under certain sea states. Excluding sum-frequency QTFs would then result in an underestimation of damage in specific bins. For the site considered in the study, the structure's overall accumulated fatigue damage was, however, found to be only weakly sensitive

to sum-frequency QTFs. (2) The impact of using sum-frequency QTFs computed from fixed bodies, i.e., neglecting first-order motions on the QTFs, was investigated. Even though differences were noted in QTFs over lower frequencies (<0.4 Hz), the impact on fatigue was limited, and (3) the impact of linearizing the JONSWAP wave spectrum, in order to avoid double counting of non-linearities in the high-frequency tail of the spectrum, indicated an increasing importance of linearisation of the spectrum with increasing periods.

Acknowledgments

The author(s) would like to thank Sebastien Lafleche for the helpful discussions regarding wave spectrum linearization. This research has been funded by the Research Council of Norway through project 352810 OptiFLEX, a collaboration between SINTEF Ocean, NTNU, Equinor, Inocean, Odfjell Oceanwind, COWI, 4subsea, Sevan Deepwater Technology, and Ocean Ventus

References

[1] Élie Rongé, Christophe Peyrard, Vengatesan Venugopal, Qing Xiao, Lars Johanning, and Michel Benoit. Evaluation of second and third-order numerical wave-loading models for floating offshore wind TLPs. *Ocean Engineering*, 288:116064, 2023.

[2] Xiaoming Ran and Erin E. Bachynski-Polić. Time-domain simulation, fatigue and extreme responses for a fully flexible tlp floating wind turbine. *Marine Structures*, 101:103778, 2025.

[3] Erin E. Bachynski and Torgeir Moan. Ringing loads on tension leg platform wind turbines. *Ocean Engineering*, 84:237–248, 2014.

[4] Thomas Sauder, Serag-Eldin Abdelmoteleb, Marius Karlsson, and Herman Schrader Bordal. INO OptiFLEX 22MW FWT - Definition and modelling of the INO OptiFLEX 22MW floating wind turbine. 2025.

[5] SINTEF. SIMA documentation. `https://sima.sintef.no/doc/latest/sima/index.html`, 2026. Accessed: 02 March 2026.

[6] Serag-Eldin Abdelmoteleb, Øyvind Ygre Rogne, Veronica Liverud Krathe, Erin E. Bachynski-Polić, and Thomas Sauder. A multi-body approach for distributing first-order hydrodynamic and hydrostatic loads on flexible structures, with application to coupled simulations of large floating wind turbines. *Marine Structures*, 2026. Submitted for publication.

[7] DNV AS. *Hydrodynamic analysis and stability analysis software - HydroD*. DNV Digital Solutions, Høvik, Norway, 2026. Version 7.4-01.

[8] DNV AS. *Frequency domain hydrodynamic analysis of stationary vessels - Wadam*. DNV Digital Solutions, Høvik, Norway, 2026.

[9] Johannes Pinkster. Low frequency second order wave exciting forces on floating structures. January 1980.

[10] DNV. DNV-RP-C205: Environmental Conditions and Environmental Loads, 2019.

[11] Thomas B. Johannessen. On the Use of Linear and Weakly Nonlinear Wave Theory in Continuous Ocean Wave Spectra: Convergence With Respect to Frequency. pages 211–217. American Society of Mechanical Engineers Digital Collection, July 2009.

[12] Bert Sweetman and Steven R. Winterstein. Second-Order Random Ocean Waves: Prediction of Temporal and Spatial Variation from Fixed and Moving References:. Technical report, Defense Technical Information Center, Fort Belvoir, VA, May 1999.

[13] DNV. DNV-RP-C203 Fatigue design of offshore steel structures, 2024.

[14] Etienne Cheynet, Lin Li, and Zhiyu Jiang. Metocean conditions at two Norwegian sites for development of offshore wind farms. *Renewable Energy*, 224:120184, April 2024.

[15] Yanira Guanche, Raúl Guanche, Paula Camus, Fernando J. Mendez, and Raúl Medina. A multivariate approach to estimate design loads for offshore wind turbines. *Wind Energy*, 16(7):1091–1106, 2013.

10th International Conference on HYDROELASTICITY IN MARINE TECHNOLOGY
Trondheim, Norway, June16th-18th, 2026

Wavelength and Wave-Steepness Effects on the Hydroelastic Response of Flexible Slender Offshore Components

Qi Zhang[1], Ould el Moctar[2], Siear Qaimi[3], Galal Galal[4], Andreas Brehm[4], Jens Neugebauer[1], and Changqing Jiang[1,*]

[1] University of Duisburg–Essen, Duisburg 47057, Germany
[2] Technische Universität Berlin, Berlin, 10623, Germany
[3] thyssenkrupp Carbon2Chem GmbH, Essen, 45143, Germany
[4] ESOS Wind GmbH, Aurich, 26603, Germany

Abstract. This paper examines how wavelength and wave steepness govern the hydroelastic response of a flexible surface-piercing cylindrical member representative of offshore wind support components. A two-way coupled CFD–FEM model is used to resolve the interaction between nonlinear wave kinematics and structural deformation. Built on the authors' previous work, this study is reframed with a sharper focus on the coupled roles of excitation frequency and wave nonlinearity in governing structural response. First, wavelength effects are isolated by varying wavelength while keeping wave steepness constant. Second, steepness effects are isolated by increasing wave height at fixed wavelength. The discussion is based on flexible-cylinder results in both the time domain and the frequency domain. The results show that wavelength affects the structural response through two coupled mechanisms: the distance between wave excitation frequency and the wet natural frequency of the structure, and the associated change in fluid-particle excursion and Keulegan–Carpenter number. By contrast, increasing wave steepness primarily intensifies nonlinear wave kinematics and redistributes response energy toward higher harmonics, which is especially evident in the structural acceleration. A unified interpretation is proposed in which hydroelastic response is governed jointly by resonance proximity and wave nonlinearity.

Key words: *Hydroelasticity; Wave kinematics; Offshore wind; Flexible cylinder; Wavelength effect; Wave steepness; CFD–FEM*

1. Introduction

Offshore wind turbines and their support structures contain many slender cylindrical members, such as monopiles, braces, and transition components, that are continuously exposed to wave-induced loading throughout their service life [1]. As offshore systems become larger and more flexible, the conventional rigid-body assumption becomes increasingly inadequate because structural deformation can modify the surrounding flow and alter the hydrodynamic load itself [2]. This fluid–structure interaction, referred to as hydroelasticity, is particularly important for vibration- and fatigue-sensitive offshore components, where variations in the spectral distribution of wave loads may significantly influence long-term performance [3].

Classical wave-load prediction approaches, including Morison-type formulations, diffraction theory, and linear potential-flow hydroelasticity, have long formed the basis of offshore design [4]. However, their applicability becomes limited when nonlinear free-surface effects, viscous contributions, higher-harmonic components, and structural deformation are significant [5]. To address these limitations, fully coupled CFD–FEM approaches have attracted increasing attention because they can capture nonlinear

*Correspondence to: changqing.jiang@uni-due.de

wave kinematics, viscous flow behavior, and two-way hydroelastic interaction within a unified framework [6]. In our previous work, such a coupled model was developed and validated for a top-fixed flexible cylinder representative of a slender offshore support member [7]. The study showed that hydroelasticity can substantially modify wave-induced loads, particularly when wave excitation is dynamically relevant to the structural modes. While that work focused on model development, validation, and broad parametric analyses, the present study concentrates on a more specific physical question: how wavelength and wave steepness separately and jointly govern the hydroelastic response of a flexible offshore member.

Although wavelength and wave steepness are mathematically related through the ratio H/λ, they represent different physical mechanisms. Wavelength primarily affects the response by changing the wave period and excitation frequency relative to the wet natural frequency of the structure, thereby influencing resonance proximity [8]. It also modifies wave kinematics, including fluid-particle excursion and the Keulegan–Carpenter (KC) number, which govern nonlinear drag and higher-order effects [9]. Wave steepness, in contrast, mainly characterizes wave nonlinearity, increasing crest–trough asymmetry and higher-harmonic content in the hydrodynamic excitation [10]. In this sense, wavelength controls the dynamic state of the system, whereas steepness controls the degree of nonlinear forcing. To clarify these roles, the study is organized into two targeted analyses. The first examines wavelength effects at constant steepness, isolating the influence of excitation frequency and wavelength-dependent kinematics. The second investigates wave steepness effects at fixed wavelength, isolating nonlinear forcing effects without changing the fundamental forcing period. The structural response is analyzed in both the time and frequency domains, allowing identification of how response energy is distributed between fundamental and higher-harmonic components. This distinction helps determine whether the response is governed primarily by resonance proximity, nonlinear harmonic enrichment, or their interaction, which is particularly relevant for fatigue-sensitive offshore structures.

The objective of this paper is therefore to provide a concise hydroelastic interpretation of the separate and combined effects of wavelength and wave steepness on the force and vibration response of a flexible slender cylinder under regular waves. The response is interpreted along two physical axes: a dynamic axis, represented by the ratio between wave frequency and wet natural frequency, and a nonlinearity axis, represented by wave steepness and the associated harmonic enrichment of the forcing. Under this framework, short waves may induce strong hydroelastic effects through resonance proximity, whereas longer or steeper waves may generate stronger local oscillations because of enhanced higher-harmonic excitation. The most pronounced hydroelastic response is therefore expected under conditions that are both dynamically relevant and strongly nonlinear.

2. Numerical framework and test matrix

The numerical framework, model configuration, and baseline validation follow the previous study [7]. Only the essential elements needed to support the present mechanism-based discussion are retained here, while the emphasis is placed on how the selected wave cases reveal the separate and combined roles of wavelength and steepness.

2.1. Coupled CFD–FEM framework

The hydrodynamic field is solved using the incompressible Navier–Stokes equations for a two-phase flow with a resolved free surface,

$$\nabla \cdot \mathbf{u} = 0, \tag{1}$$

$$\frac{\partial(\rho \mathbf{u})}{\partial t} + \nabla \cdot (\rho\, \mathbf{u}\mathbf{u}) = -\nabla p + \nabla \cdot \boldsymbol{\tau} + \rho \mathbf{g}, \tag{2}$$

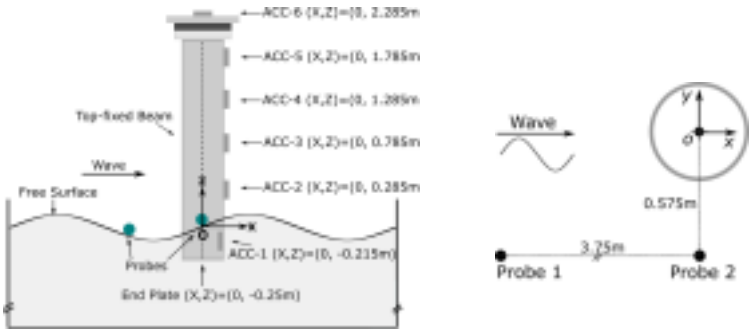


Figure 1: Overview of the structural configuration and wave definition adopted from the model test [11], as well as the authors' previous study [7].

where ρ is density, $\mathbf{u}$ velocity, p pressure, and $\boldsymbol{\tau}$ the viscous stress tensor. The structural response of the flexible cylinder is represented by the finite-element equation of motion

$$\mathbf{M}\ddot{\mathbf{d}} + \mathbf{C}\dot{\mathbf{d}} + \mathbf{K}\mathbf{d} = \mathbf{f}_{\mathrm{hyd}}, \tag{3}$$

where $\mathbf{M}$, $\mathbf{C}$, and $\mathbf{K}$ are the mass, damping, and stiffness matrices, $\mathbf{d}$ is the displacement vector, and $\mathbf{f}_{\mathrm{hyd}}$ denotes the wave-induced loads transferred from the fluid solver.

A two-way partitioned coupling is enforced at the fluid–structure interface. The fluid solver provides pressure and viscous tractions to the structural solver, while the structure returns displacement and velocity to update the moving fluid mesh. This strategy allows deformation of the cylinder to modify the local flow field and, in turn, the fluid loading. Such a framework is particularly useful when the excitation frequency approaches a wet natural frequency and/or when nonlinear wave kinematics and two-way motion feedback influence the load spectrum. For weakly nonlinear conditions and small KC, second-order potential-flow models or Morison-type formulations with higher-harmonic terms may also provide reasonable predictions of low-order (e.g. 2ω) load components; the coupled CFD–FEM framework is used here as a high-fidelity reference to resolve the combined nonlinear and hydroelastic mechanisms in a unified setting.

2.2. Structural configuration

The flexible cylinder considered in this study is a thin-walled vertical member with a total length of 2.5 m, an outer diameter of 0.125 m, an inner diameter of 0.120 m, and a wall thickness of 2.5 mm. The cylinder is top-clamped (fixed translation and rotation), with its lower end submerged to a draft of 0.25 m. The structural material properties used in the numerical model are a density of $\rho_s = 2567\ \mathrm{kg/m^3}$, a Young's modulus of $E = 2.2 \times 10^9$ Pa, and a Poisson's ratio of $\nu_s = 0.4$. The total mass of the test cylinder, including sensors, is 4.66 kg [11]. Structural accelerations are monitored at various positions along the member, and the results of Acc.1 are used through the present study.

2.3. Wave cases

To isolate wavelength effects, three regular-wave cases are considered with constant steepness $H/\lambda = 0.04$. The test matrix is summarized in Table 1. In this set, wavelength and wave period vary simultaneously, while the steepness is held fixed.

To isolate steepness effects, the wavelength of Case 2 is retained and the wave height is increased to obtain $H/\lambda = 0.06$ and 0.08. In this way, the influence of nonlinear wave shape and forcing can be studied without changing the wave frequency. For each regular-wave case, the incident-wave angular frequency is denoted by $\omega_T = 2\pi/T$.

Table 1: Wave cases used to isolate wavelength and steepness effects.

Set	Case	T [s]	λ [m]	H [m]	H/λ [-]	KC [-]
Wavelength	1	0.5	0.39	0.016	0.04	0.40
	2	1.0	1.56	0.062	0.04	1.56
	3	1.5	3.51	0.140	0.04	3.52
Steepness	2a	1.0	1.56	0.062	0.04	1.56
	2b	1.0	1.56	0.094	0.06	2.36
	2c	1.0	1.56	0.125	0.08	3.14

3. Wavelength effect at constant steepness

For Cases 1–3, the time-domain histories and FFT spectra of the in-line force and the structural acceleration at Acc.1 are presented in Figs. 2 and 3. To facilitate comparison among different wave conditions, the results are normalized. The in-line force is normalized by $\rho D^2 \zeta_a \omega^2$, where ρ is the water density, D is the cylinder diameter, ζ_a is the first-harmonic (linear) amplitude of the incident wave elevation, and ω is the wave frequency.

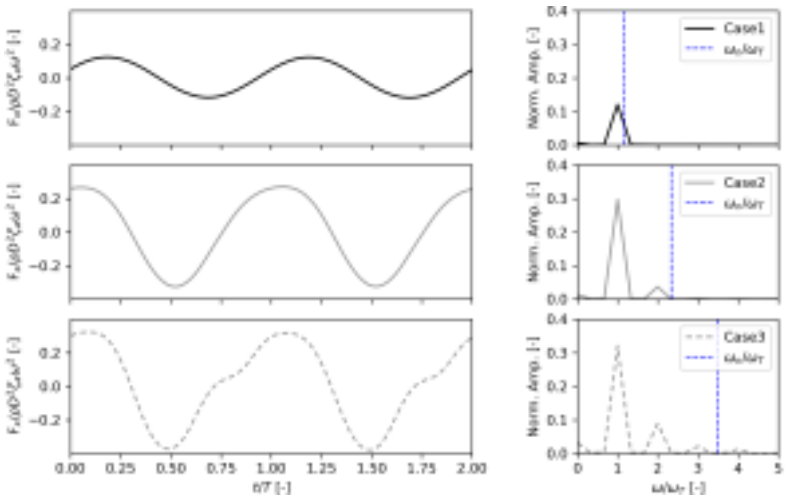


Figure 2: Time-domain histories (left) and normalized FFT spectra (right) of the in-line wave force acting on the flexible cylinder for Cases 1–3 with increasing wavelength at constant wave steepness.

The structural acceleration is normalized by $\zeta_a \omega^2$, while the frequency is normalized by the incident-wave angular frequency ω_T. In both figures, the blue dashed line denotes the normalized wet natural frequency ω_n/ω_T. This combined time-domain and frequency-domain representation is particularly useful because it not only shows how the time histories of wave elevation, inline force, and structural acceleration change with wavelength, but also reveals how the response energy is redistributed among the fundamental and higher-harmonic components.

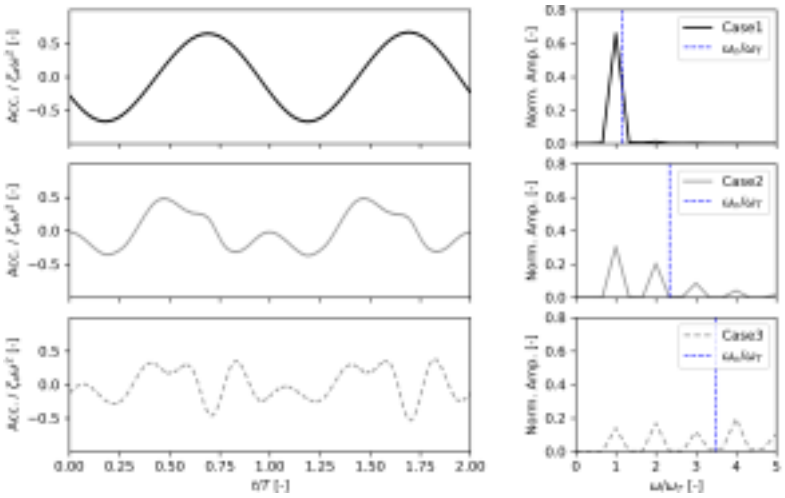


Figure 3: Time-domain histories (left) and normalized FFT spectra (right) of the structural acceleration response of the flexible cylinder for Cases 1–3 with increasing wavelength at constant wave steepness.

3.1. Why wavelength changes the response

When wave steepness is kept constant, varying the wavelength modifies the hydroelastic response through two coupled mechanisms. The first is dynamic, that is the wavelength changes the wave period and therefore the excitation frequency relative to the first wet natural frequency of the flexible cylinder. This effect can be characterized by the frequency ratio

$$r_f = \frac{\omega_T}{\omega_n}, \tag{4}$$

The second mechanism is kinematic, i.e., the wavelength changes the fluid-particle excursion and the associated KC number,

$$\mathrm{KC} = \frac{U_m T}{D}, \tag{5}$$

where U_m is a representative oscillatory velocity amplitude. As the wavelength increases, the forcing moves farther away from the fundamental structural frequency, while the flow kinematics become increasingly nonlinear and the higher-order hydrodynamic contributions become more important.

These two mechanisms leave distinct signatures in the frequency-domain results. When r_f is relatively small (close to 1) and the excitation remains dynamically relevant to the first wet mode, the response stays concentrated around the fundamental frequency and the time histories remain close to sinusoidal. By contrast, when the wavelength increases and the associated KC number becomes larger, the hydrodynamic forcing deviates increasingly from a sinusoid (sharper peaks and stronger crest–trough asymmetry), the spectrum broadens, and higher harmonics gain importance. The wavelength effect should therefore not be interpreted solely as a frequency-shift effect. It also reflects a change in the nonlinear kinematic character of the wave loading, which becomes particularly evident in the acceleration response.

3.2. Fundamental-dominated response in short waves

The short-wave regime, especially Case 1, exhibits the clearest fundamental-dominated behavior. Although the incident wave height is relatively small, the normalized wet natural frequency shown in Figs. 2 and 3 lies closest to the fundamental excitation range among the three wavelength cases. As a

result, both the force and the acceleration are governed primarily by the first harmonic, and their time histories remain nearly sinusoidal.

This behavior is confirmed by the FFT spectra. In Fig. 2, the force spectrum for Case 1 is strongly concentrated at $\omega/\omega_T = 1$, with only weak higher-harmonic contributions. The acceleration spectrum in Fig. 3 is even more distinctly fundamental-dominated, indicating that the structural motion is mainly dominated by the primary wave excitation. These results show that the strongest dynamic relevance does not necessarily occur under the largest wave height or the longest wavelength, but rather when the excitation frequency lies closest to the wet structural mode. In this regime, the response remains comparatively simple in spectral form, even though it is dynamically significant.

3.3. Stronger nonlinear harmonic content in longer waves

As the wavelength increases from Case 1 to Case 3, the in-line force becomes progressively less sinusoidal. In Case 2, the force remains primarily periodic but already exhibits a visible contribution from the second harmonic. In Case 3, the force history shows clear intra-cycle distortion and shoulder-like features, demonstrating that the load cycle is no longer governed by the fundamental component alone. This trend is fully consistent with the FFT spectra in Fig. 2, where the response evolves from a narrowly concentrated first-harmonic spectrum in Case 1 to a broader multi-harmonic spectrum in Case 3.

The structural acceleration is even more sensitive to this wavelength-induced transition. In Fig. 3, Case 1 remains largely harmonic, whereas Case 2 shows a mixed first- and second-harmonic response, and Case 3 develops multiple oscillations within a single wave period. The corresponding FFT spectra demonstrate that the response energy is redistributed over a much broader frequency range as the wavelength increases. This indicates that the structural response becomes progressively more sensitive to higher-harmonic excitation components, even though the fundamental wave frequency itself moves farther away from the first wet natural frequency. As KC increases, viscous separation and quadratic drag contributions may become more relevant and can generate odd-harmonic load components (e.g. 3ω, 5ω) in addition to wave-nonlinearity-induced harmonics; these effects are included here through the viscous CFD model.

The physical implication is that longer waves are not hydroelastically unimportant. Rather, their effect shifts from a mainly fundamental-controlled response toward a nonlinear-kinematics-dominated response in which higher harmonics play an increasingly important role in structural vibration. In the present flexible-cylinder results, this shift is seen much more clearly in the acceleration spectra than in the global force spectra, which confirms that structural acceleration is the more sensitive indicator of nonlinear hydroelastic behavior.

4. Wave steepness effect at fixed wavelength

The corresponding results for varying wave steepness at fixed wavelength are shown in Figs. 4 and 5. The same normalization is adopted as in the wavelength study so that the force and acceleration responses can be compared consistently across the steepness cases. Because the wavelength is fixed, the normalized wet natural frequency remains unchanged from Case 2a to Case 2c. The steepness study therefore isolates the role of wave nonlinearity without altering the basic dynamic position of the excitation relative to the structural mode.

4.1. Why steepness matters

When the wavelength is fixed and the wave height increases, the excitation frequency remains unchanged, but the wave kinematics become increasingly nonlinear. This provides a clean way to isolate the steepness effect because the change in response cannot be attributed to a shift in resonance condition. Instead, it reflects the progressive enhancement of crest–trough asymmetry, sharper crest-induced

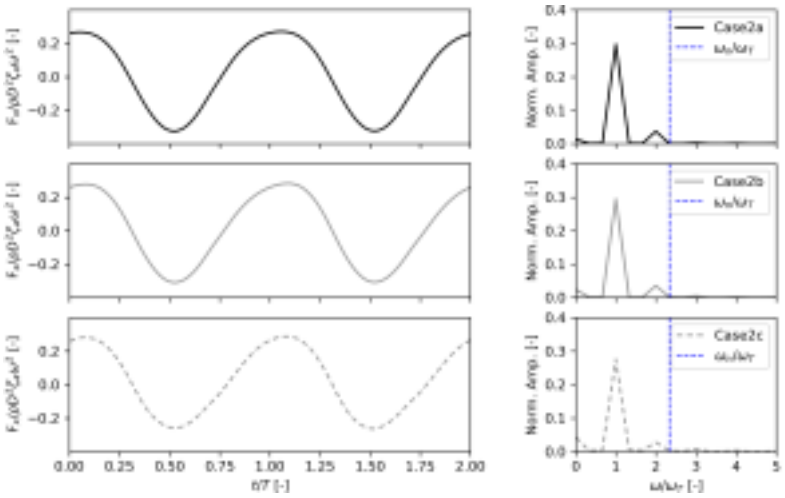


Figure 4: Time-domain histories (left) and normalized FFT spectra (right) of the in-line wave force acting on the flexible cylinder for Cases 2a–2c with increasing wave steepness at fixed wavelength.

loading, and stronger higher-harmonic content in the incident and scattered wave field. In hydroelastic terms, increasing steepness acts primarily as a forcing nonlinearity amplifier rather than as a resonance trigger.

This interpretation is directly supported by the present FFT results. As H/λ increases from Case 2a to Case 2c, the response energy is redistributed toward higher harmonics, but this redistribution is moderately stronger in the structural acceleration than in the global force. The force remains largely controlled by the fundamental wave cycle, whereas the acceleration develops an increasingly broadband character. This difference indicates that the structure filters and amplifies the nonlinear components of the hydrodynamic excitation more strongly than is apparent from the force history alone. In that sense, the steepness effect is best understood as a progressive intensification of nonlinear structural vibration within an otherwise fixed dynamic framework.

4.2. Effects on force history and structural vibration

The force histories in Fig. 4 remain dominated by the primary wave cycle for all three steepness cases, but their local shape shows only a modest increase in crest–trough asymmetry as the steepness increases. The maxima and minima depart increasingly from a sinusoidal form, and the FFT spectra show that moderate higher-order components are superimposed on the dominant first harmonic. Compared with the wavelength study, however, the steepness-induced changes in the force spectrum are more modest, indicating that the global force remains governed mainly by the fundamental wave loading even for the steepest case considered here.

A much stronger effect is observed in the structural acceleration. As shown in Fig. 5, the acceleration histories become increasingly multi-peaked within each wave period as the steepness increases from Case 2a to Case 2c. The corresponding FFT spectra show a clear growth of higher-order components, particularly around the third and fourth harmonics. Since the normalized wet natural frequency is fixed in all three steepness cases, these spectral changes cannot be attributed to any shift in the dynamic frequency ratio. They instead reflect the direct amplification of nonlinear forcing by increasing wave steepness.

This behavior is especially important for vibration-sensitive and fatigue-sensitive assessments. Even when the force response remains largely first-harmonic dominated, the structural vibration can become

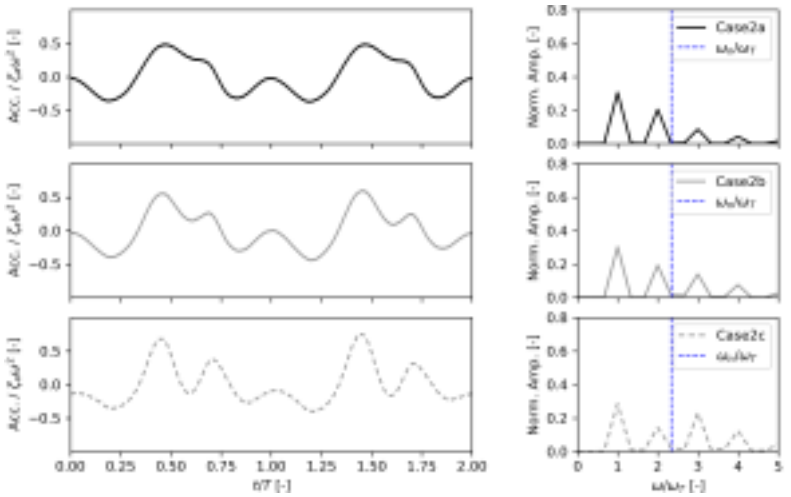


Figure 5: Time-domain histories (left) and normalized FFT spectra (right) of the structural acceleration response of the flexible cylinder for Cases 2a–2c with increasing wave steepness at fixed wavelength.

markedly richer in high-frequency content under steeper waves. The acceleration response therefore provides a more revealing measure of how steepness alters the hydroelastic behavior of the flexible member.

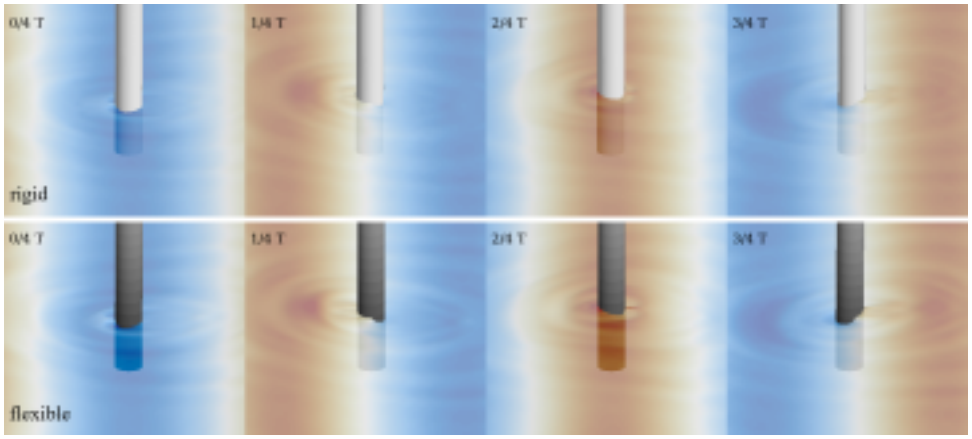


Figure 6: Instantaneous free-surface elevation field around the cylinder at successive instants over one wave period for Case 1 (top: rigid; bottom: flexible).

To provide qualitative insight into wave–structure interaction and the possible coupling between near-wake separation and the free surface, Fig. 6 shows snapshots of the instantaneous free-surface elevation field around the cylinder at quarter-period intervals for Case 1, comparing the rigid and flexible simulations. The sequence illustrates the passage of the incident crest/trough, local run-up/drawdown on the upstream face, and the generation of scattered and diffracted wave patterns that radiate away from the cylinder. In addition, a lee-side disturbance (wake imprint) is visible behind the cylinder, most clearly at $t = 1/4\,T$ and $t = 3/4\,T$, when the near-surface flow past the body is strongest. Compared

with the rigid case, the flexible case exhibits slightly stronger local elevation gradients near the body and a more pronounced (and mildly asymmetric) lee-side disturbance, consistent with motion-modulated wake dynamics that can interact with the free surface and contribute to the enhanced higher-harmonic content observed in the force response.

5. Conclusions

This paper has reinterpreted the hydroelastic response of a flexible surface-piercing cylinder under regular waves by focusing on the separate and coupled roles of wavelength and wave steepness. The combined time-domain and frequency-domain results show that wavelength and steepness affect the response through different physical pathways, and that these pathways are revealed much more clearly in the structural acceleration than in the global in-line force.

At constant steepness, wavelength affects the response through both dynamic relevance and wave kinematics. In the short-wave case, the excitation remains closest to the first wet natural frequency, and the response is therefore predominantly fundamental-dominated. As the wavelength increases, the force and acceleration histories become progressively more distorted and the FFT spectra show an increasingly broad harmonic distribution. This indicates a shift from a response dominated mainly by the primary excitation toward one increasingly influenced by nonlinear wave kinematics and higher-order forcing. The force spectrum remains centered on the first harmonic, but the acceleration spectrum shows that the structure becomes progressively more sensitive to higher-frequency excitation components as the wavelength increases.

At fixed wavelength, increasing wave steepness does not change the fundamental resonance condition, but it substantially strengthens the nonlinear character of the forcing. The force histories remain primarily first-harmonic dominated, with only moderate spectral broadening, whereas the structural acceleration develops increasingly strong higher-order components. The steepness effect is therefore best interpreted not as a direct resonance mechanism, but as an amplification of nonlinear structural vibration caused by stronger crest asymmetry and richer harmonic forcing.

Taken together, the results support a two-axis interpretation of the hydroelastic response. Wavelength governs the dynamic position of the system by changing the relationship between the excitation frequency and the wet natural frequency, while wave steepness governs the nonlinearity of the forcing by controlling the growth of higher harmonics. Under this framework, short waves exhibit strong dynamic relevance because the response remains closely tied to the fundamental excitation, whereas longer or steeper waves produce increasingly complex structural vibration because nonlinear harmonic content becomes more important. The most pronounced hydroelastic response is therefore expected when the incident wave condition is both dynamically relevant and sufficiently nonlinear.

From a practical perspective, the present results also show that structural acceleration is a more sensitive indicator of nonlinear hydroelastic behavior than the global force alone. This finding is important for offshore components whose design is governed not only by peak loading but also by vibration amplitude, local dynamic response, and fatigue accumulation. The conference-paper narrative is therefore most effectively organized around the two complementary physical axes of resonance proximity and wave nonlinearity, which together provide a clearer interpretation of how wave conditions govern the response of flexible slender offshore members.

Acknowledgments

This study is funded by the Federal Ministry for Economic Affairs and Energy (BMWE: 03SX616C), for the project FloatModular.

References

[1] Kamal Jahani, Robert G Langlois, and Fred F Afagh. Structural dynamics of offshore wind turbines: A review. *Ocean Engineering*, 251:111136, 2022.

[2] Aldert Otter, Jimmy Murphy, Vikram Pakrashi, Amy Robertson, and Cian Desmond. A review of modelling techniques for floating offshore wind turbines. *Wind Energy*, 25(5):831–857, 2022.

[3] Changqing Jiang and Ould el Moctar. Experimental decomposition of nonlinear hydrodynamic loads and hydroelastic responses in wave–structure interactions of monopile wind turbines. *Physics of Fluids*, 36(11), 2024.

[4] V Leroy, EE Bachynski-Polić, A Babarit, P Ferrant, and J-C Gilloteaux. A weak-scatterer potential flow theory-based model for the hydroelastic analysis of offshore wind turbine substructures. *Ocean Engineering*, 238:109702, 2021.

[5] Changqing Jiang, Peng Xu, Xinglan Bai, Zhichao Zhao, Ould el Moctar, and Guiyong Zhang. A review of advances in modeling hydrodynamics and hydroelasticity for very large floating structures. *Ocean Engineering*, 285:115319, 2023.

[6] Hui Li, Bingbing Han, Shengnan Liu, Sangui Chen, Zhenyang Wang, and Baoli Deng. A review of the numerical strategies for solving ship hydroelasticity based on cfd-fem technology. *Ships and Offshore Structures*, 19(11):1912–1930, 2024.

[7] Qi Zhang, Ould el Moctar, and Changqing Jiang. Hydroelasticity effects on wave-induced loads for flexible slender components in offshore wind turbines. *Marine Structures*, 107:104014, 2026.

[8] Theodosios K Papathanasiou, Angeliki E Karperaki, and Kostas A Belibassakis. On the resonant hydroelastic behaviour of ice shelves. *Ocean Modelling*, 133:11–26, 2019.

[9] CAEA Shumin, ASJ Swamidas, and JJ Sharp. Similarity method for modelling hydroelastic offshore platforms. *Ocean engineering*, 23(7):575–595, 1996.

[10] Changqing Jiang, Ould el Moctar, and Guiyong Zhang. Nonlinear modeling of wave–structure interaction for a flexible floating structure. *Ocean Engineering*, 300:117489, 2024.

[11] Wajiha Rehman, Tim Bunnik, Onno Bokhove, and Mark Kelmanson. Experimental modeling of water-wave interactions with a flexible beam. In *International Conference on Offshore Mechanics and Arctic Engineering*, volume 86892, page V007T08A022. American Society of Mechanical Engineers, 2023.

Hydrofoils

10th International Conference on HYDROELASTICITY IN MARINE TECHNOLOGY
Trondheim, Norway, June 16th-18th, 2026

A BEM-FEM model for the hydro-elastic analysis of passively controlled flexible foil-thrusters for ships and underwater vehicles

Anevlavi, D.[1] and Belibassakis, K.[2,*]

School of Naval Architecture and Marine Engineering, National Technical University of Athens, Zografos, 15780 Athens, Greece ([1]danevlavi@mail.ntua.gr, [2]kbel@fluid.mech.ntua.gr)

Abstract. Biomimetic propulsors are being studied as an alternative to conventional propellers, both for ships and autonomous underwater vehicles. Their main advantages include low-frequency operation and advanced maneuverability. In this work, a strongly coupled fluid-structure interaction model, developed to predict the hydro-elastic response of flexible flapping-thrusters, is used to support the design of passively controlled elastic thrusters for ship applications. The developed 3D FSI model consists of an unsteady BEM for the lifting-surface problem, and a FEM based on Discrete Kirchhoff Triangle approximation for thin plates with stiffness variation for the foil's structural response. Strong coupling allows the model to capture the underlying physics with engineering accuracy, given the implicitly non-linear nature of the problem involving foil-thrusters that operate fully submerged in a high-density fluid medium. Comparisons between predicted results and experimental data support the validity of the developed scheme. Finally, a horizontal T-foil wing concept, mounted at the vessel's bow, is examined as an efficient system for augmenting propulsion. Particularly, the wing's performance in irregular vertical oscillations, which are induced by head waves, characterized by a frequency spectrum, is studied and selected results are presented to showcase the potential of bow wings as energy-saving devices (ESD) for oceangoing vessels.

Key words: *Biomimetic propulsion; Flexible hydrofoil; Ship energy-saving devices*

1. Introduction

Fish locomotion remains an active research field that inspires propulsion applications for both small autonomous underwater vehicles, see, e.g., Salazar et al. (2018), and larger-scale projects targeting ocean-going vessels; see, e.g., Xing et al. (2023). Other applications of flapping foils include energy extraction of wave and tidal renewable resources, especially in coastal areas; see Xiao & Zhu (2014). The mutual existence of waves with strong following, oblique, or opposing currents at various nearshore places, which otherwise is characterized by quite a low wave potential, offers motivations for a comprehensive investigation of such resources and the development of hybrid technological devices, see, e.g., the analysis in Filippas et al. (2018) for a concept semi-activated oscillating hydrofoil device.

The combined efforts of experimental biologists and engineers identified key aspects linked to the astonishing performance of various aquatic species. These include morphology (composite materials, elastic behaviour, hydrodynamic shapes, etc.), propulsion kinematics, morphing, advanced actuation, and sensory perception. In any case, replicating a combination of biomimetic features for engineering applications is challenging, requires interdisciplinary insight into the mechanics of fish locomotion, and the development of cost-effective computational hydro-elasticity frameworks for research and design; see Korobkin et al. (2011). Recent works demonstrate that maximum efficiency

* Correspondence to: kbel@fluid.mech.ntua.gr

under design loads is possible with the use of compliant mechanisms (Heo et al. 2013) or tailor-made composite wings (Herath et al. 2017).

Thunninform locomotion (Sfakiotakis et al. 1999) lies at the core of most flapping-foil systems' operating principle, where thrust-producing kinematics are emulated using a superposition of out-of-phase heave and pitch motions. Notable efforts on foil thrust-augmentation devices for ships include the experiments conducted by Bøckmann & Steen (2014), involving rigid, actively pitch-controlled and spring-loaded oscillating foils. Soon after, this idea led to the development of WAVEFOIL's modular, retractable, bow wing retrofit solution with several installations on medium-sized vessels operating in the North Sea. In the work by Bøckmann et al. (2018), the forces generated by the foils that were mounted on the bow of the model vessel suppressed heave/pitch ship motions and led to a fuel saving of 9% when averaged over all wave directions.

Recently, in the framework of the H2020 SeaTech project (https://seatech2020.eu/) two symbiotic ship engine and propulsion innovations have been examined that lead to enhanced fuel efficiency and reduced GHG emissions. The propulsion innovation is a biomimetic dynamic wing mounted at the ship's bow to augment ship propulsion in moderate and higher sea states, capturing wave energy, producing extra thrust, and damping ship motions; see Belibassakis et al. (2022), Ntouras et al. (2022), and Bowker & Townsend (2022). Similar works involving rigid wings with angle of attack adjustment via spring-loaded mechanisms can be found in Zhang et al. (2022) and Mei et al. (2023). The bio-mimetic wings examined above as thrust-augmentation devices for ships involve rigid wing structures; thus, consideration of elasticity effects, in the sense of passive deformation, on their performance extends research toward retrofit projects for greener shipping. More specifically, literature on passively deforming flapping wings suggests that optimally tuned geometric, kinematic, and structural parameters have the potential to enhance propulsive efficiency; see Quinn et al. (2015), Richards & Oshkai (2015).

In this work, a 3D fluid-structure interaction model is employed to investigate the performance of a bio-mimetic wing operating as a thrust-augmentation device, including elasticity effects. The proposed model consists of a 3D unsteady boundary element method (BEM) strongly coupled with a finite element solver (FEM) based on discrete Kirchhoff plate elements (DKT); see Anevlavi & Belibassakis (2026). The plate model allows for variability in thickness and elastic properties. The comparison between predicted results and experimental data supports the validity of the developed scheme for analyzing wing-thruster performance. Extending the work of Papakalodoukas & Belibassakis (2025), a horizontal T-foil wing concept, mounted at the vessel's bow, is examined as an efficient system for augmenting propulsion with consideration of elasticity effects. The wing's performance in irregular vertical oscillations, induced by head waves and characterized by a known frequency spectrum, is studied, and selected results are presented to showcase the potential of bow wings as energy-saving devices (ESD) for oceangoing vessels.

2. BEM-FEM fluid-structure interaction model

In this formulation, assuming the thickness of the hydrofoil sections is sufficiently small compared to the main dimensions (chord and span), a Kirchhoff thin plate model is selected for the structural idealization of the wing. This model is suitable for the prediction of the wing's response in terms of bending. Literature shows that chordwise and spanwise bending can contribute to the enhancement of efficiency of wings operating as thrusters; see Heathcote et al. (2008), Quinn et al. (2015), Richards & Oshkai (2015). The wings studied in the present are fully submerged within the fluid medium. The free-stream velocity is equal to zero, and interactions with the free surface or other bodies/boundaries are neglected for simplicity. Hydrodynamic load prediction, due to the enforced oscillatory motion of the wing, is addressed using an unsteady lifting flow model for 3D incompressible, inviscid, and irrotational fluid flows; see Filippas & Belibassakis (2022). The rotational part of the flow is restricted in the trailing-vortex sheet emanating from the sharp trailing edge. A visualization of the trailing-edge mesh is shown in Figure 1 below. A brief description of the mathematical formulation and the strong coupling scheme introduced to transfer data between the structural and hydrodynamic models follows.

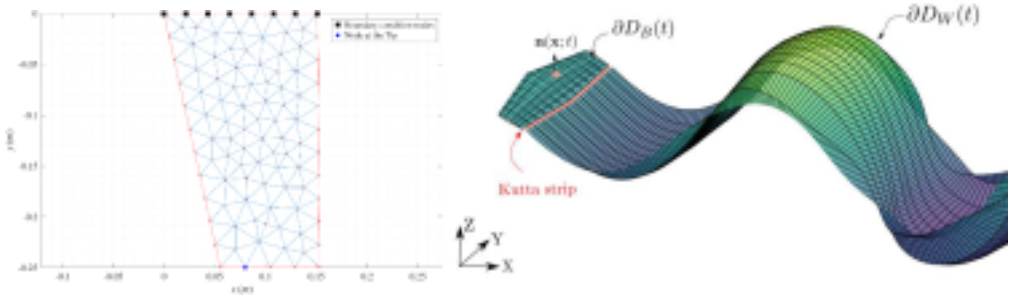


Figure 1. (a) Unstructured FEM mesh with DKT triangles on the wing's mean surface; exploiting symmetry and modelling half of the T-foil wing in a local body-fitted coordinate system [left] (b) Structured surface mesh for BEM solver with free wake in global inertial coordinate system [right].

2.1 Structural dynamics

The passive deformation caused by hydrodynamic pressure and inertial forces is solved in the local coordinate system xyz using the Kirchhoff's thin plate model based on the small displacements assumption; see Reddy (2006) for higher-order plate theories allow varying degrees of shear deformation. The thin plate assumption requires that local thickness-to-chord (or span) ratio is smaller than 0.1; which is valid for general wing shapes in marine applications. The vertical bending equation of motion (in the z-direction) for plates with variable flexural rigidity is the following 4rth order PDE,

$$D\nabla^4 w+\nabla^2 D\cdot\nabla^2 w+2\nabla D\cdot\nabla\left(\nabla^2 w\right) \\ -(1-\nu)\left(\partial_x^2 D\partial_y^2 w-2\partial_x\partial_y D\partial_x\partial_y w+\partial_y^2 D\partial_x^2 w\right)+\rho_s\tau(x)\partial_t^2 w=q_h\left(x;t\right)+q_f\left(x;t\right), \tag{1}$$

with hydrodynamic pressure difference and fictitious forces due to the non-inertial motions (enforced to the pivot point) given, respectively, by

$$q_h(x;t)=0.5\rho_f U^2\Delta C_p,\;\; q_f(x;t)=-\rho_s\tau(x)\left(x\cdot\ddot{\theta}(t)+\ddot{h}(t)\cos\theta(t)\right), \tag{2}$$

where $D(x,y)=\dfrac{E\tau^3(x)}{12(1-\nu^2)}$ denotes the flexural rigidity, E the Young's modulus, ν Poisson ratio, ρ_s the material density, $\tau(x)$ the plate thickness distribution and $\theta(t),h(t)$ the pitch/heave motion amplitudes. The above fourth order PDE is complemented by a set of natural and/or essential conditions on each edge. Common edge boundary conditions treated in the examined study cases include the clamped edge ($w=0,\;\partial_n w=0$) and the free edge conditions.

The numerical solution of Eqs. (1)-(2) is treated by means of FEM that essentially targets the equivalent variational problem. The smoothness requirements on the approximate solution poses a problem as the construction of conforming FEM schemes becomes challenging; Zienkiewicz (1990). For the numerical solution we have developed a finite element solver (FEM) based on DKT (Discrete Kirchhoff Triangle) elements. The DKT follows a C^0-formulation (Reissner-Mindlin) and satisfies the geometric Kirchhoff assumptions. The extended global equation that is derived from the Galerkin scheme using FEM assembly techniques, local-to-global numbering and Gaussian quadrature is

$$\mathbf{M}_{glob}\ddot{\mathbf{U}}+\mathbf{C}\dot{\mathbf{U}}+\mathbf{K}_{glob}\mathbf{U}=\mathbf{F}, \tag{3}$$

where $\mathbf{M}_{glob}$, $\mathbf{K}_{glob}$ stand for the global mass and stiffness matrices respectively, $\mathbf{F}_{glob}$ is the global load vector and $\mathbf{U}=[w^i,b^i{}_x,b^i{}_y,...]'$ is the vector containing the nodal unknowns for the partitioned

domain Ω^h. The selected boundary conditions are formulated by means of Lagrange multipliers and lead to an extension of the system of discretized equations; see Karperaki (2021). For the Delauney triangulation the Matlab PDE Toolbox is used. Regarding the proportional damping $\mathbf{C}=\alpha_1\mathbf{M}_{glob}+\alpha_2\mathbf{K}_{glob}$ the coefficients are defined using available experimental data. For the time-integration of the above 2nd order PDE in Eq. (3) we use the Newmark Method with $\gamma=0.5,\ \beta=0.25$,

$$\begin{aligned}\dot{\mathbf{U}}_{n+1}&=\dot{\mathbf{U}}_n+(1-\gamma)dt\ddot{\mathbf{U}}_n+\gamma dt\ddot{\mathbf{U}}_{n+1},\\ \mathbf{U}_{n+1}&=\mathbf{U}_n+dt\dot{\mathbf{U}}_n+dt^2\left(\frac{1}{2}-\beta\right)\ddot{\mathbf{U}}_n+dt^2\ddot{\mathbf{U}}_{n+1},\end{aligned} \tag{4}$$

Figure 1(a) shows the mesh corresponding to the wing of the T-foil configuration that is studied in the present work. The clamped boundary edge nodes are shown with black squares, whereas with the blue dot a node at the tip where free edge conditions apply is highlighted.

2.2 Hydrodynamic model

The wing and wake boundaries, denoted by $\partial D_B(t)$ and $\partial D_W(t)$ respectively, are modelled as surfaces of potential discontinuity in the global coordinate system XYZ. The wing surface undergoes prescribed rigid-body motions and is free to deform passively. The wake boundary represents the trailing vortex sheet that emanates from the sharp trailing edge which is modelled as a free shear layer with non-zero vorticity. The formulation of the initial boundary value problem (IBVP) problem is based on potential theory and boundary integral equations (BIE). The governing equation for the total velocity potential is the Laplace equation

$$\Delta\Phi(\mathbf{x};t)=0,\ \mathbf{x}\in D(t). \tag{5}$$

For the boundary value problem, a flow-tangency condition must be satisfied on the wing boundary

$$\partial_n\Phi(\mathbf{x};t)=\left(\mathbf{V}_{RIGID}(\mathbf{x};t)+\mathbf{n}_z(\mathbf{x};t)\frac{dw}{dt}\right)\cdot,\ \mathbf{n}_z(\mathbf{x};t)=(0,0,1),\mathbf{x}\in\partial D_B(\mathrm{t}) \quad , \tag{6}$$

where $\partial_n\Phi(\mathbf{x};t)=\nabla\Phi(\mathbf{x};t)\cdot\mathbf{n}(\mathbf{x};t)$ denotes the normal derivative with $\mathbf{n}(\mathbf{x};t)$ the unit normal vector on the body and $\mathbf{V}_{RIGID}(\mathbf{x};t)$ the instantaneous velocity of the wing due to rigid motions and $\mathbf{n}_z(\mathbf{x};t)\frac{dw}{dt}$ the velocity due to elastic displacement. To close the problem a non-linear (quadratic), pressure-type Kutta condition, requiring zero pressure difference at the trailing edge is enforced,

$$\partial_t(\Phi^u-\Phi^l)+0.5(\nabla\Phi^u+\nabla\Phi^l)\cdot(\nabla\Phi^u-\nabla\Phi^l)=0. \tag{7}$$

The above form of the pressure-type Kutta condition can be derived by using the approximate Bernoulli's theorem on the body at upper and lower sides of trailing edge along with the assumption that the trailing wake evolves in time as a material curve (based on the mean velocity); see Filippas & Belibassakis (2022). The approximate Bernoulli's theorem on an inertial frame is,

$$\frac{p(\mathbf{x};t)}{\rho_f}+\partial_t\Phi(\mathbf{x};t)+\frac{1}{2}\left[\nabla\Phi(\mathbf{x};t)\right]^2=0,\ \ \mathbf{x}\in\partial D(t). \tag{8}$$

Regarding the wake model, the vortex sheet emanates parallel to the bisector of the trailing edge and has the shape of trailing edge's path. The weakly singular Boundary Integral Equation (BIE), which holds for each $\mathbf{x}_o\in\partial D_B(t)$, is derived for the present formulation,

$$\frac{1}{2}\Phi_B(\mathbf{x}_0;t)+\int_{\partial D_B(t)}\Phi_B(\mathbf{x}_0;t)\partial_nG(\mathbf{x}_0\,|\,\mathbf{x})\mathrm{ds}(\mathbf{x})=\int_{\partial D_B(t)}b(\mathbf{x}_0;t)G(\mathbf{x}_0\,|\,\mathbf{x})\mathrm{ds}(\mathbf{x})-\int_{\partial D_W(t)}\mu_W(\mathbf{x}_0;t)\partial_nG(\mathbf{x}_0\,|\,\mathbf{x})\mathrm{ds}(\mathbf{x}), \tag{9}$$

with μ_W denoting the dipole intensity on the wake (or equivalently the potential jump) and $G(\mathbf{x}_0 \mid \mathbf{x})$ the Green function for the 3-D Laplace equation. An example of a BEM mesh with free wake modelling for the trailing wake is shown in Figure 1(b). Numerical instability mitigation due to vortex-sheet roll-up is addressed using the kernel-smoothing functions described in Filippas & Belibassakis (2022).

For the numerical solution of the above hydrodynamic problem a GPU-accelerated boundary element method (BEM) is developed, based on a formulation that is direct with respect to the potential. The pressure-type Kutta condition is the basis for the construction of the dynamical system equation and other kinematic boundary conditions are used as constraints. The discretized version of Eq. (9) based on a low-order piecewise-constant approximation is used as an algebraic constraint by means of the DtN (Dirichlet-to-Neumann) operator. Starting from a prescribed initial condition, e.g. from rest, a time-stepping method is applied to obtain the numerical solution. Particularly, the higher-order Adams-Bashforth-Moulton predictor-corrector method provides the required accuracy, stability and efficiency. The calculation of generalized forces is obtained without any further assumption by pressure integration. The latter is calculated by using an approximate Bernoulli equation.

2.3 Strong coupling

A partitioned coupling approach is implemented to treat the implicitly non-linear FSI problem. Information exchange between each step is based on the Inverse Distance Weighting method (or Shepard Interpolation). Figure 2 shows the details of the mesh interpolation scheme comprising of the BEM Control points, the centroids of each DKT triangle and the use of symmetry to treat only half of the wing in terms of the structural problem due to the T-foil boundary support. Figure 3 shows the flow chart of the procedure. More details regarding the coupling can be found in Anevlavi & Belibassakis (2026).

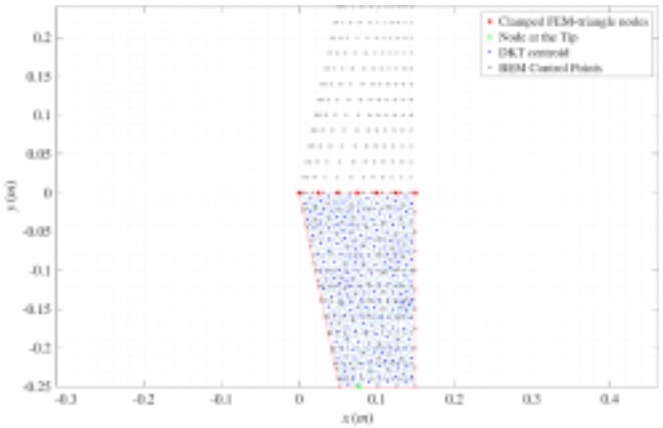


Figure 2. Swept back wing planform shape with the BEM collocation points and the FEM mesh.

3. Performance of bow T-foil thruster in irregular waves

The case study is based on previous towing tank experiments performed at the NTUA model basin for a ferry ship equipped with a bow T-foil wing; see Papakalodoukas and Belibassakis (2025). Figure 6 shows the T-foil configuration on board the ship model and a snapshot of the towing tank experiments at the NTUA basin. In the experiments, a maximum carriage running speed of 5.5m/s can be achieved, whereas the single-direction wave head waves of peak frequency between 0.3-1.2Hz with a significant wave height of 35cm are considered.

The bow T-foil is assumed to follow the exact ship motions for each sea state. Emphasis is given to the potential of the bow wing to generate net thrust under general heaving conditions, which are the result of ship motions in irregular waves. Particularly, linear wave theory is applied, assuming fully developed sea conditions with wave amplitudes that are small compared to the wavelength. The

Bretschneider frequency spectrum providing the distribution of wave energy in the frequency domain is employed to model irregular wave conditions. The wave spectrum $S(\omega)$ in the earth-fixed reference system is given by,

$$S(\omega) = \frac{1.25}{4}\frac{\omega_P^4}{\omega^5}H_S^2 exp\left(-1.25\left(\frac{\omega_P}{\omega}\right)^4\right) , \tag{10}$$

where $T_p = 2\pi / \omega_p$ denotes the modal (peak) period and H_s the significant wave height. Since, the foil responds to incident bow waves the encounter frequency ω_e needs to be taken into consideration.

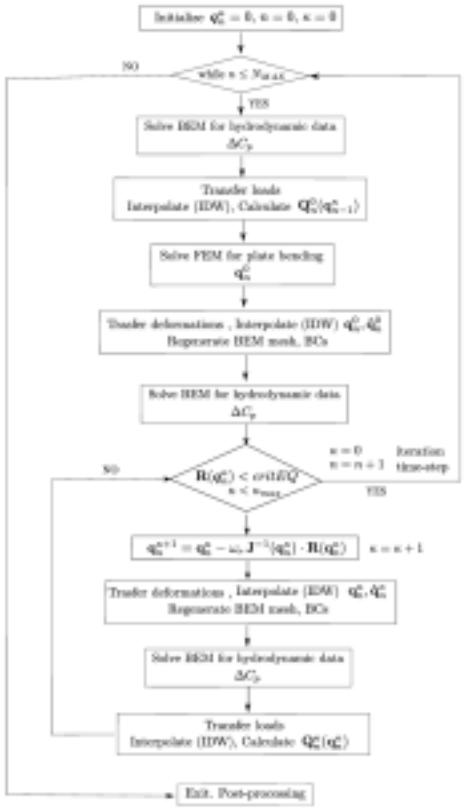


Figure 3. Flowchart for strongly coupled FSI BEM-FEM scheme; see Anevlavi & Belibassakis (2026).

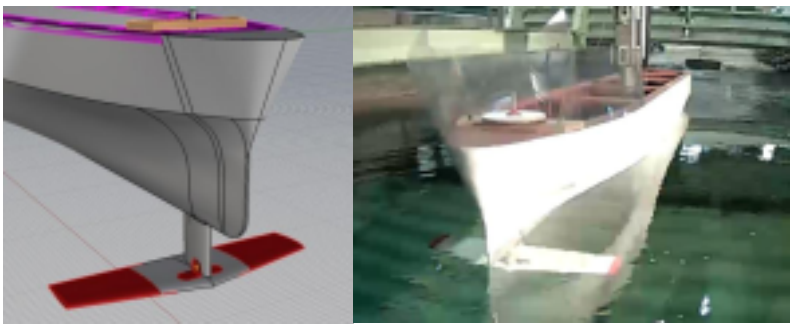


Figure 4. (a) 3D-CAD model of the ferry ship model (L=3.3m) with a T-foil arranged at the bow, and (b) Snapshot from NTUA towing tank experiments; see Papakalodoukas & Belibassakis (2025).

The wave spectrum from the perspective of a moving observer with the foil's mean velocity U is defined using,

$$S^U(\omega_e) = S(\omega)\frac{d\omega}{d\omega_e} = S(\omega)\cdot\left(1+\frac{2\omega U}{g}\right)^{-1}, \tag{11}$$

where the encounter frequency is $\omega_e = \omega + kU$, and $k = \omega^2/g$. In this work, for simplicity, we consider the Response Amplitude Operator of ship's bow motion to be $RAO_{foil}(\omega_e) = 1$, and the foil follows the wave elevation

$$S^U_{foil}(\omega_e) = S^U(\omega_e), \tag{12}$$

ans $H_s = 4\sqrt{m_o}$, where $m_o = \int_0^\infty S(\omega)d\omega = \int_0^\infty S^U(\omega_e)d\omega_e$. Consequently, the vertical motion of the T-foil can be simulated by the random-phase model; where the band of encounter frequencies is discretized into many consecutive bins of width $\delta\omega$ centered at the discrete values $\omega_{e,n}$, as follows

$$h(t) = \sum_n h_n \cos(\omega_n + \epsilon_n),\ \ h_n = \sqrt{2S^U_{foil}(\omega_{e,n})\delta\omega_e}\ , \tag{13}$$

where ϵ_n are random phases that are uniformly distributed in $[0,2\pi)$; see, e.g., Ochi (1998).

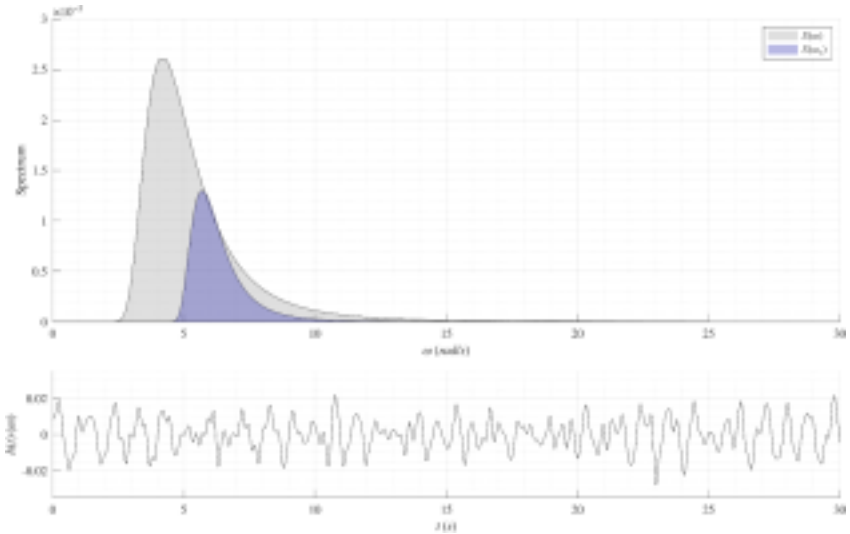


Figure 5. (a) Simulation of the foil's vertical motion for ship model speed U=1.2m/s in head waves Hs=3.5 cm and Tp=1.5s. (b) Spectrums S(ω), S(ωe) are shown with blue and orange colors respectively, where S(ω) refers to the bar graph with higher peak values.

4. Numerical results

The FSI numerical method presented above is further extended to treat more general oscillatory motions. Indicative results concerning the hydrodynamic performance of a T-foil operating as a ship energy-saving device under realistic sea state conditions are obtained and discussed. The planform shape of the examined T-foil with sectional profiles NACA0012 is shown in Figure 4. Moreover, in Figure 5 the wave frequency spectrum for a specific test case are shown, in the earth-fixed and moving frames of reference, respectively, corresponding to significant wave height Hs=3.5 cm, peak period

*T*p=1.5s, and model speed *U*=1.2m/s, as well as the simulated time history of the foil's vertical motion which is examined next in the case of rigid and elastic foil response.

4.1 Rigid wing response

In the experiments the presence of the T-foil leads to a noticeable reduction of vertical ship model oscillations and reduced added wave resistance, via stabilization of the ship in waves. Our aim here is to simulate the above condition and predict the net thrust following the simplified approach for enforcing the general heaving motions on the T-foil based on irregular wave motions of the ship. The time history of the thrust coefficient is provided below in Figure 6. The T-foil produced net thrust of Ct,foil = 0.0080 with a planform area of $S = 0.062m^2$. Numerical results are obtained using a BEM mesh comprising of NEA=25 and NEC=30 panel elements in the spanwise and chordwise direction. A time discretization of dt=0.0054s or TSR=0.35 (i.e. 0.35% percentage of Tp=1.5sec) for simulating a number of Nper = 18. All simulations are performed on a PC with Intel Core Ultra 7 (RAM 16GB) and NVIDIA GeForce RTX 4050 Laptop GPU (VRAM 8GB); supporting the argument that the present numerical tool is cost-effective and can run on various portable computers.

Present method results are generally in agreement with the findings of Papakalodoukas & Belibassakis (2025) and the greater value of net thrust is attributed to consideration of the heaving time history without filtering the data, which results in reduction of peak amplitudes. The above numerical experiment has been performed multiple times, with consideration of different seeds for generating random phase angle datasets to check the repeatability.

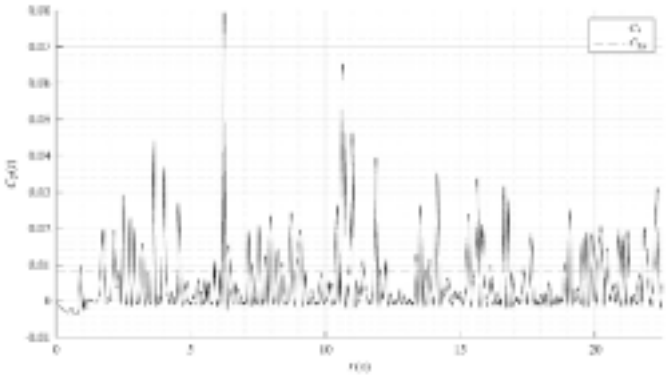


Figure 6. Thrust coefficient as calculated by the present model in irregular head waves in the same conditions as in Fig.5, The long-term average value *C*x=0.008 is indicated by using dashed line.

4.2 Flexible wing response

For the elastic wing we assume it comprises of an aluminum sheet material core with thickness τ=1mm, whereas the hydrofoil shape can be given using polyurethane rubber material; see Heathcote et al. (2008). However, only the metal sheet is used to represent the response of the wing for simplicity. For the aluminum we assume E=71GPa, ρs=2700kg/m^2 and Poisson ratio ν=0.28. Emphasis is given to the time-histories of lift, thrust and moment; with respect to [0.3c,0,0]. The predicted time histories due to the irregular head waves of Fig.5 are shown in Figure 7. Aggregated data analysis from five cycles reveal that the elastic foil produces higher lift, while thrust is shown to be reduced. The latter is attributed to the phase-lag between the enforced rigid body motions and the elastic displacement that alters hydrofoil shape by introducing "camber" to an originally symmetric section; thus, affecting vorticity shedding at the TE. Moment coefficient remains at low values. Figure 8 shows two instances of the deflected wing mid-surface with tip-displacement to chord length ratios below 3.5%; which lie within the applicability of thin plate equation. All the above supports the argument that the present FSI model provides useful information for the analysis of biomimetic thrusters supporting the design of novel thrusters.

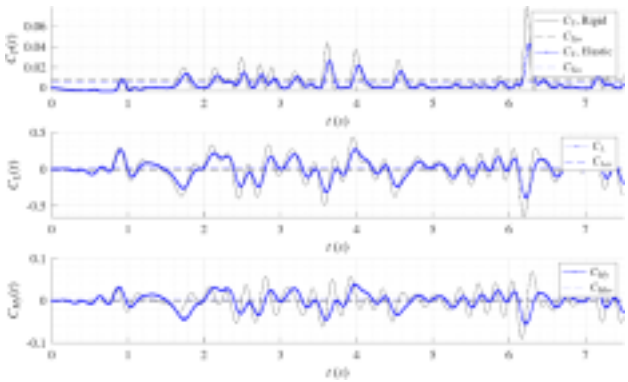


Figure 7. Lift, thrust and moment coefficient time history as calculated by the present model in irregular head waves in the same conditions as in Fig.5.

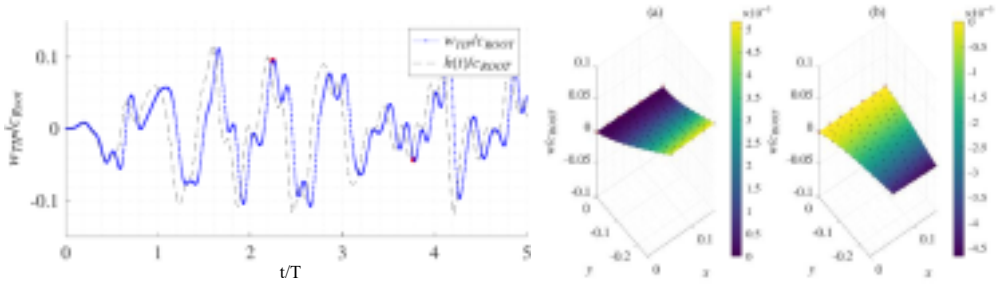


Figure 8. Time history of tip deflection in the inertial frame (left subplot). Snapshots of the deformed wing shape corresponding to the red dot time steps (right subplot).

5. Conclusions

The performance of a bio-mimetic wing operating as a thrust-augmentation device, including elasticity effects, is studied by a 3D fluid-structure interaction solver. The proposed FSI model consists of a 3D unsteady boundary element method that is strongly coupled with a finite element solver based on discrete Kirchhoff plate elements. Previous work in Anevlavi & Belibassakis (2026) supports the validity of the developed scheme for analyzing wing-thruster performance through comparisons between predicted results and experimental data. In the present work, the FSI scheme is used to predict the hydro-elastic response of a horizontal T-foil concept, installed at the vessel's bow and designed to operate as an augmenting propulsion device. For simplicity, the wing is assumed to undergo prescribed vertical oscillations induced by the vessel's response to irregular head waves and characterized by a known frequency spectrum. Incorporating elasticity into the design has been found to increase cycle-averaged lift coefficient while reducing generated thrust, compared to the equivalent rigid T-foil concept. These findings suggest that the interaction between the vessel's dynamics and the hydro-elastic response of the T-foil needs to be studied in future work to reveal whether the elastic foil has the potential to reduce further ship responses; offering significant dynamic stabilization. Moreover, future research will also focus on design space exploration involving optimal shape and material properties distribution.

References

[1] J. Xing and L. Yang, *Wave devouring propulsion: An overview of flapping foil propulsion technology*, Renewable and Sustainable Energy Reviews, 184:113589, 2023.

[2] R. Salazar, V. Fuentes and A. Abdelkefi, *Classification of biological and bioinspired aquatic systems: A review,* Ocean Engineering, 185:75-114, 2018.
[3] Q. Xiao and Q. Zhu, *A review on flow energy harvesters based on flapping foils,* Journal of Fluids and Structures, 46:176-191, 2014.
[4] E.S. Filippas, Th.P. Gerostathis and K.A. Belibassakis, *Semi-activated oscillating hydrofoil as a nearshore biomimetic energy system in waves and currents,* Ocean Engineering, 154:396-415, 2018.
[5] A. Korobkin, E.I. Parau and J.M. Vanden-Broek, *The mathematical challenges and modelling of hydroelasticity*, Philos Trans A Math Phys Eng Sci., 369: 2803-12, 2011.
[6] H. Heo, J. Ju and D.M. Kim, *Compliant cellular structures: Application to a passive morphing airfoil,* Composite Structures, 106:560-69, 2013.
[7] M.T. Herath, B.G. Prusty, A.W. Phillips and N.S. John, *Structural strength and laminate optimization of self-twisting composite hydrofoils using a Genetic Algorithm*, Composite Structures, 176:359-78, 2017.
[8] M. Sfakiotakis, D. Lane and J. Davies, *Review of fish swimming modes for aquatic locomotion,* IEEE Journal of Oceanic Engineering, 24:237-252, 1999.
[9] E. Bøckmann and S. Steen, *Experiments with actively pitch-controlled and spring-loaded oscillating foils,* Applied Ocean Research, 48:227-235, 2014.
[10] E. Bøckmann, A. Yrke and S. Steen, *Fuel savings for a general cargo ship employing retractable bow foils,* Applied Ocean Research, 76:1-10, 2018.
[11] K. Belibassakis, E. Filippas and G. Papadakis, *Numerical and experimental investigation of the performance of dynamic wing for augmenting ship propulsion in head and quartering seas,* J. Mar. Sci. Eng., 10:24, 2022.
[12] D. Ntouras, G. Papadakis, and K. Belibassakis, *Ship bow wings with ap plication to trim and resistance control in calm water and in waves*, J. Mar. Sci. Eng., 10:492, 2022.
[13] J. Bowker, N. Townsend, *A probabilistic method to evaluate bow foils for realistic seas and shipping routes*, Applied Ocean Research, 129: 103374, 2022.
[14] Y. Zhang, L. Xu, and Y. Zhou, *A wave foil with passive angle of attack adjustment for wave energy extraction for ships*, Ocean Engineering, 246:110627, 2022.
[15] L. Mei, W. Yan, J. Zhou and W. Shi, *Thrust enhancement of DTBM 5415 with elastic flapping foil in regular head waves*, Journal of Marine Science and Engineering, 11:632, 2023.
[16] D.B. Quinn, G.V. Lauder and A.J. Smith, *Maximizing the efficiency of a flexible propulsor using experimental optimization*, J. Fluid Mech., 767:430-448, 2015.
[17] A.J. Richards, P. Oshkai, *Effect of stiffness, inertia and oscillation kinematics on the thrust generation and efficiency of an oscillating-foil propulsion system*, J. Fluids and Structures, 57: 357-374, 2015.
[18] D. Anevlavi, K. Belibassakis, *A strongly coupled 3D BEM-FEM fluid–structure interaction model for the analysis of flexible biomimetic thrusters,* Journal of Fluids and Structures, 140:104464, 2026.
[19] I. Papakalodoukas, K. Belibassakis, *Performance prediction of bow-foil thrusters in waves using unsteady vortex element method,* J. Mar. Sci. Eng., 13:1152, 2025.
[20] S. Heathcote, Z. Wang and I. Gursul, *Effect of spanwise flexibility on flapping wing propulsion*, Journal of Fluids and Structures, 24:183-199, 2008.
[21] E. Filippas, K. Belibassakis, *A nonlinear time-domain BEM for the performance of 3D flapping-wing thrusters in directional waves,* Ocean Engineering 245:110157, 2022.
[22] J. Reddy, *Theory and analysis of elastic plates and shells*, Boca Raton: CRC Press, 2006.
[23] O. Zienkiewicz, R. Taylor, P. Papadopoulos. and E. Oñate, *Plate bending elements with discrete constraints: New triangular elements*, Computers & Structures 35(4) 505-522, 1990.
[24] A. Karperaki, *Hydroelastic interaction between ocean waves and large floating structures in the inhomogeneous ocean environment,* Ph.D. Thesis, School of Naval Architecture and Marine Engineering, NTUA, 2021.
[25] M.K. Ochi, *Ocean Waves. The Stochastic Approach*, Cambridge University Press, 1998.

10th International Conference on HYDROELASTICITY IN MARINE TECHNOLOGY
Trondheim, Norway, June16$^{\text{th}}$-18$^{\text{th}}$, 2026

Hydroelastic Consequences of Passive Vortex-Generator Control in Cavitating Flexible Hydrofoils

Yuxing Lin[1], Ould el Moctar[2], and Changqing Jiang[1] *

[1] University of Duisburg–Essen, Duisburg 47057, Germany
[2] Technische Universität Berlin, Berlin 10623, Germany

Abstract. Building on our earlier experimental study of cavitation–hydroelastic interaction in flexible hydrofoils with passive vortex-generator control, the present paper provides a focused interpretation of the $Re = 5 \times 10^5$ dataset. The aim is to clarify how a leading-edge wedge-type vortex generator modifies cavitation morphology and structural response in cloud and partial cavitation, and to show why cavity suppression and vibration suppression are not equivalent objectives. Two representative operating conditions are examined, namely cloud cavitation at $\sigma = 1.4$ and partial cavitation at $\sigma = 1.8$. Synchronized high-speed cavitation imaging and stereo digital image correlation are used to compare a rigid reference hydrofoil, an unmodified flexible hydrofoil, and a flexible hydrofoil equipped with the passive device. In cloud cavitation, the vortex generator breaks the large detached cavity into smaller and more rapidly condensing structures and reduces the RMS displacement of the flexible hydrofoil from 0.2309 to 0.1625 mm, which corresponds to a reduction of 29.6%. In partial cavitation, the device still shortens the cavity, but the RMS displacement rises from 0.0696 to 0.1344 mm, which corresponds to an increase of 93.1%. These results show that passive cavitation control should be assessed using both cavitation morphology and hydroelastic response, because a device that effectively suppresses large cloud cavitation can still be unfavorable for structural vibration under another operating condition.

Key words: *Hydroelasticity; Cavitation; Hydrofoil; Vortex generator; Fluid–structure interaction; Passive control*

1. Introduction

Cavitating lifting surfaces are encountered in propellers, pump and turbine blades, rudders, hydrofoils, and other marine or turbomachinery components operating under strong adverse pressure gradients [1]. Once vapor cavities form, grow, and collapse on the suction side, the resulting pressure fluctuations may generate severe vibration, erosion, noise, and performance loss [2]. In flexible components, the problem becomes hydroelastic. The structure responds to cavitation loading, while its deformation simultaneously modifies the effective angle of attack, pressure distribution, and cavity topology [3].

Among the major cavitation regimes, cloud cavitation is particularly damaging because it involves repeated shedding and collapse of large detached vapor structures [4]. The associated impulsive loading can excite substantial bending and torsional motion. Partial cavitation is often less dramatic in appearance, but it can still produce a significant structural response when the remaining unsteadiness lies close to a structural mode [5]. For engineering design, the central question is therefore not only how to reduce cavity extent, but also how to control the pathway through which cavitation-induced loading couples with the structure.

Passive cavitation-control concepts such as roughness elements, grooves, obstacles, riblets, biomimetic leading-edge modifications, and vortex generators have been explored extensively in the literature [6].

*Correspondence to: changqing.jiang@uni-due.de

Their principal role is to modify the near-wall flow, the boundary layer, or the streamwise-vorticity field, thereby changing cavity growth, re-entrant-jet development, and large-scale shedding [7]. Many of these approaches have shown encouraging results for rigid hydrofoils, but their hydroelastic implications in three-dimensional cavitating flow remain much less resolved [8].

Our recent work reported a broader experimental campaign on a rigid hydrofoil, an unmodified flexible hydrofoil, and a flexible hydrofoil equipped with a wedge-type leading-edge vortex generator, covering two Reynolds numbers and a wide range of cavitation conditions [9]. The present paper is deliberately narrower in scope. It revisits only the $Re = 5 \times 10^5$ cases from that dataset, because this Reynolds number reveals the hydroelastic trade-off particularly clearly. At this condition, the vortex generator reduces both cavity severity and vibration in cloud cavitation, whereas in partial cavitation it reduces cavity extent but increases the measured structural response. The contribution of the present paper lies in this focused interpretation rather than in the presentation of a new dataset. By restricting the discussion to one Reynolds number and two representative operating points, the paper highlights a compact design message. Passive control modifies the cavitation oscillator, and its hydroelastic consequence depends strongly on the operating regime.

2. Experimental basis

The complete facility description, uncertainty analysis, and full two-Reynolds-number dataset are documented in Ref. [9]. Only the information required for the present discussion is summarized here.

2.1. Facility and selected operating points

All data were obtained in the K23 closed-loop cavitation tunnel at the University of Duisburg–Essen. The tunnel test section measures $0.3 \times 0.3 \times 1.1\ \mathrm{m}^3$ and provides full optical access for synchronized cavitation imaging and stereo digital image correlation. The hydrofoil was mounted on the starboard wall and operated at a fixed angle of attack of 10°. Figure 1 summarizes the experimental basis used in the present paper.

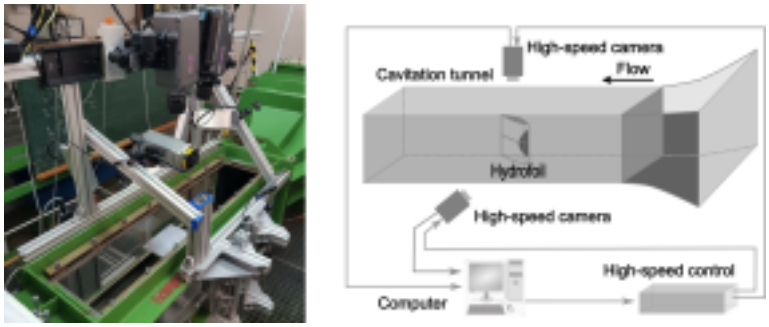


Figure 1: Experimental basis of the present study, adapted from Ref. [9].

The present paper focuses on the inflow velocity $U = 5\ \mathrm{m/s}$, which corresponds to $Re = 5 \times 10^5$ based on the hydrofoil chord length $c = 100\ \mathrm{mm}$. The cavitation number is defined as

$$\sigma = \frac{p_r - p_v}{0.5\rho U^2}, \tag{1}$$

where p_r is the upstream reference pressure, p_v is the vapor pressure, and ρ is the water density. Two representative cases are considered, namely cloud cavitation at $\sigma = 1.4$ and partial cavitation at $\sigma = 1.8$. These two operating points span the key change in hydroelastic behavior discussed in this paper.

2.2. Hydrofoil configurations and measurements

Three NACA 0015 hydrofoils were employed, namely a rigid stainless-steel reference hydrofoil, an unmodified flexible polyvinyl chloride hydrofoil, and a flexible polyvinyl chloride hydrofoil equipped with a wedge-type passive vortex generator. All hydrofoils had a chord length of $100\ \mathrm{mm}$ and a span of $200\ \mathrm{mm}$. The rigid hydrofoil is included mainly as a reference for separating structural effects from facility-induced motion. Figure 2 shows the three hydrofoil configurations and the geometry of the passive device.

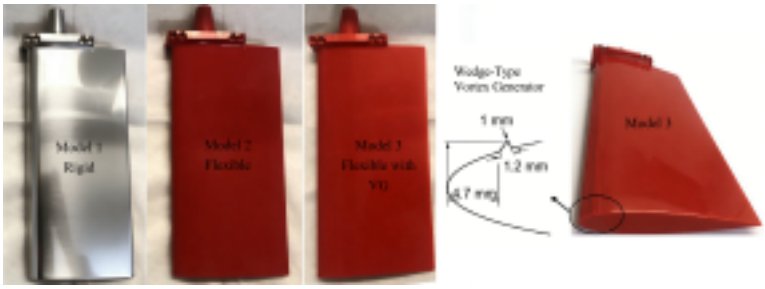


Figure 2: Hydrofoil configurations used in the experiments, adapted from Ref. [9].

The wedge-type vortex generator was installed near the leading edge so that it could modify cavitation inception and the early stage of attached-cavity development before the large-scale cloud-shedding cycle became established. Its position started at $x_0/c = 0.047$, with a base length of $l = 1.2\ \mathrm{mm}$ and a height of $h = 1.0\ \mathrm{mm}$. The design intent was to generate streamwise-vorticity forcing that fragments or shortens the attached cavity and shifts the unsteady cavitation dynamics away from the large-scale cloud-cavitation cycle.

Cavitation morphology and structural response were measured synchronously using high-speed imaging and stereo digital image correlation. The image sequences were recorded at $1500\ \mathrm{Hz}$ with approximately 2800 frames per sequence. A stochastic speckle pattern was applied to the pressure side of the flexible hydrofoils to enable digital image correlation without obstruction by the cavity on the suction side. The reconstructed out-of-plane displacement uncertainty was of order $10^{-3}\ \mathrm{mm}$. The previously reported upper-bound value under non-cavitating tunnel operation is $1.7 \times 10^{-3}\ \mathrm{mm}$, which is small relative to the cavitation-induced responses discussed below [9].

Prior to the cavitation tests, impulse measurements in water were performed to determine the first wet natural frequency of each hydrofoil. The measured values are listed in Table 1. The lower first wet frequency of the vortex-generator-equipped flexible hydrofoil is attributed to the added mass and mass redistribution introduced by the passive device and its attachment.

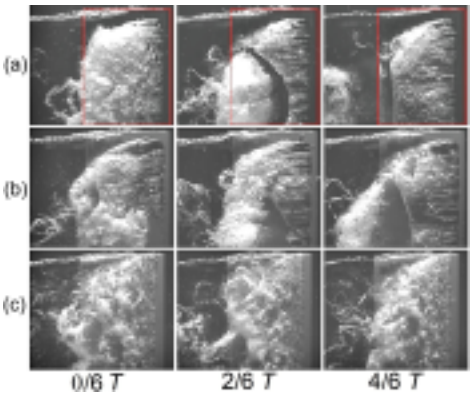
Table 1: Measured first wet natural frequencies of the hydrofoils in water

Property	Rigid	Flexible	Flexible + VG
Material	Steel	PVC	PVC
f_{e} [Hz]	77.41	36.57	30.86

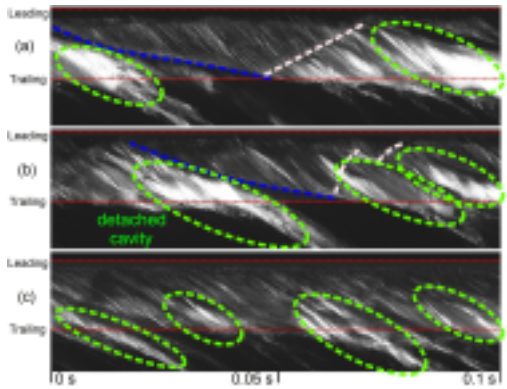
3. Cloud cavitation

3.1. Suppression of the large-scale cloud-shedding cycle

The cloud-cavitation case at $\sigma = 1.4$ provides the clearest example of beneficial passive control. In the rigid and unmodified flexible hydrofoils, the cavity evolution is governed predominantly by re-entrant-jet-driven shedding. The attached cavity grows, detaches, and forms large downstream vapor clouds that condense rapidly. Relative to the rigid reference, the flexible hydrofoil exhibits more compact detached clouds and a more disturbed shedding sequence, which indicates that hydroelastic deformation already feeds back on the cavity dynamics. Representative instantaneous cavity morphologies and the corresponding space–time cavitation signatures are presented in Fig. 3.



(a) Instantaneous cavitation morphology



(b) Representative space–time cavitation signature, blue line for cavitation development and white line for re-entrant jet movement

Figure 3: Cloud-cavitation behavior at $Re = 5 \times 10^5$, angel of attack = 10 degrees and $\sigma = 1.4$, (a) rigid hydrofoil; (b) flexible hydrofoil and (c) flexible hydrofoil with vortex generator

With the wedge-type vortex generator installed, the cavitation topology changes qualitatively. Instead of large detached clouds, the vortex-generator-equipped hydrofoil produces markedly smaller vapor structures that are shed more frequently and condense over a shorter downstream distance. A short attached cavity persists near the leading edge, but the large-scale cloud system is strongly weakened. The space–time cavitation signatures show the same tendency. The coherent low-frequency cloud pattern of the baseline hydrofoils is replaced by finer and more rapidly interrupted shedding events. In physical terms, the passive device reconfigures the cavitation oscillator from an energetic large-scale cloud cycle to a smaller-scale and higher-frequency process.

3.2. Hydroelastic response under cloud cavitation

The digital image correlation measurements show that the morphological change is accompanied by a clear reduction in structural response. At $Re = 5 \times 10^5$ and $\sigma = 1.4$, the unmodified flexible hydrofoil exhibits an RMS out-of-plane displacement of 0.2309 mm, whereas the flexible hydrofoil with vortex generator reaches 0.1625 mm. This corresponds to a reduction of 29.6%. The associated time histories of structural deformation are shown in Fig. 4.

The spectral results reported previously for this operating point show two main groups of peaks, namely a low-frequency group associated with cloud-cavitation shedding and a second group near the hydrofoil natural-frequency band [9]. The vortex generator reduces the amplitude in both groups. This

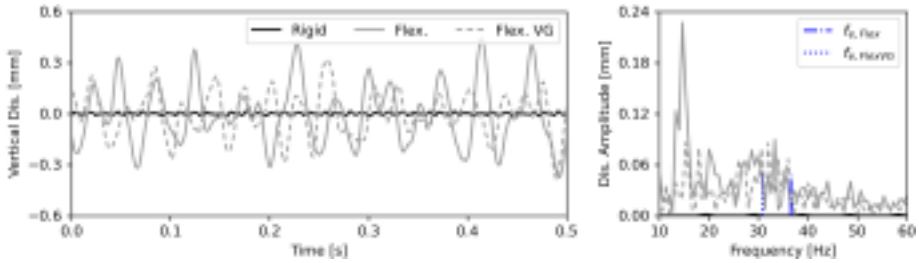


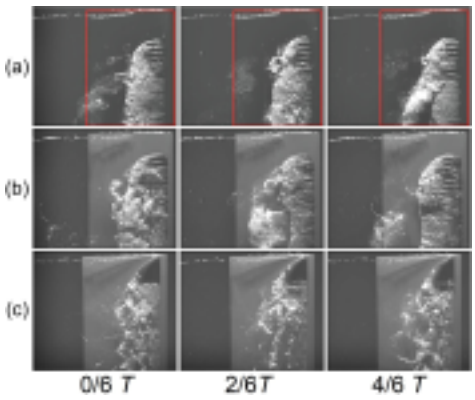
Figure 4: Time series of structural response at $Re = 5 \times 10^5$ and $\sigma = 1.4$. The vortex generator suppresses large detached cavities and reduces the flexible-hydrofoil RMS displacement from 0.2309 to 0.1625 mm

behavior is the hydroelastic signature of successful passive control in the present study. The device weakens the large-scale cloud oscillator and simultaneously reduces the structural response driven by that oscillator.

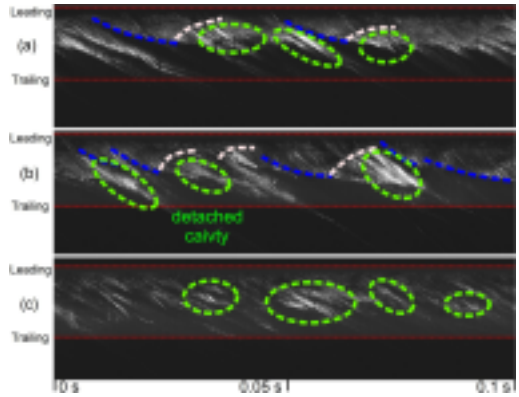
4. Partial cavitation

4.1. Reduced cavity extent and increased vibration

The partial-cavitation case at $\sigma = 1.8$ reveals the central trade-off of the paper. Compared with cloud cavitation, the attached cavity is shorter, the detached vapor structures are smaller, and the re-entrant jet is weaker. In the rigid and unmodified flexible hydrofoils, cavity detachment becomes more localized and irregular. When the vortex generator is added, the attached cavity becomes even shorter and more fragmented. From a purely flow-visualization perspective, the control effect still appears favorable, because large detached clouds do not develop. Representative cavity morphologies and space–time signatures for this regime are shown in Fig. 5.



(a) Instantaneous cavitation morphology



(b) Representative space–time cavitation signature, blue line for cavitation development and white line for re-entrant jet movement

Figure 5: Partial-cavitation behavior at $Re = 5 \times 10^5$, angel of attack = 10 degrees and $\sigma = 1.8$, (a) rigid hydrofoil; (b) flexible hydrofoil and (c) flexible hydrofoil with vortex generator

The hydroelastic measurements, however, show that this interpretation is incomplete. At $Re = 5 \times 10^5$ and $\sigma = 1.8$, the unmodified flexible hydrofoil exhibits an RMS displacement of 0.0696 mm, whereas the vortex-generator-equipped flexible hydrofoil reaches 0.1344 mm. The increase is approximately 93.1%, even though the cavity itself is reduced. The corresponding structural-response time histories are given in Fig. 6.

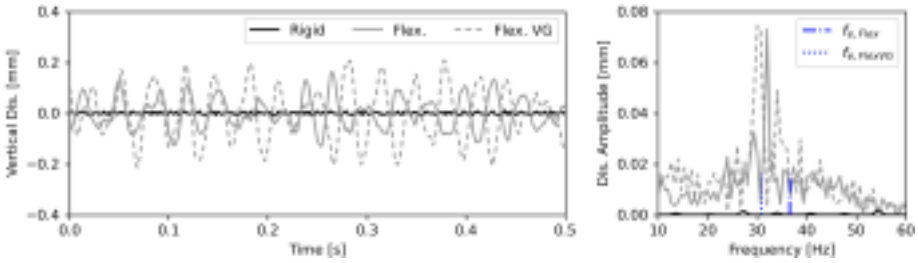


Figure 6: Time series of structural response at $Re = 5 \times 10^5$ and $\sigma = 1.8$. The vortex generator shortens the cavity but increases the flexible-hydrofoil RMS displacement from 0.0696 to 0.1344 mm

The frequency-domain results provide the key physical explanation. The low-frequency peak associated with cloud-cavitation shedding disappears in this regime, which is consistent with the absence of large detached cloud structures. The remaining vibration energy is concentrated near the first wet-mode band, and the vortex generator shifts the forcing toward this response-prone range [9]. In other words, the passive device improves the cavity morphology but reconfigures the residual unsteadiness in a way that is more effective at exciting the flexible structure.

5. Focused design interpretation

The value of restricting the conference paper to one Reynolds number is that the hydroelastic consequence of passive control becomes particularly evident. At $Re = 5 \times 10^5$, the cloud-cavitation and partial-cavitation cases already expose two distinct excitation pathways. In cloud cavitation, the large detached cavity is the dominant source of energetic forcing, so suppressing that oscillator leads simultaneously to smaller cavities and lower vibration. In partial cavitation, the cloud oscillator has largely disappeared, and the controlling issue is no longer cavity size itself but the frequency content of the residual unsteadiness. A quantitative comparison of the RMS displacement levels in the two regimes is summarized in Table 2.

Table 2: Cross-regime comparison of the flexible-hydrofoil RMS displacement.

Condition	Flexible [mm]	Flexible + VG [mm]	Change due to VG
Cloud cavitation, $\sigma = 1.4$	0.2309	0.1625	-29.6%
Partial cavitation, $\sigma = 1.8$	0.0696	0.1344	$+93.1\%$

This shift in excitation pathway explains why the same passive device can appear favorable in cavitation images and yet produce an opposite structural outcome. The vortex generator fragments the attached cavity and promotes smaller and more frequent shedding events in both regimes. In cloud cavitation, that redistribution is beneficial because it removes the energetic low-frequency cloud cycle. In

partial cavitation, the redistributed loading remains sufficiently close to the first wet-mode band that the flexible response increases rather than decreases. The main design lesson is therefore not that the vortex generator works or fails in a universal sense. Rather, the device changes the cavitation oscillator, and the structural consequence of that change depends on the operating regime.

For hydrofoils, propulsor blades, and related flexible lifting surfaces, this point has a direct engineering implication. Passive cavitation control should be evaluated using at least two classes of metrics, namely a flow-side metric related to cavity severity and a structure-side metric related to deformation or spectral response. A smaller cavity does not necessarily imply a safer hydroelastic state. Conversely, a control device that is beneficial for suppressing erosion-prone cloud cavitation may still require optimization if vibration reduction is also a design objective. This multi-objective perspective is the main added emphasis of the present conference paper.

6. Closing discussion and conclusions

This conference paper revisits the $Re = 5 \times 10^5$ subset of our previously reported experimental dataset in order to sharpen a single message. Passive vortex-generator control should be interpreted through its hydroelastic consequence rather than through cavity reduction alone. The narrower scope is intentional. By contrasting one cloud-cavitation case with one partial-cavitation case at the same Reynolds number, the paper isolates the regime dependence more clearly than a broader multi-condition narrative.

In cloud cavitation at $\sigma = 1.4$, the wedge-type vortex generator suppresses the re-entrant-jet-driven large-scale cloud-shedding cycle and replaces it with smaller and more rapidly condensing vapor structures. The structural consequence is favorable. The flexible-hydrofoil RMS displacement decreases from 0.2309 to 0.1625 mm, which corresponds to a reduction of 29.6%. Under this operating condition, the flow-control objective and the vibration-mitigation objective are aligned. The device weakens the most energetic cavitation oscillator, and the structural response decreases accordingly.

In partial cavitation at $\sigma = 1.8$, the interpretation changes. The vortex generator still shortens and fragments the cavity, so the flow field appears more benign when judged only from cavitation images. Nevertheless, the RMS displacement increases from 0.0696 to 0.1344 mm, which corresponds to an increase of 93.1%. The reason is not an increase in large detached clouds, but a redistribution of the remaining unsteady loading toward the first wet-mode response band. This case therefore demonstrates the central caution of the study. Reduced cavity extent and reduced vibration are not equivalent outcomes.

The broader design implication is that passive control should be assessed over the operating envelope and with both flow-side and structure-side diagnostics. For applications in which cloud-cavitation suppression, noise reduction, or erosion mitigation dominate the design objective, the wedge-type vortex generator is promising because it effectively suppresses the energetic large-scale cloud cycle. For applications in which vibration or fatigue is critical, however, the same device may require further optimization because the modified forcing can remain hydroelastically unfavorable in partial cavitation. Future work should therefore combine cavity morphology, full-field deformation, and direct pressure or load measurements within a unified optimization framework for passive hydroelastic cavitation control.

References

[1] Roger EA Arndt. Cavitation in fluid machinery and hydraulic structures. *Annual Review of Fluid Mechanics*, 13(1):273–326, 1981.

[2] Jean-Pierre Franc and Jean-Marie Michel. *Fundamentals of cavitation*. Springer, 2005.

[3] Antoine Ducoin, Yin Lu Young, and Jean-Franc¸ois Sigrist. Hydroelastic responses of a flexible hydrofoil in turbulent, cavitating flow. In *Fluids Engineering Division Summer Meeting*, volume 54518, pages 493–502, 2010.

[4] Y Kawanami, Hiroharu Kato, Hajime Yamaguchi, M Tanimura, and Y Tagaya. Mechanism and control of cloud cavitation. 1997.

[5] Saad Jahangir, Willian Hogendoorn, and Christian Poelma. Dynamics of partial cavitation in an axisymmetric converging-diverging nozzle. *International Journal of Multiphase Flow*, 106:34–45, 2018.

[6] Debabrata Panda, Virendra Kumar Saharan, and Sivakumar Manickam. Controlled hydrodynamic cavitation: A review of recent advances and perspectives for greener processing. *Processes*, 8(2):220, 2020.

[7] Yuxing Lin, Ebrahim Kadivar, Ould el Moctar, Jens Neugebauer, and Thomas E Schellin. Experimental investigation on the effect of fluid–structure interaction on unsteady cavitating flows around flexible and stiff hydrofoils. *Physics of Fluids*, 34(8), 2022.

[8] Mahshid Zaresharif, Florent Ravelet, David J Kinahan, and Yan Delaure. Cavitation control using passive flow control techniques. *Physics of Fluids*, 33(12), 2021.

[9] Yuxing Lin, Ould el Moctar, and Changqing Jiang. Experimental study of coupled cavitation–hydroelasticity interaction in hydrofoils with passive vortex-generator control. *Physics of Fluids*, 38(3), 2026.

Hydroelastic Problems and Methods

10th International Conference on HYDROELASTICITY IN MARINE TECHNOLOGY
Trondheim, Norway, June 16th-18th, 2026

Data-driven prediction of design global bending loads in ships from model tests

Drummen, I.*, Kaydihan, L. , Düz, B. Kurnia, R.

{i.drummen, l.kaydihan, b.duz, r.kurnia}@marin.nl
MARIN, Wageningen, Netherlands

Abstract. Knowledge of extreme global loads is essential for ensuring structural safety throughout a ship's operational life. Accurately estimating these loads allows designers to achieve sufficient structural strength without the excessive conservatism that leads to unnecessary construction and operational costs. Although several methods exist for evaluating hydrodynamic loads, no documented and unified procedure is available for predicting extreme global bending moments that consistently incorporates nonlinear and transient load components. This paper proposes an approach for using model test results with machine learning for an assessment of extreme global load effects. The example in the paper is based on model tests. Advanced CFD simulations can, however, also be used as a basis. Incorporating the nonlinear hydro structural analyses to feed this methodology enables us to include whipping in the analyses. Lastly, a proposal is made for extending the method to fatigue damage.

Key words: *Extreme values; Multifidelity; Data driven; Fatigue damage, Ships*

1. Introduction

Understanding extreme bending loads is critical in ship design to ensure safety. Accurate predictions allow for sufficient structural strength without incurring the excessive costs associated with overly conservative estimates. Over the past decades, significant research has focused on methods for predicting extreme global load effects (see, for example, [1], [2], [3]). However, these approaches rely on various assumptions, and there is no universal consensus on acceptable probabilities for classifying extreme events.

A range of numerical tools has been developed to predict extreme values, but these tools are either incomplete in terms of physical modeling or too computationally demanding for comprehensive long-term analyses. Frequency-domain methods are highly efficient for evaluating a wide range of conditions but cannot adequately account for nonlinear loads. Conversely, model tests and advanced simulations—up to RANS-based CFD methods [4], [5]—capture the physics more accurately but are limited in the number of conditions that can realistically be studied. Combining computationally efficient low-fidelity tools with high-fidelity data from model tests or advanced simulations offers a powerful approach [6].

A key aspect of high-fidelity data is the inclusion of whipping effects. For example, [2] demonstrated that hull flexibility can increase vertical bending moments by up to 35% for containerships in design-relevant sea states. Similarly, full-scale measurements reported in [7] indicate an increase of approximately 20% in amidships vertical bending moments for a frigate hull during actual sailing conditions.

Several procedures have been established to investigate the dynamics of extreme load cases. One such method is the Most Likely Response Wave (MLRW) approach [8], [9], which derives a wave train expected to produce a maximum response through reverse engineering. This involves combining wave

* Correspondence to: i.drummen@marin.nl

information with the ship's transfer function and adjusting phasing to achieve a peak response at a specific time. The resulting wave train can be reproduced in a model basin or numerical simulation, enabling efficient physical studies. [9] showed that the MLRW method can accurately predict nonlinear short-term probability distributions for rigid hulls at low forward speeds, making it suitable for long-term analysis of such hulls. However, when hull flexibility is significant, the method loses accuracy. Additionally, generating a most likely response wave in a basin is challenging due to nonlinearities in steep wave propagation.

Similarly, the Design Load Generator [10] is a numerical tool that approximates individual load peaks, enabling efficient short-term evaluation of specific events using high-fidelity models. This approach also facilitates uncertainty estimation through forward propagation of input parameter variability.

Extreme load events identified in short-term sea state evaluations must be extrapolated to long-term values, incorporating all possible environmental and operational conditions and their respective probabilities. Common approaches include the peak-over-threshold method, which uses all values exceeding a predefined threshold and typically applies a Generalized Pareto distribution [11], and the block-maxima method, which considers the maximum value from each condition combined with a Generalized Extreme Value distribution. A direct integration of short- and long-term analyses is proposed in [12], where Gaussian Process Regression (Kriging) is applied to estimate long-term extremes and quantify uncertainty. Although the case study in [12] was based on numerical results, the process accommodates tools and procedures of varying fidelity.

Drummen et al. [13] proposed a procedure for determining long-term global load effects that accounts for both strong and weak nonlinearities. Building on the concept introduced by [14], we assume that physical trends lead to a smooth, though nonlinear, transition of Weibull parameters across different operating conditions. As a case study, they investigate a frigate-type hull structure using data from both model tests and a numerical model [15], [16]. Drummen et al. [13] proposed to improve the outlined method using machine learning approaches, and possibly generalized models for the correction of the weak and strong nonlinear forces. In this paper we propose an improved approach for using model test results and with machine learning for an assessment of extreme global load effects. The example in the paper is based on model tests. Advanced CFD simulations can however, also be used as a basis. Incorporating the nonlinear hydro structural analyses to feed this methodology enables us to include the dynamic whipping factors in the analyses. Lastly, the proposed approach is extended to fatigue damage.

2. Methods

2.1 Scaled model tests

The scaled model tests used in this paper where carried out with a with a segmented model of a 120 m long frigate type hull form, [15]. The dynamic properties of the backbone structure were scaled and modelled with a tubular backbone. The properties of this backbone were chosen such that mode shapes and frequencies agreed with the full-scale results measured during the dedicated trials. The natural frequency of the two and three node vertical global flexural vibration modes were 2 Hz and 2.7 Hz, respectively. In between the segments, strain gauges were placed on the backbone so that vertical and horizontal bending moments could be inferred.

The test results of 42 runs were used in this paper for the analyses. These tests were carried out in irregular waves with a significant wave height value between 3.5 m to 9 m. Ship speed varied between 5 kn to 21 kn and relative headings with an interval of 45 degrees were tested

2.2 Approaches to long term analyses of global loads

Drummen et al. [13] provided a description of an approach for long term analyses of global load effect. A first and useful estimate of the extreme values can be obtained from a linear long term spectral analysis. The basis for this assessment is the probability of the vertical bending moment (vbm) of exceeding a certain value (x) in a given sea state [16]:

$$P(vbm, x) = e^{\left(-\frac{x}{\alpha}\right)^{\beta}} \tag{1}$$

Assuming linear behavior, the Rayleigh distribution applies, with parameters α and β equal to twice the standard deviation and two, respectively. For a given value of x, the resulting expression will differ for every combination of wave height, wave period, heading, and vessel speed.
In the long-term assessment, the probabilities are summed over all environmental and operational conditions the ship is expected to encounter. Essentially, the assessment aims to determine the value of x for which Eq. 2 holds true—representing the level that is expected to be exceeded once during the vessel's lifetime.

$$1 = \sum_{height} \sum_{period} \sum_{heading} \sum_{speed} \frac{T_c}{T_{ze;c}} e^{\left(-\frac{x}{\alpha}\right)^{\beta}} \tag{2}$$

In this equation, T_c represents the time spent in a specific condition over the vessel's lifetime, which is assumed to be 30 years. The term $T_{ze;c}$ denotes the wave-encounter period in that condition. Drummen et al. [13] argued that the approach summarized by Eq. 2 results in statistically constructed value rather than a directly occurring event. As a more intuitive alternative, they proposed performing lifetime simulations. In this case, the same 2700 conditions were considered, and the time fraction spent in each condition was derived from the environmental and operational assumptions. For each deployment, the vessel was assumed to spend 85 days at sea, operating 24 hours per day, and encountering a new condition every three hours. Thus, each deployment consists of 680 distinct conditions, each randomly selected from the time-weighted distribution. The maximum bending-moment peak during each deployment was obtained from an inverse Weibull distribution.

$$x = -\alpha(ln\ P)^{\frac{1}{\beta}} \tag{3}$$

Repeating this for 60 deployments provided an estimate of the vessel's lifetime maximum. This entire procedure was repeated 1,000 times to establish the statistical distribution of maximum lifetime values. The most probable value was found equal to 379 MNm. By repeating the analysis accounting for short-crested waves by using a cosine square distribution with a spreading over 180 degrees, a value of 266 MNm was found.

2.3 Data Driven approach

A data-driven model was used to estimate the Weibull distribution parameters of the measured vertical bending moment amidships for including of weak nonlinearities. Results are presented in Section 3.1. The purpose of the model is to provide reliable estimates of the Weibull scale parameter α and shape parameter β for a broad range of sea states and operational conditions. The predicted Weibull parameters can subsequently be combined with a wave scatter diagram to estimate the long-term extreme loads on the vessel.
Gradient Boosting Regression (GBR) was selected as the prediction model because of its ability to approximate nonlinear relationships using relatively small datasets while maintaining good generalization behavior. GBR is an ensemble learning technique in which the final prediction model is constructed as the weighted sum of multiple weak learners, typically shallow regression trees.
Separate GBR models were trained for the Weibull parameters α and β. Different feature sets and hyperparameter configurations were adopted for the two targets because preliminary investigations showed that the governing relationships differ substantially. The parameter α exhibited relatively strong deterministic dependence on the environmental conditions and could therefore be predicted with high accuracy. In contrast, β showed increased scatter, particularly for oblique and following sea conditions, requiring a more strongly regularized model configuration.
For α and β, the input vectors describing the sea-state and operational conditions is defined as

$$\boldsymbol{s}_\alpha = [H_s, T_z, U, \xi, cos(\psi), sin(\psi), U \cdot cos\,(\psi)] \tag{4}$$

$$\boldsymbol{s}_\beta = [H_s, T_z, U, \xi, \xi^2, U \cdot cos\,(\psi)] \tag{5}$$

where H_s is the significant wave height, T_z is the zero-crossing wave period, U is the ship speed, ψ is the wave heading, and ξ is the wave steepness defined as $2\pi H_s/(gT_z^2)$. For a given sea-state vector **s**, the prediction after M boosting stages is expressed as

$$\boldsymbol{F}_M(\boldsymbol{s}) = \sum_{m=0}^{M} \gamma_m \boldsymbol{h}_m(\boldsymbol{s}) \tag{6}$$

where $\boldsymbol{h}_m(\boldsymbol{s})$ represents the individual regression trees and γ_m are weighting coefficients determined during training. The initial model $\boldsymbol{F}_0$ is typically chosen as the mean value of the target variable.
At each boosting iteration, a new regression tree is fitted to the residual errors of the previous ensemble prediction. For a training dataset consisting of N samples, the residuals at iteration m are computed as

$$\boldsymbol{r}_{im} = \boldsymbol{y}_i - \boldsymbol{F}_{m-1}(\boldsymbol{s}_i) \tag{7}$$

where $\boldsymbol{y}_i$ is the target value and $\boldsymbol{F}_{m-1}(\boldsymbol{s}_i)$ is the prediction from the previous boosting stage. The new regression tree is subsequently trained to approximate these residuals.
The model is updated iteratively according to

$$\boldsymbol{F}_m(\boldsymbol{s}) = \boldsymbol{F}_{m-1}(\boldsymbol{s}) + \eta \boldsymbol{h}_m(\boldsymbol{s}) \tag{8}$$

where η is the learning rate controlling the contribution of each additional tree. Smaller learning rates generally improve generalization performance but require a larger number of boosting stages.
In the present study, shallow regression trees were used as weak learners in order to reduce overfitting and promote smooth generalization across the sea-state parameter space. The maximum tree depth was restricted to one or two levels, depending on the target parameter. This configuration effectively limits the local complexity of the model while preserving its ability to capture nonlinear relationship between input and output variables.

2.4 Numerical modelling approach for hydro structural problem

Hydro-structural modelling of ships under impulsive load is challenging due to complexity and computational costs. Potential-flow-based panel codes are still more practical and much faster than viscous-flow CFD solvers for predicting impulsive loads [17]. For this study, the PANSHIP-NL, a semi-nonlinear time-domain panel code developed at MARIN was used to predict extreme vertical bending moment including whipping response.
PANSHIP-NL solves the potential flow problems [18] using a 3D time domain panel method for large amplitude ship motion [4] [19]. It solves source distribution boundary integral equations (BIEs) by employing the transient Green's function which satisfies boundary conditions including the free surface condition. Once the BIEs is solved, the velocity potential can be obtained from the source distribution, then pressure and force can be calculated. The radiation, diffraction, wave excitation and restoring forces are determined using instantaneous submerged hull portions due to ship motions and the incident wave (body-nonlinear approach). The disturbed wave elevation along the waterline of the vessel is obtained from the hydrodynamic pressure at the waterline panels. The disturbed wave elevation is accounted for in the wave excitation and restoring forces only. Quadratic velocity terms in the Bernoulli equation for pressure as well as transom flow condition terms are considered.
Hydro-structural simulation is obtained with a built-in coupling of PANSHIP-NL and a beam element solver. The structural properties are incorporated in the beam elements. Equation of motion of the ship and the beam is solved with an iterative time integration to capture the fluid-structure interaction. The code has been validated against model tests for a 386m long container ship [19] and a 173m ferry in [20] simulating the ship response under slamming loads.

Simulation setup is described as follows. The hull was discretized into 2366 quadrilateral panels, see Figure 1. The mesh was arranged such that the panel boundaries coincide with the beam and segments. In addition to the hydrodynamic mesh, the ship structure is represented by a backbone beam structure. The input parameters such as inertia and mass of the segments are obtained from model test data and the stiffness properties of the beam tuned to obtain the dynamic properties of the ship, see Section 2.1. The natural frequency of two-node vertical mode is then verified by performing an impact response simulation and monitoring the vertical bending moment response.



Figure 1: Hull paneling used in PANSHIP-NL.

Deterministic validation of PANSHIP simulations with model tests was done by a minimization procedure to reconstruct a measured wave elevation signal, as described in [4]. The simulations of some test cases were compared to the model tests for the ship sailing in head waves with the test conditions as in Table 1. The comparison was done over 600s. Section 3.2 presents a comparison between the whipping factor obtained from model tests and PANSHIP simulations.

Table 1: Test conditions used in deterministic validation for the ship sailing in head waves.

Test Nr	Hs [m]	Tp [s]	Mean speed [kn]
427	6.5	11.16	4.1
428	3.5	8.53	15.1
430	4.5	9.84	15.0
433	6.5	9.84	14.9
435	6.5	12.47	15.6
437	8.5	11.16	15
438	3.5	9.84	19.7

3. Inclusion of nonlinear global load effects

Model tests were performed in irregular waves. Especially with higher significant wave heights, nonlinear responses start playing a role. Those nonlinearities are distinguished mainly into weak and strong nonlinearities. Froude-Krylov and hydrostatic restoring forces yield to weak nonlinearities while the strong nonlinearities are mainly the result of impact loads such as slamming loads. In this section the outcomes of the approaches defined above chapter are presented. Having a validated numerical hydro structural model allows for more data points that were not tested to help the data driven algorithm. Section 4.2 presents a comparison between the experimentally and numerically derived whipping factors.

3.1 Weak nonlinearity

As mentioned in Section 2.1, the available dataset consisted of 42 model test runs performed under different combinations of significant wave height, wave period, ship speed, and wave heading. For each run, Weibull distributions were fitted to the mid-ship VBM response, resulting in corresponding α and β parameters. Since the number of available model test runs was limited, the selected modelling approach needed to provide robust predictions while maintaining good generalization capability across the operational envelope.
The Weibull distribution given in Eq. 1. is capable of describing the weak nonlinearities. In order to be used in long term analysis, the approach given in Section 2.2 was used to derive the Weibull parameters per condition. A low pass filter was applied to the measured vertical bending moments at the midship.

The frequency was chosen around 1.75 Hz to remove the whipping response from the signal. Then data driven approach was applied to derive functions of the two parameters of Weibull distribution that was fitted to the exceedance probabilities of the sagging vertical bending moment amidship. The proposed method in Section 2.3 used the model tests results and derived a formulation for the scale and shape parameters.

The Weibull parameters α and β were modelled in logarithmic space to improve numerical stability and reduce the effect of heteroscedasticity. The transformed target vector is defined as $\boldsymbol{y} = [\log(\alpha), \log(\beta)]$, while the final prediction is obtained through inverse transformation. The final GBR models used stochastic subsampling during training, meaning that each regression tree was trained on a randomly selected subset of the available samples. This stochastic boosting approach reduces model variance and improves robustness for small datasets. The final hyperparameter configuration consisted of 200 estimators with a tree depth of 2 for the α model and 250 estimators with a tree depth of 1 for the β model, with learning rates of 0.05 and 0.07, respectively.

Because of the limited number of available model test runs, leave-one-out cross-validation was used for model validation. In this procedure, a single sample is removed from the dataset, the model is trained on the remaining samples, and the excluded sample is subsequently predicted. Repeating this process for all samples provides an approximately unbiased estimate of the model generalization performance while maximizing the amount of training data used in each iteration.

The prediction accuracy was quantified using the coefficient of determination (R^2) and the Mean Absolute Percentage Error (MAPE). The α model achieved high predictive accuracy, with R^2 value of 0.94 and MAPE value of 8.4%. The β parameter was more challenging to predict. Nevertheless, the final β model achieved R^2 value of 0.49, with a MAPE of approximately 5%.

The GBR model is a computationally efficient method for estimating Weibull parameters across a wide range of sea states while minimizing the number of required model test runs. The methodology is particularly suitable for fatigue-life assessment workflows where rapid evaluation of large scatter diagrams is required.

Performing lifetime simulations with the derived Weibull parameters and the inclusion of short-crested waves results in a most probable VBM of 312 MNm, which is 17% higher than the linear value presented in Section 2.2.

3.2 Whipping factor

The second type of nonlinearity is the strong one due to slamming and the resulting whipping. In order to include this, the approach used by [15] was adopted. Given a short term sea state, the whipping factor, w_f, here is defined as the ratio of the maximum total bending moment, $M_{T;\max}$, and the maximum wave frequency part of the bending moment $M_{WF;\max}$.

$$w_f = \frac{M_{T;max}}{M_{WF;max}} \tag{9}$$

This factor was determined for all model tests. $M_{WF;\max}$ was chosen as the maximum wave frequency moment correlated to the maximum total moment The data-driven algorithm described in Section 2.3 was used to derive a formulation for the whipping factor. The obtained model, however, performed less well than the one proposed by [13]. Therefore the latter was used for further analyses. This resulted in an updated bending moment of 401 MNm. This is 29% higher than the value without whipping.

Using PANSHIP-NL, the basis for the data-driven approach can be extended using additional conditions above those that were tested during the model tests. For this purpose, validation of the simulations against the model tests is of course essential. Figures 2 and 3 respectively show the probability of exceedance (PoE) of the (sagging) vertical bending moment at station 2 close to amidships for Test Nr 433 and 437. The simulations predicted the PoE quite well with some deviation at extreme values. The whipping contribution is quite significant as shown in both the model tests and simulations.

Figure 4 shows a comparison of the whipping factor as obtained from the model tests and the simulations. Overall good agreement can be seen. The large deviations can be seen for Run 433 and Test Nr 437. One possible explanation is that viscous damping is dominant for those cases. This contribution is modelled in PANSHIP-NL with a cross flow drag model. The coefficients of $C_{Dy} = 1$ $C_{Dz} = 0.5$ were used in the simulations. Further tuning of the simulation to the model test results is required before extending the database for the data-driven approach.

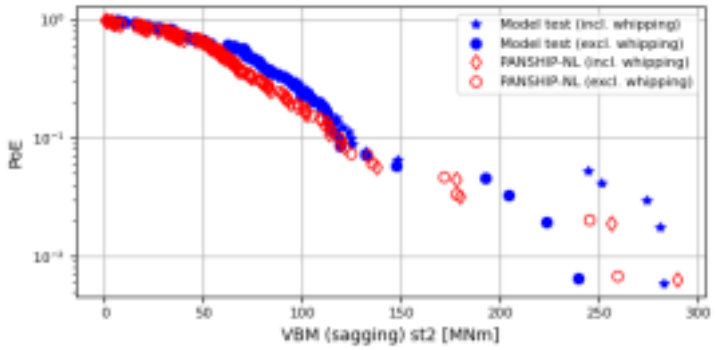


Figure 2: Effect of the whipping in an exceedance probability plot obtained from model tests and simulations with PANSHIP-NL for Test Nr 433.

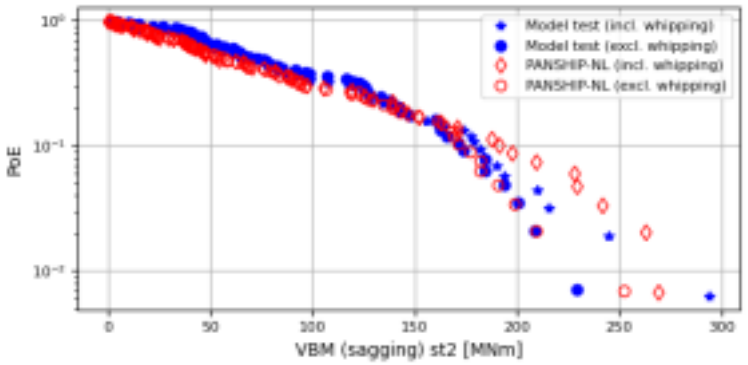


Figure 3: Effect of the whipping in an exceedance probability plot obtained from model tests and simulations with PANSHIP-NL for Test Nr 437.

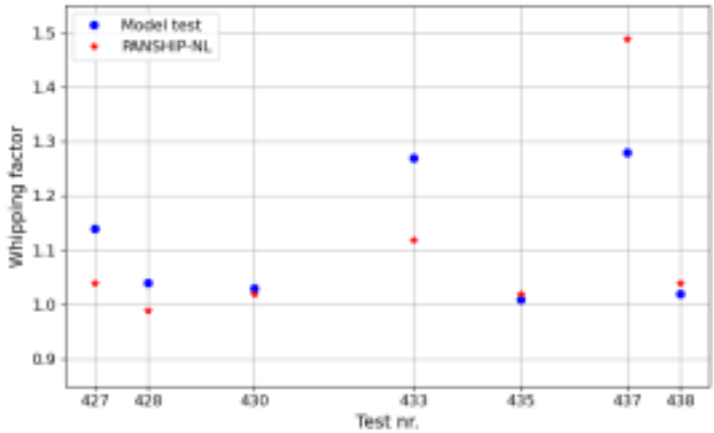


Figure 4: Whipping factor as obtained from model tests and simulations with PANSHIP-NL.

4. Extension to fatigue damage

The approach outlined above is specific for extreme values. An extension to fatigue damage can be done along the same lines as presented in [21] and combining this with [15]. For each of the performed model tests in the latter reference, the stress was determined using a matrix converting the measured horizontal and vertical bending moments to the stress in a particular fatigue sensitive location. Using again a Weibull distribution the fatigue damage, D, can be expressed as [21]:

$$D = \frac{n_0}{a}\alpha^m \Gamma\left(\frac{m}{\beta} + 1\right) \tag{10}$$

where n_0 is the mean number of stress cycles, a and m the parameters of the SN-curve and Γ represents the gamma function. The Weibull parameters α and β can be determined by fitting Eq. 9 to the damage derived from the model tests. Alternatively, the wave frequency fatigue damage can be fitted directly to the fatigue damage derived from the model tests. The whipping parameter is again obtained by dividing the total fatigue damage by the wave frequency fatigue damage [15].
Using the lifetime simulations proposed in [13] opens the door for using fracture mechanics models in the prediction of fatigue damage. In this way also loads sequencing effects can be investigated, as the crack growth rate increases under the same loading as the crack growth increases.

5. Discussion

Drummen et al. [13] presented an overview of extreme bending moments obtained using different approaches and details. The extreme value resulting from a spectral approach is equal to 372 MNm. The probability of an individual ship exceeding this value is 63.2%. If the analysis is performed in this say, a long-term maximum of 379 MNm is found. Both former values are based on long crested waves. In short crested waves this value will be lower. By including a cosine square spreading function in the analysis, a value of 266 MNm was found. Table 2 summarizes the extreme bending moment.
By performing lifetime simulations, an extreme value of 377 MNm was found. This value is, and should, be similar to the values of the spectral approach. The degree of similarity, however, depends on the number of conditions that contribute the most to the extremes. The more conditions contribute, the more extreme is a combination of events in different conditions. Weak and strong nonlinearities were included based on measurements from model tests. When only including weak nonlinearities, an extreme of 312 MNm was found. This increases to 401 MNm when it also includes strong nonlinearities.

A second advantage of the lifetime simulation approach is that it becomes more straightforward to include special periods [13]. As an illustration, lifetime simulations were repeated assuming that there is a chance of 10% of a heavy weather period during a deployment. If this is included, the extreme value increases to 445 MNm.

Table 2: Summary of extreme bending moments.

Assessment method	Including nonlinearities	Extreme moment [MNm]
PoE = 1 over lifetime	No	372
Most probable extreme value	No	379
Most probable extreme value – short-crested	No	266
Lifetime simulations	No	377
Lifetime simulations – short-crested	No	265
Lifetime simulations – short-crested	Weak nonlinearities	312
Lifetime simulations – short-crested	Weak and strong nonlinearities	401
Lifetime simulations including heavy weather period – short-crested	Weak and strong nonlinearities	445

The lifetime simulations also allow for a direct comparison against measurements. Figure 5 shows with the crosses increasing maximum vertical bending moments as obtained from measurements. Monthly values obtained during 16 deployments were used. For the lifetime simulations measured operational and environmental conditions were used. Short-crestedness and whipping were taken into account. In line with the actual numbers, 16 deployments with a duration of 60 days were simulated. The confidence interval in the lifetime simulations were obtained by simulating 1000 times. It can be seen that the both results show a slowly decreasing trend in the increase of the vertical bending moment. The average vertical bending moment after 16 deployments agree value well at a value of approximately 225 MNm. Note that the corresponding value under design conditions from Table 2 is 401 MNm.

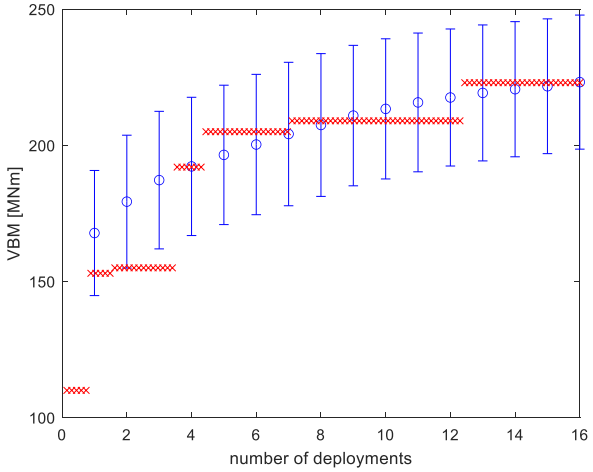


Figure 5: Comparison of measured vertical bending moment (red crosses) and lifetime simulations (blue dots with confidence interval).

6. Conclusions and Recommendations

This paper proposes an approach for using model test results and with machine learning for an assessment of extreme global load effects. The example in the paper is based on model tests. Advanced CFD simulations can, however, also be used as a basis. Despite the inherent limitation of nonlinear

hydroelastic potential flow models in capturing hydro-structural loads including whipping, their computational efficiency and robustness make them a practical tool to give insights into global responses and trends across a wide range of conditions. The results show that PANSHIP-NL predicted the probability of exceedance of vertical bending moments and whipping factors fairly accurate compared to the model tests. The use of a tuned PANSHIP_NL simulation model enables us to predict untested conditions which then can be combined with existing test conditions to increase the robustness of the outcome of the data driven approach.
In the paper, the proposed approach for extreme global loads is extended to fatigue damage calculation. The maximum vertical bending moment measuring during 16 deployments agrees very well with the one obtained from the lifetime simulations proposed in this paper.
More work should be done using the machine learning approach for incorporating the whipping effect as well as the that of short-crested waves. Moreover, it is recommended to develop an approach to incorporating the nonlinear simulations in the analyses of the long term global loads.

References

[1] ISSC, "Report of special task committee vi.1: extreme hull girder loading," in *Proceedings of the 14th international ship and ofsshore structures congress*, Japan, 2000.

[2] I. Drummen, M. Wu and T. Moan , "Experimental and numerical study of containership responses in severe head seas," *Marine Structures,* vol. 22, pp. 172-193, 2009.

[3] G. Storhaug and E. Moe, "Measurements of wave induced vibrations onboard a large container vessel operating in harsh environment," in *Proceedings of the 10th international symposium on practical design of ships and other floating structures*, US, 2007.

[4] F. van Walree, D. Sgarioto and T. Turner, "Validation of a Time Domain Panel Code for Prediction of Impulsive Loads on High Speed Ships," in *31st Symposium on Naval Hydrodynamics*, Monterey, California, 2016.

[5] J. Oberhagemann, On Prediction of Wave-Induced Loads and Vibration of Ship Structures with Finite Volume Fluid Dynamic Methods, Universität Duisburg-Essen, 2016.

[6] J. de Lauzon, Q. Derbanne and Š. Malenica, "Slamming Induced Whipping Computations on a Large Database of Container Ships," in *PRADS*, 2019.

[7] I. Drummen, L. Rogers, A. Benhamou, R. Hageman and K. Stambaugh, "Hull structure monitoring of a new class of US Coast Guard Cutters," in *ASNE-TSS*, Washington DC, 2019.

[8] J. Dietz, "Application of conditional waves as critical wave episodes for extreme loads on marine structures," Ph.D. thesis, Technical University of Denmark, Lyngby, Denmark, 2004.

[9] I. Drummen, M. Wu and T. Moan, "Numerical and experimental investigations into the application of response conditioned waves for long-term nonlinear analyses," *Marine Structures,* vol. 22, pp. 576-593, 2009.

[10] D.-H. Kim, Design Load Generator: Estimation of Extreme Environmental Loadings for Ship and Offshore Applications, Ann Arbor, Michigan, 2012.

[11] A. Naess, An introduction to extreme value analysis for engineering applications, Trondheim, Norway, 2011.

[12] O. Gramstad, C. Agrell, E. Bitner-Gregersen, B. Guo, E. Ruth and E. Vanem, "Sequential sampling method using Gaussian process regression for estimating extreme structural response," *Marine Structures,* vol. 72, 2020.

[13] I. Drummen, R. B. Hageman and K. Stambaugh, "Multifidelity approach for predicting extreme global bending load effects," in *Hydroelasticity in Marine Technology*, Rome, 2022.

[14] Q. Derbanne, J.-F. Leguen, T. Dupau and E. Hamel, "Long-term non-linear bending moment prediction," in *OMAE2008-57326*, Estoril, Portugal, 2008.

[15] I. Drummen, M. Schiere, R. Dallinga and K. Stambaugh, "Full and Model Scale testing of a New Class of US Coast Guard Cutter," in *Ship Structure Committe*, Linthicum Heights, 2014.

[16] J. Sikora, R. Michaelson and B. Ayyub, "Assessment of cumulative lifetime seaway loads for ships," *Naval Engineers Journal,* p. 167:180, Spring 2002.

[17] F. van Walree, A. Serani, M. Diez and F. Stern, "Prediction of heavy weather seakeeping of a destroyer hull formby means of time domain panel and CFD codes," in *Proceedings of the 33rd Symposium on Naval Hydrodynamics*, Osaka, Japan, 2020.

[18] Lin W.M. and Yue D., "Numerical Solutions for Large Amplitude Ship Motions in the Time Domain," in *Proceedings of the 18th Symposium on Naval Hydrodynamics*, Ann Arbor,, 1990.

[19] F. v. Walree and R. Grin., "Validation of a time domain panel code for prediction of impulsive loads on container ships," in *Proceedings of the ASME 2024 International Conference on Ocean, Offshore Arctic Engineering OMAE2024*, Singapore, 2024.

[20] R. Kurnia and F. v. Walree, "Benchmarking potential flow based models for prediction of slamming and whipping loads on a ferry," in *Proceedings of the ASME 2026 International Conference on Ocean, Offshore, Arctic Engineering OMAE2026*, Tokyo, 2026.

[21] I. Drummen, M. Wu, K. L. Mirek and T. Moan, "Numerical investigation into the application of response conditioned waves for long-term nonlinear fatigue analyses of rigid hulls," *Ocean Engineering,* no. 36, pp. 1208 - 1216, 2009.

[22] R. Hageman, I. Drummen and K. Stambaugh, "Structural fatigue loading predictions and comparisons with test data for a new class of US Coast Guard Cutters," in *Committe ship structurses symposium, Linthicum Hiehgts*, 2014.

[23] I. Drummen, L. Rogers, A. Benhamou, R. Hageman and K. Stambaugh, "Hull Structure Monitoring of a New Class of US Coast Guard Cutters," in *ASNE - Techonology, Systems & Ships*, Washington DC, 2019.

[24] M. Leadbetter, I. Rychlik and K. Stambaugh, "Estimating Dynamic Stability Event Probabilities from Simulation and Wave Modeling Methods," in *Proceedings of the 12th International Ship Stability Workshop*, Washington DC, 2011.

[25] Y. Kim, K.-H. Kim and Y. Kim, "Analysis of Hydroelasticity of Floating Shiplike Structure in Time Domain Using a Fully Coupled Hybrid BEM-FEM," in *Journal of Ship Research Vol. 53 No. 01*, 2009.

[26] R. Santjer, S. Agarwal, O. Colomés and O. Morales-Nápoles, "Gaussian copula-based Bayesian Networks for dynamic loads in mooring systems," *Applied Ocean Research,* vol. 165, no. 104809, December 2025.

[27] K. Wei, C. Zou and B. Xu, "Spatial distribution models of horizontal and vertical wave impact pressure," *Applied Ocean Research ,* vol. 125, no. 103245, August 2022.

[28] O. Gaidai, G. Storhaug and A. Naess, "Extreme large cargo ship panel stresses by bivariate ACER method," *Ocean Engineering,* vol. 123, September 2016.

[29] S. M. v. Essen and H. C. Seyffert, "Design loads for wave impacts – introducing the Probabilistic Adaptive Screening (PAS) method for predicting extreme non-linear loads on maritime structures," *Preprint,* vol. doi:10.48550/arXiv.2511.23156, 2025.

Generalized modal approach for marine and offshore engineering: key aspects and applications

Jagite G. & Malenica S.
Bureau Veritas, Paris La Defense, FRANCE

Abstract. The dynamic systems excited by the external loading include various more or less complex configurations with a single or several rigid or flexible floating bodies interacting with each other, in freely floating or moored conditions. The evaluation of the behavior of those systems, when floating and interacting with water waves, becomes increasingly cumbersome when the classical multibody approach is employed. Furthermore, for fully nonlinear problems, there is no choice but to employ direct numerical solvers and complicated coupling schemes. However, when the behavior of floating bodies can be reasonably linearized, the dynamic behavior can be represented using space-dependent generalized motion/deformation modes with time-dependent amplitudes. The critical aspect of the generalized modal approach is the definition of the generalized modes and their transfer to hydrodynamic module in the form of the body boundary conditions. The hydrodynamic module's sole role is to solve the corresponding Boundary Value Problem and return the hydrodynamic quantities: added mass, damping, restoring and excitation. Everything else constitutes postprocessing which can be customized case by case. The generalized modal approach combines elegance with exceptional versatility, making it suitable for diverse practical applications.

Key words: *Generalized modes, hydro-structure interactions, potential flow, diffraction-radiation*

1. Introduction

The evaluation of the nonlinear dynamic interaction between floating systems and water waves presents significant complexities. On the hydrodynamic side, even under the potential flow assumptions which is commonly the case, the presence of the free surface, which can experience large deformations, makes the evaluation of the fluid flow highly challenging. At the same time, describing the mechanics of the floating system, when multiple floating bodies (potentially flexible) interact with each other is also far from trivial.

1.1 Notations

Compact matrix notations are introduced where $[\boldsymbol{A}]$ is used to denote the $n \times m$ matrix with the elements A_{ij} , $(i = 1, n\,; j = 1, m)$. At the same time, any vector quantity $\boldsymbol{a} = a_x\boldsymbol{i} + a_y\boldsymbol{j} + a_z\boldsymbol{k}$ is written as a single column matrix $\{\boldsymbol{a}\}$ and, to each vector quantity, the skew symmetric matrix $[\boldsymbol{a}]$ is associated [7] which allows writing the scalar product of two vectors $\{\boldsymbol{a}\}$ and $\{\boldsymbol{b}\}$ as $\boldsymbol{a} \cdot \boldsymbol{b} = \{\boldsymbol{a}\}^T\{\boldsymbol{b}\}$ and the cross product as $\boldsymbol{a} \wedge \boldsymbol{b} = [\boldsymbol{a}]\{\boldsymbol{b}\}$.

1.2 Coordinate systems

Reference is made to Figure 1 where the two coordinate systems are identified:

- (O, X, Y, Z) Earth-fixed coordinate system with arbitrary origin
- (G, x', y', z') Body-fixed coordinate system with the origin at the body center of gravity

The two coordinate systems are related to each other through the transformation matrix $[\boldsymbol{A}]$ so that, for any vector quantity $\{\boldsymbol{u}\}$ defined in (O, X, Y, Z) , the following relation is valid:

$$\{\boldsymbol{u}\} = [\boldsymbol{A}]\{\boldsymbol{u}'\} \tag{1}$$

The transformation matrix $[\boldsymbol{A}]$ is the critical parameter in the analysis of the nonlinear body motion and the instantaneous body rotation vector $\{\boldsymbol{\Omega}'\}$ is related to the transformation matrix by:

$$[\boldsymbol{\Omega}'] = [\boldsymbol{A}]^T[\dot{\boldsymbol{A}}] \tag{2}$$

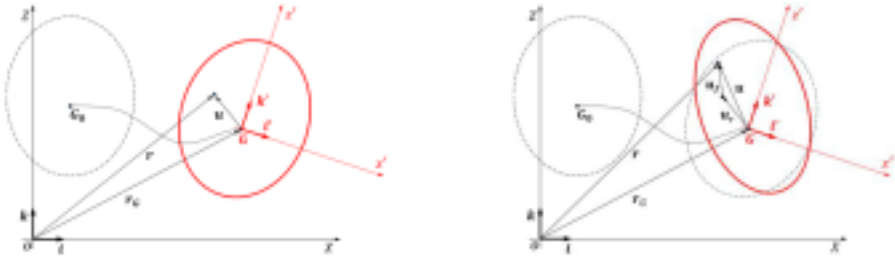


Figure 1: Rigid (left) and flexible (right) body motion and the different coordinate systems.

2. Description of the body dynamics

2.1 Body kinematics

The motion of the floating system is defined by the translation of the reference point and the additional modes of motion (rotations, deformations, etc) around it.

2.1.1 Single rigid body

In the case of a single rigid body, the natural choice for the reference point is the body center of gravity, and only three additional rotational modes need to be defined to determine the instantaneous position of the body. The motion is described by the following position, velocity and acceleration vectors:

$$\begin{aligned} \{\boldsymbol{r}\} = \{\boldsymbol{r}_G\} + [\boldsymbol{A}]\{\boldsymbol{u}'\} \quad , \quad \{\boldsymbol{v}\} = \{\boldsymbol{v}_G\} + [\boldsymbol{A}][\boldsymbol{\Omega}']\{\boldsymbol{u}'\} \\ \{\boldsymbol{a}\} = \{\boldsymbol{a}_G\} + [\boldsymbol{A}][\dot{\boldsymbol{\Omega}}']\{\boldsymbol{u}'\} + [\boldsymbol{A}][\boldsymbol{\Omega}'][\boldsymbol{\Omega}']\{\boldsymbol{u}'\} \end{aligned} \tag{3}$$

where $\{\boldsymbol{r}_G\}$, $\{\boldsymbol{v}_G\}$ and $\{\boldsymbol{a}_G\}$ are the position, velocity and acceleration of the center of gravity and $\{\boldsymbol{\Omega}'\}$ is the instantaneous rotational velocity vector.

2.1.2 Flexible body

The main difference between the rigid and the flexible body kinematics is that the distance between the points attached to the body is not constant in time when body is flexible. Reference is made to Figure 1 and the total displacement of the point attached to the body $\{\boldsymbol{u}\}$ is decomposed into its rigid $\{\boldsymbol{u}_r\}$ and the flexible part $\{\boldsymbol{u}_f\}$:

$$\{\boldsymbol{u}\} = \{\boldsymbol{u}_r\} + \{\boldsymbol{u}_f\} \tag{4}$$

It follows that the motion is described by the following position, velocity and acceleration vectors:

$$\begin{aligned} \{\boldsymbol{r}\} = \{\boldsymbol{r}_G\} + [\boldsymbol{A}]\{\boldsymbol{u}'\} \quad , \quad \{\boldsymbol{v}\} = \{\boldsymbol{v}_G\} + [\boldsymbol{A}][\boldsymbol{\Omega}']\{\boldsymbol{u}'\} + [\boldsymbol{A}]\{\dot{\boldsymbol{u}}_f'\} \\ \{\boldsymbol{a}\} = \{\boldsymbol{a}_G\} + [\boldsymbol{A}][\boldsymbol{\Omega}'][\boldsymbol{\Omega}']\{\boldsymbol{u}'\} + [\boldsymbol{A}][\dot{\boldsymbol{\Omega}}']\{\boldsymbol{u}'\} + 2[\boldsymbol{A}][\boldsymbol{\Omega}']\{\dot{\boldsymbol{u}}_f'\} + [\boldsymbol{A}]\{\ddot{\boldsymbol{u}}_f'\} \end{aligned} \tag{5}$$

In the general case, the body deformation vector $\{\boldsymbol{u}_f'\}$ can be arbitrarily large but here the deformation vector is assumed to be small, and is represented as a sum of the N_f modal contributions:

$$\{\boldsymbol{u}_f'(\boldsymbol{u}_r', t)\} = \sum_{i=1}^{N_f} \chi_{fi}(t)\{\boldsymbol{h}_{fi}'(\boldsymbol{u}_r')\} = [\boldsymbol{\hbar}_f']\{\boldsymbol{\chi}_f\} \tag{6}$$

where $\boldsymbol{h}_{fi}' = h_{fix'}'\boldsymbol{i}' + h_{fiy'}'\boldsymbol{j}' + h_{fiz'}'\boldsymbol{k}'$ is the modal displacement expressed relative to the body fixed coordinate system, and:

$$[\boldsymbol{\hbar}_f'] = \begin{bmatrix} h_{f1x'}' & h_{f2x'}' & \cdots & h_{fN_fx'}' \\ h_{f1y'}' & h_{f2y'}' & \cdots & h_{fN_fy'}' \\ h_{f1z'}' & h_{f2z'}' & \cdots & h_{fN_fz'}' \end{bmatrix} \quad , \quad \{\boldsymbol{\chi}_f\}^T = \{\chi_{f1} \quad \chi_{f2} \quad \cdots \quad \chi_{fN_f}\} \tag{7}$$

2.2 Dynamic equilibrium equation

2.2.1 Single rigid body

The body dynamics can be described relative to either coordinate system, however, for the purposes of the generalized modal description, it is more convenient to describe it relative to body fixed coordinate system (G, x', y', z'). This is because the additional modes of motion are defined relative to this coordinate system. The final expression is well known and is repeated here for the sake of completeness:

$$[\boldsymbol{m}]\{\ddot{\boldsymbol{r}}_{\boldsymbol{G}}\}' = \{\boldsymbol{F}'\} \quad , \quad [\boldsymbol{I}'_{\theta\theta}]\{\dot{\boldsymbol{\Omega}}\}' = \{\boldsymbol{M}'\} - [\boldsymbol{\Omega}'][\boldsymbol{I}'_{\theta\theta}]\{\boldsymbol{\Omega}'\} \tag{8}$$

with:

$$[\boldsymbol{m}] = \iiint_{\forall_B} [\mathbf{I}]dm \quad , \quad [\boldsymbol{I}'_{\theta\theta}] = \iiint_{\forall_B} [\boldsymbol{u}']^T[\boldsymbol{u}']dm \tag{9}$$

2.2.2 External loading

The external forces are assumed to act at discrete points at the body, and they are denoted by $\{\boldsymbol{f}'_j\}$. Herein, two main types of external forces are considered: gravity and the pressure forces:

$$\{\boldsymbol{f}'_j\} = \left\{\boldsymbol{f}_j^{g'}\right\} + \left\{\boldsymbol{f}_j^{p'}\right\} \quad , \quad \left\{\boldsymbol{f}_j^{g'}\right\} = -m_j g[\boldsymbol{A}]^T\{\boldsymbol{k}\} \quad , \quad \left\{\boldsymbol{f}_j^{p'}\right\} = P\{\boldsymbol{n}'\}dS_j \tag{10}$$

where P is the external pressure and $\{\boldsymbol{n}'\}dS_j$ is the oriented element of the wetted surface.
With these notations, the external rigid body forces and moments in (8) become:

$$\{\boldsymbol{F}'\} = \sum_{j=1}^{N}\{\boldsymbol{f}'_j\} \quad , \quad \{\boldsymbol{M}'\} = \sum_{j=1}^{N}[\boldsymbol{u}']\{\boldsymbol{f}'_j\} \tag{11}$$

2.2.3 Flexible body

The application of the D'Alembert principle of virtual work leads to the following dynamic motion equation for the flexible floating body (e.g. Shabana [7]):

$$\begin{bmatrix} [\boldsymbol{m}] & [0] & [\boldsymbol{I}'_{Rf}] \\ [0] & [\boldsymbol{I}'_{\theta\theta}] & [\boldsymbol{I}'_{\theta f}] \\ [\boldsymbol{I}'_{Rf}]^T & [\boldsymbol{I}'_{\theta f}]^T & [\boldsymbol{I}'_{ff}] \end{bmatrix} \begin{Bmatrix} \{\ddot{\boldsymbol{r}}_{\boldsymbol{G}}\}' \\ \{\dot{\boldsymbol{\Omega}}\}' \\ \{\ddot{\boldsymbol{\chi}}_f\} \end{Bmatrix} = \begin{Bmatrix} \{\boldsymbol{F}'\} \\ \{\boldsymbol{M}'\} \\ \{\boldsymbol{F}_f\} - [\boldsymbol{K}]\{\boldsymbol{\chi}_f\} \end{Bmatrix} - \begin{Bmatrix} \{\boldsymbol{Q}'_{vR}\} \\ \{\boldsymbol{Q}'_{v\theta}\} \\ \{\boldsymbol{Q}'_{vf}\} \end{Bmatrix} \tag{12}$$

where the matrix $[\boldsymbol{K}]$ denotes the structural stiffness matrix for the flexible modes.
The inertia terms related to rigid body motions ($[\boldsymbol{m}]$, $[\boldsymbol{I}'_{\theta\theta}]$) are still given by (9) and those related to the flexible modes are defined as follows:

$$[\boldsymbol{I}'_{Rf}] = \iiint_{\forall_B} [\boldsymbol{\hbar}'_f]dm \quad , \quad [\boldsymbol{I}'_{\theta f}] = \iiint_{\forall_B} [\boldsymbol{u}'_r]^T[\boldsymbol{\hbar}'_f]dm \quad , \quad [\boldsymbol{I}'_{ff}] = \iiint_{\forall_B} [\boldsymbol{\hbar}'_f]^T[\boldsymbol{\hbar}'_f]dm \tag{13}$$

Finally, $\{\boldsymbol{Q}'_{vi}\}$ in (12) are the quadratic velocity inertia force vectors which can become quite complex for arbitrary body motions/deformations. However, here only the linear dynamics is of concern so that the quadratic velocity inertia force vectors are neglected in the rest of the paper.

2.2.4 External loading

The external rigid body forces and moments remain defined by (11) and the flexible body modal forces are given by:

$$F_{fi} = \sum_{j=1}^{N}\{\tilde{\boldsymbol{h}}'_{fi}\}^T\{\boldsymbol{f}'_j\} \tag{14}$$

where $\{\tilde{\boldsymbol{h}}'_{fi}\}$ denotes the instantaneous value of the modal displacement.

2.2.5 Generalized modal description of the linear body dynamics

In the linear case it is convenient to describe the dynamics of the floating flexible body in a more compact form. For simplicity, the usual superscript " $^{(1)}$" will be omitted and the instantaneous linear position vector $\{\boldsymbol{r}\}$ of the point attached to the body is rewritten as:

$$\{\boldsymbol{r}\} = \{\boldsymbol{r}_{G_0}\} + \{\boldsymbol{u}_r\} + \{\boldsymbol{R}_G\} + [\boldsymbol{\theta}]\{\boldsymbol{u}'_r\} + [\boldsymbol{\hbar}'_f]\{\boldsymbol{\chi}_f\} = \{\boldsymbol{r}_0\} + [\boldsymbol{\hbar}']\{\boldsymbol{\xi}\} \tag{15}$$

with $\{\boldsymbol{r}_0\} = \{\boldsymbol{r}_{G_0}\} + \{\boldsymbol{u}_r\}$ and the total mode shape matrix $[\boldsymbol{\hbar}']$ reads:

$$[\boldsymbol{\hbar}'] = \begin{bmatrix} 1 & 0 & 0 & 0 & z' & -y' & h'_{f1x'} & h'_{f2x'} & \dots & h'_{fN_fx'} \\ 0 & 1 & 0 & -z' & 0 & x' & h'_{f1y'} & h'_{f2y'} & \dots & h'_{fN_fy'} \\ 0 & 0 & 1 & y' & -x' & 0 & h'_{f1z'} & h'_{f2z'} & \dots & h'_{fN_fz'} \end{bmatrix} \tag{16}$$

Similarly, the linear motion dynamic equilibrium equation can be written in a very simple form:

$$[\boldsymbol{\mathcal{M}}]\{\ddot{\boldsymbol{\xi}}\} = \{\boldsymbol{\mathcal{F}}\} \tag{17}$$

with:

$$[\boldsymbol{\mathcal{M}}] = \iiint_{\forall_B} [\boldsymbol{\hbar}']^T [\boldsymbol{\hbar}'] dm \quad , \quad \{\boldsymbol{\mathcal{F}}\} = \sum_{j=1}^{N} [\boldsymbol{\hbar}']^T \{\boldsymbol{f}'_j\} \tag{18}$$

This generalized formulation of body dynamics is valid at first order only.

3. Evaluation of the external loads

3.1 General

Gravity and pressure loads are both nonlinear in a body-fixed coordinate system: pressure is inherently nonlinear, while gravity becomes nonlinear due to coordinate transformation. This means that both types of loading require a careful linearization procedure.

3.2 Potential flow theory

In addition to the two coordinate systems defined before, here the additional coordinate system (o, x, y, z), called hydrodynamic coordinate system, is introduced as shown in Figure 2. This coordinate system is the inertial coordinate system which is parallel to the Earth-fixed coordinate system (O, X, Y, Z) with the difference that its origin is placed at the mean free surface.

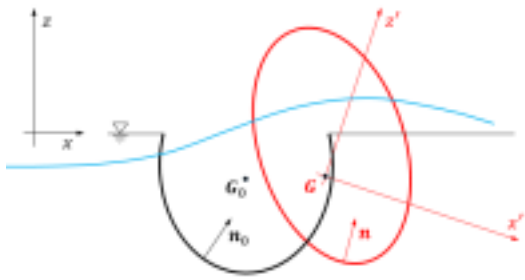


Figure 2: Small body motions/deformations.

This simply allows us to write the hydrostatic pressure as $-\varrho g z$. Furthermore, the potential flow theory is adopted and the total pressure $P(\boldsymbol{x}, t)$ is decomposed into its hydrostatic $P^{hs}(\boldsymbol{x}, t)$ and hydrodynamic part $P^{hd}(\boldsymbol{x}, t)$, with:

$$P^{hs}(\boldsymbol{x}, t) = -\varrho g z \quad , \quad P^{hd}(\boldsymbol{x}, t) = -\varrho \left[\frac{\partial \Phi}{\partial t} + \frac{1}{2}(\nabla \Phi)^2\right] \tag{19}$$

The velocity potential Φ is the main unknown in the hydrodynamic problem and is found after solving the Boundary Value Problem (BVP) which is composed of the Laplace equation in the fluid and the different conditions at the domain boundaries (free surface, body, seabed and infinity). Solving the fully nonlinear potential flow problem for general freely floating body is extremely complex and no reliable tool exists nowadays. That is why the BVP is usually linearized by assuming the small body motions.

3.2.1 Linear Boundary Value Problems

The linear problem is commonly formulated in frequency domain where it is convenient to decompose the total velocity potential φ, into the incident, diffracted and radiated parts. We recall hereafter the decomposition of the total velocity potential and the corresponding body boundary conditions for the diffraction and radiation velocity potentials:

$$\varphi = \varphi_I + \varphi_D - i\omega \sum_{j=1}^{6+N_f} \xi_j \varphi_{R_j} \quad ,with \quad \frac{\partial \varphi_D}{\partial n} = -\frac{\partial \varphi_I}{\partial n} \quad ,and \quad \frac{\partial \varphi_{R_j}}{\partial n} = \{\boldsymbol{h}_j'\}^T \{\boldsymbol{n}'\} \tag{20}$$

3.3 Linearization of the external loading

Assuming the linear velocity potential φ to be known, the following expressions are obtained for the linear generalized wave loads:

$$\mathcal{F}_i^g = -\sum_{j=1}^{N_m} m_j g \left(\{\boldsymbol{h}_i'\}^T [\boldsymbol{\theta}] + \{\boldsymbol{u}_f'\}^T [\nabla \boldsymbol{h}_i']^T \right) \{\boldsymbol{k}\} \tag{21}$$

$$\mathcal{F}_i^{hs} = -\varrho g \iint_{S_B} \left[\zeta_v \{\boldsymbol{h}_i'\}^T + z \left(\{\boldsymbol{h}_i'\}^T \left(\nabla \boldsymbol{u}_f' - \left[\nabla \boldsymbol{u}_f' \right]^T \right) + \{\boldsymbol{u}_f'\}^T [\nabla \boldsymbol{h}_i']^T \right) \right] \{\boldsymbol{n}'\} dS \tag{22}$$

$$\mathcal{F}_i^{hd} = -\varrho i\omega \iint_{S_B} \varphi \{\boldsymbol{h}_i'\}^T \{\boldsymbol{n}'\} dS \tag{23}$$

where N_m is the total number of the mass points, and ζ_v denotes the vertical displacement of the point attached to the body which, within the generalized modal approach, is given by:

$$\zeta_v = \sum_{i=1}^{6+N_f} \xi_i \{\boldsymbol{h}_i'\}^T \{\boldsymbol{k}\} = \sum_{i=1}^{6+N_f} \xi_i h_{iz'}' \tag{24}$$

The total linear hydrodynamic load $\mathcal{F}_i^{hd}$ is decomposed into the part which is independent of the body motions $\mathcal{F}_i^{hd(DI)}$ (incident + diffraction) and the parts which are dependent on the body motions $\mathcal{F}_i^{hd(Rj)}$ (radiation) and we can write:

$$\mathcal{F}_i^{hd(DI)} = i\omega\varrho \iint_{S_B} (\varphi_I + \varphi_D) \{\boldsymbol{h}_i'\}^T \{\boldsymbol{n}'\} dS \quad , \quad \mathcal{F}_i^{hd(R_j)} = \varrho\omega^2 \sum_{j=1}^{6+N_f} \iint_{S_B} \varphi_{R_j} \{\boldsymbol{h}_i'\}^T \{\boldsymbol{n}'\} dS \tag{25}$$

The radiation loading is further decomposed into the part in phase with the modal acceleration (added mass A_{ij}) and the part which is in phase with the modal velocity (damping B_{ij}):

$$\mathcal{F}_i^{hd(R_j)} = \sum_{j=1}^{6+N_f} \xi_j \left(\omega^2 \mathcal{A}_{ij} + i\omega \mathcal{B}_{ij} \right) \tag{26}$$

In parallel gravity and the hydrostatic pressure forces, which are in phase with the modal displacement, are combined and rewritten as:

$$\mathcal{F}_i^g + \mathcal{F}_i^{hs} = \sum_{j=1}^{6+N_f} \xi_j \mathcal{C}_{ij} \tag{27}$$

With this in mind the total external linear force to be used in (17) can be rewritten in matrix form as:

$$\{\boldsymbol{\mathcal{F}}^{hd}\} = \{\boldsymbol{\mathcal{F}}^{DI}\} + (\omega^2[\,\boldsymbol{\mathcal{A}}\,] + i\omega[\,\boldsymbol{\mathcal{B}}\,] - [\,\boldsymbol{\mathcal{C}}\,])\{\boldsymbol{\xi}\} \tag{28}$$

and the linear dynamic equilibrium equation (17) can be rewritten as:

$$\left[-\omega^2([\boldsymbol{\mathcal{M}}] + [\,\boldsymbol{\mathcal{A}}\,]) - i\omega[\,\boldsymbol{\mathcal{B}}\,] + [\,\boldsymbol{\mathcal{C}}\,]\right]\{\boldsymbol{\xi}\} = \{\boldsymbol{\mathcal{F}}^{DI}\} \tag{29}$$

The solution of this equation gives the modal amplitudes $\{\boldsymbol{\xi}\}$ and the problem is formally solved.

4. Numerical examples

As it is well known, it is common to employ the generalized modal approach in the context of a single flexible body where additional deformation modes occur naturally [6][8][4]. However, the same theory remains valid for many other practical applications such as multibody interactions, local loading evaluation, and many others. Several such applications are described hereafter.

4.1 Multibody interactions

When several floating bodies operate in vicinity of each other (e.g. Figure 3), the hydrodynamic interaction effects need to be considered in addition to any mechanical connections between the bodies. The multibody interaction problem can be solved in many different ways. The most intuitive approach consists in considering each body separately by keeping the other one fixed. The resulting coupled motion equation for M disconnected rigid bodies becomes:

$$\sum_{m=1}^{M}\sum_{j=1}^{6}\left[-\omega^2\left(\delta_{nm}M_{kj}^{nm} + A_{kj}^{nm}\right) - i\omega B_{kj}^{nm} + \delta_{nm}C_{kj}^{nm}\right]\xi_j^m = F_k^{DIn} \tag{30}$$

where $n = 1,2,\dots M$ and $k = 1,2,\dots 6$ and δ_{nm} denotes the Kronecker symbol.

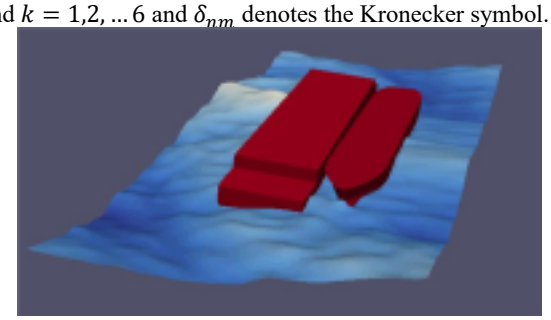


Figure 3: Two floating bodies in side-by-side configuration.

The hydrodynamic interaction between the bodies is accounted for in the hydrodynamic added mass and damping coefficients A_{kj}^{nm} and B_{kj}^{nm} , and in the excitation force F_k^{DIn}. These quantities are evaluated by integrating the corresponding velocity potential over the wetted surfaces of the different bodies. There are in total $1 + 6M$ velocity potentials to be evaluated namely one diffraction φ_D and $6M$ radiation velocity potentials φ_{Rj}^k. The corresponding body boundary conditions for each of them are:

$$\frac{\partial\varphi_D}{\partial n} = -\frac{\partial\varphi_I}{\partial n} \quad , \quad \frac{\partial\varphi_{Rj}^k}{\partial n} = \begin{cases} n_j^m & k = m \\ 0 & k \neq m \end{cases} \tag{31}$$

The excitation force and the hydrodynamic coefficients become:

$$F_k^{DIn} = i\omega\varrho\iint_{S_{B_n}}(\varphi_I + \varphi_D)n_k^n dS \quad , \quad \omega^2 A_{kj}^{nm} + i\omega B_{kj}^{nm} = \varrho\omega^2\iint_{S_{B_n}}\varphi_{Rj}^m n_k^n dS \tag{32}$$

The possible connections between the bodies are usually considered through additional equations which fix the motions dependencies with respect to the type of the connection. In order to ensure these motion

dependencies, additional unknowns (e.g. constraint equations) are added, and, in some cases, this can lead to rather complex expressions and an increased system of equations. We refer to Figure 4 where, for simplicity, two floating bodies are supposed to be connected by a hinge that allows relative rotations around the Y- axis.

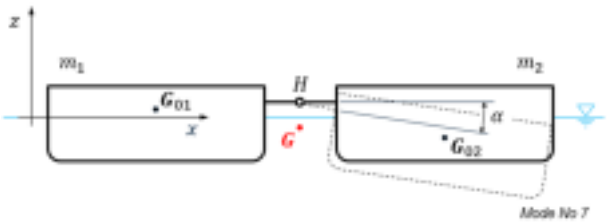


Figure 4: Two bodies linked by a hinge.

The same problem can be also solved using the generalized modal approach. The critical step is the choice of generalized modes. This can be done in many different ways and probably the simplest one is presented in Table 1. This describes the 6 rigid body modes of the two bodies assumed to be rigidly moving together, and the additional 7th mode representing the relative rotation (pitch) between them. For simplicity, the reference point for the overall rotations is at the overall center of gravity. We note that in the classical approach the number of unknowns would be 13 instead of 7 here.

Table 1 : Generalized mode shapes for 2 hinged bodies.

	i ξ_i	**1 x_G**	**2 y_G**	**3 z_G**	**4 θ_x**	**5 θ_y**	**6 θ_z**	**7 α**
m_1	$\{h_i'\}$	$\{i'\}$	$\{j'\}$	$\{k'\}$	$[i']\{u_r'\}$	$[j']\{u_r'\}$	$[k']\{u_r'\}$	0
	$[\nabla h_i']$	0	0	0	$[i']$	$[j']$	$[k']$	0
m_2	$\{h_i'\}$	$\{i'\}$	$\{j'\}$	$\{k'\}$	$[i']\{u_r'\}$	$[j']\{u_r'\}$	$[k']\{u_r'\}$	$[\boldsymbol{j}']\left(\{\boldsymbol{u}_r'\} - \{\boldsymbol{u}_H'\}\right)$
	$[\nabla h_i']$	0	0	0	$[i']$	$[j']$	$[k']$	$[\boldsymbol{j}']$

Once the generalized modes are defined, the procedure for calculating the body motions remains rather straightforward and follows strictly the previous discussions. However, the corresponding inertia and hydrostatic stiffness matrices require a few additional comments. The modal inertia matrix is defined by the expression (18) and this expression can be directly applied. In practice, however, the inertia properties of each body are known independently, and it is more convenient to use these data directly. We denote the mass of the k-th body by m_k , its center of gravity by G_{0k} and its radii of gyration with respect to the center of gravity G_{0k} by $I_{ij}^{G_{0k}}$. With these notations the matrix elements $\mathcal{M}_{ij}$ for $i = 1{,}6$ and $j = 1{,}6$ are the classical elements of the global rigid body inertia (body 1 + body 2) expressed with respect to the global center of gravity. Regarding the restoring matrix $[\boldsymbol{\mathcal{C}}]$, the expressions (27) remain valid and can be directly applied. However, similar to the mass matrix, it is more convenient to express the different elements of the restoring matrix as a function of their values for individual bodies. In that case, the matrix elements $\mathcal{C}_{ij}$ for $i = 1{,}6$ and $j = 1{,}6$ are the classical elements of the global rigid body case (body 1 + body 2) expressed with respect to the global center of gravity.

4.2 Hydrodynamic loads on part of the body

In practice, it is sometimes necessary to evaluate the hydrodynamic loading on the part of the structure only. This might be important for the evaluation of the local hydrodynamic loading to be applied on the structural model in the case of quasi static hydro-structure simulations, but it can also be required for the hydroelastic simulations where the loading needs to be projected onto the mode shapes of the finite elements. There are different ways to do that and here we demonstrate that the generalized modal approach can be used as well and that this approach has some advantages over the classical methods.

4.2.1 Partial loads on rigid structure

The problem of evaluating the loads on the part of the wetted body is in many aspects similar to the multibody problem which has been discussed above. In this case, the model is subdivided into two parts S_B^1 and S_B^1, and 12 mode shapes in total are defined (see Table 2). As can been seen, their definition is rather simple: the first 6 modes represent the rigid body motions S_B^1 while S_B^2 is kept fixed, and the last 6 modes represent the rigid body motions S_B^2 while S_B^1 is kept fixed. For a typical Floating Offshore Wind Turbine (FOWT), modes 5 and 11 are shown in Figure 5

Table 2 : Relevant mode shapes for evaluation of local hydrodynamic loads.

	i ξ_i	**1** x_G	**2** y_G	**3** z_G	**4** θ_x	**5** θ_y	**6** θ_z	**7** x_G	**8** y_G	**9** z_G	**10** θ_x	**11** θ_y	**12** θ_z
S_B^1	$\{\boldsymbol{h}_i'\}$	$\{i'\}$	$\{j'\}$	$\{k'\}$	$[i']\{u_r'\}$	$[j']\{u_r'\}$	$[k']\{u_r'\}$	0	0	0	0	0	0
	$[\nabla \boldsymbol{h}_i']$	0	0	0	$[i']$	$[j']$	$[k']$	0	0	0	0	0	0
S_B^2	$\{\boldsymbol{h}_i'\}$	0	0	0	0	0	0	$\{i'\}$	$\{j'\}$	$\{k'\}$	$[i']\{u_r'\}$	$[j']\{u_r'\}$	$[k']\{u_r'\}$
	$[\nabla \boldsymbol{h}_i']$	0	0	0	0	0	0	0	0	0	$[i']$	$[j']$	$[k']$

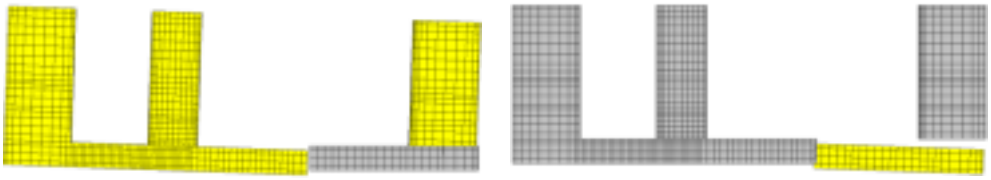


Figure 5: Modes 5 and 11 for FOWT (gray part remains fixed).

These modes are given to diffraction radiation software which outputs the hydrodynamic loads:

$$\mathcal{F}_i^{hd(DI)SS} = \quad i\omega\varrho \iint_{S_B} (\varphi_I + \varphi_D)\{\boldsymbol{h}_i'\}^T\{\boldsymbol{n}'\}dS \quad , \quad i = 1{,}12 \tag{33}$$

$$\mathcal{F}_i^{hd(R_j)SS} = \quad \varrho\omega^2 \sum_{j=1}^{12} \iint_{S_B} \varphi_{R_j}\{\boldsymbol{h}_i'\}^T\{\boldsymbol{n}'\}dS = \sum_{j=1}^{12} \left(\omega^2 \mathcal{A}_{ij}^{SS} + i\omega \mathcal{B}_{ij}^{SS}\right) \quad , \quad i = 1{,}12 \tag{34}$$

Regarding the contributions from gravity, hydrostatic pressure and inertia, they can be evaluated separately by employing directly the expressions (27) and (18). We denote them as follows:

$$[\mathcal{C}^{SS}] = \begin{bmatrix} \left[\mathcal{C}^{S_B^1}\right] & 0 \\ 0 & \left[\mathcal{C}^{S_B^2}\right] \end{bmatrix} \quad , \quad [\mathcal{M}^{SS}] = \begin{bmatrix} \left[\mathcal{M}^{S_B^1}\right] & 0 \\ 0 & \left[\mathcal{M}^{S_B^2}\right] \end{bmatrix} \tag{35}$$

where $\left[\mathcal{C}^{S_B^i}\right]$ and $\left[\mathcal{M}^{S_B^i}\right]$ are (6×6) the restoring and the inertia matrices of each substructure which are independent of each other.
Once all the coefficients are evaluated, the total loads on each substructure are given by:

$$\mathcal{F}_i^{SS} = \mathcal{F}_i^{hd(DI)SS} + \sum_{j=1}^{12} \left(\omega^2 \mathcal{A}_{ij}^{SS} + i\omega \mathcal{B}_{ij}^{SS}\right)\xi_j - \sum_{j=1}^{12} \left(\mathcal{C}_{ij}^{SS} - \omega^2 \mathcal{M}_{ij}^{SS}\right)\xi_j \quad , \quad i = 1{,}12 \tag{36}$$

Since the rigid body is in dynamic equilibrium, the sum of the loads at two substructures should be zero:

$$\mathcal{F}_i^{SS} = -\mathcal{F}_{i+6}^{SS} \quad , \quad i = 1{,}6 \tag{37}$$

It is also obvious that the same principles can be applied to any number of substructures by simply extending the number of modes. In that way we can, for example, evaluate the internal loads along the ship, which is something that is often required by industry.

4.2.2 Hydroelastic response of a ship using the beam shape function approach

The generalized modal approach is widely used to evaluate the hydroelastic response of ships by extending rigid-body motions with elastic modes. However, questions remain regarding the number of modes required for convergence and the use of wet versus dry modes. To overcome these issues and ensure exact coupling between structural FE and hydrodynamic models, the shape function approach can be applied. This involves projecting beam element shape functions onto the hydrodynamic mesh, forming boundary value problems for each function [5]. Figure 6 shows this projection for a container vessel, with continuity enforced between adjacent elements. Alternatively, shape functions may be treated independently, enabling analysis of nonlinear hydro-elastoplastic behavior under extreme conditions [3].

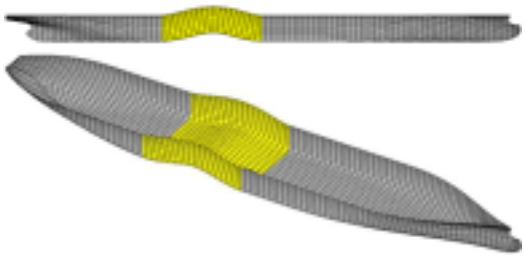


Figure 6: Projection of the typical beam shape functions onto 3D hydrodynamic mesh.

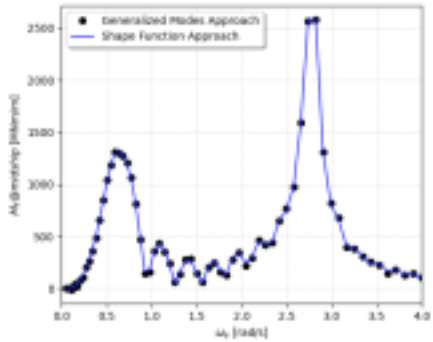


Figure 7: Comparison of the RAOs between the classic generalized modes approach and the shape function approach.

To illustrate the method, the springing response of a large container ship is analyzed using beam shape functions as the modal basis, instead of the conventional dry modes. As shown in Figure 7, excellent agreement is observed between the two approaches (errors <1%) when comparing the midship bending moment RAO. The main advantage of the approach based on the shape functions lies in its ability to account for the nonlinear hydro-plastic effects which might occur when hull sections experience buckling collapse in extreme conditions.

5. Ultimate generalized modal approach

5.1 Unit generalized modal concept

On the hydrodynamic side, the mean wetted body is defined by a number of panels N_P as can be seen in Figure 8.

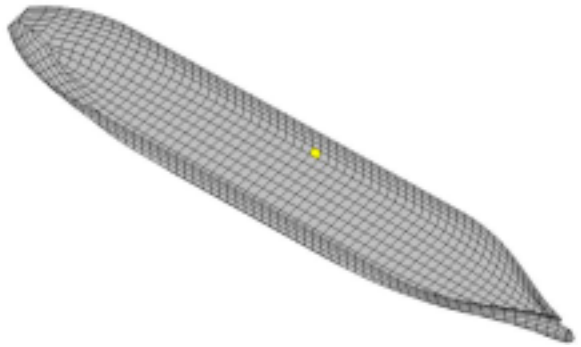


Figure 8: Hydrodynamic mesh of the floating body (panel p in yellow).

For each generalized mode, the mesh deforms according to its shape, affecting only the radiation (not diffraction) boundary condition (20). Since we are dealing with the linear problem, mode selection is arbitrary provided their sum reproduces the physical response. The ultimate choice is the unit generalized mode (see Figure 8) which is associated with each hydrodynamic panel p.

From hydrodynamic point of view, the unit generalized mode is defined by the following body boundary condition for the radiation velocity potential:

$$\frac{\partial \varphi_{R_p}^u}{\partial n} = \{\boldsymbol{h}_p'^u\}^T\{\boldsymbol{n}'\} = \begin{cases} 1 & , \quad p = j \quad , \quad j = 1, N_p \\ 0 & , \quad p \neq j \quad , \quad j = 1, N_p \end{cases} \tag{38}$$

5.1.1 External modal loading for unit generalized mode

The corresponding unit generalized modal excitation vector, the added mass and damping coefficients are defined as follows:

$$\mathcal{F}_p^{hd(DI^u)} = \quad i\omega\varrho \iint_{S_B} (\varphi_I + \varphi_D)\{\boldsymbol{h}_p'^u\}^T\{\boldsymbol{n}'\}dS \quad , \quad p = 1, N_P \tag{39}$$

$$\mathcal{F}_p^{hd(R_j^u)} = \quad \varrho\omega^2 \sum_{q=1}^{N_P} \iint_{S_B} \varphi_{R_q}^u \{\boldsymbol{h}_p'^u\}^T\{\boldsymbol{n}'\}dS = \sum_{q=1}^{N_P} \left(\omega^2 \mathcal{A}_{pq}^u + i\omega \mathcal{B}_{pq}^u\right) \quad , \quad p = 1, N_P \tag{40}$$

5.2 Physical mode shapes as a combination of the generalized unit mode shapes

Any physical mode shape $\{\boldsymbol{h}_j'\}$ can be expressed as the combination of the unit generalized mode shapes:

$$\{\boldsymbol{h}_j'\} = \sum_{p=1}^{N_P} \alpha_j^p \{\boldsymbol{h}_p'^u\} \tag{41}$$

where α_j^p is the value of the physical mode shape j at panel p.
The body boundary condition for the radiation velocity potential of physical mode j follows as:

$$\{\boldsymbol{h}_j'\}^T\{\boldsymbol{n}'\} = \sum_{p=1}^{N_P} \alpha_j^p \{\boldsymbol{h}_p'^u\}^T\{\boldsymbol{n}'\} \tag{42}$$

so that the radiation velocity potential for physical mode shape j can be expressed as:

$$\varphi_{R_j} = \sum_{p=1}^{N_P} \alpha_j^p \varphi_{R_p}^u \tag{43}$$

To clarify, as an example we consider the pitch motion where we have:

$$\alpha_5^p = \left(z_p' - z_G'\right)n_{x_P}' - \left(x_p' - x_G'\right)n_{z_P}' \tag{44}$$

where $\left(x_p', y_p', z_p'\right)$ are the coordinates of the panel p and $\left(n_{x_P}', n_{y_P}', n_{z_P}'\right)$ are the components of its normal vector.

5.2.1 External modal loading for physical modes

After some manipulations, the external hydrodynamic loading for physical modes follows as:

$$\mathcal{F}_i^{hd(DI)} = \quad i\omega\varrho \iint_{S_B} (\varphi_I + \varphi_D)\{\boldsymbol{h}_i'\}^T\{\boldsymbol{n}'\}dS = \sum_{p=1}^{N_P} \alpha_i^p \, \mathcal{F}_p^{hd(DI^u)} \tag{45}$$

$$\mathcal{F}_i^{hd(R_j)} = \quad \varrho\omega^2 \sum_{j=1}^{6+N_f} \iint_{S_B} \varphi_{R_j}\{\boldsymbol{h}_i'\}^T\{\boldsymbol{n}'\}dS = \sum_{j=1}^{6+N_f} \sum_{q=1}^{N_P} \sum_{p=1}^{N_P} \alpha_j^q \, \alpha_i^p \left(\omega^2 \mathcal{A}_{pq}^u + i\omega \mathcal{B}_{pq}^u\right)$$

In summary we have the following important identities:

$$\mathcal{F}_i^{hd(DI)} = \sum_{p=1}^{N_P} \alpha_i^p \, \mathcal{F}_p^{hd(DI^u)} \quad , \quad \mathcal{A}_{ij} = \sum_{q=1}^{N_P} \sum_{p=1}^{N_P} \alpha_j^q \, \alpha_i^p \mathcal{A}_{pq}^u \quad , \quad \mathcal{B}_{ij} = \sum_{q=1}^{N_P} \sum_{p=1}^{N_P} \alpha_j^q \, \alpha_i^p \mathcal{B}_{pq}^u \tag{46}$$

The unit generalized modal approach is useful for the evaluation of the external modal loading related to hydrodynamic pressure and it allows us to calculate the modal hydrodynamic coefficients for arbitrary physical mode shapes using the unit generalized mode shape solutions. This means that for a given wetted body surface, the solution of the hydrodynamic BVP's has to be performed only once and any particular physical situation can be modelled using those results. It has to be mentioned that the quantities $\mathcal{F}_p^{hd(DI^u)}$, $\mathcal{A}_{pq}^u$ and $\mathcal{B}_{pq}^u$ are the classical outcomes of any classical diffraction radiation solver (Hydrostar, Wamit …) and they can be evaluated in preprocessing phase. In order to evaluate the final physical response, the hydrostatic restoring and the inertial properties of the physical modes also need to be evaluated. Since these quantities do not depend on the solution of the hydrodynamic BVP they can be evaluated independently by the expressions (27) and (18) as it has been demonstrated in Section 4.1 for multibody problem. In summary the hydrodynamic database of the unit generalized hydrodynamic coefficients (39) and (40) can be used for solving all the physical problems which have been discussed here by employing the expressions (46).

6. Conclusions

Here we have summarized the generalized modal approach for solving the wave body interactions and presented several examples (rigid body motions, multibody interactions, evaluation of local loading and internal loads, hydroelastic response) where the generalized modal approach can be used. We also introduced, for the first time, what we denoted as the ultimate generalized modal approach, which allows for solving any particular physical problem by using the precalculated hydrodynamic database for the unit generalized modes. This means that the diffraction radiation code can be run only once, in preprocessing phase, without any physical considerations (other than those related to the solution of the BVP's) which can be dealt with independently in the postprocessing phase. This brings significant flexibility in using the classical diffraction-radiation software. It is the author's opinion that, up to now, the generalized modal approach has not received enough attention within the community, in spite of its extreme elegance and versatility and we hope that the discussions presented here will help in making it more popular, as it deserves.

7. References

[1] Bureau Veritas, 2024.: "Hydrostar for experts" User manual
[2] Jagite G., 2020.: "Analysis of slamming induced whipping effects over the ultimate strength of ships", PhD Thesis, Ecole Centrale de Nantes, France
[3] Jagite G., Le Sourne H., Cartraud P., Malenica S., Bigot F., De Lauzon J., Derbanne Q., 2020.: "A new approach to compute the non-linear whipping response using hydro-elastoplastic coupling", OMAE Conference, Fort Lauderdale, USA
[4] Malenica S. & Bigot F., 2020.: "On the generalized motions/deformations of the floating bodies", 25th IWWWFB, Seoul, South Korea.
[5] Malenica S., 1998.: "Hydroelastic coupling of beam structural model with 3D hydrodynamic model.", 2nd Int. Conf. on Hydroelasticity, Fukuoka, Japan.
[6] Newman J.N. 1994.: "Wave effects on deformable bodies," Applied Ocean Res., 16.
[7] Shabana A.A.1989.: "Dynamics of multibody systems", John Wiley & Sons
[8] Tuitman J.T., Malenica S. & Van't Veer R., 2013.: "Generalized modes in time domain seakeeping calculations (Extended)", Transactions of SNAME

Hydroelastic Problems in Marine Seismic Acquisition

Tønnessen, R.[1*], Oscarsson-Nagel, M.D.[2]

[1] TGS, Oslo, Norway (Rune.Tonnessen@tgs.com)
[2] TGS, Oslo, Norway (Mattias.Oscarsson-Nagel@tgs.com)

Abstract. In this paper we are discussing hydroelasticity within the field of marine geophysical exploration. That would mean offshore operations where the purpose is to generate maps of the geological structures below the sea bottom. We generally distinguish between node operations and towed streamer operations.

During node operations the nodes are placed on the seabed usually by ROV's, and the depth may be 3000m and beyond. This calls for an equivalently long umbilical subject to cross flow.

In towed streamer seismic both the streamers, the tow lead-ins, source umbilicals and all the ropes are exposed to hydrodynamic forces. Most of the focus related to hydrodynamics has been on minimizing the cross-flow forces on the cables and ropes being a part of the seismic streamer spread. Cable fairing will be discussed.

Further to this, the source itself emits a very strong hydro acoustic impulse that affects the nearby mechanics, including the float that keeps the source array afloat and the deflector wing mounted on the float. This will be discussed as well.

The paper does not aim at sharing significant new research-based insights but merely provides an overview of hydroelastic problems in this business and the impact it has.

Key words: *seismic acquisition; VIV; fairing; cavitation; airgun impulse*

1. Introduction

There exist two different methods of acquiring seismic data offshore. Traditional streamer seismic where one vessel tows a seismic source as well as one of more recording cables are likely the most known method. During recent years so-called node operations have become more popular even though this operation cost about ten times that of streamer seismic per square kilometer. The advantage in the latter is that the sensors lay still on the sea bottom in a noise free environment and the sources can move independently of the node handler vessel and hence generate data with both very short and very long offset (distance between the source and the recording node). In some parts of the world, node seismic is worth the extra cost while in other places it is not.

1.1 Ocean bottom node operations

During node operations the seismic receiver nodes are placed on the seabed by a so-called node handler vessel. See Figure 1. A node handler can carry several ROV's. The ROV's can operate at depths exceeding 3000m. A tether management system (TMS) is normally part of the ROV system. The TMS is operated through an umbilical. Normally the diameter of this umbilical is around 28-40mm. The TMS includes a winch containing the ROV's tether, paying the tether in and out when the ROV operates. Some TMS'es are equipped with thrusters. In some operations a so called High Speed Loader (HSL) is used. This is a "lift" that transports nodes from the ship and down to the depth where

* Correspondence to: rune.tonnessen@tgs.com

the ROV operates, and by doing so the ROV's does not need to go to the surface to load nodes. The ROV's load up nodes from the HSL to its own node carrying magazine. During the operation there are up to three umbilicals going from the vessel and down to the ROV's. The speed of the operation is limited by the drag of these umbilicals, and as a consequence the max speed is usually around 1 knot. In some areas, and in particular in Gulf of Mexico, operations can be hampered by severe loop currents of more than two knots. Severe strumming (VIV) can be experienced.

A reduction in drag of the umbilicals will have a huge impact on operational cost. The whole operation, including the node handler vessel and several source vessels, are often limited in efficiency due to the drag of the umbilicals.

Efforts are beeing done as some operators swap out hydraulicly driven ROV's with electrical ROV's resulting in somewhat thinner umbilicals. Cabel fairings are not used as they cause other problems when being reeled onto cable reels.

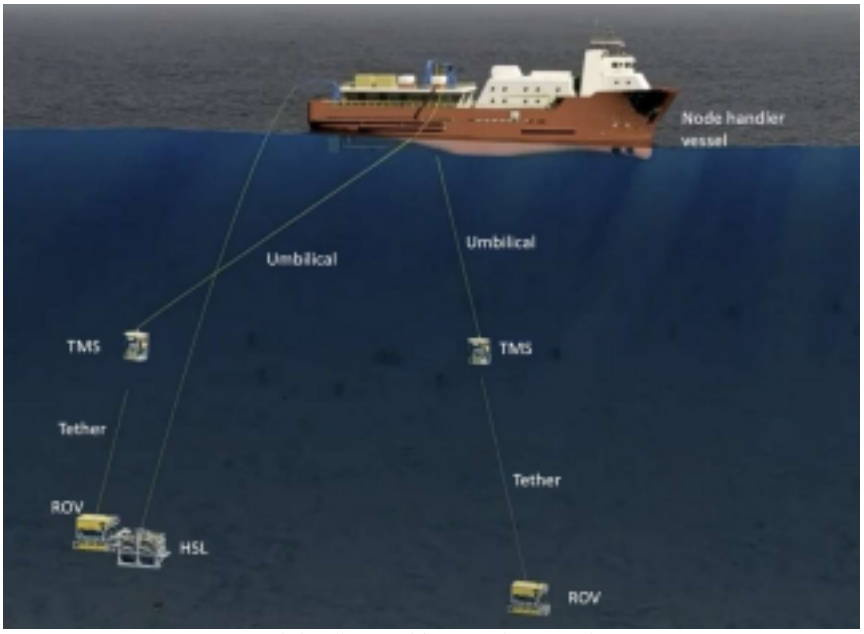


Figure 1: Node handler vessel for ocean bottom node operations.

1.2 Towed streamer seismic

Figure 2 below shows the geometry of a streamer spread illustrated by a towing simulation plot. A streamer is a long cable containing thousands of recording sensors such as hydrophones and often also accelerometers. Typical diameter is 55-65mm. The combination of hydrophones and accelerometers allows the interpreters to determine not only the strength of the acoustic wavefield received but also the direction of the wavefield. In the old days only one streamer was used but since the advent of 3D seismic vessels typically tows multiple streamers spread out by large deflectors. The streamer lengths and the separation between them vary dependent on the geophysical objective, so it can be anything between 3km and 12km lengths and streamer to streamer separations ranging between 25m and 180m. The largest spreads are typically 16 times 12km streamers with 100m distance between, so deflected out about 1500m laterally. The drag of this system often exceeds 100 tons. Typical survey speed is between 4.5 and 5 knots.

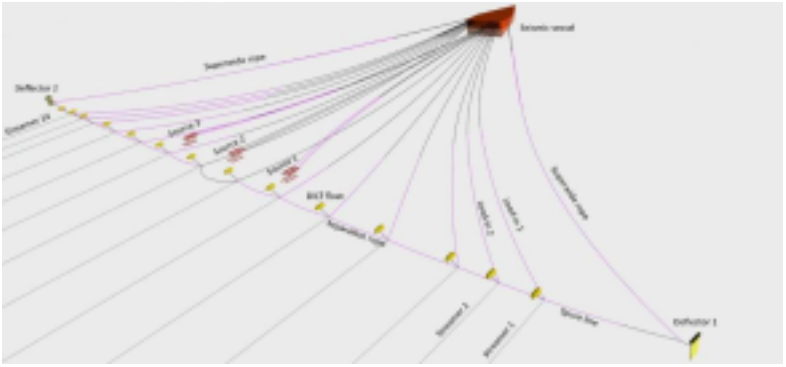


Figure 2: An example of a seismic streamer spread in the form of a simulated geometry. Streamers being truncated. Sea surface not seen.

With reference to Figure 2, the streamers are towed by so-called lead-ins, usually around 30mm in diameter. The front of the streamers is held up by so called DILT floats. The spread is spread out by deflectors. They come in different sizes; the most powerful ones can provide nearly 40tons of lift at 4.5knots. The deflectors are towed by a so-called superwide rope, which diameter is in the range of 35-50mm. The front end of the spread is held together with separation ropes. Diameter depending on load, larger diameter further out. Pink areas in the plot are areas where some sort of cable fairing is used in this particular case.

To control the streamers so-called birds are used. The simplest ones can only control the depth but the ones we use can control both depth and lateral position. We will come back to that in section 2.3. In addition to the birds a full acoustic positioning network is integrated with the streamer system, and this is again tied up to the earth fixed coordinate system by GPS'es.

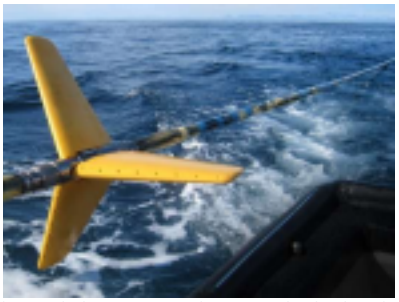


Figure 3: A steering bird inline with the streamer. This particular bird is about one meter in span.

Contrary to the Ocean Bottom Node operation, the streamer vessel operates both the sources and the recording system (streamers) simultaneously. Figure 2 shows three sources towed just in front of the streamers. A typical source string can be seen in Figure 4. Each source string (gun array plus float) typically involves several individual airguns, and together the gun array on one source string is called a sub-array. During operation the subarray are lowered to the shooting depth, typically around 5-8 meter below the float. A full source array may comprise one sub-array, two sub-arrays or eventually three sub-arrays if a large source volume is required. In Figure 2, three sources are operated, each source including two sub-arrays. A three-source string array typically emits 4200 cubic inch of air compressed to about 2000psi. (We apologize for using non-metric units, but this is standard in the industry when referring to source volume). Currently a little revolution is ongoing where the smaller airguns are replaced by one airgun of much larger volume. We talk about one airgun of 8000 cuin on each source string. A photo of an 8000 cuin source can be seen in Figure 5.



Figure 4: A seismic source sub array. Air guns hanging beneath the float during deployment. Source steering wing in closed position.

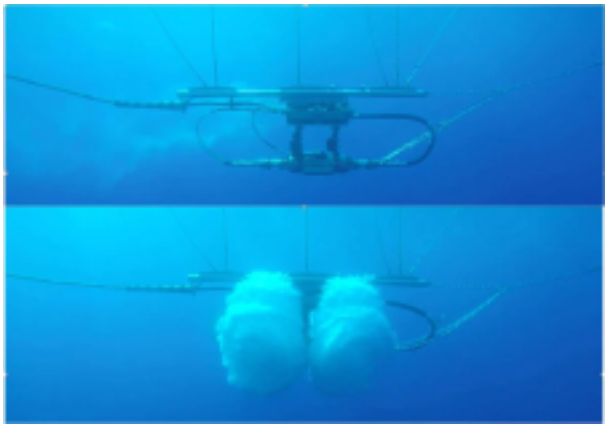


Figure 5: An 8000 cubic inch Gemini source. Upper: Source prior to firing. Lower: Source immediately after firing.

Referring again to Figure 2, one can see that the sources are spread out laterally. Traditionally the sources are spread out just a bit, typically half a streamer separation, but in recent years there has been a desire to increase the number of sources beyond the traditional two sources, sometimes up to six sources, and to spread them out wider. To achieve this, deflectors are applied to the keel of the source string. The deflector is seen as the yellow wing on Figure 4, being collapsed during source handling. To read more on the motivations and methods behind the wide-tow multiple source configurations, please refer to Widmaier et.al. (2019), Widmaier et.al (2021, SEG) and Widmaier et.al. (2021, First Break). The fairing work described in section 2.4 has to a large extent been motivated by the desire to tow the source out more widely.

In the academic field of hydrodynamics and control most of the interest has been shown towards the streamer part of the system. At least three PhD's have been written on the subject. Pedersen (1996) was the first to my knowledge being interested in the streamer technology focusing on hydrodynamic modeling of streamer behavior, while Ersdal (2004) went more into depth of the hydrodynamics of the streamer, and later Grindheim (2018) wrote about the control aspect of the streamer.

There are some interesting aspects related to steering of the streamer that we will come back in section 2.3 to but mostly it is the total drag of the system that is of interest. A one ton drag reduction typically results in 300 USD worth of fuel saved per day. Although the streamers cover a very large area, the drag of the streamers only account for about 20% of the total drag. The rest comes from the deflectors, the superwide ropes, the lead-in cables, the separation ropes and the floats. Suppressing VIV is very important when it comes to drag as a cable vibrating may have three times the drag of a non-vibrating cable. Furthermore, VIV of say lead-in cables can transmit the vibrations over to the streamers and cause noise on the recording sensors, corrupting the seismic data.

2. Hydroelastic Problems

We will discuss hydroelastic problems in marine seismic and the main focus will be on towed streamer seismic. The streamer itself is exposed to movements of the front end, for example because of the DILT floats moving up and down in waves as well as the jerking of the deflectors. I will not discuss this at any lengths. It is, however, worth mentioned that the outer streamers may be negatively affected by the tip vortices generated by the deflectors. To mitigate this a minimum length of spureline that need to be applied to get the deflector away for the streamer. There has also been put in efforts to kill the tip vortices. Note that the deflectors may have up to 40 tons of hydrodynamic lift, so the wash from the deflectors are substantial.

Further throughout this chapter we will discuss hydroelastic problems related to steering of the streamers in section 2.3, we will discuss cable fairing types and show result of fairing tests in section 2.4, discuss a very complex cavitation problem in 2.4 where hydroelasticity may play a role, and finally show an example of hydroacoustic "whipping" in in section 2.5.

2.3 Streamer hydrodynamics and control

As previously mentioned so called streamer birds are placed along the streamer. Their primary objective is to keep the streamer at the desired depth. The secondary objective is most often to keep a constant streamer separation, but this objective may vary. In some cases, one wants the streamer to operate in a fan shape, with the tails going out wide, and in some cases one wants to try to counteract a side current by steering all streamers to the side. Three degrees side steering is a well-known number for maximum steering capability, but this may vary between type of birds and the density of birds along the streamer. Normally the birds are placed every 300meter along the streamer. The direction the streamers take relative to the direction the vessel travels is called feather, and the amount the birds can steer the streamer to the side is called steered feather. Natural feather from side currents may in some areas exceed 45 degrees.

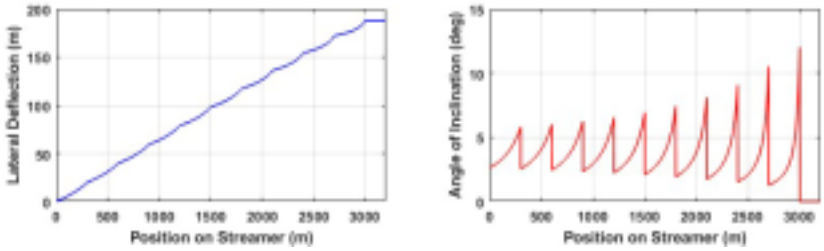


Figure 6: Left: Lateral deflection of a 3km long streamer with birds every 300m steering out laterally. Right: The angle of incident of the same streamer along the streamer.

There exists a static hydroelastic problem and its solution has potential to improve the efficiency of the streamer steering. To optimize the usage of the birds it is useful to know the real angle of attack of the bird wings relative to the ambient water flow. Today, the bird controller assumes that the bird body is parallel to the ambient flow, but that is not always the case. First, the bird body is generally in line with the streamer and if the streamer is steered sideways the steered feather may be 3degree. Then the streamer is not straight between the birds. In front of the streamer where the tension is high the streamer curvature is moderate while the further aft you get, the curvature increases. This can clearly be seen in Figure 6, where the birds are located at the position where the streamer angle of incident rapidly drops. At the tail the direction of the streamer segment just in front of a bird may be more than 10degrees off relative to the average direction of the streamer. Assuming that the bird body orients itself at an angle averaging that of the streamer in front and aft of the bird, then it will easily take an orientation 7-9 degrees relative to the flow. If one assumes that the stall angle of the wings is 15 degrees and considering that some wing effort must be used to depth control, then we see that a considerable amount of the birds steering capacity is unused. A modeling of the real orientation of the

bird considering all local forces and moments, including streamer bend resistance, forces and moments from wings, streamer tension, could be implemented as part of the steering software and hence improve the utilization of the steering capacity.

2.4 VIV and cable fairings

As mentioned in section 1.2 the main hydrodynamic focus is to reduce the overall drag of the system. Various types of cable fairings are used for this purpose. Figure 7 shows some of them. There are several compromises that must be made when it comes to fairing. The profile fairing has lowest drag coefficient. Sometimes it is as low as 0.2 and it suppresses VIV very well. However, it is difficult to store on reals and the variant shown below does not work as well when the flow is inclined (not normal to) to the cable. However there exist other variants, still rigid but in a softer material and made up of longer segments that survive reeling and performs better when inclined to the flow. The stiff profile fairing is normally used on the separation ropes. In this section I will soon be referring to some towing tank tests done in 2018. Unfortunately, the data is not public. Those tests show that there is a quite large difference in measure drag of stiff fairing when the fairing is forcefully at zero angle of attack compared to a fairing that is free rotating about the cable. It has been observed in the field that fairing segments tend to orient themselves in a staggered way (alternating tail up and down) with an increase in drag as a result.



Figure 7: Left: Cable with hairy fairing. Middle: Cable with canvas fairing. Right: Cable with profile fairing.

Figure 7 (left) shows a cable or a rope with hairy fairing. This is perhaps the most commonly used fairing in seismic. Some variants have some plastic strings inserted into the braiding of the rope instead of the rope filaments, then often referred to as ribbon fairing. The hairy/ribbon fairing suppresses VIV reasonably well albeit experience shows that some low amplitude VIV remains. This fairing type is used on the portion of the lead-in cable where more efficient fairing is not used as well as on the whole of the superwide rope. The superwide rope goes through a high number of sheaves during handling and it has proven difficult to get more efficient fairings to survive this treatment.

The canvas fairing in the middle of Figure 7 has proven to reel well onto a reel and at the same time perform better than the hairy fairing in water. It suppresses VIV better, and the drag coefficient is better, and in some cases as we will soon see the drag coefficient can be really good.

When it comes to designing a fairing there exist some pitfalls that people tend to fall into. One is to try to make an optimum foil shape stiff fairing having a nose protruding forward of the cable. This tends to make the fairing attain an angle of attack, and as a result generate lift. The other error is to make too long fairing segments without having the tail split. If the cable is curved, the tail will take a longer arc than the front and the result is that the fairing will twist and take an angle of attach, and the fairing will generate lift. You do not want the fairing to generate lift! Another pitfall is to let a canvas fairing be too loosely wrapped around the cable. The shape will then follow the pressure field, be sucked out perpendicular to the flow and you end up having a cable with significantly increased effective diameter.

We will now show some results from a towing tank test of stiff profiled fairing (not the one in Figure 7) and canvas type fairings. The test had several objectives. First, we wanted to understand to what degree the stiff profile fairings follow the crossflow principle when we vary the angle of incident. The crossflow principle assumes that we can decompose the flow into a component cross wise and in-line with the cable, and that the cross wise and in-line drag coefficient will be constant for all angles of inclination of the cable to the flow. In towed seismic we often operate the cables and ropes at very small incident angles. The crossflow principle is assumed questionable for those angles. Some data exists for circular cylinders and cables, but less so for faired cables. The towing simulations tools we apply assumes that the crossflow principle applies. The second objective was to study the efficiency of the canvas fairing shown in Figure 7 (middle).

The tests were carried out at Sintef Ocean's towing tank. A rotatable test rig was used allowing testing of several incident angles. For the free oscillation tests the rig was configured to oscillate transversely to the flow and stiffness was adjusted by application of springs. The test piece was a two meter long and 75mm thick aluminium cylinder placed between tapered end pieces, the end pieces were not part of the measurement but implemented to mitigate end effects.

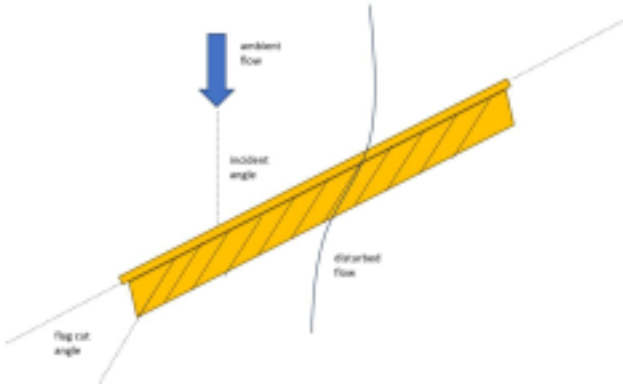


Figure 8: Nomenclature related to canvas fairing.

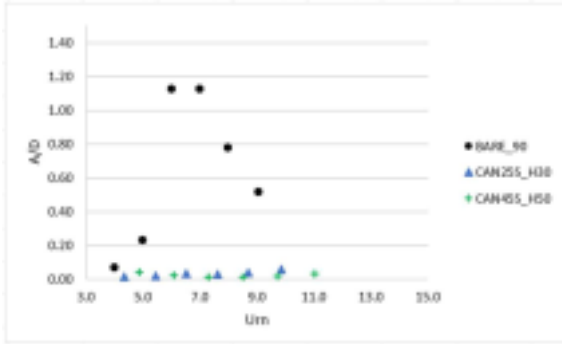


*Figure 9: Free oscillation test of circular cylinder and cylinders with canvas fairings. A/D means vibration amplitude over diameter. Urn=Un/(fn*D) is the reduced velocity, fn being the free oscillation natural frequency, D the diameter, and Un the normal velocity.*

Figure 9 shows the results from free oscillation tests from a bare cylinder and two variants of the canvas fairing. For the bare cylinder, only the results for incident angles of 90 degrees are shown here. Incident angles of 30 degree and 50 degrees were run as well, and the results compares well with that of 90 degrees. Two samples of canvas fairing were run in this test. One with a "flag cut angle" of 25 degrees (the angle the slit in the tail, or "flag", is cut in reference to the cable, ref. Figure 8) and one

where the canvas is cut at 45 degrees. The samples were run with 25 and 50 degrees incident angles respectively. No VIV were seen even with the canvas versions with short tail. We also tested fairings with longer tail. Similar free oscillation tests were run with stiff fairings and still no VIV were seen. It would be interesting, however, to test the canvas fairing where the discrepancy in cable incident angle differs a lot with the flag cut angle, in which case there is reason to believe the fairing is less effective.

Figure 10 (Left) shows the most interesting results of the test series in my opinion. Canvas fairing with flag cut angle of 25 degrees and 45 degrees were run at incident angles of 20, 30, 40 and 50 degrees and at speeds of 4.0, 4.5 and 5.5 knots. Considering the lower symbols, one can see that canvas fairing made with a flag cut angle of 25 degrees and ran at 40 and 50 degrees incident angles performed considerably better than those fairings where the cut angle and the incident angle matches approximately. Actually, the drag is halved at the lower speeds. Having watched the fairing during testing one understands why. When the cable is inclined with the flow, the flow will make a turn and locally orient itself more in line with the cable, so if one wants the flags to follow the disturbed flow one should cut the flags to an angle that is about 20 degree less than the expected inclination angle. A canvas fairing with flag parts not aligned with the local flow will easily have the flag part curled up behind the cylinder and you lose much of the drag reducing effect. More on this in a patent by Hauge & Tønnessen (2020).



Figure 10:Normal drag coefficient versus Reynolds number. Reynolds number based on the diameter of the test cylinder and the forward velocity (not normal velocity). Left: Normal drag coefficient of canvas fairing at 20, 30, 40 and 50 degrees incident angles. Towing speeds at 4.0, 4.5 and 5.5knots. Right: Normal drag coefficient for rigid profile fairing. Same speeds. Example: CAN25S_H20 – a short fairing cut at 25 degree and ran at 20 degree incident angle.

The drop in drag for the 25degree fairing ran at 30degree inclination at higher Reynolds number is more like expected when transiting from subcritical to critical flow, but it contradicts the cross-flow principle. Further at 20degree incident angles we generally see lower values for lower speeds than at say 30degree incident angles and above. This as well contradicts the cross-flow principle. If there were no Reynolds number effect and the cross-flow principle was perfect all marks should end up on top of each other along a horizontal line.

Results from rigid fairing tests shown in Figure 10 (Right). One of the objectives was to establish whether the cross-flow principle applies for foil shaped fairings. From the figure it seems that it does, and at least no worse than for bare cable or canvas fairing. The exception being low incident angles, but at incident angles as low as 20 degrees rigid foil fairing are rarely used. What we do notice, however, is the very low drag values of this fairing, and the percentage wise large increase if the fairing is not perfectly aligned with the flow, which we can see from the relatively large jump from locked fairing to free rotating fairing. In the experiment the fairing was not sectionized as is normal in seismic operations and it is reasonable to believe that sectionized fairings would lead to different results when the inclination angle deviates substantially from 90 degrees.

As an engineer in the seismic industry, one has to judge the pros and cons of various fairings. Rigid profile fairings are very effective but come with some cons in terms of the ability to go through sheaves and onto reels. If one designs a canvas fairing well, the difference between this and a rigid

profile fairing may not be that large. One must also account for the fact that the producer of the fairing often publish the Cd values based on the thickness of the fairing itself and not the rope or cable inside, and the fairing may be quite a bit thicker than the rope.

2.5 Source induced cavitation

During the last few years, we have worked towards achieving wider separations between the sources. Efficient fairing on source umbilicals was one part of it. Another effort has been the introduction of a somewhat larger deflector for the source array. The original deflector wing can be seen in Figure 4 while the new, enlarged wing, can be seen in Figure 11.



Figure 11: A source sub-array in operation with the enlarged deflector wing.

The new wing has equal chord length to the old one but a longer span and it spans deeper than the old. Four pilot series wings in composite material as well as two prototype wings in aluminium were produced. After only seven days in operation all the composite wings had holes, and the aluminium wing had some damage that looked more like someone had shot at it with a shotgun. See Figure 12 for the assessment of the damages. At first glance the damages appeared to be a result of cavitation but that was difficult to explain from assessing the hydrodynamic pressures. This damage had never been seen on the smaller wings, and strangely, a few holes were seen also on the pressure side.

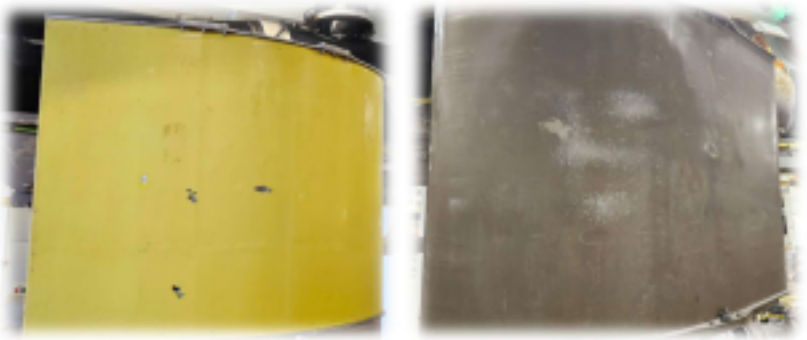


Figure 12: Left Composite wing with holes (leading edge to the right). Right: Aluminum wing with pitting damage (leading edge to the left).

DNV was approached and they were confident the damage was caused by cavitation. Two hypotheses were established. The primary hypothesis was that it was the ghost part of the airgun shots that triggered cavitation. The second hypothesis was that it was the hydroelastic chock response from the acoustic pulse that triggered cavitation. DNV performed CFD simulations while TGS did a source modeling exercise. A subset of the source signature simulations is shown in Figure 12.

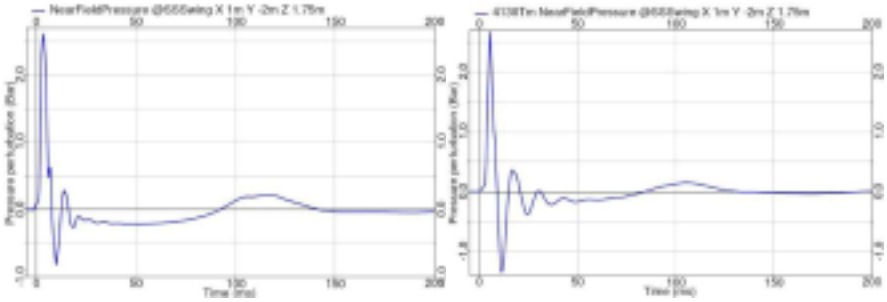


Figure 13: Source signatures at lower aft of the wings. Left: 5m source depth. Right: 8m source depth. The first pulse is the primary while the second and negative pulse is the ghost. Thereafter comes airbubble oscillations.

The signatures were calculated for several other positions on the wing as well. At the upper half of the wing both the primary and ghost pulses showed much lower values. The largest values both for primary pulse and ghost were found at the aft and lower part of the wings. DNV produced a report (not public) showing that instantaneous pressure field when the acoustic ghost pulse arrives is completely dominated by the acoustic ghost. For the case with 5m source depth the minimum pressure was about 40kPa while for the case for 8m source depth, the minimum pressure was -10kPa which is of course unphysical but clearly indicates that cavitation can occur.

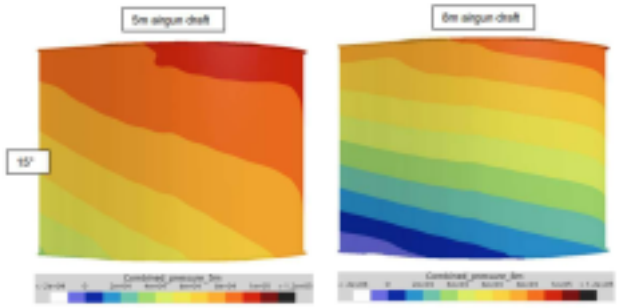


Figure 14: The complete pressure fields over the source steering wings at the moment where the source ghost hits.

Pressure fields including atmospheric pressure, hydrostatic pressure, hydrodynamic pressure as well as pressure from the source ghost are seen in Figure 14. 15 degree and 35degree angle of attack was considered, but the difference was small. In addition to the above plot DNV also plotted “Cp + cavitation number” (not shown here), but the area where “Cp + cavitation” number goes below zero, where cavitation is expected, corresponds well with the blue/purple area in the plots to the right. Now, the problem here is that this plot is for 8m airgun depth while it was with 5m airgun depth we first saw the problems, so for 5m airgun depth we should not have a cavitation problem according to this analysis. Further the cavitation pitting is not only located at the lower aft part but also further up towards the middle, and for the aluminium wing, forward of the center of the wing. See Figure 11. At this point we have not fully understood the root cause. It may very well be inaccuracies in the analysis of the source signature. The model used assumes a flat sea surface and no bodies where diffraction can occur. In Figure 11 we clearly see the sea surface is non flat as the float and the wing sets up a considerable wave. Further we should not forget the second hypothesis, that there is an element of hydro elastic response involved. The chock from the source pulse may very well trigger a response that again can trigger cavitation. This may explain the difference in location of the damage on the aluminium wing and on the composite wings as the hydro-elastic response is likely to differ from a composite wing and an aluminium wing especially given that their internal structure differs. The aluminium wing is built up of traditional ribs with welded on skin while the composite structure has a steel frame inside while the composite skin itself is more loosely attached to the frame.

2.5 Source induced "whipping"

Whipping is a well-known hydroelastic problem for merchant ships. A related problem is recently experienced in seismic exploration but now related to the source array. It was mentioned earlier that traditional source arrays are often replaced by high air volume sources shown in Figure 5. This has resulted in a longer duration of the primary pressure pulse as well as significant pressure pulses from the bubble oscillations. Figure 15 below shows some snapshots of a video of such a source firing. In the upper photo one can see the bubble just before it hits the float, and in the lower one can see the bubble hitting the float. However, already at the primary pressure peak one can see on the video that the float keel start vibrating from the shock. In addition, when the bubble hits the float, the float is exposed to hogging and sagging moments. The new type of source has led to more problems related to fatigue of the steel keel under the float. So far, we deal with the problem by regular inspections and welding when cracks are found.



Figure 15: The firing of a Gemini source and the impact on the source float. Upper: At the shot. Lower: When the bubble hits the float.

Acknowledgements

Thanks to TGS for allowing this publication and thanks to colleagues who contributed with images and facts. Acknowledgements to Sintef Ocean for the fairing experiments, and to DNV for the study in wing cavitation.

References

[1] M. Widmaier, D. O'Dowd, C. Roalkvam, *Redefining marine towed-streamer acquisition*. First Break 37, 2019.
[2] M. Widmaier, C. Roalkvam, J. Oukili, and R. Tønnessen, *Maximizing quality and efficiency with wide-tow multi-source configurations*, First Break 39, 2021.
[3] M. Widmaier, J. Oukili, C. Roalkvam, N. Halbert, and R. Tønnessen, *Maximizing quality and efficiency with of multisensory streamer seismic with an ultra-wise penta-source configuration*, SEG Technical Program Expandad Abstracts, 2021.
[4] E. Pedersen, *A Nautical Study of Towed Marine Seismic Streamer Cable Configurations*, Dr.Ing. thesis, Norwegian Institute of Technology (NTH), ISBN 82-471-0027-4, 1996.
[5] S. Ersdal, *An experimental study of Hydrodynamic Forces on Cylinders and Cables in Near Axial Flow,* Dr.Ing. thesis, Norwegian University of Science and Technology (NTNU), ISBN 978-82-471-6470-9, 2004.
[6] J.V. Grindheim, *Modeling, Prediction and control of marine towed seismic streamers*, PhD thesis, Norwegian University of Life Sciences (NMBU), ISBN 978-82-575-1522-5, 2018.
[7] T. Hauge and R. Tønnessen, *Split fairing for towed marine equipment*, Patent no. US11427285B2, published 2020, granted 2022.

10th International Conference on HYDROELASTICITY IN MARINE TECHNOLOGY
Trondheim, Norway, June16$^{\text{th}}$-18$^{\text{th}}$, 2026

Inverse Wave Force Estimation Using Frequency- and Time-Domain Hydroelastic Models

Van Zijl, C.[1,*] Jovanova, J.[1], and Grammatikopoulos, A.[1]

[1] Department of Maritime & Transport Technology, Delft University of Technology, The Netherlands

Abstract. Accurate knowledge of wave-induced loads is essential for the safe and efficient design and operation of offshore structures, yet direct measurement of hydrodynamic forces remains challenging. This study investigates whether wave excitation forces can be estimated from measured structural responses by treating the structure as a distributed force sensor. A hydroelastic state-space model incorporating frequency-dependent added mass and radiation damping, obtained through rational approximation of radiation forces, is employed. A joint input–state Kalman filter is used to estimate both dynamic states and unknown excitation forces from noisy acceleration measurements. Its performance is evaluated against frequency-domain inverse methods based on least-squares inversion of acceleration frequency response functions, including a Tikhonov-regularised formulation to address ill-conditioning. Results show that accurate force reconstruction is primarily achieved within frequency ranges where the forward operator is well conditioned, particularly near modal resonances and for lower-order modes. While Tikhonov regularisation yields the lowest estimator variance, it introduces bias and underestimates force energy for higher-order modes. The time-domain Kalman filter provides a more balanced trade-off between variance reduction and bias through implicit regularisation introduced by system dynamics. The results demonstrate that regularisation improves estimator stability but may suppress physically relevant force content when applied excessively.

Key words: *Wave load estimation; inverse problems; Tikhonov regularization; Kalman filtering*

1. Introduction

Accurate knowledge of wave-induced loads enables engineers to design marine structures that can withstand the harsh ocean environment while optimising performance and operational efficiency. In the shipping and offshore industries, reliable estimates of wave forces support safe and efficient route planning, fuel optimisation, and structural health monitoring [1, 2]. Despite their importance, wave excitation forces are difficult or impossible to measure directly on large floating structures, motivating the use of inverse methods in which forces are inferred from measured structural responses.

Inverse force estimation relies on a forward model that relates external excitation to measured responses. In marine applications, this relationship is provided by hydroelastic models that couple structural dynamics with hydrodynamic loading. In the frequency domain, the forward model is commonly expressed through frequency response functions that incorporate frequency-dependent added-mass and radiation-damping effects [3]. In the time domain, these same hydrodynamic effects appear as radiation memory terms, typically represented through convolution kernels or equivalent state-space formulations [4]. Both representations describe the same underlying physics, but lead naturally to different inverse estimation approaches.

A fundamental challenge in inverse wave load estimation is the low-frequency nature of wave excitation acting on large floating structures. In the present context, “low-frequency” refers to first-order

[*]Correspondence to: c.m.vanzijl@tudelft.nl

wave excitation in the typical ocean-wave range (approximately 0.05–0.15 Hz, corresponding to wave periods of 7–20 s), which is substantially below the first wet natural frequencies of large ship structures (typically of order 1 Hz). In this regime, hydroelastic transfer operators are often ill-conditioned, leading to significant amplification of measurement noise in inverse solutions [5]. This effect is especially pronounced for higher-order modes and can limit the reliability of frequency-domain least-squares inversion. Time-domain formulations introduce implicit regularisation through their state-space representation and noise modelling, which may mitigate low-frequency variance amplification, but at the cost of increased dependence on the assumed model structure.

The aim of this paper is to examine frequency- and time-domain inverse wave force estimation methods within a consistent hydroelastic modelling framework. The focus is on a controlled comparison of commonly used inverse formulations applied to the same linear hydroelastic model, wave excitation, and measurement conditions. The frequency-domain approach is considered in least-squares and Tikhonov-regularised form. The regularisation parameter is selected using the L-curve criterion, yielding a global regularisation level that is subsequently scaled with frequency according to the magnitude of the forward operator singular values. The time-domain approach employs a joint input–state Kalman filter, in which regularisation arises implicitly through the system dynamics and noise modelling.

The remainder of the paper is organised as follows. Section 2 introduces the hydroelastic forward model and inverse formulations. Section 3 describes the numerical model and simulation setup. Section 4 presents the results, and Section 5 summarises the main findings.

2. Theory

This section introduces the hydroelastic forward model used for inverse wave load estimation and formulates the inverse problem in both the frequency and time domains. A linear hydroelastic model is adopted, allowing a frequency-domain representation based on transfer operators and a time-domain state-space formulation that includes radiation memory effects through a rational approximation. Superscript $(\cdot)^{(m)}$ denotes modal quantities.

2.1. Hydroelastic model

The hydroelastic system is represented in a truncated modal basis containing rigid-body and flexible structural modes. The modal basis matrix $\Phi \in \mathbb{R}^{n\times n_m}$ is constructed from the dry structural eigenvalue problem

$$\big(K_s - \omega_r^2 M_s\big)\,\phi_r = 0, \tag{1}$$

where M_s and K_s denote the dry structural mass and stiffness matrices, respectively. Using the modal coordinates $\underline{Y}^{(m)} \in \mathbb{R}^{n_m}$, the coupled hydroelastic equation of motion in the frequency domain becomes

$$\Big(-\omega^2\big(M + M_h(\omega)\big) + i\omega\big(C + C_h(\omega)\big) + \big(K + K_h\big)\Big)\underline{Y}^{(m)}(\omega) = \underline{F}^{(m)}(\omega), \tag{2}$$

Here, M, C, and K denote the reduced structural mass, damping, and stiffness matrices in modal coordinates. The structural damping matrix C is assumed diagonal and constructed from prescribed modal damping ratios. Furthermore, $M_h(\omega)$ and $C_h(\omega)$ are the frequency-dependent added-mass and radiation-damping matrices and K_h is the hydrostatic restoring matrix.

2.2. Frequency-domain formulation

Define the modal hydroelastic frequency response function (FRF) as:

$$H^{(m)}(\omega) = (-\omega^2\big(M + M_h(\omega)\big) + i\omega\big(C + C_h(\omega)\big) + \big(K + K_h\big))^{-1}, \tag{3}$$

For acceleration measurements at selected physical locations, the measured response is

$$\underline{Y}(\omega) = -\omega^2\, S\Phi\, H^{(m)}(\omega)\,\underline{F}^{(m)}(\omega) \;\triangleq\; \mathcal{H}(\omega)\,\underline{F}^{(m)}(\omega), \tag{4}$$

where S maps structural degrees of freedom to sensor locations. The operator $\mathcal{H}(\omega)$ therefore constitutes the forward model for inverse force estimation.

2.3. Time-domain formulation

For implementation of the time-domain joint input–state Kalman filter introduced later, the hydroelastic model is expressed in state-space form [4]. The use of a state-space realization for radiation-memory effects in combination with Kalman-filter-based force estimation follows the approach of [6]. The present work applies this framework to a hydroelastic system; the relevant equations are therefore summarized here for completeness.

2.3.1. Radiation memory and hydrodynamic state-space model

The time-domain equation of motion corresponding to Eq. (2) is:

$$(M + M_\infty)\ddot{\underline{y}}^{(m)}(t) + C\dot{\underline{y}}^{(m)}(t) + (K + K_h)\underline{y}^{(m)}(t) + \int_0^t K_r(t-\tau)\dot{\underline{y}}^{(m)}(\tau)\,\mathrm{d}\tau = \underline{f}^{(m)}(t), \quad (5)$$

where M_∞ is the infinite-frequency added mass. Define the radiation impedance

$$Z(\omega) \triangleq C_h(\omega) + i\omega\big(M_h(\omega) - M_\infty\big). \quad (6)$$

To avoid explicit evaluation of the radiation-memory convolution in Eq. (5), the radiation impedance is approximated by a finite-dimensional state-space realization. Using vector fitting, $Z(s)$ with $s = i\omega$ is approximated as

$$Z(s) \approx C_r(sI - A_r)^{-1}B_r, \quad (7)$$

where A_r, B_r, and C_r are realization matrices whose order is determined by the number of retained poles in the fit.This yields the hydrodynamic radiation subsystem

$$\dot{\underline{x}}_r^{(m)}(t) = A_r\,\underline{x}_r^{(m)}(t) + B_r\,\dot{\underline{y}}^{(m)}(t), \quad (8)$$

$$\underline{f}_{\text{rad}}^{(m)}(t) = C_r\,\underline{x}_r^{(m)}(t). \quad (9)$$

which replaces the convolution term with a finite-dimensional dynamical system suitable for time-domain state estimation and Kalman filtering.

2.3.2. Augmented hydroelastic state-space model

Combining the structural modal dynamics with the radiation subsystem yields a finite-dimensional state-space representation suitable for time-domain inverse estimation and Kalman filtering. Defining the effective inertia matrix $M_{\text{eff}} = M + M_\infty$ the modal acceleration equation becomes

$$\ddot{\underline{y}}^{(m)}(t) = -M_{\text{eff}}^{-1}(K + K_h)\underline{y}^{(m)}(t) - M_{\text{eff}}^{-1}C\dot{\underline{y}}^{(m)}(t) - M_{\text{eff}}^{-1}C_h\underline{x}_r^{(m)}(t) + M_{\text{eff}}^{-1}\underline{f}^{(m)}(t). \quad (10)$$

Introducing the augmented modal state vector

$$\underline{x}^{(m)}(t) = \begin{bmatrix} \underline{y}^{(m)}(t) \\ \dot{\underline{y}}^{(m)}(t) \\ \underline{x}_r^{(m)}(t) \end{bmatrix}. \quad (11)$$

The continuous-time augmented model is

$$\dot{\underline{x}}^{(m)}(t) = A\,\underline{x}^{(m)}(t) + B\,\underline{f}^{(m)}(t), \quad (12)$$

with

$$A = \begin{bmatrix} 0 & I & 0 \\ -M_{\text{eff}}^{-1}(K + K_h) & -M_{\text{eff}}^{-1}C & -M_{\text{eff}}^{-1}C_r \\ 0 & B_r & A_r \end{bmatrix}, \qquad B = \begin{bmatrix} 0 \\ M_{\text{eff}}^{-1} \\ 0 \end{bmatrix}. \quad (13)$$

2.4. Discrete-time model and acceleration output

For inverse estimation, (12) is discretised with sampling interval Δt,

$$\underline{x}_{n+1}^{(m)} = A_d\,\underline{x}_n^{(m)} + B_d\,\underline{f}_n^{(m)} + \underline{w}_n, \tag{14}$$

$$\underline{y}_n = C_d\,\underline{x}_n^{(m)} + D_d\,\underline{f}_n^{(m)} + \underline{v}_n, \tag{15}$$

where $\underline{w}_n \sim \mathcal{N}(0, Q)$ and $\underline{v}_n \sim \mathcal{N}(0, R)$. The measured output consists of accelerations at selected physical DOFs. Let Φ map modal to physical coordinates and S select sensor locations. The measurement matrices are

$$C_d = S\Phi \begin{bmatrix} -M_{\text{eff}}^{-1}(K + K_h) & -M_{\text{eff}}^{-1}C & -M_{\text{eff}}^{-1}C_r \end{bmatrix}, \tag{16}$$

$$D_d = S\Phi\, M_{\text{eff}}^{-1}. \tag{17}$$

2.5. Inverse force estimation

The objective is to estimate the unknown modal excitation force $\underline{f}^{(m)}$ from measured responses, given the hydroelastic forward model.

2.5.1. Frequency-domain least-squares inversion

In the frequency domain, the forward model reads

$$\underline{Y}(\omega_k) = \mathcal{H}(\omega_k)\,\underline{F}^{(m)}(\omega_k), \tag{18}$$

Assuming $\mathcal{H}_k$ has full column rank, the corresponding closed-form least-squares solution is

$$\widehat{\underline{F}}_k^{(m)} = \left(\mathcal{H}_k^{\mathrm{H}}\mathcal{H}_k\right)^{-1}\mathcal{H}_k^{\mathrm{H}}\,\tilde{\underline{Y}}_k \tag{19}$$

where $(\cdot)^{\mathrm{H}}$ denotes the Hermitian transpose.

2.5.2. Tikhonov-regularised frequency-domain inversion

In practice, the forward operator $\mathcal{H}_k$ may be ill-conditioned, particular at low frequencies. In this case, small singular values amplify measurement noise and lead to large estimator variance. To stabilise the inversion, Tikhonov regularisation is introduced. The regularised estimate has the following closed-form solution:

$$\widehat{\underline{F}}_k^{(m)} = \left(\mathcal{H}_k^{\mathrm{H}}\mathcal{H}_k + \lambda^2\mathbf{I}\right)^{-1}\mathcal{H}_k^{\mathrm{H}}\,\tilde{\underline{Y}}_k \tag{20}$$

where $\lambda > 0$ is the regularisation parameter controlling the trade-off between variance reduction and estimation bias. The global regularisation parameter is selected using the L-curve criterion [7].

2.5.3. Time-domain joint input–state Kalman filter

The discrete-time state-space model is used within the joint input–state estimation framework of Gillijns and De Moor [8], in which both the structural state and modal excitation forces are estimated sequentially from the measured acceleration response. The formulation exploits the direct feedthrough term in the measurement equation to obtain same-step force estimates from the measurement innovation while simultaneously updating the structural state.

3. Numerical model

A numerical study is conducted on an idealised floating beam to compare frequency- and time-domain inverse force estimation under controlled modelling and measurement noise.

3.1. Hydroelastic model

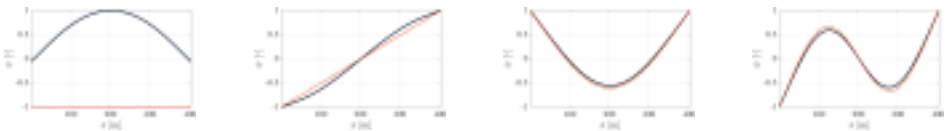
The structure is modelled as a uniform Euler–Bernoulli beam of length $L = 200$ m with circular cross-section radius $R = 10$ m and wall thickness $t = 1.7 \times 10^{-3}$ m. The Young's modulus is $E = 200$ GPa. The material density is selected such that the beam floats at an approximate draft of $R/2$ and the first dry bending natural frequency is $f_1 \approx 0.2$ Hz. The first dry natural frequency is selected to be approximately consistent with the low-frequency global structural dynamics of large container ship structures, for which first natural frequencies are often of the order of 0.2 Hz. In real vessels, these low-frequency modes may typically correspond to torsional global modes, whereas the present simplified model exhibits only vertical bending responses. The beam model is therefore not intended to represent a specific vessel directly, but rather an idealised flexible floating structure with comparable low-frequency hydroelastic behaviour.

A finite-element model with 401 elements (402 nodes) is constructed. Modal truncation retains $n_m = 8$ dry modes, including rigid-body and flexible modes. A uniform modal damping ratio $\zeta = 0.02$ is assumed for all retained modes.

Frequency-dependent hydrodynamic coefficients are computed using the potential-flow boundary element solver CAPYTAINE [9]. The wetted surface is discretised using 7360 panels. For the retained modal basis, the added-mass and radiation-damping matrices $M_h(\omega)$ and $C_h(\omega)$ are obtained over the frequency range of interest. In addition, the modal wave-excitation force transfer functions (RAOs mapping wave elevation to modal forces) are also computed using CAPYTAINE. All hydrodynamic coefficients are computed for head-wave conditions (180° wave heading). Table 1 compares the dry and wet natural frequencies for a subset of modes of the coupled hydroelastic model, while the corresponding dry and wet mode shapes are shown in Fig. 1.

Table 1: Comparison of natural frequencies (in Hz) for dry and wet/coupled models. The flexible modes (Mode 3 and 4) are labeled using the convention XnVB, where X denotes the number of nodes in the mode shape and VB stands for vertical bending.

Mode name	**Dry model**	**Wet model**
Pitch	0.00	0.139
Heave	0.00	0.140
2nVB	0.229	0.228
3nVB	0.633	0.503



(a) Heave (b) Pitch (c) 2nVB (d) 3nVB

Figure 1: Mode shapes of four modes for the dry (solid line) and wet/coupled (dashed line) models.

The radiation impedance in Eq. (6) is approximated using vector fitting as described in Section 2.1.. The open-source MATLAB package `vectfitx` [10] is employed, using $N_p = 10$ poles per retained mode.

3.2. Numerical simulation procedure

Irregular wave excitation is modelled using a JONSWAP spectrum [11] with parameters $H_s = 3$ m, $T_p = 9$ s, and $\gamma = 3.3$. The spectrum is transformed to encounter frequency for head-wave conditions and forward speed of $U = 10$ m/s. A uniform random phase realisation is used to model random waves. Modal wave-excitation forces are then obtained from the hydrodynamic excitation-force RAOs computed using CAPYTAINE.

The corresponding noise-free structural response is generated using the hydroelastic forward model introduced in Section 2.1.. The resulting acceleration signals are sampled at 20 Hz over a duration of 2000 s and contaminated with additive zero-mean Gaussian noise with standard deviation 0.01 m/s^2.

For the frequency-domain inverse method, the sampled acceleration signals are transformed using an FFT with Hanning windowing prior to least-squares or Tikhonov inversion at each discrete frequency. For the time-domain approach, the measured acceleration time histories are used directly in the discrete-time hydroelastic state-space model together with the joint input–state Kalman filter described in Section 2.5..

4. Results

The results are presented in three parts. First, the accuracy of the rational approximation of the radiation impedance is assessed, as this directly determines the fidelity of the time-domain state-space model. Second, the variance characteristics of the frequency- and time-domain inverse force estimators are compared. Finally, the quality of the reconstructed force spectra is evaluated in terms of power spectral density and root-mean-square force levels.

4.1. Radiation impedance fitting accuracy

The quality of the rational approximation of the radiation impedance is quantified using the relative fitting error. The relative fitting error is defined as

$$\frac{\sum_\omega |Z(\omega) - \hat{Z}(\omega)|}{\sum_\omega |Z(\omega)|}. \tag{21}$$

Figure 2 shows the relative error for all entries of the 8×8 impedance matrix. The lowest errors are observed for the lower-order modes (modes 1–3), while significantly larger errors occur for the highest mode (mode 8). In general, diagonal terms exhibit smaller errors than off-diagonal terms, reflecting the fact that self-radiation effects are captured more accurately than modal coupling terms. Physically, entry (i, j) represents the radiation force in mode i induced by motion in mode j.

To illustrate the quality of individual fits, Figure 3 compares the real and imaginary parts of selected impedance terms. The $(2, 2)$ entry shows an good match between the true and fitted impedance over the frequency range of interest, with only minor amplitude deviations. In contrast, the $(8, 8)$ entry exhibits noticeably larger discrepancies, particularly in amplitude, consistent with the higher relative errors reported above. These results confirm that modelling errors increase with modal order and will therefore primarily affect force estimation in the higher modes.

4.2. Variance of force estimates

Figure 4 compares the variance of the estimated modal excitation forces for Modes 1–4 under measurement noise contamination. The variance quantifies how strongly the estimated forces fluctuate across different realizations of measurement noise and therefore provides a measure of estimator robustness to sensor noise. Lage values of variance indicate strong amplification of sensor noise through the inverse problem. The plotted quantity corresponds to the variance of the real part of the estimated modal forces and therefore has units of force squared (N^2).

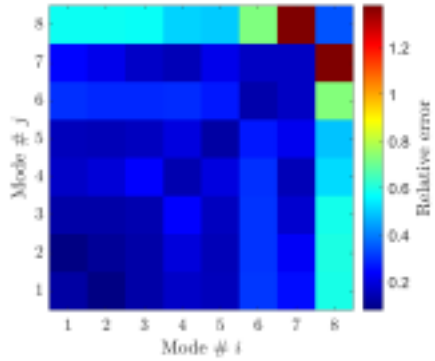


Figure 2: Relative fitting error of the rational approximation of the radiation impedance for all entries of the 8×8 modal impedance matrix. Each entry (i, j)corresponds to the radiation force in mode i induced by motion in mode j.

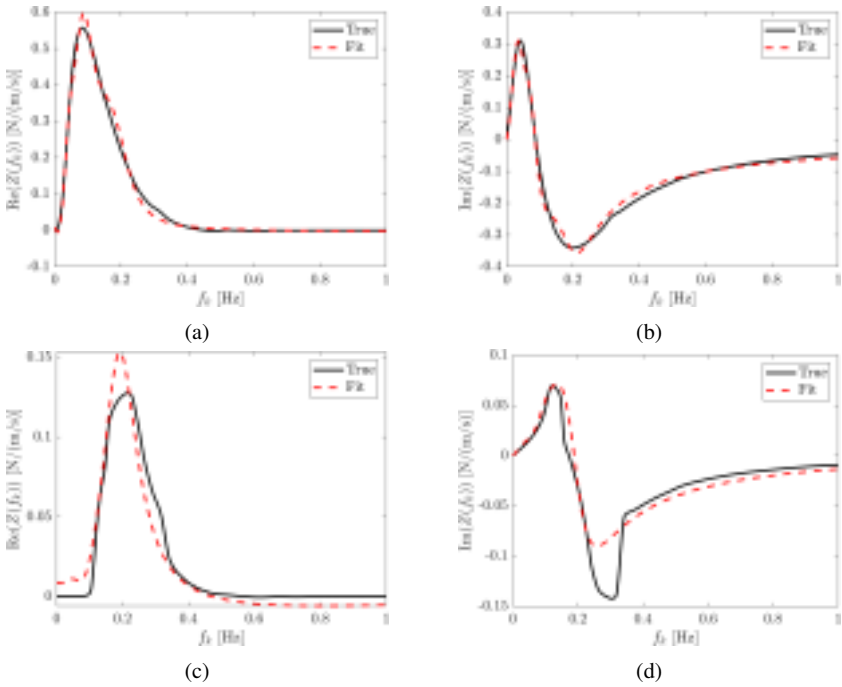
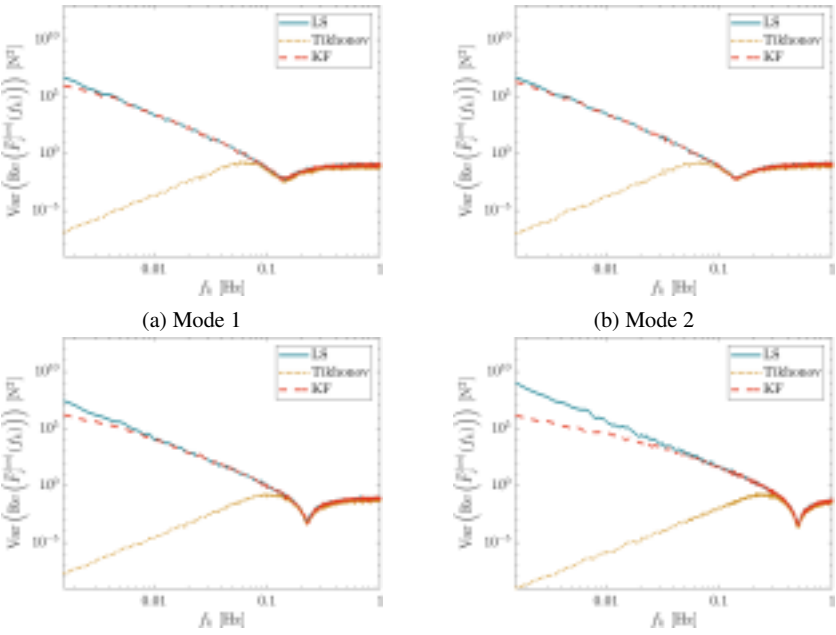


Figure 3: Comparison of the real and imaginary parts of the fitted and true radiation impedance for selected diagonal terms (2,2) and (8,8) of the modal impedance matrix over the frequency range of interest.

The large variation in variance across frequency highlights the strong frequency dependence of the inverse problem conditioning. Near the modal resonance frequencies, the measured accelerations are highly sensitive to the corresponding excitation forces, resulting in relatively low estimator variance.

Away from resonance, the differences between the estimators become pronounced. The unregularised LS solution exhibits strong variance amplification at low frequencies, particularly for higher-

order modes, due to the ill-conditioning of the forward operator. The Kalman filter reduces this effect through implicit regularisation introduced by the state-space dynamics and noise modelling. The Tikhonov estimator produces the lowest variance overall by explicitly damping weakly observable singular directions of the inverse problem. However, this variance reduction reflects stronger regularisation rather than improved observability and must therefore be interpreted together with the bias characteristics discussed in the following section.



(a) Mode 1 (b) Mode 2

(c) Mode 3 (d) Mode 4

Figure 4: Variance of the estimated modal wave-excitation forces for modes 1—4 as a function of frequency obtained using least-squares (LS), Tikhonov regularization, and the time-domain Kalman filter (KF).

4.3. Reconstruction of force spectra and RMS level

The quality of the reconstructed force spectra is examined by comparing the power spectral density (PSD) of the estimated forces with the true PSD. The area under the PSD is directly related to the root-mean-square (RMS) force contribution over a given frequency band. While the variance results in Section 4.1 indicate that the Tikhonov estimator provides the strongest stabilisation of the inverse problem, the PSD comparison reveals the associated increase in estimation bias.

For the LS estimator, the PSD is computed directly from the frequency-domain force estimate as $S_{F_jF_j}(\omega_k) = S_P\,|\hat{F}_j(\omega_k)|^2$, where S_P is a scaling factor ensuring consistency with the signal normalization. For the Kalman filter, the PSD is estimated from the time-domain force signal using Welch's method.

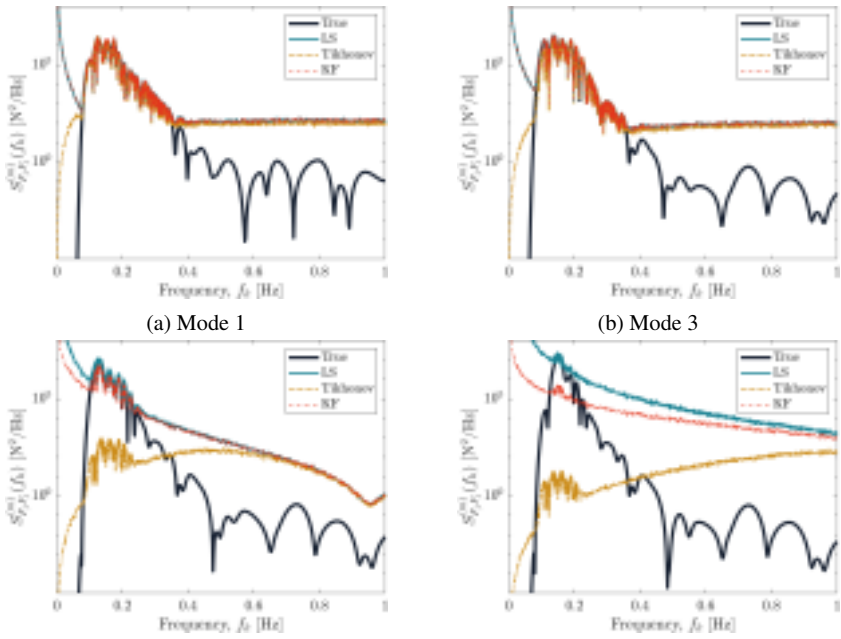
Figure 5 compares the reconstructed PSDs for Modes 1, 3, 5, and 7. For the lower-order modes, all estimators recover the true PSD reasonably well in the dominant excitation range around 0.1–0.3 Hz. Outside this range, the differences between the estimators become increasingly pronounced.

The LS estimator exhibits elevated PSD levels away from resonance due to strong amplification of

measurement noise in ill-conditioned frequency regions. The Tikhonov estimator strongly suppresses these poorly observable components through explicit regularization. For the higher-order modes, particularly Modes 5 and 7, this suppression becomes so strong that the reconstructed force energy is several orders of magnitude lower than the true PSD over parts of the frequency range. This behaviour reflects the bias–variance tradeoff inherent to Tikhonov regularization: variance is substantially reduced, but at the cost of aggressively damping weakly observable force components toward zero.

The Kalman filter achieves a more balanced behaviour. Although its variance is generally higher than that of the Tikhonov estimator, the reconstructed PSD retains more physically relevant force content within the frequency range of interest. This suggests that the dynamical constraints imposed by the state-space model provide an effective form of implicit regularization without introducing the same level of bias suppression.

Although modelling errors in the fitted radiation dynamics increase with modal order, their effect on systematic bias is not clearly distinguishable from regularisation effects in the present results.



(a) Mode 1 (b) Mode 3

(c) Mode 5 (d) Mode 7

Figure 5: Power spectral density (PSD) of the estimated modal excitation forces for modes 1,3,5, and 7 compared with the true PSD, shown as a function of frequency.

5. Conclusions

This paper examined frequency- and time-domain inverse wave force estimation methods within a consistent hydroelastic modelling framework, focusing on the role of regularisation in stabilising the inverse problem. Three formulations were considered: unregularised frequency-domain least-squares (LS) inversion, Tikhonov-regularised frequency-domain inversion, and a time-domain joint input–state Kalman filter (KF).

Accurate reconstruction of excitation forces is primarily achieved in frequency regions where the

hydroelastic forward operator is well conditioned, typically near modal resonances and for lower-order modes. In this regime, all estimators exhibit comparable performance, whereas away from resonance the LS solution shows strong variance amplification due to ill-conditioning.

Tikhonov regularisation stabilises the inversion and yields the lowest estimator variance, but introduces estimation bias by suppressing weakly observable force components. For higher-order modes this leads to underestimation of force energy and reduced reconstructed PSD, demonstrating that strong explicit regularisation may suppress physically relevant excitation content.

The time-domain Kalman filter provides a more balanced trade-off between variance reduction and bias through implicit regularisation introduced by the system dynamics. Although its variance is generally higher than that of the Tikhonov estimator, the reconstructed force spectra retain more physically relevant energy.

Overall, the results indicate that the primary limitation in inverse wave force estimation is governed by the sensitivity of the measured structural responses to the excitation forces, rather than by the specific estimation algorithm itself. In particular, poorly observable modal components and ill-conditioned frequency regions lead to strong noise amplification and increased estimation uncertainty. Explicit regularisation improves numerical stability but must be applied carefully to avoid excessive bias, while time-domain formulations benefit from incorporating temporal dynamics that naturally constrain the solution.

References

[1] U. Lajic Z. Jensen J.J. Nielsen, "Towards fault-tolerant decision support systems for ship operator guidance," *Reliability Engineering System Safety*, vol. 104, pp. 1–14, 2024.

[2] U. D. Nielsen, H. B. Bingham, A. H. Brodtkorb, T. Iseki, J. J. Jensen, M. Mittendorf, R. E. G. Mounet, Y. Shao, G. Storhaug, A. J. Sørensen, and T. Takami, "Estimating waves via measured ship responses," *Scientific Reports*, vol. 13, p. 17342, Oct. 2023. Publisher: Nature Publishing Group.

[3] Y.-S. Wu and W.-C. Cui, "Advances in the three-dimensional hydroelasticity of ships," *Proceedings of the Institution of Mechanical Engineers, Part M: Journal of Engineering for the Maritime Environment*, vol. 223, pp. 331–348, Sept. 2009.

[4] R. Taghipour, T. Perez, and T. Moan, "Hybrid frequency–time domain models for dynamic response analysis of marine structures," *Ocean Engineering*, vol. 35, pp. 685–705, May 2008.

[5] C. Van Zijl, J. Jovanova, and A. Grammatikopoulos, "Quantification of errors in frequency-domain inverse force estimation due to measurement noise," in *Proceedings of the Eleventh International Operational Modal Analysis Conference (IOMAC)*, 2025.

[6] W. Petersen, O. Øiseth, and E. Lourens, "Full-scale identification of the wave forces exerted on a floating bridge using inverse methods and directional wave spectrum estimation," *Mechanical Systems and Signal Processing*, vol. 120, pp. 708–726, Apr. 2019.

[7] Hansen, Per Christian, "Analysis of Discrete Ill-Posed Problems by Means of the L-Curve," *SIAM Review*, vol. 34, no. 4, pp. 561–580, 1992. _eprint: https://doi.org/10.1137/1034115.

[8] S. Gillijns and B. De Moor, "Unbiased minimum-variance input and state estimation for linear discrete-time systems with direct feedthrough," *Automatica*, vol. 43, pp. 934–937, May 2007.

[9] M. Ancellin and F. Dias, "Capytaine: a Python-based linear potential flow solver," *Journal of Open Source Software*, vol. 4, p. 1341, Apr. 2019.

[10] B.Gustavsen and A. Semlyen, "Rational approximation of frequency domain responses by vector fitting," *IEEE Trans. Power Delivery*, vol. 14, no. 3, pp. 1051–1061, 1999.

[11] D. E. Hasselmann, M. Dunckel, and J. A. Ewing, "Directional Wave Spectra Observed during JONSWAP 1973," *Journal of Physical Oceanography*, vol. 10, no. 8, pp. 1264 – 1280, 1980. Place: Boston MA, USA Publisher: American Meteorological Society.

10th International Conference on HYDROELASTICITY IN MARINE TECHNOLOGY
Trondheim, Norway, June16$^{\text{th}}$-18$^{\text{th}}$, 2026

New hydro-structure interface model based on Super Green functions accounting for forward-speed effects

Chen, X.B.[1,*], Nguyen, M.Q.[1], de Lauzon, J.[1], Cao, K.[2], Jagite, G.[1], and Malenica, S.[1]

[1] Research Department, Bureau Veritas Marine & Offshore, Paris, France
[2] Future Ship Team, Bureau Veritas Marine & Offshore, Shanghai, China

Abstract. HydroStar-V method based on boundary integral equations (BIE) involving Green function (GF) is presented as a new hydro-structure interface model. As a fundamental solution of free-surface flows associated with a point pulsating-translating source, GF is not directly useful but its integration on the hull and over the mean free surface is needed in BIE. The classical quadrature by the Gauss-Legendre rule with 1 (centroid), 4 (2×2) or more points is usually used in many previous works. However, it has been observed to be extremely difficult to obtain good accuracy, due to highly oscillatory behaviors of GF. Important formulations have then been developed to analytically integrate the Green function on flat panels. The analytical integration of point GF, called Super Green Functions (SGF), is applied to yields accurate solutions of BIE and construct a robust mathematical and computational framework to evaluate added-mass and damping coefficients, unsteady pressure and inertial loads applied on structure models.

Key words: *Hydro-structure interface; Forward speed; Classical GF; Super GF*

1. Introduction

The integrated hydro-structure interaction model [1] plays an important role by accomplishing tasks including the generation of eigen modes, the consistent transfer of associated hydrodynamic loading (added-mass coefficients, pressure and inertial) to Finite Element models, and the computation of global (or/and local) structure responses. In the global response analysis, the quasi-static assumption has been considered to be acceptable and the associated method has been largely applied in practice. However, there is a numerical issue concerning the accurate prediction of hydrodynamic loading at high encounter frequency, in particular, in head seas where waves of usual wave frequencies can induce loads exciting structure responses associated with first springing modes.

Within the framework of linear potential theory we have re-analyzed the boundary value problem, in Section 2, by choosing ship-shaped stream (also called double-body flow) as the base flow. The linearisation of unsteady flow over the base flow is carried out on the mean free surface and ship hull. Further to previous description in [5], we have considered the general case with flexible body. The classical modal expansion is used to express the displacement from which the boundary condition on the ship hull is explicitly given in a similar way as in [3]. In addition to BIE on the ship hull and those on the free surface in the vicinity of ship, additional BIE is imposed on the waterplane inside the ship to ensure the well-condition of resultant linear system.

Involved in the BIEs, the Green function (GF), a fundamental solution of free-surface flows associated with a point pulsating-translating source with viscous effect, is first analyzed. Its integration on the hull and over the mean free surface is needed in BIE. The classical quadrature by the Gauss-Legendre rule with 1 (centroid), 4 (2×2) or more points is usually used in many previous works. However, it has

*Correspondence to: xiao-bo.chen@bureauveritas.com

been observed to be extremely difficult to obtain good accuracy, due to highly oscillatory behaviors of GF. Important formulations have then been developed to analytically integrate the Green function on flat panels, based on application of Stokes' theorem, recently presented in [4] including the classical zero speed cases. The analytical GF integration, also called Super Green Functions (SGF) and applied in [5] and in [6], yields accurate solutions of BIE at high encounter frequencies, and construct a robust mathematical and computational framework.

The integration of fluid pressure on the deformable surface is analyzed and written by involving the modal-shape functions. Some new decomposition of radiation loads is presented in Section 3. They are composed of usual added-mass and damping coefficients, hydrostatic stiffness and speed-effect restoring forces. To shown the advantage of the present method based on the Super Green function (SGF) over the classical Green function (CGF) method, some numerical results are illustrated, in Section 4, for encounter frequencies scaled with ship length and the acceleration due to gravity up to a high value of 30. Finally, some discussion and conclusions are followed in Section 5.

2. Ship motion theory and Green function methods

We define a Cartesian coordinate system translating at the constant speed U with the ship in the positive x-direction. The z-axis is positive upwards with the origin at the undisturbed free surface. Relative to this reference frame, there exists an ambient flow (uniform stream) $-U\vec{i}$ opposite to ship forward direction.

The presence of ship changes this ambient flow into a ship-shaped stream around the hull, called base flow $\mathbf{W} = U\nabla(\bar{\phi} - x)$. In addition to this base flow, there should be a wavy steady flow $\nabla\phi$. When the ship oscillates about the reference frame or/and in incoming waves, there exist also unsteady flow $\nabla\psi$. The wavy steady and unsteady flows are called perturbation flow and represented by the velocity potential $\Phi = \phi + \psi$. All velocity potentials $(\bar{\phi}, \phi, \psi)$ satisfy the Laplace equation in the fluid. The total perturbation flow $\nabla\Phi$ satisfies the kinematic and dynamic combined condition Eq.(1) given in [5] on the free surface $z = \eta$ defined by Eq.(2) in [5].

The equation representing the boundary condition on the free surface for potentials $\Phi = \phi + \psi$ and that for wave elevations are fully nonlinear with quadratic and cubic products of potentials and the assumption of time independence concerns only the base flow $\mathbf{W}$. Direct solutions of such problems with accuracy are extremely difficult.

2.1. Linearisation based on the ship-shaped stream

In this gravity-dominant fluid domain, the reference length L, the acceleration of gravity g and the water density ρ are used to define the nondimensional coordinates $\mathbf{x} = (x, y, z)$, the time t, the fluid velocity $\mathbf{u} = (u, v, w)$, the velocity potential Φ and dynamic pressure P scaled by $(L, \sqrt{g/L}, \sqrt{gL}, \sqrt{gL^3}, \rho gL)$, respectively, while the nondimensional frequency ω, the Froude number F_{r} and the Brard number τ are

$$(\omega; F_{\mathrm{r}}; \tau) = \left(\omega_e\sqrt{L/g}; U/\sqrt{gL}; U\omega_e/g\right) \tag{1}$$

Chosen as the base flow, the ship-shaped stream is described by the velocity potential $\bar{\phi}$ satisfying

$$\begin{cases} \bar{\phi}_z = 0 & \text{on } F \\ \bar{\phi}_n = n_1 & \text{on } H \end{cases} \tag{2}$$

where F stands for the mean free surface and H for the mean ship hull.

Now we assume that the base flow $\mathbf{W} = F_{\mathrm{r}}\mathbf{w}$ with $\mathbf{w} = \nabla(\bar{\phi} - x)$ and $\bar{\phi}$ satisfying (2) is of order $O(1)$ while the perturbation flows $\Phi = \phi + \psi$ are of smaller order $o(1)$ comparing to the base flow $\mathbf{W}$. In this way, the quadratic and cubic products of (ϕ, ψ) are ignored. Furthermore, the free-surface elevation η is also assumed to be of smaller order $o(1)$ which is true for small or moderate speed. The Taylor expansion of all terms with respect to $z = 0$ are used. Finally, the frequency-domain expression of unsteady potential is written as

$$\psi = \Re\mathrm{e}\left\{\varphi\, \mathrm{e}^{-\mathrm{i}\omega_e t}\right\} \tag{3}$$

with ω_e the encounter frequency, and the base flow $\mathbf{w} = \nabla\bar{\phi} - \vec{i}$ is used to obtain the linear boundary condition

$$\varphi_z - \omega^2\varphi - 2\mathrm{i}\tau\mathbf{w}\cdot\nabla\varphi + F_\mathrm{r}^2\mathbf{w}\cdot\nabla(\mathbf{w}\cdot\nabla\varphi) + F_\mathrm{r}^2\nabla\varphi\cdot(\mathbf{w}\cdot\nabla)\mathbf{w} + \bar{\phi}_{zz}(\mathrm{i}\tau\varphi - F_\mathrm{r}^2\mathbf{w}\cdot\nabla\varphi) = 0 \quad (4)$$

on F i.e. $z = 0$. The boundary condition on the ship hull is written on H at its mean position

$$\varphi_n = \nabla\varphi\cdot\mathbf{n} = \begin{cases} -\xi_0(\nabla\varphi_I\cdot\mathbf{n}) & \text{diffraction} \\ \sum_{j=1}^{M}\left[(-\mathrm{i}\omega\xi_j)(\mathbf{h}^j\cdot\mathbf{n}) + (F_\mathrm{r}\xi_j)(\mathbf{m}^j\cdot\mathbf{n})\right] & \text{radiations} \end{cases} \quad (5)$$

in which we have used the representation by modal decomposition for the displacement

$$\mathbf{X}(\mathbf{x}) = \begin{pmatrix} X_1 \\ X_2 \\ X_3 \end{pmatrix} = \sum_{j=1}^{M}\xi_j\mathbf{h}^j(\mathbf{x}) \quad (6)$$

with $\mathbf{h}^j(\mathbf{x})$ the jth vector of modal displacement (modal shape) and ξ_j the modal amplitude, and M the total number of modes. The vector $\mathbf{m}^j(\mathbf{x})$ represents the coupling of base flow $\mathbf{w}(\mathbf{x})$ and the modal displacement $\mathbf{h}^j(\mathbf{x})$, defined in [3] by

$$\mathbf{m}^j(\mathbf{x}) = (\mathbf{w}\cdot\nabla)\mathbf{h}^j - (\mathbf{h}^j\cdot\nabla)\mathbf{w} \quad (7)$$

The potential $\varphi_I(\mathbf{x})$ in (5) representing incoming waves is known to take Airy's form

$$\varphi_I = -\omega_0^{-1}\mathbf{e}^{k_0 z + \mathrm{i}k_0(x\cos\beta + y\sin\beta)} \quad (8)$$

with the wave frequency ω_0, the wavenumber $k_0 = \omega_0^2$ and wave heading β. In (5), ξ_0 is the amplitude of incoming waves and ξ_j for $j = 1, 2, \cdots, 6$ denote the six rigid-mode motions including the translations $\mathbf{T} = (\xi_1, \xi_2, \xi_3)$ and rotations $\mathbf{R} = (\xi_4, \xi_5, \xi_6)$ around the centre of gravity. The flexible modes are denoted by $j = 7, 8, \cdots, M$. The six rigid-modal shapes are well known and given by

$$(\mathbf{h}^1, \mathbf{h}^2, \mathbf{h}^3, \mathbf{h}^4, \mathbf{h}^5, \mathbf{h}^6) = \begin{pmatrix} 1,0,0, & 0, & (z-z_G), & -(y-y_G) \\ 0,1,0, & -(z-z_G), & 0, & (x-x_G) \\ 0,0,1, & (y-y_G), & -(x-x_G), & 0 \end{pmatrix} \quad (9)$$

It can be checked that

$$(\mathbf{h}^1, \mathbf{h}^2, \mathbf{h}^3)\cdot\mathbf{n} = \mathbf{n} = (n_1, n_2, n_3); \quad (\mathbf{h}^4, \mathbf{h}^5, \mathbf{h}^6)\cdot\mathbf{n} = \mathbf{r}\wedge\mathbf{n} = (n_4, n_5, n_6) \quad (10)$$

and by using (7), we obtain

$$\begin{aligned} (\mathbf{m}^1, \mathbf{m}^2, \mathbf{m}^3)\cdot\mathbf{n} &= -(\mathbf{n}\cdot\nabla)\mathbf{w} = (m_1, m_2, m_3) \\ (\mathbf{m}^4, \mathbf{m}^5, \mathbf{m}^6)\cdot\mathbf{n} &= -(\mathbf{n}\cdot\nabla)(\mathbf{r}\wedge\mathbf{w}) = (m_4, m_5, m_6) \end{aligned} \quad (11)$$

fully consistent with that given in [7]. The position vector $\mathbf{r}$ in (10) and (11) is defined by

$$\mathbf{r} = \{x - x_G, y - y_G, z - z_G\} \quad (12)$$

with respect to the center of gravity $\mathbf{r}_G = (x_G, y_G, z_G)$.

Following the boundary condition (5) the total unsteady potential can be decomposed as

$$\varphi = \xi_0(\varphi_I + \varphi_0) + \sum_{j=1}^{M}\left[(-\mathrm{i}\omega\xi_j)\varphi_j^n + (F_\mathrm{r}\xi_j)\varphi_j^m\right] \quad (13)$$

with the known φ_I of incoming waves given by (8), the diffraction potential φ_0, M radiation potentials φ_j^n associated with the velocity $(-\mathrm{i}\omega\xi_j)$, and M radiation potentials φ_j^m associated with the displacement $(F_\mathrm{r}\xi_j)$. The sum $(\varphi_I+\varphi_0)$, and all radiation potential $(\varphi_j^n,\varphi_j^m)$ satisfy the same boundary condition (17) on the free surface F and different boundary condition on the ship hull H :

$$\nabla\varphi_0\cdot\mathbf{n}=-\nabla\varphi_I\cdot\mathbf{n};\quad \nabla\varphi_j^n\cdot\mathbf{n}=\mathbf{h}^j\cdot\mathbf{n};\quad \nabla\varphi_j^m\cdot\mathbf{n}=\mathbf{m}^j\cdot\mathbf{n} \tag{14}$$

for $j=1,2,\cdots,6$ concerning the rigid modes and $j=7,8,\cdots,M$ the flexible modes.

2.2. Boundary integral equations

The fundamental solution at the field point $\mathbf{x}(x,y,z)$ associated with a translating and pulsating source at the encouter frequency ω_e, located at $\boldsymbol{\xi}(\xi,\eta,\zeta)$, i.e., the Green function $\tilde{G}(\mathbf{x},\boldsymbol{\xi},t)$ is written by

$$\tilde{G}(\mathbf{x},\boldsymbol{\xi},t)=\left\{G(\mathbf{x},\boldsymbol{\xi})\mathrm{e}^{-\mathrm{i}\omega_e t}\right\} \tag{15}$$

in our frequency domain analysis. The Green function $G(\mathbf{x},\boldsymbol{\xi})$ satisfies the special Poisson equation

$$\nabla^2 G(\mathbf{x},\boldsymbol{\xi})=\delta(|\mathbf{x}-\boldsymbol{\xi}|) \tag{16}$$

with $\delta(\cdot)$ the Dirac delta function, in the fluid domain. Based on the formal analysis of the Laplace-Fourier transform applied to the Stokes flow, in [8], the leading effect of vorticity is represented by an additional term appearing in the boundary condition at the free surface. Indeed, the linear boundary condition with dissipation is written by

$$G_z-\omega^2 G+2\mathrm{i}\tau G_x+F_\mathrm{r}^2 G_{xx}-4\tilde{\epsilon}(F_\mathrm{r}G_{xzz}+\mathrm{i}\omega G_{zz})=0 \tag{17}$$

on $z=0$. In (17), the coefficient $\tilde{\epsilon}=\nu/\sqrt{gL^3}$ is proportional to the fluid kinematic viscosity ν. It is shown that the magnitude of elementary waves $\mathrm{e}^{kz+\mathrm{i}(\alpha x+\beta y-\omega t)}$ decays like $\mathrm{e}^{-4\epsilon\omega k^2\sqrt{x^2+y^2}}$ and more rapidly with short waves of large wavenumber. This implies that the complex singular and highly oscillatory behaviours in $G(\mathbf{x},\boldsymbol{\xi})$ due to short waves predicted in [9] just disappear.

By applying the Green's theorem to both the unknown potential φ representing φ_j^n, φ_j^m, or φ_0 and the Green function G, the new boundary integral equation (BIE) obtained in [5] is then written as

$$\frac{\varphi}{2}+\fint\!\!\!\!\!\!\iint_H \varphi G_n\,\mathrm{d}S-\iint_F\left[\mathcal{F}_0\varphi+\mathcal{F}_1\varphi_\xi+\mathcal{F}_2\varphi_\eta\right]\,\mathrm{d}S=\iint_H \varphi_n G\,\mathrm{d}S+I_F \tag{18}$$

for $\mathbf{x}\in H$ on the ship hull, which should be combined with one BIE on the free surface since $(\varphi,\varphi_\xi,\varphi_\eta)$ are unknown on F. The functions $(\mathcal{F}_0,\mathcal{F}_1,\mathcal{F}_2)$ dependent on the base flow $\bar{\phi}(\boldsymbol{\xi})$ and the Green function $G(\mathbf{x},\boldsymbol{\xi})$, and their derivatives are given by Eq.(43) in [5].

Similar to the new BIE on H, the BIE for a field point $\mathbf{x}$ on the free surface is written by

$$\varphi+\iint_H \varphi G_n\,\mathrm{d}S-\fint\!\!\!\!\!\!\iint_F\left[\mathcal{F}_0\varphi+\mathcal{F}_1\varphi_\xi+\mathcal{F}_2\varphi_\eta\right]\,\mathrm{d}S=\iint_H \varphi_n G\,\mathrm{d}S+I_F \tag{19}$$

for $\mathbf{x}\in F$. In addition, we apply the third Green theorem to a field point $\mathbf{x}$ located inside the ship, i.e., outside of the fluid domain limited by $H\cup F\cup\Sigma$. In particular, at some points on the waterplane denoted by W, the integral equation is written as

$$\iint_H \varphi G_n\,\mathrm{d}S-\iint_F\left[\mathcal{F}_0\varphi+\mathcal{F}_1\varphi_\xi+\mathcal{F}_2\varphi_\eta\right]\,\mathrm{d}S=\iint_H \varphi_n G\,\mathrm{d}S+I_F \tag{20}$$

for $\mathbf{x}\in W$ inside the ship hull.

The integral I_F on the right hand side of (18), (19) and (20) is nil ($I_F = 0$) for the radiation potentials $\varphi = \varphi_j^n$ or $\varphi = \varphi_j^m$. For the diffraction potential, $\varphi = \varphi_0$, it is associated with the forcing term due to incoming waves (8) and written by

$$I_F = \iint_F \big[\mathcal{C}_0 + \mathrm{i}k_0(\mathcal{C}_1 \cos\beta + \mathcal{C}_2 \sin\beta) - k_0^2(\mathcal{C}_3 \cos^2\beta + \mathcal{C}_4 \cos\beta \sin\beta + \mathcal{C}_5 \sin^2\beta)\big] G\varphi_I \,\mathrm{d}S \quad (21)$$

with the heading β of incoming waves, φ_I given by (8) and the base flow dependent coefficients $(\mathcal{C}_0, \mathcal{C}_1, \cdots, \mathcal{C}_5)$ are defined by Eq.(48) in [5].

The linear system combining BIE on H (18) and BIE on F (19) is of square form, i.e., the same number of equations as that of unknowns, since the tangent derivatives of unknowns on F can be transformed to unknowns $\varphi(\mathbf{x})$ by using shape functions in higher-order patch method, or any scheme of finite-difference type. In order to be sure that Green's third theorem is well respected outside of the fluid domain - zero potential inside the ship. The additional equation (20) is formulated for $\mathbf{x}$ on the waterplane W. The system is then over-determined. A linear system of rectangular form can be resolved using the standard Lapack library.

2.3. Classical Green function and Super Green functions

By applying Fourier transform to differential equations including (16) and (17) satisfied by the Green function, $G(\mathbf{x}, \boldsymbol{\xi})$ can be written by

$$G(\mathbf{x}, \boldsymbol{\xi}) = -1/r + 1/r' + G^F(\mathbf{x}, \boldsymbol{\xi}) \quad (22)$$

in which r is the distance from the field point $\mathbf{x}$ to the source point $\boldsymbol{\xi}$ and r' is that to the mirror soure point $\boldsymbol{\xi}' = (\xi, \eta, -\zeta)$. The free-surface term $G^F(\mathbf{x}, \boldsymbol{\xi})$ is initially defined by a double Fourier integral (with resepct to wavenumber and polar angle) and given in [10] after integration on wavenumber by

$$G^F(\mathbf{x}, \boldsymbol{\xi}) = \frac{1}{\pi} \int_{-\pi}^{\pi} F(Z) \,\mathrm{d}\theta \quad \text{with} \quad F(Z) = A_1 K(Z, k_1) + A_2 K(Z, k_2) + A_3 K(Z, k_3) \quad (23)$$

in which three complex wavenumbers denoted by $k_{1,2,3}(\theta) = \kappa_{1,2,3}(\theta) + \mathrm{i}\mu_{1,2,3}(\theta)$ are determined by the cubic equation derived from the boundary condition 17

$$(F_\mathrm{r} k \cos\theta - \omega)^2 - k - \mathrm{i}4\epsilon F_\mathrm{r}^3 (F_\mathrm{r} k \cos\theta - \omega) k^2 = 0 \quad (24)$$

with the non-dimensional coefficient $\epsilon = \mu g/(\rho U^3)$ involving μ the fluid dynamic viscosity. The amplitude coefficients

$$\begin{aligned} A_1 &= A_1(\theta) = \mathrm{i}k_1/[4\epsilon F_\mathrm{r}^4 \cos\theta (k_1 - k_2)(k_1 - k_3)] \\ A_2 &= A_2(\theta) = \mathrm{i}k_2/[4\epsilon F_\mathrm{r}^4 \cos\theta (k_2 - k_3)(k_2 - k_1)] \\ A_3 &= A_3(\theta) = \mathrm{i}k_3/[4\epsilon F_\mathrm{r}^4 \cos\theta (k_3 - k_1)(k_3 - k_2)] \end{aligned} \quad (25)$$

are dependent on the wavenumbers. Both $k_{1,2,3}$ and $A_{1,2,3}(\theta)$ are symmetric function of the polar angle. Furthermore, the complex variable Z is defined by

$$Z = Z(\mathbf{x}, \boldsymbol{\xi}, \theta) = \mathrm{v} - \mathrm{i}\mathrm{w} \quad \text{with} \quad \mathrm{v} = z + \zeta; \quad \mathrm{w} = (x - \xi)\cos\theta + (y - \eta)\sin\theta \quad (26)$$

and the wavenumber integral function $K(Z, k_i)$ in (23) is expressed by

$$K(Z, k_i) = \mathrm{e}^{k_i Z} E_1(k_i Z) + \mathrm{i}\pi \big[\mathrm{sgn}(\mu_i) + \mathrm{sgn}(\mu_i \mathrm{v} - \kappa_i \mathrm{w})\big] H(\kappa_i) \,\mathrm{e}^{k_i Z} \quad \text{for} \quad i = 1, 2, 3 \quad (27)$$

in [10] with the exponential integral function $E_1(\cdot)$ defined by Eq.(5.1.1) in [11], the usual sign function $\mathrm{sgn}(\cdot)$ and the Heaviside function $H(\cdot)$. The single Fourier polar integral (23) is often referred as the representation of Havelock's type of the Green function.

The surface integration of the Green function over the source surface associated with a field point is called S2P integral while the further integration of S2P integral over the field surface called S2S integral. The two-fold integration (S2S) is necessary in the evaluation of influence coefficients of the boundary integral equation based on the Galerkin scheme. First we consider a flat panel S on which a constant source is applied. The panel is of polygonal form with m vertices with the coordinates $\boldsymbol{\xi}_j = (\xi_j, \eta_j, \zeta_j)$ for $j = 1, 2, \cdots, m$, and connectivity from $\boldsymbol{\xi}_j$ to $\boldsymbol{\xi}_{j+1}$ with $\boldsymbol{\xi}_{m+1} = \boldsymbol{\xi}_1$ to close the contour. The field point is denoted by $\mathbf{x}$ and the variable $Z_j(\mathbf{x}, \boldsymbol{\xi}_j, \theta)$ connects $\mathbf{x}$ to $\boldsymbol{\xi}_j$ by its definition (26). Using the following notations

$$F(Z) = \sum_{i=1}^{3} A_i K(Z, k_i) \quad \text{and} \quad F_n(Z) = \sum_{i=1}^{3} A_i K_n(Z, k_i) \tag{28}$$

for $n \geq 1$, the integration of the Green function defined by (23) is then obtained by

$$\mathcal{G}^F(\mathbf{x}) = \iint_S G^F(\mathbf{x}, \boldsymbol{\xi})\, \mathrm{d}s(\boldsymbol{\xi}) = \frac{1}{\pi} \int_{-\pi}^{\pi} \sum_{j=1}^{m} \left[c_j F_2(Z_j) + d_j F_1(Z_j) \right] \mathrm{d}\theta \tag{29}$$

developed in [4]. The geometry-dependent coefficients (c_j, d_j) are defined by Eq.(10) in [4] In the same way, the integration of the derivatives of the Green function can be obtained and written as

$$\nabla \mathcal{G}^F(\mathbf{x}) = \iint_S \begin{pmatrix} \partial_\xi \\ \partial_\eta \\ \partial_\zeta \end{pmatrix} G^F(\mathbf{x}, \boldsymbol{\xi})\, \mathrm{d}s(\boldsymbol{\xi}) = \frac{1}{\pi} \int_{-\pi}^{\pi} \begin{pmatrix} \mathrm{i}\cos\theta \\ \mathrm{i}\sin\theta \\ 1 \end{pmatrix} \sum_{j=1}^{m} \left[c_j F_1(Z_j) + d_j F(Z_j) \right] \mathrm{d}\theta \tag{30}$$

involving the functions (F_1, F) in place of (F_2, F_1) in (29) with (F_2, F_1, F) defined in (28). In the definition (28) of $F(Z, \theta)$ and $F_n(Z, \theta)$, the functions $K_n(Z, k_i)$ for $n \geq 1$ are successive antiderivatives of $K(Z, k_i)$, i.e.

$$\partial K_n(Z, k_i)/\partial Z = K_{n-1}(Z, k_i) \quad \text{for} \quad n \geq 1 \quad \text{with} \quad K_0(Z, k_i) = K(Z, k_i) \tag{31}$$

with respect to Z. The work in [10] gives three expressions of antiderivatives:

$$K_n(Z, k_i) = k_i^{-n} \left[K(Z, k_i) + \sum_{m=0}^{n-1} (k_i Z)^m L_m(Z) \right] \tag{32}$$

$$\tilde{K}_n(Z, k_i) = \sum_{m=0}^{\infty} \left[K(Z_0, k_i) + \sum_{p=1}^{m} (-1)^p \frac{(p-1)!}{(k_i Z_0)^p} \right] \frac{(k_i \tilde{Z})^m}{(m+n)!} \tilde{Z}^n \tag{33}$$

$$\hat{K}_n(Z, k_i) = -\sum_{m=0}^{\infty} (k_i Z)^m Z^n \mathcal{L}_{m+n}(Z, k_i) \tag{34}$$

with

$$L_0(Z) = \ln(-Z) L_m(Z) = [L_{m-1}(Z) - 1/m!]/m \quad \text{for} \quad m \geq 1 \tag{35}$$

used in (32) and

$$\mathcal{L}_0(Z, k_i) = \gamma + \ln(-k_i) + \ln(-Z)\mathcal{L}_m(Z, k_i) = [\mathcal{L}_{m-1}(Z, k_i) - 1/m!]/m \quad \text{for} \quad m \geq 1 \tag{36}$$

in which $\gamma = 0.5772156649\ldots$ is the Euler's constant, $Z_0 = z_0 + \zeta_0 - \mathrm{i}[(x_0 - \xi_0)\cos\theta + (y_0 - \eta_0)\sin\theta]$ associated with a pair of reference points $(\mathbf{x}_0, \boldsymbol{\xi}_0)$, and $\tilde{Z} = Z - Z_0$, used in (33). All three antiderivatives K_n by (32), $\tilde{K}_n$ by (33) and $\hat{K}_n$ by (34) are equivalent and have a different constant (indepedent of Z) between them which does not induce any difference in their applications to super Green functions.

Now we consider the field point $\mathbf{x}$ located within a flat panel H of polygonal form with $\bar{m}$ vertices $\mathbf{x}_\ell = (x_\ell, y_\ell, z_\ell)$ for $\ell = 1, 2, \cdots, \bar{m}$. The side segments are denoted by the connection from $\mathbf{x}_\ell$ to $\mathbf{x}_{\ell+1}$

with $\mathbf{x}_{\overline{m}+1} = \mathbf{x}_1$ to close the contour. The second-fold integration of $\mathcal{G}^F(\mathbf{x})$ by (29) on the field panel H is obtained by

$$\mathscr{G}^F = \iint_H \mathcal{G}^F(\mathbf{x})\,\mathrm{d}s(\mathbf{x}) = \frac{1}{\pi}\int_{-\pi}^{\pi}\sum_{j=1}^{m}\sum_{\ell=1}^{\overline{m}}\Big[c_j\bar{c}_\ell F_4(Z_{j\ell}) + (c_j\bar{d}_\ell + d_j\bar{c}_\ell)F_3(Z_{j\ell}) + d_j\bar{d}_\ell F_2(Z_{j\ell})\Big]\mathrm{d}\theta \quad (37)$$

in which the coefficients (c_j, d_j) are given by Eq.(20) in [4]. Furthermore, The variables $Z_{j\ell}$ is defined by $Z_{j\ell} = z_\ell + \zeta_j - \mathrm{i}[(x_\ell - \xi_j)\cos\theta + (y_\ell - \eta_j)\sin\theta]$. In the same way, the integration of $\nabla\mathcal{G}^F(\mathbf{x})$ on the field panel H is expressed by

$$\nabla\mathscr{G}^F = \iint_H \nabla\mathcal{G}^F(\mathbf{x})\mathrm{d}s(\mathbf{x}) = \frac{1}{\pi}\int_{-\pi}^{\pi}\begin{pmatrix}\mathrm{i}\cos\theta\\ \mathrm{i}\sin\theta\\ 1\end{pmatrix}\sum_{j=1}^{m}\sum_{\ell=1}^{\overline{m}}\Big[c_j\bar{c}_\ell F_3(Z_{j\ell}) + (c_j\bar{d}_\ell + d_j\bar{c}_\ell)F_2(Z_{j\ell}) + d_j\bar{d}_\ell F_1(Z_{j\ell})\Big]\mathrm{d}\theta \quad (38)$$

involving the functions (F_3, F_2, F_1) in place of (F_4, F_3, F_2) in (37) with F_n for $n \geq 1$ defined in (28) using the antiderivatives $K_n(Z, k_i)$ given by (32)–(34) of the wavenumber integral function $K(Z, k_i)$ defined by (27).

3. Hydrodynamic loading and interface with structure models

Once we solve the new BIE and obtain $(\varphi_j^n, \varphi_j^m)$ for $j = 1, 2, \cdots, M$, the time-harmonic pressure scaled with $(\rho g L)$ due to radiation can be written as

$$p^R = \sum_{j=1}^{M}\Big[\omega^2\varphi_j^n + \mathrm{i}\tau\big(\mathbf{w}\cdot\nabla\varphi_j^n + \varphi_j^m\big) - F_\mathrm{r}^2\mathbf{w}\cdot\nabla\varphi_j^m\Big]\xi_j \quad (39)$$

by introducing the radiation part potentials given by (13). In the same way, the dynamic pressure due to diffraction scaled with $(\rho g a)$ is contributed by the sum of the incoming and diffraction potentials

$$p^D = -\Big[-\mathrm{i}\omega(\varphi_I + \varphi_0) + F_\mathrm{r}(\mathbf{w}\cdot\nabla)(\varphi_I + \varphi_0)\Big] \quad (40)$$

In addition, the steady pressure $\bar{p}$ composed of hydrostatic part p^H and that p^S due to steady base flow

$$\bar{p} = p^H + F_\mathrm{r}^2 p^S \quad \text{with} \quad \begin{cases} p^H = -z \\ p^S = -\dfrac{1}{2}(\mathbf{w}\cdot\mathbf{w} - 1) = -\dfrac{1}{2}\nabla\bar{\phi}\cdot\nabla\bar{\phi} + \bar{\phi}_x \end{cases} \quad (41)$$

yields the usual hydrostatic stiffness due to the variation of p^H associated with the ship motion and the speed-effect restoring force due to the variation linked to p^S associated with the same ship motion.

The radiation forces including linear forces scaled by $(\rho g L^3)$ and torque moments scaled by $(\rho g L^4)$, are defined as the reaction of fluid via pressure on the ship hull against the acceleration, velocity and displacement of the ship, under the chosen reference system associated with the mean position of ship

$$F_i^R = -\iint_H \big[p^R + (\mathbf{X}\cdot\nabla)\bar{p}\big](\mathbf{h}^i\cdot\mathbf{n})\,\mathrm{d}s - \iint_H \bar{p}(\mathbf{h}^i\cdot[\mathbf{N}]\mathbf{n})\,\mathrm{d}s - \oint_\Gamma(\eta^R - X_3)\bar{p}(\mathbf{h}^i\cdot\mathbf{n})\,\mathrm{d}l \quad (42)$$

for $i = 1, 2, \cdots, M$. In (42), the term $[\mathbf{N}]\mathbf{n}$ is a vector of order $O(|\nabla\mathbf{X}|)$ defined by

$$[\mathbf{N}]\mathbf{n} = \mathrm{Tr}[\nabla\mathbf{X}]\mathbf{n} - [\nabla\mathbf{X}]^T\mathbf{n} \quad (43)$$

and $\mathbf{X}$ the displacement vector represented by the series of modeshapes (6), and $[\nabla\mathbf{X}]^T = [X_{j,i}]$ the second-order tensor, and $\mathrm{Tr}[\nabla\mathbf{X}] = X_{1x} + X_{2y} + X_{3z} = \nabla\cdot\mathbf{X}$ the trace of $[\nabla\mathbf{X}]$. It can be checked that $\mathbf{h}^i\cdot\mathbf{n} = n_i$ already shown in (10) for the rigid modes $i = 1, 2, \cdots, 6$ and

$$[\mathbf{N}]\mathbf{n} = \mathbf{R}\wedge\mathbf{n} \quad \Rightarrow \quad \mathbf{h}^i\cdot([\mathbf{N}]\mathbf{n}) = \mathbf{h}^i\cdot(\mathbf{R}\wedge\mathbf{n}) = \{\mathbf{R}\wedge\mathbf{n}, \mathbf{R}\wedge(\mathbf{r}\wedge\mathbf{n})\} \quad (44)$$

with rotation vector $\mathbf{R} = \{\xi_4, \xi_5, \xi_6\}$. The waterline integral in (6) is resultant from the integration on the intermittant surface between the local free-surface elevation

$$\eta^R = +\mathrm{i}\omega\varphi^R - F_\mathrm{r}(\mathbf{w}\cdot\nabla\varphi^R) \tag{45}$$

and the vertical displacement X_3 defined in (44) along the mean waterline denoted by Γ. This term omitted in previous studies is kept here. The radiation forces are written by

$$F_i^R = -\sum_{j=1}^{M}\big(-\omega^2 A_{ij} - \mathrm{i}\omega B_{ij} + C_{ij}\big)\xi_j \tag{46}$$

in which A_{ij}, B_{ij} and C_{ij} on the right-hand side are called added-mass, damping and stiffness coefficients, respectively, following their respective association with the acceleration, velocity and displacement of ship.

Among all terms in (42) and (46), the simplest one concerns the hydrostatic pressure $p^H = -z$

$$-\iint_H \big[(\mathbf{X}\cdot\nabla)p^H(\mathbf{h}^i\cdot\mathbf{n}) + p^H(\mathbf{h}^i\cdot[\mathbf{N}]\mathbf{n})\big]\,\mathrm{d}s = -\sum_{j=1}^{M} H_{ij}\xi_j \tag{47}$$

in which H_{ij} is called hydrostatic restoring coefficients given in all textbooks. In a similar way, the contribution by p^S defined in (41) can be written by

$$-F_\mathrm{r}^2\iint_H \big[(\mathbf{X}\cdot\nabla)p^S(\mathbf{h}^i\cdot\mathbf{n}) + p^S(\mathbf{h}^i\cdot[\mathbf{N}]\mathbf{n})\big]\,\mathrm{d}s + F_\mathrm{r}^2\oint_\Gamma X_3 p^S(\mathbf{h}^i\cdot\mathbf{n})\,\mathrm{d}l = -F_\mathrm{r}^2\sum_{j=1}^{M} S_{ij}\xi_j \tag{48}$$

where S_{ij} is called speed-effect restoring coefficients. Concerning the radiation forces due to the time-harmonic pressure p^R defined by (39) and the free-surface elevation η^R along the waterline, we decompose them

$$-\iint_H p^R(\mathbf{h}^i\cdot\mathbf{n})\,\mathrm{d}s - F_\mathrm{r}^2\oint_\Gamma \eta^R p^S(\mathbf{h}^i\cdot\mathbf{n})\,\mathrm{d}l = -\sum_{j=1}^{M}\Big(-\omega^2 R_{ij}^{\omega} - \tau R_{ij}^{\tau} + F_\mathrm{r}^2 R_{ij}^{F\mathrm{r}}\Big)\xi_j \tag{49}$$

with the components

$$\begin{aligned}
R_{ij}^{\omega} &= -\iint_H \varphi_j^n(\mathbf{h}^i\cdot\mathbf{n})\,\mathrm{d}s - F_\mathrm{r}^2\oint_\Gamma \varphi_j^n p^S(\mathbf{h}^i\cdot\mathbf{n})\,\mathrm{d}l\\
R_{ij}^{\tau} &= -\iint_H \mathrm{i}\big(\mathbf{w}\cdot\nabla\varphi_j^n + \varphi_j^m\big)(\mathbf{h}^i\cdot\mathbf{n})\,\mathrm{d}s - F_\mathrm{r}^2\oint_\Gamma \mathrm{i}\big(\mathbf{w}\cdot\nabla\varphi_j^n + \varphi_j^m\big)p^S(\mathbf{h}^i\cdot\mathbf{n})\,\mathrm{d}l\\
R_{ij}^{F\mathrm{r}} &= -\iint_H \big(\mathbf{w}\cdot\nabla\varphi_j^m\big)(\mathbf{h}^i\cdot\mathbf{n})\,\mathrm{d}s - F_\mathrm{r}^2\oint_\Gamma \big(\mathbf{w}\cdot\nabla\varphi_j^m\big)p^S(\mathbf{h}^i\cdot\mathbf{n})\,\mathrm{d}l
\end{aligned} \tag{50}$$

By introducing (47), (48) and (49) back to (42) and following the usual notations, the coefficients (A_{ij}, B_{ij}, C_{ij}) on the right-hand side of (46) are then given by Eq.(64) in [5].

The diffraction wave loads often called the wave excitation loads $\mathbf{E} = (E_1, E_2, \cdots, E_M)$ are defined by the integration of time-harmonic pressure due to wave diffraction and of steady pressure over time-harmonic varying surface

$$E_i = -\iint_H p^D(\mathbf{h}^i\cdot\mathbf{n})\,\mathrm{d}s - F_\mathrm{r}^2\oint_\Gamma \eta^D p^S(\mathbf{h}^i\cdot\mathbf{n})\,\mathrm{d}l \tag{51}$$

with p^D given by (40) and the free-surface elevation

$$\eta^D = -\Big[-\mathrm{i}\omega(\varphi_I + \varphi_0) + F_\mathrm{r}(\mathbf{w}\cdot\nabla)(\varphi_I + \varphi_0)\Big]_{z=0} \tag{52}$$

involved in the line integral in (51) resultant from the integration of steady pressure over the intermittent surface varying with the free-surface elevation around the mean waterline Γ due to wave diffraction.

Finally, the motion equation is classically expressed by

$$\sum_{j=1}^{M}\Big\{-\omega^2(M_{ij}+A_{ij})-\mathrm{i}\omega B_{ij}+C_{ij}\Big\}\xi_j=E_i \tag{53}$$

for $i=1,2,\cdots,M$ and with M_{ij} the coefficients of inertial matrix dependent on ship mass and mass distribution, and the coefficients of radiation (A_{ij},B_{ij},C_{ij}) defined by Eq.(64) in [5].

4. Numerical results

The classical Wigley IV hull for which reliable and open experimental results are available and reported in [12] is considered here for benchmark comparisons. First, we start with the computation of added-mass and damping coefficients at zero speed. A coarse mesh composed of 72 curved patch on the hull and 96 patches on the surface is generated and each patch is then subdivided into 9 flat panels. The

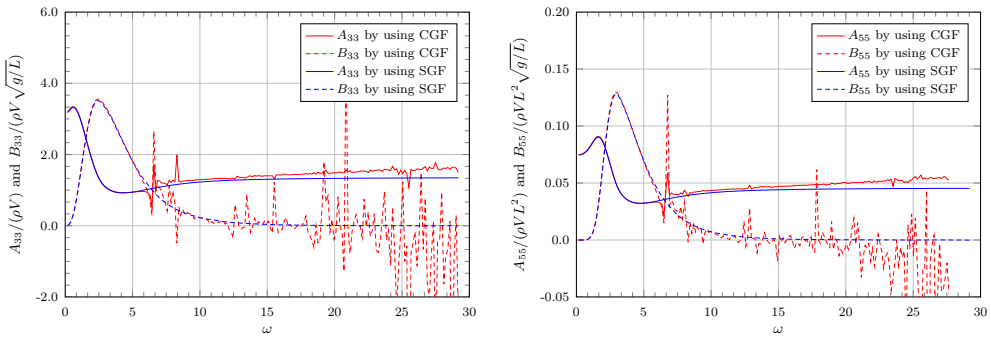


Figure 1: Added-mass & damping coefficients in heave (left) and pitch (right) at $F_\mathrm{r}=0$: CGF *vs* SGF.

results using CGF by centroid Gauss point to integrate GF on each panel are illustrated in Figure 1 by red solid and red dashed line for the added-mass and damping coefficients, respectively. The results by using SGF are depicted by blue solid line and blue dashed line. It is observed that two series of results are identical for the oscillation frequency $\omega<6$ and large discrepancy appears for $\omega>6$. It is remarkable that high oscillations in the results by using CGF which partly are due to effect of irregular frequencies. By using finer meshes, the results using CGF could be improved by pushing abnormal oscillations at high frequencies. Our tests using 4k panels, we can have correct results till $\omega=15$, while SGF method yields already good results for all $\omega<30$ using the coarse mesh.

For $F_\mathrm{r}=0.2$, CGF method is based on the encounter-frequency approximation to take account of forward-speed effect. The added-mass and damping coefficients, wave excitation loads and induced motions are reported in Figure 2. Again, CGF results are illustrated by red solid and dashed lines and SGF ones by blue solid and dashed lines. The data of experimental measurements [12] are depicted by blue symbols (circle and "x", square and "+"). The results in the limited interval of encounter-frequencies $(1<\omega<7)$ are zoomed for more clarity. The added-mass and damping coefficients in heave are plotted in top-left figure and those in pitch in top-right figure. In the middle figures, the coupling added-mass and damping coefficients in heave-pitch and pitch-heave are depicted in the middle-left figure and middle-right figure. The wave excitation loads (diffraction loads) are drawn in the bottom-left figure and motions in the bottom-right figure. In all figures, the results by using the encounter-frequency approximation (CGF) present abnormal oscillations for $\omega>6$ and quite different from those by using SGF for $\omega<6$. Numerical results by using SGF are in very good agreement with the available results of experimental measurements for $1<\omega<7$, and smooth variation everywhere.

5. Discussion and conclusions

We have presented our new hydro-structure interface model based on the new developments on hydrodynamic side. Building on the foundation in potential theory and Green function method, our new developments answer several critical issues in the seakeeping computation of ships animated with a forward speed including (1) the formulation of interaction between steady and unsteady flows, (2) the singularity and highly oscillatory behavior of the Green function near the free surface, (3) the integration of Green function (SGF), (4) the removal of irregular wavenumbers, and (5) the consistent decomposition of speed-dependent restoring forces. In particular, the boundary condition associated with the interaction with steady flow in a general way. Furthermore, the integration of unsteady and steady pressure on the ship hull associated with each modal shape is formulated in a consistent way.

Careful implementation of the present GFM has been realised in our in-house software HydroStar-V . Numerical results are validated against classical benchmark cases including Wigley hulls, Series 60, DTMB, KCS, etc. In particular, the Wigley IV hull with a larger width-to-length ratio for which the effect of steady flow is important. The most recent experimental measurements on RIOS bulk carrier

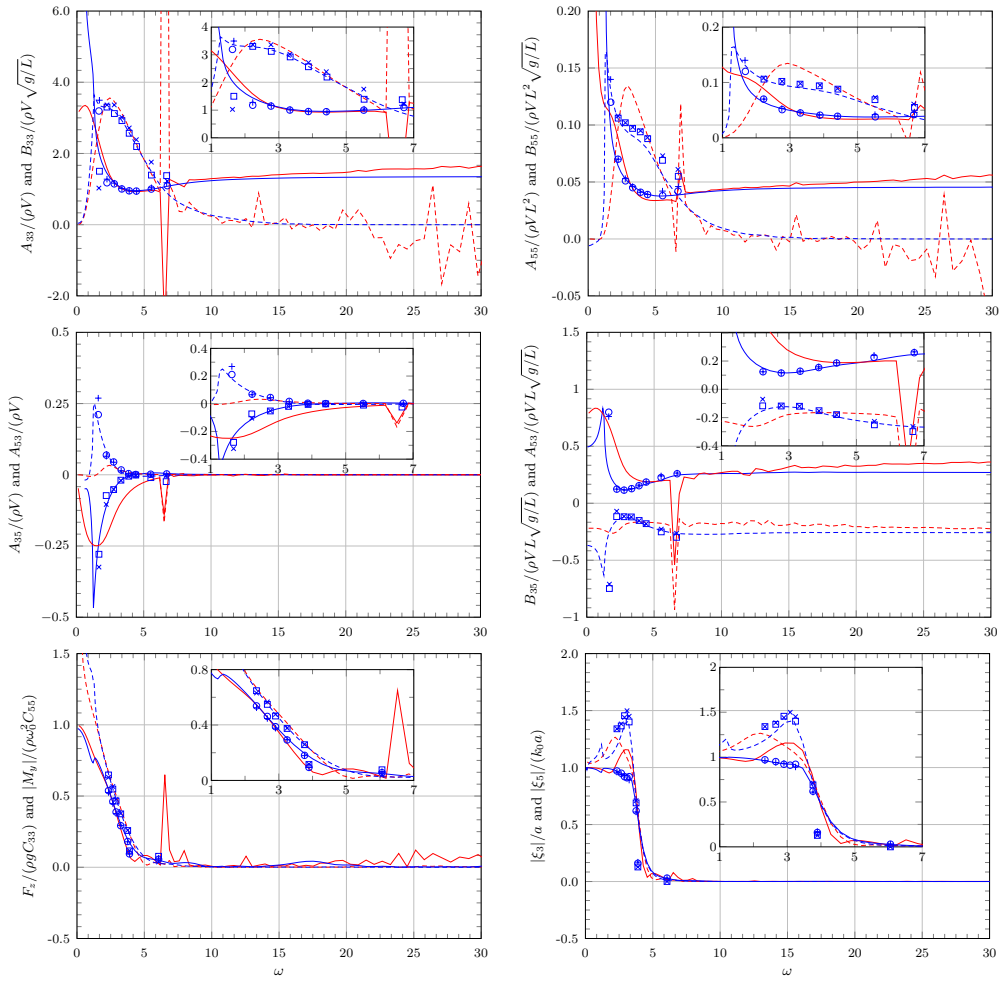


Figure 2: Added-mass & damping coefficients (top and middle), wave excitation loads (bottom-left figure) and induced motions (bottom-right figure) at $F_{\mathrm{r}} = 0.2$: CGF (encounter-frequency approximation, red lines) *vs* SGF (blue lines) and experimental results (blue symbols).

in both head and following seas described in [13], have been used. In all cases, very good agreement is obtained, with the prediction of added-mass and damping coefficients, excitation loads and induced motions typically within 5–10% of experimental values, including the challenging cases of oblique seas and following seas [14]. On the other side, the results by the "encounter-frequency" approximation are found to have large discrepancies with benchmark results. The approximation cannot capture correctly wave fields around the ship and the prediction of global seakeeping characteristics (added-mass, damping, wave excitation loads and induced motions) is not reliable. It is shown that the classical Gauss-point integration (CGF) method cannot provide convergent results (abnormal oscillations) at large encounter frequencies while the present method based on using SGF give smooth results up to $\omega = 30$, and in very good agreement with model tests in the low and moderate encounter frequencies.

The new method presented here accumulates a series of critical groundwork in both theoretical and numerical aspects. Based on sound theoretical analyses and rigorous numerical developments, the results show excellent convergence and very good agreement with benchmark results. These advances have been implemented in our in-house code HydroStar-V and Homer enabling more accurate hydro-structure analysis.

Acknowledgments

The first author likes to thank Dr Jinzhu Xia for introducing his work [3] on the boundary condition associated with modal shapes, and to Dr Chao Tian from CSSRC for some technical discussions.

References

[1] S. Malenica, Q. Derbanne, F.X. Sireta, F. Bigot, E. Tiphine, G. de-Hauteclocque & X.B. Chen (2013) HOMER – Integrated hydro-structure interactions tool for naval and offshore applications. International Conference on Computer Applications in Shipbuilding, Busan, South Korea.

[2] X.B. Chen, M.Q. Nguyen, I. Ten, C. Ouled Housseine, Y.M. Choi, L. Diebold, S. Malenica, G. de-Hauteclocque & Q. Derbanne (2022) New seakeeping computations based on potential flows linearized over the ship-shaped stream. PRADS'2022.

[3] J. Z. Xia (1996) A hydroelastic body boundary condition of floating structures. Ship Tech. Res. 43:173–174.

[4] Chen X.B., Choi Y.M., Nguyen M.Q. & Wuillaume P.Y. (2025) Surface integration of ship-motion Green function. *Proc. 40th Int. workshop on water waves and floating Bodies, Shanghai, China.*

[5] X.B. Chen, M.Q. Nguyen, I. Ten, C. Ouled Housseine, Y. M. Choi, L. Diebold, S. Malenica, G. De-Hautecloque & Q. Derbanne (2022) New seakeeping computations based on potentials linearised over the shipshaped stream. In Proceeding of the 15 Intl Symp on Practical Design of Ships and Other Floating Structures, PRADS 2022, Dubrovnik, Croatia.

[6] M.Q. Nguyen, G. de-Hauteclocque, J. de Lauzon, S. Malenica & X.B. Chen (2024) Quasi-static fluid structure interactions for ships advancing in waves with constant forward speed. Proc. 43rd OMAE conference, Singapore.

[7] J. N. Newman (1978) The theory of ship motions. Advances in Applied Mechanics, 18:221–283.

[8] X.B. Chen, F. Dias & W.Y. Duan (2011) Introduction of dissipation in potential flows. Proceeding of the 7th International Workshop on Ship Hydrodynamics, Shanghai, China.

[9] X.B. Chen & G.X. Wu (2001) On singular and highly oscillatory properties of the Green function for ship motions. Journal of Fluid Mechanics, 445(1):77–91.

[10] X.B. Chen (2023) Fundamental solutions to ship-motion problems with viscous effects. Physics of Fluids, 35(9):097130-9.

[11] M. Abramowitz & I. A. Stegun (1972) Handbook of Mathematical Functions: with Formulas, Graphs, and Mathematical Tables. Number 55. National Bureau of Standards.

[12] J. M. J. Journee (1992) Experiments and calculations on 4Wigley hull forms in head waves. Technical Report 909, Delft University of Technology.

[13] W.T. Waskito, M. Kashiwagi, H. Iwashita & M. Hinatsu (2020) Prediction of nonlinear vertical bending moment using measured pressure distribution on ship hull. Applied Ocean Research, 101.

[14] X. B. Chen, L. Diebold, H. Iwashita & P.Y. Wuillaume (2026) Analysis of ship seakeeping in following seas. In Proceeding of the 41st International Workshop on Water Waves and Floating Bodies, Plitvice, Croatia.

10^{th} International Conference on Hydroelasticity in Marine Technology
Trondheim, Norway, June16^{th}-18^{th}, 2026

Recent Developments in Modelling Flow-Induced Motions of Floating Offshore Wind Turbines During Wet-Tow

Yin, D.[1,*] Fonseca, N.[2], and Jiang, F.[2], Firoozkoohi, R.[2],
Indergård, R.[2], Braaten, H.[2], Lie, H.[2]

[1] Department of Energy and Transport, SINTEF Ocean, Trondheim, Norway
[1] Department of Ships and Ocean Structures, SINTEF Ocean, Trondheim, Norway

Abstract. Flow-induced motions (FIM) can occur in both moored and towed floating offshore wind turbines (FOWTs) due to environmental loads and towing forces. Typical semi-submersible floaters consist of multiple cylindrical elements subjected to drag, added-mass, and vortex-induced forces when the relative flow velocity exceeds certain thresholds. During wet-towing, coupled multi-degree-of-freedom responses such as vortex-induced motions, galloping, and fishtailing may develop, leading to stability challenges and potential fatigue damage. Towing tests of a 1:40 INO WINDMOOR semi-submersible were conducted at SINTEF Ocean to investigate towing resistance and FIM characteristics. Results show that the use of bridles significantly enhances directional stability and mitigates FIM responses. As part of the Transport and Installation of FOWTs Joint Industry Project (TOWIN JIP), a time-domain vortex-induced vibration model was applied to simulate the FIM of a generic semi-submersible, where vortex shedding from the columns is presumed dominant. The simulations reproduced key dynamic features observed experimentally, demonstrating the model's potential for predicting FIM during wet-towing and supporting safe and efficient floating wind transport and installation operations.

Key words: Flow-induced motion; Floating offshore wind turbine; Fluid-structure interaction; Wet-tow

1. Introduction

Floating offshore wind turbines (FOWTs) may experience flow-induced motions (FIM) during tow-to-site for installation or tow-to-port for major component replacement, repairs, or exchanges In this paper, FIM is used as an umbrella term encompassing vortex-induced motions (VIM), galloping, and fishtailing. VIM is a resonance-driven mechanism characterized by lock-in between the vortex shedding frequency and the structural natural frequency, typically resulting in bounded, self-limiting oscillations. In contrast, galloping is a self-excited instability driven by negative hydrodynamic damping, which generally occurs at higher reduced velocities where vortex shedding is less dominant. Fishtailing refers to a system-level yaw instability arising from the interaction between hydrodynamic loads, towline restoring forces, and structural inertia. These coupled low-frequency platform motions may limit towing speeds, contribute to tow line fatigue damage, and pose safety risks during towing operations. For semi-submersible FOWTs (SS-FOWTs), VIM is generally expected to be the dominant mechanism due to vortex shedding from the columns, while galloping and fishtailing may also develop depending on the floater geometry and towing configuration.

*Correspondence to: decao.yin@sintef.no

Experimental studies have confirmed that SS-FOWTs are susceptible to significant FIM responses during both moored and towing conditions. Model tests on the OC4 Phase II floater reported cross-flow VIM amplitudes up to approximately $0.7D$ (where D is the column diameter) under current loading [1], while towing tests of the same concept showed that the use of bridles reduced the transverse VIM amplitude from below $< 0.3D$ to below $< 0.15D$ [2]. Similar behaviour was observed for the INO WINDMOOR floater in both current and towing tests, where coupled sway-yaw VIM responses were measured and bridles significantly improved directional stability and reduced the motion amplitudes [3, 4].

During wet towing, the structure is subjected to complex fluid-structure interaction phenomena. For multi-column platforms with non-circular members (e.g., square columns or rectangular pontoons) capable of generating negative hydrodynamic damping, the response may transition from resonance-driven VIM to a galloping-dominated regime at higher reduced velocities. In this regime, vortex shedding can become entrained by the structural motion, leading to a non-self-limiting increase in oscillation amplitude with towing speed [5]. Fishtailing refers to system level yaw instability of the entire floating unit caused by the interplay between hydrodynamic forces, towline restoring forces, and structural inertia. Bernitsas & Kekridis [6] developed a 3-DoF fully analytical model to investigate the towing stability of a number of vessels towed by an elastic towline, found an expression to determine the equilibria of the dynamic system and applied the Routh-Hurwitz criterion to study their stability.

Previous studies have applied a range of numerical tools to analyse FOWT towing behaviour, including potential-flow models, Computational Fluid Dynamics (CFD) simulations, and coupled time-domain analyses [2, 7]. These studies have improved the prediction of towing resistance, platform motions, and towing stability. However, modelling FIM remains challenging due to the complex wake interactions between multiple columns and pontoons, shielding effects, and the coexistence of VIM, galloping, and fishtailing. In addition, experimental validation is complicated by the scaling conflict between Froude and Reynolds similarity. As a result, there remains a gap between low-fidelity potential-flow approaches and computationally expensive CFD methods, highlighting the need for efficient and validated semi-empirical models for predicting FIM during towing operations.

This paper investigates the FIM behaviour of a semi-submersible FOWT during wet towing as part of the Transport and Installation of Floating Offshore Wind Turbines Joint Industry Project (TOWIN JIP). Experimental observations from towing tests of the INO WINDMOOR concept are reviewed together with CFD-based wake visualisation and a preliminary time-domain FIM model adapted from Vortex-Induced Vibration (VIV) theory. The objective is to improve the understanding of towing-induced FIM and support the development of practical prediction methods for future towing operations. Section 2 introduces the governing equations and towing resistance formulation. Section 3 presents the experimental observations and CFD results. Section 4 describes the numerical FIM model and its application to a towing case study, followed by the main conclusions in Section 5.

2. Problem formulation

This study investigates the dynamics of SS-FOWT in a tug boat wet-tow system, where towing operation is carried out by means of a single elastic towing line, two bridles are connected to the two columns of a SS-FOWT, as illustrated in Figure 1.

2.1. Estimation of towing resistance of the FOWT

The determination of towing resistance (R_{T}) is a fundamental step in the planning and execution of wet-towing operations, as it governs the required bollard pull (BP) and towing feasibility.Wet towing is the common transport method for SS-FOWTs, as their shallow draft

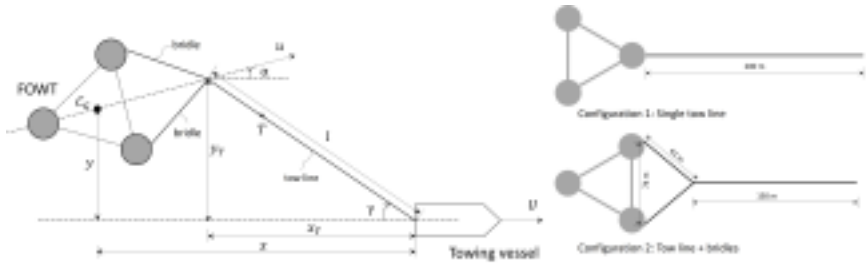


Figure 1: Top view sketch of the towing system of a SS-FOWT (Left); Two towing configurations discussed in this study (Right).

and large water-plane area provide good stability in transit conditions. Towing operations are typically performed at a reduced transit draft (e.g., 10-12 m for a typical SS) compared to the in-place draft to lower the hydrodynamic drag forces and the required BP.

The total towing resistance is composed of four principal components [7, 8]:

$$\mathbf{R}_{\mathrm{T}} = \mathbf{R}_{\mathrm{V}} + \mathbf{R}_{\mathrm{Wave}} + \mathbf{R}_{\mathrm{Added\ wave}} + \mathbf{R}_{\mathrm{Wind}} \tag{1}$$

where the steady hydrodynamic resistance is calculated using the relative velocity $\mathbf{U}_{\mathrm{rel}} = \mathbf{U}_{\mathrm{tow}} - \mathbf{U}_{\mathrm{c}}$. Following Froude's hypothesis, this is decomposed into viscous resistance ($\mathbf{R}_{\mathrm{V}}$) and wave-making (residual) resistance ($\mathbf{R}_{\mathrm{W}}$). For this bluff-bodied semi-submersible, $\mathbf{R}_{\mathrm{V}}$ is dominated by pressure (form) drag due to flow separation at the columns, while skin friction is secondary. The wave-making component $\mathbf{R}_{\mathrm{W}}$ accounts for the energy expended in generating free-surface waves and is a function of the Froude number. The added resistance in waves $\mathbf{R}_{\mathrm{Added\ wave}}$ is a second-order load consisting of mean and slowly varying components; the latter is particularly important as it may excite the natural frequency of the coupled towing system. Viscous damping corrections are necessary since potential flow models underestimate damping at resonance. Wind resistance $\mathbf{R}_{\mathrm{Wind}}$ acts on the exposed rotor, nacelle, and tower of the assembled FOWT and cannot be disregarded.

2.2. Time domain FIM analysis

The motion of a SS-FOWT in the presence of combined current, wave, aerodynamic loads and towing force is described in the time domain by the 6-DoF rigid-body equilibrium. The governing equation follows the generalized form of Newton's second law for a floating body [7], [9] and can be expressed as:

$$(\mathbf{M} + \mathbf{A}_{\infty})\ddot{\mathbf{u}}(t) + \mathbf{B}_v\dot{\mathbf{u}}(t) + \int_0^t \mathbf{K}_R(t-\tau)\dot{\mathbf{u}}(\tau)d\tau + \mathbf{K}_{\mathrm{rest}}\mathbf{u}(t) = \mathbf{F}_{\mathrm{ext}}(t) \tag{2}$$

where $(\mathbf{M} + \mathbf{A}_{\infty})$ represents the sum of structural mass and infinite-frequency added mass; $\mathbf{B}_v$ is the viscous damping matrix; $\mathbf{K}_R(t-\tau)$ is the retardation function representing frequency-dependent wave-radiation damping and added mass, derived from potential flow theory via the Ogilvie relations [10]. $\mathbf{K}_{\mathrm{rest}}$ is the total restoring stiffness matrix. For a towed FOWT, this term consistently accounts for both the hydrostatic restoring stiffness (derived from buoyancy and gravity) and the pendular restoring stiffness arising from the towline tension and geometry [6].

The external force acting on a towed FOWT $\mathrm{F}_{\mathrm{ext}}(t)$ includes the following time-varying excitation forces:

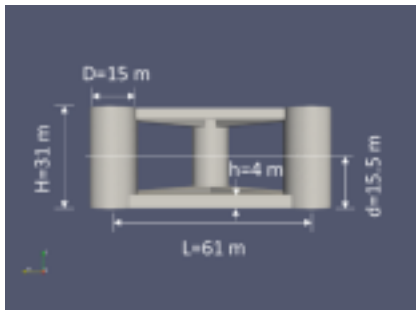
$$\mathbf{F}_{\mathrm{ext}}(t) = \mathbf{F}_{\mathrm{wind}}(t) + \mathbf{F}_{\mathrm{wave}}(t) + \mathbf{F}_{\mathrm{current}}(t) + \mathbf{F}_{\mathrm{towline}}(t) + \mathbf{F}_v(t) \tag{3}$$

where wave loads $\mathbf{F}_{\mathrm{wave}}$ include first-order diffraction/radiation forces and second-order drift loads, derived from potential flow theory. Wind loads $\mathbf{F}_{\mathrm{wind}}$ act on the parked rotor-nacelle assembly; for towing operations this contribution is typically small. Current-induced drag $\mathbf{F}_{\mathrm{current}}$

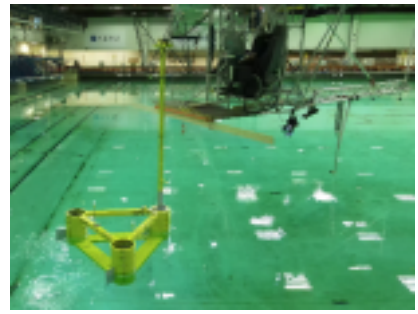
is modelled using Morison's equation along the submerged members. The towline force $\mathbf{F}_{\text{towline}}$ is modelled as a flexible finite-element structure in RIFLEX, providing non-linear restoring forces that govern yaw stability and directional behaviour during towing — the absence of stable equilibrium in non-linear models can lead to self-induced yaw oscillations, i.e., fishtailing, which is mitigated by introducing bridles to increase rotational stiffness. Vortex shedding forces $\mathbf{F}_v$ represent unsteady hydrodynamic loads arising from periodic vortex shedding, modelled using a semi-empirical time-domain formulation as described in Section 4..

3. Towing-out of INO WINDMOOR 12 MW FOWT

The 12 MW INO WINDMOOR FOWT has a triangular shaped SS platform composed of three vertical circular cylinder columns interconnected with rectangular deck beams and rectangular submerged lower pontoons. The main characteristic dimensions of the prototype floater are shown in Figure 2a. Still water towing test on a 1:40 INO WINDMOOR model was carried out in the Ocean Basin at SINTEF Ocean, one of the two towing configurations is shown in Figure 2b. Details of the test setup and program is given in [6]. The tests were conducted under Froude similarity, ensuring dynamic similarity of gravity-driven effects. However, the Reynolds number at model scale is significantly lower than at full scale due to reduced towing speed and characteristic length. This mismatch primarily affects viscous forces, and consequently, the model tests may underestimate viscous damping and vortex-shedding intensity compared to full-scale conditions.



(a) Dimensions of the INO WINDMOOR platform: D - column diameter, H - column height, d - draft, h - pontoon height, and L - centre-to-centre column distance.



(b) Model test setup in Ocean Basin.

Figure 2: Experimental set-up of INO WINDMOOR towing test.

3.1. Drag force

In the calm water towing tests with constant towing speeds, the towing force measured on the tow line is equivalent to the towing resistance force (see Equation 1), which is dominated by the drag force (F_D). The total drag force acting on a FOWT platform beneath the still water level is:

$$F_D = \frac{1}{2} C_D \rho U^2 A_p \tag{4}$$

where C_D is the total drag coefficient which will be amplified due to transverse (sway) motions. The projected area, A_p, is calculated using the dimensions defined in Figure 2a: $A_p = 3dD + h(L - 2D) = 821.5\ \text{m}^2$. The calculated total drag coefficients (C_D) of the two towing

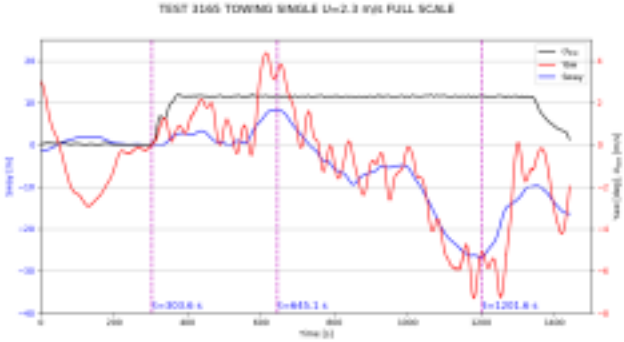
configurations falls between 0.9 – 1.0 and there is no significant difference of drag coefficients between the two towing configurations.

This drag coefficient is sensitive to the Reynolds number regime and the platform's geometry. While the model tests were conducted at a lower Reynolds number than at full scale due to Froude scaling, the drag coefficient is also affected by the low aspect ratio ($A_R = d/D \approx 1.0$) of the columns. For such platforms, the three-dimensional flow effects at the column bases and the free-surface interface typically lead to a reduction in the integrated drag coefficient compared to theoretical infinite cylinders [11, 12]. Accounting for these low aspect ratio effects, alongside the well-documented reduction of C_D at prototype Reynolds numbers [13, 14], is essential for the accurate extrapolation of model-scale resistance to full-scale operational conditions.

For a surface piercing cylinder, the surface resistance coefficient (defined as $F_S = C_S \frac{1}{2}\rho U^2 D^2$) accounts for the additional resistance arising from free-surface deformation around the column, and is governed by the Froude number $Fr = U/\sqrt{gD}$. It reaches a maximum value of about 0.9 at $Fr \approx 1$, and decreases toward zero below $Fr = 0.5$ [13]. In the towing tests of INO WINDMOOR, the maximum towing speed is 3.0 m/s, resulting in a Froude number $Fr = 0.24$, well below this threshold, so the surface resistance is negligible.

3.2. FIM

VIM may occur for both operational (moored) and transit (towed) SS-FOWT, and the sway motion and yaw motion are major concerns. The dynamics and controlling factors of VIM differ significantly between these two states, primarily due to differences in the constraints and restoring forces applied to the structure. In a towing configuration, the tow line provides transverse stiffness that can be modelled as a simple horizontal pendulum set-up [4].



(a) Time series of sway and yaw motions, plotted against towing speed.



(b) t = 303.6 s. (c) t = 645.1 s. (d) t = 1201.6 s.

Figure 3: Snapshots of bird eye video camera showing coupled sway and yaw motions of Test 3165, $U_{\text{tow}} = 2.3$ m/s. Configuration: single tow line + bridles.

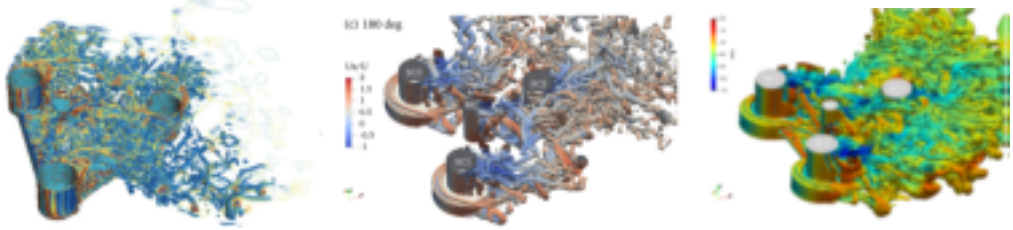
Figure 3 shows measured VIM of INO-WINDMOOR model under Ocean Basin towing test using single tow line with two bridles. The time histories presented in Figure 3a clearly show a coupled sway-yaw VIM. Three snapshots from the fixed overhead video camera are shown in

Figure 3b - Figure 3d: Figure 3b shows the initial position of the model where $U_{\text{tow}} = 0.0$ m/s, and Figure 3c and Figure 3d shows the positions of the platform where the sway motions reached the maximum and minimum values. Sway period is around 350 s, yaw period is about 65 s.

3.3. CFD visualization of wake structure

To visualize coherent vortex structures and understand wake dynamics, the λ_2-criterion [15] and the Q-criterion [16] were applied. Both methods capture swirling motion but emphasize different features depending on the local flow's strain and pressure distribution. Three CFD studies illustrated in Figure 4 employ these criteria to extract vortex iso-surfaces and illustrate the underlying wake dynamics of semi-submersible FOWT platforms with simplified mooring under uniform current. In all cases, the free surface is neglected and the problem is formulated as single-phase, incompressible flow. Turbulence modelling varies across the studies, including Reynolds-averaged Navier–Stokes (RANS) and Detached Eddy Simulation (DES) — a hybrid RANS and and Large Eddy Simulation (LES) formulation that retains near-wall RANS accuracy while resolving large-scale turbulent structures.

Multi-scale vortices generated from the three main columns interact with those shed from the pontoons (Figure 4a), heave plate and centre column (Figure 4b), and connecting structures (Figure 4c). Vortices shed from upstream columns are convected downstream, impinging on and interacting with downstream columns — directly affecting vortex shedding frequency and fluid forces. Connecting structures partially break up upstream vortices, reducing this interaction and mitigating VIM [17]. This wake complexity is directly relevant to FIM during towing, where a bridle configuration connecting two columns is more common than a single towline. Even though all the mentioned CFD works are in model scale, it is believed that the column base, heave plates and supporting structures alter the vortex shedding so the Reynolds number effects are small.



(a) INO-WINDMOOR SS-FOWT platform (1:40). Represented by λ_2 iso-surfaces and coloured by vorticity magnitude. $V_R = 8.0$, $Re = 6.2 \times 10^4$ [18].

(b) OC4 DeepWind SS-FOWT (1:50). Represented by iso-surface of $Q = 1$ and colored by non-dimensional in-line flow velocity U_x/U for platform at $V_R = 10.0$, $Re = 2.92 \times 10^4$ [17].

(c) OC4 DeepWind SS-FOWT (1:72.72). Represented by iso-surface of $Q = 1$ and coloured by non-dimensional in-line flow velocity U_x/U for platform at $V_R = 10.0$, $Re = 2.87 \times 10^4$ [19].

Figure 4: 3D wake structures of two SS-FOWT platforms under VIM.

4. FIM numerical model

To enable precise predictions of FOWT dynamics during towing operation in real sea states, a time-domain analysis with fully integrated structural models is essential. Advanced hydrodynamic load models are particularly critical to account for scaling effects, wave effects, motions of bluff bodies with low aspect ratio, wake interactions and interference – which are key factors influencing FIM of FOWT platforms.

The present FIM model is based on a set of simplifying assumptions. The vortex shedding forces are assumed to be dominated by the main columns, while contributions from pontoons,

braces, and secondary structures are not modelled explicitly. Wake interaction, interference, and shielding effects are not resolved at the flow level, but are incorporated implicitly through effective hydrodynamic coefficients. In addition, the model adopts a semi-empirical VIV-based formulation originally developed for circular cylinders, which is extended here to multi-column FOWT configurations. These assumptions are revisited when interpreting the simulation results.

4.1. Time domain FIM model

The recently developed time-domain VIV load model [20] - originally developed for modelling VIV of slender marine structures with underlying assumption of infinite length, could be a starting point to model FIM. The formulation of time-domain VIV load model is described below. Considering an oscillating circular cylinder in constant flow, the global and local coordinate systems are defined as shown in Figure 5.



Figure 5: Global (defined by the incoming flow) and local (defined by the instantaneous relative velocity) coordinate system of on cylinder plane.

The hydrodynamic force acting on a unit length of circular cylinder is [20]:

$$F_h = (C_A + 1)\rho\frac{1}{4}\pi D^2\dot{\mathbf{u}}_n - C_A\rho\frac{1}{4}\pi D^2\ddot{\mathbf{x}}_n + \frac{1}{2}\rho C_D D|\mathbf{v}_n|\mathbf{v}_n + \frac{1}{2}\rho D C_{v,y}|\mathbf{v}_n|(\mathbf{j}_3 \times \mathbf{v}_n)cos\phi_{v,y} \quad (5)$$

where $\dot{\mathbf{u}}_n$ is the component of fluid acceleration perpendicular to the cylinder, $\ddot{\mathbf{x}}_n$ is the normal component of the cylinder's acceleration perpendicular to the cylinder, $\mathbf{v}_n = \mathbf{u}_n - \dot{\mathbf{x}}_n$ is the relative velocity of the fluid perpendicular to the cylinder. C_A, C_D, and $C_{v,y}$ are the non-dimensional added mass, drag and cross-flow vortex shedding coefficients respectively. $\mathbf{j}_3$ is the unit vector along the cylinder, $\mathbf{j}_3 \times \mathbf{v}_n$ gives a vector in the instantaneous cross-flow direction with length $|\mathbf{v}_n|$. $\phi_{v,y}$ is the instantaneous phase of the cross-flow vortex shedding force.

On the right hand side:

- The first term represents the inertia force arising from the fluid acceleration and acts in the direction of that acceleration
- The second term is the inertia force due to the cylinder acceleration and acts in the direction opposite of the structural acceleration.
- The third term is the damping term given by the relative velocity normal to the cylinder $\mathbf{v}_n$ and acts in the direction of the normal relative fluid velocity.
- The fourth term represents the cross-flow vortex shedding force acts in the instantaneous cross-flow direction.

A synchronization model introduces a phase-coupling between the force and response, which effectively captures how the local vortex shedding frequency may increase or decrease to obtain lock-in. The instantaneous frequency of the cross-flow vortex shedding force is given by:

$$\frac{d\phi_{v,y}}{dt} = 2\pi f_{v,y} = 2\pi\frac{|v_n|}{D}\bar{f} \quad (6)$$

where $\bar{f} = \bar{f}_0 + \Delta\bar{f}sin(\theta)$. $\bar{f}_0$ and $\Delta\bar{f}$ are the instantaneous non-dimensional frequency and frequency range, determining the position and span of the synchronization range, respectively. $\theta = \phi_{\dot{y}_{rel}} - \phi_{v,y}$ is the difference between the instantaneous phase of the vortex shedding force and the phase of the structural velocity in the local CF direction. $\phi_{\dot{y}_{rel}}$ is the instantaneous phase of the (local) cross-flow structural velocity.

The underlying assumptions, limitations, and physical interpretation of this modelling approach are discussed in detail in [20] and [3]. It should be noted that wave–current interaction effects are not explicitly modelled at the flow level. Initial study on VIM of a spar-type turbine has demonstrated promising results [21], and thereafter it has been validated against field measurements. It is expected since the spar-type platform is a finite cylinder with surface and end effects. While for SS-FOWT, it is not straightforward. Attempt using different empirical coefficients of the time domain VIV load model on columns has been tried in [3], demonstrated the possibility of further development of the load model to include the vortex shed from the pontoons, and wake interactions. To further complicate the problem, the effects from various sea-states have to be considered for field operations.

The aim of the present study is to develop semi-empirical FIM numerical models: VIM model and galloping model. A better understanding of the wake is crucial to make proper simplifications and assumptions. Validated CFD simulation enables visualization of the wake or even calculate hydrodynamic force components of each sub-structure of SS-FOWT platform. The mainstream SS-FOWT concepts such as DeepCWind and INO WINDMOOR are composed of three main columns, with or without an additional central column, pontoons, heave plates and small scale interconnecting braces. A generic numerical hydrodynamic force model should 1) Capture the dominating vortex shedding force from the columns; 2) Model the hydrodynamic forces and damping effects from other structure components.

Modelling a towed FOWT including FIM using CFD is time consuming and costly, scaling effects and wave-current coupling pose additional challenges. Therefore, an efficient time-domain semi-empirical model is highly desirable by industry. Vortex shedding and VIV on circular cylinders are far more extensively investigated than other structural forms such as square pontoons or braces. One way is to model all the structure components explicitly, which requires a large empirical database that covers a variety of conditions: constant flow, oscillatory flow, wake flow etc. A more practical approach is to focus on the columns, which have much larger dimensions than the other components, and so the vortex shedding forces are dominating the FIM. The latter strategy is adopted in this study.

4.2. Difference between VIV and FIM

Attempts have been made to carefully tune the key empirical parameters of the time-domain VIV load model toward modelling FIM of a towed FOWT. The characteristic differences between these two phenomena are summarized in Table 1. The VIV parameters are benchmark values derived from laboratory tests on rigid and flexible pipes [20], representing high-aspect-ratio slender structures. In contrast, the FIM parameters are preliminary estimates for multi-column FOWT platforms, which are characterized by low aspect ratios, multiple-body wake interference, and 6-DOF motion [3, 1].

Table 1: Characteristic differences between VIV and FIM cross-flow empirical parameters under constant flow conditions.

Parameter	VIV		FIM during towing	
	Value [20]	Features	Value	Features
C_D	1.1	$D = \mathrm{O}(1\ m)$	0.45	$D = \mathrm{O}(10\ m)$
$C_{v,y}$	1.2	Single cross section	3.0	Multiple bodies
$\bar{f}_0$	0.13	Large A_R	4.0	Small A_R
		Ambient flow		Wake interference
$\Delta\bar{f}$	[0.11 - 0.26]	Vortex correlation	[2.0 - 6.0]	Vortex interaction
		2 DoF		6 DoF
				Restoring force

While the benchmark VIV parameters for slender structures are well-documented, they are not directly applicable to FOWT platforms due to the differing physics of multi-column interactions. A critical distinction lies in the natural period, $T_{n,y}$. For the INO WINDMOOR platform, $T_{n,y} \approx 95$ s in a moored setup [3], but increases to $T_{n,y} \approx 420$ s at $U_{\text{tow}} = 1.5$ m/s in a towing configuration [4]. This difference arises because the pendulum restoring mechanism of the towline governs the natural period, which is inversely proportional to the towing speed.

Accordingly, the reduced velocity in towing configuration can be expressed as:

$$V_{R,\text{tow}} = \frac{U_{\text{tow}} T_{n,y}}{D} = \frac{2\pi}{D}\sqrt{\frac{2(M + M_A)L_t}{\rho C_D A_p}} \tag{7}$$

The final expression indicates that the reduced velocity becomes independent of the towing speed, as the towline restoring force scales with the hydrodynamic drag. Consequently, the natural sway period varies inversely with U_{tow}, yielding a constant V_R for a given system configuration. At $U_{\text{tow}} = 1.5$ m/s, this leads to a shift in reduced velocity from 9.5 (typical VIM lock-in) to 42. The large-amplitude responses at high reduced velocity are unlikely to be classical resonance-driven VIM, and may involve galloping-type instability or nonlinear wake-structure interaction, the precise mechanism of which requires further investigation.

4.3. Case study - FIM during towing

A coupled SIMO-RIFLEX numerical model of INO WINDMOOR under towing condition is established under the SIMA workbench as shown in Figure 6. Case study has been carried out on the selected model test $U = 2.3$ m/s (Test 3165 shown in Figure 3). The numerical approach is based on the hypothesis that the global FIM response is primarily driven by the synchronized vortex shedding from the three main columns. These assumptions are consistent with those introduced in the beginning of this section and should be considered when interpreting the results.

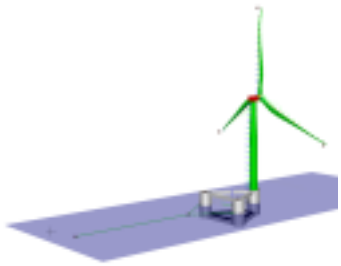


Figure 6: SIMA numerical model of INO WINDMOOR towing setup.

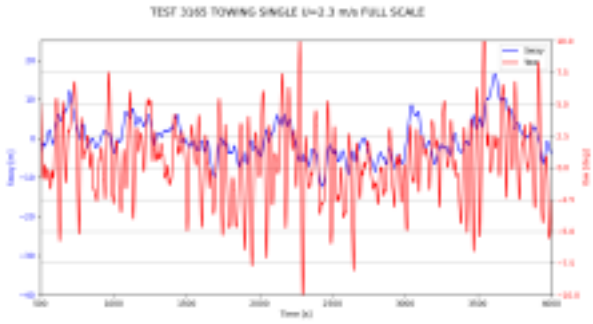


Figure 7: Time series of sway and yaw motions from FIM numerical simulation $U = 2.3$ m/s. Configuration 2: single tow line + bridles.

An attempt has been made to tune the key empirical input parameters presented in Table1 to the time-domain VIV model to get qualitatively comparable sway and yaw responses. In this semi-empirical framework, complex phenomena such as vortex shedding from pontoons, wake interference, and shielding effects are not modelled explicitly through the tracking of local wake structures. Instead, they are implicitly represented by adopting integrated hydrodynamic force coefficients that differ significantly from those of isolated slender components.

For instance, the drag coefficient C_D for the present semi-submersible FOWT is reduced to 0.45 (compared to 1.1 for VIV), reflecting the loss of span-wise vortex correlation and the disruptive effect of shielding within the column array [3, 1]. Similarly, the increased transverse added mass coefficient ($C_{v,y} = 3.0$) and the tuned frequency parameters ($\bar{f}, \Delta\bar{f}$) account for

the modified flow field between the columns. This "bulk" calibration approach ensures that the total unsteady hydrodynamic load acting on the three main columns captures the collective energy exchange between the wake and the structure without the prohibitive computational cost of explicit wake modelling [3].

These simplifications are significant and need thorough evaluation for each floater concept, either from experiments or CFD simulations. Figure 7 shows the preliminary dynamic simulation results using the time domain vortex shedding force model on the submerged columns. The numerical simulation is carried out with a duration of 4000 s; considering the natural sway period is around 300 s, the initial 500 s is removed to avoid the transient effects. The sway and yaw motions in Figure 7 are comparable to Figure 3a generally in terms of amplitude and response frequency. Sway motions are dominated by low frequency, while yaw motions are dominated by high frequency.

5. Conclusions

Wet-tow of an assembled FOWT for installation and major component replacement requires specific time window and towing speed limit and is of high cost and time consuming. TOWIN JIP aims increasing towing speeds and expanding operational weather windows, necessitating rigorous prediction of hydrodynamic phenomena. A towed FOWT is highly susceptible to nonlinear FIM, such as VIM and galloping, during transit.

The present paper reviews recent research on FIM of a FOWT, specially on towing studies. Relevant experimental work and CFD simulations are discussed, for better understanding of the dynamic responses and wake structure. Selected case from INO WINDMOOR SS-FOWT towing test is analysed and presented. The time domain VIV load model is applied on the main columns while neglect other auxiliary structures and effects. The predicted FIM are comparable to the measured motions from the experiments, demonstrating the potential for further development and application. Overall, this study integrates model-scale towing tests with a simplified time-domain VIM model, representing one of the first steps toward an operational FIM prediction framework for SS-FOWTs.

A validated and industry-ready time-domain FIM model will provide deeper insights to refine the design and support decision-making during operation for floating offshore wind. It will enable safer and more efficient marine operations: allowing for potential higher towing speeds, broader weather windows, and optimised installation and maintenance strategies. Future work will focus on experimental calibration of the FIM empirical coefficients across a wider range of floater geometries and sea states, and on extending the model to capture galloping and combined VIM-galloping responses.

References

[1] R.T. Gonçalves, M.E.F. Chame, L.S.P. Silva, A. Koop, S. Hirabayashi, and H. Suzuki. Experimental Flow-Induced Motions of a FOWT Semi-Submersible Type (OC4 Phase II Floater). Journal of Offshore Mechanics and Arctic Engineering, 143(1):012004, 09 2020.

[2] R.C. Ramachandran, J.-J. Serraris, J. Hernandez Montfort, E.-J. De Ridder, C. Desmond, and J. Murphy. Towing Analysis and Validation of a Fully Assembled Floating Offshore Wind Turbine Based on an Experimental Study. Journal of Marine Science and Engineering, 12(4), 2024.

[3] D. Yin, E. Passano, and P.A. Berthelsen. Numerical Investigation of Vortex-Induced Motions (VIM) on A Semi-Submersible Floating Offshore Wind Turbine. In Proceedings of the ASME 2024 43rd International Conference on Ocean, Offshore and Arctic Engineering, volume 7: Ocean Renewable Energy, Singapore EXPO, Singapore, 2024. V007T09A045.

[4] D. Yin, R. Indergård, H. Lie, and H. Braaten. Experimental Investigation of Towing of a Semi-submersible Floating Offshore Wind Turbine. Journal of Physics: Conference Series, 2875(012026), 2024.

[5] O.J. Waals, A.C. Phadke, and S. Bultema. Flow Induced Motions on Multi Column Floaters. In Proceedings of the ASME 2007 26th International Conference on Offshore Mechanics and Arctic Engineering, volume 1: Offshore Technology; Special Symposium on Ocean Measurements and Their Influence on Design, pages 669–678, 06 2007.

[6] M.M. Bernitsas and N.S. Kekridis. Nonlinear Stability Analysis of Ship Towed by Elastic Rope. Journal of Ship Research, 30(02):136–146, 06 1986.

[7] M. Chen, Y. Chen, T. Li, Y. Tang, J. Ye, H. Zhou, M. Ouyang, X. Zhang, W. Shi, and X. Sun. Analysis of the wet-towing operation of a semi-submersible floating wind turbine using a single tugboat. Ocean Engineering, 299:117354, 2024.

[8] DNV. DNV-RP-H103 Modelling and Analysis of Marine Operations, 2011.

[9] SINTEF Ocean. SIMA Documentation. Trondheim, Norway, 2026.

[10] T. F. Ogilvie. Recent progress toward the understanding and prediction of ship motions. In Proceedings of the Fifth Symposium on Naval Hydrodynamics, 1964.

[11] D.A. Potts, J.R. Binns, A.E. Potts, and H. Marcollo. The Effect of Aspect Ratio on the Drag of Bare Cylinders. In Proceedings of the ASME 2019 38th International Conference on Ocean, Offshore and Arctic Engineering, volume 1: Offshore Technology; Offshore Geotechnics, Glasgow, Scotland, UK, June 2019. V001T01A028.

[12] T. Kristiansen, D. Kristiansen, and A. Fredriksen. Experimental study of drag loads on open and closed low-aspect-ratio circular cylinders in steady current. Journal of Fluids and Structures, 118:103851, 2023.

[13] J.R. Chaplin and P. Teigen. Steady flow past a vertical surface-piercing circular cylinder. Journal of Fluids and Structures, 18(3):271–285, 2003. Bluff-body/Flow interactions.

[14] D. Yin, H. Lie, and R.J. Baarholm. Prototype Reynolds number VIV tests on a full-scale rigid riser. Journal of Offshore Mechanics and Arctic Engineering, 140(1), 2018. 011702.

[15] Jinhee Jeong and Fazle Hussain. On the identification of a vortex. Journal of Fluid Mechanics, 285:69–94, 1995.

[16] J.C.R. Hunt, A.A. Wray, and P. Moin. Eddies, streams, and convergence zones in turbulent flows. In Proceedings of the 1988 Summer Program, pages 193–208, 1988.

[17] Y. Liu, D. Ge, X. Bai, and L. Li. A CFD Study of Vortex-Induced Motions of a Semi-Submersible Floating Offshore Wind Turbine. Energies, 16(2), 2023.

[18] F. Jiang, D. Yin, A. Califano, and P.A. Berthelsen. Application of CFD on VIM of semi-submersible FOWT: A Case Study. IOP The Journal of Physics, 2626(012041), 2023.

[19] Y. Yang and Y. Liu. Three-degree-of-freedom vortex-induced motions of an OC4 floating offshore wind turbine platform under different current incidences. Ocean Engineering, 330:121240, 2025.

[20] J. Wu, J. Jin, D. Yin, H. Lie, E. Passano, S. Sævik, M.A. Tognarelli, G. Grytøyr, T. Andersen, D. Karunakaran, and R. Igland. Time Domain VIV Analysis Tool VIVANA-TD: Validations and Improvements. In Proceedings of the ASME 2020 39th International Conference on Ocean, Offshore and Arctic Engineering, number OMAE2020-18759, Virtual Conference, Online, August 2020.

[21] E. Passano, G. Grytøyr, H. Haslum, H. Lie, and D. Yin. Simulation of VIM of an offshore floating wind turbine. In Proceedings of the ASME 2022 41st International Conference on Ocean, Offshore and Arctic Engineering, number OMAE2022-79006, Hamburg, Germany, 2022.

Acknowledgments

The authors gratefully acknowledge the support of FME NorthWind and the TOWIN JIP and their participants.

Ice-Body-Water Interactions

10th International Conference on HYDROELASTICITY IN MARINE TECHNOLOGY
Trondheim, Norway, June16$^{\text{th}}$-18$^{\text{th}}$, 2026

Analysis of Vertical Mode Expansions for Hydroelastic Waves in Viscoelastic Floating Ice Plates

Shishmarev, K.[1,*], Ni, B.-Y.[1], Khabakhpasheva, T.[2] and Korobkin, A.[2]

[1] College of Shipbuilding Engineering, Harbin Engineering University, Harbin, China
[2] School of Engineering, Mathematics and Physics, University of East Anglia, Norwich, UK

Abstract. A two-dimensional problem describing the behaviour of a viscoelastic semi-infinite ice plate subjected to an incident wave is investigated. The solution is obtained by expanding the fluid velocity potential into vertical modes and matching their coefficients at the interfaces between regions. Complex wavenumbers satisfying the dispersion relation for a viscoelastic plate at a given real frequency are calculated and analysed. The spectrum is first examined for the elastic case, where double and triple roots are identified, and its evolution with increasing viscosity is then studied. The influence of viscosity on wave attenuation and plate deflections is analysed. The results show that, except within a narrow parameter range, the elastic plate exhibits a peak of maximum strain near its edge. The position of this peak is examined for varying ice thickness, wave frequency, and viscosity. Viscosity introduces damping of plate oscillations and modifies the strain distribution. Regions most susceptible to failure are identified, and a subsequent analysis is proposed to describe the behaviour of detached fragments. Three models are considered for the separated part: broken ice, an elastic or viscoelastic plate, and a rigid plate.

Key words: *Hydroelastic waves; Vertical mode method; Viscoelastic ice plate; Dispersion relation; Strains*

1. Introduction

Hydroelastic interaction between surface waves and floating ice plates is commonly analysed within linear potential-flow theory combined with thin-plate models. A central topic is the propagation and scattering of flexural–gravity waves generated by moving loads, incident waves, or submerged bodies. Classical formulations are summarised in [1]. Further studies include wave scattering by semi-infinite and finite plates, wave propagation near edges, interaction with coastal or offshore structures, and configurations involving multiple plates [2, 3, 4, 5, 6, 7, 8, 9].

A widely used analytical approach is the method of vertical modes (eigenfunction expansions). It has been applied to semi-infinite plate configurations and wave-scattering problems in two- and three-dimensional settings [10, 11, 12]. Mode-coupling relations were derived in [13] using the Fourier integral theorem for Laplace problems with higher-order boundary conditions. The formulation reduces to a system of algebraic equations for the modal coefficients. Modified edge conditions, waveguides, and cylindrical geometries were examined in [14, 15, 16].

The dispersion relation of the plate determines the spectral structure of the solution. Depending on the parameters, the spectrum may include real, complex, imaginary, and multiple roots [11, 17]. In the present work, the vertical-mode method is applied to a semi-infinite viscoelastic plate to study wave-induced oscillations, strain distributions, and possible fracture scenarios.

*Correspondence to: shishmarev.k@mail.ru

2. Formulation of the problem

Oscillations of a semi-infinite viscoelastic ice plate are considered in two dimensions. The plate occupies $(\hat{x} > 0)$, while $(\hat{x} < 0)$ corresponds to open water of finite depth H $(-H < \hat{z} < 0)$. Cartesian coordinates $(\hat{x}, \hat{z})$ are used and the interface between free surface and plate is located at $\hat{x} = 0$. A schematic of the configuration is shown in Fig. 1.

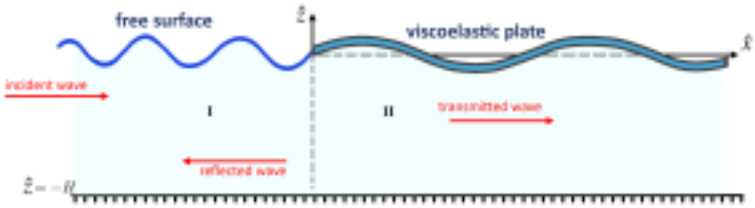


Figure 1: Schematic of the problem in dimensionless variables. Region I: free-surface flow; Region II: flow covered by a semi-infinite viscoelastic plate.

The plate is described within linear thin-plate theory with density ρ_i, thickness h_i and flexural rigidity

$$D = \frac{E h_i^3}{12(1-\nu^2)},$$

where E and ν are Young's modulus and Poisson's ratio. The fluid is inviscid, incompressible and has density ρ. Viscoelasticity is modelled by the Kelvin–Voigt law with retardation time τ.

Dimensionless variables are introduced as

$$x = \hat{x}/L_{sc}, \quad z = \hat{z}/L_{sc}, \quad t = \omega\hat{t}, \qquad h = H/L_{sc},$$

where ω is the frequency of incident wave, L_{sc} is the characteristic length scale, chosen equal to the depth H. The incident wave has the form

$$\eta_{\text{inc}} = e^{i(k_0 x - t)}, \qquad \phi_{\text{inc}} = -ie^{i(k_0 x - t)} \frac{\cosh[k_0(z+h)]}{k_0 \sinh(k_0 h)}, \tag{1}$$

where wavenumber k_0 satisfies the free-surface dispersion relation. Unknown functions, including free surface elevation η, ice deflection w and potential ϕ are sought in harmonic form

$$\eta = \eta(x)e^{-it}, \quad w = w(x)e^{-it}, \quad \phi = -i\Phi(x,z)e^{-it}. \tag{2}$$

In Region I $(x < 0)$ the governing equations are

$$\Phi_{xx} + \Phi_{zz} = 0, \quad -h < z < 0, \tag{3}$$

$$\eta - \gamma\Phi = 0, \quad \Phi_z = \eta \quad (z = 0), \qquad \Phi_z = 0 \quad (z = -h). \tag{4}$$

The radiation condition as $x \to -\infty$ is

$$\eta \sim e^{ik_0 x} + a_0 e^{-ik_0 x}.$$

In Region II ($x > 0$),

$$\Phi_{xx} + \Phi_{zz} = 0, \quad -h < z < 0, \qquad \Phi_z = 0 \ (z = -h), \tag{5}$$

$$-\gamma m w + \beta(1 - i\varepsilon) w_{xxxx} + w = \gamma\Phi, \qquad \Phi_z = w \ (z = 0). \tag{6}$$

The nondimensional parameters are

$$m = \frac{\rho_i h_i}{\rho L_{sc}}, \quad \beta = \frac{D}{\rho g L_{sc}^4}, \quad \varepsilon = \tau\omega, \quad \gamma = \frac{\omega^2 H}{g}.$$

At $x = 0$ the plate satisfies free-edge conditions

$$w_{xx} = w_{xxx} = 0, \tag{7}$$

and at the interface $x = 0, -h < z < 0$ the fluid potential satisfies

$$[\Phi] = 0, \qquad [\Phi_x] = 0. \tag{8}$$

The aim is to determine w, η and Φ, and to analyse the spatial distribution of strains proportional to w_{xx}.

3. Outline of the solution method

The boundary-value problem is solved by the vertical mode method.
In Region I,

$$\Phi_{\text{ref}} = \sum_{n=0}^{\infty} a_n e^{-ik_n x} f_n(z), \tag{9}$$

where k_n satisfy

$$k_n \tanh(k_n h) = \gamma. \tag{10}$$

For given γ, this equation has one positive real root k_0 and imaginary roots $k_n = i\alpha_n$ ($n \geq 1$). The vertical modes are

$$f_n(z) = \frac{\cosh(k_n(z+h))}{k_n \sinh(k_n h)},$$

with orthogonality

$$\int_{-h}^{0} f_n f_m \, dz = \sigma_{nn}\delta_{nm}, \qquad \sigma_{nn} = \frac{h(k_n^2 - \gamma^2) + \gamma}{2\gamma^2 k_n^2}.$$

In Region II,

$$\Phi_{\text{trn}} = \sum_{n=-2}^{\infty} b_n e^{i\xi_n x} g_n(z), \tag{11}$$

where ξ_n satisfy

$$\xi_n \tanh(\xi_n h)\big(1 - m\gamma + \beta(1 - i\varepsilon)\xi_n^4\big) = \gamma, \tag{12}$$

and corresponding vertical modes and ice deflection are

$$g_n(z) = \frac{\cosh(\xi_n(z+h))}{\xi_n \sinh(\xi_n h)}, \qquad w(x) = \sum_{n=-2}^{\infty} b_n e^{i\xi_n x}.$$

The modal series are truncated at $n = N_{\text{mod}}$. Substitution of the expansions into the continuity conditions at $x = 0$, followed by projection onto the modes $f_p(z)$ ($p = 0, \ldots, N_{\text{mod}}$), yields

$$\sigma_{pp}\, a_p - \sum_{m=-2}^{N_{\text{mod}}} F_{pm}\, b_m = -\,\sigma_{00}\, \delta_{p0}, \tag{13}$$

$$k_p\sigma_{pp}\,a_p + \sum_{m=-2}^{N_{\text{mod}}} \xi_m F_{pm}\,b_m = k_0\sigma_{00}\,\delta_{p0}, \tag{14}$$

where

$$F_{pm} = \int_{-h}^{0} f_p(z) g_m(z)\,dz.$$

The free-edge conditions (7) give two additional relations,

$$\sum_{m=-2}^{N_{\text{mod}}} \xi_m^2 b_m = 0, \qquad \sum_{m=-2}^{N_{\text{mod}}} \xi_m^3 b_m = 0. \tag{15}$$

We introduce the vectors of unknown coefficients

$$\mathbf{a} = \begin{bmatrix} a_0 & a_1 & \dots & a_{N_{\text{mod}}} \end{bmatrix}^\top, \qquad \mathbf{b} = \begin{bmatrix} b_{-2} & b_{-1} & b_0 & \dots & b_{N_{\text{mod}}} \end{bmatrix}^\top,$$

and define the diagonal matrices

$$\Sigma = \operatorname{diag}(\sigma_{00}, \dots, \sigma_{N_{\text{mod}}N_{\text{mod}}}), \qquad \mathbf{K} = \operatorname{diag}(k_0, \dots, k_{N_{\text{mod}}}),$$

$$\Xi = \operatorname{diag}(\xi_{-2}, \xi_{-1}, \dots, \xi_{N_{\text{mod}}}).$$

Let $\mathbf{F}$ be the matrix with entries F_{pm}, and

$$\mathbf{r}_2 = \begin{bmatrix} \xi_{-2}^2 & \xi_{-1}^2 & \dots & \xi_{N_{\text{mod}}}^2 \end{bmatrix}, \qquad \mathbf{r}_3 = \begin{bmatrix} \xi_{-2}^3 & \xi_{-1}^3 & \dots & \xi_{N_{\text{mod}}}^3 \end{bmatrix}.$$

Then the system (13)–(15) can then be written in block form as

$$\begin{bmatrix} \Sigma & -\mathbf{F} \\ \mathbf{K}\Sigma & \mathbf{F}\Xi \\ \mathbf{0} & \begin{bmatrix} \mathbf{r}_2 \\ \mathbf{r}_3 \end{bmatrix} \end{bmatrix} \begin{bmatrix} \mathbf{a} \\ \mathbf{b} \end{bmatrix} = \begin{bmatrix} -\sigma_{00}\mathbf{e}_0 \\ k_0\sigma_{00}\mathbf{e}_0 \\ \begin{bmatrix} 0 \\ 0 \end{bmatrix} \end{bmatrix}, \tag{16}$$

where $\mathbf{e}_0 = (1, 0, \dots, 0)^\top$.

Equation (16) is a linear algebraic system for the modal coefficients $\mathbf{a}$ and $\mathbf{b}$.

4. Numerical and analytical results

The computations of the ice-plate response were carried out for the following parameters: $\rho_i = 917$ kg/m^3, $\rho = 1024$ kg/m^3, $g = 9.8$ m/s^2, $E = 4.2 \times 10^9$ Pa, $\nu = 2$. The ice thickness varied from 0.025 to 1 m, the incident-wave frequency ω ranged from 0 to 20 s^{-1}, and the retardation time τ from 0 to 20 s. The characteristic length scale was chosen as the water depth, $L_{sc} = H$.

Before computing the deflections, it is necessary to determine the wavenumbers k_n and ξ_n. There are no particular difficulties in evaluating the fluid wavenumbers, while the calculation of plate wavenumbers requires special care due to the nature of the dispersion equation.

4.1. Discussion of wave numbers

Figure 2 shows the evolution of the wave numbers $\xi_{-2,-1,0}$ for different values of h_i and increasing $\omega \in (0, 20]$. The real root ξ_0, corresponding to the travelling wave with wavelength $2\pi/\xi_0$, increases as ω increases. Increasing thickness slows this growth; for fixed remaining parameters, ξ_0 is smaller for a thicker plate. The roots $\xi_{-2,-1}$ represent damped corrections to the plate response, and their contribution remains significantly larger than that of the purely imaginary roots (whose variations are negligible and

therefore not shown). The behaviour of $\xi_{-2,-1}$ differs from that of ξ_0. With increasing frequency, the imaginary parts of these roots increase, leading to stronger spatial damping of this contribution. Increasing thickness reduces the absolute values of these roots, similarly to the real root. A specific feature is observed as frequency varies: as shown in Figures 2(b)–(c), the roots approach a common point on the imaginary axis, forming a double root. With further increase in frequency, they split and move along the imaginary axis, may form another double root, and then separate again. This behaviour is not observed for relatively small or large thicknesses within the considered frequency range.

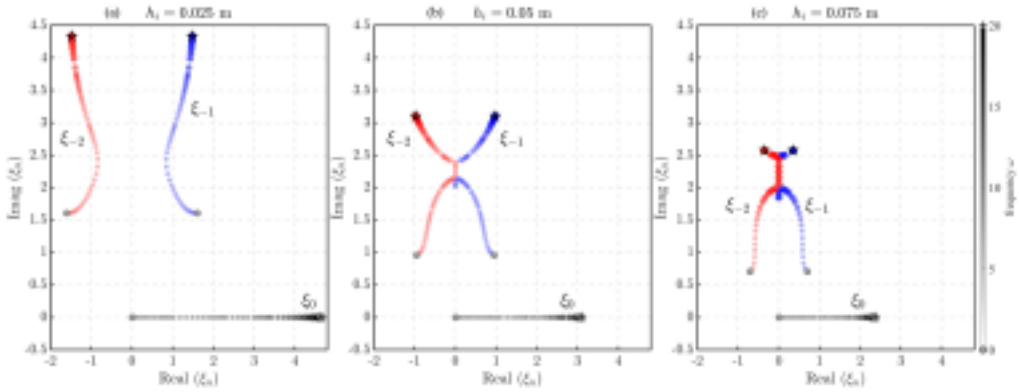


Figure 2: Evolution of the first three (primary) wave numbers of the plate with increasing frequency ω. The smallest value of $\omega = 0.01$ 1/s is marked by gray unit markers. Then, according to the color bar and frequency, the corresponding position of the root is displayed by an increasing size marker and increasing transparency. The final position is marked with an asterisk.

Figure 3 illustrates the evolution of the wave numbers $\xi_{-2,-1,0,1}$ for the viscoelastic plate for different h_i, ω, and increasing retardation time $\tau \in (0, 20]$. In most cases, the purely imaginary roots $\xi_n, n \geq 1$ are almost unaffected by viscosity. The roots $\xi_{-2,-1,0}$ move along an arc towards the origin. The real root becomes complex for any $\tau > 0$, indicating spatial damping; its real part decreases and the wavelength increases. The strongest variation of the roots occurs for relatively small τ, after which the changes become gradual (for example, around $\tau \approx 3$ s for $h_i = 0.025$ m). At higher frequencies, the magnitudes of the wave numbers are more sensitive to viscosity. The imaginary part of the former real root attains its maximum at relatively small τ. For small thicknesses, an additional feature is observed: the roots ξ_{-1} and ξ_1 may interchange as τ increases, approaching the imaginary axis. Their initial distance from the origin plays an essential role. Increasing thickness reduces the absolute values of all wave numbers; for example, at $\tau = 20$ s the magnitudes are almost twice smaller for $h_i = 0.1$ m than for $h_i = 0.025$ m. In general, Figure 2 indicates two positions of double roots $\xi_{-2,-1}$ corresponding to different frequencies. Figure 4(a) presents the curves of double roots on the (ω, h_i) plane. These curves originate from a single point and increase rapidly with ω. The region between them corresponds to configurations where $\xi_{-2,-1}$ lie on the imaginary axis. This region expands as frequency and thickness increase. For $h_i > 0.082$ m, double roots also occur, but at higher frequencies. Double roots arise only for certain combinations of (ω, h_i).

The triple point is marked in Figure 4(a). It represents the apex of the double-root curves, from which two branches emerge and then diverge without forming additional triple points. Figures 4(b)–(c) illustrate the approach and separation of the roots forming the triple point. This triple root involves ξ_{-2}, ξ_{-1} and ξ_1.

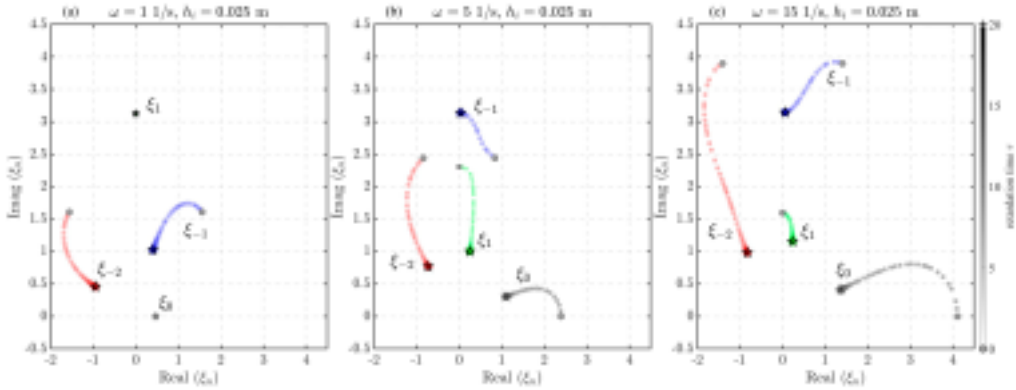


Figure 3: Evolution of the first four wave numbers of the plate with increasing retardation time τ. The smallest value of $\tau = 0.01$ s is marked by gray unit markers. Then, according to the color bar and retardation time, the corresponding position of the root is displayed by an increasing size marker and increasing transparency. The final position is marked with an asterisk.

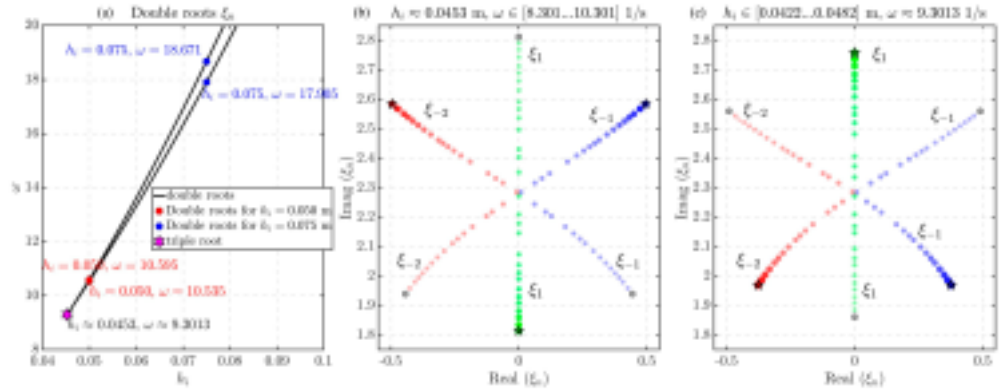


Figure 4: Lines of double roots on the (ω, h_i) plane with the single triple root marked (a). The approach and separation of the roots $\xi_{-2,-1,1}$ forming the triple root to a single value for fixed thickness (b) and frequency (c).

4.2. Discussion of plate oscillation results

The deflections of the ice were calculated for the given parameters of the problem and the range of values for ω, τ, and h_i using the vertical mode method described in section 3. An important point is considering the required number of modes for obtaining an accurate solution. In most cases, the contributions of imaginary roots ξ_n, $n \geq 10$, described by the coefficients b_n, to the deflections of the ice were negligible. For example, around 10^{-12} in most cases, and up to 10^{-7} for small ice thickness and high frequency for b_{10}, and around 10^{-15} in most cases and up to 10^{-8} for small ice thickness and high frequency for b_{20}. In our calculations, we used $N = 30$.

Figure 5 shows typical shapes of the free surface, ice deflections, and maximum strains along the plate thickness resulting from the impact of the incoming wave. The results are shown for $h_i = 0.1$ m,

$\omega = 1.75$ 1/s, and for different τ. The x axis is normalized by the wavelength, i.e., x/λ, where λ is the wavelength for each specific case. For the liquid, elastic, and viscoelastic plates, the wavelength will be different. It is important to note that for $\tau = 1$, strong damping in the ice plate is already observed. The maximum deflections occur at the plate edge, and they can be larger than the wave amplitudes on the free surface. The amplitudes of the deflections in the depth of the plate are generally always smaller than the wave amplitudes on the free surface.

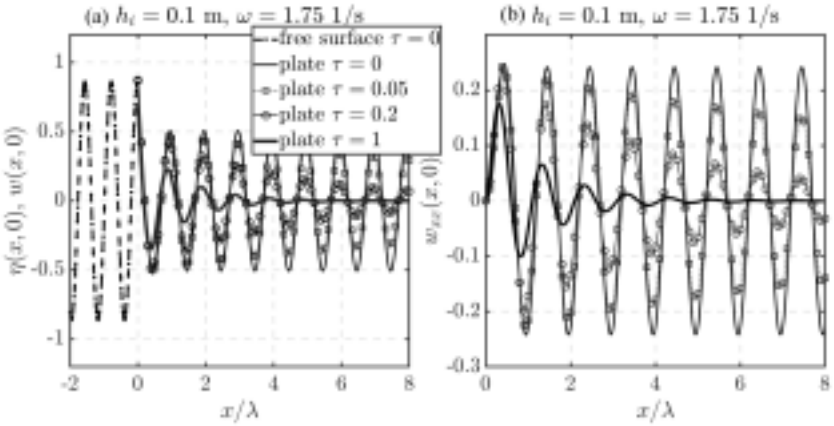


Figure 5: Typical shapes of the free surface (a), ice deflections (b), and maximum strains (c) along the plate thickness due to the impact of the incoming wave. Significant damping of deflections away from the edge is observed with increasing viscosity parameter, τ.

The primary quantities of interest in this study are the maximum absolute deflections and strains over time, which form the basis for analysis within the framework of the harmonic solution. Viscous damping has a relatively minor effect on deflections at the plate edge compared to regions farther away. The maximum strains for some frequencies exhibit a well-defined peak: they increase from zero at the edge, reach a maximum, and then decrease to a constant value. If the amplitude of the incoming wave is gradually increased such that only this peak value reaches the critical threshold, it is reasonable to assume that the ice will fail at the location of maximum strain. However, such peaks are not always present. Figure 6(a) illustrates the distributions of the maximum absolute strains in the ice cover for an elastic plate at different frequencies. For frequencies of 1 and 1.25 1/s, which do not correspond to extrema within the considered range, no distinct peak is observed. Instead, the strains increase to a local maximum near the edge, but further along the plate they attain a constant value that exceeds this initial maximum. This behavior contrasts with the viscoelastic case shown in Figure 6(b), where distinct peaks in the maximum absolute strains are consistently observed, even for very low viscosity.

Figure 7 presents a contour plot showing the distance L of the peak maximum strain's location from the plate edge, when such a peak exists, on the $[\omega, h_i]$ plane. The peak is typically observed when the ratio L/λ is less than 0.5. In Figure 7, these regions are marked in red tones, while blue regions correspond to $L/\lambda > 0.5$. As frequency increases and the wavelength decreases, a zone appears where the maximum strains are distributed along the plate. Due to numerical sensitivity, the value of L in this regime may be determined with reduced accuracy. To define the fracture location consistently, we evaluate L using the viscoelastic plate with $\tau = 10^{-5}$; otherwise, the global maximum is taken. In some cases, the potential fracture point may reach up to two wavelengths from the edge. In most cases (the pink region), the plate breaks at approximately 0.435–0.475λ from the edge.

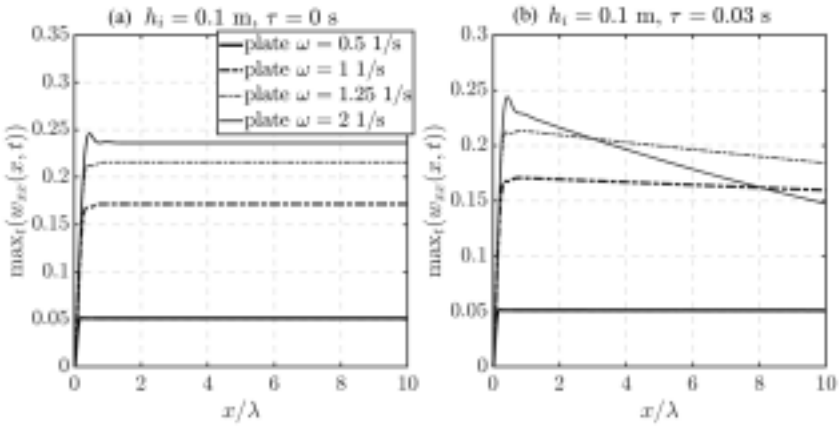


Figure 6: Absolute maximum strains over time in the ice cover for an elastic (a) and viscoelastic (b) plate at different frequencies.

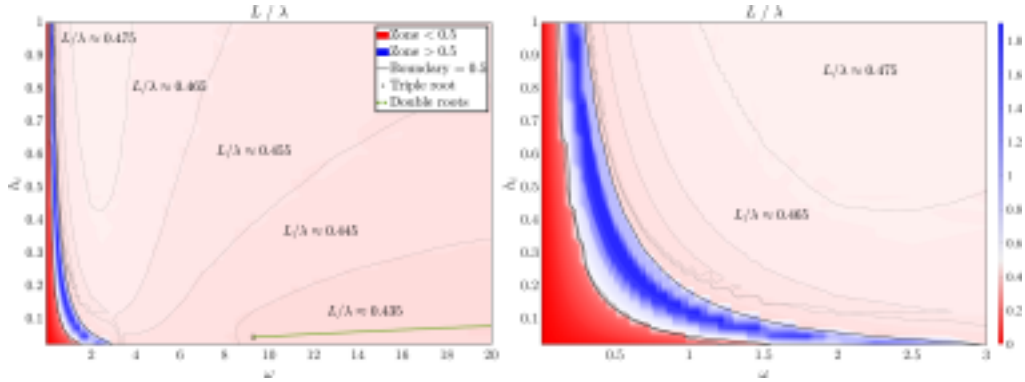


Figure 7: Distance of the peak maximum strains over time from the edge of the plate in relation to the wavelength.

5. Detached Plate at the Maximum Strain Point

Having computed the location of maximum strains in the previous section, we can now consider the following problem: Suppose that the plate completely breaks off at this point ($x = L > 0$). Then, we have a small detached plate and the remaining semi-infinite one. The boundary conditions for both plates are free edge conditions. The scheme is shown in Figure 8. On the left ($-\infty < x < 0$) is the free surface (Region I), and in the interval $0 < x < L$ (Region II), we sequentially consider three alternative physical models: broken ice (described by plate's equation with zero rigidity), finite elastic/viscoelastic plate and rigid plate. To the right of the crack, at $x > L$, is the semi-infinite plate (Region III), which is either elastic at $\varepsilon = 0$ or viscoelastic at $\varepsilon > 0$. As before, in Region I (free surface, $x < 0$), the incident wave is set, and the reflected wave is expanded using vertical modes. At the boundary between regions, the potentials satisfy the continuity conditions for the potential itself and its longitudinal derivative.

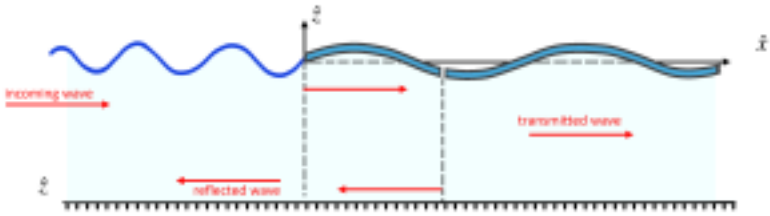


Figure 8: Scheme of the problem with a detached piece of ice.

Option A: Broken Ice on $0 < x < L$

In this model, the detached segment is treated as a layer of broken ice that possesses inertia but does not sustain bending stresses. The central region is therefore described by a modified dispersion relation that accounts only for the mass effect without flexural rigidity. The velocity potential in this region is represented by two series of vertical mode expansions, allowing for reflections at both interfaces $x = 0$ and $x = L$. Continuity of the potential and its longitudinal derivative is imposed at both boundaries, while the semi-infinite plate to the right is modelled in the same way as in the base problem. The resulting algebraic system determines the modal amplitudes in all regions.

Option B: Finite Elastic or Viscoelastic Plate on $0 < x < L$

In this case, the detached segment is modelled as a finite elastic or viscoelastic plate with free-edge conditions at both ends. Its material parameters may differ from those of the remaining semi-infinite plate. The solution in the central region is constructed using longitudinal modal expansions consistent with the plate dispersion relation. Matching conditions for the velocity potential and its derivative are imposed at $x = 0$ and $x = L$, and free-edge conditions are enforced at both edges of the finite plate. This formulation leads to a coupled algebraic system that determines the wave amplitudes in the free-surface region, the finite plate, and the semi-infinite plate.

Option C: Finite Plate Modelled by Normal Modes

In this formulation, the detached segment is represented using the normal modes of a finite beam with free edges. The plate deflection is expanded in terms of rigid-body and elastic vibration modes. For each structural mode, an associated fluid potential satisfying Laplace's equation is constructed, and an additional corrective potential is introduced to ensure matching at the interfaces. Continuity conditions at $x = 0$ and $x = L$, together with the projected plate equation, yield a linear system for the modal coefficients. The semi-infinite plate to the right is treated as in the original configuration, with its free-edge conditions preserved.

5.1. Numerical results after first break up event

Let us assume that the plate has already fractured at the point of maximum strain. The system consists of a free surface on the left, a finite floating plate in the centre (modelled in four different ways), and a remaining semi-infinite plate on the right. The main result is that, for a wide range of problem

parameters (ice thickness h_i and frequency ω), the modelling approach for the broken-off part does not play a significant role. For elastic, viscoelastic, and rigid plates, the results are nearly identical. The only major difference appears for the broken-ice model, which exhibits a distinct oscillation pattern.

The key feature of these results is that, when the time-dependent maxima of deflection and strain are computed, the spatial pattern remains similar to that observed before the first fracture. The maximum deflection occurs at the edge, and then decreases with distance, approaching a constant value. Pronounced strain peaks are also present (Figure 9). The magnitudes of these peak strains are slightly smaller than those before the first fracture. This suggests a possible sequential failure scenario: the plate may continue to fracture at approximately the same distance from the edge each time, while the amplitude of the incident wave required to induce the next fracture gradually increases.

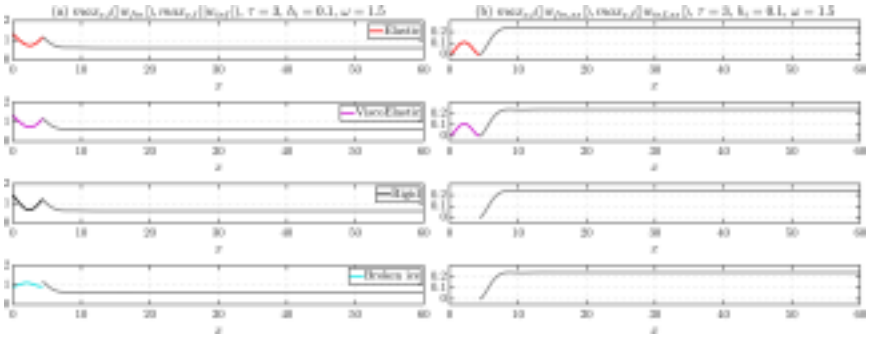


Figure 9: Maximum in time deflections of the detached and main semi-infinite parts (a), and the corresponding maximum in time strains (b) over time for four models of the broken-off plate. The case of an elastic plate, $\tau = 0$, is considered.

6. Conclusions

Oscillations of a semi-infinite viscoelastic ice plate subjected to an incident harmonic wave have been analysed within linear hydroelastic theory. The solution has been constructed by expanding the fluid velocity potential into vertical modes in each region and enforcing continuity and free-edge conditions, which reduce the problem to a system of linear algebraic equations for the modal coefficients.

The complex wave numbers determined from the plate dispersion relation have been examined as functions of frequency, thickness and viscosity. In the elastic case, the spectrum consists of one real root, a complex-conjugate pair and a countable set of imaginary roots. Double and a single triple root were identified within the considered parameter range. For the viscoelastic plate, all roots become complex and move continuously in the complex plane as viscosity increases; multiple roots were not observed in this case.

The spatial distributions of time-dependent maximum deflections and strains have been studied. The largest deflections occur at the plate edge, while the maximum strains typically form a peak at a finite distance from the edge, proportional to the wavelength. Viscosity leads to spatial damping of oscillations and reduces strain amplitudes, with the strongest effect observed for relatively small values of the retardation parameter.

After identifying the position of maximum strain, a model with a detached fragment has been considered in simplified form. Different representations of the broken-off part lead to qualitatively similar responses of the remaining semi-infinite plate, except in the case of the broken-ice model. The results

indicate that repeated fracture may occur at comparable relative distances from the plate edge under increasing wave amplitude.

Acknowledgments

The work of KS and BN is supported by the National Natural Science Foundation of China (Nos. W2433140, W2541018 and 52521009). The work of TK and AK is supported by the Leverhulme Trust (Grant RPG-2025-307).

References

[1] V.A. Squire, R. Hosking, A. Kerr, and P.J. Langhorne. *Moving Loads on Ice Plates*. Kluwer: Dordrecht, The Netherlands, 1996.

[2] E.A. Batyaev and T.I. Khabakhpasheva. Hydroelastic waves in a channel covered with a free ice sheet. *Fluid Dynamics*, 50(6):775–788, 2022.

[3] K.A. Shishmarev, T.I. Khabakhpasheva, and A.A. Korobkin. The response of ice cover to a load moving along a frozen channel. *Appl. Ocean Res.*, 59:313–326, 2016.

[4] T.A. Sibiryakova, K.E. Naidenova, and K.A. Shishmarev. Movement of a submerged body along a frozen channel covered by inhomogeneous ice (in russian). *Transactions of the Krylov State Research Centre*, Special Issue 1:177—-184, 2024.

[5] M. Kashiwagi. Research on hydroelastic responses of vlfs:recent progress and future work. *Int. J. Offshore Polar Eng.*, 10(2):81–90, 2000.

[6] E. Watanabe, T. Utsunomiya, and C.M. Wang. Hydroelastic analysis of pontoon-type vlfs:a literature survey. *Eng Struct.*, 26(2):245–256, 2004.

[7] X. Chen, Y. Wu, W. Cui, and J.J. Jensen. Review of hydroelasticity theories for global response of marine structures. *Ocean Eng.*, 33:439–457, 2006.

[8] D. Karmakar, J. Bhattacharjee, and T. Sahoo. Wave interaction with multiple articulated floating elastic plates. *J. Fluids Struct.*, 25:1065–1078, 2009.

[9] M.A. Peter, M.H. Meylan, and H. Chung. Wave scattering by acircular elastic plate in water of finite depth: a closed form solution. *Int. J. Offshore Polar .Eng.*, 14(2):81–85, 2004.

[10] F. Montiel, L. G. Bennetts, V. A. Squire, F. Bonnefoy, and P. Ferrant. Hydroelastic response of floating elastic discs to regular waves. part 2. modal analysis. *Journal of Fluid Mechanics*, 723:629–652, 2013.

[11] A. Korobkin, S. Malenica, and T. Khabakhpasheva. Interaction of flexural-gravity waves in ice cover with vertical walls. *Philos. Trans. Roy. Soc. A: Math. Phys. Eng. Sci.*, 376(2129):20170347, 2018.

[12] D.V. Evans and R. Porter. Wave scattering by narrow cracks in ice sheets floating on water of finite depth. *J. Fluid Mech.*, 484:143–165, 2003.

[13] S.R. Manam, J. Bhattacharjee, and T. Sahoo. Expansion formulae in wave structure interaction problems. *TProc. R. Soc. A*, 462:263–287, 2006.

[14] J.B. Lawrie and I.D. Abrahams. On the propagation and scattering of fluid-structural waves in a three-dimensional duct bounded by thin elastic walls. *Springer Netherlands, IUTAM Symposium on Diffraction and Scattering in Fluid Mechanics and Elasticity*, pages 279–288, 2002.

[15] J.B. Lawrie and I.D. Abrahams. An orthogonality relation for a class of problems with high-order boundary conditions; applications in sound-structure interaction. *Q. J. Mech. Appl. Math.*, 52(2):161–181, 1999.

[16] D. Alex, R. Ashok, and N. Balasubramani. Hydroelastic analysis of a forced circular elastic floating plate in the presence of porous barrier. *Applied Ocean Research*, 150:104085, 2024.

[17] L.G. Bennets. *Wave scattering by ice sheets of varying thickness*. PhD thesis, University of Reading, UK, 2007.

10th International Conference on HYDROELASTICITY IN MARINE TECHNOLOGY
Trondheim, Norway, June16th-18th, 2026

Ice Sheet Response to a High-Speed Vessel Moving in Open Water along the Ice Edge

Korobkin, A.,* Khabakhpasheva, T.

School of Engineering, Mathematics and Physics, University of East Anglia, Norwich, UK

Abstract. This paper investigates the potential fracture of a continuous ice sheet with a free edge induced by a high-speed vessel travelling at constant velocity near the ice boundary. The hydrodynamic pressure distribution along the ice–water interface is determined within the framework of linear 2D+T potential-flow theory, assuming a rigid ice cover. For high-speed vessels with a transom stern, the flow in each vertical control plane normal to the vessel's direction of motion is described using the Wagner model for two-dimensional slamming. The gravity-driven flow in the wake behind the vessel is neglected. Analytical expressions for the pressure distribution and flow velocity are derived and systematically analysed with respect to the vessel's geometry, speed, and distance from the ice edge. Far-field asymptotic solutions are obtained to provide simplified representations of the flow at large distances from the vessel. The resulting ice deflection and strain fields are then evaluated using a decoupled hydroelastic formulation, and the validity of this approximation is assessed. Finally, several ice-failure criteria are applied to identify the regions where fracture initiation is most likely to occur.

Key words: *ice sheet; 2D+T theory; decoupled approach; ice strains; ice fracture*

1. Introduction

Transportation in the Arctic on ice, under ice, and close to the ice cover can be disturbing for the environmental conditions. Navigation in the Arctic contributes to sea ice breakup as ship-generated loads reduce ice cover and accelerate global warming.

Navigation in ice-covered waters has traditionally been studied primarily in terms of the ice loads acting on ships and the associated increase in fuel consumption caused by ice present on or near the ship's route. It was shown in [1] that the influence of a continuous ice sheet on a ship navigating at low speed in open water near an ice field can be reasonably estimated by modelling the ice as rigid. However, the effect of ice flexibility becomes increasingly significant as the ship speed increases and the distance to the ice edge decreases. The rigid, undeformable ice model was also adopted in [2] for high-speed vessels operating at large distances from the ice edge.

The problem of flexural–gravity waves generated by a vessel and propagating through an ice cover remains computationally challenging, see [3]. The wave patterns produced by ships—idealised as moving pressure distributions—travelling along straight or curved trajectories have been shown to be highly complex and sensitive to the ship speed and path geometry, see [4]–[7].

In this study, the ice sheet is modelled as semi-infinite with a straight edge. A high-speed vessel moves in open water at constant speed while maintaining a fixed distance from the ice edge. Gravitational effects are neglected. The vessel geometry plays a crucial role in determining the hydrodynamic loads exerted on the ice sheet. This problem is analysed within a decoupled model using the strip theory for potential flows. In this theory, applicable to slender bodies, a vertical control plane perpendicular

*Correspondence to: a.korobkin@uea.ac.uk

to the direction of the vessel motion is introduced, and the three-dimensional flow is approximately described by a sequence of two-dimensional problems.As the vessel passes through the control plane, it generates a two-dimensional flow within this vertical section with the velocity component of the flow normal to the plane being negligible to leading order. The problem of a high-speed ship using the strip theory is equivalent to the two-dimensional problem of water impact by a contour, which changes its shape in time, see [8]. The gravity-driven flow in the wake behind the vessel is neglected. In the coordinate system moving together with the vessel, the vessel induces a stationary hydrodynamic pressure acting on the ice/water interface. For the rigid ice model, this pressure can be calculated analytically using the Wagner model of water entry.

Regarding existing high-speed vessels designed for Arctic operation, the expedition ice-class research vessel Le Commandant Charcot has a length of 150 m, a beam of 28.3 m, a draught of 10 m, and a maximum speed of 15 knots in open water. It is equipped a broad, near-vertical transom stern, which in open water behaves hydrodynamically like a conventional transom stern . In comparison, the Arctic LNG carrier Christophe de Margerie measures 299 m in length, 50 m in beam, 11.8 m in draught, and can reach speeds up to 19.5 knots. In open water, this vessel behaves as a conventional large commercial ship with a transom stern. Formally, neither vessel can be classified as high-speed, since their Froude numbers are 0.20 and 0.18, respectively, both below the conventional threshold value of 0.4. In contrast, the BAE Systems Arctic 24, a rigid inflatable boat designed for operation in severe environments and search-and-rescue missions, represents a genuinely high-speed craft, with a Froude number reaching 2.94 at its maximum speed of 50 knots. The vessel has a length of 7.8 m, a beam of 2.54 m, and a maximum draught of 0.80 m.

These examples demonstrate that modern Arctic high-speed vessels are typically slender, have relatively shallow draughts, capable of high-speed navigation, and are with transom stern. The presence of a transom stern is particularly relevant for hydrodynamic modelling, as it reduces wave formation in the wake and simplifies the 2D+T formulation by providing a well-defined flow separation point.

The problem of a vessel advancing through a lead between rigid or elastic ice sheets has been investigated numerically in [1, 9], where gravitational effects and the waves generated by the vessel were taken into account. The interaction of a high-speed vessel with rigid ice was further examined in [2], where the fully nonlinear hydrodynamic problem including gravity was solved numerically for finite water depth.

In the present paper, we focus on the hydrodynamic pressure distribution along the ice–water interface induced by a vessel travelling near the ice edge, and on the corresponding deflection of the ice sheet.

2. Formulation of the problem for elastic ice

The three-dimensional problem of a vessel travelling at constant speed U in open water near an ice sheet is formulated in a coordinate system $Oxyz$ moving with the vessel. The fluid occupies the half-space $y < 0$. The boundary of the flow domain is covered by the ice sheet for $x > 0$ and $-\infty < z < \infty$, while for $x < 0$ the surface is ice-free (see Fig. 1). The vessel moves in open water with its centreplane located at a distance d from the ice edge $x = 0$.

The liquid is assumed to be incompressible and inviscid, and the flow generated by the vessel is taken to be potential and steady in the moving reference frame. The analysis is carried out within the framework of linear hydroelasticity. The ice sheet is modelled as a thin, homogeneous elastic plate of constant thickness and zero draught, with its edge free of bending moments and shear forces.

Gravity is retained in the formulation in order to establish the conditions under which its influence may be neglected and the 2D+T approximation becomes applicable. The range of validity of the linear theory itself is not addressed here.

The linear problem is formulated in terms of the velocity potential $\phi(x, y, z)$ and the normal deflection of the ice sheet $w(x, z)$. These functions satisfy the following governing equations and boundary

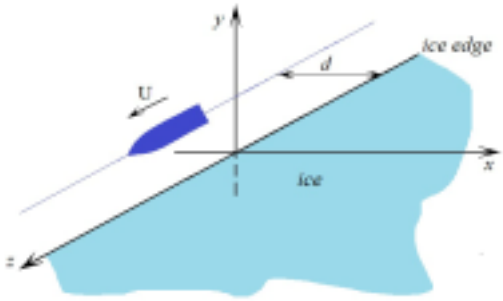


Figure 1: A vessel travelling in open water at a constant speed U parallel to the ice edge.

conditions:

$$\nabla^2\phi + \phi_{yy} = 0 \quad (y < 0, -\infty < z < \infty, -\infty < x < \infty), \tag{1}$$

$$mU^2 w_{zz} + D\nabla^4 w = p(x,0,z) \quad (x > 0, -\infty < z < \infty), \tag{2}$$

$$p(x,0,z) = \rho U \phi_z - \rho g w(x,z) \quad (x > 0, -\infty < z < \infty), \tag{3}$$

$$\phi_y = -U w_z \quad (x > 0, -\infty < z < \infty), \tag{4}$$

$$U^2\phi_{zz} + g\phi_y = 0 \quad (x < 0, -\infty < z < \infty, (x,z) \notin S_v), \tag{5}$$

$$\phi_y = f_x\phi_x + f_z(\phi_z - U) \quad (x < 0, (x,z) \in S_v), \tag{6}$$

$$w_{xx} + \nu w_{zz} = 0, \qquad w_{xxx} + (2-\nu) w_{zzx} = 0 \quad (x = 0, -\infty < z < \infty), \tag{7}$$

$$\phi(x,y,z) \to 0, \qquad w(x,z) \to 0 \quad (x^2 + y^2 + z^2 \to \infty). \tag{8}$$

In these equations, $\nabla^2 = \partial^2/\partial x^2 + \partial^2/\partial z^2$, m is the mass of the ice plate per unit area, D is the flexural rigidity of the ice sheet, ν is Poisson's ratio of the ice, $p(x,0,z)$ is the hydrodynamic pressure at the ice-water interface, ρ is the water density, g is the gravitational acceleration, S_v is the projection of the wetted part of the vessel onto the plane $y = 0$.

The function $y = f(|x + d|, z)$ appearing in the boundary condition (6) on the hull of the vessel describes the geometry of the hull surface, where d is the distance between the vessel centreplane and the ice edge. Let L denote the vessel length, B the beam, and H the draught. We assume that the vessel is slender, $\mu = B/L \ll 1$, has small draught, $\delta = H/B \ll 1$, and travels close to the ice edge, so that $\lambda = d/B = O(1)$.

We focus on the flow in the vicinity of the vessel. The corresponding dimensionless variables (denoted by a tilde) are introduced as

$$\tilde{x} = \frac{x}{B}, \quad \tilde{y} = \frac{y}{B}, \quad \tilde{z} = \frac{z}{L}, \quad \phi = \frac{HBU}{L}\tilde{\phi}(\tilde{x},\tilde{y},\tilde{z}), \quad w = \delta\mu^2\frac{\rho U^2 B^4}{D}\tilde{w}, \quad p = \rho U^2\delta\mu^2\tilde{p}, \tag{9}$$

and the shape of the hull reads now $\tilde{y} = \delta\tilde{f}(|\tilde{x} + \lambda|, \tilde{z})$. The scaling of the velocity potential follows from the body boundary condition (6). The pressure scaling is obtained from the linearised Bernoulli equation (3), while the scaling for the ice deflection is derived from the thin-plate equation (2).

Equations (1)–(8) written in the dimensionless variables (9) take the following form (the tildes are omitted hereafter for brevity):

$$\phi_{xx} + \phi_{yy} + \mu^2\phi_{zz} = 0 \quad (y < 0, -\infty < z < \infty, -\infty < x < \infty), \tag{10}$$

$$\eta_0 w_{zz} + w_{xxxx} + 2\mu^2 w_{xxzz} + \mu^4 w_{zzzz} = p(x,0,z) \quad (x > 0, -\infty < z < \infty), \tag{11}$$

$$p(x,0,z) = \phi_z - \eta_1 w(x,z) \quad (x > 0, y = 0, -\infty < z < \infty), \tag{12}$$

$$\phi_y = -\eta_2 w_z \quad (y=0, x>0, -\infty<z<\infty), \tag{13}$$

$$\phi_{zz} + \eta_3 \phi_y = 0 \quad (y=0, x<0, -\infty<z<\infty, (x,z)\notin S_v), \tag{14}$$

$$\phi_y = \delta f_x \phi_x + f_z(\delta\mu^2\phi_z - 1) \quad (y=0, x<0, (x,z)\in S_v), \tag{15}$$

$$w_{xx} + \nu\mu^2 w_{zz} = 0, \qquad w_{xxx} + (2-\nu)\mu^2 w_{zzx} = 0 \quad (x=0, -\infty<z<\infty), \tag{16}$$

$$\phi(x,y,z)\to 0, \qquad w(x,z)\to 0 \quad (x^2+y^2+z^2\to\infty). \tag{17}$$

The new parameters in (11) – (14) are

$$\eta_0 = \frac{\rho_i h_i U^2 B^4}{DL^2}, \quad \eta_1 = \frac{\rho g B^4}{D}, \quad \eta_2 = \frac{\rho U^2 B^5}{DL^2}, \quad \eta_3 = \frac{gL^2}{BU^2}, \quad D = \frac{E h_i^3}{12(1-\nu^2)}. \tag{18}$$

Here, ρ_i denotes the ice density, h_i the ice thickness, and E Young's modulus. The parameter η_0 characterises the importance of ice inertia. It increases with increasing vessel speed U. The parameter η_1 measures the relative importance of the hydrostatic pressure compared with the dynamic pressure acting on the ice. This parameter is independent of the vessel speed. The parameter η_2 governs the coupling between the hydrodynamic problem and the structural response of the ice sheet. The problem becomes decoupled when $\eta_2 \ll 1$. The parameter η_3 indicates the importance of gravity in the free-surface condition. If η_3 is small, gravitational effects may be neglected in the free-surface condition (14). If $\eta_3 \gg 1$, the free surface can be approximated as a rigid plate.

A deeper understanding of the possible regimes of ice response to the vessel-generated flow can be obtained by noting that

$$\eta_2\eta_3 = \eta_1, \quad \eta_1 = \Big(\frac{B}{L_c}\Big)^4, \quad \eta_3 = \frac{1}{Fr^2\mu}, \quad \eta_0 = \frac{\rho_i}{\rho}\frac{h_i B}{L^2}\eta_1, \quad L_c = \Big(\frac{D}{\rho g}\Big)^{1/4}, \quad Fr = \frac{U}{\sqrt{gL}}, \tag{19}$$

where L_c is the characteristic length of the ice sheet and Fr is the Froude number.

For the sea-ice parameters reported in [11], $\rho = 1026$ kg/m^3, $\rho_i = 917$ kg/m^3, $E = 4.2\times10^9$ N/m^2, $\nu = 0.33$, ice thickness $h_i = 1$ m, and for the boat BAE Systems Arctic 24 with $L = 7.8$ m, $B = 2.54$ m, $H = 0.8$ m, and $Fr = 2.94$, we have $L_c = 14$ m and

$$\mu = 0.325, \quad \delta = 0.315, \quad \eta_0 = 0.000038, \quad \eta_1 = 0.001, \quad \eta_2 = 0.0028, \quad \eta_3 = 0.356. \tag{20}$$

The values (20) indicate that the boat is slender (small μ), with shallow draught (δ is small), inertia of the ice can be neglected, $\eta_0 \ll 1$, hydrostatic pressure can be neglected compared with the dynamic pressure, $\eta_1 \ll 1$ and $\eta_3 \ll 1$, the problem is approximately decoupled, $\eta_2 \ll 1$, with the hydrodynamic pressure being independent of the ice deflection.

If only the ice thickness varies, introducing the dimensionless thickness $\bar{h}_i = h_i/1\,\text{m}$, we find that the parameters μ, δ and η_3 are independent of $\bar{h}_i$, whereas the remaining parameters scale as

$$\eta_0 = \bar{\eta}_0 \bar{h}_i^{\frac{1}{4}}, \quad \eta_1 = \bar{\eta}_1 \bar{h}_i^{-\frac{3}{4}}, \quad \eta_2 = \bar{\eta}_2 \bar{h}_i^{-\frac{3}{4}}, \tag{21}$$

where the overbar denotes the corresponding values for an ice thickness of 1 m given in (20). Relations (21) indicate that the hydroelastic problem becomes fully coupled, with $\eta_2 = O(1)$, only when $h_i = O(0.4\,\text{mm})$. Hence, for any practically relevant ice thickness, the modelling of the high-speed boat interaction with the ice plate is the same as for $h_i = 1$ m.

Within the 2D + T theory, the problem may be treated as decoupled ($\eta_2 \ll 1$) and without gravity at the free surface ($\eta_3 \ll 1$) only for sufficiently high vessel speeds and small beam B. In this regime, gravity may also be neglected in the Bernoulli equation (12), and the structural inertia becomes negligible ($\eta_0 \ll 1$). The resulting hydrodynamic problem remains non-trivial and corresponds to a water-entry problem without gravity in the presence of a semi-infinite rigid plate on the free surface. However, the associated structural problem is not expected to admit a solution, since the limiting plate

equation, $w_{xxxx} = \phi_z(x, 0, t)$, cannot satisfy simultaneously the edge conditions (16) and the far-field conditions (17). For this reason, we assume $\eta_1 \ll 1$, $\eta_2 \ll 1$, and $\eta_3 \ll 1$, while retaining η_0 in the plate equation (11) in order to regularise the simplified problem. Another possible regularisation consists in setting $\eta_0 = 0$ while retaining η_1 in equation (12) for the pressure along the ice–water interface. Both regularisations may, however, be avoided if the solution of (10)–(17) with all parameters set to zero is interpreted as an inner solution. This inner solution should then be matched to an outer solution defined on the linear spatial scale of the ship length, see [10].

3. Solution of the simplified problem

Within the leading-order approximation, the governing equations of the simplified problem follow from (10)–(17) by setting $\mu = 0$, $\eta_0 = 0$, $\eta_2 = 0$, and $\eta_3 = 0$, while retaining η_1. To emphasise the analogy between this simplified model for a slender vessel and Wagner's water-impact theory, we replace the horizontal coordinate z with a fictitious time variable $-\tau$. We choose $\tau = 0$ at the bow of the vessel and $\tau = 1$ at the stern.

The hydrodynamic part of the problem then reads

$$\begin{gathered}
\phi_{xx} + \phi_{yy} = 0 \quad (y < 0,\ -\infty < x < \infty, 0 < \tau < 1),\\
\phi_y(x, y, \tau) = -f_z(|x + \lambda|, -\tau) \quad (y = 0,\ a(\tau) < x < b(\tau)),\\
\phi_y(x, y, \tau) = 0 \quad (y = 0,\ x > 0),\\
\phi_{\tau\tau}(x, y, \tau) = 0 \quad (y = 0,\ x < a(\tau) \text{ and } b(\tau) < x < 0),\\
\phi(x, y, \tau) = 0\ (\tau < 0), \quad \phi(x, y, z) \to 0\ (x^2 + y^2 \to \infty,\ 0 < \tau < 1),
\end{gathered} \tag{22}$$

and the ice deflection is governed by the equations

$$\begin{gathered}
w_{xxxx} + 4q^4 w = P(x, \tau) \quad (x > 0,\ 0 < \tau < 1),\\
w_{xx}(0, \tau) = w_{xxx}(0, \tau) = 0, \quad w(x, \tau) \to 0 \quad (x \to \infty),
\end{gathered} \tag{23}$$

where $q = 2^{-\frac{1}{2}} B/L_c$ and $P(x, \tau) = -\phi_\tau(x, 0, \tau)$.

The solution of the problem (23) is obtained using the Green function $G(x, \xi)$,

$$w(x, \tau) = \int_0^\infty G(x, \xi) P(\xi, \tau) \mathrm{d}\xi, \tag{24}$$

$$G(x, \xi) = \frac{1}{8q^3}\Big\{h(|x - \xi|) + m(|x - \xi|) + h(x + \xi) - m(x + \xi) + 2h(\xi)h(x) + 2m(\xi)m(x)\Big\},$$

$$h(x) = \exp(-qx)\cos(qx), \quad m(x) = \exp(-qx)\sin(qx).$$

Foa a slender vessel ($\mu \ll 1$), the strains in the plate are given by

$$\epsilon(x, \tau) = \epsilon_{sc} w_{xx}(x, \tau), \quad \epsilon_{sc} = \delta\eta_2 \frac{h_i}{2B}. \tag{25}$$

where the second derivative of the deflection is calculated numerically by the integral (24) with

$$G_{xx}(x, \xi) = \frac{1}{4q}\Big\{ - h(|x - \xi|) + m(|x - \xi|) + h(x + \xi) + m(x + \xi) + 2h(\xi)m(x) - 2m(\xi)h(x)\Big\}.$$

It is seen that $G_{xx}(0, \xi) = 0$. The resulting integral is evaluated numerically once the hydrodynamic pressure $P(x, \tau)$ has been determined.

The solution of the hydrodynamic problem (22) strongly depends on the hull shape. A simple dimensional representation of the hull shape is $y = f(|x + d|, z) = |x + d| \tan\gamma + Hz/L$, where

$-L < z < 0$, γ is the deadrise angle of the hull sections (in this simple case it is taken constant along the hull), H is the draught and L is the length of the vessel. In the dimensionless variables (9) with $\delta = H/B$ and $k = \tan\gamma/\delta = O(1)$ we have $\tilde{f} = k|\tilde{x} + \tilde{d}| + \tilde{z}$. Dropping tildes and replacing z with $-\tau$ and $\tilde{d}$ with λ, the shape function in (22) becomes $f(|x + \lambda|, -\tau) = k|x + \lambda| - \tau$. Correspondingly, $f_z(|x + \lambda|, -\tau) = 1$ in the body boundary condition.

The hydrodynamic problem (22) is formulated in terms of the velocity potential $\phi(x, y, \tau)$. However, it is convenient to reformulate it in terms of the displacement potential $\phi_0(x, y, \tau)$ and the acceleration potential $\phi_2(x, y, \tau)$, defined by

$$\phi_0(x, y, \tau) = \int_0^\tau \phi(x, y, \tau_0)\,\mathrm{d}\tau_0, \qquad \phi_2(x, y, \tau) = -\phi_\tau(x, y, \tau). \tag{26}$$

We assume that $a'(\tau) < 0$ and $b'(\tau) > 0$ for $0 < \tau < 1$. These inequalities are satisfied for the selected hull geometry. Under this assumption, the boundary condition on the free surface segments can be integrated in time, yielding $\phi_0(x, 0, \tau) = 0$ and $\phi_2(x, 0, \tau) = 0$ there.

Integrating and differentiating the body boundary condition with respect to τ, we obtain for the chosen hull shape

$$\phi_{0y}(x, 0, \tau) = y_b(x, \tau) = k|x + \lambda| - \tau, \qquad \phi_{2y}(x, 0, \tau) = 0, \qquad (y = 0,\ a(\tau) < x < b(\tau)). \tag{27}$$

The remaining boundary conditions and the Laplace equation in the region $y < 0$ are the same as in (22); see [12].

Note that the boundary-value problem for $\phi_2(x, y, \tau)$ is homogeneous, i.e. it contains no forcing terms. The formulations of the problems for the displacement potential ϕ_0 and the acceleration potential ϕ_2 incorporate their required behaviour at the contact points $x = a(\tau)$ and $x = b(\tau)$. The displacement potential ϕ_0 and its first derivatives must remain bounded at the contact points [13], and the first derivatives are square-root singular at the ice edge, whereas the acceleration potential ϕ_2 exhibits a square-root singularity at the contact points and finite at the ice edge $x = 0$ [14]. The boundedness of the derivatives of ϕ_0 at $x = a(\tau)$ and $x = b(\tau)$ provides two equations for the unknown functions $a(\tau)$ and $b(\tau)$. The value of the acceleration potential at $y = 0$ for $x > 0$ determines the pressure distribution along the ice–water interface, $P(x, \tau) = \phi_2(x, 0, \tau)$.

To find the general solution of the problem for the acceleration potential, we introduce the complex potential

$$\Phi_2(z) = \phi_2(x, y, \tau) + i\psi_2(x, y, \tau), \qquad z = x + iy,$$

where $\psi_2(x, y, \tau)$ is the harmonic conjugate of ϕ_2 which is related to it through the Cauchy–Riemann relations and decays at infinity. The boundary conditions on the ice plate and on the wetted part of the hull give

$$\psi_2(x, -0, \tau) = 0 \quad (x > 0), \qquad \psi_2(x, -0, \tau) = C(\tau) \quad (y = 0,\ a(\tau) < x < b(\tau)), \tag{29}$$

where the function $C(\tau)$ should be determined using the singularity coefficients at the contact points. On the rest of the boundary, $\phi_2(x, -0, \tau) = 0$.

We also introduce the characteristic function

$$R(z) = \sqrt{z/(z - a)(z - b)},$$

defined such that $R(x - i0) = -\,r(x)$ for $x > 0$, where $r(x) = \sqrt{|x/(x - a)(x - b)|}$. In the hydrodynamic formulation, the variable τ plays the role of a parameter; therefore, for brevity it will be omitted in some of the expressions below.

The function $\Phi_2(z)/R(z)$ is analytic in $y < 0$, bounded at the boundary $y = 0$ and tends to a real constant $D(\tau)$ as $z \to \infty$. Correspondingly, the function $i[\Phi_2/R(z) - D]$ decays at infinity and its real part is equal to $C/r(x)$, where $a < x < b$ and zero otherwise.

Using the Hilbert formula, which relates the real and imaginary parts of a function analytic in the lower half-plane, we arrive at the required pressure distribution along the ice-water interface,

$$P(x,\tau) = -\sqrt{\frac{x}{(x-a)(x-b)}}\Big(D(\tau) + \frac{C(\tau)}{\pi}\int_a^b \frac{d\xi}{r(\xi)(\xi-x)}\Big) \quad (x>0). \tag{30}$$

The coefficients C and D are obtained by comparing the behaviour of the pressure within the contact region, $a<x<b$,

$$\phi_2(x,-0,\tau) = -\sqrt{\frac{|x|}{(x-a)(b-x)}}\Big(D(\tau) + \frac{C(\tau)}{\pi} P.v.\int_a^b \frac{\sqrt{(\xi-a)(b-\xi)}d\xi}{\sqrt{-\xi}(\xi-x)}\Big), \tag{31}$$

close to $x=a$ and $x=b$ with the corresponding asymptotic behaviours of the displacement potential.

The formula (31) yields

$$\phi_2(x,-0,\tau) \sim -\sqrt{\frac{|a|}{b-a}}\Big(D(\tau) + C(\tau)[bS_{-1}+S_1]](x-a)^{-\frac{1}{2}} \quad (x\to a+0),$$

$$\phi_2(x,-0,\tau) \sim -\sqrt{\frac{|b|}{b-a}}\Big(D(\tau) + C(\tau)[aS_{-1}+S_1]](b-x)^{-\frac{1}{2}} \quad (x\to b-0), \tag{32}$$

where

$$S_k = \frac{1}{\pi}\int_0^\pi (1-\omega\cos\theta)^{\frac{k}{2}} d\theta \tilde{P}^{\frac{k}{2}} = \tilde{P}^{\frac{k}{2}}\tilde{S}_k, \quad \omega = \frac{\tilde{a}+\tilde{b}}{2(\lambda-\tilde{b})+\tilde{a}+\tilde{b}}, \quad \tilde{P} = \lambda + \frac{\tilde{a}-\tilde{b}}{2},$$

$a=-\lambda-\tilde{a}$, $b=-\lambda+\tilde{b}$, $\tilde{a}$ and $\tilde{b}$ are positive functions of τ, increasing with τ, $\tilde{a}(0)=0$, $\tilde{b}(0)=0$.

It is known that the displacement potential behaves as

$$\phi_0 \sim K_a(\tau)(x-a)^{\frac{3}{2}} \quad (x\to a+0), \qquad \phi_0 \sim K_b(\tau)(b-x)^{\frac{3}{2}} \quad (x\to b-0).$$

Differentiating these asymptotic formulae twice in τ, we find

$$\phi_2 \sim -\frac{3}{4}a_\tau^2(\tau)K_a(\tau)(x-a)^{-\frac{1}{2}} \quad (x\to a+0), \quad \phi_2 \sim -\frac{3}{4}b_\tau^2(\tau)K_b(\tau)(b-x)^{-\frac{1}{2}} \quad (x\to b-0). \tag{33}$$

Comparing (32) and (33), we determine $C(\tau)$ and $D(\tau)$ for the functions $K_a(\tau)$, $K_b(\tau)$, $a(\tau)$ and $b(\tau)$, which are obtained from the solution of the problem for the complext potential $V(z)=\phi_{0x}-i\phi_{0y}$. Here

$$V(z)=O(z^{-\frac{3}{2}}), \quad V(z)=O((z-a)^{\frac{1}{2}}), \quad V(z)=O((z-b)^{\frac{1}{2}}), \quad V(z)=O(z^{-\frac{1}{2}})$$

as z tends to infinity, a, b and the edge of the ice plate, correspondingly.In addition, the condition $\phi_0=0$, where $b<x<0$, $y=0$, requires

$$\int_a^b \phi_{0x}(x,0,\tau)dx = 0. \tag{34}$$

Note that the function $\tilde{V}(z)=iV(z)R(z)$ decays at infinity, finite at the contact points and its real part is equal to $-y_b(x,\tau)r(x)$ in $a<x<b$ and is zero otherwise. The Hilbert formula provides

$$\phi_{0x}(x,0,\tau)r(x) = \frac{1}{\pi}P.v.\int_a^b \frac{y_b(\xi,\tau)r(\xi)d\xi}{\xi-x}, \tag{35}$$

where $y_b(x,\tau)=f(x)-h(\tau)$, in general, $f(x)$ is the shape function of sections of the vessel, $f(0)=0$, and $h(\tau)$ describes the draught of the vessel as the coordinate along its length.

The condition on the behaviour of the complex displacement at infinity gives

$$\int_0^\pi y_b[-\tilde{P}(1-\omega\cos\theta)]\sqrt{1-\omega\cos\theta}d\theta = 0. \tag{36}$$

Condition (34) yields

$$\int_0^\pi y_b[-\tilde{P}(1-\omega\cos\theta)]\{\pi\tilde{S}_{-1}(\omega)(1-\omega\cos\theta)^{\frac{3}{2}} + \omega^2\sin^2\theta N_0(\theta)\}d\theta = 0, \tag{37}$$

$$N_0(\theta) = \int_0^\pi \frac{d\varphi}{\sqrt{1-\omega\cos\varphi}(\sqrt{1-\omega\cos\varphi}+\sqrt{1-\omega\cos\theta})}.$$

Equations (36) and (37) determine the unknown functions $a(\tau)$ and $b(\tau)$. The coefficients $K_a(\tau)$ and $K_b(\tau)$ are obtained by analysing the behaviour of the integral in (35) as x approaches the contact points a and b, respectively.

For a large distance between the vessel route and the ice edge, $\lambda \gg 1$, the positions of the contact points are, to leading order, approximately independent of the presence of the ice. For $y_b(x,\tau) = k|x+\lambda| - \tau$ and large λ, equation (36) gives $\tilde{a}(\tau) \approx \tilde{b}(\tau) = \pi\tau/(2k)$. Furthermore, equation (35) gives $K_a = K_b = -2\sqrt{b-a}/(3\tilde{a}'(\tau))$. By comparing the asymptotic expressions (33) and (32), we obtain

$$D(\tau) = -\tilde{a}^{\frac{1}{2}}(\tau)\tilde{a}'(\tau), \quad C(\tau) = 0$$

and, consequently,

$$P(x,\tau) = \Big(\frac{\pi}{2k}\Big)^{\frac{3}{2}}\tau^{\frac{1}{2}}\frac{x^{\frac{1}{2}}}{x+\lambda} \quad (x>0), \tag{38}$$

to leading order as $\lambda \to \infty$.

The hydrodynamic pressure (38) is positive and attains its maximum value $P_{\max}(\tau)$ at $x = \lambda$. It is convenient to introduce the scaled pressure,

$$\hat{P}(\hat{x}) = \frac{2\sqrt{\hat{x}}}{\hat{x}+1}, \quad \hat{x} = x/\lambda. \tag{39}$$

Note that the hydrodynamic pressure given by (38) is not integrable.

Substituting (38) and (39) in the formula (25) for the strains yields

$$\epsilon(x,\tau) = \hat{\epsilon}_{sc}\tau^{\frac{1}{2}}\hat{\epsilon}(\hat{x}), \quad \hat{\epsilon}_{sc}\tau^{\frac{1}{2}} = \lambda\epsilon_{sc}P_{\max}(\tau)/(2q), \quad \hat{\epsilon}(\hat{x}) = \int_0^\infty E(\hat{x},\hat{\xi})\frac{\sqrt{\hat{\xi}}d\hat{\xi}}{\hat{\xi}+1}, \tag{40}$$

where $E(\hat{x},\hat{\xi}) = 4qG_{xx}(\lambda\hat{x},\lambda\hat{\xi})$.Correspondingly, for the ice deflection we obtain, see equation (24),

$$w(x,\tau) = \hat{w}_{sc}\tau^{\frac{1}{2}}\hat{W}(\hat{x}), \quad \hat{W}(\hat{x}) = \int_0^\infty F(\hat{x},\hat{\xi})\frac{\sqrt{\hat{\xi}}d\hat{\xi}}{\hat{\xi}+1},$$

where $F(\hat{x},\hat{\xi}) = 8q^3G(\lambda\hat{x},\lambda\hat{\xi})$.

4. Numerical results

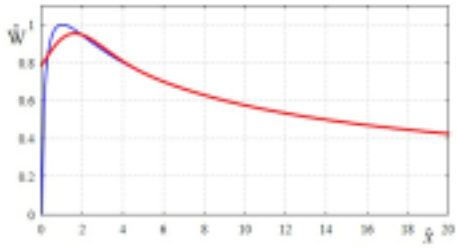
Calculations of the strains in the ice plate are performed for a vessel of length $L = 50\,\text{m}$, beam $B = 10\,\text{m}$, draft $H = 2\,\text{m}$, travelling at speed $U = 20\,\text{m/s}$, with the vessel centreplane located at a distance $d = 20\,\text{m}$ from the ice edge. The ice thickness is $h_i = 1\,\text{m}$, which corresponds to the characteristic length $L_c = 14\,\text{m}$. The corresponding dimensionless parameters are

$$\mu = \frac{1}{5}, \quad \delta = \frac{1}{5}, \quad \lambda = 2, \quad q \approx 0.5, \quad Fr = 0.9, \quad \eta_0 \approx 0.001, \quad \eta_1 = 0.26, \quad \eta_2 = 0.04, \quad \eta_3 = 6.17.$$

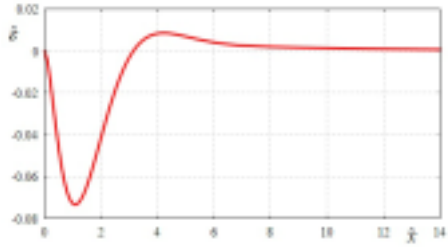
For the deadrise angle $\gamma = 30°$, we obtain $k = 2.88$ and $\epsilon_{sc} = 4 \times 10^{-4}$. The yield strain of sea ice is $\epsilon_Y = 8 \times 10^{-5}$ (see [11]). The function $\hat{\epsilon}(\hat{x})$ is shown by the red curve in Figure 2b. It can be seen that the strains remain below the yield level, with

$$\max \hat{\epsilon}(\hat{x}) \approx 0.07 < \frac{0.2}{\sqrt{\tau}}, \qquad 0 < \tau < 1.$$

In this case, the deflection scale $\hat{w}_{sc}$ is equal to $36.6\,\mathrm{cm}$. The function $\hat{W}(\hat{x})$ is shown by the red curve in Figure 2a. The predicted deflections are comparable with the ice thickness $h_i = 1\,\mathrm{m}$ and decay slowly with increasing distance from the ice edge. The blue curve in Figure 2a represents the function $\hat{P}(\hat{x})$ given by (39), which describes the pressure distribution along the ice–water interface. It is observed that, in the far field, the ice deflection follows the pressure distribution.



(a) Deflection $\hat{W}(\hat{x})$ (red line) and the pressure $\hat{P}(\hat{x})$ (blue line)



(b) Strain $\hat{\epsilon}(\hat{x})$.

Figure 2: The scaled deflection $\hat{W}(\hat{x})$ (a) and strain distribution $\hat{\epsilon}(\hat{x})$ (b) as functions of the distance from the ice edge $\hat{x}$.

5. Conclusion

The obtained deflections of the ice plate induced by a high-speed vessel travelling parallel to the ice edge closely follow the hydrodynamic pressure distribution predicted by the rigid-ice model. The magnitude of the deflections is large compared with the ice thickness, indicating that fluid–structure coupling effects may be significant. However, for the parameter values used in the numerical simulations, the resulting strains remain small and do not exceed the yield strain of the ice.

Both the hydrodynamic pressure and the associated deflections decay slowly with increasing distance from the ice edge. This suggests that a vessel moving in open water may generate a detectable mechanical response in the ice at considerable distances from the edge.

Acknowledgments

The authors gratefully acknowledge financial support from the Leverhulme Trust under the research grant “Waves and ice interaction with ice breaking and over-washing”.

References

[1] Xue, Y. Z., Zeng, L. D., Ni, B. Y., Korobkin, A. A., & Khabakhpasheva, T. I. (2021). Hydroelastic response of an ice sheet with a lead to a moving load. Physics of Fluids, 33(3).

[2] Marleaux, P., Khabakhpasheva, T., Abdel-Maksoud, M., Korobkin, A., & Maki, K. (2022). High-speed vessel moving along the edge of ice field. In 37th International Workshop on Water Waves and Floating Bodies 2022. Istituto di Ingegneria del Mare.

[3] Korobkin, A., Părău, E. I., & Vanden-Broeck, J. M. (2011). The mathematical challenges and modelling of hydroelasticity. Philosophical Transactions of the Royal Society A: Mathematical, Physical and Engineering Sciences, 369(1947), 2803-2812.

[4] Părău, E. I., & Vanden-Broeck, J. M. (2011). Three-dimensional waves beneath an ice sheet due to a steadily moving pressure. Philosophical Transactions of the Royal Society A: Mathematical, Physical and Engineering Sciences, 369(1947), 2973-2988.

[5] Dinvay, E., Kalisch, H., & Părău, E. I. (2019). Fully dispersive models for moving loads on ice sheets. Journal of Fluid Mechanics, 876, 122-149.

[6] Dinvay, E., Kalisch, H., & Părău, E. (2022). Waves generated by moving loads on ice plates: Viscoelastic approximations. Wave Motion, 114, 103011.

[7] Johnsen, K., Kalisch, H., & Părău, E. I. (2022). Ship wave patterns on floating ice sheets. Scientific Reports, 12(1), 18931.

[8] Tassin, A., Piro, D. J., Korobkin, A. A., Maki, K. J., & Cooker, M. J. (2013). Two-dimensional water entry and exit of a body whose shape varies in time. Journal of Fluids and Structures, 40, 317-336.

[9] Zhang, Z., & Maki, K. (2023). Wave resistance of a ship moving in a lead between rigid ice sheets of finite thickness. Physics of Fluids, 35(7).

[10] Fontaine, E., & Cointe, R. (1997). A slender body approach to nonlinear bow waves. Philosophical Transactions of the Royal Society of London. Series A: Mathematical, Physical and Engineering Sciences, 355(1724), 565-574.

[11] Brocklehurst, P., Korobkin, A. A., & Părău, E. I. (2010). Interaction of hydro-elastic waves with a vertical wall. Journal of Engineering Mathematics, 68(3), 215-231.

[12] Howison, S. D., Ockendon, J. R., & Wilson, S. K. (1991). Incompressible water-entry problems at small deadrise angles. Journal of Fluid Mechanics, 222, 215-230.

[13] Korobkin, A.A.(1996). Water impact problems in ship hydrodynamics. In: M. Ohkusu (ed.) Advances in Marine Hydrodynamics, pp. 323–371. Computational Mechanics, Boston.

[14] Korobkin, A.A.(2003). Cavitation in liquid impact problems. In: Fifth International Symposium on Cavitation, pp. 1–4. Osaka.

Nonlinear Interaction Between an Ice Cover of Variable Thickness and a Bottom Obstruction in Channel Flow

Liang, C.[1], Ni, B.Y.[1*], Khabakhpasheva, T.I.[2] and Semenov, Y.A.[1]

[1] College of Shipbuilding Engineering, Harbin Engineering University, Harbin, China
(liangchuang@hrbeu.edu.cn)
[2] School of Mathematics, University of East Anglia, Norwich NR4 7TJ, UK
(T.Khabakhpasheva@uea.ac.uk)

Abstract. The problem of nonlinear flexural-gravity waves due to a rectangular obstruction on the bottom of the channel covered by an elastic ice sheet of variable thickness is studied. The velocity potential theory and the theory of thin elastic shells are employed which fully account for the nonlinear boundary conditions at the ice/liquid interface and on the bottom of the channel. The integral hodograph method is employed to derive the complex velocity potential of the flow. This allows one to formulate the coupled ice/liquid interaction problem and reduce it to a system of nonlinear equations in the unknown magnitude of the velocity at the ice/liquid interface. Results are obtained for a rectangular obstruction on the channel bottom. The effects of ice thickness variation on the interface profiles are analyzed for different thickness variations of ice sheet.

Key words: *nonlinear interaction; variable ice thickness; hydroelasticity*

1. Introduction

The interaction between ice, water flow and bottom topography is of vital importance in geophysical and engineering applications, particularly in polar regions covered with ice cover. In recent years, this subject has gained renewed attention due to the impact of climate change and the accelerated melting of Arctic ice. Understanding the dynamics of ice-water interaction plays an important role in the wave propagation over bottom topography and ice response.

Most studies on ice-water interaction are primarily based on linear theories and focus on constant ice thickness. Ni et al. [1] provided a comprehensive review of theoretical and experimental studies on ice/water/structure interaction. Oblique flexural gravity wave scattering due to abrupt change in bottom topography was investigated by Karmakar et al. [2] under the assumption of linearized theory of water waves. Further investigations on the scattering of flexural gravity waves due to uneven bottom topography in the context of wave blocking were carried out by Boral, Meylan, Sahoo & Ni [3]. Other studies aimed to analyze the oscillatory response of floating elastic plates subjected to periodic waves [4]. Furthermore, the effects of a moving load or a submerged body beneath the ice in frozen channels were examined [5, 6]. These studies generally focus on the transmission and reflection coefficients or the ice/liquid interface response, and the key point of these problems is the dependence of ice response on external disturbances.

However, depending on small-amplitude approximations and linearized boundary conditions, linear theories have limitations on analyzing wave propagation in fluid-structure interaction problems, including ice-covered water flows. One major limitation of linear theories is their inability to describe wave behaviors near critical speeds. In problems involving elastic ice sheet, two critical Froude numbers

* Correspondence to: nibaoyu@hrbeu.edu.cn

exist: the first is $F = 1$, corresponding to the critical speed of surface gravity waves in a finite-depth channel, and $F = F_{cr}$, at which the wavelengths of the elastic propagating upstream and the gravity wave propagating downstream are coincided, resulting in complex superposition similar to resonance. Near these critical values, linear theories predict infinite displacement of the interface, leading to singularities in the solution. This unphysical result indicates that nonlinear effects become dominant and must be accounted for to obtain a physically meaningful solution [7].

There have been some investigations on nonlinear effects such as wave-wave coupling and amplitude-dependent dispersion in recent years. Hydroelastic solitary waves having near-minimum phase speed were calculated using a nonlinear elastic model to describe the dynamics of ice sheets by Milewski et al. [8]. Further investigations on nonlinear hydroelastic waves with a linear shear current were carried out by Gao et al. [9]. Guyenne & Părău [10] computed fully nonlinear hydroelastic solitary waves using a nonlinear Schrödinger equation. Recently, Ni et al. [11] examined the interaction between the flow in a channel with an obstruction on the bottom and an elastic ice sheet, considering the fully nonlinear boundary conditions at the elastic ice/liquid interface and the obstruction of the channel bottom.

In this paper, we investigate the effect of variable ice thickness on the nonlinear flexural-gravity waves in the channel with rectangular obstruction. The previous studies on the variable ice thickness have been explored using variational approaches by Porter & Porter [12]. Time-dependent response of a heterogeneous elastic plate with variable thickness was performed by Sturova [13]. Ice thickness variation can significantly affect the nonlinear response of ice/liquid interface. Considering the variable ice thickness can to a certain extent simulate the broken ice in polar regions, and the cracks or the polynyas in the ice zones.

We employ velocity potential theory and the integral hodograph method to develop a mathematical model that fully accounts for the nonlinear boundary conditions at both the ice/liquid interface and the channel bottom. The elastic sheet is modelled using the Cosserat theory of hyperelastic shells [14]. The fluid is considered as an ideal incompressible liquid. The boundary conditions at the ice/liquid interface are fully nonlinear.

2. Formulation of the problem

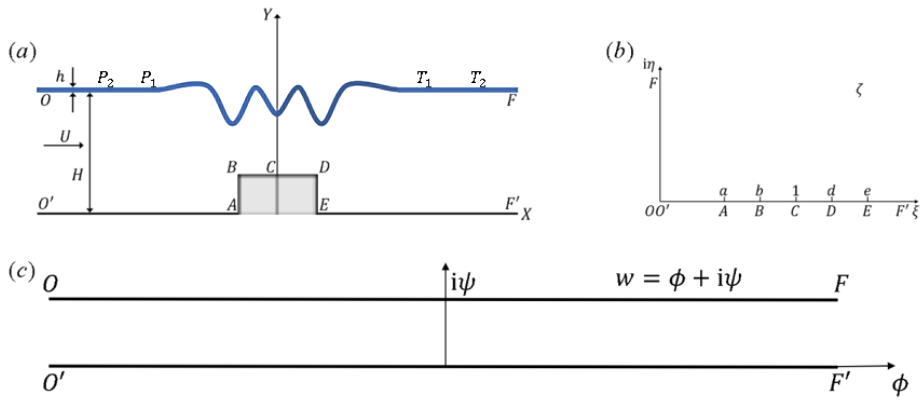


Figure 1. (*a*) Physical plane, (*b*) parameter, or ζ, plane, and (*c*) complex potential, or w, plane.

We analyse a two-dimensional steady flow through a channel with a rectangular obstruction and a thickness variable ice sheet. The flow remains uniform far upstream and downstream, with a constant velocity U and a fixed channel depth H. The ice sheet has variable thickness. The explicit form of the ice thickness will be given later.

A Cartesian coordinate system *XY* is introduced, with its origin at the centre of the rectangle. The *X*-axis is directed to the flow direction which has a uniform velocity U at infinity. The *Y*-axis is directed vertically upward. A sketch of these configurations is shown in Figure 1a. The liquid is assumed to be inviscid and incompressible, subjected to the downward gravitational acceleration g. The flow is irrotational, allowing the application of potential flow theory.

We introduce the complex velocity potential of the flow, $W(Z) = \Phi(X,Y) + \mathrm{i}\Psi(X,Y)$ where $\Phi(X,Y)$ is the velocity potential and $\Psi(X,Y)$ is the stream function, with $Z = X + \mathrm{i}Y$. The dynamic boundary condition at the ice/liquid interface, $Y = Y(X)$ is given by Bernoulli's equation:

$$\rho\frac{V^2}{2} + \rho gY + P_{ice} + P_{ext} = \rho\frac{U^2}{2} + \rho gH + P_\infty, \tag{1}$$

where $V = |\nabla\Phi|$ is the velocity magnitude, $P_{ice}(X)$ is the pressure along the ice/liquid interface, (the pressure due to the bending of the ice sheet is the same as the hydrodynamic pressure), and $P_\infty = P_a + \rho_i gh$ is its value at infinity. Here, P_a is the atmospheric pressure, ρ_i is the density of ice, h is the thickness of the ice sheet and g is gravitational acceleration. The external pressure $P_{ext}(X)$ is applied in the intervals $X_{P2} < X < X_{P1}$ and $X_{T1} < X < X_{T2}$ to ensure a waveless interface far upstream and downstream.

We seek a solution that satisfies the asymptotic condition: $Y(X)_{X\to-\infty} = H$, where H is the depth of the channel. The Euler–Bernoulli beam equation, used for structural analysis at the ice/liquid interface, is given by

$$M = D'K, \tag{2}$$

$$P_{ice} - P_a = \frac{\mathrm{d}^2M}{\mathrm{d}S^2}, \tag{3}$$

where M is the bending moment of the elastic ice sheet, $D' = \frac{Eh^3}{12(1-\nu^2)}$ is the flexural rigidity of the ice sheet, E is the Young's modulus, $h = h(S)$ is the variable ice thickness, ν is Poisson ratio, $K = \frac{Y''}{\sqrt{1-Y'^2}}$ is the curvature of the interface, and S is the arclength coordinate along the interface.

To obtain the solution, we introduce a nondimensionalization of the variables using the velocity U and the channel depth H as reference quantities. The dimensionless coordinates are defined as $x = X/H$, $y = Y/H$, $s = S/H$, and the variable ice thickness is expressed as $h^* = h/H$. The bottom and interface profiles are given by $y_b(x) = Y_b(X)/H$ and $y(x) = Y(x)/H$, respectively. Similarly, the velocity potential Φ and the stream function Ψ are normalized by the characteristic quantity UH, defining the dimensionless variables $\phi = \Phi/UH$ and $\psi = \Psi/UH$. Under this normalization, the stream function takes the values $\psi = 0$ along the channel bottom and $\psi = 1$ at the ice/liquid interface.

The explicit form of the ice thickness is described as follows:

$$h^*(s) = h^*_{aver}\left[1 + 0.5\cos\left(k_f s\right)\right], -\infty < s < \infty, \tag{4}$$

where h^*_{aver} is an average ice thickness taken as 0.005 in this paper. $h^*(s)$ varies from $h^*_{min} = 0.5h^*_{aver} = 0.0025$ to $h^*_{max} = 1.5h^*_{aver} = 0.0075$, and k_f is the frequency in the change of ice thickness.

The nondimensionalized bending moment takes the form

$$m = E_b\kappa, \tag{5}$$

where $E_b = \frac{D'}{\rho gH^4}$ is nondimensionalized flexural rigidity, $\kappa = \frac{y''}{\sqrt{1-y'^2}}$ is the nondimensionalized curvature of the interface. The nondimensionalized pressure due to the bending of the ice sheet is the

2nd derivative of equation (5) on *s*-coordinate, and since now $h^* = h^*(s)$ is a function of *s*, E_b will also be a function of *s*. It is more convenient to denote E_b as $k_{coeff}h^{*3}$, where $k_{coeff} = \frac{E}{12(1-\nu^2)\rho g H^3}$, within which only constants are included. E_b is a continuous function of *s*, so the nondimensionalized pressure takes the form

$$p_{ice} - p_a = \frac{\mathrm{d}^2 m}{\mathrm{d}s^2} = \frac{\mathrm{d}^2 E_b}{\mathrm{d}s^2}\kappa + 2\frac{\mathrm{d}E_b}{\mathrm{d}s}\frac{\mathrm{d}\kappa}{\mathrm{d}s} + \frac{\mathrm{d}^2\kappa}{\mathrm{d}s^2}E_b, \tag{6}$$

where

$$\begin{aligned} E_b &= k_{coeff}h^{*3}, \\ \frac{\mathrm{d}E_b}{\mathrm{d}s} &= k_{coeff}3h^{*2}\frac{\mathrm{d}h^*}{\mathrm{d}s}, \\ \frac{\mathrm{d}^2E_b}{\mathrm{d}s^2} &= k_{coeff}\left[6h^*\left(\frac{\mathrm{d}h^*}{\mathrm{d}s}\right)^2 + 3h^{*2}\frac{\mathrm{d}^2h^*}{\mathrm{d}s^2}\right], \end{aligned} \tag{7}$$

and

$$\begin{aligned} h^* &= h^*_{aver}\left[1 + 0.5\cos\left(k_f s\right)\right], \\ \frac{\mathrm{d}h^*}{\mathrm{d}s} &= -0.5h^*_{aver}k_f\sin\left(k_f s\right), \\ \frac{\mathrm{d}^2h^*}{\mathrm{d}s^2} &= -0.5h^*_{aver}\left(k_f\right)^2\cos\left(k_f s\right). \end{aligned} \tag{8}$$

The nondimensionalized dynamic boundary condition takes the form

$$v^2 = 1 - \frac{2(y-1)}{F^2} - \frac{2}{F^2}(p_{ice} - p_a) - \frac{2C_d}{H}v\frac{\mathrm{d}v}{\mathrm{d}s}, \tag{9}$$

where $v = |\nabla\phi| = V/U$. The Froude number, $F = \frac{U}{\sqrt{gH}}$, decides the flow regime based on the channel depth. Equation (9) expresses the velocity magnitude v along the interface in terms of the interface elevation y and its derivatives. These variables will be further related to the expressions of the complex potential and complex velocity in the subsequent sections.

2.1 Determination of complex potential and complex velocity

On the channel bottom the stream function $\psi \equiv 0$, and at the interface $\psi \equiv 1$, while the potential varies from $-\infty$ to ∞. Thus, the domain of the complex potential $w = \phi + \mathrm{i}\psi$ is the infinite strip $-\infty < \phi < \infty$ of unit width, $0 \le \psi \le 1$. Due to the simplicity of the domain of w, we can use conformal mapping to immediately write the complex potential w as a function of the parameter variable ζ

$$w(\zeta) = \frac{2}{\pi}\ln\zeta\,, \frac{\mathrm{d}w}{\mathrm{d}\zeta} = \frac{2}{\pi\zeta}. \tag{10}$$

We adopt an integral formula [15, 16] that enables us to determine a complex function based on its argument values along the real axis and its magnitude along the imaginary axis in the first quadrant. Consequently, we select the first quadrant as the region for the parameter variable $\zeta = \xi + \mathrm{i}\eta$ instead of a half-plane, as illustrated in Figure 1*b*. In the physical plane $z = x + \mathrm{i}y$ (Figure 1*a*), this parameter region corresponds to the liquid domain: the real axis represents the channel bottom, while the

imaginary axis corresponds to the interface. The conformal mapping theorem allows us to fix the positions of three points, $O(O')$ at $\zeta = 0$, CC at $\zeta = 1$, and $F(F')$ at $\zeta = \infty$, as shown in Figure 1*b*. The velocity magnitude at the ice/liquid interface is given on the imaginary axis, and the argument of the complex velocity along the channel bottom is given on the real axis of the first quadrant

$$v(\eta) = \left|\frac{\mathrm{d}w}{\mathrm{d}z}\right|, 0 \le \eta < \infty, \tag{11}$$

$$\arg\left(\frac{\mathrm{d}w}{\mathrm{d}z}\right) = \mathrm{Im}\left[\ln\left(\frac{\mathrm{d}w}{\mathrm{d}z}\right)\right] = \chi(\xi), 0 \le \xi < \infty. \tag{12}$$

The argument of the complex velocity is conjugate to the velocity direction on the bottom,

$$\chi(\xi) = \mathrm{Im}\left(\ln\frac{\mathrm{d}w}{\mathrm{d}z}\right) = \begin{cases} 0,\ 0 < \xi \le a, \eta = 0, \\ -\dfrac{\pi}{2}, a < \xi \le b, \eta = 0, \Delta\chi_A = -\dfrac{\pi}{2}, \\ 0,\ b < \xi \le d, \eta = 0, \Delta\chi_B = \dfrac{\pi}{2}, \\ \dfrac{\pi}{2}, d < \xi \le e, \eta = 0, \Delta\chi_D = -\dfrac{\pi}{2}, \\ 0,\ e < \xi < \infty, \eta = 0, \Delta\chi_E = \dfrac{\pi}{2}, \end{cases} \tag{13}$$

which undergoes a step change due to the corners at points A, B, D, and E ($\zeta = a, b, d, e$). The evaluation of the integrals over the step changes is done, for example, at point A as follows

$$\frac{1}{\pi}\int_{a-\varepsilon}^{a+\varepsilon}\frac{\mathrm{d}\chi}{\mathrm{d}\xi}\ln\frac{\xi+\zeta}{\xi-\zeta}\mathrm{d}\xi = \frac{1}{\pi}\ln\frac{a+\zeta}{a-\zeta}\int_{a-\varepsilon}^{a+\varepsilon}\frac{\mathrm{d}\chi}{\mathrm{d}\xi}\mathrm{d}\xi = \frac{\Delta\chi_A}{\pi}\ln\frac{a+\zeta}{a-\zeta}, \tag{14}$$

where the sign of the nominator is changed since the argument of the logarithm should be zero for $\zeta = \xi < a$. Doing the same for each corner point and taking into account that $v_\infty = v_0 = 1$ and $\chi_\infty = 0$, we obtain the expression for the complex velocity defined in the first quadrant of the parameter plane

$$\frac{\mathrm{d}w}{\mathrm{d}z} = \sqrt{\frac{a-\zeta}{a+\zeta}\frac{b+\zeta}{b-\zeta}\frac{d+\zeta}{d-\zeta}\frac{e-\zeta}{e+\zeta}}\exp\left[-\frac{\mathrm{i}}{\pi}\int_0^\infty\frac{\mathrm{d}\ln v}{\mathrm{d}\eta}\ln\frac{\mathrm{i}\eta-\zeta}{\mathrm{i}\eta+\zeta}\mathrm{d}\eta\right]. \tag{15}$$

The complex potential is a logarithmic function of ζ, or ζ exponentially depends on the complex potential $w = \phi + \mathrm{i}\psi$. The arc length coordinates $s_b \sim \phi$ and $s \sim \phi$ along the bottom and the interface, respectively, which means ζ exponentially depends on s. This causes difficulties in computations for a length of the computational domain larger than $5H$. We can resolve the logarithmic singularity if we eliminate the parameter variables ζ, ξ and η from (15). We introduce the variables $\phi' = \pi\phi/2$, the stream function $\psi' = \pi\psi/2$, and $w' = \pi w/2$ as independent variables and determine the variables ξ and η from equation (10):

$$\left.\begin{array}{l} \zeta = \exp(w'), w' = \phi' + \mathrm{i}\psi', \\ \eta = \exp(\phi'), -\infty < \phi' < \infty, \psi' = \pi/2, \\ \xi = \exp(\phi'), -\infty < \phi' < \infty, \psi' = 0. \end{array}\right\} \tag{16}$$

By substituting (16) into (15), we obtain the complex velocity as a function of the complex potential w, the inverse function of which is the derivative of the mapping function, $z = z(w)$

$$\frac{\mathrm{d}z}{\mathrm{d}w}=\sqrt{\frac{a+\mathrm{e}^{w'}}{a-\mathrm{e}^{w'}}\frac{b-\mathrm{e}^{w'}}{b+\mathrm{e}^{w'}}\frac{d-\mathrm{e}^{w'}}{d+\mathrm{e}^{w'}}\frac{e+\mathrm{e}^{w'}}{e-\mathrm{e}^{w'}}}\exp\left[\frac{\mathrm{i}}{\pi}\int_{-\infty}^{\infty}\frac{\mathrm{d}\ln v}{\mathrm{d}\phi'}\ln\left(\frac{\mathrm{i}\mathrm{e}^{\phi'}-\mathrm{e}^{w'}}{\mathrm{i}\mathrm{e}^{\phi'}+\mathrm{e}^{w'}}\right)\mathrm{d}\phi'\right], \tag{17}$$

where $\{a,b,d,e\}=\exp\{\pi\phi_A/2,\pi\phi_B/2,\pi\phi_D/2,\pi\phi_E/2\}$, $\phi_A,\phi_B,\phi_D,\phi_E$ are the potentials at the corner points *A*, *B*, *D*, and *E*. The kernel of the integral in (17) exponentially decays as the difference $|\phi'-w'|$ increases. The integration of (17) along $-\infty<\phi<\infty$, $\psi=1$ in the w-plane gives the interface; its integration along $-\infty<\phi<\infty$, $\psi=0$ gives the channel bottom.

2.2 System of equations for the unknowns $\phi_A,\phi_B,\phi_D,\phi_E$ and the function $v(\eta)$

The potentials $\phi_A,\phi_B,\phi_D,\phi_E$ are unknown and have to be determined from the length of the segments $|AB|,|BC|,|CD|,|DE|$:

$$|AB|=\int_{\phi_A}^{\phi_B}\frac{\mathrm{d}s_b}{\mathrm{d}\phi'}\mathrm{d}\phi',|BC|=\int_{\phi_B}^{0}\frac{\mathrm{d}s_b}{\mathrm{d}\phi'}\mathrm{d}\phi',|CD|=\int_{0}^{\phi_D}\frac{\mathrm{d}s_b}{\mathrm{d}\phi'}\mathrm{d}\phi',|DE|=\int_{\phi_D}^{\phi_E}\frac{\mathrm{d}s_b}{\mathrm{d}\phi'}\mathrm{d}\phi', \tag{18}$$

where

$$\begin{aligned}\frac{\mathrm{d}s_b}{\mathrm{d}\phi'}&=\left|\frac{\mathrm{d}z}{\mathrm{d}w}\right|_{w=\phi'}\\&=\sqrt{\left|\frac{a+\mathrm{e}^{\phi'}}{a-\mathrm{e}^{\phi'}}\frac{b-\mathrm{e}^{\phi'}}{b+\mathrm{e}^{\phi'}}\frac{d-\mathrm{e}^{\phi'}}{d+\mathrm{e}^{\phi'}}\frac{e+\mathrm{e}^{\phi'}}{e-\mathrm{e}^{\phi'}}\right|}\exp\left[\frac{\mathrm{i}}{\pi}\int_{-\infty}^{\infty}\frac{\mathrm{d}\ln v}{\mathrm{d}\phi''}\left[\pi-2\arctan\left(\mathrm{e}^{\phi''}-\mathrm{e}^{\phi'}\right)\right]\mathrm{d}\phi''\right].\end{aligned} \tag{19}$$

The velocity magnitude along the interface is found using the dynamic boundary condition, which depends on the interface shape $y(s)$, its curvature, and higher order derivatives of the curvature. The shape of the ice/liquid interface is determined by integrating the derivative of the mapping function along the upper boundary of the strip in the w-plane

$$\begin{aligned}y(\phi)&=y(-\phi^*)\\&+\mathrm{Im}\left\{\int_{-\phi^*+\mathrm{i}}^{\phi+\mathrm{i}}\sqrt{\frac{a+\mathrm{e}^{w'}}{a-\mathrm{e}^{w'}}\frac{b-\mathrm{e}^{w'}}{b+\mathrm{e}^{w'}}\frac{d-\mathrm{e}^{w'}}{d+\mathrm{e}^{w'}}\frac{e+\mathrm{e}^{w'}}{e-\mathrm{e}^{w'}}}\exp\left[\frac{\mathrm{i}}{\pi}\int_{-\infty}^{\infty}\frac{\mathrm{d}\ln v}{\mathrm{d}\phi'}\ln\left(\frac{\mathrm{i}\mathrm{e}^{\phi'}-\mathrm{e}^{w'}}{\mathrm{i}\mathrm{e}^{\phi'}+\mathrm{e}^{w'}}\right)\mathrm{d}\phi'\right]\mathrm{d}w'\right\},\end{aligned} \tag{20}$$

where $y(-\phi^*)=H$. Here, $-\phi^*$ and ϕ^* are the lower and the upper boundary of the computational region; the channel in the physical plane is truncated, and the flow outside the computational region, $|\phi|>\phi^*$, is assumed to be uniform.

In discrete form, the solution is obtained at fixed points $-\phi^*<\phi_j<\phi^*$, $j=1,\dots,N$ along the upper side of the strip w. The curvature and its derivatives are determined using spline interpolation of the nodes $y_m=y(\bar{\phi}_m)$ and $s_m=s(\bar{\phi}_m)$. The nodes $\bar{\phi}_m=\phi_{4m}$, $m=1,\dots,M$, $M=N/4$, are chosen as every fourth point on the set of the discrete points ϕ_j, $j=1,\dots,N$. We choose a fifth-order spline, which provides continuous derivatives along the interface up to the fourth derivative appearing in the pressure coefficient. By applying the dynamic boundary condition to the nodes $\bar{\phi}_m$, we can obtain the following system of nonlinear equations:

$$G_m(\bar{\boldsymbol{V}})=c_{pm}(\bar{\boldsymbol{V}})-c_{pm}^{ice}(\bar{\boldsymbol{V}})=0,m=1,\dots,M, \tag{21}$$

where $\bar{\boldsymbol{V}}=(v_1,\dots,v_M)^T$ is the vector of unknown velocities $v_m=v(\bar{\phi}_m)$,

$$c_{pm}(\bar{\boldsymbol{V}}) = 1 - v_m^2 - \frac{2[y_m(\bar{\boldsymbol{V}}) - 1]}{F^2} - C_d v_m^2 \left(\frac{\mathrm{d}v}{\mathrm{d}s}\right)_m, m = 1, \dots, M \tag{22}$$

is the pressure coefficient due to the fluid, and

$$c_{pm}^{ice}(\bar{\boldsymbol{V}}) = \frac{2}{F^2}(p_{ice} - p_a)_m, m = 1, \dots, M \tag{23}$$

is the pressure coefficient due to bending.

The system of equations (21) is solved using Newton's method. The Jacobian of the system is evaluated numerically using the central difference with $\Delta v_m = 10^{-8}$. At each evaluation of the function $G_m(\bar{\boldsymbol{V}})$, the system of nonlinear equations is solved using the Newton's method under internal iteration procedure. The velocities $v_j,\ j = 4m-3,\ 4m-2,\ 4m-1$, between the nodes s_{m-1} and s_m are determined using linear interpolation of the values $\ln v_m$ obtained from the solution of the system of equations (21), $m = 1, \dots, M$.

2.3 Analysis of the dispersion relation

We examine a steady sine-like wavy interface of small steepness δ_0, or the slope of the interface can be written as

$$\delta(s) = \mathrm{Re}\left[\delta_0 \mathrm{e}^{\mathrm{i}kHs}\right], \tag{24}$$

where kH is the nondimensional wavenumber. By differentiating equation (9) in the arclength coordinate s, we obtain

$$v^2 \frac{\mathrm{d}\ln v}{\mathrm{d}s} = -\frac{1}{F^2}[1 + E_b(kH)^4]\delta. \tag{25}$$

For the case without an ice sheet ($E_b = 0$), (25) becomes

$$v^2 \frac{\mathrm{d}\ln v}{\mathrm{d}s} = -\frac{\delta}{F^2} = -\frac{kH}{\tanh kH}\delta, \tag{26}$$

where we use the relation between the Froude number and wavenumber for free surface gravity waves in a channel of depth H. We assume that the velocity along the interface behaves the same as for the free surface case. From (25) and (26), we obtain the dispersion equation

$$F^2 \frac{kH}{\tanh kH} = 1 + E_b(kH)^4. \tag{27}$$

Figure 2 illustrates the relationship between Froude number and wavenumber obtained from the solution of equation (27) for various ice thicknesses. Usually, the dispersion relation relates wave frequency (or phase speed of a wave moving in still water) to wavenumber, $\omega^2 = k^2U^2$. In the present case, $U^2 = F^2gH$; therefore, the frequency ω and the Froude number can be expressed as $\omega^2 = k^2F^2gH$.

It can be seen in Figure 2 that, without an ice sheet ($h^* = 0$), each Froude number $F < 1$ corresponds to one wavenumber (kH). It tends to zero as the Froude number $F \to 1$. In the presence of an ice sheet, there is a minimal, or critical, Froude number F_{cr}, where the solution of the dispersion relation exists. In the range $F_{cr} < F < 1$, there are two wavenumbers, k_{gr} and k_{ice}, corresponding to the gravity and the elastic waves, respectively; the wavenumber $k_{ice} > k_{gr}$, or the elastic wave is

shorter than the gravity wave. This range of Froude number corresponds to the ice-supercritical and channel-subcritical flows. The larger the ice thickness, the smaller the wavenumber k_{ice}, and the critical Froude number approaches the channel critical Froude number, i.e. $F_{cr} \to 1$. Thus, the interval $F_{cr} < F < 1$, where both the gravity and the elastic waves exist, reduces.

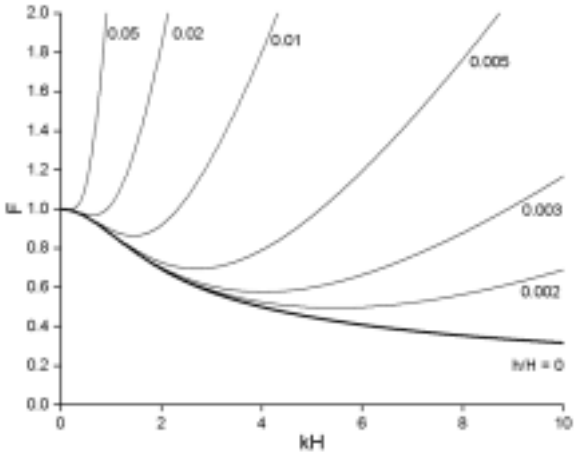
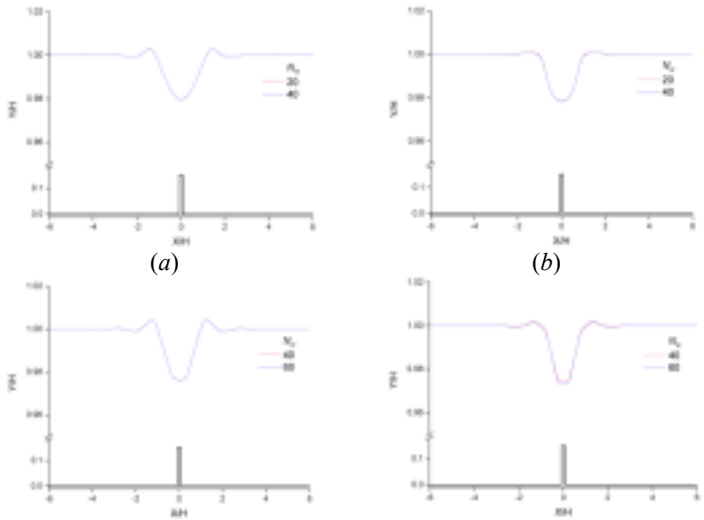


Figure 2. Froude number vs wavenumber for different ice thicknesses, h^*.

3. Results and discussion



(*a*) (*b*)

(*c*) (*d*)

Figure 3. Interface profiles for (*a*) $k_f = 0.5k_w$, $N_w = 20$(red line), $N_w = 40$(blue line); (*b*) $k_f = k_w$, $N_w = 20$(red line), $N_w = 40$(blue line); (*c*) $k_f = 2k_w$, $N_w = 40$(red line), $N_w = 60$(blue line); (*d*) $k_f = 3k_w$, $N_w = 40$(red line), $N_w = 60$(blue line). N_w represents the number of discretization points within one wavelength. Froude number $F = 0.5$, the height of the obstruction $a/H = 0.15$, length of the obstruction $b/H = 0.15$. $k_w = \frac{2\pi}{\lambda}, \lambda = 2\pi F^2$. $h^*_{min} = 0.0025$, corresponding critical Froude number $F_{cr} = 0.5744$.

Figure 3 shows the interface profiles for 4 different frequencies: (*a*) $k_f = 0.5k_w$; (*b*) $k_f = k_w$; (*c*) $k_f = 2k_w$; (*d*) $k_f = 3k_w$. Froude number is chosen to be 0.5, and since $h^*_{min} = 0.0025$, the corresponding critical Froude number $F_{cr} = 0.5744$, so the chosen Froude number is always smaller than the critical value no matter how the ice thickness changes, thus it is always a subcritical flow for the cases shown in the figure. $k_w = \frac{2\pi}{\lambda}$ is the namely wavenumber for subcritical flow, and $\lambda = 2\pi F^2$ is the namely wavelength. Red and blue lines represent different computational configurations for each case to prove convergence in terms of accuracy.

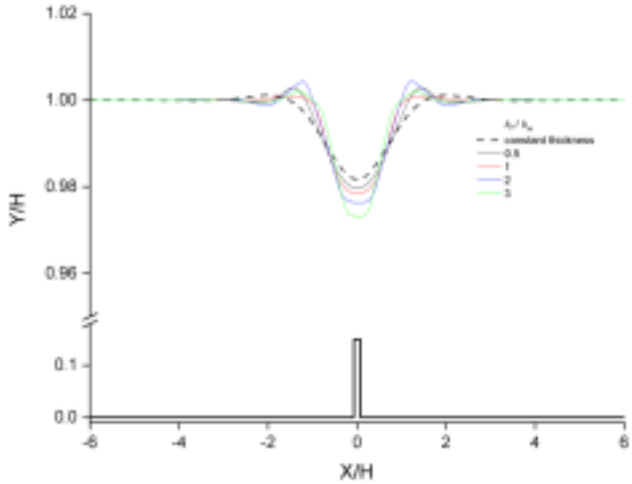


Figure 4. Comparison for different frequencies and constant ice thickness case. Froude number $F = 0.5$, the height of the obstruction $a/H = 0.15$, length of the obstruction $b/H = 0.15$. Constant thickness is taken as $h^*_{max} = 0.0075$(dash line), different frequencies are $k_f = 0.5k_w$(black solid line), $k_f = k_w$(red line), $k_f = 2k_w$(blue line), $k_f = 3k_w$(green line).

Figure 4 shows the interface profiles for different frequencies and constant ice thickness case. Constant ice thickness case could be regarded as the case where k_f tends to 0, consequently, function $h^*(s)$ will tend to $h^*_{max} = 1.5h^*_{aver} = 0.0075$. In the figure, we can see that all the cases form a symmetrical interface profile with respect to *y*-axis (*x*=0), which is consistent with the results for subcritical flows in the channel covered with constant-thickness ice [11]. A wave trough appears around the centre for each case, and the smallest depression occurs in the constant ice thickness case (dash line), then the depression deepens monotonically with the increase of k_f. The phenomenon indicates that ice thickness variation will weaken the rigidity of ice sheet, and result in larger deformation of the ice/liquid interface. Besides, more intensely the ice thickness varies, more significant this effect will be.

4. Conclusions

The problem of nonlinear flexural-gravity waves due to a rectangular obstruction on the bottom of the channel covered by an elastic ice sheet of variable thickness is studied. The potential flow theory is applied to describe the fluid, while the elastic sheet is modelled using the Cosserat theory of hyperelastic shells. Fully nonlinear boundary conditions are considered. The integral hodograph method is employed to solve the mixed boundary-value problem. The complex velocity and the complex potential are determined using the integral formula which solves the mixed boundary-value problem for the first quadrant, or the parameter plane.

The variation of ice thickness in the form of cosine function is considered. The effects of the frequency in the change of ice thickness on the interface profiles are analyzed. The deformation of the ice/liquid interface will become larger as the frequency increases, which indicates that the rigidity of ice sheet is weakened.

Acknowledgements. This work is supported by the National Natural Science Foundation of China (nos. W2541018, 52521009, 52192693, 52192690, 52350410468, W2433140), for which the authors are most grateful.

References

[1] B.Y. Ni, D.F. Han, S.C. Di, and Y.Z. Xue, *On the development of ice-water-structure interaction,* J. Hydrodyn., 32(4): 629-652, 2020.
[2] D. Karmakar, J. Bhattacharjee, and T. Sahoo, *Oblique flexural gravity-wave scattering due to changes in bottom topography,* J. Engng Maths, 66: 325–341, 2010.
[3] S. Boral, M.H. Meylan, T. Sahoo, and B.Y. Ni, *Time-dependent flexural gravity wave scattering due to uneven bottom in the paradigm of blocking dynamics,* Physics of Fluids, 35(11): 116603, 2023.
[4] K. Shishmarev, T.I. Khabakhpasheva, and A.A. Korobkin, *Ice response to an underwater body moving in a frozen channel,* Appl. Ocean Res., 91: 101877, 2019.
[5] K. Shishmarev, T.I. Khabakhpasheva, and A.A. Korobkin, *The response of ice cover to a load moving along a frozen channel,* Appl. Ocean Res., 59: 313–326, 2016.
[6] K. Shishmarev, T.I. Khabakhpasheva, and K. Oglezneva, *Steady-state motion of a load on an ice cover with linearly variable thickness in a channel,* J. Mar. Sci. Engng, 11(5): 1045, 2023.
[7] Y.A. Semenov, *Nonlinear flexural-gravity waves due to a body submerged in the uniform stream,* Phys. Fluids, 33(5): 052115, 2021.
[8] P.A. Milewski, J.M. Vanden-broeck, and Z. Wang, *Hydroelastic solitary waves in deep water,* J. Fluid Mech., 679: 628-640, 2011.
[9] T. Gao, Z. Wang, and P.A. Milewski, *Nonlinear hydroelastic waves on a linear shear current at finite depth,* J. Fluid Mech., 876: 55-86, 2019.
[10] P. Guyenne, and E.I. Părău, *Computations of fully nonlinear hydroelastic solitary waves on deep water,* J. Fluid Mech., 713: 307-329, 2012.
[11] B.Y. Ni, Y.A. Semenov, T.I. Khabakhpasheva, E.I. Părău, and A.A. Korobkin, *Nonlinear ice sheet/liquid interaction in a channel with an obstruction,* J. Fluid Mech., 983: A41, 2024.
[12] D. Porter, and R. Porter, *Approximations to wave scattering by an ice sheet of variable thickness over undulating bed topography,* J. Fluid Mech., 509: 145-179, 2004.
[13] I.V. Sturova, *Time-dependent response of a heterogeneous elastic plate floating on shallow water of variable depth*, J. Fluid Mech., 637: 305-325, 2009.
[14] P.I. Plotnikov, and J.F. Toland, *Modelling nonlinear hydroelastic waves*, Phil. Trans. R. Soc., A 369: 2942–2956, 2011.
[15] Y.A. Semenov, and A. Iafrati, *On the nonlinear water entry problem of asymmetric wedges,* J. Fluid Mech., 547: 231–256, 2006.
[16] Y.A. Semenov, and L.J. Cummings, *Free boundary Darcy flows with surface tension: analytical and numerical study*, Eur. J. Appl. Maths, 17: 607–631, 2007.

10th International Conference on HYDROELASTICITY IN MARINE TECHNOLOGY
Trondheim, Norway, June16th-18th, 2026

Wave Scattering by a Submerged Porous Circular disc with Radially Varying Porosity below an Ice-Covered Surface

Gayen, R.[1,*] and Hoque, A.[1]

[1] Department of Mathematics, Indian Institute of Technology Kharagpur, Kharagpur, 721302, West Bengal, India

Abstract. Marine and offshore structures often require materials that can adapt to varying environmental and mechanical conditions. Functionally graded porous (FGP) materials, which are a new generation of advanced materials, are receiving significant attention. They are unique in their ability to merge the variable mechanical and structural properties of functionally graded materials with the substantial energy absorption capacity of porous systems. Such materials hold great promise for coastal and polar engineering, where structures must withstand dynamic wave–ice interactions and harsh hydrodynamic conditions. This study explores the interaction of water waves with a thin, porous circular disc of radially varying porosity, submerged beneath an ice-covered surface in deep water. The ice cover, modeled as an elastic plate, introduces additional stiffness and significantly influences the wave field and hydrodynamic response. The analysis focuses on how variations in porosity distribution, submergence depth and ice rigidity affect key hydrodynamic quantities such as the hydrodynamic force and scattering cross-section. The results demonstrate that adjusting the porosity profile provides an effective means to control wave–structure interactions. Discs with higher porosity toward the edge experience reduced hydrodynamic loading and scattering, suggesting improved wave energy dissipation and structural resilience. In contrast, shallower submergence amplifies wave-induced forces, emphasizing the importance of optimized installation depth. Overall, the study highlights the potential of FGP structures as adaptable and efficient components in ice-covered waters, offering valuable design insights for floating platforms, underwater energy devices and coastal protection systems in polar and sub-Arctic regions.

Key words: *Wave scattering; Circular disc; Functionally graded porosity; Scattering cross-section; Hydrodynamic force*

1. Introduction

Wave–structure interaction in ice-covered waters is of growing importance due to increased offshore activities in polar and subpolar regions, including renewable energy installations, underwater vehicles and subsea infrastructure. In such environments, surface waves are significantly modified by the presence of ice covers, leading to altered dispersion characteristics, wave attenuation and scattering behaviour (cf. Wu et al. [20] and Perrie et al. [15]) . Understanding how submerged bodies interact with these modified wave fields is therefore essential for the safe and efficient design of marine and Arctic engineering systems.

Submerged porous structures are increasingly used in coastal and offshore engineering due to their ability to attenuate wave energy while reducing hydrodynamic loading compared to impermeable bodies. Applications include breakwaters, wave energy devices, artificial reefs and submerged protective barriers. Unlike solid bodies, porous structures allow partial fluid penetration, resulting in complex fluid–structure coupling governed by both inertia and dissipation mechanisms. While extensive studies exist on wave interaction with submerged rigid bodies in open water (cf. Porter [16], Martin and Farina

*Correspondence to: rupanwita.gayen@gmail.com

[12] and Hoque et al. [7]) and more recently under ice-covered surfaces (cf. Kundu et al. [10] and Hao et al. [6]), comparatively fewer investigations have addressed porous submerged bodies, particularly in the presence of ice cover (cf. Hoque et al. [8], Das et al. [2] and Mohapatra and Soares [13]).

Previous research on wave–ice interactions has established that ice sheets may be modelled as thin elastic plates, leading to flexural–gravity wave propagation rather than classical surface gravity waves. Several analytical and numerical studies have examined scattering by submerged plates, cylinders and discs beneath ice-covered surfaces, revealing significant changes in wave fields, scattering-cross section and hydrodynamic force compared to open-water configurations (cf. Farina and Martin [4], Hoque et al. [7] and Jiang et al. [9]). Separately, wave interaction with porous structures has been investigated under free-surface conditions, including porous breakwaters and submerged plates with uniform porosity (cf. de Freitas et al. [3] and Selvan and Behera [17]). However, the combined effects of porosity, ice cover and spatially varying permeability remain largely unexplored.

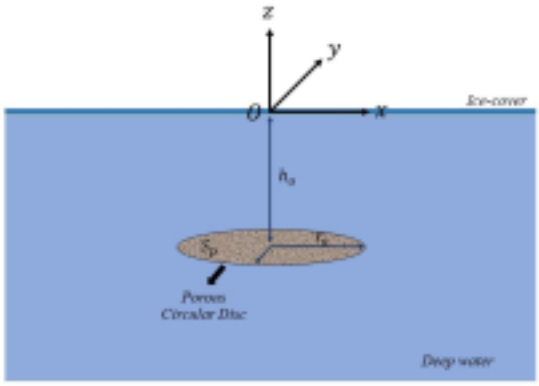
In practical applications, porous materials often exhibit non-uniform porosity and permeability due to fabrication processes, environmental degradation, or intentional functional grading to enhance mechanical performance and energy dissipation. Such spatial variations significantly modify transport properties and wave propagation, leading to altered dispersion, scattering, and attenuation compared with homogeneous porous media. Consequently, several studies have examined wave interaction with spatially non-uniform porous structures. Macaskill [11] investigated a vertical porous barrier with linearly varying permeability, while Song and Tao [18] studied a non-uniform porous cylinder. Banerjee et al. [1] and Tao et al. [19] showed that permeability variations strongly affect scattering characteristics and hydrodynamic responses for a non-uniform porous plates. Mondal et al. [14] analysed a non-uniform porous circular arc-shaped plate, and Gayen and Hoque [5] examined recently a circular disc with radially varying porosity, highlighting graded porous configurations for wave control and energy dissipation. However, functionally graded porous materials remain unexplored in water-wave scattering. Motivated by this, the porous-effect parameter in the present study is chosen such that the porosity increases radially from the centre of the disc.

The present study addresses this gap by formulating and solving the wave scattering problem for a submerged porous circular disc with radially varying porosity beneath an ice cover modeled as an elastic plate. A hypersingular integral equation is derived and solved using an expansion–collocation method to compute the velocity potential, expressed in polar coordinates and expanded in suitable basis functions. Hydrodynamic quantities, including the scattering cross-section and hydrodynamic force are evaluated to examine the effects of porosity distribution, disc submergence depth and ice rigidity. The results provide new physical insights into wave attenuation mechanisms induced by porous submerged bodies beneath ice sheets and demonstrate the potential of functionally graded porosity as a design parameter for wave control in cold-region marine engineering applications.

2. Mathematical Formulation

We consider a thin circular porous disc of radius r_o submerged horizontally at depth h_o beneath an ice-covered surface in deep water, as shown schematically in Figure 1. A cylindrical coordinate system (r,θ,z) is adopted with the z-axis directed upward, the undisturbed ice surface coinciding with the xy-plane, and the fluid domain extending to $z\to-\infty$. Flexural–gravity wave scattering is analysed in an incompressible, inviscid fluid of density ρ under irrotational flow. The disc surface S_p is defined by $S_p : 0\le r\le r_o,\ 0\le\theta\le 2\pi,\ z=-h_o$. The porosity varies radially through a prescribed seepage function $\lambda(r), 0\le r\le r_o$. Without loss of generality, spatial variables are non-dimensionalized by setting $r_o=1$.

Assuming small-amplitude oscillations, the time-harmonic velocity potential is written as $\phi(r,\theta,z,t)=\Re\{\Phi(r,\theta,z)e^{-\mathrm{i}\omega t}\}$, where $\Re$, ω, and t denote the real part, angular frequency, and time, respectively. The total potential is decomposed as $\Phi=\Phi^I+\Phi^S$, where Φ^I and Φ^S are the incident and scattered potentials, respectively.



(a)



(b)

Figure 1: Representation of the problem

Therefore, the scattering potential Φ^S satisfies the Laplace equation

$$\frac{1}{r}\frac{\partial}{\partial r}\left(r\frac{\partial \Phi^S}{\partial r}\right)+\frac{1}{r^2}\frac{\partial^2 \Phi^S}{\partial \theta^2}+\frac{\partial^2 \Phi^S}{\partial z^2}=0, \tag{1}$$

in the fluid domain, along with the linearized ice-cover condition

$$\left(1-\varepsilon k+D\nabla^4_{r,\theta}\right)\frac{\partial \Phi^S}{\partial z}-k\Phi^S=0 \quad \text{on} \quad z=0, \tag{2}$$

where $k=\omega^2/g$, g is the gravitational acceleration, $D=El_0{}^3/12(1-\mu^2)\rho g$ and $\varepsilon=\rho' l_0/\rho$. μ, E, l_0 and ρ' are the Poisson's ratio, the Young's modulus, the negligible thickness and the density of the ice-cover, respectively. ρ is the density of the water and $\nabla^4_{r,\theta}$ is the biharmonic operator defined as $\nabla^4_{r,\theta}=\frac{\partial^4}{\partial r^4}+\frac{2}{r^2}\frac{\partial^4}{\partial r^2\partial\theta^2}+\frac{1}{r^4}\frac{\partial^4}{\partial\theta^4}+\frac{2}{r}\frac{\partial^3}{\partial r^3}-\frac{2}{r^3}\frac{\partial^3}{\partial r\partial\theta^2}-\frac{1}{r^2}\frac{\partial^2}{\partial r^2}+\frac{4}{r^4}\frac{\partial^2}{\partial\theta^2}+\frac{1}{r^3}\frac{\partial}{\partial r}$.

The boundary condition on the surface of the disc is given by

$$\frac{\partial \Phi^S}{\partial z}(r,\theta,-h_o)=X^S(r,\theta,-h_o)-\mathbf{i}\nu_o G(r)[\Phi^S](r,\theta). \tag{3}$$

Here, $[\Phi^S](r,\theta)=\Phi^S(r,\theta,h_o^+)-\Phi^S(r,\theta,h_o^-)$ denotes the potential jump across the disc. X^S is the normal velocity induced by the incident potential in the scattering problem. The incident potential Φ^I is expressed as $\Phi^I=\frac{gA}{\omega}e^{\mathbf{i}\nu_o r\cos\theta}e^{\nu_o z}$, where A is the amplitude of the wave. Therefore, X^S is computed as

$$X^S=-\frac{\partial \Phi^I}{\partial z}=-\nu_o\frac{gA}{\omega}e^{\mathbf{i}\nu_o r\cos\theta}e^{\nu_o z}.$$

The complex-valued porous-effect parameter $G(r)$, which depends on the inertial coefficient S and the resistance force f, is defined following as (cf.Das et al. [2]) $G(r)=\frac{\lambda(r)(f+\mathbf{i}S)}{kl_p(f^2+S^2)}=G_r+\mathbf{i}G_i$, where $\lambda(r)$ denotes the plate porosity, defined as the ratio of the porous volume to the total plate volume and l_p is the plate thickness. The real part G_r represents the resistive effect of the porous medium, whereas the imaginary part G_i accounts for the associated inertial contribution. When $f\gg S$, G is predominantly real, corresponding to a densely packed plate, whereas for $S\gg f$, G becomes mainly imaginary, indicating a loosely packed structure. Finally, ν_o denotes the positive real root of the dispersion relation $E(\nu)\equiv\nu(D\nu^4+1-\varepsilon k)-k=0$.

The deep water condition is expressed as

$$\nabla\Phi^S \quad \to \quad 0 \quad \text{as} \quad z\to-\infty. \tag{4}$$

Also, Φ^S satisfies the radiation condition at infinity:

$$\lim_{r\to\infty} r^{\frac{1}{2}}\left(\frac{\partial}{\partial r}-\mathbf{i}\nu_o\right)\Phi^S=0. \tag{5}$$

Now we discuss a technique for converting the problems defined by Eqs. (1)-(5) into a two-dimensional hypersingular integral equation. Using Green's second identity to the potential function $\Phi^S(\mathbf{P})$ and the Green's function $\mathscr{G}(\mathbf{P},\mathbf{Q})$, the scattering velocity potential $\Phi^S(\mathbf{P})$ at any point $\mathbf{P}\equiv(r,\theta,z)$ in the fluid domain can be represented in terms of the Green's function as

$$\Phi^S(\mathbf{P})=\frac{1}{4\pi}\int_{S_p}[\Phi^S](\mathbf{q})\frac{\partial}{\partial\xi}\mathscr{G}(\mathbf{P},\mathbf{q})\,dS^p_{\mathbf{q}}, \tag{6}$$

where $\mathbf{Q}=(\alpha,\beta,\xi)$ is the source point. The Green's function $\mathscr{G}(\mathbf{P},\mathbf{Q})$ fulfilling the Laplace equation (1) in water other than the source point $\mathbf{Q}$, the ice-cover condition (2) and the bottom condition (4) takes the form

$$\mathscr{G}(\mathbf{P},\mathbf{Q})\equiv\mathscr{G}(r,\theta,z,\alpha,\beta,\xi)=\frac{1}{\sqrt{R^2+(z-\xi)^2}}+\frac{1}{\sqrt{R^2+(z+\xi)^2}}+2k\int_0^\infty f(\nu)e^{\nu(z+\xi)}\,d\nu, \tag{7}$$

where $R=[r^2+\alpha^2-2r\alpha\cos(\theta-\beta)]^{1/2}$, $f(\nu)=\frac{J_0(\nu R)}{E(\nu)}$ and J_0 is the Bessel function of the first kind of order zero.

From the above expression, the potential functions $\Phi^S(\mathbf{P})$ and $[\Phi^S]$ remain unknown. Applying the boundary condition (3) on the porous disc therefore yields the following integral equation:

$$\frac{1}{4\pi}\,\text{⨍}\!\!\!\!\!\!\int_{S_p}[\Phi^S](\mathbf{q})\frac{\partial^2}{\partial z\,\partial\xi}\mathscr{G}(\mathbf{p},\mathbf{q})dS^p_{\mathbf{q}}=X^S(\mathbf{p})-\mathbf{i}\nu_o G[\Phi^S](\mathbf{p}),\ \mathbf{p}\in S_p. \tag{8}$$

The resulting integral equation contains a hypersingular kernel, interpreted in the Hadamard finite-part sense and denoted by a "×" on the integral sign. The solution satisfies the edge condition $[\Phi^S]=0$ on ∂S_p, ensuring continuity of the velocity potential across the disc edge.

Substituting the expression for $\mathscr{G}$ from Eq. (7) into the kernel of the integral equation (8), we obtain

$$\frac{\partial^2\mathscr{G}}{\partial z\partial\xi}(\mathbf{p},\mathbf{q})=\frac{1}{R^3}+\mathscr{H}(\mathbf{p},\mathbf{q}). \tag{9}$$

From this expression, it is evident that the term $\frac{1}{R^3}$ gives rise to the hypersingular behaviour, while the remaining part $\mathscr{H}(\mathbf{p},\mathbf{q})$ is regular and is obtained by evaluating it using contour integration, the asymptotic behaviour of the Hankel function, and Jordan's lemma (cf. Hoque et al. [8]) as

$$\mathscr{H}(\mathbf{p},\mathbf{q})=\frac{12h_o^2}{(R^2+4h_o^2)^{5/2}}-\frac{1}{(R^2+4h_o^2)^{3/2}}+2\pi\mathbf{i}k\left[\frac{\nu_o^2e^{-2\nu_oh_o}}{E'(\nu_o)}H_0^{(1)}(\nu_oR)+\frac{\nu_1^2e^{-2\nu_1h_o}}{E'(\nu_1)}H_0^{(1)}(\nu_1R)-\frac{\bar{\nu}_1{}^2e^{-2\bar{\nu}_1h_o}}{E'(\bar{\nu}_1)}H_0^{(2)}(\bar{\nu}_1R)\right]$$
$$+\frac{4k}{\pi}\int_0^\infty\nu^2\frac{\{E(\nu)+k\}\sin2\nu h_o+k\cos2\nu h_o}{\{E(\nu)+k\}^2+k^2}K_0(\nu R)d\nu.$$

Substituting the kernel $\frac{\partial^2\mathscr{G}}{\partial z\partial\xi}$ and the expression of X^S, Eq. (8) can be written in polar coordinates as

$$\frac{1}{4\pi}\int_0^{2\pi}\int_0^1\frac{1}{R^3}[\Phi^S](\alpha,\beta)\alpha\,d\alpha\,d\beta+\frac{1}{4\pi}\int_0^{2\pi}\int_0^1\mathscr{H}(\alpha,\beta,r,\theta,h_o,k)[\Phi^S](\alpha,\beta)\alpha\,d\alpha\,d\beta$$
$$+\mathbf{i}\nu_oG(r)[\Phi^S](r,\theta)=-\nu_o\frac{gA}{\omega}e^{\mathbf{i}\nu_or\cos\theta}e^{-\nu_oh_o}. \tag{10}$$

To solve the resulting equation, we assume an expansion of the unknown velocity potential $[\Phi^S]$ in terms of basis functions with even angular modes due to symmetry about the x-axis.

$$[\Phi^S](\alpha,\beta)=\sum_{k=0}^{N_\alpha}\sum_{m=0}^{N_\beta}c_k^mB_k^m(\alpha,\beta)=\sum_{k=0}^{N_\alpha}\sum_{m=0}^{N_\beta}c_k^mP_{m+2k+1}^m(\sqrt{1-\alpha^2})\cos(m\beta), \tag{11}$$

where c_k^m are unknown coefficients and $P_{m+2k+1}^m(\alpha)$ denote the associated Legendre functions.

By inserting the expansion (11) into Eq. (10), the hypersingular contribution on the left-hand side can be evaluated analytically as (cf. Farina and Martin [4])

$$\int_0^{2\pi}\int_0^1\frac{1}{R^3}B_k^m(\alpha,\beta)\alpha\,d\alpha\,d\beta=D_k^m\frac{B_k^m(r,\theta)}{\sqrt{1-r^2}},\ \text{with}\ D_k^m=-4\pi2^{2m}\frac{2k+1}{2k+2m+1}\frac{\Gamma(m+k+3/2)}{\Gamma(k+1)}. \tag{12}$$

Consequently, Eq. (10) can be rewritten in the following equivalent form:

$$\frac{1}{4\pi}\sum_{k=0}^{N_\alpha}\sum_{m=0}^{N_\beta} c_k^m \left\{ D_k^m \frac{B_k^m(r,\theta)}{\sqrt{1-r^2}} + \int_0^{2\pi}\int_0^1 P_{m+2k+1}^m\left(\sqrt{1-\alpha^2}\right)\cos m\beta\, \mathscr{H}(\alpha,\beta,r,\theta,h_o,k)\alpha\, d\alpha\, d\beta \right.$$
$$\left. +4\pi \mathbf{i}\nu_o G(r) P_{m+2k+1}^m\left(\sqrt{1-r^2}\right)\cos m\theta \right\} = -\nu_o \frac{gA}{\omega} e^{\mathbf{i}\nu_o r\cos\theta} e^{-\nu_o h_o}. \quad (13)$$

To determine the unknown coefficients c_k^m, the integral equation is collocated at $(N+1)^2$ points, with $N = N_\alpha = N_\beta$. The collocation points are defined as

$$r_u = \cos\left(\frac{\theta_u}{2}\right) \text{ and } \theta_w = \frac{(2w+1)\pi}{(2N+2)}, \quad \text{where } u,w = 0,1,2\ldots N.$$

This procedure yields a linear system of the form

$$\boldsymbol{A}\boldsymbol{x} = \boldsymbol{b}, \quad (14)$$

where, $\boldsymbol{A} = (a_{jn})_{(N+1)^2\times(N+1)^2}$ denotes the coefficient matrix with entries

$$a_{jn} = D_k^m \frac{B_k^m(r_u,\theta_w)}{\sqrt{1-r_u^2}} + \int_0^{2\pi}\int_0^1 P_{m+2k+1}^m\left(\sqrt{1-\alpha^2}\right)\cos(m\beta)\,\mathscr{H}(\alpha,\beta,r_u,\theta_w,h_o,k)\,\alpha\, d\alpha\, d\beta$$
$$+4\pi\mathbf{i}\nu_o\, G(r_u)\, P_{m+2k+1}^m\left(\sqrt{1-r_u^2}\right)\cos(m\theta_w),$$

$\boldsymbol{x} = (x_n)_{(N+1)^2\times 1}$ is the unknown vector with entries $x_n = c_k^m$ and $\boldsymbol{b} = (b_j)_{(N+1)^2\times 1}$ is the known vector with entries $b_j = -4\pi\nu_o \frac{gA}{\omega} e^{\mathbf{i}\nu_o r_u\cos\theta_w} e^{-\nu_o h_o}$. Here, $j = (u,w)$ and $n = (m,k)$, with $u,w,k,m = 0,1,2,\ldots,N$.

Solving Eq. (14) provides the coefficients c_k^m, which are then substituted into Eq. (11) to determine the velocity potential difference $[\Phi^S](\alpha,\beta)$.

3. The Physical Quantities

3.1. Scattering cross-section

The scattering cross-section is a measure of the wave energy scattered by a body and is evaluated in terms of the average energy flux through a prescribed control surface. The non-dimensional scattering cross-section $\mathscr{Q}$ is defined as the ratio of the average energy flux carried by the scattered waves away from the disc to the average energy flux associated with the incident wave passing through a fixed vertical plane of unit width parallel to the wave crests.

In the far-field region, the scattered potential Φ^S and the Green's function $\mathscr{G}$ behaves asymptotically as

$$\Phi^S(r,\theta,z) \sim \frac{1}{\sqrt{\nu_o r}} f(\theta) e^{\nu_o z} e^{\mathbf{i}\nu_o r} \quad \text{as} \quad r\to\infty, \quad (15)$$

and

$$\mathscr{G}(r,\theta,z,\alpha,\beta,\xi) \sim 2k\sqrt{\frac{2\pi}{\nu_o R}} \frac{e^{\nu_o(z+\xi)+\mathbf{i}(\nu_o R+\pi/4)}}{E'(\nu_o)} \quad \text{as} \quad R\to\infty, \quad (16)$$

respectively, where $f(\theta)$ represents the angular-dependent scattering amplitude.

By substituting Eqs. (15) and (16) into Eq. (6) and employing the far-field approximation $R \sim r - \alpha\cos\theta\cos\beta - \alpha\sin\theta\sin\beta$ as $r\to\infty$, the expression for the scattering amplitude can be written as

$$\begin{aligned} f(\theta) &= k\nu_o\sqrt{\frac{1}{2\pi}} \frac{e^{\mathbf{i}\pi/4} e^{-\nu_o h_o}}{E'(\nu_o)} \int_0^{2\pi}\int_0^1 [\Phi^S](\alpha,\beta) e^{-\mathbf{i}\nu_o\alpha\cos(\theta-\beta)}\,\alpha\, d\alpha\, d\beta \\ &= k\nu_o\sqrt{\frac{1}{2\pi}} \frac{e^{\mathbf{i}\pi/4} e^{-\nu_o h_o}}{E'(\nu_o)} \int_0^{2\pi}\int_0^1 \sum_{k=0}^{N_\alpha}\sum_{m=0}^{N_\beta} c_k^m B_k^m(\alpha,\beta) e^{-\mathbf{i}\nu_o\alpha\cos(\theta-\beta)}\,\alpha\, d\alpha\, d\beta. \end{aligned} \quad (17)$$

Therefore, the total scattering-cross section in non-dimensional form is expressed as

$$\mathscr{Q} = kr_o \int_0^{2\pi} \hat{f}(\theta)\, d\theta, \tag{18}$$

where $\hat{f}(\theta) = \frac{\omega}{gA} f(\theta)$ denotes the non-dimensional scattering amplitude .

3.2. Pressure Distribution and Hydrodynamic Force

At any point $\mathbf{P} \equiv (x,y,z)$ in the fluid, the pressure $\mathscr{P}(\mathbf{P},t)$ is evaluated using Bernoulli's equation and is given by

$$\mathscr{P}(\mathbf{P},t) = -\rho \frac{\partial \phi^S(\mathbf{P},t)}{\partial t} - \rho g z = \Re\left\{\mathbf{i}\rho\omega\Phi^S(\mathbf{P})e^{-i\omega t}\right\} - \rho g z, \tag{19}$$

Here, the potential function $\Phi^S(x,y,z)$ is determined from Eq. (6) as

$$\Phi^S(x,y,z) = \frac{1}{4\pi}\int_0^{2\pi}\int_0^1 [\Phi^S](\alpha,\beta)\left(\frac{\partial \mathscr{G}}{\partial \xi}\right)_{\xi=-h_o} \alpha\, d\alpha\, d\beta = \frac{1}{4\pi}\int_0^{2\pi}\int_0^1 \sum_{k=0}^{N_\alpha}\sum_{m=0}^{N_\beta} c_k^m B_k^m(\alpha,\beta)\left(\frac{\partial \mathscr{G}}{\partial \xi}\right)_{\xi=-h_o} \alpha\, d\alpha\, d\beta, \tag{20}$$

where $\left(\frac{\partial G}{\partial \xi}\right)_{\xi=-h_o} = \frac{z+h_o}{\{R^2+(z+h_o)^2\}^{3/2}} - \frac{z-h_o}{\{R^2+(z-h_o)^2\}^{3/2}} + 2\pi\mathbf{i}k\left[\frac{\nu_o e^{\nu_o(z-h_o)}}{E'(\nu_o)}H_0^{(1)}(\nu_o R) + \frac{\nu_1 e^{\nu_1(z-h_o)}}{E'(\nu_1)}H_0^{(1)}(\nu_1 R) - \frac{\bar{\nu}_1 e^{\bar{\nu}_1(z-h_o)}}{E'(\bar{\nu}_1)}H_0^{(2)}(\bar{\nu}_1 R)\right] + \frac{4k}{\pi}\int_0^\infty \nu \frac{\{E(\nu)+k\}\cos\{\nu(z-h_o)\}+k\sin\{\nu(z-h_o)\}}{\{E(\nu)+k\}^2+k^2}K_0(\nu R)d\nu.$

Also, the hydrodynamic force on a submerged porous disc is determined by analyzing the fluid-structure interaction, which involves evaluating the pressure distribution around the surface of disc in the fluid. Therefore, the hydrodynamic force $\mathscr{F}$ is calculated as

$$\mathscr{F} = \int_{S_p} [\mathscr{P}](\mathbf{q},t) dS_q^p, \quad \mathbf{q} \in S_p, \tag{21}$$

where $[\mathscr{P}]$ denotes the pressure difference across the two faces of the disc. Substituting $\mathscr{P}(\mathbf{P},t)$ from Eq. (19) yields

$$\mathscr{F} = \int_{S_p} \Re\left\{\mathbf{i}\rho\omega[\Phi^S](\mathbf{q})e^{-i\omega t}\right\} dS_q^p. \tag{22}$$

Using the coefficients c_k^m determined from Eq. (14), the scattering potential difference $[\Phi^S]$ is computed from Eq. (11) and subsequently employed in Eq. (22) to evaluate the hydrodynamic force.

3.3. Surface Displacement

The surface displacement associated with the flexural–gravity wave field is determined from the linearized kinematic free-surface condition. Assuming small-amplitude motion and a time-harmonic dependence of the form $e^{-\mathbf{i}\omega t}$, the scattered velocity potential $\phi^S(x,y,z,t)$ and the corresponding surface elevation $\hat{\eta}(x,y,t)$ are represented as

$$\phi^S(x,y,z,t) = \Re\left\{\Phi^S(x,y,z)e^{-\mathbf{i}\omega t}\right\}, \quad \text{and} \quad \hat{\eta}(x,y,t) = \Re\left\{\eta(x,y)e^{-\mathbf{i}\omega t}\right\}, \text{respectively.} \tag{23}$$

For an incompressible and irrotational fluid, the linearized kinematic boundary condition on the free surface is given by

$$\frac{\partial \hat{\eta}}{\partial t} = \frac{\partial \phi}{\partial z}, \qquad z = 0. \tag{24}$$

Substituting the time-harmonic representations of the velocity potential and the surface elevation into the above equation yields

$$\eta(x,y) = \frac{\mathbf{i}}{\omega}\frac{\partial \Phi}{\partial z}(x,y,0). \tag{25}$$

The derivative of potential function is obtained by differentiating Eq. (8) with respect to z, which gives

$$\frac{\partial \Phi^S}{\partial z}(x,y,0) = \frac{1}{4\pi}\int_0^{2\pi}\int_0^1 [\Phi^S](\alpha,\beta)\left(\frac{\partial^2 \mathscr{G}}{\partial z \partial \xi}\right)_{\substack{z=0\\ \xi=-h_0}} \alpha\, d\alpha\, d\beta = \frac{1}{4\pi}\int_0^{2\pi}\int_0^1 \sum_{k=0}^{N_\alpha}\sum_{m=0}^{N_\beta} c_k^m B_k^m(\alpha,\beta)\left(\frac{\partial^2 \mathscr{G}}{\partial z \partial \xi}\right)_{\substack{z=0\\ \xi=-h_0}} \alpha\, d\alpha\, d\beta. \tag{26}$$

Here, $\left(\frac{\partial^2 \mathscr{G}}{\partial z \partial \xi}\right)_{\substack{z=0 \\ \xi=-h_0}} = \frac{1}{\left(R^2+h_0^2\right)^{3/2}} - \frac{3h_0^2}{\left(R^2+h_0^2\right)^{5/2}} - \frac{1}{\left(R^2+h_0^2\right)^{3/2}} + \frac{3h_0^2}{\left(R^2+h_0^2\right)^{5/2}} + 2\pi i k \left[\frac{\nu_0^2 e^{-\nu_0 h_0}}{E'(\nu_0)} H_0^{(1)}(\nu_0 R) + \frac{\nu_1^2 e^{-\nu_1 h_0}}{E'(\nu_1)} H_0^{(1)}(\nu_1 R) - \frac{\bar{\nu}_1^2 e^{-\bar{\nu}_1 h_0}}{E'(\bar{\nu}_1)} H_0^{(2)}(\bar{\nu}_1 R) \right] + \frac{4k}{\pi} \int_0^\infty \nu^2 \frac{\{E(\nu)+k\}\sin(\nu h_0)+k\cos(\nu h_0)}{\{E(\nu)+k\}^2+k^2} K_0(\nu R)\, d\nu$ and $R = \sqrt{(x-r\cos\alpha)^2+(y-r\sin\alpha)^2}$.

4. Numerical Results

This section presents numerical results for wave scattering by a submerged porous circular disc beneath an ice-covered surface, focusing on the effects of porosity distribution, submergence depth, and ice rigidity on the hydrodynamic force and scattering cross-section. All quantities are non-dimensionalized using the disc radius r_o as well as pressure distribution and hydrodynamic force force are scaled by $\rho g/k$ and $\rho g A r_o^2$, respectively. The hypersingular integral equation is solved using an expansion–collocation method with associated Legendre polynomials and Fourier modes. The numerical results are computed with $N_\alpha = N_\beta = 5$ and are found to converge to an accuracy of at least four decimal places. The porosity distribution is modeled as $G(r) = G_0\left(1+ar^b\right)$, where G_0 is the reference porosity, $a \in [-1,1]$ controls grading, and $b \geq 1$ governs radial variation. Here, $a = 0$, $a > 0$, and $a < 0$ correspond to uniform, edge-increasing, and edge-decreasing porosity, respectively. Unless stated otherwise, results are shown for $G_0 = 0.2$, $a = 0.5$, and $b = 2$.

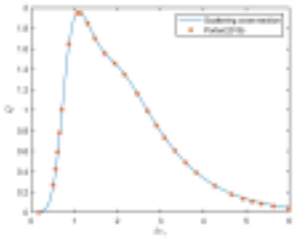


Figure 2: Comparison between the present scattering cross-section results and those obtained by Porter [16] for $h_o/r_o = 0.4$, $G = 0$, $D/r_o^4 = 0$, and $\varepsilon/r_o = 0$.

4.1. Validation

Figure 2 shows a comparison of the scattering cross-section $\mathscr{Q}$ with the wavenumber parameter kr_o for a submerged rigid circular disc ($G = 0$) beneath an free surface ($D/r_o^4 = 0$ and ε/r_o) in deep water. The solid curve represents the present numerical results, while the symbols star correspond to the benchmark solutions of Porter [16]. Excellent agreement is observed over the entire range of kr_o, validating the accuracy of the present formulation and numerical implementation.

Figure 3 compares the hydrodynamic force $\mathscr{F}/(\rho g A r_o^2)$ obtained in the present study with the results reported by Das et al. [2] for a porous disc with uniform porosity porosity $G = 0.1$ at the submergence $h_o/r_o = 0.3$ below an free surface ($D/r_o^4 = 0$ and ε/r_o). The figure demonstrates excellent agreement between the two sets of results, confirming the accuracy and reliability of the numerical method employed.

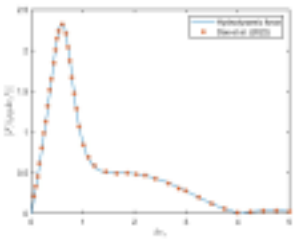


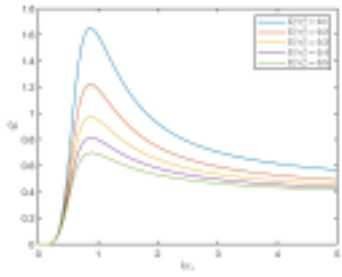
Figure 3: Comparison between the present hydrodynamic force $\mathscr{F}/(\rho g A r_o^2)$ and the results of Das et al. [2] for $h_o/r_o = 0.3$, $G = 0.1$, $D/r_o^4 = 0$, and $\varepsilon/r_o = 0$.

4.2. New Results

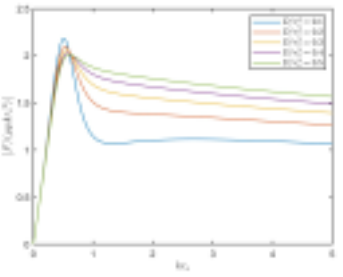
This section examines the results for a submerged porous disc with radially increasing porosity beneath an ice cover, focusing on the effects of submergence depth, ice rigidity, and porosity distribution

on the scattering cross-section and hydrodynamic force. Unless stated otherwise, the parameters are set as $D/r_o^4 = 0.1$, $\varepsilon/r_o = 0.001$ and $h_o/r_o = 0.2$.

Figure 4 shows the effect of ice rigidity on the scattering cross-section and hydrodynamic force of a submerged porous disc with $G(r) = 0.2(1+0.5r^2)$, $\varepsilon/r_o = 0.001$, and $h_o/r_o = 0.2$. Figure 4a presents $\mathscr{Q}$ versus kr_o for different D/r_o^4, while Figure 4b shows the corresponding hydrodynamic force. As the ice rigidity increases, the scattering cross-section decreases because a stiffer ice cover suppresses vertical surface deformation, thereby reducing wave energy radiation and reflection from the submerged disc. Near $kr_o \approx 0.5$, smaller rigidity produces larger hydrodynamic forces due to stronger disc–wave coupling and enhanced pressure fluctuations. At higher kr_o, the hydrodynamic force increases with rigidity as stiffer ice transmits wave-induced stresses more effectively to the fluid

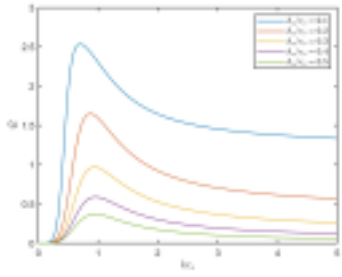


(a) Scattering cross-section

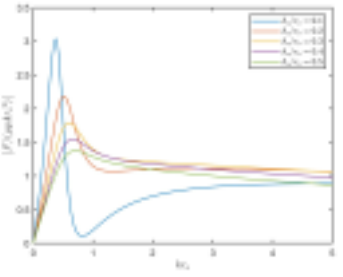


(b) Hydrodynamic force

Figure 4: Comparison of the scattering cross-section $\mathscr{Q}$ and hydrodynamic force $\mathscr{F}/(\rho g A r_o^2)$ for different values of ice rigidity D/r_o^4, with $\varepsilon/r_o = 0.001$, $h_o/r_o = 0.2$ and $G(r) = 0.2(1+0.5r^2)$.



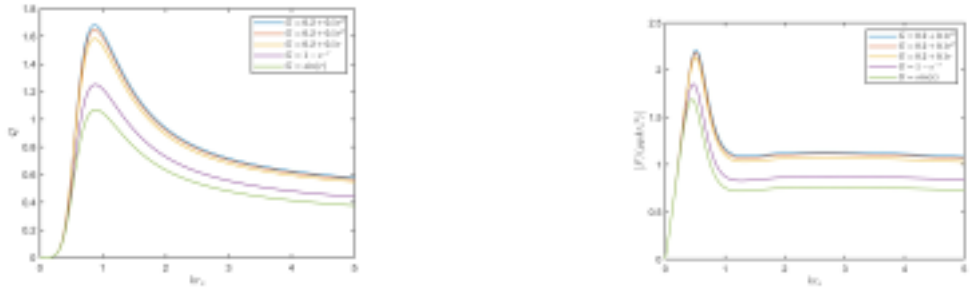
(a) Scattering cross-section



(b) Hydrodynamic force

Figure 5: Comparison of the scattering cross-section $\mathscr{Q}$ and hydrodynamic force $\mathscr{F}/(\rho g A r_o^2)$ for different values of the submerged depth h_o/r_o with $D/r_o^4 = 0.1$, $\varepsilon/r_o = 0.001$ and $G(r) = 0.2(1+0.5r^2)$.

Figure 5 illustrates the influence of submergence depth on wave interaction with a porous disc beneath an ice-covered surface. As shown in Figure 5, the scattering cross-section and hydrodynamic force decrease with increasing submerged depth h_o/r_o due to the exponential decay of the wave-induced pressure and velocity fields with depth, which weakens the wave–structure coupling and suppresses the resonance peaks. In particular, Figure 5b shows a significant reduction in the hydrodynamic force near the resonance region ($kr_o \approx 0.4$), where the wave–body interaction is most pronounced. For smaller submergence depths, stronger pressure gradients and enhanced fluid acceleration generate larger hy-



(a) Scattering cross-section

(b) Hydrodynamic force

Figure 6: Comparison of the scattering cross-section $\mathscr{Q}$ and hydrodynamic force $\mathscr{F}/(\rho g A r_o^2)$ for different radially increasing porosity distribution functions $G(r)$ with $D/r_o^4 = 0.1$, $\varepsilon/r_o = 0.001$ and $h_o/r_o = 0.2$.



(a) $D/r_o^4 = 0.1$

(b) $D/r_o^4 = 0.2$

Figure 7: Contour plots of pressure distribution $(k\mathscr{P}/\rho g)$ for two values of the ice rigidity D/r_o^4. The other parameters are fixed: $kr_o = 1$, $G(r) = 0.2 + 0.1r^2$, $\varepsilon/r_o = 0.001$ and $h_o/r_o = 0.2$.



(a) $d/r_o = 0.1$

(b) $d/r_o = 0.2$

Figure 8: Comparison of the surface elevation amplitude $|\eta/A|$ for two different submerged depths h_o/r_o at the resonance frequency $kr_o = 0.7$, for $G(r) = 0.2 + 0.1r^2$, $D/r_o^4 = 0.1$, and $\varepsilon/r_o = 0.001$.

drodynamic forces, whereas deeper submergence attenuates these effects, resulting in reduced force amplitudes and smoother resonance behaviour.

Figures 6a and 6b present the scattering cross-section and hydrodynamic force of a submerged porous disc with depth $h_o/r_o = 0.2$, ice rigidity $D/r_o^4 = 0.1$ and submerged ice thickness $\varepsilon/r_o = 0.001$, for various radially increasing porosity distributions $G(r)$. The results show that the porosity distribution

$G(r) = 0.2 + 0.1r^3$ yields relatively higher scattering cross-section and hydrodynamic force values than quadratic, linear, exponential, and trigonometric distributions because it attains lower radial porosity compared to the others. This reduced permeability limits fluid leakage through the disc, strengthens pressure gradients and enhances wave reflection, leading to increased hydrodynamic loading and scattering.

Figure 7 shows contour plots of the non-dimensional pressure distribution $(k\mathscr{P}/\rho g)$ over the submerged porous disc for two ice rigidity values $D/r_o^4 = 0.1$ and $D/r_o^4 = 0.2$, with other parameters fixed. In both cases, the pressure is maximum near the disc center and decreases smoothly toward the edge, indicating radially symmetric loading. As the ice rigidity decreases, the pressure field becomes more concentrated and intense near the center, reflecting stronger transmission of wave-induced stresses to the fluid and the submerged disc through the more flexible ice cover.

Figure 8 illustrates the variation of the normalized surface elevation amplitude $|\eta/A|$ for two different submerged depths h_o/r_o at the resonance frequency $kr_o = 0.7$. It is observed that the surface elevation is significantly larger for the smaller submergence depth, indicating stronger wave–disc interaction near the ice-covered surface. As the disc is placed deeper in the fluid, the free-surface response decreases due to the exponential decay of the flexural–gravity wave field with depth through the factor $e^{-\nu_0 h_o}$. Consequently, the scattered wave field becomes weaker and more smoothly distributed for larger h_o/r_o. The pronounced oscillatory behaviour near the disc region confirms the resonance amplification of the scattered wave field caused by constructive interaction between the incident and scattered flexural–gravity waves.

5. Conclusion

This study examines wave interaction with a submerged porous disc of radially varying porosity beneath an ice cover using a hypersingular integral equation solved by an expansion–collocation method. The effects of porosity distribution, submergence depth, and ice rigidity on scattering and hydrodynamic force are analysed and validated against uniform-disc results. Functionally graded porous (FGP) materials significantly enhance wave energy dissipation and reduce hydrodynamic loading. Increased ice rigidity suppresses surface deformation and lowers scattering, while its influence on force depends on frequency. Shallower submergence amplifies both scattering and force, highlighting the potential of FGP structures for marine engineering in ice-covered environments, including floating platforms, underwater energy devices, and coastal protection systems. Furthermore, the free-surface elevation results demonstrate that shallower submerged discs produce stronger resonance amplification and larger surface oscillations.

Acknowledgement

A.H. gratefully acknowledges financial support and research facilities provided by the University Grants Commission (Grant No. 211610172464).

References

[1] Banerjee, S., Mondal, D., and Banerjea, S. (2024). Wave response to a non-uniform porous vertical plate. *Journal of Marine Science and Application*, 23(4):867–876.

[2] Das, A., De, S., and Mandal, B. (2022). Radiation and scattering of flexural-gravity waves by a submerged porous disc. *Meccanica*, 57(7):1557–1573.

[3] de Freitas, I. M., Farina, L., and Miller, J. J. (2021). The heaving motion of a porous disc submerged in deep water. *Ocean Engineering*, 219:108290.

[4] Farina, L. and Martin, P. (1998). Scattering of water waves by a submerged disc using a hypersingular integral equation. *Applied Ocean Research*, 20(3):121–134.

[5] Gayen, R. and Hoque, A. (2026). A note on the radiation of water waves by a nonuniform porous disk. *Journal of Fluids Engineering*, 148(3):034501.

[6] Hao, L., Pan, Z., and Wu, B. (2020). Three-dimensional green-function method to predict the water wave radiation of a submerged body with ice cover. *Applied Ocean Research*, 101:102297.

[7] Hoque, A., Farina, L., Datta, R., and Gayen, R. (2025a). Hydrodynamic response of a submerged elliptic disc to surface water waves. *Applied Ocean Research*, 154:104327.

[8] Hoque, A., Gayen, R., Farina, L., and Datta, R. (2025b). The interaction of flexural-gravity waves with a submerged porous elliptic disk in deep water: Scattering and radiation analysis. *Physics of Fluids*, 37(7).

[9] Jiang, S. C., Gou, Y., and Teng, B. (2014). Water wave radiation problem by a submerged cylinder. *Journal of Engineering Mechanics*, 140(5):06014003.

[10] Kundu, S., Datta, R., Gayen, R., and Islam, N. (2019). The interaction of flexural-gravity waves with a submerged rigid disc. *Applied Ocean Research*, 92:101912.

[11] Macaskill, C. (1979). Reflexion of water waves by a permeable barrier. *Journal of Fluid Mechanics*, 95(1):141–157.

[12] Martin, P. and Farina, L. (1997). Radiation of water waves by a heaving submerged horizontal disc. *Journal of Fluid Mechanics*, 337:365–379.

[13] Mohapatra, S. and Soares, C. G. (2021). Surface gravity wave interaction with a horizontal flexible floating plate and submerged flexible porous plate. *Ocean Engineering*, 237:109621.

[14] Mondal, D., Samanta, A., Das, G., and Banerjea, S. (2024). Effect of nonuniform porosity in curved breakwater on water waves. *The ANZIAM Journal*, 66(3):201–221.

[15] Perrie, W., Meylan, M. H., Toulany, B., and Casey, M. P. (2022). Modelling wave–ice interactions in three dimensions in the marginal ice zone. *Philosophical Transactions of the Royal Society A*, 380(2235):20210263.

[16] Porter, R. (2015). Linearised water wave problems involving submerged horizontal plates. *Applied Ocean Research*, 50:91–109.

[17] Selvan, S. A. and Behera, H. (2020). Wave energy dissipation by a floating circular flexible porous membrane in single and two-layer fluids. *Ocean Engineering*, 206:107374.

[18] Song, H. and Tao, L. (2010). An efficient scaled boundary fem model for wave interaction with a nonuniform porous cylinder. *International Journal for Numerical Methods in Fluids*, 63(1):96–118.

[19] Tao, L., Song, H., and Chakrabarti, S. (2009). Wave interaction with a perforated circular breakwater of non-uniform porosity. *Journal of Engineering Mathematics*, 65(3):257–271.

[20] Wu, T., Luo, W., Jiang, D., Deng, R., and Huang, S. (2020). Numerical study on wave-ice interaction in the marginal ice zone. *Journal of Marine Science and Engineering*, 9(1):4.

Marine Membrane Structures

10th International Conference on HYDROELASTICITY IN MARINE TECHNOLOGY
Trondheim, Norway, June16$^{\text{th}}$-18$^{\text{th}}$, 2026

Assessing large hydroelastic parameter spaces through a table-top Faraday experiment

H. Pot[1,*] B. Christiaens[2,*] P. Wellens[1,*] S. Schreier[1,*] J. Westerweel[2]

[1] Department of Maritime and Transport Technology, Delft University of Technology, Delft, The Netherlands
[2] Laboratory of Aero and Hydrodynamics, Delft University of Technology, Delft, The Netherlands

Abstract. This study investigates the influence of stiffness on the hydroelastic wave-structure interactions of floating sheets, a concept for offshore photovoltaics. We propose an experimental method in which we can vary models, amplitudes and frequencies effortless, since conventional experimental methods have limitations, especially for large out-of-plane deformations. Moreover, green water effects which often occur for steep waves are eliminated with this setup. This study investigates the applicability of linear hydroelastic theory with the measurements on two floating membranes with different thickness. The measured hydroelastic wavelengths are for both membranes larger than the predictions by the theoretical hydroelastic dispersion. We find that the measurements of both thicknesses can be matched if an in-plane tension is added to the linear hydroelastic dispersion relation. This study demonstrates that the measurements are not well predicted by the linear theory and the stresses in the structure are most likely underestimated by this prediction.

Key words: *Fluid-structure interactions; Hydroelastic dispersion; Floating membrane; Experiments, Synthetic Schlieren*

1. Introduction

Certain offshore structures evolve into increasingly flexible designs with vast principal dimensions. Such designs include floating airports [16], flexible breakwaters [17], wave energy converters [18, 19] and floating solar [20, 12, 21]. The latter may be most economically beneficial when it covers large spatial domains, and when investment cost are minimized by using a flexible floater design [22]. Flexible designs in offshore waves environments may be prone to out-of-plane deflections much larger than their own thickness [23]. This may induce loads beyond the often used linear approximations.

Figure 1 shows an often used characterisation for large floating structures such as floating airports, sea ice, and floating solar [16, 23]. This logarithmic figure stresses the vast range of scales associated with these designs: there are large variations in structure lengths, in hydroelastic stiffness (characteristic length), and the ratio between the structure length and the wavelength. Most numerical models are limited to linear plate theory [23]. However, the magnitude of the out-of-plane deformations is often not within the intended range of the linear plate theory and linear approximations most likely underestimates the strains in the structure [24, 23, 25]. Including geometrically nonlinear strains could therefore improve the load predictions. This however requires advanced modeling approaches.

In experimental research, the large surface coverage poses challenges since common facilities such as towing tanks have limited widths. Therefore, blocking effects or reflections can affect the response [26]. Therefore, large and expensive basins are generally necessary if scaling of the principal dimensions is required [27, 28, 4]. Secondly, often only a narrow parameter space and a single or a few models are tested, since exchanging models is labor intensive [27, 12, 29, 1, 4]. Experimental attempts in steep

*Correspondence to: h.m.pot@tudelft.nl

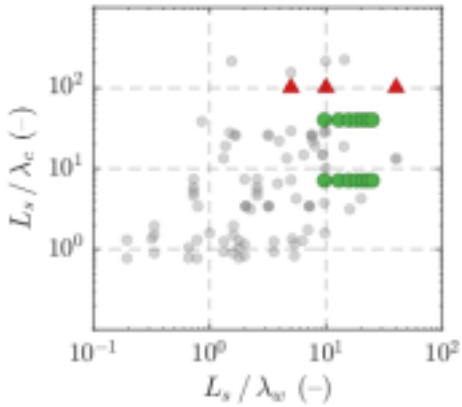


Figure 1: Typical characterisation of large floating structures, with experimental measurements reported in other studies (grey ○), the measurements of the current study (green ○), and the foreseen real scale application (red △). The literature data includes experimental studies to sea ice [1, 2, 3, 4, 5, 6, 7, 8, 9], Very Large Floating Structure (VLFS) [10, 11], floating PV [12], and small scale ($L_{basin} < 1$ m) floating membranes experiments [13, 14, 15]. The characteristic length is defined as a relation between the bending rigidity D and the hydrostatic stiffness ρg, $\lambda_c = (\frac{D}{\rho g})^{1/4}$.

waves report challenges regarding green water [29]. Moreover, when the models are delicate membranes, direct strain measurements are often difficult to perform, since strain gauges may be stiffer that the model itself, and optical strain measurements are not always possible due to large model motions. The typical foreseen non-dimensional parameters for the real scale application of floating solar are presented by the red triangles in Figure 1. Almost no experimental systematic variations of the stiffness are performed in this region. The proposed systematic variations are however necessary to understand the loads in the structure, especially for significant wave amplitudes.

In sea ice predictions and large scale floating membranes one-dimensional dispersion relations are often used to predict the hydroelastic wave-structure interaction [7, 30, 31, 32, 8]. When the planar dimensions increase, the hydroelastic deformations are the dominant response [33]. Therefore, hydroelastic dispersion relations may be suitable to model the response of a large floating sheet in waves. Hydroelastic dispersion relations can yield various load contributions, including mass, bending rigidity, pretension and gravity. Therefore it may be possible to study the relative contribution of different load terms by fitting the dispersion relation to measured responses. In experimental small-scale studies, the hydroelastic waves are well described by linear dispersion relations [31, 13, 14]. In analytical studies, nonlinear steepness is often added via perturbations. Such studies are however rarely validated with experimental data. Therefore, it is not certain if and how nonlinearities in the structure appear, and whether or not that is correctly modeled by the analytical approaches.

In this study, we propose a table-top experimental method to study the loads within a membrane under wave loading. A Faraday experiment is employed in which a small basin is vertically excited by a shaker through which standing waves are generated. The setup allows for a large parameter space to be explored, as illustrated in Figure 1. We compare the measurements with linear hydroelastic dispersion relations, since these are used to study the governing loads in the structure and to relate the small scale findings to real scale application size. Also, we aim to obtain insights in the response variations when the deformation amplitude increases.

2. Theory

2.1. Faraday Waves

Faraday waves are standing waves excited by a vertical vibration of the basin. The surface deformation ζ of the medium can be described by a Mathieu equation. In ship hydrodynamics, this equation is used to describe parametric roll. For an ideal fluid with phenomenological damping, this equation reads [34]:

$$\ddot{\zeta} + 2\gamma\dot{\zeta} + \omega[1 - \hat{a}\cos(\omega_e t)]\zeta = 0, \tag{1}$$

with ω_e the oscillating frequency of the shaker, ω the wave frequency, and $\hat{a}$ the non-dimensional amplitude of the shaker. Likewise the onset of parametric roll, the onset of Faraday waves starts when the energy inserted in the system by the shaker exceeds the viscous damping. The onset follows so-called stability tongues, with its minima occurring at $\omega_e/\omega = 2/n$ for n = 1, 2, 3, ... The lowest harmoninic response thus occurs at the subharmonic frequency $\omega = \omega_e/2$.

The relation between the sub-harmonic wave frequency and the wavelength is for fluids well described by the dispersion relation. An important note hereby is, that right after the onset amplitude of the waves, the geometry of the basin demands the wave patterns. For a circular basin, this results in a circular wave pattern which looks like Bessel functions. Above the onset amplitude, the pattern is indifferent of geometry of the basin [35]. Therefore the same wave patterns can be generated in for instance circular or square basins. In this study we focus on wave patterns independent of geometry of the basin.

2.2. Dispersion relations

The dispersion relation for water waves yields [36]:

$$\omega^2 = \left(g + \frac{\sigma}{\rho}k^2\right) k \tanh kd, \tag{2}$$

and describes the fixed relation between the wave frequency ω and wave number k through the gravitational acceleration g, the surface tension σ, the density of the fluid ρ, and the water depth d. Now, we assume a free floating thin plate with thickness h, structural mass per unit area $\rho_s h$, and bending rigidity $D = \frac{Eh^3}{12(1-\nu^2)}$, with Young's Modulus E, and Poisson ratio ν. With the classical thin plate theory, the governing equation becomes [32]:

$$D\nabla^4\zeta - T\nabla^2\zeta + \rho_s h\zeta_{tt} = p, \tag{3}$$

with ζ the vertical sheet displacement, p the pressure acting on the bottom of the sheet imposed by the fluid, which is defined by the linearised Bernoulli equation, and ∇^2 and ∇^4 the Laplacian and bi-Laplacian operators, defined as $\nabla^2 = \frac{\partial^2}{\partial x^2} + \frac{\partial^2}{\partial y^2}$ and $\nabla^4 = \frac{\partial^4}{\partial x^4} + 2\,\frac{\partial^4}{\partial x^2 \partial y^2} + \frac{\partial^4}{\partial y^4}$, respectively. Here, T can be uniform and isotropic tension [14] or compression [32] in the sheet. We assess the limit in which the inertia of the sheet is much lower than the inertia of the fluid, and therefore neglect the sheet inertia. The dispersion relation is than derived as [32]:

$$\omega^2 = \left(g + \frac{T}{\rho}k^2 + \frac{D}{\rho}k^4\right) k \tanh kd. \tag{4}$$

In the limit where capillary effects are non-negligible, the air-water interface surface tension σ as presented in Eq. 2 is a component of T, acting as a dynamic, wave motion dependent tension. Therefore, T is defined as $\sigma + T_{add}$, with T_{add} being any other in-plane tension, if present. In the limit of a very small thickness compared to the wavelength, or the material being extremely flexible, the bending rigidity is negligible, through which the sheet is often referred to as membrane. In this limit, pretension is necessary to prevent the membrane from wrinkling or folding.

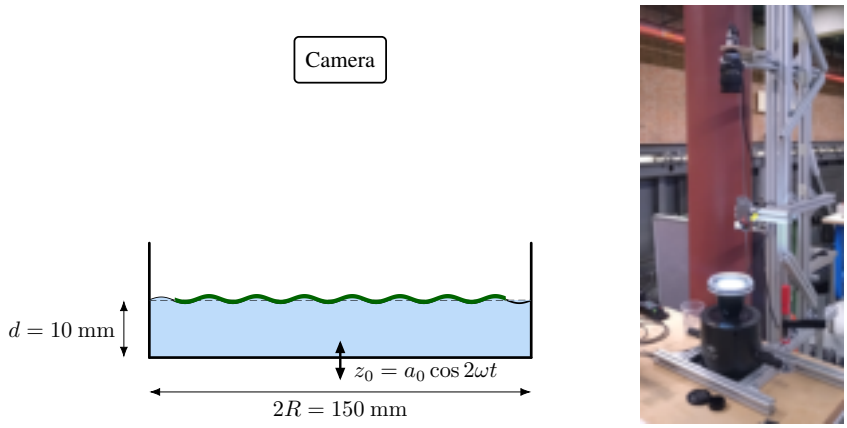


Figure 2: Experimental setup with an oscillating basin, a thin floating sheet, and a camera positioned above the basin.

3. Methods

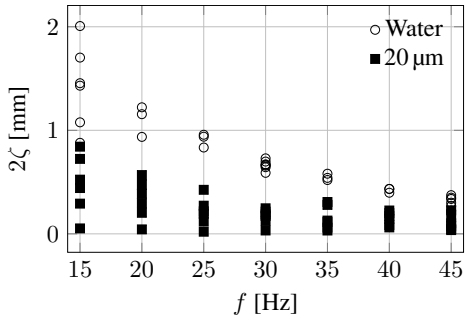
Measurements are performed in a vertically shaking fluid basin (Figure 2). The fluid basin is a cylindrical container with a diameter of 150 mm. The shaker is a Brüel & Kjaer Vibration Exciter Type 4808, driven by a Brüel & Kjaer Power Amplifier Type 2719. The oscillations are controlled by a NF Electronic Instruments 1930A multifunction synthesizer. The fluid depth is 10 ± 0.8 mm. The ambient temperature of the laboratory and the fluid is 20 ± 2 °C.

A 2.3 MP Basler a2A1920-150μm camera (1920×1200 pixels) is mounted 800 mm above the tank. The exposure time is 2 ms, and the gain is 12. The lens is a Nikon Af-S NIKKOR 24-85 mm f/3.5-4.5G ED VR. A random dot pattern with a dot diameter of 0.25 mm on transparent paper is placed under the basin to perform optical correlation with *Synthetic Schlieren* [37]. To enhance the speckle contrast, a circular LED light of 70 mm diameter is positioned directly below the dot pattern. The shaker accelerations are measured with an accelerometer connected to the shaker, using a PCB Model 482B11 ICP signal conditioner (accuracy $\pm$ 1.6 %). The image acquisition is phase-locked using a frequency divider to minimize errors due to phase shifting. The camera is triggered by a TTL output from the shaker excitator. The acquisition rate is directly related to the shaker frequency and is approximately 4 Hz. Pylon viewer (Basler, Germany) is used for image acquisition.

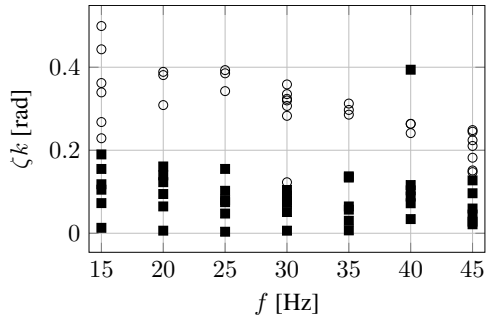
Circular samples of transparent elastic films (ELASTOSIL Film 2030, Wacker Chemie AG) with diameters of 120 mm are free floating on the fluid, leaving an average space of 15 mm with the walls of the basin. The samples have a thickness of 20 ± 0.4 μm and 200 ± 4.0 μm, respectively, by manufacturer's statement. The material density is 1.075 ± 0.025 g/cm^3, and a Poisson ratio of 1/2 is assumed. The manufacturer's stress-strain test for small strains reports a Young's Modulus of 0.58 ± 0.02 MPa. With a static hydroelastic wrinkle test [38] this is verified as 0.6 ± 0.2 MPa. The characteristic length $\lambda_c = (\frac{D}{\rho g})^{1/4}$ is 0.48 mm and 2.7 mm for the thin and the thick sheet, respectively.

Demineralised water is used as a test fluid, which is refreshed at the start of each day to minimize contamination. During the experiments, the sheets remained in a stable position, without making contact with the side walls of the tank. Trapped air bubbles and water drops are carefully removed prior to testing. The shaker frequency is varied from 30 Hz to 90 Hz with steps of 10 Hz, resulting in a subharmonic response frequency of half the shaker frequency. For clarity, the subharmonic response frequency is used in the latter of this work. Six wave amplitudes are tested at each frequency. Figure 3 shows the measured response heights and steepness per frequency.

Prior to each test a reference image is acquired. The displacement fields of 100 images are com-



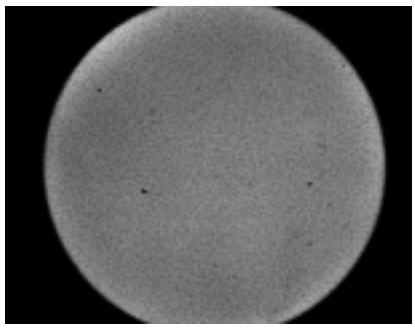
(a) Measured deformation amplitudes per frequency.



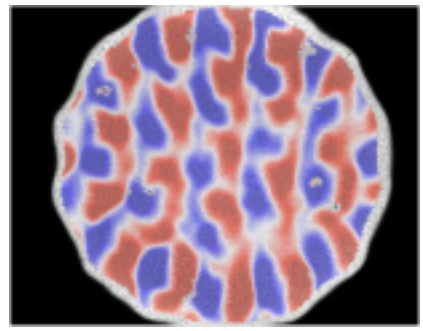
(b) Measured deformation steepness per frequency.

Figure 3: (a) Measured amplitudes (b) steepness for water waves and the floating membrane of thickness $h = 20\mu$m. The classic thin plate assumptions are considered valid for $\zeta k \leq 0.1$, with $0.1 < \zeta k < 0.2$ a transition regime. For fluids, $\zeta k > 0.2$ is known as strongly nonlinear waves.

puted via cross-correlation with the reference image using commercial software (DaVis 11 Strainmaster, LaVision GmbH, Göttingen, Germany), and a window size of 25 $\times$ 25 px^2 and stepsize of 9 px (0.54 mm). The raw images and computed displacements are shown in Figure 4. The amplitude fields are reconstructed from the displacement fields using the PIVMAT MATLAB library developed by [37]. Amplitude field analysis is performed with a 2D Fourier spectrum. Zero-padding is applied to improve peak localisation. Thereafter, the 2D spectrum is azimuthally averaged to obtain the 1D power spectrum. An average power spectrum is computed from all processed images of each test. The width of the dominant peak at 80% (arbitrarily chosen) of its maximum amplitude is used as an estimate of the wavelength uncertainty.



(a) Raw camera image.



(b) Displacement field.

Figure 4: (a) Raw camera image at still water and (b) DIC displacement field computed by cross-correlation in DAVIS. Note that these do not represent the actual deformation amplitudes, which are subsequently computed in MATLAB using the refractive method *Synthetic Schlieren*.

4. Results

Figure 5 shows the instantaneous hydroelastic deformation fields for $h = 20$ μm at wave frequencies of 15 Hz and 45 Hz, respectively. Note that the shaker frequency here is 30 Hz and 90 Hz, respectively,

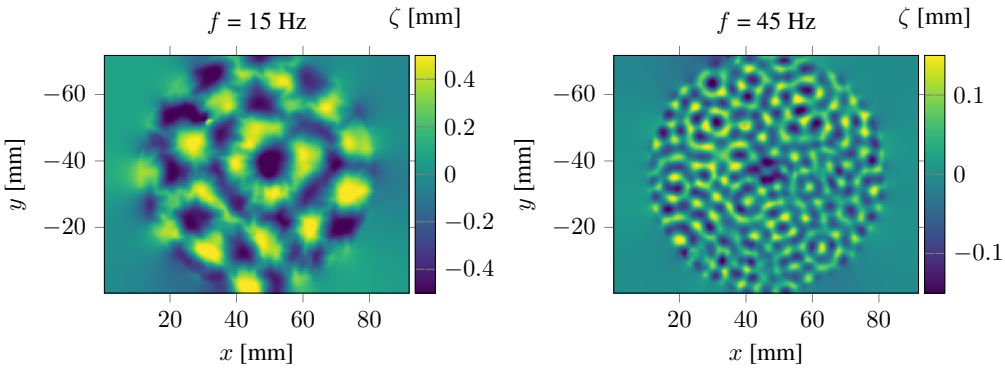


Figure 5: Instantaneous deformation field $\zeta(x, y)$ for the h = 20 μm membrane at (a) f = 15 Hz and (b) f = 45 Hz.

and that the wave frequency is subharmonic with respect to the shaker frequency (see Eq. 1). The Figure shows that the hydroelatic standing waves appear with a distinctive wavelength. The orientation of the waves is not influenced by the circular edges of the basin. The basin edges only have an effect when the shaker frequency is close to the natural frequency of the basin and the fluid, or when the wave amplitude is just above onset amplitude [35]. Above these thresholds, the waves are omnidirectional and the wavelengths are, for bare fluids, governed by dispersion relations [39].

Figure 6 shows the measured wavelengths over the range of frequencies for water and floating sheets of h = 20 μm and h = 200 μm. The effective surface tension of the air-water interface is computed by fitting Eq. 2 to the measurements with bare water, with σ = with 28 mN/m. This fitted surface tension is significantly lower than the theoretical value of 72 mN/m. However, contamination of water is well known to drastically decrease the surface tension, and various studies report similar values [40, 31, 39].

Figure 6 shows that the theoretical dispersion relation (red dotted line) for h = 20 μm is nearly identical to the dispersion relation of water. Here, the magnitude of the bending rigidity D of Eq. 4 is very small due to the thinness of the membrane. The measured wavelength for h = 20 μm are however slightly larger than this theoretical relation. Since the bending rigidity is near zero, this effect is more likely explained by an additional tension term. Indeed, if a tension term scaling to $\sim k^3$ of T_{add} is added to the theoretical dispersion relation, all measurement data of smallest steepness bin of h = 20 μm ly on the dispersion curve. $T_{add} = 10$ mN/m fits best for this thickness.

A possible explanation for this may be the presence of a uniform pre-tension as a result of the surface tension. A graphical explanation of this is shown in Figure 7. Due to the capillary effect of the fluid, the surface tension may impose a static pulling force on the edges of the membrane, a phenomena also observed at the edges of vertical walls [41]. Since this occurs along the circumference of the membrane, the effect may impose a uniform pretension. We test this hypotheses by drastically decreasing the surface tension by adding a surfactant (soap) when the membrane is at rest. In that case, the membrane shows wrinkles and folds and is not able to form a flat floating layer. We therefore conclude that some effect of static pre-tension is acting on the edges of the membrane caused by the surface tension. Note that the *dynamic* surface tension as included in Eq. 2 is also still present in the force balance, but only in dynamic conditions as it is curvature dependent. The interested reader is referred to [41] in which a thorough explanation of this concept is found. However, in-plane tensions from other sources also lead to longer wavelengths. They can originate from the nonlinear membrane effect (vón Kármàn strains). Note that in the current setup we cannot differentiate between the relative influence of the two in-plane tensions.

The measured wavelengths for h = 200 μm are significantly longer than for h = 20 μm. The theoretical dispersion relation for h = 200 μm (dash-dotted line) predicts significantly longer wavelengths

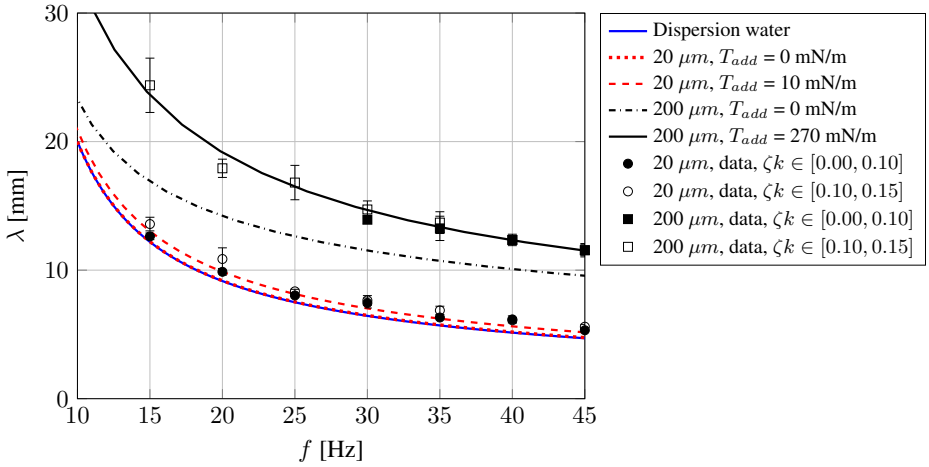


Figure 6: Theoretical dispersion relations (Eq. 4) and the measured data for h = 20 μm and h = 200 μm. The data is binned by steepness. The filled markers indicate a steepness range $\zeta k \in [0.00, 0.10]$, while the open markers indicate a steepness range $\zeta k \in [0.10, 0.15]$. The theoretical dispersion relations for h = 20 μm and h = 200 μm are displayed by the red dotted line and the black dash-dotted line, respectively. The red dashed line is fitted to the data of the lowest steepness bin of h = 20 μm by adding T_{add} = 10 mN/m to Eq. 4, and the black solid line to the data in the lowest bin of h = 200 μm with T_{add} = 270 mN/m. The data of both thicknesses is well described by the dispersion relations with the additional tension term. The dispersion relation for water with $\sigma = 28$ mN/m is shown in blue.



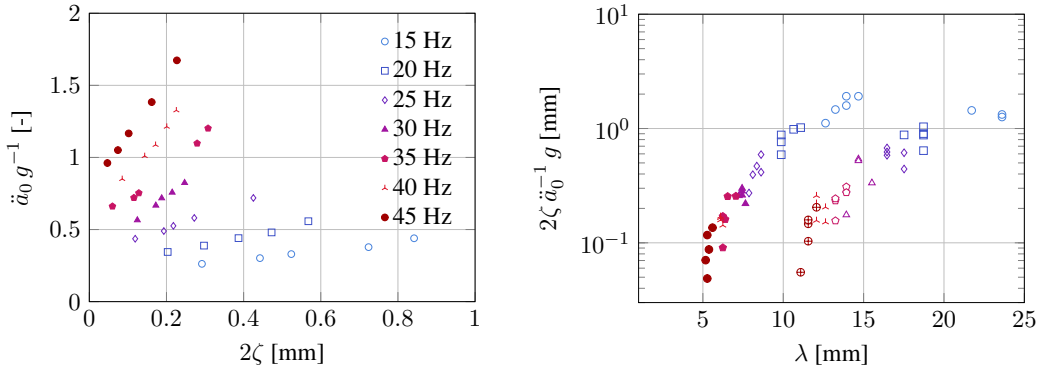
Figure 7: Capillary effect the fluid acting on the edges of the membrane. The angle of the capillary arc influences the magnitude of the horizontally applied tension to the membrane [41].

than the theoretical dispersion relation for h = 20 μm does (dotted line). This indicates the significant theoretical influence of the bending rigidity. The theoretical curve however largely under-predicts the measured wavelengths, and indicates that additional stresses are present under the loading. We therefore add a tension of T_{add} = 270 mN/m to Eq. 4 which closely fits all measurement data, likewise the addition of $T_{add} = 10$ mN/m for h = 20 μm. The wavelengths of both thicknesses can be accurately described by the theoretical dispersion relation including an additional tension term which scales with $\sim k^3$ in the dispersion relation. Therefore we assume that a different stress-strain relation may be more applicable for the membranes.

In Figure 6 the individual measurements are binned per response steepness ζk, where the filled markers indicate a steepness range $\zeta k \in [0.00, 0.10]$ and the open markers indicate a steepness range $\zeta k \in [0.10, 0.15]$. Despite uncertainties in the wavelengths, a larger wavelength is generally found for measurements with larger steepness. This may indicate that the steepness of current measurements already exceed the linear regime in which the dispersion relation of Eq. 4 is valid.

Figure 8a shows that the deformation amplitude linearly increases with the oscillation acceleration. Higher frequencies require a larger acceleration magnitude for similar size deformation amplitudes. The data also shows that a trend line would not pass through (0,0), indicating the presence of a typical Faraday experiment characteristic: the viscous threshold before waves start appearing at the surface. Figure

8b shows the measured wavelength against $2\zeta\, \ddot{a}_0^{-1}\, g$, which collapses the measurements of different frequencies. The frequencies are sorted by the same markers as in Figure 8a. For h = 20 μm, this results in a nearly straight line with narrow bandwidth. For a few frequencies, clearly different wavelengths are measured. This indicates the presence of nonlinear effects in the amplitude. The amplitude dependent effects are clearly non included in the linear dispersion relation of Eq. 4, clearly indicating the limitations for the current measurements. The 200 μm membrane shows a much larger spread in the wavelengths. The differences between both thicknesses indicate thickness-dependent nonlinear effects which may be a result of additional stress-strain relations in the thicker membrane or the Poisson penalty.



(a) Shaker accelerations against the deformation amplitude for $t = 20$ μm.

(b) Deformation amplitude over shaker acceleration against the wavelength.

Figure 8: Dynamic response of the membrane relative to the shaker acceleration. (a) The shaker accelerations against the deformation amplitude for h = 20 μm. The different frequencies are marked by colors ranging from blue (lowest frequencies) to red (highest frequencies) and are in detail shown in the legend. (b) The deformation amplitude over shaker acceleration against the wavelength. The same color- and marker scheme is used as in (a). The left data cloud is for h = 20 μm and the right data cloud for h = 200 μm.

5. Conclusions

This study shows that an additional tension in the linear hydroelastic dispersion relation is needed to predict the wavelengths in the floating membranes measured with the Faraday setup, which generates standing waves. For the thin membrane with h = 20 μm, the bending rigidity is insignificant compared to the gravitational loads, the surface tension and the additional tension. The measured wavelengths of the thin sheet are closely predicted by the linear dispersion relation, but the wavelengths of the thicker sheet are largely under-predicted by the linear dispersion relation. This observation disagrees with similar sized unidirectional progressive wave experiments [31, 13], where the linear dispersion relation serves as an excellent prediction for the wavelengths. The hydroelastic wavelengths of both membranes are excellently predicted when an additional tension scaling to $\sim k^3$ is added to the linear dispersion relation. We therefore attribute the discrepancy with linear theory to the effect of nonlinear stress-strain relations (vón Kármàn strains), although a direct confirmation of this effect with strain measurements is not possible with the current setup. In the current small scale setup, systematic variation of frequencies, amplitudes and floating models could effortless be measured. Due to the standing waves, no green water entered the floating model, a common challenge when measuring steep waves. This makes the setup useful for systematic variations and measurements on steep waves.

Acknowledgments

This study was funded by the Dutch Research Council (NWO) under the Grant Number 19002 ('FlexFloat') in the Open Technology Program (OTP). The authors are grateful for the fruitful discussions with prof. Willem van de Water, and the technical support by S. Tokgöz, C. P. Poot, J G den Ouden, F J Sterk, P Taudin Chabot, and A Piras.

References

[1] M. Meylan, L. Bennetts, C. Cavaliere, A. Alberello, and A. Toffoli. Experimental and theoretical models of wave-induced flexure of a sea ice floe. *Phys. Fluids*, 27:041704, 2015.

[2] K. Iijima, C. Ma, A. Pambela, and T. Maeda. DIC measurement of deflection waves travelling along a thin flexural plate floating at water surface. *Ocean Eng.*, 266:113079, 12 2022.

[3] M. Meylan. *The behaviour of sea ice in ocean waves*. PhD thesis, University of Otago, New Zealand.

[4] F. Montiel, F. Bonnefoy, P. Ferrant, L. Bennetts, V. Squire, and P. Marsault. Hydroelastic response of floating elastic discs to regular waves part 1: wave basin experiments. *J. Fluid Mech.*, 723:604–628, 2013.

[5] A. Pambela, C. Ma, T. Maeda, and K. Iijima. Stokes wave traveling along a thin elastic plate floating at water surface. *J. Fluids Struct.*, 120:103919, 2023.

[6] S. Parra, D. Sree, D. Wang, E. Rogers, J. Lee, C. Collins, A. Law, and A. Babanin. Experimental study on surface wave modifications by different ice covers. *Cold Regions Sci. Technol.*, 174:103042, 6 2020.

[7] S. Sakai and K. Hanai. Empirical formula of dispersion relation of waves in sea ice. In *Ice in the Environment: Proc. 16th IAHR Intern. Symp. on Ice*, pages 2–6. Intern. Assoc. Hydraulic Eng. Research, 12 2002.

[8] D. Sree, A. Law, and H. Shen. An experimental study on the interactions between surface waves and floating viscoelastic covers. *Wave Motion*, 70:195–208, 2017.

[9] D. Sree, A. Law, and H. Shen. An experimental study on gravity waves through a floating viscoelastic cover. *Cold Regions Sci. Technol.*, 155:289–299, 2018.

[10] H. Kagemoto, M. Fujino, and M. Murai. Theoretical and experimental predictions of the hydroelastic response of a very large floating structure in waves. *Appl. Ocean Res.*, 20:135–144, 1998.

[11] S. Schreier and G. Jacobi. Experimental investigation of wave interaction with a thin floating sheet. *Int. J. Offshore Polar Eng.*, 31(4):435–444, 2021.

[12] T. Kristiansen, P. Gron, and O. Faltinsen. A floating membrane solar island study. *Proc. 9th Int. Conf. Hydroelasticity Mar. Technol.*, pages 445–454, 2022.

[13] L. Domino, M. Fermigier, E. Fort, and A. Eddi. Dispersion-free control of hydroelastic waves down to sub-wavelength scale. *Eur. Phys. Lett.*, 121(1):14001, 2018.

[14] L. Deike, J. Bacri, and E. Falcon. Nonlinear waves on the surface of a fluid covered by an elastic sheet. *J. Fluid Mech.*, 733:394–413, 2013.

[15] L. Deike, M. Berhanu, and E. Falcon. Experimental observation of hydroelastic three-wave interactions. *Phys. Rev. Fluids*, 2:064803, 2017.

[16] H. Suzuki, B. Bhattacharya, M. Fujikubo, D. Hudson, H. Riggs, H. Seto, H. Shin, T. Shugar, Y. Yasuzawa, and Z. Zong. Very large floating structures. In *Proc. Int. Ship Offshore Struct. Congr.*, volume 2, pages 391–442, 2006.

[17] Y. Guo, S. Mohapatra, and C. Soares. Review of developments in porous membranes and net-type structures for breakwaters and fish cages. *Ocean Eng.*, 200, 2020.

[18] J. Orphin, A. Fleming, and C. Algie. Physical scale model testing of a flexible membrane wave energy converter: videogrammetric analysis of membrane operation. *Int. J. Mar. Energy*, 20:135–150, 2017.

[19] Y. Ye, J. Gan, H. Liu, W. Wu, S. Wang, and C. Soares. *A review of developments, material and mechanics of floating inflatable membrane structures for marine applications*, pages 649–657. CRC Press, 1 edition, 4 2025.

[20] S. Agarwal, O. Colomés, and A. Metrikine. Dynamic analysis of viscoelastic floating membranes using monolithic finite element method. *J. Fluids Struct.*, 129:104167, 2024.

[21] S. Oliveira-Pinto and J. Stokkermans. Marine floating solar plants: an overview of potential, challenges and feasibility. *Proc. Inst. Civ. Eng. Marit. Eng.*, 173:120–135, 2020.

[22] K. Trapani, D. Millar, and H. Smith. Novel offshore application of photovoltaics in comparison to conventional marine renewable energy technologies. *Renew. Energy*, 50:879–888, 2013.

[23] M. Zhang and S. Schreier. Review of wave interaction with continuous flexible floating structures. *Ocean Eng.*, 264:112404, 2022.

[24] M. Zhang and S. Schreier. Application of modal expansion method to very flexible floating structures (VFFSs). In *International Ocean and Polar Engineering Conference*, 6 2022.

[25] X. Chen, J. Jensen, W. Cui, and S. Fu. Hydroelasticity of a floating plate in multidirectional waves 1. *Ocean Eng.*, 30:1997–2017, 2003.

[26] A. Tassin, V. Cognet, A. Eddi, and M. Fermigier. Very large floating structure (VLFS) interacting with water waves: large scale laboratory experiments and numerical modelling. In *The 39th International Workshop on Water Waves and Floating Bodies*, 4 2024.

[27] S. Michele, S. Zheng, F. Buriani, A. Borthwick, and D. Greaves. Floating hydroelastic circular plate in regular and irregular waves. *Eur. J. Mech. B Fluids*, 99:148–162, 2023.

[28] Y. Cheng, C. Ji, G. Zhai, and G. Oleg. Oblique wave-induced responses of a VLFS edged with a pair of inclined perforated plates. *China Ocean Eng.*, 32:14–25, 2018.

[29] H. Pot, J. Westerweel, and S. Schreier. Stereoscopic digital image correlation for hydroelastic waves of floating membranes. *Meas. Sci. Technol.*, 36, 12 2025.

[30] P. Xu and P. Wellens. Fully nonlinear hydroelastic modeling and analytic solution of large-scale floating photovoltaics in waves. *J. Fluids Struct.*, 109:103446, 2022.

[31] J. Ono-Dit-Biot, M. Trejo, E. Loukiantcheko, M. Lauch, Raphaél, K. Dalnoki-Veress, and T. Salez. Hydroelastic wake on a thin elastic sheet floating on water. *Phys. Rev. Fluids*, 4:014808, 2019.

[32] R. Schulkes, R. Hosking, and A. Sneyd. Waves due to a steadily moving source on a floating ice plate. Part 2. *J. Fluid Mech.*, 180:297–318, 1987.

[33] P. Xu and P. Wellens. Theoretical analysis of nonlinear fluid–structure interaction between large-scale polymer offshore floating photovoltaics and waves. *Ocean Eng.*, 249, 2022.

[34] K. Kumar and L. Tuckermant. Parametric instability of the interface between two fluids. *J. Fluid Mech.*, 279:49–68, 1994.

[35] W. Edwards and S. Fauve. Patterns and quasi-patterns in the Faraday experiment. *J. Fluid Mech.*, 278:123–148, 11 1994.

[36] H. Lamb. *Hydrodynamics*. Dover Publications, 6 edition, 1932.

[37] F. Moisy, M. Rabaud, and K. Salsac. A synthetic schlieren method for the measurement of the topography of a liquid interface. *Exp. Fluids*, 46(6):1021–1036, 2009.

[38] D. Vella, P. Aussillous, and L. Mahadevan. Elasticity of an interfacial particle raft. *Europhys. Lett.*, 68:212–218, 2004.

[39] S. Douady. Experimental study of the Faraday instability. *J. Fluid Mech.*, 221:383–409, 1990.

[40] A. Ponce-Torres and E. Vega. The effects of ambient impurities on the surface tension. *EPJ Web Conf.*, 114, 2016.

[41] D. Vella. *The Fluid Mechanics of Floating and Sinking*. PhD thesis, University of Cambridge, 8 2007.

10th International Conference on HYDROELASTICITY IN MARINE TECHNOLOGY
Trondheim, Norway, June16$^{\text{th}}$-18$^{\text{th}}$, 2026

Effect of damping of floating flexible membrane exposed to water waves

Maugsten, O. P. [1,*] and Grue, J.[1]

[1] Section for Mechanics, Department of Mathematics, University of Oslo, Oslo, Norway

Abstract. The hydrodynamic response of a floating porous membrane is investigated using linear potential theory combined with a Darcy-type resistance model. The membrane is allowed to deform, and both rigid-body and flexible modes are included in the analysis. Response amplitude operators and mean horizontal drift forces are evaluated for varying pretension, porosity, and aspect ratio.

Increasing pretension shifts the behaviour from a flexible, bending-dominated regime toward rigid-body motion. This transition modifies both the modal response and the wavelength dependence of the drift force. Porosity reduces response amplitudes, while its influence on the mean drift force depends on the structural regime. Changing the aspect ratio alters the deformation pattern and significantly affects the drift force, with elongated membranes exhibiting reduced horizontal drift compared to square configurations.

The results show how pretension, porosity, and aspect ratio can be used to control wave-induced loads on floating membrane structures.

Key words: *Flexible membrane; Darcy damping; Drift force; Boundary element method; Fluid-structure interaction*

1. Introduction

Floating thin membranes interacting with surface gravity waves are relevant to applications such as floating solar platforms, and ice–wave interaction problems in polar regions. In recent years, renewed attention has been given to wave–ice dynamics due to climate-driven changes in Arctic sea-ice extent and thickness [1]. As ice covers thin and become more fragmented, wave-induced deformation, attenuation, and drift forces play an increasingly important role in large-scale ice evolution.

The hydrodynamics of flexible and porous floating structures have been studied extensively. Flexible membranes were analysed by [2], while wave-attenuation experiments for compliant surface covers were reported by [3]. Porous and resistive models have been shown to modify both scattering and drift forces by altering the balance between reflection, transmission, and dissipation [4, 5]. The link between attenuation and mean drift forces has been shown by [6], demonstrating that energy dissipation directly influences steady wave loading.

In a recent study (Maugsten and Grue [7]), we developed a three-dimensional potential-flow model for a floating square membrane with viscous damping represented through a linear porosity condition. That work established the coupled membrane–wave formulation, derived the associated energy relations, and demonstrated how porosity modifies far-field scattering and mean horizontal drift forces.

The present conference paper extends this earlier work by providing a more detailed parametric investigation of the membrane response. In particular, we examine how variations in pretension, porosity, and aspect ratio influence the amplitude response, and mean horizontal drift force. Special attention is given to the wavelength-dependent behaviour of the drift force and its connection to changes in reflected wave energy.

*Correspondence to: johng@uio.no

We particularly investigate wave effects due to a) a membrane of a given nondimensional pretension in the range: $T/\rho g L_1^2 \sim 10^{-2}$ to 10^{-4} (T pretension, ρ density of the water, g acceleration due to gravity, L_1 length of the membrane) and wavenumber KL_1 up to 30 (K wavenumber of the incoming waves), b) non-porous or porous membrane, c) the damping effect of the porosity, d) appearance of the RAOs in the respective cases, and e) the mean drift force. Membranes of quadratic or elongated fashion are investigated.

1.1. Comments on the Basic Assumptions

The membrane in consideration may be flooded. A membrane of positive buoyancy will float up. Practical experiments with sheets of density less than the water show this. Water on a porous membrane will be drained. A practical application of the problem in consideration is groups of interconnected PV panels floating directly on the water. In practice a uniform pretension will be defined by moorings organized in a clever way. A finding of the paper is that a nondimensional pretension of 10^{-3} or 10^{-4} gives similar responses and drift forces. Minor variations of the pretension may not be critical. A square floater may well be added to the boundaries of the membrane. A long and wide membrane occupies a large area compared to the floater, and similarly dominates over the floater as regards production of wave scattering. The floater is a minimal scatterer.

The assumption of a linear pressure drop model of a porous membrane exposed to water waves is encouraged by practical experiments connecting the porous effect parameter to the opening rate [8]. An alternative quadratic pressure drop formulation is not pursued here. Regarding the drift force, the tension effect (membrane) is more important than the bending stiffness (flexible plate). The membrane causes a significant drift force, while a non-porous flexible plate does not, see [9]. A porous flexible plate causes some drift force, however.

1.2. Outline

The paper is organized as follows. Section 2 briefly summarizes the mathematical formulation. Section 3 discusses the mean drift force. Section 4 presents the numerical results, focusing on the effects of pretension, porosity, and aspect ratio. Section 5 provides a discussion of the main findings, and conclusions are drawn in Section 6.

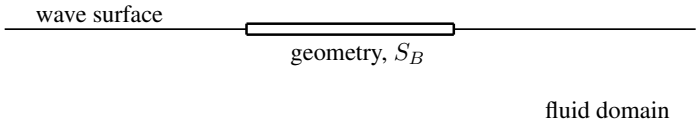


Figure 1: A porous floating membrane exposed to water waves

2. Method

Coordinates are introduced with (x, y) in the horizontal plane and z along the vertical. t is time. The linear wave-membrane problem is studied. Time-harmonic motion of the frequency ω is assumed.

2.1. Motion of the Membrane

A membrane of rectangular shape is floating on the water surface. This has length L_1 along the x-direction and width L_2 along the y-direction. The pretension T is expressed in nondimensional terms by $\Pi_1 = T/\rho g L_1^2$ (ρ density of the fluid, g acceleration of gravity). The vertical excursion of the membrane

is represented by: $W_0(x,y,t) = Re(w_0(x,y)e^{i\omega t})$, and modes of the membrane determined from the homogeneous wave equation: $-\rho_m h\omega^2 w_0(x,y) - T\nabla_h^2 w_0(x,y)$, with ρ_m the membrane density, h membrane thickness and ∇_h^2 the horizontal Laplace operator. The membrane response is expanded by: $w_0(x,y) = \sum_j \xi_j w_j(x,y) = \sum_j \xi_j X_j(x) Y_j(y)$. Clamped boundary conditions imposed along the boundaries with $w_0(x = \pm L_1/2, y) = 0$ and $w_0(x, y = \pm L_2/2) = 0$ obtain:

$$X_n(x) = a_n \cos[(2n-1)\pi x/L_1] + b_n \sin[2n\pi x/L_1], \tag{1}$$

$$Y_m(y) = c_m \cos[(2m-1)\pi y/L_2] + d_m \sin[2m\pi y/L_2]. \tag{2}$$

The rigid modes corresponding to heave, pitch and roll are represented by $w_{0,rigid} = \xi_1 + \xi_2 x + \xi_3 y$.

2.2. Boundary Condition at the Membrane

A porous floating membrane of given pretension is investigated (see Figure 1). This kind of flexible geometry is assumed to model several interconnected members separated by small gaps. A series of floating solar panels linked together may be an example. The porosity modifies the dynamics and damping of the floater.

The boundary condition along the membrane is modelled using a linear Darcy-type law, which relates the vertical bulk velocity through the membrane, $\bar{W}$, to the pressure difference across it, ΔP [10, 11]. The relation is expressed as

$$\frac{b}{\mu}\Delta P = \bar{W}. \tag{3}$$

The pressure jump is determined by $\Delta P = P_{fluid} - P_{air} = -\rho\partial\Phi/\partial t$, where Φ denotes the velocity potential that governs the fluid motion. The parameter b denotes the permeability of the membrane, and μ is the dynamic viscosity of the fluid. The velocity $\bar{W}$ is connected to the normal velocity of the fluid below the plate and the vertical velocity of the plate by

$$\bar{W} = \partial\Phi/\partial z - \partial W_0/\partial t, \tag{4}$$

where the components of the fluid velocity are obtained by $(\partial\Phi/\partial x, \partial\Phi/\partial y, \partial\Phi/\partial z)$. A nondimensional porosity parameter is introduced by: $B\omega\rho/(\mu K)$. The parameter $\Pi_2 = B/\sqrt{KL_1}$ is used in the computations. The wavenumber $K = \omega^2/g$. By experiments, Zhao et al. [8] have connected the porous effect parameter to the opening rate τ of a porous membrane exposed to water waves. For waveslope $KA = 0.02$, parameters B and τ are connected by: $(B,\tau) = (0.07, 0.02)$, $(0.26, 0.04)$, $(0.56, 0.06)$, $(2.0, 0.12)$. This gives some indication of the relation between the porosity parameter and the opening rate of the porous membrane.

The resulting boundary condition on the geometry is of combined Neumann-Dirichlet type, and is in the field of applied mathematics termed as a Robin boundary condition, and is subject of vital mathematical research [12, 13, 14, 15].

2.3. Fluid Motion

The fluid motion is represented by the wave potential

$$\Phi(x,y,z,t) = Re[A\tilde{\phi}e^{i\omega t}], \text{ where } \tilde{\phi} = \phi_D + i\omega\sum_j(\xi_j)\phi_j. \tag{5}$$

Here, $\phi_D = \phi_0 + \phi_s$, with $\phi_0 = (ig/\omega)\exp(Kz - iKr[\cos(\theta - \theta_0)])$, $x = r\cos\theta$, $y = r\sin\theta$, θ_0 the incoming wave heading, ϕ_s the scattering potential, and infinite water depth is assumed. The boundary condition at the geometry reads $\partial\phi_D/\partial z = -iKB\phi_D$ (diffraction) and $\partial\phi_j/\partial z = -iKB\phi_j + w_j$ (radiation). The potentials satisfy $-\omega^2/\tilde{\phi} + g\partial\tilde{\phi}/\partial z = 0$ at the wave surface, ϕ_j represent outgoing

waves in the far field, and decays with the depth. The wave potentials are solved by a set of integral equations. The membrane responses are calculated from the response equation,

$$\sum_j (K_{ij} + c_{ij} - \omega^2(M_{ij} + a_{ij} + i\omega b_{ij})\frac{\xi_j}{A} = X_i, \tag{6}$$

where K_{ij} is the stiffness matrix due to the membrane tension, c_{ij} restoring force matrix, M_{ij} mass matrix, a_{ij} added mass matrix, and X_i the exciting force in mode number j. More details are found in Maugsten and Grue [7].

2.4. Drift Force

The mean wave drift force is a second-order wave effect arising from the steady transfer of wave momentum to a floating structure. It is derived from first-order potential solutions and plays a critical role in the positioning and mooring design of floating bodies. Following the far-field momentum-flux formulation of [16], the non-dimensional drift force components in the horizontal plane are expressed as:

$$\frac{F_x^\infty}{\rho g L_1 A^2} = -\frac{1}{4}\left(\int_0^{2\pi} \cos\theta\, |\hat{U}(\theta)|^2\, d\theta + 2\cos\theta_0\ \mathrm{Re}\left\{\sqrt{\frac{2\pi}{\nu}}\, e^{i\pi/4}\hat{U}^*(\theta_0)\right\}\right), \tag{7}$$

$$\frac{F_y^\infty}{\rho g L_1 A^2} = -\frac{1}{4}\left(\int_0^{2\pi} \sin\theta\, |\hat{U}(\theta)|^2\, d\theta + 2\sin\theta_0\ \mathrm{Re}\left\{\sqrt{\frac{2\pi}{\nu}}\, e^{i\pi/4}\hat{U}^*(\theta_0)\right\}\right), \tag{8}$$

where F_x^∞ and F_y^∞ are the far-field contributions, and normalization by $\rho g L_1 A^2$ yields dimensionless quantities.

For a porous membrane, an additional contribution to the drift force arises from the momentum flux across the membrane surface S_B, resulting from the normal fluid flux through the boundary. This term is given by:

$$(F_x^{S_b}, F_y^{S_B}) = -\int_{S_B} \rho\, \overline{(U_x, U_y)\,\bar{W}}\, dS. \tag{9}$$

Using the porous boundary condition, the non-dimensional form becomes:

$$\frac{F_x^{S_B}}{\rho g L_1 A^2} = -\frac{1}{2}\,\frac{B\nu}{gL_1}\ \mathrm{Im}\int_{S_b} \tilde{\phi}\,\tilde{\phi}_x^*\, dS, \tag{10}$$

with an analogous expression for $F_y^{S_B}$. Here, $\Phi = \mathrm{Re}(Ae^{i\omega t}\tilde{\phi})$ and * denotes complex conjugation.

The total mean drift force is obtained by summing the far-field and membrane-surface contributions:

$$(F_x, F_y) = (F_x^\infty, F_y^\infty) + (F_x^{S_B}, F_y^{S_B}). \tag{11}$$

Although the membrane-surface contribution is relatively small at short wavelengths, it becomes significant in the long-wave limit. In this regime, it partially cancels the dominant far-field component and is essential for obtaining physically consistent predictions of the drift force.

3. Results

We examine the influence of porous damping, pretension, and aspect ratio on the membrane response. Response amplitude operators (RAOs) and mean drift force coefficients are presented as functions of the dimensionless wave number $KL_1 \in [0, 30]$. The membrane thickness is $10^{-6}L$.

Modes 1–3 correspond to rigid-body motions (heave, pitch, and roll). Flexible modes enter from mode 4 onward: mode 4 and 6 represent the first and second bending modes in the x-direction, while

modes 5 and 7 represent the corresponding modes in the y-direction. Higher modes exist but are not shown, as their contribution is secondary in the present parameter range (see Maugsten and Grue, 2026 for a detailed modal description).

Unless otherwise stated, the membranes are square. The incident waves propagate from $0°$.

3.1. Effect of Porous Damping and Pretension

Figure 2 shows RAOs for a compliant membrane with low pretension ($\Pi_1 = 10^{-3}$). The response is dominated by rigid-body heave and pitch (modes 1 and 2), with a significant contribution from the first flexible mode in the x-direction (mode 4). Modes 5 and 7 contribute primarily at long wavelengths. Introducing porosity ($\Pi_2 = 0.1$) consistently reduces the response amplitude across all modes, demonstrating the dissipative effect of porous damping. (The heave RAO tends to 1 at zero wavenumber.)

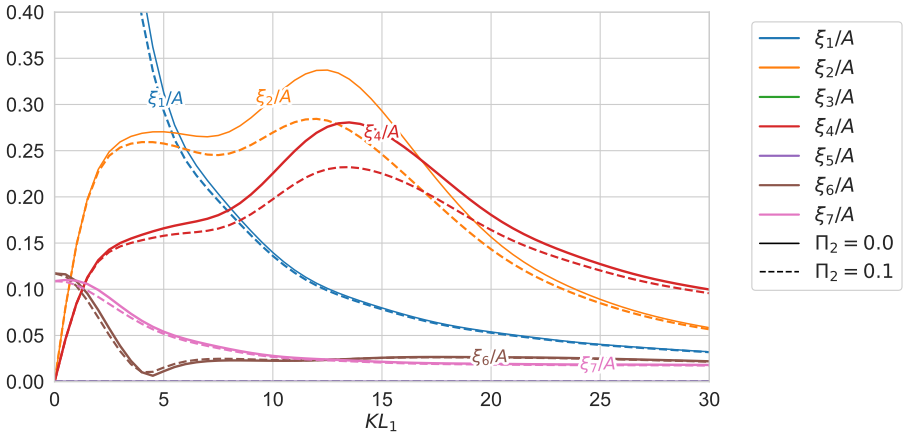


Figure 2: RAOs for membranes with pretension $\Pi_1 = 10^{-3}$. The non-porous case ($\Pi_2 = 0.0$) is shown with solid lines, while the porous case ($\Pi_2 = 0.1$) is shown with dashed lines.

Figure 3 shows that increasing the pretension to $\Pi_1 = 10^{-2}$ shifts the response toward higher wave numbers. Flexible modes remain important, but their peaks occur at shorter wavelengths, reflecting the increased membrane stiffness. Porosity continues to reduce the overall response.

For high pretension ($\Pi_1 = 10^{-1}$, Figure 4), the membrane response approaches rigid-body behaviour. Flexible mode amplitudes are strongly suppressed, with only mode 4 remaining visible as a secondary contribution. The system thus transitions from a flexible, wave-compliant structure to an effectively rigid membrane as Π_1 increases.

Figure 5 presents the mean horizontal drift force coefficient. A non-zero drift force is observed for all configurations, demonstrating that even an infinitely thin membrane experiences wave-induced drift.

The compliant membrane ($\Pi_1 = 10^{-3}$) exhibits relatively small drift forces at long wavelengths, with a pronounced increase toward shorter waves. In contrast, the stiff membrane ($\Pi_1 = 10^{-1}$) shows significantly larger drift forces at long wavelengths, while the force decays more rapidly for shorter waves. Increased pretension therefore shifts the drift response toward longer wavelengths and enhances its magnitude in that regime.

Porosity modifies the drift behaviour in a wavelength-dependent manner. For the flexible membranes ($\Pi_1 = 10^{-3}$ and 10^{-2}), porosity increases the drift force at long wavelengths and reduces it at short wavelengths. For the high-pretension membrane, the trend reverses. Porosity reduces the long-wave drift and increases it at shorter wavelengths.

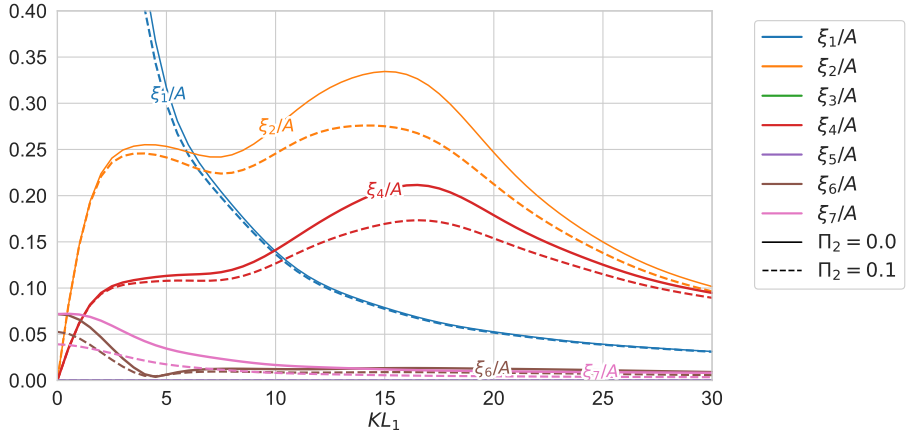


Figure 3: RAOs for membranes with pretension $\Pi_1 = 10^{-2}$. The non-porous case ($\Pi_2 = 0.0$) is shown with solid lines, while the porous case ($\Pi_2 = 0.1$) is shown with dashed lines.

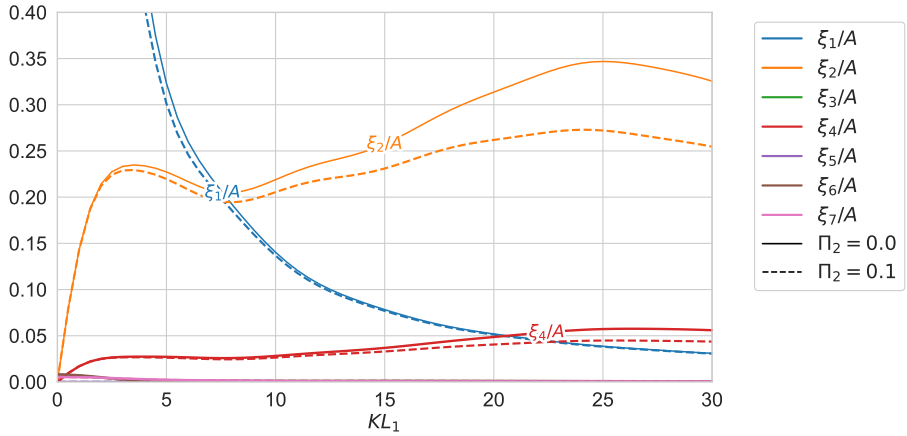


Figure 4: RAOs for membranes with pretension $\Pi_1 = 10^{-1}$. The non-porous case ($\Pi_2 = 0.0$) is shown with solid lines, while the porous case ($\Pi_2 = 0.1$) is shown with dashed lines.

3.2. Effect of Aspect Ratio

The membrane geometry, and in particular its aspect ratio, significantly influences the hydrodynamic response. In this section, the pretension is fixed at $\Pi_1 = 10^{-3}$ while the aspect ratio is increased from 1:1 (square) to 4:1. Figure 6 shows the RAOs for the elongated membrane. Compared to the square case, additional flexible modes of high number (notably modes 8 and 10) become significant. The aspect ratio therefore changes both the magnitude and the modal distribution of the response. Porosity reduces the overall amplitudes but does not substantially alter the modal pattern.

The corresponding mean drift force is shown in Figure 7. Increasing the aspect ratio to 4:1 leads to a substantial reduction in the drift force compared to the square membrane. The elongated geometry therefore weakens the net wave-induced horizontal loading. For this configuration, introducing porosity ($\Pi_2 = 0.1$) has only a minor influence on the drift force, indicating that geometric effects dominate over porous dissipation in determining the mean load for highly elongated membranes.

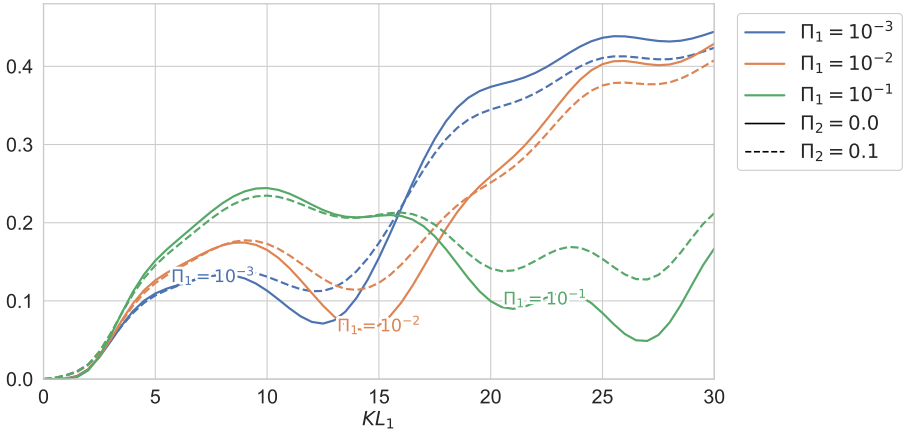


Figure 5: Mean horizontal drift force coefficient $F_x/(\rho g L_1 A^2)$ for membranes with varying pretension Π_1. Non-porous membranes are shown with solid lines. Porous membranes ($\Pi_2 = 0.1$) are shown with dashed lines.

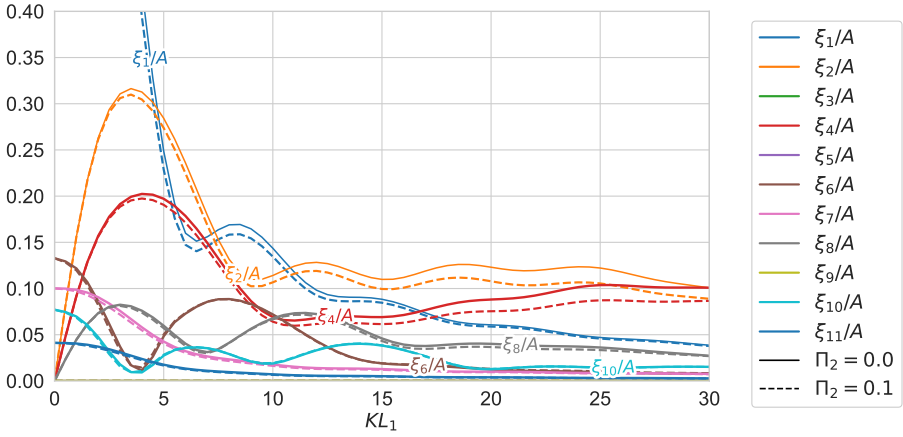


Figure 6: Response amplitude operators (RAOs) for a membrane with aspect ratio 4:1 (four times longer in the x-direction than in the y-direction) at fixed pretension $\Pi_1 = 10^{-3}$. Compared to the square membrane, additional higher-order flexible modes (notably modes 8 and 10) become dynamically significant. Solid lines: non-porous membrane ($\Pi_2 = 0$). Dashed lines: porous membrane ($\Pi_2 = 0.1$).

4. Discussion

The results show how pretension, porosity, and aspect ratio affect the behaviour of a floating flexible membrane. These parameters do not only change the size of the response, but also which modes contribute and how the mean drift force behaves.

Increasing the pretension moves the membrane from a flexible regime toward rigid-body behaviour. For low pretension Π_1 (Figure 2), bending modes contribute significantly to the response, especially in the wave-propagation direction. As Π_1 increases (Figure 3), the natural frequencies shift to higher wave numbers, and the flexible modes become less important within the range considered here. For high pretension (Figure 4), the response is mainly governed by rigid-body modes. This change also affects

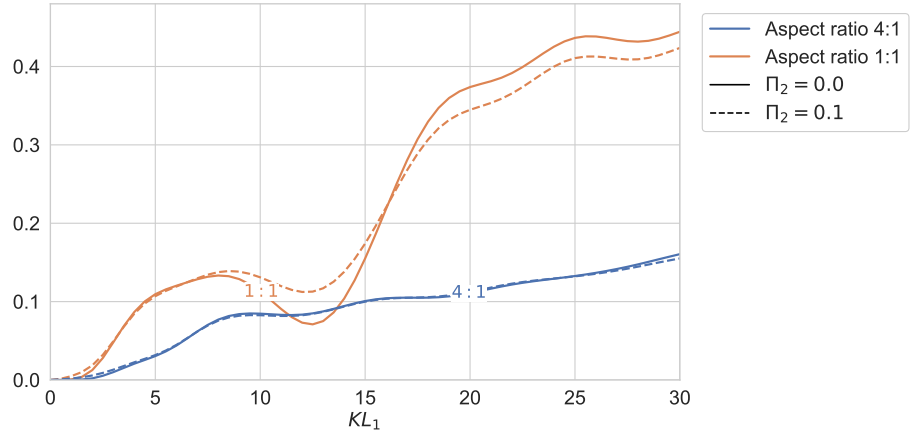


Figure 7: Mean horizontal drift force coefficient $F_x/(\rho g L_1 A^2)$ for membranes with aspect ratios 1:1 and 4:1 at $\Pi_1 = 10^{-3}$. Blue curves: 4:1 membrane. Orange curves: square membrane. Solid lines denote non-porous cases; dashed lines denote porous cases ($\Pi_2 = 0.1$).

the drift force (Figure 5). Flexible membranes show larger drift at shorter waves, while stiff membranes show larger drift at longer waves.

Porosity reduces the RAO amplitudes in all cases (Figures 2–4 and 6). Its effect on the mean drift force (Figure 5) is more complex. For flexible membranes, porosity increases the drift at long wavelengths and reduces it at short wavelengths. For stiff membranes, the trend is reversed. This shows that the effect of porosity depends on how flexible the structure is. Since the drift force is related to wave reflection and transmission, even small changes in the scattering can influence the load.

Change of the aspect ratio modifies the membrane deformations (Figure 6). The 4:1 membrane activates additional bending modes of high number. A dominant response in the longitudinal direction is found. At the same time, the mean drift force is much smaller than for the square membrane (Figure 7). In this case, geometry has a stronger influence on the drift than porosity.

From a practical point of view, both pretension and geometry can be used to control wave-induced loads. Higher pretension increases long-wave drift force (Figure 5), while a larger aspect ratio reduces the force (Figure 7). Porosity reduces oscillatory motion, but its influence on steady forces depends on the modal regime.

5. Concluding Remarks

The hydrodynamic response of a floating porous membrane is strongly influenced by pretension, porosity, and aspect ratio. Increasing pretension shifts the behaviour from a flexible, bending-dominated regime toward rigid-body motion. This transition changes both the modal response and the wavelength dependence of the mean drift force.

Porosity consistently reduces response amplitudes. Its effect on the mean drift force depends on the structural regime, showing different trends for flexible and stiff membranes. This demonstrates that dissipative effects interact with structural stiffness in determining steady wave loads.

The aspect ratio primarily modifies the deformation pattern and modal distribution. Elongating the membrane activates additional bending modes and significantly reduces the mean horizontal drift force compared to the square configuration.

Overall, stiffness and geometry provide effective means of controlling wave-induced loads, while porosity offers additional damping of motion. The present results are based on linear potential theory

and a linear porous resistance model.

References

[1] V. A. Squire. *Ocean wave interactions with sea ice: A reappraisal*, Annu. Rev. Fluid Mech., 52:37–60, 2020.

[2] I. H. Cho and M. H. Kim. *Interactions of a horizontal flexible membrane with oblique incident waves*, J. Fluid Mech., 367:139–161, 1998.

[3] G. Sutherland, T. Halsne, J. Rabault and A. Jensen. *The attenuation of monochromatic surface waves due to the presence of an inextensible cover*, Wave Motion, 68:88–96, 2017.

[4] J. Dokken, J. Grue and L. P. Karstensen. *Wave analysis of porous geometry with linear resistance law*, J. Marine Sci. Appl., 16(4):480–489, 2017.

[5] E. Mackay, H. Liang and L. Johanning. *A BEM model for wave forces on structures with thin porous elements*, J. Fluids Struct., 102:103246, 2021.

[6] K. H. Christensen and E. Terrile. *Drift and deformation of oil slicks due to surface waves*, J. Fluid Mech., 620:313–332, 2009.

[7] O. P. Maugsten and J. Grue. *Wave dissipation effects of a floating membrane*, J. Fluids. Struct., 144, 104548-1-18, 2026.

[8] F. Zhao, W. Bao, T. Kinoshita and H. Itakura. *Theoretical and experimental study on a porous cylinder floating in waves*, J. Offshore Mech. and Arct. Eng., 133/011301-1-10, 2011.

[9] K. H. McGuire, H. R. L. Jacobsen and and J. Grue. *Wave effects on a floating, flexible and porous plate in 3D*, J. Fluids. Struct., 137, 104361-1-18, 2025.

[10] G. I. Taylor. *Fluid flow in regions bounded by porous surfaces*, Proc. R. Soc. Lond. A, 234(1199), 456–475, 1956.

[11] A. T. Chwang. *A porous-wavemaker theory*, J. Fluid Mech., 132, 395–406, 1983.

[12] M. M. Schiffer. *Boundary-value problems in elliptical partial differential equations*, In: Modern Mathematics for the Engineer, ed. by E. F. Beckenbach, McGraw-Hill, 1956.

[13] A. Romeo and A. Saharian. *Casimir effect for scalar fields under Robin boundary conditions on plates*, J. Physics A; Math. Gen., 35:1297-1320, 2002..

[14] W. Arendt and M. Warma. *The Laplacian with Robin boundary conditions on arbitrary domains*, Potential Analysis, 19:341-363, 2003.

[15] J. E. H. Weber. *Surface wave damping by a Robin boundary condition*, Eur. J. Mech. B/Fluids, 109:243–252, 2025.

[16] J. Nossen, J. Grue and E. Palm. *Wave forces on three-dimensional floating bodies with small forward speed*, J. Fluid Mech., 227, 135–160, 1991.

10th International Conference on HYDROELASTICITY IN MARINE TECHNOLOGY
Trondheim, Norway, June16th-18th, 2026

Non-linear hydro-elastic analysis of a vertical pre-tensioned membrane in waves.

Moreau M.[1,*] and Kristiansen T.[1]

[1] Department of Marine Technology, Norwegian University of Science and Technology, Trondheim, Norway

Abstract. This study investigates the non-linear deformations and stresses of a pre-tensioned vertical membrane attached to a rectangular floater, free to heave under regular waves of low steepness. Fully non-linear simulations are first performed in a two-dimensional wave tank, where the membrane is modeled as a series of trusses. In parallel, a more computationally efficient reduced-order analytical model is proposed, based on a modal representation of the membrane displacements coupled with linear frequency-dependent hydrodynamic loads. The main second-order effects—a mean set-down of the floater and second-harmonic oscillations—are captured by the modal analysis, although the resonant periods of the out-of-plane displacements are shifted compared to the fully non-linear truss model, a discrepancy that requires further investigation.

Key words: *Hydro-elasticity, membrane, non-linear analysis*

1. Introduction

Membrane materials are increasingly used in marine applications due to their low cost and high flexibility, which allows them to deform with waves rather than transmit energy to attached structures. Linear frequency-domain models have been developed to predict the global motions of marine membrane structures, intended to be used in early-stage design. Such works have been derived for instance for circular floating membranes supporting solar panels or membrane-based hemispherical aquaculture farm [1], describing the displacements in terms of mode shape functions. Coupled with experiments, some of these studies highlight the importance of non-linear effects; for instance, [2] reports a mean set-down of the floater collar supporting a membrane aquaculture farm in waves without currents, which cannot be captured by linear analysis.

Time-domain hydro-elastic models have also been derived for horizontal floating thin plates, first with linear hydrodynamics [3] and later with a full third-order structural and hydrodynamic model [4] solved via perturbation methods for low wave steepness. Fully numerical solutions can capture non-linear behavior but at high computational cost. In our previous work [5], a taut membrane fixed to a rectangular floater was simulated in a 2D wave tank modeling the membrane as a system of trusses and lumped masses, and revealing significant second-order responses in both floater motions and membrane stresses. In the present work, the same truss model is used, but also develop reduced-order non-linear models for a taut membrane in waves, with the objective to both identify the main cause responsible for non-linear responses and to calculate these responses in a reasonable time. First, the fully non-linear truss model is introduced, then, a second-order analytical model for the membrane, coupled with linear frequency-domain hydrodynamic loads, is proposed and compared with the truss simulations.

*Correspondence to: mael.k.i.moreau@ntnu.no

2. Numerical wave tanks

We consider a two-dimensional numerical wave tank, where a vertical flexible membrane is attached to a rectangular floater that is free to heave and restrained in the other degrees of freedom. The analysis focuses on the wave-induced heave response of the floater and the non-linear deformation and stress distribution along the membrane. The membrane is initially stretched at the center of the tank at a given pre-tension T_0 from the tank's bottom to the floater, and is assumed to remain taut in waves. Bodies and notations are shown together with a tank's mesh in Fig. 1.

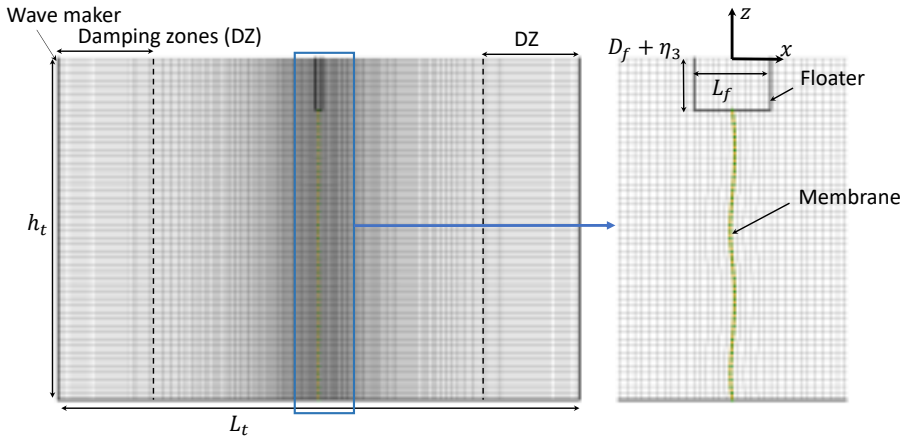


Figure 1: Grid mesh and notation of the two-dimensional wave tank with a vertical membrane and rectangular floater placed in its center. The membrane is initially stretched with a pre-tension T_0, fixed at the bottom to the tank's floor and at its top to the floater that is free to heave. For non-linear simulations, the mesh deforms with the membrane (on this figure, $T_0 = 28$N/m, $T = 1s$,$\epsilon = 1/80$, $t = 41.5$s, $L_f = 0.15$m, $D_f = 0.15$m).

The system is initially in static equilibrium. Neglecting the mass and displacement of the membrane, the mass of the floater for a given pre-tension T_0 is

$$M_f = \rho D_f L_f - T_0/g. \tag{1}$$

Regular waves are generated at the left boundary of the tanks, and dissipated at the outlet by a numerical damping zone, while reflected waves are also dissipated at the inlet. The fluid equations are derived under the assumption of inviscid fluid and potential flow. The free-surface boundary condition is linearised, and the Laplace equation is solved for the velocity potential ϕ in the fluid domain using a finite volume method. The free surface and body boundaries are advanced in time using an implicit–explicit time-marching scheme.

Two numerical wave tanks are then implemented, using either non-linear or linear body-boundary conditions on the surfaces of the membrane and floater. The purpose of each solver is discussed in the following sections, while a detailed description of both numerical schemes is given in [5].

2.1. Fully non-linear truss model (TM)

First, a non-linear hydro-elastic model is implemented, which serves as reference model in our study. The fully non-linear membrane equation

$$\rho_m \frac{\partial^2 \mathbf{r}}{\partial t^2} = \frac{\partial T \boldsymbol{\tau}}{\partial s} + \Delta p \tag{2}$$

is solved by a system of trusses and lump masses. In (2), ρ_m is the membrane surface density, $\mathbf{r}$ the position vector, T the tension, s the arc length and τ the tangential vector along the membrane. The tension in each truss is calculated at each time step from Hook law $T = Ed(l - l_u)/l_u$ where E is the Young modulus, d the membrane's thickness, l the length of the truss at a given time step, and l_u the un-stretched length of the truss. The hydrodynamic pressure

$$p = -\rho \frac{\partial \phi}{\partial t} - \frac{1}{2}\rho \nabla^2 \phi - \rho g z \tag{3}$$

is calculated at the instantaneous position of the membrane.

The floater equation is given by

$$M_f \frac{\partial^2 \eta_3}{\partial t^2} + \rho g L_f \eta_3 = -M_f g + F_h + F_c, \tag{4}$$

where F_c is the contact force exerted by the membrane on the floater, and F_h is the hydrodynamic pressure integrated over the instantaneous position of the floater's bottom. The non-linear body-boundary condition are handled with a Eulerian-Lagrangian method, allowing the mesh to follow the body motions at each time steps (see Fig. 1).

2.2. Linear hydrodynamic model

In parallel, a linear hydrodynamic model is implemented to solve the diffraction and radiation problems for prescribed motions of the floater and membrane. The obtained frequency-dependent added mass and damping coefficients as well and exciting force's amplitude and phase are used in the modal analysis presented in Section 3.

For the diffraction problems, the bodies are fixed and incident waves are generated which are diffracted and reflected by the bodies. For the radiation problems, no incident waves are generated, and forced oscillatory motions of period T are imposed through the linear kinematic body-boundary conditions, either for η_3 or for a prescribed deformation mode of the membrane $\mathcal{G}(z)$. Both for the diffraction and radiation problems, time series are generated, and the instantaneous generalised hydrodynamic loads $F(t)$ is obtained by integration of the linear dynamic pressure over the mean surface S_0 of the bodies:

$$F(t) = \rho \int_{S_0} \frac{\partial \phi}{\partial t}\, n dS, \tag{5}$$

where n is the projection of the vector normal to the body surface on a given degree of freedom, either $n = -1$ for the floater heave motion or $n = \mathcal{G}(z)$ for the membrane flexible modes (cf. [6]). From the computed hydrodynamic loads time series, harmonic analysis is performed once steady-state conditions are reached. The force signal is decomposed into components that are in phase and in quadrature with the prescribed body motions for the radiation problem, or with the incident waves for the diffraction problem. These components are then used to determine the frequency-dependent added-mass and damping coefficients, as well as exciting forces and phases.

3. Second order membrane equations: a modal analysis

A non-linear model for the membrane displacements is developed by Taylor expanding the fully non-linear membrane equation (2), assuming small displacements. The membrane equations for the vertical and horizontal displacements, denoted respectively v and w and also referred to as in-plane and out-of-plane displacements, are solved in time domain by a modal decomposition approach. On the other hand, generalised frequency-dependent linear hydrodynamic loads are applied.

We apply the Green-Lagrange strain-displacement relationship given by (cf. [7])

$$\varepsilon(z) = \frac{\partial v}{\partial z} + \frac{1}{2}\left(\frac{\partial w}{\partial z}\right)^2 + \frac{1}{2}\left(\frac{\partial v}{\partial z}\right)^2. \tag{6}$$

The tension in the membrane is the sum of the initial pre-tension T_0 and of the dynamic tension predicted by Hook law,

$$T(z) = T_0 + Ed\ \varepsilon(z). \tag{7}$$

E is the Young modulus and d the membrane thickness. The dynamic equations for v and w are obtained from Newton's 2nd law

$$\rho_m \frac{\partial^2 w}{\partial t^2} = \frac{\partial}{\partial z}\left[T(z)\sin\theta(z)\right] + \Delta p_{\text{lin}}, \tag{8}$$

$$\rho_m \frac{\partial^2 v}{\partial t^2} = \frac{\partial}{\partial z}\left[T(z)\cos\theta(z)\right], \tag{9}$$

where p_{lin} is the linear hydrodynamic pressure applying on both sides of the membrane in $x = 0$, and $\theta(z)$ is the local angle between the membrane's tangent and the vertical axis, i.e. $\tan(\theta) = \dfrac{\partial w}{\partial z}$.

3.1. Second order model (SOM)

A complete second order model is first derived for the membrane equations, which also includes a third order structural load in the out-of-plane direction. Eqs. (6) and (7) are inserted into Eqs. (8) and (9), which are then expanded at the second order in term of both the displacements v and w or their partial derivatives

$$\rho_m \frac{\partial^2 w}{\partial t^2} = T_0 \frac{\partial^2 w}{\partial z^2} + Ed\frac{\partial v}{\partial z}\frac{\partial^2 w}{\partial z^2} + Ed\frac{\partial^2 v}{\partial z^2}\frac{\partial w}{\partial z} + \frac{3}{2}(Ed - T_0)\left(\frac{\partial w}{\partial z}\right)^2 \frac{\partial^2 w}{\partial z^2} + p_{lin}, \tag{10}$$

$$\rho_m \frac{\partial^2 v}{\partial t^2} = Ed\frac{\partial^2 v}{\partial z^2} + (Ed - T_0)\frac{\partial w}{\partial z}\frac{\partial^2 w}{\partial z^2} + Ed\frac{\partial v}{\partial z}\frac{\partial^2 v}{\partial z^2}. \tag{11}$$

The first term in the right-hand sides of Eqs. (10) and (11) represent the linear structural restoring. A third order structural restoring force is also included in the out-of-plane equation, which is commonly found in the literature for $T_0 = 0$ for thin plates (see for instance [4]). At the connection with the floater, the kinematic boundary conditions at $z_f = -D_f + \eta_3$ are Taylor expanded at the second order:

$$w(z_f, t) \simeq w(-D_f, t) + \frac{\partial w}{\partial z}(-D_f, t)\eta_3(t) = 0, \tag{12}$$

$$v(z_f, t) \simeq v(-D_f, t) + \frac{\partial v}{\partial z}(-D_f, t)\eta_3(t) = \eta_3(t). \tag{13}$$

The displacements are represented as series of mode shape functions and time-dependent modal coefficients:

$$w(z,t) = \sum_{k=1}^{\infty} \bar{w}_k(t)\Psi_k(z) + \bar{w}_p(t)l(z), \tag{14}$$

$$v(z,t) = \sum_{k=1}^{\infty} \bar{v}_k(t)\Psi_k(z) + l(z)\eta_3(t) + \bar{v}_p(t)g(z), \tag{15}$$

where $\Psi(z) = \sin\left(k\dfrac{\pi(z+D_f)}{L_m}\right)$, and $l(z)$ and $g(z)$ are given in Appendix A. The first term in the right-hand side of Eqs. (14) and (15) represent homogeneous modes, in the sense that they give zero displacement at the upper membrane boundary. For the out-of-plane displacement, these homogeneous modes are sufficient to describe the linear solution. In Eq. (15), the second term represents the exact linear solution for v, while the last terms in Eqs. (14) and (15) are additional particular solution introduced to statisfy the non-linear kinematic boundary conditions (12) and (13). Because these last equations are non-linear, an iterative scheme is implemented at each time step to calculate w_p and v_p, typically converging with very few iterations.

In this model, the floater's heave equation (4) includes both linear hydrodynamic loads F_h and a non-linear contact force

$$F_c = -T\cos\theta \tag{16}$$

expanded at the second order at $z = -D_F$:

$$F_c \simeq -T_0 - Ed\frac{\partial v}{\partial z} + \frac{1}{2}(T_0 - Ed)\left(\frac{\partial w}{\partial z}\right)^2 - \frac{1}{2}Ed\left(\frac{\partial v}{\partial z}\right)^2 - \eta_3 Ed\frac{\partial^2 v}{\partial z^2}. \tag{17}$$

3.2. Simplified second order model (SSOM)

A simplified second-order model is derived from the one presented in Sec. 3.1., in which only the terms quadratic in w are retained. This is justified by that in taut configuration, w is typically of higher order of magnitude than v and η_3. The membrane equations becomes

$$\rho_m\frac{\partial^2 w}{\partial t^2} = T_0\frac{\partial^2 w}{\partial z^2} + \Delta p_{lin}, \tag{18}$$

$$\rho_m\frac{\partial^2 v}{\partial t^2} = Ed\frac{\partial^2 v}{\partial z^2} + (Ed - T_0)\frac{\partial w}{\partial z}\frac{\partial^2 w}{\partial z^2}. \tag{19}$$

The upper kinematic boundary conditions for v and w are linearised at $z = -D_f$, i.e. $w = 0$ and $v = \eta_3$. The modal representation of the displacements simplifies to

$$w(z,t) = \sum_{k=1}^{\infty}\bar{w}_k(t)\Psi_k(z), \tag{20}$$

$$v(z,t) = \sum_{k=1}^{\infty}\bar{v}_k(t)\Psi_k(z) + l(z)\eta_3(t), \tag{21}$$

and the contact force on the floater

$$F_c \simeq -T_0 - Ed\frac{\partial v}{\partial z} + \frac{1}{2}(T_0 - Ed)\left(\frac{\partial w}{\partial z}\right)^2. \tag{22}$$

3.3. Modal equations

The modal equations for the unknown coefficients $\bar{v}_k$ and $\bar{w}_k$ are derived by projection of the membrane equations (10) and (11), respectively Eqs. (18) and (19) for the simplified model, on each homogeneous modes Ψ_j by integration over the membrane's length:

$$\int_{L_m}[\text{ Eq. (10), Eq. (11), Eq. (18), Eq. (19) }]\,\Psi_j(z)\,\mathrm{d}z \tag{23}$$

The series of homogeneous modes are truncated. The number of modes retained for w and v are denoted N_w and N_v, respectively. A time marching scheme is implemented to solve the modal equation

in the time domain, that is implicit for the motions, and explicit for the velocities. The modal coefficients $\bar{w}_j$, $\bar{v}_j$ and their time derivatives are hence solved at the time $n+1$ from the following equations:

$$\bar{w}_j^{n+1} - \Delta t \dot{\bar{w}}_j^{n+1} = \bar{w}_j^n, \tag{24}$$

$$\bar{v}_j^{n+1} - \Delta t \dot{\bar{v}}_j^{n+1} = \bar{v}_j^n, \tag{25}$$

$$\sum_{k=1}^{N_w} [a_{n,k}(\omega) + m_j \delta_{k,j}] \, \dot{\bar{w}}_j^{n+1} = \sum_{k=1}^{N_w} [a_{n,k}(\omega) + m_j \delta_{k,j}] \, \dot{\bar{w}}_j^{n} + \Delta t L_j^w(w^n, v^n) + \Delta t f_j^{n+1}, \quad j \in [1, N_w], \tag{26}$$

$$m_j \dot{\bar{v}}_j^{n+1} = m_j \dot{\bar{v}}_j^{n} + \Delta t L_j^v(w^n, v^n), \quad j \in [1, N_v], \tag{27}$$

where m_j are the modal mass coefficients, δ the Kroenecker symbol, and $a_{m,k}$ the generalised added mass coefficients calculated in Sec. 2.2.. $L_j^w(w^n, v^n)$ and $L_j^v(w^n, v^n)$ represent the modal forces computed using the displacements from the previous time step. These forces account not only for the non-linear internal stresses but also for the inertia of the particular solutions and the linear wave radiation damping. Finally, f_j^{n+1} is the linear instantaneous exciting force acting on the j-th sine mode of the membrane.

4. Results

Simulations were run on a Linux-based computing cluster using an Intel Xeon Gold 6238R processor. Time series of 50s were generated from the moment the first train of waves reached the model. Each TM, SOM and SSOM simulations were solved on a single core, requiring around 4.1 days of CPU time for the TM, compared to around 20min for both the SOM and SSOM. These CPU times for the TM are higher than those reported in [5] due to the use of a finer mesh, result of a mesh convergence study that is not presented here. $N_v = N_w = 19$ sine modes were used in the SOM and SSOM to represent the displacements v and w.
All the simulations were run for regular incident waves of period $T = 1$s and initial pre-tensions ranging from $T_0 = 20$N/m to $T_0 = 150$N/m. The physical properties of the membrane and the dimensions of the system are given in Table 1. The mass of the floater was defined for each given pre-tension T_0 in order to satisfy the initial static equilibrium (1). Results presented in this section focuses on the steady-state part of the system's response time series.

Table 1: Membrane properties and dimensions of the system.

Parameter	**Unit**	**Value**	**Description**
h_t	[m]	1.0	Water depth
D_f	[m]	0.15	Floater draught
L_f	[m]	0.15	Floater width
L_m	[m]	0.85	Membrane length
d	[m]	1.25×10^{-4}	Membrane thickness
E	[Pa]	40.0×10^6	Membrane Young's modulus
ρ_m	[kg/m^2]	0.18	Membrane surface density

First, waves were generated with a low steepness $\epsilon = 2\pi\zeta_A/\lambda = 1/200$, where λ is the wave length and ζ_A the wave height. The two main second order effects observed in the floater response - a mean set-down and second harmonic component - are presented in Fig. 2 as function of the intial pre-tension T_0.

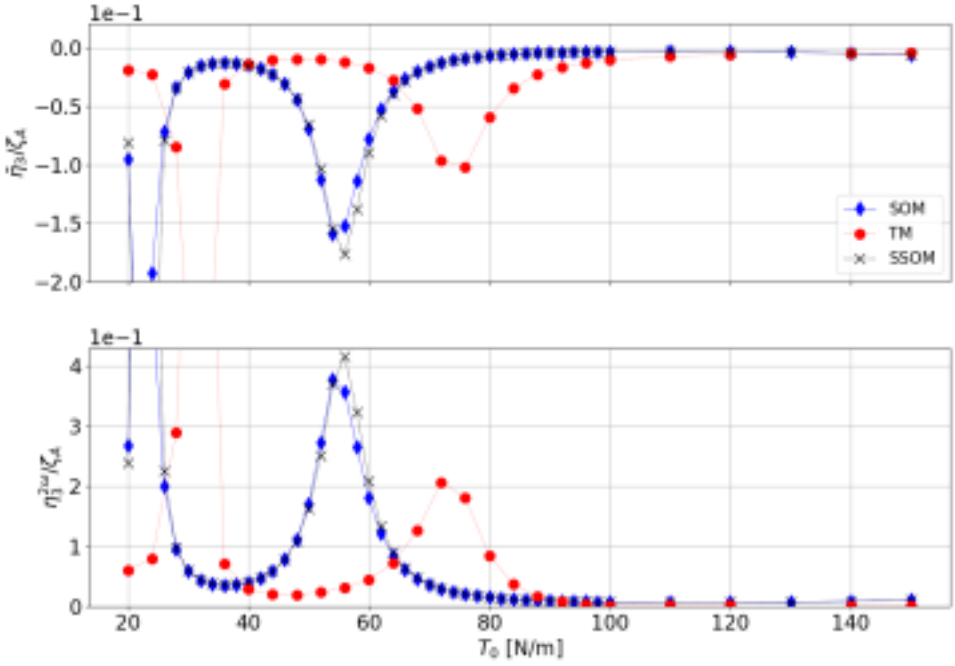


Figure 2: Top: mean set-down of the floater, normalised by the wave height ζ_A, as function of the initial pre-tension T_0. Results from the three non-linear models are presented for the wave steepness $\epsilon = 1/200$ and the wave period $T = 1$s. Bottom: amplitude of the floater's heave motion second harmonic, normalised by the wave height.

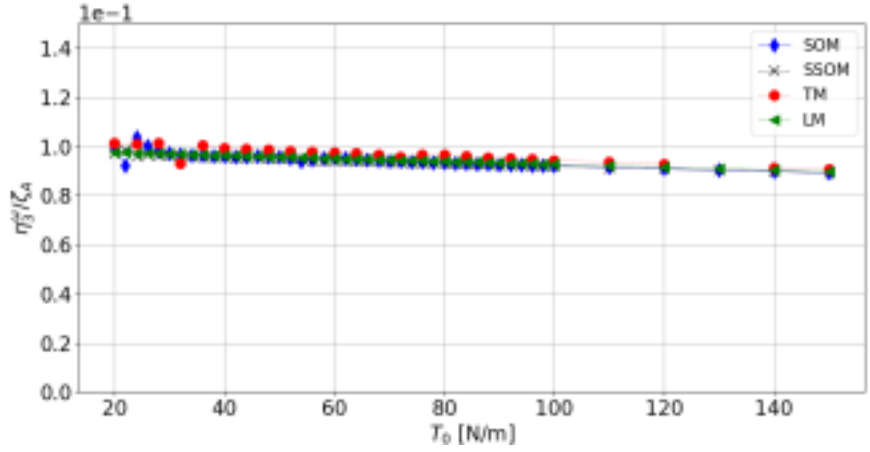


Figure 3: First harmonic amplitude of the floater's heave motion. $\epsilon = 1/200$, $T = 1$s. Non-linear results are compared the linear solution (LM).

Despite the low wave excitation, significant second order effects are observed in the floater's response, confirming the observations already made in [5] for $T_0 = 20$N/m and $T_0 = 100$N/m. Resonant peaks are observed with both the TM and the second-order models. However, there is a clear shift in the resonant peak locations with respect to T_0 between the TM and SOM/SSOM, suggesting that the second-order models are missing a key physical component. In contrast, the SOM and SSOM results show much better agreement with each other. This indicates, in particular, that the out-of-plane displacement's linear response dominates the vertical non-linear behavior in the SOM, and that non-linear kinematic boundary condition with the floater has little influence on the results.
The first harmonic amplitude of the floater's heave motion is shown in Fig. 3. The harmonic response of the three non-linear models are all close to the linear solution (LM). This linear solution was obtained similar to the SSOM, without the quadratic terms in Eqs. (21) and (22). In particular, the linear problem for the out-of-plane displacement is entirely decoupled from the linear in-plane displacement and floater's heave equations. The linear solution shows a low-dependency on T_0. That was expected as $T = 1$s is far from the linear heave resonance of the floater. Linearly, the membrane acts like a spring of stiffness Ed/L_m on the floater (see Appendix A), causing a very narrow resonant peak of η_3's RAO at periods $T < 0.45$s for this range of pre-tensions. It can also be noted that near resonance of the second order responses in Fig. 2, both the mean and second harmonic amplitude reaches similar or higher magnitude than the first harmonic component. In particular for the TM at $T_0 = 32$N/m, $|\bar{\eta}_3/\zeta_A|$ is more than five time higher than η_3^{ω}/ζ_A, while $\eta_3^{2\omega}/\zeta_A$ is more than ten times higher then η_3^{ω}/ζ_A, confirming that second order effects dominate the floater's response compared to the linear solution for this pre-tension.
A major limitation of the second-order model is that it uses frequency-dependent coefficients evaluated at the wave frequency, which may not accurately predict the linear loads for pre-tensions near resonance. Introducing a retardation function to model time-dependent linear hydrodynamic loads could provide a solution in future work.

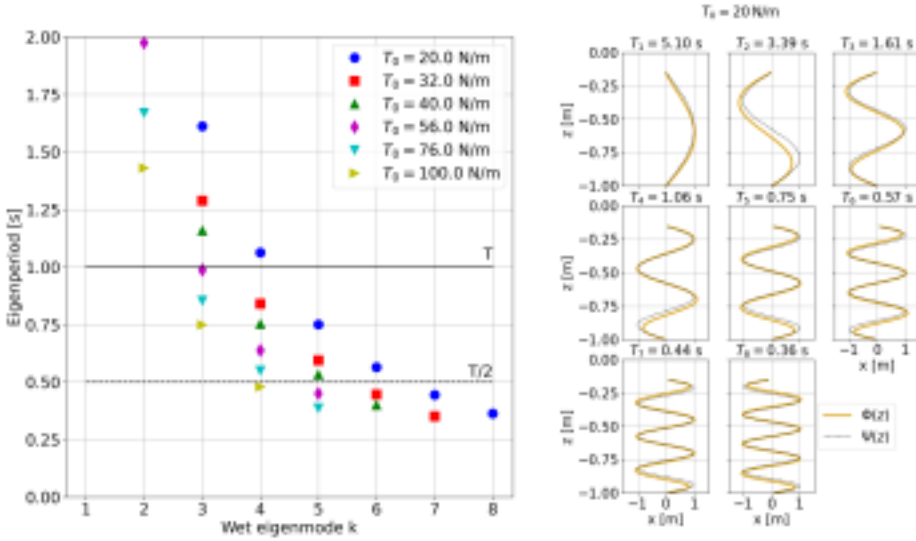


Figure 4: Left: wet eigenperiod of each mode for several pre-tension calculated from the linear model. Right: wet eigenmodes $\Phi_k(z)$ for $T_0 = 20$. Dash line: sine mode $\Psi_k(z)$.

Further analysis of the out-of-plane displacement's resonant modes is presented below, as they are identified as potential causes of the non-linear resonant peaks in Fig. 2. Using the linear modal equa-

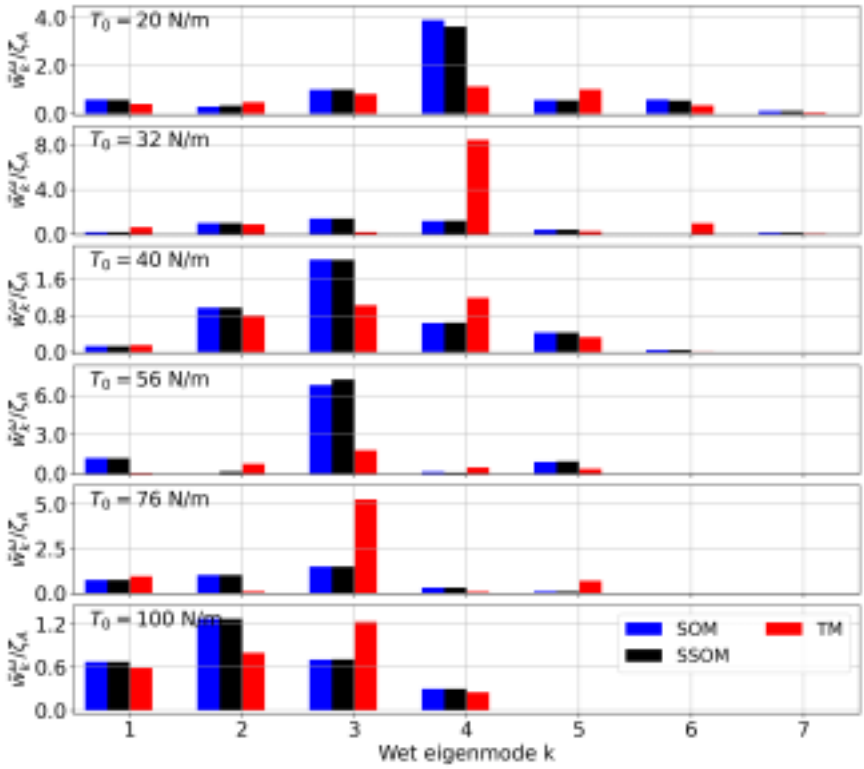


Figure 5: First harmonic amplitude of the modal coefficients $\tilde{w}_k$ for several selected pre-tensions T_0. $\epsilon = 1/200$, $T = 1$s. Values displayed on the ordinate differ along the subplots.

tions for w from the SSOM, an eigenvalue analysis was performed to determine the wet eigenperiods T_k and the corresponding wet eigenmodes $\Phi_k(z)$ of the out-of-plane displacement. The eigenperiods and modes are ordered by decreasing T_k, with T_1 being the highest period. Results of this linear eigenvalue analysis are shown in Fig. 4. The out-of-plane response of the membrane from both the TM and the second-order models can be expressed as a series of wet eigenmodes, $w = \sum_{k=1}^{\infty} \tilde{w}_k(t)\Phi_k(z)$, where the modal coefficients $\tilde{w}_k$ are obtained by projecting the total response w from the numerical simulations onto the basis $\Phi_k(z)$. The RAO of the modal coefficients $\tilde{w}_k$ are presented in Fig. 5 for selected pre-tensions. In both the TM and the second-order models, the resonance of η_3's second-order response in Fig. 2 is strongly correlated with the resonance of one of w's eigenmodes. This can be observed, for example, in the TM at $T_0 = 76$N/m and in the second-order models at $T_0 = 56$N/m. It should be emphasised that w's second harmonic amplitude was observed to be two order of magnitudes lower than the first harmonic component (not shown here).

For the second-order models, a given eigenmode is excited when its eigenperiod is close to the wave period, $T = 1$s. For example, at $T_0 = 56$ N/m, $T_3 = 0.99$s and $\tilde{w}_3^{\omega}/\zeta_A = 3.8$ (SOM) and 3.6 (SSOM), which dominate the out-of-plane response. For the truss model, the excited wet eigenmodes have eigenperiods shorter than the wave period. For instance, at $T_0 = 76$ N/m, $\tilde{w}_3^{\omega}/\zeta_A$ calculated from the TM reaches its maximum, corresponding to an eigenperiod $T_3 = 0.86$s. This indicates that w's resonant periods may be shifted to higher values compared to the linear eigenperiods due to non-linear effects absent in the second-order models. This is presently under investigation.

Simulations were also performed for a higher wave steepness, $\epsilon = 1/80$. Results are shown in Fig. 6. The mean set-down and the second-harmonic amplitude of the floater increase for all non-linear models, with the amplitude of the peak increasing by a factor of ranging from 2 to 3 compared to $\epsilon = 1/200$. The resonant peak from the truss model, however, occurs at the same pre-tension as for $\epsilon = 1/200$. This suggests that, at such low steepnesses, the frequency shift between the second-order models and the truss model is not caused by missing non-linear hydrodynamic loads in the SOM and SSOM.
For $\epsilon = 1/80$, the difference between the SOM and SSOM is more pronounced than for $\epsilon = 1/200$, which was expected as the motions becomes more and more linear for higher steepness, and with the SOM predicting lower amplitudes and a shift in the resonant peak to lower pre-tensions relative to the SSOM.

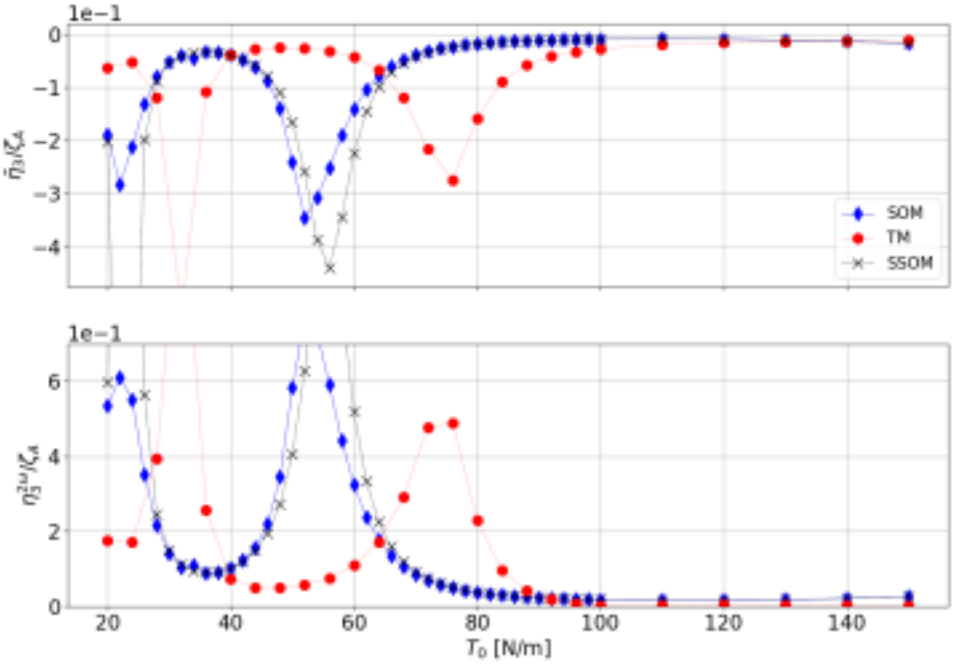


Figure 6: Top: mean set-down of the floater normalised by the wave height. Bottom: amplitude of the floater's heave motion second harmonic, normalised by the wave height. $\epsilon = 1/80$, $T = 1$s

5. Conclusion

Second-order analytical models, based on Taylor expansions of the membrane equations for small displacements and linear frequency-dependent hydrodynamics were solved using modal representations of these displacements and spatial integration. The comparisons with the fully non-linear truss model simulations showed mixed results: if the main second order effects were caught by the second-order models, a shift of the out-of-plane resonant modes to lower periods was observed compared to the truss model.

Limitations of the second-order models include the limited ability to capture very localised stress variations in the membrane due to the integral formulation, as well as the single-frequency representation of the linear hydrodynamic loads, which does not account for the 2ω oscillations of the floater near resonant modes. Future work will include further analytical investigations of membrane non-linearity, which remains a promising approach due to the substantial reduction in computational time compared to fully numerical models.

References

[1] M.M. Sabara, T. Kristiansen, M. Moreau, S. Sævik, P.F. Lader and D. Kristiansen, *Development of a linear numerical model for closed membrane-type fish cage in waves*, Journal of Fluids and Structures, 2026.

[2] M.M. Sabara, P.F. Lader, D. Kristiansen, T. Kristiansen and M. Kanazawa, *Bag and floater motions of a fabric membrane cage*, Journal of Fluids and Structures, Vol. 106, https://doi.org/10.1016/j.jfluidstructs.2021.103353, 2021.

[3] P. Xu and P.R. Wellens, *Theoretical analysis of nonlinear fluid–structure interaction between large-scale polymer offshore floating photovoltaics and waves*, Ocean Engineering, Vol. 250, https://doi.org/10.1016/j.oceaneng.2022.110829, 2021a.

[4] P. Xu and P.R. Wellens, *Fully nonlinear hydroelastic modeling and analytic solution of large-scale floating photovoltaics in waves*, Journal of Fluids and Structures, Vol. 109, https://doi.org/10.1016/j.jfluidstructs.2021.103446, 2022.

[5] M. Moreau and T. Kristiansen, *Numerical investigations of non-linear responses of a vertical membrane in waves*, in Proceedings of the 16th International Symposium on Practical Design of Ships and Other Floating Structures (PRADS2025), Ann Arbor, USA, October 2025.

[6] J.N. Newman, *Wave effects on deformable bodies*, Applied Ocean Research, Vol. 16, No. 1, pp. 47–59, https://doi.org/10.1016/0141-1187(94)90013-2, 1994.

[7] C. Mittelstedt, *Theory of Plates and Shells*, Springer-Verlag, Berlin, Germany, 2023, https://doi.org/10.1007/978-3-662-66805-4.

A Appendix

The linear solution for the vertical displacement of the membrane is given by

$$v(z,t) = l(z)\eta_3(t) = \left[\frac{\sin(k_v h_t)\cos(k_v z) + \cos(k_v h_t)\sin(k_v z)}{\sin(k_v h_t)\cos(k_v D_f) - \sin(k_v D_f)\cos(k_v h_t)}\right]\eta_3(t), \tag{28}$$

where $k_v = \sqrt{\frac{\omega\rho_m}{Ed}}$ is the spatial wave number. For low density membranes with $k_v h_t << 1$, a good approximation of this linear solution is $v \simeq \frac{ht+z}{L_m}\eta_3$. The tension in the membrane is then $Ed\frac{\partial v}{\partial z} \simeq Ed/L_m\eta_3$.

A candidate for the particular mode shape function $g(z)$ in Eq. (15) that is used in the present work is given by

$$g(z) = \sinh\left(\frac{z+h_t}{L_m}\right). \tag{29}$$

10th International Conference on HYDROELASTICITY IN MARINE TECHNOLOGY
Trondheim, Norway, June16$^{\text{th}}$-18$^{\text{th}}$, 2026

Surge Motion and Hydroelastic Response of a Membrane-Based Floating Solar Island: An Uncertainty Study

Skare, A.[1,*] and Kristiansen, T.[1]

[1] Department of Marine Technology, Norwegian University of Science and Technology, Trondheim, Norway

Abstract. This study investigates the hydroelastic response of a membrane-based floating solar island through a combined numerical and experimental uncertainty analysis. The system consists of a thin circular membrane attached to a circular elastic floating collar. The response is obtained from a frequency-domain modal solver. Validation data from model-scale experiments are presented. A systematic parameter-identification study is performed to determine the effective membrane pretension and the floater's flexural rigidity by minimizing the mismatch between numerical and experimental point RAOs. Friction mechanisms associated with surge motion are examined. In particular, viscous boundary-layer friction on the membrane and Coulomb-type friction in the mooring pulleys are introduced to investigate discrepancies at low kR. The results provide an improved understanding of uncertainty in modeling the membrane-based floating solar island.

Key words: *Floating membrane; Hydroelastic response; Floating solar;*

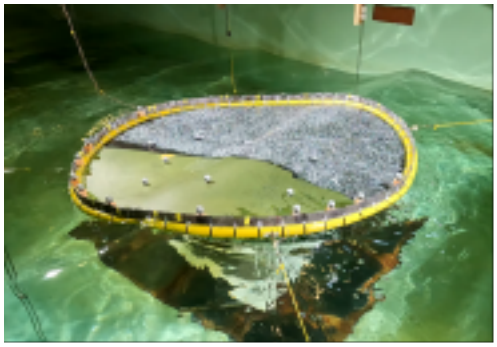
1. Introduction

The present work further investigates the behavior of a membrane-based floating solar island in regular waves, with a focus on uncertainties in both our numerical model and supporting experiments. The vertical formulation developed in [1] and its in-plane extension in [2] form the basis of the present analysis, both employing an improved rim-constraint formulation that avoids the incorrect Lagrangian-multiplier treatment used in [3, 4]. Using the vertical model of [1], we perform a quantitative curve-fit analysis of experimental RAOs to more accurately identify the effective membrane pretension T_0 and floater stiffness EI_z, parameters that influence not only the vertical response but also the surge motion through hydrodynamic coupling of the lowest ($m = 1$) Fourier modes. Surge is examined using the in-plane framework of [2], extended here to include the laminar boundary-layer shear forces acting on the membrane. This effect, together with the (unwanted) pulley friction observed in the model tests, is evaluated to clarify sources of discrepancy between numerical predictions and experimental measurements. We also briefly discuss additional experimental uncertainty sources and practical challenges encountered during model tests. By addressing this, we aim to clarify the dominant uncertainty mechanisms influencing the solar island's behavior and contribute to improved modeling developments.

2. Model Tests

Physical model tests were carried out in NTNU's small towing tank during the summer of 2023. The tests have been partly presented in [1, 2]. The 1:50-scale model is shown in Fig. 1a, and key parameters are listed in Table 1. The model was positioned on the tank centerline, 15.3 m from the wavemaker, with waves propagating in the positive x-direction for consistency with the numerical coordinate system.

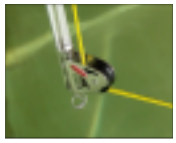
*Correspondence to: aurora.n.skare@ntnu.no



(a) The solar island in waves.



(b) Marker on fencing.



(c) Pulleys for mooring.

Figure 1: The model-scale (1:50) solar island. Instrumentation details are shown in (b) and (c).

The model's floater was constructed from piecewise Divinycell cylinder sections with a continuous PVC core, which determined the out-of-plane flexural rigidity, EI_z, and provided the attachment point for the membrane fabric. The design aimed to reproduce the simplified membrane–floater interface assumed in our numerical model. To limit overtopping at model scale, a lightweight plastic fence was added along the outer edge. A thin elastic rubber between segments prevented water leakage onto the membrane without significantly altering the floater's stiffness.

Qualisys markers on the floater were mounted on small Divinycell blocks on the inside of the fence (Fig. 1b). Because the structure is extremely lightweight ($\simeq 1$ kg), any additional mass placed on the membrane surface influences its dynamic behavior, making additional sensors challenging to accommodate. In total, 19 reflective Qualisys markers were mounted on the left half of the floater and membrane. The right half of the membrane was instead covered with a speckled pattern to enable Digital Image Correlation (DIC). Although the DIC measurements provided useful qualitative information, the quantitative results presented here rely primarily on the Qualisys system due to challenges in DIC tracking. Eight wave probes were installed upstream, downstream, and to the sides of the model, and each mooring line was instrumented with a force ring to measure dynamic tension. The mooring lines pass through a small pulley, shown in Fig. 1c, before they are attached to a vertical spring at the tank-wall. A trigger signal synchronized the optical systems with wave-probe acquisition.

A total of 80 regular wave conditions were tested, spanning wavenumbers $k = 1.76$–20.0 m^{-1} in constant increments. Three wave steepnesses, $H/\lambda = 1/60$, $1/45$, and $1/30$, were examined to assess linearity. Each full sequence of 80 wave trains was repeated four times. Each train contained 60 steady-state waves, for each test, the central 20 waves were extracted and band-pass filtered around the first harmonic to compute point-wise RAOs. These processed time series form the basis for the RAOs presented in the following sections.

In August 2024, free-decay tests of the membrane in air were conducted to estimate the pretension, $T_0 = \left(m_b + a^{air}_{(01,01)}\right)(\omega_{n,01}/\lambda_{01})^2$, by measurements of the first clamped-edge mode frequency, $\omega_{n,01}$ ($\simeq 19$ s^{-1}). The corresponding modal wave number is denoted λ_{01}. The membrane's the added mass in air, $a^{air}_{01,01}$, is included as it is of similar size to the membrane's mass per unit area, m_b. This was obtained from twice the infinite frequency modal added mass from WAMIT, being $\simeq 0.2$ kg m^{-2}.

3. Theory

This section summarizes the linear hydroelastic formulation used to model the coupled response of the membrane and floating collar. In addition, we describe the inclusion of viscous shear friction on the membrane.

Table 1: Parameters from model tests (2023) in NTNU's small towing tank. The model is of scale 1:50.

Description	**Notation**	**Model Scale**	**Full Scale (1:50)**	**Unit**
Membrane properties				
Diameter	$2R_0$	1.17	58.5	m
Thickness	d	0.13	6.5	mm
Mass (per unit area)	m_b	0.18	9	kg m^{-2}
Floater properties				
Center-line diameter	$2R$	1.20	60	m
Cross-sectional diameter	$2a$	0.03	1.5	m
Mass (per unit length)	m_f	0.34	850	kg m^{-1}
Mooring line pretension	T_p	1.80	2.3×10^6	N
Instrumentation and wave tank				
OQUS reflective sphere mass	$m_{oq.}$	0.004	50	kg
Tank width	–	2.5	125	m
Water depth	h	0.7	35	m

3.1. The Numerical Solver

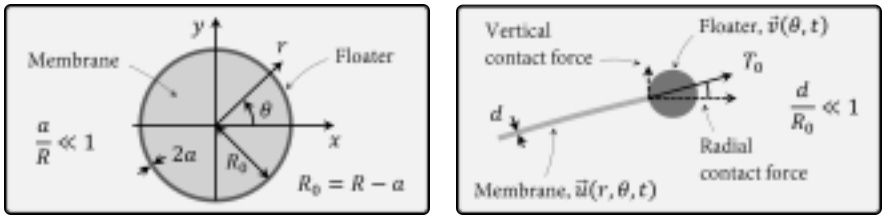
We refer to [1] and [2] for a complete description. Here, we explain only the essence of the modal approach and the modal representation of vertical membrane and floater motions. For the membrane, we assume a constant pretension, T_0, and model its motion, $\vec{u}(r, \theta, t)$, based on the linearized membrane equations. The floater's motion, $\vec{v}(r, \theta, t)$, is modeled using modified Euler-Bernoulli beam equation, accounting for curvature. The geometry of the membrane-floater system and relevant notation for its parameters are illustrated in Figs. 2a and 2b.

At the membrane-floater interface, we must enforce two constraints: the kinematic constraint, which forces the membrane's rim to be at the same spatial location as the floater at all times, and the dynamic constraint, ensuring an equal but opposite contact force acting on the membrane's rim as that acting on the floater. To enforce these constraints and model the contact forces, the membrane motion is decomposed into what we refer to as homogeneous and particular modes. The particular modes enforce the kinematic constraint by matching the floater displacement at the rim. The contact force is represented through homogeneous modes, which have a non-zero angle at the rim (and thereby a non-zero force), but zero displacement. This choice of modal boundary conditions is referred to as "Method 1" in [2, 1].

The vertical membrane motion is represented by a sum of Fourier-Bessel modes, where the modal wave numbers are chosen to ensure that the modes obey the clamped and free edge modal boundary conditions. The indexing is such that a generic modal wave number k_{mn} is the n'th root of the m'th modal frequency equation. The number of particular modes must match the number of floater Fourier modes, and thus we only include the first ($n = 1$) mode for every m'th particular mode (similar for horizontal motion). For more details, see [1]. We solve for the unknown, frequency dependent modal amplitudes of the homogeneous- and particular modes. Note that rigid-body heave and pitch are now introduced explicitly, as particular modes for $m = 0$ and $m = 1$, respectively. For in-plane motions using Method 1, surge will be the particular membrane mode for $m = 1$. Surge is thereby coupled with the vertical motions via pitch and the $m = 1$ modes. This is important as surge is dominant for mooring.

3.2. Viscous Friction on Membrane

We represent the shear stress in a simplified manner, by assuming the classical solution to Stokes' second problem over the entire membrane. This means we disregard effects related to the floater. In Stokes' second problem, the shear stress and boundary layer velocity depend only on the relative motion between the considered oscillatory wall and the fluid. This justifies its application when accounting for



(a) Bird's eye view. (b) Cross-sectional view.

Figure 2: Schematic of the membrane-based floating solar island. Incident wave along positive x-axis.

viscous boundary layer effects on surge motions of the membrane. We assume a laminar boundary layer flow, which is relevant in model scale. Since the shear stress is then linear with respect to the relative velocity, we consider contributions from the fluid motion and the membrane motion separately, such that, $\tau_{w0} = \mu\sqrt{\omega/\nu}\,(\omega\zeta_a)\cos(\omega t - kx + \pi/4)$ and $\tau_{w1} = -\mu\sqrt{\omega/\nu}\,(\omega\eta_{1a})\cos(\omega t - \varepsilon_1 + \pi/4)$, respectively. The incident wave amplitude is denoted ζ_a, the kinematic and dynamic viscosity are given by ν and μ, and the surge motion by its amplitude η_{1a}, and its phase ε_1. Note that we only include the incident flow velocity, and not the flow velocity due to diffraction. In reality, this will also matter. The total force on the membrane due to viscous shear stress is obtained by integrating over the membrane. The resulting force will consist of a damping term, proportional to the surge velocity, and an excitation term, proportional to the incident wave velocity. In total, we obtain in frequency representation,

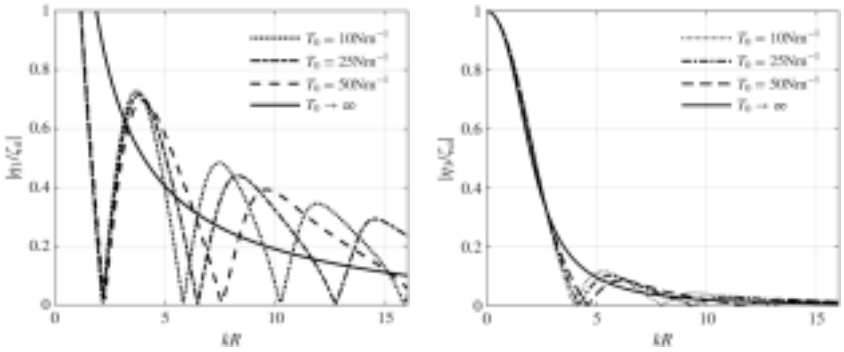
$$\frac{\hat{F}_1^{(visc.)}}{\zeta_a} = \mu\sqrt{\frac{\omega}{\nu}}\omega\, e^{i\frac{\pi}{4}}\pi R_0\left(\frac{2}{k}J_1(kR_0) - R_0\frac{\eta_{1,a}}{\zeta_a}e^{i\varepsilon_1}\right). \tag{1}$$

4. Results

We investigate the effect of EI_z and T_0 on the vertical membrane motions first. Next, the effect of viscous shear on surge motion. The hydrodynamic coefficients used throughout were obtained using WAMIT 7.5, based on the model-scale geometry and assuming linear potential flow. The structural response of the coupled membrane and floating collar was computed in the frequency–domain, with $M = 9$ circumferential modes and $N = 20$ radial modes, selected based on modal convergence tests in [1]. The numerical response is reconstructed from the full set of Fourier–Bessel modes to obtain the total response for every marker position.

4.1. Parameter Identification and Best-Fit Vertical Hydroelastic Response

We first provide theoretical results illustrating the main effects of the two parameters T_0 and EI_z. We look at surge and heave of the membrane, which are particular modes, and next at the vertical membrane motion at a selected point. In Figs. 3a and 3b, the theoretical surge and heave response of the membrane are plotted for selected values of the membrane pretension, T_0, as a function of the non-dimensional incident wave-number, kR. As the pretension increases, $T_0 \to \infty$, the membrane response converges to that of a rigid body; and so the membrane is less able to follow the incident wave for the same kR range. This happens at $T_0 \simeq 1000\ \mathrm{Nm}^{-1}$ for heave motion and at $T_0 \simeq 10\,000\ \mathrm{Nm}^{-1}$ for surge motion. Since these are totally unrealistic values in practice, the island will always be highly compliant, which is the intention in the first place. We observe that cancellation points for both heave and surge move towards higher kR values as T_0 increases. A similar trend can be seen for the point RAO response in Fig. 4a. Figure 4b illustrates the effects of increasing EI_z. As $EI_z \to \infty$, the floater becomes rigid. At the membrane center (not shown), this has negligible effect on the response. However, as we approach the membrane's rim ($r = R_0$), the increasingly stiff floater will affect the local point response of the



(a) Surge sensitivity to pretension, T_0. (b) Heave sensitivity to pretension, T_0.

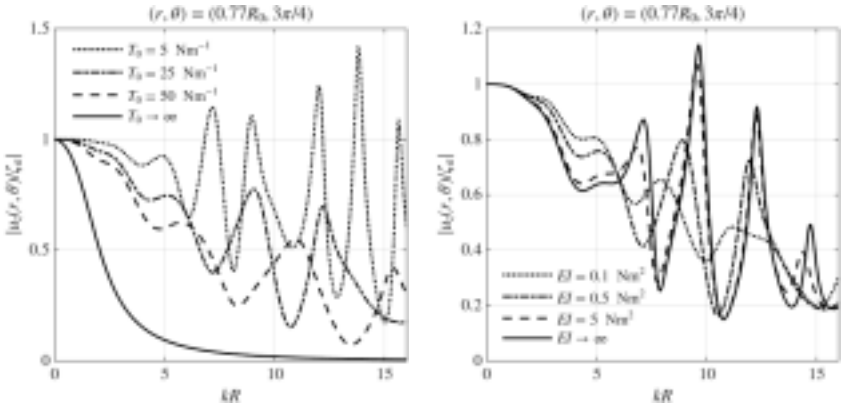
Figure 3: Surge (a) and heave (b) RAOs of the membrane for selected values of the membrane pretension T_0, plotted as functions of the non-dimensional wavenumber kR. As T_0 increases, the membrane response approaches that of a rigid body.

membrane. This illustrates the importance of structural parameters T_0 and EI_z when predicting the vertical response of the membrane.

We next attempt to identify the best-fit structural parameters by minimizing the mismatch between numerical and experimental point-wise RAOs. Previous work [1] identified "best-fit" values for T_0 and EI_z by a qualitative, visual comparison of numerical and experimental point RAOs, yeilding $T_0 = 15\ \text{Nm}^{-1}$ and $EI_z = 0.5\ \text{Nm}^2$. In the present study, a more rigorous and quantitative parameter identification study is performed. Both T_0 and EI_z are varied systematically, and the discrepancy between numerical and experimental point responses is evaluated using an L_2 error metric. We define the local residual as $\delta_j(k_iR) = \left|\text{RAO}_j^{num.} - \text{RAO}_j^{exp.}\right|$, that is, the model–experiment mismatch at a given wavenumber, k_i, for a given point, (r_j, θ_j). The frequency aggregated L_2 discrepancy is defined as, $e_j = ||\delta_j(k_iR)||_2$. Lastly, the global error for a defined set of N_p points is defined as the average over the frequency aggregated L_2 discrepancy, such that $\bar{E} = \frac{1}{N_p}\sum_{j=1}^{N_p} e_j$. The global error provides a reproducible and objective basis for determining the effective membrane pretension and the circumferential flexural rigidity of the floater in the physical model, by minimizing the global mismatch for a parameter pair (T_0, EI_z). A sequence of progressively refined parameter sweeps are performed. Contour plots of the error landscape for the successive refinement stages are shown in Fig. 5, where the color levels represent the global error, for the set of membrane markers.

The best-fit values obtained from the membrane marker subset, the floater marker subset and the combined set are listed in Table 2. The independent sweeps using only membrane markers and only floater markers yield consistent, but slightly different minima. This behavior is expected, as the floater is dominated by its circumferential stiffness, EI_z, whereas the membrane response is primarily governed by the pretension, T_0. A combined sweep using all markers results in a minimum in the overlap of the low-error regions identified by the two subsystems. The proximity of these minima demonstrates that the fitted model parameters are physically meaningful within the uncertainty of the experiments. Still, the effective experimental pretension in the physical model inferred from the best-fit analysis is substantially higher than the estimate from the free decay tests in air ($T_0 \simeq 9.5\ \text{Nm}^{-1}$). This may be due to long-term material relaxation, as the decay measurements were conducted approximately a year after the test campaign. Similarly, the floater behaves substantially stiffer than the nominal design value of $EI_z = 0.12\ \text{Nm}^2$. This is hypothesized to be due to additional reinforcements added throughout the test campaign, as there was water leakage onto the membrane due to wear of the rubber material between the Divinycell cylinders and the fencing structure.

Figures 6 and 7 show a selection of membrane- and floater point RAOs respectively, where numerical



(a) RAO sensitivity to pretension, T_0. (b) RAO sensitivity to flexural rigidity, EI_z.

Figure 4: Example of a selected point RAO showing the influence of membrane pretension T_0 (a) and floater flexural rigidity EI_z (b). Increasing T_0 reduces membrane compliance and shifts resonance and cancellation features to higher kR. Increasing EI_z primarily influences the local hydroelastic behavior near the membrane's rim.

Table 2: Best-fit parameters (T_0, EI_z) using membrane, floater and combined marker RAOs.

Sweep Type	$T_{0,\text{best}}$ [N/m]	$EI_{z,\text{best}}$ [Nm^2]
Membrane Subset	24.8	0.58
Floater Subset	21.5	0.50
Set of All Markers	23.4	0.53

results are based on the best-fit parameters involving all markers. This is compared with experimental results, of wave steepness $H/\lambda = 1/45$. The gray baseline markers show the local, frequency-dependent residual, δ_j. The vertical error bars represent the experimental standard deviation $\sigma_{exp.}$, obtained from four repetitions of each regular-wave test. These quantify only measurement uncertainty, and should not be confused with the error metric used for parameter identification. In general, the results demonstrate that the linear numerical solver is able to reproduce the membrane's vertical hydroelastic response in regular waves across most marker locations. The largest discrepancies arise predominantly at higher wavenumbers, where the experimental uncertainty, $\sigma_{exp.}$, is intrinsically greater. This is partly a consequence of limitations in the Qualisys motion-capture system, which operates at a maximum sampling frequency of 50 Hz and with a positional uncertainty on the order of 1 mm, making small-amplitude motions more difficult to resolve accurately. In addition, the wave maker has reduced precision in generating very short waves. There are also still large discrepancies for the front and aft points on the floater ($\theta = 0$ and π) for $kR \simeq 3$. We have not been able to explain these. They are not due to nonlinear effects, as experiments with $H/\lambda = 1/30$ and $1/60$ deviate only a little [1].

4.2. Effects of Friction on the Surge Response

Figure 8 illustrates the sensitivity of the surge RAO to two different frictional mechanisms. The baseline curve represents the inviscid results without any drag or friction effects. The dashed curve includes the laminar boundary-layer shear force on the membrane, $\hat{F}_1^{visc.}$, computed using the formulation in Eq. 1. To explore the potential influence of substantially larger viscous forces, a third curve includes three times the laminar viscous drag as an illustrative case. Lastly, a pulley-friction curve is shown,

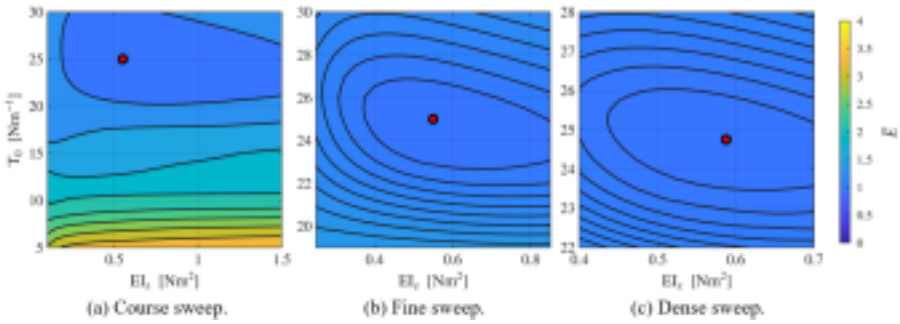


Figure 5: Global model error $\bar{E}_{membr.}$ over the parameter space of membrane pretension T_0 and floater flexural rigidity EI_z, for membrane marker subset. The error metric is defined as the mean of the marker-level, frequency aggregated L_2 discrepancy, e_j, across the selected set of markers. Lower values indicate better agreement between numerical and experimental RAOs. The red marker denotes the optimal parameter pair identified in each sweep.

which adds a simple Coulomb friction model for the mooring pulleys, $F_C = -\mu_c N \text{sgn}(\dot{\eta}_1)$, on top of the laminar viscous model, with N given by the mooring-line pretension. All numerical results are compared with experimental RAOs for wave steepness $H/\lambda = 1/45$.

In our model-scale conditions, the oscillatory Reynolds number, $Re = \zeta_a^2 \omega/\nu$, lies between 300 and 6000, well below typical transition thresholds for oscillatory boundary-layer flow. A laminar Stokes-type boundary layer is therefore a reasonable assumption for the present experiments. In contrast, full-scale estimates show Reynolds numbers reaching 2×10^6 at low kR, placing the flow in the turbulent regime, where shear stresses can be several times larger than those predicted by laminar boundary layer theory. The "3 $\times$ viscous drag" case is not intended as a representative turbulent boundary layer estimate, but rather to examine how sensitive the surge response is to an increased drag, as is the case under full-scale turbulent conditions.

The results indicate that, as kR decreases, the experimental surge response is more consistent with numerical predictions that include viscous shear drag, $\hat{F}_1^{visc.}$. The trend suggests that laminar boundary-layer shear on the membrane introduces appreciable additional damping at low wavenumbers, particularly for $kR \simeq$ 2-6, partially mitigating the over-prediction observed in the inviscid results. Adding pulley friction increases the surge response at cancellation points. Our friction model is highly simplified, but appears to partially explain observed discrepancies around $kR \simeq 2$. For $kR > 5.5$, the Coulomb friction produces a non-physical amplification, the curve is therefore truncated beyond this point. Pulley-based mooring arrangements should in any case be avoided in future experiments for this type of light weight structure.

4.3. Other Experimental Sources of Uncertainty

The plastic fencing added on top of the floater to reduce overtopping introduced several new challenges for motion tracking and data quality. The fence prevented the markers from being placed directly on the floater surface, such that each marker was mounted on a Divinycell cube attached on the inside of the fence, as shown in Fig. 1b. This shifted both the vertical and the radial position with respect to the floater's centerline, requiring correction during postprocessing and contributing to uncertainty, particularly for in-plane motion data. Additionally, the fencing cast a persistent shadow over the outer part of the membrane, such that Qualisys markers could not be positioned close to the rim, and DIC tracking failed in the region closest to the collar. This is the region most critical for the structure's integrity, as failure of the membrane-floater connection would compromise the entire system, and therefore the region most critical for validating the numerical implementation of the membrane–floater interaction. It is

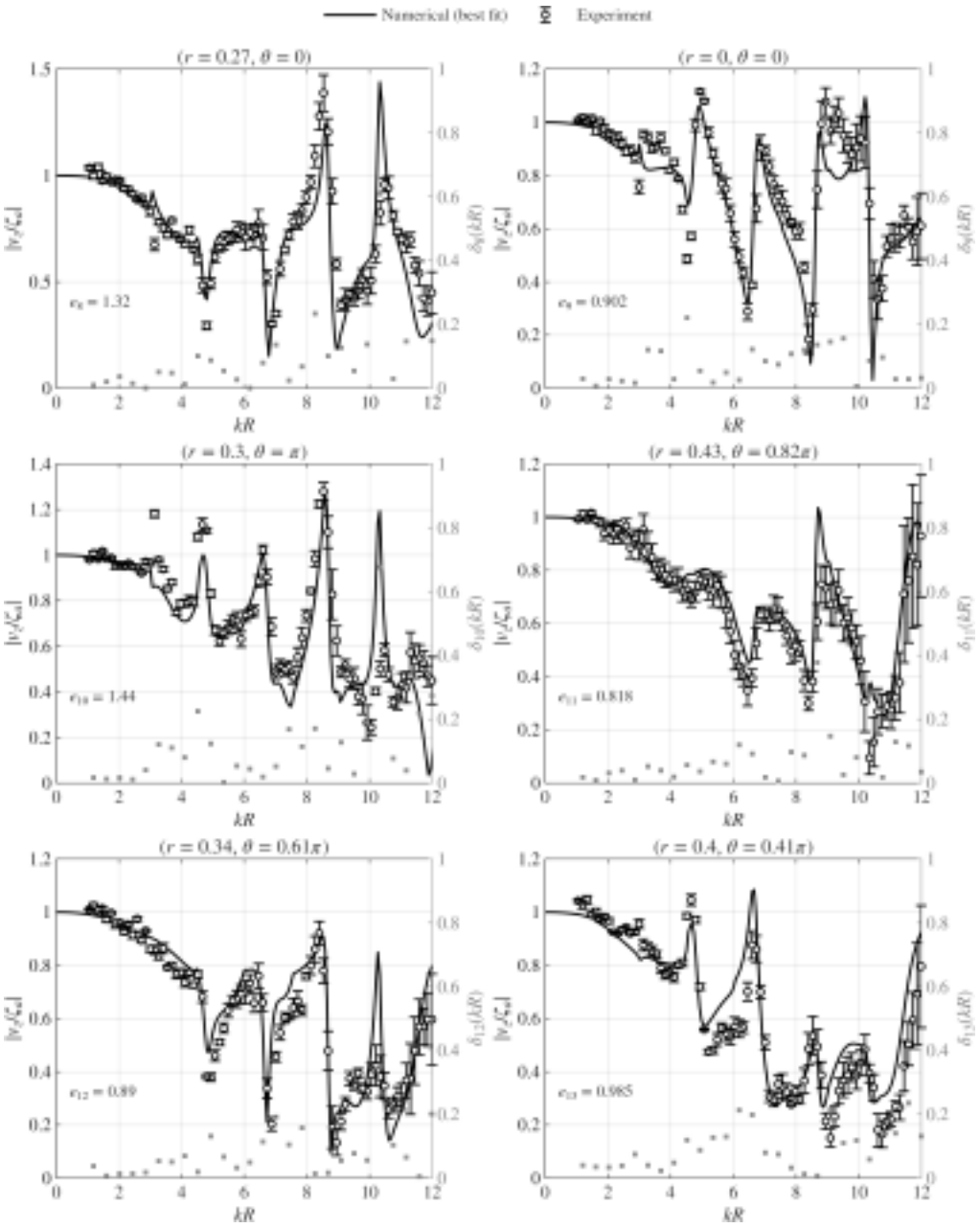


Figure 6: Point-wise Response Amplitude Operators (RAOs) as functions of the non-dimensional wavenumber kR for markers on the membrane. Experimental measurements are compared with the numerical predictions evaluated at the best-fit parameters, $(T_0, EI_z) = (23.4\ \mathrm{Nm}^{-1}, 0.53\ \mathrm{Nm}^2)$, including tank-wall effects. Error bars represent the experimental standard deviation $\sigma_{exp.}(kR)$, obtained from four repetitions of each wave train. Gray markers show the point-wise numerical–experimental discrepancy, $\delta_j(k_iR)$, for marker j. Each plot is labeled with the marker-level L_2 discrepancy, e_j, aggregated over all frequencies for that marker.

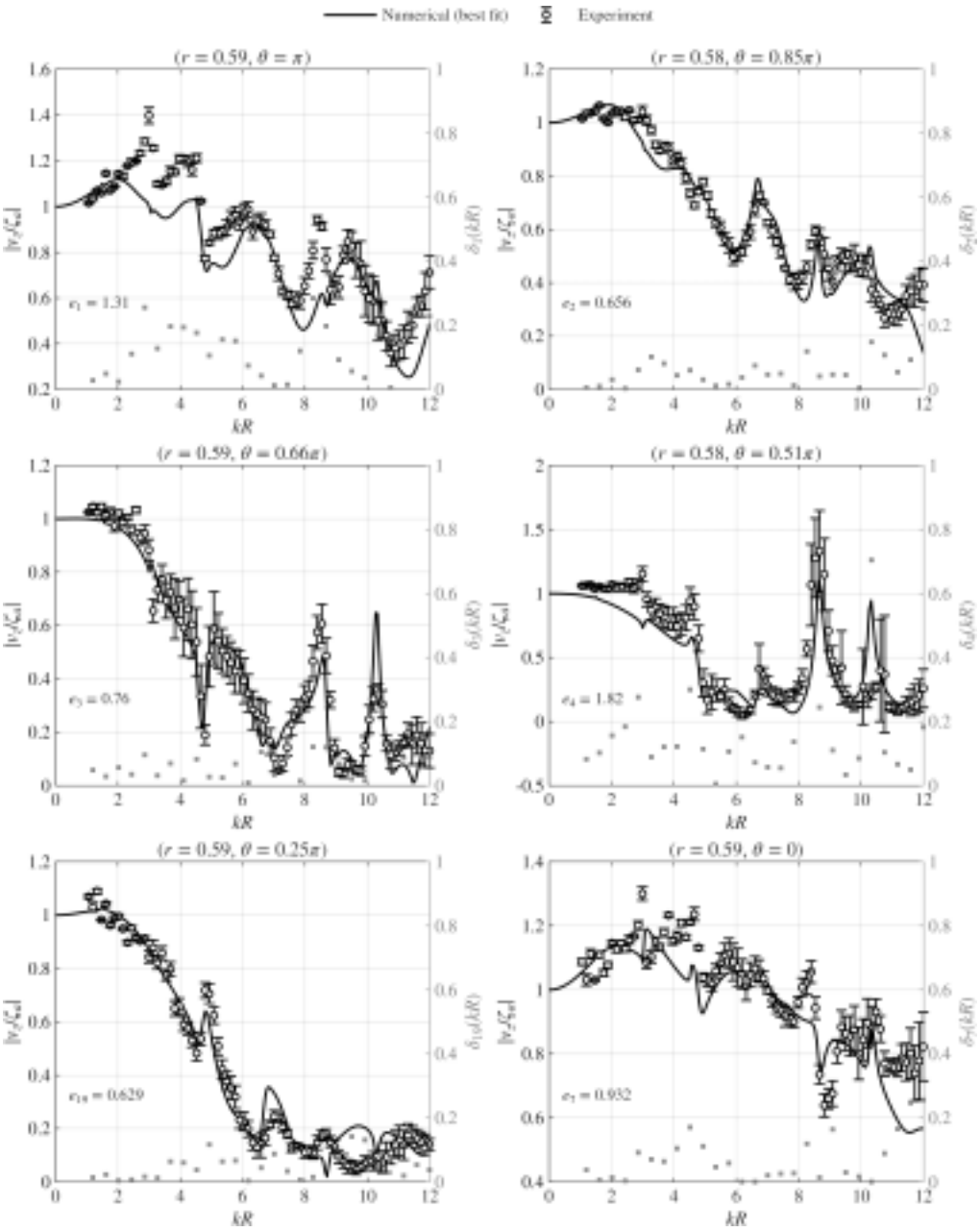


Figure 7: Point-wise Response Amplitude Operators (RAOs) as functions of the non-dimensional wavenumber kR for markers on the floater. Experimental measurements are compared with the numerical predictions evaluated at the best-fit parameters, $(T_0, EI_z) = (23.4\ \mathrm{Nm}^{-1}, 0.53\ \mathrm{Nm}^2)$, including tank-wall effects. Error bars represent the experimental standard deviation $\sigma_{exp.}(kR)$, obtained from four repetitions of each wave train. Gray markers show the point-wise numerical–experimental discrepancy, $\delta_j(k_iR)$, for marker j. Each plot is labeled with the marker-level L_2 discrepancy, e_j, aggregated over all frequencies for that marker.

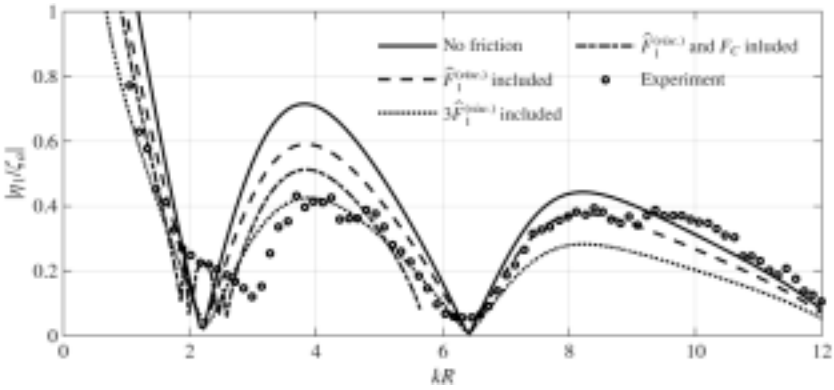


Figure 8: Surge RAO of the membrane as a function of the non-dimensional wavenumber kR. Experimental results are compared with the numerical predictions evaluated at the best-fit structural parameters, with and without friction effects.

still uncertain how to overcome these practical problems in future experiments; avoiding water-on-deck while avoiding unwanted shadowing.

5. Conclusion

A combined numerical and experimental study was performed to evaluate the hydroelastic response of a membrane-based floating solar island. The frequency-domain model reproduced the measured RAOs well, and parameter identification yielded consistent estimates of the membrane pretension and the floater's circumferential rigidity. Additional uncertainty sources – viscous shear friction on membrane, pulley friction, marker-placement offsets, and limited measurements near the collar – had localized effects. The results refine the effective structural parameters and clarify the primary uncertainty mechanisms relevant for modeling membrane-based floating solar islands.

Acknowledgments

This work was supported by the Research Council of Norway through SFI BLUES, grant number 309281.

References

[1] Aurora Skare and Trygve Kristiansen. Modeling wave-induced vertical motion and contact forces for a floating membrane solar island. *Journal of Hydrodynamics*, pages 1–11, 2026.

[2] Aurora Skare and Trygve Kristiansen. Modeling a membrane based floating solar island in waves. In *The 16th International Symposium on Practical Design of Ships and other Floating Structures (PRADS), Ann Arbor, MI, USA.*, October 2025.

[3] Trygve Kristiansen, P Grøn, and Odd Magnus Faltinsen. A floating membrane solar island study. In *Proceedings of the 9th International Conference on HYDROELASTICITY IN MARINE TECHNOLOGY*, 2022.

[4] Yifan Zhang, Xiantao Zhang, Yongqiang Chen, Xinliang Tian, and Xin Li. A frequency-domain hydroelastic analysis of a membrane-based offshore floating photovoltaic platform in regular waves. *Journal of Fluids and Structures*, 127:104125, 2024.

Ship Loads and Responses

10th International Conference on HYDROELASTICITY IN MARINE TECHNOLOGY
Trondheim, Norway, June 16th-18th, 2026

Comparative experimental investigation on springing responses of a 14,000 TEU containership

Ye, Y.[1,2], Fu, S.[1,2,*], Jiang, J.[1,2,3], Chen, X.[1,2] and Huang, W.[1,2]

[1] State Key Laboratory of Ocean Engineering, Shanghai Jiao Tong University, Shanghai, China
[2] Collaborative Innovation Centre for Advanced Ship and Deep-Sea Exploration, Shanghai, China
[3] COSCO Shipping Heavy Industry Co. Ltd, Shanghai, China

Abstract. The increasing dimension of container ships may lead to the natural frequencies of their flexible modes falling within the range of wave encounter frequencies. As a result, the springing response of the large container ships under sailing conditions may be triggered. In this study, a comparative springing experimental investigation of a 14,000 TEU containership is conducted. The segmented containership model with backbone is used. To investigate the effect of structural stiffness on springing responses, two types of backbones are adopted: a variable U-shaped section backbone which is designed similar to the real ship stiffness distribution, and a uniform U-shaped section backbone with lower bending stiffness in which linear springing can be triggered. The springing responses of the ship model with forward speed under a series of regular wave tests are studied. The results show that the vertical bending moment at elastic mode resonance frequency is lower than the maximum result in the non-resonant interval. Nonlinear springing, which occurred in real stiffness backbone, significantly affects the amplitude of the vertical bending moment.

Key words: *Hydroelasticity; Large containership; Springing; Segmented model experiment*

1. Introduction

With the increasing demand for maritime transportation, large container ships are more popular all over the world. However, the large particulars have brought some problems in the design of the large container ship. Their low relative stiffness reduces the structure natural frequency, making it closer to the encounter frequency when the ships sail in the sea. This causes springing response, which will alter the sectional forces and cause structure failure potential.

In recent years, more and more studies focus on the numerical method of the hydroelastic response in large containership. Based on the body surface condition, the hydroelastic method can be divided into three types: modal superposition method [1], direct coupling method [2] and beam-connected-discrete-module (BCDM) method [3]. In the modal superposition method, the modal hydroelastic equation is established by solving the generalized hydrodynamics in the modal space, then determining the hydroelasticity response. Senjanović et al. [4] used a thin-walled beam model combined with three-dimensional potential flow theory to analyze the hydroelastic response of a large container ship. The direct coupling method completes the hydroelastic response analysis by exchanging information between the structural domain and the fluid domain at each time step. It can effectively solve the nonlinear problems such as slamming by using CFD-FEM coupling method [5]. Recently, the BCDM method has been developed to solve hydroelastic response. It analyses the hydroelastic response by discretizing the ship into several modules connected by a hull girder, coupling the multibody hydrodynamic force with the structural stiffness matrix to obtain global hydroelastic response equation [6]. This method has been applied to a navigating large container ship [7].

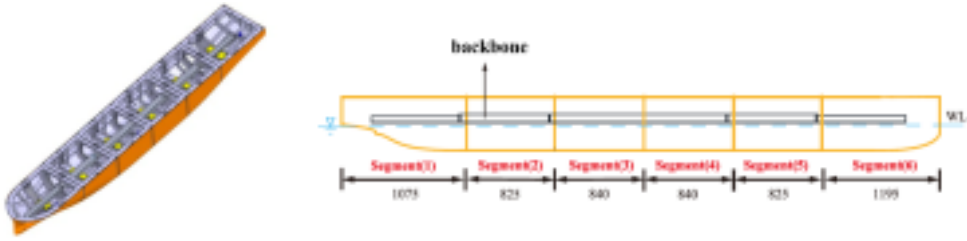
* Correspondence to: shixiao.fu@sjtu.edu.cn

Although significant progress has been made in numerical methods, model experiments are often carried out to analyze the hydroelastic response of large container ship more precisely. To determine the sectional load responses, segmented ship model with backbone is always used [8]. Lin et al. [9] carried out a segmented model experiment of 10,000 TEU container ship, and the springing and whipping phenomenon were investigated. Tang et al. [10] investigated the nonlinear bending moments of a 10,000 TEU container ship in extreme waves by segmented model. The results indicate high order harmonics in extreme waves. Korea Research Institute of Ships and Ocean engineering (KRISO) carried out Wave Induced Loads on Ships Joint Industry Project (WILS JIP), in which the hydroelastic response of the container ship was investigated. Firstly, the global wave loads of a 6,500 TEU containership were conducted [11], and later a 10,000 TEU containership model was used to investigate the springing and whipping response [12]. China Ship Scientific Research Center (CSSRC) also carried out a Joint Industry Project named 'Comparative Study on Springing Responses of 20,000 TEU Containership'. Two types of backbone were used in the segmented ship model. Firstly, two circular steel backbones were utilized to represent the modal feature of the containership [13] and then investigate the springing response of vertical bending moment [14]. Later, considering the low torsion stiffness in large container ship, a U-shaped backbone made of acrylonitrile butadiene-styrene-polycarbonate (ABSPC) was used, which can simultaneously characterize the vertical, horizontal, and torsional stiffness and the shear center of the container ship. A novel method was developed to measure the torsional moment and shear force of the U-shaped backbone [15]. Both the springing [16] and whipping [17] were analyzed. The experimental results indicate a significant influence of the flexible torsion mode in the hydroelastic response of large container ship.

However, linear springing at the first order vertical bending mode frequency, which always requires high frequency regular wave in model test, is little studied in the above studies. In this paper, two types of backbone were used in a segmented ship model experiment: a variable U-shaped section backbone, which is designed similar to the real ship stiffness distribution, and a uniform U-shaped section backbone with lower bending stiffness, in which first order vertical bending mode can be triggered.

2. Basin model setup

A 14,000 TEU container ship model, which is the same in Ye et al. [18], was used to investigate the hydroelastic response. The scale ratio is 1:60 and the main particulars of full loaded condition are shown in Table 1. The model consists of six segments connected by a U-shaped section steel backbone. The whole model is illustrated in Fig. 1.



(a) Overview by 3D modeling. (b) Arrangements of segments and backbone.

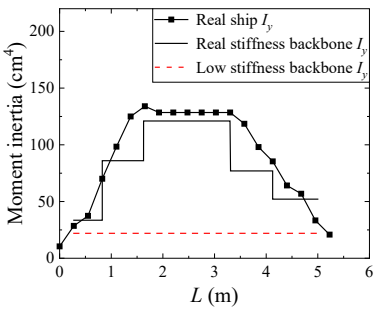
Figure 1: Model design.

Table 1: Main particulars of containership

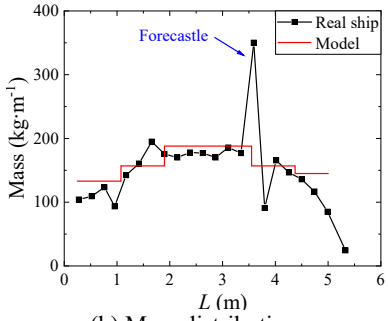
Particulars	Full-scale	Model
Scale	1/1	1/60
L (m)	335.90	5.599
B (m)	51	0.850
H (m)	29.9	0.498
D (m)	14.5	0.242
X_{CG} (m)	160.23	2.671

Z_{CG} (m)	22.71	0.379
r_{xx} (m)	17.558	0.293
r_{yy} (m)	82.925	1.382
r_{zz} (m)	84.550	1.409

Two types of backbone were used in this experiment, including a variable U-shaped backbone, whose bending stiffness is similar to that of the real ship, and a low stiffness U-shaped backbone. The vertical bending stiffness of the two backbones compared with the real ship stiffness in model scale is illustrated in Fig. 2(a). The Young's modulus of the backbone is 2.06×10^{11} Pa, and the details of the bending stiffness are shown in Table 2. The mass distribution is shown in Fig. 2(b). The local effect of the forecastle is neglected, because the natural frequency of 1st order vertical bending in 3D FEM with forecastle is 4.01 rad/s while 4.10 rad/s without forecastle. To measure bending moment, Fiber Bragg Grating (FBG) strain sensors were utilized. Fig. 3 (a) shows the section type and the arrangement of FBG strain sensors. The cantilever beam model was used to calibrate the FBG sensors, as shown in Fig. 3 (b). By using the optical motion measurement system, six degrees of freedom (DOF) of ship motions were measured, with markers placed on the ship.



(a) Bending stiffness distribution.

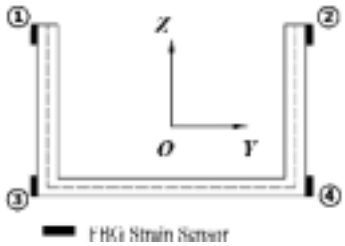


(b) Mass distribution.

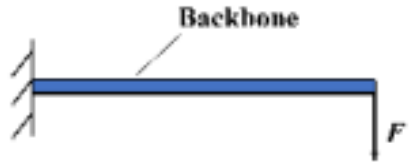
Figure 2: Bending stiffness and mass distribution of the model.

Table 2: Bending stiffness distribution of the backbones

Length (m)	Real stiffness I_y (cm^4)	Low stiffness I_y (cm^4)
0 ~ 0.825	33	22
0.825 ~ 1.625	86	
1.625 ~ 3.3	121	
3.3 ~ 4.125	77	
4.125 ~ 5	52	



(a) Section type and arrangements of FBG sensors.



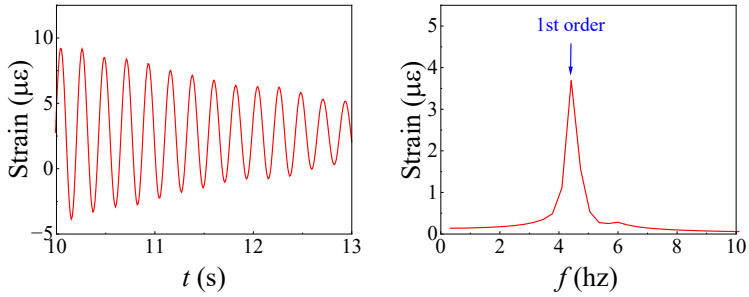
(b) Calibration model

Figure 3: Arrangements and calibration of FBG sensors.

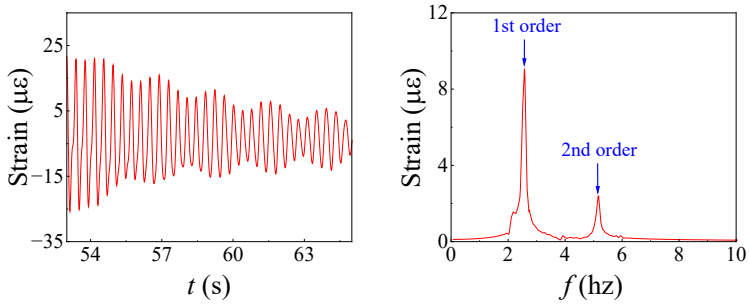
3. Hammering test

The purpose of the hammering test is to derive the structure natural frequency and the damping ratio, which is topic in the springing response. Both the dry and wet modes were measured. In the dry mode

test, the model was hung by several springs. The decay history and spectrum of the natural frequency of both types of the backbone are shown in Fig. 4, and the results are listed in Table 3. In the real stiffness backbone, only the 1st order vertical bending mode was triggered, while the 1st and 2nd order vertical bending mode were triggered in the low stiffness backbone.



(a) Decay history and spectrum of strain of real stiffness backbone.



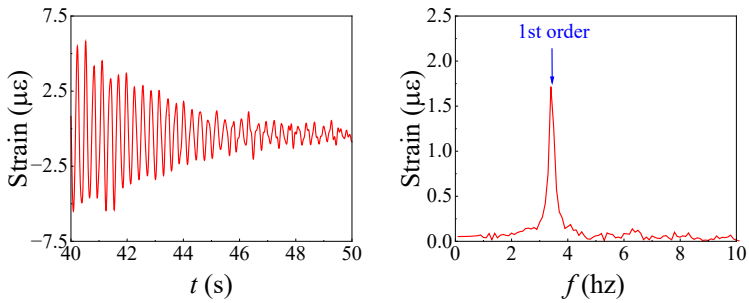
(b) Decay history and spectrum of strain of low stiffness backbone.

Figure 4: Dry mode test.

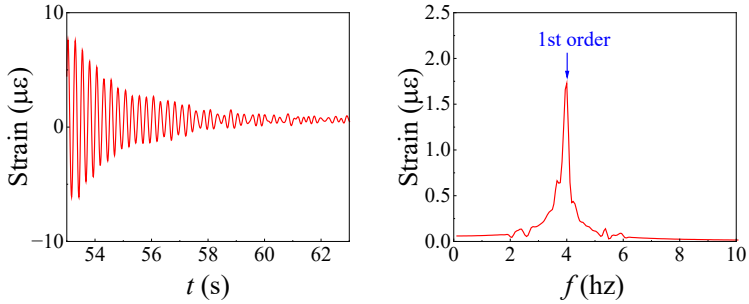
Table 3: Dry mode results.

Vertical bending mode		Real stiffness	Low stiffness
1st order	Natural frequency (Hz)	4.41	2.58
	Damping ratio	0.83%	0.72%
2nd order	Natural frequency (Hz)	-	5.17
	Damping ratio	-	1.33%

In the wet mode test, the model was set in the basin. The decay time history and spectrum of the strain are shown in Fig.5, and Table 4 lists the results. Compared to the dry mode, the wet mode exhibits lower natural frequencies, indicating that the hydrodynamic coefficient reduces the vibration frequency of the container ship in waves.



(a) Decay history and spectrum of strain of real stiffness backbone.



(b) Decay history and spectrum of strain of low stiffness backbone.
Figure 5: Wet mode test.

Table 4: Wet mode results.

Vertical bending mode		Real stiffness	Low stiffness
1st order	Natural frequency (Hz)	3.40	1.73
	Damping ratio	1.68%	2.06%

4. Springing results

Linear RAO tests and springing tests were carried out at the towing tank of State Key Laboratory of Ocean Engineering (SKLOE), Shanghai Jiao Tong University. Four towing mooring springs with stiffness of 4903 N/m were used to tow the model. The model was towed in the head sea. The photo of the test is shown in Fig.6. The ship speed was 22kn (real scale).



Figure 6: Photo of springing test.

4.1 RAO results

Markers were positioned on the 2nd and 4th segments to measure the ship motions. Based on the rigid-body kinematics theory, the measured motion of each segment was transformed to the center of gravity (CG) of the ship, as shown in Fig.7. The difference between the motions of CG measured by two segments reflects the elastic deformation of the backbone. Fig.8 illustrates the motion amplitude under unit wave amplitude. The results derived from rigid bodies in the 2nd segment (solid line) and 4th segment (dashed line) are depicted respectively. The experimental results show that the motion for the low stiffness backbone is larger than those for the real stiffness backbone, especially for the linear springing frequency (1st order vertical bending natural frequency ω_n equals to wave encounter frequency ω_e) of low stiffness backbone. Furthermore, the difference between the two segments is more pronounced for the low stiffness backbone than for the real stiffness backbone. This indicates that the low stiffness backbone undergoes significant elastic deformation.

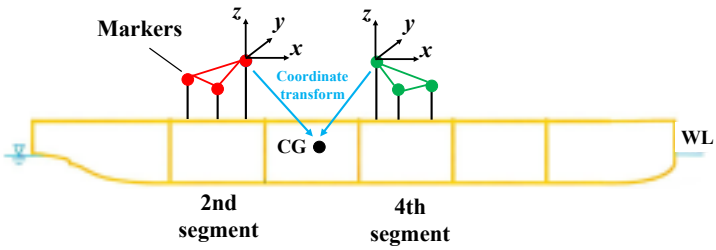


Figure 7: Motion measured by markers.

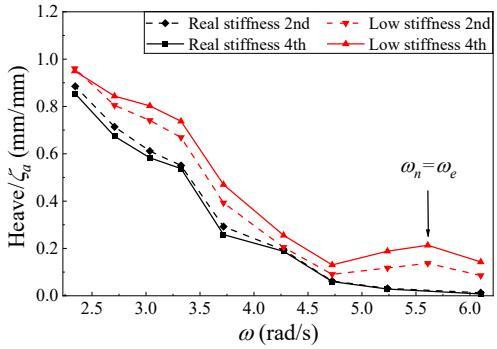


Figure 8: Motion amplitude of the CG measured by 2 segments.

Fig.9 shows the RAO results of vertical bending moment (VBM) under unit wave amplitude in model scale. At the low wave frequency interval (2.5 rad/s < ω < 4.0 rad/s), the difference between two types of the backbone is lower than the high wave frequency interval (ω > 4.0 rad/s). Notably, for the low stiffness backbone linear resonance cases, the resonance peak result is smaller than the maximum result in the non-resonance cases, which is different from most numerical results. This may be due to the large hydrodynamic damping coefficient in the model experiment.

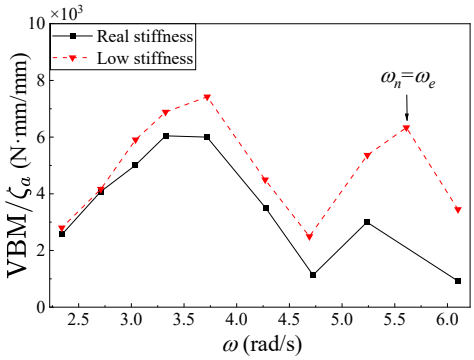


Figure 9: Amplitude of VBM at midship.

To further investigate the linear springing effect along the ship length, Fig.10 illustrates the amplitude of VBM of the low stiffness backbone along the ship length at the linear springing frequency and the wave frequency ω = 3.72 rad/s, where VBM is maximum in non-resonant interval. It can be found that the distinction between linear springing and non-resonant vibration is primarily evident beyond the aft part (x/L > 0.3), reaching its maximum at midship. The peak amplitude of non-resonant peak is approximately 1.2 times that of the springing vibration. At the aft part (x/L < 0.3), the amplitudes of both frequencies are essentially equivalent.

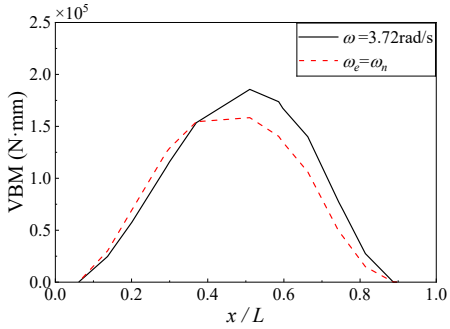


Figure 10: Amplitude of VBM along ship length.

4.2 Nonlinear springing

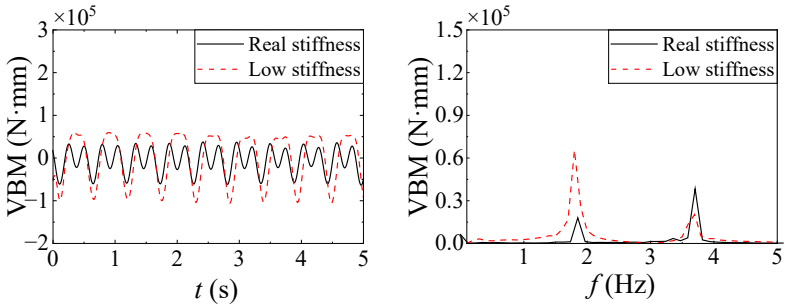
For large container ship, due to some nonlinear factors, nonlinear springing may occur in short wave length cases [16]. Several nonlinear cases were set, as shown in Table 5. The wave height was 3m (real scale).

Table 5: Nonlinear springing cases.

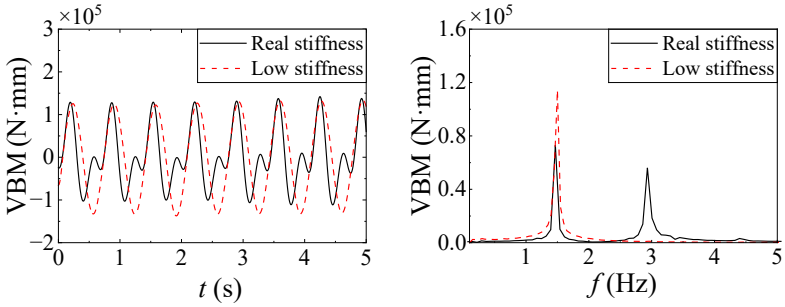
Case ID	Wave length to ship length ratio λ/L	Wave steepness	Wave frequency (rad/s)		Natural frequency to encounter frequency ratio ω_n / ω_e	
			Full scale	Model	Real stiffness	Low stiffness
C1	0.3	0.030	0.78	0.101	1.87	0.95
C2	0.4	0.022	0.68	0.087	2.28	1.16
C3	0.5	0.018	0.61	0.078	2.69	1.37
C4	0.6	0.015	0.55	0.071	3.06	1.56

Fig.11 compares the nonlinear results of two types of the backbones. Both the time series and the spectrum of the VBM at midship are shown. As shown in Fig.11, for the real stiffness backbone, the nonlinear wave-induced vibration phenomenon occurred in every condition. Furthermore, when the 1st order vertical bending natural frequency nearly equals to the integer multiple of wave encounter frequency, the elastic mode was triggered, increasing amplitude of VBM. For real stiffness backbone. In case C2, the second order nonlinear springing occurred, and the amplitude of the second order harmonic was almost twice as large as the wave encounter frequency component. Similarly, in case C4, the third order nonlinear springing was triggered. For the low stiffness backbone, the nonlinear wave-induced vibration phenomenon was less pronounced compared with the real stiffness backbone. Only in case C1, nonlinear vibration could be significantly observed in low stiffness backbone, as shown in Fig.11(a). This suggests that nonlinear wave-induced vibration relates not only to non-linear external excitation [16] but also to the stiffness of the ship hull.

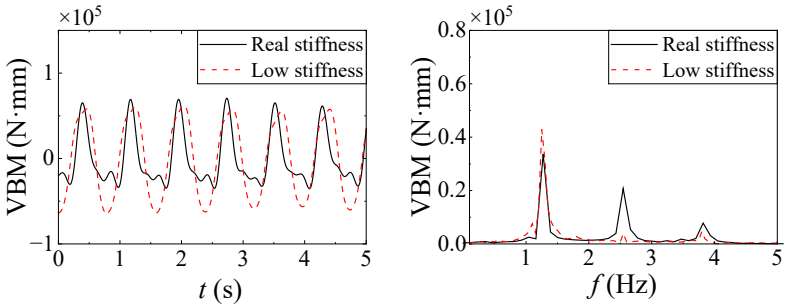
The main reason for the nonlinear excitation may be the variation of the wet surface in the experiment, as shown in Fig.12. Due to the significant changes of the body plan near the waterline at the bow and stern, the hydrodynamic forces exhibit strong nonlinearity. The frequency of the nonlinear forces is the integer times of the wave encounter frequency. Therefore, when the encounter frequency approaches the structure natural frequency, the elastic mode is triggered.



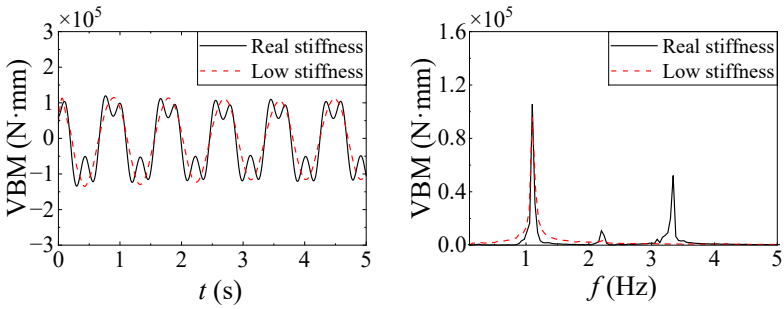
(a) Comparison of VBM in Case C1 (λ/L=0.3).



(b) Comparison of VBM in Case C2 (λ/L=0.4).



(c) Comparison of VBM in Case C3 (λ/L=0.5).



(d) Comparison of VBM in Case C4 (λ/L=0.6).

Figure 11: Comparison of VBM at midship in nonlinear springing cases.

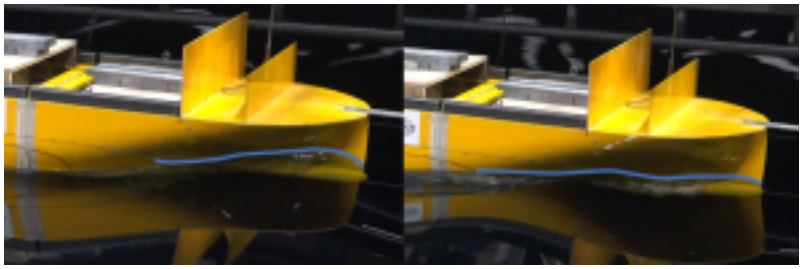


Figure 12: Transient wet surface variation of the ship.

4.3 Brief summary

In Section 4, the RAO results and springing results of the containership are analyzed, including real stiffness backbone and low stiffness backbone. In Fig.8 and Fig.9, the RAO results of motion and VBM are shown respectively. The low stiffness backbone exhibited larger elastic deformation and sectional forces than real stiffness backbone. Fig.10 further investigates the springing effect on VBM along ship length by comparing the results of resonant frequency with maximum non-resonant frequency. Finally, the nonlinear springing phenomenon is analyzed from Fig.11.

5. Conclusions

In this paper, two types of backbones were used in a 14,000 TEU containership segmented model experiment to investigate the springing responses of the containership. Two types of backbones were designed: one to simulate the actual bending stiffness of the real ship hull, and the other low stiffness backbone to investigate linear elastic vibration responses. The dry and wet modes were determined by the hammering test. Both the linear springing and the nonlinear springing were investigated. The main conclusions are below:

(1) In linear RAO tests, the low stiffness backbone exhibited significant elastic deformation compared with the real stiffness backbone. For low stiffness backbone, the amplitude of bending moment at the resonance frequency is smaller than the maximum value in the non-resonant frequency range. Under long-wave conditions, the results of the low stiffness backbone and the real stiffness backbone are largely consistent.

(2) In nonlinear springing tests, the real stiffness backbone exhibited pronounced nonlinear wave-induced vibration. Furthermore, the elastic mode was triggered when the structural natural frequency was an integer multiple of the wave encounter frequency. The amplitude of the second order harmonic can be up to twice as large as the wave encounter frequency component. Conversely, little nonlinear springing behavior was observed for the low stiffness backbone.

In future research, the whipping phenomenon can be investigated on this large container ship.

Acknowledgements

The authors gratefully acknowledge the National Science Fund for Distinguished Young Scholars (Grant No. 52425102).

References

[1] Y. Wu. *Hydroelasticity of floating bodies.* PhD thesis, University of Brunel, 1984.
[2] Yooil Kim, Kyoung-Hwan Kim, and Yonghwan Kim. Springing analysis of a seagoing vessel using fully coupled bem–fem in the time domain. *Ocean Engineering*, 36(11):785–796, 2009.
[3] Wei Wei, Shixiao Fu, Torgeir Moan, Ziqi Lu, and Shi Deng. A discrete-modules-based frequency domain hydroelasticity method for floating structures in inhomogeneous sea conditions. *Journal of Fluids and Structures*, 74:321–339, 2017.

[4] Ivo Senjanović, Stipe Tomašević, and Nikola Vladimir. An advanced theory of thin-walled girders with application to ship vibrations. *Marine structures*, 22(3):387–437, 2009.
[5] Jialong Jiao, Songxing Huang, and C Guedes Soares. Viscous fluid–flexible structure interaction analysis on ship springing and whipping responses in regular waves. *Journal of Fluids and Structures*, 106:103354, 2021.
[6] Shiyuan Zhang, Shixiao Fu, Zhiyuan Pan, Kaijia Han, and Yusong Ye. Springing responses of ships with forward speed based on a multi-module hydroelastic method. *Marine Structures*, 101:103733, 2025.
[7] Yusong Ye, Shixiao Fu, and Shiyuan Zhang. Hydroelastic analysis of a large container ship with forward speed based on multi-module method. In *Proceedings of the Fourth World Conference on Floating Solutions: WCFS2024; 2–4 December; Hong Kong*, pages 507–517, Singapore, 2025. Springer Nature Singapore.
[8] Apostolos Grammatikopoulos. A review of physical flexible ship models used for hydroelastic experiments. *Marine Structures*, 90:103436, 2023.
[9] Yuan Lin, Ning Ma, Xiechong Gu, and Deyu Wang. Experimental study on the asymmetric impact loads and hydroelastic responses of a very large container ship. *International Journal of Naval Architecture and Ocean Engineering*, 12:226–240, 2020.
[10] Ying Tang, Shi-Li Sun, Rui-Song Yang, Hui-Long Ren, Xin Zhao, and Jia-Long Jiao. Nonlinear bending moments of an ultra large container ship in extreme waves based on a segmented model test. *Ocean Engineering*, 243:110335, 2022.
[11] SY Hong, JH Kyoung, YS Kim, KH Song, S Kim, S Malenica, M Lindgren, H Rathje, and C Ge. Validation of wave loads on a large container ship in oblique waves. In *Proc. 6th Colloquium on Seakeeping and Stability of Ships*, pages 109–117, 2008.
[12] Sa Young Hong, Byoung Wan Kim, and Bo Woo Nam. Experimental study on torsion springing and whipping of a large container ship. In *ISOPE International Ocean and Polar Engineering Conference*, pages ISOPE–I. ISOPE, 2011.
[13] Ye Lu, Juan Liu, Bei Teng, Chao Tian, Hailong Si, Qingyun Zhou, and Xinyun Ni. Modal investigation on a large-scale containership model for hydroelastic analysis. *Shock and Vibration*, 2022(1):2539870, 2022.
[14] Ye Lu, Juan Liu, Bei Teng, Chao Tian, Hailong Si, and Xinyun Ni. Linear springing assessment of ultra large container ships. In *ISOPE International Ocean and Polar Engineering Conference*, pages ISOPE–I. ISOPE, 2022.
[15] Hailong Si, Xuekang Gu, and Jiajun Hu. Model experiment method of container ship's torsion moment and shear force. *Journal of Ship Mechanics*, 24(12):1657–1667, 2020.
[16] Hailong Si, Chao Tian, Jun Yang, Yanchao Geng, Nan Zhao, Jiajun Hu, and Junhua Zhan. Experimental investigation of nonlinear springing of ultra-large container ship in regular waves. *Marine Structures*, 99:103697, 2025.
[17] Hailong Si, Chao Tian, Caixia Jiang, Peng Yang, Nan Zhao, and Zhijia Wu. Experimental slamming and whipping investigation of ultra large container ships in waves. *Ocean Engineering*, 325:120759, 2025.
[18] Yusong Ye, Jijiang Jiang, Shiyuan Zhang, Shixiao Fu, Zhiyuan Pan, and Shaobo Wu. Global and structural hydroelastic analysis of a large container ship with forward speed using multi-module method. *Journal of Ocean Engineering and Science*, 2026.

10th International Conference on HYDROELASTICITY IN MARINE TECHNOLOGY
Trondheim, Norway, June16$^{\text{th}}$-18$^{\text{th}}$, 2026

Experimental Study on Influence of Bow Flare Shape above Waterline on Whipping Response of 14,000 TEU Container Ship

Suzuki, K.[1,*] Takeda, K.[1], Sugimoto, K.[1], Harada. M.[1], Oka, M.[2], and Matsui, S.[2]

[1] Nippon Kaiji Kyokai (ClassNK), Tokyo, Japan
[2] National Maritime Research Institute, Tokyo, Japan

Abstract. This study investigates the influence of bow flare geometry above the waterline on the whipping response of a 14,000 TEU container ship using segmented model experiments in irregular waves. Three interchangeable bow segments—L-flare, M-flare, and S-flare—were tested, differing only in their above-water flare shape while sharing identical underwater geometry. All experiments were conducted under identical incident-wave time series generated using the same wavemaker input. Ship motions, vertical accelerations, vertical bending moments, and hull-surface pressures were measured. While global ship motions showed negligible differences among the three models, clear differences were observed in accelerations and vertical bending moments. Peak accelerations measured at the fore and aft perpendiculars and vertical bending moments near midship increased with increasing flare size. The whipping factor, defined as the peak value of the raw time series divided by the corresponding rigid-body peak, was approximately 1.3 on average for the L-flare model and approximately 1.2 on average for the S-flare model. The measured pressure time series further indicated that larger flare geometries induce stronger bow flare slamming loads.

Key words: *Whipping; Bow flare geometry; Segmented model experiments; Vertical bending moment; 14K-TEU container ship*

1. Introduction

In recent decades, the pursuit of higher transportation efficiency has led to the continuous enlargement of container ships. As of 2025, ultra-large container ships with capacities of approximately 24,000 TEU and lengths of around 400 m have been constructed and are currently in operation. For such large vessels, elastic hull girder responses cannot be regarded as small, and the loads induced by whipping are superposed on the vertical bending moment of the rigid-body. Accordingly, IACS Unified Requirement S11A[1] specifies that the influence of whipping on the vertical bending moment shall be considered in the ultimate strength assessment of large container ships meeting the specified conditions. In ClassNK, the effect of whipping is incorporated through the introduction of a partial safety factor γ_{wh}[2, 3]. The partial safety factor for whipping represents a safety margin accounting for elastic responses relative to the rigid-body vertical bending moment, and a constant value of $\gamma_{wh} = 1.5$ is adopted. This value was determined based on irregular-wave analyses of multiple full-scale ships and was selected conservatively to cover the range of obtained results. Consequently, the adopted partial safety factor implicitly includes the combined effects of various factors influencing whipping responses. However, whipping behaviour is known to depend on several factors, such as bow geometry[4, 5, 6], forward speed[7, 8, 9], and wave conditions[7, 10, 11]. From a rational design perspective, it is therefore important to accumulate knowledge on how each factor contributes to whipping responses.

Although many previous studies have investigated whipping through both computational[12, 13, 14, 15, 16, 17] and experimental[4, 5, 6, 7, 8, 9, 10, 11] approaches, studies focusing solely on the influence

*Correspondence to: kan-suzuki@classnk.or.jp

of flare shape are limited. Thus, an experimental investigation was conducted using segmented model tests in a towing tank. In the experiments, a segmented model of a publicly available 14,000 TEU container ship[18, 19] was used. By employing interchangeable bow segments that differ only in their flare geometry above the waterline and by applying the same wavemaker input signal to all test cases, aiming to generate identical incident-wave time series, the present study aims to clarify the influence of bow flare shape on whipping-induced responses in irregular head waves. The effects of bow flare variation are examined through comparisons of ship motions, accelerations, vertical bending moments, and hull surface pressures.

2. Towing tank tests

2.1. Ship model: NK-14KTEU container ship

In the experiments, a 14,000 TEU container ship referred to as NK-14KTEU[18, 19] was used. This ship is an original hull form developed by ClassNK for research purposes and is publicly available. The principal particulars of NK-14KTEU are summarised in Table 1, and the body plan is shown in Fig. 1. In order to measure elastic responses, the model was constructed as an eight-segment model, with the segments connected by a backbone structure. To investigate the influence of differences in bow flare shape on the vertical bending moment induced by the whipping, interchangeable bow segments were prepared. Only the flare shape above the waterline of the segments forward of station S.S. 8.5 differs.

Hereafter, the three models with different bow flare shapes are referred to as the L-flare, M-flare, and S-flare models in descending order of the projected area of the flare. The origin is located at the midship on the centerline at the draft line in calm water. The translational motions follow a right-handed coordinate system, with the z-axis pointing vertically upward. For rotational motions, the positive direction is defined according to the right-hand rule. The positive directions of accelerations are defined consistently with this coordinate system. With respect to the vertical bending moment, hogging is defined as

Table 1: Principal particulars of NK-14KTEU.

Item	Value (Scale 1:64)		Unit
	full	model	
Ship overall length: L_{oa}	370.3	5.786	m
Ship length: $L_{pp}(\equiv L)$	352.0	5.500	m
Ship breadth: B	50.0	0.781	m
Draft: d	15.0	0.234	m
Displacement volume: ∇	178,459	0.681	m^3
Block coefficient: C_b	0.676	0.676	-
Horizontal center of gravity: $x_G(=L_{cb})$	-6.687	-0.104	m
Vertical center of gravity from keel: KG	21.0	0.328	m
Pitch gyration radius: κ_{yy}/L_{pp}	0.250	0.250	-

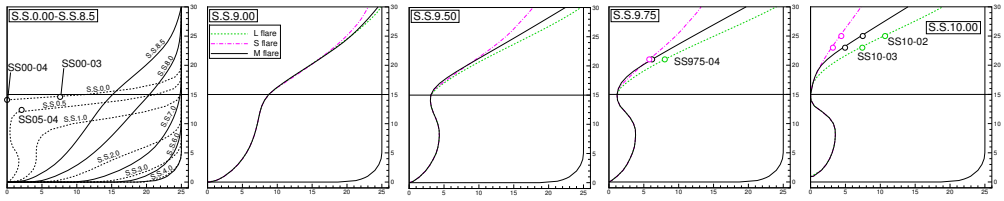


Figure 1: Body plan of L, M and S flare. Circle markers represent attached FBG pressure sensors.

Table 2: Measured and calculated natural frequency of NK-14KTEU model in elastic modes in model scale.

Elastic mode	Node	Natural frequency [Hz]		
		Cal. (U=0.0 knot)	Exp. (U=0.0 knot)	Exp. (U=5.0 knot)
First	2	3.6	3.5	3.5
Second	3	5.4	5.4	5.7
Third	4	7.5	7.2	8.8
Fourth	5	15.6	12.6	13.9

positive.

The backbone structure was designed so as to reproduce the elastic characteristics of the full-scale 14,000 TEU container ship with respect to its natural frequencies in the first elastic mode. Before the wave experiments, impact hammer tests were carried out in the towing tank to identify the elastic natural frequencies of the model. The measured frequencies were then compared with those obtained from FEM analysis, and the results are summarised in Table 2. It can be confirmed from the table that the model exhibits good agreement with the numerical predictions for the first three elastic modes.

2.2. Setting and measurements

The experiments in irregular head waves were conducted in 2022 at the large towing tank of the Akishima Laboratories, whose dimensions are 220 m in length, 14 m in breadth, and 6.5 m in depth. The ship speed was fixed at 5 knots, corresponding to operational conditions in severe seas, which gives a Froude number of 0.044. Regarding the wave condition, a significant wave height H_s of 12.0 m and a mean wave period of $T_{01} = 11.5$ s based on the ISSC spectrum were specified. The experiments for the three flare shape models were conducted under the same wave conditions by applying identical input signals to the wavemaker. Therefore, ideally, the same incident wave time series should be generated in all cases. The time of starting to move the ship model forward after wave generation was set to be identical in all experiments.

The measured responses included surge, heave, and pitch motions; vertical bending moments at seven sections connected by eight segments; vertical accelerations at the aft perpendicular (AP), midship, and fore perpendicular (FP); and pressures acting on the hull surface. All signals were recorded at a sampling rate of 100 Hz. For the measurement of hull surface pressures, Fiber Bragg Grating (FBG) pressure sensors (version 7)[20] were utilised. The locations of the installed FBG sensors are indicated in Fig. 1 as a circle.

3. Analysis

3.1. Extraction of peak values

In Sections 4.1.,4.2..4.3., the peak values obtained from the measured time series data are discussed. Those peak values are obtained by the following way, which is explained using the example of the time series vertical bending moment shown in Fig. 2. The period is defined by zero-up crossing analysis based on the low-pass filtered time series for the M-flare model. Within this period, the positive and negative peak values for the three flare models are extracted from the raw time-series data. The extracted extreme values are plotted in scatter diagrams, where the horizontal axis represents the values obtained from the M-flare model and the vertical axis represents those obtained from the L- or S-flare model, as shown in Fig. 3.

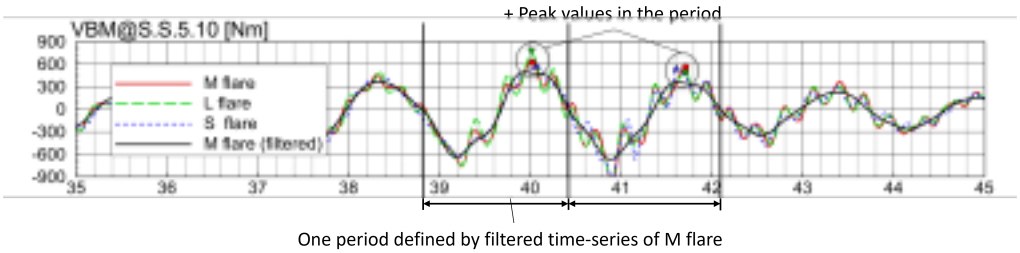


Figure 2: Example of a time history of the vertical bending moment illustrating the extraction of peak values within a period. The inverted triangles, circles, and triangles represent the positive peak values of the L-, M-, and S-flare cases, respectively, in each period.

3.2. Whipping factor

To quantify the amplification of the response in vertical bending moment due to elastic vibration, the whipping factor f_i defined in the form is introduced.

$$f_i = \frac{p_i^{\text{raw}}}{p_i^{\text{rigid}}} \tag{1}$$

where p_i^{raw} and p_i^{rigid} are the extreme values of the raw and rigid-body time series, respectively, in the i-th period defined using the procedure described in the previous section.

3.3. Vertical velocity

To discuss the pressure behaviour from the viewpoint of relative velocity, which is one of the key factors in estimating slamming loads, the vertical velocity $v(x,t)$ is calculated from the measured heave $\xi_3(t)$ and pitch $\xi_5(t)$, which are approximated by a Fourier series expansion, as follows:

$$\xi_j(t) \sim \xi_j^{(0)} + \sum_n^N \text{Re}\left[X_j^{(n)} e^{in\omega t}\right], (j = 3,\ 5) \tag{2}$$

$$v(x,t) = -\left\{\dot{\xi}_3(t) - x\dot{\xi}_5(t)\right\} \tag{3}$$

where $X_j^{(n)}$ denotes complex amplitude of the n-th harmonic component calculated from the measured time-series data, and ω is defined by the analysis interval T_a as $\omega = 2\pi/T_a$. Note that the positive direction of the vertical velocity is defined as downward here, whereas that of the displacement is defined as upward.

In principle, slamming loads should be discussed based on the relative velocity between the hull and the free surface. However, since information on the free-surface elevation was not available in the present experiments, the pressure time series is discussed using only the vertical velocity in Eq. (3).

4. Results and discussion

4.1. Incident waves

To investigate the reproducibility of the incident waves in each experiment, the peak values are compared. Figure 3 presents a comparison of the extreme values of the incident waves for the L- and S-flare models against those of the M-flare model. From Fig. 3, it can be seen that, for both the L- and

S-flare models relative to the M-flare model, the linear regression lines are almost aligned with the 45-degree line, although the scatter of the S-flare data is larger than that of the L-flare data. This indicates that the incident wave time series generally follow the trend of that for the M-flare model.

The significant wave height H_s and the mean wave period T_{01} in each test were calculated by spectral analysis. The results are shown in Fig. 4 (a) and Table 3. The frequency range $\omega_0 = 3.0$ to 4.0, in which the power spectral density function exhibits large values, corresponds to a ratio between wavelength and ship length $\lambda/L = 0.70$ to 1.25. The figure and the table indicate that the differences in H_s and T_{01} among the tests are small, although deviations from the target values are observed.

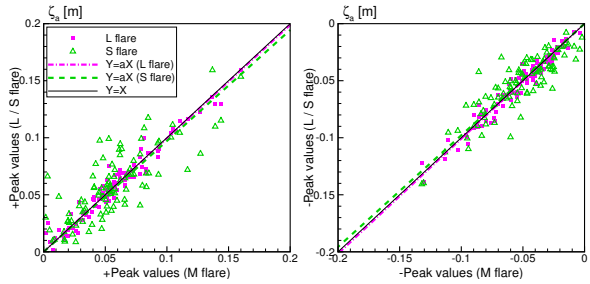


Figure 3: Comparisons of the extreme values of the incident waves for the L-flare and S-flare models against those of the M-flare model (sample size: 99). Positive values are defined as upwards.

Table 3: Significant wave height and mean wave period in each test, which are expressed in full scale.

	Target	L-flare test	M-flare test	S-flare test
H_s [m]	12.00	10.92	10.86	10.88
T_{01} [s]	11.5	13.15	13.21	13.16

4.2. Ship motions and accelerations

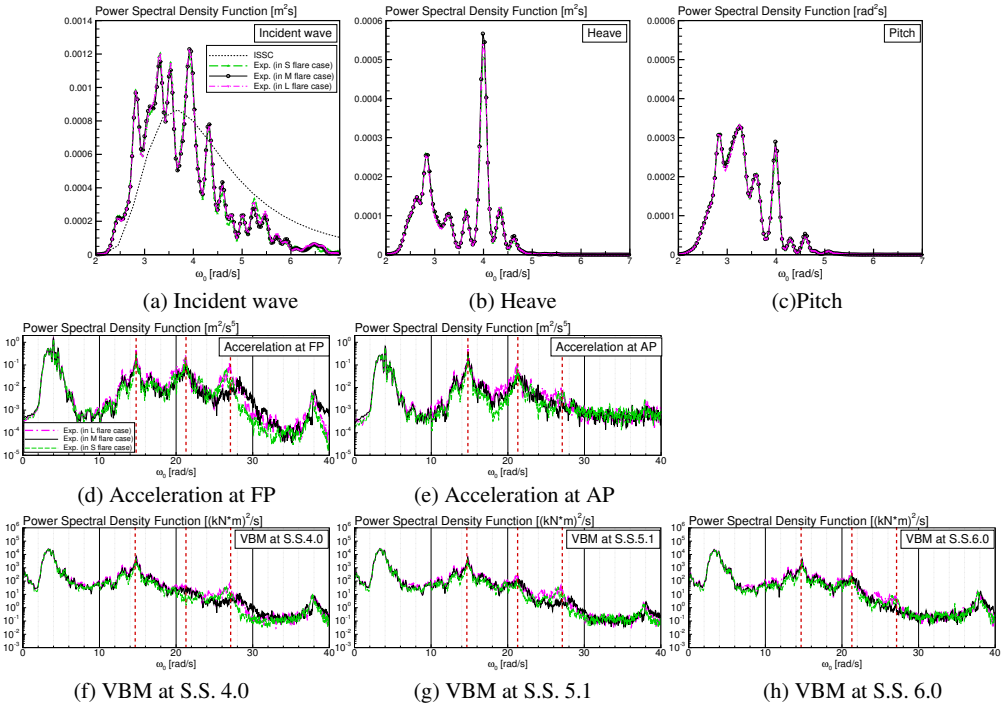
In Fig. 4 (b) and (c), the power spectral density function of heave and pitch is shown, respectively. The results among the three ship models do not show a significant difference in both heave and pitch.

The power spectral density functions of the accelerations at the FP and AP are shown in Fig. 4 (d) and (e) on a logarithmic scale. In these figures, resonance phenomena are observed at $\omega_0 \sim 14.7,\ 21.6,$ and $27.6\ \mathrm{rad/s}$. Red dotted lines are shown at these frequencies. When these frequencies are converted to the encounter wave frequencies corresponding to a towing speed of 5 knots for the full-scale ship, they become about $3.5,\ 5.9,$ and 8.4 Hz, respectively. These frequencies are in close agreement with the resonance frequencies identified in the hammering tests, as shown in Table 2.

Subsequently, the peak acceleration values of the L- and S-flare models were compared with those of the M-flare model, following the procedure described in Section 3.1.. The peak values together with the linear regression lines are presented in Fig. 5. These values are normalised using the corresponding values listed in Table 3. As shown in Fig. 5, the peak values at both the FP and AP increase with increasing bow flare size. Since the ship motions show no significant difference among the three models, the observed differences are attributed to whipping induced by slamming.

4.3. Vertical bending moment

In Fig. 4 (f) to (h), the power spectral density functions of vertical bending moments as S.S. 4.0, 5.1, and 6.0 are shown, respectively. From the panels, the natural frequencies are observed at the same frequencies as observed in accelerations. Following the analysis described in Section 3.1., the peak

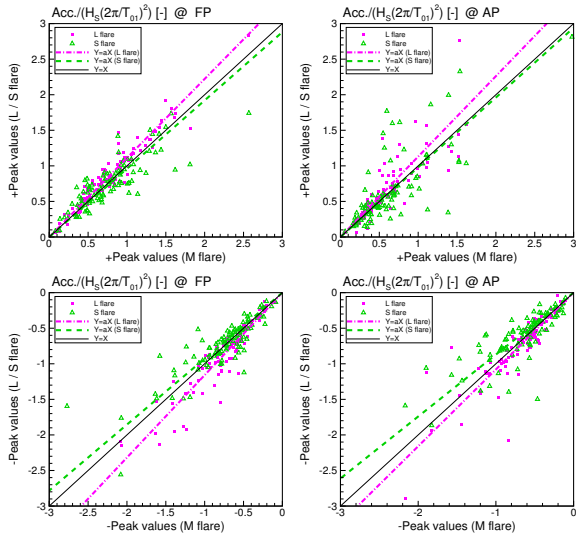


(a) Incident wave (b) Heave (c)Pitch

(d) Acceleration at FP (e) Acceleration at AP

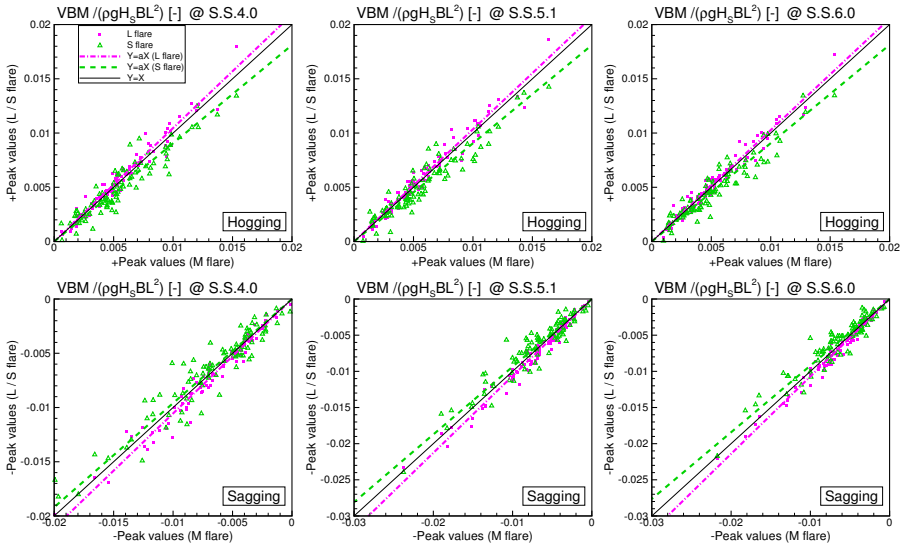
(f) VBM at S.S. 4.0 (g) VBM at S.S. 5.1 (h) VBM at S.S. 6.0

Figure 4: Power spectral density functions of incident wave, heave, pitch, accelerations at FP and AP, and vertical bending moment at S.S. 4.0, 5.1, and 6.0.



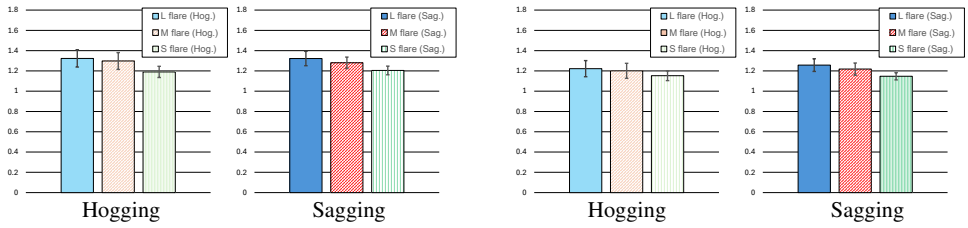
(a) at FP (b) at AP

Figure 5: Comparison of peak values regarding measured accelerations at FP and AP (sample size: about 90). Positive values are defined as upwards.



(a) at S.S. 4.0 (b) at S.S. 5.1 (c) at S.S. 6.0

Figure 6: Comparison of peak values regarding measured vertical bending moment at S.S. 4.0, 5.1, and 6.0 (sample size: about 100). Positive values (upper panels) indicate hogging condition.



(a) $H_s = 12.0$ m, $T_{01} = 11.5$ s (b) $H_s = 9.0$ m, $T_{01} = 11.5$ s

Figure 7: Whipping factors of three bow flare ship models at S.S. 5.1.

vertical bending moment values of the L- and S-flare models, together with their linear regression lines, were compared with those of the M-flare model in Fig. 6. The results at S.S. 4.0, 5.1, and 6.0 were selected because they are located around midship. At these sections, a clear trend is observed in which larger bow flare results in larger vertical bending moments in both sagging and hogging conditions.

In addition, the whipping factors of the three models are shown in Fig. 7. The figure includes not only the results for the condition with $H_s = 12.0$ m and $T_{01} = 11.5$ s (Fig. 7 (a)), but also $H_s = 9$ m and $T_{01} = 11.5$ s (Fig. 7 (b)). Although extreme values corresponding to a probability of $1/N$ are often evaluated using statistical distributions such as the Weibull distribution, this approach was not adopted in this study because the number of experimental cases was insufficient to discuss a probability of $1/N$ using the average and error bar. Instead, to increase the number of available data samples, the present analysis focuses on peak values obtained in idealically same waves. The number of data samples used to calculate the mean and standard error is approximately 30, which corresponds to the upper third of the peak in the rigid-body time series of the M-flare model. The upper one-third of the peaks is used to avoid including cases with very small denominators in Eq. (1), which would yield excessively large whipping factors and should therefore be excluded from the evaluation. The bars on each side represent twice the standard error, which implies that the mean value is included within the 95 % confidence

interval. In Fig. 7 (a), the whipping factors increase with increasing bow flare size in both hogging and sagging modes. This tendency can also be confirmed in the case of Fig. 7 (b). The whipping factor averaged approximately 1.3 for the L-flare model and approximately 1.2 for the S-flare model in both hogging and sagging conditions for the case of $H_s = 12.0$ m. This difference confirms the influence of bow flare geometry on the vertical bending moment. In addition, the whipping factor of the L-flare model for $H_s = 12.0$ m reaches a maximum averaged value of approximately 1.4. Considering that the partial safety factor for whipping, γ_{wh}, is defined as 1.5, it can be inferred that bow flare geometry has a significant influence on the amplification of the vertical bending moment due to whipping. It should be noted that the partial safety factor was derived based on analyses employing Weibull distribution fitting, whereas the estimation method of the whipping factor adopted in this study is different.

From the comparison between Fig. 7 (a) and (b), which correspond to different wave heights, it is confirmed that the whipping factor increases for all models with increasing wave height.

4.4. Pressures

To deepen the understanding of the amplification of vertical bending moment induced by whipping, the pressure time series is discussed here. The pressure measured at the position indicated in Fig. 1, accelerations at FP and AP, and vertical velocity estimated in Eq. (3) in time history are shown in Fig. 8. The values are normalised by significant wave height and other appropriate physical quantities. This figure shows an example of a time interval extracted from the measured time history, in which the occurrence of strong slamming can be identified from the acceleration time series. To improve the readability of the figure, and because a strong correlation of incident waves was observed in the time-series responses, only the L-flare and M-flare models are shown, while the S-flare model is omitted. In the figure, bow flare slamming is considered to occur at around T=10.2 s, as high-frequency vibrations in the acceleration at the FP are amplified. At this moment, the pressure sensors around the bow flare (SS10-02, SS10-03, and SS975-04) record moderate or weak slamming pressures. Unlike a sinusoidal response, the pressure exhibits an abrupt initial rise, although it does not show a spike-like behaviour. After this time, from T=14.2 s, the acceleration vibrations at the FP for the L-flare model are further amplified, and an amplification of vibration can also be observed in the acceleration at the AP. At this

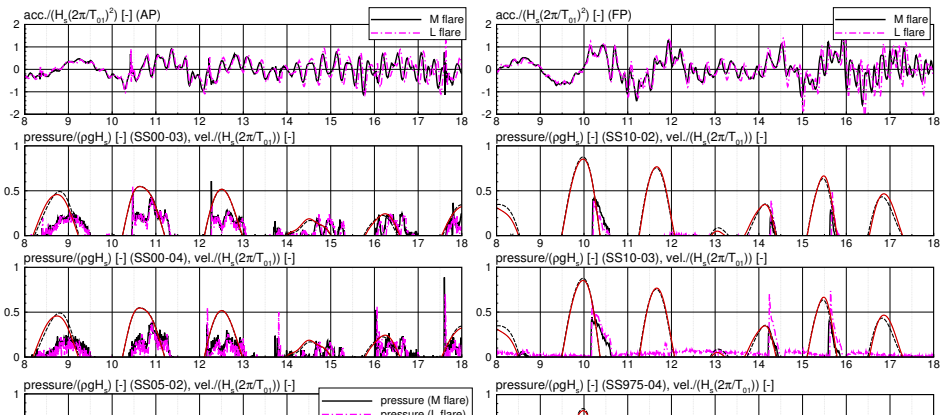


Figure 8: Time histories of pressure measured at the position indicated in Fig. 1, accelerations at FP and AP, and vertical velocity estimated in Eq. (2) in time history between the L-flare model and the M-flare model.

moment, the pressures measured on the L-flare, particularly at SS10-03, show larger values than those for the M-flare. In contrast, the vertical velocities show little difference between the two models at the time when the impact is observed. Since slamming loads are theoretically evaluated based on the relative velocity between the hull and the free surface, as well as the local angle between the free surface and the flare geometry, the observed differences in pressure behavior are considered to be primarily induced by the flare shape itself, rather than by differences in global ship motions although the detailed free-surface motion was not measured in the present experiments.

Subsequently, the pressure behaviour around the stern is discussed. The authors initially considered the possibility that stern pressures might also be influenced by the bow flare shape through changes in ship motions. However, as discussed in Section 4.2., the differences in ship motions among the three model tests are small. Consequently, no significant differences in vertical velocity or stern pressure are observed between the two models, as shown in Fig. 8. Therefore, the amplification of vibrations observed at approximately $T = 14.2$ s is considered to be caused by whipping induced by bow flare slamming, rather than by stern slamming. It should be noted that small differences in spike-like pressure peaks can be observed at, for example, $T = 12.2$, 14.8, and 17.6 s. These discrepancies in peak values are considered to be mainly caused by the small sampling frequency of the pressure measurements.

5. Conclusions

This study experimentally investigated the influence of bow flare geometry above the waterline on the whipping response of a 14,000 TEU container ship through segmented model experiments in irregular head waves. Three types of models, differing only in their above-water flare geometry, were tested under identical incident-wave time series generated using the same wavemaker input. By reproducing the same incident waves for all tests, the effects of bow flare geometry on the measured responses were isolated. The obtained results are as follows.

1) Experiments were conducted in irregular waves corresponding to a full-scale significant wave height of $H_s = 12$ m and a mean wave period of $T_{01} = 11.5$ s, with the model towed at a speed of 5 knots. The extreme values and spectral characteristics derived from the measured incident-wave time series were compared among the tests, confirming that the incident waves were almost identical in all experiments.

2) Under the wave condition, the heave and pitch motions showed almost no difference among the experiments conducted with models having different bow flare shapes. In contrast, the accelerations measured at the FP and AP exhibited high-frequency components corresponding to elastic-mode resonance frequencies, and the peak values tended to increase as the bow flare size increased.

3) At the midship sections, the peak values of the vertical bending moment increased with increasing bow flare size for both sagging and hogging. Using the whipping factor, defined as the amplification ratio relative to the rigid-body component, a clear difference was observed. The average whipping factor at S.S. 5.1 was evaluated from the extreme values corresponding to the upper one-third of the rigid-body peak values obtained from the M-flare model. The factor was approximately 1.3 for the L-flare model and 1.2 for the S-flare model in both sagging and hogging.

4) The pressure time histories were examined at a time interval when high-frequency acceleration vibrations were prominently observed in the experiments with the L-flare and M-flare models. At the moment, little difference was found in the downward vertical velocity derived from the ship motions. However, the pressure rise at the bow of the L-flare model was confirmed to be larger than that of the M-flare model. Although it was initially anticipated that differences in bow flare shape might also influence stern slamming through changes in ship motions, no significant differences were observed around the stern, because the motion differences among the models were negligible.

Acknowledgments

The authors gratefully acknowledge Dr. Toichi Fukasawa of the National Maritime Research Institute for his valuable advice and support in the course of this study.

References

[1] IACS. *UR S11A Longitudinal Strength Standard for Container Ships*, June, 2015.

[2] ClassNK(Nippon Kaiji Kyokai). *Rules for the survey and construction of steel ships, Part C, Part 2*, June 2025

[3] ClassNK(Nippon Kaiji Kyokai). *Explanation of Amendments to the Rules for the Survey and Construction of Steel Ships, Parts A and C, and Related Survey Guidelines*, Nippon Kaiji Kyokai Kaishi, Vol. 314(I), pp. 5–21, 2016 (in Japanese).

[4] I. Watanabe, M. Ueno and H. Sawada. *Effects of bow flare shape on the wave loads of a container ship*, J. Soc. Nav. Archit. Jpn., No. 166, pp. 259–266, 1989.

[5] G. Storhaug and T. Moan. *The effect of bow shape on the springing/whipping response of a large ocean-going vessel investigated by an experimental method*, Proc. OMAE, Vol. 42703, pp. 367–378, 2007.

[6] S. Zhu and T. Moan. *A comparative study of the influence of bow shape on hull girder vibrations through two backbone models*, Proc. HYEL, pp. 19–21, 2012.

[7] S. Zhu, M. Wu and T. Moan. *Experimental investigation of hull girder vibrations of a flexible backbone model in bending and torsion*, Appl. Ocean Res., Vol. 33(4), pp. 252–274, 2011.

[8] J. Jiao and H. Ren. *Characteristics of bow-flare slamming and hydroelastic vibrations of a vessel in severe irregular waves investigated by segmented model experiments*, J. Vibroeng., Vol. 18(4), pp. 2475–2494, 2016.

[9] J. Zou, H. Li, Z. Sun, B. Han and Z. Wang. *Experimental analysis of bow flare slamming and whipping responses in a ship at different sailing speeds*, Ocean Eng., Vol. 305, 117896, 2024.

[10] H. Si, C. Tian, C. Jiang, P. Yang, N. Zhao and Z. Wu. *Experimental slamming and whipping investigation of ultra-large container ships in waves*, Ocean Eng., Vol. 325, 120759, 2025.

[11] H. Si, C. Tian, J. Yang, Y. Geng, N. Zhao, J. Hu and J. Zhan. *Experimental investigation of nonlinear springing of ultra-large container ship in regular waves*, Mar. Struct., Vol. 99, 103697, 2025.

[12] R. Miyake, T. Zhu, T. Matsumoto and A. Kumano. *Effect of bow flare shape to the vertical wave bending moment of container ships*, Proc. JASNAOE, Vol. 3, pp. 137–140, 2006 (in Japanese).

[13] J.-H. Kim and Y. Kim. *Numerical analysis on springing and whipping using fully-coupled FSI models*, Ocean Eng., Vol. 91, pp. 28–50, 2014.

[14] J. de Lauzon, Q. Derbanne and Š. Malenica. *Slamming induced whipping computations on a large database of container ships*, Proc. PRADS, pp. 857–877, 2019.

[15] A. Oto, T. Okada, Y. Kawamura, T. Miyashita and T. Nagashima. *Influences of bow flare shape on whipping response of a large container ship*, Proc. JASNAOE, Vol. 30, pp. 45–51, 2020 (in Japanese).

[16] J. Jiao, Z. Chen, C. Chen and H. Ren, *Time-domain hydroelastic analysis of nonlinear motions and loads on a large bow-flare ship advancing in high irregular seas*, J. Mar. Sci. Technol., Vol. 25(2), pp. 426–454, 2020.

[17] Z. Chen, J. Jiao, S. Chen, F. Zhang and Q. Feng. *CFD–FEM simulation of hydroelastic responses and slamming loads of a bow-flare ship advancing in head regular waves*, Ships Offshore Struct., Vol. 20(10), pp. 1523–1539, 2025.

[18] K. Takeda, S. Matsui and K. Sugimoto. *A study on validation of linear seakeeping codes with benchmark tank tests for container ship and VLCC*, Proc. OMAE, Vol. 87790, 2024.

[19] S. Matsui, K. Takeda and K. Sugimoto. *Difference in ship response in waves between strip and 3D methods based on integrated formulation*, Ocean Eng., Vol. 305, 117908, 2024.

[20] K. Suzuki, H. Iwashita, M. Kashiwagi, M. Wakahara, T. Iida and M. Minoura. *Temperature interference in improved FBG pressure sensor for towing tank test*, J. Mar. Sci. Technol., Vol. 28(2), pp. 351–369, 2023.

10th International Conference on HYDROELASTICITY IN MARINE TECHNOLOGY
Trondheim, Norway, June 16th-18th, 2026

Variable-Stiffness Ship Elastic Models for Hydroelastic Digital Twinning

Dessi, D.[1*], Passacantilli, F.[1], Venturi, A.[1], Delgado, D.[2], Van Dijke, R.[2]
Terroba F.[3], Bardiani, J.[4], Sbaruffati, C.[4], Sandström, J.[5], Haridas, A.[6]

[1] Institute of Marine Engineering - NationTal Research Council - Rome, Italy
[2] Damen Naval - Vlissingen, Netherlands
[3] Instituto Nacional de Tecnica Aerospacial - Campus "El Pardo" - Madrid
[4] Politecnico di Milano, Department of Mechanical Engineering - Milano, Italy
[5] Saab Naval AB - Karlskrona, Sweden
[6] Testia GmbH - Bremen, Germany

Abstract. Nowadays, scale-model testing with elastic segmented hulls offers a new opportunity for verifying digital twinning techniques by combining numerical models and sensor data. The previous statement provided the main motivation to build an elastically scaled model capable of tracking closely structural modifications within the project "Digital Ship Structural Health Monitoring project" (dTHOR), granted by the European Defence Fund. On the hydroelasticity side, the scope of this paper is two-fold: first, to show the possibility of building variable-stiffness elastic models and secondly, to investigate how the variations in the longitudinal bending stiffness affect the whipping response of the ship. The physical model was designed and built thanks to a strong collaboration among several partners which leveraged a realistic representation of the ship modal properties in vertical bending as dry and wet vibration tests demonstrated. The elastic segmented model was tested in the towing-tank under regular and random waves with a quite large array of sensors spanning from accelerometers, strain-gauges and fibre-optics. Load and whipping responses were extensively acquired in intact and reduced stiffness conditions.

Key words: *Scale-model testing; Variable stiffness; Structural assessment; Digital twinning; Technology Readiness Level.*

1. Introduction

Traditionally, hydro-elastic experiments in naval architecture and ocean engineering have focused on identifying loads, responses and system properties, such as modal parameters, using a wide range of laboratory-scale, large-scale, and, more recently, full-scale tests. At model scale, condensation of the ship's relevant structural properties to allow for dynamic coupling with fluid loads is constrained by fulfilling the Froude similarity law. Recently, structural monitoring on real vessels is gaining prominence due to growing attention to structural integrity and regulatory review. Nonetheless, one key issue highlighted several times by the research community is the absence of extensive research projects which investigate ship responses via a combination of full and model-scale problems, both experimentally and numerically. Recently, due to the growing attention to data-driven models, it has also emerged the attractive possibility of using digital twinning principles and methods to build hybrid models (sensor data plus numerical predictions) of real ships. In this framework, structural degradation affecting the serviceability of ship structures is assumed to produce detectable changes in the structural

* Correspondence to: daniele.dessi@cnr.it

stiffness distribution and, consequently, in the dynamic response and modal properties of the vessel [1]. In this perspective, scale-models can offer an interesting benchmark for the pipelines and computational modules to achieve a dynamic digital twin of an existing object through its lifespan evolution, often characterized by structural degradation. Thus, to verify digital twinning techniques, a new paradigm for scaled experiments has been introduced within the dTHOR project: the structural configuration itself is incrementally modified to test our capability of sensing changes in key parameters. Although this begins as a controlled demonstration, it enables raising the Technology Readiness Level of the entire technology which includes collecting heterogeneous data (encounter waves, rigid-body absolute and relative motion, deformations and accelerations) through different acquisition systems during seakeeping tests. The large set of collected data enables precise validation of hydroelasticity codes as well as the generation of hybrid models to capture the relevant physics. The present analyses and data collection have been done under the scope of the European Defence Fund (EDF) project "Digital Ship Structural Health Monitoring" (dTHOR) project (https://dthor.eu/). The objective of the dTHOR project was to develop a system based on innovative utilization of large amounts of load and response measurements from robust and advanced sensors, a digital framework complying with recognized open standards for data exchange, and hybrid analysis and modelling which combines physics-based and data-driven models, in the perspective of improving technological leadership of European navies in structural design and ship asset management.

2. Scale-model

2.1 Requirements and concept design

The objectives of the experimental campaign within the dTHOR project necessitated innovations in the physical model design, experimental setup, and testing procedures. Beyond ensuring a strong hydro-elastic correspondence between the scale model and the full-scale ship, particular attention was given to the ability to alter the structural configuration and to generate a sufficient amount of data for implementing digital twin technology on the scale model. Moreover, validating damage identification tools necessitated demonstrating that scale-model testing achieved a higher TRL compared to tests conducted separately in a laboratory "dry" environment. The test set-up was required to produce accurate and large volume data under well-documented conditions for future reusability. The latter further demanded for integrating different sensors and data collection methods on the same platform.

Several types of scaled models have been used in hydroelastic tests of ships in a model basin. According to the ITTC Recommended Procedures and Guidelines [2], the global load experiment of a ship is performed with either a 'segmented model' or a 'hydro-structural model.' Segmented and elastically scaled models of ships have been used since the fifties for different purposes, and their applications have increased in the last few decades. The 'hydro-structural model' is a scaled-down version of the actual ship structure, including hull plating. Though the hydro-structural model offers interesting opportunities to realistically reduce the stiffness to simulate local failures, grounding or ship collision, the design of the hydro-structural models is complex, and fabrication is costly and time consuming. The segmented model is divided instead into several independent segments to quantify the global load at discrete locations. The elastic segmented model is featured by a backbone or flexible connections between the segments. A more comprehensive review of the segmented model technique can be found in [3]. The metallic backbone (aluminium or steel) is essential for reproducing global ship deformation in segmented models. These construction approaches were reviewed in the perspective of introducing stiffness variations leading to adopting the segmented model approach as a more affordable way to build a scale demonstrator for the dTHOR project.

2.2 Reference ship data and scaling

The reference ship is a frigate built in the 1970s and 1980s that served in the German and Dutch navies from 1982 to 2022. A scale ratio of 1:28 was selected for the scale-model based on towing-tank constraints (carriage capacity, wave-maker limits), manufacturing feasibility, and project budget. Hydroelastic similarity was enforced by using Froude scaling for both hydrodynamic and structural

properties. Thus, the backbone beam was dimensioned to reproduce, at model scale, the global bending and torsional stiffness of the full-scale frigate. Ballast distribution was adjusted to match the mass, centre of gravity position, and inertial properties, ensuring correct rigid-body dynamics and realistic whipping behaviour. The resulting properties of the physical model that was built by INTA in Spain are provided in Table 1, while Figure 1 shows some geometric characteristics of the physical model.

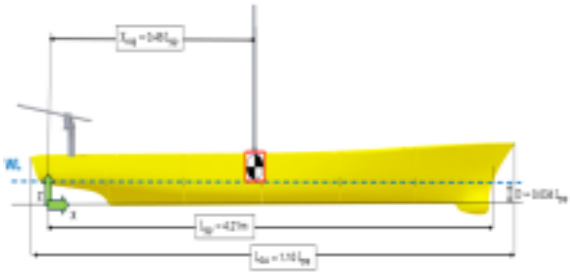


Figure 1: Scale-model basic geometric characteristics (not in scale between vertical and horizontal dimensions).

Item	Value
Length between Perpendiculars L_{pp}	4.21 m
Length overall L_{OA}	1.10 L_{pp}
Beam B	0.12 L_{pp}
Draft D	0.034 L_{pp}
Displacement	154.2 kg
Centre of Gravity longitudinal position (X_{cog})	0.48 L_{pp}

Table 1: Segmented scale-model main characteristics.

2.3 Stiffness scaling and modification devices

The horizontal and vertical bending as well as the torsional stiffness along the ship *x*-axis were condensed to a longitudinal distribution applying Finite Element Analysis (FEA) to the full-scale ship. It is worth underlining that a stiffness-similarity approach was chosen rather than a modal-frequency optimization. In the adopted approach, the equivalent sectional stiffness of ten selected portions of the full-scale ship is first evaluated from the finite element model and then scaled according to Froude similarity. The geometry of the backbone beam sections is subsequently defined to reproduce the target bending stiffness distribution along the hull. The stiffness-similarity approach ensures a physically consistent representation of the hull stiffness distribution rather than an exact reproduction of individual modal frequencies. The backbone is an aluminium hollow beam, with rectangular cross section (Figure 2), to which the legs supporting the segments are directly connected. The beam transversal sections were shaped by varying the thickness of the four sides to coherently obtain an overall beam stiffness matching the reference one. The performed vertical bending distribution is closely related to the target distribution (Figure 3) and satisfactory results were obtained also for the horizontal bending. Though relevant rotational inertia was provided by the ballast mass extending vertically above the beam and by the segments, the core beam is quite slender and the possibility of reproducing torsional stiffness was limited. Each module allows controlled symmetric or asymmetric reductions of the longitudinal bending stiffness by removing or replacing specific metallic plates on the backbone. The plates are screwed to the main beam, enabling modification and restoration of the intact configuration (Figure 4). Stiffness variations are obtained by progressively removing the cover plates shown in Figure 5 according to the sequence reported in Table 2.

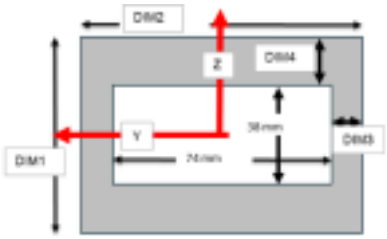


Figure 2: Hollow beam section.

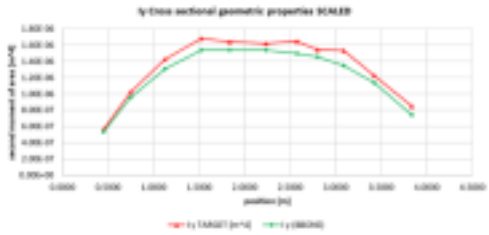


Figure 3: Vertical bending stiffness distributions.

Configurations D1-D5 correspond to increasing damage (i.e., decreasing stiffness), whereas D6 represents the return path toward the intact condition. It is important to note that the configuration numbering reflects damage severity rather than the chronological order of testing. Each label simply identifies a specific backbone configuration, independent of the experimental sequence.



(a) Undamaged condition D0 (b) Damage condition D2.

Figure 4: Backbone detail before (a) and after (b) removal of the plates.



Figure 5: Position and labels of the removable plates.

Table 2: Backbone stiffness variations.

Reduced stiffness configuration	D0	D1	D2	D3	D4	D5	D6
Removed Plate	0	1	1,2	1,2,3	1,2,3,4,5	1,2,3,4,5,6	6
Relative vert. bend. stiffness reduction [%]	0	23 %	46 %	50%	39 %	42 %	5 %
Length [mm]	--	200	200	200	200	200	200

3. Experimental set-up

3.1 Sensor equipment

As a part of a collaborative effort among dTHOR partners, the segmented model was transported to CNR-INM towing-tank in Rome for the planned experimental campaign. The scale model was then equipped with a distributed sensing network designed to directly capture encountered wave profile, rigid-body motions, global and local structural responses. From the acquired signals, additional information such as hydrodynamic loads can be derived. Table 3 lists the observed variables, sensor types, and number of measurement points. Because the total sensor count exceeded the channel capacity of any single DAQ unit, a distributed acquisition architecture was implemented. Each partner supplied acquisition hardware dedicated to specific sensor families. Synchronisation across units was ensured through electrical triggers and recorded mechanical impulses. The resulting system guarantees consistency across all time-aligned signals and enables multi-source modal and load identification.

Table 3: List of sensors installed on the physical model.

Observed variables	Sensors	N. sensors
Heave, Pitch	Optical system: Krypton Rodym DMM	1
Wave elevation	Servo type (finger) probe: Kenek SSH301N	2
Strain	Strain-gauge: HBM LY43-3-350	12
	Fibre-Bragg Grating distributed	30+30
Accelerations	Uniaxial accelerometer: PCB 333B32	11
	Triaxial accelerometer: HBK 4506-B-003	10

4. Physical model assessment and calibration

4.1 Dry static tests

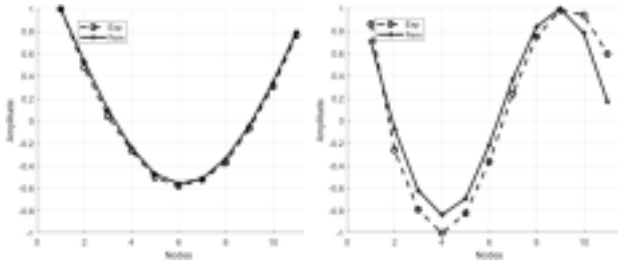
As a first step to achieve a digital twin, several structural tests were conducted to verify or update the FE model of the segmented model at the CNR-INM Laboratory of Structural Dynamics and Diagnostics. The static tests involved the bare backbone and aimed also at validating the installation and calibration of the strain measurements. The backbone was simply supported at the beam ends and loads of increasing magnitude were applied to induce reference bending moments. After zeroing the gauges, each loading step was applied and removed to verify repeatability of the measurements. The recorded values agreed with numerical predictions under linearity assumptions.

4.2 Vibration tests

The dry vibration tests focused on the assessment of the modal properties of the segmented hull in the final intact configuration. To approximate free-free boundary conditions, the model was suspended using soft springs as shown in Figure 6. Stiffness and position of the springs were selected to ensure that heave and pitch frequencies remained below one fifth of the first bending natural frequency, minimising coupling between rigid-body and elastic modes. An output-only techniques for system identification, named stochastic subspace identification (SSI), was used to extract the modal properties from the acceleration measurements. The unmeasured stochastic excitation was provided through a hammer impacting randomly on the backbone. Five vertical bending modes are experimentally identified (modes #1 and #2 are shown in Figure 7). The correlation between experimental and numerical mode shapes, the latter obtained by the FEA, is quantified using the Modal Assurance Criterion (MAC) in Figure 8, while natural frequencies are reported in Table 4. MAC values close to unity for the first and second modes indicate high fidelity of the FE model in dry conditions.



Figure 6: Dynamic vibration tests in the Lab under spring suspension.



(a) 1st mode (b) 2nd mode

Figure 7: Numerical vs. experimental (dry) vertical bending modes comparison (modes 1-2).



Figure 8: MAC between num. and exp. modes

Table 4: Dry natural frequencies.

Mode	1st mode	2nd mode	3rd mode	4th mode	5th mode
FEA [Hz]	9.78	21.3	31.5	44.1	50.1
Exp [Hz]	9.94	20.1	34.1	49.3	56.4
Diff %	1.6	5.9	7.6	10.5	11.1

In wet modal identification tests, the scale-model was mechanically connected to the carriage by the seakeeping equipment that allows heave and pitch DoFs (Figure 9). Under wave excitation, the 'wet' mode shapes were identified via SSI (modes #1 and #2 in Figure 10). The FE model was extended to account for hydrodynamic added mass via the MFLUID module in NX Nastran. The natural frequencies comparison between experimental and numerical 'wet' modes reveals higher frequency shifts if compared to dry conditions (Table 5). The 1st vertical bending mode remains almost unchanged (0.3 % deviation), whereas higher modes show noticeable reductions (up to 18 %). The MAC between FE and experimental mode shapes (Figure 11) highlights some differences for the fundamental modes due to unmodelled FSI effects or errors in identification. It is interesting to examine the correspondence between wet and dry modes by using the MAC as an indicator of the similarity between corresponding modal shapes sorted by their natural frequency (Figure 12). A strong correspondence is observed between dry and wet modes for the first two modes. The overall damping in wet conditions generally grows with the forward speed as shown in Figure 13.

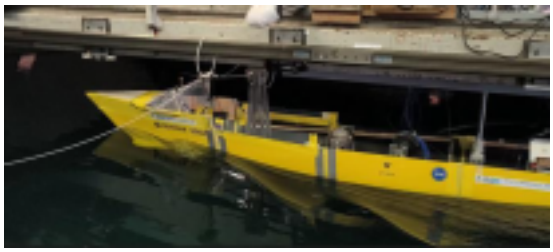


Figure 9: Side view of the segmented model during a typical test in head waves.

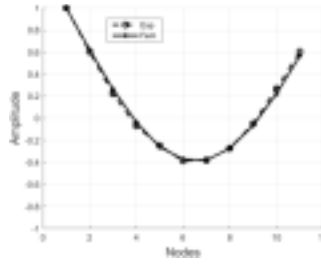


Figure 10: Num. vs. experimental 1st wet vertical bending modes comparison.

Table 5: Wet natural frequencies.

Mode	1st mode	2nd mode	3rd mode	4th mode
FEA [Hz]	7.19	14.8	23.3	32.8
Exp [Hz]	7.17	14.1	28.2	40.0
Diff %	0.3	4.9	17.3	18.0

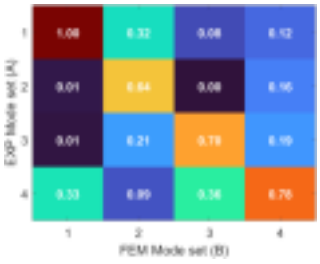


Figure 11: MAC between wet numerical and exp. modes.

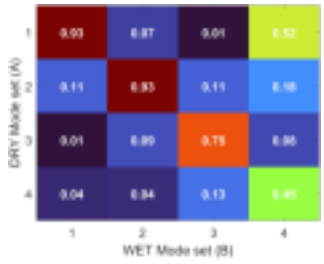


Figure 12: MAC between exp. wet and dry modes.

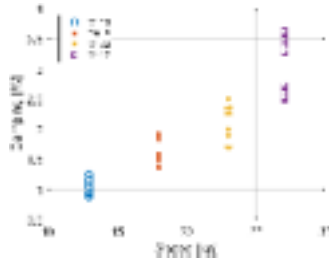


Figure 13: Damping variation with the forward speed.

5. Wave basin tests

5.1 Wave-induced loads under rigid-body assumption

The segmented model was subjected to a series of experiments in regular and irregular head-sea conditions to characterize the hydrodynamic excitation and the resulting response (rigid-body motion and elastic vibrations). Wave parameters were selected to cover a representative combination of wavelengths and amplitudes, ensuring realistic full-scale equivalents and favouring the onset of slamming and whipping events. Though not critical in present analysis, a correct representation of the

sea spectra would be beneficial for correlating wave loads and stress fatigue. In Figure 14 the Power Spectral Densities (PSDs) of the wave elevation measured by the leading-edge/front probe (cyan curve) and by the side probe (black curve) are compared. This comparison is intended to assess the consistency of the incident wave field generated in the towing tank. Indeed, both wave probes were mounted on the towing carriage and positioned sufficiently far from the ship model, so that their measurements were not significantly affected by wave radiation and diffraction associated with the wave–ship interaction. Under these conditions, the two PSDs are expected to be close to each other, with possible minor differences due to local wave-field non-uniformities, probe positioning, and measurement uncertainty. The blue curve represents instead the wave spectrum in earth-bound reference system as obtained from the front wave probe and exhibits a good correspondence with the nominal sea spectrum (purple curve). Internal loads were assessed through strain measurements gathered from both metallic strain gauges and fibre-optic sensors distributed along the backbone. Using calibrated strain–moment relationships, vertical bending moments (VBMs) and shear forces can be reconstructed along the hull girder. Thus, the non-dimensional response operators for the can be then calculated for each towing-tank run.

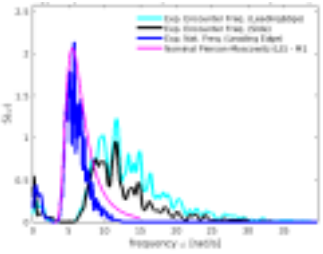


Figure 14: Nominal and measured sea spectra ($V = 18\text{kn}, H_s = 1\text{m}, T_s = 6\text{s}$).

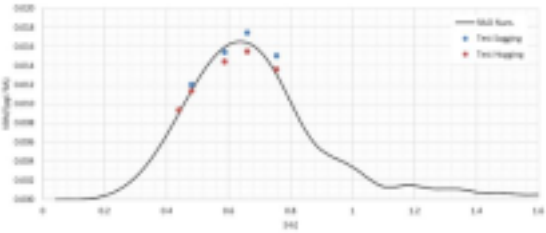


Figure 15: RAO of VBM from SECAL with respect to the encounter wave compared with regular wave tests.

The ship hydrodynamics in the frequency domain are analysed using SEACAL, which employs a three-dimensional panel method based on zero-speed Green's functions with forward-speed corrections. The hull wetted surface is discretized with a 0.046×0.046 m panel mesh to ensure accurate potential-flow calculations while balancing geometric resolution and computational cost. An example of VBM calculations in regular waves at zero speed is shown in Figure 15. Time-domain rigid-body responses are computed using PRETTI. The same three-dimensional hull mesh is extended above and below the still waterline to account for both submerged and exposed geometry. At each time step, the instantaneous wetted surface is updated through the dynamic waterline, and Froude–Krylov forces are evaluated by integrating the incident pressure over the submerged panels. In Figure 16, the blue curve shows the PSD from the PRETTI time-domain simulation, the red curve the experimental PSD, and the black curve the PSD obtained from the SEACAL RAO combined with the encountered wave spectrum. In Figure 17, dashed curves indicate exceedance distributions from PRETTI, continuous lines the experimental measurements, and the black line the Rayleigh distribution derived from the frequency-domain solution, corresponding to the FD RAO line in Figure 16.

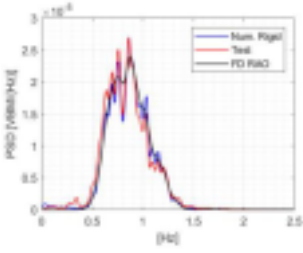


Figure 16: Comparison between RAOs obtained with time-domain solution, frequency-domain and experimental data relative to amidship ($V = 13\text{kn}$, $H_s = 3.5\text{m}$, and $T_s = 12\text{s}$)..

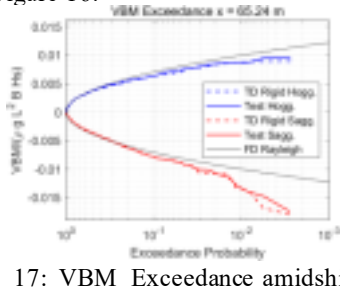


Figure 17: VBM Exceedance amidship from time-domain solution compared to experimental data and Rayleigh model ($V = 13\text{kn}$, $H_s = 3.5\text{m}$, and $T_s = 12\text{s}$)..

5.2 Wave-induced elastic response and missing data reconstruction

A preliminary analysis of the effect of ship flexibility on the VBM is conducted using Panship NL (non-linear). In this process, the hydrodynamic pressures exerted on the hull panels are transferred to the structural nodes. Subsequently, the nodal equations of motion are solved to determine displacements, velocities, and accelerations. This nodal kinematics are then fed back into the hydrodynamic model to update the panel loads. This iterative loop continues until successive iterations reveal no further changes in nodal motion, thereby indicating convergence. This initial hydro-elastic assessment is shown in Figure 18, highlighting the presence of whipping as in the recorded signal. As outlined before, strain measurements were carried out with both standard strain-gauge patches and fibre-optics. Strain-gauge time histories are shown in Figure 19. The implementation of strain measurements based on fibre-optics (FBGs with 60 measurement points, as described in Section 3.1) introduce additional possibilities both in terms of quantity and quality of data. The FBGs strain signals are processed to provide real-time displacements using a code based on the inverse finite element method (iFEM), for which a detailed formulation is available in [4]. Figure 20 illustrates the strain time history for sensor 10, which is affixed to the fibre on the upper side of the backbone, positioned 1.453m from the rear perpendicular, in relation to run #72 ($V = 13\text{kn}, H_s = 1.0\text{m}$, and $T_s = 6\text{s}$). Since this sensor is mounted on the top surface, a clear relationship between strain and vertical displacement is observed. Negative (compressive) strain corresponds to upward curvature of the backbone and therefore globally positive vertical displacements shown in Figure 21 and Figure 22. Conversely, positive (tensile) strain indicates reversing of the curvature and produces globally negative vertical displacements, shown in Figure 23 and Figure 24. These results confirm the physical consistency of the recorded strains with the vertical displacement reconstructed via iFEM. The alternating compression-tension pattern follows the generated wave frequency, confirming the accuracy of the measurement system and proper synchronization among sensors. Furthermore, this analysis helps detect possible irregularities in the response, such as asymmetric deformation or phase lags relative to the excitation, which could indicate local stiffness reduction or structural damage.

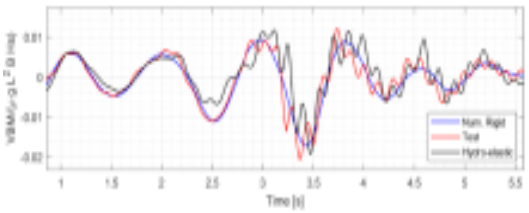


Figure 18: Comparison between experimental data and numerical solutions with and w/o ship flexibility.

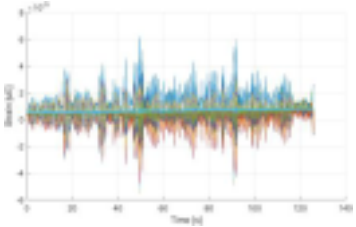


Figure 19: Strain time history for run #105 ($V = 18\text{kn}$, $H_s = 3\text{m}$, $T_s = 8\text{s}$).

Because the backbone is excited by head waves, the structural response is dominated by vertical bending with negligible torsion as clear by comparing top and side strains. In fact, top sensors record clear tensile-compressive cycles, while lateral sensors show much smaller amplitudes, often close to the noise floor. Their signals remain phase-coherent with the top measurements, consistent with symmetric excitation and minimal torsional or out-of-plane effects. The previous results address the ship response to continuous wave loading.

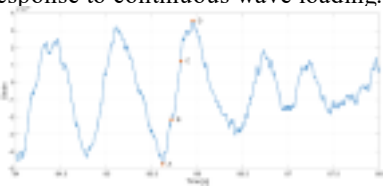


Figure 20: Strain time history for the measurement point no. 10 of the run #72 ($V = 13\text{kn}$, $H_s = 1\text{m}$, $T_s = 6\text{s}$).

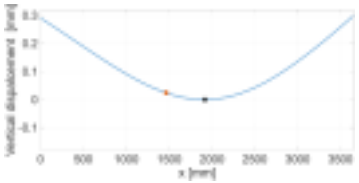


Figure 21: Displacement reconstruction of instant "A" of Figure 20.

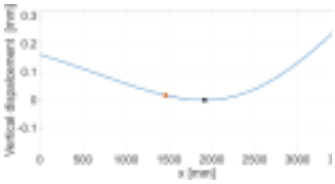


Figure 22: Displacement reconstruction of instant "B".

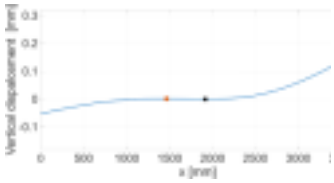


Figure 23: Displacement reconstruction of instant "C".

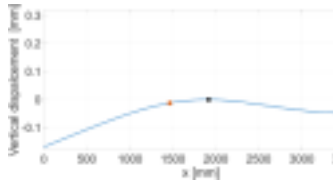


Figure 24: Displacement reconstruction of instant "D".

5.3 Whipping response and the effect of stiffness variation

A key objective of the test campaign was to investigate how longitudinal stiffness variations influence the onset and magnitude of whipping responses. For this purpose, selected "damaged" configurations were tested under identical wave conditions to isolate the effect of stiffness reduction. Figure 25 illustrates the tracking of the system's first natural frequency, as determined by applying the Stochastic Subspace Identification with Extended Unweighted Principal Component (SSI-UPCX) method to the signals from uniaxial accelerometers. The effect of the progressive reduction in beam stiffness is clearly reflected in the shifts of the first natural frequency. The different degraded configurations do not represent the same level of structural modification: configurations D4–D5 (runs #67-#77) correspond to the most severe stiffness reductions, producing the largest and most detectable frequency shifts. These configurations can be distinguished more reliably from the reference condition. Conversely, configuration D6 (runs #78-#84), obtained by removing a single lateral plate, cannot be clearly recognized. In fact, this modification has limited influence on the flexural stiffness distribution governing the vertical bending modes considered in the analysis. Consequently, the induced frequency shift is too small to separate from experimental variability and measurement uncertainty.

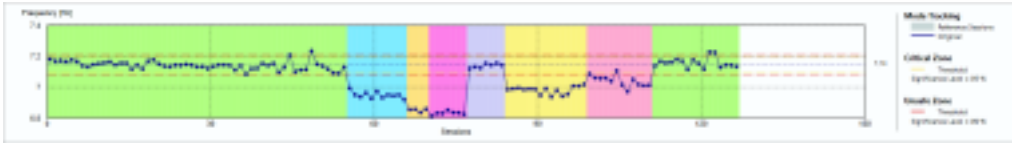


Figure 25: Mode tracking for the first vertical bending mode across multiple tests. The coloured areas refer to different damaged states, while green stands for intact.

A subsequent analysis was conducted to compare the stress response and accumulated fatigue damage at a specific strain gauge location between the intact and damaged configurations. This comparison was performed under identical sea state conditions for both structural scenarios. The sensor under examination is the strain gauge installed beneath the stern plates (SG8). The initial comparison focused on the standard deviation (STD) of the stress signal for each sea state, as illustrated in Figure 26. A subsequent comparison evaluated the accumulated fatigue damage for each sea state, utilizing a rainflow cycle counting procedure in conjunction with a stress–life (S–N) approach and the Palmgren–Miner linear damage rule (Figure 27). Both the stress STD and fatigue damage were derived from the total vibration response, combining effects of wave excitation and whipping-induced structural response. The damaged configuration consistently exhibits higher stress fluctuations and accumulated fatigue damage across all examined sea states. This behaviour suggests that the removal of the plates effectively diminishes the local stiffness of the backbone, thereby resulting in increased internal stresses.

6. TRL Evaluation

The experimental platform served as a critical testbed for assessing the Technology Readiness Level (TRL) of sensing and analytics components developed within the dTHOR project for ship-scale digital twinning. It provided a controlled yet realistic environment in which the system's ability to deliver high-fidelity data was evaluated, even when subjected to structural perturbations such as deliberate

variations in longitudinal stiffness. This capability is essential for validating digital-twin robustness under evolving structural conditions. The TRL assessment encompassed several maturity dimensions. First, the evaluation of Sensor and Hardware Maturity confirmed that key components, including multiple data acquisition (DAQ) units, accelerometers, and strain gauges, achieved TRL 4. These devices were successfully integrated and tested in non-operational laboratory settings, demonstrating stable measurements and hardware robustness. Second, Data Acquisition and Integration maturity was quantified through the Integration Readiness Level (IRL) framework. The platform validated end-to-end data flow, synchronization, and logging across heterogeneous subsystems. Several critical interfaces reached IRL 7–8 following successful real-world data transfer, indicating reliable integration performance under representative testing conditions. Finally, the overall System Readiness Level (SRL) was calculated at approximately 0.346, placing the platform within the Technology Development phase (TRL 4-5). At this stage, component compatibility has been characterized, and baseline system performance has been defined. These findings confirm that the experimental backbone demonstrator offers a realistic, scalable environment for validating digital-twin technologies. By effectively tracking structural modifications, it establishes the foundation for progression toward TRL 6, where integrated subsystems will be validated at pilot scale under representative operational conditions.

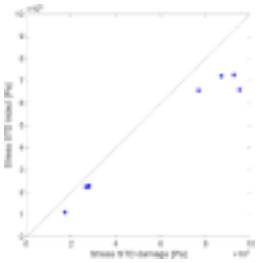


Figure 26: Comparison of stress STD on SG8 between intact and damaged configurations.

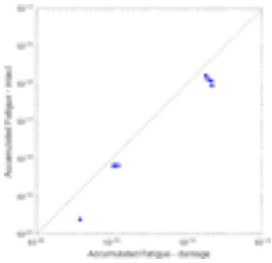


Figure 27: Comparison of accumulated fatigue on SG8 between intact and damaged configurations.

7. Conclusions

The integration of modern sensor technology with advanced signal processing facilitates the generation of high-quality, extensive datasets, elucidating complex fluid-structure interactions and advancing data-driven or hybrid models in the field of hydroelasticity. The concept of elastic physical models incorporating components with adjustable stiffness offers a novel approach to further exploring more complex issues, such as the progressive collapse of ships under significant fluid-structure coupling.

Acknowledgements

The authors acknowledge the support of the dTHOR project that has received funding from the European Defence Fund (EDF) under Grant agreement 101103257-dTHOR-EDF-2021-NAVAL-R-2.

References

[1] Y. Zhang, J. Guo, Y. Xie and J. Xu, *Warship damage identification using mode curvature shapes method*, Applied Ocean Research 152, 2022.
[2] ITTC – Recommended Procedures and Guidelines, 2017, 7.5-02-07-02.6, Global Loads Seakeeping Procedure.
[3] D. Dessi et al. *ISSC Report of the Technical Committee V.2: Experimental Methods*. 20th International Ship and Offshore Structure Congress, P. Rigo and M. Kaminski editor, 2018.
[4] A. Kefal, I. Emami, M. Yildiz, A. Tessler, *A smoothed iFEM approach for efficient shape-sensing applications*, Numerical and experimental validation on composite structures. Mech. Syst. Signal Process. 152, 107486, 2021.

Slamming Problems

10th International Conference on HYDROELASTICITY IN MARINE TECHNOLOGY
Trondheim, Norway, June 16th-18th, 2026

Decomposition of Structural Response to Slamming Loads Based on Rigid Body Motions

Ying-xu Ma[1], Zhe Sun[2*], A. Korobkin[3] and T. Khabakhpasheva[4]

[1]Dalian University of Technology (mayingxu@mail.dlut.edu.cn)
[2]Dalian University of Technology (zsun@dlut.edu.cn)
[3]University of East Anglia, UK (a.korobkin@uea.ac.uk)
[4]University of East Anglia, UK (t.khabakhpasheva@ uea.ac.uk)

Abstract. The slamming force decomposition model, originally developed for rigid bodies, is extended in this study to flexible structures. Within the rigid-body framework, the total vertical slamming force in both two- and three-dimensional water-entry problems can be represented as the sum of three contributions: a velocity-dependent term, an acceleration-dependent term, and a gravity-related term, with the corresponding coefficients depending solely on the instantaneous penetration depth. This force-decomposition model has been previously validated by the authors. To investigate a similar decomposition framework for elastic responses, a numerical model based on Modified Logvinovich Model and superposition theory is used to simulate the water-entry slamming of elastic wedge. Numerical simulations are conducted for ranges of constant entry velocities and deadrise angles to determine the corresponding stress distributions. The relationships between the elastic stresses and the rigid-body motion parameters are established and analyzed. The results show that, for constant entry velocity, the structural stress—at least up to its peak value—scales with the square of the entry velocity, in agreement with the rigid-body slamming force decomposition theory.

Key words: *slamming; decomposition; elastic structure; FSI*

1 Introduction

When ships and offshore structures navigate or operate in waves, their sections may experience violent slamming, generating extremely high transient loads that pose a serious threat to structural integrity. Therefore, accurately and efficiently predicting slamming loads and structural responses is one of the critical issues in naval architecture. For rigid structures, slamming problems have been extensively studied. Von Kármán [1] and Wagner [2] established the theoretical foundation, followed by the development of a series of semi-analytical models such as the Modified Logvinovich Model (MLM) [3] and the Generalized Wagner Model (GWM) [4], significantly enhancing the ability to handle complex geometries and flow nonlinearities. Notably, Korobkin et al. [5] proposed a force decomposition theory that breaks down the total impact force into the sum of velocity-squared coefficients and acceleration coefficients, both solely dependent on penetration depth. This approach enables rapid prediction of impact forces for arbitrary motion histories, effectively reducing computational costs in direct numerical simulations. Subsequently, Seng [6] observed that force decomposition methods often fail when objects move at low velocities. Sun et al. [7] further refined the original impact force decomposition model by incorporating a gravity term. Recent studies have demonstrated that the hydrodynamic pressure at a given point on the structural surface admits a similar decomposition.

* Correspondence to: zsun@dlut.edu.cn

However, real structures exhibit elasticity, leading to strong coupling between hydrodynamic loads and structural deformation—known as hydroelastic effects. This causes the dynamic stress response within the structure to potentially differ significantly from predictions based on rigid-body assumptions. Currently, stress response prediction for hydroelastic impact relies primarily on fully coupled Computational Fluid Dynamics (CFD) and Finite Element Method (FEM) approaches. While highly accurate, these methods consume substantial computational resources, making them impractical for rapid evaluation and parameter optimization during early design stages. In recent years, MLM has been increasingly applied to elastic structure immersion analysis. Sun et al. [8] further combined MLM with the modal superposition method to establish a semi-analytical coupled model for two-dimensional symmetric elastic body immersion. Results indicate that MLM outperforms the traditional Wagner model in predicting impact deflection and stress in the partially wetted stage of elastic structure water entry.

Nevertheless, a systematic framework for predicting stress responses in elastic bodies—analogous to the efficient force decomposition theory for rigid bodies—remains unexplored. It is worth noting that existing studies on slamming stress scaling are mostly scenario-specific, with conclusions linked to their respective fluid-structure interaction mechanisms. For wave impact on horizontal elastic plates, Faltinsen et al. [9] and Korobkin & Khabakhpasheva [10] reported a linear stress-velocity relationship, attributed to plate-liquid energy equilibrium during penetration. However, few studies have focused on high-speed constant vertical water entry of elastic wedges where inertial effects dominate. Therefore, the stress characteristics under this condition still require further exploration.

This paper therefore proposes an innovative analytical framework extending the core principles of rigid-body impact force decomposition to predict stress responses in elastic structures. By integrating the efficient MLM hydroelastic analysis with the modal superposition method, this study seeks to establish explicit quantitative relationships between internal structural stresses and entry motion parameters as well as structural modal characteristics. This ultimately forms a decomposition model capable of rapidly forecasting impact stresses in elastic structures in the partially wetted stage.

2 Theoretical Fundamentals

2.1 Coupled Model for Hydroelastic Slamming Analysis

This study employs the two-dimensional water-elastic impact semi-analytical method developed by Sun et al. [8] This method couples the Modified Logvinovich Model (MLM) hydrodynamic solver with a structural dynamics solver based on the modal superposition method through an iterative coupling procedure, thereby achieving a balance between computational efficiency and accuracy. It is suitable for analyzing the transient response of a symmetric elastic body undergoing vertical water impact.

2.1.1 MLM Hydrodynamic Model

The MLM model serves as the hydrodynamic core of hydroelastic slamming analysis. It solves the nonlinear hydrodynamic equations to obtain the pressure distribution on the structural surface, with its core advantage lying in the consideration of the feedback effect of elastic deflection on hydrodynamic loads. This approach enables an accurate representation of fluid–structure interaction (FSI), with the MLM yielding more reliable predictions of impact deflection and structural stress than the traditional Wagner model [8]. Notably, the MLM framework is only valid for the partially wetted stage of elastic

wedge water entry and fails to capture the hydroelastic response characteristics of the fully wetted stage [8,11]. For some impact conditions, the maximum stress may occur after the wedge is fully wetted, where the hydrodynamic load mechanism shifts from nonlinear free surface effects to resonant loads on the fully wetted structure, and MLM is no longer applicable [11].

2.1.2 Mode Superposition Method for Structural Response

The elastic deformation of the structure is described using the mode superposition method, which decomposes the complex dynamic deflection field of a structure into a linear combination of the natural dry modes of the structure. This method greatly simplifies the solution process of structural dynamics problems.

The coordinate x denotes the position along the inclined plane of the elastic wedge, with x=0 located at the fixed vertex of the wedge and x=L at the free distal end, where L is the length of the wedge beam. The positive direction of x points from the fixed vertex to the free end.

The instantaneous deflection field $w(\boldsymbol{x}, t)$, obtained from three-dimensional numerical simulations or experiments, is expressed as a linear superposition of the first N natural modes $\Phi_i(\boldsymbol{x})$ of the structure:

$$w(x,t) \approx \sum_{i=1}^{N} q_i(t)\ \phi_i(x) \tag{1}$$

where $q_i(t)$ is the modal coefficient (or generalized coordinate) of the i-th mode at time t, which directly reflects the contribution of this mode to the current structural deformation. The mode shapes $\Phi_i(\boldsymbol{x})$ are known for simple beam structures.

2.1.3 Solution Strategy for Fluid-Structure Interaction

The FSI solution in this study is based on a partitioned coupling strategy with prediction-correction iteration, and combines the Newmark implicit time integration method to achieve step-by-step solution in the time domain. The details of the coupling can be found in our previous work [8].

2.2 Slamming Force Decomposition Model

2.2.1 Slamming Force Decomposition Model for Rigid body

The core of the slamming force decomposition model is to decompose the vertical slamming force acting on a body during water entry into three components: a velocity-related term, an acceleration-related term, and a gravity-related term that cannot be neglected at low speeds. The three coefficients $F_V(H)$, $F_W(H)$ and $F_G(H)$ are all solely dependent on the body shape and the dimensionless penetration depth H ($H = h/X_h$, where h is the actual penetration depth and X_h is the characteristic length of the body), and are independent of the motions [8].

For both two- and three-dimensional slamming problems, the vertical slamming force acting on the body at any instant can be expressed as:

$$F = \rho v^2 X_h F_V\left(H\right) + \rho a X_h^2 F_W\left(H\right) + \rho g X_h^2 F_G\left(H\right) \tag{2}$$

where ρ is the fluid density; v is the falling velocity of the body; $a = \frac{dv}{dt}$ is the acceleration of the body; X_h represents the characteristic length of the body, which is taken as the vertical dimension of the body in this study.

For a body with a specified shape, the slamming force coefficients $F_V(H)$, $F_W(H)$ and $F_G(H)$ can be pre-determined via numerical simulation or experimental methods. Subsequently, for a given body, once the time history of its motion is prescribed, the vertical slamming force acting on the body during water entry can be rapidly evaluated using Eqn. (2), without solving the full transient flow field through complex nonlinear models. This method transforms the complex slamming problem into a coefficient analysis problem, which greatly improves the efficiency of slamming force prediction for bodies under various complex water entry conditions.

2.2.2 Hypothesis of Elastic Slamming Stress Decomposition

Based on the rigid-body formulation in section 2.2.1, it is conjectured that the stress of elastic structures during high-speed water entry follows a similar decomposition law. In this paper, we start from a simplified yet more important scenario, i.e. the slamming with constant entry velocity. Therefore, the influences of the acceleration term and the gravity term are neglected, and the following formula is assumed:

$$\sigma = \rho v^2 X_h S_V(H) \tag{3}$$

In this equation, $S_V(H)$ represents the dimensionless stress decomposition coefficient.It is assumed to depend only on the body shape and the dimensionless penetration depth H , being independent of the entry velocity v.

To verify the rationality of this hypothesis, the slamming coefficients $S_V(H)$ at different velocities are extracted under different entry velocities, and their variations with velocity and penetration depth are analyzed in detail. It is important to clarify that this quadratic relationship between stress and entry velocity only applies to the high-speed constant vertical water entry of elastic wedges, within the partially wetted stage where the MLM model is valid.

3 Geometric Model and Computation Parameters

To systematically separate and quantify the influence of motion parameters on structural stress responses, this study takes the validated model of Sun[8], i.e. elastic wedge as research object. A schematic diagram of the wedge structure and the midpoint of the beam is shown in Fig. 1. and the key parameters are listed in Table 1.

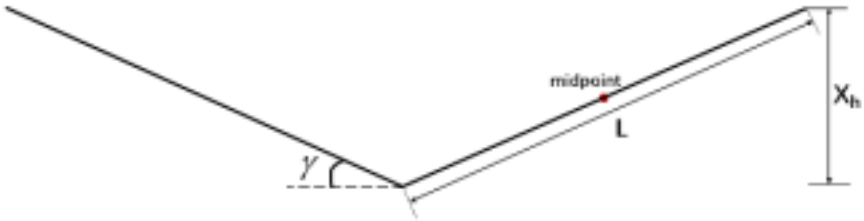


Fig. 1 Sketch of the wedge and the midpoint position of the beam

Table 1 Geometric and Material Parameters of the Wedge Structure

Parameter	Value
Wedge rise angle γ	22°,10°
Beam length (along the inclined plane) L	0.13 m
Plate thickness h	0.018 m
Boundary condition	Cantilever beam (wedge vertex fixed, distal end free)
Material	Aluminum
Youngs modulus E	6.89×10^{10} Pa
Material density ρ_s	2700 kg/m³

As mentioned before, this study focuses on the influence of water entry velocity on the structural stress response during slamming under constant entry velocity. A total of 7 velocity values are set in this study with a velocity gradient of 1 m/s. The specific velocity values are 4 m/s, 5 m/s… 10 m/s in sequence. The velocity magnitude falls into the high-speed water entry range, so the gravity effect can be neglected.

To ensure the study focuses on the partially wetted stage valid for the MLM model, the present work deliberately avoids impact conditions where the maximum stress occurs after full wetting, thereby ensuring that the maximum stress in the wedge is generated within the intended scope of this study [11].

4 Results and Discussions

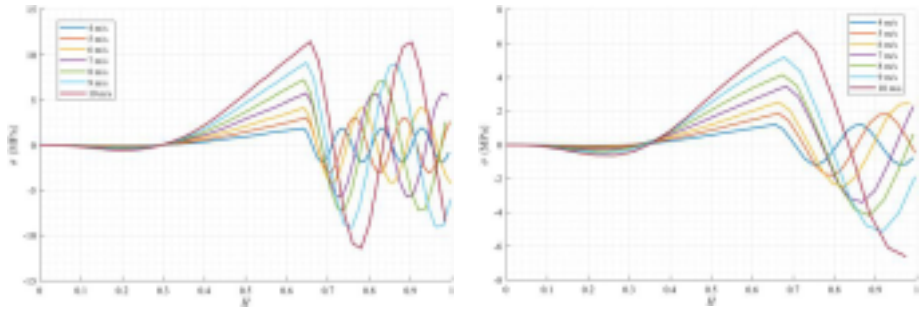
4.1 Stress-peak and velocity correlation analysis

To reveal the intrinsic correlation between structural slamming stress and water entry velocity, two models with different deadrise angles are taken as the research objects in this section. The stress peaks at the beam midpoint under each uniform velocity water entry condition are extracted to conduct a stress-peak and velocity correlation analysis.

The stress-penetration depth curves under different velocities are compared in Fig. 2, with the corresponding peak values presented in Fig. 3. The stress peaks at the beam midpoint under different velocities were fitted. In the Fig.3., blue circles denote the peak stress values under different velocity conditions, and the red lines represent the quadratic fitting curves based on the relationship between these peak values and velocity. For both models with different rise angles, the slamming stress peaks increase with the increase of water entry velocity, and the data points are highly consistent with the quadratic relationship:

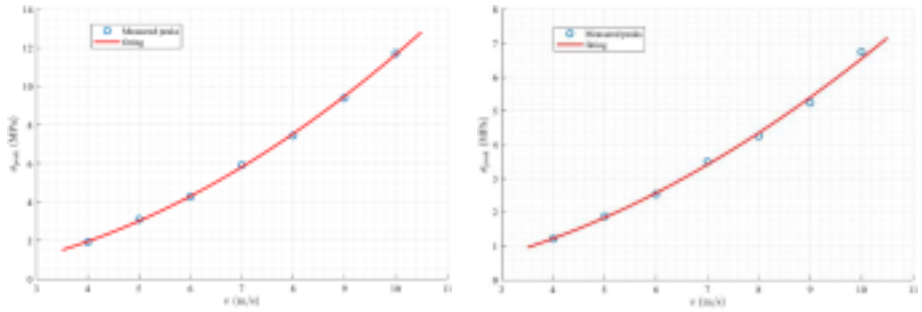
$$\sigma \propto v^2 \tag{4}$$

More specifically, the fitted velocity exponents k are 1.9524 and 1.83 for the wedge with deadrise angle of 22° and 10° respectively, which are very close to the hypothesis value of 2.0, with the coefficient of determination R^2 both greater than 0.99. This proves that the slamming stress peak is approximately proportional to the square of the water entry velocity, which is consistent with the hypothesis in Eqn. (3).



(a) $\gamma = 22^\circ$ (b) $\gamma = 10^\circ$

Fig. 2 Comparison of stress-penetration depth curves at the beam midpoint under different velocities



(a) $\gamma = 22^\circ$ (b) $\gamma = 10^\circ$

Fig. 3 Fitting curves of stress peaks at the beam midpoint under different velocities

4.2 The Discussion of Stress Decomposition Coefficient $S_V(H)$

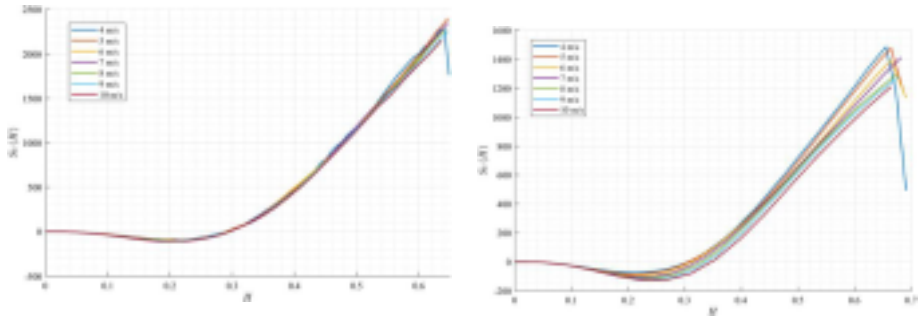
Based on the velocity-squared effect, the stress decomposition hypothesis theory in Eqn. (3), the stress decomposition coefficient can be calculated as follows:

$$S_V(H) = \frac{\sigma}{\rho v^2 X_h} \tag{5}$$

For the two models with different rise angles, the $S_V(H)$ corresponding to multiple velocity curves are extracted and compared respectively in Fig. 4. As described in Section 2.2.2, the stress decomposition coefficient $S_V(H)$ is a dimensionless function that depends only on the body geometry and the dimensionless penetration depth H, and is independent of the entry velocity. Since the deadrise angle is the key parameter determining the geometric characteristics of a wedge, the $S_V(H)$ curves corresponding to different deadrise angles differ significantly and must be determined separately for each specific deadrise angle.

The results show that for the same model at the same penetration depth, $S_V(H)$ is basically independent of velocity and is only a function of H. The above phenomenon fully indicates that the stress decomposition formula is valid under high uniform velocity water entry conditions.

It has to be noted that, as shown in Fig. 2, the features of the stress after the peak is rather complicated and its dependency on velocity seems not to be as simple as Eqn. (3). This is beyond the scope of this work and the research of the decomposition after the peak is planned in the future.



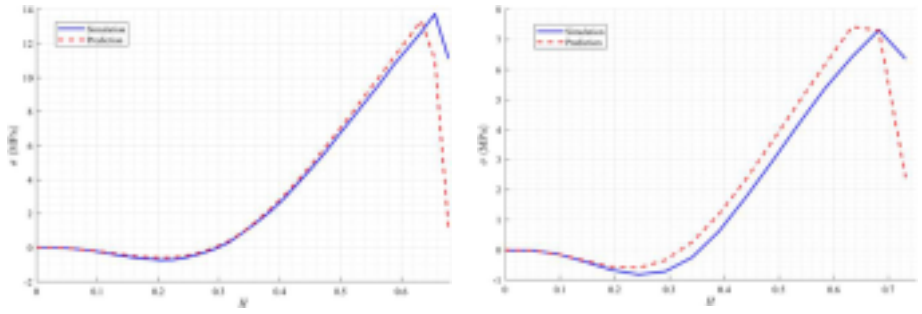
(a) $\gamma = 22^\circ$ (b) $\gamma = 10^\circ$

Fig. 4 Comparison of S_V-penetration depth curves under different velocities

4.3 Stress Prediction Based on Decomposition Theory

Using the obtained universal stress decomposition coefficient $S_V(H)$, the slamming stress is predicted for a new velocity condition (v=12 m/s) that is not involved in the fitting in Fig. 5. A comparison between the predicted stress curve and the direct numerical simulation results shows that the two curves are highly consistent, with the relative errors of the peaks being 2.84% and 1.55%, respectively. This proves that the stress decomposition coefficient $S_V(H)$ has working condition universality: the slamming stress history of the same model under any velocity can be predicted rapidly and accurately by obtaining $S_V(H)$ from only one set of working conditions.

This preliminary results indicate that the proposed prediction method can potentially be used for the rapid evaluation of water entry slamming strength for different ship types/structural forms, significantly reducing the cost of repetitive numerical calculations. It should be emphasized that the present prediction is only valid within the partially wetted stage where the MLM model applies.



(a) $\gamma = 22^\circ$ (b) $\gamma = 10^\circ$

Fig. 5 Comparison between predicted stress and numerical simulation results

5 Conclusions

This paper extends the classical rigid body slamming force decomposition theory to elastic structures and constructs a hydroelastic slamming stress decomposition model. It is found that under constant velocity water entry condition, the slamming stress of elastic structures is proportional to the square of entry velocity. This proportionality coefficient $S_V(H)$ is only a function of the dimensionless penetration depth H and is independent of the water entry velocity.

To verify the proposed theory, the elastic wedge slamming scenario was simulated by a combined MLM-mode superposition model. Based on the precomputed stress decomposition coefficient $S_V(H)$, the slamming stress of a new velocity condition is predicted, and the results are highly consistent. It has to be noted that the current research only covers the range before the stress peak, and dynamics after the peak value is more complicated and is planned to be investigated in the future.

The stress decomposition model established in this paper is potentially useful for rapid prediction of slamming stress for the same structural model. This method provides a novel and efficient analytical approach for the rapid assessment of slamming strength and the optimization of structural design parameters in the field of naval architecture and ocean engineering.

Funding: This research was funded by China National Defense Basic Scientific Research Program grant number 2024206B040.

References

[1] T. Von Karman, *The impact on seaplane floats during landing*, National Advisory Committee for Aeronautics, Washington D.C., 1929.
[2] H. Wagner, *Phenomena associated with impacts and sliding on liquid surfaces*, Zeitschrift für Angewandte Mathematik und Mechanik, 12(4): 193-215, 1932.
[3] G.V. Logvinovich, *Hydrodynamics of flows with free boundaries*, Naukova Dumka, Kiev, 1969.
[4] R. Zhao, O.M. Faltinsen, J.V. Aarsnes. *Water entry of arbitrary two-dimensional sections with and without flow separation*, Journal of Ship Research, 40(3): 208-220, 1996.
[5] A.V. Korobkin, T.A. Khabakhpasheva, S. Malenica, et al., *A comparison study of water impact and water exit models*, International Journal of Naval Architecture and Ocean Engineering, 6(4): 1182-1196, 2014.
[6] S. Seng, *Slamming and whipping analysis of ships*, Technical University of Denmark, Lyngby, 2012.
[7] Z. Sun, X. Sui, A.V. Korobkin, et al., *Slamming force decomposition with gravity effect*, Journal of Fluids and Structures, 114: 103694, 2022.
[8] Z. Sun, A.V. Korobkin, X.P. Sui, et al., *A semi-analytical model of hydroelastic slamming*, Journal of Fluids and Structures, 101: 103200, 2021.
[9] T.I. Khabakhpasheva, A.A. Korobkin, *Regular wave impact onto an elastic plate*, Journal of Engineering Mathematics, 55(2): 127-150,2006.
[10] T.I. Khabakhpasheva, A.A. Korobkin, *Elastic wedge impact onto a liquid surface: Wagner's solution and approximate models*, Journal of Fluids and Structures, 36: 32-49, 2013.
[11] O.M. Faltinsen, J. Kvålsvold, J.V. Aarsnes, *Wave impact on a horizontal elastic plate*, Journal of Marine Science and Technology, 2(2): 87-100, 1997.

10th International Conference on HYDROELASTICITY IN MARINE TECHNOLOGY
Trondheim, Norway, June 16th-18th, 2026

From hydroelasticity to hydro-elastoplasticity and hydroplasticity of structural responses subjected to extreme water impacts

Yu, Z.[1*] and Fimreite, S.B.[1]

[1] Department of Marine Technology, Norwegian University of Science and Technology, Trondheim, Norway (zhaolong.yu@ntnu.no)

Abstract. Extreme water impacts can occur for ocean structures subjected to extreme waves as well as aeronautical vehicles during emergency water landing. The problem involves complicated fluid structure interaction (FSI) effects between fluid flow pressures and structural responses. The structural responses are, however, not limited to elastic responses, but can potentially induce elastoplastic responses or even large plastic structural damage in extreme cases. The FSI effects in such extreme conditions are termed as hydro-elastoplasticity and hydroplasticity, the mechanisms of which are not well understood. This paper summarizes recent progresses in hydroplastic/hydro-elastoplastic slamming and shows the potential that a complete hydro-elastoplastic slamming model may become an alternative to the current pressure based approach widely used in the industry, which is often overly conservative. The need for significant research efforts in this area is highlighted.

Key words: *extreme water slamming; hydroplasticity; hydro-elastoplasticity; structural design; fluid structure interactions*

1. Introduction

Studies on slamming and water impact problems have been lasting for about one century since the pioneering work of von Karman and Wagner. In the late 1920s, von Karman [1] presented the first analytical work for 2D rigid wedges entering calm water when studying problems related to water landing of seaplanes based on potential flow theory assuming incompressible, inviscid and irrotational fluid flow. The model was later generalized by Wagner [2] to account for the local uprise of water. A number of follow-up water impact studies and design approaches since then have used the rigid body assumption that the hydrodynamic loading is the same as if the structures were rigid.

It was realized in the 1970s that the rigid body assumption will be inaccurate in many cases and water impact loads can be strongly influenced by structural deformations both globally and locally. The term 'hydroelasticity' was created to describe the FSI effects during water impacts in the sense that (1) hydrodynamic loads induce structural elastic vibrations, and (2) structural vibrations in return affect the hydrodynamic loads through causing a fluid flow with a pressure field. Faltinsen [3] showed that structures could be considered as rigid for the hydrodynamic problem if the ratio of the wetting time and structural natural period, is large. The structural responses can then be estimated by a quasi-static approach. When the wetting time becomes small or comparable to the structural natural period, hydroelastic effects matter and the rigid body assumption is inaccurate. Hydroelastic response of structures (notably flat panels and wedges) under water impacts has been studied extensively in the past several decades e.g. Kvalsvold and Faltinsen [4], Korobkin et al. [5] and Faltinsen [6]. Hydroelastic theories generally consider the structural responses as the sum of a series of structural vibration modes and the hydrodynamic pressure acting on the structures depends on structural vibrations as well as rigid body motions. This will give a coupled formulation. A good overview of rigid body and hydroelastic water impact is given in Abrate [7] and Faltinsen [8].

In events of more extreme water impacts, large deformations with plastic deformations can occur. The coupling effects between hydrodynamics and large elastoplastic/fully plastic structural deformations are termed as hydro-elastoplasticity and hydroplasticity, respectively, and have not been well studied and understood. A good example of a hydro-elastoplastic slamming event is the tragic incident that occurred on the offshore drilling rig COSL Innovator in the North Sea in 2015 [9]. A steep

* Correspondence to: zhaolong.yu@ntnu.no

horizontal wave struck the unit on the front bulkhead of the living quarter (see Fig. 1a). Water intrusion caused extensive damage to the cabins. One crew member was killed and four were injured. Similar accidents have been recorded for the maritime sector with slamming events leading to injuries, failure of superstructures and wet deck damage of catamarans (see Fig.1b). Light weight structures made of e.g., aluminum and composites are increasingly used, and they are especially vulnerable to extreme water impacts compared with steel structures. In the aeronautical industry, the impact on water of aeronautical structures is of concern as soon as an aircraft is designed to operate over sea. According to reviews documented in [10], over 24% of the world helicopter accidents occurred on water. Statistics [11] available for helicopters operating in the offshore industry in UK stated that approximately 90,000 hours were flown each year. Between 1976 and 2004, 12 fatal accidents associated with offshore operations occurred claiming a total of 118 lives. Fig. 1(c) and (d) shows the drop test of a full-scale WG30 helicopter and the associated damage.

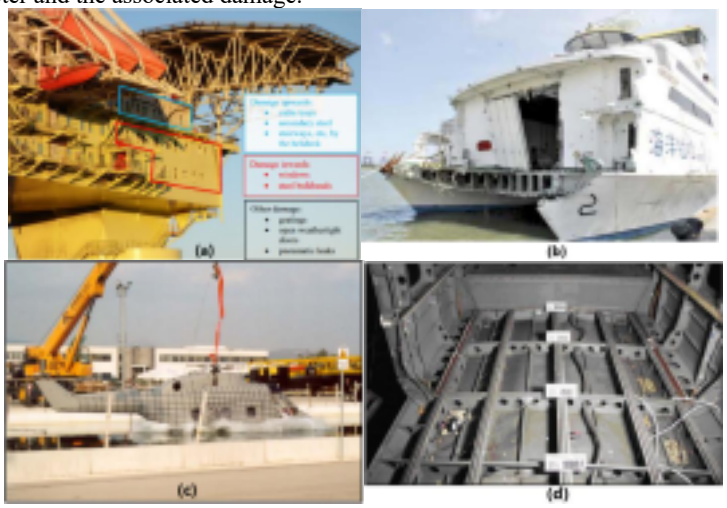


Figure. 1: (a). Damaged region of the COSL Innovator accident in 2015 [9] (b). Damage sustained by Ocean LaLa following an extreme wet-deck slamming event on 9th August 2010 [12]. (c) and (d). The CAST project with drop of a full-scale WG30 helicopter that was out of service, at a measured velocity of 7.95 m/s and the resulting damage [13]. (e) and (f). The CAST project with drop of subfloor components from a full-scale WG30 helicopter at a measured velocity of 8 m/s and the resulting damage [14].

Studies on the extreme water impact responses of structures with elasoplastic responses were mostly through experiments [13] and numerical simulations, e.g. CFD [15], SPH [16] and ALE [17]. Fundamental understanding of the hydroelastoplastic/hydroplastic interactions between hydrodynamic pressures and large elastoplastic responses of structures remains limited. This paper summarizes recent developments of the hydro-elastoplastic/hydroplastic theories for the extreme water impact events and highlights the needs for significant efforts for future research in this area. In addition, gaps between hydroelastic theories and practical needs for structural design against slamming are pointed out. The potential of a complete hydro-elastoplastic approach is indicated as a more accurate and reliable alternative to the current pressure-based industry design practice.

2. Hydroplastic response models in extreme water impacts

The hydroplastic theory assumes the structural elastic energy to be small compared to the plastic energy such that all the kinetic energy should be dissipated by plastic deformations. The hydroplastic models for water impact problems are generally developed by coupling hydrodynamic pressures from the potential flow theory and rigid plastic solutions for structures. Rigid plastic solutions are widely used for structural responses under quasi-static loads (e.g. ship collisions [18] or dropped objects) and transient loads (e.g. explosions [19]). More details on the rigid plastic solutions for beams and plates can be found in books of [20, 21].

In 2019, Yu et al [22] made a first attempt to derive a coupled hydroplastic solution for extreme water impact damage of beams and stiffened panels in 2D conditions. The model was verified to be of good accuracy by comparison with ALE simulations in [17]. In 2020, Abrahamsen et al. [23] derived a hydroplastic response model for thin plates in 3D conditions, and the model was validated to be of good accuracy with drop test results. The above two models are the existing hydroplastic models in the literature as far as the authors are aware of, and will be reviewed in some detail. Both models were derived for flat water entry of structures with instantaneous wetting, which are considered critical for structural design.

2.1 Hydroplastic model by Yu et al [22] for plates and stiffened panels

The hydro-plastic model by Yu et al [22] was formulated for plate strips and one-bay stiffened panel in 2D conditions as shown in Fig. 2. Flat or virtually flat water impacts were considered. For the considered flat water impacts, structural responses were categorized into two phases, i.e. the structural inertia phase (also called the acoustic phase) and the free deflection phase. In the structural inertia phase, the structure was subjected to intensive pressure impulses that are characterized by large pressure peaks and very short durations. At the end of the structural inertia phase, the structure was assumed to be imparted a beam averaged deflection velocity equal to the initial drop velocity. The duration of this phase was, however, too short for the structure to build up any visible deflection.

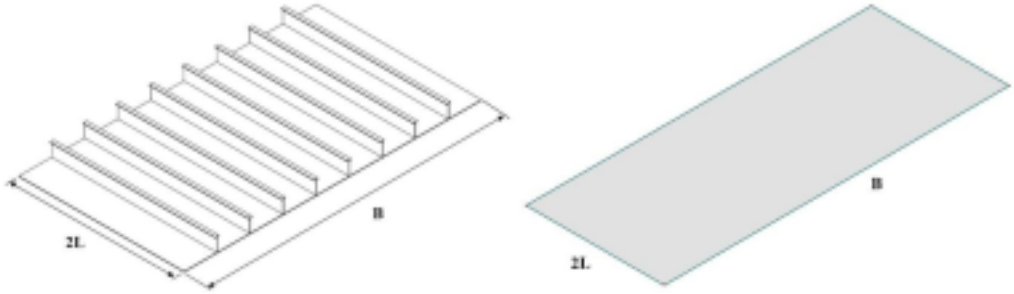


Figure. 2. (left) stiffened panels and (right) plates

In the free deflection phase, the structure would deform under the initial deflection velocity and undergo three possible deformation modes following rigid plastic theories as shown in Fig. 3. The deformation modes are considerably different from elastic analysis. For a given beam, it is stated that when the acting pressure $\boldsymbol{p}$ is larger than three times the value of static structural collapse pressure in bending $\boldsymbol{p_c}$, i.e., $\boldsymbol{p/p_c>3}$, plastic hinges will not form in the beam midspan as in a static collapse, but somewhere in between the end and the middle of the beam. The hinges will travel towards the middle of the beam over time and merge. During the deflection, the beam bending moment and axial membrane force interact through the interaction curves based on generalized forces.

During the deformations, significant coupling exists between large plastic deflection and the water pressure, denoted as hydroplasticity. With the assumed structural deflection modes, the hydrodynamic pressure was calculated using the potential flow theory by solving for the velocity potential in Fig. 4. In stage 2 and 3, water pressure acted as an added mass effect and pushed the decelerating structure to deform. For stage 1, apart from an added-mass term, an additional pressure term exists related to the time change of added masses, which results from the moving hinges leading to a time change of structural modes. By equating the rate of change of internal and external work, the governing motion equations were obtained and solved numerically.

Results from the hydro-plastic model by Yu et al [22] showed a dominant nondimensional parameter, i.e. the nondimensional velocity $V_{nd} = V_0\sqrt{\dfrac{\rho L^3}{M_0 h/b}}$ that governed the structural damage as shown in Fig. 5. V_0 is the initial water impact velocity, ρ is the water density and $2L, b, h$ are the length, width and height of the beam, respectively. M_0 is the fully plastic bending moment for the beam cross section.

From Fig. 5, nondimensional permanent deflections vary virtually linearly with nondimensional velocities for plates but the relationship is quite nonlinear for stiffened panels.

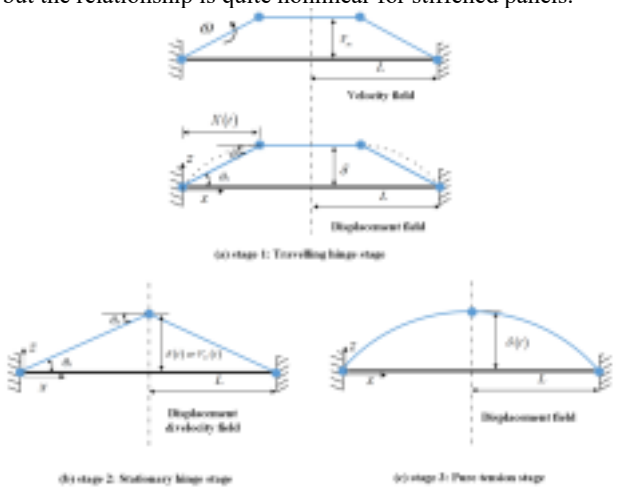


Figure. 3. Deformation modes of a beam during extreme water impacts (Yu et al [22])

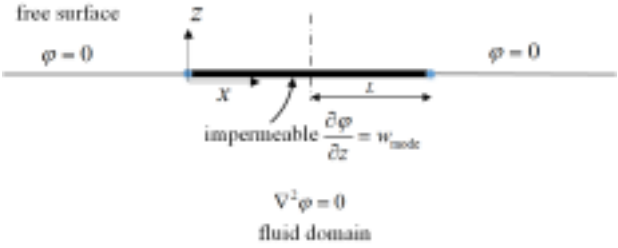


Figure. 4. Boundary value problem for the velocity potential φ (Yu et al [22])

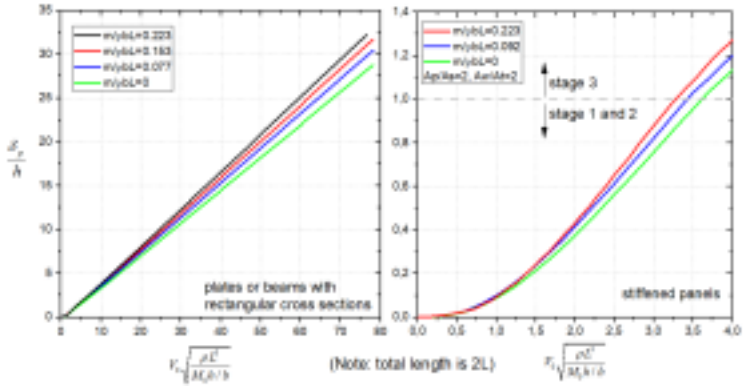


Figure. 5. Nondimensional permanent deflections versus nondimensional velocities for (left) plates and (right) stiffened panels (Yu et al [22])

The hydroplastic theories was verified by comparison with ALE simulations [17] as shown in Fig. 6(a) for the T2 stiffened panel cross section and test results [24]. Dimensions of the T2 stiffened panel are given in Fig. 6(a) with the same plate thickness of 10 mm for the plate flange, web and the top flange. Good agreement was generally obtained with both structural deformations (see Fig. 6b) and slamming pressures (see Fig. 6c).

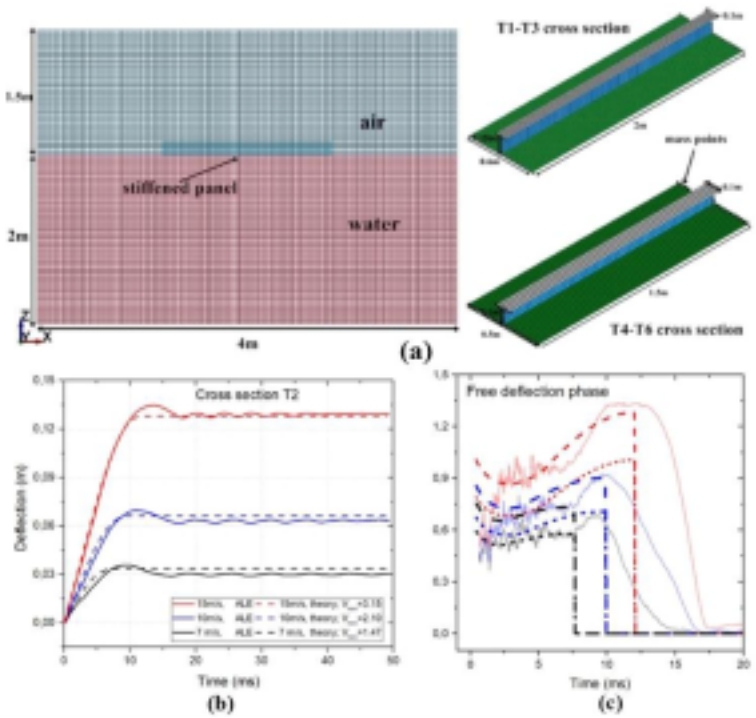
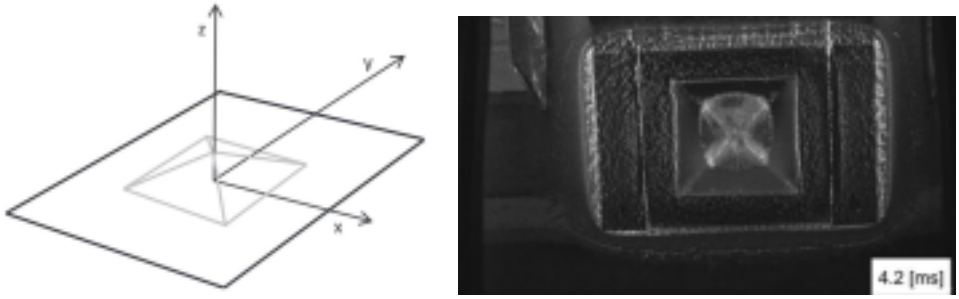


Figure. 6. (a) ALE modelling of water entry of stiffened panels; (b): Deflections of T2 stiffened panels with different initial impact velocities; Dimensions of the T2 stiffened panel are given in (a) with the same plate thickness of 10 mm for the plate flange, web and top flange. (c) slamming pressures on the T2 stiffened panel from ALE simulations and the hydroplastic theory from Yu et al. [17] and Yu [24].

2.2 Hydroplastic model by Abrahamsen et al. [23] for thin plates



(a) (b)

Figure. 6. (a) A pyramid shaped deformation mode; (b) bottom view a thin plate with plastic damage during the drop test. (from Abrahamsen et al. [23])

The hydro-plastic model by Abrahamsen et al. [23] was developed for thin square plates in 3D condtions, where membrane stretching dominated and bending effects were neglected. A pyramid shaped deformation model was considered reasonable for plastic responses of thin plates and the resistance formulations were according to Jones [25]. On the hydrodynamic side, potential flow theory with the infinite frequency free-surface condition was applied. Initial drop velocities were used as inputs of the model as done in Faltinsen [3] and Yu et al [22].

Drop tests were conducted to study large plastic deformations of a square plate and to validate the hydroplastic model. Dual cameras were used to monitor the deforming plate from above, and the deformations were tracked using the 3D-DIC technique that was often used for monitoring explosion responses. The complex hydrodynamics of the impact were captured as shown in Fig. 6. Good agreement was obtained in general between test results and the theory.

3. Development of a complete hydro-elastoplastic response model in extreme water impacts

A complete analytical hydro-elastoplastic model that captures the coupling between hydrodynamic pressures and elastoplastic responses of structures is not yet available in the literature. Work is, however, underway by the authors. The development of a hydro-elastoplastic water impact response model is much more complicated than a hydroplastic model, and the increased complexity lies mostly on the structural response side.

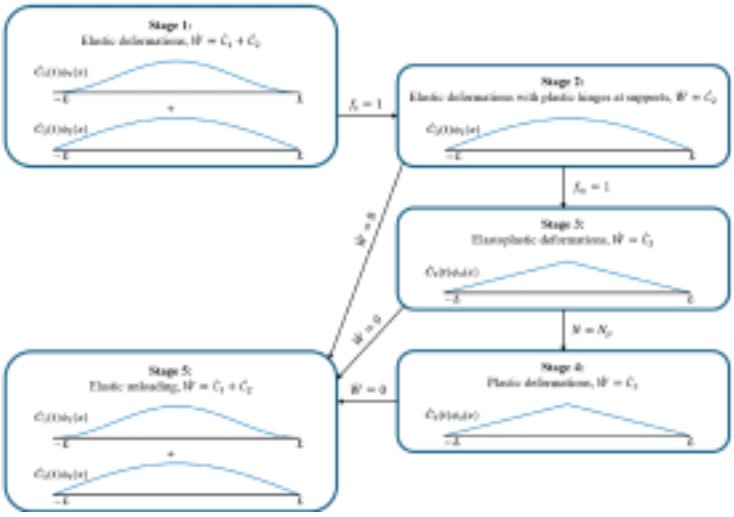


Figure. 7. Elastoplastic responses of a beam subjected to lateral pressures (from Fimreite and Yu [26])

On the structural response side, the structures may go through several deformation stages depending on the loading intensities. The main effects include transient flexural elastic waves [27], coupling of elastic and plastic responses, and stationary and moving plastic hinges. During the deformation process, the effects of bending, membrane stretching and shear will constantly interact with each other. The interaction functions are more complicated for a stiffened panel cross section [18, 28] than for a rectangular cross section. Fimreite and Yu [26] proposed an elastoplastic response model for beams with rectangular and stiffened panel cross sections using the Lagrange's equation of motion. Five deformation stages were included as shown in Fig. 7 covering pure elastic response, elastoplastic development, fully plastic response and elastic unloading in the end. No moving hinges were introduced for simplicity. The analytical model was validated to be of good accuracy by comparing with nonlinear finite element ABAQUS simulations considering varied loading intensities that cause elastic, elastoplastic and large plastic responses. More elastoplastic models subjected to lateral pressures can be found in e.g. Gauch et al. [27] and Yuan et al.[29].

On the hydrodynamic side, the modal analysis approach is used assuming dry modes of elastoplastic responses in Fig. 7. Work is underway to couple both hydrodynamic pressures and structural responses. An alternative viable solution for a complete hydro-elastoplastic slamming model can be achieved by combining finite element solutions for the structural responses and the potential flow theory for hydrodynamics.

4. Design of structures against extreme water impacts: Gaps between academia and industry practices

Although significant progress has been made by the hydrodynamic experts on slamming phenomena, most existing studies stop at the hydroelastic coupling between hydrodynamics and structural responses. Their findings are not always applicable to the practical design work of structural engineers in the industry. The current industrial practice for slamming design typically follows a two-step approach:

- Estimating hydrodynamic pressures from wave impacts under the assumption that the structure is rigid.
- Applying these pressures to detailed structural models in finite element (FE) software such as ABAQUS, to compute structural responses.

This one-way coupling approach often leads to overly conservative structural design [30], which in return increases material costs and carbon emissions. A way to avoid being overly conservative is to introduce a reduction factor that accounts for the FSI effects. However, it is not clear how to determine the reduction factor and the theoretical basis for it. Given the industry needs for more accurate slamming analysis and design tools, a new design approach based on the hydroplastic/hydro-elastoplastic slamming model was proposed by Yu [24] as shown in Fig. 8 as an alternative to the current design practice. The new design approach uses impact velocities as the main design parameter and contains two main parts. The first is to use data from model tests or field measurements to establish design slamming events corresponding to ULS and ALS conditions with the critical impact velocity and impact angle as an indicator. Given the design event, the next is to use the hydroplastic/hydro-elastoplastic model to design reliable structures to withstand the design events that satisfy the acceptance criterion. By doing so, direct use of pressure histories, which are often overly conservative, can be avoided while the coupled nature of the problem is preserved. A complete hydro-elastoplastic slamming model that covers the entire response ranges will be desirable in the design and remains to be developed.

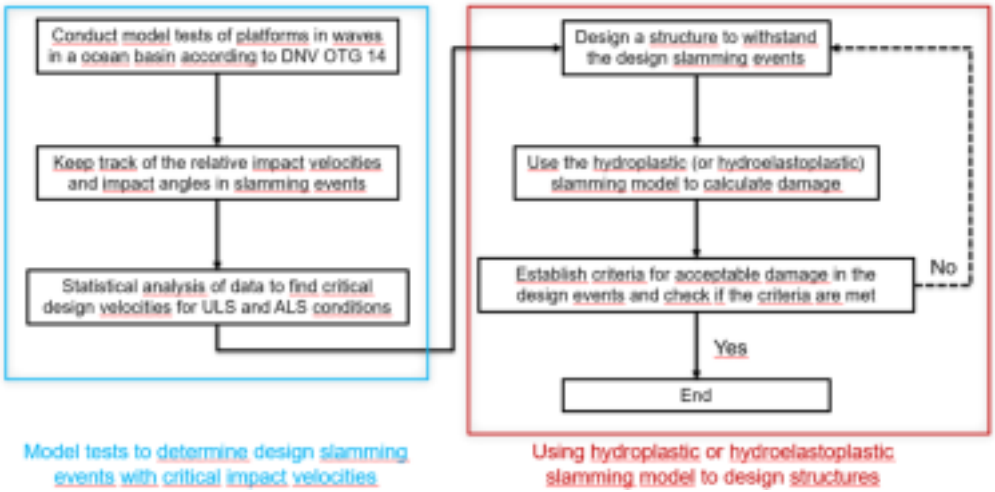


Figure 8. A new design approach for designing against extreme wave impacts (Yu [24]).

5. Conclusions

Water impacts may induce elastoplastic structural responses or even significant plastic deformations in extreme conditions, where hydro-elastoplasticity/ hydroplasticity matters. This paper reviews the recent theoretical development in the emerging field of hydro-elastoplastic/hydroplastic structural responses in extreme water impacts. Two hydroplastic models were reviewed, where the elastic effects were assumed to be small and negligible. The rigid plastic deformation models under large impulsive

loads characterized by moving hinges make it quite different from modes for elastic responses. The challenges for deriving a complete hydro-elastoplastic slamming model are reviewed, where correct representation of the elastoplastic beam responses can be critical. Hydro-elastoplastic slamming models are shown to be a good alternative to the current pressure based design approaches. The method avoids the direct use of pressures in design, and captures the coupled nature of the problem. The needs for more research efforts in this field are highlighted.

Acknowledgements

The author gratefully acknowledges the support from high performance computation resources from the Norwegian national e-infrastructures, Project NN9585K - Accidental actions on strait crossings and offshore platforms.

References

[1] Von Karman T. The impact on seaplane floats during landing. 1929.
[2] Wagner H. Über stoß-und gleitvorgänge an der oberfläche von flüssigkeiten. ZAMM-Journal of Applied Mathematics and Mechanics/Zeitschrift für Angewandte Mathematik und Mechanik. 1932;12:193–215.
[3] Faltinsen OM. Hydrodynamics of high-speed marine vehicles: Cambridge university press; 2005.
[4] Kvalsvold J, Faltinsen OM. Hydroelastic modeling of wet deck slamming on multihull vessels. Journal of ship research. 2021;39:225–39.
[5] Korobkin A, Gueret R, Malenica Š. Hydroelastic coupling of beam finite element model with Wagner theory of water impact. Journal of Fluids and Structures. 2006;22:493–504.
[6] Faltinsen OM. Water entry of a wedge by hydroelastic orthotropic plate theory. Journal of ship research. 1999;43:180–93.
[7] Abrate S. Hull slamming. Applied Mechanics Reviews. 2011;64:060803.
[8] Faltinsen OM. Hydroelastic slamming. Journal of Marine Science and Technology. 2000;5:49–65.
[9] Viste-Ollestad I, Andersen T, Oma N, Zachariassen S. Investigation of an incident with fatal consequences on COSLInnovator. Norway's Petroleum Safety Authority, Investigation report. 2016:1–47.
[10] WH-Limited. An analysis of the response of helicopter structures to water impact. Stress department report SDR156 1995.
[11] Authority CA. Summary report on helicopter ditching and crashworthiness research. UK: Station Off Norwich. 2005.
[12] Lavroff J, Davis M, Holloway D, Thomas G, McVicar J. Wave impact loads on wave-piercing catamarans. Ocean Engineering. 2017;131:263–71.
[13] Pentecôte N, Vigliotti A. Crashworthiness of helicopters on water: Test and simulation of a full-scale WG30 impacting on water. International journal of crashworthiness. 2003;8:559–72.
[14] Hughes K, Vignjevic R, Campbell J. Experimental observations of an 8 m/s drop test of a metallic helicopter underfloor structure onto water: part 2. Journal of Aerospace Engineering. 2007;221:679–90.
[15] Truong DD, Jang B-S, Janson C-E, Ringsberg JW, Yamada Y, Takamoto K, et al. Benchmark study on slamming response of flat-stiffened plates considering fluid-structure interaction. Marine Structures. 2021;79:103040.
[16] Hassoon OH, Tarfaoui M, El Moumen A, Qureshi Y, Benyahia H, Nachtane M. Mechanical performance evaluation of sandwich panels exposed to slamming impacts: Comparison between experimental and SPH results. Composite structures. 2019;220:776–83.
[17] Yu Z, Amdahl J, Greco M, Xu H. Hydro-plastic response of beams and stiffened panels subjected to extreme water slamming at small impact angles, part II: Numerical verification and analysis. Marine Structures. 2019;65:114–33.
[18] Yu Z, Amdahl J, Sha Y. Large inelastic deformation resistance of stiffened panels subjected to lateral loading. Marine Structures. 2018;59:342–67.
[19] Symonds PS, Mentel TJ. Impulsive loading of plastic beams with axial constraints. Journal of the Mechanics and Physics of Solids. 1958;6:186–202.

[20] Jones N. Structural impact: Cambridge university press; 2011.
[21] Stronge WJ, Yu T. Dynamic models for structural plasticity: Springer Science & Business Media; 2012.
[22] Yu Z, Amdahl J, Greco M, Xu H. Hydro-plastic response of beams and stiffened panels subjected to extreme water slamming at small impact angles, Part I: An analytical solution. Marine Structures. 2019;65:53–74.
[23] Abrahamsen BC, Alsos HS, Aune V, Fagerholt E, Faltinsen OM, Hellan Ø. Hydroplastic response of a square plate due to impact on calm water. Physics of Fluids. 2020;32.
[24] Yu Z. Water impact damage considering hydro-plastic interactions: Extensive experimental and numerical validation, and structural design recommendations. Marine Structures. 2025;101:103766.
[25] Jones N. A theoretical study of the dynamic plastic behavior of beams and plates with finite-deflections. International Journal of Solids and Structures. 1971;7:1007–29.
[26] Fimreite SB, Yu z. Dynamic responses of elastoplastic beams with rectangular and asymmetric I-profiles subjected to lateral pressure loads. under review. 2025.
[27] Gauch HL, Montomoli F, Tagarielli VL. The response of an elastic-plastic clamped beam to transverse pressure loading. International Journal of Impact Engineering. 2018;112:30–40.
[28] Yu Z. On the rigid plastic solutions for large deformation resistance of stiffened panels. Journal of Marine Science and Applications. 2026.
[29] Yuan Y, Tan P, Shojaei K, Wrobel P. Large deformation, damage evolution and failure of ductile structures to pulse-pressure loading. International Journal of Solids and Structures. 2016;96:320–39.
[30] Fimreite SB, Yu Z, Amdahl J, Greco M. Numerical analysis of extreme water slamming damage and residual strength of ring-stiffened columns of a semi-submersible floating offshore wind turbine. Marine Structures. 2026;105:103900.

10th International Conference on HYDROELASTICITY IN MARINE TECHNOLOGY
Trondheim, Norway, June16$^{\text{th}}$-18$^{\text{th}}$, 2026

Hydroelastic impacts with aerated water

Wellens P.R.[1,*] and Bockstael, M.M.[1,2]

[1] Ship Hydromechanics Laboratory, Delft University of Technology, The Netherlands
[2] Maritime Research Institute (MARIN), Wageningen, The Netherlands

Abstract. Green water can enact impact loads on deck structures of ships sailing through heavy seas. The water that flows on deck likely has some air entrained, originating from wave breaking. We call that entrained air aeration, and the water aerated water. The maximum pressures in impacts with aerated water can be reduced compared to pressures in water without air. A novel set of experiments was devised in order to study controlled hydroelastic impacts on models of deck structures in the presence of aeration. The plates, with varying stiffness, could take on different angles with respect to the flow direction of the water front. The water front could have different angles, so that a relative angle between water front and plate could be defined. The tests were conducted without aeration and with 4 different percentages of air in water (by volume). The impacts were measured by means of force gauges and pressure gauges, the water front was registered by means of resistive free surface gauges and a set of high-speed cameras. The deformations of the plates were measured by means of laser distance meters. Impacts following from the same starting configuration were repeated so that variations could be studied.

Key words: *Wave-structure interaction; Hydroelasticity; Compressibility*

1. Introduction

With rising wave heights due to climate change, understanding wave behaviour and its interaction with ships and offshore structures has become more critical. Wave breaking in heavy seas entrains air in water, apparent from the white crests. Aerated water has a demonstrated effect in fluid-structure interaction, but has not yet been quantified for all loading mechanisms. Green water is a loading mechanism that results from large relative wave heights and the subsequent flow of water on deck. Deck structures in the path of the flow, often intended to protect sensitive equipment, need to be low weight and fail-safe. The study in this paper aims to advance knowledge of fluid-structure interactions in the context of wave impacts. The key focus is the role of hydroelastic effects in the presence of aerated water.

Hydroelasticity is about the two-way coupling between the wave loading and structure response. Faltinsen defined the importance of hydroelasticity for an elastic hull with wedge-shaped cross-sections penetrating an initially calm water surface based on the ratio between the wetting time of the structure and the largest wet natural period of the stiffened plating using orthotropic plate theory [1]. Faltinsen introduced the following non-dimensional parameter

$$\xi = \frac{tan(\beta)}{V\sqrt{\rho L^3/EI}}, \tag{1}$$

in which L is the length of the analysed longitudinal stiffener between two successive transverse frames, β is the dead rise angle, V is the impact velocity, ρ is the water density, and EI represents the bending stiffness. The parameter ξ is comparable to the ratio used by Bereznitski [2] between the wetting time of the rigid wedge, which is the load duration T_d, and highest natural period T_{n1} of the stiffener

*Correspondence to: p.r.wellens@tudelft.nl

$$Ratio = \frac{T_d}{T_{n1}} \tag{2}$$

Bereznitski [2] found that the ratio between the impact duration and the period of first mode of vibration of dry structure is the key factor in determining the importance of hydroelastic effects. A value of the ratio near 1 means that hydroelasticity is important and values of the ratio near 2 or 3 mean that hydroelasticity is not important.

Air entrainment in waves appears both as distributed aeration with bubble clouds and void fractions dispersed in the water column and as large-scale entrapment such as cavities of air trapped beneath overturning jets. The degree of aeration has strong implications for wave dynamics, energy dissipation, and impact loads on marine structures. Peregrine [3] notes that significant reductions in pressure may occur even with relatively small amounts of entrained air in violent, confined flows. With a novel numerical method by Van der Eijk and Wellens [4], which was validated by dedicated experiments with falling wedges, it was found that aeration causes large differences in impact pressure with respect to impacts without air in water.

Based on the existing literature, the effect of both hydroelasticity and aeration on impacts does not yet seem to have been investigated for free surface waves. This paper describes an experiment in which wave-structure interaction with aerated water is systematically studied. The green water loading mechanism is emulated by sloshing a water-filled container until the (strongly nonlinear) run-up along the side walls of the container impacts with a cantilevered plate.

2. Experimental Setup

The interaction between waves and flexible structures is highly complex and nonlinear and difficult to capture accurately using numerical simulations alone. A carefully designed experimental setup with known accuracy is a time-efficient means of obtaining insight into the problem. In order to be an accessible benchmark for the validation of numerical methods, the setup was kept two-dimensional (2D) as much as possible. It consists of a water-filled container that is equipped with an instrumented internal support structure for a clamped cantilever plate, or beam in 2D, and a false floor with porous stones that provide a continuous supply of micro-bubbles of air in the water to make it aerated. The plate thickness and the angle with respect to the horizontal could be varied. A visual representation of the setup is shown in Figure 1, its global dimensions are given in Table 1.

The container is oscillated in surge direction (in the direction of the tank length L_t) with a fixed amplitude and varying oscillation frequency, generating a free surface wave and run-up on the side walls. The mass of fluid in the run-up is wedge-shaped representing the progression of water on deck with a characteristic velocity and approach angle varying with the varying sloshing frequency of the tank. The setup offers a precise, controlled and repeatable environment to study hydroelastic wave impacts in detail.

Compared to the deadrise angle β of the falling wedge in Faltinsen [1], a modified angle β_r is defined, , see Figure 2, representing the difference between plate angle θ and angle β_w (steepness) of the approaching wave run-up front. The connection between angle and wetting time (or loading time) remains.

To investigate the effect of hydroelasticity, four stainless steel plates are used, ranging from stiff (4 mm, almost rigid) to highly flexible (0.5 mm). The plate angle, θ, can be adjusted using clamping blocks with different inclinations. These blocks are secured with bolts, allowing plates of varying thicknesses to be mounted, while any gap created by thinner plates is filled with shim plates to maintain correct alignment. By comparing the pressures, forces and deflections measured on the flexible plates with those obtained from the rigid plate, the degree of hydroelastic behaviour can be assessed.

The level of aeration in the fluid can be controlled using a flow system controller which is connected to the valve controlling the input of the Pentax DYPFP24 Micro-bubble air diffusers, which have a

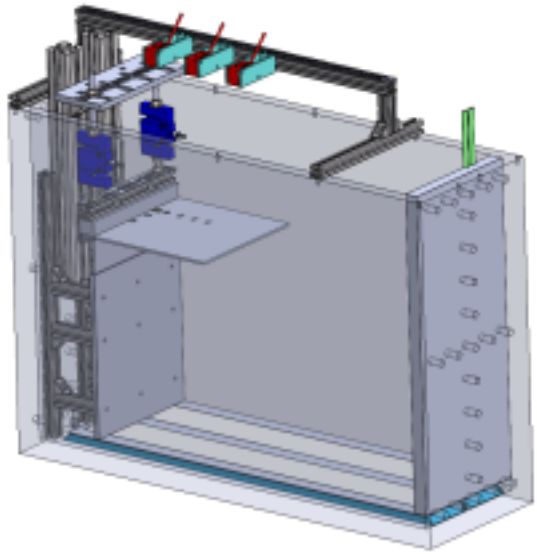


Figure 1: A CAD model of the experimental setup in the sloshing tank. The water height is measured using a water level gauge (green), plate deformation with laser distance sensors (red), the impact force with the load cells (dark blue), aeration is produced with air bubble diffusers (blue/white) and the impact pressure is measured with pressure sensors (yellow).

Table 1: Tank parameters.

Parameters	**Symbol**	**Value**	**Unit**
Tank length bottom	L_t	583	mm
Tank width bottom	W_t	200	mm
Tank height	H_t	496	mm
Relative plate height	H_p	307	mm
Plate density (RVS)	ρ_p	8000	kg/m^3
Young's Modulus (RVS)	E_p	$193 \cdot 10^9$	Pa
Relative still water level	H_w	145	mm

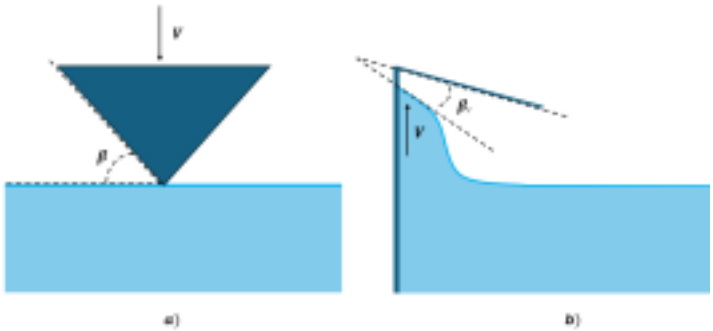


Figure 2: Definition of the dimensionless number: (a) the setup of Faltinsen [1], and (b) the current setup.

maximum flow capacity of 7 liters per minute, or 345 kPa. The level of aeration is measured using an aeration float [4].

The loads on the plate will be measured using pressure sensors. The impact load varies along the length of the plate; since the location of the peak pressure shifts with increasing sloshing frequency, pressure sensors must be distributed across the entire plate. Pressure sensors will only be placed on the rigid 4mm plate as sensor readings are influenced by local deformation of the elastic plates and vice versa. By mounting sensors on an elastic plate its stiffness and mass distribution as well as the natural frequencies and vibration modes are affected. Besides measuring the local pressures, the total load is also be examined. As a result, all the added equipment influences the response of the setup. A sufficient amount of sensors must be placed to ensure a high resolution, while at the same time they should not interfere with the system's accuracy.

Two types of pressure sensors are used to enable verification of the pressure response and peak pressure at different locations along the plate. The precise spacing of the pressure sensors (Figure 3) was determined using numerical simulations.

To investigate the pressure behaviour, piezo-resistive sensors are implemented. This type of sensor can measure both static and dynamic pressures by detecting changes in electrical resistance that occur when the sensing diaphragm undergoes mechanical deformation. For this purpose, the SMI 5420E-30-AHS sensors were selected. They feature an operating pressure range of 0–30 PSI and a maximum (proof) pressure of 90 PSI. The sensor combines MEMS piezoresistive sensing with integrated signal-conditioning electronics that perform temperature and offset compensation, providing a stable and linear output suitable for both static and moderately dynamic measurements.

In addition, piezoelectric sensors are used to capture rapid pressure peaks. These sensors are recommended for high-frequency measurements due to their fast response times [5]. Their high natural frequencies help prevent resonance effects associated with wave interactions or entrapped air bubbles, enabling accurate detection of sharp pressure peaks during impact events. Accordingly, PCB 113B24 piezoelectric sensors are used to identify pressure peaks during wave impacts. However, it is important to note that piezoelectric sensors are limited to measuring dynamic pressures and cannot record static or slowly varying loads due to the inherent signal decay.

The deformation of the elastic plates is measured using three Panasonic HG-C1400 laser distance sensors with ID numbers 169,170 and 171. Laser 169 is measuring at 50mm from the wall, laser 170 measures at 100mm from the wall and laser 171 measures approximately at the plate tip. Because of changes in the plate angle, the exact positions of the laser 171 measurements on the plate will vary.

The sloshing tank will accelerate towards the desired frequency and is influenced by factors as break release and inertia of the tank. Three complete surge oscillations of the tank per test were performed. The position and acceleration of the tank will be measured by a linear Waycon position sensor. The

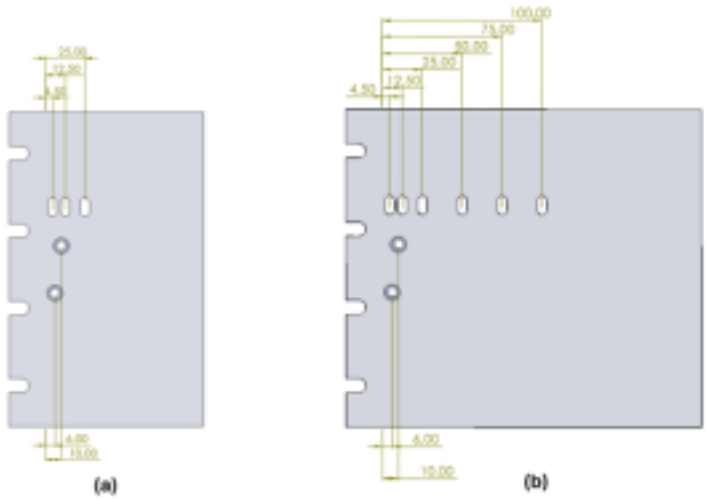


Figure 3: Location of the pressure sensors: for the 100 mm plate (a): SMI7, SMI8, SMI9 (numbering increases from left to right); and for the 200 mm plate, (b): SMI1, SMI2, SMI3, SMI4, SMI5, SMI6. SMI sensors were placed in the oval holes. PCB sensors were placed in the round holes. PCB1 and PCB3 are interchanged between the two plates.

Table 2: The test parameters for the experiment in the sloshing tank.

Plate Thickness (mm)	**Wave Approach Angle (°)**	**Plate Angle (°)**	**Aeration Percentage**
4.0	0	0	0%
1.5	10	10	1%
1.0	20	20	2%
0.5	30	30	4%

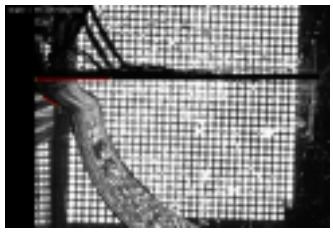
measured position can then be used as input for numerical simulations.

The test matrix for this study is designed to systematically investigate the impact of waves on a plate under a wide range of physical conditions. With 4 different plate thicknesses, 4 wave approach angles, 4 plate angles and 4 aeration conditions a total of 256 unique test cases are created. The plate thicknesses are chosen based on the ratio between the impact period and the first natural period of the plate [1], [2]. To ensure sufficient reliability of the results, each test case will be repeated three times. Additional calibration and control tests were conducted to validate measurement consistency and system performance. A test lasted between 3 and 4 seconds, with 5 seconds of measuring time. Three minutes were taken in between tests to allow the free surface oscillations to dampen out until they could no longer be distinguished from measurement noise.

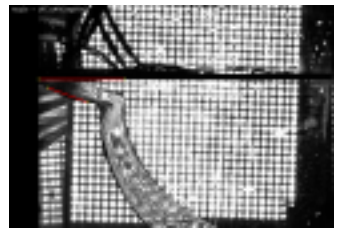
The first dry natural frequency of the experimental plates is identified using a free decay test, with the tip motion measured by laser distance sensor 171. By placing the plate in the sub-assembly and exciting it with a short impulse, such as a hit with a hammer, the plate will vibrate. By plotting the measured signal of the lasers, the experimental natural frequency of the plate can be approximated. Subsequently, to predict the wetted natural frequency of the plate (assuming a full wetted length) with added mass, the water level is raised to exactly the height of the plate such that the bottom side of the plate is in contact with the water surface. Again, the plate is excited with a short impulse and the natural frequency is

Table 3: Natural frequencies of the plates with varying lengths and thicknesses.

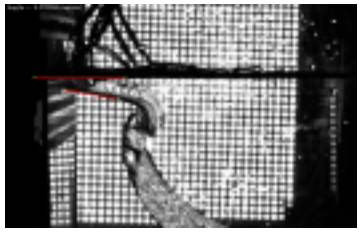
Plate Length [mm]	**Plate Thickness [mm]**	$f_{n1a,\text{dry}}$ **[Hz]**	$f_{n1m,\text{dry}}$ **[Hz]**	$f_{n1m,\text{wet}}$ **[Hz]**	**Error** $f_{n,\text{dry}}$ **[%]**
200	0.5	9.88	8.63	2.46	12.65
	1.0	19.77	19.23	8.77	2.73
	1.5	29.65	27.30	11.63	7.92
	4.0	79.06	-	-	-



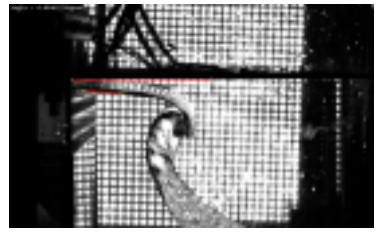
(a) 30° wave approach angle, 0.85 Hz



(b) 20° wave approach angle, 1.00 Hz



(c) 10° wave approach angle, 1.15 Hz



(d) 5° wave approach angle, 1.40 Hz

Figure 4: Resulting wave shapes for different wave approach angles β_w and sloshing frequencies: (a) 30° at 0.85 Hz, (b) 20° at 1.00 Hz, (c) 10° at 1.15 Hz, and (d) 5° at 1.40 Hz.

retrieved from the signal of the laser distance sensors.

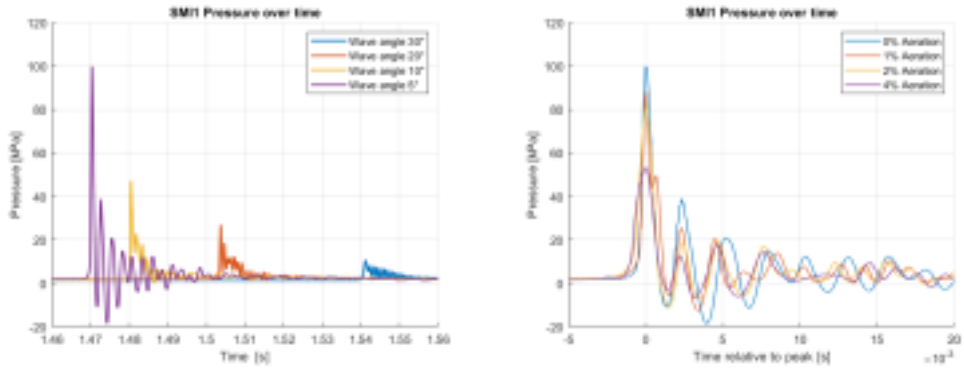
The resulting natural frequency of the plates are presented in Table 3. The error is calculated as the difference between the measured dry natural frequency f_{n1m} and the analytical dry natural frequency f_{n1a}. Measured results are not present for the 4 mm plate because the response could not be distinguished from the elastic response of the force gauges.

3. Results

Key response parameters from the experiment are the maximum pressure and the plate deformation. These signals were measured at a frequency of 100 kHz. The start time of the high-frequency measurements was not always the same. For this reason all signals were synchronized by means of a trigger signal for the high-speed cameras that was always the same.

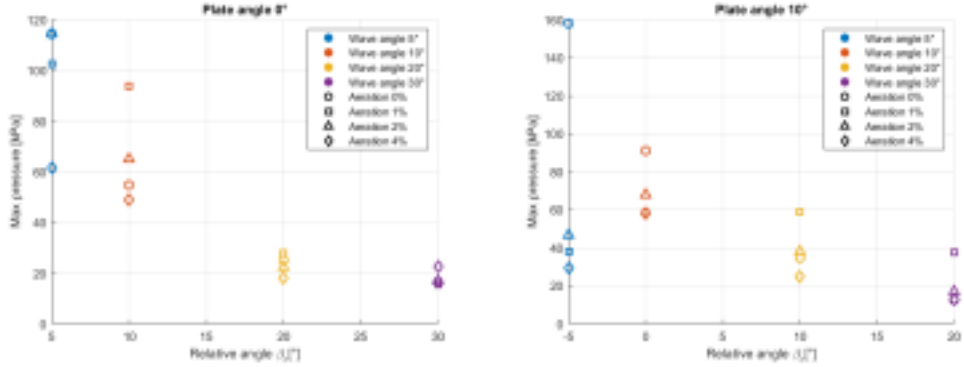
In Figure 4 the wave approach angles β_w are shown with the corresponding frequency of the surge motion of the tank. When the resulting wave approach angles are larger than the plate angle ($\beta_r < 0$), air entrapment occurs in the corner between the vertical wave and the impact plate.

The pressures were measured using the SMI pressure sensors positioned as described in Figure 3. The sensor positioning has a significant influence on the measured pressures, as local pressure effects oc-



(a) (b)

Figure 5: Pressure signals:(a) pressure development over time for different wave approach angles for a plate angle of $0°$ and 0% aeration, and (b) effect of aeration on the pressure development over time for a plate angle of $0°$. Pressures were only measured with the 4 mm thick plate.

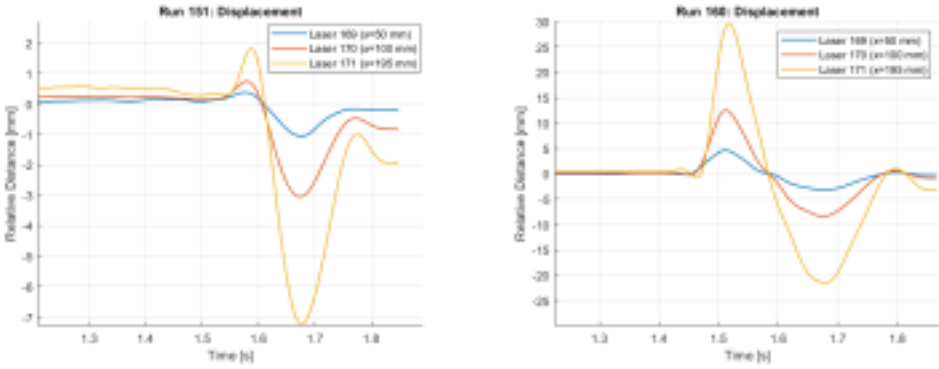


(a) (b)

Figure 6: Max pressures vs. relative angle β_r for different wave approach angles β_w, levels of aeration and plate angles θ: (a) $\theta = 0°$ and (b) $\theta = 10°$.

cur along the entire plate length. Locally entrapped air and minor disturbances of the free water surface, such as those caused by airflow or falling droplets, can also affect the measured pressures. Figure 5a is showing the difference in impact time and pressure behaviour at SMI1 for different wave approach angles. Larger wave angles with lower velocity impact the pressure sensor later in time with respect to the smaller wave angles with higher approach velocities. The effect of aeration is shown in Figure 5b, where the reduction in the peak pressure is a result of higher levels of aeration. Greater aeration leads to a broader initial pressure peak, demonstrating that aeration reduces the pressure maximum but increases the impact duration.

Figure 6 shows the maximum pressure in a time signal as a function of relative angles β_r for different wave angles and levels of aeration. Results are shown for two different plate angles, $\theta = 0$ and $\theta = 10°$. The pressures in the figures are based on the mean of the repeated tests. At each relative angle, increasing the percentage (by volume) of aeration, reduces the maximum pressure. A relative angle $\beta_r = 0$ means that the plate and wave front have the same orientation and that the plate is impacted by water over the entire length of the wave front at (almost) the same time. A negative relative angle means that an



(a) (b)

Figure 7: Displacement of a horizontal 0.5mm plate at different locations for 0% aeration for (a) wave approach angle of 30° and (b) wave approach angle of 5°.

air pocket was entrapped. Increasing the relative angle β_r between plate angle θ and wave approach angle β_w also reduces the maximum pressure. Note that for the plate with $\theta = 10°$ in Figure 6b, the trends for the cases with levels of aeration higher than 0 are discontinuous. At a relative angle $\beta_r = -5$ the maximum pressures for the tests with aeration are much lower than the test without aeration. Why entrapped air would behave so differently with or without aeration in the water, is something that at present we cannot explain. The results for the pressure indicate that even at low levels of aeration the compressibility of water plays a significant role during wave impacts.

The deformation of the plates is measured using the three laser distance sensors. The horizontal positioning of laser 171 is influenced by the plate's angle and thickness, since plate deformation under impact can reduce the effective horizontal distance of the plate due bending deformation. For this reason, the measured maximum deflections are based solely on the vertical deformation of the plate at plate and angle specific horizontal locations, which should be considered when interpreting the results.

Figure 7 shows the displacement at 3 locations on the plate for two wave approach angles for a 0.5mm plate. The displacement was fully elastic (not the entire signal in time is shown). Depending on the wave approach angle, the largest deformation may occur on initial impact (Figure 7b) or when the plate moves downwards again on the secondary loading due to the wave's mass further exciting the plate or a possible vacuum effect in the corner of the plate. Depending on the plate thickness, plate angle and wave approach angle the motion of the water mass following the plate can reinforce or oppose the oscillations depending on timing and phase.

The influence of aeration on the displacement of elastic plates was investigated for different plate thicknesses. Figure 8 illustrates that the effect of aeration varies with plate thickness. For the thinnest plate considered (0.5 mm), which exhibits high elasticity, increasing aeration appears to increase the maximum displacement. In contrast, for the thicker plate (1.5 mm), which is comparatively stiffer, the trend is reversed: increasing aeration tends to reduce the maximum displacement.

This behaviour can be explained by the interaction of two phenomena. First, the presence of air can increase the loading duration, which is the dominant factor for highly elastic plates such as the 0.5 mm case, leading to larger displacements due to prolonged excitation. Second, for stiffer plates the presence of air primarily reduces the peak impact force, and since the maximum force governs deformation in these cases, the resulting displacement decreases.The transition between these two responses for aerated wave impacts occurs at an intermediate plate thickness, where neither mechanism fully dominates.

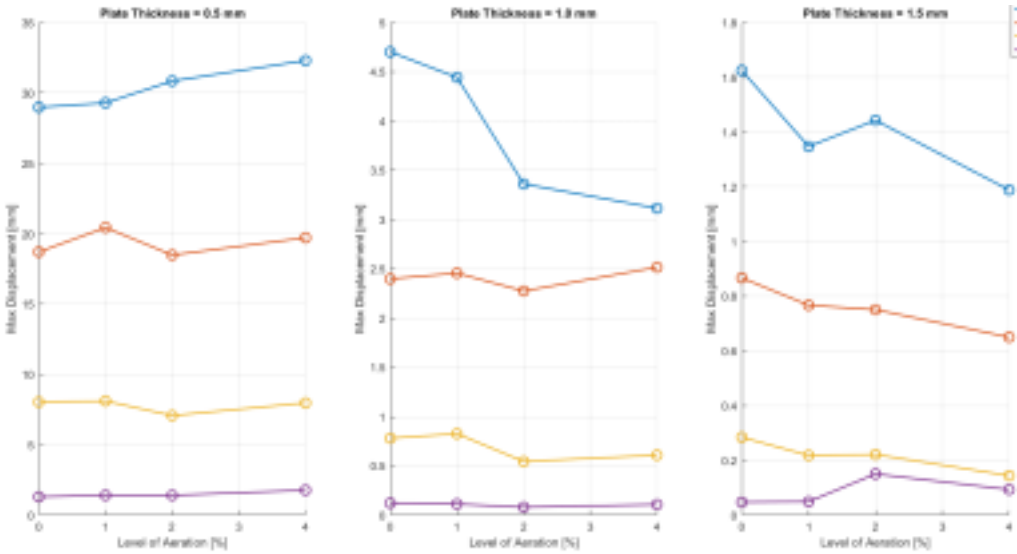


Figure 8: The effect of aeration on maximum plate deflection for different plate thicknesses and relative angles β_r.

4. Conclusions

This study examined hydroelastic wave impacts on a flexible plate through an experimental approach. The investigation explored the combined influence of aeration, relative impact angle, and structural flexibility on the magnitude and distribution of impact loads and structural responses.

The measured pressures strongly depend on the relative angle β_r between the plate and the approaching wave. When the plate and wave are almost aligned $-5 < \beta_r < 5$, the impact is close to normal to the surface, producing the highest peak pressures. For negative relative angles, entrapped air pockets form near the lower edge, causing variability with sometimes higher pressures and sometimes cushioning of the impact, reducing the pressure amplitude while increasing the impact duration. Positive relative angles result in lower pressures

In the present setup, the plate thickness has a greater influence on maximum deformation and hydroelastic effects than reported in wedge impact investigations.

Higher levels of aeration lower the pressure amplitude but increase the duration of loading, demonstrating that air reduces the intensity of the impact while spreading it over a longer time interval. Overall, maximum pressures occur for $\beta_r \approx 0$ and minimal aeration, while both higher aeration and greater relative angles ($|\beta_r| > 5$) lead to a notable decrease in impact intensity.

The plate deformation is dependant on the relative influence of aeration versus the plate stiffness. Aeration and plate deformation both extend the impact duration when considered individually. Aeration reduces the peak loads, resulting in smaller deformations that can counteract the increase of the impact duration induced by plate flexibility. This interaction demonstrates the nonlinear coupling between aeration and structural elasticity: although each factor independently increases the impact duration, their simultaneous presence can diminish each other's influence.

Acknowledgments

We would like to express our gratitude to the staff of the Ship Hydromechanics laboratory, without whom experiments could not be conducted: Pascal Chabot, Jasper den Ouden, Angela Piras, Peter Poot,

Sebastian Schreier, Frits Sterk, Sedat Tokgöz and Ton Veer.

References

[1] O. M. Faltinsen, "Water entry of a wedge by hydroelastic orthotropic plate theory," *Journal of Ship Research*, vol. 43, no. 3, 1999, ISSN: 00224502. DOI: 10.5957/jsr.1999.43.3.180.

[2] A. Bereznitski, "Slamming: The role of hydroelasticity," *International Shipbuilding Progress*, vol. 48, no. 4, 2001, ISSN: 0020868X.

[3] D. H. Peregrine and L. Thais, "The effect of entrained air in violent water wave impacts," *Journal of Fluid Mechanics*, vol. 325, 1996, ISSN: 00221120. DOI: 10.1017/S0022112096008166.

[4] M. van der Eijk and P. Wellens, "An efficient pressure-based multiphase finite volume method for interaction between compressible aerated water and moving bodies," *Journal of Computational Physics*, vol. 514, p. 113 167, Oct. 2024, ISSN: 0021-9991. DOI: 10.1016/J.JCP.2024.113167.

[5] S. Y. Kim, K. H. Kim, and Y. Kim, "Comparative study on pressure sensors for sloshing experiment," *Ocean Engineering*, vol. 94, 2015, ISSN: 00298018. DOI: 10.1016/j.oceaneng.2014.11.014.

10th International Conference on HYDROELASTICITY IN MARINE TECHNOLOGY
Trondheim, Norway, June 16th-18th, 2026

Hydroelastic simulation for water entry slamming of a flat plate based on two-way CFD-FEM method

Zhihao Wang, Jianhua Wang*, Jiawei Xiao, Decheng Wan

Computational Marine Hydrodynamics Lab (CMHL), School of Ocean and Civil Engineering, Shanghai Jiao Tong University, Shanghai, China (jianhuawang@sjtu.edu.cn;)

Abstract. A CFD–FEM coupling method based on the preCICE library is proposed to investigate the hydroelastic response of flat-plate water-entry slamming, which simplifies bow slamming. The flow is solved by RANS (OpenFOAM) and the structure by FEM (CalculiX). A three-dimensional flat plate is studied at three entry velocities; the plate is held fixed while water moves upward for computational efficiency. Results for rigid and elastic plates agree well with experiments and literature. Rigid slamming exhibits earlier onset, shorter duration, and higher peak pressures. As velocity increases, peak pressures rise, impulse duration decreases, and the pressure difference between rigid and elastic plates grows. The Dynamic Amplification Factor (DAF) demonstrates that when load duration is far shorter than the structural natural period, structural inertia filters extreme slamming pressure peaks (DAF < 1), primarily because local deformation creates an inclination angle that reduces tangential velocity and lowers slamming pressure.

Key words: *Hydroelastic, Flat plate, CFD-FEM, Water entry, Flexible slamming*

1. Introduction

Hydroelasticity describes the mutual interaction between fluid motion and structural deformation, and is critical for accurate prediction of slamming loads. Since a ship bottom has almost zero deadrise angle, flat-plate water entry is a severe and widely used idealization that features air cushion effects and, for elastic plates, intensified pressure oscillations and structural response. Early contributions include Verhagen's air-cushion theory, Chuang's experiments highlighting the influence of entrapped air and structural elasticity, and Mori's drop tests on stiffened panels. With the development of coupled CFD–FEM methods, recent studies (e.g., Xie et al., Yamada, Truong et al., Tavakoli et al.) have revealed multi-mode hydroelastic behavior and demonstrated that equivalent loads depend on both impact velocity and plate stiffness. Kvalsvold and Faltinsen further showed that maximum stress is governed by the structural natural period rather than by peak pressure. Despite these advances, the coupled evolution of the free-surface pressure field and structural deformation, and specifically the quantitative filtering effect of structural inertia on instantaneous pressure peaks via a deformation-induced local inclination angle, have not been systematically characterized. This paper addresses this gap through a partitioned CFD–FEM simulation of the constant-velocity water entry of a three-dimensional elastic flat plate. The analysis focuses on the influence of elasticity on slamming pressure and load duration, the structural response under different entry velocities, and the introduction of the Dynamic Amplification Factor to quantify how the local inclination caused by structural deformation reduces tangential velocity and attenuates slamming pressure (DAF < 1).

2. Numerical method

2.1 Fluid part

The interFoam solver in OpenFOAM ESI v2306 is employed in the fluid part simulations. The governing equations include the mass conservation equation and the momentum equation as shown below.

* Correspondence to: jianhuawang@sjtu.edu.cn

$$\nabla \cdot U = 0 \tag{1}$$

$$\frac{\partial \rho U}{\partial t} + \nabla \cdot \left[\rho(U - U_g)U\right] = -\nabla p_d - g \cdot x \nabla \rho + \nabla \cdot \left(\mu_{eff} \nabla U\right) + (\nabla U) \cdot \nabla \mu_{eff} + f_s \tag{2}$$

In the equation above, U is the velocity field; U_g is the grid moving speed; $p_d = p - \rho g x$ is the fluid dynamic pressure; ρ is the density of liquid or gas; g is the gravitational acceleration vector; $\mu_{eff} = \rho(v + v_t)$ is the effective dynamic viscosity, where v and v_t are called kinematic viscosity and turbulent eddy viscosity, respectively, and the latter is solved by the turbulence model; and f_s is the source term applied in the extinction region.

The VOF method with artificial compression technique is used to capture the free surface. The transport equation of the phase fraction is:

$$\frac{\partial \alpha}{\partial t} + \nabla \cdot \left[(U - U_g)\alpha\right] + \nabla \cdot \left[U_r(1 - \alpha)\alpha\right] = 0 \tag{3}$$

where α is the phase fraction between 0 and 1.

2.2 Solid part

The structural responses are calculated using CalculiX, a free software three-dimensional structural finite element program, which could make use of the ABAQUS input format and commercial pre-processors.

The dynamic movement of the beam is described via displacement field $\boldsymbol{u}$ and the equation is shown below:

$$M\ddot{\boldsymbol{u}} + C\dot{\boldsymbol{u}} + K\boldsymbol{u} = q \tag{4}$$

Where M, C, K are the structure mass, damping $\boldsymbol{n} \times \boldsymbol{n}$ matrix and stiffness. The damping matrix uses Rayleigh damping which is a linear combination of mass and stiffness of the structure. The structural problem is solved by using finite element method. Further details can be found in the CalculiX documentation.

2.3 Two way coupled part

This paper utilizes the open-source Multiphysics coupling library preCICE to couple the fluid and structure solvers, thereby achieving a bidirectional coupled solver. preCICE employs adapters as interfaces to directly interpolate and exchange data without modifying the underlying code of each open-source program. It only requires calling the libpreCICE library within each respective open-source program. This method has been used in studying several FSI problems (Zhang et al. (2025), Xiao et al. (2024, 2025)).

The specific analysis procedure in Figure 1 can be summarized as follows:

① Within each time step, calculate the hydrodynamic loads acting on the structural interface.

② Obtain data such as the displacement $\boldsymbol{u}$, velocity $\dot{\boldsymbol{u}}$, and acceleration $\ddot{\boldsymbol{u}}$ of the structural elements from the previous structural analysis step.

③ Substitute the hydrodynamic loads generated by the fluid at the fluid-structure interface and the structural element information from step ② into equation (4) to compute the new structural displacement data.

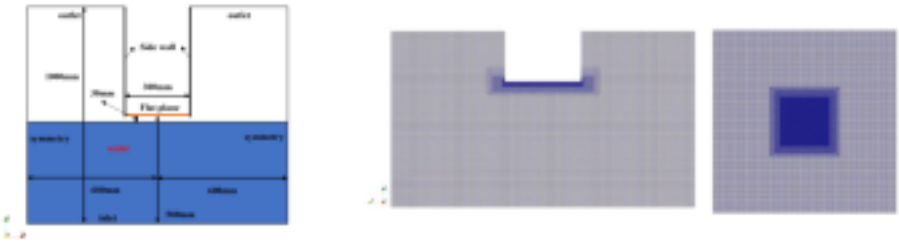
④ Based on the updated structural displacement data obtained in step ③, update the fluid mesh and flow field accordingly.



Figure 1. Schematic of coupled method.

3. Geometric model

Yan et al. (2022) numerically studied an elastic flat plate using STAR-CCM+ coupled with Abaqus. The tank was simplified to a 1.2 m × 1.2 m × 1 m rectangular domain, as shown in Figure 2(a), with a 0.3 m square plate centered at mid-height. Constant-velocity water entry was modeled by fixing the plate and imposing an upward flow from the bottom inlet; the top was set as an outlet and the sides as symmetry planes, with the region above the plate excluded. The initial free surface was placed 30 mm below the plate to save time and allow flow development. The fluid domain was discretized with a hexahedral mesh, illustrated in Figure 2(b), refined near the free surface and the plate. The plate, depicted in Figure 3 and detailed in Table 1, was 4.7 mm thick POM with a Young's modulus of 2800 MPa, a Poisson's ratio of 0.3, and a density of 1410 kg/m³. Outermost boundaries were constrained in x and y; 16 pins at 18 mm from the edge restricted z-displacement; and an inner boundary at 25.3 mm from the edge was fully fixed.



(a) Fluid domain. (b) Fluid mesh distribution.

Figure 2. Flat plate fluid domain and mesh set up.



Figure 3. Flat plate structure domain set up.

Table 1 Structure material parameters.

Parameter	
Plate thickness	4.7mm
Young's modulus E	2800MPa
Poisson's ratio	0.3
Density	1410kg/m3

To measure the slamming pressure on the plate and structural responses such as stress and strain, three pressure measurement points and two strain measurement points were arranged on the flat plate, as shown in Figure 4. Among these, P2r and P2e represent the pressure measurement points set on the rigid plate and the elastic plate, respectively. The pressure gauges were attached to the impact side of the plate, while the strain gauges were mounted on the back side.

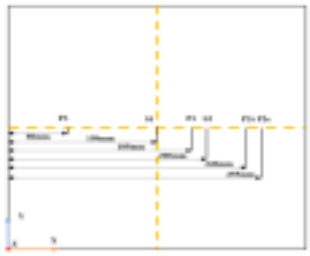


Figure 4. Sensors distribution on the flat plate.

4. Results and discussions

4.1 Grid sensitivity study

This section focuses on the mesh convergence verification for the fluid and structural domains. Three sets of meshes with different sizes are employed to investigate the slamming of a rigid flat plate with a water entry velocity of 1.041 m/s. The mesh sizes include a coarse mesh of 0.00125 m, a medium mesh of 0.000625 m, and a fine mesh of 0.0003125 m. Figure 5(a) presents the pressure time-history curves at measurement point P1, specifically comparing the time segment containing the slamming pressure peak. Convergence analysis is conducted using the Grid Convergence Index (GCI), with the following settings:

$$R_G = \frac{S_2 - S_1}{S_3 - S_2} \tag{5}$$

Different R_G correspond to different convergence forms:

Monotonic: $0 < R_G < 1$;

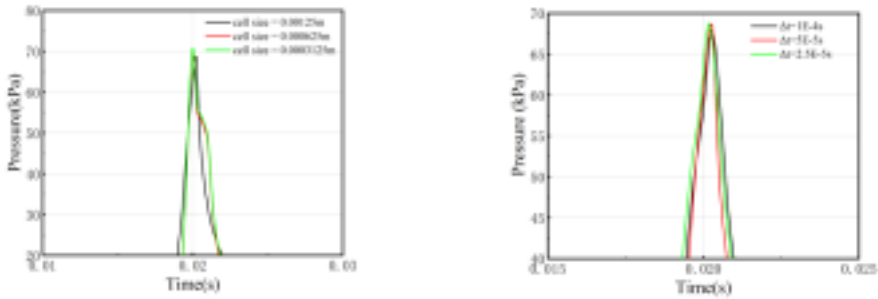
Oscillatory: $R_G < 0$;

Divergence: $R_G > 1$;

As shown in Table 2, the convergence index is 0.67, indicating that the fluid mesh is monotonically convergent. Since hexahedral meshes are employed, a full mesh refinement would result in a substantial increase in the total cell count. Therefore, the coarse mesh with a grid size of 0.00125 m is adopted for the calculations, corresponding to a total of 2.5 million cells.

Table 2 Fluid domain convergence.

Cell type	Peak impact pressure (kPa)	R_G
Coarse	S_1=68.68	0.67
Medium	S_2=69.52	
Fine	S_3=70.78	



(a) Mesh convergence study (b) Time step convergence study

Figure 5. Mesh and time step convergence study of fluid part.

To evaluate the influence of the time step size on slamming pressure, three time steps—1×10^{-4} s, 5×10^{-5} s, and 2.5×10^{-5} s—are employed for convergence analysis. Figures 5(b) presents a comparison of the time histories of peak slamming pressure at the measurement points under different time steps. It can be observed that, under the current mesh configuration, the time step size has a limited effect on the slamming pressure predictions. Considering the requirements of structural calculations, a time step of 5×10^{-5} s is adopted for the subsequent numerical simulations.

In structural modeling, the flat plate structure is discretized using eight-node shell elements (S8R), which are then employed in solid element calculations. In CalculiX, shell elements are automatically extruded into solid elements. This transformation method is illustrated in Figure 6. Specifically, starting from the S8R elements, 20 nodes are extruded along the element normal direction based on the thickness parameter, thereby generating 20-node solid elements (C3D20). Compared to the four-node shell elements (S4R), the S8R elements are more effective at capturing stress concentrations.

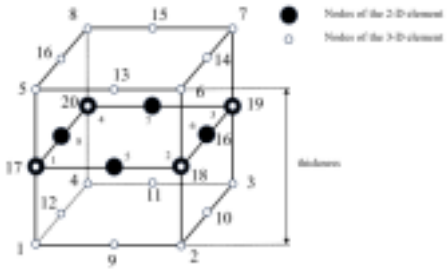


Figure 6. Expansion of a 2D 8-node element into a 3D 20-node solid element.

The structural element size is set to 3 mm. To ensure stability in high-frequency calculations, Rayleigh damping with a stiffness-proportional damping ratio of 4% (at the fundamental frequency) is adopted, based on values reported in the literature and in the experiment. As shown in Figure 7, the point mass representing the sensor also has a significant impact on the structural response. The dry natural frequency without considering the sensor mass is 181.0 Hz, which decreases to 147.3 Hz after incorporating the sensor mass. Table 3 compares the dry natural frequencies under different conditions. After accounting for the sensor mass, the natural frequency shows better agreement with the experimental dry natural frequency; therefore, this mesh configuration is adopted for the subsequent calculations. The fundamental natural frequency in the numerical simulation assumes vacuum conditions, whereas the experimental value includes the influence of the added mass of the surrounding air. This is one of the factors contributing to the discrepancy between the numerical and experimental natural frequencies.

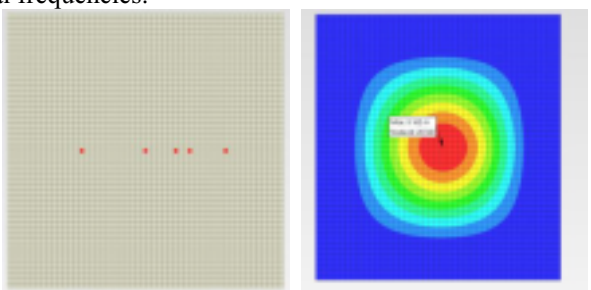


Figure 7. Structure mesh set up.

Table 3 Fundamental natural frequency of the plate

Type	dry modal frequency
without considering the sensor mass	181.0Hz
considering the sensor mass	147.3Hz
Literature result	148.9Hz
Experiment result	147.1Hz

4.2 Method validation study

The study investigates three drop-induced slamming cases with different water-entry velocities, as reported in the literature. The working conditions are listed in Table 4, with water-entry slamming velocities of 0.519 m/s, 0.782 m/s, and 1.041 m/s, respectively. Validation was first performed for rigid-body water-entry slamming. The peak slamming pressures at measurement point P1 are presented in Table 5, with the maximum error of 5.2% occurring at a slamming velocity of 0.519 m/s. The predicted slamming pressure shows satisfactory accuracy.

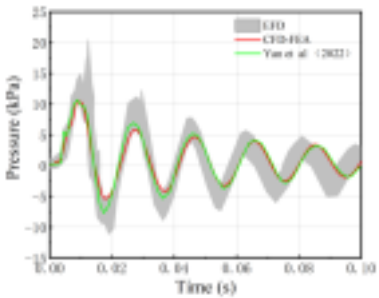
Table 4 Case set up.

Case	Impact velocity (m/s)
Case 1	0.519
Case 2	0.782
Case 3	1.041

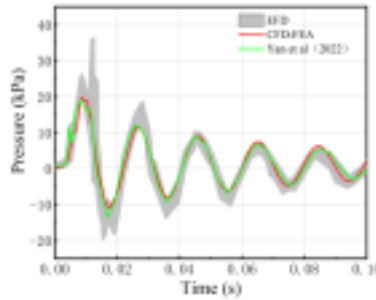
Table 5 Validation of peak slamming pressure for rigid plate at P1.

Case	CFD (kPa)	EFD (kPa)	Error
Case 1	16.17	17.05	5.2%
Case 2	38.89	37.96	2.4%
Case 3	68.68	67.88	1.2%

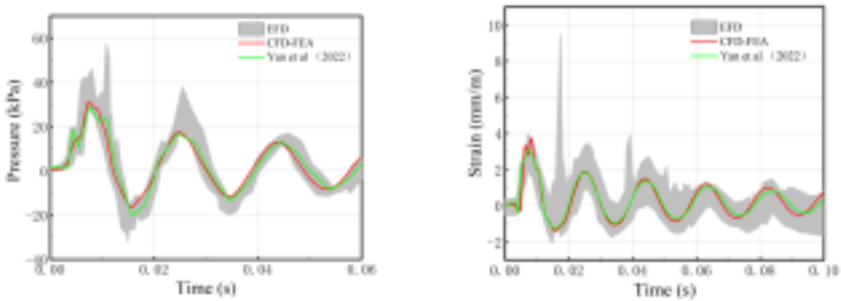
This study compares the slamming pressure time histories at point P1 for the elastic plate under three entry conditions against experimental and literature data. As shown in Figure 8, initial peak pressures differ substantially from experiments, with first-peak discrepancies potentially exceeding 50%, and the overall vibration frequency is lower than measured. Nevertheless, agreement with literature is good, with a maximum error of 6.5% for Case 3. The discrepancies are attributed to differences in equivalent structural stiffness: greater deformation—i.e., lower stiffness—dissipates more energy and yields lower peak pressures. In the experiments, the top constraints likely increased the equivalent stiffness and reduced trapped air, so in later stages where deformation is smaller the pressure peaks align closely. Compared with 30 repeated experimental trials, the present numerical results generally fall within the experimental envelope.



Case 1



Case 2



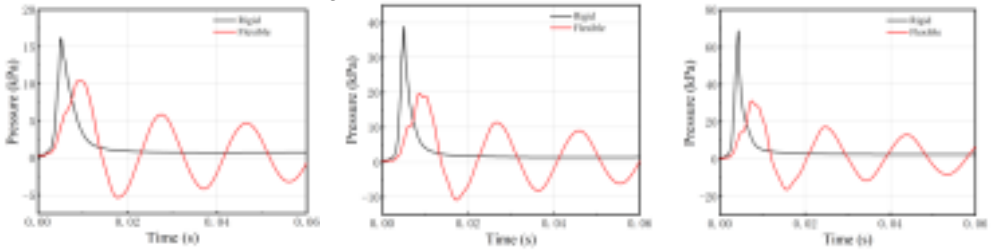
Case 3 Case 3 Strain

Figure 8. Comparison of time histories of flexible flat plate P1 impact pressure and strain.

Figure 8 also compares the strain time history at node S1 for Case 3 with experiments and literature. The peak strain matches the measurements, but a second abnormal peak present in the experiment is absent in the simulation. This stems primarily from trapped air: as the elastic plate rebounds, the entrapped air undergoes secondary compression and generates an extra pressure pulse, consistent with the air-cushion effect described by Verhagen in 1967 and Chuang in 1970. The CFD–FEM model, with its limited two-phase resolution, cannot fully reproduce this mechanism. Transient nonlinear behavior in the experimental boundary conditions and possible excitation of higher vibration modes may also contribute. Despite this, the simulated first-peak amplitude and vibration frequencies agree well with experiments, and the results lie within the scatter band of 30 repeated tests, confirming their overall physical validity.

4.3 Elastic effects

To investigate the influence of hydroelasticity on flat plate slamming, the time histories of slamming pressure at measurement point P1 were compared between rigid and elastic plates under different working conditions. P1 was selected because it is closer to the center of the plate, where stress, strain, and hydroelastic responses are more pronounced. As shown in Figure 9, under the same slamming velocity, the first peak of slamming pressure for the elastic plate lags that of the rigid plate.



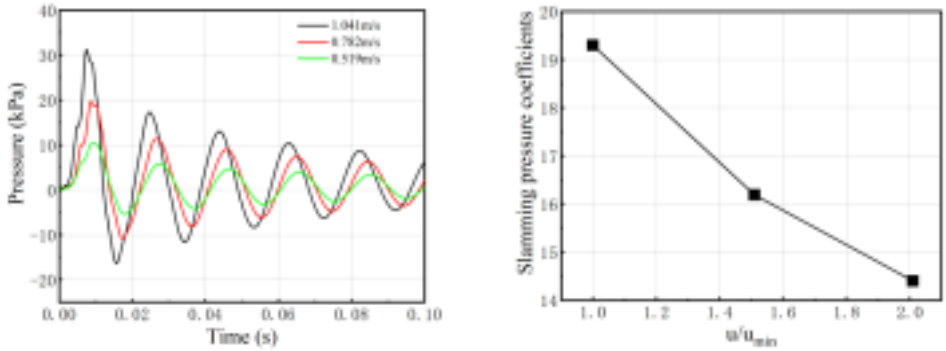
(a) Case 1 (b) Case 2 (c) Case 3

Figure 9. Comparison of time histories of flexible flat plate P1 impact pressure.

It can be observed that the difference in peak slamming pressure between the rigid and elastic plates increases with higher impact velocities, which is closely related to the deformation of the plate. Figure 10(a) presents the slamming pressure time histories at measurement point P1 for the various conditions. During the slamming process, the slamming pressure is primarily derived from the conversion of the impact velocity. When elasticity is considered, the upward and downward vibrational deformation of the plate dissipates part of the impact energy, thereby reducing the peak slamming pressure.

Figure 10(b) compares the slamming pressure coefficients corresponding to the first pressure peak at point P1 across the different working conditions. The slamming pressure coefficient is given by the formula $K = \frac{p_m}{0.5\rho v_m^2}$, where p_m is the slamming pressure, v_m is the slamming velocity, and ρ is the fluid density. The horizontal axis represents the dimensionless slamming velocity, where u_{min} = 0.519

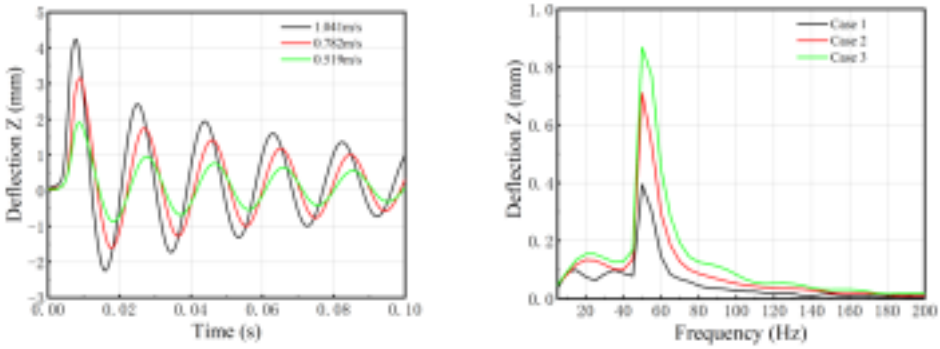
m/s. The slamming pressure coefficient for the flat plate decreases as the slamming velocity increases, and this relationship is not linear, reflecting the nonlinear characteristics of the slamming process.



(a) Time histories of slamming pressure at P1 (b) Variation of slamming pressure coefficients

Figure 10. Time histories of slamming pressure and slamming pressure coefficients.

Figure 11(a) compares the deformation time histories at measurement point P1 under different conditions. It can be observed that the differences in deformation across different conditions are primarily determined by the velocity. The time-history curves are further analyzed using the Fast Fourier Transform (FFT), as shown in Figure 11(b). The results indicate that the dominant frequencies for all three cases are around 50 Hz, which is close to the first-order wet natural frequency (53 Hz) reported in the literature. Additionally, due to the three-layer fixed boundary configuration, the presence of higher-order components during the plate slamming process is minimal.



(a) Time histories of deflection at P1 (b) Frequency analysis of deflection at P1

Figure 11. Comparisons of time histories frequency analysis of deflection at P1.

As mentioned above, the influence of elasticity on slamming pressure primarily stems from the loss of impact velocity caused by the vertical deformation of the plate structure under slamming pressure. The following analysis compares the slamming pressure time history at measurement point P1 with the deformation time history of the plate at the same point under case 3. As shown in Figure 12, it can be observed that the oscillation period of the slamming pressure aligns with that of the deformation oscillation.

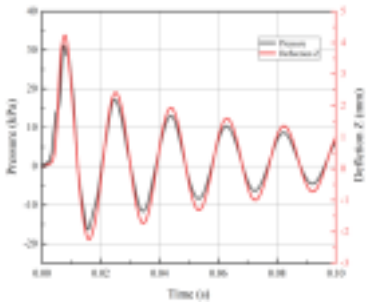


Figure 12. Time histories of impact pressure and deflection of P1.

High-speed water entry generates instantaneous and extremely high slamming pressures. When evaluating hydroelastic structural responses, it is necessary to consider two-way coupling. If these extreme pressures are directly applied to the structure in a quasi-static manner., through one-way coupling may lead to significant overestimation of structural response. Here, the Dynamic Amplification Factor (DAF) by Malenica et al. (2022) is introduced to investigate the necessity of two-way coupling. The DAF is a ratio that quantifies the amplification of the structural response under dynamic loading relative to the equivalent static loading. In this section, it is defined as the maximum Z-direction deformation at measurement point P1 under quasi-static loading:

$$\omega_{max} = \beta \frac{qa^4}{Eh^3} \tag{6}$$

With β = 0.0138, q taken as the peak rigid-body slamming pressure at P1, a = 300 mm, h = 4.7 mm, and E = 2800 MPa, Figure 13 shows $DAF = \omega_{p1max}/\omega_{max}$ versus t_w/t_l — the ratio of load duration to the first structural natural period (53 Hz). Here ω_{p1max} is the maximum deformation from Figure 11(a), and t_w is half the slamming pressure duration from onset to the first peak's return to zero, as marked in Figure 10(a). Three regimes are identified: impulsive (DAF < 1 due to structural inertia filtering), dynamic (DAF amplifies response), and quasi-static (DAF ≈ 1, one-way coupling adequate). As entry velocity increases, pressure duration shrinks and DAF decreases. Neglecting elasticity overestimates the slamming load, while a quasi-static approach overestimates structural response; therefore, two-way hydroelastic coupling is essential.

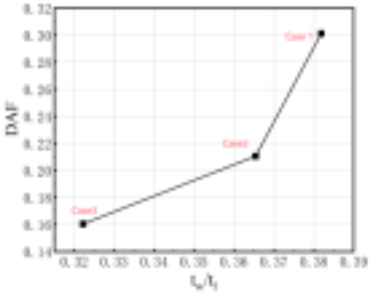


Figure 13. Distribution of different cases' DAF at P1.

Figure 14 presents the deformation contour maps of the plate and the temporal and spatial evolution of the fluid pressure field around the plate at identical time instants over 1 slamming cycles during the plate's water entry. As can be seen from the figure, in the initial stage of slamming, most areas of the plate have not yet undergone deformation. As the slamming pressure region expands, deformation begins to develop near the center of the plate. Moreover, the moment when the slamming pressure reaches its peak at the plate center essentially coincides with the moment of peak deformation, which is consistent with the observations from Figure 13.

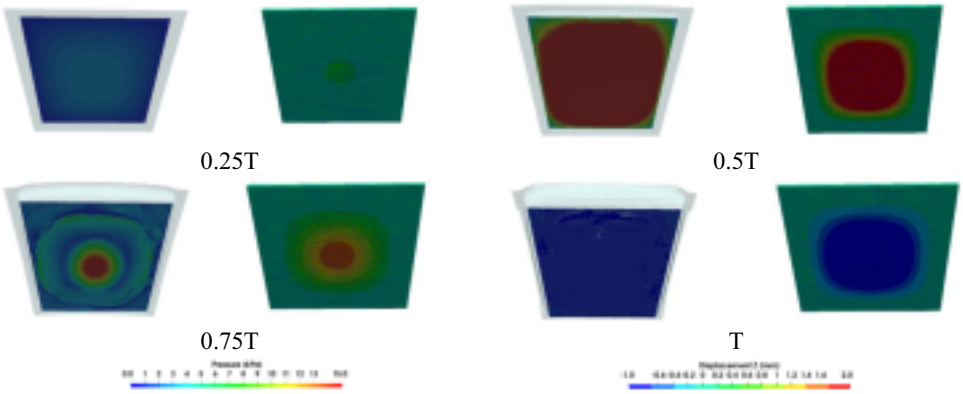


Figure 14. The evolution of impact pressure and deflection of Case 3.

5. Conclusions

This study simulates the constant-velocity water entry of a three-dimensional elastic flat plate, validating the proposed CFD–FEM method. The main conclusions are:

The method is applicable to such slamming problems. Maximum errors in slamming pressure at P1 are 5.2% for the rigid plate and 6.5% for the elastic plate, while the maximum strain error at S1 is 5.8%. The simulated flow and structural evolution agree well with experiments.

Hydroelastic effects are significant. The Dynamic Amplification Factor (DAF < 1) quantitatively demonstrates that when the load duration is far shorter than the structural natural period, structural inertia produces a pronounced filtering effect on extreme slamming pressure peaks. This is primarily caused by a deformation-induced local inclination angle that reduces tangential velocity and thus attenuates the pressure. The slamming pressure coefficient decreases with increasing water-entry velocity, and plate deformation correlates positively with the local inclination angle.

The slamming exhibits clear three-dimensional effects. Pressure decreases from the plate center toward the edges because the deformation-induced inclination angle is smaller near the center, resulting in less tangential velocity loss and a smaller pressure reduction.

Acknowledgements

This work was supported by the National Natural Science Foundation of China (52471335, 52131102), to which the authors are most grateful.

References

[1] S. Chuang. *Experiments on flat-bottom slamming. Journal of Ship Research,* 10: 10-17. 1966.
[2] S. Chuang. *Investigation of impact of rigid and elastic bodies with water.* David Taylor Naval Ship Research and Development Centre. 1970.
[3] S. Malenica, S. Seng, L. Diebold, Y.M. Scolan, A.A. Korobkin, T. Khabakhpasheva, *On three dimensional hydroelastic impact.* 9th International Conference on Hydroelasticity in marine technology Rome, Italy. 2022
[4] J. Xiao, C. Liu, B. Han, D. Wan, J. Wang, *A two-way coupled fluid–structure interaction method for predicting the slamming loads and structural responses on a stiffened wedge*, Physics of Fluids, 36, 077123 2024.
[5] J. Xiao, X. Wen, J. Wang, D. Wan, *Two-Way Coupled CFD-FEA Method for Dam-Break Flows Impacting on the Elastic Beam*, International Journal of Offshore and Polar Engineering, 35(2): 168–176 2025.
[6] J. Kvalsvold, O. M. Faltinsen. *Hydroelastic modeling of wet deck slamming on multihull vessels.* Journal of Ship Research, 39(03): 225-239. 1995.

[7] K. Mori. *Response of the bottom plate of high-speed crafts under impulsive water pressure.* J Soc Nav Archit Jpn 142:297–305. 1977.

[8] S. Tavakoli, T. Mikkola, S. Hirdaris. *A fluid−solid momentum exchange method for the prediction of hydroelastic responses of flexible water entry problems.* Journal of Fluid Mechanics 965, A19. 2023.

[9] D. D. Truong, B. S. Jang, C. E. Janson, J.W. Ringsberg, Y. Yamada, K. Takamoto. *Benchmark study on slamming response of flat-stiffened plates considering fluid-structure interaction*. Marine structure 79, 103030. 2021.

[10] J. H. G. Verhagen. *The impact of a flat plate on a water surface.* Journal of Ship Research, 11(04): 211-223. 1967.

[11] W. Zhang, J. Wang, H. Guo, Y. Liu, D. Wan, *Numerical investigations of ship hydroelasticity of a 20,000 TEU containership based on CFD-MBD method,* Ocean Engineering, 317: 120061. 2025.

[12] W. Zhang, Y. Zhuang, D. Wan, J. Wang, *Hydroelastic performance of an ultra-large containership in irregular and freak waves*, Physics of Fluids, 37, 027190. 2025.

[13] H. Xie, H. Ren, S. Qu, H. Tang. *Numerical and experimental study on hydroelasticity in water-entry problem of a composite ship-hull structure.* Composite Structures 201, 942–957. 2018.

[14] H. Xie, H. Ren, H. Li, K. Tao. *Quantitative analysis of hydroelastic characters for one segment of hull structure entering into water*. Ocean Engineering 173, 469–490. 2019.

[15] Y. Yamada, K. Takamoto, T. Nakanishi, M. Chong, Y. Komoriyama. *Numerical study on the slamming impact of stiffened flat panel using ICFD method: effect of structural rigidity on the slamming impact.* In: International Conference on Offshore Mechanics and Arctic Engineering, 84331. American Society of Mechanical Engineers. V02BT02A006. 2020.

[16] D. Yan, T. Mikkola, A. Lakshmynarayanan, S. T¨odter, T.E. Schellin, J. Neugebauer, B. Ould el Moctar, S. Hirdaris. *A study into the FSI modelling of flat plate water entry and related uncertainties.* Marine Structures 86, 103296. 2022.

10th International Conference on HYDROELASTICITY IN MARINE TECHNOLOGY
Trondheim, Norway, June16th-18th, 2026

Hydroelastoplasticity Effects on Water Impact Loads

Tödter, S.[1,*] Linde, J.[1], Neugebauer, J.[1], and el Moctar, O.[1]

[1] University of Duisburg-Essen, Institute of Sustainable and Autonomous Maritime Systems, Duisburg, Germany

Abstract. The assessment of water impact loads on seagoing vessels and watering aircrafts is crucial for their structural design. However, there are barely no studies analysing the influence of hydroelastoplasticity on impact loads. In the presented study, flat plate impact tests with 0° inclination against the calm water surface were carried out using test specimens which were almost rigid, elastic and plastically deformable under the considered test conditions. An impact velocity of $1.0\,\mathrm{ms}^{-1}$ was used. The tests were performed in a controlled manner, allowing to keep the velocity constant during the water impact and to measure the integral impact forces. Additionally, deformations occurring during the water impacts were measured by Digital Image Correlation and plastic deformations were quantified by a laser scanning technique. The measurement results highlight significant influences of the mechanical properties of the test specimens, i.e. whether they are rigid, elastic, or plastically deformable, on the water loads, structural responses and the distribution of trapped air.

Key words: *Hydroelastoplasticity; Hydroelasticity; Water Impact Experiments; Digital Image Correlation; Laser Scanning Technique; Fluid-Structure Interaction*

1. Introduction

Water impacts are critical processes, which have to be considered in a wide range of engineering fields ranging from naval architecture to aerospace application (see Seddon and Moatamedi [1]). Resulting impact-induced loads are highly dynamic, differ spatially and introduce vibrations or affect the structural integrity of the impacting structure. The slamming phenomenon was studied for decades in the context of maritime application but still lacks details to be understood completely (Kapsenber [2]; Dias and Ghidagli [3]). Kapsenberg highlighted the complex nature of the local phenomenon emphasizing the influence of air cushioning and bubbles in the fluid. This effect becomes most prominent at small deadrise angles where impulse forces are the largest.

A long history of studies considered local impact loads originating from the initial work of von Karman [4]. Subsequently, investigations focused on the water impact of rigid bodies at small deadrise angles as it can be found for example in Tenzer et al. [5], El Malki Alaoui et al. [6] and Wang et al. [7]. Huera-Huarte et al. [8] systematically decreased the deadrise angle. When the deadrise angle approaches 0 deg, the cushioning effect of trapped air, damping the impact loads, becomes important (Verhagen [9]; Lewison and Maclean [10]).

Consequently, Okada and Sumi [11] divided water impacts into three categories: Flat water impacts at 0 deg deadrise angle, water impacts having deadrise angles larger than 3 deg, and the intermediate region. They also emphasized that the load cushioning effect of trapped air was amplified for hydroelastic water impacts. Tödter et al. [12] showed how hydroelasticity damps impact loads and changes the distribution of trapped air. Here, a ring of trapped bubbles was formed and oscillated in phase with structural response of the plate at the plate's wet natural frequency.

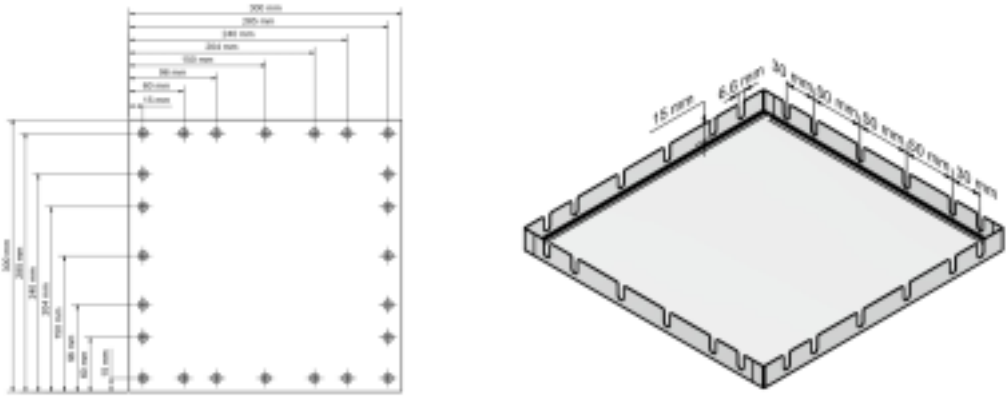
*Correspondence to: simon.toedter@uni-due.de

However, water impact loads often do not only induce elastic vibrations but induce plastic deformation, affecting the structural integrity of ships and ditching aircraft (Jones [13]). Henke [14] used a finite-difference method to simulate elasto-plastic deformations of plates. Liu et al. [15] simulated the impact of a flat stiffened aluminium panel and modelled the resulting plastic deformations. Zhu et al. [16] performed drop tests using thin steel plates. They measured the material properties as well as impact-induced pressures, strains and deflections. They also compared the measurements with numerical simulations using LS-DYNA.
Abrahamsen et al. [17] performed drop tests using a cantilever impacting on a water surface. They used Digital Image Correlation (DIC) to measure plate deformations, and captured the air trapping underneath the plate. Measured plastic displacements were compared with an analytic approach, which matched favourably. Yu et al. [18, 19] developed an analytic model to quantify slamming-induced hydroplastic deformations, and used Arbitrary Lagrangian Eulerian (ALE) methods to validate their model through simulations. Seo and Shin [20] performed repetitive impact tests using large-scale cylindrical and wedge-shaped test bodies and measured impact pressures as well as commutative deformations. Katsuno and el Moctar [21] used two-way coupled simulations to model hydroelastoplastic fluid-structure-interactions during helicopter ditching. The study focussed on deformations of the helicopter's landing gear.
The literature review shows that only few studies on hydro-elastoplastic impacts were carried-out by means of physical testing. Those studies were drop tests, making measurements of the force on the impacting test specimens impossible. Further on, the velocity of test specimens changes inevitably during drop tests, which introduces additional uncertainty for the validation of numerical studies. In the present study, we performed water impact tests with constant impact velocity. The test specimens were designed in a manner to experience hydroelastic and hydroelastoplastic deformations during water impact. Hydrodynamic impact forces as well as elastoplastic and plastic deformations were measured. Impact loads, structural displacements and air trapping were compared for rigid, hydroelastic and hydroelastoplastic impact cases.

2. Experimental setup

2.1. Test case description

Two different materials were employed in the physical testing campaign. Test results are compared with published data from rigid water impact tests by Tödter et al. [12]. The first test plate was made of polyoxymethylene (POM) type C plate with a thickness of 3 mm, representing the elastic test specimen. The second plate type was made of titanium zinc (EN 988) with a thickness of 0.5 mm and represented the plastically deformable test specimens. The specified material thickness tolerance was ± 0.03 mm. However, the actual material thickness was not monitored. Since the plastic deformations could not be reversed, one titanium zinc plate had to be used for each test repetition. Thus, ten plates were manufactured out of the same titanium zinc sheet. The material properties of titanium zinc were quantified performing tensile tests according to DIN EN ISO 6892-1. The tests were repeated three times to evaluate mean values. Consequently, the resulting mean Young's modulus was $E = 98$ GPa, the mean yield stress was $R_{p0.2} = 162$ MPa, the mean tensile strength was $R_M = 193.3$ MPa and the mean fracture strain was $\epsilon_B = 18\,\%$. Those properties differ significantly from literature values, which emphasizes the importance to quantify actual material properties.
The test specimens were mounted to an aluminium frame to carry out water impact tests. The flat POM plate was mounted to the frame's bottom using M4 countersunk screws, while the screws were covered with wax to provide a smooth surface. The screw arrangement as well as the plate dimensions are drawn in Figure 1a. The frame had an outer dimension of 300 x 300 mm^2, an inner dimension of 260 x 260 mm^2 and a thickness of 25 mm. Thus, the inner 260 x 260 mm^2 of the mounted plates were free to deform.
The titanium zinc plates were bent to be flush-mounted inside the frame. The horizontal parts of the



(a) (b)

Figure 1: Design of the POM (a) and titanium zinc (b) test specimens

plates had a length and width of 258 mm. An inner radius of 1 mm was applied to bend the plates. The corners of the plates were not closed, allowing water to enter onto the plate. However, the time duration required for water to flow through the tiny openings was much longer than the water impact duration itself. Thus, entering water did not influence the plate behavior during water impact. The bent plate is displayed in Figure 1b.

Figure 2 depicts the detailed mounting of a titanium zinc sheet (blue) inside the frame. The design was initially inspired by the setup used by Abrahamsen et al. [17]. The bent titanium zinc plate was fixed by pressing four brackets, mounted by screws, against the inside of the frame with the vertically bent flange in between. Aluminium walls were mounted on top of the frame to prevent water from entering onto the test specimen. Using this setup, the inner plate area of 249 x 249 mm^2 was free to deform inwards and outwards.

To quantify the natural frequencies of the specimens, hammering tests were performed in air. Those hammering test were also performed for the test specimen used by Tödter et al. [12]. The titanium zinc test specimens could not be subjected to hammering tests in water because the specimens would have to remain submerged for a significant amount of time and water consequently flowing onto the specimens during that time would have significantly influenced the natural frequency of the specimens. For POM, the dry and wet natural frequencies were 88.35 and 27.5 Hz, respectively. The titanium zinc plate had a lower natural frequency of 63.2 Hz, while the natural frequency of the aluminium plate was 1758.9 Hz.

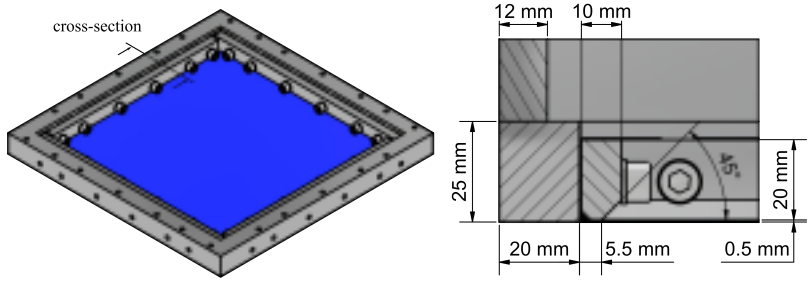


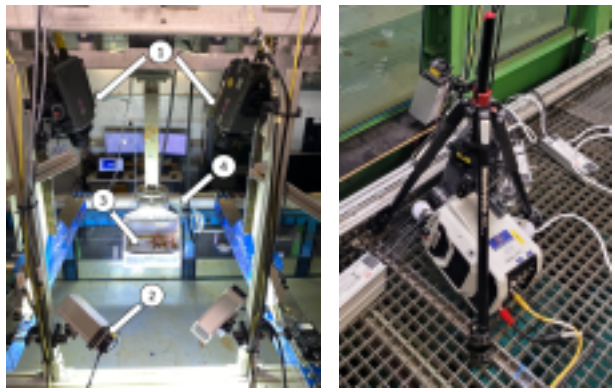
Figure 2: Mounting of the titanium zinc test specimens

2.2. Test facility and instrumentation

The water impact test facility consisted of a vertically traversing platform, driven by an electric motor, guiding rails, a load cell, mounted on a vertical beam underneath the platform, and a test body, containing the test specimen mounted below the load cell. A control loop maintained a constant velocity during the water impacts. The test facility was placed over a water basin having a length of 6 m, a width of 1.5 m and a water depth set to 378 mm.
A magnetostrictive position sensor of type Balluff BTL5 measured the position of the platform with a resolution of 4 μm and a sampling rate of 1 kHz.
Integral push and pull forces on the test specimens were measured using a load cell of type HBM U3/10, which had a measuring range of up to 10 kN. A PCB 353B34 mono-axial ICP accelerometer measured dynamic accelerations in the vertical direction up to 4905 ms^{-2}. All sensor signals were acquired by coupled and synchronised QuantumX MX410B data acquisition systems. The data acquisition systems had a resolution of 24 bit for analogue/digital-conversion, allowing a sufficient resolution of highly dynamic sensor readings. A sampling rate of 96 kHz was used to acquire force and acceleration signals. Tenzer et al. [5] showed that this sampling rate is sufficient to accurately capture impact peak loads at the studied impact conditions. A trigger signal generated by the test device was used to synchronise the impact tests with the data acquisition system and the optical measurement systems.

2.3. Optical displacement measurements and high-speed imaging

Elastoplastic displacements of the test specimens during water impact were measured using the optical measurement technique Digital Image Correlation (DIC). Figure 3a shows the setup for DIC measurements. Two high-speed cameras (1) of type phantom v9.1 recorded a speckle pattern (3) applied to the inner surface of each test specimen (4). Multiple LED spotlights (2) illuminated the field of view (FoV). The cameras' sampling rates were set to 3300 fps capturing a field of view of 263.7 x 212.5 mm^2 at a resolution of 3.32 pixel/mm. For the spatial calibration, a calibration plate was placed at multiple positions, taking the plate's motion in the cameras' depth-of-field direction into account. The fitting error of the calibration was 0.1364 pixel.
A phantom v2012 high-speed camera, which is shown in Figure 3b, was used to record the air trapping below the test specimens. The camera's frame rate was set to 50000 fps at a resolution of 768 x 480 pixels. The exposure time was set to 17.7 μs to avoid motion blur.



(a) (b)

Figure 3: Setup for Digital Image Correlation measurements (a) and high-speed imaging (b)

It was not possible to use DIC to measure plastic deformations, because splashing water blocked the camera view before the elastic components of the deformations decayed completely. Thus, plastic deformations of the titanium zinc test specimens were measured by performing laser scans of each test specimen before and after the impact test. A 3D scanner of type Creaform peel 3 was used to measure the geometry of the test specimen and to digitally reconstruct the test specimen. The scanner had a volumetric uncertainty of 0.05 mm.

2.4. Test procedure and data processing

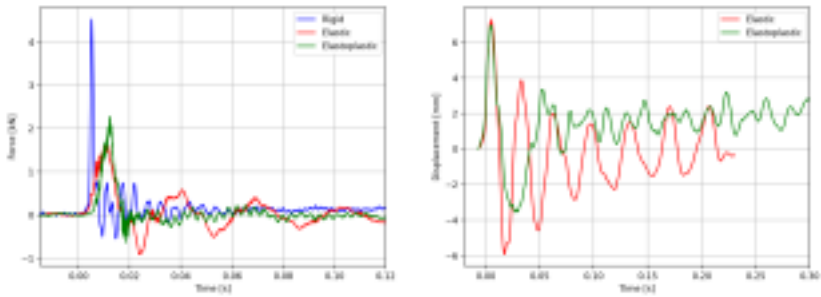
Impact-induced loads tend to scatter at small impact angles due to free-surface roughness and liquid fragmentation during air escape (Dias and Ghidaglia [3]). Thus, repetitive impact tests were required to statistically analyse the impact loads. Here, impact tests were repeated thirty times for the rigid impact case, five times for the hydroelastic impact case, and ten times for the hydroelastoplastic water impact case. To ensure a sufficient test repeatability, ambient conditions had to be identical for each test run. The water surface was calm and smooth. Each test specimen subjected to plastic deformations was used only once. Thus, a new and dry test sample was used for each impact test in which hydroelastoplasticity occurred. Each impact process consisted of the same travel distance, the same velocity of $1.0\,\mathrm{ms}^{-1}$ as well as identical acceleration and deceleration phases of the test rig. The actual mean impact velocities of the rigid, hydroelastic and hydroelastoplastic test cases were 1.041, 0.998 and $1.003\,\mathrm{ms}^{-1}$, having standard deviations of 0.013, 0.002 and $0.004\,\mathrm{ms}^{-1}$, respectively. The influence of external conditions on impact loads were previously evaluated by van Nuffel et al. [22]. The findings of the study were followed to maximise the test accuracy.
The test samples' positions, the forces acting on the test specimens and vertical accelerations of the test specimens were measured during each test run. The velocity of each test specimen was quantified using the time derivative of the position signal. To determine the hydrodynamic force, the measured force was corrected by the buoyancy force and the inertia force, consisting of the test specimens' mass and acceleration. Additionally, DIC was used to measure elastoplastic displacements during water impacts. To get the elastoplastic deformations, DIC measurements were corrected by the global test specimen's motion recorded by the position sensor.
The plastic deformation was quantified by comparing the scans of a test specimen prior and after the water impact. A best-fit algorithm was applied, using the commercial software VXelements 11, to map both scans onto each other. This algorithm minimised the sum of all displacements. Thus, it decreased actual displacements at the plate's centre and increased displacements at the rigid frame, where no plastic deformations occurred – compare Figure 6a. However, considering that no plastic deformations occurred at the frame allowed to correct the displacements evaluated by the best-fit algorithm.

3. Results

The results of the tests using the three different test specimen types, one behaving rigid, one deforming only elastically and the last, allowing for elastoplastic deformations, were compared. The comparison considered the peak forces and displacements during the impact, the evolution of the force and displacement time histories as well as the characteristic distribution of trapped air. Additionally, the plastic deformation resulting from the water impact case was analysed. During discussion of the results, tests and results obtained using the rigid test specimen are referred to as *rigid case*. In the same manner, tests and results obtained using the test specimens allowing elastic and elastoplastic deformations are referred to as *elastic case* and *elastoplastic case*, respectively.

Figure 4 plots the force (a) and displacement (b) time histories recorded for one water impact. The force signal of rigid case shows a distinct sharp peak at 4.53 kPa. In contrast, the force time histories of the elastic and elastoplastic cases had longer peak durations but reached lower peak forces of 1.65 and 2.29 kN, respectively. After the peak, the force of the rigid case oscillated for three periods within 0.02 s

before decaying. The hydroelastic case oscillated with a frequency of approximately 29 Hz, which was close to the plate's wet natural frequency. In contrast, the force signal of the hydroelastoplastic case did not exhibit oscillations of higher amplitude, but instead showed high-frequency vibrations that decayed after 0.1 s. Graph b of Figure 4 depicts the time histories of the displacement at the position $x = 150$ mm and $y = 165$ mm of the hydroelastic and hydroelastoplastic cases. The first displacement peak of the hydroelastic reached a value of 7.3 mm. Subsequently, the displacement oscillated around the plate's initial position with decaying amplitudes up to 4.6 mm and a frequency that matched the force oscillation frequency. The displacement evolution of the hydroelastoplastic case exhibits a very similar shape of the first peak, with a peak value which is slightly lower at 6.94 mm. However, the displacement signal shows a sudden change of the displacement decay rate at $t = 0.005$ s, which might result from plastic deformation. Subsequently, the plate deformed convexly once and then remained concavely deformed, oscillating around the plastic displacement amplitude of 1.84 mm. The oscillation did not have a dominant frequency for this case.

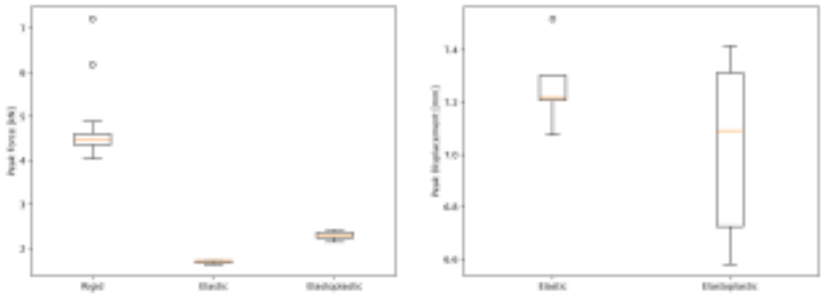


(a) (b)

Figure 4: Time histories of impact force (a) and displacement (b) during water impact

Figure 5 depicts the distribution of peak displacements and peak forces resulting from the three impact cases. The rigid, hydroelastic and hydroelastoplastic cases were repeated thirty times, five times, and ten times, respectively. The peak forces of the rigid case exhibits the highest scattering, with a standard deviation of 0.6 kN. Both other impact cases showed highly repeatable peak forces, having standard deviations of less than 0.18 kN. Peak forces of the hydroelastic and hydroelastoplastic cases are significantly lower compared to the rigid case. For the rigid case, a median peak force of 4.48 kN was reached, while the hydroelastic case reduced the median peak force down to 1.7 kN. However, the hydroelastoplastic case generated a higher median peak force of 2.2 kN compared to the hydroelastic case. This indicates that plastic deformations reduced the capability to cushion impact loads.

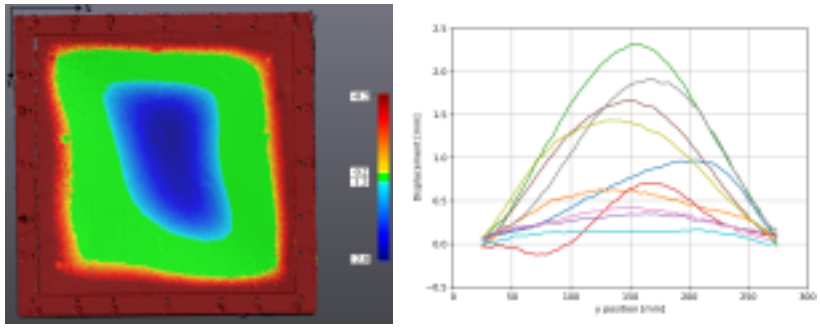
The comparison of the distribution of peak displacements shows an increased scatter for the hydroelastoplastic case. While median peak displacements were similar at 7.22 and 7.09 mm, standard distributions for the hydroelastic and hydroelastoplastic cases were 0.15 and 0.33 mm, respectively.
Plastic displacements were evaluated by comparing two laser scans, performed prior and after each impact test. Figure 6a depicts the spatial distribution of plastic displacements of a titanium zinc test specimen mounted inside the rigid frame. Positive displacements represent a concave plate deformation when observed from below the test body (i.e. the center of the bottom plate buckles away from the observer and towards the inside of the test body). The displacements were not corrected regarding the error induced by the best-fit mapping method, yet. Thus, plastic displacements were up to -0.2 mm at the rigid frame. However, maximum plastic displacements occurred at the plate's centre. This is also the case for plastic displacements in the plates' cross-section at $x = 150$ mm, presented in Figure 6b. The maximum plastic displacement occurred at the plates' centre in eight out of ten test runs. Those tests ex-



(a) (b)

Figure 5: Distribution of peak forces (a) and peak displacements (b) during water impacts

hibit that the plastic displacement is completely convex within the considered cross-section. One test run caused a different deformed shape with both, plastic convex and concave displacements, appearing like a sine shape. The other test run depicts a displacement maximum, which is significantly shifted towards the edge of the test specimen at a higher y-position (dark blue curve). Overall, the maximum plastic displacement scattered significantly. The plastic displacements at the plates' centre were between 0.14 and 2.3 mm. Recall, that all test specimens were manufactured from the same sheet to avoid influences of material thickness tolerances. For two test runs, the low plastic displacement could be explained by the fact that the plate was partially displaced in convex and concave direction balancing maximum displacements.



(a) (b)

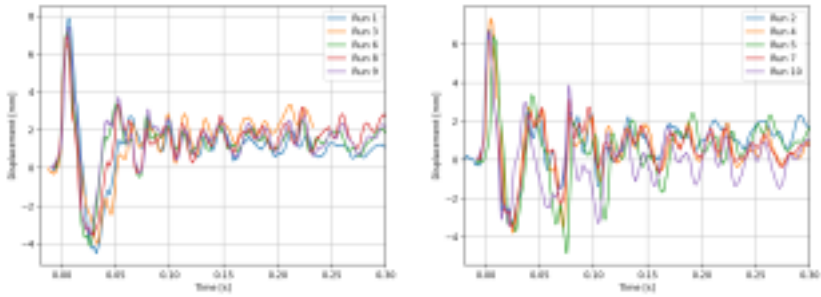
Figure 6: Spatial distribution of plastic deformations for one test run (without correction of the best-fit mapping) (a) and plastic deformations along the cross-section at $x = 150\,\text{mm}$ of the repetitive impact test (b)

Table 1 lists the plastic deformations at the centre of the plates for all test runs. Based on the plastic displacements, the test runs could be classified into two groups. The first group consists of those test runs causing plastic deformations larger than 0.7 mm. The second group contains the residual test runs. Figure 7 plots the time histories of displacements during water impacts for both groups. Both groups show similar peaks of similar magnitudes and identical durations. Differences occur subsequently to the peak. For the group causing higher plastic deformations, the plate remained concavely deformed after one convex deformation. Here, the displacement oscillated around the plastic displacement amplitude. For the other group, displacements oscillated around the initial plate displacement of 0 mm after the

peak. This resembled the hydroelastic water impact case. However, there is no dominant oscillation frequency. This emphasizes that plastic deformation is a result of the peak impact load. Further on, plastic deformations influenced the evolution of forces and structural responses after their highest peak. For water impacts of flat plates without inclination against the calm water surface, the cushioning effect of trapped air has a significant influence on impact loads and structural responses. Thus, the air trapping was recorded for the three test cases. For the rigid case, an air pocket was observed below the plate's centre. This air pocket was compressed with increasing immersion depth of the test specimen. The pocket remained at the plate's centre even after the test body motion was stopped. For the hydroelastic case, there was an air pocket below the plate's centre at the impact. As the plate started to subsequently oscillate and deformed convexly, the air pocket reshaped into a ring of bubbles, surrounding the convexly deformed part of the POM plate. The bubble ring oscillated at the plate's wet natural frequency, in synchrony with the force and plate displacement. Meanwhile, the bubble ring's diameter expanded, and the ring fell apart during the subsequent process.

Table 1: Plastic displacements at the plate centre of all test runs

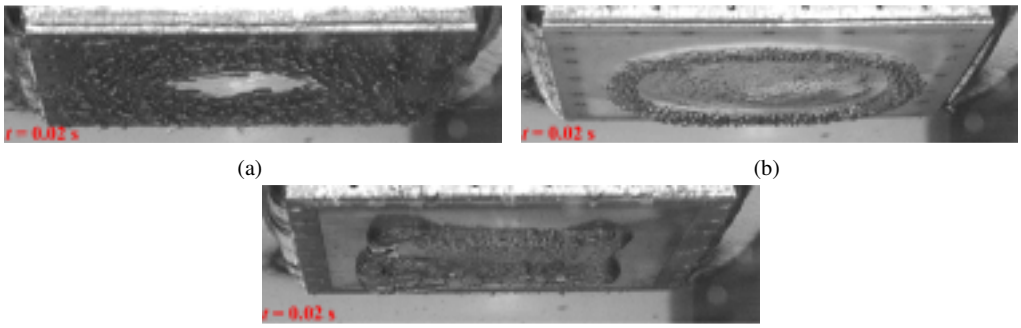
Test run	1	2	3	4	5	6	7	8	9	10
Displacement [mm]	0.764	0.619	2.302	0.632	0.344	1.659	0.417	1.837	1.417	0.141



(a) (b)

Figure 7: Time histories of displacements of all impact test runs showing maximum plastic deformations above (a) and below (b) 0.7 mm

For the hydroelastoplastic case, an initial air pocket was also trapped at the plate's centre. In contrast to the hydroelastic case, this air pocket exhibited a rectangular shape with rounded corners. The air pocket was afterwards transformed into a bubble ring structure, resembling the shape of the previously trapped air pocket. Subsequently, the bubble ring structure did not oscillate, but its size expanded asymmetrically with increasing immersion depth of the test specimen. Finally, the ring structure fell apart as well. Figure 8 depicts images, depicting the characteristic distribution of trapped air below the test specimens for the three test cases at a time instance of 0.02 s after the first contact between the test specimens and the water surface. At this time instance, the generation of the bubble ring structures were completed for the hydroelastic and hydroelastoplastic cases. The different distributions of trapped air have a major influence on the void fraction of the water-air mixture. Consequently, compressibility effects must be considered differently for hydroelastic and hydroelastoplastic water impacts.



(a) (b)

(c)

Figure 8: Images of the bottom of the test bodies, depicting the air trapping for a rigid (a), a hydroelastic (b), and a hydroelastoplastic (c) case, 0.02 s after the first contact of the test specimens with the water surface

4. Conclusion

Water impact tests with test specimens leading to a hydroelastic and hydroelastoplastic behavior were performed to investigate the influence of the different mechanical behavior on the peak loads, structural responses and air trapping. The results were also compared with those resulting from a rigid test specimen. Peak loads were dominant for the rigid case, reaching 198 and 275 % of the peak forces of the hydroelastoplastic and hydroelastic cases, respectively. The slightly higher peak force caused by the hydroelastoplastic case compared to the hydroelastic case indicated that plasticity effects reduced the load cushioning of elastic materials. Subsequently to the peak, the force time history of the hydroelastoplastic case did not show significant oscillations in contrast to the hydroelastic test case.
Peak displacements at the plate centre were similar for the hydroelastic and hydroelastoplastic cases. While displacements of the hydroelastic case oscillated at a frequency close to the plate's wet natural frequency, the elastoplastic test specimen vibrated around the plastic displacement amplitude.
The distribution of trapped air differed for the three investigated cases. For the rigid case, an air pocket was trapped at the plate's centre, being compressed while the test specimen immersed. For the hydroelastic case, the initially trapped air pocket was transformed into an rounded air bubble ring, oscillating synchronously with the plate. The hydroelastoplastic case generated a rectangular air pocket with rounded corners, which transformed into a rectangular bubble ring structure which did not oscillate. The different distributions of trapped air indicated that plasticity effects alter the compressibility effects on impact loads by changing the void fraction of the water-air mixture underneath a test specimen.

Acknowledgments

This study was part of the research project EvoS-BraWa, funded by the Bavarian Ministry of Economic Affairs and the Regional Development and Energy (StMWi) of the Bavarian Aviation Research Program (BayLu25), under grant ROB-2-3410.20-04-10-36 / BLU-2109-0036.

References

[1] C.M. Seddon and M. Moatamedi. Review of water entry with applications to aerospace structures. *International Journal of Impact Engineering*, 32(7):1045–1067, 2006.

[2] G. K. Kapsenberg. Slamming of ships: where are we now? *Philosophical Transactions of the Royal Society A: Mathematical, Physical and Engineering Sciences*, 369(1947):2892–2919, 2011.

[3] F. Dias and J.-M. Ghidaglia. Slamming: Recent progress in the evaluation of impact pressures. *Annual Review of Fluid Mechanics*, 50:243–273, 2018.

[4] T. von Karman. The impact on sea plane floats during landing. Technical Report Technical Note No. 321, National Advisory Committee for Aeronautics, 1929.

[5] M. Tenzer, O. el Moctar, and T. E. Schellin. Experimental investigation of impact loads during water entry. *Ship Technology Research*, 62:47–59, 2015.

[6] A. El Malki Alaoui, A. Nême, A. Tassin, and N. Jacques. Experimental study of coefficients during vertical water entry of axisymmetric rigid shapes at constant speeds. *Applied Ocean Research*, 37:183–197, 2012.

[7] J. Wang, C. Lugni, and O. M. Faltinsen. Experimental and numerical investigation of a freefall wedge vertically entering the water surface. *Applied Ocean Research*, 51:181–203, 2015.

[8] F.J. Huera-Huarte, D. Jeon, and M. Gharib. Experimental investigation of water slamming loads on panels. *Ocean Engineering*, 38(11):1347–1355, 2011.

[9] J. H. G. Verhagen. The impact of a flat plate on a water surface. *Journal of Ship Research*, 11(04):211–223, 1967.

[10] G. Lewison and W. M. Maclean. On the cushioning of water impact by entrapped air. *Journal of Ship Research*, 12(02):116–130, 1968.

[11] S. Okada and Y. Sumi. On the water impact and elastic response of a flat plate at small impact angles. *Journal of Marine Science and Technology*, 5:31–39, 2000.

[12] S. Tödter, O. el Moctar, J. Neugebauer, and T. E. Schellin. Experimentally measured hydroelastic effects on impact-induced loads during flat water entry and related uncertainties. *Journal of Offshore Mechanics and Arctic Engineering*, 142(1):011604, 2019.

[13] N. Jones. Slamming damage. *Journal of Ship Research*, 17(2):80–86, 1973.

[14] D. J. Henke. Transient respone of plates to travelling loads with application to slamming damage. *International Journal of Impact Engineering*, 15(6):769–784, 1993.

[15] B. Liu, R. Villavicencio, K. Liu, L. Zhu, and C. Guedes Soares. Response of an aluminum stiffened plate under extreme slamming loadings. *Journal of Offshore Mechanics and Arctic Engineering*, 141(5):051606, 2019.

[16] Z. Zhu, L. Zhu, K. Guo, and X. Wang. Analysis of saturated impulse for square plates under flat slamming impact: Experimental and numerical investigation. *Journal of Marine Science and Technology*, 12:1730, 2024.

[17] B. C. Abrahamsen, H. S. Alsos, V. Aune, E. Fagerholt, O. M. Faltinsen, and O. Hellan. Hydroplastic response of a square plate due to impact on calm water. *Physics of Fluids*, 32:082103, 2020.

[18] Z. Yu, J. Amdahl, M. Greco, and H. Xu. Hydro-plastic response of beams and stiffened panels subjected to extreme water slamming at small impact angles, part i: An analytical solution. *Marine Structures*, 65:53–74, 2019.

[19] Z. Yu, J. Amdahl, M. Greco, and H. Xu. Hydro-plastic response of beams and stiffened panels subjected to extreme water slamming at small impact angles, part ii: Numerical verification and analysis. *Marine Structures*, 65:114–133, 2019.

[20] B. Seo and H. Shin. Experimental study of slamming effects on wedge and cylindrical surfaces. *Applied Sciences*, 10(4), 2020.

[21] E. T. Katsuno and O. el Moctar. Hydroelastoplasticity in helicopter ditching using strongly coupled two-way fluid-structure interaction. *Aerospace Science and Technology*, 166:110595, 2025.

[22] D. van Nuffel, K.S. Vepa, I. De Baere, J. Degrieck, J. De Rouck, and W. Van Paepegem. Study on the parameters influencing the accuracy and reproducibility of dynamic pressure measurements at the surface of a rigid body during water impact. *Journal of Marine Science and Technology*, 53:131–144, 2013.

10th International Conference on HYDROELASTICITY IN MARINE TECHNOLOGY
Trondheim, Norway, June16$^{\text{th}}$-18$^{\text{th}}$, 2026

Investigation of the Dynamic Response of Elastic Circular Cylinders Subjected to Water Impact

Taussé Kamdoum, F.L.[1], Hascoët, R.[1], El Malki Alaoui, A.[1], and Jacques, N.[1,*]

[1] IRDL, UMR CNRS 6027, ENSTA, Institut Polytechnique de Paris,
Bretagne INP, Univ. Brest, Univ. Bretagne Sud, Brest, France

Abstract. The present paper describes a semi-analytical model and an experimental study of the hydroelastic response of a tubular structure due to a hydrodynamic impact. In the semi-analytical model, the hydrodynamic loading is estimated using a Wagner-type approach, while the structural response is modeled using Euler-Bernoulli's beam theory. The water impact model relies on the Modified Logvinovich Model (MLM) and the Fictitious Body Continuation (FBC) technique proposed by Tassin et al. (2014) to account for flow separation. A modal decomposition technique is used to formulate the impact problem as a system of ordinary differential equations which is solved numerically. The model predictions are compared with experimental results obtained from a dedicated experimental campaign. Experiments were conducted on an aluminium tube using the shock machine of the ENSTA laboratory. The transient response of the beam was monitored using accelerometers and strain gauges mounted at different locations along the tube. A reasonably good agreement was found between the analytical approach and the experiments. The results show that hydro-structure couplings play an important role. In particular, they affect the peak strain reached during the impact and the damping of the subsequent vibration.

Key words: *Hydroelasticity; slamming; hydrodynamic damping; Wagner's theory; Modal decomposition*

1. Introduction

The design of marine structures requires accurate predictions of the hydrodynamic forces they will experience throughout their lifespan. In the case of ships, these forces can cause high-frequency vibrations of the hull, leading to the phenomenon of whipping – see [1, 2]. Due to slamming, the bow experiences a sudden vertical deceleration, resulting in a flexural vibration of the hull beam. This phenomenon can increase the wave-induced stress in the hull by up to 20% [3], creating a risk of failure by exceeding the ultimate strength or by fatigue. This is what happened with the MSC Napoli, where whipping caused a structural rupture near the engine room [4].

Impulsive wave loading and hydroelastic responses are also central for offshore and coastal structures that are largely tubular, such as monopiles and jacket substructures used in offshore wind turbines and fixed platforms. These structures include slender circular members (piles, legs, braces) that may experience steep- and breaking-wave impacts (slamming), leading to short-duration impulses and subsequent structural vibrations that can govern extreme response and contribute to fatigue accumulation. Breaking-wave impacts on slender circular piles have been investigated experimentally and theoretically, showing that the impulsive force history, the effective impact area (often described via a curling factor), and the slamming coefficient are key parameters for design-level load models [5]. For offshore wind turbines, recent studies have further emphasized that the combination of non-linear hydrodynamics and structural flexibility may excite significant modal responses (ringing/whipping-like events), and

*Correspondence to: nicolas.jacques@ensta.fr

that simplified engineering load models may misrepresent the balance between modal contributions [6, 7]. Similarly, for jacket structures, dedicated experimental programs report a large variability of global slamming forces and highlight the need for controlled benchmarks to support load modelling and structural-response prediction [8, 9]. In this context, canonical experiments on instrumented circular cylinders under well-controlled impact conditions are valuable to analyse physical mechanisms (slamming-induced vibration, added mass, hydroelastic damping) that apply to tubular offshore members.

Bereznitski [10] proposed a parameter that indicates the need for considering hydroelastic coupling. This parameter is the ratio between the impact duration from a rigid body water penetration model and the first period of vibration of the dry structure. If this ratio is greater than 2, a hydroelastic approach is not necessary, as the structure response is quasi-static. Faltinsen [11] observed in the case of an elastic wedge entering water that when this parameter is less than 0.25, hydroelastic effects become important and maximum pressure cannot be used to estimate maximum slamming induced stresses. Therefore, neglecting hydroelastic coupling may lead to large errors in the determination of the maximum response of a structure [10].

Various studies have been conducted on predicting the response of elastic structures to hydrodynamic impacts – see [12, 13, 11, 14, 15, 16, 17]. However, due to the complexity of the impact phenomenon and the existence of different interaction regimes, it can be challenging to describe the induced hydroelastic response [18]. As discussed in [19], the development of analytical models and dedicated impact tests for simple configurations and well-controlled impact conditions is of great interest. This is important both for understanding the fluid-structure interaction mechanisms and for validating more complex simulation tools.

The present study is devoted to the investigation of the dynamic response of elastic circular cylinders subjected to water impact, with two mains objectives: (i) to develop a semi-analytical model for this configuration to analyse the influence of hydro-structure couplings; (ii) to carry out experiments for well-controlled conditions to monitor the dynamic response of a tube during a water impact.

2. Hydroelastic response model

2.1. Formulation

The considered water entry problem is represented in Fig. 1. The impacting body is a tube of external radius *R* hinged at one end by a rotational spring of stiffness *K* and free at the other end. The rotational spring was introduced into the model to represent the stiffness of the fastening system used to hold the tube on the machine. The point *M* moves vertically at a velocity $V(t)$ through an imposed motion. The tube is inclined at an angle γ and impacts the free surface of a liquid that is initially at rest. The coordinate system (x, z) is fixed in the laboratory reference frame, with the x-axis coinciding with the initial free surface. The coordinate system $(M, \tilde{x}, \tilde{z})$ is attached to the body. The penetration depth of a section of the tube, denoted as h, is measured perpendicular to the tube, between the plane of the initial free surface and the lowest point of the section (in Fig. 1, h is negative as the section is not submerged yet).

The hydrodynamic loading is modeled using a strip $(2D+t)$ approach. In each strip (associated with a given position $\tilde{x}$), the two-dimensional impact problem is modeled using a Wagner-type model. The tube is modeled as a homogeneous Euler-Bernoulli beam of length L, linear mass density ρ_l, Young's modulus E, and quadratic moment of area I. Let $u(\tilde{x}, t)$ be the transverse relative displacement induced by the beam deformation measured in the frame $(M, \tilde{x}, \tilde{z})$ (see Fig. 1-a), and f_l the force per unit of length acting on the beam (in the $\tilde{z}$ direction). Neglecting material damping, the differential equation governing the beam response may be written as:

$$\rho_l \frac{\partial^2 u(\tilde{x},t)}{\partial t^2} + EI \frac{\partial^4 u(\tilde{x},t)}{\partial \tilde{x}^4} = f_l(t, \tilde{x}, u(\tilde{x},t), \dot{u}(\tilde{x},t), \ddot{u}(\tilde{x},t)) + \rho_l \dot{V}(t) \cos(\gamma). \tag{1}$$

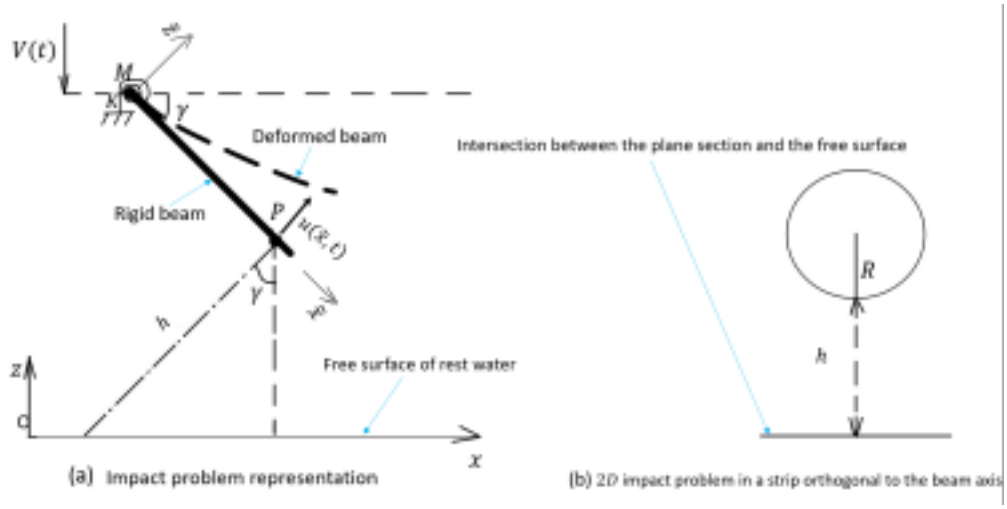


Figure 1: Illustration of the considered impact problem

The following boundary conditions are considered:

$$\begin{aligned} &u(0,t) = 0 \quad \text{and} \quad K\frac{\partial u(\tilde{x},t)}{\partial \tilde{x}}|_{\tilde{x}=0} = EI\frac{\partial^2 u(\tilde{x},t)}{\partial \tilde{x}^2}|_{\tilde{x}=0}, \\ &\frac{\partial^2 u(\tilde{x},t)}{\partial \tilde{x}^2}|_{\tilde{x}=L} = \frac{\partial^3 u(\tilde{x},t)}{\partial \tilde{x}^3}|_{\tilde{x}=L} = 0, \end{aligned} \tag{2}$$

The hydrodynamic load per unit of length f_l depends a priori on the deformation of the structure and thus on $u(\tilde{x},t)$. This dependence gives rise to hydro-elastic coupling. Using a Wagner-type approach, hydro-elastic coupling can be modeled, through a dependence of f_l on the variables u, $\dot{u}$, and $\ddot{u}$, where $\dot{u}$, and $\ddot{u}$ are the first and second time derivatives of u, respectively. The inertia term $\rho_l \dot{V}(t)\cos(\gamma)$ is due to the fact that the beam dynamics is described in a non-Galilean reference frame.

As mentioned previously, the hydrodynamic load on the beam is modeled using a $(2D+t)$ strip approach. In each strip, the hydrodynamic load is modeled using a two-dimensional Wagner-type model. More specifically, the pressure acting on a given section is estimated using the Modified Logvinovitch Model (MLM) [20]. Flow separation (associated to the formation of a cavity behind the section at large penetration depths) is treated using the Fictitious Body Continuation (FBC) concept [21]. In this framework, the hydrodynamic force per unit length on a section of the tube, with outer radius R and section area $S = \pi R^2$, can be written as:

$$f_l = \rho_f R C_s(h/R) w^2 + \rho_f S C_a(h/R)\dot{w}\,, \tag{3}$$

where ρ_f is the mass density of the fluid. C_s and C_a are respectively the slamming and added coefficients computed using the MLM-FBC model. The first term of the right-hand side of Eq. (3) is a slamming term which is proportional to the square of the penetration velocity w, and the second term is the added-mass term, which is proportional to the acceleration $\dot{w}$. The penetration velocity projected onto the plane of the cross section, w, and the penetration depth, h, can be written as:

$$w(t,\dot{u}(\tilde{x},t)) = v(t) - \dot{u}(\tilde{x},t)\,, \tag{4}$$

$$h(\tilde{x},t,u(\tilde{x},t)) = h_0(\tilde{x},t) - u(\tilde{x},t)\,, \tag{5}$$

with $v(t) = V(t)\cos(\gamma)$ and h_0 being the penetration depth of the non-deformable tube. The evolution of the slamming (C_s) and added-mass (C_a) coefficients as a function of h is shown in Fig. 2, where experimental results from the literature derived from the works of [22, 23] are also presented for C_s .

Considering Eqs. (3-5) and adopting the following notation

$$\begin{aligned}\rho_a(\tilde{x},t) &= \rho_l + \rho_f S C_a(h_0(\tilde{x},t) - u(\tilde{x},t)),\\ \rho_s(\tilde{x},t) &= \rho_f R C_s(h_0(\tilde{x},t) - u(\tilde{x},t)),\end{aligned} \tag{6}$$

Eq. (1) can be rewritten in the following form:

$$\frac{\partial^2 u(\tilde{x},t)}{\partial t^2} + \frac{EI}{\rho_a(\tilde{x},t)}\frac{\partial^4 u(\tilde{x},t)}{\partial \tilde{x}^4} = \frac{\rho_s(\tilde{x},t)}{\rho_a(\tilde{x},t)}\left(v(t) - \frac{\partial u(\tilde{x},t)}{\partial t}\right)^2 + \dot{v}(t). \tag{7}$$

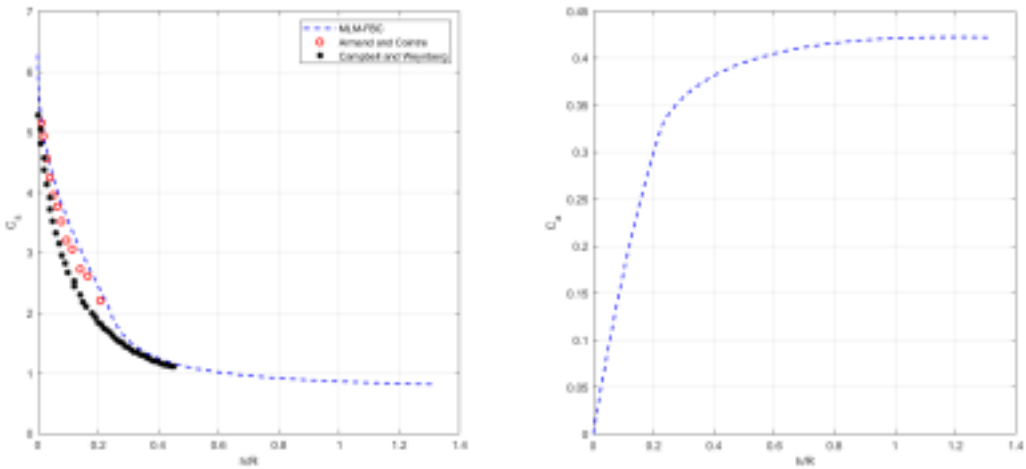


Figure 2: Evolution of the slamming coefficient C_s and the added-mass coefficient C_a with the normalized penetration depth obtained with the MLM-FBC approach.

2.2. Modal decomposition approach

To solve Eq. (7), the sought solution is projected onto the basis of the first natural modes of the dry beam:

$$u(\tilde{x},t) \simeq \sum_{k=1}^{N} \alpha_k(t)\hat{u}_k(\tilde{x}), \tag{8}$$

where $\alpha_k(t)$ and $\hat{u}_k(\tilde{x})$ are the amplitude and spatial shape of the k^{th} mode, respectively. The number of modes retained, N, depends on the desired precision. The modes of an Euler-Bernoulli beam take the form [24]:

$$\hat{u}_k(\tilde{x}) = B_k\left[\sin(\mu_k\tilde{x}) - \Omega_{1k}\sinh(\mu_k\tilde{x}) - \Omega_{2k}\left(\cos(\mu_k\tilde{x}) - \cosh(\mu_k\tilde{x})\right)\right]. \tag{9}$$

The methodology to compute the wavenumber μ_k and the coefficients $B_k, \Omega_{1k}, \Omega_{2k}$ is described in [24]. By substituting Eq. (8) into Eq. (7) one obtains:

$$\begin{aligned}\ddot{\alpha}_j(t) + EI\int_0^L \frac{\hat{u}_j(\tilde{x})}{\rho_a(\tilde{x},t)}\sum_{k=1}^{N}\alpha_k(t)\mu_k^4\hat{u}_k(\tilde{x})d\tilde{x} = \int_0^L \frac{\rho_s(\tilde{x},t)}{\rho_a(\tilde{x},t)}\hat{u}_j(\tilde{x})\left(v(t) - \sum_{k=1}^{N}\dot{\alpha}_k(t)\hat{u}_k(\tilde{x})\right)^2 d\tilde{x}\\ + \dot{v}(t)\int_0^L \hat{u}_j(\tilde{x})d\tilde{x}\,, \quad \text{for } j = 1, ..., N.\end{aligned} \tag{10}$$

The system of equations (10) is integrated numerically using a fourth-order Runge-Kutta scheme.

It is interesting to point out that in the case of an horizontal tube (γ=0), at the first order, Eq. (10) reduces to:

$$\ddot{\alpha}_j(t) + 2v(t)\frac{\rho_s(t)}{\rho_a(t)}\dot{\alpha}_j(t) + \frac{EI}{\rho_a(t)}\mu_j^4\alpha_j(t) = \left(\dot{v}(t) + v^2(t)\frac{\rho_s(t)}{\rho_a(t)}\right)\int_0^L \hat{u}_j(\tilde{x})d\tilde{x}\,. \tag{11}$$

The second term of the left-hand side of Eq. (11) is a modal damping term due to fluid-structure coupling. It is interesting to notice that this damping term is proportional to the velocity at which the tube penetrates water.

3. Experimental set-up

The experiments aim to analyze the hydroelastic response of a hollow aluminium tube as it impacts the free surface of still water ($\rho_f = 1000$ kg/m^3) horizontally ($\gamma = 0°$) at a controlled velocity (tests have been also performed with an inclination angle $\gamma = 5°$, but they will not be described in the present paper).

We used the ENSTA shock machine [25] shown in Fig. 3. This machine has a load capacity of 200 kN with a maximum velocity of 20 m/s. The water tank is 2 meters wide, 3 meters long, and 2 meters deep. We expect that the tank dimensions do not have any influence on the experimental results. Indeed, the mock-up is relatively small compared with the tank, as shown in the figure below. The total length of the specimen is 0.684 m, while the width of the tank is 2 m. The tube diameter is 25 mm, which is very small compared with the distance between the free ends of the tube and the lateral tank walls (658 mm). Moreover, the ratio between the projected area of the mock-up and that of the tank is equal to 2.85×10^{-3}. For the hydrodynamic impact tests, the tank is moved to a position under the machine and then filled with water to a given height (1.2 m for the present tests). The characteristics of the instrumented tubes are given in Table 1.

The tube instrumentation, displayed in Fig. 4, consists of four strain gauges – G_1, G_2, G_{1s}, and G_{2s} – placed at precise locations such that the positions of G_1 and G_{1s} are symmetrical to each other, as are those of G_2 and G_{2s}. Three accelerometers, A_1, A_{1s}, and A_0, are also used. A_1 and A_{1s} are placed at symmetrical positions at the ends of the tube. The water entry velocity, $V(t)$ is obtained by integrating the signal from accelerometer A_0. Four different target impact velocities have been considered: 3 m/s, 5 m/s, 6.6 m/s and 8.5 m/s.

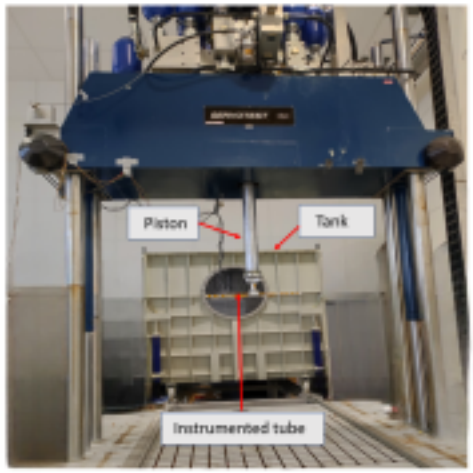
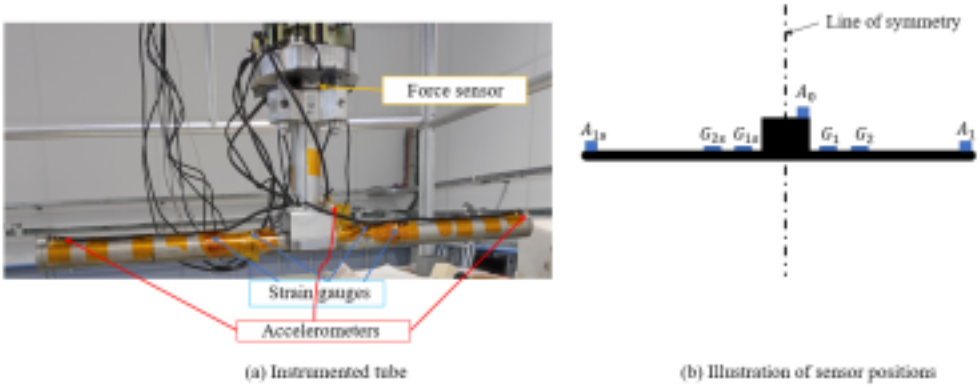


Figure 3: Hydraulic shock machine at ENSTA laboratory.

Table 1: Characteristics of the tube.

Parameters	Values	Units
E	70×10^9	Pa
ρ_V	2.833×10^3	kg/m^3
R	12.5×10^{-3}	m
e	2×10^{-3}	m
L	312×10^{-3}	m



(a) Instrumented tube (b) Illustration of sensor positions

Figure 4: Instrumented tubular specimen.

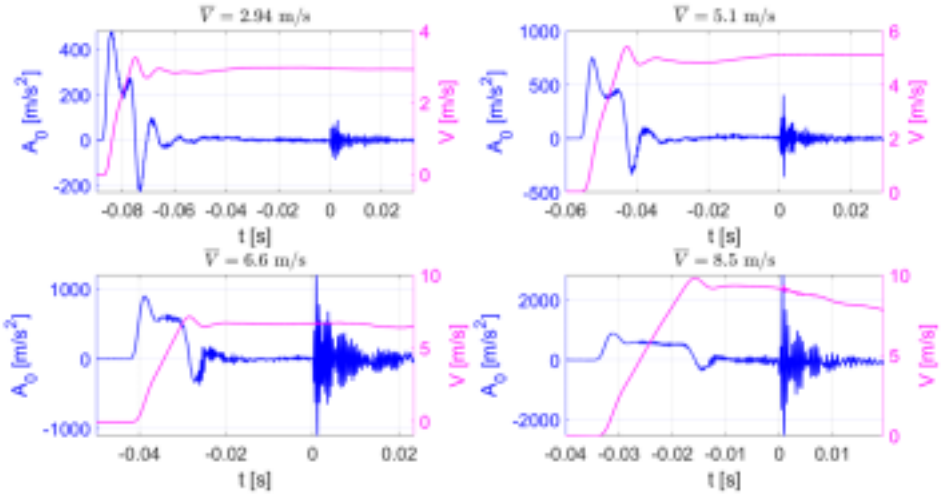


Figure 5: Signals from accelerometer A_0 and the corresponding velocity evolutions for different target impact velocities.

Fig. 5 shows examples of acceleration signals recorded by accelerometer A_0, as well as the corresponding velocity evolutions $V(t)$ obtained by integrating the acceleration signals. For each case, the impact between the tube and the water occurs at $t = 0$, and the average velocity (for $t > 0$) during the penetration of the tube into the water is indicated above each curve. We observe that for average velocities ranging from $\overline{V} = 2.96$ m/s to $\overline{V} = 6.6$ m/s, the penetration of the tube into the water occurs at an almost constant velocity (the difference between the velocity at the moment of impact and the average penetration velocity is less than 1%). In the case $\overline{V} = 8.5$ m/s, the velocity variation during the penetration stage is more pronounced: a velocity decrease of 7% is observed. Additionally, we observe for all tests a fluctuation of the acceleration signal A_0 after impact probably due to a vibration of the specimen fixation system.

4. Results and discussion

Fig. 6 shows a comparison between experimental results and theoretical predictions for the strain evolution at gauge G_1. We used the signal from A_0 to set the forced motion $V(t)$ used in the calculations in order to be as close as possible to the experimental conditions. The impact occurs at $t = 0$. Notice that, before this moment, the beam is not at rest due to the initial acceleration of the machine piston.

Interestingly, a decay of the oscillations after the impact is observed for both the experimental and theoretical signals. In the theoretical model, which does not include structural damping, the decay of the oscillations is solely due to the hydrodynamic damping induced by the fluid-structure coupling (see the end of section 2.2). A hydrodynamic damping has also been observed by Tassin et al. [26] in the case of a parabola mounted on a spring and by Abrahamsen et al. [17] in the case of elastic curved shells. The hydrodynamic damping will be further characterised and discussed in the following.

Shortly after impact, the strain reaches its peak, with the theoretical model providing a higher value than the one observed experimentally. The relative differences between the model and the experiments for the peak strain range from 15% to 20%, depending on the impact velocity. This difference suggests that in the modeling the load acting on the beam during the impact is overestimated. It is possible that

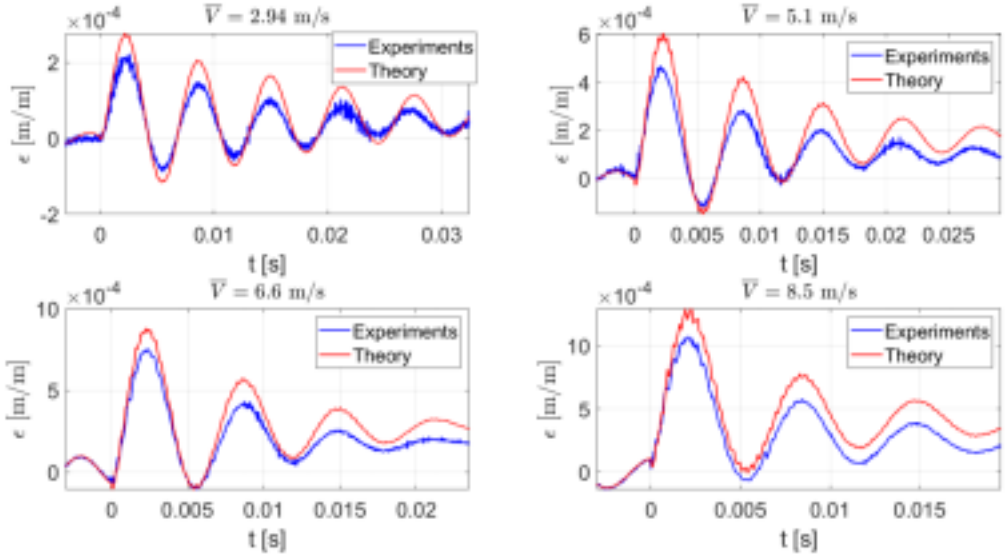


Figure 6: Time evolution of the strain at gauge at G_1. The theoretical results are compared to experimental recordings.

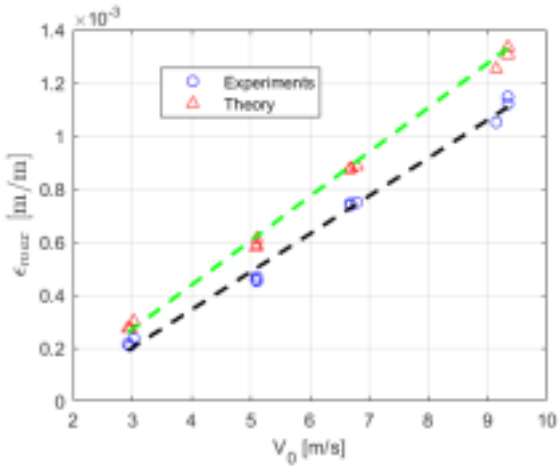


Figure 7: Maximum strain as a function of impact velocity. The dashed lines correspond to linear fits of the experimental and theoretical results.

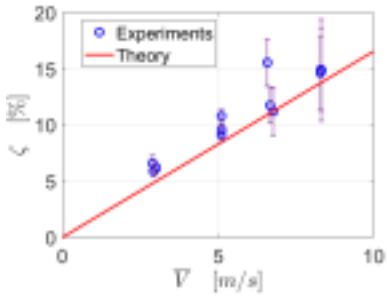


Figure 8: Damping ratio as a function of velocity. In this figure the error bars correspond to a 95% confidence interval, under the assumption that the residuals from the damping ratio estimate are Gaussian.

this difference is related to the strip approach, which does not take into account 3D effects. These effects are expected to induce smaller slamming loads as shown by Seng et al. [27] and Wang et al. [28].

For all the tests conducted, the impact duration is shorter than the first natural period of the tube. Consequently, the considered phenomenon occurred in an impulse response regime [29]. In this regime, the maximum strain is expected to be proportional to the penetration velocity. Observations of both experimental and theoretical results, as shown in Fig. 7, are consistent with this expected trend.

To gain a more quantitative understanding of the damping of deformation signals (damping of the first mode), we estimated an average damping factor from the amplitude decay of the oscillation during the penetration stage. Fig. 8 shows the evolution of this damping ratio as a function of the impact velocity (taken as the average velocity during the tube penetration stage). The damping ratio identified from the experiments is compared to the hydrodynamic damping ratio derived from the theoretical model. It appears that the damping ratio depends linearly on the water penetration velocity in both experimental results and theoretical predictions. This suggests that the damping due to fluid-structure coupling is the predominent damping mechanism for the considered configuration.

5. Conclusion

In this article, a semi-analytical model to simulate the hydroelastic response of tubular structures subjected to hydrodynamic impact is proposed. To validate this model, an experimental campaign in which a hollow aluminium tube impacts a still water surface has been performed.

Overall, a fairly good agreement between model and experiments is observed. Particular attention was paid to the damping of the tube oscillations during the entry stage. This analysis revealed that this damping is mainly due to fluid-structure coupling. The model predicts that the fluid-structure damping increases linearly with impact velocity. This trend is confirmed by experimental results. The model also provides a good estimation of the maximum strain induced by the impacts. The observed discrepancies are attributed to 3D effects not accounted for by the hydrodynamic model (strip method).

Additional results obtained with an inclined tube ($\gamma = 5°$) will be presented during the conference.

Acknowledgments

This work was conducted as part of a Doctoral thesis. The authors would like to express their gratitude to ENSTA and the Brittany region for their financial support and to all the technicians who contributed to its completion.

References

[1] M Kawakami, J-i Michimoto, and K Kobayashi. Prediction of long-term whipping vibration stress due to slamming of large full ship in rough seas. *International Shipbuilding Progress*, 24(272):83–110, 1977.

[2] G Storhaug. Experimental investigation of wave induced vibrations and their effect on the fatigue loading of ships. 2007.

[3] I Senjanović, N Vladimir, M Tomić, N Hadžić, and Š Malenica. Some aspects of structural modelling and restoring stiffness in hydroelastic analysis of large container ships. *Ships and Offshore Structures*, 9(2):199–217, 2014.

[4] Marine Accident Investigation Branch. Report on the investigation of the structural failure of MSC Napoli English Channel on 18 January 2007. 2008.

[5] J. Wienke and H. Oumeraci. Breaking wave impact force on a vertical and inclined slender pile—theoretical and large-scale model investigations. *Coastal Engineering*, 52(5):435–462, 2005.

[6] Loup Suja-Thauvin, Jørgen R. Krokstad, Erin E. Bachynski, and Erik-Jan de Ridder. Experimental results of a multimode monopile offshore wind turbine support structure subjected to steep and breaking irregular waves. *Ocean Engineering*, 146:339–351, 2017.

[7] Loup Suja-Thauvin, Jørgen R. Krokstad, and Erin E. Bachynski. Critical assessment of non-linear hydrodynamic load models for a fully flexible monopile offshore wind turbine. *Ocean Engineering*, 164:87–104, 2018.

[8] Ying Tu, Zhengshun Cheng, and Michael Muskulus. Global slamming forces on jacket structures for offshore wind applications. *Marine Structures*, 58:53–72, 2018.

[9] Shaofeng Wang, Torben Juul Larsen, and Henrik Bredmose. Experimental and numerical investigation of a jacket structure subject to steep and breaking regular waves. *Marine Structures*, 72:102744, 2020.

[10] A Bereznitski. Slamming: the role of hydroelasticity. *International Shipbuilding Progress*, 48(4):333–351, 2001.

[11] OM Faltinsen. Hydroelastic slamming. *Journal of Marine Science and Technology*, 5:49–65, 2000.

[12] O Faltinsen, O Kjaerland, A Nøttveit, and T Vinje. Water impact loads and dynamic response of horizontal circular cylinders in offshore structures. In *Offshore Technology Conference*, pages OTC–2741, 1977.

[13] A Korobkin and TI Khabakhpasheva. Plane linear problem of the immersion of an elastic plate in an ideal incompressible fluid. *Journal of applied mechanics and technical physics*, 40(3):491–500, 1999.

[14] Y-M Scolan. Hydroelastic behaviour of a conical shell impacting on a quiescent-free surface of an incompressible liquid. *Journal of Sound and Vibration*, 277(1-2):163–203, 2004.

[15] OM Faltinsen. *Hydrodynamics of High-Speed Marine Vehicles*. Cambridge University Press, 2006.

[16] M Jalalisendi and M Porfiri. Water entry of cylindrical shells: Theory and experiments. *AIAA journal*, 56(11):4500–4514, 2018.

[17] BC Abrahamsen, F Grytten, O Hellan, TH Søreide, and OM Faltinsen. Hydroelastic response of concrete shells during impact on calm water. *Journal of Fluids and Structures*, 116:103804, 2023.

[18] L Suja-Thauvin, JR Krokstad, and EE Bachynski. Critical assessment of non-linear hydrodynamic load models for a fully flexible monopile offshore wind turbine. *Ocean Engineering*, 164:87–104, 2018.

[19] TI Khabakhpasheva, A Korobkin, and Š Malenica. Water entry of an elastic conical shell. *Journal of Fluid Mechanics*, 980:A34, 2024.

[20] A Korobkin. Analytical models of water impact. *European Journal of Applied Mathematics*, 15(6):821–838, 2004.

[21] A Tassin, AA Korobkin, and MJ Cooker. On analytical models of vertical water entry of a symmetric body with separation and cavity initiation. *Applied Ocean Research*, 48:33–41, 2014.

[22] IMC Campbell and PA Weynberg. *Measurement of parameters affecting slamming*. University of Southampton, Department of Aeronautics and Astronautics, 1980.

[23] R Cointe and J-L Armand. Hydrodynamic impact analysis of a cylinder. 1987.

[24] KR Chun. Free vibration of a beam with one end spring-hinged and the other free. 1972.

[25] A El Malki Alaoui, A Nême, A Tassin, and N Jacques. Experimental study of coefficients during vertical water entry of axisymmetric rigid shapes at constant speeds. *Applied Ocean Research*, 37:183–197, 2012.

[26] A Tassin, F Hulin, and N Jacques. A direct multimode method for the reduction of vibration induced oscillations on force signals during "pseudo-rigid" water impact experiments. *Journal of Sound and Vibration*, 581:118378, 2024.

[27] S Seng, JJ Jensen, and PT Pedersen. Numerical prediction of slamming loads. *Proceedings of the Institution of Mechanical Engineers, Part M: Journal of Engineering for the Maritime Environment*, 226(2):120–134, 2012.

[28] S Wang, G Xiang, and CG Soares. Assessment of three-dimensional effects on slamming load predictions using openfoam. *Applied Ocean Research*, 112:102646, 2021.

[29] R Hascoët and N Jacques. On the risk of fatigue failure of structural elements exposed to bottom wave slamming–impulse response regime. *Applied Ocean Research*, 154:104411, 2025.

10th International Conference on HYDROELASTICITY IN MARINE TECHNOLOGY
Trondheim, Norway, June16th-18th, 2026

Mitigation of Hydroelastic Perturbations on Force Measurements During Water Impact Experiments with Pseudo-Rigid Impactors: Solutions and Challenges

Tassin, A.[1,*] and Jacques, N.[2]

[1] Ifremer, RDT, F-29280 Plouzané, France
[2] IRDL, UMR CNRS 6027, ENSTA, Institut Polytechnique de Paris, Bretagne INP, Univ. Brest, Univ. Bretagne Sud, F-29200 Brest, France

Abstract. In the present paper, we investigate numerically the hydroelastic effects occuring during water impact experiments with a pseudo-rigid impactor. The objective of this study is to assess the method proposed recently in Tassin *et al.* 2024 [1] to mitigate the effect of the vibrations on the force measurements and to explore possible improvements to the method. For this purpose, we have simulated numerically the water entry of a two-dimensional stiff elastic parabolic beam impacting a calm free surface. A constant vertical velocity is imposed at the nodes located at both extremities of the parabola. The reaction force at these nodes, which can be seen as a virtual load cell, differs (a lot) from the hydrodynamic force acting on the beam because of the structure vibrations. With the mitigation method presented in Tassin et al. 2024, it is possible to recover the hydrodynamic force from the reaction force and the nodal acceleration numerical signals. Our results show that it is possible to mitigate the effect of 11 modes of vibrations with 12 accelerometers. The residual perturbations of the hydrodynamic force (related to the beam flexibility) are analysed using a Wagner-type model. It appears that these perturbations are mainly due to an added-mass effect resulting from the structure deformation.

Key words: *Water impact; Hydroelasticity; Slamming; CFD; Finite Elements, Wagner model*

1. Introduction

Water impact experiments are often carried out to assess the accuracy of analytical models and numerical simulations of water impact. In that context, measuring the hydrodynamic force acting on a rigid impactor entering water at constant speed has been the motivation for a number of experimental test campaigns (*e.g.* [2, 3, 4, 5, 6]). Such experimental results are a convenient way of validating the ability of the models to predict the hydrodynamic force in "simple" well defined conditions. However, achieving perfect rigidity in the experiments is illusionnal despite the efforts to make the impactor and the test rig as stiff as possible. Due to the impulsive nature of the water impact loads, the structures (impactor and/or test rig) used in water impact experiments are prone to vibrations which may affect the hydrodynamic force measurements. This aspect was already clearly mentioned in the early work of Campbell and Weynberg [2] who observed oscillations of the force measurements with an amplitude equal to the expected maximum force in the case of circular cylinder. To circumvent this issue, experimentalists may have to filter (*e.g.* low-pass) quite drastically their force measurements to make comparisons with theoretical results, and by doing so they may remove a part of the useful signal, which can lead to

*Correspondence to: alan.tassin@ifremer.fr

This work is licensed under CC BY 4.0

inaccurate measurements of the hydrodynamic force acting on the body and in particular of the peak force.

An alternative approach to filtering was recently proposed in [1] to mitigate the effect of the vibrations on the force measurements during the water entry of pseudo-rigid (*i.e.* very stiff) impactors. This method consists in recording the response of the structure at different points with a set of accelerometers and to remove the contribution of the solid body inertia from the measured force. With this method, we showed in [1] that it was possible to mitigate the effect of several modes of vibration on a rather complex three-dimensional structure by performing dry hammer tests with an instrumented hammer. We were also able to significantly reduce the level of oscillations on the force signals recorded during breaking wave impact experiments carried out with the same structure, but we observed higher residual oscillations on the force signals for the most severe impact cases (see section 4.3 in [7]). We also observed a frequency shift in the spikes of the spectra which probably indicates an added-mass effect.

The present study aims at assessing and improving the vibration mitigation approach described in [1]. In particular, we aim to gain a better undertsanding on how fluid-structure couplings affect the hydrodynamic loads acting on the body and the mitigation methodology. For this purpose, we have simulated numerically the water entry of a two-dimensional stiff elastic parabolic beam impacting a calm free surface. A constant vertical velocity is imposed at the nodes located at both extremities of the parabola. The reaction force at these nodes, which differs (a lot) from the hydrodynamic force acting on the beam because of the structure vibrations, is considered to be the load measured by a load cell. In the numerical simulations, we have access to all the unknowns, and in particular to the nodal accelerations and to the hydrodynamic force, which makes it very interesting for the development of the mitigation method. Comparisons with numerical simulations for a perfectly rigid impactor are also possible.

The paper is organized as follows. Section 2. describes the numerical approach used for the simulations. In section 3. we identify the coefficients of the mitigation method using numerical hammer tests. The mitigation method is applied in section 4. to the hydroelastic impact simulations to recover the hydrodynamic force from the reaction force and the accelerations at some points of the structure. In section 5. we employ a Wagner-type model to compute the hydrodynamic force acting on a body whose shape, velocity and acceleration corresponds to those obtained from the high-fidelity numerical simulations. This make it possible to estimate the relative effect of the added-mass and of the velocity on the hydrodynamic force fluctuations. Some conclusions are finally drawn in section 6.

2. High-fidelity numerical simulation approach

Numerical simulations of water impact of an elastic curved (parabolic) beam have been performed with the finite element solver ABAQUS/Explicit. The considered configuration is illustrated in Fig. 1 below.

The initial geometry of the impacting beam is given by the following relation:

$$y = \frac{x^2}{2R_c}, \tag{1}$$

where R_c is the radius of curvature of the beam at its centre, $R_c = 0.22\,\text{m}$. The half length L_b (dimension in the x direction) of the beam is of $0.128\,\text{m}$ and its thickness t_b of $0.02\,\text{m}$. A linear elastic behaviour is assumed. The mechanical properties correspond to those of steel: Young modulus $E = 200 \times 10^9\,\text{Pa}$, Poisson ratio $\nu = 0.3$ and mass density $\rho_0 = 7800\,\text{kg/m}^3$. Owing to symmetry, only half of the beam is meshed with 131 2-node shear-flexible (Timoshenko theory) beam elements (ABAQUS B21). The following boundary and initial conditions are considered:

$$\begin{aligned} &v_x = v_{rz} = 0, && \text{at } x = 0 \text{ (beam centre)},\\ &v_x = v_{rz} = 0,\ v_y = -V_{\text{imp}}, && \text{at } x = L_b \text{ (beam end)},\\ &v_x = v_{rz} = 0,\ v_y = -V_{\text{imp}}, && \text{at } t = 0. \end{aligned} \tag{2}$$

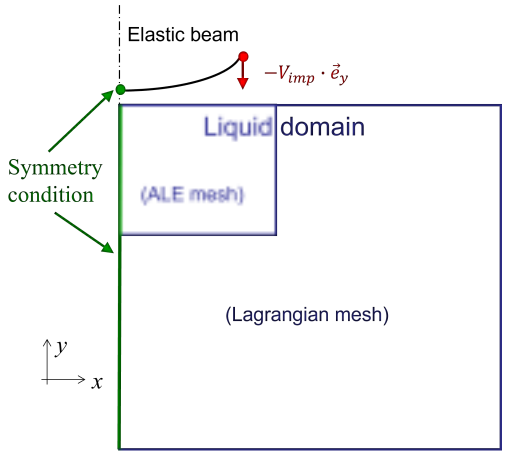


Figure 1: Illustration of the configuration considered in the numerical simulations of hydroelastic water impacts.

where v_x denotes the horizontal velocity, v_y the vertical velocity, v_{rz} the rotational velocity and V_{imp} the prescribed impact velocity. The liquid is initially at rest and is assumed to be inviscid and compressible. The flow is assumed two-dimensional ($v_z = 0$) and the effect of gravity is neglected. A linear equation of state is used to describe the compressibility:

$$p = \rho_0 c_0^2 \left(1 - \frac{\rho_0}{\rho_l}\right) \tag{3}$$

with ρ_0 and ρ_l being respectively the initial and current mass density of the fluid, and c_0 the speed of sound. Note that $\rho_0 c_0^2$ corresponds to the bulk modulus. For the present simulations, we have taken $\rho_0 = 1000\,\text{kg/m}^3$. After considering the typical speed of sound to the water ($c_0 \approx 1425$ m/s), the speed of sound was increased to $c_0 = 2850$ m/s in order to limit compressibility effects with an impact velocity of 5 m/s.

Water impact problems are generally associated with an intense deformation of the fluid and cannot be treated within a pure Lagrangian framework. For this reason, the ALE (Arbitrary Euler-Lagrange) adapting meshing technique of ABAQUS has been employed. This method makes it possible to maintain a high-quality mesh under severe material deformation by allowing the mesh to move independently of the underlying material.

The ALE adapting meshing is used in a region in the vicinity of the impact zone (see Fig. 1). This region is meshed with 189,901 two-dimensional 4-node bilinear elements (ABAQUS CPE4R), see for instance [8] for more details about finite elements and explicit methods. The element size is of 150 μm in the x direction and 200 μm in the y direction. For the rest of the fluid domain, where the fluid deformation is moderate, a Lagrangian mesh involving 104,601 3-node triangular linear elements is adopted. Frictionless contact is used to model the interaction between the liquid and the beam. The time step used in the simulations is of 5×10^{-9} s. A computation required about 6 hours using 8 cores on a workstation.

In addition to the water impact simulations, “dry hammer tests” simulations have been carried out. In these simulations, there is no water and a concentrated transient force is applied at the centre of the beam (node being in the symmetry plane). These simuations have been used to identify the coefficients of the mitigation method (see section 3.).

3. Dry hammer test calibration

The mitigation approach consists in correcting the reaction force signal at the beam end, $F_{\text{meas}}(t)$, with a linear combination of the node vertical acceleration signals, $\gamma_i(t)$, where i corresponds to the node index:

$$F_{corr}(t) = F_{meas}(t) + \sum_{i=1}^{N} \alpha_i \gamma_i(t), \tag{4}$$

where F_{corr} is the corrected hydrodynamic force measurement and N is the number of acceleration signals used for the force correction. The correction coefficients, α_i, may be identified from a test during which the load acting on the structure is known or can be accurately measured, for instance a hammer test with an intrumentated hammer. For this purpose, we have simulated a numerical hammer test during which a vertical force was applied to the node located in the plane of symmetry. The evolution of the force exherted by the hammer, F_{hammer}, as a function of time was triangular, as depicted in Fig. 2 below. Note that the hammer force rises faster than it decreases (rise time of 2×10^{-5} s and total load duration of 10^{-4} s). The measured force (reaction force in the vertical direction at the clamped end of the beam), which is also depicted in Fig. 2, is very much affected by the vibrations of the structure. The amplitude of the oscillations is about two times the magnitude of the impulse force. The correction coefficients are identified such as to minimize the following cost function ϵ:

$$\epsilon = \sum_{k=1}^{n} \left(F_{hammer}(t^k) - F_{meas}(t^k) - \sum_{i=1}^{N} \alpha_i \gamma_i(t^k) \right)^2, \tag{5}$$

where $t^{k=1\rightarrow n}$ represent the time-instants at which the signals are discretized. As it can be seen in Fig.2, the corrected force obtained with these coefficients matches very well the theoretical hammer force. In this example, the acceleration signal of 12 nodes (almost) evenly distributed along the beam was used and a low-pass filter with a cut-off frequency of 74.7 kHz was applied to the force and acceleration signals. This cut-off frequency is located just below the natural frequency of the 12$^{\text{th}}$ dry mode of the structure. The 20 first dry natural frequencies of the structure computed with ABAQUS are given in table 1 for reference. The amplitude spectra corresponding to the different force components are depicted in Fig. 3. One can see that the frequency content of the corrected force is very close to that of the hammer force signal up-to the cut-off frequency of the low-pass filter, which shows that the mitigation method successfully removes the effect of the first 11 natural modes of the structure.

Mode	1	2	3	4	5	6	7	8	9	10
Freq. (Hz)	3084	6758	14748	19020	24369	34725	37677	45575	56313	56714

(a) Modes 1 to 10

Mode	11	12	13	14	15	16	17	18	19	20
Freq. (kHz)	67.82	75.11	78.97	82.68	89.51	91.11	93.84	100.4	102.4	112.3

(b) Modes 11 to 20

Table 1: First dry natural frequencies of the structure.

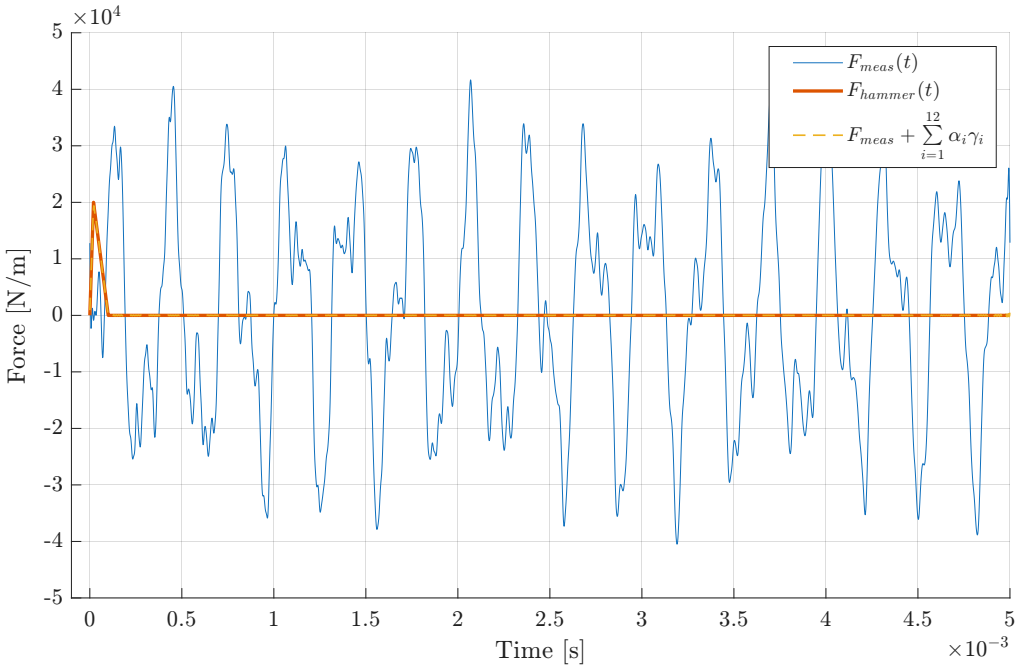


Figure 2: Force signals recorded during a dry hammer test on the parabolic beam.

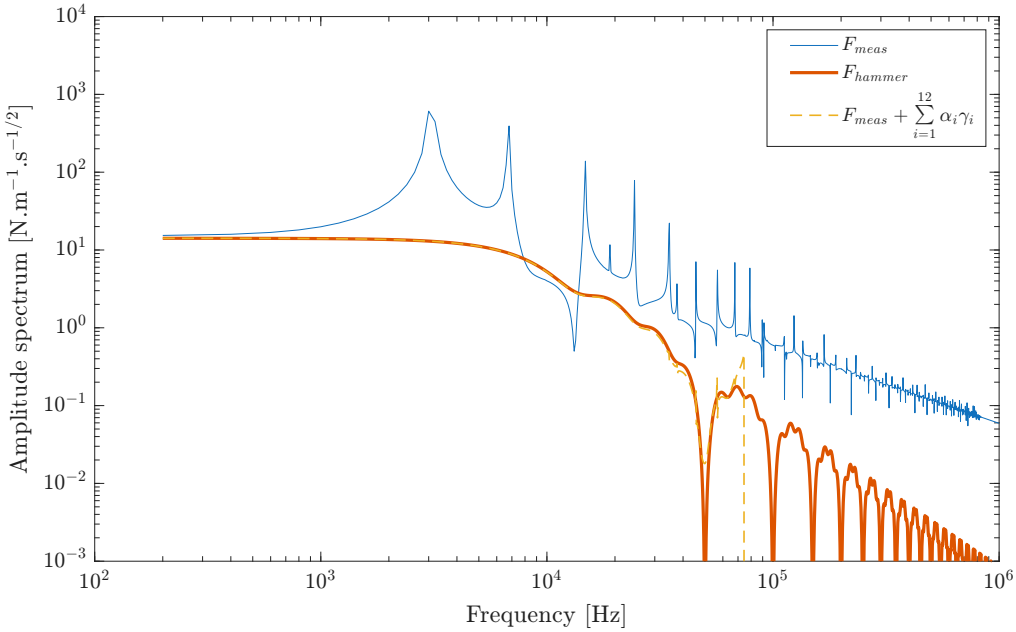


Figure 3: Amplitude spectra of the force signals recorded during a dry hammer test on the parabolic beam. (see color version online)

4. Application of the mitigation method to water impact numerical simulations

Let us now apply the mitigation method to the "force measurements" obtained from the water impact numerical simulations presented in section 2. for an impact velocity of 5 m/s using the correction coefficients identified with the hammer tests. The force results obtained with the mitigation method are depicted in Fig. 4 together with the force measured at the beam end, F_{meas}, and the hydrodynamic force acting on the beam wetted surface, F_{hydro}, obtained from the numerical simulations. The corrected force and the hydrodynamic force are so close that we can hardly distinguish one from the other, showing the ability of the mitigation method to compensate for the effect of the structure inertia and to recover the hydrodynamic force. The numerical force obtained with a rigid impactor, F_{rigid}, is also depicted for comparison. Note that a low-pass Fourier filter with a cut-off frequency of 74.7 kHz was also applied to the different signals presented in Fig. 4. One can see that the hydrodynamic force obtained with the deformable impactor oscillates around the force obtained with the rigid impactor, hence indicating that the hydrodynamic force is affected by the vibrations of the impactor. The amplitude of these oscillations is nevertheless much smaller than the force perturbations due to the solid body inertia, especially at the beginning of the impact. The Power Spectral Densities (PSD) of the different signals normalized with respect to the integral of the PSD of each signal are depicted in Fig. 5. We can see that the main difference between the rigid force spectrum and the elastic hydrodynamic force is located in the frequency range of the three first modes, where some extra energy appears in the elastic hydrodynamic force. Moreover, by comparing the spectra of the measured forces for the hammer test and the water impact test, a shift of the frequency peaks towards lower frequencies, which is consistent with an increased added mass, is visible in the case of the water impact test. Indeed, given that the structure is rather stiff and heavy, the mode shapes are expected to be only slightly modified by the added mass and the natural frequencies of the wet modes are expected to be lower than that of the dry modes. In the next section, the contribution of the added mass to the oscillations of the hydrodynamic force is investigated using a Wagner-type model.

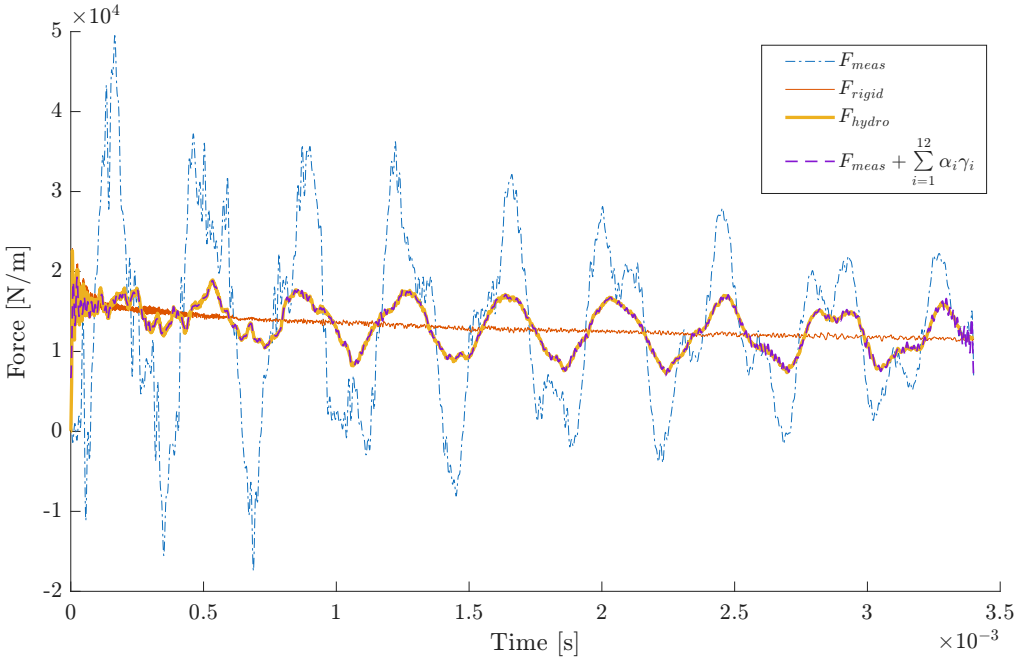


Figure 4: Force evolution as a function of time on the half-parabola. (see color version online)

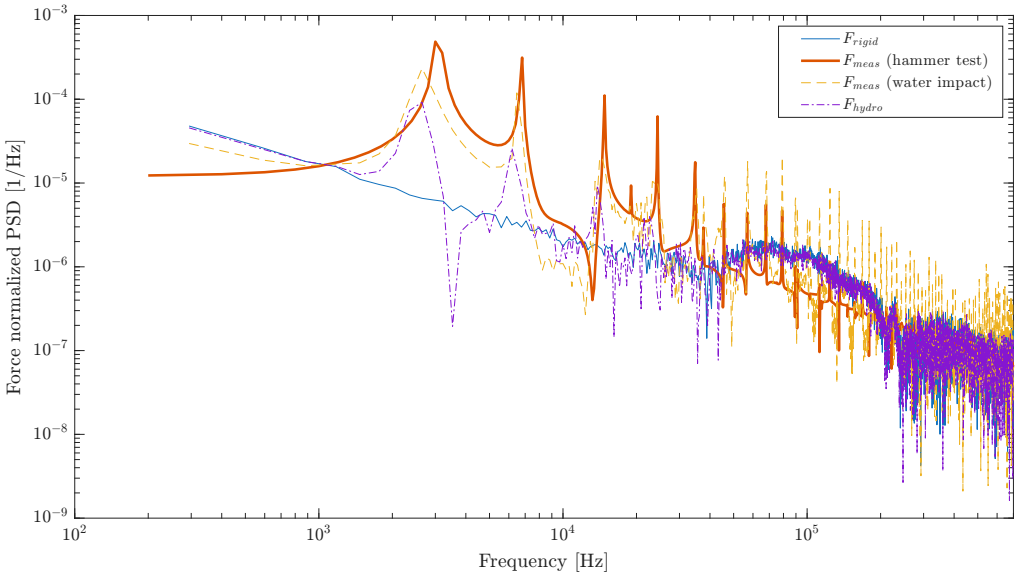


Figure 5: Force normalised PSD as a function of frequency. (see color version online)

5. Decomposition of the hydrodynamic force using a Wagner-type model

In this section we analyse the hydrodynamic force acting on the elastic parabola using the analytical (Wagner) model presented in [9]. This model was developped to compute the force acting on a body whose shape varies in time and is used here to compute the hydrodynamic force using the body shape evolution obtained from the high-fidelity hydro-elastic numerical simulation presented in the previous section. As a result of the pressure formulation used in [9], the hydrodynamic force can be decomposed into two terms: a slamming term, F_{vel}, and an added-mass term, F_{acc}, which depend only on the velocity and the acceleration of the body shape, respectively. The results obtained with this model are presented in Fig. 6 below. One can see that the velocity term F_{vel} is much less affected by the deformation of the body than the acceleration term (note that $F_{acc} = 0$ for a rigid-body impact at constant velocity). This observation suggests that a better prediction of the rigid-body hydrodynamic force could potentially be obtained if one were able to mitigate the added mass effect. However, as it is well know, the added mass evolves in time as the body becomes wetter and wetter. In fact, the increase of the added mass is the source of the slamming force. The analytical model makes it possible to compute the evolution of the vertical added mass, $m_a^i(t)$, of the first dry modes. These functions correspond to the vertical hydrodynamic force generated by unitary modal accelerations along each mode at the different time instants of the water entry (as the wetted surface increases). The evolution of the vertical added mass of the 10 first modes as a function of time is depicted in Fig. 7 below. Note that the magnitude of the added mass is only indicative because it depends on the normalization of the mode shapes. Except for the first mode whose vertical added mass increases monotonically, the vertical added mass of the other modes changes sign during the water entry. Such a behaviour makes it very difficult to infer the evolution of the added mass without knowing precisely the mode shapes and the shape of the wetted surface. This suggests that it will be very hard, if not impossible, to develop a general method able to mitigate the hydrodynamic force fluctuations due to hydro-elasticity occuring in water impact experiments. Morevover, the problem is probably even more complicated for three-dimensional problems such as breaking wave impacts on a structure.

6. Conclusion

We have shown through numerical simulations that the mitigation approach presented in [1] makes it possible to retreive the hydrodynamic force acting on a pseudo-rigid impactor entering water despite very high levels of oscillations on the measured force. With 12 accelerometer signals, we have shown that it was possible to mitigate the effect of 11 modes of vibration. However, the hydrodynamic force is affected by the deformation of the structure and exhibits some residual oscillations. Nevertheless, the amplitude of these residual oscillations is one order of magnitude smaller than the initial amplitude of the perturbations before applying the mitigation method. The hydrodynamic force computations obtained from the analytical model of [9] indicate that these residual oscillations are mainly due to an added mass effect rather than to velocity fluctuations. However, the analytical model has also shown that the vertical added mass of the different modes evolves non-monotically during the water entry, and even worse, the sign of the added mass changes for all the modes, except for the first mode. These observations tend to show that it will be hard, if not impossible, to mitigate the added mass effect without a direct measurement of the evolution of the vertical component of the modal added mass (as it is the case during experiments).

Acknowledgments

Part of this work was carried out within the DIMPACT+ project. The DIMPACT+ project receives funding from France Energies Marines and its members and partners, as well as French State funding managed by the French National Research Agency under the France 2030 investment plan (agreement no. ANR-10-IEED-0006-34).

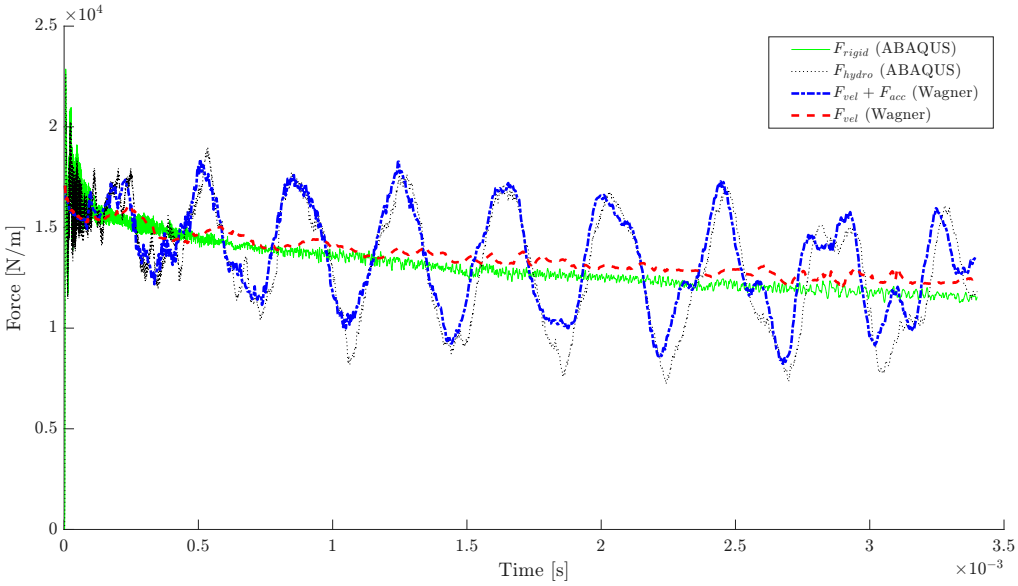


Figure 6: Force evolution as a function of time on the half-parabola (see color version online).

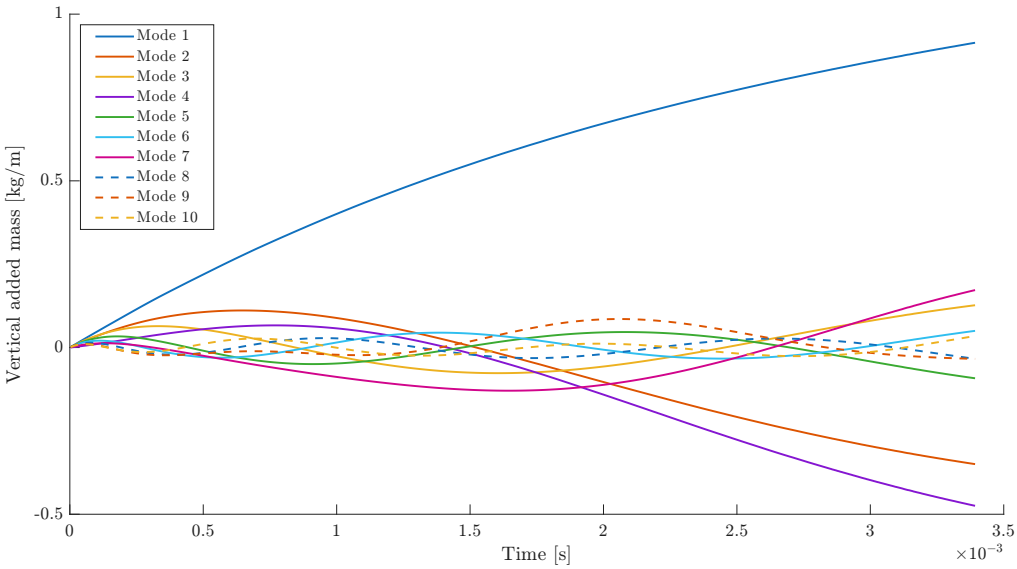


Figure 7: Vertical added mass of the first dry modes as function of time (see color version online).

References

[1] Alan Tassin, Florian Hulin, and Nicolas Jacques. A direct multimode method for the reduction of vibration induced oscillations on force signals during "pseudo-rigid" water impact experiments. *Journal of Sound and Vibration*, 581:118378, 2024.

[2] I. M. C. Campbell and P. A. Weynberg. *Measurement of parameters affecting slamming*. University of Southampton, Department of Aeronautics and Astronautics, 1980.

[3] A. Tassin, N. Jacques, A. El Malki Alaoui, A. Nême, and B. Leblé. Hydrodynamic loads during water impact of three-dimensional solids: Modelling and experiments. *Journal of Fluids and Structures*, 28:211–231, 2012.

[4] T. Breton, A. Tassin, and N. Jacques. Experimental investigation of the water entry and/or exit of axisymmetric bodies. *Journal of Fluid Mechanics*, 901:A37, 2020.

[5] Emanuele Spinosa and Alessandro Iafrati. A noise reduction method for force measurements in water entry experiments based on the ensemble empirical mode decomposition. *Mechanical Systems and Signal Processing*, 168:108659, 2022.

[6] Aref H Moalemi, Henrik Bredmose, Amin Ghadirian, and Trygve Kristiansen. Cylinder water entry on a perturbed water surface. *Journal of Fluid Mechanics*, 965:A16, 2023.

[7] Florian Hulin, Alan Tassin, Jean-François Filipot, and Nicolas Jacques. Experimental characterisation of breaking wave impact loads on a vertical cylinder. *Journal of Fluid Mechanics*, 1027:A27, 2026.

[8] T. Belytschko, W. K. Liu, and B. Moran. *Nonlinear Finite Elements for Continua and Structures*. Wiley J., 2000.

[9] A. Tassin, D. J. Piro, A. A. Korobkin, K. J. Maki, and M. J. Cooker. Two-dimensional water entry and exit of a body whose shape varies in time. *Journal of Fluids and Structures*, 40:317–336, 2013.

10th International Conference on HYDROELASTICITY IN MARINE TECHNOLOGY
Trondheim, Norway, June16th-18th, 2026

Physical and Numerical Experiment with Extreme Hydroelastic Wave Impacts at Scale

Bockstael, M.M.[1,2,*] and Wellens, P.R.[1,*]

[1] Ship Hydromechanics Laboratory, Delft University of Technology, Delft, Netherlands
[2] Maritime Research Institute Netherlands, Wageningen, Netherlands

Abstract. This study concerns repeatable wave impacts, including large variations of the interfaces and hydroelastic structural response, using physical and numerical tests at scale. The physical tests consist of a rectangular, oscillating tank that produces a sloshing wave impact against a flexible, overhanging, cantilever plate. The numerical setup consists of a hydrostructural model, where the hydrodynamic part is a two-phase finite-volume Navier-Stokes solver. The structural part is a finite-element discretisation of a beam, which is monolithically coupled to the fluid solver. Comparing physical and numerical results serves both the validation of the numerical model and the interpretation of the physical tests.

Key words: *Wave impact; Cantilever; Overhang; CFD; Monolithic coupling*

1. Introduction

Extreme wave impacts can exert high loads on maritime structures, which can lead to damage or failure. In literature, commonly mentioned categories of wave impact are slamming [1], sloshing [2] and green water [3]. The occurrence of the most extreme wave impacts is rare, which makes it hard to obtain converged statistics of extreme values [4, 5]. Controlled, artificially generated wave impacts are therefore important tools for the study of the expected value and variability of these events. The dynamics of extreme wave impacts involve large variations of the interfaces and response of the impacted structure, which are among the main sources of nonlinearities in slamming [6]. The hydrodynamic loads and structural response depend on their fluid-structure interaction, which should be taken into account as hydroelasticity during wave impacts [7, 8].

A recent review on flexible fluid-structure interactions in the ocean by [6] provides comprehensive lists of slamming studies and tests. The authors provide a history of the development of efficient and accurate semi-analytical models, but state their main limitation is in addressing more complex scenarios, such as those involving cavitation, air cushions and compressibility. For sloshing impacts these complex physical effects should be considered, but correct numerical modelling and scaling of the fluid-structure interactions is still beyond the state of the art [2]. Computational fluid dynamics (CFD) methods may address this complexity in the future, but challenges remain in developing efficient and appropriate methods for coupling the fluid and structural solvers [6]. Numerical methods, like CFD, do not require expensive physical setup and are less limited in configuration compared to analytical models. Additionally, the ability to define independent material properties is valuable for identifying scaling effects relevant to wave impacts [9]. Modelling these additional physical effects will require rigorous validation benchmarks.

This study concerns repeatable wave impacts using numerics and physical tests at scale. The experimental wave impact setup used in this study includes a free surface and a flexible structure, but differs

*Correspondence to: m.m.bockstael@tudelft.nl, p.r.wellens@tudelft.nl

from the more common wedge or plate drop tests. The tests consist of a rectangular, oscillating tank that produces a sloshing wave impact against a flexible, overhanging, cantilever plate. A numerical hydrodynamic model, specifically developed for extreme wave impacts, is coupled to a structural model of a cantilever beam. The hydrodynamic model consists of a two-phase finite-volume discretisation of the Navier-Stokes equations [10]. The structural model consists of a finite-element discretisation of the Euler-Bernoulli beam equation. The hydrostructural coupling is done using a monolithic approach to resolve the two-way interaction, and includes the geometric deformation of the beam. This allows the comparison between simulated and measured structural deflection, which is used to validate the numerical model. The combination of physical and numerical experiments increases confidence in the accuracy and interpretation of the results.

In section 2 the hydrostructural model is introduced. The physical experiment and its numerical reproduction are described in section 3. The validation of the numerical model is presented in section 4. Finally, section 5 discusses hydroelastic effects and is followed by concluding remarks.

2. Numerical model

2.1. Hydrodynamic model

The hydrodynamic model of [10] is adopted, which is based on the conservation equations for mass (Eq. 1) and momentum (Eq. 2) of the fluid. Viscous stresses are left out of the momentum equation, because their effect of is assumed negligible during the short duration of an impact.

$$\frac{\partial \rho}{\partial t} + \nabla \cdot \rho \vec{u} = 0 \tag{1}$$

$$\frac{\partial \left(\rho \vec{u}\right)}{\partial t} + \nabla \cdot \rho \vec{u} \vec{u}^T = -\nabla p + \rho g \tag{2}$$

Here ρ is the fluid density, $\vec{u}$ its velocity, p the pressure, and g the gravitational acceleration. In accordance with the Volume-of-Fluid method (VoF), Eq. 3 for colour function α is used to track the interface between air and water, where $\alpha = 0$ and 1, respectively.

$$\frac{\partial \alpha}{\partial t} + \nabla \cdot \alpha \vec{u} - \alpha \nabla \cdot \vec{u} = \frac{D\alpha}{Dt} = 0 \tag{3}$$

An aggregated fluid density can be defined by averaging over volume V as $\rho = |V|^{-1} \int_V \rho(\vec{x})\, dV$. By doing the same for α, both are related by Eq. 4 using constant (incompressible flow) densities of the two separate phases: water (ρ_1) and air (ρ_2).

$$\rho = \alpha \rho_1 + (1 - \alpha)\rho_2 \tag{4}$$

Throughout the description of the aggregated fluid model, quantities refer to their volume-averaged values according to a finite-volume discretisation. A staggered arrangement of control volumes on the cartesian cell faces is adopted for velocities, whereas all other variables, such as density, colour function and pressure, are defined over control volumes that coincide with grid cells. The advection of the free surface via α in Eq. 3 is done using the symmetric, split (COSMIC) scheme in two dimensions [11, 12]. The interfaces are reconstructed as piecewise lines (PLIC) using the analytic relations by [13].

Extreme wave impacts involve large free surface deformations and loads depend mainly on the inertia of the fluid. To accurately model the free surface dynamics, consistency between mass and momentum transport on the staggered control volumes is required [14]. Therefore, an intermediate ($*$) step is used in the advection of momentum using Eq. 5, where intermediate density ρ^* is found by solving Eq. 6 on the staggered control volumes. Without this approach, the simulated wave impact differed significantly from the physical experiment.

$$\frac{\rho^* \vec{u}^* - \rho^n \vec{u}^n}{\delta t^{n+1}} + \nabla \cdot \rho^\alpha \vec{u}^n (\vec{u}^n)^T = 0 \tag{5}$$

$$\frac{\rho^* - \rho^n}{\delta t^{n+1}} + \nabla \cdot \rho^\alpha \vec{u}^n = 0 \tag{6}$$

Here ρ^α indicates that the mass fluxes are based on the transport of mass via α in Eq. 3. Advecting velocities are determined using the first-order upwind scheme, and the time integration scheme is forward Euler as shown in Eqs. 5 and 6. The time step $\delta t^{n+1} = t^{n+1} - t^n$ is adapted to satisfy criteria that guarantee numerical stability.

The rest of the solution strategy consists of the projection method, which results in a single Poisson equation that has to be solved. Eq. 2 is rewritten to the velocity update Eq. 7.

$$\frac{\vec{u}^{n+1} - \vec{u}^*}{\delta t^{n+1}} = -\frac{1}{\rho^{n+1}} \nabla p^{n+1} + g\,. \tag{7}$$

The Poisson Eq. 8 for the pressure update $\delta p^{n+1} = p^{n+1} - p^n$ is then obtained by substituting Eq. 7 into $\nabla \cdot \vec{u}^{n+1} = 0$.

$$\delta t^{n+1} \nabla \cdot \frac{1}{\rho^{n+1}} \nabla \delta p^{n+1} = \nabla \cdot \left(\vec{u}^* - \frac{\delta t^{n+1}}{\rho^{n+1}} \nabla p^n + \delta t^{n+1} g \right) \tag{8}$$

Eq. 8 can be written to the linear system in Eq. 9 with matrix A and vector r.

$$\delta t^{n+1} \mathrm{A}^n \, \delta p^{n+1} = r^n(\delta t^{n+1}) \tag{9}$$

2.2. Structural model and coupling

The flexible plate is modelled as a 1D dynamic Euler-Bernoulli beam, with governing equation

$$\mu \frac{\partial^2 w(t,s)}{\partial t^2} + EI w''''(t,s) = q(t,s) \tag{10}$$

where w is the deflection normal to length-coordinate s. The term EIw'''' is the constant bending stiffness multiplied by the fourth spatial derivative of the deflection. The remaining terms are constant mass per unit length μ and distributed load $q(t,s)$.

A finite-element (FE) discretisation with cubic Hermite elements is applied to Eq. 10. The same symbols w and q now represent discrete nodal values in the resulting system Eq. 11 of differential equations, with mass and stiffness matrices M and K, respectively.

$$\mathrm{M} \frac{\partial^2 w(t)}{\partial t^2} + \mathrm{K}\, w(t) = q(t) \tag{11}$$

The system of linear Eqs. 12 and 13 is obtained using backward Euler time discretisation, where the first time derivative $\dot{w}$ is introduced as an additional variable. Coupling matrix C_p is introduced to express variable load q^{n+1} in terms of piecewise-constant fluid pressures p.

$$\mathrm{M} \frac{\dot{w}^{n+1} - \dot{w}^n}{\delta t^{n+1}} + \mathrm{K}\, w^{n+1} = \mathrm{C}_p\, p^{n+1} \tag{12}$$

$$\frac{w^{n+1} - w^n}{\delta t^{n+1}} = \dot{w}^{n+1} \tag{13}$$

The monolithic hydrostructural coupled system Eq. 14 is then completed by the coupling matrix $\mathrm{C}_{\dot{w}}$ that relates $\dot{w}$ to fluid velocities $\vec{u}$.

$$\begin{bmatrix} \delta t^{n+1}\mathrm{A}^n & \mathrm{C}^n_{\dot{w}} & \\ \delta t^{n+1}\mathrm{C}^n_p & \mathrm{M} & \delta t^{n+1}\mathrm{K} \\ & \delta t^{n+1}\mathrm{I} & -\mathrm{I} \end{bmatrix} \begin{bmatrix} \delta p \\ \dot{w} \\ w \end{bmatrix}^{n+1} = \begin{bmatrix} r^n(\delta t^{n+1}) \\ \mathrm{M}\,\dot{w}^n - \delta t^{n+1}\mathrm{C}^n_p\, p^n \\ w^n \end{bmatrix} \tag{14}$$

During coupled hydrostructural simulation, the beam deformation is applied to the fluid domain using cut cells, as shown for example in Fig. 1. Cut cells define regions that are open to fluid flow using cell volume and face apertures. It is continuously ensured that there is a staircase-like sequence of fully closed fluid cell faces along the length of the beam. The minimum thickness of the beam representation in the fluid domain is thus related to the fluid cell height.

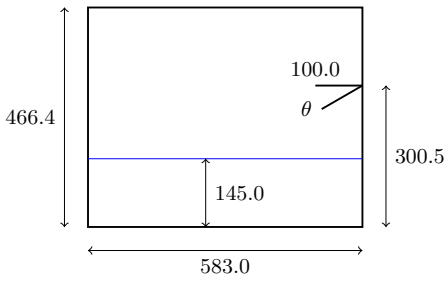


Figure 1: A visualisation of cut cells around a deformed beam. The continuous green curve shows the deformation of the beam compared to the dotted, zero deflection line. Fluid cell volume apertures are indicated by cell colours ranging from fully open (red) to closed (blue). Face apertures are shown by (dotted) black lines for (partly) closed faces.

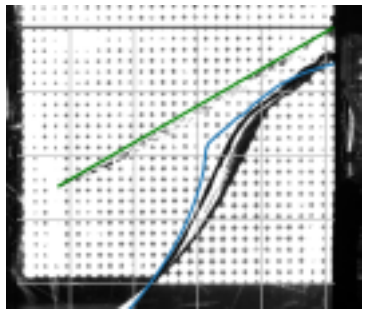
3. Wave impact experiment

3.1. Physical setup

The physical experiment simulates wave impacts on a cantilever overhang by sloshing waves in a rectangular tank, with dimensions as drawn in Fig. 2a. From standstill, the tank is excited in horizontal oscillatory motion close to the natural frequency of the fluid. This generates fast run up of a fluid wedge along the wall that impacts the overhanging plate, as seen in Figs. 2b and 2c. The thinnest and thickest plates tested have thicknesses $d_t = 0.4$ and 4.0 mm, respectively.



(a) Dimensions of the domain in millimetres. Depth of the fluid domain into the page is 200.0 mm. The plate has a clearance of 1.0 mm at both sides.



(b) Overlay of numerical simulation on video snapshot. Not exactly synchronised.



(c) Incoming wave impact on thick 4.0 mm plate instrumented with multiple, different pressure sensors. Zemic H3 50 kg reaction load cell at the top.

Figure 2: Experimental setup

The instrumentation of the measurement setup consists of reaction load cells and pressure sensors (Fig. 2c), and three laser distance sensors of type Panasonic HG-C1400 at different positions along the

plate (not shown). Only the 4.0 mm plate was instrumented with pressure sensors, since it is so stiff that no significant deflection occurs. The thinner plate was not instrumented with pressure sensors, in order not to affect plate inertia. Strain gauges could give insight into plate stress, but were not used in this setup. The combination of total reaction load, pressure and deflection is considered enough data to validate the hydrostructural model.

3.2. Numerical reproduction

The physical experiment is numerically reproduced according to the dimensions in Fig. 2a. Gravitational acceleration is assumed $g = 9.81$ m s^{-2} and the only fluid properties are the densities of water $\rho_1 = 1000$ kg m^{-3} and air $\rho_2 = 1.2$ kg m^{-3}. Fluid viscosity and surface tension are not modelled. The bending moment of inertia I of the plate is determined from its width $d_w = 198.0$ mm and its thickness d_t. The assumed structural properties of the stainless steel plate are its density of 8010 kg m^{-3} and Young's modulus $E = 195$ GPa.

The only remaining input to recreate the wave impact is the sloshing acceleration of the tank. An equation of the form Eq. 15 is fitted to the measured tank position. Note that only the position signal is used for the fit, but its second derivative still matches the measured accelerations, as shown in Fig. 3. The sloshing amplitude $a = 60.0$ mm is given constant for all tests.

$$x(t) = \begin{cases} c_0 + c_2 t^2 + c_3 t^3 + c_4 t^4 + c_5 t^5 + c_6 t^6 & \text{if } 0 \leq t \leq t_r \\ -a \cos(\omega[t - t_\varphi]) & \text{else} \end{cases} \tag{15}$$

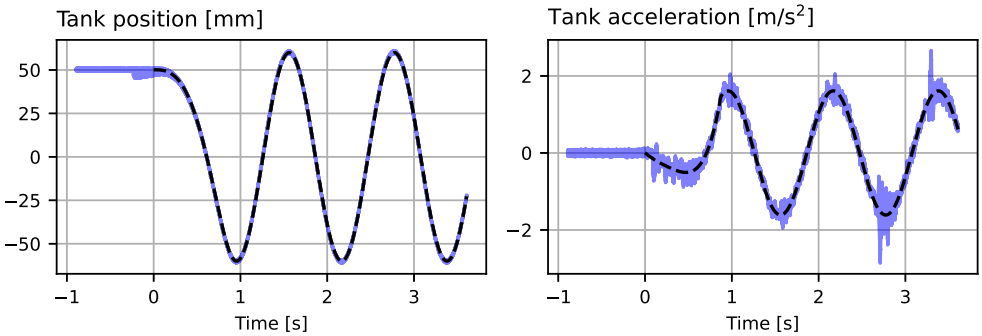


Figure 3: Example of motion fit for one test case ($\theta = 0°$, $d_t = 4.0$ mm, run no. 337).

Differences between repetitions of the same test case are small, so the mean of the coefficients is used to obtain a single fit for each test case. Coefficients $c_{4,5,6}$ are not averaged, but solved based on C^0 continuity of $(x, \dot{x}, \ddot{x})$ at $t = t_r$. The parameters required to reproduce the accelerations are given in Table 1.

For all simulations, the fluid domain of Fig. 2a is divided into square cells. The number of degrees of freedom are given in Table 2 for three refinement levels. The 1D structural domain is subdivided by placing FE nodes on vertical grid lines of the fluid domain. The subdivisions are chosen such that the same fluid domain can be used for both the horizontal and tilted plate. The tilted plate requires less cells for the same length, because it intersects fewer vertical grid lines. The two rightmost columns in Table 2 show the plate length as represented in the fluid domain resulting from these choices. Dynamic deflections are projected to the vertical grid lines corresponding to the initial state. When the beam is tilted, this projection causes a difference in the geometrical representation of the beam length in the fluid, which is accepted for the current implementation.

θ	d_t	$a\omega^2$	t_φ	t_r	$2c_2$	$6c_3t_r$	$12c_4t_r^2$	$20c_5t_r^3$	$30c_6t_r^4$
[deg.]	[mm]	[m s^{-2}]	[s]	[s]	[m s^{-2}]	[m s^{-2}]	[m s^{-2}]	[m s^{-2}]	[m s^{-2}]
0	4.0	1.6099	0.9538	0.8667	0.0331	-2.2801	5.5865	-10.6677	8.7772
0	0.4	1.6514	0.9599	0.8857	0.0426	-2.1469	4.3879	-8.3103	7.5546
30	4.0	1.6135	0.9539	0.8748	0.0018	-1.7344	3.0352	-6.4711	6.6482
30	0.4	1.6057	0.9533	0.8607	0.0718	-3.2192	10.1072	-17.8087	12.2741

Table 1: Sloshing acceleration parameters for considered test cases. Values are presented in a form that can be used directly in the second derivative $\ddot{x}(t)$ of Eq.15.

N_{F1}	N_{F2}	$\Delta x_{1,2}$	N_F	N_{S0}	N_{S30}	Δs_{30}	$N_{S0}\Delta x_1$	$N_{S30}\Delta s_{30}$
		[mm]				[mm]	[mm]	[mm]
175	140	3.331	24,500	30	26	3.847	99.94	100.02
350	280	1.666	98,000	60	52	1.923	”	”
700	560	0.833	392,000	120	104	0.962	”	”

Table 2: Degrees of freedom N_F and N_S for the fluid and structure domains, respectively. A distinguishment is made between the horizontal ($\cdot_0$) and tilted ($\cdot_{30}$) plates. Cell sizes are given for the fluid $\Delta x_{1,2}$ and the structure Δs_{30}. Note that $\Delta s_0 = \Delta x_1$.

4. Validation

The four test cases of Table 1 are reproduced numerically to validate the hydrostructural model for wave impact. In the results that follow, multiple physical test realisations are shown in the same figure using transparent blue curves to demonstrate the repeatability. Filtering is applied to the physical measurement signals by removing frequency components above 400 Hz using forward and inverse Fast Fourier Transform.

The plate deflection is shown only for the 0.4 mm plate in Fig. 4, because the 4.0 mm plate does not deform significantly compared to the laser precision. In the following text and figures, the 0.4 and 4.0 mm plates are also referred to as flexible and rigid, respectively. The comparison of deflection is interpreted mostly qualitatively, due to uncertainty in the exact position of the laser distance sensor in the physical measurement. The comparison shows similar temporal behaviour of the plate deflection in the measurements and the coupled simulation. The quasi-static deflection curves are discussed later in section 5.

Reaction forces are compared in Fig. 5, where a clear difference is the absence of oscillations in the simulations of the rigid plate. These force oscillations for the rigid plate are attributed to the elasticity of the load cell and is discussed further in section 5. Besides these oscillations, the reaction forces are of similar magnitude and temporal dynamics. The tilted, flexible case clearly shows large oscillations that can be attributed to the hydroelastic response of the plate itself. For the horizontal plate the magnitude of the peaks are similar, but the tilted plate experiences around two times higher peak forces in the simulation with the highest resolution.

Pressure measurements are compared in Fig. 6, where the values are relative to atmospheric pressure. For the horizontal plate, the magnitudes of measured and simulated pressure peaks are similar. The tilted plate, however, experiences around two times higher peak pressures in the simulation with the highest resolution. The lack of convergence of peaks values upon refinement on the tilted plate is thought to be related to the small relative wave impact angle, as shown in Fig. 2b.

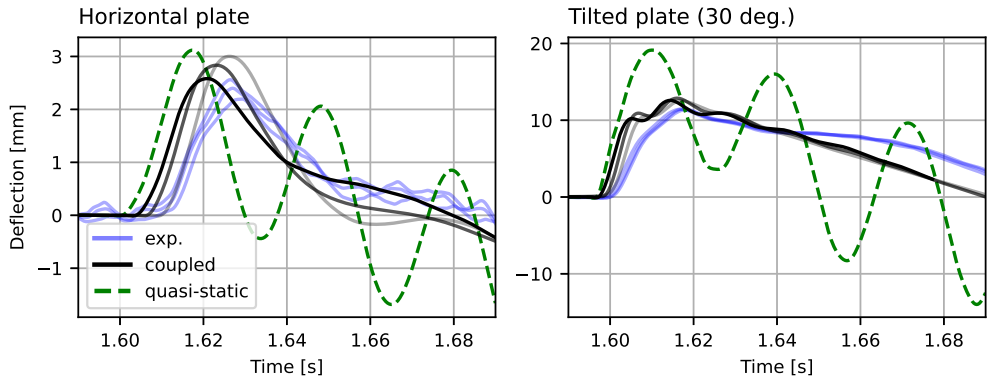


Figure 4: Comparison of measured and simulated deformation of the flexible 0.4 mm plate. Results for increasing grid resolution are shown with with decreasing transparency.

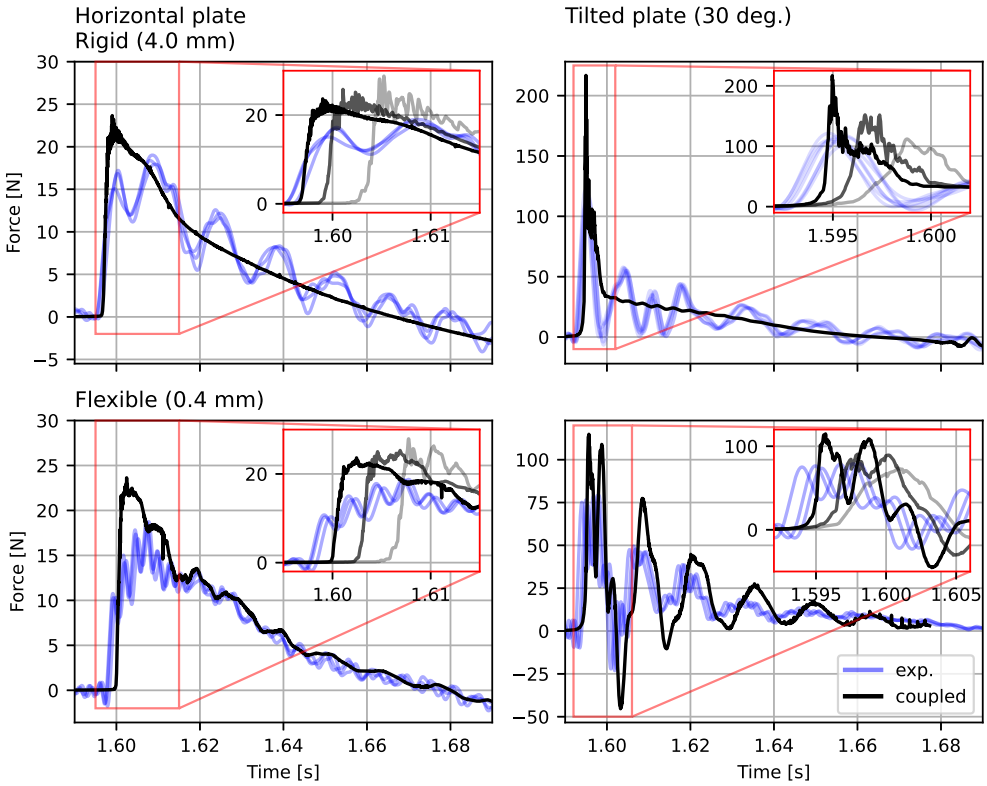


Figure 5: Measured and simulated reaction force. The insets show results for increasing grid resolution with decreasing transparency.

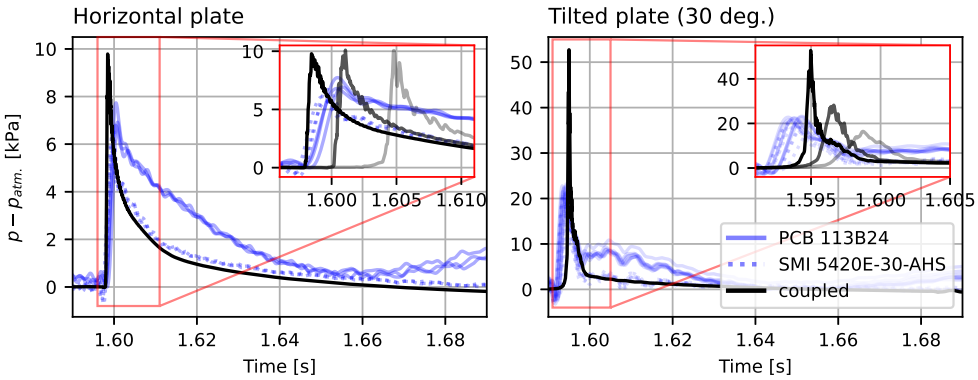


Figure 6: Measured and simulated pressure at a distance of 11 mm from the clamp. Two types of pressure sensors (PCB 113B24 and SMI 5240E-30-AHS) were used simultaneously at this length coordinate, placed at different locations in the third dimension. The insets show results for increasing grid resolution with decreasing transparency.

5. Hydroelasticity

In this section we discuss the observed effects of hydroelasticity in the wave impact experiment of the previous section. The elasticity of the reaction load cell is first discussed, followed by the effects of modelling plate elasticity on the total response.

5.1. Elasticity of the reaction load cell

The physical reaction force measurement for the rigid plate in Fig. 5 contains oscillations that can not be attributed to the plate deflection. These oscillations are absent in the numerical simulation of the same plate, which supports this statement. Instead, they are attributed to the excitation of a natural frequency of the measurement system originating from the combination of load cell stiffness and supporting clamp mass. For the lighter, flexible plate, the oscillations are of higher frequency due to its lower mass. The oscillations likely influence the response of the plate, making it difficult to separate the hydroelastic contributions of the support and plate bending. Steps to correct for the elasticity of the load cell, such as filtering out specific frequencies of the measurements, are not taken.

5.2. Elasticity of the plate

Two different numerical approaches for determining the structural response are compared. The first approach consists of two steps: Calculate hydrodynamic loads on a rigid plate and then apply these loads to a dynamic structural model of a thin plate. This approach does not take into account the hydroelastic interaction, so it is referred to as the quasi-static method. The second approach is the monolithically coupled hydroelastic model introduced in section 2, and is referred to as the coupled method.

The difference in deformation calculated with the quasi-static and coupled methods is visualised in Fig. 4. The maximum deflection of the horizontal plate is overestimated around 20 % by the quasi-static method compared to the coupled method. Additionally, without the modelling of the fluid-structure interaction, large oscillations in structural deformation remain after the initial excitation. These are not observed in the measurements or the coupled simulations.

The maximum deflection of the tilted plate is overestimated even more. This may be expected when looking at the duration of the impulse versus the first natural period of the plate, which is 31.3 ms accord-

ing to analytical solution of Eq. 10. This natural period is also observed in the quasi-static oscillations after impact. The duration of the force peak on the rigid, tilted plate is clearly below 0.01 s, while the natural period is more than a factor 3 higher. Consistent with literature, this impact can be placed in the impulsive regime where dynamic, coupled response is reduced compared to the quasi-static estimate.

6. Conclusion

This work introduced a model for hydroelastic simulation of wave impact on thin plates. A physical reference experiment is used for model validation and instructions for its numerical reproduction are presented. The following conclusions are drawn based on the presented results.

The importance of accompanying physical experiments with suitable numerical ones is highlighted by the observations in the measured reaction forces. For the impacts on the rigid plate, the elasticity of the reaction load cell caused oscillations in its measured value, which were absent in the numerical simulations without a load cell. The numerical results are thus important for the correctness of and confidence in the interpretation of the physical measurements. For the most severe wave impact considered, the hydroelastic analysis resulted in significantly lower structural deformations compared to the quasi-static analysis, highlighting the importance of hydroelasticity from a structural perspective.

The lack of numerical convergence for small relative wave impact angles requires further investigation, such as the inclusion of additional physics in the model.

Acknowledgments

The authors thank Jimme Bromlewe for his work on the physical experiment referred to in this study.

References

[1] G. K. Kapsenberg. Slamming of ships: where are we now? *Philosophical Transactions of the Royal Society A: Mathematical, Physical and Engineering Sciences*, 369(1947):2892–2919, 07 2011.

[2] S. Malenica, L. Diebold, S. Hong Kwon, and D. Cho. Sloshing assessment of the lng floating units with membrane type containment system where we are? *Marine Structures*, 56:99–116, 2017.

[3] B. Buchner. *Green water on ship-type offshore structures*. PhD thesis, Delft University of Technology, 2002.

[4] S. van Essen and H. Seyffert. Finding dangerous waves—review of methods to obtain wave impact design loads for marine structures. *Journal of Offshore Mechanics and Arctic Engineering*, 145(6):060801, 03 2023.

[5] A. D. Boon and P. R. Wellens. Probability and distribution of green water events and pressures. *Ocean Engineering*, 264:112429, 2022.

[6] S. Tavakoli, M. Singh, S. Hosseinzadeh, Z. Hu, Y. Shao, S. Wang, L. Huang, A. Grammatikopoulos, Y. Pearl Li, D. Khojasteh, J. Liu, A. Dolatshah, H. Cheng, and S. Hirdaris. A review of flexible fluid-structure interactions in the ocean: Progress, challenges, and future directions. *Ocean Engineering*, 342:122545, 2025.

[7] O. M. Faltinsen. Hydroelastic slamming. *Journal of Marine Science and Technology*, 5(2):49–65, 2000.

[8] A. Bereznitski. Slamming: The role of hydroelasticity. *International Shipbuilding Progress*, 48(4):333–351, 2001.

[9] F. Dias and J. M. Ghidaglia. Slamming: Recent progress in the evaluation of impact pressures. *Annual Review of Fluid Mechanics*, 50(Volume 50, 2018):243–273, 2018.

[10] M. van der Eijk and P. R. Wellens. An efficient pressure-based multiphase finite volume method for interaction between compressible aerated water and moving bodies. *Journal of Computational Physics*, 514:113167, 2024.

[11] B. P. Leonard, A. P. Lock, and M. K. MacVean. Conservative explicit unrestricted-time-step multidimensional constancy-preserving advection schemes. *Monthly weather review*, 124(11):2588–2606, 1996.

[12] B. Duz, M. J. A. Borsboom, A. E. P. Veldman, P. R. Wellens, and R. H. M. Huijsmans. Efficient and accurate plic-vof techniques for numerical simulations of free surface water waves. *Proceedings of the 9th International Conference on Computational Fluid Dynamics-ICCFD9, Istanbul, Turkey*, 2016.

[13] R. Scardovelli and S. Zaleski. Analytical relations connecting linear interfaces and volume fractions in rectangular grids. *Journal of Computational Physics*, 164(1):228–237, 2000.

[14] M. van der Eijk and P. R. Wellens. Two-phase free-surface flow interaction with moving bodies using a consistent, momentum preserving method. *Journal of Computational Physics*, 474:111796, 2023.

Sloshing

10th International Conference on HYDROELASTICITY IN MARINE TECHNOLOGY
Trondheim, Norway, June 16th-18th, 2026

Effect of Liquid Materials on Sloshing Flows and Hydrodynamic Impact on a Rectangular Tank

Park, G.[1], Hwang, J.[2], Park, T.[3], Kim, Y.[4*]

[1] Department of Naval Architecture and Ocean Engineering, Seoul National University, Seoul, Korea (hjk1028@snu.ac.kr)
[2] Department of Naval Architecture and Ocean Engineering, Seoul National University, Seoul, Korea (mannalgoge@snu.ac.kr)
[3] Department of Naval Architecture and Ocean Engineering, Seoul National University, Seoul, Korea (thth0325@snu.ac.kr)
[4] Department of Naval Architecture and Ocean Engineering, Seoul National University, Seoul, Korea (yhwankim@snu.ac.kr)

Abstract. Sloshing impact of liquid on cargo containment structures depend strongly on the properties of the liquid and the structural configuration. Therefore, observing sloshing behavior for different liquid materials is essential to understand the underlying physical phenomena and to predict sloshing-induced loads on ship structures. This issue is particularly critical for liquefied ammonia, which is emerging as a next-generation marine energy carrier. In this study, sloshing experiments were conducted in a rectangular tank to investigate differences in sloshing impact pressures for different liquids. Phase transition effects were specifically considered by maintaining constant liquid–gas density conditions representative of liquefied ammonia cargo. Based on the experimental framework proposed by Lee et al. (2021), a precise experimental system was developed to control depressurized ullage pressure and temperature, which govern the physical properties and phase transition behavior. Comparative single-impact sloshing experiments were performed using air–water and HFE-7300 under various ullage pressure conditions. The results demonstrate the significant influence of phase transitions on sloshing impact pressures. These findings are expected to provide valuable insights into the hydroelastic responses of systems subjected to evaporation and condensation processes.

Key words: *Sloshing impact, Phase change, Ullage depressurization, Liquefied ammonia, HFE-7300*

1. Introduction

Over the past few decades, extensive experimental databases have been established to clarify how key physical parameters, such as liquid-gas density ratio, affect LNG sloshing loads, leading to a practical design framework that relies on air/water and heavy-gas/water model tests for LNG containment systems [1-3]. With stricter IMO carbon regulations, ammonia is emerging as a next generation marine fuel, however sloshing in liquefied ammonia is not yet supported by sufficient dedicated data. For ammonia, the high liquid density combined with the low vapor density suggests that sloshing impact loads may become more severe than LNG, making a more rigorous experimental base is necessary as interest in ammonia containment system growing.

At present, however, the established LNG-oriented testing practice provides limited evidence for liquefied ammonia conditions. In particular, conventional water and air tests offer a baseline but do not systematically address thermodynamic conditions relevant to phase change. Moreover, since sloshing loads arise from complexed local flow around structural body and can vary with fluid properties, observing and comparing sloshing behavior across different working fluids is necessary for

* Correspondence to: yhwankim@snu.ac.kr

strengthening physical understanding and improving load prediction for cargo containment structures. In this context, the main purpose of this work is to establish an extended experimental basis for liquefied ammonia sloshing assessment through comparative single impact tests under density ratio similar conditions, with controlled thermodynamic environments relevant to phase change.

Sloshing impact pressures have been shown to vary with the working fluid [4, 5]. Under comparable global sloshing regimes with a various gas liquid density ratio, the density ratio was identified as a significant parameter governing the impact pressure. Studies were also conducted to relate phase transition effects to impact pressure characteristics with boiling water and found that boiling condition can influence the sloshing impact [2, 6]. Based on the founds of the boiling water test, phase transition theory based on one dimensional piston model was introduced [7]. In addition, two-dimensional model tank experimental system capable of realizing phase transition using Novec 7000 was developed, and the respective influences of density ratio and phase transition on impact pressure were measured [8].

Rapid heat exchange across the gas-liquid interphase during sloshing was also observed using Novec fluids [9, 10]. Consistent trends between Novec based tests and nitrogen/oxygen experiments were demonstrated, and also the Jakob number was proposed as a key property governing sloshing induced phase transition. More recently, phase change related sloshing experiments have continued. Impact pressures were measured for water with a vapor–air ullage mixture and for thermally saturated vapor–water waves in a flume tank [11, 12]. Overall, these results indicate that sloshing can trigger rapid interfacial heat transfer between the gas and liquid phases, leading to increased pressures during evaporation and pressure reductions during condensation.

In this study, single impact sloshing experiments were conducted using water and air, and non-aqueous working fluid material to enable controlled comparison across different thermodynamic conditions. Comparative tests were performed under three fluid conditions: air/water at atmospheric pressure, HFE-7300 at 20℃ with ullage air pressurization to 1.15 barA, and saturated HFE-7300 at 45℃ operated at an ullage pressure of 0.15 barA. Two types of single impact were considered to obtain physical insight under different flow behavior. For comparative tests while maintaining a constant gas-to-liquid density ratio, the model-tank temperature and ullage pressure were adjusted, including operation at non-atmospheric ullage pressures. Based on the previous works conducted by Lee et al. (2021), a precise experimental system was developed to control temperature and ullage pressure that determine the physical properties and phase transition behavior.

2. Experimental Set-Up

For physical similarity, we considered density ratio and slope of the Jakob number, defined here as the ratio between specific heat of liquid to the latent heat of evaporation (c_p/h_v). The conventional water and air test at 1.0 atmospheric pressure was adopted as a baseline case because its gas to liquid density ratio is similar to that of liquefied ammonia under the reference cargo condition. However, when phase transition is to be represented, achieving similarity using only the saturated vapor and liquid of a single substance becomes challenging because ammonia features a small density ratio and a low Jakob number slope. Operating the model tank under reduced ullage pressure enables the targeted density ratio to be achieved under single substance conditions. As a reference working fluid for comparison with the water and air case, we employed HFE-7300 (1,1,1,2,2,3,4,5,5,5 - decafluoro-3-methoxy-4-(trifluoromethyl)pentane) considering feasible test condition and moderate Jakob number. HFE-7300 is a colorless, odorless, non-toxic, and non-flammable fluid with a normal boiling point of 98℃ at 1.0 atmospheric pressure.

Comparative experiments were conducted under three fluid conditions: water and air, HFE-7300 at 20℃ with ullage air pressurization, and saturated HFE-7300 at 45℃. At 45℃, HFE-7300 reaches saturation at about 0.15 barA and under this saturated condition the density ratio between vapor and liquid becomes similar to that of liquefied ammonia and air/water at 1.0 atmospheric pressure, thereby satisfying the targeted density ratio parameter. However at 20℃, the saturation vapor pressure is lower (approximately 0.05barA). Therefore, air was injected into the model tank and the ullage pressure was increased to 1.15 barA to recover the same density ratio similarity condition. The thermodynamic properties of HFE-7300 vapor were evaluated using the Peng-Robinson equation of state [13]. The key physical properties of ammonia and each test condition are summarized in Table 1.

Table 1: Fluid properties

Fluid	Pressure (barA)	Liquid density (kg/m^3)	Density ratio (ρ_{gas}/ρ_{liquid})	Jakob Number Slope (1/K)
Ammonia	1.0	682	0.0012	0.0034
Air/Water	1.0	997		-
20℃ HFE-7300	1.15	1670		-
45℃ HFE-7300	0.15	1610		0.01

The present experimental arrangement was developed based on works done by Lee et al. (2021). A model tank of height (H) 600 mm, length (L) 1000 mm, and width (W) 100 mm was manufactured for the experiments. To allow the interior of tank to be maintained under vacuum while also obtaining efficient heat transfer, the main body was constructed from aluminum rather than acrylic. The front face of the tank was fitted with a pressure resistance tempered glass window to enable flow visualization. An RTD (resistance temperature detector) was embedded at the back plate to measure the temperature of the heating wall, allowing active monitoring and precise control of the liquid heating plate. Additional RTD sensors installed inside the tank measured the local liquid temperature at multiple locations. Figure 1 shows the manufactured model tank with the features described above.

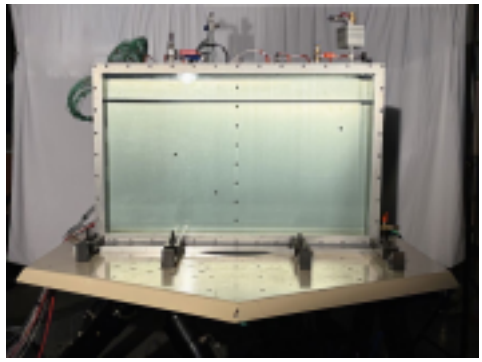


Figure 1: Experiment model tank: 1,000x600 x 100mm.

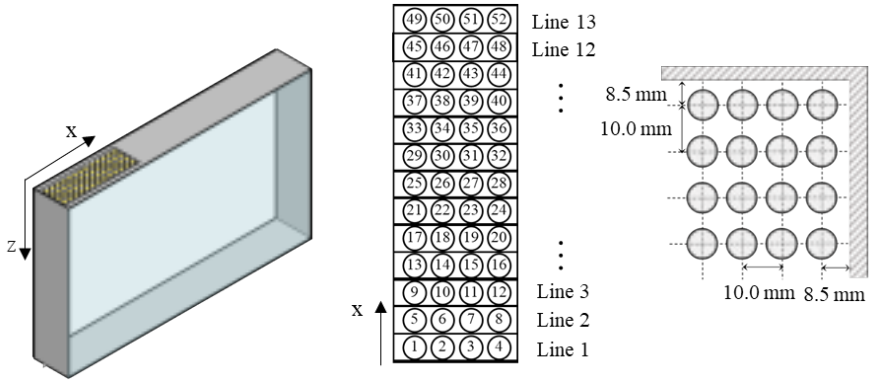


Figure 2: Location of the panel (left), numberings of sensor and lines (middle), and sensor arrangements (right).

The model tank was mounted on a 6 DOF Stewart motion platform with a maximum payload capacity of 1.5 tons. On the upper wall of the tank, an array of dynamic pressure sensors was installed for

measuring impact pressure of the fluid, arranged in 4 rows and 13 columns, for a total 52 sensors. The sensor panel and the measurement lines are illustrated in Figure 2. Because experiments were conducted at elevated temperature, sensor named 601CBA (manufactured by Kistler) with a high temperature capability were selected to ensure stable measurements. We conducted a comparative test between a conventional pressure sensor, 211B5, and the present sensor, 601CBA. Under cool-water conditions, the measured pressures were similar for both sensors. However, under heated-liquid conditions, the 601CBA sensor provided much more robust and reliable pressure measurements than the conventional sensor. The sampling rate was set to 20kHz, and undesired low frequency bias in the dynamic pressure signal was removed using a high pass filter following the Lee et al. (2021)'s work. During platform excitation, a high speed camera which is synchronized with the DAQ system recorded the internal flow, enabling direct observation of local flow features that can vary with the working fluid and phase change.

A schematic of the experimental set-up is shown in Figure 3. At the beginning of each setting, a vacuum pump was used to remove air and moisture from the model tank. After evacuation, the liquid was heated and partially vaporized. During this process, both the liquid temperature and ullage pressure increased. Once the target pressure was reached, the generated vapor was vented to the outside as boil-off gas. A pressure regulator controlled the discharge rate of ullage gas to maintain a nearly constant ullage pressure. A high capacity condenser rapidly condensed the boil-off gas, maintaining very low downstream pressure and preventing the ullage pressure from rising due to back pressure effects.

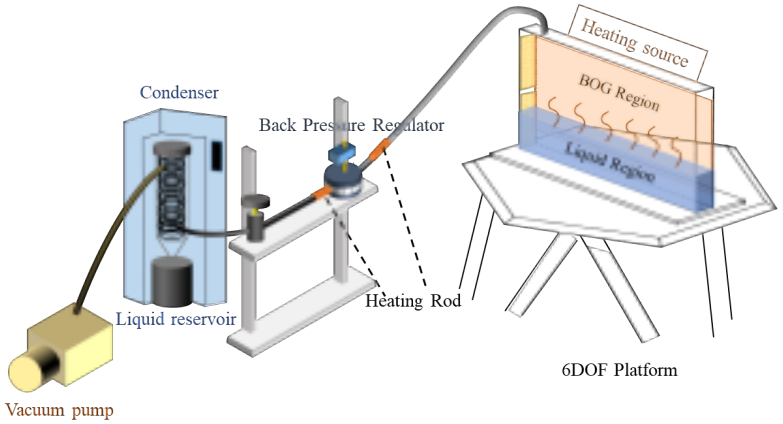


Figure 3: Schematic of experimental set-up.

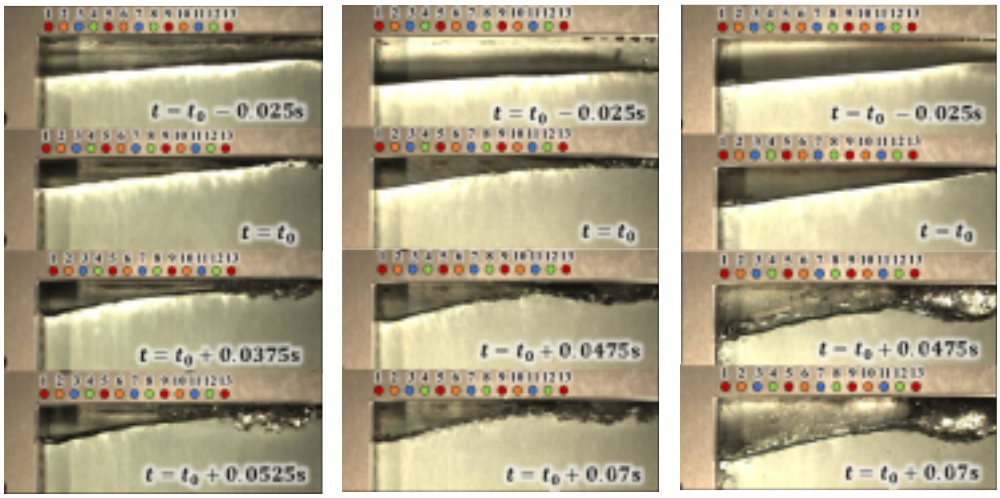
In the present study, single impact tests were performed at a filling level of 80% of the tank height. Platform motion was prescribed using a combined hyperbolic tangent and sine function [8, 14]. The function is described as follows:

$$A(t) = \begin{cases} A\tanh\left(\pi\frac{t^2}{T}\right)\sin\left(2\pi\frac{t}{T}\right) & if\ t \le T \\ A\tanh\left(\pi\frac{(2T-t)^2}{T}\right)\sin\left(2\pi\frac{t}{T}\right) & if\ T < t \le 2T \end{cases} \quad (1)$$

Two types of impact events were considered: impacts involving a gas pocket and regular impacts where the liquid directly contacts the wall without an entrapped gas pocket. For gas pocket impacts, an excitation amplitude of 1/25 of the tank length and an excitation frequency of 1.15 times of the resonant frequency were used. For regular impacts, an amplitude of 1/20 of the tank length and 0.75 times of the resonant frequency were used. Following the Froude's law on the pressure, measured pressures were non-dimensionalized by dividing by ρgL, where ρ is the liquid density, g is the gravitational acceleration, and L is the tank length. For each condition, repeated tests were conducted to assess convergence and repeatability.

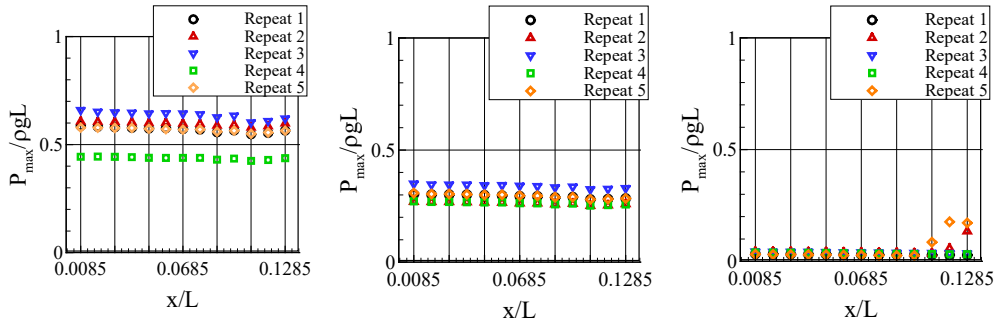
3. Results

Figure 4 and Figure 5 present, respectively, the high speed captured images of gas pocket dynamics and the maximum impact pressures of each lines measured during gas pocket impacts for water and air, 20℃ HFE-7300, and 45℃ HFE-7300. In figure 4, snapshots are shown at selected time intervals referenced to t_0, defined as the moment when the first major pressure peak occurs, so that the subsequent oscillatory behavior can be clearly compared across cases.



(a) Air/Water (b) 20℃ HFE-7300 (c) 45℃ HFE-7300

Figure 4: Snapshots of local flow during gas pocket impacts.



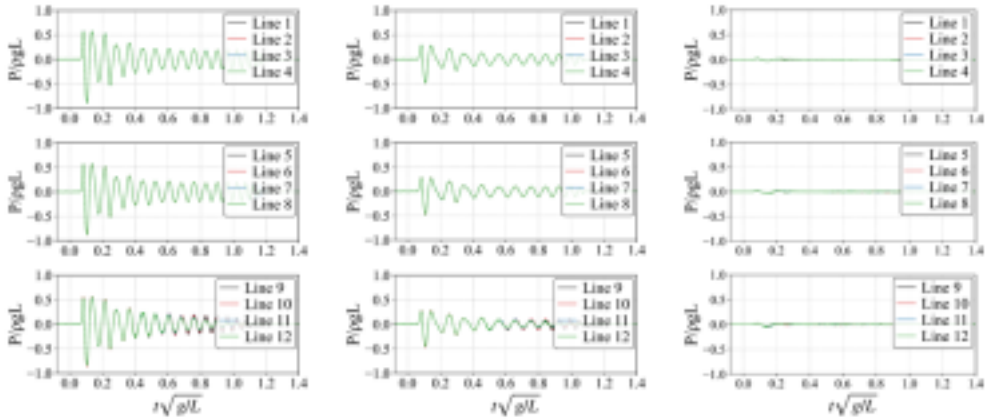
(a) Air/Water (b) 20℃ HFE-7300 (c) 45℃ HFE-7300

Figure 5: Distribution of the maximum gas pocket impact pressure.

For air/water and HFE-7300 at 20℃ conditions, in which phase change is negligible, the overall gas pocket shape and size were similar under identical excitation, and the observed gas pocket motion showed similar dynamics. In contrast, when phase change occurred at 45℃ HFE-7300 at the near saturation, condensation weakened the gas liquid interface, leading to noticeable gas pocket deformation. Moreover, earlier liquid intrusion into the gas pocket was observed, followed by a sweep along the upper wall. Regarding the non-dimensional maximum impact pressure, air/water case produced the largest peaks, consistent with Lee et al. (2021). When phase change occurred, the impact

load was not effectively transmitted to the upper wall, resulting in significantly smaller measured pressures. When phase change was absent, similar maximum peak pressures were obtained along the tank length. In contrast, under phase-change conditions, the outermost measurement lines (Lines 11-13) exhibited distinct peak levels and larger scatter between repeated tests, consistent with the observed deformation.

The measured pressure time histories during gas pocket impacts are shown in Figure 6. Clear pressure oscillations were observed for the two non-phase change cases. In air/water case, oscillations occurred at higher frequency than in 20℃ HFE-7300, primarily due to differences in thermophysical properties [15]. Specifically, the larger mean molecular weight and lower adiabatic index (c_p/c_v) of the HFE-7300 vapor and air mixture lead to a lower gas pocket oscillation frequency than in air/water. In the saturated HFE-7300 case at 45℃, the gas pocket oscillations largely vanished, which is interpreted as suppression of gas pocket expansion and contraction due to ongoing interfacial phase change. This observation suggests that, in typical aerated or gas pocket impact events, phase change can mitigate the impact pressure by damping the gas pocket induced loadings.



(a) Air/Water (b) 20℃ HFE-7300 (c) 45℃ HFE-7300

Figure 6: Pressure signals in time series of gas pocket impact.

Figure 7 shows the flow evolution under regular impact conditions, referenced to t_0, the moment of maximum impact. The liquid climbs along the wall, directly strikes the upper corner without an entrapped gas pocket, and then sweeps across the upper wall. Unlike gas pocket impacts, the overall flow pattern under direct impacts was similar for all fluid conditions.

The non-dimensional maximum pressures for direct impacts shown in Figure 8 were comparable across fluid media conditions. This may be attributed to the short impulse time. The impact event ends before sufficient thermodynamic interaction between the gaseous and liquid phase develops, so phase transition does not significantly influence the impact pressure. The 20℃ HFE-7300 condition exhibited relatively large scatter in the maximum peak. This may be explained by compositional stratification in the ullage gas mixture. Because the components of the mixture have very large differences in density, small variations in the local gas composition can occur between repeated tests. This can change the local ullage gas density and, consequently, increase the scatter in the measured maximum pressures.

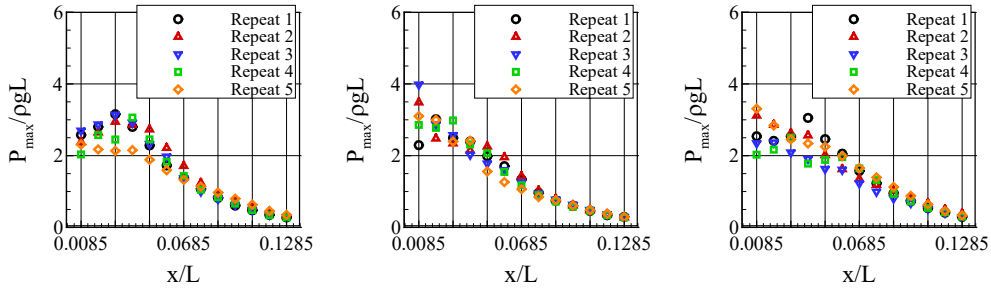
Figure 9 presents the non-dimensional pressure time histories for the regular impact case. In contrast to gas pocket impacts, the pressure develops clearly sequential behavior across the measurement lines. The earliest peak appears in the upstream lines where the initial liquid – wall contact occurs, and subsequent peaks are recorded later at downstream lines with progressively smaller amplitudes. Both the peak levels and the arrival times of these peaks are similar across the tested fluids, indicating that phase change has small influence on this short duration event. Overall, the results suggest that, for bubble free direct impacts under the present single impact conditions, the density ratio effect seems to

dominate over other fluid property effects. Those results are associated with previous density ratio-based estimations for liquefied cargo sloshing loads.



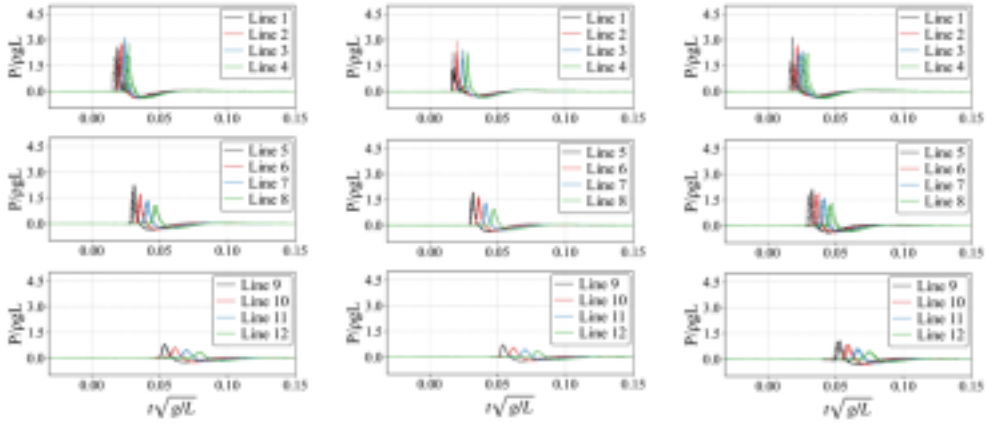
(a) Air/Water (b) 20°C HFE-7300 (c) 45°C HFE-7300

Figure 7: Snapshots of local flow during regular impacts.



(a) Air/Water (b) 20°C HFE-7300 (c) 45°C HFE-7300

Figure 8: Distribution of the maximum impact pressure during regular flow.



(a) Air/Water (b) 20°C HFE-7300 (c) 45°C HFE-7300

Figure 9: Pressure signals in time series of liquid direct impact

4. Conclusion

In this study, the effect of working fluids on sloshing loads was investigated through comparative single-impact experiments in a rectangular tank. Two representative impact conditions at an 80% filling level were examined: gas pocket impacts formed by gas entrapment at the tank corner and regular impacts without gas entrapment. Distinct differences in impact responses were observed between these two flow regimes, and the following conclusions are drawn:

- For gas pocket impacts, phase transition significantly modified the global gas pocket dynamics and markedly reduced the transmitted wall loads. Consistent with previous studies, the vapor–liquid interface weakened under phase-change conditions, and gas pocket oscillations were suppressed. In contrast, under non–phase-change conditions, differences in the thermodynamic properties of the working fluids influenced the characteristic oscillation frequency when oscillations occurred.
- For direct regular impacts without bubbles, the influence of phase transition was less pronounced. The local flow features were similar across all tested cases, and the maximum nondimensional impact pressures were comparable under conditions with similar density ratios. These results indicate that, for bubble-free impacts, the density ratio is the dominant governing parameter, whereas phase transition plays a critical role when gas pockets are involved.
- Overall, the findings demonstrate that phase transition can significantly affect fluid impact in sloshing phenomena. Therefore, reliable design load assessment should be supported by model tests that consider not only density ratio similarity but also the effects of phase change.

Acknowledgements

This experimental equipment, facility and research are supported by Lloyd's Register Foundation (LRF) Research Center at Seoul National University (SNU), Project GCY-100002. Also, this research is supported by the HD Hyundai Heavy Industries (HD HHI) and Samsung Heavy Industries (SHI). Their support is greatly appreciated.

References

[1] S.Y. Kim, Y. Kim, J.J. Park, B. Kim, *Experimental study of sloshing load on LNG tanks for unrestricted filling operation*, Proceedings of the 26th International Ocean and Polar Engineering Conference (ISOPE), Rhodes, 2016.

[2] S. Maillard, L. Brosset, *Influence of density ratio between liquid and gas on sloshing model test results,* Proceedings of the 19th International Offshore and Polar Engineering Conference (ISOPE), Osaka, 2009.

[3] Y. Kim, T.H. Park, J. Lee, Y. Ahn, S.Y. Kim, *Observation on effects of liquid-gas density ratio in sloshing pressure for LNG cargo design,* Proceedings of the 40th International Workshop on Water Waves and Floating Body (IWWWFB), Shanghai, 2025.

[4] Y. Ahn, Y. Kim, S.Y. Kim, *Experimental study and method of sloshing model test considering gas-liquid density ratio*, International Journal of Offshore and Polar Engineering, 29(3):257-268, 2019.

[5] M.R. Karimi, L. Brosset, M.L. Kaminski, J.M. Ghidaglia, *Effects of ullage gas and scale on sloshing loads*, European Journal of Mechanics B/Fluids, 62:59-85, 2017.

[6] Y. Kim, J. Lee, J. Kim, *Experimental observation of the effects of liquid temperature and bubbles on impact pressure inside gas pocket*, International Journal of Offshore and Polar Engineering, 27(01):1-10, 2017.

[7] J.P. Braeunig, L. Brosset, F. Dias, J.M. Ghidaglia, *On the effect of phase transition on impact pressure due to sloshing*, Proceedings of the 20th International Offshore Polar Engineering Conference (ISOPE), Beijing, 2010.

[8] J. Lee, Y. Ahn, Y. Kim, *Experimental study of effect of density ratio and phase transition during sloshing impact in rectangular tank*, Ocean Engineering, 242, 2021.

[9] S.P. Das, E.J. Hopfinger, *Mass transfer enhancement by gravity waves at a liquid-vapour*

interface, International Journal of Heat and Mass Transfer, 52:1400-1411, 2009.

[10] C. Ludwig, M.E. Dreyer, E.J. Hopfinger, *Pressure variations in a cryogenic liquid storage tank subjected to periodic excitations*, International Journal of Heat and Mass Transfer, 66:223-234, 2013.

[11] R. Ezeta, L. Kimmoun, L. Brosset, *Influence of ullage pressure on wave impacts induced by solitary waves in a flume tank*, Proccedings of the 33rd International Ocean and Polar Engineering Conference (ISOPE), Ottawa, 2013.

[12] R. Ezeta, B.P. Muniz, Y.L.E. Fan, N. Kim, N. Couty, L. Brosset, D. Van Der Meer, *Large-scale wave impact of a boiling liquid*, Journal of Fluid Mechanics, 1008, 2025.

[13] A. Aminian, D. Celný, E. Mickoleit, A. Jäger, V. Vinš, *Ideal gas heat capacity and critical properties of HFE-type engineering fluids:Ab initio predictions of* C_p^{ig}*, modeling of phase behavior and thermodynamic properties using Peng-Robinson and volume-translated Peng-Robinson equations of state*, International Journal of Thermodynamics, 43, 2022.

[14] T. Loysel, E. Gervaise, S. Moreau, L. Brosset, *Results of the 2012-2013 sloshing model test benchmark*, Proceedings of the 23rd International Offshore and Polar Engineering Conference (ISOPE), Alaska, 2013.

[15] B.C. Abrahamsen, O.M. Faltinsen, *The natural frequency of the pressure oscillations inside a water-wave entrapped air pocket on a rigid wall,* Journal of Fluids and Structures, 35:200-212, 2012.

10th International Conference on HYDROELASTICITY IN MARINE TECHNOLOGY
Trondheim, Norway, June 16th-18th, 2026

Experimental and Numerical Studies on Sloshing Flows in a Rectangular Tank with a Hyper-elastic Baffle

Park, T.[1], Park, C.J.[2], Kim, Y.[3*], and Lee, J.[4]

[1] Department of Naval Architecture and Ocean Engineering, Seoul National University, Seoul, Republic of Korea (thth0325@snu.ac.kr)
[2] Hyundai Maritime Research Institute, HD Hyundai Heavy Industry Co., Ltd., Sungnam, Republic of Korea (cjpark@hd.com)
[3] Department of Naval Architecture and Ocean Engineering, Seoul National University, Seoul, Republic of Korea (yhwankim@snu.ac.kr)
[4] Hyundai Maritime Research Institute, HD Hyundai Heavy Industry Co., Ltd., Sungnam, Republic of Korea (ishoti@hd.com)

Abstract. This study investigated the hydro-elastic effects of a flexible vertical baffle on sloshing flows using a combined framework of model experiments, semi-analytic eigenvalue analysis, and numerical simulations. A beam-type hyper-elastic baffle was installed at the bottom center of a rectangular tank to examine its influence on sloshing flows induced by horizontal tank motion. Unlike previous studies that primarily focused on violent sloshing regimes, this work emphasized the transition from linear to nonlinear responses, with particular attention to small-amplitude excitations (A = 10 and 20 mm). A semi-analytic formulation was adopted as a theoretical reference to solve the coupled eigenvalue problem, enabling the prediction of hydro-elastic natural frequencies and mode shapes of the fluid–structure system. The experimental results showed that, at small excitation amplitudes, the pressure asymmetry across the baffle was a more sensitive indicator of hydro-elastic resonance than the tip displacement, exhibiting strong agreement with the theoretically predicted eigenfrequencies. Furthermore, a two-way implicit fluid–structure interaction coupling between Star-CCM+ and Abaqus was implemented to assess the baffle's dynamic response and phase-lag characteristics. The numerical model successfully reproduced the dominant resonant behaviors observed in the experiments, although it tended to underestimate high-frequency nonlinear fluctuations in more violent sloshing conditions. By clarifying the applicability limits of linear eigenvalue theory and validating the predictive capability of nonlinear fluid–structure interaction models, this study provides a reliable benchmark for the design and assessment of elastic internal structures in liquid cargo tanks.

Key words: *Sloshing; Fluid-Structure interaction; Hydroelasticity; Flexible baffle*

1. Introduction

Liquid sloshing, defined as the free-surface oscillation of a partially filled tank, remains a critical challenge in naval architecture and ocean engineering. The dynamic loads induced by sloshing can lead to significant structural damage, stability issues, and operational hazards in marine vessels, particularly in liquefied natural gas (LNG) carriers and offshore storage units. When the frequency of the external vessel motion approaches the natural frequency of the internal fluid, resonance occurs, resulting in amplified wave elevations and impact pressures on the tank walls. To mitigate these effects, various internal structures, such as swash bulkheads and baffles, have been widely adopted to dissipate kinetic energy and shift the system's resonance characteristics.

* Correspondence to: yhwankim@snu.ac.kr

Traditionally, research on sloshing suppression has focused on rigid baffles. Foundational studies by Abramson (1966) and Faltinsen (2017) established the understanding of fluid behavior in moving containers and nonlinear sloshing. Focusing on the internal structures [1-2], Evans and McIver (1987) and Jeyakumaran and McIver (1995) investigated the shift in sloshing natural frequencies induced by thin rigid baffles using potential flow theory and variational principles. Subsequent experimental studies [3-4], such as those by Xue et al. (2017), have extensively quantified the pressure reduction efficiency of various rigid baffle configurations [5]. However, as structural designs become increasingly lightweight and specialized materials are introduced, the assumption of absolute rigidity is often challenged by hydro-elastic interactions.

Flexible baffles introduce complexity through inherent fluid-structure coupling, where energy absorption and resonance modification via hydro-elasticity offer potentially more efficient damping than rigid alternatives. Recent analytical efforts, such as Meng et al. (2021), provided semi-analytical solutions for linear regimes, while numerical studies using various fluid-structure interaction (FSI) frameworks have attempted to capture this interaction [6].

In a previous study, Park et al. (2025) [7] conducted experimental observations of violent sloshing flows (with excitation amplitudes of A = 30 to 70 mm) in a rectangular tank equipped with hyper-elastic baffles, characterizing the impact pressures and large-scale deformations in highly nonlinear regimes. While that study provided valuable insights into extreme sloshing events, the fundamental relationship between the linear hydro-elastic natural frequencies and the onset of nonlinearity remained somewhat obscured by the dominance of violent flow features. There is a clear research gap in understanding how the system transitions from a linear hydro-elastic state to a nonlinearly detuned state, and how accurately simplified eigenvalue theories can predict resonance at lower excitation levels.

To address this gap, the present study extends the work of Park et al. (2025) [7] by focusing on the small-amplitude excitation range (A = 10 and 20 mm) to clarify the fundamental resonance characteristics. The primary objective is to evaluate the validity of a linear hydro-elastic eigenvalue framework through detailed experimental measurements and numerical computations. Unlike the previous emphasis on violent impacts, this paper highlights pressure asymmetry as a sensitive indicator of resonance in the small-amplitude regime. A semi-analytic eigenvalue formulation, expanding upon the methods of Evans and McIver and Meng et al., is employed as a theoretical baseline. Furthermore, a two-way implicit FSI coupling between Star-CCM+ and Abaqus is utilized to replicate the experiments, providing a quantitative assessment of the numerical model's ability to capture frequency shifts and damping effects. The findings of this study establish a robust link between linear theoretical predictions and nonlinear experimental observations, providing a comprehensive benchmark for the design of flexible internal structures in containment systems.

2. Eigenvalue Analysis for Sloshing Natural Modes

2.1 Baseline Eigenvalue Problem for a Rigid Vertical Baffle

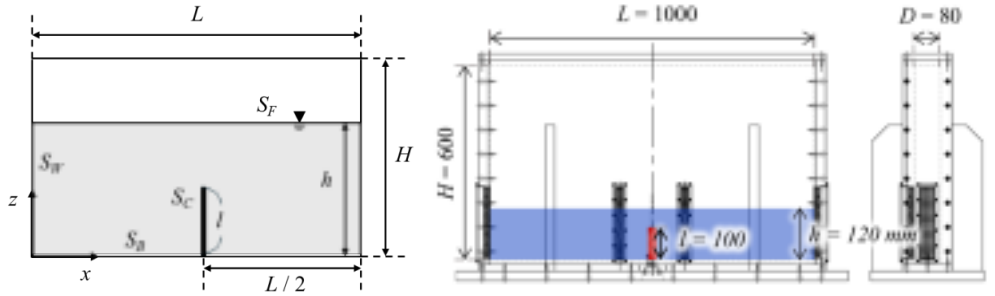


Figure 1: Schematic diagram and notations of the rectangular tank (*left*) and detailed geometric dimensions of the experimental model (*right*). All dimensions are in mm.

In this section, the sloshing natural modes in a rectangular tank with a vertical internal baffle are formulated as an eigenvalue boundary value problem (BVP) within the framework of potential flow theory. The fluid is assumed to be incompressible, inviscid, and irrotational.

Consider a rectangular with length L and filling height h. The velocity potential $\phi(x,z,t) = Re[\Phi(x,z)e^{i\omega t}]$ satisfies the Laplace equation within the fluid domain, subject to the linearized free-surface boundary condition $K\Phi - \partial\Phi/\partial z = 0$ on $z = h$, and the impermeability condition $\partial\Phi/\partial n = 0$ on the fixed rigid boundaries S_w and S_B. For a rigid internal baffle, the same Neumann condition is enforced on the baffle surface.

2.2 Rigid-baffle Configuration: Narrow-Gap Approximation

Following the approach of Evans and McIver [3], the problem can be reformulated using the horizontal gap velocity $u(z)$ at the clearance between the baffle and the free surface:

$$u(z) = \frac{\partial\Phi}{\partial z} \quad \text{at the gap.} \tag{1}$$

The gap represents the distance between the baffle tip and the free surface. This leads to an exact eigenvalue condition expressed in the following determinant form:

$$\det|\mathbf{C} - \mathbf{A}(K)\mathbf{B}| = 0. \tag{2}$$

In this expression, **C** represents the uncoupled sloshing operator of the non-compartmented tank, **B** denotes the modal coupling induced by the baffle, and **A** is a coupling coefficient depending on the eigenvalue *K*.

2.3 Rigid-baffle Configuration: Thin Bottom-mounted Limit

When the baffle thickness is small compared to the tank length, the eigenvalue shift can be evaluated using Green's identity [4]. For a bottom-mounted thin baffle located at $x = x_0$, the eigenvalue *K* can be approximated in the following closed form:

$$K \approx k_m \tanh(k_m h)\left[1 - \frac{2\pi^2 \sin^2(k_m(x_0 + L/2))}{L \sinh(2k_m h)}\left(\frac{l}{L}\right)^2\right] \tag{3}$$

where $k_m = m\pi/L$ is the horizontal wavenumber of the *m*-th unperturbed sloshing mode and *l* is the baffle height.

2.4 Eigenvalue Problem with a Flexible Baffle Configuration

For a flexible baffle, the rigid boundary condition on the baffle surface is replaced by the kinematic compatibility condition [6]:

$$\frac{\partial\Phi}{\partial x} = i\omega W(z) \tag{4}$$

where $W(z)$ is the lateral deflection of the baffle, assuming harmonic time-dependence of the form $w(z,t) = W(z)e^{i\omega t}$. The baffle is modeled as a vertical Euler-Bernoulli beam clamped at the bottom center of the tank, governed by:

$$EI\frac{d^4W(z)}{dz^4} - \mu\omega^2 W(z) = \Delta P(z). \tag{5}$$

Here, *EI* is the flexural rigidity, μ is the mass per unit length of the baffle, and $\Delta P(z)$ is the spatial amplitude of the differential pressure ($\Delta p(z,t) = \Delta P(z)e^{i\omega t}$).

By expanding the potential and the baffle deflection into their respective modal bases, the hydro-elastic problem is reduced to a coupled generalized eigenvalue problem:

$$\mathbf{K}_{coupled}\mathrm{x} = \omega^2 \mathbf{M}_{coupled}\mathrm{x}. \tag{6}$$

In the limit of infinite stiffness $(EI \to \infty)$, the formulation recovers the rigid-baffle condition. These theoretical natural frequencies are used as a baseline for interpreting the hydro-elastic responses observed in the experiments, particularly in identifying resonance peaks at small excitation amplitudes. Table 1 summarizes the natural frequencies (ω_n) predicted from the eigenvalue analyses.

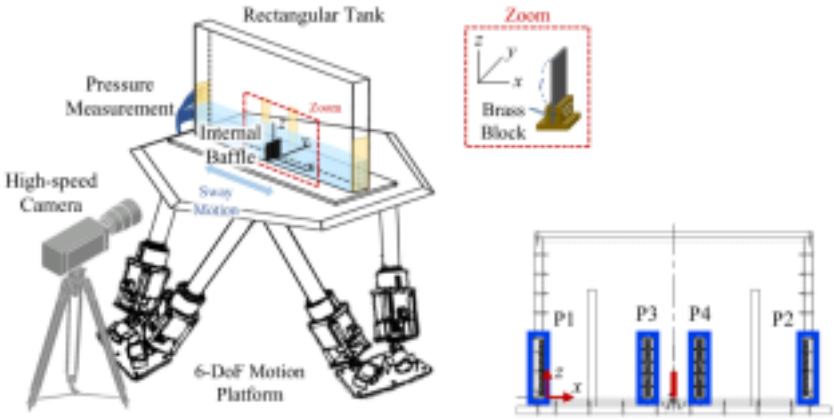
Table 2: Comparison of eigenfrequencies of fundamental sloshing mode.

h / H (%)	$\omega_n (L/g)^{1/2}$		
	without baffle	with rigid baffle	with flexible baffle
		from Eq. (6)	from Eq. (9)
20	1.064	0.928	0.853

3. Experimental Scheme and Test Conditions

3.1 Experimental Setup and Pressure Measurement

The experimental setup in this study follows the configuration established by Park et al. (2025) [7], utilizing the same tank dimensions defined in Figure 1. For this study, a flexible vertical baffle made of Nitrile Butadiene Rubber with 80 degrees hardness (NBR 80) was mounted at the bottom center of the tank in a cantilever configuration using two brass blocks depicted in Figure 2. Based on linear elastic indentation hardness, a relation between the hardness (S) for Shore 'A' and the Young's modulus (E) can be expressed in Eq. (7) [8]. The detailed properties of the baffle are summarized in Table 3. The baffle dimensions were 100 x 79.5 x 4 mm. All tests were performed at a shallow-water filling level of h / H = 20% (h = 120 mm).



(a) Experiment setup (b) Pressure sensor panels location

Figure 2: Schematic of the experimental setup including the motion platform, high-speed camera system (a), and the spatial distribution of clustered pressure sensors on the walls (b).

$$E_{shore\ A} = \frac{0.0981(56+7.62336\,S)}{0.137505(254-2.54\,S)}. \tag{7}$$

Table 3: The material properties of the flexible baffle.

	Unit	Value
Material hardness (S)	Shore 'A'	81
Young's modulus (E)	MPa	9.96
Flexural rigidity (EI)	N·m^2	4.22 x 10^{-3}
Density (ρ)	kg/m^3	1300
Mass per unit length (μ)	kg/m	0.4134

To capture the hydrodynamic loads, clustered pressure sensors were mounted on the tank walls. The sensor layout is illustrated in Figure 2(b); Panel 1 (P1) and 2 (P2) were installed on the side walls, while the remaining panels were positioned on the rear wall, symmetrically 100 mm away from the tank centerline. Dynamic pressure signals were recorded at a sampling frequency of 20 kHz [9]. To quantify the flow asymmetry induced by the baffle's hydro-elastic response, the differential pressure (Δp) was defined as:

$$\Delta p(t) = p_{left}(t) - p_{right}(t). \tag{8}$$

To ensure statistical reliability and capture the steady-state characteristics, the asymmetry was evaluated using the Root Mean Square (RMS) value of Δp averaged over 500 consecutive cycles, defined as:

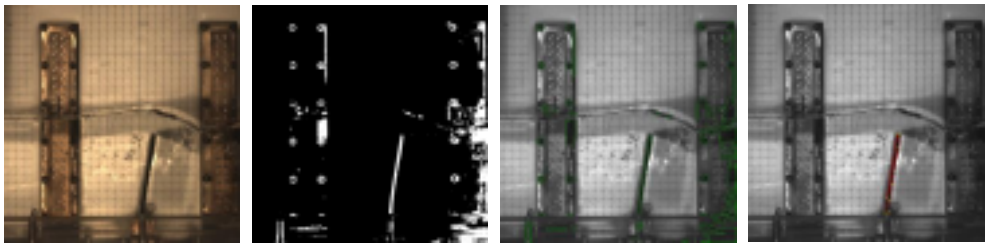
$$\Delta p_{RMS} = \sqrt{\frac{1}{T}\int_{t_0}^{t_0+T}[\Delta p(t)]^2 dt}. \tag{9}$$

where T represents the duration corresponding to 500 periods. The continuous integration over an extensive duration of 500 periods ensures that the hydro-elastic response is fully developed and strictly stationary. This robust temporal averaging effectively filters out random experimental uncertainties and transient noises, guaranteeing the statistical convergence of the evaluated resonance peaks.

This differential metric was applied to both the side wall panels (P1 vs. P2) and the rear wall panels (P3 vs. P4). Finally, the pressure signals were synchronized with the tank motion to ensure precise phase-lag analysis between the fluid excitation and the structural response.

3.2 OpenCV-based Baffle Displacement Detection

To overcome the limitations of manual grid-paper-based measurement – specifically low processing speed and potential human error – this study implemented an automated image-processing algorithm using the OpenCV library (version 4.9.0).



(a) Original (b) Preprocessing (c) Noise Removal (d) Detection

Figure 3: Sequential stages of baffle tip displacement detection: (a) original image, (b) preprocessing, (c) noise removal, and (d) detected baffle's configuration.

The baffle's tip displacement was extracted through a multi-stage process:

- Preprocessing: High-speed camera recording (100 fps) was converted to grayscale and binarized using a heuristically optimized threshold to account for varying ambient lighting conditions in the laboratory.
- Noise Removal: A morphology transformation ('Opening' operation) was applied to eliminate image noise caused by sensor clusters or air bubbles during violent sloshing events.
- Detection & Calibration: The baffle was identified based on its geometric features (clamped base and high aspect ratio), and the (x, z) coordinates of the uppermost vertices were tracked. These pixel coordinates were then converted to physical units (mm) using a pre-recorded grid calibration image.

3.3 Test Conditions

The test conditions focused on the small-amplitude regime to evaluate the system's linear hydro-elastic characteristics. Table 4 summarizes the detailed test parameters used in this study.

Table 4 : Test conditions.

Parameter	Value
Filling Height (h / H)	20%
Excitation Motion	Regular sway motion
Test Cycle	At least 500 cycles
Excitation Amplitudes (A)	10, 20 mm
Excitation Frequency (ω)	$0.7 \leq \omega_n/\omega_{n,\text{ no baffle}} \leq 1.5$ (Steps: 0.05 – 0.1) (where $\omega_{n,\text{ no baffle}} (L / g)^{1/2} = 1.064$)

4. Computational Methodology

4.1 Fluid-Structure Interaction (FSI) Framework

To investigate the complex hydro-elastic interaction between the sloshing flow and the flexible baffle, a strongly coupled two-way fluid-structure interaction (FSI) analysis was performed. This study adopted a partitioned coupling approach, where the fluid and structural governing equations are solved individually by specialized solvers. Star-CCM+ was utilized as the fluid solver to capture free-surface elevations and hydrodynamic pressures, while Abaqus was employed as the structural solver to compute the nodal displacements and deformations of the baffle [12-13].

The two solvers are coupled through an implicit co-simulation scheme. This implicit coupling involves an iterative correction loop within each time step to ensure equilibrium at the fluid-structure interface. Unlike explicit coupling, this synchronized exchange of pressure loads and structural deformations eliminates time lags in force-displacement transfer, providing numerical stability even in resonant regimes where the structural response is significant.

4.2 Numerical Setup and Material Modeling

To precisely replicate the experimental setup, a pressure outlet was applied to the top vent, and side-wall symmetry conditions were enforced for two-dimensional (2D) flow efficiency. The fluid domain was discretized into 213,307 finite volumes with refined layers near the free-surface and baffle, while the structural baffle comprised 1,600 finite elements to resolve high-order bending modes. Transient fluid flow was resolved using a segregated solver with a second-order implicit unsteady time-integration scheme, iteratively coupling momentum and pressure-correction equations. The liquid-gas interface was tracked via the Volume of Fluid (VoF) method combined with the High Resolution Interface Capturing (HRIC) scheme to minimize numerical diffusion. A laminar flow assumption was adopted

since hydrodynamic loads on the baffle are predominantly governed by pressure gradients rather than viscous shear stresses. The experimental tank motion, including the ramp-up phase, was directly imposed to ensure consistency with the physical tests. To capture large-strain behavior, the flexible baffle was modeled as a geometrically nonlinear hyper-elastic body using a second-order Ogden model, with parameters summarized in Table 5.

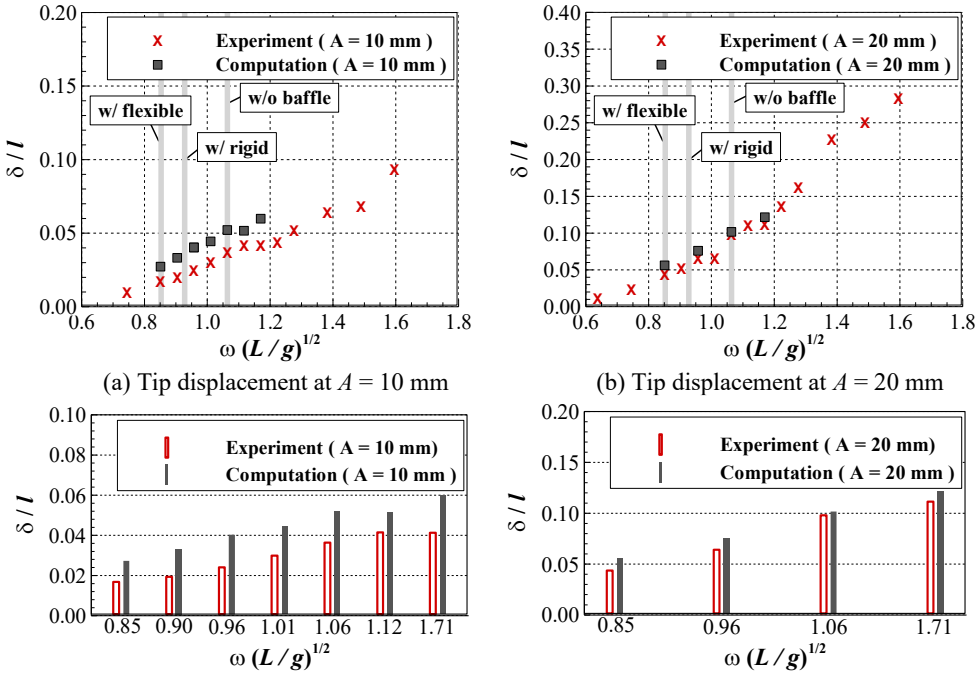
Table 5 : The material constants of the Ogden model for the flexible baffle.

Parameter	N	μ_1	α_1	μ_2	α_2
NBR 80	2	1.33×10^6	7.4	6.14×10^6	-4.7

5. Results and Observations

5.1 Comparative Analysis of Baffle Tip Displacement

The maximum normalized displacement (δ / l) of the baffle was compared between the experimental measurements and the numerical computations across a range of excitation frequencies (ω) as shown in Figure 4.



(a) Tip displacement at A = 10 mm

(b) Tip displacement at A = 20 mm

(c) Comparison of displacement at A = 10 mm

(d) Comparison of displacement at A = 20 mm

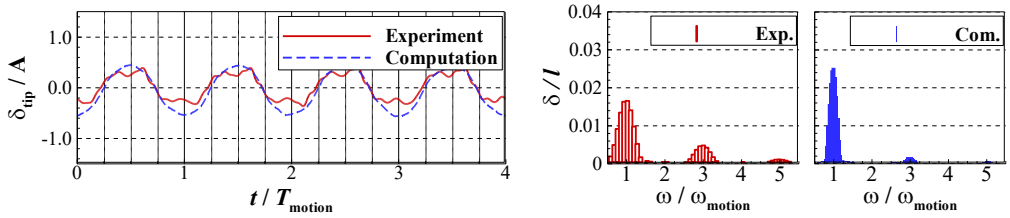
Figure 4: Normalized baffle tip displacement (δ / l) for different excitation amplitudes (A = 10, 20 mm). The results contrast experimental data with numerical computations, where vertical lines denote the theoretical natural frequencies for various internal configurations.

Overall, the numerical model effectively reproduced the frequency response trends observed in the experiments. However, a consistent overestimation of the displacement by the simulations was observed across most frequency bands. This discrepancy was particularly pronounced at the lower excitation

amplitude (A = 10 mm), where the experimental response remained relatively subtle. Such overestimation is likely attributable to the numerical damping characteristics inherent in the Ogden material model or the omission of secondary experimental factors – such as mechanical friction at the mounting block and localized fluid resistance – that were not fully accounted for in the idealized numerical environment.

5.2 Nonlinearity and Higher-order Vibration Modes

To investigate discrepancies between experimental and numerical results, time-series and Fast Fourier Transform (FFT) analyses were performed. Figure 5 presents a representative case (A = 10 mm and ω $(L$ / g$)^{1/2}$ = 0.85), where experimental data exhibits distinct high-frequency fluctuations superimposed on the primary oscillation, while computational results show a smooth sinusoidal form. The FFT spectra in Figure 5(b) clearly reveals complex dynamic behavior, specifically identifying higher-order vibration modes at $3\omega_{motion}$ and $5\omega_{motion}$ in response to fluid impacts. In contrast, the numerical simulation fails to capture these nonlinear fluctuations. This limitation is primarily attributed to artificial numerical physical components. Furthermore, explicit structural model updating – such as tuning numerical damping ratios via dry-state modal tests – was not executed prior to FSI computations. The absence of empirically calibrated structural damping, combined with numerical dissipation, primarily leads to the filtering of the high-frequency harmonics observed experimentally.



(a) Time-history of tip displacement (b) FFT results for tip displacement

Figure 5: Comparison of baffle tip displacement at A = 10 mm, and ω $(L/g)^{1/2}$ = 0.85: (a) time-history of tip displacement (δ_{tip}/A); and (b) Fast Fourier Transform (FFT) results comparing computation (*blue and dash*) and experimental (*red and solid*) frequency response.

5.3 Pressure Asymmetry as a Sensitive Resonance Indicator

The relationship between the root-mean-square of the differential pressure (Δp_{RMS}) and the resonance phenomenon was evaluated to assess its effectiveness as a diagnostic tool. The normalized pressure difference defined using the fluid density (ρ), motion parameters (A, ω), and tank length (L), exhibits distinct peaks near the predicted hydro-elastic natural frequency bands. This trend confirms that the linear eigenvalue framework provides a reliable theoretical foundation for identifying resonance under small-amplitude excitations.

Notably, the pressure difference measured at the rear wall panels (P3 and P4) shows significantly higher sensitivity to the resonant response compared to the side wall measurements (P1 and P2). This finding suggests that the flow field disturbed by the internal flexible structure exerts a more direct impact near the baffle.

5.4 Phase-lag Analysis and Resonant Behavior

The phase relationship between the external tank motion and the resulting baffle deformation provides further physical insight into the system's resonant characteristics. The phase lag, defined as $\Delta\phi = \Delta\phi_{tank} - \Delta\phi_{baffle}$, exhibits a consistent increasing trend with respect to the excitation frequency across all tested amplitudes.

As shown in Figure 7, the phase lag consistently approaches zero near the predicted hydro-elastic natural frequency. This convergence serves as a classic physical indicator of resonant behavior in coupled fluid-structure systems. Furthermore, the phase-lag trajectories for different amplitudes (A = 10 and 20 mm) remain remarkably stable and nearly identical. This suggests that the fundamental hydro-elastic mode shapes are preserved even as the free-surface nonlinearity increases within the tested range, confirming the robustness of the linear eigenvalue framework in predicting the primary resonance point.

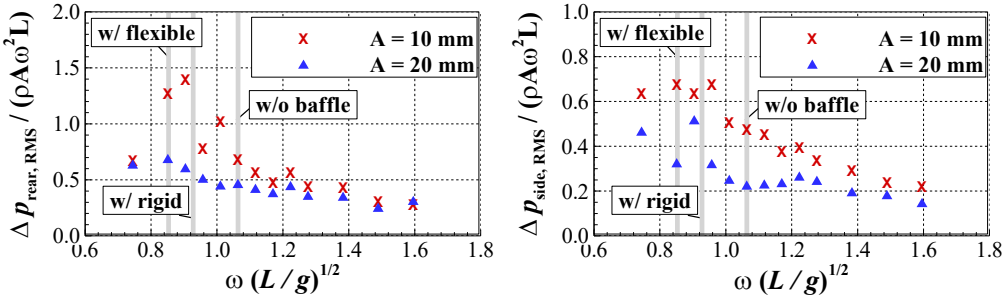


Figure 6: Normalized differential pressure ($\Delta p_{RMS}/\rho A\omega^2 h$) at different sensor panels: (left) rear wall panels (P3 and P4), and (right) side wall panels (P1 and P2). For two motion amplitudes, A = 10 mm (red crosses) and A = 20 mm (blue triangles), the rear wall panels exhibit higher sensitivity in identifying the hydro-elastic resonance peak.

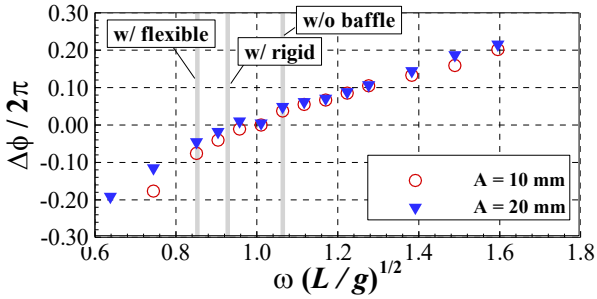


Figure 7: Phase relationship between the external tank motion and the baffle tip deformation: Normalized phase lag ($\Delta\phi$ / 2π) as a function of the normalized excitation frequency $\omega\,(L/g)^{1/2}$ for A = 10 mm (*red circles*) and 20 mm (*blue gradients*).

6. Conclusion

This study investigated the hydro-elastic sloshing characteristics and the dynamic response of a flexible vertical baffle through a combined framework of theoretical eigenvalue analysis, model-scale experiments, and two-way implicit FSI computations. Focusing on the small-amplitude regime to clarify the transition from linear hydro-elasticity to nonlinear flow regimes, the key findings are summarized as follows:

- Theoretical Validation: The semi-analytic eigenvalue formulation successfully predicted the shift in sloshing natural frequencies induced by baffle elasticity. It showed excellent agreement with experimental resonance peaks at small excitation amplitudes, validating the theoretical baseline for coupled fluid–structure systems.
- Diagnostic Sensitivity: At low excitation amplitudes (A = 10, 20 mm), pressure asymmetry across the baffle proved to be a significantly more sensitive indicator of resonance than the baffle's tip

displacement. Sensors located on the rear wall panels exhibited the highest sensitivity in capturing these resonant fluctuations.

- Phase-lag Characteristics: The phase relationship between the tank motion and baffle deformation serves as a robust physical benchmark for identifying resonance, with the phase lag consistently approaching zero near the predicted natural frequencies.
- Numerical Fidelity and Limitations: While the strongly coupled FSI framework accurately replicated dominant resonant trends and phase-lag characteristics, the numerical model tended to overestimate maximum displacement at low forcing levels. Furthermore, it failed to fully resolve the higher-order vibration modes (3ω and $5\omega_{\text{motion}}$) captured in experimental FFT analysis.

In conclusion, the integration of linear eigenvalue theory with high-precision experimental and numerical analysis provides a comprehensive understanding of hydro-elastic sloshing phenomena. These results establish a reliable benchmark for the optimized design and reliable validation of flexible damping structures in marine liquid containment systems.

Acknowledgements

This study was supported by Lloyd's Register Foundation (LRF)-Funded Research Center in Seoul National University, project GCY-100002. Their support is highly appreciated.

References

[1] H.N. Abramson, *The dynamic behavior of liquids in moving containers, with applications to space vehicle technology*, NASA-SP-106, 1966.
[2] O.M. Faltinsen, A.N. Timokha, *Sloshing*, Cambridge University Press, London, 2017.
[3] D.V. Evans, P. McIver, Resonant frequencies in a container with a vertical baffle, Journal of Fluid Mechanics, 175:295-307, 1987.
[4] R. Jeyakumaran, P. McIver, *Approximations to sloshing frequencies for rectangular tanks with internal structures*, Journal of engineering mathematics, 29(6): 537-556, 1995
[5] M.A. Xue, J. Zheng, P. Lin, and X. Yuan, *Experimental study on vertical baffles of different configurations in suppressing sloshing pressure*, Ocean Engineering, 136: 178-189. 2017.
[6] X. Meng, D. Zhou, and J. Wang, *Effect of vertical elastic baffle on liquid sloshing in rectangular rigid container*, International Journal of Structural Stability and Dynamics, 21(12): 2150167, 2021.
[7] T. Park, C.J. Park, J. Lee, and Y. Kim, *Experimental observation on violent sloshing flows inside rectangular tank with flexible baffles*, Applied Ocean Research, 154: 104307, 2025.
[8] A.N. Gent, *On the relation between indentation hardness and Young's modulus*, Rubber Chemistry and Technology, 31(4): 896-906, 1958
[9] S.Y. Kim, Y. Kim, and K.H. Kim, *Statistical analysis of sloshing-induced random impact pressures*, Journal of Engineering for the Maritime Environment, 228(3): 235-248, 2014.
[10] A.H. Nayfeh, D.T. Mook. *Nonlinear oscillations*. John Wiley & Sons, 2024.
[11] Y. Ren, M.A. Xue, and P. Lin, *Experimental study of sloshing characteristics in a rectangular tank with elastic baffles*. Journal of Fluids and Structures, 122:103984, 2023.
[12] S.C. Hwang, J.C. Park, H. Gotoh, A. Khayyer, and K.J. Kang, *Numerical simulations of sloshing flows with elastic baffles by using a particle-based fluid–structure interaction analysis method*. Ocean Engineering, 118:227-241, 2016.
[13] S.R. Idelsohn, J. Marti, A. Souto-Iglesias, and E. Onate, *Interaction between an elastic structure and free-surface flows: experimental versus numerical comparisons using the PFEM,* Computational Mechanics, 43(1):125-132, 2008.

10th International Conference on HYDROELASTICITY IN MARINE TECHNOLOGY
Trondheim, Norway, June 16th-18th, 2026

Numerical Study of Hydroelastic Response due to Slosh-Induced Impact

Yang, K.-K.[1*] Kim, D.-H. and Kang, D.-Y.[1]

[1] Chungnam National University, Daejeon, Korea

Abstract. This study presents a detailed numerical analysis of the hydroelastic response of an LNG carrier's cargo tank subjected to slosh-induced impact loads, using computational fluid dynamics (CFD) and coupled fluid-structure interaction (FSI) simulations. A unified finite volume framework based on OpenFOAM and solids4foam is adapted and a partitioned FSI approach is employed to capture the complex coupling between fluid momentum and structural elasticity. Numerical simulations were performed under harmonic sway excitation, successfully capturing a violent flip-through impact on the side wall. The analysis specifically highlights the variations in added mass resulting from the rapidly changing wetted area during the impact process, which significantly influences the dynamic characteristics of the system. While initial findings clarify the localized deformation patterns and basic stress distributions, detailed signal processing and spectral analysis of the hydroelastic response are currently ongoing.

Key words: *Sloshing; CFD; Hydroelastic impact; Added mass*

1. Introduction

Recently, global environmental regulations have tightened and the demand for eco-friendly energy has increased, leading to a need for larger liquefied natural gas (LNG) carriers and more diverse operating conditions. In the past, it was recommended that LNG vessels operate only in either fully loaded or empty conditions. However, the necessity for partial filling operations has grown significantly in recent years. In such partial filling states, sloshing—the violent motion of liquid inside the cargo tank—occurs. The localized impact loads caused by sloshing are a critical factor threatening the structural integrity of the membrane and cargo containment system (CCS) [1,2,3].

Fluid impact due to sloshing exhibits highly complex physical characteristics depending on the shape of the free surface, the velocity of the liquid, and the presence of trapped gas. When the duration of the impact load is similar to the natural period of the structure, hydroelasticity effects, driven by fluid-structure interaction (FSI), become significant [4,5].

Traditional ship design has primarily relied on quasi-static approaches or indirect dynamic analysis, where pressures measured on rigid walls (through tank tests or numerical simulations) are simply applied as loads for structural analysis. However, assuming a rigid wall ignores the coupling effect of structural deformation on the fluid flow, such as changes in added mass. This limitation can lead to overestimating or underestimating the actual structural response during an impact [2].

Therefore, this study aims to analyze the hydroelastic impact phenomena caused by sloshing flow through computational fluid dynamics (CFD) and FSI analysis. Using an integrated numerical environment of OpenFOAM 9 and solids4foam [6], a finite volume-finite volume (FV-FV) coupling method is applied. The global flow patterns are first examined to observe the overall development of the sloshing flow field where periodic impacts occur. Subsequently, a localized flow analysis is performed to numerically simulate the flip-through phenomenon and evaluate the resulting axial stress

* Correspondence to: kkyang@cnu.ac.kr

characteristics on the elastic wall. While these initial findings clarify the localized deformation patterns and basic stress distributions, detailed signal processing and spectral analysis of the hydroelastic response are currently ongoing to further quantify the structural integrity under extreme conditions.

2. Numerical methods

2.1 Fluid region

In general, hydroelastic analysis is conducted by coupling a finite element method (FEM)-based structural solver with a fluid solver. However, this study adopts a unified approach using solids4foam [6] and OpenFOAM 9, where both the fluid and solid structures are discretized using the finite volume method (FVM). The governing equations for an incompressible Newtonian fluid consist of the continuity equation and the Navier-Stokes equations, which represent the conservation of momentum, as follows:

$$\frac{\partial}{\partial t}\int_V \rho dV + \int_S \rho\left(u_i - W_{g,i}\right)n_i dS = 0 \tag{1}$$

$$\frac{\partial}{\partial t}\int_V \rho u_i dV + \int_S \rho u_i\left(u_j - W_{g,j}\right)n_j dS = -\int_S p n_i dS + \int_S \tau_{ij} n_j dS + \int_V \rho f_{b,i} dV \tag{2}$$

where u_i and $W_{g,i}$ represent the fluid and grid velocities in the i-direction, respectively. p denotes the pressure, τ_{ij} is the viscous stress tensor, and n_j is the unit outward normal vector to the surface S enclosing the control volume V. Also, $f_{b,i}$ denotes the body force, which accounts for both the gravitational force and the inertial forces arising from the adoption of a non-inertial coordinate system fixed to the tank.

For spatial discretization, the cell-centered finite volume method was applied. The convection terms were discretized using a second-order total variation diminishing limiter scheme, while the diffusion terms were treated with the central differencing scheme (CDS). To accurately capture free-surface behavior, the volume-of-fluid (VOF) method was employed with the piecewise linear interface calculation technique and an interfacial compression scheme. The coupling between velocity and pressure was achieved using the pressure-implicit with splitting of operators (PISO) algorithm.

2.2 Solid region

While solids4foam provides various non-linear models to account for large deformations and rotations, the linear geometry model was selected for this research. The structural deformations of the LNG CCS under sloshing impact are relatively small compared to the overall dimensions, allowing for a small-strain and small-rotation approximation. In this FVM-based structural solver, the governing equation for the conservation of linear momentum is expressed in terms of the total displacement vector w_i as follows:

$$\int_V \rho_s \frac{\partial^2 w_i}{\partial t^2} dV = \int_S \sigma_{ij} n_j dS + \int_V \rho_s f_{b,i} dV \tag{3}$$

where ρ_s is the density of the solid and σ_{ij} is the Cauchy stress tensor, which is determined by the constitutive law of the material.

For the boundary conditions, the traction vector t_i on the surface is defined as:

$$t_i = \sigma_{ij} n_j. \tag{4}$$

In the case of FSI, this traction is coupled with the fluid pressure and viscous forces acting on the interface, ensuring the continuity of stress across the fluid-solid boundary.

2.3 Fluid-structure coupling

The interaction between the sloshing fluid and the structural containment system is resolved using a partitioned FSI approach. In this partitioned procedure, the fluid and solid equations are solved sequentially within each time step until the interfacial conditions are satisfied. At the fluid-structure interface, both kinematic and dynamic conditions must be met to ensure the continuity of the physical fields.

The kinematic condition requires that the velocity and displacement of the fluid and the structure be identical at the boundary. This ensures that the two domains move together without separation or penetration. The dynamic condition requires the equilibrium of forces acting on the interface. The traction exerted by the fluid must be equal in magnitude and opposite in direction to the traction experienced by the structure as follows:

$$t_i = \left(-p\delta_{ij} + \tau_{ij}\right) n_j^f \tag{5}$$

Where the superscript *f* denotes the fluid region. These interfacial conditions are enforced iteratively within the partitioned coupling scheme. Specifically, the fluid solver calculates the pressure and viscous forces to provide the traction for the solid solver, while the solid solver calculates the resulting deformation to update the boundary and mesh position of the fluid domain.

To maintain numerical stability and ensure convergence between the two solvers, a fixed under-relaxation technique was applied to the interface displacement. During the iterative process, the displacement at the fluid-solid interface was updated as follows:

$$w_{interface}^{(k+1)} = w_{interface}^{(k)} + \alpha R^{(k)} \tag{6}$$

where $w_{interface}$ is the interface displacement, R represents the FSI residual, which is defined as the difference between the displacement predicted by the solid solver and the current fluid interface position and α is the relaxation factor. For the present study, a relaxation factor of $\alpha = 0.4$ was selected to ensure robust convergence during the violent sloshing impact events. The sub-iteration loop continues until the L_2-norm of the FSI residual falls below the specified tolerance.

3. Results and discussion

3.1 Test condition

In this study, a flip-through impact at the side wall was selected as the target phenomenon to investigate the hydroelastic response of the containment system [5]. The dimensions of the tank and the arrangement of pressure sensors are illustrated in Fig. 1. The ullage pressure was maintained at an atmospheric pressure of 101,325 Pa, and the initial filling height of the tank was set to $h/L = 0.122$. To induce the target flip-through event, the tank was subjected to a simple harmonic sway motion with a time-varying excitation period as follows:

$$x(t) = A\cos\left(\frac{2\pi}{T(t)}t\right) \tag{7}$$

where A represents the sway excitation amplitude, set at a non-dimensional ratio of $A/L = 0.03$. The excitation period $T(t)$ is defined as a function of time as follows:

$$T(t) = T_0 + \left(T_1 - T_0\right) e^{-\left(t/T_a\right)^2} \tag{8}$$

were the parameters $T_0 = 1.6$ s, $T_1 = 4$ s, and $T_a = 0.05$ s. Under these conditions, the flip-through event occurs on the left wall during the third cycle of the tank motion. At this specific moment, the hydroelastic response of the structural wall within the impact zone was observed and analyzed in detail.

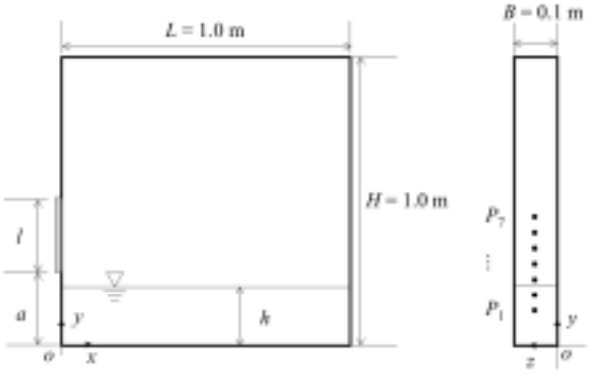


Figure 1: Schematic illustration of the model tank and pressure probe arrangement.

3.2 Global flow characteristics

Before examining the localized hydroelastic response, the global flow features within the tank were observed to understand the overall sloshing flows. Figure 2 illustrates the snapshots of the free-surface evolution during the third excitation cycle.

As shown in the figure, the liquid motion exhibits periodic impact patterns synchronized with the harmonic sway excitation. Prior to the target flip-through impact occurring on the left wall during the third cycle, a significant impact event is observed at the right wall (see Fig. 2(c)). As the liquid hits the wall, high-velocity jet flows are generated along the vertical boundary. As these jets subsequently descend and merge with the bulk liquid, they induce a highly complex flow field characterized by free-surface fragmentation and entrapped air bubbles.

Furthermore, it is observed that the repeated impact events over multiple cycles introduce a degree of irregularity to the flow. Specifically, the free surface approaching the walls becomes increasingly disturbed compared to the initial cycles, deviating from a simple standing wave profile. This non-linear evolution of the free surface, coupled with the interaction of descending jets, sets the complex initial conditions for the subsequent flip-through event on the left wall, where the most intense hydroelastic response is expected to be captured.

Figure 3 presents the time history of the dimensionless pressure ($p/\rho gh$) measured at a height of $y/L = 0.175$ from the tank bottom on the both side walls. The pressure profiles clearly exhibit the periodic nature of the sloshing impact induced by the harmonic sway motion. In the early stages of the excitation, the pressure peaks remain relatively low. However, the impact intensity gradually increases as the cycles progress. During the third excitation cycle, a significant impact event is first captured on the right wall at approximately $t/T_0 \approx 2.2$. This is followed by a much more severe impact on the left wall at $t/T_0 \approx 2.7$, which corresponds to the target flip-through impact. The pressure peak recorded during the flip-through event on the left wall is substantially higher than those of previous impacts, reaching a dimensionless value of nearly 3.8. Following these primary impact peaks, high-frequency oscillations are observed in the pressure signal. These fluctuations are attributed to the disturbed flows caused by descending jets and merging liquid masses.

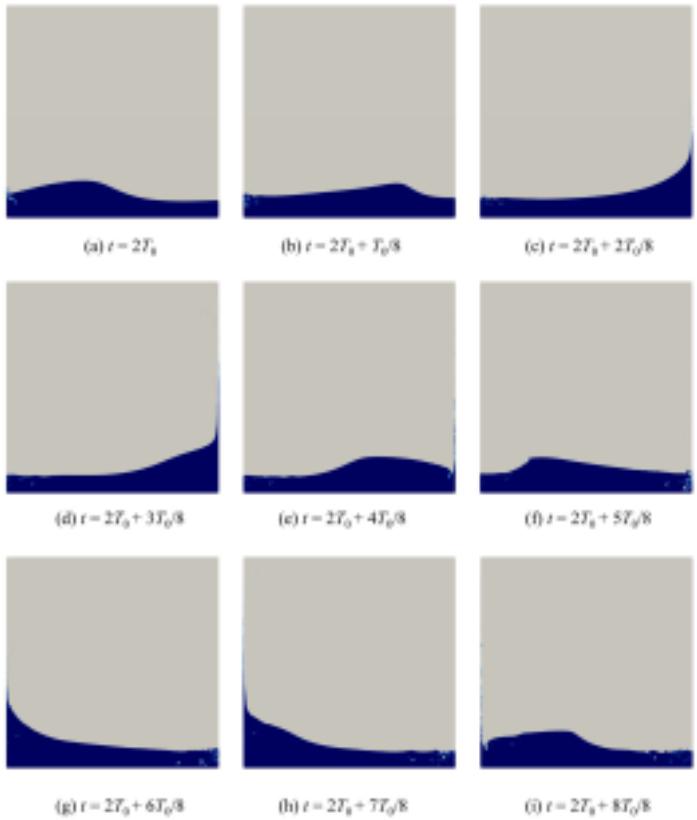


Figure 2: Snapshots of free-surface evolution during the third excitation cycle.

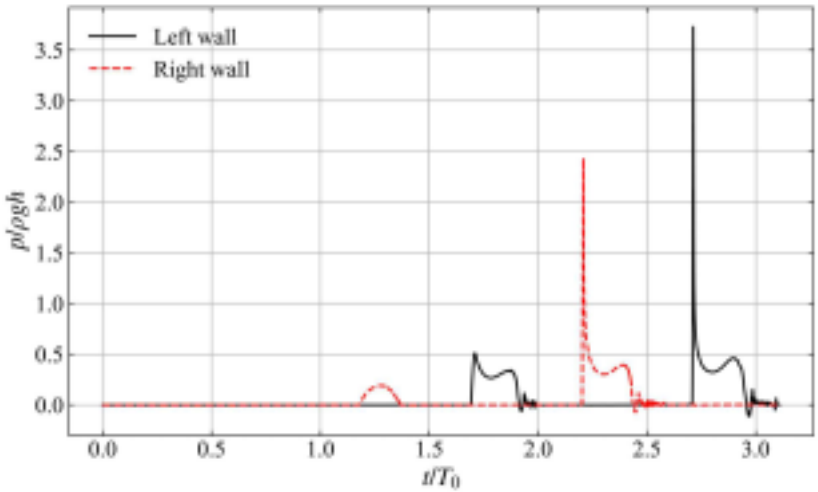


Figure 3: Time history of pressure measured at $y/L = 0.175$ on the side walls.

3.3 Local hydroelastic characteristics

To obtain a deeper understanding of the hydroelasticity during the peak impact period, the localized flow and structural response on the left wall were analyzed. Figure 4 illustrates the evolution of the flip-through impact at three distinct stages. In these snapshots, the structural displacement is magnified by a factor of 1,000 to clearly visualize the hydroelastic deformation. The time of maximum axial stress, σ/σ_Y, is defined as t^*.

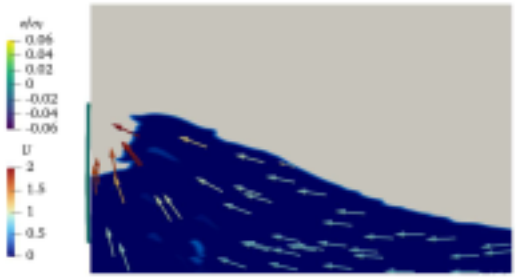
The flip-through process is characterized by the following three stages:

- Stage (a) $t = t^* - 10$ ms: As the wave trough approaches the left wall, the free surface begins to rise rapidly. The velocity vectors indicate a strong convergence of the fluid toward the wall. At this pre-impact stage, the structure begins to experience initial hydrodynamic pressure, leading to the onset of deformation.
- Stage (b) $t = t^*$ (Maximum Stress): This represents the critical moment of the flip-through event. The wave trough flips upward, generating a very thin, high-speed jet along the wall. This stage coincides with the maximum axial stress within the structural part. The 1,000 times magnified displacement shows a clear concave deformation of the wall toward the fluid.
- Stage (c) $t = t^* + 10$ ms: Following the peak impact, the jet flow continues to develop and surge upward. The velocity magnitude remains high near the interface, and the structural response evolves as the impact energy is redistributed. The stress distribution along the wall shows that the structural vibration persists even after the primary jet has formed.

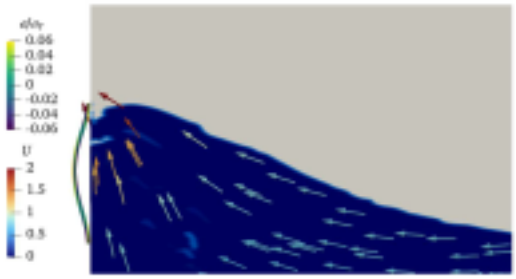
These observations confirm that the flip-through impact induces highly localized and intense structural loads. The coupling between the rapid fluid acceleration and the structural flexibility results in a dynamic response that cannot be fully captured by rigid-body assumptions.

The time histories of the axial stress at various vertical locations around the impact zone are shown in Fig. 5. At the center of the impact zone ($y/L = 0.175$), the axial stress exhibits a negative peak at t^*, reaching a dimensionless value of approximately -0.08. Since the measurement is taken on the fluid-contacting surface and the wall is bending outward, this negative sign indicates that the inner surface is subjected to compression. In contrast, the stress measured at the vertical boundaries of the impact region ($y/L = 0.142$ and 0.208) shows positive values. This confirms that while the center of the impact zone is compressed, the peripheral areas experience tension as the structure resists the localized outward displacement.

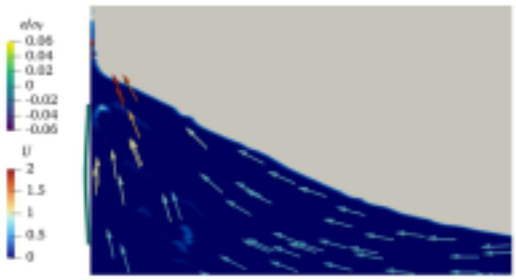
The stress signals are also characterized by high-frequency oscillations that persist well after the primary impact peak. These fluctuations represent the structural membrane continues to vibrate at its natural frequencies following the rapid energy transfer from the fluid. These oscillations are most intense at the impact center ($y/L = 0.175$) and show a gradual decay as the fluid jet surges upward and the localized pressure gradient diminishes. The clear presence of these dynamic vibrations and the spatial variation in stress signs underscore the necessity of a fully coupled FSI approach. This is because the structural response is dictated not only by the magnitude of the impact but also by the complex interaction between fluid momentum and structural elasticity, especially the variations in added mass resulting from the rapidly changing wetted area during the impact process, which significantly alters the dynamic characteristics of the system.



(a) $t = t^* - 10$ms



(b) $t = t^*$ (max. stress)



(c) $t = t^* + 10$ ms

Figure 4: Localized flow field and hydroelastic response on the left wall during the flip-through event: (Displacement is magnified by 1,000×).

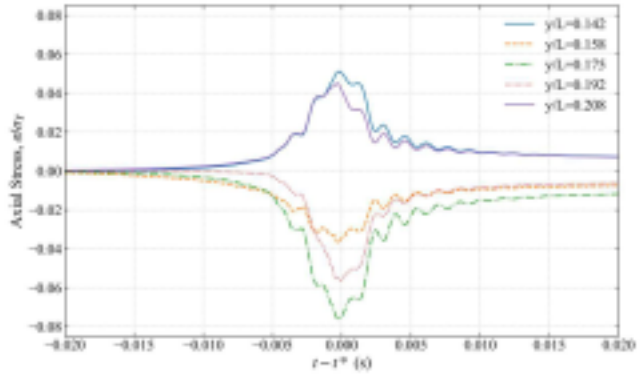


Figure 5: Time histories of axial stress measured on the fluid-contacting surface at various vertical locations during the flip-through event.

4. Conclusion

In this study, a unified FVM-FVM FSI solver was utilized to analyze the detailed hydroelastic response during sloshing-induced impact. The primary conclusions derived from this research are as follows:

- A robust numerical environment was established using the linear model in solids4foam, enabling stable and accurate simulation of the complex interaction between violent free-surface evolution and structural flexibility.
- The flip-through event on the tank wall clearly demonstrated the hydroelastic deformation and the axial stress analysis on the inner side of the wall revealed a typical localized bending behavior.
- The persistent high-frequency oscillations observed after the primary impact peak confirm that the dynamic characteristics of the structure play an important role in stress distribution and structural integrity assessment.

Future research will focus on the quantitative time-frequency analysis of these hydroelastic responses utilizing the Hilbert-Huang Transform (HHT) and Empirical Mode Decomposition (EMD). This will further enhance safety diagnostic technologies for LNG containment systems by identifying the spectral characteristics of impact-induced vibrations.

Acknowledgements

This study was partly supported by the Korea Institute for Advancement of Technology (KIAT) grant funded by the Korea Government (MOTIE) (RS-2023-KI002688, HRD Program for Industrial Innovation) and by Lloyd's Register Foundation, Grant No. CGY 100002. We gratefully acknowledge the support.

References

[1] O.M. Faltinsen, A.N. Timokha, *Sloshing*, Cambridge University Press, Cambridge, 2010.
[2] S. Malenica, L. Diebold, S.H. Kwon, D.S. Cho, *Sloshing assessment of the LNG floating units with membrane type containment system where we are?*, Marine Structures, 56:99-116, 2017.
[3] T. Park, C.J. Park, J. Lee, Y. Kim, *Experimental observation on violent sloshing flows inside rectangular tank with flexible baffles*, Applied Ocean Research, 154:104307, 2025.
[4] C. Lugni, M. Brocchini, O.M. Faltinsen, *Wave impact loads: the role of the flip-through*, Physics of Fluids, 18:122101, 2006.
[5] C. Lugni, A. Bardazzi, O.M. Faltinsen, G. Graziani, *Hydroelastic slamming response in the evolution of a flip-through event during shallow-liquid sloshing*, Physics of Fluids, 26:032108, 2014.
[6] Ž. Tuković, A. Karač, P. Cardiff, H. Jasak, A. Ivanković, *OpenFOAM finite volume solver for fluid-solid interaction*, Transactions of FAMENA, 42:1-31, 2018.

Wave-Energy Concepts

10th International Conference on HYDROELASTICITY IN MARINE TECHNOLOGY
Trondheim, Norway, June16th-18th, 2026

Enhancing Floating Breakwater and Wave Energy Converter Performance Using Local Resonators

Agarwal, S.[1], Liang, C.[1], Faragau, A.[1] and Colomés, O.[1,*]

[1] Faculty of Civil Engineering and Geosciences, Delft University of Technology, Delft, The Netherlands

Abstract. This paper presents a floating membrane equipped with local resonators as a dual-function system for wave energy harvesting and wave attenuation. Conventional floating breakwaters need to be very long to interact with long, low-frequency ocean waves, where most of the ocean's energy is concentrated. This concept uses a resonator to achieve the same effect, thereby, removing the need for a long floating breakwater. A coupled membrane–fluid–resonator model is developed to study the effect of the resonators on the wet natural frequencies, modal interaction, and wave reflection/transmission. The results show that properly tuned resonators can increase energy absorption at low frequencies while simultaneously reducing transmitted wave amplitude. The proposed system demonstrates how locally resonant concepts can be translated to hydroelastic structures to combine coastal protection and renewable energy harvesting within a single platform.

Key words: *Hydroelastic metamaterials; Wave energy harvesting; Floating breakwaters; Locally resonant metamaterials*

1. Introduction

Coastal regions are increasingly exposed to rising sea levels and intensifying wave climates, while simultaneously being identified as prime locations for large-scale renewable energy extraction. This dual pressure calls for infrastructure that does not merely resist wave action, but interacts with it in a productive manner. Conventional floating breakwaters are designed to attenuate wave energy through reflection and dissipation, whereas wave energy converters aim to maximize energy capture, often as standalone devices. These approaches are typically treated separately, leading either to passive protection systems or to energy harvesters with limited coastal shielding. Bridging this divide requires structural concepts that simultaneously attenuate incident waves and convert their energy into usable power.

Hydroelastic structures provide a promising framework for such multi-functionality [1]. Unlike rigid barriers, floating flexible membranes deform under wave loading, enabling distributed interaction with the wave field over an extended footprint. If appropriately engineered, this deformation can be exploited to both reduce transmitted wave energy and activate energy conversion mechanisms integrated with the structure [2]. The challenge arises from the requirement that a floating breakwater must be comparable in length to the wavelength of the waves it interacts with. Low-frequency ocean waves, which carry most of the ocean's energy, can have very long wavelengths, making the required structure impractically large. Therefore, the objective of this work is to enable the interaction of floating flexible structures with low-frequency ocean waves, without the need for impractically large structures.

Recent advances in metamaterials offer a pathway toward this objective. Metamaterials were first developed in electro-magnetics to achieve unconventional wave manipulation through engineered sub-wavelength structures. Shortly thereafter, the concept of locally resonant inclusions was translated to acoustics and elastodynamics, where subwavelength bandgaps were demonstrated using internal resonators [3]. In mechanical and structural systems, such locally resonant elements have since been

*Correspondence to: j.o.colomesgene@tudelft.nl

exploited for vibration suppression [4], band-gap formation [5], and enhanced energy harvesting by concentrating wave energy into discrete oscillators [6]. Early demonstrations showed that metamaterial-inspired wave focusing and localization can dramatically amplify piezoelectric harvesting from structure-borne waves [7]. Subsequent metastructure concepts combining distributed resonators with piezoelectric elements further established the dual functionality of attenuation and energy extraction [8, 9]. Translating these concepts to hydroelastic floating systems enables frequency-selective amplification of membrane deformation, thereby improving harvesting efficiency while simultaneously inducing wave attenuation through resonant energy trapping mechanisms.

In this paper, we investigate a floating membrane equipped with one row of local resonators as a dual-function system that acts both as a wave-energy harvester and as a floating breakwater, see sketch in Figure 1. The analysis focuses on the coupled hydroelastic dynamics and on the role of the resonator in modifying the system's natural frequencies, modal interactions, and energy dissipation characteristics. Through this framework, we assess the potential of resonator-enhanced hydroelastic structures to provide integrated coastal protection and renewable energy extraction within a single scalable platform.

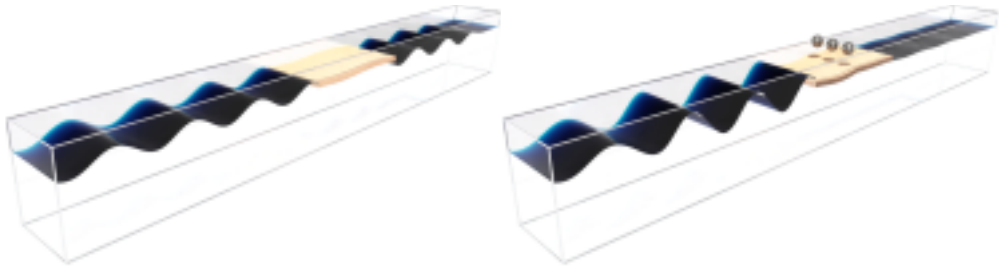


Figure 1: Sketch of the response of a floating flexible membrane under regular waves (left), and response of a floating flexible membrane with a row of resonators (right).

2. Problem setting

In this work we consider a floating flexible structure with negligible bending stiffness, i.e. floating membrane, with a row of resonators mounted on top. The resonators are represented as point masses attached to the structure through a linear spring and linear damper. At its turn, the structure is floating in fluid domain, denoted as Ω. The fluid domain is bounded by inlet and outlet surfaces, Γ_{in} and Γ_{out}, respectively, an irregular bottom surface, Γ_{b}, fluid free-surface, Γ_{fs}, and thin flexible structure (membrane) surface, Γ_{m}. Note that the upper boundary of the fluid domain is composed by the union of free-surface and structure surface, $\Gamma_{\text{fs}} \cup \Gamma_{\text{m}}$, and that the intersection of the free-surface and structure surface define the boundary of the structure, denoted by Λ_{m}, i.e. $\Lambda_{\text{m}} = \Gamma_{\text{fs}} \cap \Gamma_{\text{m}}$. In Figure 2 we depict a sketch of a 2D section of the floating hydroelastic structure with a mounted resonator where all these domains are defined.

We assume the fluid to be incompressible and inviscid and the flow to be irrotational, which enables a unique definition of the flow by means of the velocity potential. We also assume that free-surface wave amplitudes are small compared to the wave-length and water-depth. In that case, the fluid motion can be described via linearised potential flow theory. Furthermore, we assume that there is no separation between floating structure and fluid, thus, the deflection of a structure with negligible draft is equal to the free-surface elevation in Γ_{fs}. For the sake of simplicity we consider homogeneous structural properties, but the same formulation could be used for inhomogenous, i.e. space-dependent, material properties, see [10]. In this work we do not consider nonlinear waves nor nonlinear structural deformations.

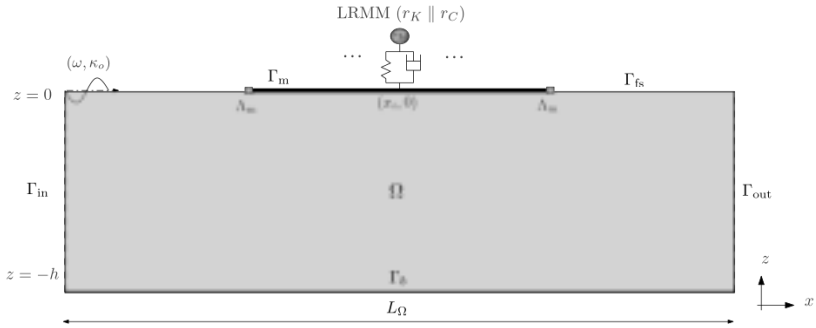


Figure 2: Schematic of the 2D computational domain of the floating hydroelastic structure with attached local resonators.

2.1. Governing equations

Let us consider a scalar velocity potential field, ϕ, defined in the fluid domain, Ω, such that the fluid velocity can be defined as $\mathbf{u} = \nabla\phi$. The fluid is assumed to be incompressible, i.e. $\nabla \cdot \mathbf{u} = 0$, leading to the potential flow governing equation

$$\Delta\phi = 0 \qquad \text{in } \Omega. \tag{1}$$

The governing equation of the fluid is supplemented by appropriate kinematic boundary conditions.

$$\mathbf{n} \cdot \nabla\phi = 0 \text{ on } \Gamma_{\text{b}}, \tag{2a}$$
$$\mathbf{n} \cdot \nabla\phi = u_{\text{in}} \text{ on } \Gamma_{\text{in}}, \tag{2b}$$
$$\mathbf{n} \cdot \nabla\phi = u_{\text{out}} \text{ on } \Gamma_{\text{out}}, \tag{2c}$$
$$\mathbf{n} \cdot \nabla\phi = \kappa_t \text{ on } \Gamma_{\text{fs}}, \tag{2d}$$
$$\mathbf{n} \cdot \nabla\phi = \eta_t \text{ on } \Gamma_{\text{m}}. \tag{2e}$$

In (2), $\mathbf{n}$ is the outward normal to the domain boundary, u_{in} is the velocity component normal to the inlet boundary, u_{out} is the velocity component normal to the outlet boundary, κ_t is the time derivative of the free-surface elevation and η_t is the time derivative of the structure deflection. From the linearized Bernoulli equation, we can relate pressure with free-surface elevation and velocity potential.

$$p = -\rho\phi_t - \rho g\kappa, \qquad \text{on } \Gamma_{\text{fs}}, \qquad p = -\rho\phi_t - \rho g\eta, \qquad \text{on } \Gamma_{\text{m}}. \tag{3}$$

Where ρ is the fluid density and g the gravitational acceleration. We assume that the pressure at the free-surface Γ_{fs} is equal to the atmospheric pressure, which is considered zero in this work. Then, the dynamic boundary condition at the free-surface reads

$$\phi_t = -g\kappa, \qquad \text{on } \Gamma_{\text{fs}}. \tag{4}$$

Let us consider a resonator of mass r_M, attached to the flexible structure with a spring of elastic constant r_K and a damper with damping coefficient r_C, see Figure 2. In this study we consider a pre-tensioned viscoelastic membrane with uniform tension per unit width $T\,(N/m)$, uniform mass per unit length $m\,(kg/m)$ (or unit area in the case of 3 dimensions) and uniform viscous damping parameter τ. The deflection of the membrane coupled with an elastically mounted resonator is given by the governing equations

$$m\eta_{tt} - \nabla \cdot (T\,(\nabla\eta + \tau\nabla\eta_t)) + (r_K(\eta - \xi) + r_C(\eta_t - \xi_t))\,\delta(\mathbf{x}_r) = p, \qquad \text{on } \Gamma_{\text{m}}, \tag{5a}$$
$$r_M\xi_{tt} + r_C\,(\xi_t - \eta_t(\mathbf{x}_r)) + r_K\,(\xi - \eta(\mathbf{x}_r)) = 0. \tag{5b}$$

In equation (5a), η_{tt} is the second derivative with respect to time of the membrane deflection, i.e. acceleration. The variable ξ is the vertical displacement of the resonator, and ξ_t and ξ_{tt} the respective velocity and acceleration. Also in equation (5a), we use $\delta(\mathbf{x}_r)$ to denote the Dirac delta function evaluated at the membrane location, $\mathbf{x}_r$, where the resonator is attached. The governing equation of the membrane should be supplemented with appropriate boundary conditions. Here we assume that the structure boundaries are free, that is

$$T\left(\nabla\eta + \tau\nabla\eta_t\right)\cdot\mathbf{n} = 0 \qquad \text{on } \Lambda_{\text{m}}. \tag{6}$$

Note that the pressure felt by the fluid in equation (3) has to be equal to the pressure felt by the structure in equation (5a). Therefore, we can merge the two equations, resulting into a modified dynamic boundary condition for the fluid at Γ_{m} given by

$$r_{M,\rho}\eta_{tt} - \nabla\cdot\left(T_\rho\left(\nabla\eta + \tau\nabla\eta_t\right)\right) + \left(r_{K,\rho}(\eta-\xi) + r_{C,\rho}(\eta_t - \xi_t)\right)\delta(\mathbf{x}_r) + \phi_t + g\eta = 0, \qquad \text{on } \Gamma_{\text{m}}. \tag{7}$$

Where the subscript $(\cdot)_\rho$ denotes quantities normalized by the fluid density, e.g. $r_{M,\rho} = r_M/\rho$.

Therefore, the dynamic behaviour of locally resonant hydroelastic structures is governed by the set of coupled equations (1, 4, 7 and 5b), which can be used to determine the system variables $\{\phi, \kappa, \eta, \xi\}$, with boundary conditions defined by equations (2) and (6) .

Since we have a linear system, using separation of variables, for a problem with regular waves of frequency ω we can express the system unknowns as $s(\mathbf{x}, t) = \bar{s}(\mathbf{x})\exp(-\imath\omega t)$, for $s = \phi, \kappa, \eta, \xi$. Where the variable $\bar{s}$ represents the space-dependent amplitudes of the velocity potential, free-surface elevation, structure deflection and resonators vertical motion, respectively. For the sake of simplicity, hereinafter we will neglect the over-bar notation and assume that, in the frequency domain context, the variables ϕ, κ, η and ξ will refer to solution amplitudes.

2.2. Numerical Formulation

In this section we describe the numerical formulation based on a finite element approximation of the coupled fluid-structure-resonators problem. We use the finite element method with a monolithic formulation, i.e. solving a unique fully coupled system, extending the formulation firstly proposed for the hydroelastic analysis of floating beams and plates in [11] and later extended to membranes in [12]. Here we first derive the continuous weak form of the problem, followed by the discrete version.

Let us define the inner product between two functions defined in Ω as $(u, v) = \int_\Omega u(\mathbf{x})v(\mathbf{x})\, d\Omega$.Let $\mathcal{V}$ be a suitable functional space in Ω, $\mathcal{V}_{\Gamma_{\text{fs}}}$ the trace space of $\mathcal{V}$ on the free surface Γ_{fs} and $\mathcal{V}_{\Gamma_{\text{m}}}$ the trace space of $\mathcal{V}$ on the structure Γ_{m}, *i.e.* $\mathcal{V}_{\Gamma_{\text{fs}}} = \{v|_{\Gamma_{\text{fs}}} : v \in \mathcal{V}\}$ and $\mathcal{V}_{\Gamma_{\text{m}}} = \{v|_{\Gamma_{\text{m}}} : v \in \mathcal{V}\}$, respectively. We define the velocity potential $\phi \in \mathcal{V}$ and the associated test function $w \in \mathcal{V}$, the free-surface elevation function $\kappa \in \mathcal{V}_{\Gamma_{\text{fs}}}$ and its associated test function $u \in \mathcal{V}_{\Gamma_{\text{fs}}}$ and the membrane deflection $\eta \in \mathcal{V}_{\Gamma_{\text{m}}}$ with associated test function $v \in \mathcal{V}_{\Gamma_{\text{m}}}$. Let us also consider the set of complex numbers $\mathcal{Q} = \mathbb{C}$, containing the value of the resonator motion amplitude and its associated test function, i.e. $\xi \in \mathcal{Q}$ and $q \in \mathcal{Q}$, respectively. Using this notation, the weak form of the problem in the frequency domain, for a given wave frequency ω, reads: *Find* $[\phi, \kappa, \eta, \xi] \in \mathcal{V} \times \mathcal{V}_{\Gamma_{fs}} \times \mathcal{V}_{\Gamma_m} \times \mathcal{Q}$ *such that*:

$$B_\omega([\phi, \kappa, \eta, \xi], [w, v, u, q]) = L_\omega([w, v, u, q]) \qquad \forall [w, v, u, q] \in \mathcal{V} \times \mathcal{V}_{\Gamma_{\text{fs}}} \times \mathcal{V}_{\Gamma\text{m}} \times \mathcal{Q}, \tag{8}$$

with

$$\begin{aligned} B_\omega([\phi, \kappa, \eta, \xi], [w, v, u, q]) = {} & (\nabla\phi, \nabla w)_\Omega + (i\omega\kappa, w)_{\Gamma_{fs}} + (i\omega\eta, w)_{\Gamma_m} + \\ & (-i\omega\phi + g\kappa, \beta(v + \alpha w))_{\Gamma_{fs}} + \\ & \left(-i\omega\phi + \left(-m_\rho\omega^2 + g\right)\eta, u\right)_{\Gamma_m} + \left(T_\rho(1 - i\omega\tau)\nabla\eta, \nabla u\right)_{\Gamma_m} + \\ & \left(r_{K,\rho} - i\omega r_{C,\rho}\right)\left(\eta(\mathbf{x}_r) - \xi\right)u(\mathbf{x}_r) + \\ & \left(-r_{M,\rho}\omega^2\xi + \left(r_{K,\rho} - i\omega r_{C,\rho}\right)\left(\xi - \eta(\mathbf{x}_r)\right)\right)q, \end{aligned} \tag{9}$$

$$L_\omega([w, v, u, q]) = (u_{in}, w)_{\Gamma_{in}} + (u_{out}, w)_{\Gamma_{out}}. \tag{10}$$

The weak form (8) results from standard finite element derivations, we refer the reader to [11, 12] for a detailed explanation of the derivations. Note that the contribution from the resonators results in point-wise evaluations of membrane deflection and corresponding test function, $\eta(\mathbf{x}_r)$ and $u(\mathbf{x}_r)$. The equation of motion of the resonator, equation (5b), is added by testing against the respective test function q, recalling that these is a space-independent scalar complex value.

We use a finite element solver to obtain the solution to the continuous form (8). Here we follow the same approach as proposed in [11, 12, 10], leading to a unique monolithic algebraic system after discretization. Let us consider a triangulation, Ω_h, of the domain Ω, and the corresponding conformal triangulations of the domain boundaries, $\Gamma_{\text{fs,h}}$, $\Gamma_{\text{m,h}}$, $\Gamma_{\text{in,h}}$, $\Gamma_{\text{out,h}}$ and $\Gamma_{\text{b,h}}$. We define the finite-dimensional finite-element spaces for the velocity potential $\mathcal{V}_h$ as follows:

$$\mathcal{V}_h = \left\{ w_h \in \mathcal{C}^0(\Omega) : \; w_h|_K \in \mathbb{P}_r(K), \forall K \in \Omega_h \right\}, \tag{11}$$

and the free surface elevation and membrane elevation, $\mathcal{V}_{\Gamma_{\text{fs}},h}$ and $\mathcal{V}_{\Gamma_{\text{m}},h}$, are the trace spaces of $\mathcal{V}_h$ on the free surface and membrane, respectively. In (11), $\mathbb{P}_r(K)$ is the space of Lagrange polynomials of degree r in an element K, and E are facets of dimension $d-1$, with d being the topological dimension of the domain Ω. In particular we use $r = 2$ in this work. We recall that the space $\mathcal{Q}$ is a finite-dimensional space containing a single complex scalar value.

Using this notation, the final discrete form in the frequency domain reads: *Find* $[\phi_h, \kappa_h, \eta_h, \xi] \in \times\mathcal{V}_{\Gamma_{fs},h} \times \mathcal{V}_{\Gamma_m,h} \times \mathcal{Q}$ *such that for all* $[w_h, v_h, u_h, q] \in \mathcal{V} \times \mathcal{V}_{\Gamma_{fs}} \times \mathcal{V}_{\Gamma_m} \times \mathcal{Q}$:

$$B_\omega([\phi_h, \kappa_h, \eta_h, \xi], [w_h, v_h, u_h, q]) = L_\omega([w_h, v_h, u_h, q]). \tag{12}$$

With B_ω and L_ω as given by equations (9) and (10), respectively.

3. Results

In this section we assess the behaviour of the proposed floating membrane with resonator system. We assume a structure with infinite width, with long-crested regular waves coming in the direction aligned with the structure longitudinal axis. With these assumptions the problem simplifies to a floating 1-dimensional membrane on a 2-dimensional fluid domain. We also assume deep water regime and flat bottom, see sketch in Figure 2.

The length of the membrane is $L_m = 2h$, placed in 2D water domain with depth $h = 10\,(m)$, and length $L_\Omega = 3L_m$. The membrane is made of polyethylene with density of $\rho_s = 922.5(kg/m^3)$ and a thickness of $1m$, thereby resulting in mass per-unit-area of $m = 922.5(kg/m^2)$ and a submerged draft of $0.9(m)$. The membrane is tensioned with a tension per-unit-width $T = 10\rho g$, where $\rho = 1025\,(kg/m^3)$ is the water density. This pre-tensioning can be achieved via floaters, which are not modelled in this analysis. On top of the membrane we place a resonator with variable mass. Otherwise stated, we use a resonator mass of $r_M = 1000\,(kg/m)$ and natural frequency of $2.4\,(rad/s)$. Note that the material properties used in this study might not necessarily lead to a feasible engineering solution, but are selected to highlight the combined effect of hydroelastic structures with local resonators.

3.1. Influence of local resonator on system natural frequencies

As discussed in the introduction, the purpose of the local resonator is to complement the membrane's ability to efficiently harvest energy at specific wave frequencies. As demonstrated in [12], the membrane effectively harvests energy at the natural frequencies of the coupled membrane–fluid system, referred to as the *wet natural frequencies*. Ideally, the local resonator should not significantly alter these wet natural frequencies, but rather enhance the system's performance by enabling efficient energy harvesting at lower frequencies. Accordingly, this section investigates the extent to which the wet natural frequencies are influenced by the addition of the local resonator. For a detailed description of the identification

procedure for the wet natural frequencies and their associated mode shapes, the reader is referred to [12].

In particular, we vary the natural frequency $\omega_r = \sqrt{\frac{r_k}{r_M}}$ of the resonator, by varying r_k and keeping a constant mass $r_M = 1000\,(kg/m)$. In Figure 3 we depict how the first 6 natural frequencies of the system, $\omega_n^{(i)}$ with $i = \{0, ..., 5\}$, change when we vary the resonator natural frequency in the range $\omega_r \in [1.0, 5.0]\,(rad/s)$.

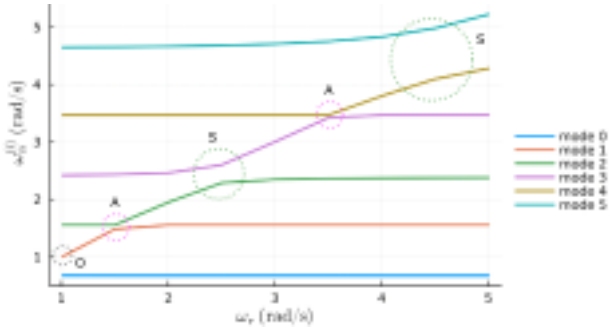


Figure 3: The influence of the natural frequency of the resonator $\omega_r = \sqrt{\frac{r_k}{r_M}}$ on the first 6 natural frequencies of the whole system.

Before discussing the figure, it is important to recall that the resonator is placed at the centre of the membrane and the membrane has two kinds of elastic modes: anti-symmetric (A), where the centre is a node with nearly zero displacement, and symmetric (S), where the centre is an anti-node with significant displacement.

Now coming to Figure 3, consider first the case of $\omega_r = 1$ rad/s. Here we mark 6 natural frequencies of the system $\omega_n^{(i)}$,of which five correspond to the hydroelastic modes of the membrane, while the sixth is governed by the resonator, denoted by marker O. In this configuration, the resonator does not alter the hydroelastic natural frequencies of the membrane.

As we increase ω_r, at some point ω_r approaches one of the hydroelastic natural frequencies of membrane. If the resonator frequency is close a anti-symmetric mode of the membrane, where the centre of the membrane is a node, then the influence of the resonator remains minimal, as seem by markers A. In fact, it appears as if the resonator-dominated mode vanishes. In contrast, when ω_r approaches a symmetric natural frequency, strong modal interaction occurs, as indicated by markers S. This region contains two strongly coupled modes and introduces a band-gap, which may be of interest for exploring meta-material behaviour of this structure.

This result highlights the frequency-selective nature of the coupled system of floating membranes with resonators, which has the ability to inject new modal content into the system close to the resonator natural frequency.

3.2. Response of the undamped system

After assessing the influence of the resonator on the system natural frequencies, we proceed to examine the steady-state dynamic response of the coupled system under monochromatic wave excitation. The incoming wave field is prescribed with a target amplitude $|\kappa_{\text{in}}| = \kappa_0$, assuming linear wave Airy theory, and wave frequency ω. In this section we look into wave reflection, transmission, and absorption coefficients under various incoming wave frequencies without material damping.

Let κ_{in}, κ_{r} and κ_{t} denote the complex-valued wave amplitudes associated with the incident, reflected, and transmitted waves, respectively. With the wave amplitudes we can then compute the corresponding reflection coefficient $K_r = \frac{P_r}{P_{\text{in}}}$ and transmission coefficient $K_t = \frac{P_{\text{total}}}{P_{\text{in}}}$, with the respective power fluxes, P_{in}, P_r, P_t defined as

$$P_{\text{in}} = \frac{1}{2}\rho g|\kappa_{\text{in}}|^2 C_g, \qquad P_{\text{r}} = \frac{1}{2}\rho g|\kappa_{\text{r}}|^2 C_g, \qquad P_{\text{total}} = \frac{1}{2}\rho g|\kappa_{\text{t}}|^2 C_g, \tag{13}$$

with

$$C_g = \frac{1}{2}\frac{\omega}{k}\left(1 + \frac{2kh}{\sinh(2kh)}\right). \tag{14}$$

In equation (14), C_g is the wave group velocity and k the wave number associated to ω, the incoming wave frequency. As a baseline, the dynamic response of the membrane-only configuration is first examined. The computed wet natural frequencies are $\omega^w_{mem} = \{1.553,\ 2.413,\ 3.467,\ 4.642\}$ rad/s, which serve as reference values for interpreting the coupled response. We then consider the undamped coupled system ($\tau = 0$, $r_C = 0$) subjected to a regular wave with $\omega = 2.4$ rad/s, coinciding with ω_r and close to the second wet natural frequency of the membrane.

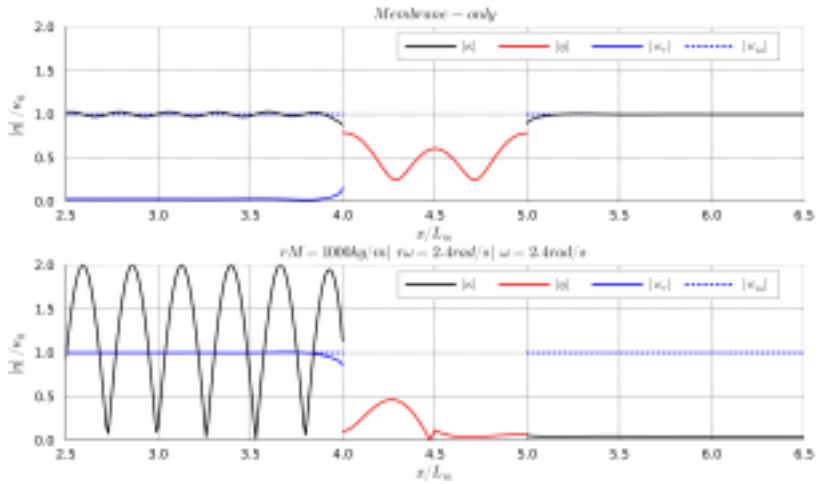


Figure 4: Amplitudes of the structural deflection η, incoming wave κ_{in}, reflected wave κ_r, transmitted wave κ_t, and total free-surface elevation, for an incident wave frequency close to one of the natural frequencies of the membrane-fluid (top) and of the local resonator (bottom).

The spatial amplitudes of the free-surface elevation κ and membrane deflection η are shown in Figure 4, where the upstream field is decomposed into the incident wave κ_{in} and the reflected component $\kappa_r = \kappa - \kappa_{in}$, and the downstream solution represents the transmitted wave $\kappa_t = \kappa$. For the membrane-only case (top Figure. 4), excitation near resonance results in nearly complete transmission with minimal reflection. In contrast, when the resonator frequency coincides with the excitation frequency, strong resonant motion is triggered, leading to almost total reflection and strongly reduced transmission (bottom Figure. 4). This demonstrates that the addition of the resonator enables selective wave-energy capture for frequencies that would otherwise fully transmit through the membrane.

To further investigate the system's dynamic characteristics without material damping, we perform a series of simulations using monochromatic waves with $\omega = [1, 5]$ rad/s, and evaluate the amplitude of the structural response and wave fields at each frequency. The resulting response contours and energy coefficients are shown in Figure 5 and Figure 6.

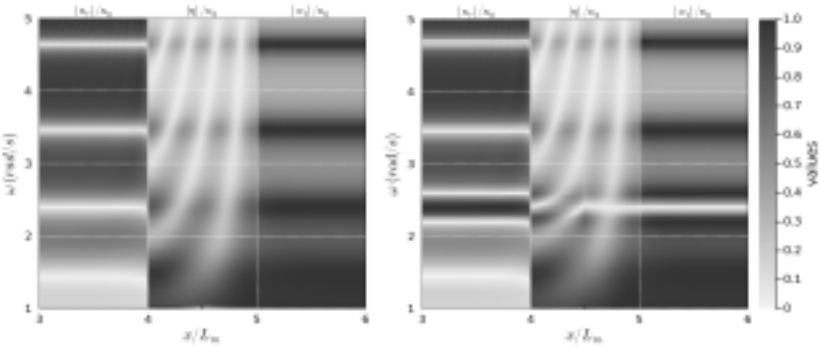


Figure 5: Response contour plots of the normalized amplitude of the deflection η, reflected wave κ_r, and transmitted wave κ_t in the vicinity of the structure for wave frequency $\omega = [1,\ 5]\ rad/s$ for the membrane only (left) and coupled system (right).

Figure 5 compares the membrane-only and coupled responses in terms of the normalized amplitudes of η, κ_r, and κ_t over space and frequency. For the membrane alone, lower frequencies produce larger deflections, whereas higher frequencies yield reduced response, indicating compliance to long waves and relative stiffness to short waves. With the introduction of a local resonator ($\omega_r = 2.4\,\mathrm{rad/s}$), a pronounced amplification of reflected waves emerges near the resonant frequency, demonstrating strong frequency-selective reflection accompanied by a corresponding suppression of the transmitted wave amplitude, while maintaining a structural response comparable to the uncoupled membrane.

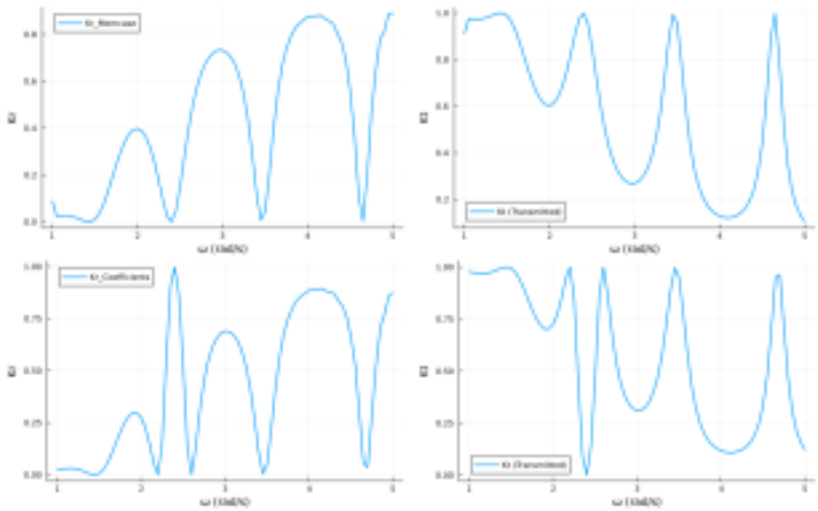


Figure 6: Plots of reflection coefficient K_r (left), transmitted coefficient K_t (right) under monochrome frequency $\omega = [1:5]\ rad/s$ for the membrane-only (top) and coupled system (bottom).

This frequency-selective behavior is further quantified by the energy coefficients shown in Figure 6. For the membrane-only system, the structure acts as a frequency-dependent filter: low-frequency waves are largely transmitted, while higher frequencies are reflected. Near the wet natural frequency, K_r exhibits pronounced troughs and K_t corresponding peaks, forming passbands centered around the struc-

tural resonance. With the introduction of the resonator, this filtering pattern is fundamentally modified near ω_r. As shown in Figure 6 (bottom row), K_r increases sharply while K_t decreases around the resonator frequency. Extreme flips in K_r and K_t are observed, which reflect the emergence of a bandgap around the resonator frequency.

3.3. Response of the damped system

Having explored the dynamic response of the coupled system in the absence of material damping, we now investigate the influence of resonator damping on the wave–structure interaction. To isolate this effect, the membrane viscoelastic parameter is set to $\tau = 0$ and only internal resonator damping is considered. To characterize the damping within each resonator, we adopt a classical mass-spring-dashpot viscoelastic model, where the damping coefficient r_C is defined through the damping ratio ζ as $r_C = 2\zeta\sqrt{r_K r_M}$. The power dissipated by the resonator damping and the corresponding absorbed wave energy coefficient are defined as

$$P_a = \frac{1}{2} r_C \omega^2 \left|\xi - \kappa\right|^2, \qquad K_a = \frac{P_a}{P_{in}}. \tag{15}$$

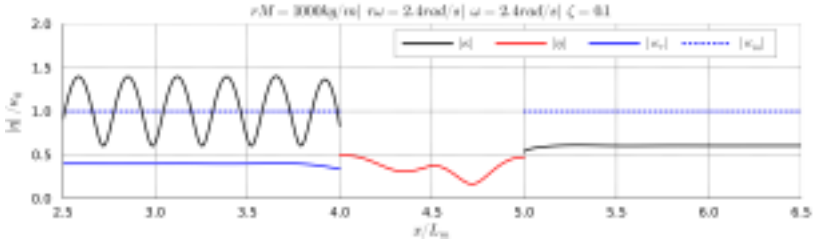


Figure 7: Plot of amplitude of structure deflectionη, incoming wave $\kappa_i n$, reflected wave κ_r, transmitted wave κ_t, and total free-surface elevation for the case with damping ratio $\zeta = 0.1$.

Figure 7 shows the spatial amplitude distribution with resonator damping. We have seen that in the undamped case, see Figure 4 (bottom), the system operates in a nearly fully reflective regime, with negligible transmission. When damping is introduced, the resonant structural amplification is suppressed and the reflected wave amplitude decreases, while transmission increases from nearly zero to a finite level. Since the transmitted wave remains smaller than the incident wave, the redistribution between reflection and transmission is incomplete, indicating that a portion of the incoming energy is dissipated through the resonator damping mechanism. This initial observation suggests that damping can effectively tune the energy partition between reflection and absorption.

Figure 8 shows the normalized amplitudes of η, κ_r, and κ_t for $\zeta = 0.1$ over a range of excitation frequencies. Compared to the undamped configuration result in Figure 5b, the frequency-selective behaviour in Figure 8 becomes less pronounced when resonator damping is introduced. The reflected wave amplitude is lower than in the undamped case, but remains significantly higher than in the membrane-only case. Similarly, the transmission coefficient is higher than in the undamped case, but significantly lower than in the membrane-only case shown in Figure 5a. These observations indicate a redistribution of energy from narrow-band response at the resonator frequency to a wider band response around the resonator frequency, enabled by increased energy dissipation by the resonator.

To further quantify the influence of resonator damping, the frequency domain simulations are repeated for different damping ratios ζ, and the corresponding wave-energy coefficients are computed. The resulting reflection, transmission, and absorption coefficients are shown in Figure 9. As the damp-

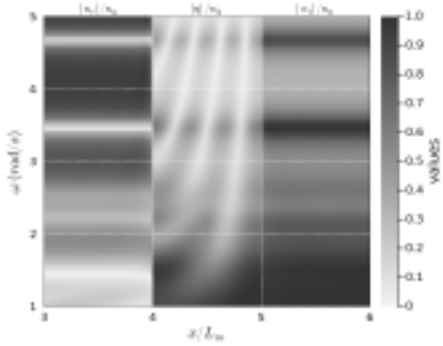


Figure 8: Response contour of coupled system and vicinity water domain with damping ratio $\zeta = 0.1$.

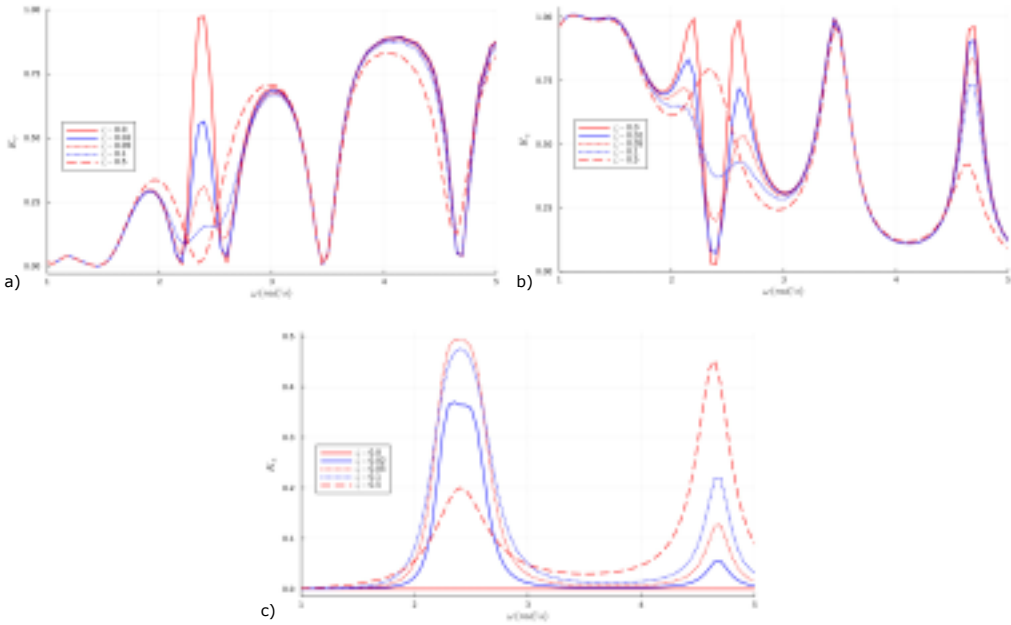


Figure 9: Plots of a) reflection coefficient K_r, b) transmitted coefficient K_t, and c) absorption coefficients K_a for $\zeta = [0.01, 0.02, 0.05, 0.1, 0.5]$ under monochrome frequency $\omega = [1:5]\ rad/s$.

ing ratio increases, a clear redistribution of energy between reflection, transmission, and absorption is observed. For low damping values (e.g., $\zeta = 0.02$), the reflection coefficient K_r near the resonant frequencies remains high, although reduced compared with the undamped case, consistent with the strong wave rejection observed previously. As ζ increases further (e.g., $\zeta = 0.05$ and $\zeta = 0.1$), K_r continues to decrease while the absorption coefficient K_a increases and becomes dominant near resonance, indicating that a significant portion of the incoming wave energy is dissipated by the resonator. The pronounced peaks of K_a around the resonant frequencies confirm the damping-enhanced selective absorption capacity of the system. At very high damping (e.g., $\zeta = 0.5$), the influence of the resonator becomes less pronounced, although K_a remains non-negligible, both K_r and K_t gradually approach the membrane-only behavior.

4. Conclusions

The inclusion of local resonator introduces a strong frequency-dependent energy modulation. The resonator disrupts the original passband structure by creating a localized bandgap around ω_r, where wave reflection is significantly enhanced, showing its potential in reflecting and/or absorbing certain-frequency energy. The addition of damping in the coupled system introduces a tunable mechanism to control both wave reflection and transmission characteristics. Low damping preserves selective filtering with extreme peak–dip transitions in both K_r and K_t around the resonant frequency. Moderate damping smooths this transitions and redistributes energy over broader frequencies. Excessive damping neutralizes local resonator's effects, rendering the system nearly equivalent to the baseline membrane. These findings highlight the critical sensitivity of wave-structure interactions to the damping level and offer practical insights for engineering resonator-based coastal or floating systems.

Acknowledgments

This publication is part of the project "Hydroelastic Black Holes for Offshore Renewable Energy" with file number OCENW.XS24.2.127 of the research programme ENW-XS which is financed by the Dutch Research Council (NWO).

References

[1] Miguel Lamas-Pardo, Gregorio Iglesias, and Luis Carral. A review of very large floating structures (vlfs) for coastal and offshore uses. *Ocean Engineering*, 109:677–690, 2015.

[2] XL Zhao, DZ Ning, QP Zou, DS Qiao, and SQ Cai. Hybrid floating breakwater-wec system: A review. *Ocean engineering*, 186:106126, 2019.

[3] Z. Liu, X. Zhang, Y. Mao, Y. Y. Zhu, Z. Yang, C. T. Chan, and P. Sheng. Locally resonant sonic materials. *Science*, 289(5485):1734–1736, 2000.

[4] G. L. Huang and C. T. Sun. Band gaps in a multiresonator acoustic metamaterial. *Journal of Vibration and Acoustics*, 131(3):031003, 2009.

[5] Y. Xiao, J. Wen, and X. Wen. Flexural wave band gaps in locally resonant beams with periodically attached resonators. *Journal of Physics D: Applied Physics*, 45(19):195401, 2012.

[6] M. Carrara, M. R. Cacan, M. J. Leamy, M. Ruzzene, and A. Erturk. Dramatic enhancement of structure-borne wave energy harvesting using an elliptical acoustic mirror. *Applied Physics Letters*, 100(20):204105, 2012.

[7] M. Carrara, M. Ruzzene, and A. Erturk. Metamaterial-inspired structures and concepts for elastoacoustic wave energy harvesting. *Smart Materials and Structures*, 22(6):065004, 2013.

[8] G. Hu, L. Tang, A. Banerjee, and R. Das. Metastructure with piezoelectric element for simultaneous vibration suppression and energy harvesting. *Journal of Vibration and Acoustics*, 139(1):011012, 2017.

[9] J. Li, X. Zhou, G. Huang, and G. Hu. Acoustic metamaterials capable of both sound insulation and energy harvesting. *Smart Materials and Structures*, 25(4):045013, 2016.

[10] Kareem El Sayed, Shagun Agarwal, Andrei Metrikine, and Oriol Colomés. Adjoint-based PDE-constrained optimization of viscoelastic floating membrane for maximum wave power absorption. *Structural and Multidisciplinary Optimization*, 69(3):71, February 2026.

[11] Oriol Colomés, Francesc Verdugo, and Ido Akkerman. A monolithic finite element formulation for the hydroelastic analysis of very large floating structures. *International Journal for Numerical Methods in Engineering*, 124(3):714–751, 2023.

[12] Shagun Agarwal, Oriol Colomés, and Andrei V Metrikine. Dynamic analysis of viscoelastic floating membranes using monolithic finite element method. *Journal of Fluids and Structures*, 129:104167, 2024.

10th International Conference on HYDROELASTICITY IN MARINE TECHNOLOGY
Trondheim, Norway, June16th-18th, 2026

Hydroelastic Response and Power Extraction in Wave-Energy-Integrated Aquaculture Systems

Mi, S.[1], Cheng, H.[2], Avital, E.J.[1,*],
Chatjigeorgiou, I.K.[3], Konispoliatis, D.N.[3], Papadakis, G.[3], and Samad, A.[4]

[1] School of Engineering and Materials Science, Queen Mary University of London, UK
[2] AKVA GROUP ASA, Bergen, Norway
[3] School of Naval Architecture and Marine Engineering, National Technical University of Athens, Greece
[4] Department of Ocean Engineering, IIT Madras, India

Abstract. Wave-energy-integrated aquaculture systems can provide local renewable power but also change the hydrodynamic loads on deformable cage components in energetic seas. This paper presents a viscous two-phase numerical framework that resolves the coupled free-surface hydrodynamics, structural dynamics, and power-take-off (PTO) response in such systems. The model is built on the Basilisk two-phase viscous flow solver with geometrical volume-of-fluid (VOF) interface capturing and a piecewise linear interface construction (PLIC)-centroid immersed boundary method (IBM) on adaptive Cartesian grids, loosely coupled to the Project Chrono multibody dynamics library for rigid-body and structural dynamics. A lumped PTO module is implemented via a rotational damping model to quantify the absorbed power. The framework is validated against benchmark problems including the free heave of a floating cylinder, the rotation of an oscillating wave surge converter (OWSC) under regular waves, and wave loading on a fixed rigid planar net. A representative WEC-integrated aquaculture configuration is then simulated in regular waves to illustrate the coupled behaviour of flap motion, absorbed power, and net loading. The results show that these quantities vary periodically with the incident waves and are strongly correlated in time, pointing to future parametric studies on PTO tuning and operating strategies.

Key words: *Hydroelasticity; Wave–Structure Interaction; Aquaculture Structures; Fluid–Structure Interaction; Wave Energy Converters*

1. Introduction

Offshore aquaculture is moving toward more energetic sites to mitigate nearshore environmental pressure and access larger farming space. This transition exposes cage–net–mooring systems to stronger wave climates and raises both the structural-load level [1, 2] and the operational-energy demand (feeding, monitoring, cleaning, etc.), for which renewable supply offshore is increasingly attractive [3]. A promising option is to co-locate or mechanically integrate wave energy converters (WECs) with aquaculture structures, sharing marine space and infrastructure. Recent assessments indicate that wave energy can be a viable contributor to offshore farm power supply and that WECs may also provide partial wave shielding [4, 3]. Concept developments range from co-location planning and integrated multi-purpose platforms [5] to more focused hybrid concepts that couple WEC devices directly with cage systems [6, 7].

The engineering design of such concepts faces a coupled multi-physics problem in which the incident and radiated wave field interacts with WEC motion and power-take-off (PTO) dynamics, the unsteady flow modifies loads on deformable nets and slender members, and structural deformation feeds back to

*Correspondence to: e.avital@qmul.ac.uk

the hydrodynamics. Experiments and simulations have shown that net systems exhibit significant wave- and current-induced deformation and highly unsteady loading [1, 2], motivating modelling approaches that resolve both the free-surface flow and the hydroelastic response.

Many design-stage models for wave energy converters (WECs) obtain wave–body hydrodynamic coefficients using linear potential-flow boundary element methods (BEM), due to their computational efficiency in large-scale parametric and control studies [8]. For aquaculture cages, nets and moorings are commonly represented using reduced-order hydrodynamic load models coupled with lumped-mass/truss structural discretisations to enable practical time-domain simulations at farm scale [9, 10, 11]. Such approaches are efficient; however, when viscous effects, flow separation, or strongly nonlinear free-surface phenomena become important near moving components and flexible structures, viscous free-surface CFD can be beneficial [12]. In the present framework, we adopt a hybrid strategy: grid-resolved bodies and the two-phase free surface are solved with viscous VOF–IBM CFD, while unresolved slender members (nets/moorings) are loaded using Morison-type models, enabling robust coupling with multibody/flexible dynamics and a PTO module.

In this work, we develop a viscous two-phase numerical framework for wave-energy-integrated aquaculture problems by coupling a two-phase viscous free-surface solver with an immersed boundary representation of grid-resolved bodies and a nonlinear multibody/flexible-structure solver. The fluid solver is implemented in Basilisk [13] using a geometrical VOF method with PLIC reconstruction, and grid-resolved immersed bodies are handled using a PLIC-centroid immersed boundary method on adaptive Cartesian grids. Structural dynamics of rigid components and line-type members (nets/moorings) are advanced in Project Chrono [14] using a staggered coupling strategy, with hydrodynamic loads assembled from IBM surface integration for grid-resolved bodies and Morison-type reduced-order models for unresolved slender structures. A lumped PTO module is included to quantify absorbed power. The framework is validated against benchmark problems involving a free-heaving floating cylinder, an oscillating wave surge converter (OWSC) under regular waves, and wave loading on a rigid planar net. A demonstrative WEC-integrated aquaculture configuration is then presented to illustrate the coupled response of WEC motion, absorbed power, and net loading under regular waves, supporting the use of the framework for future parametric studies and operating-mode exploration.

2. Numerical Framework

2.1. Governing Equations

The numerical work is implemented in the open-source code Basilisk [13]. Basilisk is widely used and validated for multiphase flow simulation and supports adaptive mesh refinement (AMR) on quadtree/octree Cartesian grids.

For incompressible flows, the governing equations can be written as

$$\rho\left(\partial_t \mathbf{u} + (\mathbf{u}\cdot\nabla)\mathbf{u}\right) = -\nabla p + \nabla\cdot(2\mu\mathbf{D}) + \rho\mathbf{g} + \sigma\kappa\,\delta_s\,\mathbf{n} + \rho\,\mathbf{a}_{\mathrm{IB}}, \tag{1}$$

$$\nabla\cdot\mathbf{u} = 0, \tag{2}$$

where $\mathbf{u} = (u, v, w)$ is the velocity field, p is the pressure, and $\mathbf{D}$ is the deformation tensor defined as

$$D_{ij} \equiv \frac{1}{2}\left(\partial_i u_j + \partial_j u_i\right). \tag{3}$$

The density ρ and viscosity μ vary in space and time through the fluid volume fraction C_f (see Section 2.2.), e.g., $\rho(C_f) = C_f\rho_w + (1 - C_f)\rho_a$ and $\mu(C_f) = C_f\mu_w + (1 - C_f)\mu_a$, where the subscripts w and a denote water and air, respectively.

The surface tension force is represented by $\sigma\kappa\,\delta_s\,\mathbf{n}$, where σ is the surface tension coefficient, κ is the interface curvature, $\mathbf{n}$ is the interface normal, and δ_s is a Dirac distribution concentrated on the interface [13]. In this study, immersed boundary force $\mathbf{a}_{\mathrm{IB}}$ is assembled as an acceleration field (per unit mass) which is added to the face acceleration term used by the projection scheme (see Section 2.3.).

2.2. Interface Capturing Method

Two geometrical interfaces are handled on the same Eulerian grid: (i) the moving air–water free surface, and (ii) the solid–fluid boundary of immersed bodies. Throughout this section "fluid" refers collectively to the air–water two-phase mixture, while "water" and "air" denote the individual phases. Both interfaces are reconstructed using Basilisk's geometrical volume-of-fluid (VOF) framework with piecewise linear interface construction (PLIC), in which the local interface in each interfacial cell is approximated by a straight line segment in 2D (or a plane in 3D) whose position and orientation match the prescribed volume fraction and local normal [15].

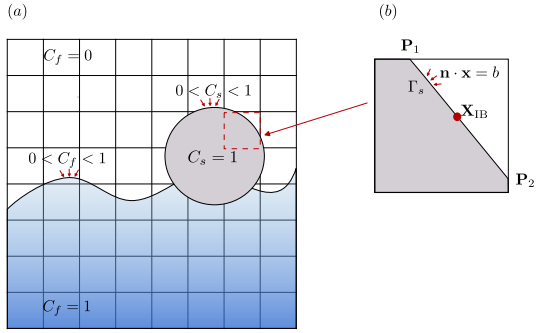


Figure 1: Illustration of the interface capture method. (a) Definitions of the water volume fraction C_f and solid volume fraction C_s for air, water, and solid regions. (b) A representative cell partially occupied by the solid phase, showing the PLIC-reconstructed solid boundary, interface normal $\mathbf{n}$, intersection points $\mathbf{P}_1$ and $\mathbf{P}_2$ with cell edges, and the position of the immersed boundary (IB) point $\mathbf{X}_{\text{IB}}$.

For the air–water interface, we define $C_f \in [0, 1]$ as the water volume fraction in each control volume (see Fig. 1(a)): $C_f = 1$ in water, $C_f = 0$ in air, and $0 < C_f < 1$ in mixed cells indicating the free surface. The scalar field C_f is advected by

$$\partial_t C_f + \nabla \cdot (C_f \mathbf{u}) = 0, \tag{4}$$

and the PLIC reconstruction in each mixed cell is used to compute geometrical fluxes and to maintain a sharp free surface [13].

As shown in Fig. 1(a), the solid volume fraction $C_s \in [0, 1]$ is defined to indicate the interface between fluid and solid: $C_s = 1$ and $C_s = 0$ denote the solid and the fluid cells respectively, and $0 < C_s < 1$ marks cells partially occupied by the solid. Note that the solid–fluid interface defined by C_s implicitly contains both solid–water and solid–air segments, depending on whether the adjacent fluid is water ($C_f = 1$) or air ($C_f = 0$). The material properties at the air–water–solid junction are treated as described in Section 2.3..

In contrast to C_f, the field C_s is not transported by an advection equation. Instead, at each time step it is rebuilt from the current solid configuration (position and shape), e.g. by evaluating a signed-distance function and converting it into volume fractions (see Section 2.4.). In each cut cell ($0 < C_s < 1$), the same PLIC procedure is used to reconstruct the solid–fluid interface, from which the immersed boundary point $\mathbf{X}_{\text{IB}}$ is then defined as the centroid of the reconstructed interface fragment (see Fig. 1(b)).

2.3. Immersed Boundary Method

A PLIC-centroid immersed boundary method (IBM) is employed to resolve the hydrodynamics of grid-resolved bodies (e.g. floaters and WEC components) on Basilisk adaptive Cartesian grids, following

a multi-direct forcing (MDF) strategy on quadtree/octree meshes [16]. The IB effect is introduced as an acceleration field $\mathbf{a}_{\mathrm{IB}}$ in the momentum equation (Eq. 1). Within one time step, after the standard convection and viscous-diffusion substeps [17, 18, 13], an auxiliary velocity $\widetilde{\mathbf{u}}$ is assembled and the no-slip condition $\mathbf{u}(\mathbf{X}_{\mathrm{IB}}) = \mathbf{U}_s(\mathbf{X}_{\mathrm{IB}})$ at each IB point is enforced iteratively by an MDF correction. At iteration k,

$$\mathbf{a}_{\mathrm{IB}}^{(k)}(\mathbf{X}_{\mathrm{IB}}) = \frac{\mathbf{U}_s(\mathbf{X}_{\mathrm{IB}}) - \widetilde{\mathbf{U}}^{(k)}(\mathbf{X}_{\mathrm{IB}})}{\Delta t}, \tag{5}$$

where $\widetilde{\mathbf{U}}^{(k)}(\mathbf{X}_{\mathrm{IB}})$ is obtained by interpolating $\widetilde{\mathbf{u}}^{(k)}$ to the IB point using the four-point Peskin delta kernel [19]. The Eulerian IB acceleration is then spread back to nearby cell centres, and $\widetilde{\mathbf{u}}$ is updated by $\widetilde{\mathbf{u}}^{(k+1)} = \widetilde{\mathbf{u}}^{(k)} + \Delta t\, \mathbf{a}_{\mathrm{IB}}^{(k)}$. After N_{iter} iterations the total IB acceleration is $\mathbf{a}_{\mathrm{IB}} = \sum_{k=1}^{N_{\mathrm{iter}}} \mathbf{a}_{\mathrm{IB}}^{(k)}$, and the face velocity is projected to be divergence-free with p^{n+1} obtained from the standard variable-coefficient Poisson equation. To avoid spurious currents near the air–water–solid junction, the material properties inside the solid region are set to those of the heavier phase [20], i.e. $\rho_s = \rho_w$, $\mu_s = \mu_w$, leading to $\rho_{\mathrm{eff}} = C_s\rho_s + (1 - C_s)\rho(C_f)$ and $\mu_{\mathrm{eff}} = C_s\mu_s + (1 - C_s)\mu(C_f)$.

2.4. Coupling with Project Chrono

The two-phase VOF–IBM flow solver is coupled with Project Chrono [14] to simulate the multibody and flexible dynamics of wave-energy-integrated aquaculture systems. Because such systems involve components with vastly different characteristic length scales, structures are split into two categories: *grid-resolved bodies* (floating collars, WEC flaps), whose geometry is represented on the Eulerian grid via C_s and whose hydrodynamic loads are obtained by integrating pressure and viscous stresses over the reconstructed immersed boundary Γ_s using the IB-point centroids [16]; and *unresolved slender structures* (mooring lines, net twines), whose diameters are smaller than the local grid spacing, modelled with 1D cable/bar elements in Chrono and loaded by a Morison-type formulation that uses locally interpolated Eulerian flow kinematics, following our previous work [10, 21].

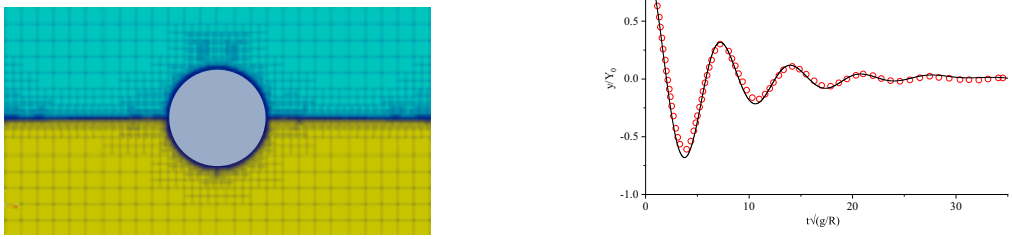
A loosely coupled staggered scheme advances the system from t^n to t^{n+1} in four substeps: (i) given the Chrono states at t^n, the geometry of IBM-resolved bodies is reconstructed and C_s^n is reassembled on the grid; (ii) the two-phase flow is advanced to obtain $(\mathbf{u}^{n+1}, p^{n+1}, C_f^{n+1})$; (iii) the IBM surface loads on grid-resolved bodies and the Morison nodal loads on slender members are evaluated; and (iv) the rigid-body and 1D structural dynamics are advanced in Chrono under these loads and constraints to give the updated structural states at t^{n+1}.

3. Validation Cases

3.1. Free heave of a cylinder on an air-water interface

This case validates the fully coupled fluid–structure interaction between a floating rigid body and a two-phase flow, using the experiment of [22]. A cylinder ($R = 0.0762$ m, $\rho_s = 500$ kg/m^3) is released from rest with an initial heave offset $Y_0 = R/3$ above the equilibrium position. The computational domain is a two-dimensional slice of the experimental tank with length $L = 12$ m, height $H = 3$ m and water depth $d = 1.22$ m. Adaptive mesh refinement (AMR) is used to resolve the small oscillations of the cylinder, with the grid refined around the cylinder boundary and the air–water interface (Fig. 2(a)).

Fig. 2(b) compares the predicted heave time history with the experimental data. The numerical results capture both the oscillation period and the decay rate, with peak amplitudes within a few percent of the experimental values, indicating that the present coupled solver can accurately reproduce the heave dynamics of a floating body on a free surface.



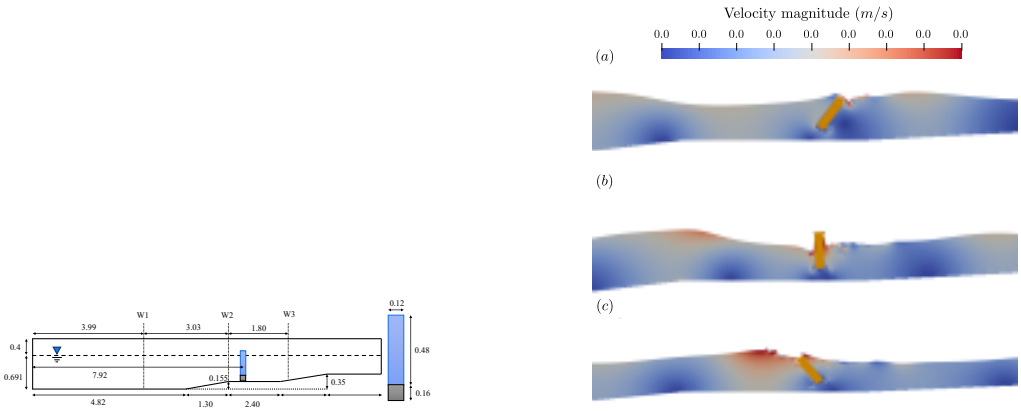
(a) (b)

Figure 2: Free heave of a floating cylinder: (a) snapshot of the AMR distribution around the cylinder and the air–water interface; (b) time history of the cylinder heave displacement compared with the experimental data of [22].

3.2. Rotation of OWSC under waves

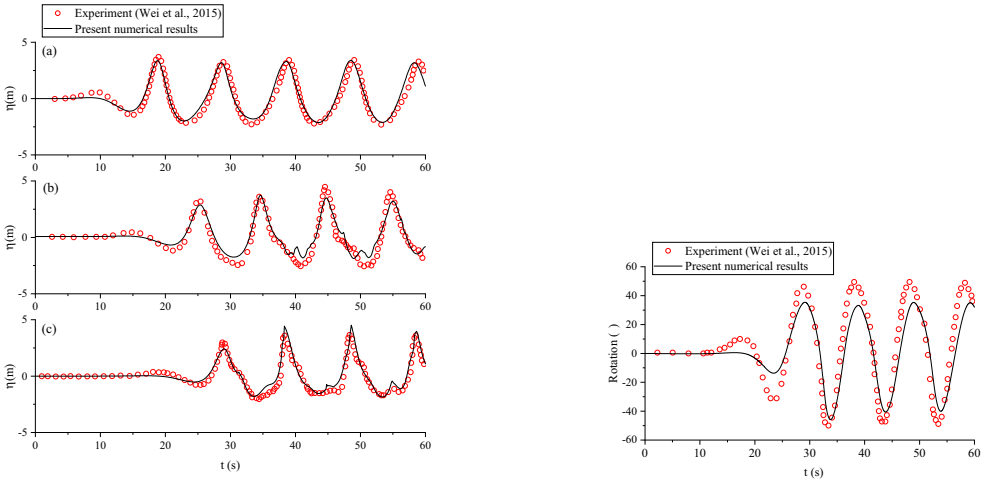
Oscillating wave surge converters (OWSCs) are flap-type WECs that extract energy from incident waves through large-amplitude oscillatory rotation. Their dynamics have been extensively studied experimentally and numerically and provide a practical benchmark for validating solvers for renewable energy applications [23, 24, 25]. We consider a two-dimensional OWSC configuration based on the experimental work of [23] and use the present model to reproduce the coupled free-surface deformation and flap rotational response under regular waves.

The numerical setup is illustrated in Fig. 3(a). Following [23], the wave tank is 18 m long, 4.58 m wide and 1.0 m high in the experiment. Here, we consider a two-dimensional slice and adopt a 1:25 scale. Regular waves with $H = 0.2$ m and $T = 2.0$ s are generated at the inlet, corresponding to $H = 5$ m and $T = 10$ s at full scale. Quantities in this section are reported at full scale following [23]. The OWSC is modelled as a rigid rectangular flap hinged near the tank bottom, with mass 33.0 kg and moment of inertia 1.84 kg m^2/m about the hinge axis. Three wave gauges (W1–W3) along the tank record the free-surface elevation.



(a) (b)

Figure 3: OWSC validation setup and instantaneous flow field: (a) two-dimensional numerical setup, with the rigid flap (blue) hinged to a fixed base (grey) and three wave probes W1–W3; (b) instantaneous free-surface profile and velocity magnitude contours at $t = 30$, 32.5, and 35 s (top to bottom).



(a) (b)

Figure 4: OWSC validation: (a) time history of the free-surface elevation at probes W1–W3; (b) time history of the flap rotation angle. Both panels compare the present simulation with the experimental data of [23].

Fig. 3(b) shows instantaneous snapshots of the free surface and flap rotation at three time instants ($t = 30$, 32.5, and 35 s). The flap motion near the free surface induces clear wave scattering on both the upstream and downstream sides, qualitatively confirming that the present solver captures the coupled dynamics among incident waves, flap rotation, and the perturbed flow field.

Fig. 4(a) compares the predicted free-surface elevation at the three wave probes with the experimental data. At the upstream probe W1, the predicted elevation follows the experimental trace closely in both amplitude and phase. At probes W2 and W3, located closer to the flap, slight differences in the peak crests are observed between the simulation and the experiment, while the dominant wave period and the overall trend of the surface elevation are well captured. These local peak-level differences are attributed to the 2D approximation, which cannot reproduce the 3D wave diffraction around the lateral edges of the finite-width flap.

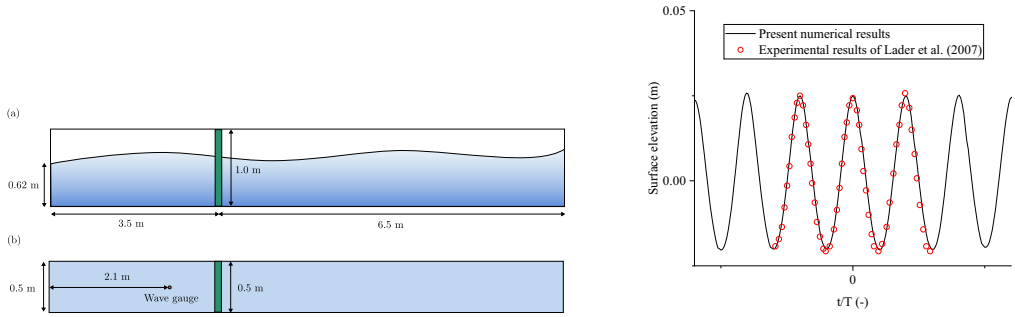
Fig. 4(b) further compares the flap rotation time history with the measurements. The predicted response captures the dominant oscillation period and the overall phase, and the peak rotation angles agree with the experiment to within roughly 5–10%, with the present model slightly underestimating the rotation amplitude. A similar small discrepancy is also observed in the simulation of [25].

3.3. A fixed rigid planar net under wave loads

We use the experimental data of [2] to validate the present model for wave loading on nets. The experiment measured the hydrodynamic loads on planar nets of different geometries under several wave conditions. Among the available cases we adopt the condition with $f = 1.42$ Hz and $H = 0.045$ m, because it (i) corresponds to a moderate wave steepness representative of operational conditions for net cages; (ii) is reported with complete drag, lift and free-surface measurements for all three net configurations and is therefore best suited for assessing the model's sensitivity to net geometry; and (iii) is the most extensively documented case in the experimental dataset. Additional wave conditions are left for future systematic studies.

The numerical setup is illustrated in Fig. 5(a). The computational domain is a wave tank of length 10 m, width 0.5 m, and height 1 m, with water depth 0.62 m. A fixed rigid planar net of width 0.5 m and

height 1.0 m is placed vertically at $x = 3.5$ m from the inlet, and a wave gauge at $x = 2.1$ m records the free-surface elevation. Fig. 5(b) shows that the simulated surface elevation at this gauge agrees with the experimental data, confirming that the prescribed wave field is correctly generated. The twine length and diameter for the three net cases are given in Table 1.



(a) (b)

Figure 5: Fixed planar net validation: (a) numerical setup (top: side view; bottom: top view); (b) time history of the free-surface elevation at the wave gauge for $f = 1.42$ Hz and $H = 0.045$ m, compared with the experimental data of [2].

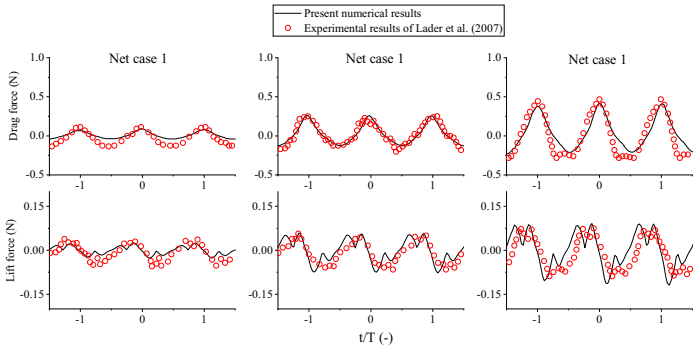


Figure 6: Time development of the drag (top row) and lift (bottom row) forces acting on the rigid planar net for the three net cases of Table 1, compared with the experimental data of [2].

Table 1: Parameters for the three planar nets used in the numerical cases of Section 3.3., corresponding to Fig. 6.

	Net case 1	Net case 2	Net case 3
Twine length (mm)	21	16	25
Twine diameter (mm)	1.0	1.8	3.6
Solidity (S_n)	0.095	0.225	0.288

As shown in Fig. 6, the simulated drag and lift forces for the three net cases are compared with the experimental data of [2]. Under the same wave load, the peak drag force increases with the net's solidity, a trend well captured by the present model. Slight differences in the drag and lift peaks are observed between the simulation and the experiment, but the overall trends agree well across all three cases. Overall, the validation demonstrates that the present model reproduces the hydrodynamic loading trends on planar nets under regular waves and provides a reliable basis for simulating more complex aquaculture structures.

4. Results

To demonstrate the coupled hydroelastic response and power extraction of a WEC-integrated aquaculture concept, we consider a simplified configuration comprising a floating cylinder, two symmetric flap-type WECs hinged on its $\pm x$ sides, a flexible net panel suspended beneath the cylinder, and four mooring lines (Fig. 7). The computational domain is a cube of side $8L_c$ with water depth $1.5L_c$, where $L_c = 1$ m is the cylinder length. The cylinder ($D_c = 0.4$ m) is centred at $x = 2.5L_c$, each flap has length $1.5D_c$, thickness $0.3D_c$, and width L_c, and the net of size $L_c \times L_c$ is linked to the cylinder along its top edge with weights of 0.01 N at the bottom nodes. Mooring-line properties and anchor/fairlead positions are summarised in Table 2, and regular waves with $H = 0.25$ m and $T = 1.5$ s are generated at the inlet.

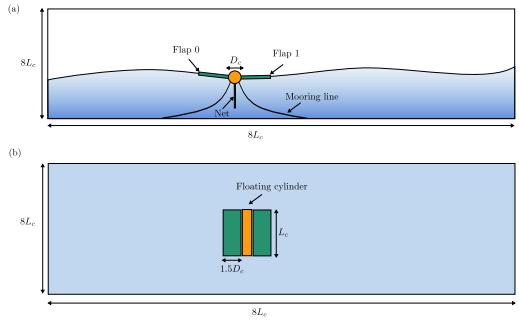


Figure 7: Numerical setup for the WEC-integrated aquaculture system in waves: (a) side view, (b) top view.

Table 2: Mooring-line properties and connection geometry for the WEC-integrated aquaculture case (fairleads in the cylinder frame, anchors in the global frame).

Property	Value	Connection	Position (m)
Number of lines	4	Fairlead L1, L2 (left)	$(-0.07,\ -0.06,\ \pm 0.4)$
Diameter	3.5 mm	Fairlead L3, L4 (right)	$(+0.07,\ -0.06,\ \pm 0.4)$
Rest length	2.3 m	Anchor L1, L2	$(1,\ -1.5,\ \pm 0.4)$
Young's modulus	5×10^6 Pa	Anchor L3, L4	$(4,\ -1.5,\ \pm 0.4)$
Mass per length	0.06 kg/m		

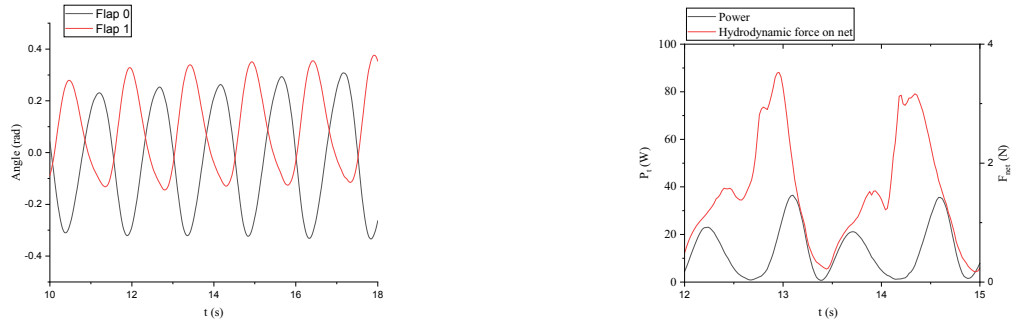
Fig. 8(a) presents a representative snapshot of the coupled system at $t = 16.6$ s, showing the floating structure at the free surface and the velocity magnitude in the surrounding flow. The incident waves



(a) (b)

Figure 8: WEC-integrated aquaculture system: (a) snapshot of the floating structure and surrounding flow at $t = 16.6$ s; (b) motion and deformation of the system at $t = 17$, 17.5, and 18 s. The colour on the net indicates the magnitude of the total hydrodynamic force.

induce strong wave scattering and a disturbed flow field around the cylinder and the flaps. Fig. 8(b) illustrates the motion and deformation of the net panel, mooring lines, and flaps at three instants ($t = 17$, 17.5, and 18 s) over approximately one wave period. The net undergoes a clear hydroelastic response to the oscillatory wave-induced flow: at $t = 17$ s and 17.5 s, the net appears more stretched and exhibits a broader distribution of elevated hydrodynamic forces, qualitatively demonstrating the time-varying coupling among wave kinematics, WEC motion, and the deformable net structure.



(a) (b)

Figure 9: Time histories of the WEC-integrated aquaculture case: (a) flap rotation angles θ_0 and θ_1 of the two WECs; (b) PTO power (left axis) and total net hydrodynamic force (right axis).

The time histories of flap rotation, PTO power, and net loading provide quantitative support for the above observations. Fig. 9(a) shows that both flaps exhibit periodic oscillations with amplitudes of approximately ± 0.3 rad, with the two rotation signals largely out of phase due to the symmetric layout on opposite sides of the cylinder. The power take-off is modelled as a linear rotational damper with torque $T_{\mathrm{pto}} = -B\omega$ and absorbed power $P_{\mathrm{abs}} = B\omega^2 \geq 0$, where ω is the hinge angular velocity. With $B = 10$ N m s/rad, Fig. 9(b) shows that P_{abs} oscillates with the wave period and reaches peaks on the order of tens of watts, while the total net hydrodynamic force exhibits a comparable periodic variation with elevated load levels close in time to the power peaks. This indicates a strong coupling between energy extraction and structural loading, suggesting that PTO tuning and operating strategy can influence both the harvested power and the load environment of the deformable net cage components.

5. Conclusions

A viscous two-phase numerical framework has been developed for coupled free-surface flow and structural dynamics in wave-energy-integrated aquaculture systems. The framework combines a two-

phase VOF solver with a PLIC-reconstructed IBM in Basilisk and a loosely coupled interface to Project Chrono. Large components are grid-resolved while slender members are treated with reduced-order Morison-type loading. Validation against (i) free heave of a floating cylinder, (ii) OWSC rotation under regular waves, and (iii) wave loading on a fixed rigid planar net reproduces the experimentally observed free-surface evolution, oscillation periods and wave-induced loading trends, with small local discrepancies near the OWSC flap and in the net force peaks that are consistent with the 2D approximation and explicitly discussed in Section 3. A demonstrative WEC-integrated aquaculture case further shows that flap motion, absorbed power, and net loading vary periodically with the incident waves and are strongly correlated in time, supporting the use of the framework for preliminary design exploration of such integrated concepts. More extensive parametric studies and operating-mode comparisons are reserved for future work.

References

[1] Trygve Kristiansen and Odd M Faltinsen. Experimental and numerical study of an aquaculture net cage with floater in waves and current. *Journal of Fluids and Structures*, 54:1–26, 2015.

[2] Pål Lader, Atle Jensen, Johan Kristian Sveen, Arne Fredheim, Birger Enerhaug, and Dave Fredriksson. Experimental investigation of wave forces on net structures. *Applied Ocean Research*, 29(3):112–127, 2007.

[3] Lysel Garavelli, Mikaela C Freeman, Levy G Tugade, David Greene, and Jim McNally. A feasibility assessment for co-locating and powering offshore aquaculture with wave energy in the united states. *Ocean & Coastal Management*, 225:106242, 2022.

[4] Daniel Clemente, P Rosa-Santos, Tiago Ferradosa, and F Taveira-Pinto. Wave energy conversion energizing offshore aquaculture: Prospects along the portuguese coastline. *Renewable Energy*, 204:347–358, 2023.

[5] Liang Li, Carlo Ruzzo, Maurizio Collu, Yan Gao, Giuseppe Failla, and Felice Arena. Analysis of the coupled dynamic response of an offshore floating multi-purpose platform for the blue economy. *Ocean Engineering*, 217:107943, 2020.

[6] Yong Cheng, Jiale Gong, and Jian Zhang. Hydrodynamic investigation on a single-point moored offshore cage-wave energy converter hybrid system. *Ocean Engineering*, 299:116848, 2024.

[7] Yong Cheng, Yinong Hu, Deshuang Yu, Saishuai Dai, Zhiming Yuan, Atilla Incecik, and Gang Wang. Hydrodynamic characteristics of a wave energy converter array-offshore aquaculture cage group hybrid system. *Energy*, 328:136522, 2025.

[8] Louis Papillon, Ronan Costello, and John V Ringwood. Boundary element and integral methods in potential flow theory: A review with a focus on wave energy applications. *Journal of Ocean Engineering and Marine Energy*, 6(3):303–337, 2020.

[9] Trygve Kristiansen and Odd M Faltinsen. Modelling of current loads on aquaculture net cages. *Journal of Fluids and Structures*, 34:218–235, 2012.

[10] Shuo Mi, Mingyang Wang, Eldad Jitzchak Avital, John JR Williams, and Ioannis K Chatjigeorgiou. An implicit eulerian–lagrangian model for flow-net interaction using immersed boundary method in openfoam. *Ocean Engineering*, 264:112843, 2022.

[11] Hui Cheng, Lin Li, Karl Gunnar Aarsæther, and Muk Chen Ong. Typical hydrodynamic models for aquaculture nets: A comparative study under pure current conditions. *Aquacultural Engineering*, 90:102070, 2020.

[12] Tobias Martin, Andrei Tsarau, and Hans Bihs. A numerical framework for modelling the dynamics of open ocean aquaculture structures in viscous fluids. *Applied Ocean Research*, 106:102410, 2021.

[13] Stéphane Popinet. An accurate adaptive solver for surface-tension-driven interfacial flows. *Journal of Computational Physics*, 228(16):5838–5866, 2009.

[14] Alessandro Tasora, Radu Serban, Hammad Mazhar, Arman Pazouki, Daniel Melanz, Jonathan Fleischmann, Michael Taylor, Hiroyuki Sugiyama, and Dan Negrut. Chrono: An open source multi-physics dynamics engine. In *international conference on high performance computing in science and engineering*, pages 19–49. Springer, 2015.

[15] Ruben Scardovelli and Stéphane Zaleski. Direct numerical simulation of free-surface and interfacial flow. *Annual Review of Fluid Mechanics*, 31(1):567–603, 1999.

[16] Spencer Schwartz and Yue Ling. An eulerian-based immersed boundary method using direct forcing on piecewise linear constructed interface. *Computers & Fluids*, page 106727, 2025.

[17] John B Bell, Phillip Colella, and Harland M Glaz. A second-order projection method for the incompressible navier-stokes equations. *Journal of computational physics*, 85(2):257–283, 1989.

[18] Stéphane Popinet. Gerris: a tree-based adaptive solver for the incompressible euler equations in complex geometries. *Journal of computational physics*, 190(2):572–600, 2003.

[19] Charles S Peskin. The immersed boundary method. *Acta numerica*, 11:479–517, 2002.

[20] Nishant Nangia, Neelesh A Patankar, and Amneet Pal Singh Bhalla. A dlm immersed boundary method based wave-structure interaction solver for high density ratio multiphase flows. *Journal of Computational Physics*, 398:108804, 2019.

[21] Shuo Mi, Eldad Jitzchak Avital, John JR Williams, and Ioannis K Chatjigeorgiou. Development of a novel multi-component coupled numerical model for aquaculture systems in openfoam. *Applied Ocean Research*, 151:104146, 2024.

[22] Sōichi Itō. *Study of the transient heave oscillation of a floating cylinder.* PhD thesis, Massachusetts Institute of Technology, 1977.

[23] Yanji Wei, Ashkan Rafiee, Alan Henry, and Frederic Dias. Wave interaction with an oscillating wave surge converter, part i: Viscous effects. *Ocean Engineering*, 104:185–203, 2015.

[24] Chi Zhang, Yanji Wei, Frederic Dias, and Xiangyu Hu. An efficient fully lagrangian solver for modeling wave interaction with oscillating wave surge converter. *Ocean Engineering*, 236:109540, 2021.

[25] Yaru Ren, Pengzhi Lin, Chi Zhang, and Xiangyu Hu. An efficient correction method in riemann sph for the simulation of general free surface flows. *Computer Methods in Applied Mechanics and Engineering*, 417:116460, 2023.

10th International Conference on HYDROELASTICITY IN MARINE TECHNOLOGY
Trondheim, Norway, June16th-18th, 2026

Preliminary investigation into fully coupled solvers for flexible wave energy converters

Salvatore Capasso[1,2,*], Giacomo Moretti[3], Gianluca Rizzello[4], Kathrin Flaßkamp[4], Iván Martínez-Estévez[5], Corrado Altomare[1], Alejandro J.C. Crespo[5], and Tomohiro Suzuki[2].

[1] Universitat Politècnica de Catalunya – BarcelonaTech, Spain [2] Dept. of Civil Engineering, KU Leuven, Belgium [3] Department of Industrial Engineering, Università di Trento, Italy [4] Faculty of Natural Sciences and Technology, Universität des Saarlandes, Germany [5] EPhysLab, CIM-Uvigo, Universidade de Vigo, Spain

Abstract. Future wave energy converters (WEC) may be structured around highly deformable membranes accommodating wave loads and converting mechanical deformation into usable electricity. Such distributed Power Take-off (PTO) systems establish a complex hydro-mechanical-electrical coupling, for which holistic numerical approaches are yet to be developed. In this paper, we take a first step towards this overarching objective by proposing a 2-D dynamic model of a Dielectric Elastomer Generator (DEG), suitable for acting as PTO in a flexible WEC. By leveraging the Project Chrono multiphysics library, a lumped approach is developed, including hyperelastic material characterization, electric force contribution and power electronics logic to simulate cyclical DEG operations. This model shows promising capabilities of modeling electroactive polymers, as well as high versatility for straightforward coupling with high-fidelity fluid solvers.

Key words: *Wave Energy Converters; Dielectric Elastomer Generators; Multibody Dynamics; Electroactive Materials; Project Chrono.*

1. Introduction

Among offshore engineering challenges, development of efficient and cost-effective wave energy converters (WECs) stands out for its inherent complexity: technological and modeling limitations quickly gain the upper hand when dealing with systems ideally seeking resonant motion, with complex machinery and operating in harsh environments [1]. Unorthodox yet refreshing studies have attributed these long-standing issues to inherent inadequacy of rigid-body architectures in open seas, visualizing conceptually opposite approaches grounded on flexible wave interfaces. As such, manufacturing costs would be reduced, and WECs resilience would benefit from vast use of elastomeric materials, which can accommodate strong wave loads for thousands of cycles [2]. A further step constists in imagining fully flexible WEC concepts within which the primary mover features a distributed Power Take-off (PTO) unit, strongly reducing the overall system complexity.

To develop such WECs at large scales, electrostatic devices, such as Dielectric Elastomer Generators (DEGs) [3], have shown significant potential [4]. These converters harvest electrical energy through a variable capacitance principle, the capacitance depending on the deformation state of a dielectric elastomer. With proper system design, wave loads can drive large stretches for these membranes and effectively convert mechanical into electric energy [5].

However conceptually straightforward and mechanically advantageous due to the superposition of primary mover and PTO, hydrodynamic modeling of DEG-based WECs is extremely challenging. These devices establish a peculiar hydroelastic case study, within which energy harvesting has to be precisely characterized, as it features nonlinear time- and input-dependent electrostatic actions on the elastomer. Moreover, the geometrical and mechanical features of dielectric materials are comparable to extremely

*Correspondence to: salvatore.capasso@upc.edu

thin membranes with strongly nonlinear viscoelastic properties. This combination of factors justifies the lack of comprehensive approaches in literature, which instead appear somehow fragmented between accurate hydroelastic coupled solvers with excessive approximation of DEG behavior [6], and precise electroactive polymer modeling [7] but with simplified hydrodynamics.

Taking the first step towards bridging this gap, here we propose a dynamic DEG model suitable for straightforward coupling with computational fluid dynamics (CFD) solvers. In particular, we leverage the multiphysics library Project Chrono [8] to implement a lumped parameter model (LPM) capable of describing the electro–mechanical coupled behavior of dielectric membranes in operational scenarios. This choice is motivated by both the capabilities of the chosen environment to handle multiphysics problems with embedded control logic, and its suitability for ensuing hydroelastic coupling. In fact, the core module of Project Chrono is coupled with the Smoothed Particle Hydrodynamics (SPH)-based solver DualSPHysics [9, 10], which offers a versatile numerical environment to deal with fluid–structure interaction cases, supporting large deformations of flows and structures alike. The proposed model is an enhanced version of the linear elastic LPM already validated in the DualSPHysics–Chrono framework for 2- and 3- dimensional structural elements [11], which however did not include hyperelastic constitutive model and coupled electrical effects – novelties herein introduced.

The objective of this preliminary study is to establish a coherent and comprehensive dynamic modeling framework for DEGs. Firstly, physical description of Dielectric Elastomers (DE) is provided in Section 2 considering a reduced-order model. Section 3 describes the 2-D LPM approach and the electromechanical coupling within the Chrono framework, leading to the applications of Section 4 under cyclic loads – mimicking ideal operational conditions. Finally, Section 5 draws the conclusion and positions this work along the envisioned development trajectory of fully-coupled hydroelastic solvers for the next generation of WECs.

2. Dielectric elastomer generators in 2D

Dielectric elastomers exhibit coupled electromechanical behavior, requiring a global energy balance to assess their dynamics. On the one hand, the mechanical features of a DE membrane are described by hyperelastic models, capable of capturing strain-hardening effects at very large stretches, possibly including viscoelastic dissipation for cyclic loads. On the other hand, electrical models assume DE as linear dielectric, with electrostatic stresses induced by the electric fields, namely the Maxwell stress [12], with losses possibly modeled as in linear circuits of capacitive and resistive elements. For the purposes of this investigation, we assume ideal DEG operation, i.e., no electrical or mechanical dissipation, and uniform distribution of the electric field.

We tackle DEG topologies that can be described by a single generalized coordinate q, common practice for DEGs deformation kinematics [13]. The following mathematical derivation of mechanical and electrical force contributions considers $q \equiv x$ for simplicity, identifying stresses with single-coordinate expressions. Nevertheless, in the 2-D simulation space described in Section 3, x is considered as a local co-rotational axis that remains tangent to the deformed membrane at any given point: this naturally translates to the longitudinal axis connecting any pair of adjacent bodies which discretize the elastomer. Along this relative axis, the scalar magnitude of the computed forces is applied.

2.1. Coupled mechanical–electrical states

To begin with, let us define the principal stretches $\lambda_i = x_i/X_i$, which entirely describe the deformed state of an elastomer. x_i and X_i are the deformed and initial length, respectively, in the principal directions ($i = 1, 2, 3$), with $X_1 = l_0$, $X_2 = w_0$, $X_3 = t_0$ (Figure 1(a)). As introduced, the global energy balance conveniently frames DEG behavior. Its infinitesimal change reads:

$$\mathrm{d}U_e + \mathrm{d}U_m = \delta W_e + \delta W_m, \tag{1}$$

with U_e and U_m being the electric and mechanical potential energy, and δW_e and δW_m the work of electric and mechanical forces, respectively. The potential terms read:

$$U_e = \int_\Omega \frac{\varepsilon E^2}{2} \mathrm{d}\Omega, \text{ and} \tag{2}$$

$$U_m = \int_\Omega \Psi \mathrm{d}\Omega, \tag{3}$$

where $\Omega = l_0 w_0 t_0$ is the volume, ε the dielectric constant, E the electric field, and Ψ the strain energy function. With uniformly distributed electric field, the following relations between the electric charge Q, the voltage V and the electric field E hold true:

$$V = t_0 \lambda_3 E = x_3 E, \tag{4}$$

$$Q = \varepsilon \lambda_1 l_0 \lambda_2 w_0 E = CV, \tag{5}$$

where we introduce the capacitance of a parallel-plate capacitor, $C = \varepsilon x_1 x_2 / x_3$. These equations are written for uniform stretches, yet they remain valid also for non-uniform stretches in the present model, as voltage is spatially constant and assumed as global electric variable, and capacitance is a global quantity computed for the entire membrane. Substituting in Eq. 1 while considering electric and external force contributions gives:

$$\mathrm{d}\left(\frac{\Omega \varepsilon V^2}{2 x_3^2}\right) + \mathrm{d}(\Psi \Omega) = V \,\mathrm{d}Q + F \,\mathrm{d}q, \tag{6}$$

where $F\,\mathrm{d}q$ represents the mechanical work of an external force F against the generalized coordinate. Manipulating Eq. 6, using the electrical relations (4) and (5), gives an intuitive form of the energy balance for a membrane:

$$F \,\mathrm{d}q = \Omega \mathrm{d}\,\Psi - \frac{V^2}{2} \mathrm{d}C \tag{7}$$

as $U_e = CV^2/2$. The work of the external forces causes a variation in the total elastic energy density, referred to as mechanical state, and in the electric charge of the electrodes, identified as electrical state. To these states directly correspond elastic and Maxwell forces, that will now be derived.

2.2. Hyperelastic material characterization

To address the mechanical state, it is necessary to obtain the relevant stress components by solving the strain energy potential variation. The deformation is linked to the internal stress by a strain energy function via the three stress invariants, I_1, I_2, and I_3. DEGs are considered incompressible in the vast majority of the applications, hence $\lambda_1 \lambda_2 \lambda_3 = 1$. Being the material also isotropic, the principal nominal stress and the strain energy functions are related by the 1st Piola–Kirchhoff stress tensor:

$$P_i = \frac{\partial \Psi}{\partial \lambda_i} - \frac{1}{\lambda_i} p = \frac{\sigma_i}{\lambda_i}, \; i = 1, 2, 3, \tag{8}$$

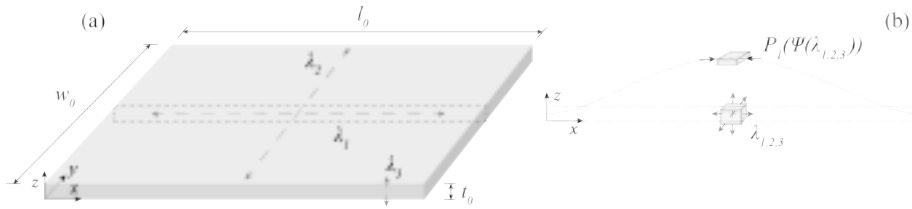


Figure 1: Visualization of the global frame of reference of a planar membrane (a), and corresponding principal nominal stress according to a 2D representation of its central axis (b).

with p representing a *hydrostatic* pressure contribution accounting for incompressibility, and σ_i the true (Cauchy) stress. For thin membranes, it is reasonable to discard vertical stress components developing along the thickness, hence $\sigma_3 = 0$: pressure can be thus defined by solving the boundary value problem, giving $p = \lambda_3 \partial\Psi/\partial\lambda_3$. The literature offers several material models with different characteristics and range of validity [14]. For this investigation we adopt the Yeoh strain energy model [15], which considers the first invariant in a cubic formulation, effectively capturing the hardening effects of elastomeric materials at large strains. It reads:

$$\Psi = c_1(I_1 - 3) + c_2(I_1 - 3)^2 + c_3(I_1 - 3)^3, \tag{9}$$

with c_1, c_2 and c_3 denoting material parameters usually fitted to match experimental stress-strain characterizations. As aforementioned, the deformation state in proposed DEG model is described by a single generalized coordinate q, here coincident with the undeformed x axis (Figure 1(b)). The reference strain along this direction is $\lambda_1 = \lambda$, from now on. Rearranging Eq. 8 accordingly and using the chain rule ($\frac{\partial\Psi}{\partial\lambda_i} = \frac{\partial\Psi}{\partial I_1}\frac{\partial I_1}{\partial\lambda_i}$), also considering the boundary conditions, gives a general expression for in-plane axial nominal stress:

$$P_q = 2\frac{\partial\Psi}{\partial I_1}\left(\lambda - \frac{\lambda_3^2}{\lambda}\right). \tag{10}$$

Eq. 10 relates the deformed state with the axial stress, also considering shrinking along y and z dictated by the incompressibility conditions, being suitable for describing membranes under uniaxial and equibiaxial tension, or pure shear.

2.3. DEG topology and states derivation: pure shear case

Given a topological configuration, DEG kinematics can be further characterized starting from the generalized expressions of the previous paragraphs. In this work, we consider a *pure shear* homogeneous deformation mode, appropriate for sheets with a much larger width than length to realize negligible deformation perpendicular to the loading direction. While this model is suitable for single-coordinate descriptions, it holds explicit dependence from the principal stretches in both mechanical and electrical states, being a suitable yet sufficiently complex model for identifying a realistic 2-D DEG.

2.3.1. Mechanical state

Let us define the elastic force contribution from Equation (7) considering the principal direction x:

$$F_{elastic} = \Omega\frac{\mathrm{d}\Psi}{\mathrm{d}x_1} = \frac{\Omega}{X_1}\frac{\mathrm{d}\Psi}{\mathrm{d}\lambda}. \tag{11}$$

Applying the chain rule and considering that

$$\frac{dI_1}{d\lambda} = 2\lambda - \frac{2}{\lambda^3\lambda_2^2}, \tag{12}$$

the single-coordinate energy approach of Eq. 11 is equivalent to the stress-derived Eq. 10. In pure shear, $\lambda_2 = \lambda_p$, λ_p being a given pre-stretch in the y direction; also, material incompressibility dictates $\lambda_3 = \frac{1}{\lambda_1\lambda_p}$, which finally leads to a coherent axial elastic force expression:

$$F_{elastic} = w_0 t_0 P_1 = 2w_0 t_0 \frac{\partial\Psi}{\partial I_1}\left(\lambda - \frac{1}{\lambda^3\lambda_p^2}\right). \tag{13}$$

2.3.2. Electrical state

The single-coordinate Maxwell stress equation, referred to the x axis, follows from Eq. 7:

$$F_{electric} = -\frac{V^2}{2}\frac{\mathrm{d}C}{\mathrm{d}q} = -\frac{V^2}{2}\frac{\mathrm{d}C}{\mathrm{d}x}. \tag{14}$$

Using the capacitance definition and considering a pure shear topology gives the updated capacitance depending on the deformed state:

$$C = \frac{\varepsilon \Omega}{t_0^2} \lambda^2 \lambda_p^2. \tag{15}$$

The electric force contribution depends on the spatial derivative of the capacitance, which gives the final electric force contribution, explicitly dependent on the deformation state, the pre-stretch value and the square of the voltage:

$$F_{electric} = -V^2 \varepsilon \frac{w_0}{t_0} \lambda \lambda_p^2. \tag{16}$$

The minus sign implies that this force pulls together upper and lower electrodes, causing reduction in thickness and hence planar expansion of the elastomer. Since the voltage is applied during the contraction phase, this contribution is resisting the elastic recovery.

3. Numerical implementation

3.1. Chrono Core Engine

Project Chrono is a comprehensive multiphysics engine which provides simulation support for a wide range of applications, including discrete and finite element solvers. The core module of Chrono offers different solutions to model dielectric elastomer membranes:

- Finite Element Analysis Module: it implements volumes, surfaces and beams supporting large deformations; if solid elements are used, it is possible to define nonlinear elastic models such as Neo–Hookean or Mooney–Rivlin, with high order nodal functions, i.e., the gradient-deficient absolute nodal coordinates formulation (ANCF), to efficiently handle complex deformation mechanics within multi-body systems.
- Multi-body module and actuators: Chrono easily handles large multi-body systems with kinematic/dynamic restrictions, which can be conveniently manipulated to match the specific physical features of the target elastomer.

Even though the first option offers a stable environment for solid mechanics with significant bending and/or torsion, it is inherently limited when attempting the simulation of DE membranes undergoing 200–400% stretching cycles, and the implementation of different hyperelastic models is not straightforward, as well as its coupling with hydrodynamic solvers. On the contrary, personalized actuators in a multi-body system can directly enforce both mechanical and electrical stress components which can be characterized to be effective at any configuration, including extreme stretching. As such, a lumped parameter model is implemented, using rigid body elements and linear actuators. Chrono implements a Differential Algebraic Equations (DAEs) solver for articulated systems of rigid bodies [8]:

$$\frac{\mathrm{d}\boldsymbol{q}}{\mathrm{d}t} = \boldsymbol{L}(\boldsymbol{q})\boldsymbol{u}, \tag{17}$$

$$\boldsymbol{M}(\boldsymbol{q})\frac{\mathrm{d}\boldsymbol{u}}{\mathrm{d}t} = \boldsymbol{f}(t, \boldsymbol{q}, \boldsymbol{u}) - \boldsymbol{g}_{\boldsymbol{q}}^T(t, \boldsymbol{q})\mathcal{L}, \tag{18}$$

$$0 = \boldsymbol{g}_{\boldsymbol{q}}^T(t, \boldsymbol{q}). \tag{19}$$

In Eq. 17 the generalized position $\boldsymbol{q}$ time derivative is related to the velocities $\boldsymbol{u}$ via linear transformation defined by $\boldsymbol{L}(\boldsymbol{q})$. Eq. 18 expresses the force balance, with $\boldsymbol{M}$ being the inertia matrix and $\boldsymbol{f}$ the total force contribution; $\boldsymbol{g}_{\boldsymbol{q}}^T(t, \boldsymbol{q})$ groups the perfect bilateral constraint forces and $\mathcal{L}$ indicates the Lagrangian multipliers. A second order accurate implicit HHT integrator, based on the Hilber–Hughes–Taylor formula, is adopted to update the system, without numerical damping unless explicitly stated.

3.2. Dynamic Lumped Parameters DEG model

Within the Chrono framework, the membrane is discretized in a set of N rigid bodies carrying inertial properties. These bodies are connected by $N - 1$ internal linear actuators (translational spring–

damper-actuators – *ChLinkTSDA*), which are characterized with a custom force functor to cope with the mechanical property of the continuous material and the electrostatic stress:

$$\boldsymbol{f}_A = f(F_{\text{elastic}}, F_{\text{electric}}), \tag{20}$$

the force components defined as in Section 2. $\boldsymbol{f}_A$ is aligned with the axis connecting two subsequent bodies j and $j+1$, hence locally satisfying the 1-D derivation of Section 2, and globally reconstructing the deformed shape of the whole membrane through integration of the system of links and bodies – i.e. the generalized coordinate q. Notably, in Eq. 13 and Eq. 16, the magnitude of the principal stress component is computed locally, depending on the distance between interconnected bodies, whereas the voltage is considered globally over the elastomeric membrane. This approach is consistent with uniform electric field assumption and established electrode coating procedures. Moreover, rotational spring-damper-actuators (*ChLinkRSDA*) connect the N bodies, and their contribution is based on a constant spring parameter computed as $K_R = EI_{sec}/l_\Delta$, with $E \approx 6c_1$ being the estimated Young's Modulus at small strains [15], I_{sec} the moment of inertia of the cross section, and $l_\Delta = l_0/N$ [16]. These links are treated as linear elastic with properties considered valid for small deformations. Their overall contribution to the dynamics is negligible, purely serving numerical stability purposes.

3.3. DEG operation logic

DEGs' working principle is illustrated in Figure 2(a), using a three-axis configuration reporting stretch, voltage and electric charge. The DEG state is identified by four configurations (A–D) and four phases (1–4), as schematized in the central panel (Figure 2(b)):

- **A** Initial undeformed configuration: no mechanical load applied and neutral electrical state, with base value of capacitance.
- (1) *Expansion*: external loads act on the DEG, resulting in a deformation which increases the capacitance.
- **B** Fully deformed configuration: maximum capacitance is reached according to the topology.
- (2) *Priming*: the electric circuit is closed and voltage is introduced spending electrical energy to increase the electrical charge of the device.
- **C** Deformed and charged state: the DEG possesses potential elastic energy, and a uniform electric field is present between the electrodes.
- (3) *Return phase*: elastic forces, and possibly external loads, make work towards the undeformed state, while the maxwell stress counters the contraction. The electric circuit is open and the voltage increase is inversely proportional to the diminishing capacitance: electrostatic energy is produced.
- **D** Charged, undeformed configuration: base capacitance is reached and voltage is at its maximum.
- (4) *Harvesting*: closing the circuit, the DEG is discharged and electrical energy is stored. Finally, state A is reached again.

In a dynamic cycle, the membrane initially responds as a pure elastic solid, and eventually electric contribution affects its dynamics depending on the electric field. As such, the system undergoes different operational states: three dedicated functions have been implemented in the solver to identify the state and operate the power electronics (Figure 2(c)):

- *Strain sensor*: this function computes the total stretch by summing up the local stretches measured by the actuator.
- *Node sensor*: a simple yet effective sensor tracking a point of interest can quickly describe the operational phase depending on the DEG topology and the external forcing condition; information on position and velocity identify the return phase ($q\dot{q} < 0$).
- *Electric controller*: this class gathers information from the sensors, computes voltage, capacitance and charge, feeding information to the TSDA functor to compute the maxwell forces; it also handles the circuit switches for priming/harvesting phases.

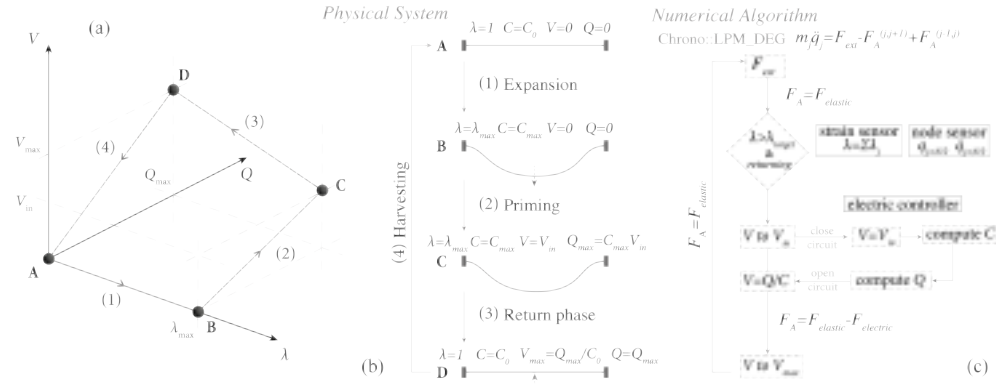


Figure 2: Overview of the DEG working cycle: $\lambda - Q - V$ chart (a), schematic of the successive states (b), and corresponding numerical logic in Project Chrono (c).

4. Model suitability

The model mechanical features are firstly evaluated by numerically replicating a tensile test performed in [17]. A thin membrane of ELASTOSTIL 2030 silicone film, with undeformed width much larger than its length, is longitudinally stretched at quasi-static rate. The sample dimension and properties are listed in Table 1. The reference paper also provides the Yeoh's model parameters to fit the strain–hardening experimental curve. The experimental prestretch λ_p is not provided in the reference material and was deduced by the minimum value of principal stretch and set as $\lambda_p = 2$. The membrane is discretized with a limited number of elements ($N = 20$), as the test features stretches purely along its longitudinal axis, i.e. no bending. The number of elements has negligible impact on the results.

Figure 3 visualizes the stretch–strain curve for the sample, pairing experimental, fitted Yeoh model, and numerical solution. The proposed approach perfectly agrees with the fitted curve, which is the target analytical reference, up to a stretch of 200%, but slightly deviates at higher stretches showing an excess of nominal stress, maybe due to a not perfectly consistent pre-stretch value. However, the Chrono model proves its capabilities of handling largely nonlinear elasticity and extreme deformations. The following

Table 1: Physical parameters of the ELASTOSTIL 2030 by Wacker Chemie AG [17].

Length	l_0	0.010	[m]		c_1	169000	[Pa]
Width	w_0	0.200	[m]	Yeoh's constants	c_2	0	[Pa]
Thickness	t_0	0.0002	[m]		c_3	577.4	[Pa]
Density	ρ_s	1100	[kg/m^3]	Dielectric permittivity	ε	$2.5 \times 8.85 \times 10^{-12}$	[F/m]

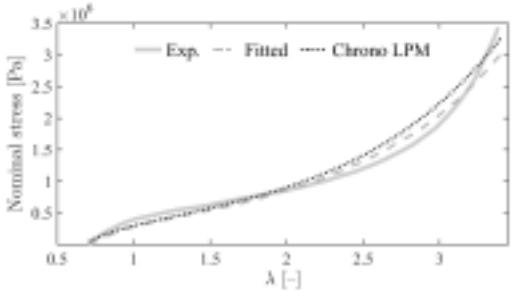


Figure 3: Pure shear tensile test for the ELASTOSTIL 2030 commercial silicone film [17].

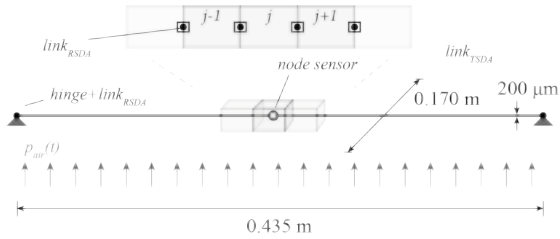


Figure 4: Schematic of the beam discretization for the dynamic test case.

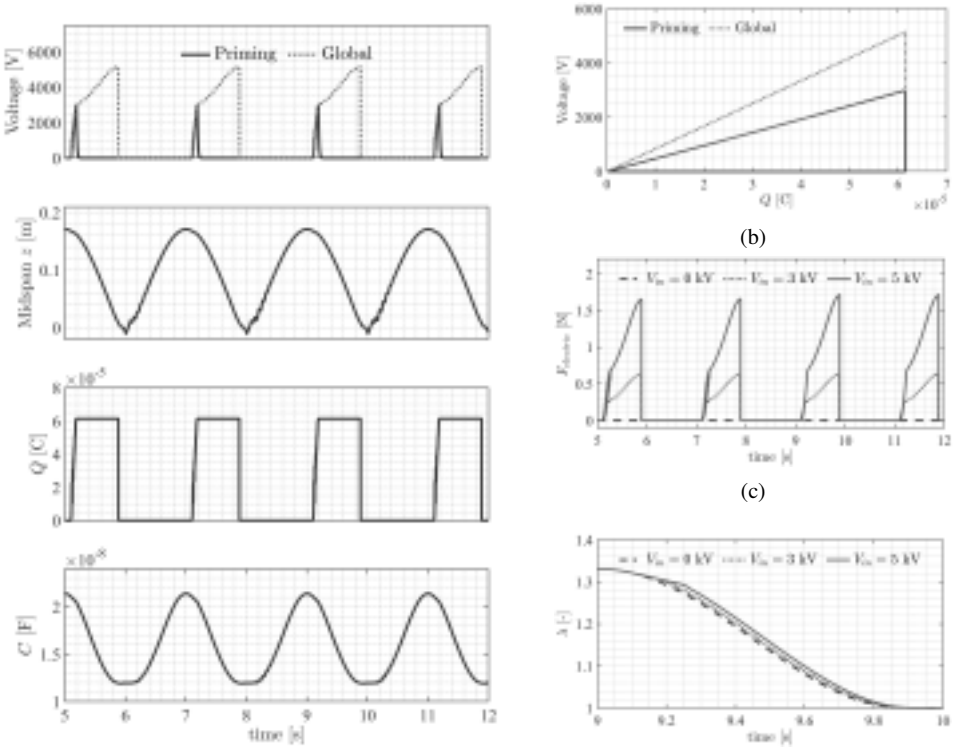


Figure 5: Response of the DEG membrane and electric quantities under cyclical loads, with V_{in} = 3.00 kV (a); comparison of input and output voltage during a complete cycle for V_{in} = 3.00 kV (b); electric force in the central section of the beam with different priming voltages (c); total principal stretch during the return phase with different priming voltages (d).

test case demonstrates the applicability of the model to comprehensively describe dynamic operations of a DE membrane subject to cyclical loads. Figure 4 shows the membrane setup and relevant dimensions. The considered material and the initial thickness are the same as in Table 1, but the dimensions are inspired by the device described in [17] (l_0 = 0.430, and w_0 = 0.170 m), as well as the priming voltage values. In the latter device, the DEG seals a pressurized chamber providing negative stiffness to improve performance [18]: for this test, a cyclic pressure differential is applied for mimicking a feasible operational scenario for submerged DEGs, but no water column is considered. The differential pressure,

hence, equals the applied pressure, which reads:

$$p_{air} = \frac{p_{max}}{2}(1 - \cos 2\pi t/T), \tag{21}$$

with $p_{max} = 500$ Pa being the maximum pressure, t the time, and $T = 2.00$ s the period – values chose to obtain significant stretch and enable relatively regular DEG operation. The membrane is pre-stretched in the longitudinal and transversal directions: $\lambda_{1p} = 1.15$ and $\lambda_p = 1.05$. The representative section modeled in Chrono is double clamped via a combination of hinges and RDSA links with twice the bending stiffness values [16], and a total of $N = 80$ blocks are used with a time step fixed at 0.5×10^{-5} s. Under a uniformly distributed pressure, the DEG kinematic response is primarily akin to a symmetric vertical bowing. Consequently, the node controller follows the state of the central node (midspan) to operate the power electronics, effectively representing the global kinematic state of the DEG.

Figure 5a shows an overview of the DEG cycles with $V_{in} = 3.00$ kV pairing voltage, tip displacement, charge and capacitance. Voltage is injected when maximum capacitance is reached (maximum tip displacement), charging the electrodes. At constant charge, the beam returns towards the equilibrium because of the reducing pressure and the elastic potential energy, causing a spike in the voltage. It is worth noticing that the tip motion presents some high-order oscillations near the equilibrium, that is, when pressure is around zero and electricity is extracted from the system. This can be easily motivated by the extremely high natural frequencies of the membrane, especially when significantly pre-tensioned: the inertia accumulated during the return faces no external countering, triggering vibrations which are eventually absorbed by yet again increasing external loads. In realistic submerged applications, added mass effects would significantly reduce this undesired event.

In Figure 5b, namely the $Q - V$ plane, the continuous and dashed lines identify the energy spent and generated during a single oscillation, respectively. The reported behavior well aligns with theoretical DE generation, and the magnitudes at play are reasonably comparable with experimental evidence for elastomer of this thickness [17]. Figure 5c and Figure 5d frame the Maxwell stress contribution to the dynamics of the membrane, showing the local value of F_{electric} at the central node for three different priming voltages, and the corresponding time-series of the total principal stretch λ. As expected, the electromechanical coupling established in the return phase causes a delay in recovering the equilibrium configuration, this effect being amplified by high priming voltages.

5. Conclusion and future work

This preliminary study proposed a dynamic 2-D lumped parameter model to simulate DEGs operating with pure shear topological configuration, including hyperelastic characterization and Maxwell stress induced by the electric field, as well as detection/action logic mimicking the energy harvesting process. Results showed promising suitability for realistic applications, and highlighted the importance of correctly defining the different forces at play influencing electroactive polymers' dynamics: state-dependent behavior is clearly recognized when energy harvesting control policies are enforced, increasing motion and strain nonlinearity. These findings confirm that simulating energy harvesting of flexWECs with simplified approaches based on viscous losses may be misleading and lead to significant inaccuracies on both structural stress and power absorption. Moreover, the proposed solver configuration can handle *any* deformation pattern, including multi-modal responses, making it a useful test-rig for assessing monitoring strategies when membranes experience non-uniform loading distribution.

This model paves the way for a subsequent development of a realistic hydroelastic modeling scenario for DEGs and electroactive polymers in general, based on the implementation of these new physical components within the well-established lumped model available in the DualSPHysics–Chrono environment. The envisioned two-way coupling is currently under development, with encouraging preliminary results but with significant numerical challenges to overcome in future work, for which this conference offers a privileged setting for constructive discussions. Simulating such thin membranes with extreme stretches of above 300%, in fact, may not be straightforward even in capable SPH-based codes, and most likely requires ad hoc implementations to guarantee numerical stability.

Acknowledgments

S. Capasso gratefully acknowledges B. Tagliafierro for the insightful discussions on multi-body dynamics. C. Altomare acknowledges funding from Spanish government and the European Social Found (ESF) under the programme 'Ramón y Cajal 2020' (RYC2020-030197-I/AEI/10.13039/501100011033)

References

[1] D. Magagna and A. Uihlein, "Ocean energy development in europe: Current status and future perspectives," *International Journal of Marine Energy*, vol. 11, pp. 84–104, 2015.

[2] I. Collins, M. Hossain, W. Dettmer, and I. Masters, "Flexible membrane structures for wave energy harvesting: A review of the developments, materials and computational modelling approaches," *Renewable and Sustainable Energy Reviews*, vol. 151, p. 111478, 2021.

[3] G. Moretti, S. Rosset, R. Vertechy, I. Anderson, and M. Fontana, "A review of dielectric elastomer generator systems," *Advanced Intelligent Systems*, vol. 2, no. 10, p. 2000125, 2020.

[4] P. Kerr, *Radical innovation for the wave energy sector: an investigation of the potential of direct conversion as an enabling technology*. PhD thesis, The University of Edinburgh, 2024.

[5] G. Moretti, M. Santos Herran, D. Forehand, M. Alves, H. Jeffrey, R. Vertechy, and M. Fontana, "Advances in the development of dielectric elastomer generators for wave energy conversion," *Renewable and Sustainable Energy Reviews*, vol. 117, p. 109430, 2020.

[6] C. Wang, Y. Wei, W. Chen, and L. Huang, "Hydroelastic modelling of a deformable wave energy converter including power take-off," *Marine Structures*, vol. 98, p. 103678, 2024.

[7] M. Righi, G. Moretti, D. Forehand, L. Agostini, R. Vertechy, and M. Fontana, "A broadbanded pressure differential wave energy converter based on dielectric elastomer generators," *Nonlinear Dynamics*, vol. 105, no. 4, pp. 2861–2876, 2021.

[8] A. Tasora, R. Serban, H. Mazhar, A. Pazouki, D. Melanz, J. Fleischmann, M. Taylor, H. Sugiyama, and D. Negrut, "Chrono: An Open Source Multi-physics Dynamics Engine," pp. 19–49, 06 2016.

[9] J. M. Domínguez, G. Fourtakas, C. Altomare, R. B. Canelas, A. Tafuni, O. García-Feal, I. Martínez-Estévez, A. Mokos, R. Vacondio, A. J. C. Crespo, B. D. Rogers, P. K. Stansby, and M. Gómez-Gesteira, "DualSPHysics: from fluid dynamics to multiphysics problems," *Computational Particle Mechanics*, vol. 9, pp. 867–895, September 2022.

[10] I. Martínez-Estévez, J. M. Domínguez, B. Tagliafierro, R. B. Canelas, O. García-Feal, A. J. C. Crespo, and M. Gómez-Gesteira, "Coupling of an SPH-based solver with a multiphysics library," *Computer Physics Communications*, vol. 283, p. 108581, February 2023.

[11] S. Capasso, I. Martínez-Estévez, B. Tagliafierro, M. Göteman, C. Altomare, J. M. Domínguez, K. Thiagarajan, M. Gómez-Gesteira, G. Viccione, and A. J. C. Crespo, "Towards a comprehensive design tool for flexible wave energy converters: Multiphysics-augmented sph-based framework," vol. Volume 4: CFD, FSI and AI of *International Conference on Offshore Mechanics and Arctic Engineering*, p. V004T08A023, 06 2025.

[12] L. Dorfmann and R. Ogden, *Nonlinear Theory of Electroelastic and Magnetoelastic Interactions*. 11 2013.

[13] G. Moretti, M. Santos Herran, D. Forehand, M. Alves, H. Jeffrey, R. Vertechy, and M. Fontana, "Advances in the development of dielectric elastomer generators for wave energy conversion," *Renewable and Sustainable Energy Reviews*, vol. 117, p. 109430, 2020.

[14] P. Steinmann, M. Hossain, and G. Possart, "Hyperelastic models for rubber-like materials: Consistent tangent operators and suitability for treloar's data," *Archive of Applied Mechanics*, vol. 82, 09 2012.

[15] O. H. Yeoh, "Some forms of the strain energy function for rubber," *Rubber Chemistry and Technology*, vol. 66, pp. 754–771, 1993.

[16] S. Capasso, B. Tagliafierro, I. Martínez-Estévez, J. Domínguez, A. Crespo, and G. Viccione, "A DEM approach for simulating flexible beam elements with the Project Chrono core module in DualSPHysics," *Computational Particle Mechanics*, 2022.

[17] M. Caselli, A. Carloni, A. Cherubini, G. Moretti, M. Fontana, and R. Vertechy, "Submerged stadium-shaped pressure differential dielectric elastomer generator for wave energy conversion," *IEEE Access*, vol. 13, pp. 197912–197925, 2025.

[18] G. Moretti, G. P. Rosati Papini, L. Daniele, D. Forehand, D. Ingram, R. Vertechy, and M. Fontana, "Modelling and testing of a wave energy converter based on dielectric elastomer generators," *Proceedings of the Royal Society A: Mathematical, Physical and Engineering Sciences*, vol. 475, no. 2222, p. 20180566, 2019.

10th International Conference on HYDROELASTICITY IN MARINE TECHNOLOGY
Trondheim, Norway, June16th-18th, 2026

Wave energy conversion by a 3-raft piezoelectric system

Dessi, D.[1,*]

[1] Institute of Marine Engineering - Consiglio Nazionale delle Ricerche, Rome, Italy

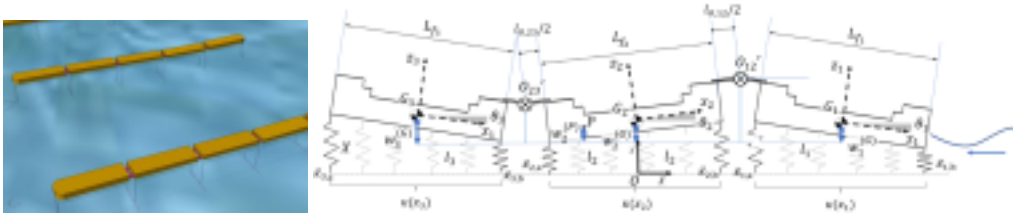
Abstract. Harvesting ocean energy based on the continuous deformation of elongated elastic bodies can be achieved by converting wave energy. Lumped models for harvesters inspired by the wave-carpet concept offer advantages, such as simplified analysis, reduced computational complexity, and easier integration with control or power take-off systems. The investigated device comprises three rafts interconnected by piezoelectric elastic elements. Cummins' equations were recast in a pure differential form by introducing additional differential equations for the radiation forces, which allowed for a more straightforward analysis of the system's behavior over time. The performance of the system was calculated in terms of the response amplitude operators of the relative motion between the floaters, which is the parameter driving the energy conversion by the power take-off system (PTO). The PTO was designed as a multilayer piezoelectric beam, and its mathematical model was simplified to be included in the system ROM. To obtain indications about the effect of the number of rafts on the energy conversion, the developed 3-raft system is then compared with the 2-raft configuration for which experimental data for validation were available.

Key words: *Wave energy conversion; Wave carpet; Cummins' equations; Reduced-order model; Piezoelectric converter*

1. Introduction

In the last years, to exploit the huge energy potential carried by surface waves, a multitude of wave energy converters (WECs) have been conceived, leading to different engineering solutions in terms of mechanical configurations and power take-off (PTO) systems. Among different ways for converting wave power into mechanical energy, one of the most promising approaches is exploiting the relative motion of mutually and flexibly constrained floating bodies, as implemented in DUCK, LEANCON, Pelamis, SeaBeavl, SeaPower, DEXAwave and M4. The latter systems belongs to a category of WECs extensively studied in literature because closely related to wave absorption systems, starting with the Cockerell's device, consisting in a long train of hinged floating rafts (see Wooley and Platts [2]). Haren and Mei [3] went a step further by identifying optimal combinations of parameters based on an analytical formulation of system response. In particular, they underlined as no great advantages in energy extraction can be obtained when the number of rafts is arbitrarily increased beyond three. Newman [4] came to the same conclusion in terms of absorption width, specifically introduced to measure device performances, highlighting also the practical advantages of elongated bodies with small beam-length ratio. The problem of finding the optimum configuration of an articulated raft system is still present nowadays (see, *e.g.*, , Noad and Porter [5]). If PTO system is included in the theoretical model, the detailed representation of the connection between floaters allows for a more realistic representation of the response to wave excitation and estimation of the electrical power. Limiting to 2-raft systems, the PTO is typically presented with lumped elements (Zheng *et al.* [6]), but more accurate descriptions of the PTO can be found for instance in Liu *et al.* [7], who proposed a combined hydrodynamic and hydraulic model with increasing levels of details. All the WECs mentioned above require complex electro-mechanical

*Correspondence to: danaiele.dessi@cnr.it



(a) Piezoelctric floater concept. (b) Geometry and main dimensions of the investigated device.

Figure 1 Energy harvesting system and its small-scale implementation considered in this paper.

PTO systems, difficult to maintain in offshore conditions. Nonetheless, WECs aimed to production of electrical energy for the grid generally benefit from increase in dimensions if sea spectrum wavelengths, installation procedures, impact on near-shore activities allow for. On a small scale, energy harvesting based on wave excitation must efficiently and compactly power electronic instrumentation, multi-functional systems, and monitoring stations on site. Thus, with a main focus on wave energy harvesting, but stretching to consider also small-scale WEC applications, the piezoelectric floating system analysed in this paper extends the concept design from the 2-raft case already considered in [1] to the case of three rafts. In its simplest arrangement, the floaters are linked on the short side with flexible bars as shown in Fig. 1(a). Arrays of piezoelectric elements are embedded at these connections and actuated by the relative body motion under wave excitation, producing electrical energy because of bending of the connecting bars. As the PTO mainly exploits the relative pitch motion between the two bodies, the device better performs with its x-axis aligned with the wave direction. Mooring lines are then needed to keep the whole system in a fixed position with respect to the seabed, and a proper layout (*e.g.*, like that of wind vane or swinging mooring on double anchor) can also guarantee the correct alignment with respect to the incoming waves for small changes in the wave direction.

Extending the mathematical model developed in [1] for a 2-raft system, a reduced-order model of three rafts elastically connected by piezoelectric beams is defined and the prediction of the system's response to incoming regular waves is simulated in the time-domain. The elastic connection is represented through a hinge exerting a restoring (torsional spring) and damping torques (dissipation due to energy conversion). The spring stiffness is experimentally identified from the 2-raft physical model, while the damping coefficients reflects the electrical load of a simple circuit at model scale. The hydrodynamic model for calculating the loads is based on linear potential flow theory, including the restoring hydrostatic and Froude-Kryloff forces, the added mass term, and the diffraction and radiation forces. The latter are obtained by introducing additional differential equations following the modified Prony method. The relative pitch rotation and the deflection of the piezoelectric element, significantly related to the harvester's performances, are calculated to find the wave lengths (and response frequencies) at which energy conversion is maximum. Though some additional analyses are needed to fully explain the system's behaviour, this is the first step to include the mathematical reduced-order model as a solver upon which the power production can be easily evaluated and system optimization can be performed as done in [1].

2. Hydro-piezo-mechanical equations

2.1. Mechanical equations

The considered floating structure consists of three elongated bodies lying on a hydrostatic spring bed, aligned with respect to the wave direction and elastically constrained to each other. The elastic constrain is provided by two piezoelectric beams placed above the waterline, which are composed by a supporting layer and one (unimorph) or two (bimorph, symmetrically arranged) piezoelectric patches. Because the

longitudinal axis of the streamlined configuration is supposed to be self-aligned with the direction of incoming waves, the three rafts are free only to heave and pitch in the longitudinal plane as shown in Fig. 1(b), and the problem is intrinsically two-dimensional. Disregarding surge is a consequence of not considering mooring lines, though the time-domain model is suitable to be coupled with mooring line dynamics as done by Dessi *et al.* for a similar problem [11]. Thus, the reduced-order model (ROM) is based on a separate and linearised description of each floater, which are mutually constrained by kinematic relations and mechanically coupled via equivalent torsional spring and dampers; these idealised elements simulate the structural link and mechanical energy absorption of the piezoelectric beam, respectively, as it will be further discussed in Sec. 2.2..

With respect to the inertial reference system (XOY), as shown in Fig. 1(b), the vertical displacement $w_i^{(P)}$ of a generic point P placed at position x_i in the local frame of reference $(x_i G_i y_i)$ of the i-th floater $(i = 1, \dots, 3)$ is described by the linearised kinematic relation $w_i^{(P)}(x_i, t) = w_i^{(G)}(t) + \theta_i(t)(x_i - x_i^{(G)})$ where $w_i^{(G)}(t)$ is the heave relative to the center of gravity G_i placed at position $x_i^{(G)}$ from the mid-point, assumed positive upward, and $\theta_i(t)$ is the pitch angle, positive counterclockwise, also referred to point G_i. In the following, we will assume that the CoG point G_i coincides with the floater mid-point because of symmetry. The floaters are connected by the two hinges located in O'_{12} and O'_{23} at a distance l_i from G_i. These constraints imply the following relations:

$$w_2^{(G)}(t) = w(t) \qquad w_1^{(G)}(t) = w(t) - \theta_1(t) l_1 - \theta_2(t) l_2, \qquad w_3^{(G)}(t) = w(t) + \theta_2(t) l_2 + \theta_3(t) l_3, \quad (1)$$

where $w(t)$ is the heave at floater's midpoint. For the sake of simplicity, it is further assumed that $L_{\text{fl}1} = L_{\text{fl}2} = L_{\text{fl}3} = L_{\text{fl}}$ and, consequently, $l_1 = l_2 = l_3 = l$. Next, the CoG of the mid raft is assumed as pole for the equilibrium of force and moments for the three floaters. Being each floater characterized by the same mass $m_i = m$ and rotational inertia $J_i = J$ the following equations are obtained:

$$(J + ml^2)\ddot{\theta}_1 + ml^2\ddot{\theta}_2 - ml\,\ddot{w} + c_\theta(\dot{\theta}_1 - \dot{\theta}_2) + k_\theta\,(\theta_1 - \theta_2) = M_1 + lF_1 \quad (2)$$

$$(J + 2ml^2)\ddot{\theta}_2 + ml^2\ddot{\theta}_1 + ml^2\ddot{\theta}_3 + c_\theta(2\,\dot{\theta}_2 - \dot{\theta}_1 - \dot{\theta}_3) + k_\theta\left(2\,\dot{\theta}_2 - \dot{\theta}_1 - \dot{\theta}_3\right) = \\ = M_2 + l(F_3 - F_1) \quad (3)$$

$$(J + ml^2)\ddot{\theta}_3 + ml^2\ddot{\theta}_2 + ml\,\ddot{w} + c_\theta(\dot{\theta}_3 - \dot{\theta}_1) + k_\theta\,(\theta_3 - \theta_1) = M_3 + lF_3 \quad (4)$$

$$m_{tot}\ddot{w} - ml\ddot{\theta}_1 + ml\ddot{\theta}_3 = F_1 + F_2 + F_3 \quad (5)$$

with $m_{tot} = 3\,m$ the overall system mass and k_θ and c_θ are respectively the stiffness and damping of the hinges at $O'_{i,i+1}$, and F_i and M_i are the force and moment, acting on (and referred to) each floater, respectively. The loads at r.h.s. include also the restoring force (relative buoyancy) due to the spring bed as it will be explained later. The torsional spring represents the restoring moment exerted by a flexible element connecting the two barges, opposing to differences in pitch angles. Introducing the vector of generalized displacements $\mathbf{u} = \{\theta_1, \theta_2, \theta_3, w\}^T$, Eqs. 2-5 are recast in matrix form:

$$\mathbf{M}\,\ddot{\mathbf{u}} + \mathbf{C}_\theta\dot{\mathbf{u}} + \mathbf{K}_\theta\mathbf{u} = \mathbf{f} \quad (6)$$

where $\mathbf{M}$, $\mathbf{C}_\theta$ and $\mathbf{K}_\theta$ are inertial mass, structural damping and stiffness matrices, respectively.

2.2. Piezoelectric equations

The governing equations of the piezoelectric beam connecting adjacent rafts is:

$$\begin{cases} \mu\ddot{w}_e + (c_s J\dot{w}_e{}'' + \bar{D}w_e'')'' - \eta\big[\delta'(x)(\xi - \xi_A) - \delta'(x)(\xi - \xi_B)\big]V = 0 \\ C_p\dot{V} + \int_0^{l_0} \eta\Big[H(\xi - \xi_A) - H(\xi - \xi_B)\Big]\dot{w}_e{}''\,d\xi = -I_c(t) \end{cases}, \quad (7)$$

where $w_e(x, t)$ represents the elastic displacement along the beam, μ is the mass per unit length, $c_s J$ is the coefficient of Rayleigh's damping model, $\bar{D}$ is the uniform bending stiffness, l_0, ξ_A and ξ_B are the

piezoelectric beam length, starting and ending point along the beam covered by the piezoelectric patch, respectively, V is the electric voltage, C_p is the piezeoelectric capacitance, η the electromechanical coupling coefficient, δ and H are the Dirac and Heaviside distributions, $I_c(t)$ the electrical current which is for the simplest (dissipation) circuit is given by V/R, with R the circuit resistance. The beam can be supposed clamped at both ends, *i.e.*, $w_e(0) = w'_e(0) = w_e(l_0) = w'_e(l_0)$. The elastic displacement of the linking beam hosting the piezoelectric element can be approximated with a cubic curve satisfying geometrical BCs at the element edges, as typically done for defining Euler-Bernoulli beam elements. Setting the origin of reference system at the beam midpoint, *i.e.*, $\xi \in [-l_0/2, l_0/2]$ ($l_0 = L_{\text{gap}}$), and imposing the hinge constraint between the displacements $w^{(A)}, w^{(B)}$ and slopes $\theta^{(A)}, \theta^{(B)}$, the curve necessarily takes the quadratic expression (the case of the beam connecting raft #1 and #2 is considered below):

$$w_e(\xi, t) = w + \frac{\theta_2 - \theta_1}{8} l_0 + \frac{\theta_1 + \theta_2}{2}\xi + \frac{\theta_2 - \theta_1}{l_0}\frac{\xi^2}{2}, \tag{8}$$

which has constant curvature equal to $w''_e = \Delta\theta/l_0$. Substituting Eq. 8 into the second of Eqs. 7, one obtains:

$$C_p\dot{V} + V/R + \eta(\dot{\theta}_2 - \dot{\theta}_1) = 0 \tag{9}$$

The first equation is replaced by a torsional hinge with stiffness k_{PTO} and damping c_{PTO}. Regarding the damping, the dissipated energy by the piezoelectric circuit must equal the nonconservative work done by the hinge, *i.e.*,

$$\frac{V^2}{R} = M_{\text{damp}}(\dot{\theta}_2 - \dot{\theta}_1) = M_{\text{damp}}\Delta\dot{\theta} \tag{10}$$

Thus,

$$M_{\text{damp}} = \frac{1}{R}\left(\frac{V}{\Delta\dot{\theta}}\right)^2 \Delta\dot{\theta} = c^{(\text{p})}_{\text{PTO}}\Delta\dot{\theta} \tag{11}$$

Neglecting the dependence on time of V in the second equations, it follows that $V/\Delta\dot{\theta} = \eta R$, and finally

$$c^{(\text{p})}_{\text{PTO}} = R\eta^2 \tag{12}$$

which indicates that the damping increases with electromechanical coupling coefficient and the resistive load.

2.3. Fluid-loads and pure differential form of the coupled system

From the hydrodynamic point of view, the main simplifying assumption in building the system's equations is to neglect the hydrodynamic interaction between the floaters in both radiation and diffraction, which affects the system behaviour at certain wavelengths, though weakly in the case of mutually constrained bodies. As outlined before, it is further supposed that the streamlined configuration remains perfectly aligned with respect to the wave direction, and the hydrodynamic loads are exerted on each floater only in terms of vertical forces and pitching moment. The generalised force vector $\mathbf{f} = \{M_1 - lF_1, M_2 - lF_1 + lF_3, M_3 + lF_3, F_1 + F_2 + F_3\}^T$ can be separated into three components:

$$\mathbf{f} = \mathbf{f}^{(res)} + \mathbf{f}^{(rad)} + \mathbf{f}^{(w)} \tag{13}$$

where the first term on the r.h.s. is the restoring force due to gravity and buoyancy, the second term corresponds to the radiation forces arising from the change in momentum of the fluid due to the motion of the structure, and the third term represents the pressure forces due to the incoming waves, which includes Froude–Krylov (pressure forces due to the undisturbed wave field) and diffraction forces (taking into account the modification of wave field due to the presence of the structure). For zero forward-speed case, the linear pressure-induced radiation forces can be expressed as:

$$\mathbf{f}^{(rad)} = -\mathbf{A}_\infty\ddot{\mathbf{u}} - \int_{-\infty}^{t} \mathbf{B}(t-\tau)\,\dot{\mathbf{u}}\,d\tau \tag{14}$$

The first term $\mathbf{A}_\infty\,\ddot{\mathbf{u}}$ in the r.h.s. of Eq. 14 accounts for the pressure forces due to the accelerations of the structure, with $\mathbf{A}_\infty$ a constant positive-definite matrix with elements given by the added mass coefficients. The integral term represents fluid-memory effects that capture the energy transfer from the motion of the structure into the fluid in terms of radiated waves on the free surface. Substituting Eq. 14 into Eq. 13 and expressing the linearised restoring forces as $\mathbf{f}^{(res)} = -\mathbf{K}_{hys}\mathbf{u} + \mathbf{f}^{(g)}$, with the latter term indicating the gravity force, the Cummins equation (Ref. [8]) is obtained:

$$(\mathbf{M} + \mathbf{A}_\infty)\,\ddot{\mathbf{u}} + \mathbf{C}_\theta\dot{\mathbf{u}} + \int_{-\infty}^{t} \mathbf{B}(t-\tau)\,\dot{\mathbf{u}}\,d\tau + (\mathbf{K}_\theta + \mathbf{K}_{hys})\,\mathbf{u} = \mathbf{f}^{(w)} + \mathbf{f}^{(g)} \tag{15}$$

The form of this integral-differential equation is not suitable to be numerically solved in an efficient way because of the radiation damping term. The modified Prony method [9], already used for the evaluation of the integral term in a similar configuration [11], was proved by Armesto *et al.* [12] to be equivalent to both the impulse response function and the state-space methods. Therefore, the generic element $B_{rs}(t)$ of the kernel function matrix $\mathbf{B}(t)$ in Eq. 14 can be approximated as:

$$B_{rs}(t) = \sum_{p=1}^{P} I_p(t), \tag{16}$$

where the element indexes are omitted for sake of conciseness in the introduced decomposition terms I_p (or added variables), which are defined as:

$$I_p(t) = \int_0^t \alpha_p e^{\beta_p(t-\tau)}\,d\tau, \tag{17}$$

with coefficients α_p and β_p of the exponential to be determined numerically or experimentally. Thus, Eq. 15 can be finally written as a system of differential equations in the unknowns $I_p(t)$, the total number of unknowns depending on the number of non-zero B_{rs} elements and the number of exponentials P employed in the approximation. In the present work the number of poles is $P = 3$ with one couple of complex conjugate poles ($p = 1, 2$) and a unique real pole ($p = 3$). With respect to the case of heaving floater discussed in [12], all the 'radiation damping' equations are recast in real form. Under the hypothesis of small displacements, the hydrostatic stiffness matrix $\mathbf{K}_{hys}$ providing the buoyancy force is obtained by assuming that the hydrostatic stiffness per unit length κ is constant along the raft. By a first-order linear theory, the expression of the generalized wave force for a floating body (Froude-Krylov and diffraction terms) can be generally expressed in case of monochromatic incident waves as $\mathcal{F}_i = Re[\mathcal{H}(\omega_\zeta)A_\zeta e^{i(\omega_\zeta t - k_\zeta X_i^{(G)} + \phi_w)}]$, where, in the present case, the generalised load vector reduces to two components $\mathcal{F} = \{F_i, M_i\}^T$, the transfer function $\mathcal{H}(\omega_\zeta)$ is the same for all the the floaters, A_ζ, ω_ζ, ϕ_w and $X_i^{(G)}$ are the wave amplitude, angular frequency, phase and floater position, respectively. Because of the rectangular, slender shape of the floaters, the expression of transfer function $\mathcal{H}(\omega_\zeta)$ can be computed analytically by using the strip theory on the basis of long wavelength assumption with respect to the relative cross-section (see [13]). At the end, the system is finally recast in first order form. Setting the state-space vector $\mathbf{q} = \{\mathbf{u}, \dot{\mathbf{u}}, \mathbf{r}\}^T$, where the vector $\mathbf{r}$ includes the added variables for describing radiation terms, the differential system takes the form:

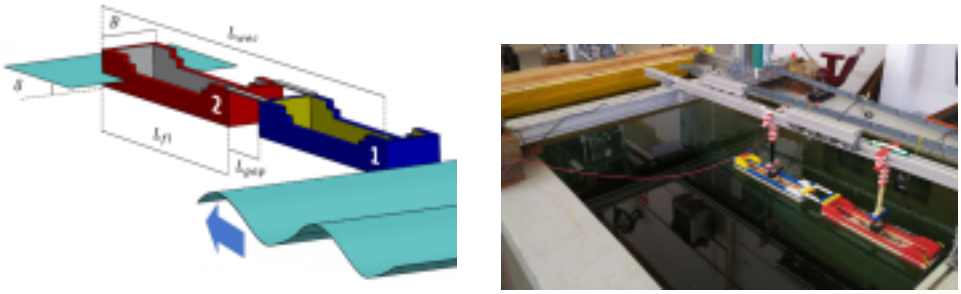
$$\hat{\mathbf{A}}\,\dot{\mathbf{q}} = \hat{\mathbf{B}}\,\mathbf{q} + \hat{\mathbf{f}} \tag{18}$$

where $\hat{\mathbf{f}} = \{\mathbf{0}, \mathbf{f}, \mathbf{0}\}^{\mathbf{T}}$, and the matrices $\hat{\mathbf{A}}$ and $\hat{\mathbf{B}}$ are given in [1] for the 2-raft case. The time-marching numerical solution of Eq. 18 is then obtained using the ode45 solver in MATLAB.

3. Experimental validation of the 2-raft system

3.1. Experimental set-up

As illustrated in [1], a floating system made of two identical box-shaped floating bodies elastically connected (Fig. 2(a)) was tested to validate the dynamical model. The principal dimensions are re-



(a) Geometry and main dimensions of the tested device. (b) View of the test facility with wavemaker at the end.

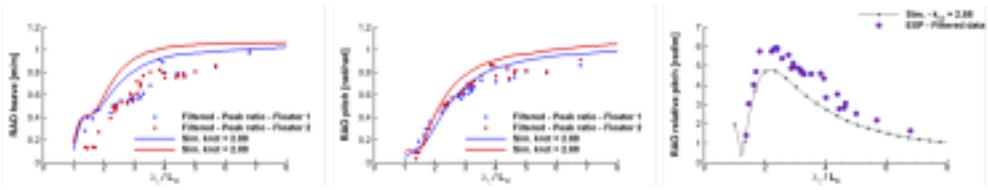
Figure 2 Experimental set-up.

ported in Table 1. A scale factor of $\chi = 4$ was considered representative for the preliminary validation of numerical tools modelling a device aimed to power sea-based instrumentation in remote locations, while larger scales (up to $\chi \geq 10$) could satisfy the energy demand of larger stations depending on wave conditions. The rafts have a slenderness ratio $L_{\text{fl}}/B = 4$, a configuration that enhances relative rotation for a given waterplane area and allows the hydrodynamic forces to be evaluated using linear potential theory. Another key parameter is the gap between the rafts L_{gap}, selected close to the optimal value for the chosen raft length (see [1]). The physical model is constructed using LEGO™ bricks for both hulls and elastic connections (Fig. 2(b)). This modular approach allows rapid modification of the configuration during testing, for instance by adjusting the ratio $L_{\text{gap}}/L_{\text{fl}}$ to enhance relative motion. To ensure watertightness, the brick structure is sealed with a removable plastic film covering the wetted hull surfaces. The elastic link, which represents the stiffness of piezoelectric benders, is also assembled using selected LEGO elements providing a suitable equivalent stiffness. Experiments were performed in a wave basin $11.7, \text{m}$ long, $1.44, \text{m}$ wide and $1.57, \text{m}$ deep, equipped with a plunge wavemaker. The wedge is driven by a stepper motor controlled through Arduino, generating waves with heights between 0.01 and $0.05, \text{m}$. The wavemaker transfer function is characterized by measuring the wedge motion with an ultrasonic probe and correlating it with the generated wave elevation measured by a KENEK finger-type wave probe positioned near the device connection. The ratio (about 15 in both directions) between the longitudinal and transversal dimensions of the wave basin and floating system, along with a wave absorber at the end of the basin, guarantees a negligible or acceptable interference with disturbances due to waves reflected on the different sides of the towing-tank.

The raft's motion was measured using a small inertial measurement unit (DS-IMU, DEWESoft) installed at the centre of gravity of each raft. Each IMU includes a triaxial accelerometer and gyroscope, and the signals are acquired at $100, \text{Hz}$. Angular displacements are obtained directly from the acquisition software, while linear displacements are reconstructed by numerical integration of accelerations. The mass of each IMU and its cable is approximately $50, \text{g}$, about 10% of the floater mass. To minimize disturbances due to the cables, they are supported by a suspension system that keeps them aligned while exerting negligible forces on the floating bodies.

Table 1 Main dimensions of the floating system.

Symbol	Quantity	Value	Symbol	Quantity	Value
L_{wec}	Overall WEC's length	0.864 m	L_{fl}	Floater length	0.384 m
L_{gap}	Gap between the rafts	0.096 m	B	Width	0.096 m
δ	Immersion	0.0137 m	m_{fl}	Raft's mass (hull+sensor+cable)	0.51 kg



(a) RAO heave. (b) RAO pitch. (c) RAO relative pitch.

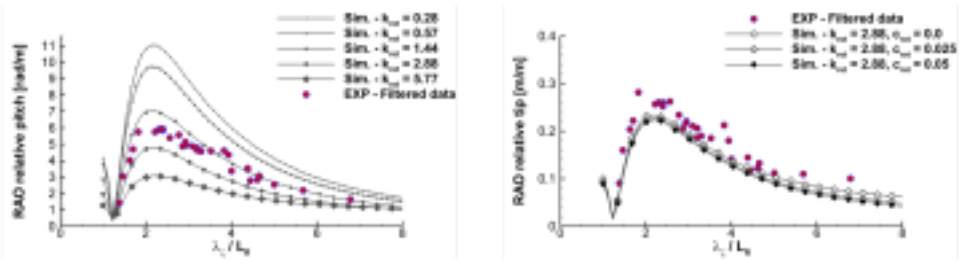
Figure 3 Comparison between numerical and experimental RAOs of heave, ptich and relative pitch (2-raft case).

Another critical aspect in modeling the floater response in water is tuning the coefficients of the equations modeling the radiation damping. Based on theory, the retardation functions $B_{33}(t)$ and $B_{55}(t)$ can be calculated and then approximated using the modified Prony method [9]-[10]. This procedure was followed by Dessi *et al.* [11] for a similar problem consisting of three box-shaped pontoons linked with cables. To improve the correspondence with free-decay oscillation tests, the Prony coefficients used to approximate the theoretical retardation function (as obtained from hydrodynamic coefficients) were slightly modified to take into account also the prsence of viscous damping. Thus, transient oscillations of single floater or full-system in heave or pitch modes are excited by setting proper initial conditions in draft or trim angle. In [1] the numerical model captures correctly the transient pitch oscillations using 3-pole approximation. However, the prediction is less accurate when the free-decay tests involve both barges because of apparent increase in frequency after the first oscillation; this is likely to depend on neglected hydrodynamic interactions. The inclusion of additional poles in the Prony's approximation, though feasible, is not considered to keep the number of additional equations low in this first investigation.

3.2. Comparison with experimental data

The comparison with experimental results in the 2-raft case does not provide strict validation of the 3-rafts dynamical model for obvious reasons. However, it is indicative of the level of accuracy that can be achieved under the simplifying assumptions upon which the dynamical models were developed. The predicted values of the heave RAO (line) in Fig. 3(a) are in general larger than the corresponding experimental ones, whereas the agreement is better on the predicted pitch motions (Fig. 3(b)). It is worth to underline that the comparison here is relative to RAO built on the band-pass filtered around the excitation frequency. Nonetheless, as shown in [1], these values are very close to those obtained using the corresponding standard deviations. The RAO curve relative to the forward floater (blue line) always keeps above that relative to the rear floater (red curve) while experimental data show more interlacing trends. At lower wavelengths, numerical prediction overestimates the second floater heave motion as if exposed to longer waves (the numerical values seem horizontally shifted with respect the experimental ones for $\lambda_\zeta/L_{\text{fl}} < 2$). In the case of pitch (Fig. 3(b)), numerical prediction of RAOs is far better both in terms of amplitudes and general prevalence of the rear floater motion with respect the forward one. Differences occur only for $\lambda_\zeta/L_{\text{fl}} < 2$ where the simulation do not catch that the pitch oscillations of the forward floater overcome those relative to the rear one. In Fig. 3(c), the bigger circles represent experimental data and lines and dots indicate the numerical results at the value of the torsional spring coefficient experimentally identified, *i.e.*, $k_{rot} = 2.88\,\text{Nm}$. The numerical simulations underestimate the relative pitch amplitudes around the peak and for longer waves, with differences getting smaller for $\lambda_\zeta/L_{\text{fl}} > 4$ or $f_\zeta < 1\,\text{Hz}$.

It is worthwhile considering how RAO prediction is affected when the rotational stiffness is changed as shown in Fig. 4(a). The curves tends to flatten toward lower values as stiffness is increased since it constrains more relative motion. Relaxing the constraint between the floaters, *i.e.*, reducing the stiffness, tends to amplify relative motion, toward the limit condition where the floaters oscillates independently



(a) RAO of relative pitch.

(b) RAO of relative tip displacement.

Figure 4 Numerical sensitivity of the relative motion RAOs with respect to rotational spring stiffness and PTO equivalent damping coefficient (k_{rot} values are expressed at model scale in Nm).

from each other. Thus, phasing between floater's motion appears to be driven mainly by the arrival time of the travelling wave on the floaters mid-point. For both relative pitch and displacement, results appear to be bounded between the nominal stiffness ($k_{rot} = 2.88\,\mathrm{Nm}$) and half its value ($k_{rot} = 1.44\,\mathrm{Nm}$). The damping value c_θ is then varied between zero and a value twice that assigned in all the regular simulations (Fig. 4(b)). This value affects the RAO response in the range from medium to long wavelengths, but the prediction of the RAO peak does not change significantly.

4. Numerical comparison between the 3-raft and 2-raft systems

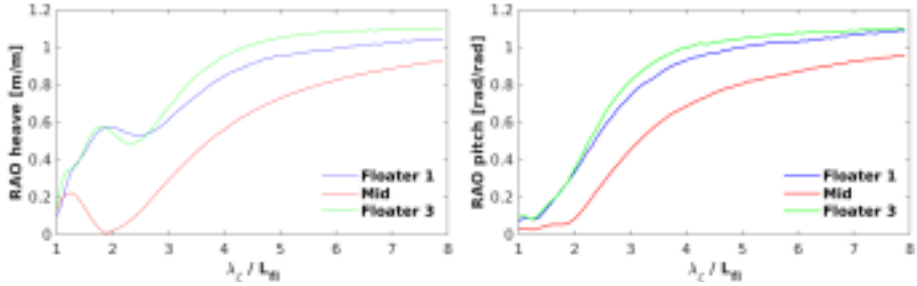
A time-marching solution of the numerical model describing the 3-raft system was obtained for several regular wave excitation. The coefficients of Eq. 18 are the same used for the 2-raft configuration that was tested in the towing tank and presented in Sec. 3.2.. In Fig. 5 the heave and pitch RAOs show that floaters # 1 and # 3 respond in a similar, although not identical, way to incoming waves. The mid-raft response is weaker; therefore convergence to the RAO asymptotic values is slower. On the other hand, the mid-raft exhibits a clear peak due to resonance peak at frequency $\lambda_\zeta/L_{\mathrm{fl}} \simeq 1.1$ close to the value of system's natural frequency. In Fig. 6 the two curves correspond to the front and rear relative rotations of the 3-raft system. The relative motion between raft # 2 and # 3 shows a higher peak amplitude than that between raft # 1 and # 2. The non-dimensional wave lengths at which the RAO maxima occur are close instead. The RAO peak value for the front hinge (between raft # 1 and # 2) relative to the 3-raft case occurs at a wavelength higher ($\lambda_\zeta^{(\max)}/L \simeq 2.8 - 2.9$) than that predicted for the 2-raft case ($\lambda_\zeta^{(\max)}/L \simeq 2.2$). Nonetheless, the peaks for both configurations exhibit peak amplitudes (see Fig. 7). These differences in the behaviour of the 2-raft and 3-raft configurations can be explained by diagonalizing the governing equations. In [1], the following coordinate transformations were introduced:

$$\bar{\theta} = 1/2(\theta_1 + \theta_2) =: \theta_a \qquad \Delta\theta = 1/2(\theta_1 - \theta_2) =: \theta_s \tag{19}$$

which decoupled the original coupled equations into two subsystems, one describing the average pitch motion $\bar{\theta}$, and the second coupling hinge heave w and the (half) relative pitch $\Delta\theta$. It is worth noting that on the r.h.s. new variable notations have been introduced; θ_a highlights anti-symmetric motion, such as average (global) pitch, while θ_s indicates local deformation. In the 3-raft case, the coordinate transformations are:

$$\theta_a = 1/2(\theta_1 + \theta_3) \qquad \theta_s = 1/2(\theta_1 - \theta_3) \tag{20}$$

which decouples the 3-rafts equations into two subsystems: one describing the system's global motion, given by θ_2 and $w = w_2$, and the other providing the deformation modes, symmetric θ_s and anti-symmetric θ_a (Eq. 20). The system's deformation modes are shown in Fig. 8. It is worth to note that θ_a has a peak at $\lambda_\zeta \simeq 2$ which corresponds to an anti-symmetric mode similar to the 3-node mode of



(a) Heave RAO. (b) Pitch RAO.

Figure 5 RAO of the rigid-body motions (heave and pitch) for the three rafts ($k_{rot} = 2.88\,\mathrm{N/m}$).

a ship bending in the vertical plane (known as 'second-mode' according to sorting criterion based on modal frequency). The symmetric mode θ_s is negligible where the anti-symmetric one has its maximum, then it grows as the wave length increases, and reaches its highest value at about $\lambda_\zeta \simeq 3.2$, where the anisymmetric mode drops. It is interesting to observe that the relative pitch peaks depend mostly on the symmetric mode contribution, but the steep slope is provided by the contribution of the antisymmetric one. Since the symmetric mode is responsible for the main fraction of energy production (alone for the 2-raft system, overlapping with the anti-symmetric one for the 3-raft configuration), it is excited by longer wavelengths as the system length increases passing from 2 to 3 rafts.

5. Conclusions

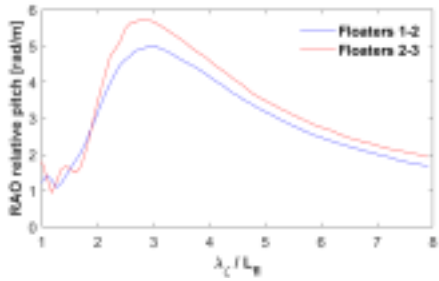
This study confirms the possibility of obtaining a preliminary, fast and robust prediction of the energy conversion capacity of a floating system made by elastically connected bodies using reduced-order models which exhibits a clear dependence on key design parameters. Though, for the sake of conciseness, electrical power has not been computed, it directly depends on the square of the relative angular velocity, as demonstrated in [1], where it was shown that $P_{ave}^{(ele)}(\omega) = 1/2R\eta^2\omega_\zeta^2|\Delta\theta(\omega)|^2\alpha(RC,\omega)$ (the function α includes resistance and capacity of the equivalent piezo and load circuit in a simplified way.) Though some assumptions introduced to simplify the mathematical model and speed-up calculations can be removed, such as not considering mooring lines, viscous damping, and neglecting the two-way coupling with piezoelectric equations, the mathematical model retain the basic physical phenomena governing the relative pitch motions of the rafts. Following the same approach as in [1], the 3-raft model will allow for a simple assessment of the dependence of the energy production on design variables and their optimization. The comparison between the 2- and 3-raft configurations indicates an advantage obtained with the 3-raft configuration in terms of power generation; while the front rafts relative motion remains substantially unchanged, the rear rafts add a relevant contribution as shown in Fig. 6(a). Along with experimental validation, upscaling of power production is another aspect worth to receive further attention in the future extending the relationship presented in [1].

References

[1] D. Dessi, F. Passacantilli, G. Leonardi. *Experimental and numerical modeling of a piezoelectric floating system for wave energy harvesting*, Applied Ocean Research, 122, art. no. 103120, 2022.

[2] M. Wooley, J. Platts. *Energy on the crest of a wave*, New Scientist, 241–243, 1975.

[3] P. Haren. *Wave power extraction by a train of rafts: hydrodynamic theory and optimum design*, Applied Ocean Research 1 (3), 147–157, 1979.



(a) vs non-dimensional wave length.

(b) vs. dimensional frequency.

Figure 6 RAO of the relative pitch between floaters 1-2 and 2-3 (3-raft case, $k_{rot} = 2.88\,\mathrm{N/m}$ and $c_{rot} = 0.025$).

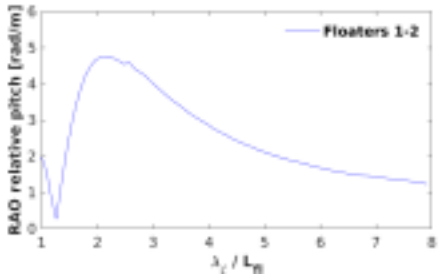


Figure 7 RAO of the relative raft pitch between floaters (2-raft case, $k_{rot} = 2.88\,\mathrm{N/m}$)

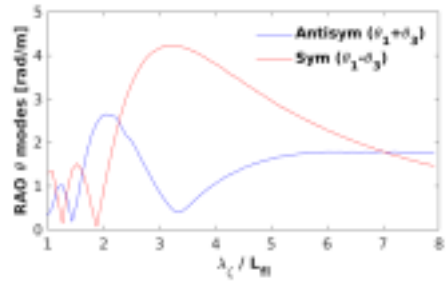


Figure 8 RAO of symmetric and antisymmetric θ-modes (3-raft case).

[4] J. Newman. *Absorption of wave energy by elongated bodies*, Applied Ocean Research 1 (4), 189–196, 1979.

[5] L. Moad, R. Porter. *Modeling an articulated raft wave energy converter*, Renewable Energy (114), 1146–1159, 2017.

[6] S. Zheng, Y. Zhang. *Analysis for wave power capture capacity of two interconected floats in regular waves*, Journal of fluids and structures (75), 158–173, 2017.

[7] C. Liu, M. Hu, W. Gao, Y. Zeng, D. Wei, Q. Yang, G. Bao. *A high-precise model for the hydraulic power take-off of a raft-type wave energy converter*, Energy (215) 119107, 2017b.

[8] W. E. Cummins. *The Impulse Response Function and Ship Motions*, in: International Symposium on Ship Theory, vol. 8, Hamburg, Germany, 1962.

[9] M. Osborne, G. A. Smyth. *Modified Prony algorithm exactly the configuration running on the numerical for fitting sums of exponential functions*, SIAM J. Sci. Comput. 16 119–138, 1995.

[10] G. Duclos, A. H. Clément, G. Chatry, *Absorption of Outgoing Waves In a Numerical Wave Tank Using a Self-Adaptive Boundary Condition*, International Journal of Offshore and Polar Engineering 11 (3), , 2001.

[11] D. Dessi, A. Carcaterra, G. Diodati. *Experimental Investigation versus Numerical Simulation of the Dynamic Response of a Moored Floating Structure to Waves*, Institution of Mechanical Engineers Part M: Journal of Engineering for the Maritime Environment 3, 153–165, 2004.

[12] J. A. Armesto, R. Guanche, F. del Jesus, A. Iturrioz, L. I. J. *Comparative analysis of the methods to compute the radiation term in Cummins' equation*, J. Ocean Engineering in Marine Energy 35 685–705, 2015.

[13] O. M. Faltinsen. *Sea Loads on Ships and Offshore Structures*, Cambridge University Press 1990.

Wave-Plate Interaction

10th International Conference on HYDROELASTICITY IN MARINE TECHNOLOGY
Trondheim, Norway, June16$^{\text{th}}$-18$^{\text{th}}$, 2026

Comparative study of energy dissipation under capillary-gravity wave scattering by submerged porous, poroelastic, and porous piezoelectric plates

Singh, M.[1,*]

[1] Mathematical Institute for Machine Learning and Data Science, Katholische Universität Eichstätt–Ingolstadt, Ingolstadt 85049, Germany

Abstract. This study presents a comparative analysis of energy dissipation due to the scattering of linear capillary–gravity waves by vertically submerged plates of three types: rigid porous, poroelastic, and porous piezoelectric. The primary objective is to examine the role of surface tension in modulating the energy dissipation mechanisms associated with each configuration. For the porous plate, fluid flow through the structure is modeled using Darcy's law. The poroelastic plate formulation accounts for the dynamic response governed by Kirchhoff plate theory coupled with porosity. The porous piezoelectric plate extends this model by incorporating electromechanical coupling, enabling mechanical-to-electrical energy conversion. For all cases, the boundary value problem is formulated within linear potential flow theory, with the free-surface boundary condition modified to include both gravitational and capillary effects. The resulting problem is solved using the Green's function method, which effectively handles the Robin-type boundary conditions on the plate and the higher-order free-surface condition. The investigation focuses on how surface tension and porosity influence energy dissipation across the three plate types and how this influence varies with the incident wavenumber, highlighting changes in dissipation mechanisms as material complexity increases.

Key words: *Capillary-gravity waves; Surface tension; Energy dissipation; Poroelastic plate; Porous piezoelectric plate*

1. Introduction

Wave–structure interaction problems involving flexible and porous marine structures are central to applications including wave energy conversion, offshore infrastructure design, and coastal protection. The ability of submerged structures to dissipate or harvest wave energy has motivated extensive research into porous barriers, hydroelastic plates, and smart structures incorporating piezoelectric materials. While most existing studies focus on gravity-wave-dominated regimes, surface tension becomes increasingly important for short waves, laboratory-scale experiments, ice-covered seas, and micro- to meso-scale energy harvesting devices.

Porous plates have long been employed as effective wave attenuators due to their ability to dissipate energy through fluid seepage, typically modeled using Darcy-type boundary conditions [1, 2]. Poroelastic plates extend this concept by allowing elastic deformation of the structure, thereby introducing hydroelastic energy exchange mechanisms alongside viscous dissipation through porosity [3, 4, 5]. More recently, porous piezoelectric plates have emerged as promising candidates for wave energy converters, where mechanical deformation induced by wave loading is converted into electrical energy via electromechanical coupling [6, 7, 8]. In practical marine deployments, piezoelectric layers are typically

[*]Correspondence to: mansi.maths.iitkgp@gmail.com; Mansi.Singh@ku.de

bonded to a compliant substrate that may develop cavities, microvoids, or permeable regions due to material fatigue, biofouling, or manufacturing constraints [9]. Incorporating a porous elastic substrate within a piezoelectric bimorph configuration is therefore both physically realistic and advantageous.

Despite these advances, the role of surface tension in governing energy dissipation across different plate types remains poorly understood. While capillary–gravity wave scattering has been studied for rigid bodies [10, 11], step bottom [12] and bottom modulations [13], and hydroelastic wave problems have been widely investigated under pure gravity-wave assumptions [14, 15, 16, 17], a systematic comparison of energy dissipation mechanisms induced by surface tension across porous, poroelastic, and piezoelectric plates is notably absent from the literature.

The inclusion of surface tension is physically motivated by several considerations. First, surface tension becomes comparable to gravity when the characteristic wavelength is of the order of a few centimetres [18, 19], a regime routinely encountered in laboratory wave flumes and scaled testing of wave energy devices. In marginal ice zones and grease-ice fields, the water surface is covered by thin, deformable, and often porous layers, leading to wave dynamics strongly influenced by capillarity. Emerging micro- and meso-scale wave energy harvesting systems and piezoelectric marine sensors operate in regimes where capillary effects govern the efficiency of mechanical-to-electrical energy transfer [20]. Second, from a mathematical standpoint, retaining surface tension changes the free-surface boundary condition from first-order to third-order, constituting a singular perturbation that alters the number of evanescent wave modes supported by the free surface and modifies the near-field pressure distribution around the plate edges. The gravity-wave-only formulation is therefore not simply the vanishing-surface-tension limit of the full capillary–gravity theory. Third, the capillary–gravity Green's function is more singular than its pure gravity counterpart, and its correct treatment via the hypersingular boundary integral formulation provides a validated benchmark for future studies operating in capillary-dominated regimes.

Existing studies typically treat these plate types in isolation and neglect surface tension, thereby hindering their applicability to short-wave regimes and small-scale systems. Moreover, the transition in dominant dissipation mechanisms from seepage in porous plates, to elastic deformation in poroelastic plates, and to electromechanical conversion in piezoelectric plates, has not been examined within a unified theoretical framework. Such a comparison is essential for understanding how material complexity and coupling mechanisms interact with capillary effects to influence wave energy dissipation.

The present study addresses this gap by conducting a comparative investigation of linear capillary-gravity wave scattering by submerged porous, poroelastic, and porous piezoelectric plates. The problem is formulated within linear potential flow theory, with surface tension explicitly included in the free-surface condition. A Green's function-based boundary integral method is employed to ensure a consistent treatment of the fluid-structure interaction across all configurations. By focusing on energy dissipation and its modulation by surface tension and porosity, this work provides new physical insight into capillary–hydroelastic interactions and establishes a theoretical foundation for the design of efficient wave attenuation and energy harvesting devices operating in capillary-influenced regimes.

2. Mathematical formulation

We consider the two–dimensional scattering of linear capillary–gravity waves by a thin, vertically submerged plate of draft d located at $x = 0$ in a fluid of infinite depth. A Cartesian coordinate system (x, z) is adopted with the undisturbed free surface at $z = 0$ and the z–axis pointing vertically downwards. The fluid is assumed to be inviscid, incompressible, and the flow irrotational.
The fluid motion is described by a velocity potential $\Phi(x, z, t) = \Re\{\phi(x, z)\mathrm{e}^{-\mathrm{i}\omega t}\}$, where ω is the angular frequency. The spatial potential $\phi(x, z)$ satisfies Laplace's equation in the fluid domain:

$$\nabla^2\phi = 0, \qquad 0 < z < \infty, \quad x \neq 0. \tag{1}$$

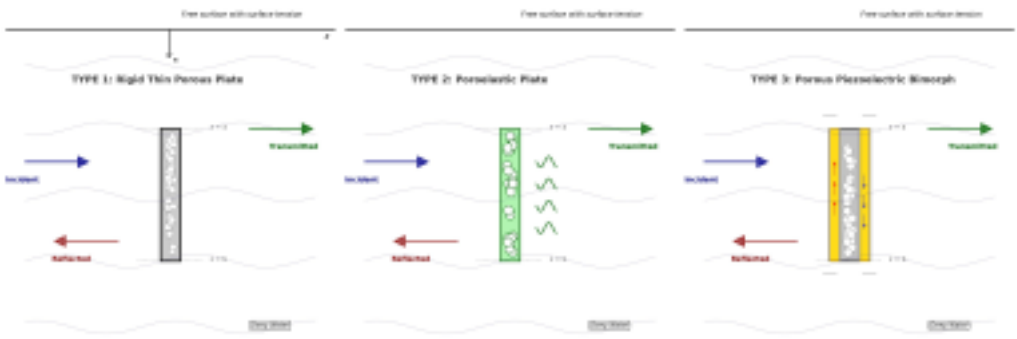


Figure 1: Schematic diagram of the fluid-plate system.

The linearized free-surface boundary condition incorporating surface tension is given by

$$\omega^2\phi + g\frac{\partial\phi}{\partial z} + \frac{T_s}{\rho}\frac{\partial^3\phi}{\partial z^3} = 0 \quad \text{on } z = 0, \tag{2}$$

where g is the acceleration due to gravity, T_s is the surface tension coefficient, and ρ is the fluid density. The condition for no motion at infinite depth is

$$\nabla\phi \to 0 \quad \text{as } z \to \infty. \tag{3}$$

At $x \to \pm\infty$, the radiation condition is imposed such that the scattered field represents outgoing waves

$$\phi(x,z) \to \begin{cases} T\left(\frac{igA}{\omega}\right)\mathrm{e}^{-k_0 z + \mathrm{i}k_0 x} & \text{as } x \to \infty, \\ \left(\frac{igA}{\omega}\right)\mathrm{e}^{-k_0 z + \mathrm{i}k_0 x} + R\left(\frac{igA}{\omega}\right)\mathrm{e}^{-k_0 z - \mathrm{i}k_0 x} & \text{as } x \to -\infty, \end{cases} \tag{4}$$

where R and T denote the unknown complex-valued reflection and transmission coefficients. The incident capillary–gravity wave potential is prescribed as

$$\phi^{\mathrm{I}} = \frac{\mathrm{i}gA}{\omega}\,\mathrm{e}^{-k_0 z + \mathrm{i}k_0 x}, \tag{5}$$

where A is the incident wave amplitude and k_0 (real and positive) satisfies the capillary–gravity dispersion relation [21]

$$\omega^2 = gk + \frac{T_s}{\rho}k^3. \tag{6}$$

The total potential is expressed as $\phi = \phi^{\mathrm{I}} + \phi^{\mathrm{S}}$, where ϕ^{S} is the scattered potential.

Plate boundary conditions

On the plate surface ($x = 0$, $a < z < b$), continuity of normal velocity requires

$$\frac{\partial\phi}{\partial x} = V(z), \tag{7}$$

where the plate-normal velocity is written in the unified form

$$V(z) = -\mathrm{i}\omega\eta(z) + \mathrm{i}k_0\mu\,\Delta\phi, \tag{8}$$

with $\Delta\phi = \phi(0^-, z) - \phi(0^+, z)$ denoting the jump in velocity potential across the plate. The complex parameter μ accounts for porous dissipation [1] and reduces to zero for an impermeable plate.
The plate displacement $\eta(z)$ satisfies the generalized thin-plate equation

$$\mathcal{D}(\omega)\,\frac{d^4\eta}{dz^4} - m\omega^2\eta = \mathrm{i}\omega\rho\,\Delta\phi, \tag{9}$$

where $\mathcal{D}(\omega)$ denotes an effective *dynamic flexural rigidity* and m is the mass per unit length of the plate. The coefficient $\mathcal{D}(\omega)$ reduces to different limiting forms depending on the plate type:

- *Rigid porous plate*: $\eta = 0$, $\mu \neq 0$.
- *Poroelastic plate*: $\mathcal{D}(\omega) = D$ (real constant), $\mu \neq 0$.
- *Porous piezoelectric plate*: $\mu \neq 0$ and

$$\mathcal{D}(\omega) = D\left(1 + \frac{\beta^2\zeta_e\omega}{\mathrm{i} + \zeta_e\omega}\right), \tag{10}$$

  is now frequency-dependent, where $\beta = \theta/\sqrt{DC}$ is the electromechanical coupling coefficient, $\zeta_e = C/G$ is the electrical time constant, and $m = I_b$ is the surface density of the bimorph. Details of the electromechanical parameters follow Renzi [22] and Zheng *et al.* [23].

The unified formulation (8)–(9) provides a consistent framework for comparing energy dissipation mechanisms. In the short-circuit limit, $\zeta_e \to 0$, the porous piezoelectric plate reduces to a poroelastic plate. Further, in the limit $D \to \infty$, the formulation degenerates to a rigid porous plate. If the upper end of the plate is clamped and the lower end is free, the boundary conditions are

$$\eta(a) = \eta'(a) = 0, \qquad \eta''(b) = \eta'''(b) = 0. \tag{11}$$

Near the sharp edges of the plate, the velocity potential satisfies the edge condition $\phi \sim O(r^{1/2})$ as $r \to 0$, where r denotes the distance from either plate edge. In the regions not occupied by the plate, the velocity potential and its normal derivative are continuous across $x = 0$:

$$\phi(0^-, z) = \phi(0^+, z), \qquad \frac{\partial\phi}{\partial x}(0^-, z) = \frac{\partial\phi}{\partial x}(0^+, z), \quad \text{for } z \in (0, a) \cup (b, \infty). \tag{12}$$

These continuity conditions, together with the plate boundary conditions (8)–(9) and the clamped–free edge conditions (11), complete the mathematical specification of the coupled fluid–structure interaction problem.

3. Solution method and energy balance

3.1. Boundary integral formulation

The boundary value problem is solved using a Green's function based boundary integral method. Applying Green's second identity to the scattered potential ϕ^{S} and the capillary–gravity Green's function G [10, 21], the velocity potential is expressed as

$$\phi(x, z) = \phi^{\mathrm{I}}(x, z) + \frac{1}{2\pi}\int_a^b \Delta\phi(0, \zeta)\,\frac{\partial G}{\partial \xi}(0, \zeta; x, z)\,d\zeta, \tag{13}$$

where $\Delta\phi(0, \zeta)$ denotes the jump in velocity potential across the plate. Differentiating (13) with respect to x and taking the limit $x \to 0$ yields

$$\frac{\partial\phi}{\partial x}(0, z) = \frac{\partial\phi^{\mathrm{I}}}{\partial x}(0, z) + \frac{1}{2\pi}\,\text{⨍}\!\!\!\!\!\!-_a^b \Delta\phi(0, \zeta)\,\frac{\partial^2 G}{\partial x\partial \xi}(0, \zeta; 0, z)\,d\zeta, \tag{14}$$

where the integral is interpreted as a Hadamard finite-part integral of order two.

3.2. Coupling with plate dynamics

The plate displacement $\eta(z)$ is solved using a plate Green's function $g_e(\zeta, z)$ obtained via the eigenfunction expansion method [15]:

$$g_e(\zeta,z)=\begin{cases}0, & \text{rigid porous plate},\\ g_{pe}(\zeta,z), \quad \left(D\,\dfrac{d^4}{dz^4}-m\omega^2\right)g_{pe}=\delta(z-\zeta), & \text{poroelastic plate},\\ g_{pp}(\zeta,z), \quad \left(\mathcal{D}(\omega)\,\dfrac{d^4}{dz^4}-m\omega^2\right)g_{pp}=\delta(z-\zeta), & \text{porous piezoelectric plate},\end{cases} \tag{15}$$

subject to the edge conditions (11). Once $g_e(\zeta, z)$ is determined, we can write

$$\eta(z)=\int_a^b \mathrm{i}\omega\rho\,\Delta\phi(0,\zeta)\,g_e(\zeta,z)\,d\zeta. \tag{16}$$

Substituting into the unified velocity condition and combining with (14) leads to a Fredholm integral equation of the second kind:

$$\frac{1}{2\pi}\,\text{⨍}\!\!\!\!\!\!-\!\!\!\!\!\!\int_a^b \Delta\phi(0,\zeta)\,\frac{\partial^2 G}{\partial x\partial\xi}(0,\zeta;0,z)\,d\zeta-\rho\omega^2\int_a^b\Delta\phi(0,\zeta)\,g_e(\zeta,z)\,d\zeta \\ -\mathrm{i}k_0\mu\,\Delta\phi(0,z)=\frac{gAk_0}{\omega}e^{-k_0 z},\quad a<z<b. \tag{17}$$

The integral equation (17) is discretised using an expansion collocation scheme handling the square-root edge singularity [10, 24]. Once $\Delta\phi$ is determined, the reflection coefficient is extracted as

$$R=\frac{-\mathrm{i}\omega k_0}{gA}\left(\frac{1+Mk_0^2}{1+3Mk_0^2}\right)\int_a^b \mathrm{e}^{-k_0 z}\,\Delta\phi(0,z)\,\mathrm{d}z, \tag{18}$$

and $T=1-R$, where $M=T_s/(\rho g)$ denotes the surface tension parameter.

3.3. Energy balance and dissipation

Employing Green's integral theorem with the free surface condition (2), bottom condition (3), and far-field condition (4) yields

$$\int_\Gamma\left(\phi\,\frac{\partial\phi^*}{\partial n}-\phi^*\,\frac{\partial\phi}{\partial n}\right)\mathrm{d}s+\frac{\mathrm{i}g^2A^2}{\omega^2}\left(|T|^2+|R|^2-1\right)\left(1+\frac{2gk_0^3M}{\omega^2}\right)=0, \tag{19}$$

where Γ denotes the contour along the submerged plate, whose boundary conditions depend on the plate type, and $(\cdot)^*$ denotes complex conjugation. The global energy balance is $|R|^2+|T|^2=1-\mathcal{D}_e$, where $\mathcal{D}_e$ is the total non-dimensional dissipation coefficient. It is evaluated as

$$\mathcal{D}_e=\frac{\omega^2}{g^2A^2}\left(\frac{\omega^2}{\omega^2+2gk_0^3M}\right)\left[2k_0\int_a^b\Re(\mu)\,|\Delta\phi|^2\,\mathrm{d}z-\omega\int_a^b\left(\eta\,\Delta\phi^*+\eta^*\,\Delta\phi\right)\,\mathrm{d}z\right]. \tag{20}$$

For a rigid porous plate ($\eta=0$), dissipation reduces to

$$\mathcal{D}_e\equiv\mathcal{D}_\mathrm{p}=\frac{2k_0\omega^2}{g^2A^2}\left(\frac{\omega^2}{\omega^2+2gk_0^3M}\right)\int_a^b\Re(\mu)\,|\Delta\phi|^2\,\mathrm{d}z. \tag{21}$$

For a poroelastic plate, the total dissipation is denoted $\mathcal{D}_\mathrm{pe}$, while for a porous piezoelectric plate:

$$\mathcal{D}_\mathrm{pp}=\mathcal{D}_\mathrm{p}-\mathcal{D}_\mathrm{elec}=\mathcal{D}_\mathrm{p}-\frac{2\omega^3}{g^2A^2}\left(\frac{\omega^2}{\omega^2+2gk_0^3M}\right)\int_a^b\Re(\eta\,\Delta\phi^*)\,\mathrm{d}z, \tag{22}$$

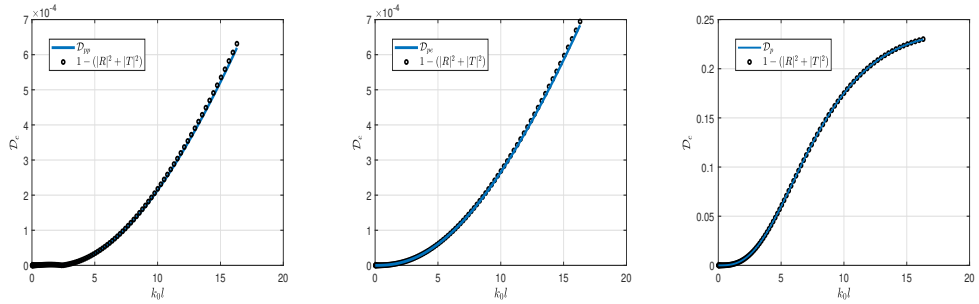
where $\mathcal{D}_{\text{elec}}$ represents the electrical power extracted by the piezoelectric layers. It should be noted that electrical extraction reduces hydrodynamic loss. In summary, energy dissipation in the coupled plate–fluid system arises from a combined interplay of multiple mechanisms, whose relative importance depends on the plate model. Surface tension influences dissipation indirectly by modifying wave dispersion and near-field hydrodynamics.

4. Results and discussion

Numerical results are presented to illustrate the influence of surface tension on energy dissipation by submerged porous, poroelastic, and porous piezoelectric plates. Additional results include the relative contributions of porosity, elastic deformation, and electromechanical effects to the total energy balance, as well as variations with incident wavenumber and surface tension. These results provide a systematic framework for comparing dissipation mechanisms across increasingly complex plate models.

All quantities are non-dimensionalised with respect to the plate length $l = (b - a) = 10\,\text{m}$, with $\frac{a}{l} = 0.1$, $\frac{b}{l} = 1.1$. The dimensionless surface tension parameter is $\frac{M}{l^2} = \frac{T_s}{\rho g l^2}$. Unless otherwise stated, $\frac{M}{l^2} = 7.16 \times 10^{-8}$, corresponding to clean seawater ($T_s \approx 0.072\,\text{N m}^{-1}, \rho \approx 1025\,\text{kg m}^{-3}$). The porosity parameter is $\mu = 0.5 + 0.1\text{i}$, where $\Re(\mu) = 0.5$ sets a moderate resistive permeability consistent with perforated plates and woven mesh barriers [2], and $\Im(\mu) = 0.1$ represents a small inertial correction appropriate for the low-Reynolds-number Darcy seepage regime. The total plate thickness is $d = 0.0101\,\text{m}$. For the poroelastic plate, $\frac{\tilde{D}}{l^4} = 2.99 \times 10^{-6}$ and $\frac{m}{\rho l} = 1.254 \times 10^{-3}$, corresponding to rigid PVC (uPVC) with Young's modulus $E = 3 \times 10^9\,\text{N/m}^2$. For the porous piezoelectric bimorph, $\frac{\tilde{D}}{l^4} = 4.78 \times 10^{-7}$, $\frac{m}{\rho l} = 1.254 \times 10^{-3}$, $\beta = 0.24$ and $\zeta_e\sqrt{g/l} = 1$ (see [23] for details), corresponding to a porous silicon-rubber substrate bonded with PVDF piezoelectric layers. The rigid porous plate is recovered by taking large D and $\beta \to 0$.

The adopted parameters ensure a consistent comparison between the three plate types while maintaining identical geometry and mass. The chosen parameter set is physically realistic and representative of lightweight submerged vertical panels interacting with capillary–gravity waves in the upper ocean. Thin porous and poroelastic plates model practical submerged wave screens and silt curtains used in harbours and coastal protection systems, where attenuation is achieved through seepage and hydroelastic deformation. In contrast, the porous piezoelectric bimorph plate represents emerging smart marine panels designed for distributed wave-energy harvesting, self-powered sensing, and adaptive damping.



(a) Porous piezoelectric plate (b) Poroelastic plate (c) Porous plate

Figure 2: Variation of the dissipation coefficient $\mathcal{D}_e$ against $k_0 l$ for the three plate types.

In Fig. 2, $\mathcal{D}_e$ is presented as a function of $k_0 l$ for the three plate configurations. The poroelastic plate is recovered from the piezoelectric bimorph by setting $\beta \to 0$, and the rigid porous plate by tak-

ing $D \to \infty$. The porous piezoelectric and poroelastic plates exhibit nearly identical dissipation, with the poroelastic case showing slightly higher $\mathcal{D}_e$ for $k_0 l > 15$, indicating that electromechanical coupling redistributes energy into electrical form rather than enhancing total dissipation. The rigid porous plate produces up to three orders of magnitude higher dissipation, confirming that without structural compliance, energy is predominantly dissipated through porous flow. The star markers representing $1 - (|R|^2 + |T|^2)$ agree excellently with the directly computed $\mathcal{D}_e$, validating the energy balance and numerical implementation. Since electrical extraction diverts a portion of the hydroelastic energy into electrical form, the hydrodynamic loss is reduced relative to the poroelastic case, which in turn dissipates less than the rigid porous plate due to structural compliance. This yields the dissipation hierarchy $\mathcal{D}_{\text{pp}} \leq \mathcal{D}_{\text{pe}} \leq \mathcal{D}_{\text{p}}$, which is consistently observed across all wavenumbers in Fig. 2. Importantly, transforming a porous plate into a porous piezoelectric bimorph enables a portion of the dissipated energy to be converted into usable electrical power.

Figs. 3 and 4 illustrate the influence of flexibility and porosity on dissipation. Increasing $\frac{\tilde{D}}{l^4}$ from 4.78×10^{-7} to 2.99×10^{-6} approximately doubles dissipation, while a further increase to 2.99×10^{-5} yields nearly a fourfold enhancement, indicating that stiffer poroelastic plates dissipate wave energy more effectively. The influence of porosity is even more pronounced: increasing $\Re(\mu)$ directly strengthens seepage-driven dissipation, while increasing $\Im(\mu)$ reduces dissipation through reactive porous effects. A non-porous piezoelectric plate ($\mu = 0$) exhibits significantly lower dissipation, confirming the dominant role of porosity in hydrodynamic energy attenuation.

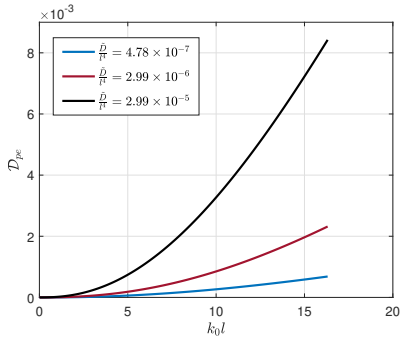


Figure 3: Variation of $\mathcal{D}_{pe}$ against $k_0 l$ for various values of $\frac{\tilde{D}}{l^4}$ for the poroelastic plate.

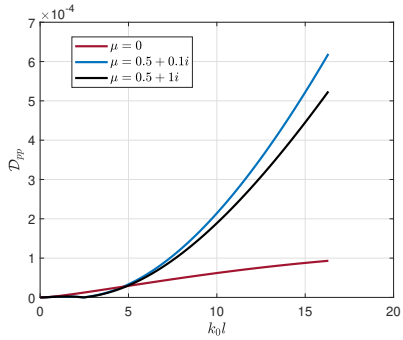


Figure 4: Variation of $\mathcal{D}_{pp}$ against $k_0 l$ for various values of μ for the porous piezoelectric plate.

Figs. 5 and 6 show $\mathcal{D}_{pp}$ and $\mathcal{D}_{\text{elec}}$ over an extended wavenumber range. In the gravity-dominated regime ($k_0 l < 30$), both increase with wavenumber. In the gravity–capillary transition regime ($30 \lesssim k_0 l \lesssim 100$), $\mathcal{D}_{\text{elec}}$ peaks and then decays. For $k_0 l \gtrsim 100$ (capillary-dominated), total dissipation rapidly decreases and approaches zero beyond $k_0 l \approx 300$. Increasing $|\mu|$ enhances overall dissipation but suppresses piezoelectric harvesting, revealing a fundamental trade-off: high porosity favours wave damping, whereas moderate porosity is more suitable for energy harvesting in short-wavelength environments.

To investigate the theoretical influence of surface tension on $\mathcal{D}_e$, we treat $\frac{M}{l^2}$ as an independent control parameter, varying it over 10^{-6} to 10^{-1}. Since all quantities are non-dimensionalised with respect to l, this parameter cannot be interpreted by simply rescaling the plate length; rather, it controls where the gravity–capillary crossover falls relative to the non-dimensional wavenumber $k_0 l$. The crossover occurs when $k^2 M \approx 1$, i.e., at $k_0 l \approx l/\sqrt{M} = (M/l^2)^{-1/2}$, giving $k_0 l \approx 1000$ at $\frac{M}{l^2} = 10^{-6}$ (gravity-dominated for all plotted wavenumbers) and $k_0 l \approx 3.2$ at $\frac{M}{l^2} = 10^{-1}$ (capillary effects active across the entire range). The lower bound $\frac{M}{l^2} = 10^{-6}$ is close to the physical value for seawater (7.16×10^{-8})

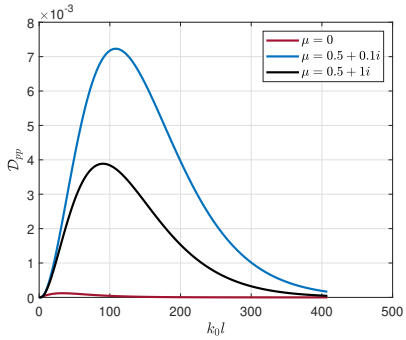


Figure 5: Variation of $\mathcal{D}_{pp}$ against $k_0 l$ for various values of μ for the porous piezoelectric plate.

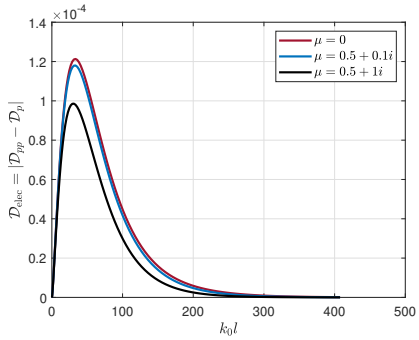


Figure 6: Variation of $\mathcal{D}_{\text{elec}} = |\mathcal{D}_{pp} - \mathcal{D}_p|$ against $k_0 l$ for various values of μ for the porous piezoelectric plate.

and anchors the study in the gravity-dominated baseline. The upper bound $\frac{M}{l^2} = 10^{-1}$ is chosen so that the gravity–capillary transition falls within the plotted wavenumber range, enabling complete visualisation of the regime transition. Extending beyond 10^{-1} would place the entire wavenumber range in the capillary-dominated limit, adding no further insight. Physically elevated values of M/l^2 arise in fluids with reduced density or enhanced surface tension (e.g., surfactant-laden interfaces, thin fluid films, or effective surface-tension models for grease-ice covers) and in laboratory wave flumes where fluid properties can be independently controlled.

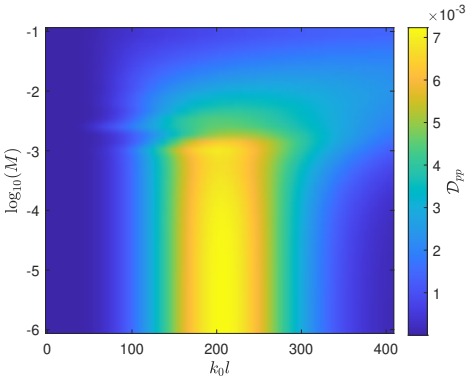


Figure 7: Intensity plots of $\mathcal{D}_{pp}$ against $k_0 l$ for various values of $\frac{M}{l^2}$ for the porous piezoelectric plate.

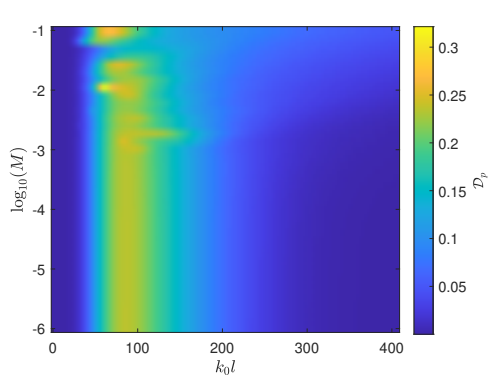


Figure 8: Intensity plots of $\mathcal{D}_p$ against $k_0 l$ for various values of $\frac{M}{l^2}$ for the rigid porous plate.

Figs. 7 and 8 present intensity plots of $\mathcal{D}_{pp}$ and $\mathcal{D}_p$ as functions of $\frac{M}{l^2}$ and $k_0 l$. For the porous piezoelectric plate, maximum dissipation occurs around $k_0 l = 200$ for $10^{-6} \lesssim \frac{M}{l^2} \lesssim 10^{-3}$, indicating strong capillary–hydroelastic coupling. The rigid porous plate exhibits dissipation approximately two orders of magnitude larger, with peak dissipation in the band $60 \lesssim k_0 l \lesssim 100$ across the entire $\frac{M}{l^2}$ range. These results demonstrate that surface tension critically governs both the magnitude and spectral localisation of dissipation, with rigid porous structures favouring strong attenuation and flexible porous piezoelectric plates exhibiting more selective, capillary-enhanced dissipation suitable for energy harvesting.

5. Conclusion

This study has demonstrated that surface tension plays a crucial and previously underexplored role in governing energy dissipation by vertically submerged porous, poroelastic, and porous piezoelectric plates interacting with capillary–gravity waves. By formulating a unified energy balance and systematically comparing rigid, flexible, and electromechanically coupled plate models under identical geometric and mass constraints, we have shown that porosity is the primary mechanism driving wave energy attenuation, while structural flexibility and piezoelectric coupling modulate both the magnitude and spectral distribution of dissipation. Rigid porous plates yield the highest dissipation, particularly in intermediate to high wavenumber regimes, making them effective for wave-damping and protection applications. In contrast, poroelastic and porous piezoelectric plates exhibit comparable total dissipation levels, with flexibility enabling controlled deformation and smoother energy redistribution across wavenumbers. Importantly, the porous piezoelectric bimorph plate reveals a fundamental trade-off between hydrodynamic attenuation and electrical energy extraction, increasing porosity enhances overall wave damping but suppresses deformation-driven electromechanical coupling, thereby limiting harvesting efficiency. Extended wavenumber and surface-tension parametric studies further identify distinct gravity-dominated and capillary-influenced regimes in which surface tension substantially modifies hydroelastic dissipation, highlighting the importance of capillary effects for short-wavelength waves. Overall, the results provide clear physical guidance for tailoring porosity, flexibility, and electromechanical coupling in submerged vertical structures, enabling the design of devices optimized either for wave attenuation or for efficient energy harvesting in capillary–gravity wave environments.

References

[1] X. Yu and A. T. Chwang. Water waves above submerged porous plate. *Journal of engineering mechanics*, 120(6):1270–1282, 1994.

[2] Y. Li, Y. Liu, and B. Teng. Porous effect parameter of thin permeable plates. *Coastal Engineering Journal*, 48(4):309–336, 2006.

[3] S. Zheng, M. H. Meylan, L. Fan, D. Greaves, and G. Iglesias. Wave scattering by a floating porous elastic plate of arbitrary shape: A semi-analytical study. *Journal of Fluids and Structures*, 92:102827, 2020.

[4] M. J. A. Smith, M. A. Peter, I. D. Abrahams, and M. H. Meylan. On the wiener–hopf solution of water-wave interaction with a submerged elastic or poroelastic plate. *Proceedings of the Royal Society A*, 476(2242):20200360, 2020.

[5] Q. Y. Wu, T. I. Khabakhpasheva, B. Y. Ni, and A. A. Korobkin. Small-amplitude waves in a floating poroelastic plate forcing by vertical pitching plate. *Physics of Fluids*, 35(11), 2023.

[6] A. K. Vashishth and V. Gupta. Reflection and transmission of plane waves from a fluid-porous piezoelectric solid interface. *The Journal of the Acoustical Society of America*, 129(6):3690–3701, 2011.

[7] G. Martínez-Ayuso, M. I. Friswell, S. Adhikari, H. H. Khodaparast, and C. A. Featherston. Energy harvesting using porous piezoelectric beam with impacts. *Procedia engineering*, 199:3468–3473, 2017.

[8] M. Askari, E. Brusa, and C. Delprete. On wave propagation and free vibration of piezoelectric sandwich plates with perfect and porous functionally graded substrates. *Journal of Intelligent Material Systems and Structures*, 33(16):2049–2073, 2022.

[9] S. Zeng, B. L. Wang, and K. F. Wang. Nonlinear vibration of piezoelectric sandwich nanoplates with functionally graded porous core with consideration of flexoelectric effect. *Composite Structures*, 207:340–351, 2019.

[10] M. Singh and R. Gayen. Scattering of linear gravity-capillary waves by a completely submerged vertical porous elastic plate. *Waves in Random and Complex Media*, 35(6):11084–11104, 2022.

[11] G. Liu and L. Zhang. Theory of capillary-gravity wave scattering by a fixed, semi-immersed cylindrical barrier with contact line dissipation. *Journal of Fluid Mechanics*, 1013:A27, 2025.

[12] M. H. Meylan and Y. A. Stepanyants. Scattering of gravity-capillary waves on a bottom step. *Physics of Fluids*, 36(1), 2024.

[13] S. Mohapatra. The effect of free-surface tension on scattering of water waves by small bottom undulation. *The Proceedings of ANZIAM*, 58:E39–E80, 2016.

[14] J. Bhattacharjee and C. Guedes Soares. Flexural gravity wave over a floating ice sheet near a vertical wall. *Journal of Engineering Mathematics*, 75(1):29–48, 2012.

[15] M. Singh, M. H. Meylan, and R. Gayen. Time-domain motion of a floating or obliquely submerged non-uniform elastic plate. *Physics of Fluids*, 35(4), 2023.

[16] M. Singh. Analysing wave power absorption by deformable plate wave energy converter placed under an ice cover using a novel numerical technique. *Ocean Engineering*, 321:120373, 2025.

[17] S. Tavakoli, M. Singh, S.d Hosseinzadeh, Z. Hu, Y. Shao, S. Wang, L. Huang, A. Grammatikopoulos, Y. P. Li, D. Khojasteh, et al. A review of flexible fluid-structure interactions in the ocean: Progress, challenges, and future directions. *Ocean Engineering*, 342:122545, 2025.

[18] C. Xiao-Bo, D. Wen-Yang, and L. Dong-Qiang. Gravity waves with effect of surface tension and fluid viscosity. *Journal of Hydrodynamics, Ser. B*, 18(3):171–176, 2006.

[19] R. Harter, I. D. Abrahams, and M. J. Simon. The effect of surface tension on trapped modes in water-wave problems. *Proceedings of the Royal Society A: Mathematical, Physical and Engineering Sciences*, 463(2088):3131–3149, 2007.

[20] M. A. Gorgui, M. S. Faltas, and A. Z. Ahmed. Capillary-gravity waves in the presence of infinite porous plates. *Il Nuovo Cimento D*, 15(5):793–808, 1993.

[21] P. F. Rhodes-Robinson. Fundamental singularities in the theory of water waves with surface tension. *Bulletin of the Australian Mathematical Society*, 2(3):317–333, 1970.

[22] E. Renzi. Hydroelectromechanical modelling of a piezoelectric wave energy converter. *Proceedings of the Royal Society A: Mathematical, Physical and Engineering Sciences*, 472(2195):20160715, 2016.

[23] S. Zheng, M. H. Meylan, X. Zhang, G. Iglesias, and D. Greaves. Performance of a plate-wave energy converter integrated in a floating breakwater. *IET Renewable Power Generation*, 15(14):3206–3219, 2021.

[24] N. F. Parsons and P. A. Martin. Scattering of water waves by submerged plates using hypersingular integral equations. *Applied Ocean Research*, 14(5):313–321, 1992.

10th International Conference on HYDROELASTICITY IN MARINE TECHNOLOGY
Trondheim, Norway, June16th-18th, 2026

Flexural Gravity Wave Blocking in a Floating-Submerged Plate System Involving Compressive Force

Boral, S.[1,*] Sahoo, T.[2], and Basu, B.[1]

[1] School of Engineering, Trinity College Dublin, Ireland
[2] Dept. of Ocean Engineering and Naval Architecture, IIT Kharagpur, Kharagpur 721302, India

Abstract The interaction between a very large floating structure (VLFS) and a submerged elastic plate resting on an elastic foundation is a significant unresolved issue in hydroelasticity, with applications including submerged tunnels, underwater decks, wave energy converters and flexible foundation-supported marine structures. A two-dimensional linear hydroelastic model is developed to investigate the interaction between surface gravity waves and a coupled system consisting of a flexible plate floating on the free surface and a flexible plate immersed and infinitely extended supported by a Winkler foundation, which models the plate as being supported by a continuous array of independent springs. The fluid domain is assumed to be irrotational, inviscid and incompressible, and is of finite depth. Subsequently, the linear potential flow theory is used to model the boundary value problem (BVP), with boundary conditions ensuring pressure and velocity continuities at the bottom and the two plate-water interfaces. For the coupled floating-submerged plate system, an analytical solution of the BVP produces a modified dispersion relation. Two hydroelastic branches, corresponding to the surface and submerged modes, are observed in the resultant dispersion characteristics. The system permits up to three propagating waves in each mode for a range of frequencies and compressive force combinations when a Winkler foundation supports the submerged plate. The dispersion behaviour undergoes notable qualitative changes as the compressive force approaches the critical buckling limit: depending on the excitation frequency, the surface-wave branch can support at most three propagating modes, whereas the submerged-plate branch can sustain up to five propagating modes. However, the combined wave system can admit as many as six distinct propagating modes simultaneously. Remarkably, when subjected to the buckling limit compressive force, the surface plate mode does not buckle; however, the submerged plate displays two types of localised hydroelastic buckling. Geometric studies indicate that in-plane compression and foundation stiffness have a significant impact on wave properties and system resilience. In contrast to higher values of compressive force, which increase reflection and encourage instability, increased foundation stiffness improves wave transmission and stabilises the structure.

Key words: *Flexural-gravity wave; Floating and submerged plate; Wave blocking; Dispersion relation*

1. Introduction

Hydroelastic interactions between ocean waves and flexible structures play a central role in many marine and geophysical systems, including very large floating structures (VLFSs), floating ice covers, and compliant offshore platforms. When a deformable plate is present at the free surface, surface gravity waves are replaced by flexural-gravity waves, in which fluid motion is coupled to plate bending. This coupling introduces an additional dispersive mechanism, giving rise to modified phase and group velocities and, in some regimes, multiple propagating waves. The theoretical foundations of flexural-gravity wave scattering and transmission beneath floating elastic plates were established in early studies motivated by sea-ice dynamics and VLFS applications [1, 2].

*Correspondence to: borals@tcd.ie

A particularly important factor in hydroelastic wave propagation is the presence of in-plane compressive force in the plate. Such compression may arise from thermal stresses, ice convergence, mooring loads, or structural confinement. Compression alters the balance between bending stiffness and fluid restoring forces and can lead to profound changes in dispersion. In particular, increasing compressive load may generate extrema in the dispersion relation where the group velocity vanishes, resulting in wave blocking. In this regime, several real wavenumbers may coexist for a given frequency, producing strong mode multiplicity and enhanced sensitivity of wave fields to small parameter variations [3]. Wave blocking has important physical and engineering consequences. Near blocking points, energy transport is strongly modified, leading to wave localisation, amplified reflection, and enhanced hydroelastic stresses. These effects become especially significant in the presence of structural irregularities such as cracks or discontinuities, where blocking can promote mode conversion and stress concentration [4]. Extensions of blocking theory to layered fluid systems have further shown that multiple interfaces introduce additional hydroelastic branches, enriching the range of possible blocking and resonance phenomena [5].

Despite this progress, most existing studies have focused on a single floating elastic plate. However, not much is known about systems involving multiple coupled elastic interfaces. In particular, configurations consisting of a floating plate and a submerged elastic plate [6] supported by an elastic foundation arise in VLFS concepts, wave-mitigation devices, and submerged compliant barriers [7]. The interaction between the surface and submerged plates introduces coupled hydroelastic modes, while compressive forces and foundation stiffness provide additional mechanisms for tuning the dispersion and stability of the system.

The present work aims to investigate linear flexural-gravity wave propagation in a finite-depth fluid containing a floating elastic plate and a submerged elastic plate subjected to uniform in-plane compression. By deriving and analysing the coupled dispersion relation, we examine how compression, submergence depth, and foundation stiffness control the emergence of wave blocking, mode multiplicity, and hydroelastic localisation. The results provide new insight into wave-structure interaction in coupled elastic plate systems and suggest pathways for controlling wave propagation through structural and foundation design.

2. Mathematical formulation

In this section, a mathematical model associated with surface gravity wave interaction with a floating and submerged plate system is developed. Here, the floating and submerged plates are considered to be infinitely extended, floating, and elastic. The study is conducted in a two-dimensional Cartesian coordinate system in the water of uniform depth H with the x-axis being extended along the mean floating plate-covered surface in the horizontal direction and the y-axis being in the vertically downward direction as in Fig. 1. The submerged elastic plate is placed at $y = h$, which is resting on a Winkler foundation with Winkler constant c_1. The homogeneous fluid domain is separated into two subdomains by the submerged plate at a submergence depth of h. The upper domain is defined by $0 < y < h$, $-\infty < x < \infty$, and the lower domain by $h < y < H$, $-\infty < x < \infty$. The fluid is assumed to be inviscid and incompressible, and the flow is irrotational. Here, the mathematical problem is carried out using linear water wave theory, and the fluid motion is considered to be simple harmonic in time with angular frequency ω. The plates are thin, homogeneous, isotropic, and are under the action of a lateral compressive force Q.

We further assume that $\Phi(x,y,t)$ is the velocity potential in the homogeneous fluid domain. Thus, the fluid motion is described by the velocity potential, $\Phi(x,y,t) = \mathrm{Re}\{\phi(x,y)e^{-\mathrm{i}\omega t}\}$ where $\phi(x,y)$ is the spatial velocity potential. The floating and submerged plate deflections are considered to be $\tilde{\eta}_1(x,t) = \mathrm{Re}\left\{\eta_1(x)e^{-\mathrm{i}\omega t}\right\}$ and, $\tilde{\eta}_2(x,t) = \mathrm{Re}\left\{\eta_2(x)e^{-\mathrm{i}\omega t}\right\}$ respectively. Here, the floating and submerged plates' deflections are associated with plane waves propagating from left to right. The velocity potentials $\phi(x,y)$

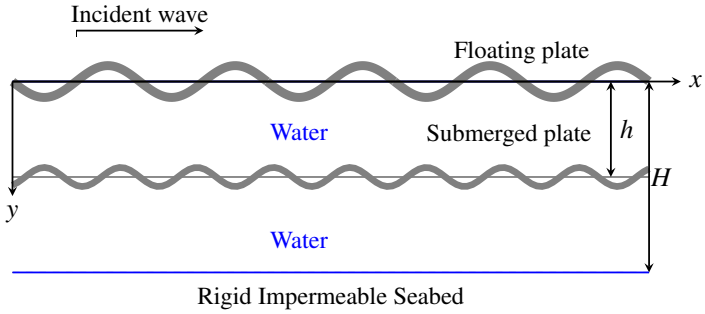


Figure 1: Schematic diagram of a floating elastic plate and a submerged elastic plate with wave-induced deformations in finite water depth.

satisfy the Laplace equation as the governing equation,

$$\frac{\partial^2\phi}{\partial x^2}+\frac{\partial^2\phi}{\partial y^2}=0, \tag{1}$$

the linearized plate-covered boundary condition ([3]),

$$\left(D_1\frac{\partial^4}{\partial x^4}+Q_1\frac{\partial^2}{\partial x^2}+1\right)\frac{\partial\phi}{\partial y}=\frac{\omega^2}{g}\phi \qquad \text{on } y=0, \tag{2}$$

where D_1 is the rigidity of the floating elastic plate and Q_1 is the floating plate compression.

The no-flow condition on the rigid seabed is given by

$$\frac{\partial\phi}{\partial y}=0 \quad \text{on} \quad y=H. \tag{3}$$

The linearised kinematic condition on the submerged flexible plate is given by

$$-\mathrm{i}\omega\eta_2=\left.\frac{\partial\phi}{\partial y}\right|_{y=h^+}=\left.\frac{\partial\phi}{\partial y}\right|_{y=h^-} \quad \text{on} \quad y=h. \tag{4}$$

The deflection of the submerged plate $\eta(x)$ under the action of lateral compressive force satisfies [5]

$$\left(E_2I_2\frac{\partial^4}{\partial x^4}+N_2\frac{\partial^2}{\partial x^2}-m_2\omega^2\right)\eta_2=F_1-F_2, \tag{5}$$

where E_2I_2 is the submerged plate rigidity with $I_2=d_2^3/\{12(1-\nu_2^2)\}$, d_2 is the plate thickness, ν_2 being the Poisson ratio, N_2 being the lateral compressive force, m_2 being the plate mass density, $F_1=-[P(x,y)|_{y=h^+}-P(x,y)|_{y=h^-}]$ with $P=\rho\,(\mathrm{i}\omega\phi+g\eta_2)$ being the hydrodynamic pressure and $F_2=c_l\eta_2$ being the force due to the elastic foundation. Here, c_l is the elastic foundation constant.
Eliminating $\eta_2(x)$ from Eqs. (4) and (5), it is derived that

$$\left(D_2\frac{\partial^4}{\partial x^4}+Q_2\frac{\partial^2}{\partial x^2}-\frac{m_2}{\rho g}\omega^2\right)\left.\frac{\partial\phi}{\partial y}\right|_{y=h^+}=-\frac{\omega^2}{g}\left(\phi\big|_{y=h^+}-\phi\big|_{y=h^-}\right)-\frac{c_l}{\rho g}\left.\frac{\partial\phi}{\partial y}\right|_{y=h^+}, \tag{6}$$

where $D_2=E_2I_2/\rho g$ and $Q_2=N_2/\rho g$.

3. Plane wave solution

Assuming $\eta_1(x) = \zeta_0 e^{ikx}$, $\eta_2(x) = \eta_0 e^{ikx}$ with ζ_0 and η_0 being the amplitudes of floating and submerged plate deflections, respectively, and using Eq. (1) along with the boundary conditions in Eqs. (2)-(4) and (6), the spatial velocity potential $\phi(x,y)$ is obtained as

$$\phi(x,y) = \begin{cases} -\dfrac{i\omega}{k}(\psi_0 \cosh(ky) + \sinh(ky))\ \eta_1(x) & \text{for} \quad 0 < y < h, \\ \dfrac{i\omega}{k}\dfrac{\cosh\{k(H-y)\}}{\sinh\{k(H-h)\}}\ \eta_2(x) & \text{for} \quad h < y < H, \end{cases} \tag{7}$$

where

$$\psi_0 = \frac{K\{1+\coth(kh)\coth k(H-h)\} - P\coth(kh)}{K\{\coth(kh)+\coth\{k(H-h)\}\} - P},\ \ K = \frac{\omega^2}{g}, P = k(D_2k^4 - Q_2k^2 + A),\ A = c_l/\rho g.$$

The amplitude ratio of the surface elevation to that of the submerged plate deflection is given by

$$\frac{\zeta_0}{\eta_0} = \frac{\sinh kh[K\{\coth kh + \coth k(H-h)\} - P]}{K}. \tag{8}$$

Using Eq. (7) in Eq. (6), the dispersion relation is obtained as [3]

$$R\omega^4 - T\omega^2 + V = 0, \tag{9}$$

where

$$R = 1 + \coth kh \coth k(H-h),\ T = gk\{A_2 \coth kh + A_1\{\coth(kh) + \coth(k(H-h))\}\},$$
$$V = g^2k^2A_1A_2,\ \ A_1 = D_1k^4 - Q_1k^2 + 1,\ \text{ and }\ A_2 = D_2k^4 - Q_2k^2 + A.$$

Here, the inertia term is assumed to be small with $m_2/(\rho g)\omega^2 \ll 1$ and thus neglected in the subsequent analysis as discussed in [3]. Thus, the solution of the dispersion relation in Eq. (9) in terms of ω^2 is obtained as

$$\omega_\pm^2 = \frac{T \pm \sqrt{T^2 - 4RV}}{2R}, \tag{10}$$

where ω_+ corresponds with the waves in the floating elastic plate-covered surface and ω_- is linked to the waves in the submerged elastic plate-covered interface. Using this relation, the phase velocities $c_\pm$ and group velocities $c_{g\pm}$ can be obtained using the formulae $c_\pm = \omega_\pm/k$ and $c_{g\pm} = d\omega_\pm/dk$.

3.1. Wave blocking in deep water

Under the assumption of deep water approximation, i.e., $kh \gg 1$ and $k(H-h) \gg 1$, the dispersion relation (9) is reduced to the form

$$(\omega^2 - gkA_1)\left\{2\omega^2 - gkA_2\right\} = 0, \tag{11}$$

which yields $\omega_+^2 = gk(D_1k^4 - Q_1k^2 + 1)$ and $\omega_-^2 = gk(D_2k^4 - Q_2k^2 + A)/2$. The solution associated with ω_+ corresponds to the flexural-gravity waves in deep water; see [3]. Besides, the solution ω_- corresponds to the wave motion induced due to the interaction of the surface gravity wave with the submerged plate in the presence of the Winkler foundation. Hence, the phase velocities in surface and submerged plate modes are obtained as

$$c_+ = \sqrt{\frac{g(D_1k^4 - Q_1k^2 + 1)}{k}}, \qquad c_- = \sqrt{\frac{g(D_2k^4 - Q_2k^2 + A)}{2k}}. \tag{12}$$

It can be easily derived that the phase velocity c_+ attains zero minimum for $Q_1 = Q_{c_+} = 2\sqrt{D_1}$ and $k = k_{c_+} = (1/D_1)^{1/4}$, and the phase velocity c_- attains zero minimum for $Q_2 = Q_{c_-} = 2\sqrt{AD_2}$ and $k = k_{c_-} = (A/D_2)^{1/4}$. Hereafter, $Q_{c_\pm}$ is known as the buckling limit of compressive force and $k_{c_\pm}$ is the critical wavenumber as in [5]. Further, the group velocities $c_{g\pm}$ yield

$$c_{g+} = \frac{1}{2}\sqrt{\frac{g}{k}}\frac{5D_1k^4 - 3Q_1k^2 + 1}{\sqrt{D_1k^4 - Q_1k^2 + 1}}, \qquad c_{g-} = \frac{1}{4}\sqrt{\frac{g}{k}}\frac{5D_2k^4 - 3Q_2k^2 + A}{\sqrt{D_2k^4 - Q_2k^2 + A}}. \tag{13}$$

Proceeding similarly as in the case of phase velocity, it can be easily derived that the group velocity c_{g+} attains a zero minimum for $Q_1 = Q_{c_{g+}} = 2\sqrt{5D_1}/3$ and $k = k_{c_{g+}} = (1/5D_1)^{1/4}$. Also, c_{g-} attains zero minimum for $Q_2 = Q_{c_{g-}} = 2\sqrt{5D_2A}/3$ and $k = k_{c_{g-}} = (A/5D_2)^{1/4}$. Here, the compressive force Q_{cg} is referred to as the threshold of the blocking limit of compressive force and k_{cg} as the saddle point [5].

It is noteworthy from equation (12), which reveals that for $c_l = 0$ and $Q_2 = 0$, a single plane wave propagation is possible in the submerged plate mode ω_-. However, wave propagation is not possible in ω_- for $0 < k < \sqrt{Q_2/D_2}$ with $c_l = 0$ as ω_-^2 becomes negative, infeasible for any real frequency. Further, for $c_l = 0$ and $k = \sqrt{Q_2/D_2}$, no wave exists in the submerged plate, ω_-.

3.2. Wave blocking in finite water depth

Here, the occurrence of wave blocking in both the floating and submerged elastic plates is discussed by analysing the dispersion relation (10) in finite water depth. Various parametric values are considered as $EI = 5 \times 10^8$ Nm, $\rho = 1025$ kgm^{-3}, $g = 9.81$ ms^{-2}, $c_l = 5 \times 10^3$ Nm^{-3} and $h/H = 0.5$ with $H = 40$ m unless otherwise specified.

Figure 2 demonstrates the effect of increasing in-plane compressive force, Q, on the dispersion characteristics of the coupled floating-submerged plate system, as derived in Eq. (9). Here, the dispersion curves associated with the floating plate-covered surface mode are shown by dashed lines, whereas the submerged plate-covered interface is presented by solid lines. In Fig. 2a, where the compressive forces on the floating and submerged plates are equal ($Q_2 = Q_1$), a progressive flattening of the dispersion curves associated with the floating plate-covered surface is observed as Q_1 increases, accompanied by the formation of pronounced local extrema. These turning points correspond to vanishing group velocity and indicate the onset of wave blocking. As the compressive force approaches the critical buckling limit Q_{c+} of the floating plate, the minimum of the dispersion curve converges towards the critical wavenumber k_{c+}, at which the group velocity becomes discontinuous; see [3]. In contrast, the dispersion curve associated with the submerged plate in the absence of an elastic foundation exhibits no local extrema, and consequently, no plate buckling or wave-blocking behaviour is observed. Figure 2b shows that when the submerged plate is supported by a Winkler foundation and the corresponding compressive force is taken as $Q_2 = \sqrt{A}\,Q_1$, the resulting elastic restraint substantially alters the dispersion characteristics of the coupled system. In this case, the dispersion branch associated with the submerged plate exhibits both local maxima and minima over a finite range of wavenumbers, indicating extrema at which the group velocity vanishes and wave blocking occurs. The presence of the foundation, therefore, allows three propagating wave solutions to coexist for a given frequency and compressive force in the submerged plate mode. The near-critical regime is examined in Fig. 2c, where small variations in Q_1 close to the buckling limit, Q_{c+}, lead to the emergence of multiple closely spaced minima in the submerged plate mode dispersion curves. As a result, for a given frequency ω, up to five progressive wave solutions may exist in the submerged plate mode. In contrast, no plate buckling is observed in the floating plate mode. However, both primary and secondary wave blocking occur for different values of frequency and wavenumbers. This behaviour signifies strong hydroelastic coupling and the coexistence of several propagating wave components, indicating the development of closely situated wave blocking in the submerged plate resting on an elastic foundation, while the floating plate mode remains globally stable.

Figure 3 reveals the influence of the submergence depth ratio h/H on the dispersion characteristics of the coupled floating-submerged plate system in the near-critical compressive force with $Q_1 = 1.95\sqrt{D_1}$.

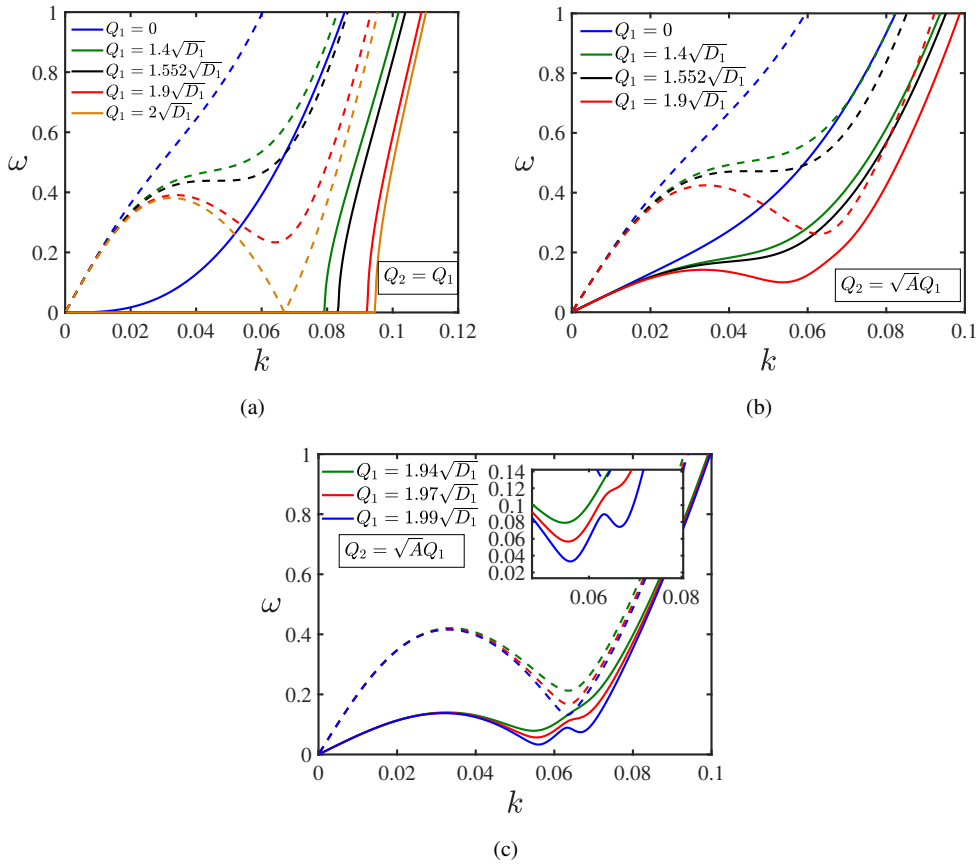
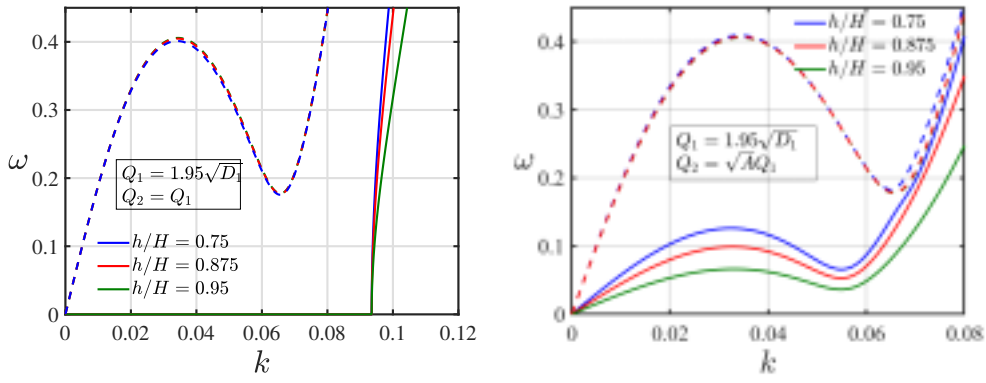


Figure 2: Dispersion curves showing the influence of compressive force Q on the coupled floating-submerged plate system: (a) $Q_2 = Q_1$; (b) Winkler foundation with $Q_2 = \sqrt{A}Q_1$; (c) near-critical compression Q_{c+}, where multiple extrema appear in the submerged-plate mode, indicating wave blocking and multi-valued wavenumbers. Dashed curves represent the floating plate (surface) mode, while solid curves correspond to the submerged plate mode

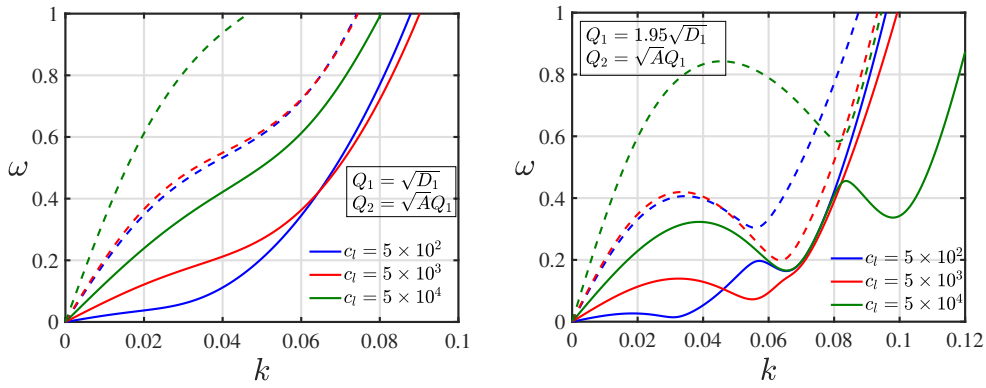
.

In Fig. 3a, where equal compressive forces are applied on both plates ($Q_2 = Q_1$), the dispersion curves associated with the floating plate mode (dashed lines) are virtually insensitive to changes in h/H, indicating that the surface-mode dynamics are governed predominantly by the floating plate properties and are only weakly affected by the submerged plate location. In contrast, the submerged plate mode (solid lines) exhibits a pronounced dependence on h/H, with the corresponding dispersion branches shifting towards higher wavenumbers as the submerged plate is placed deeper in the water column, reflecting the strong influence of the vertical fluid structure on the hydroelastic coupling. When the submerged plate is supported by a Winkler foundation and its compressive force is scaled as $Q_2 = \sqrt{A}\,Q_1$, as shown in Fig. 3b, the submerged-mode dispersion curves develop distinct local maxima and minima, signifying the occurrence of wave blocking. The position and depth of these extrema vary systematically with h/H, demonstrating that geometric configuration alone can significantly modify the blocking position and the number of coexisting propagating waves in the internal mode, while the floating plate mode remains globally stable across the considered parameter range.



(a) (b)

Figure 3: Effect of submergence ratio h/H on dispersion of the coupled floating-submerged plate system: dashed curves show the surface mode and solid curves present the submerged-plate mode with (a) $Q_2 = Q_1$; (b) with Winkler foundation and $Q_2 = \sqrt{A}Q_1$, showing blocking-related extrema in the submerged mode.



(a) (b)

Figure 4: Effect of the Winkler foundation constant c_l on the dispersion characteristics of the coupled floating-submerged elastic plate system in finite water depth for (a) $Q < Q_{c_{g^+}}$ and (b) $Q > Q_{c_{g^+}}$. Dashed curves represent the floating plate (surface) mode, while solid curves correspond to the submerged plate mode.

Figure 4 demonstrates the effect of the Winkler foundation constant c_l on the dispersion characteristics of the coupled floating-submerged plate system under different values of compressive force before and after the threshold of blocking $Q_{c_{g^+}}$. In Fig. 4a, corresponding to compressive forces $Q_1 = \sqrt{D_1}$ and $Q_2 = \sqrt{A}\,Q_1$, an increase in the foundation constant systematically elevates the submerged plate mode dispersion curves, indicating that a stiffer elastic foundation provides an enhanced restoring force that effectively increases the hydroelastic rigidity of the submerged plate and facilitates wave transmission. In this regime, the dispersion curves remain smooth, and no pronounced extrema are observed in both floating and submerged plate modes. On the contrary, Fig. 4b, which corresponds to a near-critical compressive force ($Q_1 = 1.95\sqrt{D_1}$ and $Q_2 = \sqrt{A}\,Q_1$), reveals that higher values of c_l with $c_l = 5 \times 10^3$

promote the emergence of multiple local maxima and minima in the submerged-mode dispersion curves, signifying the occurrence of more than two wave blocking at which root coalescence takes place. As the values of c_l decrease to $c_l = 5 \times 10^2$, these extrema become less pronounced and extend over a wider range of wavenumbers and frequencies, indicating that a stiffer elastic foundation enhances hydroelastic coupling and facilitates localisation and blocking of flexural-gravity waves in the submerged plate mode. Physically, the Winkler foundation provides an additional restoring force that modifies the effective stiffness of the submerged plate, leading to enhanced hydroelastic interactions among multiple progressive internal waves and repeated wave blocking in the near-critical regime. In contrast, the floating plate mode remains largely unaffected by variations in the foundation stiffness, as its dynamics are dominated by the free-surface condition.

4. Conclusions

A linear hydroelastic model has been developed to investigate flexural-gravity wave interaction with a coupled floating-submerged elastic plate system subjected to in-plane compressive forces, with the submerged plate supported by a Winkler-type elastic foundation. An analytical solution yields a modified dispersion relation that reveals two coupled hydroelastic branches associated with the surface and submerged plate modes in finite water depth. The dispersion characteristics are shown to be strongly influenced by compressive force, submergence depth, and foundation stiffness. As the compressive force approaches the critical buckling limit, pronounced non-monotonic behaviour emerges in the dispersion curves, leading to vanishing group velocity and wave blocking. A key and previously unreported finding of this study is that, for a given frequency, the submerged plate mode can support up to five distinct propagating waves, arising from the presence of the multiple closely spaced local extrema in the dispersion relation. In contrast, even at the critical buckling limit, the floating plate mode does not undergo buckling and continues to support propagating waves with positive phase velocity when the submerged plate is supported by an elastic foundation. The analysis demonstrates that for a fixed frequency, multiple real roots can exist either in the floating plate mode or in the submerged plate mode, irrespective of the specific values of compressive force, submergence depth ratio, or Winkler foundation constant. This highlights the inherently multi-valued nature of wave propagation in coupled hydroelastic systems. The results provide new physical insight into wave blocking, root coalescence, and hydroelastic localisation in floating-submerged plate configurations, with important implications for the design and stability assessment of very large floating structures and submerged flexible systems. The present framework offers a foundation for future investigations incorporating finite plate length, nonlinear effects, and three-dimensional geometries.

Acknowledgments: This work was funded by the Sustainable Energy Authority of Ireland (SEAI) National Energy Research, Development & Demonstration (RD&D) Programme; Award Number 23/RDD/942, 'Innovation in Dynamic Cables for Offshore Renewable Energy (InDyCORE).

References

[1] J. Ding, Y. Wu, Z. Xie, W. Yang, S. Wang, J. Yu, and T. Yu. Overview: Research on hydroelastic responses of vlfs in complex environments. *Marine Structures*, 78:102978, 2021.

[2] B.-Y. Ni, H. Xiong, D. Han, L. Zeng, L. Sun, and H. Tan. A review of ice deformation and breaking under flexural-gravity waves induced by moving loads. *Journal of Marine Science and Application*, 24(1):35–52, 2025.

[3] T. Sahoo, M. H. Meylan, Y. Stepanyants, S. Boral, and S. Das. *Flexural Gravity Waves: The Mathematical Theory and Applications*. CRC Press, 2025.

[4] S. C. Barman, S. Boral, and T. Sahoo. Bragg scattering of flexural-gravity waves by a series of polynyas in the context of blocking dynamics. *Physics of Fluids*, 35(1), 2023.

[5] S. Boral, B.-Y. Ni, and A. Korobkin. Interactions of flexural-gravity and interfacial waves in a two-layer fluid with a discontinuous background mean flow. *Journal of Fluid Mechanics*, 1015:A22, 2025.

[6] G. Polly, A. Mérigaud, B. Thiria, and R. Godoy-Diana. Experiments on water-wave interactions with a horizontal submerged elastic plate. *J. Fluid Mech.*, 1007:R4, 2025.

[7] S. Boral and T. Sahoo. Flexural gravity wave blocking due to a floating submerged plate resting on a viscoelastic foundation. In *Proceedings of the 9th International Conference on Hydroelasticity in Marine Technology (HYEL 2023)*, pages 247–257, 2023.

Author Index

Abdelmoteleb, S. E., 177
Agarwal, S., 529
Aloisio, G., 73
Altomare, C., 553
Alexandre, A., 157
Anevlavi, D., 201
Arredondo-Galeana, A., 109
Avital, E.J., 541

Bachynski-Polić, E.E., 177
Bardiani, J., 403
Basu, B., 585
Belibassakis, K., 201
Bockstael, M.M., 435, 487
Boral, S., 585
Boyer, R., 53
Braaten, H., 279
Brennan, F., 109
Brehm, A., 189
Brown, S., 109

Caiwei, S., 157
Capasso, S., 553
Cao, K., 267
Chatjigeorgiou, I.K., 541
Chen, X., 267, 383
Cheng, H., 541
Christiaens, B., 339
Ciappi, E., 73
Colomés, O., 529
Costantino Muniz, G., 73
Crespo, A., 553

de Koning, J., 131
De Lauzon, J., 267
Delgado, D., 403
Dessi, D., 403, 563
Drummen, I., 221
Düz, B., 221

El Malki Alaoui, A., 467
El Moctar, O., 189, 211, 457

Faltinsen, O.M., 3, 85
Faragau, A., 529
Fernandes, A.C., 119
Fimreite, S.B., 425
Firoozkoohi, R., 279
Flaßkamp, K., 553
Fonseca, N., 279
Fredriksen, A.G., 17
Fu, S., 383

Galal, G., 189
Gayen, R., 325
Grammatikopoulos, A., 131, 257
Greaves, D., 109, 145
Greco, M., 63
Grue, J., 349
Guedes Soares, C., 39
Guichard, J., 145

Halbout, C., 167
Hann, M., 145
Harada, M., 393
Haridas, A., 403

Hascoët, R., 467
Hoque, A., 325
Hoogendoorn, D., 131
Huang, W., 383
Hwang, J., 153

Indergård, R., 279

Jacques, N., 467, 477
Jagite, G., 233, 267
Ji, J., 39
Jiang, C., 189, 211
Jiang, F., 279
Jiang, J., 383
Jovanova, J., 257

Kang, D.-Y., 173
Kaydihan, L., 221
Khabakhpasheva, T., 293, 305, 315, 415
Kim, D.-H., 173
Kim, S., 97
Kim, Y., 153, 509
Konispoliatis, D.N., 541
Korobkin, A., 293, 305, 415
Kristiansen, D., 17
Kristiansen, T., 17, 359, 371
Kurnia, R., 221

Lee, J., 509
Liang, C., 315, 529
Linde, J., 457
Lin, Y., 211
Lopes, F.S., 119
Lugni, C., 63
Lie, H., 279

Malenica, S., 233, 267
Martínez-Estévez, I., 553
Matsui, S., 393
Maugsten, O.P., 349
Mi, S., 541
Mohapatra, S.C., 39
Moreau, M., 359
Moretti, G., 553

Nguyen, M., 267
Ni, B.-Y., 293, 315
Norvik, C., 63
Neugebauer, J., 189, 457

Oka, M., 393
Ogden, D., 109
Oscarsson-Nagel, M.D., 245
Ouvrard, T., 167

Palaversa, M., 27
Paifelman, E., 73
Papadakis, G., 541
Park, C., 509
Park, G., 153
Park, T., 153, 509
Pascoaleto, V., 119
Passacantilli, F., 403
Peyrard, C., 167
Pot, H., 339

Qaimi, S., 189

Rajasree, V.R.N., 177
Rizzello, G., 553
Robaux, F., 167
Rogne, Ø.Y., 189
Ruesen, J., 131

Sahoo, T., 585
Samad, A., 541
Sandström, J., 403
Sauder, T., 177
Sbaruffati, C., 403
Schreier, S., 339
Sellini, M., 73
Semenov, Y.A., 315
Shao, Y., 53
Shishmarev, K., 293
Singh, M., 1109
Skare, A., 371
Song, J., 97
Sugimoto, K., 393
Sun, Z., 415
Suzuki, K., 393
Suzuki, T., 553
Sævik, S., 27

Taussé Kamdoum, F.L., 467
Takeda, K., 393
Tassin, A., 477
Tödter, S., 457
Tønnessen, R., 245
Tosdevin, T., 145
Terroba Ramirez, F., 403

Van Dijk, R., 403
Van Zijl, C., 257
Venturi, A., 403

Wan, D., 445
Wang, J., 445
Wang, Z., 445
Wei, Z., 53
Wellens, P., 339
Wellens, P.R., 435, 487
Westerweel, J., 339
Wenzhe, Z., 157
Won-Ho, L., 157

Xiang, X., 85
Xiao, J., 445

Yang, K.-K., 173
Ye, Y., 383
Yin, D., 279
Ying-xu, M., 415
Yu, Z., 27, 425

Zhang, Q., 189
Zhiyuan, P., 157